

# Real-Time Rendering

Third Edition



Tomas Akenine-Möller

Eric Haines

Naty Hoffman

# Real-Time Rendering

## Third Edition



# Real-Time Rendering

## Third Edition

Tomas Akenine-Möller  
Eric Haines  
Naty Hoffman



A K Peters, Ltd.  
Natick, Massachusetts

CRC Press  
Taylor & Francis Group  
6000 Broken Sound Parkway NW, Suite 300  
Boca Raton, FL 33487-2742

© 2008 by Taylor & Francis Group, LLC  
CRC Press is an imprint of Taylor & Francis Group, an Informa business

No claim to original U.S. Government works  
Version Date: 20120214

International Standard Book Number-13: 978-1-4398-6529-3 (eBook - PDF)

This book contains information obtained from authentic and highly regarded sources. Reasonable efforts have been made to publish reliable data and information, but the author and publisher cannot assume responsibility for the validity of all materials or the consequences of their use. The authors and publishers have attempted to trace the copyright holders of all material reproduced in this publication and apologize to copyright holders if permission to publish in this form has not been obtained. If any copyright material has not been acknowledged please write and let us know so we may rectify in any future reprint.

Except as permitted under U.S. Copyright Law, no part of this book may be reprinted, reproduced, transmitted, or utilized in any form by any electronic, mechanical, or other means, now known or hereafter invented, including photocopying, microfilming, and recording, or in any information storage or retrieval system, without written permission from the publishers.

For permission to photocopy or use material electronically from this work, please access [www.copyright.com](http://www.copyright.com) (<http://www.copyright.com/>) or contact the Copyright Clearance Center, Inc. (CCC), 222 Rosewood Drive, Danvers, MA 01923, 978-750-8400. CCC is a not-for-profit organization that provides licenses and registration for a variety of users. For organizations that have been granted a photocopy license by the CCC, a separate system of payment has been arranged.

**Trademark Notice:** Product or corporate names may be trademarks or registered trademarks, and are used only for identification and explanation without intent to infringe.

**Visit the Taylor & Francis Web site at**  
<http://www.taylorandfrancis.com>

**and the CRC Press Web site at**  
<http://www.crcpress.com>

Dedicated to Eva, Felix, and Elina  
T. A-M.

Dedicated to Cathy, Ryan, and Evan  
E. H.

Dedicated to Dorit, Karen, and Daniel  
N. H.



# Contents

[book's figures for download](#)

|   |           |
|---|-----------|
| Preface   | xi        |
| <b>1 Introduction</b>                                     | <b>1</b>  |
| 1.1    Contents Overview . . . . .                        | 2         |
| 1.2    Notation and Definitions . . . . .                 | 4         |
| <b>2 The Graphics Rendering Pipeline</b>                  | <b>11</b> |
| 2.1    Architecture . . . . .                             | 12        |
| 2.2    The Application Stage . . . . .                    | 14        |
| 2.3    The Geometry Stage . . . . .                       | 15        |
| 2.4    The Rasterizer Stage . . . . .                     | 21        |
| 2.5    Through the Pipeline . . . . .                     | 25        |
| <b>3 The Graphics Processing Unit</b>                     | <b>29</b> |
| 3.1    GPU Pipeline Overview . . . . .                    | 30        |
| 3.2    The Programmable Shader Stage . . . . .            | 30        |
| 3.3    The Evolution of Programmable Shading . . . . .    | 33        |
| 3.4    The Vertex Shader . . . . .                        | 38        |
| 3.5    The Geometry Shader . . . . .                      | 40        |
| 3.6    The Pixel Shader . . . . .                         | 42        |
| 3.7    The Merging Stage . . . . .                        | 44        |
| 3.8    Effects . . . . .                                  | 45        |
| <b>4 Transforms</b>                                       | <b>53</b> |
| 4.1    Basic Transforms . . . . .                         | 55        |
| 4.2    Special Matrix Transforms and Operations . . . . . | 65        |
| 4.3    Quaternions . . . . .                              | 72        |
| 4.4    Vertex Blending . . . . .                          | 80        |
| 4.5    Morphing . . . . .                                 | 85        |
| 4.6    Projections . . . . .                              | 89        |
| <b>5 Visual Appearance</b>                                | <b>99</b> |
| 5.1    Visual Phenomena . . . . .                         | 99        |
| 5.2    Light Sources . . . . .                            | 100       |

|          |  |            |
|----------|--|------------|
| 5.3      | Material . . . . .                                 | 104        |
| 5.4      | Sensor . . . . .                                   | 107        |
| 5.5      | Shading . . . . .                                  | 110        |
| 5.6      | Aliasing and Antialiasing . . . . .                | 116        |
| 5.7      | Transparency, Alpha, and Compositing . . . . .     | 134        |
| 5.8      | Gamma Correction . . . . .                         | 141        |
| <b>6</b> | <b>Texturing</b>                                   | <b>147</b> |
| 6.1      | The Texturing Pipeline . . . . .                   | 148        |
| 6.2      | Image Texturing . . . . .                          | 156        |
| 6.3      | Procedural Texturing . . . . .                     | 178        |
| 6.4      | Texture Animation . . . . .                        | 180        |
| 6.5      | Material Mapping . . . . .                         | 180        |
| 6.6      | Alpha Mapping . . . . .                            | 181        |
| 6.7      | Bump Mapping . . . . .                             | 183        |
| <b>7</b> | <b>Advanced Shading</b>                            | <b>201</b> |
| 7.1      | Radiometry . . . . .                               | 202        |
| 7.2      | Photometry . . . . .                               | 209        |
| 7.3      | Colorimetry . . . . .                              | 210        |
| 7.4      | Light Source Types . . . . .                       | 217        |
| 7.5      | BRDF Theory . . . . .                              | 223        |
| 7.6      | BRDF Models . . . . .                              | 251        |
| 7.7      | BRDF Acquisition and Representation . . . . .      | 264        |
| 7.8      | Implementing BRDFs . . . . .                       | 269        |
| 7.9      | Combining Lights and Materials . . . . .           | 275        |
| <b>8</b> | <b>Area and Environmental Lighting</b>             | <b>285</b> |
| 8.1      | Radiometry for Arbitrary Lighting . . . . .        | 286        |
| 8.2      | Area Light Sources . . . . .                       | 289        |
| 8.3      | Ambient Light . . . . .                            | 295        |
| 8.4      | Environment Mapping . . . . .                      | 297        |
| 8.5      | Glossy Reflections from Environment Maps . . . . . | 308        |
| 8.6      | Irradiance Environment Mapping . . . . .           | 314        |
| <b>9</b> | <b>Global Illumination</b>                         | <b>327</b> |
| 9.1      | Shadows . . . . .                                  | 331        |
| 9.2      | Ambient Occlusion . . . . .                        | 373        |
| 9.3      | Reflections . . . . .                              | 386        |
| 9.4      | Transmittance . . . . .                            | 392        |
| 9.5      | Refractions . . . . .                              | 396        |
| 9.6      | Caustics . . . . .                                 | 399        |
| 9.7      | Global Subsurface Scattering . . . . .             | 401        |

|           |   |            |
|-----------|---|------------|
| 9.8       | Full Global Illumination . . . . .          | 407        |
| 9.9       | Precomputed Lighting . . . . .              | 417        |
| 9.10      | Precomputed Occlusion . . . . .             | 425        |
| 9.11      | Precomputed Radiance Transfer . . . . .     | 430        |
| <b>10</b> | <b>Image-Based Effects</b>                  | <b>439</b> |
| 10.1      | The Rendering Spectrum . . . . .            | 440        |
| 10.2      | Fixed-View Effects . . . . .                | 440        |
| 10.3      | Skyboxes . . . . .                          | 443        |
| 10.4      | Light Field Rendering . . . . .             | 444        |
| 10.5      | Sprites and Layers . . . . .                | 445        |
| 10.6      | Billboarding . . . . .                      | 446        |
| 10.7      | Particle Systems . . . . .                  | 455        |
| 10.8      | Displacement Techniques . . . . .           | 463        |
| 10.9      | Image Processing . . . . .                  | 467        |
| 10.10     | Color Correction . . . . .                  | 474        |
| 10.11     | Tone Mapping . . . . .                      | 475        |
| 10.12     | Lens Flare and Bloom . . . . .              | 482        |
| 10.13     | Depth of Field . . . . .                    | 486        |
| 10.14     | Motion Blur . . . . .                       | 490        |
| 10.15     | Fog . . . . .                               | 496        |
| 10.16     | Volume Rendering . . . . .                  | 502        |
| <b>11</b> | <b>Non-Photorealistic Rendering</b>         | <b>507</b> |
| 11.1      | Toon Shading . . . . .                      | 508        |
| 11.2      | Silhouette Edge Rendering . . . . .         | 510        |
| 11.3      | Other Styles . . . . .                      | 523        |
| 11.4      | Lines . . . . .                             | 527        |
| <b>12</b> | <b>Polygonal Techniques</b>                 | <b>531</b> |
| 12.1      | Sources of Three-Dimensional Data . . . . . | 532        |
| 12.2      | Tessellation and Triangulation . . . . .    | 534        |
| 12.3      | Consolidation . . . . .                     | 541        |
| 12.4      | Triangle Fans, Strips, and Meshes . . . . . | 547        |
| 12.5      | Simplification . . . . .                    | 561        |
| <b>13</b> | <b>Curves and Curved Surfaces</b>           | <b>575</b> |
| 13.1      | Parametric Curves . . . . .                 | 576        |
| 13.2      | Parametric Curved Surfaces . . . . .        | 592        |
| 13.3      | Implicit Surfaces . . . . .                 | 606        |
| 13.4      | Subdivision Curves . . . . .                | 608        |
| 13.5      | Subdivision Surfaces . . . . .              | 611        |
| 13.6      | Efficient Tessellation . . . . .            | 629        |

|   |     |
|---|-----|
| <b>14 Acceleration Algorithms</b>                       | 645 |
| 14.1 Spatial Data Structures . . . . .                  | 647 |
| 14.2 Culling Techniques . . . . .                       | 660 |
| 14.3 Hierarchical View Frustum Culling . . . . .        | 664 |
| 14.4 Portal Culling . . . . .                           | 667 |
| 14.5 Detail Culling . . . . .                           | 670 |
| 14.6 Occlusion Culling . . . . .                        | 670 |
| 14.7 Level of Detail . . . . .                          | 680 |
| 14.8 Large Model Rendering . . . . .                    | 693 |
| 14.9 Point Rendering . . . . .                          | 693 |
| <b>15 Pipeline Optimization</b>                         | 697 |
| 15.1 Profiling Tools . . . . .                          | 698 |
| 15.2 Locating the Bottleneck . . . . .                  | 699 |
| 15.3 Performance Measurements . . . . .                 | 702 |
| 15.4 Optimization . . . . .                             | 703 |
| 15.5 Multiprocessing . . . . .                          | 716 |
| <b>16 Intersection Test Methods</b>                     | 725 |
| 16.1 Hardware-Accelerated Picking . . . . .             | 726 |
| 16.2 Definitions and Tools . . . . .                    | 727 |
| 16.3 Bounding Volume Creation . . . . .                 | 732 |
| 16.4 Geometric Probability . . . . .                    | 735 |
| 16.5 Rules of Thumb . . . . .                           | 737 |
| 16.6 Ray/Sphere Intersection . . . . .                  | 738 |
| 16.7 Ray/Box Intersection . . . . .                     | 741 |
| 16.8 Ray/Triangle Intersection . . . . .                | 746 |
| 16.9 Ray/Polygon Intersection . . . . .                 | 750 |
| 16.10 Plane/Box Intersection Detection . . . . .        | 755 |
| 16.11 Triangle/Triangle Intersection . . . . .          | 757 |
| 16.12 Triangle/Box Overlap . . . . .                    | 760 |
| 16.13 BV/BV Intersection Tests . . . . .                | 762 |
| 16.14 View Frustum Intersection . . . . .               | 771 |
| 16.15 Shaft/Box and Shaft/Sphere Intersection . . . . . | 778 |
| 16.16 Line/Line Intersection Tests . . . . .            | 780 |
| 16.17 Intersection Between Three Planes . . . . .       | 782 |
| 16.18 Dynamic Intersection Testing . . . . .            | 783 |
| <b>17 Collision Detection</b>                           | 793 |
| 17.1 Collision Detection with Rays . . . . .            | 795 |
| 17.2 Dynamic CD using BSP Trees . . . . .               | 797 |
| 17.3 General Hierarchical Collision Detection . . . . . | 802 |
| 17.4 OBBTree . . . . .                                  | 807 |

|                     |   |             |
|---------------------|---|-------------|
| 17.5                | A Multiple Objects CD System . . . . .      | 811         |
| 17.6                | Miscellaneous Topics . . . . .              | 816         |
| 17.7                | Other Work . . . . .                        | 826         |
| <b>18</b>           | <b>Graphics Hardware</b>                    | <b>829</b>  |
| 18.1                | Buffers and Buffering . . . . .             | 829         |
| 18.2                | Perspective-Correct Interpolation . . . . . | 838         |
| 18.3                | Architecture . . . . .                      | 840         |
| 18.4                | Case Studies . . . . .                      | 859         |
| <b>19</b>           | <b>The Future</b>                           | <b>879</b>  |
| 19.1                | Everything Else . . . . .                   | 879         |
| 19.2                | You . . . . .                               | 885         |
| <b>A</b>            | <b>Some Linear Algebra</b>                  | <b>889</b>  |
| A.1                 | Euclidean Space . . . . .                   | 889         |
| A.2                 | Geometrical Interpretation . . . . .        | 892         |
| A.3                 | Matrices . . . . .                          | 897         |
| A.4                 | Homogeneous Notation . . . . .              | 905         |
| A.5                 | Geometry . . . . .                          | 906         |
| <b>B</b>            | <b>Trigonometry</b>                         | <b>913</b>  |
| B.1                 | Definitions . . . . .                       | 913         |
| B.2                 | Trigonometric Laws and Formulae . . . . .   | 915         |
| <b>Bibliography</b> |   | <b>921</b>  |
| <b>Index</b>        |   | <b>1003</b> |



# Preface

How much has happened in six years! Luckily for us, there has not been a paradigm shift (yet), but the amount of creative energy that has gone into the field these past years is incredible. To keep up with this ever-growing field, we are fortunate this time to be three authors instead of two. Naty Hoffman joins us this edition. He has years of experience in the field and has brought a fresh perspective to the book.

Since the second edition in 2002, researchers have produced hundreds of articles in the area of interactive computer graphics. At one point Naty filtered through conference proceedings, saving articles he thought were worth at least a mention. From just the research conferences alone the list grew to over 350 references; this did not include those in journals, book series like *GPU Gems* and *ShaderX*, or web articles. We realized we had a challenge ahead of us. Even a thorough survey of each area would make for a book of nothing but surveys. Such a volume would be exhaustive, but exhausting, and ultimately unsatisfying. Instead, we have focused on theory, algorithms, and architectures that we felt are key in understanding the field. We survey the literature as warranted, but with the goal of pointing you at the most recent work in an area and at resources for learning more.

This book is about algorithms that create synthetic images fast enough that the viewer can interact with a virtual environment. We have focused on three-dimensional rendering and, to a limited extent, on user interaction. Modeling, animation, and many other areas are important to the process of making a real-time application, but these topics are beyond the scope of this book.

We expect you to have some basic understanding of computer graphics before reading this book, as well as computer science and programming. Some of the later chapters in particular are meant for implementers of various complex algorithms. If some section does lose you, skim on through or look at the references. One of the most valuable services we feel we can provide is to have you realize what others have discovered and that you do not yet know, and to give you ways to learn more someday.

We make a point of referencing relevant material wherever possible, as well as providing a summary of further reading and resources at the end of

most chapters. Time invested in reading papers and books on a particular topic will almost always be paid back in the amount of implementation effort saved later.

Because the field is evolving so rapidly, we maintain a website related to this book at: <http://www.realtimerendering.com>. The site contains links to tutorials, demonstration programs, code samples, software libraries, book corrections, and more. This book's reference section is available there, with links to the referenced papers.

+ book's figures

Our true goal and guiding light while writing this book was simple. We wanted to write a book that we wished we had owned when we had started out, a book that was both unified yet crammed with details not found in introductory texts. We hope that you will find this book, our view of the world, of some use in your travels.

### Acknowledgments

Special thanks go out to a number of people who went out of their way to provide us with help. First, our graphics architecture case studies would not have been anywhere as good without the extensive and generous cooperation we received from the companies making the hardware. Many thanks to Edvard Sørgard, Borgar Ljosland, Dave Shreiner, and Jørn Nystad at ARM for providing details about their Mali 200 architecture. Thanks also to Michael Dougherty at Microsoft, who provided extremely valuable help with the Xbox 360 section. Masaaki Oka at Sony Computer Entertainment provided his own technical review of the PLAYSTATION® 3 system case study, while also serving as the liaison with the Cell Broadband Engine™ and RSX® developers for their reviews.

In answering a seemingly endless stream of questions, fact-checking numerous passages, and providing many screenshots, Natalya Tatarchuk of ATI/AMD went well beyond the call of duty in helping us out. In addition to responding to our usual requests for information and clarification, Wolfgang Engel was extremely helpful in providing us with articles from the upcoming *ShaderX*<sup>6</sup> book and copies of the difficult-to-obtain *ShaderX*<sup>2</sup> books.<sup>1</sup> Ignacio Castaño at NVIDIA provided us with valuable support and contacts, going so far as to rework a refractory demo so we could get just the right screenshot.

The chapter reviewers provided an invaluable service to us. They suggested numerous improvements and provided additional insights, helping us immeasurably. In alphabetical order they are: Michael Ashikhmin, Dan Baker, Willem de Boer, Ben Diamond, Ben Discoe, Amir Ebrahimi,

<sup>1</sup>Check our website; he and we are attempting to clear permissions and make this two-volume book [307, 308] available for free on the web.

Christer Ericson, Michael Gleicher, Manny Ko, Wallace Lages, Thomas Larsson, Gr  gory Massal, Ville Miettinen, Mike Ramsey, Scott Schaefer, Vincent Scheib, Peter Shirley, K.R. Subramanian, Mauricio Vives, and Hector Yee.

We also had a number of reviewers help us on specific sections. Our thanks go out to Matt Bronder, Christine DeNezza, Frank Fox, Jon Hasselgren, Pete Isensee, Andrew Lauritzen, Morgan McGuire, Jacob Munkberg, Manuel M. Oliveira, Aurelio Reis, Peter-Pike Sloan, Jim Tilander, and Scott Whitman.

We particularly thank Rex Crowle, Kareem Ettouney, and Francis Pang from Media Molecule for their considerable help in providing fantastic imagery and layout concepts for the cover design.

Many people helped us out in other ways, such as answering questions and providing screenshots. Many gave significant amounts of time and effort, for which we thank you. Listed alphabetically: Paulo Abreu, Timo Aila, Johan Andersson, Andreas Bærentzen, Louis Bavoil, Jim Blinn, Jaime Borasi, Per Christensen, Patrick Conran, Rob Cook, Erwin Coumans, Leo Cubbin, Richard Daniels, Mark DeLoura, Tony DeRose, Andreas Dietrich, Michael Dougherty, Bryan Dudash, Alex Evans, Cass Everitt, Randy Fernando, Jim Ferwerda, Chris Ford, Tom Forsyth, Sam Glassenberg, Robin Green, Ned Greene, Larry Gritz, Joakim Grundwall, Mark Harris, Ted Himlan, Jack Hoxley, John “Spike” Hughes, Ladislav Kavan, Alicia Kim, Gary King, Chris Lambert, Jeff Lander, Daniel Leaver, Eric Lengyel, Jennifer Liu, Brandon Lloyd, Charles Loop, David Luebke, Jonathan Maïm, Jason Mitchell, Martin Mittring, Nathan Monteleone, Gabe Newell, Hubert Nguyen, Petri Nordlund, Mike Pan, Ivan Pedersen, Matt Pharr, Fabio Policarpo, Aras Pranckevičius, Siobhan Reddy, Dirk Reiners, Christof Rezk-Salama Eric Risser, Marcus Roth, Holly Rushmeier, Elan Ruskin, Marco Salvi, Daniel Scherzer, Kyle Shubel, Philipp Slusallek, Torbjörn Söderman, Tim Sweeney, Ben Trumbore, Michal Valient, Mark Valledor, Carsten Wenzel, Steve Westin, Chris Wyman, Cem Yuksel, Billy Zelsnack, Fan Zhang, and Renaldas Zioma.

We also thank many others who responded to our queries on public forums such as GD Algorithms. Readers who took the time to send us corrections have also been a great help. It is this supportive attitude that is one of the pleasures of working in this field.

As we have come to expect, the cheerful competence of the people at A K Peters made the publishing part of the process much easier. For this wonderful support, we thank you all.

On a personal note, Tomas would like to thank his son Felix and daughter Elina for making him understand (again) just how fun it can be to play computer games (on the Wii), instead of just looking at the graphics, and needless to say, his beautiful wife Eva...

Eric would also like to thank his sons Ryan and Evan for their tireless efforts in finding cool game demos and screenshots, and his wife Cathy for helping him survive it all.

Naty would like to thank his daughter Karen and son Daniel for their forbearance when writing took precedence over piggyback rides, and his wife Dorit for her constant encouragement and support.

Tomas Akenine-Möller

Eric Haines

Naty Hoffman

*March 2008*

### *Acknowledgements for the Second Edition*

One of the most agreeable aspects of writing this second edition has been working with people and receiving their help. Despite their own pressing deadlines and concerns, many people gave us significant amounts of their time to improve this book. We would particularly like to thank the major reviewers. They are, listed alphabetically: Michael Abrash, Ian Ashdown, Ulf Assarsson, Chris Brennan, Sébastien Dominé, David Eberly, Cass Everitt, Tommy Fortes, Evan Hart, Greg James, Jan Kautz, Alexander Keller, Mark Kilgard, Adam Lake, Paul Lalonde, Thomas Larsson, Dean Macri, Carl Marshall, Jason L. Mitchell, Kasper Høy Nielsen, Jon Paul Schelter, Jacob Ström, Nick Triantos, Joe Warren, Michael Wimmer, and Peter Wonka. Of these, we wish to single out Cass Everitt at NVIDIA and Jason L. Mitchell at ATI Technologies for spending large amounts of time and effort in getting us the resources we needed. Our thanks also go out to Wolfgang Engel for freely sharing the contents of his upcoming book, *ShaderX* [306], so that we could make this edition as current as possible.

From discussing their work with us, to providing images or other resources, to writing reviews of sections of the book, many others helped in creating this edition. They all have our gratitude. These people include: Jason Ang, Haim Barad, Jules Bloomenthal, Jonathan Blow, Chas. Boyd, John Brooks, Cem Cebenoyan, Per Christensen, Hamilton Chu, Michael Cohen, Daniel Cohen-Or, Matt Craighead, Paul Debevec, Joe Demers, Walt Donovan, Howard Dortsch, Mark Duchaineau, Phil Dutré, Dave Eberle, Gerald Farin, Simon Fenney, Randy Fernando, Jim Ferwerda, Nickson Fong, Tom Forsyth, Piero Foscari, Laura Fryer, Markus Giegl, Peter Glaskowsky, Andrew Glassner, Amy Gooch, Bruce Gooch, Simon Green, Ned Greene, Larry Gritz, Joakim Grundwall, Juan Guardado, Pat Hanrahan, Mark Harris, Michael Herf, Carsten Hess, Rich Hilmer, Kenneth Hoff III, Naty Hoffman, Nick Holliman, Hugues Hoppe, Heather Horne, Tom Hubina, Richard Huddy, Adam James, Kaveh Kardan, Paul Keller,

David Kirk, Alex Klimovitski, Jason Knipe, Jeff Lander, Marc Levoy, J.P. Lewis, Ming Lin, Adrian Lopez, Michael McCool, Doug McNabb, Stan Melax, Ville Miettinen, Kenny Mitchell, Steve Morein, Henry Moreton, Jerris Mungai, Jim Napier, George Ngo, Hubert Nguyen, Tito Pagán, Jörg Peters, Tom Porter, Emil Praun, Kekoa Proudfoot, Bernd Raabe, Ravi Ramamoorthi, Ashutosh Rege, Szymon Rusinkiewicz, Carlo Séquin, Chris Seitz, Jonathan Shade, Brian Smits, John Spitzer, Wolfgang Straßer, Wolfgang Stürzlinger, Philip Taylor, Pierre Terdiman, Nicolas Thibieroz, Jack Tumblin, Fredrik Ulfves, Thatcher Ulrich, Steve Upstill, Alex Vlachos, Ingo Wald, Ben Watson, Steve Westin, Dan Wexler, Matthias Wloka, Peter Woytiuk, David Wu, Garrett Young, Borut Zalik, Harold Zatz, Hansong Zhang, and Denis Zorin. We also wish to thank the journal *ACM Transactions on Graphics* for continuing to provide a mirror website for this book.

Alice and Klaus Peters, our production manager Ariel Jaffee, our editor Heather Holcombe, our copyeditor Michelle M. Richards, and the rest of the staff at A K Peters have done a wonderful job making this book the best possible. Our thanks to all of you.

Finally, and most importantly, our deepest thanks go to our families for giving us the huge amounts of quiet time we have needed to complete this edition. Honestly, we never thought it would take this long!

Tomas Akenine-Möller  
Eric Haines  
May 2002

### *Acknowledgements for the First Edition*

Many people helped in making this book. Some of the greatest contributions were made by those who reviewed parts of it. The reviewers willingly gave the benefit of their expertise, helping to significantly improve both content and style. We wish to thank (in alphabetical order) Thomas Barregren, Michael Cohen, Walt Donovan, Angus Dorbie, Michael Garland, Stefan Gottschalk, Ned Greene, Ming C. Lin, Jason L. Mitchell, Liang Peng, Keith Rule, Ken Shoemake, John Stone, Phil Taylor, Ben Trumbore, Jorrit Tyberghein, and Nick Wilt. We cannot thank you enough.

Many other people contributed their time and labor to this project. Some let us use images, others provided models, still others pointed out important resources or connected us with people who could help. In addition to the people listed above, we wish to acknowledge the help of Tony Barkans, Daniel Baum, Nelson Beebe, Curtis Beeson, Tor Berg, David Blythe, Chas. Boyd, Don Brittain, Ian Bullard, Javier Castellar, Satyan Coorg, Jason Della Rocca, Paul Diefenbach, Alyssa Donovan, Dave Eberly, Kells Elmquist, Stuart Feldman, Fred Fisher, Tom Forsyth, Marty Franz, Thomas Funkhouser, Andrew Glassner, Bruce Gooch, Larry Gritz, Robert

Grzeszczuk, Paul Haeberli, Evan Hart, Paul Heckbert, Chris Hecker, Joachim Helenklaken, Hugues Hoppe, John Jack, Mark Kilgard, David Kirk, James Klosowski, Subodh Kumar, André LaMothe, Jeff Lander, Jens Larsson, Jed Lengyel, Fredrik Liliegren, David Luebke, Thomas Lundqvist, Tom McReynolds, Stan Melax, Don Mitchell, André Möller, Steve Molnar, Scott R. Nelson, Hubert Nguyen, Doug Rogers, Holly Rushmeier, Gernot Schaufler, Jonas Skeppstedt, Stephen Spencer, Per Stenström, Jacob Ström, Filippo Tampieri, Gary Tarolli, Ken Turkowski, Turner Whitted, Agata and Andrzej Wojaczek, Andrew Woo, Steve Worley, Brian Yen, Hans-Philip Zachau, Gabriel Zachmann, and Al Zimmerman. We also wish to thank the journal *ACM Transactions on Graphics* for providing a stable website for this book.

Alice and Klaus Peters and the staff at AK Peters, particularly Carolyn Artin and Sarah Gillis, have been instrumental in making this book a reality. To all of you, thanks.

Finally, our deepest thanks go to our families and friends for providing support throughout this incredible, sometimes grueling, often exhilarating process.

Tomas Möller  
Eric Haines  
*March 1999*

# Chapter 1

## Introduction

Real-time rendering is concerned with making images rapidly on the computer. It is the most highly interactive area of computer graphics. An image appears on the screen, the viewer acts or reacts, and this feedback affects what is generated next. This cycle of reaction and rendering happens at a rapid enough rate that the viewer does not see individual images, but rather becomes immersed in a dynamic process.

The rate at which images are displayed is measured in frames per second (fps) or Hertz (Hz). At one frame per second, there is little sense of interactivity; the user is painfully aware of the arrival of each new image. At around 6 fps, a sense of interactivity starts to grow. An application displaying at 15 fps is certainly real-time; the user focuses on action and reaction. There is a useful limit, however. From about 72 fps and up, differences in the display rate are effectively undetectable.

Watching images flicker by at 60 fps might be acceptable, but an even higher rate is important for minimizing response time. As little as 15 milliseconds of temporal delay can slow and interfere with interaction [1329]. There is more to real-time rendering than interactivity. If speed was the only criterion, any application that rapidly responded to user commands and drew anything on the screen would qualify. Rendering in real-time normally means three-dimensional rendering.

Interactivity and some sense of connection to three-dimensional space are sufficient conditions for real-time rendering, but a third element has become a part of its definition: graphics acceleration hardware. While hardware dedicated to three-dimensional graphics has been available on professional workstations for many years, it is only relatively recently that the use of such accelerators at the consumer level has become possible. Many consider the introduction of the 3Dfx Voodoo 1 in 1996 the real beginning of this era [297]. With the recent rapid advances in this market, add-on three-dimensional graphics accelerators are as standard for home computers as a pair of speakers. While it is not absolutely required for real-



**Figure 1.1.** A wonderful image from the Toy Shop demo [1246, 1247, 1249], generated at interactive rates. (*Image courtesy of Natalya Tatarchuk, ATI Research, Inc.*)

time rendering, graphics accelerator hardware has become a requirement for most real-time applications. An excellent example of the results of real-time rendering made possible by hardware acceleration is shown in Figure 1.1.

In the past few years advances in graphics hardware have fueled an explosion of research in the field of interactive computer graphics. We will focus on providing methods to increase speed and improve image quality, while also describing the features and limitations of acceleration algorithms and graphics APIs. We will not be able to cover every topic in depth, so our goal is to introduce concepts and terminology, give a sense of how and when various methods can be applied, and provide pointers to the best places to go for more in-depth information. We hope our attempts to provide you with tools for understanding this field prove to be worth the time and effort you spend with our book.

## 1.1 Contents Overview

What follows is a brief overview of the chapters ahead.

**Chapter 2, The Graphics Rendering Pipeline.** This chapter deals with the heart of real-time rendering, the mechanism that takes a scene description and converts it into something we can see.

**Chapter 3, The Graphics Processing Unit.** The modern GPU implements the stages of the rendering pipeline using a combination of fixed-function and programmable units.

**Chapter 4, Transforms.** Transforms are the basic tools for manipulating the position, orientation, size, and shape of objects and the location and view of the camera.

**Chapter 5, Visual Appearance.** This chapter begins discussion of the definition of materials and lights and their use in achieving a realistic surface appearance. Also covered are other appearance-related topics, such as providing higher image quality through antialiasing and gamma correction.

**Chapter 6, Texturing.** One of the most powerful tools for real-time rendering is the ability to rapidly access and display data such as images on surfaces. This chapter discusses the mechanics of this technique, called texturing, and presents a wide variety of methods for applying it.

**Chapter 7, Advanced Shading.** This chapter discusses the theory and practice of correctly representing materials and the use of point light sources.

**Chapter 8, Area and Environmental Lighting.** More elaborate light sources and algorithms are explored in this chapter.

**Chapter 9, Global Illumination.** Shadow, reflection, and refraction algorithms are discussed, as well as such topics as radiosity, ray tracing, pre-computed lighting, and ambient occlusion.

**Chapter 10, Image-Based Effects.** Polygons are not always the fastest or most realistic way to describe objects or phenomena such as lens flares or fire. In this chapter, alternate representations based on using images are discussed. Post-processing effects such as high-dynamic range rendering, motion blur, and depth of field are also covered.

**Chapter 11, Non-Photorealistic Rendering.** Attempting to make a scene look realistic is only one way of rendering it. This chapter discusses other styles, such as cartoon shading.

**Chapter 12, Polygonal Techniques.** Geometric data comes from a wide range of sources, and sometimes requires modification in order to be rendered rapidly and well. This chapter discusses polygonal data and ways to clean it up and simplify it. Also included are more compact representations, such as triangle strips, fans, and meshes.

**Chapter 13, Curves and Curved Surfaces.** Hardware ultimately deals in points, lines, and polygons for rendering geometry. More complex surfaces offer advantages such as being able to trade off between quality and rendering speed, more compact representation, and smooth surface generation.

**Chapter 14, Acceleration Algorithms.** After you make it go, make it go fast. Various forms of culling and level of detail rendering are covered here.

**Chapter 15, Pipeline Optimization.** Once an application is running and uses efficient algorithms, it can be made even faster using various optimization techniques. This chapter is primarily about finding the bottleneck and deciding what to do about it. Multiprocessing is also discussed.

**Chapter 16, Intersection Test Methods.** Intersection testing is important for rendering, user interaction, and collision detection. In-depth coverage is provided here for a wide range of the most efficient algorithms for common geometric intersection tests.

**Chapter 17, Collision Detection.** Finding out whether two objects touch each other is a key element of many real-time applications. This chapter presents some efficient algorithms in this evolving field.

**Chapter 18, Graphics Hardware.** While GPU accelerated algorithms have been discussed in the previous chapters, this chapter focuses on components such as color depth, frame buffers, and basic architecture types. Case studies of a few representative graphics accelerators are provided.

**Chapter 19, The Future.** Take a guess (we do).

We have included appendices on linear algebra and trigonometry.

## 1.2 Notation and Definitions

First, we shall explain the mathematical notation used in this book. For a more thorough explanation of many of the terms used in this section, see Appendix A.

### 1.2.1 Mathematical Notation

Table 1.1 summarizes most of the mathematical notation we will use. Some of the concepts will be described at some length here.

The angles and the scalars are taken from  $\mathbb{R}$ , i.e., they are real numbers. Vectors and points are denoted by bold lowercase letters, and the

| Type             | Notation                         | Examples  |
|------------------|----------------------------------|---|
| angle            | lowercase Greek                  | $\alpha_i, \phi, \rho, \eta, \gamma_{242}, \theta$  |
| scalar           | lowercase italic                 | $a, b, t, u_k, v, w_{ij}$   |
| vector or point  | lowercase bold                   | $\mathbf{a}, \mathbf{u}, \mathbf{v}_s$ $\mathbf{h}(\rho), \mathbf{h}_z$                           |
| matrix           | capital bold                     | $\mathbf{T}(\mathbf{t}), \mathbf{X}, \mathbf{R}_x(\rho)$  |
| plane            | $\pi$ : a vector and<br>a scalar | $\pi : \mathbf{n} \cdot \mathbf{x} + d = 0,$<br>$\pi_1 : \mathbf{n}_1 \cdot \mathbf{x} + d_1 = 0$ |
| triangle         | $\triangle$ 3 points             | $\triangle \mathbf{v}_0 \mathbf{v}_1 \mathbf{v}_2, \triangle \mathbf{cba}$                        |
| line segment     | two points                       | $\mathbf{uv}, \mathbf{a}_i \mathbf{b}_j$  |
| geometric entity | capital italic                   | $A_{OBB}, T, B_{AABB}$  |

**Table 1.1.** Summary of the notation used in this book.

components are accessed as

$$\mathbf{v} = \begin{pmatrix} v_x \\ v_y \\ v_z \end{pmatrix},$$

that is, in column vector format, which is now commonly used in the computer graphics world. At some places in the text we use  $(v_x, v_y, v_z)$  instead of the formally more correct  $(v_x \ v_y \ v_z)^T$ , since the former is easier to read.

In homogeneous coordinates (see Section A.4), a coordinate is represented by  $\mathbf{v} = (v_x \ v_y \ v_z \ v_w)^T$ , where a vector is  $\mathbf{v} = (v_x \ v_y \ v_z \ 0)^T$  and a point is  $\mathbf{v} = (v_x \ v_y \ v_z \ 1)^T$ . Sometimes we use only three-element vectors and points, but we try to avoid any ambiguity as to which type is being used. For matrix manipulations, it is extremely advantageous to have the same notation for vectors as for points (see Chapter 4 on transforms and Section A.4 on homogeneous notation). In some algorithms, it will be convenient to use numeric indices instead of  $x$ ,  $y$ , and  $z$ , for example  $\mathbf{v} = (v_0 \ v_1 \ v_2)^T$ . All of these rules for vectors and points also hold for two-element vectors; in that case, we simply skip the last component of a three-element vector.

The matrix deserves a bit more explanation. The common sizes that will be used are  $2 \times 2$ ,  $3 \times 3$ , and  $4 \times 4$ . We will review the manner of accessing a  $3 \times 3$  matrix  $\mathbf{M}$ , and it is simple to extend this process to the other sizes. The (scalar) elements of  $\mathbf{M}$  are denoted  $m_{ij}$ ,  $0 \leq (i, j) \leq 2$ ,

where  $i$  denotes the row and  $j$  the column, as in Equation 1.2:

$$\mathbf{M} = \begin{pmatrix} m_{00} & m_{01} & m_{02} \\ m_{10} & m_{11} & m_{12} \\ m_{20} & m_{21} & m_{22} \end{pmatrix}. \quad (1.2)$$

The following notation, shown in Equation 1.3 for a  $3 \times 3$  matrix, is used to isolate vectors from the matrix  $\mathbf{M}$ :  $\mathbf{m}_{:,j}$  represents the  $j$ th column vector and  $\mathbf{m}_{i,:}$  represents the  $i$ th row vector (in column vector form). As with vectors and points, indexing the column vectors can also be done with  $x$ ,  $y$ ,  $z$ , and sometimes  $w$ , if that is more convenient:

$$\mathbf{M} = (\mathbf{m}_{:,0} \quad \mathbf{m}_{:,1} \quad \mathbf{m}_{:,2}) = (\mathbf{m}_x \quad \mathbf{m}_y \quad \mathbf{m}_z) = \begin{pmatrix} \mathbf{m}_0^T \\ \mathbf{m}_1^T \\ \mathbf{m}_2^T \end{pmatrix}. \quad (1.3)$$

A plane is denoted  $\pi : \mathbf{n} \cdot \mathbf{x} + d = 0$  and contains its mathematical formula, the plane normal  $\mathbf{n}$  and the scalar  $d$ . The normal is a vector describing what direction the plane faces. More generally (e.g., for curved surfaces), a normal describes this direction for a particular point on the surface. For a plane the same normal happens to apply to all its points.  $\pi$  is the common mathematical notation for a plane. The plane  $\pi$  is said to divide the space into a *positive half-space*, where  $\mathbf{n} \cdot \mathbf{x} + d > 0$ , and a *negative half-space*, where  $\mathbf{n} \cdot \mathbf{x} + d < 0$ . All other points are said to lie in the plane.

A triangle can be defined by three points  $\mathbf{v}_0$ ,  $\mathbf{v}_1$ , and  $\mathbf{v}_2$  and is denoted by  $\triangle \mathbf{v}_0 \mathbf{v}_1 \mathbf{v}_2$

Table 1.2 presents a few additional mathematical operators and their notation. The dot, cross, determinant, and length operators are covered in Appendix A. The transpose operator turns a column vector into a row vector and vice versa. Thus a column vector can be written in compressed form in a block of text as  $\mathbf{v} = (v_x \ v_y \ v_z)^T$ . Operator 4 requires further explanation:  $\mathbf{u} \otimes \mathbf{v}$  denotes the vector  $(u_x v_x \ u_y v_y \ u_z v_z)^T$ , i.e., component  $i$  of vector  $\mathbf{u}$  and component  $i$  of vector  $\mathbf{v}$  are multiplied and stored in component  $i$  of a new vector. In this text, this operator is used exclusively for color vector manipulations. Operator 5, introduced in *Graphics Gems IV* [551], is a unary operator on a two-dimensional vector. Letting this operator work on a vector  $\mathbf{v} = (v_x \ v_y)^T$  gives a vector that is perpendicular to  $\mathbf{v}$ , i.e.,  $\mathbf{v}^\perp = (-v_y \ v_x)^T$ . We use  $|a|$  to denote the absolute value of the scalar  $a$ , while  $|\mathbf{A}|$  means the determinant of the matrix  $\mathbf{A}$ . Sometimes, we also use  $|\mathbf{A}| = |\mathbf{a} \ \mathbf{b} \ \mathbf{c}| = \det(\mathbf{a}, \mathbf{b}, \mathbf{c})$ , where  $\mathbf{a}$ ,  $\mathbf{b}$ , and  $\mathbf{c}$  are column vectors of the matrix  $\mathbf{A}$ . The ninth operator, factorial, is defined as shown

|     | <b>Operator</b> | <b>Description</b>                   |
|-----|-----------------|--------------------------------------|
| 1:  | $\cdot$         | dot product                          |
| 2:  | $\times$        | cross product                        |
| 3:  | $\mathbf{v}^T$  | transpose of the vector $\mathbf{v}$ |
| 4:  | $\otimes$       | piecewise vector multiplication      |
| 5:  | $\perp$         | the unary, perp dot product operator |
| 6:  | $  \cdot  $     | determinant of a matrix              |
| 7:  | $  \cdot  $     | absolute value of a scalar           |
| 8:  | $\  \cdot \ $   | length (or norm) of argument         |
| 9:  | $n!$            | factorial                            |
| 10: | $\binom{n}{k}$  | binomial coefficients                |

**Table 1.2.** Notation for some mathematical operators.

below, and note that  $0! = 1$ :

$$n! = n(n - 1)(n - 2) \cdots 3 \cdot 2 \cdot 1. \quad (1.4)$$

The tenth operator, the binomial factor, is defined as shown in Equation 1.5:

$$\binom{n}{k} = \frac{n!}{k!(n - k)!}. \quad (1.5)$$

Further on, we call the common planes  $x = 0$ ,  $y = 0$ , and  $z = 0$  the *coordinate planes* or *axis-aligned planes*. The axes  $\mathbf{e}_x = (1 \ 0 \ 0)^T$ ,  $\mathbf{e}_y = (0 \ 1 \ 0)^T$ , and  $\mathbf{e}_z = (0 \ 0 \ 1)^T$  are called *main axes* or *main directions* and often the *x-axis*, *y-axis*, and *z-axis*. This set of axes is often called the *standard basis*. Unless otherwise noted, we will use orthonormal bases (consisting of mutually perpendicular unit vectors; see Appendix A.3.1).

The notation for a range that includes both  $a$  and  $b$ , and all numbers in between is  $[a, b]$ . If you want all number between  $a$  and  $b$ , but not  $a$  and  $b$  themselves, then we write  $(a, b)$ . Combinations of these can also be made, e.g.,  $[a, b)$  means all numbers between  $a$  and  $b$  including  $a$  but not  $b$ .

The C-math function `atan2(y, x)` is often used in this text, and so deserves some attention. It is an extension of the mathematical function  $\arctan(x)$ . The main differences between them are that  $-\frac{\pi}{2} < \arctan(x) < \frac{\pi}{2}$ , that  $0 \leq \text{atan2}(y, x) < 2\pi$ , and that an extra argument has been added to the latter function. This extra argument avoids division by zero, i.e.,  $x = y/x$  except when  $x = 0$ .

|    | Function                  | Description              |
|----|---------------------------|--------------------------|
| 1: | <code>atan2(y, x)</code>  | two-value arctangent     |
| 2: | $\overline{\cos}(\theta)$ | clamped cosine           |
| 3: | $\log(n)$                 | natural logarithm of $n$ |

**Table 1.3.** Notation for some specialized mathematical functions.

Clamped-cosine,  $\overline{\cos}(\theta)$ , is a function we introduce in order to keep shading equations from becoming difficult to read. If the result of the cosine function is less than zero, the value returned by clamped-cosine is zero.

In this volume the notation  $\log(n)$  always means the natural logarithm,  $\log_e(n)$ , not the base-10 logarithm,  $\log_{10}(n)$ .

We use a right-hand coordinate system (see Appendix A.2) since this is the standard system for three-dimensional geometry in the field of computer graphics.

Colors are represented by a three-element vector, such as (*red, green, blue*), where each element has the range [0, 1].

## 1.2.2 Geometrical Definitions

The basic rendering primitives (also called drawing primitives) used by most graphics hardware are points, lines, and triangles.<sup>1</sup>

Throughout this book, we will refer to a collection of geometric entities as either a *model* or an *object*. A *scene* is a collection of models comprising everything that is included in the environment to be rendered. A scene can also include material descriptions, lighting, and viewing specifications.

Examples of objects are a car, a building, and even a line. In practice, an object often consists of a set of drawing primitives, but this may not always be the case; an object may have a higher kind of geometrical representation, such as Bézier curves or surfaces, subdivision surfaces, etc. Also, objects can consist of other objects, e.g., we call a car model's door an object or a subset of the car.

## Further Reading and Resources

The most important resource we can refer you to is the website for this book: <http://www.realtimerendering.com>. It contains links to the latest information and websites relevant to each chapter. The field of real-time rendering is changing with real-time speed. In the book we have attempted

---

<sup>1</sup>The only exceptions we know of are Pixel-Planes [368], which could draw spheres, and the NVIDIA NV1 chip, which could draw ellipsoids.

to focus on concepts that are fundamental and techniques that are unlikely to go out of style. On the website we have the opportunity to present information that is relevant to today's software developer, and we have the ability to keep up-to-date.



# Chapter 2

## The Graphics Rendering Pipeline

*“A chain is no stronger than its weakest link.”*

—Anonymous

This chapter presents what is considered to be the core component of real-time graphics, namely the *graphics rendering pipeline*, also known simply as the pipeline. The main function of the pipeline is to generate, or *render*, a two-dimensional image, given a virtual camera, three-dimensional objects, light sources, shading equations, textures, and more. The rendering pipeline is thus the underlying tool for real-time rendering. The process of using the pipeline is depicted in Figure 2.1. The locations and shapes of the objects in the image are determined by their geometry, the characteristics of the environment, and the placement of the camera in that environment. The appearance of the objects is affected by material properties, light sources, textures, and shading models.

The different stages of the rendering pipeline will now be discussed and explained, with a focus on function and not on implementation. Implementation details are either left for later chapters or are elements over which the programmer has no control. For example, what is important to someone using lines are characteristics such as vertex data formats, colors, and pattern types, and whether, say, depth cueing is available, not whether lines are implemented via Bresenham’s line-drawing algorithm [142] or via a symmetric double-step algorithm [1391]. Usually some of these pipeline stages are implemented in non-programmable hardware, which makes it impossible to optimize or improve on the implementation. Details of basic draw and fill algorithms are covered in depth in books such as Rogers [1077]. While we may have little control over some of the underlying hardware, algorithms and coding methods have a significant effect on the speed and quality at which images are produced.

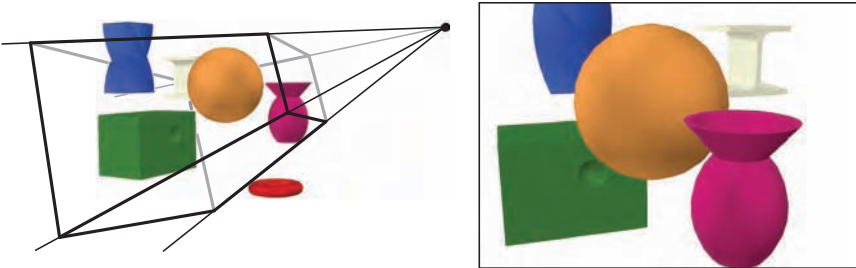


**Figure 2.1.** In the left image, a virtual camera is located at the tip of the pyramid (where four lines converge). Only the primitives inside the view volume are rendered. For an image that is rendered in perspective (as is the case here), the view volume is a frustum, i.e., a truncated pyramid with a rectangular base. The right image shows what the camera “sees.” Note that the red donut shape in the left image is not in the rendering to the right because it is located outside the view frustum. Also, the twisted blue prism in the left image is clipped against the top plane of the frustum.

## 2.1 Architecture

In the physical world, the pipeline concept manifests itself in many different forms, from factory assembly lines to ski lifts. It also applies to graphics rendering.

A pipeline consists of several stages [541]. For example, in an oil pipeline, oil cannot move from the first stage of the pipeline to the second until the oil already in that second stage has moved on to the third stage, and so forth. This implies that the speed of the pipeline is determined by the slowest stage, no matter how fast the other stages may be.

Ideally, a nonpipelined system that is then divided into  $n$  pipelined stages could give a speedup of a factor of  $n$ . This increase in performance is the main reason to use pipelining. For example, a ski chairlift containing only one chair is inefficient; adding more chairs creates a proportional speedup in the number of skiers brought up the hill. The pipeline stages execute in parallel, but they are stalled until the slowest stage has finished its task. For example, if the steering wheel attachment stage on a car assembly line takes three minutes and every other stage takes two minutes, the best rate that can be achieved is one car made every three minutes; the other stages must be idle for one minute while the steering wheel attachment is completed. For this particular pipeline, the steering wheel stage is the *bottleneck*, since it determines the speed of the entire production.

This kind of pipeline construction is also found in the context of real-time computer graphics. A coarse division of the real-time rendering pipeline into three *conceptual stages*—*application*, *geometry*, and *rasterizer*—is shown in Figure 2.2. This structure is the core—the engine of the rendering

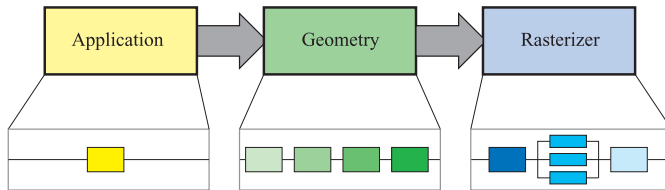


**Figure 2.2.** The basic construction of the rendering pipeline, consisting of three stages: application, geometry, and the rasterizer. Each of these stages may be a pipeline in itself, as illustrated below the geometry stage, or a stage may be (partly) parallelized, as shown below the rasterizer stage. In this illustration, the application stage is a single process, but this stage could also be pipelined or parallelized.

pipeline—which is used in real-time computer graphics applications and is thus an essential base for discussion in subsequent chapters. Each of these stages is usually a pipeline in itself, which means that it consists of several substages. We differentiate between the conceptual stages (application, geometry, and rasterizer), functional stages, and pipeline stages. A functional stage has a certain task to perform but does not specify the way that task is executed in the pipeline. A pipeline stage, on the other hand, is executed simultaneously with all the other pipeline stages. A pipeline stage may also be parallelized in order to meet high performance needs. For example, the geometry stage may be divided into five functional stages, but it is the implementation of a graphics system that determines its division into pipeline stages. A given implementation may combine two functional stages into one pipeline stage, while it divides another, more time-consuming, functional stage into several pipeline stages, or even parallelizes it.

It is the slowest of the pipeline stages that determines the *rendering speed*, the update rate of the images. This speed may be expressed in *frames per second* (fps), that is, the number of images rendered per second. It can also be represented using *Hertz* (Hz), which is simply the notation for  $1/\text{seconds}$ , i.e., the frequency of update. The time used by an application to generate an image usually varies, depending on the complexity of the computations performed during each frame. Frames per second is used to express either the rate for a particular frame, or the average performance over some duration of use. Hertz is used for hardware, such as a display, which is set to a fixed rate. Since we are dealing with a pipeline, it does not suffice to add up the time it takes for all the data we want to render to pass through the entire pipeline. This, of course, is a consequence of the pipeline construction, which allows the stages to execute in parallel. If we could locate the bottleneck, i.e., the slowest stage of the pipeline, and measure how much time it takes data to pass through that stage, then

we could compute the rendering speed. Assume, for example, that the bottleneck stage takes 20 ms (milliseconds) to execute; the rendering speed then would be  $1/0.020 = 50$  Hz. However, this is true only if the output device can update at this particular speed; otherwise, the true output rate will be slower. In other pipelining contexts, the term *throughput* is used instead of rendering speed.

**EXAMPLE: RENDERING SPEED.** Assume that our output device's maximum update frequency is 60 Hz, and that the bottleneck of the rendering pipeline has been found. Timings show that this stage takes 62.5 ms to execute. The rendering speed is then computed as follows. First, ignoring the output device, we get a maximum rendering speed of  $1/0.0625 = 16$  fps. Second, adjust this value to the frequency of the output device: 60 Hz implies that rendering speed can be 60 Hz,  $60/2 = 30$  Hz,  $60/3 = 20$  Hz,  $60/4 = 15$  Hz,  $60/5 = 12$  Hz, and so forth. This means that we can expect the rendering speed to be 15 Hz, since this is the maximum constant speed the output device can manage that is less than 16 fps.  $\square$

As the name implies, the *application stage* is driven by the application and is therefore implemented in software running on general-purpose CPUs. These CPUs commonly include multiple cores that are capable of processing multiple *threads of execution* in parallel. This enables the CPUs to efficiently run the large variety of tasks that are the responsibility of the application stage. Some of the tasks traditionally performed on the CPU include collision detection, global acceleration algorithms, animation, physics simulation, and many others, depending on the type of application. The next step is the *geometry stage*, which deals with transforms, projections, etc. This stage computes what is to be drawn, how it should be drawn, and where it should be drawn. The geometry stage is typically performed on a graphics processing unit (GPU) that contains many programmable cores as well as fixed-operation hardware. Finally, the *rasterizer stage* draws (renders) an image with use of the data that the previous stage generated, as well as any per-pixel computation desired. The rasterizer stage is processed completely on the GPU. These stages and their internal pipelines will be discussed in the next three sections. More details on how the GPU processes these stages are given in Chapter 3.

## 2.2 The Application Stage

The developer has full control over what happens in the application stage, since it executes on the CPU. Therefore, the developer can entirely determine the implementation and can later modify it in order to improve

performance. Changes here can also affect the performance of subsequent stages. For example, an application stage algorithm or setting could decrease the number of triangles to be rendered.

At the end of the application stage, the geometry to be rendered is fed to the geometry stage. These are the *rendering primitives*, i.e., points, lines, and triangles, that might eventually end up on the screen (or whatever output device is being used). This is the most important task of the application stage.

A consequence of the software-based implementation of this stage is that it is not divided into substages, as are the geometry and rasterizer stages.<sup>1</sup> However, in order to increase performance, this stage is often executed in parallel on several processor cores. In CPU design, this is called a *superscalar* construction, since it is able to execute several processes at the same time in the same stage. Section 15.5 presents various methods for utilizing multiple processor cores.

One process commonly implemented in this stage is *collision detection*. After a collision is detected between two objects, a response may be generated and sent back to the colliding objects, as well as to a force feedback device. The application stage is also the place to take care of input from other sources, such as the keyboard, the mouse, a head-mounted helmet, etc. Depending on this input, several different kinds of actions may be taken. Other processes implemented in this stage include texture animation, animations via transforms, or any kind of calculations that are not performed in any other stages. Acceleration algorithms, such as hierarchical view frustum culling (see Chapter 14), are also implemented here.

## 2.3 The Geometry Stage

The geometry stage is responsible for the majority of the per-polygon and per-vertex operations. This stage is further divided into the following functional stages: model and view transform, vertex shading, projection, clipping, and screen mapping (Figure 2.3). Note again that, depending on the implementation, these functional stages may or may not be equivalent to pipeline stages. In some cases, a number of consecutive functional stages form a single pipeline stage (which runs in parallel with the other pipeline stages). In other cases, a functional stage may be subdivided into several smaller pipeline stages.

---

<sup>1</sup>Since a CPU itself is pipelined on a much smaller scale, you could say that the application stage is further subdivided into several pipeline stages, but this is not relevant here.



**Figure 2.3.** The geometry stage subdivided into a pipeline of functional stages.

For example, at one extreme, all stages in the entire rendering pipeline may run in software on a single processor, and then you could say that your entire pipeline consists of one pipeline stage. Certainly this was how all graphics were generated before the advent of separate accelerator chips and boards. At the other extreme, each functional stage could be subdivided into several smaller pipeline stages, and each such pipeline stage could execute on a designated processor core element.

### 2.3.1 Model and View Transform

On its way to the screen, a model is transformed into several different *spaces* or *coordinate systems*. Originally, a model resides in its own *model space*, which simply means that it has not been transformed at all. Each model can be associated with a *model transform* so that it can be positioned and oriented. It is possible to have several model transforms associated with a single model. This allows several copies (called *instances*) of the same model to have different locations, orientations, and sizes in the same scene, without requiring replication of the basic geometry.

It is the vertices and the normals of the model that are transformed by the model transform. The coordinates of an object are called *model coordinates*, and after the model transform has been applied to these coordinates, the model is said to be located in *world coordinates* or in *world space*. The world space is unique, and after the models have been transformed with their respective model transforms, all models exist in this same space.

As mentioned previously, only the models that the camera (or observer) sees are rendered. The camera has a location in world space and a direction, which are used to place and aim the camera. To facilitate projection and clipping, the camera and all the models are transformed with the *view transform*. The purpose of the view transform is to place the camera at the origin and aim it, to make it look in the direction of the negative  $z$ -axis,<sup>2</sup> with the  $y$ -axis pointing upwards and the  $x$ -axis pointing to the right. The actual position and direction after the view transform has been applied are dependent on the underlying application programming interface (API). The

<sup>2</sup>We will be using the  $-z$ -axis convention; some texts prefer looking down the  $+z$ -axis. The difference is mostly semantic, as transform between one and the other is simple.

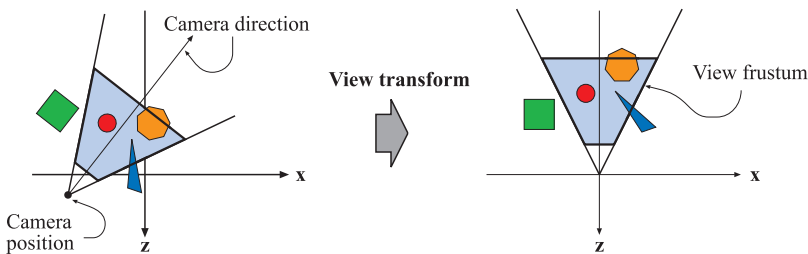


**Figure 2.4.** In the left illustration, the camera is located and oriented as the user wants it to be. The view transform relocates the camera at the origin, looking along the negative  $z$ -axis, as shown on the right. This is done to make the clipping and projection operations simpler and faster. The light gray area is the view volume. Here, perspective viewing is assumed, since the view volume is a frustum. Similar techniques apply to any kind of projection.

space thus delineated is called the *camera space*, or more commonly, the *eye space*. An example of the way in which the view transform affects the camera and the models is shown in Figure 2.4. Both the model transform and the view transform are implemented as  $4 \times 4$  matrices, which is the topic of Chapter 4.

### 2.3.2 Vertex Shading

To produce a realistic scene, it is not sufficient to render the shape and position of objects, but their appearance must be modeled as well. This description includes each object's material, as well as the effect of any light sources shining on the object. Materials and lights can be modeled in any number of ways, from simple colors to elaborate representations of physical descriptions.

This operation of determining the effect of a light on a material is known as *shading*. It involves computing a *shading equation* at various points on the object. Typically, some of these computations are performed during the geometry stage on a model's vertices, and others may be performed during per-pixel rasterization. A variety of material data can be stored at each vertex, such as the point's location, a normal, a color, or any other numerical information that is needed to compute the shading equation. Vertex shading results (which can be colors, vectors, texture coordinates, or any other kind of shading data) are then sent to the rasterization stage to be interpolated.

Shading computations are usually considered as happening in world space. In practice, it is sometimes convenient to transform the relevant entities (such as the camera and light sources) to some other space (such

as model or eye space) and perform the computations there. This works because the relative relationships between light sources, the camera, and the models are preserved if all entities that are included in the shading calculations are transformed to the same space.

Shading is discussed in more depth throughout this book, most specifically in Chapters 3 and 5.

### 2.3.3 Projection

After shading, rendering systems perform *projection*, which transforms the view volume into a unit cube with its extreme points at  $(-1, -1, -1)$  and  $(1, 1, 1)$ .<sup>3</sup> The unit cube is called the *canonical view volume*. There are two commonly used projection methods, namely *orthographic* (also called *parallel*)<sup>4</sup> and *perspective* projection. See Figure 2.5.

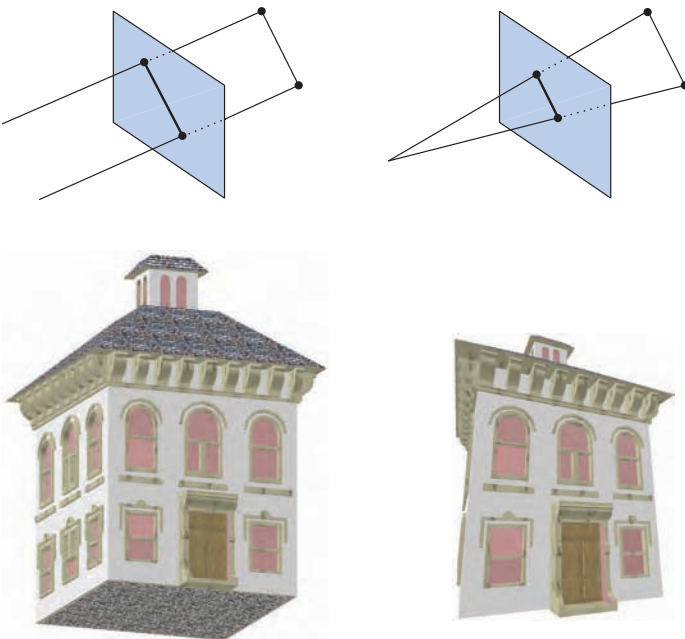


**Figure 2.5.** On the left is an orthographic, or parallel, projection; on the right is a perspective projection.

---

<sup>3</sup>Different volumes can be used, for example  $0 \leq z \leq 1$ . Blinn has an interesting article [102] on using other intervals.

<sup>4</sup>Actually, orthographic is just one type of parallel projection. For example, there is also an oblique parallel projection method [516], which is much less commonly used.

The view volume of orthographic viewing is normally a rectangular box, and the orthographic projection transforms this view volume into the unit cube. The main characteristic of orthographic projection is that parallel lines remain parallel after the transform. This transformation is a combination of a translation and a scaling.

The perspective projection is a bit more complex. In this type of projection, the farther away an object lies from the camera, the smaller it appears after projection. In addition, parallel lines may converge at the horizon. The perspective transform thus mimics the way we perceive objects' size. Geometrically, the view volume, called a *frustum*, is a truncated pyramid with rectangular base. The frustum is transformed into the unit cube as well. Both orthographic and perspective transforms can be constructed with  $4 \times 4$  matrices (see Chapter 4), and after either transform, the models are said to be in *normalized device coordinates*.

Although these matrices transform one volume into another, they are called projections because after display, the  $z$ -coordinate is not stored in the image generated.<sup>5</sup> In this way, the models are projected from three to two dimensions.

### 2.3.4 Clipping

Only the primitives wholly or partially inside the view volume need to be passed on to the rasterizer stage, which then draws them on the screen. A primitive that lies totally inside the view volume will be passed on to the next stage as is. Primitives entirely outside the view volume are not passed on further, since they are not rendered. It is the primitives that are partially inside the view volume that require *clipping*. For example, a line that has one vertex outside and one inside the view volume should be clipped against the view volume, so that the vertex that is outside is replaced by a new vertex that is located at the intersection between the line and the view volume. The use of a projection matrix means that the transformed primitives are clipped against the unit cube. The advantage of performing the view transformation and projection before clipping is that it makes the clipping problem consistent; primitives are always clipped against the unit cube. The clipping process is depicted in Figure 2.6. In addition to the six clipping planes of the view volume, the user can define additional clipping planes to visibly chop objects. An image showing this type of visualization, called *sectioning*, is shown in Figure 14.1 on page 646. Unlike the previous geometry stages, which are typically performed by programmable processing units, the clipping stage (as well as the subsequent screen mapping stage) is usually processed by fixed-operation hardware.

---

<sup>5</sup>Rather, the  $z$ -coordinate is stored in a  $Z$ -buffer. See Section 2.4.

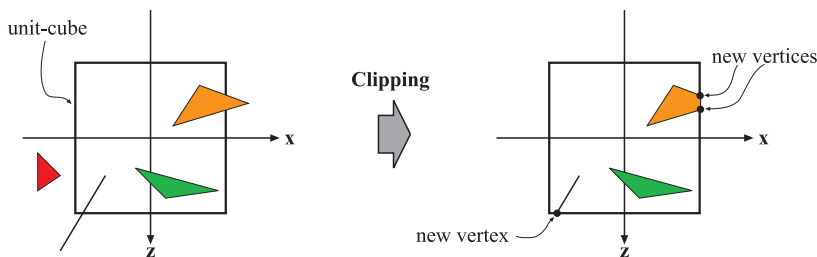


**Figure 2.6.** After the projection transform, only the primitives inside the unit cube (which correspond to primitives inside the view frustum) are needed for continued processing. Therefore, the primitives outside the unit cube are discarded and primitives totally inside are kept. Primitives intersecting with the unit cube are clipped against the unit cube, and thus new vertices are generated and old ones are discarded.

### 2.3.5 Screen Mapping

Only the (clipped) primitives inside the view volume are passed on to the screen mapping stage, and the coordinates are still three dimensional when entering this stage. The  $x$ - and  $y$ -coordinates of each primitive are transformed to form *screen coordinates*. Screen coordinates together with the  $z$ -coordinates are also called *window coordinates*. Assume that the scene should be rendered into a window with the minimum corner at  $(x_1, y_1)$  and the maximum corner at  $(x_2, y_2)$ , where  $x_1 < x_2$  and  $y_1 < y_2$ . Then the screen mapping is a translation followed by a scaling operation. The  $z$ -coordinate is not affected by this mapping. The new  $x$ - and  $y$ -coordinates are said to be screen coordinates. These, along with the  $z$ -coordinate ( $-1 \leq z \leq 1$ ), are passed on to the rasterizer stage. The screen mapping process is depicted in Figure 2.7.

A source of confusion is how integer and floating point values relate to pixel (and texture) coordinates. DirectX 9 and its predecessors use a

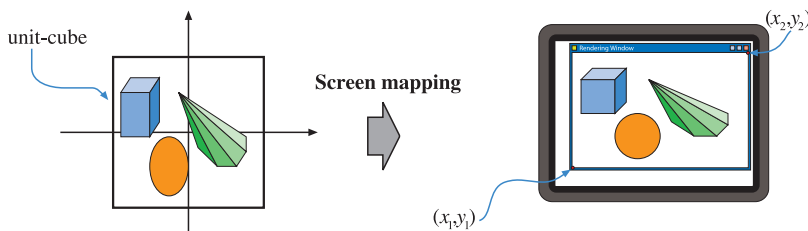


**Figure 2.7.** The primitives lie in the unit cube after the projection transform, and the screen mapping procedure takes care of finding the coordinates on the screen.

coordinate system where 0.0 is the center of the pixel, meaning that a range of pixels [0, 9] cover a span from [−0.5, 9.5). Heckbert [520] presents a more logically consistent scheme. Given a horizontal array of pixels and using Cartesian coordinates, the left edge of the leftmost pixel is 0.0 in floating point coordinates. OpenGL has always used this scheme, and DirectX 10 and its successors use it. The center of this pixel is at 0.5. So a range of pixels [0, 9] cover a span from [0.0, 10.0). The conversions are simply

$$d = \text{floor}(c), \quad (2.1)$$

$$c = d + 0.5, \quad (2.2)$$

where  $d$  is the discrete (integer) index of the pixel and  $c$  is the continuous (floating point) value within the pixel.

While all APIs have pixel location values that increase going from left to right, the location of zero for the top and bottom edges is inconsistent in some cases between OpenGL and DirectX.<sup>6</sup> OpenGL favors the Cartesian system throughout, treating the lower left corner as the lowest-valued element, while DirectX sometimes defines the upper left corner as this element, depending on the context. There is a logic to each, and no right answer exists where they differ. As an example, (0, 0) is located at the lower left corner of an image in OpenGL, while it is upper left for DirectX. The reasoning for DirectX is that a number of phenomena go from top to bottom on the screen: Microsoft Windows uses this coordinate system, we read in this direction, and many image file formats store their buffers in this way. The key point is that the difference exists and is important to take into account when moving from one API to the other.

## 2.4 The Rasterizer Stage

Given the transformed and projected vertices with their associated shading data (all from the geometry stage), the goal of the rasterizer stage is to compute and set colors for the pixels<sup>7</sup> covered by the object. This process is called *rasterization* or *scan conversion*, which is thus the conversion from two-dimensional vertices in screen space—each with a  $z$ -value (depth-value), and various shading information associated with each vertex—into pixels on the screen.

---

<sup>6</sup> “Direct3D” is the three-dimensional graphics API component of DirectX. DirectX includes other API elements, such as input and audio control. Rather than differentiate between writing “DirectX” when specifying a particular release and “Direct3D” when discussing this particular API, we follow common usage by writing “DirectX” throughout.

<sup>7</sup> Short for *picture elements*.

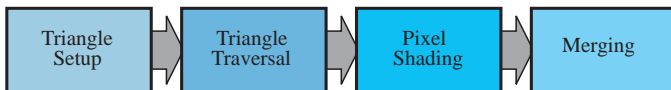


**Figure 2.8.** The rasterizer stage subdivided into a pipeline of functional stages.

Similar to the geometry stage, this stage is divided into several functional stages: triangle setup, triangle traversal, pixel shading, and merging (Figure 2.8).

### 2.4.1 Triangle Setup

In this stage the differentials and other data for the triangle's surface are computed. This data is used for scan conversion, as well as for interpolation of the various shading data produced by the geometry stage. This process is performed by fixed-operation hardware dedicated to this task.

### 2.4.2 Triangle Traversal

Here is where each pixel that has its center (or a sample) covered by the triangle is checked and a *fragment* generated for the part of the pixel that overlaps the triangle. Finding which samples or pixels are inside a triangle is often called *triangle traversal* or *scan conversion*. Each triangle fragment's properties are generated using data interpolated among the three triangle vertices (see Chapter 5). These properties include the fragment's depth, as well as any shading data from the geometry stage. Akeley and Jermoluk [7] and Rogers [1077] offer more information on triangle traversal.

### 2.4.3 Pixel Shading

Any per-pixel shading computations are performed here, using the interpolated shading data as input. The end result is one or more colors to be passed on to the next stage. Unlike the triangle setup and traversal stages, which are usually performed by dedicated, hardwired silicon, the pixel shading stage is executed by programmable GPU cores. A large variety of techniques can be employed here, one of the most important of which is *texturing*. Texturing is treated in more detail in Chapter 6. Simply put, texturing an object means “gluing” an image onto that object. This process is depicted in Figure 2.9. The image may be one-, two-, or three-dimensional, with two-dimensional images being the most common.



**Figure 2.9.** A dragon model without textures is shown in the upper left. The pieces in the image texture are “glued” onto the dragon, and the result is shown in the lower left.

#### 2.4.4 Merging

The information for each pixel is stored in the *color buffer*, which is a rectangular array of colors (a red, a green, and a blue component for each color). It is the responsibility of the merging stage to combine the fragment color produced by the shading stage with the color currently stored in the buffer. Unlike the shading stage, the GPU subunit that typically performs this stage is not fully programmable. However, it is highly configurable, enabling various effects.

This stage is also responsible for resolving visibility. This means that when the whole scene has been rendered, the color buffer should contain the colors of the primitives in the scene that are visible from the point of view of the camera. For most graphics hardware, this is done with the *Z-buffer* (also called *depth buffer*) algorithm [162].<sup>8</sup> A *Z-buffer* is the same size and shape as the color buffer, and for each pixel it stores the *z*-value from the camera to the currently closest primitive. This means that when a primitive is being rendered to a certain pixel, the *z*-value on that primitive at that pixel is being computed and compared to the contents of the *Z-buffer* at the same pixel. If the new *z*-value is smaller than the *z*-value in the *Z-buffer*, then the primitive that is being rendered is closer to the camera than the primitive that was previously closest to the camera at that pixel. Therefore, the *z*-value and the color of that pixel are updated

---

<sup>8</sup>When a *Z-buffer* is not available, a *BSP tree* can be used to help render a scene in back-to-front order. See Section 14.1.2 for information about BSP trees.

with the  $z$ -value and color from the primitive that is being drawn. If the computed  $z$ -value is greater than the  $z$ -value in the  $Z$ -buffer, then the color buffer and the  $Z$ -buffer are left untouched. The  $Z$ -buffer algorithm is very simple, has  $O(n)$  convergence (where  $n$  is the number of primitives being rendered), and works for any drawing primitive for which a  $z$ -value can be computed for each (relevant) pixel. Also note that this algorithm allows most primitives to be rendered in any order, which is another reason for its popularity. However, partially transparent primitives cannot be rendered in just any order. They must be rendered after all opaque primitives, and in back-to-front order (Section 5.7). This is one of the major weaknesses of the  $Z$ -buffer.

We have mentioned that the color buffer is used to store colors and that the  $Z$ -buffer stores  $z$ -values for each pixel. However, there are other channels and buffers that can be used to filter and capture fragment information. The *alpha channel* is associated with the color buffer and stores a related opacity value for each pixel (Section 5.7). An optional *alpha test* can be performed on an incoming fragment before the depth test is performed.<sup>9</sup> The alpha value of the fragment is compared by some specified test (equals, greater than, etc.) to a reference value. If the fragment fails to pass the test, it is removed from further processing. This test is typically used to ensure that fully transparent fragments do not affect the  $Z$ -buffer (see Section 6.6).

The *stencil buffer* is an offscreen buffer used to record the locations of the rendered primitive. It typically contains eight bits per pixel. Primitives can be rendered into the stencil buffer using various functions, and the buffer's contents can then be used to control rendering into the color buffer and  $Z$ -buffer. As an example, assume that a filled circle has been drawn into the stencil buffer. This can be combined with an operator that allows rendering of subsequent primitives into the color buffer only where the circle is present. The stencil buffer is a powerful tool for generating special effects. All of these functions at the end of the pipeline are called *raster operations* (ROP) or *blend operations*.

The *frame buffer* generally consists of all the buffers on a system, but it is sometimes used to mean just the color buffer and  $Z$ -buffer as a set. In 1990, Haeberli and Akeley [474] presented another complement to the frame buffer, called the *accumulation buffer*. In this buffer, images can be accumulated using a set of operators. For example, a set of images showing an object in motion can be accumulated and averaged in order to generate motion blur. Other effects that can be generated include depth of field, antialiasing, soft shadows, etc.

---

<sup>9</sup>In DirectX 10, the alpha test is no longer part of this stage, but rather a function of the pixel shader.

When the primitives have reached and passed the rasterizer stage, those that are visible from the point of view of the camera are displayed on screen. The screen displays the contents of the color buffer. To avoid allowing the human viewer to see the primitives as they are being rasterized and sent to the screen, *double buffering* is used. This means that the rendering of a scene takes place off screen, in a *back buffer*. Once the scene has been rendered in the back buffer, the contents of the back buffer are swapped with the contents of the *front buffer* that was previously displayed on the screen. The swapping occurs during *vertical retrace*, a time when it is safe to do so.

For more information on different buffers and buffering methods, see Sections 5.6.2 and 18.1.

## 2.5 Through the Pipeline

Points, lines, and triangles are the rendering primitives from which a model or an object is built. Imagine that the application is an interactive *computer aided design* (CAD) application, and that the user is examining a design for a cell phone. Here we will follow this model through the entire graphics rendering pipeline, consisting of the three major stages: application, geometry, and the rasterizer. The scene is rendered with perspective into a window on the screen. In this simple example, the cell phone model includes both lines (to show the edges of parts) and triangles (to show the surfaces). Some of the triangles are textured by a two-dimensional image, to represent the keyboard and screen. For this example, shading is computed completely in the geometry stage, except for application of the texture, which occurs in the rasterization stage.

### *Application*

CAD applications allow the user to select and move parts of the model. For example, the user might select the top part of the phone and then move the mouse to flip the phone open. The application stage must translate the mouse move to a corresponding rotation matrix, then see to it that this matrix is properly applied to the lid when it is rendered. Another example: An animation is played that moves the camera along a predefined path to show the cell phone from different views. The camera parameters, such as position and view direction, must then be updated by the application, dependent upon time. For each frame to be rendered, the application stage feeds the camera position, lighting, and primitives of the model to the next major stage in the pipeline—the geometry stage.

### *Geometry*

The view transform was computed in the application stage, along with a model matrix for each object that specifies its location and orientation. For

each object passed to the geometry stage, these two matrices are usually multiplied together into a single matrix. In the geometry stage the vertices and normals of the object are transformed with this concatenated matrix, putting the object into eye space. Then shading at the vertices is computed, using material and light source properties. Projection is then performed, transforming the object into a unit cube’s space that represents what the eye sees. All primitives outside the cube are discarded. All primitives intersecting this unit cube are clipped against the cube in order to obtain a set of primitives that lies entirely inside the unit cube. The vertices then are mapped into the window on the screen. After all these per-polygon operations have been performed, the resulting data is passed on to the rasterizer—the final major stage in the pipeline.

### Rasterizer

In this stage, all primitives are rasterized, i.e., converted into pixels in the window. Each visible line and triangle in each object enters the rasterizer in screen space, ready to convert. Those triangles that have been associated with a texture are rendered with that texture (image) applied to them. Visibility is resolved via the Z-buffer algorithm, along with optional alpha and stencil tests. Each object is processed in turn, and the final image is then displayed on the screen.

## Conclusion

This pipeline resulted from decades of API and graphics hardware evolution targeted to real-time rendering applications. It is important to note that this is not the only possible rendering pipeline; offline rendering pipelines have undergone different evolutionary paths. Rendering for film production is most commonly done with *micropolygon* pipelines [196, 1236]. Academic research and *predictive rendering* applications such as architectural pre-visualization usually employ *ray tracing* renderers (see Section 9.8.2).

For many years, the only way for application developers to use the process described here was through a *fixed-function pipeline* defined by the graphics API in use. The fixed-function pipeline is so named because the graphics hardware that implements it consists of elements that cannot be programmed in a flexible way. Various parts of the pipeline can be set to different states, e.g., Z-buffer testing can be turned on or off, but there is no ability to write programs to control the order in which functions are applied at various stages. The latest (and probably last) example of a fixed-function machine is Nintendo’s Wii. Programmable GPUs make it possible to determine exactly what operations are applied in various sub-stages throughout the pipeline. While studying the fixed-function pipeline provides a reasonable introduction to some basic principles, most new de-

velopment is aimed at programmable GPUs. This programmability is the default assumption for this third edition of the book, as it is the modern way to take full advantage of the GPU.

## Further Reading and Resources

Blinn's book *A Trip Down the Graphics Pipeline* [105] is an older book about writing a software renderer from scratch, but is a good resource for learning about some of the subtleties of implementing a rendering pipeline. For the fixed-function pipeline, the venerable (yet frequently updated) *OpenGL Programming Guide* (a.k.a., the “Red Book”) [969] provides a thorough description of the fixed-function pipeline and algorithms related to its use. Our book’s website, <http://www.realtimerendering.com>, gives links to a variety of rendering engine implementations.



# Chapter 3

## The Graphics Processing Unit

*“The display is the computer.”*

—Jen-Hsun Huang

Historically, hardware graphics acceleration has started at the end of the pipeline, first performing rasterization of a triangle’s scanlines. Successive generations of hardware have then worked back up the pipeline, to the point where some higher level application-stage algorithms are being committed to the hardware accelerator. Dedicated hardware’s only advantage over software is speed, but speed is critical.

Over the past decade, graphics hardware has undergone an incredible transformation. The first consumer graphics chip to include hardware vertex processing (NVIDIA’s GeForce256) shipped in 1999. NVIDIA coined the term *graphics processing unit* (GPU) to differentiate the GeForce 256 from the previously available rasterization-only chips, and it stuck [898]. Over the next few years, the GPU evolved from configurable implementations of a complex fixed-function pipeline to highly programmable “blank slates” where developers could implement their own algorithms. Programmable *shaders* of various kinds are the primary means by which the GPU is controlled. The vertex shader enables various operations (including transformations and deformations) to be performed on each vertex. Similarly, the pixel shader processes individual pixels, allowing complex shading equations to be evaluated per pixel. The geometry shader allows the GPU to create and destroy geometric primitives (points, lines, triangles) on the fly. Computed values can be written to multiple high-precision buffers and reused as vertex or texture data. For efficiency, some parts of the pipeline remain configurable, not programmable, but the trend is towards programmability and flexibility [123].

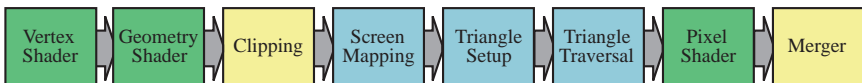


**Figure 3.1.** GPU implementation of the rendering pipeline. The stages are color coded according to the degree of user control over their operation. Green stages are fully programmable. Yellow stages are configurable but not programmable, e.g., the clipping stage can optionally perform culling or add user-defined clipping planes. Blue stages are completely fixed in their function.

## 3.1 GPU Pipeline Overview

The GPU implements the geometry and rasterization conceptual pipeline stages described in Chapter 2. These are divided into several hardware stages with varying degrees of configurability or programmability. Figure 3.1 shows the various stages color coded according to how programmable or configurable they are. Note that these physical stages are split up slightly differently than the functional stages presented in Chapter 2.

The vertex shader is a fully programmable stage that is typically used to implement the “Model and View Transform,” “Vertex Shading,” and “Projection” functional stages. The geometry shader is an optional, fully programmable stage that operates on the vertices of a primitive (point, line or triangle). It can be used to perform per-primitive shading operations, to destroy primitives, or to create new ones. The clipping, screen mapping, triangle setup, and triangle traversal stages are fixed-function stages that implement the functional stages of the same names. Like the vertex and geometry shaders, the pixel shader is fully programmable and performs the “Pixel Shading” function stage. Finally, the merger stage is somewhere between the full programmability of the shader stages and the fixed operation of the other stages. Although it is not programmable, it is highly configurable and can be set to perform a wide variety of operations. Of course, it implements the “Merging” functional stage, in charge of modifying the color, Z-buffer, blend, stencil, and other related buffers.

Over time, the GPU pipeline has evolved away from hard-coded operation and toward increasing flexibility and control. The introduction of programmable shader stages was the most important step in this evolution. The next section describes the features common to the various programmable stages.

## 3.2 The Programmable Shader Stage

Modern shader stages (i.e., those that support Shader Model 4.0, DirectX 10 and later, on Vista) use a *common-shader core*. This means that the

vertex, pixel, and geometry shaders share a programming model. We differentiate in this book between the common-shader core, the functional description seen by the applications programmer, and unified shaders, a GPU architecture that maps well to this core. See Section 18.4. The common-shader core is the API; having unified shaders is a GPU feature. Earlier GPUs had less commonality between vertex and pixel shaders and did not have geometry shaders. Nonetheless, most of the design elements for this model are shared by older hardware; for the most part, older versions' design elements are either simpler or missing, not radically different. So, for now we will focus on Shader Model 4.0 and discuss older GPUs' shader models in later sections.

Describing the entire programming model is well beyond the scope of this book, and there are many documents, books, and websites that already do so [261, 338, 647, 1084]. However, a few comments are in order. Shaders are programmed using C-like *shading languages* such as *HLSL*, *Cg*, and *GLSL*. These are compiled to a machine-independent assembly language, also called the *intermediate language* (IL). Previous shader models allowed programming directly in the assembly language, but as of DirectX 10, programs in this language are visible as debug output only [123]. This assembly language is converted to the actual machine language in a separate step, usually in the drivers. This arrangement allows compatibility across different hardware implementations. This assembly language can be seen as defining a virtual machine, which is targeted by the shading language compiler.

This virtual machine is a processor with various types of registers and data sources, programmed with a set of instructions. Since many graphics operations are done on short vectors (up to length 4), the processor has 4-way SIMD (*single-instruction multiple-data*) capabilities. Each register contains four independent values. 32-bit single-precision floating-point scalars and vectors are the basic data types; support for 32-bit integers has recently been added, as well. Floating-point vectors typically contain data such as positions ( $xyzw$ ), normals, matrix rows, colors ( $rgba$ ), or texture coordinates ( $uvwq$ ). Integers are most often used to represent counters, indices, or bit masks. Aggregate data types such as structures, arrays, and matrices are also supported. To facilitate working with vectors, *swizzling*, the replication of any vector component, is also supported. That is, a vector's elements can be reordered or duplicated as desired. Similarly, *masking*, where only the specified vector elements are used, is also supported.

A *draw call* invokes the graphics API to draw a group of primitives, so causing the graphics pipeline to execute. Each programmable shader stage has two types of inputs: *uniform* inputs, with values that remain constant throughout a draw call (but can be changed between draw calls),

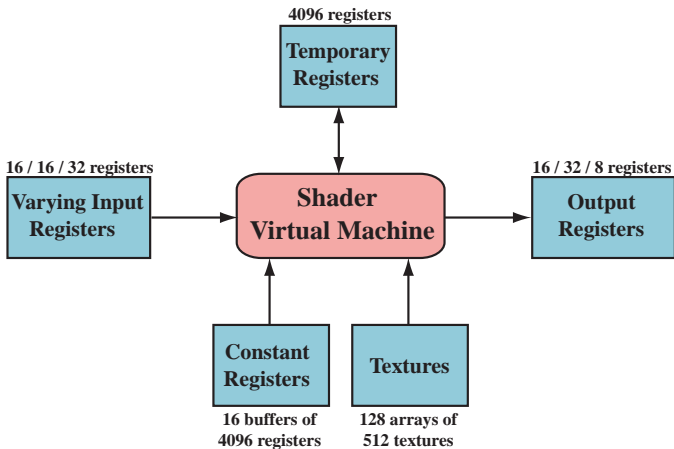


**Figure 3.2.** Common-shader core virtual machine architecture and register layout, under DirectX 10. The maximum available number is indicated next to each resource. Three numbers separated by slashes refer to the limits for vertex, geometry, and pixel shaders (from left to right).

and *varying* inputs, which are different for each vertex or pixel processed by the shader. A texture is a special kind of uniform input that once was always a color image applied to a surface, but that now can be thought of as any large array of data. It is important to note that although shaders have a wide variety of inputs, which they can address in different ways, the outputs are extremely constrained. This is the most significant way in which shaders are different from programs executing on general-purpose processors. The underlying virtual machine provides special registers for the different types of inputs and outputs. Uniform inputs are accessed via read-only *constant registers* or *constant buffers*, so called because their contents are constant across a draw call. The number of available constant registers is much larger than the number of registers available for varying inputs or outputs. This is because the varying inputs and outputs need to be stored separately for each vertex or pixel, and the uniform inputs are stored once and reused across all the vertices or pixels in the draw call. The virtual machine also has general-purpose *temporary registers*, which are used for scratch space. All types of registers can be array-indexed using integer values in temporary registers. The inputs and outputs of the shader virtual machine can be seen in Figure 3.2.

Operations that are common in graphics computations are efficiently executed on modern GPUs. Typically, the fastest operations are scalar and vector multiplications, additions, and their combinations, such as multiply-add and dot-product. Other operations, such as reciprocal, square root,

sine, cosine, exponentiation, and logarithm, tend to be slightly more costly but still fairly speedy. Texturing operations (see Chapter 6) are efficient, but their performance may be limited by factors such as the time spent waiting to retrieve the result of an access. Shading languages expose the most common of these operations (such as additions and multiplications) via operators such as `*` and `+`. The rest are exposed through *intrinsic functions*, e.g., `atan()`, `dot()`, `log()`, and many others. Intrinsic functions also exist for more complex operations, such as vector normalization and reflection, cross products, matrix transpose and determinant, etc.

The term *flow control* refers to the use of branching instructions to change the flow of code execution. These instructions are used to implement high-level language constructs such as “if” and “case” statements, as well as various types of loops. Shaders support two types of flow control. *Static flow control* branches are based on the values of uniform inputs. This means that the flow of the code is constant over the draw call. The primary benefit of static flow control is to allow the same shader to be used in a variety of different situations (e.g., varying numbers of lights). *Dynamic flow control* is based on the values of varying inputs. This is much more powerful than static flow control but is more costly, especially if the code flow changes erratically between shader invocations. As discussed in Section 18.4.2, a shader is evaluated on a number of vertices or pixels at a time. If the flow selects the “if” branch for some elements and the “else” branch for others, both branches must be evaluated for all elements (and the unused branch for each element is discarded).

Shader programs can be compiled offline before program load or during run time. As with any compiler, there are options for generating different output files and for using different optimization levels. A compiled shader is stored as a string of text, which is passed to the GPU via the driver.

### 3.3 The Evolution of Programmable Shading

The idea of a framework for programmable shading dates back to 1984 with Cook’s *shade trees* [194]. A simple shader and its corresponding shade tree are shown in Figure 3.3. The RenderMan Shading Language [30, 1283] was developed from this idea in the late 80’s and is still widely used today for film production rendering. Before GPUs supported programmable shaders natively, there were several attempts to implement programmable shading operations in real time via multiple rendering passes. The *Quake III: Arena* scripting language was the first widespread commercial success in this area in 1999 [558, 604]. In 2000, Peercy et al. [993] described a system that translated RenderMan shaders to run in multiple passes on graphics hardware. They found that GPUs lacked two features that would make this approach

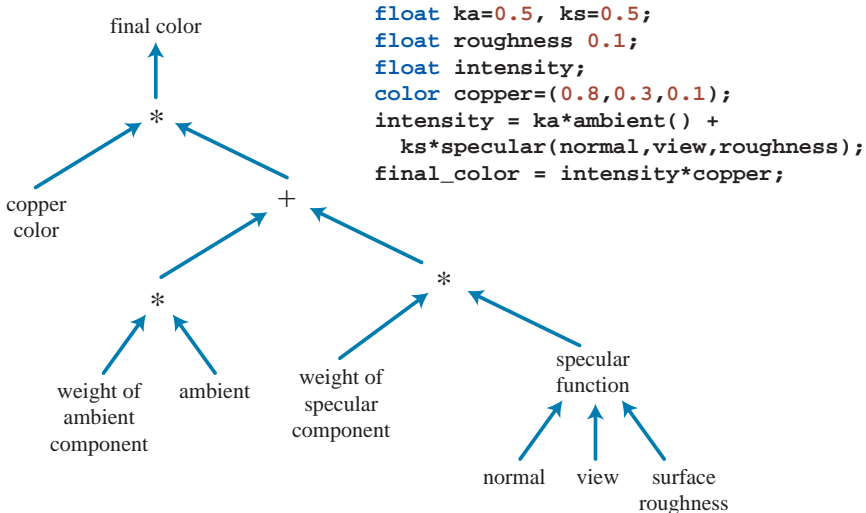


**Figure 3.3.** Shade tree for a simple copper shader, and its corresponding shader language program. (After Cook [194].)

very general: the ability to use computation results as texture coordinates (*dependent texture reads*), and support for data types with extended range and precision in textures and color buffers. One of the proposed data types was a novel (at the time) 16-bit floating point representation. At this time, no commercially available GPU supported programmable shading, although most had highly configurable pipelines [898].

In early 2001, NVIDIA's GeForce 3 was the first GPU to support programmable vertex shaders [778], exposed through DirectX 8.0 and extensions to OpenGL. These shaders were programmed in an assembly-like language that was converted by the drivers into microcode on the fly. Pixel shaders were also included in DirectX 8.0, but pixel shader SM 1.1 fell short of actual programmability—the very limited “programs” supported were converted into texture blending states by the driver, which in turn wired together hardware “register combiners.” These “programs” were not only limited in length (12 instructions or less) but also lacked the two elements (dependent texture reads<sup>1</sup> and float data) that Peercy et al. had identified as crucial to true programmability.

Shaders at this time did not allow for flow control (branching), so conditionals had to be emulated by computing both terms and selecting or interpolating between the results. DirectX defined the concept of a

<sup>1</sup>The GeForce 3 did support a dependent texture read of sorts, but only in an extremely limited fashion.

*Shader Model* to distinguish hardware with different shader capabilities. The GeForce 3 supported vertex shader model 1.1 and pixel shader model 1.1 (shader model 1.0 was intended for hardware that never shipped). During 2001, GPUs progressed closer to a general pixel shader programming model. DirectX 8.1 added pixel shader models 1.2 to 1.4 (each meant for different hardware), which extended the capabilities of the pixel shader further, adding additional instructions and more general support for dependent texture reads.

The year 2002 saw the release of DirectX 9.0 including Shader Model 2.0 (and its extended version 2.X), which featured truly programmable vertex and pixel shaders. Similar functionality was also exposed under OpenGL using various extensions. Support for arbitrary dependent texture reads and storage of 16-bit floating point values was added, finally completing the set of requirements identified by Peercy et al. in 2000 [993]. Limits on shader resources such as instructions, textures, and registers were increased, so shaders became capable of more complex effects. Support for flow control was also added. The growing length and complexity of shaders made the assembly programming model increasingly cumbersome. Fortunately, DirectX 9.0 also included a new shader programming language called HLSL (High Level Shading Language). HLSL was developed by Microsoft in collaboration with NVIDIA, which released a cross-platform variant called Cg [818]. Around the same time, the OpenGL ARB (Architecture Review Board) released a somewhat similar language for OpenGL, called GLSL [647, 1084] (also known as GLslang). These languages were heavily influenced by the syntax and design philosophy of the C programming language and also included elements from the RenderMan Shading Language.

Shader Model 3.0 was introduced in 2004 and was an incremental improvement, turning optional features into requirements, further increasing resource limits and adding limited support for texture reads in vertex shaders. When a new generation of game consoles was introduced in late 2005 (Microsoft’s Xbox 360) and 2006 (Sony Computer Entertainment’s PLAYSTATION® 3 system), they were equipped with Shader Model 3.0–level GPUs. The fixed-function pipeline is not entirely dead: Nintendo’s Wii console shipped in late 2006 with a fixed-function GPU [207]). However, this is almost certainly the last console of this type, as even mobile devices such as cell phones can use programmable shaders (see Section 18.4.3).

Other languages and environments for shader development are available. For example, the *Sh* language [837, 838] allows the generation and combination [839] of GPU shaders through a C++ library. This open-source project runs on a number of platforms. On the other end of the spectrum, several visual programming tools have been introduced to allow artists (most of whom are not comfortable programming in C-like languages) to

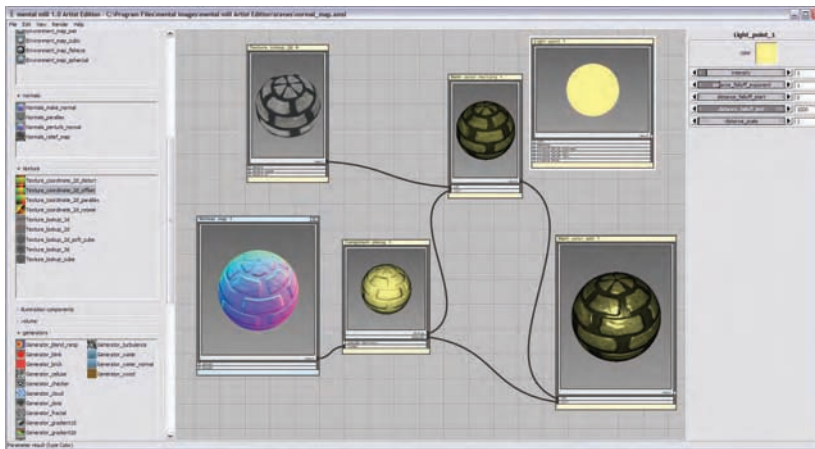


**Figure 3.4.** A visual shader graph system for shader design. Various operations are encapsulated in function boxes, selectable on the left. When selected, each function box has adjustable parameters, shown on the right. Inputs and outputs for each function box are linked to each other to form the final result, shown in the lower right of the center frame. (*Screenshot from “mental mill,” mental images, inc.*)

design shaders. Such tools include visual graph editors used to link predefined shader building blocks, as well as compilers to translate the resulting graphs to shading languages such as HLSL. A screenshot of one such tool (*mental mill*, which is included in NVIDIA’s FX Composer 2) is shown in Figure 3.4. McGuire et al. [847] survey visual shader programming systems and propose a high-level, abstract extension of the concept.

The next large step in programmability came in 2007. Shader Model 4.0 (included in DirectX 10.0 [123] and also available in OpenGL via extensions), introduced several major features, such as the geometry shader and stream output.

Shader Model 4.0 included a uniform programming model for all shaders (vertex, pixel and geometry), the common-shader core described earlier. Resource limits were further increased, and support for integer data types (including bitwise operations) was added. Shader Model 4.0 also is notable in that it supports only high-level language shaders (HLSL for DirectX and GLSL for OpenGL)—there is no user-writable assembly language interface, such as found in previous models.

GPU vendors, Microsoft, and the OpenGL ARB continue to refine and extend the capabilities of programmable shading. Besides new versions of existing APIs, new programming models such as NVIDIA’s *CUDA* [211] and AMD’s *CTM* [994] have been targeted at non-graphics applications. This area of general-purpose computations on the GPU (GPGPU) is briefly discussed in Section 18.3.1.

### 3.3.1 Comparison of Shader Models

Although this chapter focuses on Shader Model 4.0 (the newest at time of writing), often developers need to support hardware that uses older shading models. For this reason we give a brief comparison between the capabilities of several recent shading models: 2.0 (and its extended version of 2.X), 3.0 and 4.0.<sup>2</sup> A listing of all the differences is beyond the scope of this book; detailed information is available from the Microsoft Developer Network (MSDN) and their DirectX SDK [261].

We focus on DirectX here, because of its distinct releases, versus OpenGL's evolving levels of extensions, some approved by the OpenGL Architecture Review Board (ARB), some vendor-specific. This extension system has the advantage that cutting-edge features from a specific *independent hardware vendor* (IHV) can be used immediately. DirectX 9 and earlier support IHW variations by exposing “capability bits” that can be examined to see if a GPU supports a feature. With DirectX 10, Microsoft has moved sharply away from this practice and toward a standardized model that all IHWs must support. Despite the focus here on DirectX, the following discussion also has relevance to OpenGL, in that the associated underlying GPUs of the same time periods have the same features.

Table 3.1 compares the capabilities of the various shader models. In the table, “VS” stands for “vertex shader” and “PS” for “pixel shader” (Shader Model 4.0 introduced the geometry shader, with capabilities similar to those of the vertex shader). If neither “VS” nor “PS” appears, the row applies to both vertex and pixel shaders. Since the virtual machine is 4-way SIMD, each register can store between one and four independent values. “Instruction Slots” refers to the maximum number of instructions that the shader can contain. “Max. Steps Executed” indicates the maximum number of instructions that can be executed, taking branching and looping into account. “Temp. Registers” shows the number of general-purpose registers that are available for storing intermediate results. “Constant Registers” indicates the number of constant values that can be input to the shader. “Flow Control, Predication” refers to the ability to compute conditional expressions and execute loops via branching instructions and predication (i.e., the ability to conditionally execute or skip an instruction). “Textures” shows the number of distinct textures (see Chapter 6) that can be accessed by the shader (each texture may be accessed multiple times). “Integer Support” refers to the ability to operate on integer data types with bitwise operators and integer arithmetic. “VS Input Registers” shows the number of varying input registers that can be accessed by the vertex shader. “Interpolator Registers” are output registers for the vertex shader and input

---

<sup>2</sup>Shader Models 1.0 through 1.4 were early, limited versions that are no longer actively used.

|                                  | <b>SM 2.0/2.X</b>     | <b>SM 3.0</b>  | <b>SM 4.0</b>      |
|----------------------------------|-----------------------|----------------|--------------------|
| <b>Introduced</b>                | DX 9.0, 2002          | DX 9.0c, 2004  | DX 10, 2007        |
| <b>VS Instruction Slots</b>      | 256                   | $\geq 512^a$   | 4096               |
| <b>VS Max. Steps Executed</b>    | 65536                 | 65536          | $\infty$           |
| <b>PS Instruction Slots</b>      | $\geq 96^b$           | $\geq 512^a$   | $\geq 65536^a$     |
| <b>PS Max. Steps Executed</b>    | $\geq 96^b$           | 65536          | $\infty$           |
| <b>Temp. Registers</b>           | $\geq 12^a$           | 32             | 4096               |
| <b>VS Constant Registers</b>     | $\geq 256^a$          | $\geq 256^a$   | $14 \times 4096^c$ |
| <b>PS Constant Registers</b>     | 32                    | 224            | $14 \times 4096^c$ |
| <b>Flow Control, Predication</b> | Optional <sup>d</sup> | Yes            | Yes                |
| <b>VS Textures</b>               | None                  | 4 <sup>e</sup> | $128 \times 512^f$ |
| <b>PS Textures</b>               | 16                    | 16             | $128 \times 512^f$ |
| <b>Integer Support</b>           | No                    | No             | Yes                |
| <b>VS Input Registers</b>        | 16                    | 16             | 16                 |
| <b>Interpolator Registers</b>    | 8 <sup>g</sup>        | 10             | $16/32^h$          |
| <b>PS Output Registers</b>       | 4                     | 4              | 8                  |

<sup>a</sup>Minimum requirement (more can be used if available).

<sup>b</sup>Minimum of 32 texture and 64 arithmetic instructions.

<sup>c</sup>14 constant buffers exposed (+2 private, reserved for Microsoft/IHVs), each of which can contain a maximum of 4096 constants.

<sup>d</sup>Vertex shaders are required to support static flow control (based on constant values).

<sup>e</sup>SM 3.0 hardware typically has very limited formats and no filtering for vertex textures.

<sup>f</sup>Up to 128 texture arrays, each of which can contain a maximum of 512 textures.

<sup>g</sup>Not including 2 color interpolators with limited precision and range.

<sup>h</sup>Vertex shader outputs 16 interpolators, which the geometry shader can expand to 32.

**Table 3.1.** Shader capabilities, listed by DirectX shader model version [123, 261, 946, 1055].

registers for the pixel shader. They are so called because the values output from the vertex shader are interpolated over the triangle before being sent to the pixel shader. Finally, “PS Output Registers” shows the number of registers that can be output from the pixel shader—each one is bound to a different buffer, or *render target*.

## 3.4 The Vertex Shader

The vertex shader is the first stage in the functional pipeline shown in Figure 3.1. While this is the first stage that does any graphical processing, it is worth noting that some data manipulation happens before this stage. In what DirectX calls the *input assembler* [123, 261], a number of streams of data can be woven together to form the sets of vertices and primitives sent down the pipeline. For example, an object could be represented by one array of positions and one array of colors. The input assembler would create

this object’s triangles (or lines or points) by essentially creating vertices with positions and colors. A second object could use the same array of positions (along with a different model transform matrix) and a different array of colors for its representation. Data representation is discussed in detail in Section 12.4.5. There is also support in the input assembler to perform *instancing*. This allows an object to be drawn a number of times with some varying data per instance, all with a single draw call. The use of instancing is covered in Section 15.4.2. The input assembler in DirectX 10 also tags each instance, primitive, and vertex with an identifier number that can be accessed by any of the shader stages that follow. For earlier shader models, such data has to be added explicitly to the model.

A triangle mesh is represented by a set of vertices and additional information describing which vertices form each triangle. The vertex shader is the first stage to process the triangle mesh. The data describing what triangles are formed is unavailable to the vertex shader; as its name implies, it deals exclusively with the incoming vertices. In general terms, the vertex shader provides a way to modify, create, or ignore values associated with each polygon’s vertex, such as its color, normal, texture coordinates, and position. Normally the vertex shader program transforms vertices from model space to homogeneous clip space; at a minimum, a vertex shader must always output this location.

This functionality was first introduced in 2001 with DirectX 8. Because it was the first stage on the pipeline and invoked relatively infrequently, it could be implemented on either the GPU or the CPU, which would then send on the results to the GPU for rasterization. Doing so made the transition from older to newer hardware a matter of speed, not functionality. All GPUs currently produced support vertex shading.

A vertex shader itself is very much the same as the common core virtual machine described earlier in Section 3.2. Every vertex passed in is processed by the vertex shader program, which then outputs a number of values that are interpolated across a triangle or line.<sup>3</sup> The vertex shader can neither create nor destroy vertices, and results generated by one vertex cannot be passed on to another vertex. Since each vertex is treated independently, any number of shader processors on the GPU can be applied in parallel to the incoming stream of vertices.

Chapters that follow explain a number of vertex shader effects, such as shadow volume creation, vertex blending for animating joints, and silhouette rendering. Other uses for the vertex shader include:

- Lens effects, so that the screen appears fish-eyed, underwater, or otherwise distorted.

---

<sup>3</sup>Older shader models also supported output of the size of a point sprite particle object, but sprite functionality is now part of the geometry shader.



**Figure 3.5.** On the left, a normal teapot. A simple shear operation performed by a vertex shader program produces the middle image. On the right, a noise function creates a field that distorts the model. (*Images produced by FX Composer 2, courtesy of NVIDIA Corporation.*)

- Object definition, by creating a mesh only once and having it be deformed by the vertex shader.
- Object twist, bend, and taper operations.
- Procedural deformations, such as the movement of flags, cloth, or water [592].
- Primitive creation, by sending degenerate meshes down the pipeline and having these be given an area as needed. This functionality is replaced by the geometry shader in newer GPUs.
- Page curls, heat haze, water ripples, and other effects can be done by using the entire frame buffer's contents as a texture on a screen-aligned mesh undergoing procedural deformation.
- Vertex texture fetch (available in SM 3.0 on up) can be used to apply textures to vertex meshes, allowing ocean surfaces and terrain height fields to be applied inexpensively [23, 703, 887].

Some deformations done using a vertex shader are shown in Figure 3.5.

The output of the vertex shader can be consumed in a number of different ways. The usual path is for each instance's triangles to then be generated and rasterized, and the individual pixel fragments produced sent to the pixel shader program for continued processing. With the introduction of Shader Model 4.0, the data can also be sent to the geometry shader, streamed out, or both. These options are the subject of the next section.

## 3.5 The Geometry Shader

The geometry shader was added to the hardware-accelerated graphics pipeline with the release of DirectX 10, in late 2006. It is located immediately

after the vertex shader in the pipeline, and its use is optional. While a required part of Shader Model 4.0, it is not used in earlier shader models.

The input to the geometry shader is a single object and its associated vertices. The object is typically a triangle in a mesh, a line segment, or simply a point. In addition, extended primitives can be defined and processed by the geometry shader. In particular, three additional vertices outside of a triangle can be passed in, and the two adjacent vertices on a polyline can be used. See Figure 3.6.

The geometry shader processes this primitive and outputs zero or more primitives. Output is in the form of points, polylines, and triangle strips. More than one triangle strip, for example, can be output by a single invocation of the geometry shader program. As important, no output at all can be generated by the geometry shader. In this way, a mesh can be selectively modified by editing vertices, adding new primitives, and removing others.

The geometry shader program is set to input one type of object and output one type of object, and these types do not have to match. For example, triangles could be input and their centroids be output as points, one per triangle input. Even if input and output object types match, the data carried at each vertex can be omitted or expanded. As an example, the triangle's plane normal could be computed and added to each output vertex's data. Similar to the vertex shader, the geometry shader must output a homogeneous clip space location for each vertex produced.

The geometry shader is guaranteed to output results from primitives in the same order as they are input. This affects performance, because if a number of shader units run in parallel, results must be saved and ordered. As a compromise between capability and efficiency, there is a limit in Shader Model 4.0 of a total of 1024 32-bit values that can be generated per execution. So, generating a thousand bush leaves given a single leaf as input is not feasible and is not the recommended use of the geometry shader. Tessellation of simple surfaces into more elaborate triangle meshes is also not recommended [123]. This stage is more about programmatically modifying incoming data or making a limited number of copies, not about

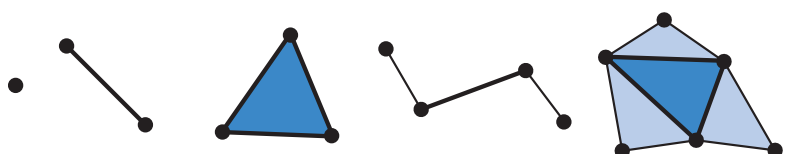


**Figure 3.6.** Geometry shader input for a geometry shader program is of some single type: point, line segment, triangle. The two rightmost primitives, which include vertices adjacent to the line and triangle objects, can also be used.



**Figure 3.7.** Some uses of the geometry shader. On the left, metaball isosurface tessellation is performed on the fly using the GS. In the middle, fractal subdivision of line segments is done using the GS and stream out, and billboards are generated by the GS for display. On the right, cloth simulation is performed by using the vertex and geometry shader with stream out. (*Images from NVIDIA SDK 10 [945] samples courtesy of NVIDIA Corporation.*)

massively replicating or amplifying it. For example, one use is to generate six transformed copies of data in order to simultaneously render the six faces of a cube map; see Section 8.4.3. Additional algorithms that can take advantage of the geometry shader include creating various sized particles from point data, extruding fins along silhouettes for fur rendering, and finding object edges for shadow algorithms. See Figure 3.7 for still more. These and other uses are discussed throughout the rest of the book.

### 3.5.1 Stream Output

The standard use of the GPU’s pipeline is to send data through the vertex shader, then rasterize the resulting triangles and process these in the pixel shader. The data always passed through the pipeline and intermediate results could not be accessed. The idea of *stream output* was introduced in Shader Model 4.0. After vertices are processed by the vertex shader (and, optionally, the geometry shader), these can be output in a stream, i.e., an ordered array, in addition to being sent on to the rasterization stage. Rasterization could, in fact, be turned off entirely and the pipeline then used purely as a non-graphical stream processor. Data processed in this way can be sent back through the pipeline, thus allowing iterative processing. This type of operation is particularly useful for simulating flowing water or other particle effects, as discussed in Section 10.7.

## 3.6 The Pixel Shader

After the vertex and geometry shaders perform their operations, the primitive is clipped and set up for rasterization, as explained in the last chapter.

This section of the pipeline is relatively fixed in its processing steps, not programmable.<sup>4</sup> Each triangle is traversed and the values at the vertices interpolated across the triangle's area. The pixel shader is the next programmable stage. In OpenGL this stage is known as the *fragment shader*, which in some ways is a better name. The idea is that a triangle covers each pixel's cell fully or partially, and the material portrayed is opaque or transparent. The rasterizer does not directly affect the pixel's stored color, but rather generates data that, to a greater or lesser extent, describes how the triangle covers the pixel cell. It is then during merging that this fragment's data is used to modify what is stored at the pixel.

The vertex shader program's outputs effectively become the pixel shader program's inputs. A total of 16 vectors (4 values each) can be passed from the vertex shader to the pixel shader in Shader Model 4.0.<sup>5</sup> When the geometry shader is used, it can output 32 vectors to the pixel shader [261].

Additional inputs were added specifically for the pixel shader with the introduction of Shader Model 3.0. For example, which side of a triangle is visible was added as an input flag. This knowledge is important for rendering a different material on the front versus back of each triangle in a single pass. The screen position of the fragment is also available to the pixel shader.

The pixel shader's limitation is that it can influence only the fragment handed it. That is, when a pixel shader program executes, it cannot send its results directly to neighboring pixels. Rather, it uses the data interpolated from the vertices, along with any stored constants and texture data, to compute results that will affect only a single pixel. However, this limitation is not as severe as it sounds. Neighboring pixels can ultimately be affected by using image processing techniques, described in Section 10.9.

The one case in which the pixel shader can access information for adjacent pixels (albeit indirectly) is the computation of gradient or derivative information. The pixel shader has the ability to take any value and compute the amount by which it changes per pixel along the  $x$  and  $y$  screen axes. This is useful for various computations and texture addressing. These gradients are particularly important for operations such as filtering (see Section 6.2.2). Most GPUs implement this feature by processing pixels in groups of  $2 \times 2$  or more. When the pixel shader requests a gradient value, the difference between adjacent pixels is returned. One result of this implementation is that gradient information cannot be accessed in parts of the shader affected by dynamic flow control—all the pixels in a group must be processing the same instructions. This is a fundamental limitation which exists even in offline rendering sys-

---

<sup>4</sup>The notable exception is that the pixel shader program can specify what type of interpolation is used, e.g., perspective corrected or screen space (or none at all).

<sup>5</sup>In DirectX 10.1 the vertex shader will both input and output 32 vectors.

tems [31]. The ability to access gradient information is a unique capability of the pixel shader, not shared by any of the other programmable shader stages.

Pixel shader programs typically set the fragment color for merging in the final merging stage. The depth value generated in the rasterization stage can also be modified by the pixel shader. The stencil buffer value is not modifiable, but rather is passed through to the merge stage. In SM 2.0 and on, a pixel shader can also discard incoming fragment data, i.e., generate no output. Such operations can cost performance, as optimizations normally performed by the GPU cannot then be used. See Section 18.3.7 for details. Operations such as fog computation and alpha testing have moved from being merge operations to being pixel shader computations in SM 4.0 [123].

Current pixel shaders are capable of doing a huge amount of processing. The ability to compute any number of values in a single rendering pass gave rise to the idea of *multiple render targets* (MRT). Instead of saving results of a pixel shader’s program to a single color buffer, multiple vectors could be generated for each fragment and saved to different buffers. These buffers must be the same dimensions, and some architectures require them each to have the same bit depth (though with different formats, as needed). The number of PS output registers in Table 3.1 refers to the number of separate buffers accessible, i.e., 4 or 8. Unlike the displayable color buffer, there are other limitations on any additional targets. For example, typically no anti-aliasing can be performed. Even with these limitations, MRT functionality is a powerful aid in performing rendering algorithms more efficiently. If a number of intermediate results images are to be computed from the same set of data, only a single rendering pass is needed, instead of one pass per output buffer. The other key capability associated with MRTs is the ability to read from these resulting images as textures.

## 3.7 The Merging Stage

As discussed in Section 2.4.4, the merging stage is where the depths and colors of the individual fragments (generated in the pixel shader) are combined with the frame buffer. This stage is where stencil-buffer and Z-buffer operations occur. Another operation that takes place in this stage is color blending, which is most commonly used for transparency and compositing operations (see Section 5.7).

The merging stage occupies an interesting middle point between the fixed-function stages, such as clipping, and the fully programmable shader stages. Although it is not programmable, its operation is highly configurable. Color blending in particular can be set up to perform a large

number of different operations. The most common are combinations of multiplication, addition, and subtraction involving the color and alpha values, but other operations are possible, such as minimum and maximum, as well as bitwise logic operations. DirectX 10 added the capability to blend two colors from the pixel shader with the frame buffer color—this capability is called *dual-color blending*.

If MRT functionality is employed, then blending can be performed on multiple buffers. DirectX 10.1 introduced the capability to perform different blend operations on each MRT buffer. In previous versions, the same blending operation was always performed on all buffers (note that dual-color blending is incompatible with MRT).

## 3.8 Effects

This tour of the pipeline has focused so far on the various programmable stages. While vertex, geometry, and pixel shader programs are necessary to control these stages, they do not exist in a vacuum. First, an individual shader program is not particularly useful in isolation: A vertex shader program feeds its results to a pixel shader. Both programs must be loaded for any work to be done. The programmer must perform some matching of the outputs of the vertex shader to the inputs of the pixel shader. A particular rendering effect may be produced by any number of shader programs executed over a few passes. Beyond the shader programs themselves, state variables must sometimes be set in a particular configuration for these programs to work properly. For example, the renderer’s state includes whether and how the Z-buffer and stencil buffer are each used, and how a fragment affects the existing pixel value (e.g., replace, add, or blend).

For these reasons, various groups have developed effects languages, such as HLSL FX, CgFX, and COLLADA FX. An effect file attempts to encapsulate all the relevant information needed to execute a particular rendering algorithm [261, 974]. It typically defines some global arguments that can be assigned by the application. For example, a single effect file might define the vertex and pixel shaders needed to render a convincing plastic material. It would expose arguments such as the plastic color and roughness so that these could be changed for each model rendered, but using the same effect file.

To show the flavor of an effect file, we will walk through a trimmed-down example taken from NVIDIA’s FX Composer 2 effects system. This DirectX 9 HLSL effect file implements a very simplified form of *Gooch shading* [423]. One part of Gooch shading is to use the surface normal and compare it to the light’s location. If the normal points toward the light, a warm tone is used to color the surface; if it points away, a cool tone is used.

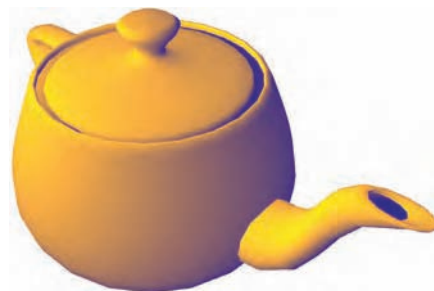


**Figure 3.8.** Gooch shading, varying from a warm orange to a cool blue. (*Image produced by FX Composer 2, courtesy of NVIDIA Corporation.*)

Angles in between interpolate between these two user-defined colors. This shading technique is a form of non-photorealistic rendering, the subject of Chapter 11. An example of this effect in action is shown in Figure 3.8.

Effect variables are defined at the beginning of the effect file. The first few variables are “untweakables,” parameters related to the camera position that are automatically tracked for the effect:

```
float4x4 WorldXf    : World;
float4x4 WorldITXf : WorldInverseTranspose;
float4x4 WvpXf      : WorldViewProjection;
```

The syntax is *type id : semantic*. The type `float4x4` is used for matrices, the name is user defined, and the semantic is a built-in name. As the semantic names imply, the `WorldXf` is the model-to-world transform matrix, the `WorldITXf` is the inverse transpose of this matrix, and the `WvpXf` is the matrix that transforms from model space to the camera’s clip space. These values with recognized semantics are expected to be provided by the application and not shown in the user interface.

Next, the user-defined variables are specified:

```
float3 Lamp0Pos : Position <
    string Object = "PointLight0";
    string UIName = "Lamp 0 Position";
    string Space  = "World";
> = {-0.5f, 2.0f, 1.25f};

float3 WarmColor <
    string UIName   = "Gooch Warm Tone";
    string UIWidget = "Color";
> = {1.3f, 0.9f, 0.15f};
```

```

float3 CoolColor <
    string UIName    = "Gooch Cool Tone";
    string UIWidget = "Color";
> = {0.05f, 0.05f, 0.6f};

```

Here some additional annotations are provided inside the angle brackets “`<>`” and then default values are assigned. The annotations are application-specific and have no meaning to the effect or to the shader compiler. Such annotations can be queried by the application. In this case the annotations describe how to expose these variables within the user interface.

Data structures for shader input and output are defined next:

```

struct appdata {
    float3 Position : POSITION;
    float3 Normal   : NORMAL;
};

struct vertexOutput {
    float4 HPosition : POSITION;
    float3 LightVec  : TEXCOORD1;
    float3 WorldNormal : TEXCOORD2;
};

```

The `appdata` defines what data is at each vertex in the model and so defines the input data for the vertex shader program. The `vertexOutput` is what the vertex shader produces and the pixel shader consumes. The use of `TEXCOORD*` as the output names is an artifact of the evolution of the pipeline. At first, multiple textures could be attached to a surface, so these additional datafields are called *texture coordinates*. In practice, these fields hold any data that is passed from the vertex to the pixel shader.

Next, the various shader program code elements are defined. We have only one vertex shader program:

```

vertexOutput std_VS(appdata IN) {
    vertexOutput OUT;
    float4 No = float4(IN.Normal,0);
    OUT.WorldNormal = mul(No,WorldITXf).xyz;
    float4 Po = float4(IN.Position,1);
    float4 Pw = mul(Po,WorldXf);
    OUT.LightVec = (Lamp0Pos - Pw.xyz);
    OUT.HPosition = mul(Po,WvpXf);
    return OUT;
}

```

This program first computes the surface's normal in world space by using a matrix multiplication. Transforms are the subject of the next chapter, so we will not explain why the inverse transpose is used here. The position in world space is also computed by applying the offscreen transform. This location is subtracted from the light's position to obtain the direction vector from the surface to the light. Finally, the object's position is transformed into clip space, for use by the rasterizer. This is the one required output from any vertex shader program.

Given the light's direction and the surface normal in world space, the pixel shader program computes the surface color:

```
float4 gooch_PS(vertexOutput IN) : COLOR
{
    float3 Ln = normalize(IN.LightVec);
    float3 Nn = normalize(IN.WorldNormal);
    float ldn = dot(Ln,Nn);
    float mixer = 0.5 * (ldn + 1.0);
    float4 result = lerp(CoolColor, WarmColor, mixer);
    return result;
}
```

The vector  $Ln$  is the normalized light direction and  $Nn$  the normalized surface normal. By normalizing, the dot product  $ldn$  of these two vectors then represents the cosine of the angle between them. We want to linearly interpolate between the cool and warm tones using this value. The function `lerp()` expects a mixer value between 0 and 1, where 0 means to use the `CoolColor`, 1 the `WarmColor`, and values in between to blend the two. Since the cosine of an angle gives a value from  $[-1, 1]$ , the `mixer` value transforms this range to  $[0, 1]$ . This value then is used to blend the tones and produce a fragment with the proper color. These shaders are functions. An effect file can consist of any number of functions and can include commonly used functions from other effects files.

A *pass* typically consists of a vertex and pixel (and geometry) shader,<sup>6</sup> along with any state settings needed for the pass. A *technique* is a set of one or more passes to produce the desired effect. This simple file has one technique, which has one pass:

```
technique Gooch < string Script = "Pass=p0;" > {
    pass p0 < string Script = "Draw=geometry;" > {
        VertexShader = compile vs_2_0 std_VS();
        PixelShader = compile ps_2_a gooch_PS();
```

---

<sup>6</sup>A pass can also have no shaders and control the fixed-function pipeline, in DirectX 9 and earlier.



**Figure 3.9.** A wide range of materials and post-processing effects are possible with programmable shaders. (*Images produced by FX Composer 2, courtesy of NVIDIA Corporation.*)

```

    ZEnable = true;
    ZWriteEnable = true;
    ZFunc = LessEqual;
    AlphaBlendEnable = false;
}
}

```

These state settings force the  $Z$ -buffer to be used in the normal way—enabled for reading and writing, and passing if the fragment’s depth is less than or equal to the stored  $z$ -depth. Alpha blending is off, as models using this technique are assumed to be opaque. These rules mean that if the fragment’s  $z$ -depth is equal to or closer than whatever was stored, the computed fragment color is used to replace the corresponding pixel’s color. In other words, standard  $Z$ -buffer usage is used.

A number of techniques can be stored in the same effect file. These techniques are usually variants of the same effect, each targeted at a different shader model (SM 2.0 versus SM 3.0, for example). A huge range of effects are possible. Figure 3.9 gives just a taste of the power of the modern programmable shader pipeline. An effect usually encapsulates related techniques. Various methods have been developed to manage sets of shaders [845, 847, 887, 974, 1271].

We are at the end of the tour of the GPU itself. There is much else the GPU can do, and many ways in which its functions can be used and combined. Relevant theory and algorithms tuned to take advantage of these capabilities are the central subjects of this book. With these basics in place, the focus will move to providing an in-depth understanding of transforms and visual appearance, key elements in the pipeline.

## Further Reading and Resources

David Blythe’s paper on DirectX 10 [123] has a good overview of the modern GPU pipeline and the rationale behind its design, as well as references to related articles.

Information about programming vertex and pixel shaders alone can easily fill a book. Our best advice for jumping right in: Visit the ATI [50] and NVIDIA [944] developer websites for information on the latest techniques. Their free *FX Composer 2* and *RenderMonkey* interactive shader design tool suites provide an excellent way to try out shaders, modify them, and see what makes them tick. Sander [1105] provides an implementation of the fixed-function pipeline in HLSL for SM 2.0 capable hardware.

To learn the formal aspects of shader programming takes some work. The *OpenGL Shading Language* book [1084] picks up where the Red

Book [969] leaves off, describing GLSL, the OpenGL programmable shading language. For learning HLSL, the DirectX API continues to evolve with each new release; for related links and books beyond their SDK, see this book’s website (<http://www.realtimerendering.com>). O’Rorke’s article [974] provides a readable introduction to effects and effective ways to manage shaders. The Cg language provides a layer of abstraction, exporting to many of the major APIs and platforms, while also providing plug-in tools for the major modeling and animation packages. The Sh metaprogramming language is more abstract still, essentially acting as a C++ library that works to map relevant graphics code to the GPU.

For advanced shader techniques, read the *GPU Gems* and *ShaderX* series of books as a start. The *Game Programming Gems* books also have a few relevant articles. The DirectX SDK [261] has many important shader and algorithm samples.



# Chapter 4

## Transforms

*“What if angry vectors veer  
Round your sleeping head, and form.  
There’s never need to fear  
Violence of the poor world’s abstract storm.”*

—Robert Penn Warren

A *transform* is an operation that takes entities such as points, vectors, or colors and converts them in some way. For the computer graphics practitioner, it is extremely important to master transforms. With them, you can position, reshape, and animate objects, lights, and cameras. You can also ensure that all computations are carried out in the same coordinate system, and project objects onto a plane in different ways. These are only a few of the operations that can be performed with transforms, but they are sufficient to demonstrate the importance of the transform’s role in real-time graphics, or, for that matter, in any kind of computer graphics.

A *linear transform* is one that preserves vector addition and scalar multiplication. Specifically,

$$\begin{aligned} \mathbf{f}(\mathbf{x}) + \mathbf{f}(\mathbf{y}) &= \mathbf{f}(\mathbf{x} + \mathbf{y}), \\ k\mathbf{f}(\mathbf{x}) &= \mathbf{f}(k\mathbf{x}). \end{aligned} \tag{4.1}$$

As an example,  $\mathbf{f}(\mathbf{x}) = 5\mathbf{x}$  is a transform that takes a vector and multiplies each element by five. This type of transform is linear, as any two vectors multiplied by five and then added will be the same as adding the vectors and then multiplying. The scalar multiplication condition is clearly fulfilled. This function is called a scaling transform, as it changes the scale (size) of an object. The rotation transform is another linear transform that rotates a vector about the origin. Scaling and rotation transforms, in fact all linear transforms for 3-element vectors, can be represented using a  $3 \times 3$  matrix.

However, this size of matrix is usually not large enough. A function for a three element vector  $\mathbf{x}$  such as  $\mathbf{f}(\mathbf{x}) = \mathbf{x} + (7, 3, 2)$  is not linear. Performing this function on two separate vectors will add each value of  $(7, 3, 2)$  twice to form the result. Adding a fixed vector to another vector performs a translation, e.g., it moves all locations by the same amount. This is a useful type of transform, and we would like to combine various transforms, e.g., scale an object to be half as large, then move it to a different location. Keeping functions in the simple forms used so far makes it difficult to easily combine them.

Combining linear transforms and translations can be done using an *affine transform*, typically stored as a  $4 \times 4$  matrix. An affine transform is one that performs a linear transform and then a translation. To represent 4-element vectors we use *homogeneous notation*, denoting points and directions in the same way (using bold lowercase letters). A direction vector is represented as  $\mathbf{v} = (v_x \ v_y \ v_z \ 0)^T$  and a point as  $\mathbf{v} = (v_x \ v_y \ v_z \ 1)^T$ . Throughout the chapter, we will make extensive use of the terminology explained in Appendix A. You may wish to review this appendix now, especially Section A.4, page 905, on homogeneous notation.

All translation, rotation, scaling, reflection, and shearing matrices are affine. The main characteristic of an affine matrix is that it preserves the parallelism of lines, but not necessarily lengths and angles. An affine transform may also be any sequence of concatenations of individual affine transforms.

This chapter will begin with the most essential, basic affine transforms. These are indeed *very* basic, and this section could be seen as a “reference manual” for simple transforms. More specialized matrices are then described, followed by a discussion and description of quaternions, a powerful transform tool. Then follows vertex blending and morphing, which are two simple but more powerful ways of expressing animations of meshes. Finally, projection matrices are described. Most of these transforms, their notations, functions, and properties are summarized in Table 4.1.

Transforms are a basic tool for manipulating geometry. Most graphics application programming interfaces (APIs) include matrix operations that implement many of the transforms discussed in this chapter. However, it is still worthwhile to understand the real matrices and their interaction behind the function calls. Knowing what the matrix does after such a function call is a start, but understanding the properties of the matrix itself will take you further. For example, such an understanding enables you to discern when you are dealing with an orthogonal matrix, whose inverse is its transpose (see page 904), making for faster matrix inversions. Knowledge like this can lead to accelerated code.

| Notation  | Name                    | Characteristics  |
|---|-------------------------|--|
| $\mathbf{T}(\mathbf{t})$                              | translation matrix      | Moves a point.<br>Affine.  |
| $\mathbf{R}_x(\rho)$                                  | rotation matrix         | Rotates $\rho$ radians around the $x$ -axis.<br>Similar notation for the $y$ - and $z$ -axes.<br>Orthogonal & affine.                  |
| $\mathbf{R}$  | rotation matrix         | Any rotation matrix.<br>Orthogonal & affine.   |
| $\mathbf{S}(\mathbf{s})$                              | scaling matrix          | Scales along all $x$ -, $y$ -, and $z$ -axes according to $\mathbf{s}$ .<br>Affine.  |
| $\mathbf{H}_{ij}(s)$                                  | shear matrix            | Shears component $i$ by a factor $s$ , with respect to component $j$ .<br>$i, j \in \{x, y, z\}$ . Affine.                             |
| $\mathbf{E}(h, p, r)$                                 | Euler transform         | Orientation matrix given by the Euler angles head (yaw), pitch, roll.<br>Orthogonal & affine.  |
| $\mathbf{P}_o(s)$                                     | orthographic projection | Parallel projects onto some plane or to a volume. Affine.  |
| $\mathbf{P}_p(s)$                                     | perspective projection  | Projects with perspective onto a plane or to a volume.   |
| $\text{slerp}(\hat{\mathbf{q}}, \hat{\mathbf{r}}, t)$ | slerp transform         | Creates an interpolated quaternion with respect to the quaternions $\hat{\mathbf{q}}$ and $\hat{\mathbf{r}}$ , and the parameter $t$ . |

**Table 4.1.** Summary of most of the transforms discussed in this chapter.

## 4.1 Basic Transforms

This section describes the most basic transforms, such as translation, rotation, scaling, shearing, transform concatenation, the rigid-body transform, normal transform (which is not so normal), and computation of inverses. For the experienced reader, this can be used as a reference manual for simple transforms, and for the novice, it can serve as an introduction to the subject. This material is necessary background for the rest of this chapter and for other chapters in this book. We start with the simplest of transforms—the translation.

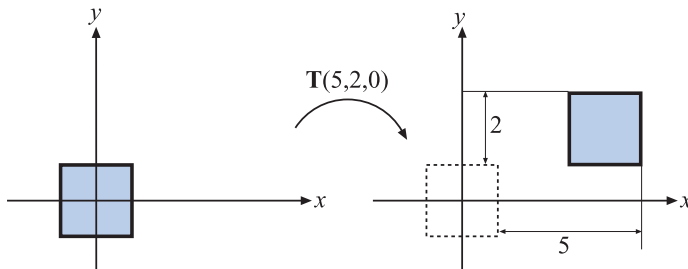


**Figure 4.1.** The square on the left is transformed with a translation matrix  $\mathbf{T}(5, 2, 0)$ , whereby the square is moved 5 distance units to the right and 2 upwards.

### 4.1.1 Translation

A change from one location to another is represented by a translation matrix,  $\mathbf{T}$ . This matrix translates an entity by a vector  $\mathbf{t} = (t_x, t_y, t_z)$ .  $\mathbf{T}$  is given below by Equation 4.2:

$$\mathbf{T}(\mathbf{t}) = \mathbf{T}(t_x, t_y, t_z) = \begin{pmatrix} 1 & 0 & 0 & t_x \\ 0 & 1 & 0 & t_y \\ 0 & 0 & 1 & t_z \\ 0 & 0 & 0 & 1 \end{pmatrix}. \quad (4.2)$$

An example of the effect of the translation transform is shown in Figure 4.1. It is easily shown that the multiplication of a point  $\mathbf{p} = (p_x, p_y, p_z, 1)$  with  $\mathbf{T}(\mathbf{t})$  yields a new point  $\mathbf{p}' = (p_x + t_x, p_y + t_y, p_z + t_z, 1)$ , which is clearly a translation. Notice that a vector  $\mathbf{v} = (v_x, v_y, v_z, 0)$  is left unaffected by a multiplication by  $\mathbf{T}$ , because a direction vector cannot be translated. In contrast, both points and vectors are affected by the rest of the affine transforms. The inverse of a translation matrix is  $\mathbf{T}^{-1}(\mathbf{t}) = \mathbf{T}(-\mathbf{t})$ , that is, the vector  $\mathbf{t}$  is negated.

### 4.1.2 Rotation

A rotation transform rotates a vector (position or direction) by a given angle around a given axis passing through the origin. Like a translation matrix, it is a *rigid-body transform*, i.e., it preserves the distances between points transformed, and preserves handedness (i.e., it never causes left and right to swap sides). These two types of transforms are clearly useful in computer graphics for positioning and orienting objects. An *orientation matrix* is a rotation matrix associated with a camera view or object that defines its orientation in space, i.e., its directions for up and forward. Commonly-used rotation matrices are  $\mathbf{R}_x(\phi)$ ,  $\mathbf{R}_y(\phi)$ , and  $\mathbf{R}_z(\phi)$ , which

rotate an entity  $\phi$  radians around the  $x$ -,  $y$ -, and  $z$ -axes respectively. They are given by Equations 4.3–4.5:

$$\mathbf{R}_x(\phi) = \begin{pmatrix} 1 & 0 & 0 & 0 \\ 0 & \cos \phi & -\sin \phi & 0 \\ 0 & \sin \phi & \cos \phi & 0 \\ 0 & 0 & 0 & 1 \end{pmatrix}, \quad (4.3)$$

$$\mathbf{R}_y(\phi) = \begin{pmatrix} \cos \phi & 0 & \sin \phi & 0 \\ 0 & 1 & 0 & 0 \\ -\sin \phi & 0 & \cos \phi & 0 \\ 0 & 0 & 0 & 1 \end{pmatrix}, \quad (4.4)$$

$$\mathbf{R}_z(\phi) = \begin{pmatrix} \cos \phi & -\sin \phi & 0 & 0 \\ \sin \phi & \cos \phi & 0 & 0 \\ 0 & 0 & 1 & 0 \\ 0 & 0 & 0 & 1 \end{pmatrix}. \quad (4.5)$$

For every  $3 \times 3$  rotation matrix,<sup>1</sup>  $\mathbf{R}$ , that rotates  $\phi$  radians around any axis, the trace (see page 898 for a definition) is constant independent of the axis, and is computed as [742]:

$$\text{tr}(\mathbf{R}) = 1 + 2 \cos \phi. \quad (4.6)$$

The effect of a rotation matrix may be seen in Figure 4.4 on page 62. What characterizes a rotation matrix,  $\mathbf{R}_i(\phi)$ , besides the fact that it rotates  $\phi$  radians around axis  $i$ , is that it leaves all points on the rotation axis,  $i$ , unchanged. Note that  $\mathbf{R}$  will also be used to denote a rotation matrix around any axis. The axis rotation matrices given above can be used in a series of three transforms to perform any arbitrary axis rotation. This procedure is discussed in Section 4.2.1. Performing a rotation around an arbitrary axis directly is covered in Section 4.2.4.

All rotation matrices have a determinant of one and are orthogonal, easily verified using the definition of orthogonal matrices given on page 904 in Appendix A. This also holds for concatenations of any number of these transforms. There is another way to obtain the inverse:  $\mathbf{R}_i^{-1}(\phi) = \mathbf{R}_i(-\phi)$ , i.e., rotate in the opposite direction around the same axis. Also, the determinant of a rotation matrix is always one, since the matrix is orthogonal.

**EXAMPLE: ROTATION AROUND A POINT.** Assume that we want to rotate an object by  $\phi$  radians around the  $z$ -axis, with the center of rotation being a certain point,  $\mathbf{p}$ . What is the transform? This scenario is depicted in

---

<sup>1</sup>If the bottom row and rightmost column is deleted from a  $4 \times 4$  matrix, a  $3 \times 3$  matrix is obtained.

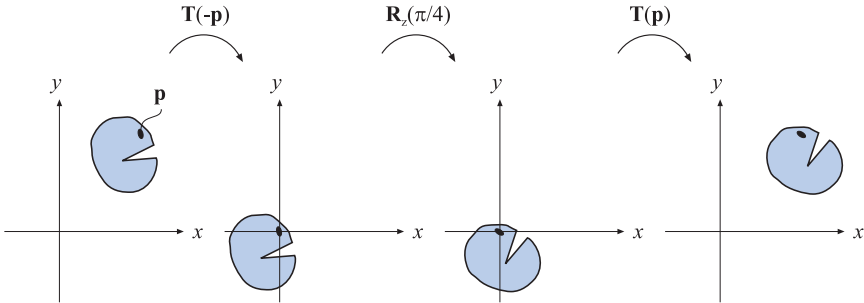


**Figure 4.2.** Example of rotation around a specific point  $\mathbf{p}$ .

Figure 4.2. Since a rotation around a point is characterized by the fact that the point itself is unaffected by the rotation, the transform starts by translating the object so that  $\mathbf{p}$  coincides with the origin, which is done with  $\mathbf{T}(-\mathbf{p})$ . Thereafter follows the actual rotation:  $\mathbf{R}_z(\phi)$ . Finally, the object has to be translated back to its original position using  $\mathbf{T}(\mathbf{p})$ . The resulting transform,  $\mathbf{X}$ , is then given by

$$\mathbf{X} = \mathbf{T}(\mathbf{p})\mathbf{R}_z(\phi)\mathbf{T}(-\mathbf{p}). \quad (4.7)$$

□

### 4.1.3 Scaling

A scaling matrix,  $\mathbf{S}(\mathbf{s}) = \mathbf{S}(s_x, s_y, s_z)$ , scales an entity with factors  $s_x$ ,  $s_y$ , and  $s_z$  along the  $x$ -,  $y$ -, and  $z$ -directions respectively. This means that a scaling matrix can be used to enlarge or diminish an object. The larger the  $s_i$ ,  $i \in \{x, y, z\}$ , the larger the scaled entity gets in that direction. Setting any of the components of  $\mathbf{s}$  to 1 naturally avoids a change in scaling in that direction. Equation 4.8 shows  $\mathbf{S}$ :

$$\mathbf{S}(\mathbf{s}) = \begin{pmatrix} s_x & 0 & 0 & 0 \\ 0 & s_y & 0 & 0 \\ 0 & 0 & s_z & 0 \\ 0 & 0 & 0 & 1 \end{pmatrix}. \quad (4.8)$$

Figure 4.4 on page 62 illustrates the effect of a scaling matrix. The scaling operation is called *uniform* if  $s_x = s_y = s_z$  and *nonuniform* otherwise. Sometimes the terms *isotropic* and *anisotropic* scaling are used instead of uniform and nonuniform. The inverse is  $\mathbf{S}^{-1}(\mathbf{s}) = \mathbf{S}(1/s_x, 1/s_y, 1/s_z)$ .

Using homogeneous coordinates, another valid way to create a uniform scaling matrix is by manipulating matrix element at position (3, 3), i.e., the

element at the lower right corner. This value affects the  $w$ -component of the homogeneous coordinate, and so scales every coordinate transformed by the matrix. For example, to scale uniformly by a factor of 5, the elements at  $(0, 0)$ ,  $(1, 1)$ , and  $(2, 2)$  in the scaling matrix can be set to 5, or the element at  $(3, 3)$  can be set to  $1/5$ . The two different matrices for performing this are shown below:

$$\mathbf{S} = \begin{pmatrix} 5 & 0 & 0 & 0 \\ 0 & 5 & 0 & 0 \\ 0 & 0 & 5 & 0 \\ 0 & 0 & 0 & 1 \end{pmatrix}, \quad \mathbf{S}' = \begin{pmatrix} 1 & 0 & 0 & 0 \\ 0 & 1 & 0 & 0 \\ 0 & 0 & 1 & 0 \\ 0 & 0 & 0 & 1/5 \end{pmatrix}. \quad (4.9)$$

In contrast to using  $\mathbf{S}$  for uniform scaling, using  $\mathbf{S}'$  must always be followed by homogenization. This may be inefficient, since it involves divides in the homogenization process; if the element at the lower right (position  $(3, 3)$ ) is 1, no divides are necessary. Of course, if the system always does this division without testing for 1, then there is no extra cost.

A negative value on one or three of the components of  $\mathbf{s}$  gives a *reflection matrix*, also called a *mirror matrix*.<sup>2</sup> If only two scale factors are  $-1$ , then we will rotate  $\pi$  radians. Reflection matrices usually require special treatment when detected. For example, a triangle with vertices in a counterclockwise order will get a clockwise order when transformed by a reflection matrix. This order change can cause incorrect lighting and back-face culling to occur. To detect whether a given matrix reflects in some manner, compute the determinant of the upper left  $3 \times 3$  elements of the matrix. If the value is negative, the matrix is reflective.

**EXAMPLE: SCALING IN A CERTAIN DIRECTION.** The scaling matrix  $\mathbf{S}$  scales along only the  $x$ -,  $y$ -, and  $z$ -axes. If scaling should be performed in other directions, a compound transform is needed. Assume that scaling should be done along the axes of the orthonormal, right-oriented vectors  $\mathbf{f}^x$ ,  $\mathbf{f}^y$ , and  $\mathbf{f}^z$ . First, construct the matrix  $\mathbf{F}$  as below:

$$\mathbf{F} = \begin{pmatrix} \mathbf{f}^x & \mathbf{f}^y & \mathbf{f}^z & \mathbf{0} \\ 0 & 0 & 0 & 1 \end{pmatrix}. \quad (4.10)$$

The idea is to make the coordinate system given by the three axes coincide with the standard axes, then use the standard scaling matrix, and then transform back. The first step is carried out by multiplying with the transpose, i.e., the inverse, of  $\mathbf{F}$ . Then the actual scaling is done, followed by a transform back. The transform is shown in Equation 4.11:

$$\mathbf{X} = \mathbf{F}\mathbf{S}(\mathbf{s})\mathbf{F}^T. \quad (4.11)$$

□

---

<sup>2</sup>According to some definitions of a reflection matrix, the negative component(s) must equal  $-1$ .

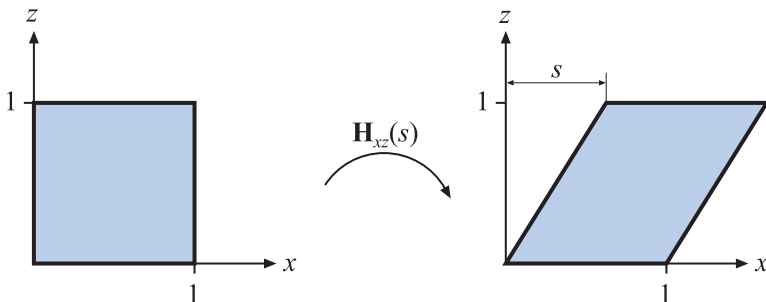


**Figure 4.3.** The effect of shearing the unit square with  $\mathbf{H}_{xz}(s)$ . Both the  $y$ - and  $z$ -values are unaffected by the transform, while the  $x$ -value is the sum of the old  $x$ -value and  $s$  multiplied by the  $z$ -value, causing the square to be tilted.

#### 4.1.4 Shearing

Another class of transforms is the set of shearing matrices. These can, for example, be used in games to distort an entire scene in order to create a psychedelic effect or to create fuzzy reflections by jittering (see Section 9.3.1). There are six basic shearing matrices,<sup>3</sup> and they are denoted  $\mathbf{H}_{xy}(s)$ ,  $\mathbf{H}_{xz}(s)$ ,  $\mathbf{H}_{yx}(s)$ ,  $\mathbf{H}_{yz}(s)$ ,  $\mathbf{H}_{zx}(s)$ , and  $\mathbf{H}_{zy}(s)$ . The first subscript is used to denote which coordinate is being changed by the shear matrix, while the second subscript indicates the coordinate which does the shearing. An example of a shear matrix,  $\mathbf{H}_{xz}(s)$ , is shown in Equation 4.12. Observe that the subscript can be used to find the position of the parameter  $s$  in the matrix below; the  $x$  (whose numeric index is 0) identifies row zero, and the  $z$  (whose numeric index is 2) identifies column two, and so the  $s$  is located there:

$$\mathbf{H}_{xz}(s) = \begin{pmatrix} 1 & 0 & s & 0 \\ 0 & 1 & 0 & 0 \\ 0 & 0 & 1 & 0 \\ 0 & 0 & 0 & 1 \end{pmatrix}. \quad (4.12)$$

The effect of multiplying this matrix with a point  $\mathbf{p}$  yields a point:  $(p_x + sp_z \ p_y \ p_z)^T$ . Graphically, this is shown for the unit square in Figure 4.3. The inverse of  $\mathbf{H}_{ij}(s)$  (shearing the  $i$ th coordinate with respect to the  $j$ th coordinate, where  $i \neq j$ ), is generated by shearing in the opposite direction, that is,  $\mathbf{H}_{ij}^{-1}(s) = \mathbf{H}_{ij}(-s)$ .

---

<sup>3</sup>Actually, there are *only* six shearing matrices, because we shear in planes orthogonal to the main axes. However, a general shear matrix can shear orthogonally to any plane.

Some computer graphics texts [348, 349] use a slightly different kind of shear matrix:

$$\mathbf{H}'_{xy}(s, t) = \begin{pmatrix} 1 & 0 & s & 0 \\ 0 & 1 & t & 0 \\ 0 & 0 & 1 & 0 \\ 0 & 0 & 0 & 1 \end{pmatrix}. \quad (4.13)$$

Here, however, both subscripts are used to denote that these coordinates are to be sheared by the third coordinate. The connection between these two different kinds of descriptions is  $\mathbf{H}'_{ij}(s, t) = \mathbf{H}_{ik}(s)\mathbf{H}_{jk}(t)$ , where  $k$  is used as an index to the third coordinate. The right matrix to use is a matter of taste and API support.

Finally, it should be noted that since the determinant of any shear matrix  $|\mathbf{H}| = 1$ , this is a volume preserving transformation.

### 4.1.5 Concatenation of Transforms

Due to the noncommutativity of the multiplication operation on matrices, the order in which the matrices occur matters. Concatenation of transforms is therefore said to be order-dependent.

As an example of order dependency, consider two matrices,  $\mathbf{S}$  and  $\mathbf{R}$ .  $\mathbf{S}(2, 0.5, 1)$  scales the  $x$ -component by a factor two and the  $y$ -component by a factor 0.5.  $\mathbf{R}_z(\pi/6)$  rotates  $\pi/6$  radians counterclockwise around the  $z$ -axis (which points outwards from page of this book). These matrices can be multiplied in two ways, with the results being totally different. The two cases are shown in Figure 4.4.

The obvious reason to concatenate a sequence of matrices into a single one is to gain efficiency. For example, imagine that you have an object that has several thousand vertices, and that this object must be scaled, rotated, and finally translated. Now, instead of multiplying all vertices with each of the three matrices, the three matrices are concatenated into a single matrix. This single matrix is then applied to the vertices. This composite matrix is  $\mathbf{C} = \mathbf{TRS}$ . Note the order here: The scaling matrix,  $\mathbf{S}$ , should be applied to the vertices first, and therefore appears to the right in the composition. This ordering implies that  $\mathbf{TRSp} = (\mathbf{T}(\mathbf{R}(\mathbf{Sp})))$ .<sup>4</sup>

It is worth noting that while matrix concatenation is order-dependent, the matrices can be grouped as desired. For example, say that with  $\mathbf{TRSp}$  you would like to compute the rigid-body motion transform  $\mathbf{TR}$  once. It

---

<sup>4</sup> Another valid notational scheme sometimes seen in computer graphics uses matrices with translation vectors in the bottom row. In this scheme, the order of matrices would be reversed, i.e., the order of application would read from left to right. Vectors and matrices in this notation are said to be in *row-major* form since the vectors are rows. In this book, we use *column-major* form.

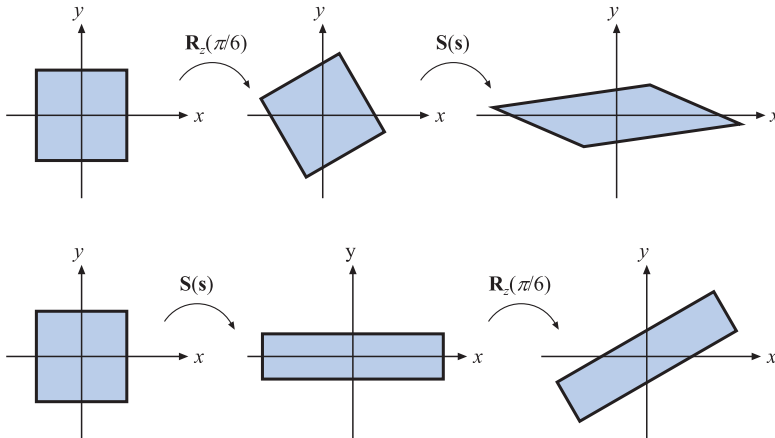


**Figure 4.4.** This illustrates the order dependency when multiplying matrices. In the top row, the rotation matrix  $R_z(\pi/6)$  is applied followed by a scaling,  $S(s)$ , where  $s = (2, 0.5, 1)$ . The composite matrix is then  $S(s)R_z(\pi/6)$ . In the bottom row, the matrices are applied in the reverse order, yielding  $R_z(\pi/6)S(s)$ . The results are clearly different. It generally holds that  $MN \neq NM$ , for arbitrary matrices  $M$  and  $N$ .

is valid to group these two matrices together,  $(\mathbf{TR})(\mathbf{Sp})$ , and replace with the intermediate result. Thus, matrix concatenation is *associative*.

#### 4.1.6 The Rigid-Body Transform

When a person grabs a solid object, say a pen from a table, and moves it to another location, perhaps to her shirt pocket, only the object's orientation and location change, while the shape of the object generally is not affected. Such a transform, consisting of concatenations of only translations and rotations, is called a *rigid-body transform* and has the characteristic of preserving lengths, angles, and handedness.

Any rigid-body matrix,  $\mathbf{X}$ , can be written as the concatenation of a translation matrix,  $\mathbf{T}(\mathbf{t})$ , and a rotation matrix,  $\mathbf{R}$ . Thus,  $\mathbf{X}$  has the appearance of the matrix in Equation 4.14:

$$\mathbf{X} = \mathbf{T}(\mathbf{t})\mathbf{R} = \begin{pmatrix} r_{00} & r_{01} & r_{02} & t_x \\ r_{10} & r_{11} & r_{12} & t_y \\ r_{20} & r_{21} & r_{22} & t_z \\ 0 & 0 & 0 & 1 \end{pmatrix}. \quad (4.14)$$

The inverse of  $\mathbf{X}$  is computed as  $\mathbf{X}^{-1} = (\mathbf{T}(\mathbf{t})\mathbf{R})^{-1} = \mathbf{R}^{-1}\mathbf{T}(\mathbf{t})^{-1} = \mathbf{R}^T\mathbf{T}(-\mathbf{t})$ . Thus, to compute the inverse, the upper left  $3 \times 3$  matrix of  $\mathbf{R}$  is transposed, and the translation values of  $\mathbf{T}$  change sign. These two new matrices are multiplied together in opposite order to obtain the inverse.

Another way to compute the inverse of  $\mathbf{X}$  is to consider  $\mathbf{R}$  (making  $\mathbf{R}$  appear as  $3 \times 3$  matrix) and  $\mathbf{X}$  in the following notation:

$$\begin{aligned}\bar{\mathbf{R}} = (\mathbf{r}_{,0} & \quad \mathbf{r}_{,1} & \quad \mathbf{r}_{,2}) = \begin{pmatrix} \mathbf{r}_0^T \\ \mathbf{r}_1^T \\ \mathbf{r}_2^T \end{pmatrix}, \\ \mathbf{X} &\xrightarrow{=} \begin{pmatrix} \bar{\mathbf{R}} & \mathbf{t} \\ \mathbf{0}^T & 1 \end{pmatrix}.\end{aligned}\quad (4.15)$$

Here,  $\mathbf{0}$  is a  $3 \times 1$  column vector filled with zeros. Some simple calculations yield the inverse in the expression shown in Equation 4.16:

$$\mathbf{X}^{-1} = \begin{pmatrix} \mathbf{r}_0, & \mathbf{r}_1, & \mathbf{r}_2, & -\bar{\mathbf{R}}^T \mathbf{t} \\ 0 & 0 & 0 & 1 \end{pmatrix}. \quad (4.16)$$

### 4.1.7 Normal Transform

A single matrix can be used to consistently transform points, lines, polygons, and other geometry. The same matrix can also transform tangent vectors following along these lines or on the surfaces of polygons. However, this matrix cannot always be used to transform one important geometric property, the surface normal (and also the vertex lighting normal). Figure 4.5 shows what can happen if this same matrix is used.

Instead of multiplying by the matrix itself, the proper method is to use the transpose of the matrix's adjoint [156]. Computation of the adjoint is

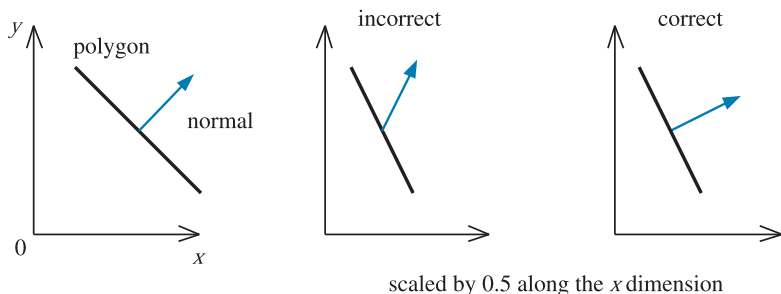


**Figure 4.5.** On the left is the original geometry, a polygon and its normal shown from the side. The middle illustration shows what happens if the model is scaled along the  $x$ -axis by 0.5 and the normal uses the same matrix. The right figure shows the proper transform of the normal.

described in Section A.3.1. The adjoint is always guaranteed to exist. The normal is not guaranteed to be of unit length after being transformed, so typically needs to be normalized.

The traditional answer for transforming the normal is that the transpose of the inverse is computed [1277]. This method normally works. The full inverse is not necessary, however, and occasionally cannot be created. The inverse is the adjoint divided by the original matrix's determinant. If this determinant is zero, the matrix is singular, and the inverse does not exist.

Even computing just the adjoint for a full  $4 \times 4$  matrix can be expensive, and is usually not necessary. Since the normal is a vector, translation will not affect it. Furthermore, most modeling transforms are affine. They do not change the  $w$  component of the homogeneous coordinate passed in, i.e., they do not perform projection. Under these (common) circumstances, all that is needed for normal transformation is to compute the adjoint of the upper-left  $3 \times 3$  components.

Often even this adjoint computation is not needed. Say we know the transform matrix is composed entirely of a concatenation of translations, rotations, and uniform scaling operations (no stretching or squashing). Translations do not affect the normal. The uniform scaling factors simply change the length of the normal. What is left is a series of rotations, which always yields a net rotation of some sort, nothing more. A rotation matrix is defined by the fact that its transpose is its inverse. The transpose of the inverse can be used to transform normals, and two transposes (or two inverses) cancel each other out. Put together, the result is that the original transform itself can also be used directly to transform normals under these circumstances.

Finally, fully renormalizing the normal produced is not always necessary. If only translations and rotations are concatenated together, the normal will not change length when transformed by the matrix, so no renormalizing is needed. If uniform scalings are also concatenated, the overall scale factor (if known, or extracted—Section 4.2.3) can be used to directly normalize the normals produced. For example, if we know that a series of scalings were applied that makes the object 5.2 times larger, then normals transformed directly by this matrix are renormalized by dividing them by 5.2. Alternately, to create a normal transform matrix that would produce normalized results, the original matrix's  $3 \times 3$  upper-left could be divided by this scale factor once.

Note that normal transforms are not an issue in systems where, after transformation, the surface normal is derived from the triangle (e.g., using the cross product of the triangle's edges). Tangent vectors are different than normals in nature, and are always directly transformed by the original matrix.

### 4.1.8 Computation of Inverses

Inverses are needed in many cases, for example, when changing back and forth between coordinate systems. Depending on the available information about a transform, one of the following three methods of computing the inverse of a matrix can be used.

- If the matrix is a single transform or a sequence of simple transforms with given parameters, then the matrix can be computed easily by “inverting the parameters” and the matrix order. For example, if  $\mathbf{M} = \mathbf{T}(\mathbf{t})\mathbf{R}(\phi)$ , then  $\mathbf{M}^{-1} = \mathbf{R}(-\phi)\mathbf{T}(-\mathbf{t})$ .
- If the matrix is known to be orthogonal, then  $\mathbf{M}^{-1} = \mathbf{M}^T$ , i.e., the transpose is the inverse. Any sequence of rotations is a rotation, and so is orthogonal.
- If nothing in particular is known, then the adjoint method (Equation A.38 on page 902), Cramer’s rule, LU decomposition, or Gaussian elimination could be used to compute the inverse (see Section A.3.1). Cramer’s rule and the adjoint method are generally preferable, as they have fewer branch operations; “if” tests are good to avoid on modern architectures. See Section 4.1.7 on how to use the adjoint to inverse transform normals.

The purpose of the inverse computation can also be taken into account when optimizing. For example, if the inverse is to be used for transforming vectors, then only the  $3 \times 3$  upper left part of the matrix normally needs to be inverted (see the previous section).

## 4.2 Special Matrix Transforms and Operations

In this section, a number of matrix transforms and operations that are essential to real-time graphics will be introduced and derived. First, we present the Euler transform (along with its extraction of parameters), which is an intuitive way to describe orientations. Then we touch upon retrieving a set of basic transforms from a single matrix. Finally, a method is derived that rotates an entity around an arbitrary axis.

### 4.2.1 The Euler Transform

This transform is an intuitive way to construct a matrix to orient yourself (i.e., the camera) or any other entity in a certain direction. Its name comes from the great Swiss mathematician Leonhard Euler (1707–1783).

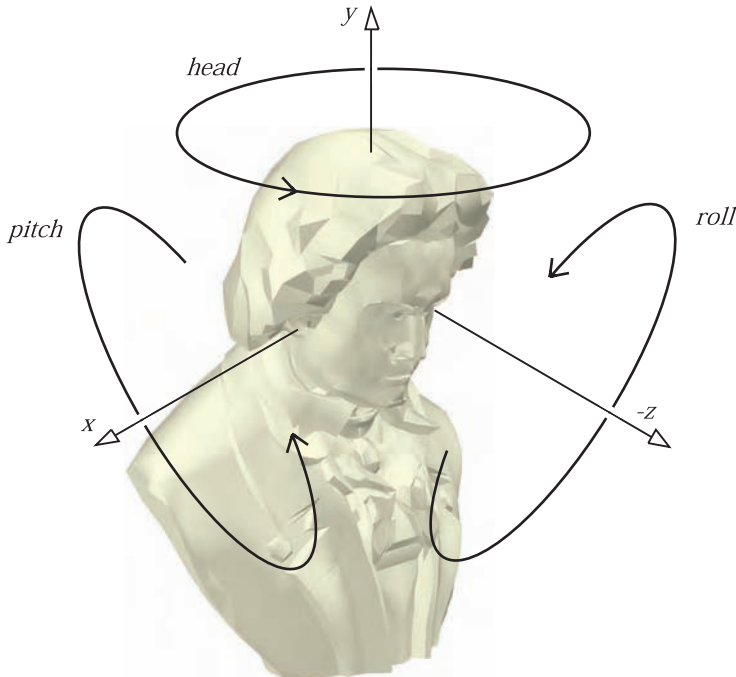


**Figure 4.6.** Depicting the way, in terms of the Euler transform, you turn your *head*, *pitch*, and *roll*. The default view direction is shown, looking along the negative *z*-axis with the head oriented along the *y*-axis.

First, some kind of default view direction must be established. Most often it lies along the negative *z*-axis with the head oriented along the *y*-axis, as depicted in Figure 4.6. The Euler transform is the multiplication of three matrices, namely the rotations shown in the figure. More formally, the transform, denoted **E**, is given by Equation 4.17:<sup>5</sup>

$$\mathbf{E}(h, p, r) = \mathbf{R}_z(r)\mathbf{R}_x(p)\mathbf{R}_y(h). \quad (4.17)$$

Since **E** is a concatenation of rotations, it is also clearly orthogonal. Therefore its inverse can be expressed as  $\mathbf{E}^{-1} = \mathbf{E}^T = (\mathbf{R}_z\mathbf{R}_x\mathbf{R}_y)^T = \mathbf{R}_y^T\mathbf{R}_x^T\mathbf{R}_z^T$ , although it is, of course, easier to use the transpose of **E** directly.

The Euler angles *h*, *p*, and *r* represent in which order and how much the head, pitch, and roll should rotate around their respective axes.<sup>6</sup> This

<sup>5</sup> Actually, the order of the matrices can be chosen in 24 different ways [1179], but we choose this one because it is commonly used.

<sup>6</sup>Sometimes the angles are all called “rolls,” e.g., our “head” is the “*y*-roll” and our “pitch” is the “*x*-roll.” Also, “head” is sometimes known as “yaw,” for example, in flight simulation.

transform is intuitive and therefore easy to discuss in layperson's language. For example, changing the head angle makes the viewer shake his head "no," changing the pitch makes him nod, and rolling makes him tilt his head sideways. Rather than talking about rotations around the  $x$ -,  $y$ -, and  $z$ -axes, we talk about altering the head, pitch, and roll. Note that this transform can orient not only the camera, but also any object or entity as well. These transforms can be performed using the global axes of the world's space or relative to a local frame of reference.

When you use Euler transforms, something called *gimbal lock* may occur [1176, 1330]. This happens when rotations are made so that one degree of freedom is lost. For example, say the order of transforms is  $x/y/z$ . Consider a rotation of  $\pi/2$  around just the  $y$ -axis, the second rotation performed. Doing so rotates the local  $z$ -axis to be aligned with the original  $x$ -axis, so that the final rotation around  $z$  is redundant.

Another way to see that one degree of freedom is lost is to set  $p = \pi/2$  and examine what happens to the Euler matrix  $\mathbf{E}(h, p, r)$ :

$$\begin{aligned}\mathbf{E}(h, \pi/2, r) &= \begin{pmatrix} \cos r \cos h - \sin r \sin h & 0 & \cos r \sin h + \sin r \cos h \\ \sin r \cos h + \cos r \sin h & 0 & \sin r \sin h - \cos r \cos h \\ 0 & 1 & 0 \end{pmatrix} \\ &= \begin{pmatrix} \cos(r+h) & 0 & \sin(r+h) \\ \sin(r+h) & 0 & -\cos(r+h) \\ 0 & 1 & 0 \end{pmatrix}. \end{aligned} \quad (4.18)$$

Since the matrix is dependent on only one angle ( $r+h$ ), we conclude that one degree of freedom has been lost.

While Euler angles are commonly presented as being in  $x/y/z$  order in modeling systems, a rotation around each local axis, other orderings are feasible. For example,  $z/x/y$  is used in animation and  $z/x/z$  in both animation and physics. All are valid ways of specifying three separate rotations. This last ordering,  $z/x/z$ , can be superior for some applications, as only when rotating  $\pi$  radians around  $x$  (a half-rotation) does gimbal lock occur. That said, by the "hairy ball theorem" gimbal lock is unavoidable, there is no perfect sequence that avoids it.

While useful for small angle changes or viewer orientation, Euler angles have some other serious limitations. It is difficult to work with two sets of Euler angles in combination. For example, interpolation between one set and another is not a simple matter of interpolating each angle. In fact, two different sets of Euler angles can give the same orientation, so any interpolation should not rotate the object at all. These are some of the reasons that using alternate orientation representations such as quaternions, discussed later in this chapter, are worth pursuing.

## 4.2.2 Extracting Parameters from the Euler Transform

In some situations, it is useful to have a procedure that extracts the Euler parameters,  $h$ ,  $p$ , and  $r$ , from an orthogonal matrix. This procedure is shown in Equation 4.19:<sup>7</sup>

$$\mathbf{F} = \begin{pmatrix} f_{00} & f_{01} & f_{02} \\ f_{10} & f_{11} & f_{12} \\ f_{20} & f_{21} & f_{22} \end{pmatrix} = \mathbf{R}_z(r)\mathbf{R}_x(p)\mathbf{R}_y(h) = \mathbf{E}(h, p, r). \quad (4.19)$$

Concatenating the three rotation matrices in Equation 4.19 yields

$$\mathbf{F} = \begin{pmatrix} \cos r \cos h - \sin r \sin p \sin h & -\sin r \cos p & \cos r \sin h + \sin r \sin p \cos h \\ \sin r \cos h + \cos r \sin p \sin h & \cos r \cos p & \sin r \sin h - \cos r \sin p \cos h \\ -\cos p \sin h & \sin p & \cos p \cos h \end{pmatrix}. \quad (4.20)$$

From this it is apparent that the pitch parameter is given by  $\sin p = f_{21}$ . Also, dividing  $f_{01}$  by  $f_{11}$ , and similarly dividing  $f_{20}$  by  $f_{22}$ , gives rise to the following extraction equations for the head and roll parameters:

$$\begin{aligned} \frac{f_{01}}{f_{11}} &= \frac{-\sin r}{\cos r} = -\tan r, \\ \frac{f_{20}}{f_{22}} &= \frac{-\sin h}{\cos h} = -\tan h. \end{aligned} \quad (4.21)$$

Thus, the Euler parameters  $h$  (head),  $p$  (pitch), and  $r$  (roll) are extracted from a matrix  $\mathbf{F}$  using the function `atan2(y, x)` (see page 7 in Chapter 1) as in Equation 4.22:

$$\begin{aligned} h &= \text{atan2}(-f_{20}, f_{22}), \\ p &= \arcsin(f_{21}), \\ r &= \text{atan2}(-f_{01}, f_{11}). \end{aligned} \quad (4.22)$$

However, there is a special case we need to handle. It occurs when  $\cos p = 0$ , because then  $f_{01} = f_{11} = 0$ , and so the `atan2` function cannot be used. Having  $\cos p = 0$  implies that  $\sin p = \pm 1$ , and so  $\mathbf{F}$  simplifies to

$$\mathbf{F} = \begin{pmatrix} \cos(r \pm h) & 0 & \sin(r \pm h) \\ \sin(r \pm h) & 0 & -\cos(r \pm h) \\ 0 & \pm 1 & 0 \end{pmatrix}. \quad (4.23)$$

The remaining parameters are obtained by arbitrarily setting  $h = 0$  [1265], and then  $\sin r / \cos r = \tan r = f_{10} / f_{00}$ , which gives  $r = \text{atan2}(f_{10}, f_{00})$ .

---

<sup>7</sup>The  $4 \times 4$  matrices have been abandoned for  $3 \times 3$  matrices, since the latter provide all the necessary information for a rotation matrix; i.e., the rest of the  $4 \times 4$  matrix always contains zeros and a one in the lower right position.

Note that from the definition of  $\arcsin$  (see Section B.1),  $-\pi/2 \leq p \leq \pi/2$ , which means that if  $\mathbf{F}$  was created with a value of  $p$  outside this interval, the original parameter cannot be extracted. That  $h$ ,  $p$ , and  $r$  are not unique means that more than one set of the Euler parameters can be used to yield the same transform. More about Euler angle conversion can be found in Shoemake's 1994 article [1179]. The simple method outlined above can result in problems with numerical instability, which is avoidable at some cost in speed [992].

**EXAMPLE: CONSTRAINING A TRANSFORM.** Imagine you are holding a wrench snatched to a screw bolt and to get the screw bolt in place you have to rotate the wrench around the  $x$ -axis. Now assume that your input device (mouse, VR gloves, space-ball, etc.) gives you an orthogonal transform for the movement of the wrench. The problem that you encounter is that you do not want to apply that transform to the wrench, which supposedly should rotate around only the  $x$ -axis. So to restrict the input transform, called  $\mathbf{P}$ , to a rotation around the  $x$ -axis, simply extract the Euler angles,  $h$ ,  $p$ , and  $r$ , using the method described in this section, and then create a new matrix  $\mathbf{R}_x(p)$ . This is then the sought-after transform that will rotate the wrench around the  $x$ -axis (if  $\mathbf{P}$  now contains such a movement).  $\square$

### 4.2.3 Matrix Decomposition

Up to this point we have been working under the assumption that we know the origin and history of the transformation matrix we are using. This is often not the case: For example, nothing more than a concatenated matrix may be associated with some transformed object. The task of retrieving various transforms from a concatenated matrix is called *matrix decomposition*.

There are many reasons to retrieve a set of transformations. Uses include:

- Extracting just the scaling factors for an object.
- Finding transforms needed by a particular system. For example, VRML [1310] uses a *Transform* node (see Section 4.1.5) and does not allow the use of an arbitrary  $4 \times 4$  matrix.
- Determining whether a model has undergone only rigid-body transforms.
- Interpolating between keyframes in an animation where only the matrix for the object is available.
- Removing shears from a rotation matrix.

We have already presented two decompositions, those of deriving the translation and rotation matrix for a rigid-body transformation (see Section 4.1.6) and deriving the Euler angles from an orthogonal matrix (Section 4.2.2).

As we have seen, it is trivial to retrieve the translation matrix, as we simply need the elements in the last column of the  $4 \times 4$  matrix. We can also determine if a reflection has occurred by checking whether the determinant of the matrix is negative. To separate out the rotation, scaling, and shears takes more determined effort.

Fortunately, there are a number of articles on this topic, as well as code available online. Thomas [1265] and Goldman [414, 415] each present somewhat different methods for various classes of transformations. Shoemake [1178] improves upon their techniques for affine matrices, as his algorithm is independent of frame of reference and attempts to decompose the matrix in order to obtain rigid-body transforms.

#### 4.2.4 Rotation about an Arbitrary Axis

Sometimes it is convenient to have a procedure that rotates an entity by some angle around an arbitrary axis. Assume that the rotation axis,  $\mathbf{r}$ , is normalized and that a transform should be created that rotates  $\alpha$  radians around  $\mathbf{r}$ .

To do this, first find two more arbitrary axes of unit length that are mutually orthogonal with themselves and with  $\mathbf{r}$ , i.e., orthonormal. These then form a basis.<sup>8</sup> The idea is to change bases (Section A.3.2) from the standard basis to this new basis, and then rotate  $\alpha$  radians around, say, the  $x$ -axis (which then should correspond to  $\mathbf{r}$ ) and finally transform back to the standard basis [214]. This procedure is illustrated in Figure 4.7.

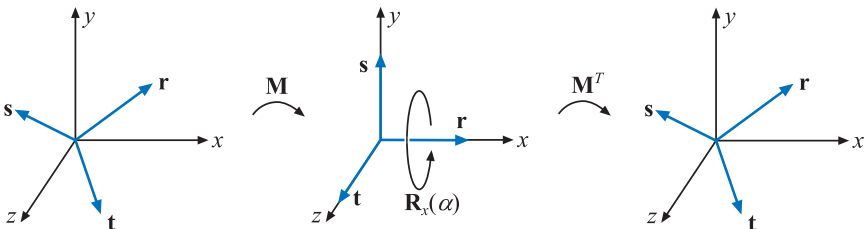


**Figure 4.7.** Rotation about an arbitrary axis,  $\mathbf{r}$ , is accomplished by finding an orthonormal basis formed by  $\mathbf{r}$ ,  $\mathbf{s}$ , and  $\mathbf{t}$ . We then align this basis with the standard basis so that  $\mathbf{r}$  is aligned with the  $x$ -axis. The rotation around the  $x$ -axis is performed there, and finally we transform back.

<sup>8</sup>An example of a basis is the standard basis, which has the axes  $\mathbf{e}_x = (1, 0, 0)$ ,  $\mathbf{e}_y = (0, 1, 0)$ , and  $\mathbf{e}_z = (0, 0, 1)$ .

The first step is to compute the orthonormal axes of the basis. The first axis is  $\mathbf{r}$ , i.e., the one we want to rotate around. We now concentrate on finding the second axis,  $\mathbf{s}$ , knowing that the third axis,  $\mathbf{t}$ , will be the cross product of the first and the second axis,  $\mathbf{t} = \mathbf{r} \times \mathbf{s}$ . A numerically stable way to do this is to find the smallest component (in absolute value) of  $\mathbf{r}$ , and set it to 0. Swap the two remaining components, and then negate the first<sup>9</sup> of these. Mathematically, this is expressed as [576]:

$$\begin{aligned}\bar{\mathbf{s}} &= \begin{cases} (0, -r_z, r_y), & \text{if } |r_x| < |r_y| \text{ and } |r_x| < |r_z|, \\ (-r_z, 0, r_x), & \text{if } |r_y| < |r_x| \text{ and } |r_y| < |r_z|, \\ (-r_y, r_x, 0), & \text{if } |r_z| < |r_x| \text{ and } |r_z| < |r_y|, \end{cases} \\ \mathbf{s} &= \bar{\mathbf{s}} / \|\bar{\mathbf{s}}\|, \\ \mathbf{t} &= \mathbf{r} \times \mathbf{s}.\end{aligned}\quad (4.24)$$

This guarantees that  $\bar{\mathbf{s}}$  is orthogonal (perpendicular) to  $\mathbf{r}$ , and that  $(\mathbf{r}, \mathbf{s}, \mathbf{t})$  is an orthonormal basis. We use these three vectors as the rows in a matrix as below:

$$\mathbf{M} = \begin{pmatrix} \mathbf{r}^T \\ \mathbf{s}^T \\ \mathbf{t}^T \end{pmatrix}. \quad (4.25)$$

This matrix transforms the vector  $\mathbf{r}$  into the  $x$ -axis ( $\mathbf{e}_x$ ),  $\mathbf{s}$  into the  $y$ -axis, and  $\mathbf{t}$  into the  $z$ -axis. So the final transform for rotating  $\alpha$  radians around the normalized vector  $\mathbf{r}$  is then

$$\mathbf{X} = \mathbf{M}^T \mathbf{R}_x(\alpha) \mathbf{M}. \quad (4.26)$$

In words, this means that first we transform so that  $\mathbf{r}$  is the  $x$ -axis (using  $\mathbf{M}$ ), then we rotate  $\alpha$  radians around this  $x$ -axis (using  $\mathbf{R}_x(\alpha)$ ), and then we transform back using the inverse of  $\mathbf{M}$ , which in this case is  $\mathbf{M}^T$  because  $\mathbf{M}$  is orthogonal.

Another method for rotating around an arbitrary, normalized axis  $\mathbf{r}$  by  $\phi$  radians has been presented by Goldman [412]. Here, we simply present his transform:

$$\begin{aligned}\mathbf{R} &= \\ &\begin{pmatrix} \cos \phi + (1 - \cos \phi)r_x^2 & (1 - \cos \phi)r_x r_y - r_z \sin \phi & (1 - \cos \phi)r_x r_z + r_y \sin \phi \\ (1 - \cos \phi)r_x r_y + r_z \sin \phi & \cos \phi + (1 - \cos \phi)r_y^2 & (1 - \cos \phi)r_y r_z - r_x \sin \phi \\ (1 - \cos \phi)r_x r_z - r_y \sin \phi & (1 - \cos \phi)r_y r_z + r_x \sin \phi & \cos \phi + (1 - \cos \phi)r_z^2 \end{pmatrix}.\end{aligned}\quad (4.27)$$

In Section 4.3.2, we present yet another method for solving this problem, using quaternions. Also in that section are more efficient algorithms for related problems, such as rotation from one vector to another.

---

<sup>9</sup>In fact, either of the nonzero components could be negated.

## 4.3 Quaternions

Although quaternions were invented back in 1843 by Sir William Rowan Hamilton as an extension to the complex numbers, it was not until 1985 that Shoemake [1176] introduced them to the field of computer graphics. Quaternions are a powerful tool for constructing transforms with compelling features, and in some ways, they are superior to both Euler angles and matrices, especially when it comes to rotations and orientations. Given an axis & angle representation, translating to or from a quaternion is straightforward, while Euler angle conversion in either direction is challenging. Quaternions can be used for stable and constant interpolation of orientations, something that cannot be done well with Euler angles.

A complex number has a real and an imaginary part. Each is represented by two real numbers, the second real number being multiplied by  $\sqrt{-1}$ . Similarly, quaternions have four parts. The first three values are closely related to axis of rotation, with the angle of rotation affecting all four parts (more about this in Section 4.3.2). Each quaternion is represented by four real numbers, each associated with a different part. Since quaternions have four components, we choose to represent them as vectors, but to differentiate them, we put a hat on them:  $\hat{\mathbf{q}}$ . We begin with some mathematical background on quaternions, which is then used to construct interesting and useful transforms.

### 4.3.1 Mathematical Background

We start with the definition of a quaternion.

**Definition.** A quaternion  $\hat{\mathbf{q}}$  can be defined in the following ways, all equivalent.

$$\begin{aligned}\hat{\mathbf{q}} &= (\mathbf{q}_v, q_w) = iq_x + jq_y + kq_z + q_w = \mathbf{q}_v + q_w, \\ \mathbf{q}_v &= iq_x + jq_y + kq_z = (q_x, q_y, q_z), \\ i^2 &= j^2 = k^2 = -1, \quad jk = -kj = i, \quad ki = -ik = j, \quad ij = -ji = k.\end{aligned}\tag{4.28}$$

The variable  $q_w$  is called the real part of a quaternion,  $\hat{\mathbf{q}}$ . The imaginary part is  $\mathbf{q}_v$ , and  $i$ ,  $j$ , and  $k$  are called imaginary units.  $\square$

For the imaginary part,  $\mathbf{q}_v$ , we can use all the normal vector operations, such as addition, scaling, dot product, cross product, and more. Using the definition of the quaternion, the multiplication operation between two quaternions,  $\hat{\mathbf{q}}$  and  $\hat{\mathbf{r}}$ , is derived as shown below. Note that the multiplication of the imaginary units is noncommutative.

**Multiplication :**

$$\begin{aligned}
 \hat{\mathbf{q}}\hat{\mathbf{r}} &= (iq_x + jq_y + kq_z + q_w)(ir_x + jr_y + kr_z + r_w) \\
 &= i(q_y r_z - q_z r_y + r_w q_x + q_w r_x) \\
 &\quad + j(q_z r_x - q_x r_z + r_w q_y + q_w r_y) \\
 &\quad + k(q_x r_y - q_y r_x + r_w q_z + q_w r_z) \\
 &\quad + q_w r_w - q_x r_x - q_y r_y - q_z r_z = \\
 &= (\mathbf{q}_v \times \mathbf{r}_v + r_w \mathbf{q}_v + q_w \mathbf{r}_v, \ q_w r_w - \mathbf{q}_v \cdot \mathbf{r}_v).
 \end{aligned} \tag{4.29}$$

As can be seen in this equation, we use both the cross product and the dot product to compute the multiplication of two quaternions.<sup>10</sup> Along with the definition of the quaternion, the definitions of addition, conjugate, norm, and an identity are needed:

$$\text{Addition : } \hat{\mathbf{q}} + \hat{\mathbf{r}} = (\mathbf{q}_v, q_w) + (\mathbf{r}_v, r_w) = (\mathbf{q}_v + \mathbf{r}_v, q_w + r_w).$$

$$\text{Conjugate : } \hat{\mathbf{q}}^* = (\mathbf{q}_v, q_w)^* = (-\mathbf{q}_v, q_w).$$

$$\begin{aligned}
 \text{Norm : } n(\hat{\mathbf{q}}) &= \sqrt{\hat{\mathbf{q}}\hat{\mathbf{q}}^*} = \sqrt{\hat{\mathbf{q}}^*\hat{\mathbf{q}}} = \sqrt{\mathbf{q}_v \cdot \mathbf{q}_v + q_w^2} \\
 &= \sqrt{q_x^2 + q_y^2 + q_z^2 + q_w^2}.
 \end{aligned} \tag{4.30}$$

$$\text{Identity : } \hat{\mathbf{i}} = (\mathbf{0}, 1).$$

When  $n(\hat{\mathbf{q}}) = \sqrt{\hat{\mathbf{q}}\hat{\mathbf{q}}^*}$  is simplified (result shown above), the imaginary parts cancel out and only a real part remains. The norm is sometimes denoted  $\|\hat{\mathbf{q}}\| = n(\hat{\mathbf{q}})$  [808]. A consequence of the above is that a multiplicative inverse, denoted by  $\hat{\mathbf{q}}^{-1}$ , can be derived. The equation  $\hat{\mathbf{q}}^{-1}\hat{\mathbf{q}} = \hat{\mathbf{q}}\hat{\mathbf{q}}^{-1} = 1$  must hold for the inverse (as is common for a multiplicative inverse). We derive a formula from the definition of the norm:

$$\begin{aligned}
 n(\hat{\mathbf{q}})^2 &= \hat{\mathbf{q}}\hat{\mathbf{q}}^* \\
 &\iff \\
 \frac{\hat{\mathbf{q}}\hat{\mathbf{q}}^*}{n(\hat{\mathbf{q}})^2} &= 1.
 \end{aligned} \tag{4.31}$$

This gives the multiplicative inverse as shown below:

$$\text{Inverse : } \hat{\mathbf{q}}^{-1} = \frac{1}{n(\hat{\mathbf{q}})^2}\hat{\mathbf{q}}^*. \tag{4.32}$$

The formula for the inverse uses scalar multiplication, which is an operation derived from the multiplication seen in Equation 4.29:  $s\hat{\mathbf{q}} = (\mathbf{0}, s)(\mathbf{q}_v, q_w)$

---

<sup>10</sup>In fact, the quaternion multiplication is the origin of both the dot product and the cross product.

$= (s\mathbf{q}_v, sq_w)$ , and  $\hat{\mathbf{q}}s = (\mathbf{q}_v, q_w)(\mathbf{0}, s) = (s\mathbf{q}_v, sq_w)$ , which means that scalar multiplication is commutative:  $s\hat{\mathbf{q}} = \hat{\mathbf{q}}s = (s\mathbf{q}_v, sq_w)$ .

The following collection of rules are simple to derive from the definitions:

**Conjugate rules:**

$$\begin{aligned} (\hat{\mathbf{q}}^*)^* &= \hat{\mathbf{q}}, \\ (\hat{\mathbf{q}} + \hat{\mathbf{r}})^* &= \hat{\mathbf{q}}^* + \hat{\mathbf{r}}^*, \\ (\hat{\mathbf{q}}\hat{\mathbf{r}})^* &= \hat{\mathbf{r}}^*\hat{\mathbf{q}}^*. \end{aligned} \quad (4.33)$$

**Norm rules:**

$$\begin{aligned} n(\hat{\mathbf{q}}^*) &= n(\hat{\mathbf{q}}), \\ n(\hat{\mathbf{q}}\hat{\mathbf{r}}) &= n(\hat{\mathbf{q}})n(\hat{\mathbf{r}}). \end{aligned} \quad (4.34)$$

**Laws of Multiplication:**

**Linearity:**

$$\begin{aligned} \hat{\mathbf{p}}(s\hat{\mathbf{q}} + t\hat{\mathbf{r}}) &= s\hat{\mathbf{p}}\hat{\mathbf{q}} + t\hat{\mathbf{p}}\hat{\mathbf{r}}, \\ (s\hat{\mathbf{p}} + t\hat{\mathbf{q}})\hat{\mathbf{r}} &= s\hat{\mathbf{p}}\hat{\mathbf{r}} + t\hat{\mathbf{q}}\hat{\mathbf{r}}. \end{aligned} \quad (4.35)$$

**Associativity:**

$$\hat{\mathbf{p}}(\hat{\mathbf{q}}\hat{\mathbf{r}}) = (\hat{\mathbf{p}}\hat{\mathbf{q}})\hat{\mathbf{r}}.$$

A unit quaternion,  $\hat{\mathbf{q}} = (\mathbf{q}_v, q_w)$ , is such that  $n(\hat{\mathbf{q}}) = 1$ . From this it follows that  $\hat{\mathbf{q}}$  may be written as

$$\hat{\mathbf{q}} = (\sin \phi \mathbf{u}_q, \cos \phi) = \sin \phi \mathbf{u}_q + \cos \phi, \quad (4.36)$$

for some three-dimensional vector  $\mathbf{u}_q$ , such that  $\|\mathbf{u}_q\| = 1$ , because

$$\begin{aligned} n(\hat{\mathbf{q}}) &= n(\sin \phi \mathbf{u}_q, \cos \phi) = \sqrt{\sin^2 \phi (\mathbf{u}_q \cdot \mathbf{u}_q) + \cos^2 \phi} \\ &= \sqrt{\sin^2 \phi + \cos^2 \phi} = 1 \end{aligned} \quad (4.37)$$

if and only if  $\mathbf{u}_q \cdot \mathbf{u}_q = 1 = \|\mathbf{u}_q\|^2$ . As will be seen in the next section, unit quaternions are perfectly suited for creating rotations and orientations in a most efficient way. But before that, some extra operations will be introduced for unit quaternions.

For complex numbers, a two-dimensional unit vector can be written as  $\cos \phi + i \sin \phi = e^{i\phi}$ . The equivalent for quaternions is

$$\hat{\mathbf{q}} = \sin \phi \mathbf{u}_q + \cos \phi = e^{\phi \mathbf{u}_q}. \quad (4.38)$$

The log and the power functions for unit quaternions follow from Equation 4.38:

**Logarithm :**  $\log(\hat{\mathbf{q}}) = \log(e^{\phi \mathbf{u}_q}) = \phi \mathbf{u}_q,$

**Power :**  $\hat{\mathbf{q}}^t = (\sin \phi \mathbf{u}_q + \cos \phi)^t = e^{\phi t \mathbf{u}_q} = \sin(\phi t) \mathbf{u}_q + \cos(\phi t).$  (4.39)

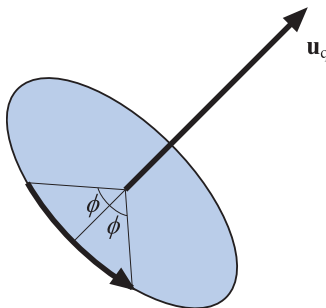


**Figure 4.8.** Illustration of the rotation transform represented by a unit quaternion,  $\hat{\mathbf{q}} = (\sin \phi \mathbf{u}_q, \cos \phi)$ . The transform rotates  $2\phi$  radians around the axis  $\mathbf{u}_q$ .

### 4.3.2 Quaternion Transforms

We will now study a subclass of the quaternion set, namely those of unit length, called *unit quaternions*. The most important fact about unit quaternions is that they can represent any three-dimensional rotation, and that this representation is extremely compact and simple.

Now we will describe what makes unit quaternions so useful for rotations and orientations. First, put the four coordinates of a point or vector  $\mathbf{p} = (p_x \ p_y \ p_z \ p_w)^T$  into the components of a quaternion  $\hat{\mathbf{p}}$ , and assume that we have a unit quaternion  $\hat{\mathbf{q}} = (\sin \phi \mathbf{u}_q, \cos \phi)$ . Then

$$\hat{\mathbf{q}} \hat{\mathbf{p}} \hat{\mathbf{q}}^{-1} \quad (4.40)$$

rotates  $\hat{\mathbf{p}}$  (and thus the point  $\mathbf{p}$ ) around the axis  $\mathbf{u}_q$  by an angle  $2\phi$ . Note that since  $\hat{\mathbf{q}}$  is a unit quaternion,  $\hat{\mathbf{q}}^{-1} = \hat{\mathbf{q}}^*$ . This rotation, which clearly can be used to rotate around any axis, is illustrated in Figure 4.8.

Any nonzero real multiple of  $\hat{\mathbf{q}}$  also represents the same transform, which means that  $\hat{\mathbf{q}}$  and  $-\hat{\mathbf{q}}$  represent the same rotation. That is, negating the axis,  $\mathbf{u}_q$ , and the real part,  $q_w$ , creates a quaternion that rotates exactly as the original quaternion does. It also means that the extraction of a quaternion from a matrix can return either  $\hat{\mathbf{q}}$  or  $-\hat{\mathbf{q}}$ .

Given two unit quaternions,  $\hat{\mathbf{q}}$  and  $\hat{\mathbf{r}}$ , the concatenation of first applying  $\hat{\mathbf{q}}$  and then  $\hat{\mathbf{r}}$  to a quaternion,  $\hat{\mathbf{p}}$  (which can be interpreted as a point  $\mathbf{p}$ ), is given by Equation 4.41:

$$\hat{\mathbf{r}}(\hat{\mathbf{q}}\hat{\mathbf{p}}\hat{\mathbf{q}}^*)\hat{\mathbf{r}}^* = (\hat{\mathbf{r}}\hat{\mathbf{q}})\hat{\mathbf{p}}(\hat{\mathbf{r}}\hat{\mathbf{q}})^* = \hat{\mathbf{c}}\hat{\mathbf{p}}\hat{\mathbf{c}}^*. \quad (4.41)$$

Here,  $\hat{\mathbf{c}} = \hat{\mathbf{r}}\hat{\mathbf{q}}$  is the unit quaternion representing the concatenation of the unit quaternions  $\hat{\mathbf{q}}$  and  $\hat{\mathbf{r}}$ .

### Matrix Conversion

Since some systems have matrix multiplication implemented in hardware and the fact that matrix multiplication is more efficient than Equation 4.40, we need conversion methods for transforming a quaternion into a matrix and vice versa. A quaternion,  $\hat{\mathbf{q}}$ , can be converted into a matrix  $\mathbf{M}^q$ , as expressed in Equation 4.42 [1176, 1177]:

$$\mathbf{M}^q = \begin{pmatrix} 1 - s(q_y^2 + q_z^2) & s(q_x q_y - q_w q_z) & s(q_x q_z + q_w q_y) & 0 \\ s(q_x q_y + q_w q_z) & 1 - s(q_x^2 + q_z^2) & s(q_y q_z - q_w q_x) & 0 \\ s(q_x q_z - q_w q_y) & s(q_y q_z + q_w q_x) & 1 - s(q_x^2 + q_y^2) & 0 \\ 0 & 0 & 0 & 1 \end{pmatrix}. \quad (4.42)$$

Here, the scalar is  $s = 2/n(\hat{\mathbf{q}})$ . For unit quaternions, this simplifies to

$$\mathbf{M}^q = \begin{pmatrix} 1 - 2(q_y^2 + q_z^2) & 2(q_x q_y - q_w q_z) & 2(q_x q_z + q_w q_y) & 0 \\ 2(q_x q_y + q_w q_z) & 1 - 2(q_x^2 + q_z^2) & 2(q_y q_z - q_w q_x) & 0 \\ 2(q_x q_z - q_w q_y) & 2(q_y q_z + q_w q_x) & 1 - 2(q_x^2 + q_y^2) & 0 \\ 0 & 0 & 0 & 1 \end{pmatrix}. \quad (4.43)$$

Once the quaternion is constructed, *no* trigonometric functions need to be computed, so the conversion process is efficient in practice.

The reverse conversion, from an orthogonal matrix,  $\mathbf{M}^q$ , into a unit quaternion,  $\hat{\mathbf{q}}$ , is a bit more involved. Key to this process are the following differences made from the matrix in Equation 4.43:

$$\begin{aligned} m_{21}^q - m_{12}^q &= 4q_w q_x, \\ m_{02}^q - m_{20}^q &= 4q_w q_y, \\ m_{10}^q - m_{01}^q &= 4q_w q_z. \end{aligned} \quad (4.44)$$

The implication of these equations is that if  $q_w$  is known, the values of the vector  $\mathbf{v}_q$  can be computed, and thus  $\hat{\mathbf{q}}$  derived. The trace (see page 898) of  $\mathbf{M}^q$  is calculated by

$$\begin{aligned} \text{tr}(\mathbf{M}^q) &= 4 - 2s(q_x^2 + q_y^2 + q_z^2) = 4 \left( 1 - \frac{q_x^2 + q_y^2 + q_z^2}{q_x^2 + q_y^2 + q_z^2 + q_w^2} \right) \\ &= \frac{4q_w^2}{q_x^2 + q_y^2 + q_z^2 + q_w^2} = \frac{4q_w^2}{n(\hat{\mathbf{q}})}. \end{aligned} \quad (4.45)$$

This result yields the following conversion for a unit quaternion:

$$\begin{aligned} q_w &= \frac{1}{2} \sqrt{\text{tr}(\mathbf{M}^q)}, & q_x &= \frac{m_{21}^q - m_{12}^q}{4q_w}, \\ q_y &= \frac{m_{02}^q - m_{20}^q}{4q_w}, & q_z &= \frac{m_{10}^q - m_{01}^q}{4q_w}. \end{aligned} \quad (4.46)$$

To have a numerically stable routine [1177], divisions by small numbers should be avoided. Therefore, first set  $t = q_w^2 - q_x^2 - q_y^2 - q_z^2$ , from which it follows that

$$\begin{aligned} m_{00} &= t + 2q_x^2, \\ m_{11} &= t + 2q_y^2, \\ m_{22} &= t + 2q_z^2, \\ u &= m_{00} + m_{11} + m_{22} = t + 2q_w^2, \end{aligned} \tag{4.47}$$

which in turn implies that the largest of  $m_{00}$ ,  $m_{11}$ ,  $m_{22}$ , and  $u$  determine which of  $q_x$ ,  $q_y$ ,  $q_z$ , and  $q_w$  is largest. If  $q_w$  is largest, then Equation 4.46 is used to derive the quaternion. Otherwise, we note that the following holds:

$$\begin{aligned} 4q_x^2 &= +m_{00} - m_{11} - m_{22} + m_{33}, \\ 4q_y^2 &= -m_{00} + m_{11} - m_{22} + m_{33}, \\ 4q_z^2 &= -m_{00} - m_{11} + m_{22} + m_{33}, \\ 4q_w^2 &= \text{tr}(\mathbf{M}^q). \end{aligned} \tag{4.48}$$

The appropriate equation of the ones above is then used to compute the largest of  $q_x$ ,  $q_y$ , and  $q_z$ , after which Equation 4.44 is used to calculate the remaining components of  $\hat{\mathbf{q}}$ . Luckily, there is code for this—see the *Further Reading and Resources* at the end of this chapter.

### Spherical Linear Interpolation

Spherical linear interpolation is an operation that, given two unit quaternions,  $\hat{\mathbf{q}}$  and  $\hat{\mathbf{r}}$ , and a parameter  $t \in [0, 1]$ , computes an interpolated quaternion. This is useful for animating objects, for example. It is not as useful for interpolating camera orientations, as the camera's "up" vector can become tilted during the interpolation, usually a disturbing effect [349].

The algebraic form of this operation is expressed by the composite quaternion,  $\hat{\mathbf{s}}$ , below:

$$\hat{\mathbf{s}}(\hat{\mathbf{q}}, \hat{\mathbf{r}}, t) = (\hat{\mathbf{r}}\hat{\mathbf{q}}^{-1})^t\hat{\mathbf{q}}. \tag{4.49}$$

However, for software implementations, the following form, where *slerp* stands for spherical linear interpolation, is much more appropriate:

$$\hat{\mathbf{s}}(\hat{\mathbf{q}}, \hat{\mathbf{r}}, t) = \text{slerp}(\hat{\mathbf{q}}, \hat{\mathbf{r}}, t) = \frac{\sin(\phi(1-t))}{\sin \phi} \hat{\mathbf{q}} + \frac{\sin(\phi t)}{\sin \phi} \hat{\mathbf{r}}. \tag{4.50}$$

To compute  $\phi$ , which is needed in this equation, the following fact can be used:  $\cos \phi = q_x r_x + q_y r_y + q_z r_z + q_w r_w$  [224]. For  $t \in [0, 1]$ , the slerp function computes (unique<sup>11</sup>) interpolated quaternions that together

---

<sup>11</sup>If and only if  $\hat{\mathbf{q}}$  and  $\hat{\mathbf{r}}$  are not opposite.

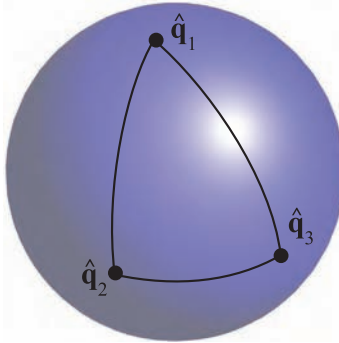


**Figure 4.9.** Unit quaternions are represented as points on the unit sphere. The function slerp is used to interpolate between the quaternions, and the interpolated path is a great arc on the sphere. Note that interpolating from  $\hat{q}_1$  to  $\hat{q}_2$  and interpolating from  $\hat{q}_1$  to  $\hat{q}_3$  to  $\hat{q}_2$  are not the same thing, even though they arrive at the same orientation.

constitute the shortest arc on a four-dimensional unit sphere from  $\hat{\mathbf{q}}$  ( $t = 0$ ) to  $\hat{\mathbf{r}}$  ( $t = 1$ ). The arc is located on the circle that is formed from the intersection between the plane given by  $\hat{\mathbf{q}}$ ,  $\hat{\mathbf{r}}$ , and the origin, and the four-dimensional unit sphere. This is illustrated in Figure 4.9. The computed rotation quaternion rotates around a fixed axis at constant speed. A curve such as this, that has constant speed and thus zero acceleration, is called a *geodesic* curve [263].

The slerp function is perfectly suited for interpolating between two orientations and it behaves well (fixed axis, constant speed). This is not the case with when interpolating using several Euler angles. In practice, computing a slerp directly is an expensive operation involving calling trigonometric functions. Li [771, 772] provides much faster incremental methods to compute slerps that do not sacrifice any accuracy.

When more than two orientations, say  $\hat{\mathbf{q}}_0, \hat{\mathbf{q}}_1, \dots, \hat{\mathbf{q}}_{n-1}$ , are available, and we want to interpolate from  $\hat{\mathbf{q}}_0$  to  $\hat{\mathbf{q}}_1$  to  $\hat{\mathbf{q}}_2$ , and so on until  $\hat{\mathbf{q}}_{n-1}$ , slerp could be used in a straightforward fashion. Now, when we approach, say,  $\hat{\mathbf{q}}_i$ , we would use  $\hat{\mathbf{q}}_{i-1}$  and  $\hat{\mathbf{q}}_i$  as arguments to slerp. After passing through  $\hat{\mathbf{q}}_i$ , we would then use  $\hat{\mathbf{q}}_i$  and  $\hat{\mathbf{q}}_{i+1}$  as arguments to slerp. This will cause sudden jerks to appear in the orientation interpolation, which can be seen in Figure 4.9. This is similar to what happens when points are linearly interpolated; see the upper right part of Figure 13.2 on page 578. Some readers may wish to revisit the following paragraph after reading about splines in Chapter 13.

A better way to interpolate is to use some sort of spline. We introduce quaternions  $\hat{\mathbf{a}}_i$  and  $\hat{\mathbf{a}}_{i+1}$  between  $\hat{\mathbf{q}}_i$  and  $\hat{\mathbf{q}}_{i+1}$ . Spherical cubic interpola-

tion can be defined within the set of quaternions  $\hat{\mathbf{q}}_i$ ,  $\hat{\mathbf{a}}_i$ ,  $\hat{\mathbf{a}}_{i+1}$ , and  $\hat{\mathbf{q}}_{i+1}$ . Surprisingly, these extra quaternions are computed as shown below [294]<sup>12</sup>:

$$\hat{\mathbf{a}}_i = \hat{\mathbf{q}}_i \exp \left[ -\frac{\log(\hat{\mathbf{q}}_i^{-1} \hat{\mathbf{q}}_{i-1}) + \log(\hat{\mathbf{q}}_i^{-1} \hat{\mathbf{q}}_{i+1})}{4} \right]. \quad (4.51)$$

The  $\hat{\mathbf{q}}_i$ , and  $\hat{\mathbf{a}}_i$  will be used to spherically interpolate the quaternions using a smooth cubic spline, as shown in Equation 4.52:

$$\begin{aligned} \text{squad}(\hat{\mathbf{q}}_i, \hat{\mathbf{q}}_{i+1}, \hat{\mathbf{a}}_i, \hat{\mathbf{a}}_{i+1}, t) = \\ \text{slerp}(\text{slerp}(\hat{\mathbf{q}}_i, \hat{\mathbf{q}}_{i+1}, t), \text{slerp}(\hat{\mathbf{a}}_i, \hat{\mathbf{a}}_{i+1}, t), 2t(1-t)). \end{aligned} \quad (4.52)$$

As can be seen above, the **squad** function is constructed from repeated spherical interpolation using slerp (see Section 13.1.1 for information on repeated linear interpolation for points). The interpolation will pass through the initial orientations  $\hat{\mathbf{q}}_i$ ,  $i \in [0, \dots, n-1]$ , but not through  $\hat{\mathbf{a}}_i$ —these are used to indicate the tangent orientations at the initial orientations.

### *Rotation from One Vector to Another*

A common operation is transforming from one direction  $\mathbf{s}$  to another direction  $\mathbf{t}$  via the shortest path possible. The mathematics of quaternions simplifies this procedure greatly, and also shows the close relationship the quaternion has with this representation. First, normalize  $\mathbf{s}$  and  $\mathbf{t}$ . Then compute the unit rotation axis, called  $\mathbf{u}$ , which is computed as  $\mathbf{u} = (\mathbf{s} \times \mathbf{t}) / \|\mathbf{s} \times \mathbf{t}\|$ . Next,  $e = \mathbf{s} \cdot \mathbf{t} = \cos(2\phi)$  and  $\|\mathbf{s} \times \mathbf{t}\| = \sin(2\phi)$ , where  $2\phi$  is the angle between  $\mathbf{s}$  and  $\mathbf{t}$ . The quaternion that represents the rotation from  $\mathbf{s}$  to  $\mathbf{t}$  is then  $\hat{\mathbf{q}} = (\sin \phi \mathbf{u}, \cos \phi)$ . In fact, simplifying  $\hat{\mathbf{q}} = (\frac{\sin \phi}{\sin 2\phi}(\mathbf{s} \times \mathbf{t}), \cos \phi)$ , using the half-angle relations (see page 919) and the trigonometric identity (Equation B.9) gives [853]

$$\hat{\mathbf{q}} = (\mathbf{q}_v, q_w) = \left( \frac{1}{\sqrt{2(1+e)}}(\mathbf{s} \times \mathbf{t}), \frac{\sqrt{2(1+e)}}{2} \right). \quad (4.53)$$

Directly generating the quaternion in this fashion (versus normalizing the cross product  $\mathbf{s} \times \mathbf{t}$ ) avoids numerical instability when  $\mathbf{s}$  and  $\mathbf{t}$  point in nearly the same direction [853]. Stability problems appear for both methods when  $\mathbf{s}$  and  $\mathbf{t}$  point in opposite directions, as a division by zero occurs. When this special case is detected, any axis of rotation perpendicular to  $\mathbf{s}$  can be used to rotate to  $\mathbf{t}$ .

Sometimes we need the matrix representation of a rotation from  $\mathbf{s}$  to  $\mathbf{t}$ . After some algebraic and trigonometric simplification of Equation 4.43,

---

<sup>12</sup>Shoemake [1176] gives another derivation.

the rotation matrix becomes [893]

$$\mathbf{R}(\mathbf{s}, \mathbf{t}) = \begin{pmatrix} e + hv_x^2 & hv_xv_y - v_z & hv_xv_z + v_y & 0 \\ hv_xv_y + v_z & e + hv_y^2 & hv_yv_z - v_x & 0 \\ hv_xv_z - v_y & hv_yv_z + v_x & e + hv_z^2 & 0 \\ 0 & 0 & 0 & 1 \end{pmatrix}. \quad (4.54)$$

In this equation, we have used the following intermediate calculations:

$$\begin{aligned} \mathbf{v} &= \mathbf{s} \times \mathbf{t}, \\ e &= \cos(2\phi) = \mathbf{s} \cdot \mathbf{t}, \\ h &= \frac{1 - \cos(2\phi)}{\sin^2(2\phi)} = \frac{1 - e}{\mathbf{v} \cdot \mathbf{v}} = \frac{1}{1 + e}. \end{aligned} \quad (4.55)$$

As can be seen, all square roots and trigonometric functions have disappeared due to the simplifications, and so this is an efficient way to create the matrix.

Note that care must be taken when  $\mathbf{s}$  and  $\mathbf{t}$  are parallel or near parallel, because then  $\|\mathbf{s} \times \mathbf{t}\| \approx 0$ . If  $\phi \approx 0$ , then we can return the identity matrix. However, if  $2\phi \approx \pi$ , then we can rotate  $\pi$  radians around *any* axis. This axis can be found as the cross product between  $\mathbf{s}$  and any other vector that is not parallel to  $\mathbf{s}$  (see Section 4.2.4). Möller and Hughes use Householder matrices to handle this special case in a different way [893].

**EXAMPLE: POSITIONING AND ORIENTING A CAMERA.** Assume that the default position for a virtual camera (or viewpoint) is  $(0 \ 0 \ 0)^T$  and the default view direction  $\mathbf{v}$  is along the negative  $z$ -axis, i.e.,  $\mathbf{v} = (0 \ 0 \ -1)^T$ . Now, the goal is to create a transform that moves the camera to a new position  $\mathbf{p}$ , looking in a new direction  $\mathbf{w}$ . Start by orienting the camera, which can be done by rotating the default view direction into the destination view direction.  $\mathbf{R}(\mathbf{v}, \mathbf{w})$  takes care of this. The positioning is simply done by translating to  $\mathbf{p}$ , which yields the resulting transform  $\mathbf{X} = \mathbf{T}(\mathbf{p})\mathbf{R}(\mathbf{v}, \mathbf{w})$ . In practice, after the first rotation another vector-vector rotation will most likely be desired to rotate the view's up direction to some desired orientation.  $\square$

## 4.4 Vertex Blending

Imagine that an arm of a digital character is animated using two parts, a forearm and an upper arm, as shown to the left in Figure 4.10. This model could be animated using rigid-body transforms (Section 4.1.6). However, then the joint between these two parts will not resemble a real elbow. This

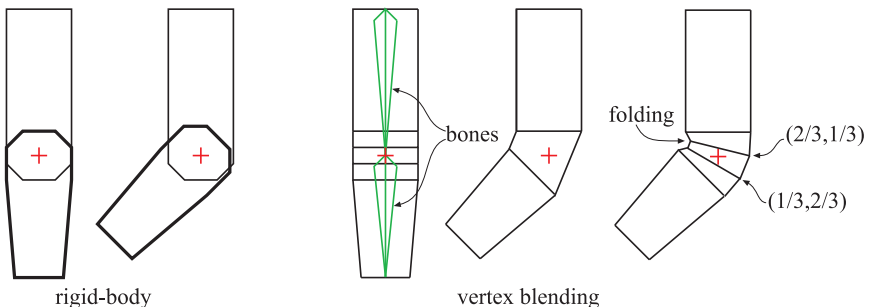


**Figure 4.10.** An arm consisting of a forearm and an upper arm is animated using rigid-body transforms of two separate objects to the left. The elbow does not appear realistic. To the right, vertex blending is used on one single object. The next-to-rightmost arm illustrates what happens when a simple skin directly joins the two parts to cover the elbow. The rightmost arm illustrates what happens when vertex blending is used, and some vertices are blended with different weights:  $(2/3, 1/3)$  means that the vertex weighs the transform from the upper arm by  $2/3$  and from the forearm by  $1/3$ . This figure also shows a drawback of vertex blending in the rightmost illustration. Here, folding in the inner part of the elbow is visible. Better results can be achieved with more bones, and with more carefully selected weights.

is because two separate objects are used, and therefore, the joint consists of overlapping parts from these two separate objects. Clearly, it would be better to use just one single object. However, static model parts do not address the problem of making the joint flexible.

*Vertex blending* is one possible solution to this problem [770, 1376]. This technique has several other names, such as *skinning*, *enveloping*, and *skeleton-subspace deformation*. While the exact origin of the algorithm presented here is unclear, defining bones and having skin react to changes is an old concept in computer animation [807]. In its simplest form, the forearm and the upper arm are animated separately as before, but at the joint, the two parts are connected through an elastic “skin.” So, this elastic part will have one set of vertices that are transformed by the forearm matrix and another set that are transformed by the matrix of the upper arm. This results in triangles whose vertices may be transformed by different matrices, in contrast to using a single matrix per triangle. See Figure 4.10. This basic technique is sometimes called *stitching* [1376].

By taking this one step further, one can allow a single vertex to be transformed by several different matrices, with the resulting locations weighted and blended together. This is done by having a skeleton of bones for the animated object, where each bone’s transform may influence each vertex by a user-defined weight. Since the entire arm may be “elastic,” i.e., all vertices may be affected by more than one matrix, the entire mesh is often called a *skin* (over the bones). See Figure 4.11. Many commercial model-

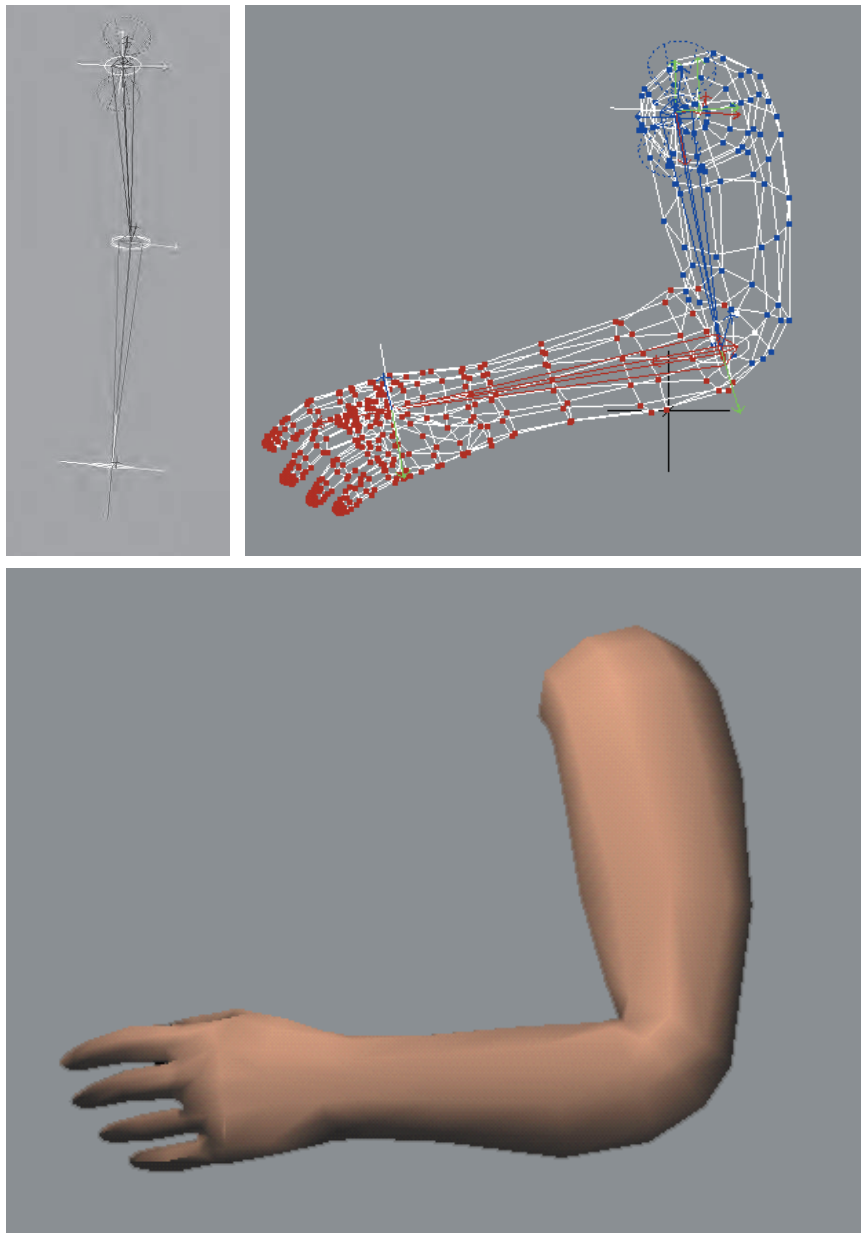


**Figure 4.11.** A real example of vertex blending. The top left image shows the two bones of an arm, in an extended position. On the top right, the mesh is shown, with color denoting which bone owns each vertex. Bottom: the shaded mesh of the arm in a slightly different position. (*Images courtesy of Jeff Lander [717].*)

ing systems have this same sort of skeleton-bone modeling feature. Despite their name, bones do not need to necessarily be rigid. For example, Mohr and Gleicher [889] present the idea of adding additional joints to enable effects such as muscle bulge. James and Twigg [599] discuss animation skinning using bones that can squash and stretch.

Mathematically, this is expressed in Equation 4.56, where  $\mathbf{p}$  is the original vertex, and  $\mathbf{u}(t)$  is the transformed vertex whose position depends on the time  $t$ . There are  $n$  bones influencing the position of  $\mathbf{p}$ , which is expressed in world coordinates. The matrix  $\mathbf{M}_i$  transforms from the initial bone's coordinate system to world coordinates. Typically a bone has its controlling joint at the origin of its coordinate system. For example, a forearm bone would move its elbow joint to the origin, with an animated rotation matrix moving this part of the arm around the joint. The  $\mathbf{B}_i(t)$  matrix is the  $i$ th bone's world transform that changes with time to animate the object, and is typically a concatenation of a number of matrices, such as the hierarchy of previous bone transforms and the local animation matrix. One method of maintaining and updating the  $\mathbf{B}_i(t)$  matrix animation functions is discussed in depth by Woodland [1376]. Finally,  $w_i$  is the weight of bone  $i$  for vertex  $\mathbf{p}$ . The vertex blending equation is

$$\mathbf{u}(t) = \sum_{i=0}^{n-1} w_i \mathbf{B}_i(t) \mathbf{M}_i^{-1} \mathbf{p}, \quad \text{where } \sum_{i=0}^{n-1} w_i = 1, \quad w_i \geq 0. \quad (4.56)$$

Each bone transforms a vertex to a location with respect to its own frame of reference, and the final location is interpolated from the set of computed points. The matrix  $\mathbf{M}_i$  is not explicitly shown in some discussions of skinning, but rather is considered as being a part of  $\mathbf{B}_i(t)$ . We present it here as it is a useful matrix that is almost always a part of the matrix concatenation process.

In practice, the matrices  $\mathbf{B}_i(t)$  and  $\mathbf{M}_i^{-1}$  are concatenated for each bone for each frame of animation, and each resulting matrix is used to transform the vertices. The vertex  $\mathbf{p}$  is transformed by the different bones' concatenated matrices, and then blended using the weights  $w_i$ —thus the name *vertex blending*. The weights are nonnegative and sum to one, so what is occurring is that the vertex is transformed to a few positions and then interpolated among them. As such, the transformed point  $\mathbf{u}$  will lie in the convex hull of the set of points  $\mathbf{B}_i(t) \mathbf{M}_i^{-1} \mathbf{p}$ , for all  $i = 0 \dots n - 1$  (fixed  $t$ ). The normals usually can also be transformed using Equation 4.56. Depending on the transforms used (e.g., if a bone is stretched or squished a considerable amount), the transpose of the inverse of the  $\mathbf{B}_i(t) \mathbf{M}_i^{-1}$  may be needed instead, as discussed in Section 4.1.7.

Vertex blending is well suited for use on the GPU. The set of vertices in the mesh can be placed in a static buffer that is sent to the GPU one time

and reused. In each frame, only the bone matrices change, with a vertex shader computing their effect on the stored mesh. In this way, the amount of data processed on and transferred from the CPU is minimized, allowing the GPU to efficiently render the mesh. It is easiest if the model's whole set of bone matrices can be used together; otherwise the model must be split up and some bones replicated.<sup>13</sup>

When using vertex shaders, it is possible to specify sets of weights that are outside the range  $[0, 1]$  or do not sum to one. However, this makes



**Figure 4.12.** The left side shows problems at the joints when using linear blend skinning. On the right, blending using dual quaternions improves the appearance. (*Images courtesy of Ladislav Kavan et al., model by Paul Steed [1218].*)

<sup>13</sup>DirectX provides a utility `ConvertToIndexedBlendedMesh` to perform such splitting.

sense only if some other blending algorithm, such as *morph targets* (see Section 4.5), is being used.

One drawback of basic vertex blending is that unwanted folding, twisting, and self-intersection can occur [770]. See Figure 4.12. One of the best solutions is to use *dual quaternions*, as presented by Kavan et al. [636]. This technique to perform skinning helps to preserve the rigidity of the original transforms, so avoiding “candy wrapper” twists in limbs. Computation is less than  $1.5\times$  the cost for linear skin blending and the results are excellent, which has led to rapid adoption of this technique. The interested reader is referred to the paper, which also has a brief survey of previous improvements over linear blending.

## 4.5 Morphing

Morphing from one three-dimensional model to another can be useful when performing animations [16, 645, 743, 744]. Imagine that one model is displayed at time  $t_0$  and we wish it to change into another model by time  $t_1$ . For all times between  $t_0$  and  $t_1$ , a continuous “mixed” model is obtained, using some kind of interpolation. An example of morphing is shown in Figure 4.13.

Morphing consists of two major problems, namely, the *vertex correspondence* problem and the *interpolation* problem. Given two arbitrary models, which may have different topologies, different number of vertices, and different mesh connectivity, one usually has to begin by setting up these vertex correspondences. This is a difficult problem, and there has been much research in this field. We refer the interested reader to Alexa’s survey [16].

However, if there is a one-to-one vertex correspondence between the two models, then interpolation can be done on a per-vertex basis. That is, for each vertex in the first model, there must exist only one vertex in the second model, and vice versa. This makes interpolation an easy task. For example, linear interpolation can be used directly on the vertices (see Section 13.1 for other ways of doing interpolation). To compute a morphed vertex for time  $t \in [t_0, t_1]$ , we first compute  $s = (t - t_0)/(t_1 - t_0)$ , and then the linear vertex blend,

$$\mathbf{m} = (1 - s)\mathbf{p}_0 + s\mathbf{p}_1, \quad (4.57)$$

where  $\mathbf{p}_0$  and  $\mathbf{p}_1$  correspond to the same vertex but at different times,  $t_0$  and  $t_1$ .

An interesting variant of morphing, where the user has more intuitive control, is often referred to as *morph targets* or *blend shapes* [671]. The basic idea can be explained using Figure 4.14.

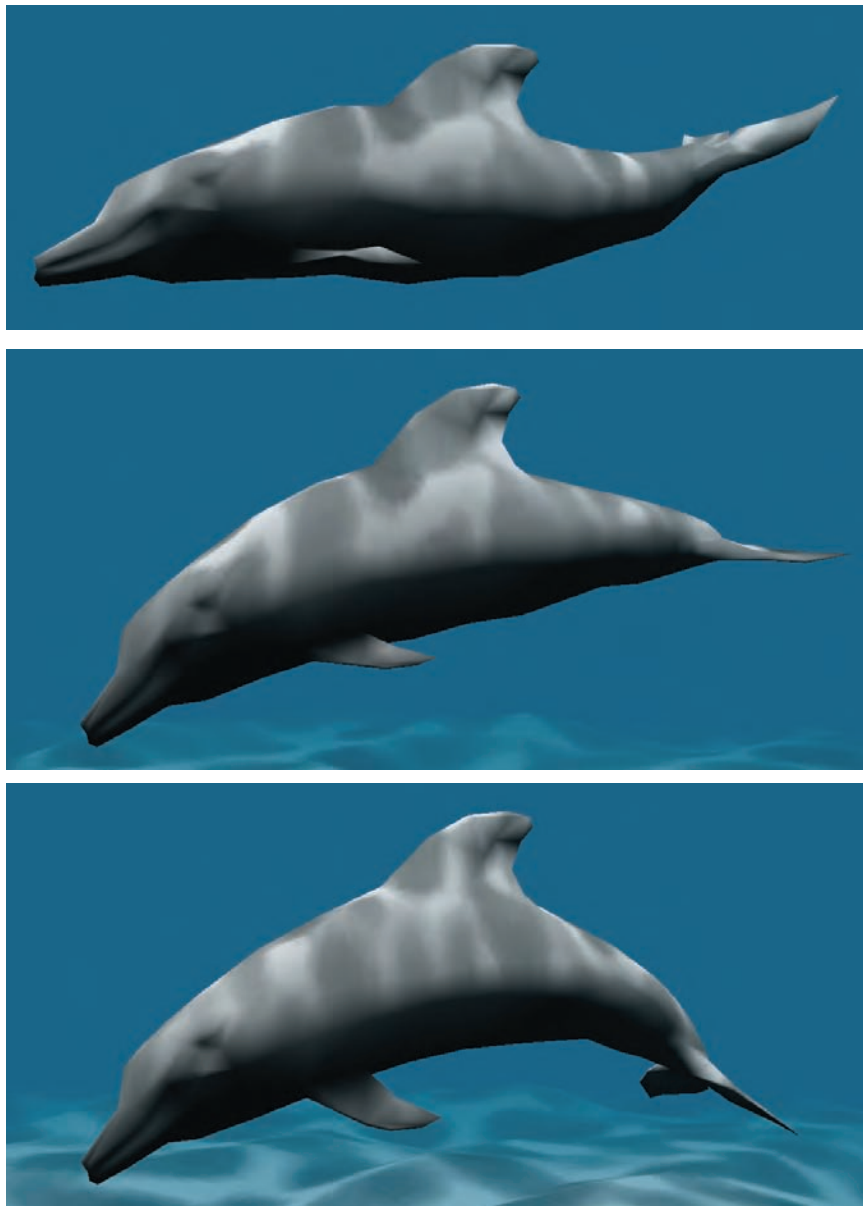


**Figure 4.13.** Vertex morphing. Two locations and normals are defined for every vertex. In each frame, the intermediate location and normal are linearly interpolated by the vertex shader. (*Images courtesy of NVIDIA Corporation.*)

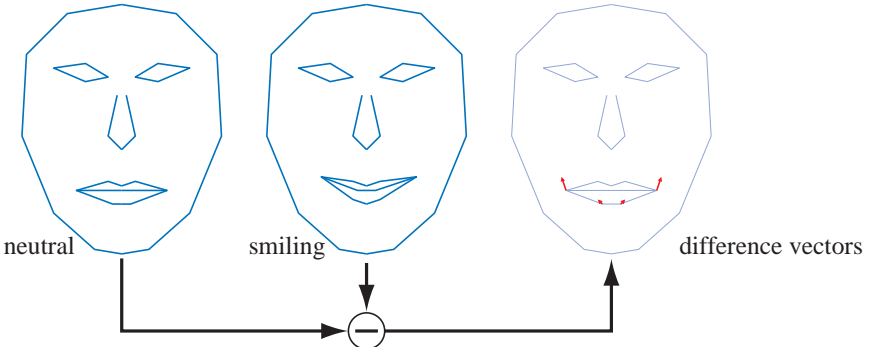


**Figure 4.14.** Given two mouth poses, a set of difference vectors is computed to control interpolation, or even extrapolation. In morph targets, the difference vectors are used to “add” movements onto the neutral face. With positive weights for the difference vectors, we get a smiling mouth, while negative weights can give the opposite effect.

We start out with a neutral model, which in this case is a face. Let us denote this model by  $\mathcal{N}$ . In addition, we also have a set of different face poses. In the example illustration, there is only one pose, which is a smiling face. In general, we can allow  $k \geq 1$  different poses, which are denoted  $\mathcal{P}_i$ ,  $i \in [1, \dots, k]$ . As a preprocess, the “difference faces” are computed as:  $\mathcal{D}_i = \mathcal{P}_i - \mathcal{N}$ , i.e., the neutral model is subtracted from each pose.

At this point, we have a neutral model,  $\mathcal{N}$ , and a set of difference poses,  $\mathcal{D}_i$ . A morphed model  $\mathcal{M}$  can then be obtained using the following formula:

$$\mathcal{M} = \mathcal{N} + \sum_{i=1}^k w_i \mathcal{D}_i. \quad (4.58)$$

This is the neutral model, and on top of that we add the features of the different poses as desired, using the weights,  $w_i$ . For Figure 4.14, setting  $w_1 = 1$  gives us exactly the smiling face in the middle of the illustration. Using  $w_1 = 0.5$  gives us a half-smiling face, and so on. One can also use negative weights and weights greater than one.

For this simple face model, we could add another face having “sad” eyebrows. Using a negative weight for the eyebrows could then create “happy” eyebrows. Since displacements are additive, this eyebrow pose could be used in conjunction with the pose for a smiling mouth. Morph targets are a powerful technique that provides the animator with much control, since different features of a model can be manipulated independently of the others. Lewis et al. [770] introduce *pose-space deformation*, which combines vertex blending and morph targets. Hardware supporting DirectX 10 can use stream-out and other improved functionality to allow

many more targets to be used in a single model and the effects computed exclusively on the GPU [793].

A real example of using both skinning and morphing is shown in Figure 4.15.

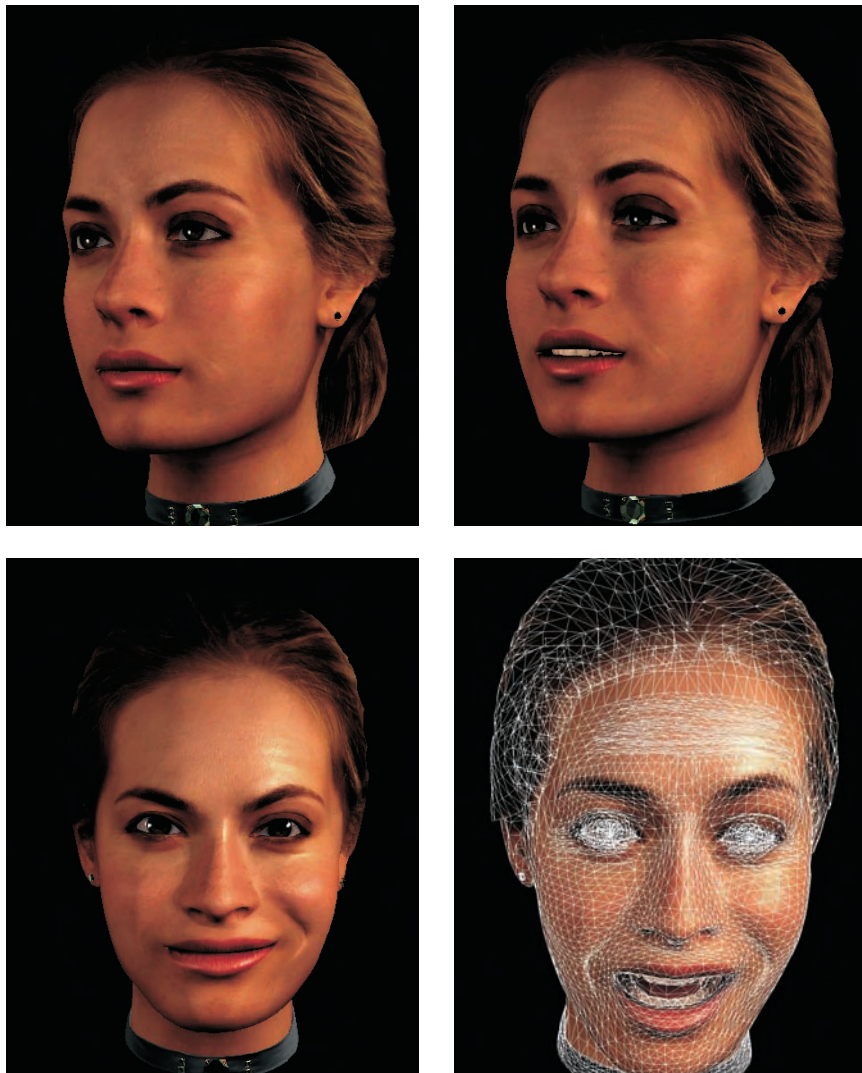


**Figure 4.15.** The Rachel character's facial expressions and movements are controlled by skinning and vertex morphing, which are accelerated by using graphics hardware support. (Images by Alex Vlachos, John Isidoro, Dave Gosselin, and Eli Turner; courtesy of ATI Technologies Inc. and LifeFX.)

## 4.6 Projections

Before one can actually render a scene, all relevant objects in the scene must be projected onto some kind of plane or into some kind of simple volume. After that, clipping and rendering are performed (see Section 2.3).

The transforms seen so far in this chapter have left the fourth component, the  $w$ -component, unaffected. That is, points and vectors have retained their types after the transform. Also, the bottom row in the  $4 \times 4$  matrices has always been  $(0 \ 0 \ 0 \ 1)$ . *Perspective projection matrices* are exceptions to both of these properties: The bottom row contains vector and point manipulating numbers, and the homogenization process is often needed (i.e.,  $w$  is often not 1, so a division by  $w$  is needed to obtain the nonhomogeneous point). *Orthographic projection*, which is dealt with first in this section, is a simpler kind of projection that is also commonly used. It does not affect the  $w$  component.

In this section, it is assumed that the viewer is looking along the negative  $z$ -axis, with the  $y$ -axis pointing up and the  $x$ -axis to the right. This is a right-handed coordinate system. Some texts and software, e.g., DirectX, use a left-handed system in which the viewer looks along the positive  $z$ -axis. Both systems are equally valid, and in the end, the same effect is achieved.

### 4.6.1 Orthographic Projection

A characteristic of an orthographic projection is that parallel lines remain parallel after the projection. Matrix  $\mathbf{P}_o$ , shown below, is a simple orthographic projection matrix that leaves the  $x$ - and  $y$ -components of a point unchanged, while setting the  $z$ -component to zero, i.e., it orthographically projects onto the plane  $z = 0$ :

$$\mathbf{P}_o = \begin{pmatrix} 1 & 0 & 0 & 0 \\ 0 & 1 & 0 & 0 \\ 0 & 0 & 0 & 0 \\ 0 & 0 & 0 & 1 \end{pmatrix}. \quad (4.59)$$

The effect of this projection is illustrated in Figure 4.16. Clearly,  $\mathbf{P}_o$  is non-invertible, since its determinant  $|\mathbf{P}_o| = 0$ . In other words, the transform drops from three to two dimensions, and there is no way to retrieve the dropped dimension. A problem with using this kind of orthographic projection for viewing is that it projects both points with positive and points with negative  $z$ -values onto the projection plane. It is usually useful to restrict the  $z$ -values (and the  $x$ - and  $y$ -values) to a certain interval,

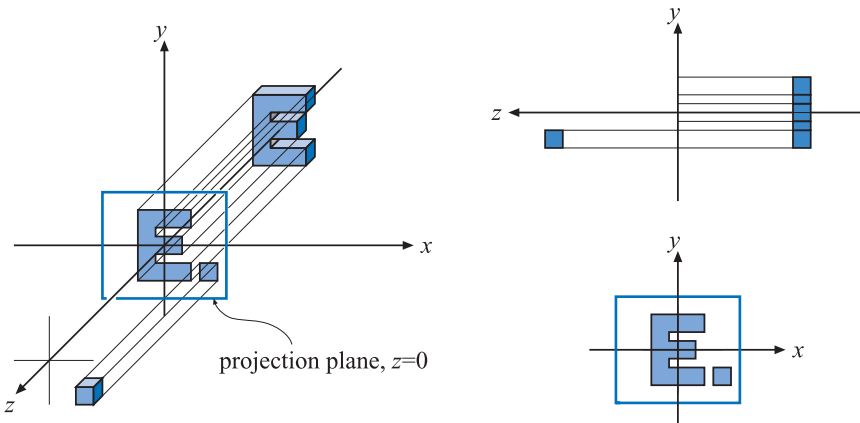


**Figure 4.16.** Three different views of the simple orthographic projection generated by Equation 4.59. This projection can be seen as the viewer is looking along the negative  $z$ -axis, which means that the projection simply skips (or sets to zero) the  $z$ -coordinate while keeping the  $x$ - and  $y$ -coordinates. Note that objects on both sides of  $z = 0$  are projected onto the projection plane.

from, say  $n$  (near plane) to  $f$  (far plane).<sup>14</sup> This is the purpose of the next transformation.

A more common matrix for performing orthographic projection is expressed in terms of the six-tuple,  $(l, r, b, t, n, f)$ , denoting the left, right, bottom, top, near, and far planes. This matrix essentially scales and translates the AABB (*Axis-Aligned Bounding Box*; see the definition in Section 16.2) formed by these planes into an axis-aligned cube centered around the origin. The minimum corner of the AABB is  $(l, b, n)$  and the maximum corner is  $(r, t, f)$ . It is important to realize that  $n > f$ , because we are looking down the negative  $z$ -axis at this volume of space. Our common sense says that the near value should be a lower number than the far. OpenGL, which also looks down the negative  $z$ -axis, presents their input near value as less than far in the orthographic matrix creation call `glOrtho`, then internally negates these two values. Another way to think of it is that OpenGL's near and far values are (positive) distances along the view direction (the negative  $z$ -axis), not  $z$  eye coordinate values.

In OpenGL the axis-aligned cube has a minimum corner of  $(-1, -1, -1)$  and a maximum corner of  $(1, 1, 1)$ ; in DirectX the bounds are  $(-1, -1, 0)$  to  $(1, 1, 1)$ . This cube is called the *canonical view volume* and the coordinates in this volume are called *normalized device coordinates*. The transformation

<sup>14</sup>The near plane is also called the *front plane* or *hither*; the far plane is also the *back plane* or *yonder*.

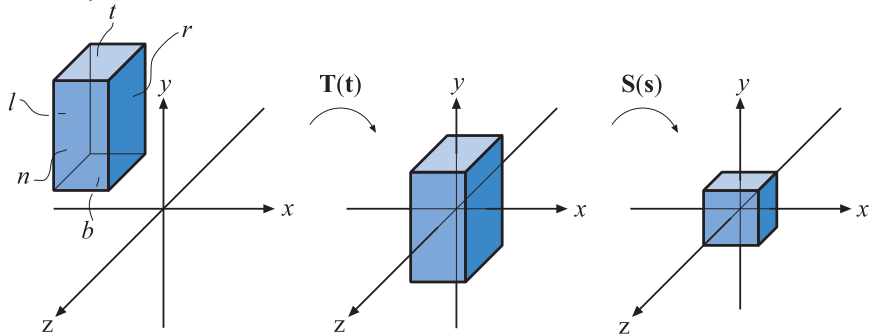


**Figure 4.17.** Transforming an axis-aligned box on the canonical view volume. The box on the left is first translated, making its center coincide with the origin. Then it is scaled to get the size of the canonical view volume, shown at the right.

procedure is shown in Figure 4.17. The reason for transforming into the canonical view volume is that clipping is more efficiently performed there.

After the transformation into the canonical view volume, vertices of the geometry to be rendered are clipped against this cube. The geometry not outside the cube is finally rendered by mapping the remaining unit square to the screen. This orthographic transform is shown here:

$$\begin{aligned} \mathbf{P}_o &= \mathbf{S}(\mathbf{s})\mathbf{T}(\mathbf{t}) = \begin{pmatrix} \frac{2}{r-l} & 0 & 0 & 0 \\ 0 & \frac{2}{t-b} & 0 & 0 \\ 0 & 0 & \frac{2}{f-n} & 0 \\ 0 & 0 & 0 & 1 \end{pmatrix} \begin{pmatrix} 1 & 0 & 0 & -\frac{l+r}{2} \\ 0 & 1 & 0 & -\frac{t+b}{2} \\ 0 & 0 & 1 & -\frac{f+n}{2} \\ 0 & 0 & 0 & 1 \end{pmatrix} \\ &= \begin{pmatrix} \frac{2}{r-l} & 0 & 0 & -\frac{r+l}{r-l} \\ 0 & \frac{2}{t-b} & 0 & -\frac{t+b}{t-b} \\ 0 & 0 & \frac{2}{f-n} & -\frac{f+n}{f-n} \\ 0 & 0 & 0 & 1 \end{pmatrix}. \end{aligned} \quad (4.60)$$

As suggested by this equation,  $\mathbf{P}_o$  can be written as the concatenation of a translation,  $\mathbf{T}(\mathbf{t})$ , followed by a scaling matrix,  $\mathbf{S}(\mathbf{s})$ , where  $\mathbf{s} = (2/(r-l), 2/(t-b), 2/(f-n))$ , and  $\mathbf{t} = (-(r+l)/2, -(t+b)/2, -(f+n)/2)$ . This matrix is invertible,<sup>15</sup> i.e.,  $\mathbf{P}_o^{-1} = \mathbf{T}(-\mathbf{t})\mathbf{S}((r-l)/2, (t-b)/2, (f-n)/2)$ .

---

<sup>15</sup>If and only if  $n \neq f$ ,  $l \neq r$ , and  $t \neq b$ ; otherwise, no inverse exists.

In computer graphics, a left-hand coordinate system is most often used after projection—i.e., for the viewport, the  $x$ -axis goes to the right,  $y$ -axis goes up, and the  $z$ -axis goes into the viewport. Because the far value is less than the near value for the way we defined our AABB, the orthographic transform will always include a mirroring transform. To see this, say the original AABBs is the same size as the goal, the canonical view volume. Then the AABB's coordinates are  $(-1, -1, 1)$  for  $(l, b, n)$  and  $(1, 1, -1)$  for  $(r, t, f)$ . Equation 4.60 yields

$$\mathbf{P}_o = \begin{pmatrix} 1 & 0 & 0 & 0 \\ 0 & 1 & 0 & 0 \\ 0 & 0 & -1 & 0 \\ 0 & 0 & 0 & 1 \end{pmatrix}, \quad (4.61)$$

which is a mirroring matrix. It is this mirroring that converts from the right-handed viewing coordinate system (looking down the negative  $z$ -axis) to left-handed normalized device coordinates.

DirectX maps the  $z$ -depths to the range  $[0, 1]$  instead of OpenGL's  $[-1, 1]$ . This can be accomplished by applying a simple scaling and translation matrix applied after the orthographic matrix, that is,

$$\mathbf{M}_{st} = \begin{pmatrix} 1 & 0 & 0 & 0 \\ 0 & 1 & 0 & 0 \\ 0 & 0 & 0.5 & 0.5 \\ 0 & 0 & 0 & 1 \end{pmatrix}. \quad (4.62)$$

So the orthographic matrix used in DirectX is

$$\mathbf{P}_{o[0,1]} = \begin{pmatrix} \frac{2}{r-l} & 0 & 0 & -\frac{r+l}{r-l} \\ 0 & \frac{2}{t-b} & 0 & -\frac{t+b}{t-b} \\ 0 & 0 & \frac{1}{f-n} & -\frac{n}{f-n} \\ 0 & 0 & 0 & 1 \end{pmatrix}. \quad (4.63)$$

which is normally presented in transposed form, as DirectX uses a row-major form for writing matrices.

## 4.6.2 Perspective Projection

A much more interesting transform than orthographic projection is perspective projection, which is used in the majority of computer graphics applications. Here, parallel lines are generally not parallel after projection; rather, they may converge to a single point at their extreme. Perspective

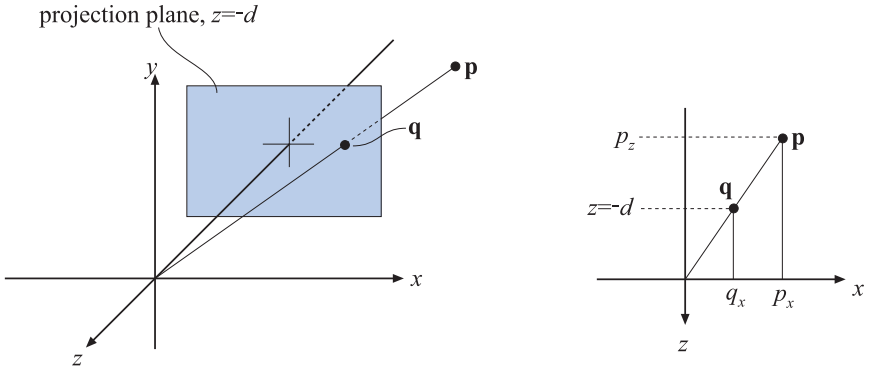


**Figure 4.18.** The notation used for deriving a perspective projection matrix. The point  $\mathbf{p}$  is projected onto the plane  $z = -d$ ,  $d > 0$ , which yields the projected point  $\mathbf{q}$ . The projection is performed from the perspective of the camera's location, which in this case is the origin. The similar triangle used in the derivation is shown for the  $x$ -component at the right.

more closely matches how we perceive the world, i.e., objects further away are smaller.

First, we shall present an instructive derivation for a perspective projection matrix that projects onto a plane  $z = -d$ ,  $d > 0$ . We derive from world space to simplify understanding of how the world-to-view conversion proceeds. This derivation is followed by the more conventional matrices used in, for example, OpenGL [970].

Assume that the camera (viewpoint) is located at the origin, and that we want to project a point,  $\mathbf{p}$ , onto the plane  $z = -d$ ,  $d > 0$ , yielding a new point  $\mathbf{q} = (q_x, q_y, -d)$ . This scenario is depicted in Figure 4.18. From the similar triangles shown in this figure, the following derivation, for the  $x$ -component of  $\mathbf{q}$ , is obtained:

$$\frac{q_x}{p_x} = \frac{-d}{p_z} \quad \Leftrightarrow \quad q_x = -d \frac{p_x}{p_z}. \quad (4.64)$$

The expressions for the other components of  $\mathbf{q}$  are  $q_y = -dp_y/p_z$  (obtained similarly to  $q_x$ ), and  $q_z = -d$ . Together with the above formula, these give us the perspective projection matrix,  $\mathbf{P}_p$ , as shown here:

$$\mathbf{P}_p = \begin{pmatrix} 1 & 0 & 0 & 0 \\ 0 & 1 & 0 & 0 \\ 0 & 0 & 1 & 0 \\ 0 & 0 & -1/d & 0 \end{pmatrix}. \quad (4.65)$$

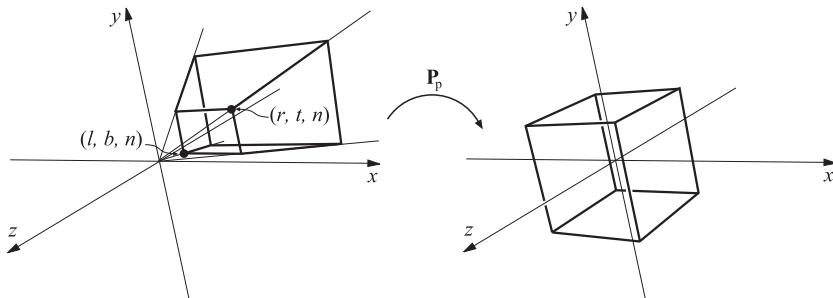


**Figure 4.19.** The matrix  $\mathbf{P}_p$  transforms the view frustum into the unit cube, which is called the canonical view volume.

That this matrix yields the correct perspective projection is confirmed by the simple verification of Equation 4.66:

$$\mathbf{q} = \mathbf{P}_p \mathbf{p} = \begin{pmatrix} 1 & 0 & 0 & 0 \\ 0 & 1 & 0 & 0 \\ 0 & 0 & 1 & 0 \\ 0 & 0 & -1/d & 0 \end{pmatrix} \begin{pmatrix} p_x \\ p_y \\ p_z \\ 1 \end{pmatrix} = \begin{pmatrix} p_x \\ p_y \\ p_z \\ -p_z/d \end{pmatrix} \Rightarrow \begin{pmatrix} -dp_x/p_z \\ -dp_y/p_z \\ -d \\ 1 \end{pmatrix}. \quad (4.66)$$

The last step comes from the fact that the whole vector is divided by the  $w$ -component (in this case  $-p_z/d$ ), in order to get a 1 in the last position. The resulting  $z$  value is always  $-d$  since we are projecting onto this plane.

Intuitively, it is easy to understand why homogeneous coordinates allow for projection. One geometrical interpretation of the homogenization process is that it projects the point  $(p_x, p_y, p_z)$  onto the plane  $w = 1$ .

As with the orthographic transformation, there is also a perspective transform that, rather than actually projecting onto a plane (which is non-invertible), transforms the view frustum into the canonical view volume described previously. Here the view frustum is assumed to start at  $z = n$  and end at  $z = f$ , with  $0 > n > f$ . The rectangle at  $z = n$  has the minimum corner at  $(l, b, n)$  and the maximum corner at  $(r, t, n)$ . This is shown in Figure 4.19.

The parameters  $(l, r, b, t, n, f)$  determine the view frustum of the camera. The horizontal field of view is determined by the angle between the left and the right planes (determined by  $l$  and  $r$ ) of the frustum. In the same manner, the vertical field of view is determined by the angle between the top and the bottom planes (determined by  $t$  and  $b$ ). The greater the field of view, the more the camera “sees.” Asymmetric frustums can be created by  $r \neq -l$  or  $t \neq -b$ . Asymmetric frustums are, for example, used for stereo viewing (see Section 18.1.4) and in CAVEs [210].

The field of view is an important factor in providing a sense of the scene. The eye itself has a physical field of view compared to the computer screen. This relationship is

$$\phi = 2 \arctan(w/(2d)), \quad (4.67)$$

where  $\phi$  is the field of view,  $w$  is the width of the object perpendicular to the line of sight, and  $d$  is the distance to the object. For example, a 21-inch monitor is about 16 inches wide, and 25 inches is a minimum recommended viewing distance [27], which yields a physical field of view of 35 degrees. At 12 inches away, the field of view is 67 degrees; at 18 inches, it is 48 degrees; at 30 inches, 30 degrees. This same formula can be used to convert from camera lens size to field of view, e.g., a standard 50mm lens for a 35mm camera (which has a 36mm wide frame size) gives  $\phi = 2 \arctan(36/(2 * 50)) = 39.6$  degrees.

Using a narrower field of view compared to the physical setup will lessen the perspective effect, as the viewer will be zoomed in on the scene. Setting a wider field of view will make objects appear distorted (like using a wide angle camera lens), especially near the screen's edges, and will exaggerate the scale of nearby objects. However, a wider field of view gives the viewer a sense that objects are larger and more impressive, and has the advantage of giving the user more information about the surroundings.

The perspective transform matrix that transforms the frustum into a unit cube is given by Equation 4.68:<sup>16</sup>

$$\mathbf{P}_p = \begin{pmatrix} \frac{2n}{r-l} & 0 & -\frac{r+l}{r-l} & 0 \\ 0 & \frac{2n}{t-b} & -\frac{t+b}{t-b} & 0 \\ 0 & 0 & \frac{f+n}{f-n} & -\frac{2fn}{f-n} \\ 0 & 0 & 1 & 0 \end{pmatrix}. \quad (4.68)$$

After applying this transform to a point, we will get another point  $\mathbf{q} = (q_x, q_y, q_z, q_w)^T$ . The  $w$ -component,  $q_w$ , of this point will (most often) be nonzero and not equal to one. To get the projected point,  $\mathbf{p}$ , we need to divide by  $q_w$ :  $\mathbf{p} = (q_x/q_w, q_y/q_w, q_z/q_w, 1)^T$ . The matrix  $\mathbf{P}_p$  always sees to it that  $z = f$  maps to +1 and  $z = n$  maps to -1. After the perspective transform is performed, clipping and homogenization (division by  $w$ ) is done to obtain the normalized device coordinates.

To get the perspective transform used in OpenGL, first multiply with  $\mathbf{S}(1, 1, -1)$ , for the same reasons as for the orthographic transform. This simply negates the values in the third column of Equation 4.68. After this mirroring transform has been applied, the near and far values are

---

<sup>16</sup>The far plane can also be set to infinity. See Equation 9.8 on page 345 for this form.

entered as positive values, with  $0 < n' < f'$ , as they would traditionally be presented to the user. However, they still represent distances along the world's negative  $z$ -axis, which is the direction of view. For reference purposes, here is the OpenGL equation:<sup>17</sup>

$$\mathbf{P}_{OpenGL} = \begin{pmatrix} \frac{2n'}{r-l} & 0 & \frac{r+l}{r-l} & 0 \\ 0 & \frac{2n'}{t-b} & \frac{t+b}{t-b} & 0 \\ 0 & 0 & -\frac{f'+n'}{f'-n'} & -\frac{2f'n'}{f'-n'} \\ 0 & 0 & -1 & 0 \end{pmatrix}. \quad (4.69)$$

Some APIs (e.g., DirectX) map the near plane to  $z = 0$  (instead of  $z = -1$ ) and the far plane to  $z = 1$ . In addition, DirectX uses a left-handed coordinate system to define its projection matrix. This means DirectX looks along the positive  $z$ -axis and presents the near and far values

as positive numbers. Here is the DirectX equation:

$$\mathbf{P}_{p[0,1]} = \begin{pmatrix} \frac{2n'}{r-l} & 0 & -\frac{r+l}{r-l} & 0 \\ 0 & \frac{2n'}{t-b} & -\frac{t+b}{t-b} & 0 \\ 0 & 0 & \frac{f'}{f'-n'} & -\frac{f'n'}{f'-n'} \\ 0 & 0 & 1 & 0 \end{pmatrix}. \quad (4.70)$$

DirectX uses row-major form in its documentation, so this matrix is normally presented in transposed form.

One effect of using a perspective transformation is that the computed depth value does not vary linearly with the input  $p_z$  value. For example, if  $n' = 10$  and  $f' = 110$  (using the OpenGL terminology), when  $p_z$  is 60 units down the negative  $z$ -axis (i.e., the halfway point) the normalized device coordinate depth value is 0.833, not 0. Figure 4.20 shows the effect of varying the distance of the near plane from the origin. Placement of the near and far planes affects the precision of the  $Z$ -buffer. This effect is discussed further in Section 18.1.2.

---

<sup>17</sup>So, to test that this really works in the  $z$ -direction, we can multiply  $\mathbf{P}_{OpenGL}$  with  $(0, 0, -n', 1)^T$ . The  $z$ -component of the resulting vector will be  $-1$ . If we instead use the vector  $(0, 0, -f', 1)^T$ , the  $z$ -component will be  $+1$ , as expected. A similar test can be done for  $\mathbf{P}_{p[0,1]}$ .

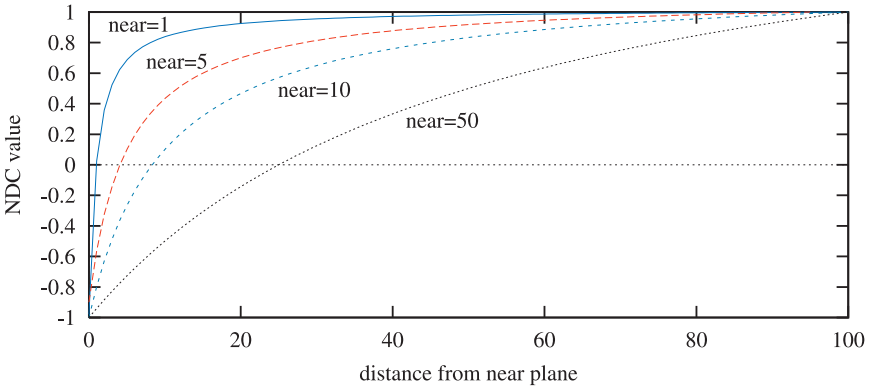


**Figure 4.20.** The effect of varying the distance of the near plane from the origin. The distance  $f' - n'$  is kept constant at 100. As the near plane becomes closer to the origin, points nearer the far plane use a smaller range of the normalized device coordinate depth space. This has the effect of making the Z-buffer less accurate at greater distances.

## Further Reading and Resources

One of the best books for building up one's intuition about matrices in a painless fashion is Farin and Hansford's *The Geometry Toolbox* [333]. Another useful work is Lengyel's *Mathematics for 3D Game Programming and Computer Graphics* [761]. For a different perspective, many computer graphics texts, such as Hearn and Baker [516], Shirley [1172], Watt and Watt [1330], and the two books by Foley et al. [348, 349], also cover matrix basics. The *Graphics Gems* series [36, 405, 522, 667, 982] presents various transform-related algorithms and has code available online for many of these. Golub and Van Loan's *Matrix Computations* [419] is the place to start for a serious study of matrix techniques in general. See: <http://www.realtimerendering.com> for code for many different transforms, including quaternions. More on skeleton-subspace deformation/vertex blending and shape interpolation can be read in Lewis et al.'s SIGGRAPH paper [770].

Hart et al. [507] and Hanson [498] provide visualizations of quaternions. Pletinckx [1019] and Schlag [1126] present different ways of interpolating smoothly between a set of quaternions. Vlachos and Isidoro [1305] derive formulae for  $C^2$  interpolation of quaternions. Related to quaternion interpolation is the problem of computing a consistent coordinate system along a curve. This is treated by Dougan [276].

Alexa [16] and Lazarus & Verroust [743] present surveys on many different morphing techniques.



# Chapter 5

# Visual Appearance

*“A good picture is equivalent to a good deed.”*

—Vincent Van Gogh

When you render images of three-dimensional models, the models should not only have the proper geometrical shape, they should also have the desired visual appearance. In many cases (but not all—see Chapter 11) the goal is photorealism—an appearance very close to photographs of real objects. To reach this goal, it is worthwhile to use reality as our guide. This chapter first discusses some of the ways in which light and materials behave in the real world. A simple lighting and surface model is used as an example of how such models can be implemented by using programmable shaders.

The remainder of the chapter introduces additional techniques that can be used to give rendered models a realistic appearance. These include transparency, antialiasing, and compositing.

## 5.1 Visual Phenomena

When performing a realistic rendering of a scene such as the one in Figure 5.1, it helps to understand the relevant physical phenomena. These are:

- Light is emitted by the sun or other sources (natural or artificial).
- Light interacts with objects in the scene; part is absorbed, part is scattered and propagates in new directions.
- Finally, light is absorbed by a sensor (human eye, electronic sensor, or film).

In Figure 5.1, we can see evidence of all three phenomena. Light is emitted from the lamp and propagates directly to the objects in the room.



**Figure 5.1.** A photograph of a room showing a light source and various objects.

The object surfaces absorb some and scatter some into new directions. The light not absorbed continues to move through the environment, encountering other objects. A tiny portion of the light traveling through the scene enters the sensor used to capture the image, in this case the electronic sensor of a digital camera.

In the following sections we will discuss these phenomena and how they can be portrayed using the rendering pipeline and GPU shaders from previous chapters.

## 5.2 Light Sources

Light is variously modeled as geometric rays, electromagnetic waves, or photons (quantum particles with some wave properties). Regardless of how it is treated, light is electromagnetic radiant energy—electromagnetic energy that travels through space. *Light sources* emit light, rather than scattering or absorbing it.

Light sources can be represented in many different ways for rendering purposes. Here we will discuss a simple light model—more complex and expressive models will be discussed in Section 7.4 and Chapter 8. Extremely distant light sources like the sun are simplest to simulate; their light travels in a single direction that is the same throughout the scene. For this reason they are called *directional lights*. For rendering purposes, the directionality of such a light source is described by the *light vector  $\mathbf{l}$* , specified in world space. The vector  $\mathbf{l}$  is always assumed to be of length 1 whenever encoun-

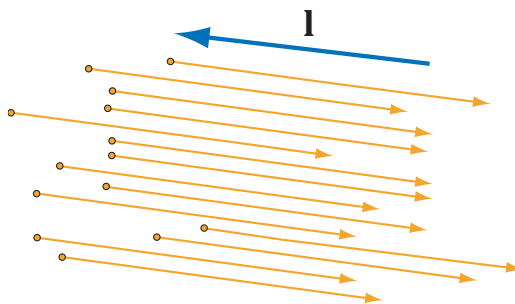


**Figure 5.2.** The light vector  $\mathbf{l}$  is defined opposite to the direction the light is traveling.

tered in this book. For directional lights,  $\mathbf{l}$  is typically normalized (scaled to a length of 1) by the application to avoid the need to renormalize it during shading. The light vector  $\mathbf{l}$  is usually defined pointing in a direction *opposite* to the direction the light is traveling (see Figure 5.2). The reason behind this will become clear shortly.

Besides the light's direction, the amount of illumination it emits also needs to be specified. The science of measuring light, *radiometry*, will be discussed in Section 7.1; this chapter will present only the relevant concepts. The emission of a directional light source can be quantified by measuring power through a unit area surface perpendicular to  $\mathbf{l}$  (see Figure 5.3). This

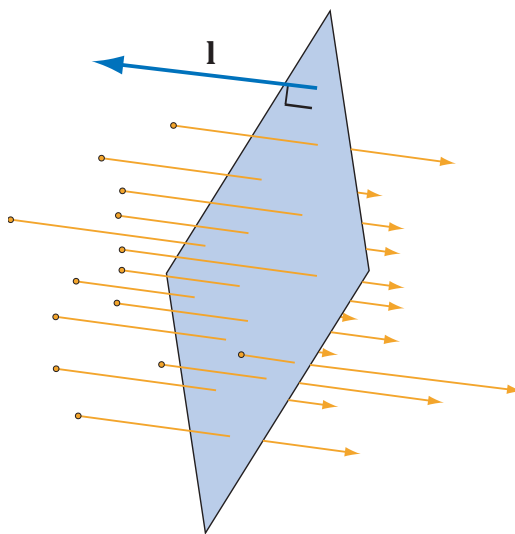


**Figure 5.3.** Measuring the magnitude of light emitted by a directional light source.

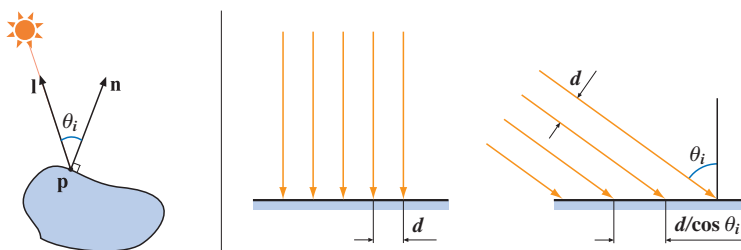


**Figure 5.4.** The diagram on the left shows the lighting geometry. In the center, light is shown hitting a surface straight-on, and on the right it is shown hitting the surface at an angle.

quantity, called *irradiance*, is equivalent to the sum of energies of the photons passing through the surface in one second.<sup>1</sup> Light can be colored, so we will represent irradiance as an RGB vector containing three numbers: one for each of red, green and blue (in Section 7.3 the subject of color will be treated in a more rigorous manner). Note that unlike colors in painting applications, RGB irradiance values can exceed 1 and in theory can be arbitrarily large.

Even if there is just one primary light source, light bouncing off other objects and the room walls will illuminate the object as well. This type of surrounding or environmental light is called *ambient light*. In Chapters 8 and 9 we will see various ways to model ambient light, but for simplicity we will not discuss any of them in this chapter. In our simple lighting model, surfaces not directly illuminated are black.

Although measuring irradiance at a plane perpendicular to  $\mathbf{l}$  tells us how bright the light is in general, to compute its illumination on a surface, we need to measure irradiance at a plane parallel to that surface (i.e., perpendicular to the surface normal  $\mathbf{n}$ ). The surface irradiance is equal to the irradiance measured perpendicularly to  $\mathbf{l}$ , times the cosine of the angle  $\theta_i$  between  $\mathbf{l}$  and  $\mathbf{n}$  (see the left side of Figure 5.4).

The center and right illustrations in Figure 5.4 show a geometric interpretation of this cosine factor. In the center, the light rays are shown hitting the surface perpendicularly. The irradiance is proportional to the density of the rays and inversely proportional to the distance  $d$  between them. In this case the irradiance at the surface and the irradiance perpendicular to  $\mathbf{l}$  are the same. On the right, the light rays are shown coming from a different direction. They make an angle  $\theta_i$  with the normal of the plane. The distance between the light rays where they hit the surface is

<sup>1</sup>If treating light as waves, irradiance is proportional to the wave amplitude (in the plane of measurement) squared.

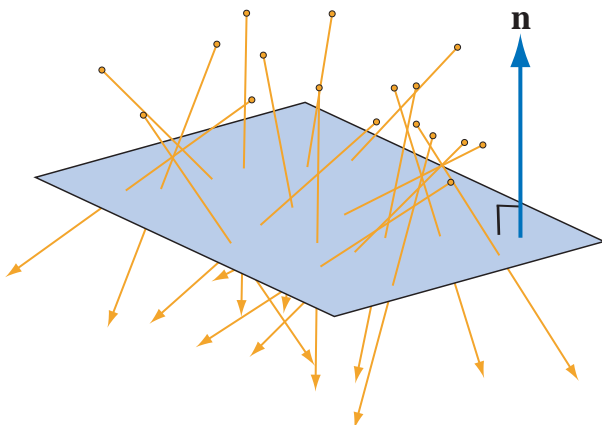


**Figure 5.5.** Irradiance measures light from all incoming directions.

$d/\cos\theta_i$ . Since the irradiance is inversely proportional to this distance, this means that it must be proportional to  $\cos\theta_i$ . This cosine can be easily computed in a shader by taking the dot product of the two vectors (note that both  $\mathbf{l}$  and  $\mathbf{n}$  are always assumed to be of length 1). Here we see why it is convenient to define the light vector  $\mathbf{l}$  opposite to the light's direction of travel; otherwise we would have to negate it before performing the dot product.

$E$  is used in equations for irradiance, most commonly for irradiance perpendicular to  $\mathbf{n}$ . We will use  $E_L$  for irradiance perpendicular to  $\mathbf{l}$ . Note that a negative value of the cosine corresponds to the case where light comes from below the surface. In this case the light does not illuminate the surface at all, so we will use the cosine clamped to non-negative values (symbolized by  $\overline{\cos}$ ):

$$\begin{aligned} E &= E_L \overline{\cos} \theta_i \\ &= E_L \max(\mathbf{n} \cdot \mathbf{l}, 0). \end{aligned} \tag{5.1}$$

In Figures 5.3 and 5.4 all the light is traveling in a constant direction. However, irradiance in general measures light going in arbitrary directions. The definition of irradiance is still the same: light energy crossing a unit-area plane in one second (see Figure 5.5). This quantity has a real-world device related to it: the light meter. This meter measures irradiance over a set of wavelengths, multiplied by a perceptual curve for light, and so gives the perceived amount of light reaching a (small) area oriented in a particular direction.

Note that irradiance is *additive*; the total irradiance from multiple directional light sources is the sum of individual irradiance values,

$$E = \sum_{k=1}^n E_{L_k} \overline{\cos} \theta_{i_k}, \quad (5.2)$$

where  $E_{L_k}$  and  $\theta_{i_k}$  are the values of  $E_L$  and  $\theta_i$  for the  $k$ th directional light source.

## 5.3 Material

In rendering, scenes are most often presented using the surfaces of objects. Object appearance is portrayed by attaching materials to models in the scene. Each material is associated with a set of shader programs, textures, and other properties. These are used to simulate the interaction of light with the object. This section starts with a description of how light interacts with matter in the real world, and then presents a simple material model. A more general treatment of material models will be presented in Chapter 7.

Fundamentally, all light-matter interactions are the result of two phenomena: *scattering* and *absorption*.<sup>2</sup>

Scattering happens when light encounters any kind of optical discontinuity. This may be the interface between two substances with different optical properties, a break in crystal structure, a change in density, etc. Scattering does not change the amount of light—it just causes it to change direction.

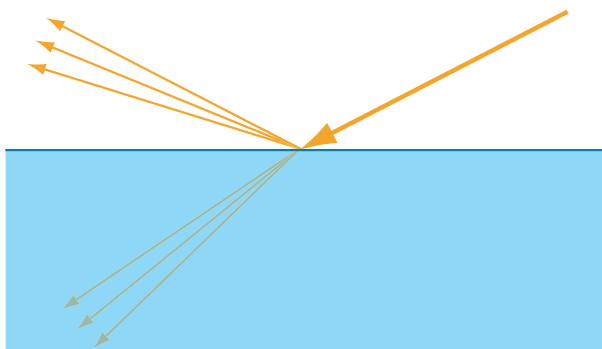


**Figure 5.6.** Light scattering at a surface—reflection and refraction.

---

<sup>2</sup>Emission is a third phenomenon. It pertains to light sources, which were discussed in the previous section.

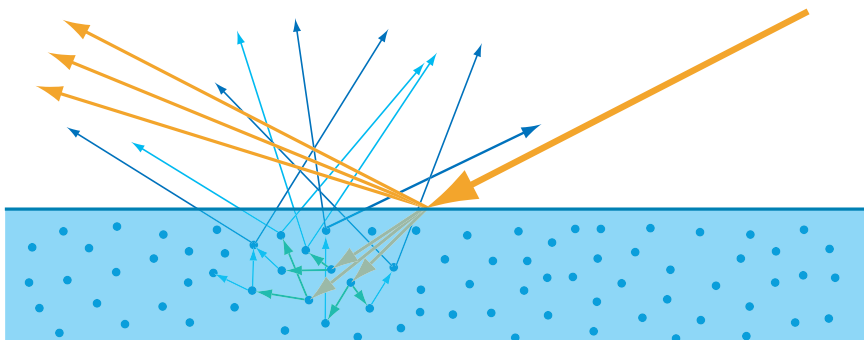


**Figure 5.7.** Interactions with reflected and transmitted light.

Absorption happens inside matter and causes some of the light to be converted into another kind of energy and disappear. It reduces the amount of light but does not affect its direction.

The most important optical discontinuity in rendering is the interface between air and object that occurs at a model surface. Surfaces scatter light into two distinct sets of directions: into the surface (*refraction* or *transmission*) and out of it (*reflection*); see Figure 5.6 for an illustration.

In transparent objects, the transmitted light continues to travel through the object. A simple technique to render such objects will be discussed in Section 5.7; later chapters will contain more advanced techniques. In this section we will only discuss opaque objects, in which the transmitted light undergoes multiple scattering and absorption events, until finally some of it is re-emitted back away from the surface (see Figure 5.7).

As seen in Figure 5.7, the light that has been reflected at the surface has a different direction distribution and color than the light that was transmitted into the surface, partially absorbed, and finally scattered back out. For this reason, it is common to separate surface shading equations into two terms. The *specular term* represents the light that was reflected at the surface, and the *diffuse term* represents the light which has undergone transmission, absorption, and scattering.

To characterize the behavior of a material by a shading equation, we need to represent the amount and direction of outgoing light, based on the amount and direction of incoming light.

Incoming illumination is measured as surface irradiance. We measure outgoing light as *exitance*, which similarly to irradiance is energy per second per unit area. The symbol for exitance is  $M$ . Light-matter interactions are *linear*; doubling the irradiance will double the exitance. Exitance divided by irradiance is a characteristic property of the material. For surfaces that do not emit light on their own, this ratio must always be between 0

and 1. The ratio between exitance and irradiance can differ for light of different colors, so it is represented as an RGB vector or color, commonly called the *surface color*  $\mathbf{c}$ . To represent the two different terms, shading equations often have separate *specular color* ( $\mathbf{c}_{\text{spec}}$ ) and *diffuse color* ( $\mathbf{c}_{\text{diff}}$ ) properties, which sum to the overall surface color  $\mathbf{c}$ . As RGB vectors with values between 0 and 1, these are regular colors that can be specified using standard color picking interfaces, painting applications, etc. The specular and diffuse colors of a surface depend on its composition, i.e., whether it is made of steel, colored plastic, gold, wood, skin, etc.

In this chapter we assume that the diffuse term has no directionality—it represents light going uniformly in all directions. The specular term does have significant directionality that needs to be addressed. Unlike the surface colors that were primarily dependent on the composition of the surface, the directional distribution of the specular term depends on the surface smoothness. We can see this dependence in Figure 5.8, which shows diagrams and photographs for two surfaces of different smoothness. The beam of reflected light is tighter for the smoother surface, and more spread out for the rougher surface. In the accompanying photographs we can see the visual result of this on the reflected images and highlights. The smoother surface exhibits sharp reflections and tight, bright highlights; the rougher surface shows blurry reflections and relatively broad, dim highlights.

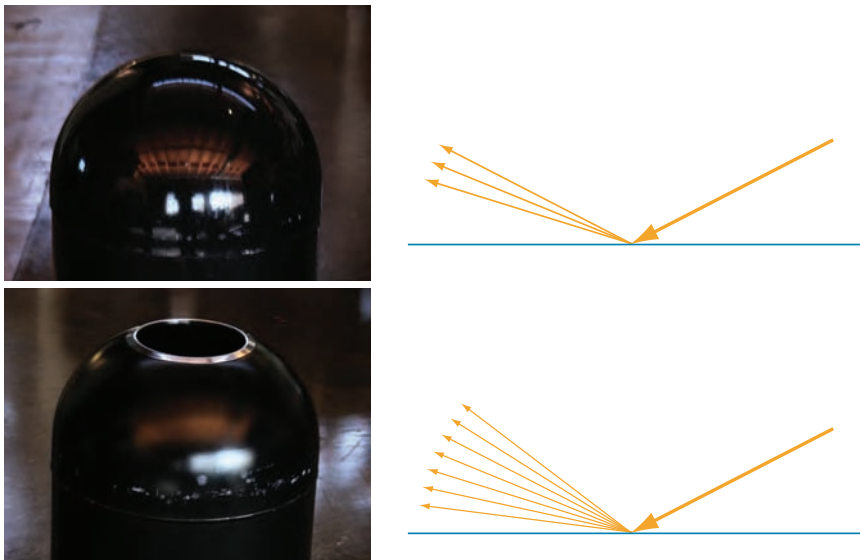


**Figure 5.8.** Light reflecting off surfaces of different smoothness.



**Figure 5.9.** Rendering the same object at different scales.

lights. Shading equations typically incorporate a smoothness parameter that controls the distribution of the specular term.

Note that, geometrically, the objects in the Figure 5.8 photographs appear quite similar; we do not see any noticeable irregularities in either surface. These irregularities *are* present, but they are too small to see in these photographs. Whether surface detail is rendered directly as geometry and texture, or indirectly by adjusting parameters in a shading equation depends on the scale of observation. In Figure 5.9 we see several views of the same object. In the first photograph on the left we see a magnified view of the surface of a single leaf. If we were to render this scene, the vein patterns would be modeled as textures. In the next photograph we see a cluster of leaves. If we were to render this image, each leaf would be modeled as a simple mesh; the veins would not be visible, but we would reduce the smoothness parameter of the shading equation to take account of the fact that the veins cause the reflected light to spread out. The next image shows a hillside covered with trees. Here, individual leaves are not visible. For rendering purposes, each tree would be modeled as a triangle mesh and the shading equation would simulate the fact that random leaf orientations scatter the light further, perhaps by using a further reduced smoothness parameter. The final (rightmost) image shows the forested hills from a greater distance. Here, even the individual trees are not visible. The hills would be modeled as a mesh, and even effects such as trees shadowing other trees would be modeled by the shading equation (perhaps by adjusting the surface colors) rather than being explicitly rendered. Later in the book we shall see other examples of how the scale of observation affects the rendering of visual phenomena.

## 5.4 Sensor

After light is emitted and bounced around the scene, some of it is absorbed in the imaging sensor. An imaging sensor is actually composed of many small sensors: rods and cones in the eye, photodiodes in a digital camera,

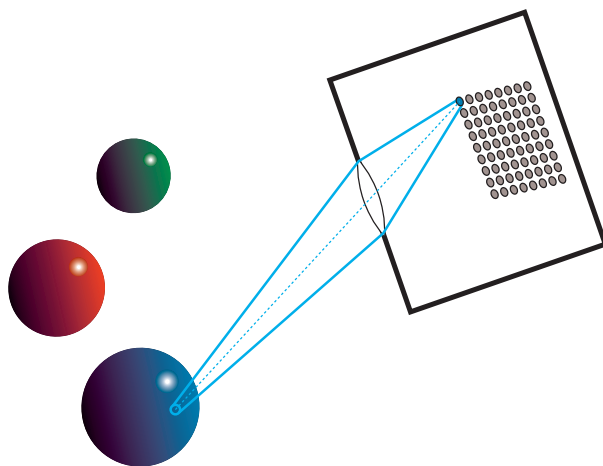


**Figure 5.10.** Imaging sensor viewing a scene.

or dye particles in film. Each of these sensors detects the irradiance value over its surface and produces a color signal. Irradiance sensors themselves cannot produce an image, since they average light rays from all incoming directions. For this reason, a full imaging system includes a light-proof enclosure with a single small *aperture* (opening) that restricts the directions from which light can enter and strike the sensors. A lens placed at the aperture focuses the light so that each sensor only receives light from a small set of incoming directions. Such a system can be seen in Figure 5.10.

The enclosure, aperture and lens have the combined effect of causing the sensors to be *directionally specific*; they average light over a small area *and* a small set of incoming directions. Rather than measuring average irradiance (the density of light flow—from all directions—per surface area), these sensors measure average *radiance*. Radiance is the density of light flow per area and per incoming direction. Radiance (symbolized as  $L$  in equations) can be thought of as the measure of the brightness and color of a single ray of light. Like irradiance, radiance is represented as an RGB vector with theoretically unbounded values. Rendering systems also “measure” (compute) radiance, similarly to real imaging systems. However, they use a simplified and idealized model of the imaging sensor, which can be seen in Figure 5.11.

In this model, each sensor measures a single radiance sample, rather than an average. The radiance sample for each sensor is along a ray that goes through a point representing the sensor and a shared point  $p$ , which is also the center of projection for the perspective transform discussed in Section 4.6.2. In rendering systems, the detection of radiance by the sensor

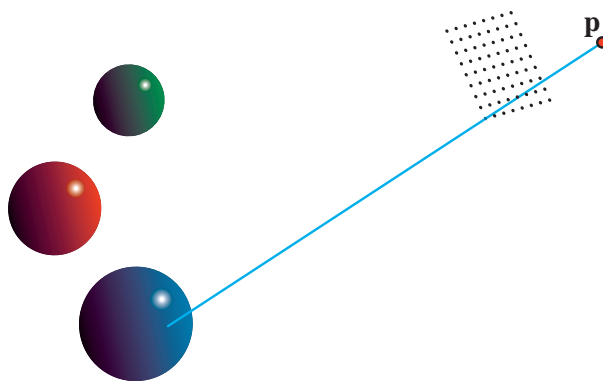


**Figure 5.11.** Idealized computer graphics model of imaging sensor.

is replaced by shader equation evaluation. The purpose of each evaluation is to compute the radiance along the appropriate ray. The direction of this ray is represented in the shading equation by the *view vector*  $\mathbf{v}$  (see Figure 5.12). The vector  $\mathbf{v}$  is always assumed to be of length 1 (i.e., normalized) whenever encountered in this book.

The relationship between the radiance value at a sensor and the signal the sensor produces is complex and often nonlinear. It depends on many factors and can vary as a function of time and spatial location. In addition, the range of radiance values detected by the sensor is often much larger than that supported by the display device (especially the “virtual sensor” used in rendering, which has an almost unlimited range). Scene radiances need to be mapped to display radiances in an appropriate manner, often in such a way as to mimic the behavior of physical sensors like film or the human eye. Relevant techniques will be discussed in Sections 5.8, 10.11, and 10.12.

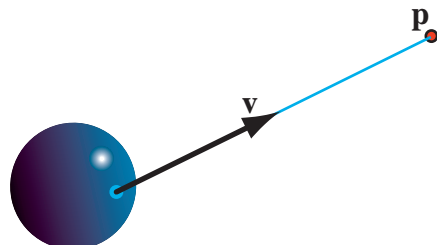


**Figure 5.12.** The view vector, a normalized direction pointing toward the sensor’s location.

There are important differences between physical imaging sensors as shown in Figure 5.10 and the idealized model shown in Figure 5.11. Physical sensors measure an average value of radiance over their area, over incoming directions focused by the lens, and over a time interval; the evaluation of a shader equation computes radiance in a single ray at a single instant. The problems caused by these differences, and various solutions to them, will be discussed in Sections 5.6, 10.13, and 10.14.

## 5.5 Shading

*Shading* is the process of using an equation to compute the outgoing radiance  $L_o$  along the view ray,  $\mathbf{v}$ , based on material properties and light sources. Many possible shading equations will be discussed in Chapter 7. Here we will present a relatively simple one as an example, and then discuss how to implement it using programmable shaders.

The shading equation we will use has diffuse and specular terms. The diffuse term is simple. From the definitions in the previous section, we get the diffuse exitance  $M_{\text{diff}}$  as a function of the light's irradiance  $E_L$ , its direction vector  $\mathbf{l}$  and the diffuse color  $\mathbf{c}_{\text{diff}}$ :

$$M_{\text{diff}} = \mathbf{c}_{\text{diff}} \otimes E_L \overline{\cos} \theta_i, \quad (5.3)$$

where the  $\otimes$  symbol is used to denote piecewise vector multiply (the quantities being multiplied are both RGB vectors).

Since the outgoing diffuse radiance  $L_{\text{diff}}$  is assumed to be the same in all directions, the following relationship holds (a justification is given in Section 7.5.1):

$$L_{\text{diff}} = \frac{M_{\text{diff}}}{\pi}. \quad (5.4)$$

Combining Equations 5.3 and 5.4 yields the shading equation for the diffuse term:

$$L_{\text{diff}} = \frac{\mathbf{c}_{\text{diff}}}{\pi} \otimes E_L \overline{\cos} \theta_i. \quad (5.5)$$

This type of diffuse shading term is also called *Lambertian* after Lambert's law, which states that for ideally diffuse surfaces, outgoing radiance is proportional to  $\overline{\cos} \theta_i$ . Note that this clamped cosine factor (often referred to as the *n dot l factor*, since it is equal to  $\max(\mathbf{n} \cdot \mathbf{l}, 0)$ ) is not specific to Lambertian surfaces; as we have seen, it holds for irradiance in general. The defining characteristic of Lambertian surfaces is that outgoing radiance is proportional to irradiance. For anyone who has seen Lambertian shading code, Equation 5.5 should look familiar, except for the  $1/\pi$  factor. This factor is typically folded into the value of  $E_L$  in real time shading (this is discussed in more detail in Section 7.5).

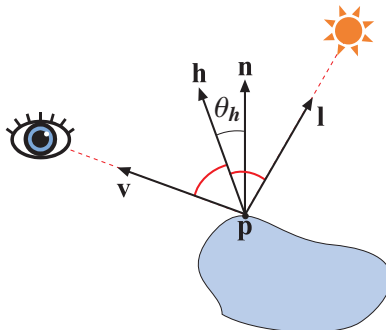


**Figure 5.13.** The half vector forms equal angles (shown in red) with the light and view vectors.

Similarly to Equation 5.3, the following holds for the specular exitance:

$$M_{\text{spec}} = \mathbf{c}_{\text{spec}} \otimes E_L \overline{\cos} \theta_i. \quad (5.6)$$

The specular term is more complex than the diffuse term due to its directional dependence. For specularity, the shading equation uses the *half vector*  $\mathbf{h}$ ,<sup>3</sup> which is so called because it is halfway between the view vector  $\mathbf{v}$  and the light vector  $\mathbf{l}$  (see Figure 5.13). It is computed thus:

$$\mathbf{h} = \frac{\mathbf{l} + \mathbf{v}}{\|\mathbf{l} + \mathbf{v}\|}, \quad (5.7)$$

where the sum of  $\mathbf{v}$  and  $\mathbf{l}$  is divided by its length  $\|\mathbf{l} + \mathbf{v}\|$  to get a unit-length result.

The following equation is used to define the distribution of the outgoing specular radiance  $L_{\text{spec}}$  (this is explained in Section 7.6):

$$L_{\text{spec}}(\mathbf{v}) = \frac{m + 8}{8\pi} \overline{\cos}^m \theta_h M_{\text{spec}}, \quad (5.8)$$

where  $\theta_h$  is the angle between  $\mathbf{h}$  and  $\mathbf{n}$  (see Figure 5.13).

Note that unlike  $L_{\text{diff}}$ ,  $L_{\text{spec}}$  depends on  $\mathbf{v}$  (indirectly via its dependence on  $\mathbf{h}$ ).  $L_{\text{spec}}$  increases when the angle  $\theta_h$  between  $\mathbf{h}$  and  $\mathbf{n}$  decreases. The rapidity of this change depends on the parameter  $m$ , which represents the surface smoothness. Increasing  $m$  causes the specular highlights to be smaller and brighter. Combining Equations 5.6 and 5.8 yields the shading equation for the specular term:

$$L_{\text{spec}}(\mathbf{v}) = \frac{m + 8}{8\pi} \overline{\cos}^m \theta_h \mathbf{c}_{\text{spec}} \otimes E_L \overline{\cos} \theta_i. \quad (5.9)$$

---

<sup>3</sup>The significance of the half vector and its use in shading will be explained in more detail in Section 7.5.6.

The complete shading equation combines the two terms to get the total outgoing radiance  $L_o$ :

$$L_o(\mathbf{v}) = \left( \frac{\mathbf{c}_{\text{diff}}}{\pi} + \frac{m+8}{8\pi} \overline{\cos}^m \theta_h \mathbf{c}_{\text{spec}} \right) \otimes E_L \overline{\cos} \theta_i. \quad (5.10)$$

This shading equation is similar to the “Blinn-Phong” equation, in common use since it was first presented by Blinn in 1977 [97]:<sup>4</sup>

$$L_o(\mathbf{v}) = \left( \overline{\cos} \theta_i \mathbf{c}_{\text{diff}} + \overline{\cos}^m \theta_h \mathbf{c}_{\text{spec}} \right) \otimes B_L. \quad (5.11)$$

$B_L$  is used here rather than  $E_L$  because, historically, this equation has not been used with physical illumination quantities, but with ad hoc “brightness” values assigned to light sources. The original formulations [97, 1014] had no representation of the light intensity at all. If we take  $B_L = E_L/\pi$ , then this is quite similar to our equation, with only two differences: It lacks the  $(m+8)/8$  factor, and the specular term is not multiplied by  $\overline{\cos} \theta_i$ . Physical and visual justifications for these differences will be given in Chapter 7.

### 5.5.1 Implementing the Shading Equation

Shading equations such as Equation 5.10 are typically evaluated in vertex and pixel shaders. In this chapter we will focus on a simple implementation of the shading equation, where the material properties ( $\mathbf{c}_{\text{diff}}$ ,  $\mathbf{c}_{\text{spec}}$ , and  $m$ ) are constant across the mesh. The use of textures to vary material properties will be discussed in Chapter 6.

Equation 5.10 is for a single light source. However, scenes often contain multiple light sources. Lighting is additive in nature, so we can sum the contributions of the individual light sources to get the overall shading equation:

$$L_o(\mathbf{v}) = \sum_{k=1}^n \left( \left( \frac{\mathbf{c}_{\text{diff}}}{\pi} + \frac{m+8}{8\pi} \overline{\cos}^m \theta_{h_k} \mathbf{c}_{\text{spec}} \right) \otimes E_{L_k} \overline{\cos} \theta_{i_k} \right), \quad (5.12)$$

where  $\theta_{h_k}$  is the value of  $\theta_h$  for the  $k$ th light source.

Various issues and implementation options relating to multiple light sources will be discussed in Section 7.9. Here we will use the shader’s

---

<sup>4</sup>Blinn’s paper was actually talking about a different shading equation altogether, and the “Blinn-Phong” equation was mentioned only briefly in a section discussing previous work (it is a variant of an equation presented by Phong [1014] two years earlier). Curiously, the “Blinn-Phong” equation gained rapid acceptance and the paper’s main contribution was all but ignored until the Cook-Torrance paper four years later [192].

dynamic branching capabilities to loop over the light sources, which is a simple (but not necessarily optimal) approach.

When designing a shading implementation, the computations need to be divided according to their *frequency of evaluation*. The lowest frequency of evaluation is *per-model*: Expressions that are constant over the entire model can be evaluated by the application once, and the results passed to the graphics API. If the result of the computation is constant over each of the primitives comprising the model (most usually triangles, but sometimes quads or line segments), then *per-primitive* evaluation can be performed. Per-primitive computations are performed by the geometry shader<sup>5</sup> and the result is reused for all pixels in the primitive. In *per-vertex* evaluation, computations are performed in the vertex shader and the results are linearly interpolated over the triangle for use by the pixel shader. Finally, the highest frequency of evaluation is *per pixel*, where the computation is performed in the pixel shader (the various shader stages were discussed in Section 3.1).

Separating out the per-model subexpressions of Equation 5.12 results in

$$L_o(\mathbf{v}) = \sum_{k=1}^n ((K_d + K_s \overline{\cos}^m \theta_{h_k}) \otimes E_{L_k} \overline{\cos} \theta_{i_k}), \quad (5.13)$$

where  $K_d = \mathbf{c}_{\text{diff}}/\pi$  and  $K_s = ((m+8)/8\pi)\mathbf{c}_{\text{spec}}$  are computed by the application. Since we only use directional light sources,  $\mathbf{l}_k$  and  $E_{L_k}$  are constant and can be set once. The remaining variables  $\theta_{h_k}$  and  $\theta_{i_k}$  vary over the mesh. As we have seen,  $\overline{\cos} \theta_{i_k}$  is computed by performing a clamped dot product between  $\mathbf{l}_k$  and  $\mathbf{n}$ . Similarly,  $\overline{\cos} \theta_{h_k}$  is computed with a dot product between  $\mathbf{h}_k$  and  $\mathbf{n}$ .

The view vector  $\mathbf{v}$  can be computed from the surface position  $\mathbf{p}$  and the view position  $\mathbf{p}_v$ :

$$\mathbf{v} = \frac{\mathbf{p}_v - \mathbf{p}}{\|\mathbf{p}_v - \mathbf{p}\|}. \quad (5.14)$$

Following which Equation 5.7 can be used to compute  $\mathbf{h}_k$ . Note that all points and vectors need to be in a consistent space—here we will use world space.

The last remaining variable is the surface normal  $\mathbf{n}$ . Values for  $\mathbf{n}$  at various locations are part of the geometric description of the model. Each triangle has a unique surface normal, and it may seem to make sense to

---

<sup>5</sup>Per-primitive computations can also be performed in the vertex shader, as long as they do not require data from adjacent primitives. This is done by associating each primitive's properties (e.g., a triangle's normal) with its first vertex and disabling vertex value interpolation. Disabling interpolation causes the value from the first vertex to be passed to all pixels in the primitive. DirectX 10 allows disabling interpolation for each vertex value separately by using the `nointerpolate` directive; in older APIs this is done for all vertex values at once by setting the *shading mode* to “flat.”

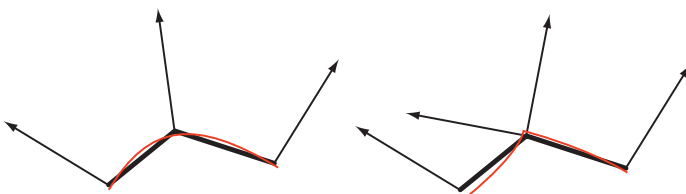


**Figure 5.14.** Side views of triangle meshes (in black, with vertex normals) representing curved surfaces (in red). On the left smoothed vertex normals are used to represent a smooth surface. On the right the middle vertex has been duplicated and given two normals, representing a crease.

use the triangle normals directly for shading. However, triangle meshes are typically used to represent an underlying curved surface. To this end, the model description includes surface normals specified at each vertex (Section 12.3.4 will discuss methods to compute vertex normals). Figure 5.14 shows side views of two triangle meshes that represent curved surfaces, one smooth and one with a sharp crease.

At this point we have all the math needed to fully evaluate the shading equation. A shader function to do so is:

```
float3 Shade(float3 p,
            float3 n,
            uniform float3 pv,
            uniform float3 Kd,
            uniform float3 Ks,
            uniform float m,
            uniform uint lightCount,
            uniform float3 l[MAXLIGHTS],
            uniform float3 EL[MAXLIGHTS])
{
    float3 v = normalize(pv - p);
    float3 Lo = float3(0.0f, 0.0f, 0.0f);
    for (uint k = 0; k < lightCount; k++)
    {
        float3 h = normalize(v + l[k]);
        float cosTh = saturate(dot(n, h));
        float cosTi = saturate(dot(n, l[k]));
        Lo += ((Kd + Ks * pow(cosTh, m)) * EL[k] * cosTi);
    }
    return Lo;
}
```

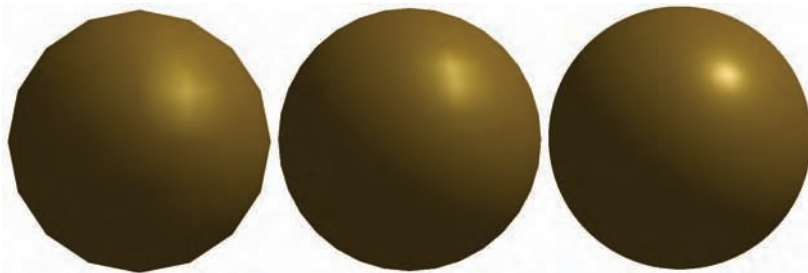


**Figure 5.15.** Per-vertex evaluation of shading equations can cause artifacts that depend on the vertex tessellation. The spheres contain (left to right) 256, 1024, and 16,384 triangles.

The arguments marked as `uniform` are constant over the entire model. The other arguments (`p` and `n`) vary per pixel or per vertex, depending on which shader calls this function. The `saturate` intrinsic function returns its argument clamped between 0 and 1. In this case we just need it clamped to 0, but the argument is known not to exceed 1, and `saturate` is faster than the more general `max` function on most hardware. The `normalize` intrinsic function divides the vector passed to it by its own length, returning a unit-length vector.

So which frequency of evaluation should we use when calling the `Shade()` function? When vertex normals are used, per-primitive evaluation of the shading equation (often called *flat shading*) is usually undesirable, since it results in a faceted look, rather than the desired smooth appearance (see the left image of Figure 5.17). Per-vertex evaluation followed by linear interpolation of the result is commonly called *Gouraud shading* [435]. In a Gouraud (pronounced *guh-row*) shading implementation, the vertex shader would pass the world-space vertex normal and position to `Shade()` (first ensuring the normal is of length 1), and then write the result to an interpolated value. The pixel shader would take the interpolated value and directly write it to the output. Gouraud shading can produce reasonable results for matte surfaces, but for highly specular surfaces it may produce artifacts, as seen in Figure 5.15 and the middle image of Figure 5.17.

These artifacts are caused by the linear interpolation of nonlinear lighting values. This is why the artifacts are most noticeable in the specular highlight, where the lighting variation is most nonlinear.

At the other extreme from Gouraud shading, we have full per-pixel evaluation of the shading equation. This is often called *Phong shading* [1014]. In this implementation, the vertex shader writes the world-space normals and positions to interpolated values, which the pixel shader passes to `Shade()`. The return value is written to the output. Note that even if

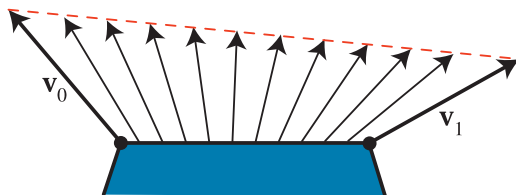


**Figure 5.16.** Linear interpolation of unit normals at vertices across a surface gives interpolated vectors that are less than a length of one.

the surface normal is scaled to length 1 in the vertex shader, interpolation can change its length, so it may be necessary to do so again in the pixel shader. See Figure 5.16.

Phong shading is free of interpolation artifacts (see the right side of Figure 5.17) but can be costly. Another option is to adopt a hybrid approach where some evaluations are performed per vertex and some per pixel. As long as the vertex interpolated values are not highly nonlinear, this can often be done without unduly reducing visual quality.

Implementing a shading equation is a matter of deciding what parts can be simplified, how frequently to compute various expressions, and how the user will be able to modify and control the appearance. This section has presented a model derived from theory, but that ignores some physical phenomena. More elaborate shading effects and equations will be presented in the chapters that follow. The next sections will cover sampling and filtering, transparency, and gamma correction.

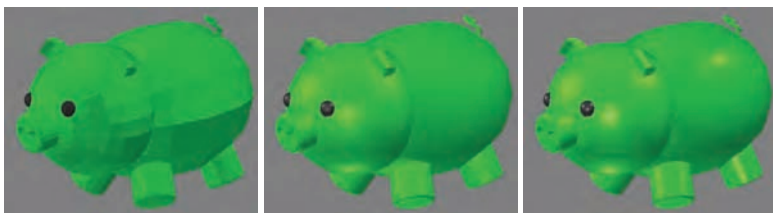


**Figure 5.17.** Flat, Gouraud, and Phong shading. The flat-shaded image has no specular term, as shininess looks like distracting flashes for flat surfaces as the viewer moves. Gouraud shading misses highlights on the body and legs from this angle because it evaluates the shading equation only at the vertices.

## 5.6 Aliasing and Antialiasing

Imagine a large black triangle moving slowly across a white background. As a screen grid cell is covered by the triangle, the pixel value representing

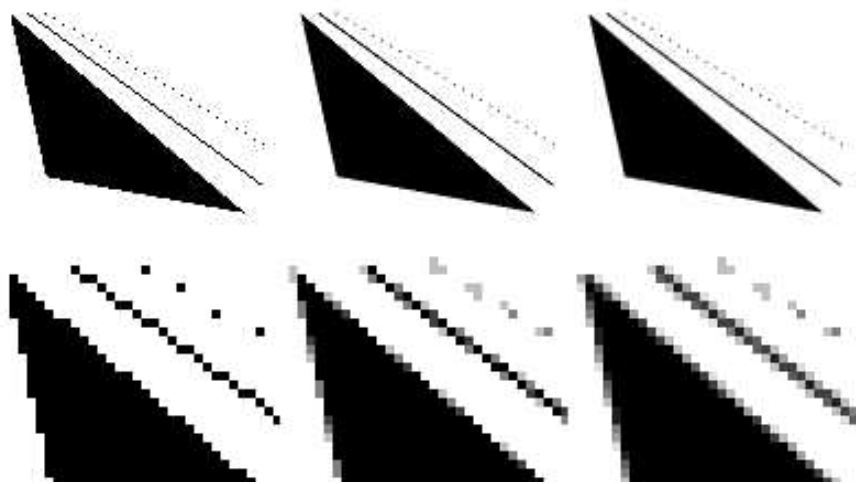


**Figure 5.18.** The upper row shows three images with different levels of antialiasing of a triangle, a line, and some points. The lower row images are magnifications of the upper row. The leftmost column uses only one sample per pixel, which means that no antialiasing is used. The middle column images were rendered with four samples per pixel (in a grid pattern), and the right column used eight samples per pixel (in a  $4 \times 4$  checkerboard). All images were rendered using InfiniteReality graphics [899].

this cell should smoothly drop in intensity. What typically happens in basic renderers of all sorts is that the moment the grid cell's center is covered, the pixel color immediately goes from white to black. Standard GPU rendering is no exception. See the leftmost column of Figure 5.18.

Polygons show up in pixels as either there or not there. Lines drawn have a similar problem. The edges have a jagged look because of this, and so this visual artifact is called “the jaggies,” which turn into “the crawlies” when animated. More formally, this problem is called *aliasing*, and efforts to avoid it are called *antialiasing* techniques.<sup>6</sup>

The subject of sampling theory and digital filtering is large enough to fill its own book [422, 1035, 1367]. As this is a key area of rendering, the basic theory of sampling and filtering will be presented. Then, we will focus on what currently can be done in real time to alleviate aliasing artifacts.

### 5.6.1 Sampling and Filtering Theory

The process of rendering images is inherently a sampling task. This is so since the generation of an image is the process of sampling a three-

<sup>6</sup>Another way to view this is that the jaggies are not actually due to aliasing—it is only that the edges are “forced” into the grid formed by the pixels [1330, 1332].

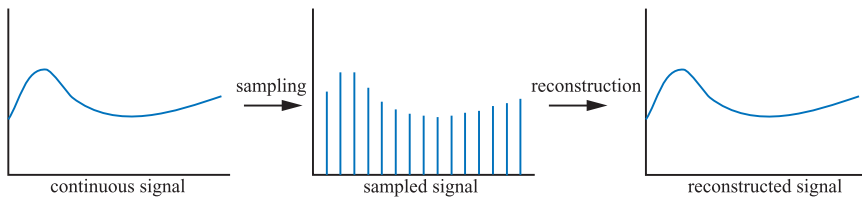
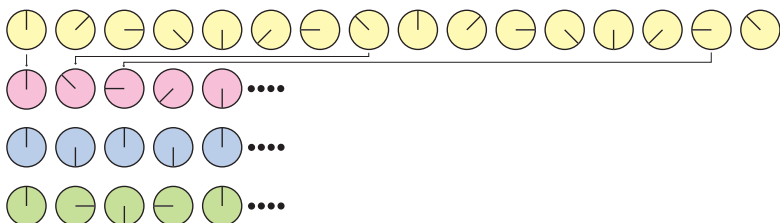


**Figure 5.19.** A continuous signal (left) is sampled (middle), and then the original signal is recovered by reconstruction (right).

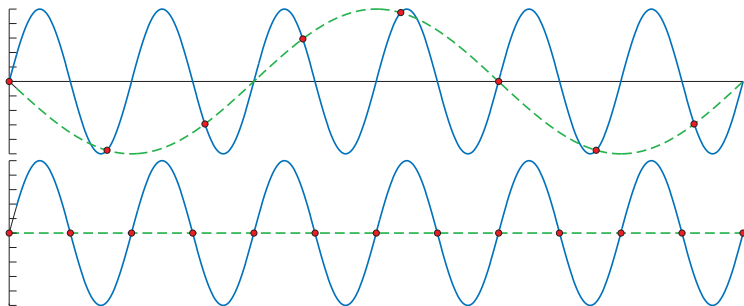
dimensional scene in order to obtain color values for each pixel in the image (an array of discrete pixels). To use texture mapping (see Chapter 6), texels have to be resampled to get good results under varying conditions. To generate a sequence of images in an animation, the animation is often sampled at uniform time intervals. This section is an introduction to the topic of sampling, reconstruction, and filtering. For simplicity, most material will be presented in one dimension. These concepts extend naturally to two dimensions as well, and can thus be used when handling two-dimensional images.

Figure 5.19 shows how a continuous signal is being sampled at uniformly spaced intervals, that is, discretized. The goal of this *sampling* process is to represent information digitally. In doing so, the amount of information is reduced. However, the sampled signal needs to be *reconstructed* in order to recover the original signal. This is done by *filtering* the sampled signal.

Whenever sampling is done, aliasing may occur. This is an unwanted artifact, and we need to battle aliasing in order to generate pleasing images. In real life, a classic example of aliasing is a spinning wheel being filmed by



**Figure 5.20.** The top row shows a spinning wheel (original signal). This is inadequately sampled in second row, making it appear to move in the opposite direction. This is an example of aliasing due to a too low sampling rate. In the third row, the sampling rate is exactly two samples per revolution, and we cannot determine in which direction the wheel is spinning. This is the Nyquist limit. In the fourth row, the sampling rate is higher than two samples per revolution, and we suddenly can see that the wheel spins in the right direction.



**Figure 5.21.** The solid blue line is the original signal, the red circles indicate uniformly spaced sample points, and the green dashed line is the reconstructed signal. The top figure shows a too low sample rate. Therefore, the reconstructed signal appears to be of lower frequency. The bottom shows a sampling rate of exactly twice the frequency of the original signal, and the reconstructed signal is here a horizontal line. It can be proven that if the sampling rate is increased ever so slightly, perfect reconstruction is possible.

a movie camera [404]. Because the wheel spins much faster than the camera records images, the wheel may appear to be spinning slowly (backwards or forwards), or may even look like it is not rotating at all. This can be seen in Figure 5.20. The effect occurs because the images of the wheel are taken in a series of time steps, and is called *temporal aliasing*.

Common examples of aliasing in computer graphics are the “jaggies” of a rasterized line or polygon edge, flickering highlights, and when a texture with a checker pattern is minified (see Section 6.2.2).

Aliasing occurs when a signal is being sampled at too low a frequency. The sampled signal then appears to be a signal of lower frequency than the original. This is illustrated in Figure 5.21. For a signal to be sampled properly (i.e., so that it is possible to reconstruct the original signal from the samples), the sampling frequency has to be more than twice the maximum frequency of the signal to be sampled. This is often called the *sampling theorem*, and the sampling frequency is called the *Nyquist<sup>7</sup> rate* [1035, 1367] or *Nyquist limit* [1332]. The Nyquist limit is also illustrated in Figure 5.20. The fact that the theorem uses the term “maximum frequency” implies that the signal has to be *bandlimited*, which just means that there are not any frequencies above a certain limit. Put another way, the signal has to be smooth enough relative to the spacing between neighboring samples.

A three-dimensional scene is normally never bandlimited when rendered with point samples. Edges of polygons, shadow boundaries, and other phenomena produce a signal that changes discontinuously and so produces frequencies that are essentially infinite [170]. Also, no matter how closely

<sup>7</sup> After Harry Nyquist [1889-1976], Swedish scientist, who discovered this in 1928.

packed the samples are, objects can still be small enough that they do not get sampled at all. Thus, it is impossible to entirely avoid aliasing problems when using point samples to render a scene. However, at times it is possible to know when a signal is bandlimited. One example is when a texture is applied to a surface. It is possible to compute the frequency of the texture samples compared to the sampling rate of the pixel. If this frequency is lower than the Nyquist limit, then no special action is needed to properly sample the texture. If the frequency is too high, then schemes to bandlimit the texture are used (see Section 6.2.2).

### *Reconstruction*

Given a bandlimited sampled signal, we will now discuss how the original signal can be reconstructed from the sampled signal. To do this, a filter must be used. Three commonly used filters are shown in Figure 5.22. Note that the area of the filter should always be one, otherwise the reconstructed signal can appear to grow or shrink.

In Figure 5.23, the box filter (nearest neighbor) is used to reconstruct a sampled signal. This is the worst filter to use, as the resulting signal is a noncontinuous stair case. Still, it is often used in computer graphics because of its simplicity. As can be seen in the illustration, the box filter is placed over each sample point, and then scaled so that the topmost point of the filter coincides with the sample point. The sum of all these scaled and translated box functions is the reconstructed signal shown to the right.

The box filter can be replaced with any other filter. In Figure 5.24, the tent filter, also called the triangle filter, is used to reconstruct a sampled signal. Note that this filter implements linear interpolation between

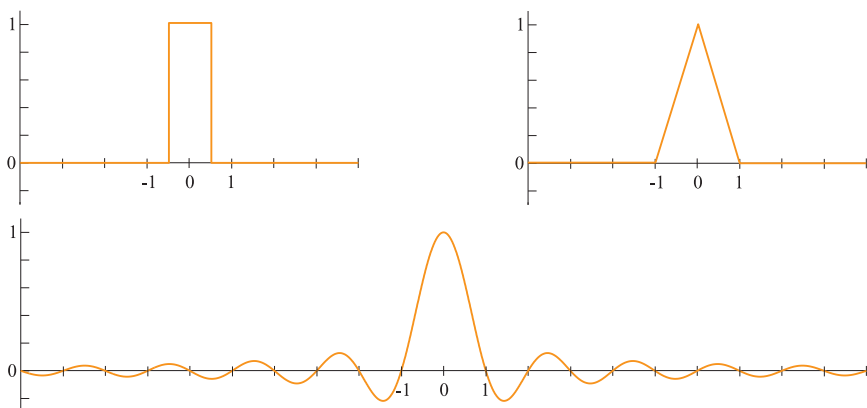


**Figure 5.22.** The top left shows the box filter, and the top right the tent filter. The bottom shows the sinc filter (which has been clamped on the  $x$ -axis here).

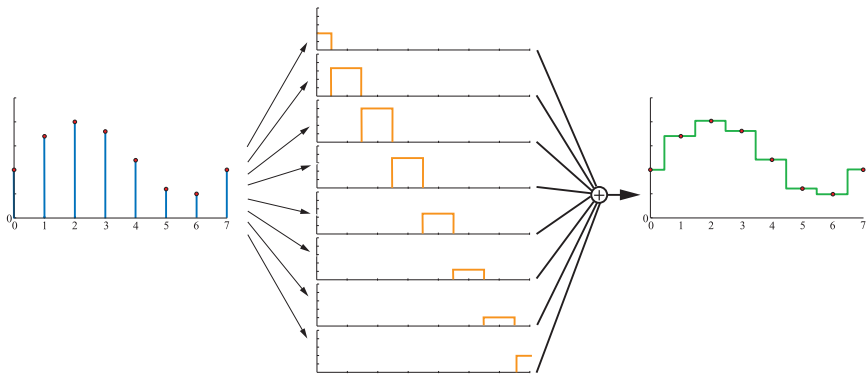


**Figure 5.23.** The sampled signal (left) is reconstructed using the box filter. This is done by placing the box filter (see Figure 5.22) over each sample point, and scaling it in the  $y$ -direction so that the height of the filter is the same as the sample point. The sum is the reconstruction signal (right).

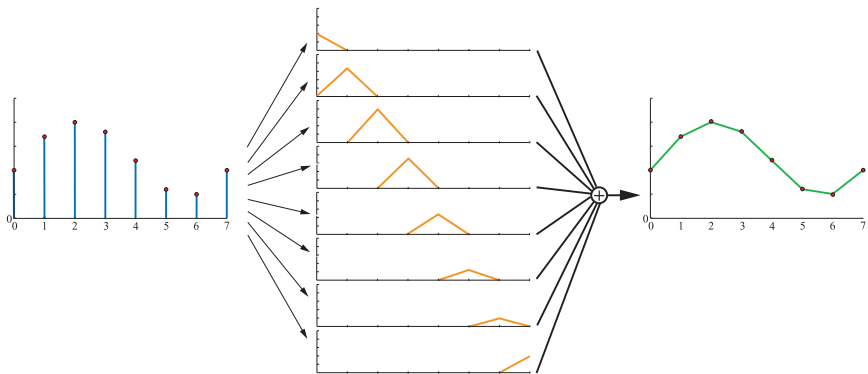


**Figure 5.24.** The sampled signal (left) is reconstructed using the tent filter. The reconstructed signal is shown to the right.

neighboring sample points, and so it is better than the box filter, as the reconstructed signal now is continuous.

However, the smoothness of the reconstructed signal using a tent filter is not very good; there are sudden slope changes at the sample points. This has to do with the fact that the tent filter is not a perfect reconstruction filter. To get perfect reconstruction the ideal *lowpass filter* has to be used. A frequency component of a signal is a sine wave:  $\sin(2\pi f)$ , where  $f$  is the frequency of that component. Given this, a lowpass filter removes all frequency components with frequencies higher than a certain frequency defined by the filter. Intuitively, the lowpass filter removes sharp features

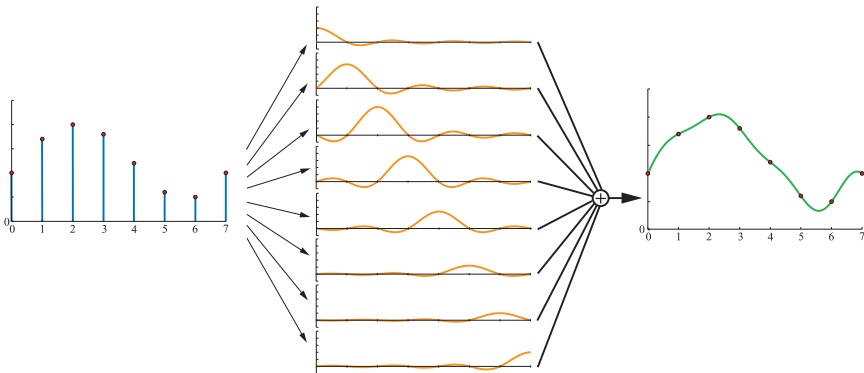


**Figure 5.25.** Here, the sinc filter is used to reconstruct the signal. The sinc filter is the ideal lowpass filter.

of the signal, i.e., the filter blurs it. The ideal lowpass filter is the sinc filter (Figure 5.22 bottom):

$$\text{sinc}(x) = \frac{\sin(\pi x)}{\pi x}. \quad (5.15)$$

Using the sinc filter to reconstruct the signal gives a smoother result, as shown in Figure 5.25.<sup>8</sup>

What can be seen is that the sampling process introduces high frequency components (abrupt changes) in the signal, and the task of the lowpass filter is to remove these. In fact, the sinc filter eliminates all sine waves with frequencies higher than 1/2 the sampling rate. The sinc function, as presented in Equation 5.15, is the perfect reconstruction filter when the sampling frequency is 1.0 (i.e., the maximum frequency of the sampled signal must be smaller than 1/2). More generally, assume the sampling frequency is  $f_s$ , that is, the interval between neighboring samples is  $1/f_s$ . For such a case, the perfect reconstruction filter is  $\text{sinc}(f_s x)$ , and it eliminates all frequencies higher than  $f_s/2$ . This is useful when resampling the signal (next section). However, the filter width of the sinc is infinite and also is negative at times, so it is rarely useful in practice.

There is a useful middle ground between the low-quality box and tent filters on one hand, and the impractical sinc filter on the other. Most widely used filter functions [872, 941, 1276, 1367] are between these extremes. All

<sup>8</sup>The theory of Fourier analysis [1035] explains why the sinc filter is the ideal lowpass filter. Briefly, the reasoning is as follows. The ideal lowpass filter is a box filter in the frequency domain, which removes all frequencies above the filter width when it is multiplied with the signal. Transforming the box filter from the frequency domain to the spatial domain gives a sinc function. At the same time, the multiplication operation is transformed into the *convolution* function, which is what we have been using in this section, without actually describing the term.

of these filter functions have some approximation to the sinc function, but with a limit on how many pixels they influence. The filters that most closely approximate the sinc function have negative values over part of their domain. For applications where negative filter values are undesirable or impractical, filters with no negative lobes (often referred to generically as Gaussian filters, since they either derive from or resemble a Gaussian curve) are typically used. Section 10.9 discusses filter functions and their use in more detail.

After using any filter, a continuous signal is obtained. However, in computer graphics we cannot display continuous signals directly, but we can use them to resample the continuous signal to another size, i.e., either enlarging the signal, or diminishing it. This is discussed next.

### *Resampling*

Resampling is used to magnify or minify a sampled signal. Assume that the original sample points are located at integer coordinates  $(0, 1, 2, \dots)$ , that is, with unit intervals between samples. Furthermore, assume that after resampling we want the new sample points to be located uniformly with an interval  $a$  between samples. For  $a > 1$ , minification (downsampling) takes place, and for  $a < 1$ , magnification (upsampling) occurs.

Magnification is the simpler case of the two, so let us start with that. Assume the sampled signal is reconstructed as shown in the previous section. Intuitively, since the signal now is perfectly reconstructed and continuous, all that is needed is to resample the reconstructed signal at the desired intervals. This process can be seen in Figure 5.26.

However, this technique does not work when minification occurs. The frequency of the original signal is too high for the sampling rate to avoid

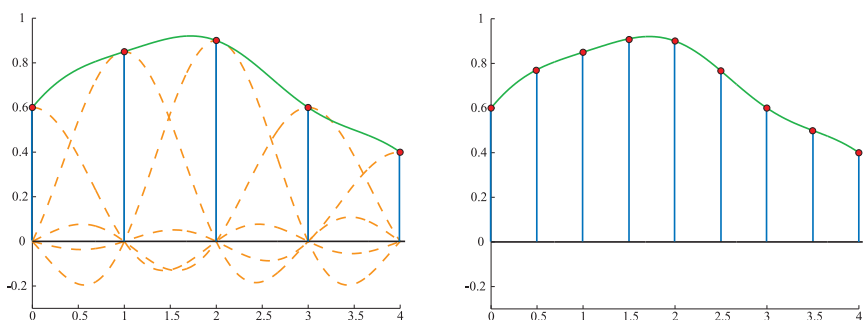


**Figure 5.26.** On the left is the sampled signal, and the reconstructed signal. On the right, the reconstructed signal has been resampled at double the sample rate, that is, magnification has taken place.

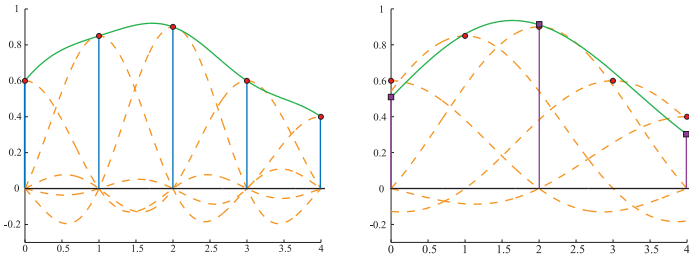


**Figure 5.27.** On the left is the sampled signal, and the reconstructed signal. On the right, the filter width has doubled in order to double the interval between the samples, that is, minification has taken place.

aliasing. Instead it has been shown that a filter using  $\text{sinc}(x/a)$  should be used to create a continuous signal from the sampled one [1035, 1194]. After that, resampling at the desired intervals can take place. This can be seen in Figure 5.27. Said another way, by using  $\text{sinc}(x/a)$  as a filter here, the width of the lowpass filter is increased, so that more of the signal's higher frequency content is removed. As shown in the figure, the filter width (of the individual sinc's) is doubled in order to decrease the resampling rate to half the original sampling rate. Relating this to a digital image, this is similar to first blurring it (to remove high frequencies) and then resampling the image at a lower resolution.

With the theory of sampling and filtering available as a framework, the various algorithms used in real-time rendering to reduce aliasing are now discussed.

## 5.6.2 Screen-Based Antialiasing

Edges of polygons produce noticeable artifacts if not sampled and filtered well. Shadow boundaries, specular highlights, and other phenomena where the color is changing rapidly can cause similar problems. The algorithms discussed in this section help improve the rendering quality for these cases. They have the common thread that they are screen based, i.e., that they operate only on the output samples of the pipeline and do not need any knowledge of the objects being rendered.

Some antialiasing schemes are focused on particular rendering primitives. Two special cases are texture aliasing and line aliasing. Texture antialiasing is discussed in Section 6.2.2. Line antialiasing can be performed in a number of ways. One method is to treat the line as a quadrilateral one pixel wide that is blended with its background; another is to consider it an infinitely thin, transparent object with a halo; a third is to render the line as an antialiased texture [849]. These ways of thinking about the line

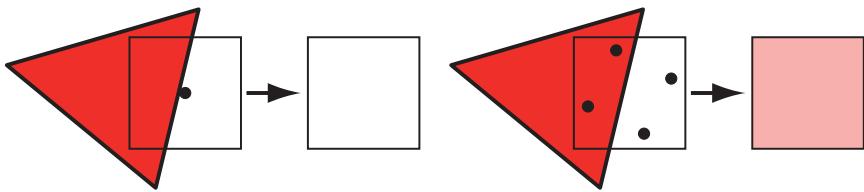


**Figure 5.28.** On the left, a red triangle is rendered with one sample at the center of the pixel. Since the triangle does not cover the sample, the pixel will be white, even though a substantial part of the pixel is covered by the red triangle. On the right, four samples are used per pixel, and as can be seen, two of these are covered by the red triangle, which results in a pink pixel color.

can be used in screen-based antialiasing schemes, but special-purpose line antialiasing hardware can provide rapid, high-quality rendering for lines. For a thorough treatment of the problem and some solutions, see Nelson’s two articles [923, 924]. Chan and Durand [170] provide a GPU-specific solution using prefiltered lines.

In the black triangle example in Figure 5.18, one problem is the low sampling rate. A single sample is taken at the center of each pixel’s grid cell, so the most that is known about the cell is whether or not the center is covered by the triangle. By using more samples per screen grid cell and blending these in some fashion, a better pixel color can be computed.<sup>9</sup> This is illustrated in Figure 5.28.

The general strategy of screen-based antialiasing schemes is to use a sampling pattern for the screen and then weight and sum the samples to produce a pixel color,  $\mathbf{p}$ :

$$\mathbf{p}(x, y) = \sum_{i=1}^n w_i \mathbf{c}(i, x, y), \quad (5.16)$$

where  $n$  is the number of samples taken for a pixel. The function  $\mathbf{c}(i, x, y)$  is a sample color and  $w_i$  is a weight, in the range  $[0, 1]$ , that the sample will contribute to the overall pixel color. The sample position is taken based on which sample it is in the series  $1, \dots, n$ , and the function optionally also uses the integer part of the pixel location  $(x, y)$ . In other words, where the sample is taken on the screen grid is different for each sample, and optionally the sampling pattern can vary from pixel to pixel. Samples are normally point samples in real-time rendering systems (and most other rendering systems, for that matter). So the function  $\mathbf{c}$  can be thought of as

---

<sup>9</sup>Here we differentiate a pixel, which consists of an RGB color triplet to be displayed, from a screen grid cell, which is the geometric area on the screen centered around a pixel’s location. See Smith’s memo [1196] and Blinn’s article [111] to understand why this is important.

two functions. First a function  $\mathbf{f}(i, n)$  retrieves the floating-point  $(x_f, y_f)$  location on the screen where a sample is needed. This location on the screen is then sampled, i.e., the color at that precise point is retrieved. The sampling scheme is chosen and the rendering pipeline configured to compute the samples at particular subpixel locations, typically based on a per-frame (or per-application) setting.

The other variable in antialiasing is  $w_i$ , the weight of each sample. These weights sum to one. Most methods used in real-time rendering systems give a constant weight to their samples, i.e.,  $w_i = \frac{1}{n}$ . Note that the default mode for graphics hardware, a single sample at the center of the pixel, is the simplest case of the antialiasing equation above. There is only one term, the weight of this term is one, and the sampling function  $\mathbf{f}$  always returns the center of the pixel being sampled.

Antialiasing algorithms that compute more than one full sample per pixel are called *supersampling* (or *oversampling*) methods. Conceptually simplest, *full-scene antialiasing* (FSAA) renders the scene at a higher resolution and then averages neighboring samples to create an image. For example, say an image of  $1000 \times 800$  pixels is desired. If you render an image of  $2000 \times 1600$  offscreen and then average each  $2 \times 2$  area on the screen, the desired image is generated with 4 samples per pixel. Note that this corresponds to  $2 \times 2$  grid sampling in Figure 5.29. This method is costly, as all subsamples must be fully shaded and filled, with a  $Z$ -buffer depth per sample. FSAA's main advantage is simplicity. Other, lower quality versions of this method sample at twice the rate on only one screen axis, and so are called  $1 \times 2$  or  $2 \times 1$  supersampling.

A related method is the *accumulation buffer* [474, 815]. Instead of one large offscreen buffer, this method uses a buffer that has the same resolution as, and usually more bits of color than, the desired image. To obtain a  $2 \times 2$  sampling of a scene, four images are generated, with the view moved half a pixel in the screen  $x$ - or  $y$ -direction as needed. Essentially, each image generated is for a different sample position within the grid cell. These images are summed up in the accumulation buffer. After rendering, the image is averaged (in our case, divided by 4) and sent to the display. Accumulation buffers are a part of the OpenGL API [9, 1362]. They can also be used for such effects as *motion blur*, where a moving object appears blurry, and *depth of field*, where objects not at the camera focus appear blurry. However, the additional costs of having to rerender the scene a few times per frame and copy the result to the screen makes this algorithm costly for real-time rendering systems.

Modern GPUs do not have dedicated accumulation buffer hardware, but one can be simulated by blending separate images together using pixel operations [884]. If only 8 bit color channels are used for the accumulated image, the low-order bits of each image will be lost when blending, po-

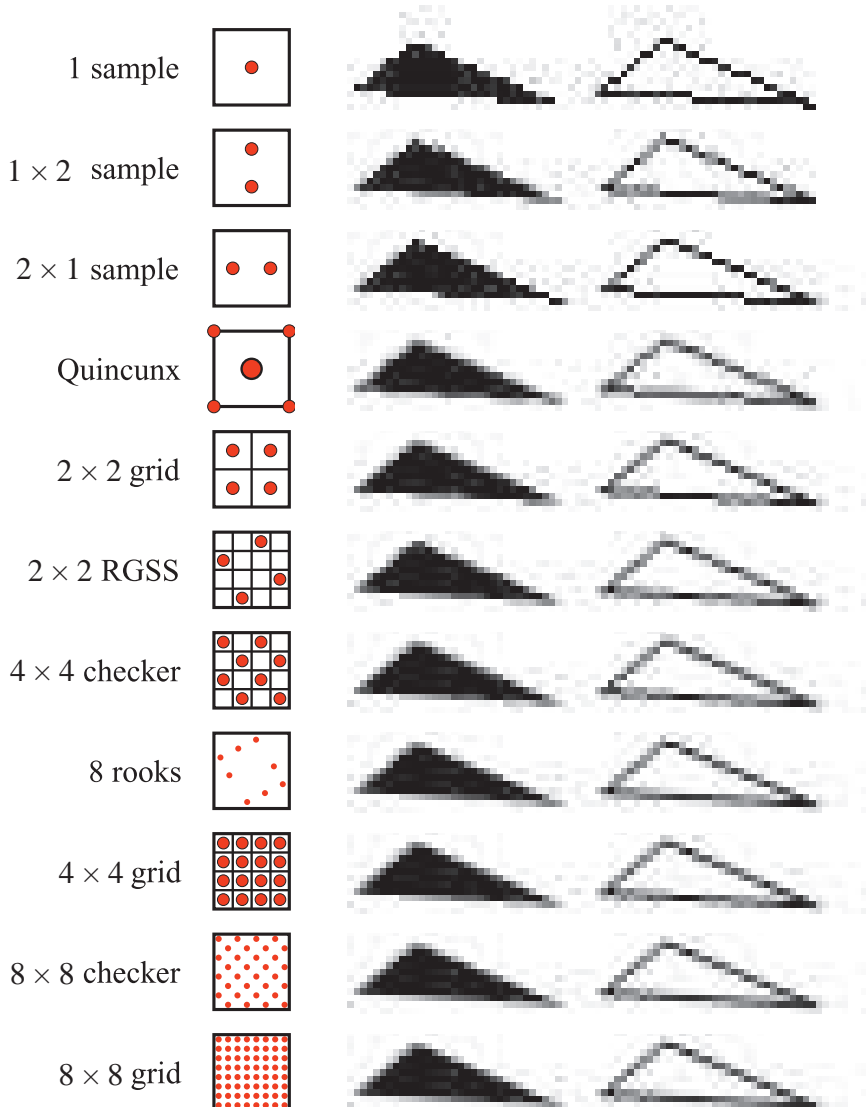


**Figure 5.29.** A comparison of some pixel sampling schemes. The  $2 \times 2$  rotated grid captures more gray levels for the nearly horizontal edge than a straight  $2 \times 2$  grid. Similarly, the 8 rooks pattern captures more gray levels for such lines than a  $4 \times 4$  grid, despite using fewer samples.

tentially causing color banding. Higher-precision buffers (most hardware supports buffers with 10 or 16 bits per channel) avoid the problem.

An advantage that the accumulation buffer has over FSAA (and over the *A*-buffer, which follows) is that sampling does not have to be a uniform orthogonal pattern within a pixel's grid cell. Each pass is independent of the others, so alternate sampling patterns are possible. Sampling in a rotated square pattern such as  $(0, 0.25)$ ,  $(0.5, 0)$ ,  $(0.75, 0.5)$ ,  $(0.25, 0.75)$  gives more vertical and horizontal resolution within the pixel. Sometimes called *rotated grid supersampling* (RGSS), this pattern gives more levels of antialiasing for nearly vertical or horizontal edges, which usually are most in need of improvement. In fact, Naiman [919] shows that humans are most disturbed by aliasing on near-horizontal and near-vertical edges. Edges with near 45 degrees slope are next to most disturbing. Figure 5.29 shows how the sampling pattern affects quality.

Techniques such as supersampling work by generating samples that are fully specified with individually computed shades, depths, and locations. The cost is high and the overall gains relatively low; in particular, each sample has to run through a pixel shader. For this reason, DirectX does not directly support supersampling as an antialiasing method. *Multisampling* strategies lessen the high computational costs of these algorithms by sampling various types of data at differing frequencies. A multisampling algorithm takes more than one sample per pixel in a single pass, and (unlike the methods just presented) shares some computations among the samples. Within GPU hardware these techniques are called *multisample antialiasing* (MSAA) and, more recently, *coverage sampling antialiasing* (CSAA).

Additional samples are needed when phenomena such as object edges, specular highlights, and sharp shadows cause abrupt color changes. Shadows can often be made softer and highlights wider, but object edges remain as a major sampling problem. MSAA saves time by computing fewer shading samples per fragment. So pixels might have 4  $(x, y)$  sample locations per fragment, each with their own color and  $z$ -depth, but the shade is computed only once for each fragment. Figure 5.30 shows some MSAA patterns used in practice.

If all MSAA positional samples are covered by the fragment, the shading sample is in the center of the pixel. However, if the fragment covers fewer positional samples, the shading sample's position can be shifted. Doing so avoids shade sampling off the edge of a texture, for example. This position adjustment is called *centroid sampling* or *centroid interpolation* and is done automatically by the GPU, if enabled.<sup>10</sup>

---

<sup>10</sup>Centroid sampling can cause derivative computations to return incorrect values, so it should be used with care.

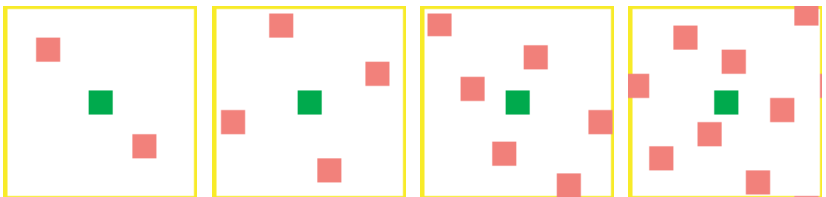


**Figure 5.30.** MSAA sampling patterns for ATI and NVIDIA graphics accelerators. The green square is the location of the shading sample, and the red squares are the positional samples computed and saved. From left to right: 2x, 4x, 6x (ATI), and 8x (NVIDIA) sampling. (*Generated by the D3D FSAA Viewer.*)

MSAA is faster than a pure supersampling scheme because the fragment is shaded only once. It focuses effort on sampling the fragment's pixel coverage at a higher rate and sharing the computed shade. However, actually storing a separate color and  $z$ -depth for each sample is usually unnecessary. CSAA takes advantage of this observation by storing just the coverage for the fragment at a higher sampling rate. Each subpixel stores an index to the fragment with which it is associated. A table with a limited number of entries (four or eight) holds the color and  $z$ -depth associated with each fragment. For example, for a table holding four colors and  $z$ -depths, each subpixel needs only two bits of storage to index into this table. In theory a pixel with 16 samples could hold 16 different fragments, in which case CSAA would be unable to properly store the information needed, possibly resulting in artifacts. For most data types it is relatively rare to have more than four fragments that are radically different in shade visible in a pixel, so this scheme performs well in practice.

This idea of separating coverage from shading and depth storage is similar to Carpenter's *A*-buffer [157], another form of multisampling. This algorithm is commonly used in software for generating high-quality renderings, but at noninteractive speeds. In the *A*-buffer, each polygon rendered creates a *coverage mask* for each screen grid cell it fully or partially covers. See Figure 5.31 for an example of a coverage mask.

Similar to MSAA, the shade for the polygon associated with this coverage mask is typically computed once at the centroid location on the fragment and shared by all samples. The  $z$ -depth is also computed and stored in some form. Some systems compute a pair of depths, a minimum and maximum. Others also retain the slope of the polygon, so that the exact  $z$ -depth can be derived at any sample location, which allows interpenetrating polygons to be rendered properly [614]. The coverage mask, shade,  $z$ -depth, and other information make up a stored *A*-buffer fragment.

A critical way that the *A*-buffer differs from the *Z*-buffer is that a screen grid cell can hold any number of fragments at one time. As they

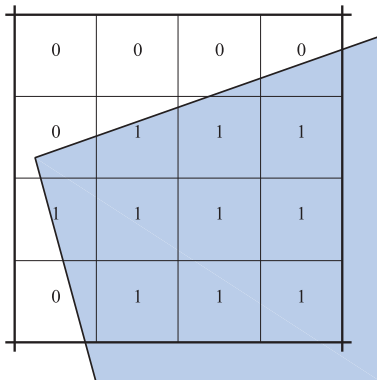


**Figure 5.31.** The corner of a polygon partially covers a single screen grid cell associated with a pixel. The grid cell is shown subdivided into a  $4 \times 4$  subgrid, and those cells that are considered covered are marked by a 1. The 16-bit mask for this cell is 0000 0111 1111 0111.

collect, fragments can be discarded if they are hidden. For example, if an opaque fragment  $A$  has a coverage mask that fully covers fragment  $B$ , and fragment  $A$  has a maximum  $z$ -depth less than the minimum  $z$ -depth of  $B$ , then fragment  $B$  can be safely discarded. Coverage masks can also be merged and used together. For example, if one opaque fragment covers one part of a pixel and another opaque fragment covers another, their masks can be logically ORed together and the larger of their maximum  $z$ -depths used to form a larger area of coverage. Because of this merging mechanism, fragments are often sorted by  $z$ -depth. Depending on the design, such merging can happen when a fragment buffer becomes filled, or as a final step before shading and display.

Once all polygons have been sent to the  $A$ -buffer, the color to be stored in the pixel is computed. This is done by determining how much of the mask of each fragment is visible, and then multiplying this percentage by the fragment's color and summing the results. See Figure 5.18 for an example of multisampling hardware in use. Transparency effects, one of the  $A$ -buffer's strengths, are also folded in at this time.

Though this sounds like an involved procedure, many of the mechanisms for rendering a triangle into a  $Z$ -buffer can be reused to implement the  $A$ -buffer in hardware [1362]. Storage and computation requirements are usually considerably lower than for simple FSAA, as the  $A$ -buffer works by storing a variable number of fragments for each pixel. One problem with this approach is that there is no upper limit on the number of semitransparent fragments stored. Jouppi & Chang [614] present the  $Z^3$  algorithm, which uses a fixed number of fragments per pixel. Merging is forced to

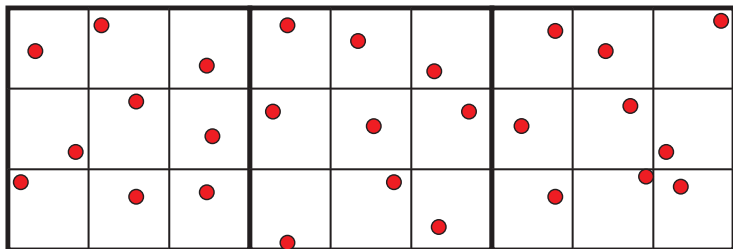


**Figure 5.32.** A typical jitter pattern for three pixels, each divided into a  $3 \times 3$  set of subcells. One sample appears in each subcell, in a random location.

occur when the storage limit is reached. Bavoil et al. [74, 77] generalize this approach in their  $k$ -buffer architecture. Their earlier paper also has a good overview of the extensive research that has been done in the field.

While all of these antialiasing methods result in better approximations of how each polygon covers a grid cell, they have some limitations. As discussed in the previous section, a scene can be made of objects that are arbitrarily small on the screen, meaning that no sampling rate can ever perfectly capture them. So, a regular sampling pattern will always exhibit some form of aliasing. One approach to avoiding aliasing is to distribute the samples randomly over the pixel, with a different sampling pattern at each pixel. This is called *stochastic sampling*, and the reason it works better is that the randomization tends to replace repetitive aliasing effects with noise, to which the human visual system is much more forgiving [404].

The most common kind of stochastic sampling is *jittering*, a form of *stratified sampling*, which works as follows. Assume that  $n$  samples are to be used for a pixel. Divide the pixel area into  $n$  regions of equal area, and place each sample at a random location in one of these regions.<sup>11</sup> See Figure 5.32. The final pixel color is computed by some averaged mean of the samples. *N-rooks sampling* is another form of stratified sampling, in which  $n$  samples are placed in an  $n \times n$  grid, with one sample per row and column [1169]. Incidentally, a form of *N-rooks* pattern is used in the Infinite-Reality [614, 899], as it is particularly good for capturing nearly horizontal and vertical edges. For this architecture, the same pattern is used per pixel and is subpixel-centered (not randomized within the subpixel), so it is not performing stochastic sampling.

AT&T Pixel Machines and Silicon Graphics' VGX, and more recently ATI's SMOOTHVISION scheme, use a technique called *interleaved sampling*. In ATI's version, the antialiasing hardware allows up to 16 samples per pixel, and up to 16 different user-defined sampling patterns that can

<sup>11</sup>This is in contrast to accumulation buffer screen offsets, which can allow random sampling of a sort, but each pixel has the same sampling pattern.



**Figure 5.33.** On the left, antialiasing with the accumulation buffer, with four samples per pixel. The repeating pattern gives noticeable problems. On the right, the sampling pattern is not the same at each pixel, but instead patterns are interleaved. (*Images courtesy of Alexander Keller and Wolfgang Heidrich.*)

be intermingled in a repeating pattern (e.g., in a  $4 \times 4$  pixel tile, with a different pattern in each). The sampling pattern is not different for every pixel cell, as is done with a pure jittering scheme. However, Molnar [894], as well as Keller and Heidrich [642], found that using interleaved stochastic sampling minimizes the aliasing artifacts formed when using the same pattern for every pixel. See Figure 5.33. This technique can be thought of as a generalization of the accumulation buffer technique, as the sampling pattern repeats, but spans several pixels instead of a single pixel.

There are still other methods of sampling and filtering. One of the best sampling patterns known is *Poisson disk sampling*, in which nonuniformly distributed points are separated by a minimum distance [195, 260]. Molnar presents a scheme for real-time rendering in which unweighted samples are arranged in a Poisson disk pattern with a Gaussian filtering kernel [894].

One real-time antialiasing scheme that lets samples affect more than one pixel is NVIDIA’s older Quincunx method [269], also called *high resolution antialiasing* (HRAA). “Quincunx” means an arrangement of five objects, four in a square and the fifth in the center, such as the pattern of five dots on a six-sided die. In this multisampling antialiasing scheme, the sampling pattern is a quincunx, with four samples at the pixel cell’s corners and one sample in the center (see Figure 5.29). Each corner sample value is distributed to its four neighboring pixels. So instead of weighting each sample equally (as most other real-time schemes do), the center sample is given a weight of  $\frac{1}{2}$ , and each corner sample has a weight of  $\frac{1}{8}$ . Because of this sharing, an average of only two samples are needed per pixel for the Quincunx scheme, and the results are considerably better than two-sample FSAA methods. This pattern approximates a two-dimensional tent filter, which, as discussed in the previous section, is superior to the box filter. While the Quincunx method itself appears to have died out, some newer GPUs are again using sharing of a single sample’s results among pixels

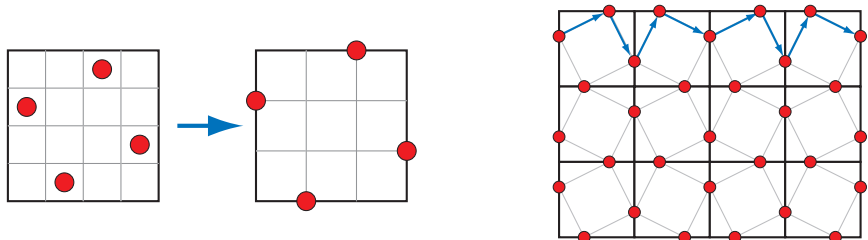


**Figure 5.34.** To the left, the RGSS sampling pattern is shown. This costs four samples per pixel. By moving these out to the pixel edges, sample sharing can occur across edges. However, for this to work out, every other pixel must have a reflected sample pattern, as shown on the right. The resulting sample pattern is called FLIPQUAD and costs two samples per pixel

for higher quality signal reconstruction. For example, the ATI Radeon HD 2000 introduced *custom filter antialiasing* (CFAA) [1166], with the capabilities of using narrow and wide tent filters that extend slightly into other pixel cells. It should be noted that for results of the highest visual quality, samples should be gathered from a much larger area, such as a  $4 \times 4$  or even  $5 \times 5$  pixel grid [872]; at the time of writing, Sun Microsystem's defunct XVR-4000 is the only graphics hardware to perform this level of filtering in real time [244].

It should be noted that sample sharing is also used for antialiasing in the mobile graphics context [13]. The idea is to combine the clever idea of sample sharing in Quinquin with RGSS (Figure 5.29). This results in a pattern, called FLIPQUAD, which costs only two samples per pixel, and with similar quality to RGSS (which costs four samples per pixel). The sampling pattern is shown in Figure 5.34. Other inexpensive sampling patterns that exploit sample sharing are explored by Hasselgren et al. [510].

Molnar presents a sampling pattern for performing adaptive refinement [83]. This is a technique where the image improves over time by increasing the number of samples taken. This scheme is useful in interactive applications. For example, while the scene is changing, the sampling rate is kept low; when the user stops interacting and the scene is static, the image improves over time by having more and more samples taken and the intermediate results displayed. This scheme can be implemented using an accumulation buffer that is displayed after certain numbers of samples have been taken.

The rate of sampling can be varied depending on the scene information being sampled. For example, in MSAA the focus is on increasing the number of samples to improve edge detection while computing shading samples at lower rates. Persson [1007] discusses how the pixel shader can be used to improve quality on a per-surface basis by gathering additional texture sam-



**Figure 5.35.** Magnified grayscale antialiased and subpixel antialiased versions of the same word. When a colored pixel is displayed on an LCD screen, the corresponding colored vertical subpixel rectangles making up the pixel are lit. Doing so provides additional horizontal spatial resolution. (*Images generated by Steve Gibson's "Free & Clear" program.*)

ples. In this way, supersampling can be applied selectively to the surfaces that would most benefit from it.

The eye is more sensitive to differences in intensity than to differences in color. This fact has been used since at least the days of the Apple II [393] to improve perceived spatial resolution. One of the latest uses of this idea is Microsoft's ClearType technology, which is built upon one of the characteristics of color *liquid-crystal display* (LCD) displays. Each pixel on an LCD display consists of three vertical colored rectangles, red, green, and blue—use a magnifying glass on an LCD monitor and see for yourself. Disregarding the colors of these subpixel rectangles, this configuration provides three times as much horizontal resolution as there are pixels. Using different shades fills in different subpixels. The eye blends the colors together and the red and blue fringes become undetectable. See Figure 5.35.

In summary, there are a wide range of schemes for antialiasing edges, with tradeoffs of speed, quality, and manufacturing cost. No solution is perfect, nor can it be, but methods such as MSAA and CSAA offer reasonable tradeoffs between speed and quality. Undoubtedly, manufacturers will offer even better sampling and filtering schemes as time goes on. For example, in the summer of 2007, ATI introduced a high quality (and computationally expensive) antialiasing scheme based on fragment edge detection, called *edge detect antialiasing*.

## 5.7 Transparency, Alpha, and Compositing

There are many different ways in which semitransparent objects can allow light to pass through them. In terms of rendering algorithms, these can be roughly divided into view-based effects and light-based effects. View-based effects are those in which the semitransparent object itself is being rendered. Light-based effects are those in which the object causes light to be attenuated or diverted, causing other objects in the scene to be lit and rendered differently.

In this section we will deal with the simplest form of view-based transparency, in which the semitransparent object acts as a color filter or constant attenuator of the view of the objects behind it. More elaborate view- and light-based effects such as frosted glass, the bending of light (refraction), attenuation of light due to the thickness of the transparent object, and reflectivity and transmission changes due to the viewing angle are discussed in later chapters.

A limitation of the  $Z$ -buffer is that only one object is stored per pixel. If a number of transparent objects overlap the same pixel, the  $Z$ -buffer alone cannot hold and later resolve the effect of all the visible objects. This problem is solved by accelerator architectures such as the  $A$ -buffer, discussed in the previous section. The  $A$ -buffer has “deep pixels” that store a number of fragments that are resolved to a single pixel color after all objects are rendered. Because the  $Z$ -buffer absolutely dominates the accelerator market, we present here various methods to work around its limitations.

One method for giving the illusion of transparency is called *screen-door transparency* [907]. The idea is to render the transparent polygon with a checkerboard fill pattern. That is, every other pixel of the polygon is rendered, thereby leaving the object behind it partially visible. Usually the pixels on the screen are close enough together that the checkerboard pattern itself is not visible. The problems with this technique include:

- A transparent object looks best when 50% transparent. Fill patterns other than a checkerboard can be used, but in practice these are usually discernable as shapes themselves, detracting from the transparency effect.
- Only one transparent object can be convincingly rendered on one area of the screen. For example, if a transparent red object and transparent green object are rendered atop a blue object, only two of the three colors can appear on the checkerboard pattern.

That said, one advantage of this technique is its simplicity. Transparent objects can be rendered at any time, in any order, and no special hardware (beyond fill pattern support) is needed. The transparency problem essentially goes away by making all objects opaque. This same idea is used for antialiasing edges of cutout textures, but at a subpixel level, using a feature called *alpha to coverage*. See Section 6.6.

What is necessary for more general and flexible transparency effects is the ability to blend the transparent object’s color with the color of the object behind it. For this, the concept of *alpha blending* is needed [143, 281, 1026]. When an object is rendered on the screen, an RGB color and a  $Z$ -buffer depth are associated with each pixel. Another component, called

alpha ( $\alpha$ ), can also be defined for each pixel the object covers. Alpha is a value describing the degree of opacity of an object fragment for a given pixel. An alpha of 1.0 means the object is opaque and entirely covers the pixel's area of interest; 0.0 means the pixel is not obscured at all.

To make an object transparent, it is rendered on top of the existing scene with an alpha of less than 1.0. Each pixel covered by the object will receive a resulting  $\text{RGB}\alpha$  (also called  $\text{RGBA}$ ) from the rendering pipeline. Blending this value coming out of the pipeline with the original pixel color is usually done using the **over** operator, as follows:

$$\mathbf{c}_o = \alpha_s \mathbf{c}_s + (1 - \alpha_s) \mathbf{c}_d \quad [\text{over operator}], \quad (5.17)$$

where  $\mathbf{c}_s$  is the color of the transparent object (called the *source*),  $\alpha_s$  is the object's alpha,  $\mathbf{c}_d$  is the pixel color before blending (called the *destination*), and  $\mathbf{c}_o$  is the resulting color due to placing the transparent object **over** the existing scene. In the case of the rendering pipeline sending in  $\mathbf{c}_s$  and  $\alpha_s$ , the pixel's original color  $\mathbf{c}_d$  gets replaced by the result  $\mathbf{c}_o$ . If the incoming  $\text{RGB}\alpha$  is, in fact, opaque ( $\alpha_s = 1.0$ ), the equation simplifies to the full replacement of the pixel's color by the object's color.

To render transparent objects properly into a scene usually requires sorting. First, the opaque objects are rendered, then the transparent objects are blended on top of them in back-to-front order. Blending in arbitrary order can produce serious artifacts, because the blending equation is order dependent. See Figure 5.36. The equation can also be modified so that blending front-to-back gives the same result, but only when rendering



**Figure 5.36.** On the left the model is rendered with transparency using the *Z*-buffer. Rendering the mesh in an arbitrary order creates serious errors. On the right, depth peeling provides the correct appearance, at the cost of additional passes. (Images courtesy of NVIDIA Corporation.)

the transparent surfaces to a separate buffer, i.e., without any opaque objects rendered first. This blending mode is called the *under operator* and is used in volume rendering techniques [585]. For the special case where only two transparent surfaces overlap and the alpha of both is 0.5, the blend order does not matter, and so no sorting is needed [918].

Sorting individual objects by, say, their centroids does not guarantee the correct sort order. Interpenetrating polygons also cause difficulties. Drawing polygon meshes can cause sorting problems, as the GPU renders the polygons in the order given, without sorting.

If sorting is not possible or is only partially done, it is often best to use Z-buffer testing, but no  $z$ -depth replacement, for rendering the transparent objects. In this way, all transparent objects will at least appear. Other techniques can also help avoid artifacts, such as turning off culling, or rendering transparent polygons twice, first rendering backfaces and then frontfaces [918].

Other methods of correctly rendering transparency without the application itself needing to sort are possible. An advantage to the  $A$ -buffer multisampling method described on page 128 is that the fragments can be combined in sorted order by hardware to obtain high quality transparency. Normally, an alpha value for a fragment represents either transparency, the coverage of a pixel cell, or both. A multisample fragment's alpha represents purely the transparency of the sample, since it stores a separate coverage mask.

Transparency can be computed using two or more depth buffers and multiple passes [253, 643, 815]. First, a rendering pass is made so that the opaque surfaces'  $z$ -depths are in the first  $Z$ -buffer. Now the transparent objects are rendered. On the second rendering pass, the depth test is modified to accept the surface that is both closer than the depth of the first buffer's stored  $z$ -depth, and the farthest among such surfaces. Doing so renders the backmost transparent object into the frame buffer and the  $z$ -depths into a second  $Z$ -buffer. This  $Z$ -buffer is then used to derive the next-closest transparent surface in the next pass, and so on. See Figure 5.37.

The pixel shader can be used to compare  $z$ -depths in this fashion and so perform *depth peeling*, where each visible layer is found in turn [324, 815]. One initial problem with this approach was knowing how many passes were sufficient to capture all the transparent layers. This problem is solved using the *pixel draw counter*, which tells how many pixels were written during rendering; when no pixels are rendered by a pass, rendering is done. Alternatively, peeling could be cut short when the number of pixels rendered by a pass falls below some minimum.

While depth peeling is effective, it can be slow, as each layer peeled is a separate rendering pass of all transparent objects. Mark and Proudfoot [817] discuss a hardware architecture extension they call the “F-buffer”



**Figure 5.37.** Each depth peel pass draws one of the transparent layers. On the left is the first pass, showing the layer directly visible to the eye. The second layer, shown in the middle, displays the second-closest transparent surface at each pixel, in this case the backfaces of objects. The third layer, on the right, is the set of third-closest transparent surfaces. Final results can be found on page 394. (*Images courtesy of Louis Bavoil.*)

that solves the transparency problem by storing and accessing fragments in a stream. Bavoil et al. [74] propose the *k*-buffer architecture, which also attacks this problem. Liu et al. [781] and Pangerl [986] explore the use of multiple render targets to simulate a four-level deep *A*-buffer. Unfortunately, the method is limited by the problem of concurrently reading and writing to the same buffer, which can cause transparent fragments to be rendered out of order. Liu et al. provide a method to ensure the fragments are always sorted properly, though at the cost of performance. Nonetheless, they can still render depth-peeled transparency layers about twice as fast in overall frame rate. That said, DirectX 10 and its successors do not allow concurrent read/write from the same buffer, so these approaches cannot be used with newer APIs.

The **over** operator can also be used for antialiasing edges. As discussed in the previous section, a variety of algorithms can be used to find the approximate percentage of a pixel covered by the edge of a polygon. Instead of storing a coverage mask showing the area covered by the object, an alpha can be stored in its place. There are many methods to generate alpha values that approximate the coverage of an edge, line, or point.

As an example, if an opaque polygon is found to cover 30% of a screen grid cell, it would then have an alpha of 0.3. This alpha value is then used to blend the object’s edge with the scene, using the **over** operator. While this alpha is just an approximation of the area an edge covers, this interpretation works fairly well in practice if generated properly. An example of a poor way to generate alphas is to create them for every polygon edge. Imagine that two adjacent polygons fully cover a pixel, with each covering 50% of it. If each polygon generates an alpha value for its edge, the two alphas would

combine to cover only 75% of the pixel, allowing 25% of the background to show through. This sort of error is avoided by using coverage masks or by blurring the edges outwards, as discussed in the previous section.

To summarize, the alpha value can represent transparency, edge coverage, or both (if one multiplies the two alphas together).

**EXAMPLE: BLENDING.** A teapot is rendered onto a background using anti-aliasing techniques. Say that at some pixel the shade of the surface is a beige,  $(0.8, 0.7, 0.1)$ , the background is a light blue,  $(0.7, 0.7, 0.9)$ , and the surface is found to cover 0.6 of the pixel. The blend of these two colors is

$$0.6(0.8, 0.7, 0.1) + (1 - 0.6)(0.7, 0.7, 0.9),$$

which gives a color of  $(0.76, 0.7, 0.42)$ . □

The **over** operator turns out to be useful for blending together photographs or synthetic renderings of objects. This process is called *compositing* [143, 1197]. In such cases, the alpha value at each pixel is stored along with the RGB color value for the object. The alpha channel is sometimes called the *matte* and shows the silhouette shape of the object. See Figure 6.24 on page 182 for an example. This  $\text{RGB}\alpha$  image can then be used to blend it with other such *elements* or against a background.

There are a number of other blending operators besides **over** [143, 1026], but most are not as commonly used in real-time applications. One exception is *additive blending*, where pixel values are simply summed. That is,

$$\mathbf{c}_o = \alpha_s \mathbf{c}_s + \mathbf{c}_d. \quad (5.18)$$

This blending mode has the advantage of not requiring sorting between triangles, since addition can be done in any order. It can work well for glowing effects that do not attenuate the pixels behind them but only brighten them. However, this mode does not look correct for transparency, as the opaque surfaces do not appear filtered [849]. For a number of layered semitransparent surfaces, such as smoke or fire, additive blending has the effect of saturating the colors of the phenomenon [928].

The most common way to store synthetic  $\text{RGB}\alpha$  images is with *premultiplied alphas* (also known as *associated alphas*). That is, the RGB values are multiplied by the alpha value before being stored. This makes the compositing **over** equation more efficient:

$$\mathbf{c}_o = \mathbf{c}'_s + (1 - \alpha_s)\mathbf{c}_d, \quad (5.19)$$

where  $\mathbf{c}'_s$  is the premultiplied source channel. Also important, premultiplied alphas allow cleaner theoretical treatment [1197]. Note that with premultiplied  $\text{RGB}\alpha$  values, the RGB components are normally not greater than the alpha value.

Rendering synthetic images meshes naturally with premultiplied alphas. An antialiased opaque object rendered over a black background provides premultiplied values by default. Say a white  $(1, 1, 1)$  polygon covers 40% of some pixel along its edge. With (extremely precise) antialiasing, the pixel value would be set to a gray of 0.4—we would save the color  $(0.4, 0.4, 0.4)$  for this pixel. The alpha value, if stored, would also be 0.4, since this is the area the polygon covered. The RGBA value would be  $(0.4, 0.4, 0.4, 0.4)$ , which is a premultiplied value.

Another way images are stored is with *unmultiplied alphas*, also known as *unassociated alphas* (or even as the mind-bending term *nonpremultiplied alphas*). An unmultiplied alpha is just what it says: The RGB value is not multiplied by the alpha value. This is rarely used in synthetic image storage, since the final color we see at a pixel is not the shade of the polygon; it is the shade multiplied by alpha, blended with the background. For the white polygon example, the unmultiplied color would be  $(1, 1, 1, 0.4)$ . This representation has the advantage of storing the polygon’s original color, but this color would always need to be multiplied by the stored alpha to be displayed correctly. It is normally best to use premultiplied whenever filtering and blending is performed, as operations such as linear interpolation do not work correctly using unmultiplied alphas [67, 104].

For image-manipulation applications, an unassociated alpha is useful to mask a photograph without affecting the underlying image’s original data. Image file formats that support alpha include TIFF (both types of alpha) and PNG (unassociated alpha only) [912].

A concept related to the alpha channel is *chroma-keying* [143]. This is a term from video production, in which actors are filmed against a blue, yellow, or (increasingly common) green screen and blended with a background. In the film industry this process is called *green-screen* or *blue-screen masking*. The idea here is that a particular color is designated to be considered transparent; where it is detected, the background is displayed. This allows images to be given an outline shape by using just RGB colors—no alpha needs to be stored. One drawback of this scheme is that the object is either entirely opaque or transparent at any pixel, i.e., alpha is effectively only 1.0 or 0.0. As an example, the GIF format allows one color (actually, one palette entry; see Section 18.1.1) to be designated as transparent.

The **over** operator can be used for rendering semitransparent objects on top of whatever has been rendered before, e.g., opaque objects and more distant transparent objects. This works, in the sense that we perceive something as transparent whenever the objects behind can be seen through it [554]. But the **over** operator is more correctly used to represent some approximation of how much an opaque object covers a pixel’s cell. A more representative formula for how a transparent object acts is to represent it by a combination of filtering and reflection. To filter, the scene behind the

transparent object should be multiplied by the transparent object’s spectral opacity [1348]. For example, a yellow piece of stained glass multiplies the scene’s color by its RGB yellow color. The stained glass itself might reflect some light toward the eye, a contribution that should then be added in. To simulate this with alpha blending, we would need to multiply the frame buffer by one RGB color and then add another RGB color. Doing this in a single pass cannot be done with regular alpha blending, but is possible with *dual-color blending*, added in DirectX 10 (see Section 3.7). Physically correct transparency is discussed in Sections 7.5.3, 9.4, and 9.5.

One last note on alpha: This channel can be used to store whatever you like. For image file formats, the stored alpha usually has a specific meaning, either unmultiplied or premultiplied. During shader computations, however, the alpha channel is sometimes a convenient place to store a grayscale specular contribution, power, or other scaling factor. An understanding of the available blending modes can make a variety of effects rapid to compute.

## 5.8 Gamma Correction

Once the pixel values have been computed, we need to display them on a monitor. In the early years of digital imaging, *cathode-ray tube* (CRT) monitors were almost exclusively used. CRT monitors exhibit a power law relationship between input voltage and display radiance, which turns out to nearly match the inverse of light sensitivity of the human eye [1028]. The consequence of this fortunate coincidence is that an encoding proportional to CRT input voltage is roughly *perceptually uniform* (the perceptual difference between a pair of encoded values  $N$  and  $N+1$  is roughly constant over the displayable range). This near-optimal distribution of values minimizes *banding* artifacts, which can be particularly bothersome when the number of distinct values is small (as is the case with color buffers storing 8 bits or less per channel). Now that CRT displays are rare, perceptual uniformity is one reason for using power-law encodings. The desire for compatibility with existing images is another important factor. LCDs have different tone response curves than CRTs, but hardware adjustments are usually made to provide compatibility [329, 1157].

The *transfer functions* that define the relationship between radiance<sup>12</sup> and encoded pixel values are slightly modified power curves. It is customary to characterize such a function by the power curve that most closely

---

<sup>12</sup>Actually, a normalized radiance value that ranges from 0 (for display *black level*) to 1 (for maximum display radiance).

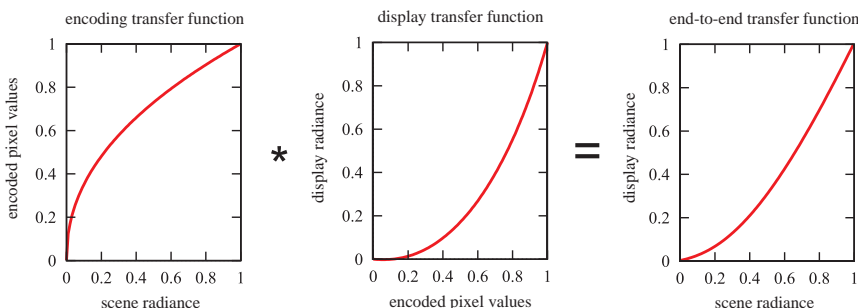


**Figure 5.38.** On the left is the function relating normalized scene radiance to encoded pixel values. In the middle is the function relating encoded pixel values to normalized display radiance. The concatenation of the two functions gives the end-to-end transfer function of the imaging system, shown to the right.

approximates it in the 0 to 1 range:

$$f_{\text{xfer}}(x) \approx x^\gamma, \quad (5.20)$$

or more precisely, by the exponent  $\gamma$  (gamma) of this curve.

Two gamma values are needed to fully characterize an imaging system. The *encoding gamma* describes the *encoding transfer function*, which is the relationship between scene radiance values captured by an imaging device (such as a camera) and encoded pixel values. The *display gamma* characterizes the *display transfer function*, which is the relationship between encoded pixel values and displayed radiance. The product of the two gamma values is the overall or *end-to-end gamma* of the imaging system, which describes the *end-to-end transfer function* (see Figure 5.38). If this product were equal to 1, then displayed radiance would be proportional to captured scene radiance. This might seem ideal, and it would be if the display could exactly reproduce the viewing conditions of the original scene. However, in practice there are two significant differences between the viewing conditions of the original scene and the displayed version. The first difference is that absolute display radiance values are several orders of magnitude less than the scene radiance values (due to limitations in display device technology). The second difference, called the *surround effect*, refers to the fact that the original scene radiance values fill the entire field of view of the observer, while the display radiance values are limited to a screen surrounded by ambient room illumination. This illumination may be very dark (as in a movie theater), dim (as in the average television-watching environment) or bright (as in an office). These two differences in viewing conditions cause the perceived contrast to be dramatically reduced compared to the original scene. To counteract this, non-unit end-to-end

gamma is used (the recommended value varies from 1.5 for a dark movie theater to 1.125 for a bright office [1028]), to ensure that the display is perceptually similar to the original scene.

The relevant gamma for rendering purposes is encoding gamma. Rec. 709 for HDTV uses an encoding gamma of about 0.5 [1028], which is appropriate for applications using television displays. Personal computers use a standard called *sRGB* [1223], which has an encoding gamma of about 0.45.<sup>13</sup> This gamma is intended for bright office environments. These encoding gamma values are designed to work with a display gamma of 2.5 to produce the appropriate end-to-end gamma. This display gamma is typical of CRT monitors—newer displays include built-in adjustments to match CRT display gamma for compatibility.<sup>14</sup>

**EXAMPLE: GAMMA CORRECTION.** A relative color of  $(0.3, 0.5, 0.6)$  is computed for a pixel. To display it correctly, each value is raised to a power of 0.45 ( $1/2.22$ ), giving  $(0.582, 0.732, 0.794)$ . For a display with eight bits per channel, these values are multiplied by 255 to give  $(148, 187, 203)$ , which is stored in the frame buffer. □

It is the responsibility of the renderer to convert physical radiance values (computed in the shader) into nonlinear frame buffer values by applying the appropriate transfer function. In the past this was commonly neglected, leading to various visual artifacts [107, 459]. The main problem with neglecting this *gamma correction* is that shading computations that are correct for physically linear radiance values are performed on nonlinear values instead. An example of this can be seen in Figure 5.39.

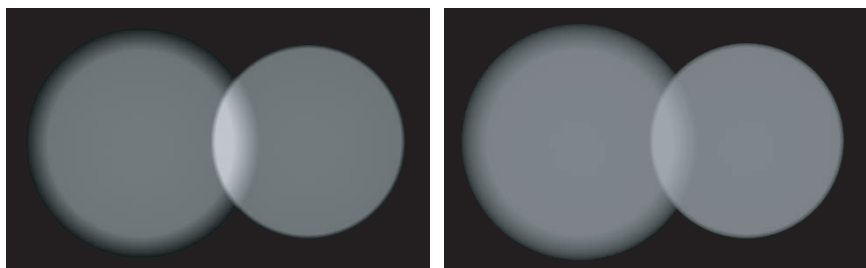


**Figure 5.39.** Two overlapping spotlights illuminating a plane. In the left image, the light values have been combined in a nonlinear space (i.e., gamma correction was not performed). In the right image, proper gamma correction has resulted in the light values being combined in linear space. Note the overbrightening of the overlap region in the left image; the right image is correct.

<sup>13</sup>Apple Macintosh computers use an encoding gamma of about 0.55 [1028].

<sup>14</sup>At least they do if properly calibrated, which unfortunately is often not the case.



**Figure 5.40.** On the left, four pixels covered by the edge of a white polygon on a black (shown as gray) background, with true area coverage shown. If gamma correction is not performed, the darkening of midtones will cause the perception of the edge to be distorted, as seen on the right.

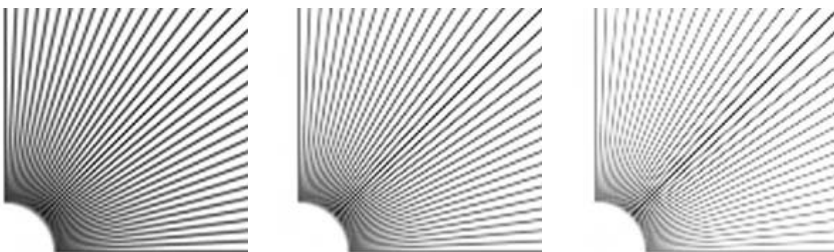


**Figure 5.41.** On the left, the set of antialiased lines are gamma-corrected; in the middle, the set is partially corrected; on the right, there is no gamma correction. (*Images courtesy of Scott R. Nelson.*)

Ignoring gamma correction also affects the quality of antialiased edges. For example, say a polygon edge covers four screen grid cells (Figure 5.40). The polygon's normalized radiance is 1 (white); the background's is 0 (black). Left to right, the cells are covered  $\frac{1}{8}$ ,  $\frac{3}{8}$ ,  $\frac{5}{8}$ , and  $\frac{7}{8}$ . So if we are using a box filter, we want to represent the normalized scene radiance of the pixels as 0.125, 0.375, 0.625, and 0.875. The correct approach is to perform antialiasing in linear space, applying the encoding transfer function to the four resulting values. If this is not done, the represented scene radiance for the pixels will be too dark, resulting in a perceived deformation of the edge as seen in the right side of the figure. This artifact is called *roping*, because the edge looks somewhat like a twisted rope [107, 923]. Figure 5.41 shows this effect.

Fortunately, modern GPUs can be set to automatically apply the encoding transfer function (typically the sRGB transfer function) when values are written to the color buffer.<sup>15</sup> The first GPUs including this feature did

<sup>15</sup>In DirectX the texture sampler call is `D3DSAMP_SRGBTTEXTURE` and the render state is `D3DRS_SRGBWRITENABLE`. DirectX 9's implementation incorrectly converts before blending, but is fine for opaque surfaces. DirectX 10's works for all cases, converting after blending.

not implement it properly for blending and MSAA antialiasing (both of which were—incorrectly—performed on nonlinear values), but more recent hardware has resolved these issues.

Although the GPU is capable of correctly converting linear radiance values to nonlinear pixel encodings, artifacts will result if the feature is unused or misused. It is important to apply the conversion at the final stage of rendering (when the values are written to the display buffer for the last time), and not before. If post-processing is applied after gamma correction, post-processing effects will be computed in nonlinear space, which is incorrect and will often cause visible artifacts. So operations such as tone mapping (see Section 10.11) can be applied to images to adjust luminance balance, but gamma correction should always be done last.

This does not mean that intermediate buffers cannot contain nonlinear encodings (in fact, this is preferable if the buffers use low-precision formats, to minimize banding), but then the buffer contents must be carefully converted back to linear space before computing the post-processing effect.

Applying the encoding transfer function at the output of the rendering pipeline is not sufficient—it is also necessary to convert any nonlinear input values to a linear space as well. Many textures (such as reflectance maps) contain values between 0 and 1 and are typically stored in a low-bit-depth format, requiring nonlinear encoding to avoid banding. Fortunately, GPUs now available can be set to convert nonlinear textures automatically by configuring them as sRGB textures. As for the output correction discussed above, the first GPUs to implement sRGB textures did so incorrectly (performing texture filtering in nonlinear space), but newer hardware implements the feature properly. As noted in Section 6.2.2, mipmap generation must also take any nonlinear encoding into account.

Applications used for authoring textures typically store the results in a nonlinear space, not necessarily the same one used by the GPU for conversion. Care must be taken to use the correct color space when authoring, including calibration of the display used. Any photographic textures require calibration of the camera as well. The Munsell ColorChecker chart [189] (formerly known as the Macbeth or GretagMacbeth ColorChecker chart) is a standard color chart that can be quite useful for these calibrations.

Various shader inputs other than textures may be encoded nonlinearly and require similar conversion before use in shading. Color constants (such as tint values) are often authored in a nonlinear space; the same may apply to vertex colors. Care must be taken not to “convert” values already in linear space!

## Further Reading and Resources

A good introduction to lights, color, signal processing, and other topics discussed in this chapter can be found in *Fundamentals of Computer Graphics, Second Edition* [1172] by Shirley et al.

Blinn's article "What Is a Pixel?" [111] provides an excellent tour of a number of areas of computer graphics while discussing different definitions. Wolberg's book [1367] is an exhaustive guide to sampling and filtering for computer graphics. Foley et al. cover the topic in some depth in a section of their classic book [349]. Blinn's *Dirty Pixels* book [106] includes some good introductory articles on filtering and antialiasing, as well as articles on alpha, compositing, and gamma correction.

Shirley has a useful summary of sampling patterns used in computer graphics [1169]. A summary of practical antialiasing methods for consoles and PCs is provided by Mitchell [884]. This article also touches on solutions to problems caused by interlaced television displays. A good quick read that helps correct the misconception that a pixel is a little square is Smith's article on the topic [1196], and Smith's tutorials on sampling and filtering are also of interest [1194, 1195]. Gritz and d'Eon [459] have an excellent summary of gamma correction issues. Poynton's *Digital Video and HDTV: Algorithms and Interfaces* [1028] gives solid coverage of gamma correction in various media, as well as other color-related topics.

# Chapter 6

## Texturing

*“All it takes is for the rendered image to look right.”*

—Jim Blinn

A surface’s texture is its look and feel—just think of the texture of an oil painting. In computer graphics, texturing is a process that takes a surface and modifies its appearance at each location using some image, function, or other data source. As an example, instead of precisely representing the geometry of a brick wall, a color image of a brick wall is applied to a single polygon. When the polygon is viewed, the color image appears where the polygon is located. Unless the viewer gets close to the wall, the lack of geometric detail (e.g., the fact that the image of bricks and mortar is on a smooth surface) will not be noticeable. Color image texturing also provides a way to use photographic images and animations on surfaces.

However, some textured brick walls can be unconvincing for reasons other than lack of geometry. For example, if the mortar is supposed to be glossy, whereas the bricks are matte, the viewer will notice that the gloss is the same for both materials. To produce a more convincing experience, a second image texture can be applied to the surface. Instead of changing the surface’s color, this texture changes the wall’s gloss, depending on location on the surface. Now the bricks have a color from the color image texture and a gloss value from this new texture.

Once the gloss texture has been applied, however, the viewer may notice that now all the bricks are glossy and the mortar is not, but each brick face appears to be flat. This does not look right, as bricks normally have some irregularity to their surfaces. By applying *bump mapping*, the surface normals of the bricks may be varied so that when they are rendered, they do not appear to be perfectly smooth. This sort of texture wobbles the direction of the polygon’s original surface normal for purposes of computing lighting.

From a shallow viewing angle, this illusion of bumpiness can break down. The bricks should stick out above the mortar, obscuring it from view. Even from a straight-on view, the bricks should cast shadows onto



**Figure 6.1.** Texturing. Color, bump, and parallax occlusion texture mapping methods are used to add complexity and realism to a scene. (*Image from “Toyshop” demo courtesy of Natalya Tatarchuk, ATI Research, Inc.*)

the mortar. Parallax and relief mapping use a texture to appear to deform a flat surface when rendering it. *Displacement mapping* actually displaces the surface, creating triangles between the texels. Figure 6.1 shows an example.

These are examples of the types of problems that can be solved with textures, using more and more elaborate algorithms. In this chapter, texturing techniques are covered in detail. First, a general framework of the texturing process is presented. Next, we focus on using images to texture surfaces, since this is the most popular form of texturing used in real-time work. Procedural textures are briefly discussed, and then some common methods of getting textures to affect the surface are explained.

## 6.1 The Texturing Pipeline

Texturing, at its simplest, is a technique for efficiently modeling the surface’s properties. One way to approach texturing is to think about what happens for a single shaded pixel. As seen in the previous chapter, the color is computed by taking into account the lighting and the material, as well as the viewer’s position. If present, transparency also affects the sam-

ple. Texturing works by modifying the values used in the shading equation. The way these values are changed is normally based on the position on the surface. So, for the brick wall example, the diffuse color at any point on the surface is replaced by a corresponding color in the image of a brick wall, based on the surface location. The pixels in the image texture are often called *texels*, to differentiate them from the pixels on the screen. The gloss texture modifies the gloss value, and the *bump texture* changes the direction of the normal, so each of these change the result of the lighting equation.

Texturing can be described by a generalized texture pipeline. Much terminology will be introduced in a moment, but take heart: Each piece of the pipeline will be described in detail. Some steps are not always under explicit user control, but each step happens in some fashion.

A location in space is the starting point for the texturing process. This location can be in world space, but is more often in the model's frame of reference, so that as the model moves, the texture moves along with it. Using Kershaw's terminology [646], this point in space then has a *projector* function applied to it to obtain a set of numbers, called *parameter-space values*, that will be used for accessing the texture. This process is called *mapping*, which leads to the phrase *texture mapping*.<sup>1</sup> Before these new values may be used to access the texture, one or more *corresponder* functions can be used to transform the parameter-space values to texture space. These texture-space locations are used to obtain values from the texture, e.g., they may be array indices into an image texture to retrieve a pixel. The retrieved values are then potentially transformed yet again by a *value transform* function, and finally these new values are used to modify some property of the surface, such as the material or shading normal. Figure 6.2 shows this process in detail for the application of a single texture. The reason for the complexity of the pipeline is that each step provides the user with a useful control.

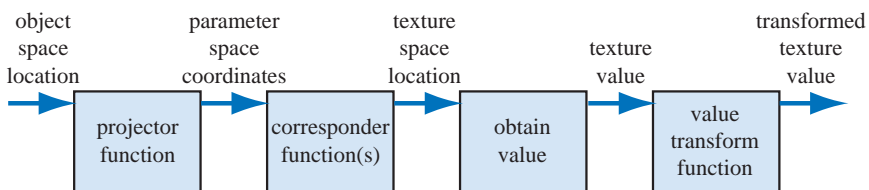


**Figure 6.2.** The generalized texture pipeline for a single texture.

<sup>1</sup>Sometimes the texture image itself is called the *texture map*, though this is not strictly correct.

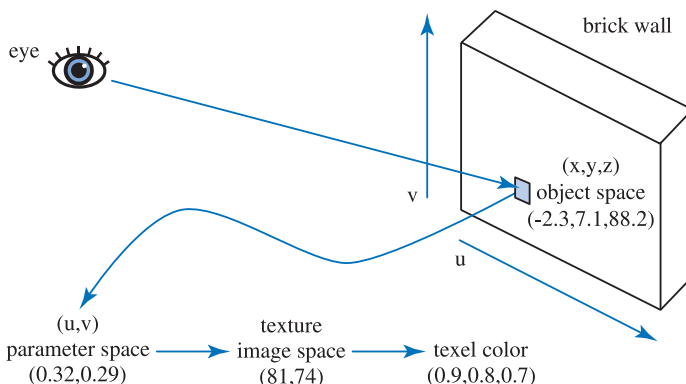


**Figure 6.3.** Pipeline for a brick wall.

Using this pipeline, this is what happens when a polygon has a brick wall texture and a sample is generated on its surface (see Figure 6.3). The  $(x, y, z)$  position in the object's local frame of reference is found; say it is  $(-2.3, 7.1, 88.2)$ . A projector function is then applied to this position. Just as a map of the world is a projection of a three-dimensional object into two dimensions, the projector function here typically changes the  $(x, y, z)$  vector into a two-element vector  $(u, v)$ . The projector function used for this example is equivalent to an orthographic projection (see Section 2.3.3), acting something like a slide projector shining the brick wall image onto the polygon's surface. To return to the wall, a point on its plane could be transformed into a pair of values ranging from 0 to 1. Say the values obtained are  $(0.32, 0.29)$ . These parameter-space values are to be used to find what the color of the image is at this location. The resolution of our brick texture is, say,  $256 \times 256$ , so the correspond function multiplies the  $(u, v)$  by 256 each, giving  $(81.92, 74.24)$ . Dropping the fractions, pixel  $(81, 74)$  is found in the brick wall image, and is of color  $(0.9, 0.8, 0.7)$ . The original brick wall image is too dark, so a value transform function that multiplies the color by 1.1 is then applied, giving a color of  $(0.99, 0.88, 0.77)$ . This color is then used in the shading equation as the diffuse color of the surface.

### 6.1.1 The Projector Function

The first step in the texture process is obtaining the surface's location and projecting it into parameter space, usually two-dimensional  $(u, v)$  space. Modeling packages typically allow artists to define  $(u, v)$  coordinates per vertex. These may be initialized from projector functions or from mesh unwrapping algorithms. Artists can edit  $(u, v)$  coordinates in the same way

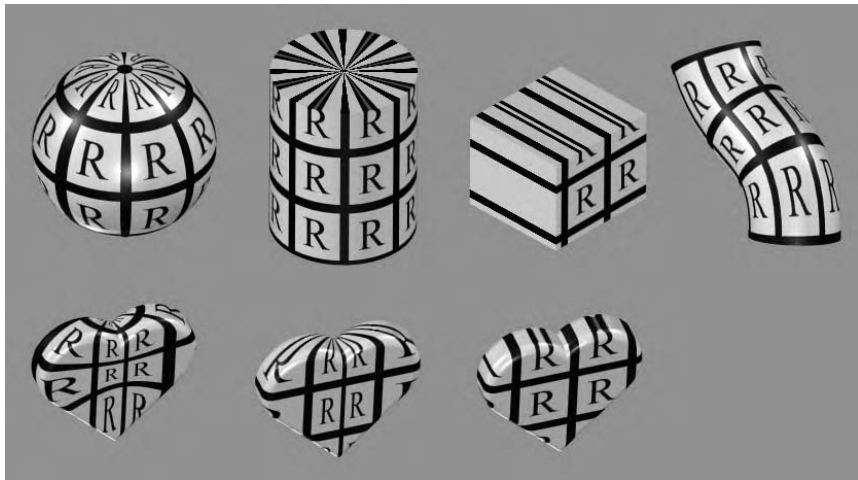


**Figure 6.4.** Different texture projections. Spherical, cylindrical, planar, and natural  $(u, v)$  projections are shown, left to right. The bottom row shows each of these projections applied to a single object (which has no natural projection).

they edit vertex positions. Projector functions typically work by converting a three-dimensional point in space into texture coordinates. Projector functions commonly used in modeling programs include spherical, cylindrical, and planar projections [85, 646, 723]. Other inputs can be used to a projector function. For example, the surface normal can be used to choose which of six planar projection directions is used for the surface. Problems in matching textures occur at the seams where the faces meet; Geiss [386, 387] discusses a technique of blending among them. Tarini et al. [1242] describe *polycube maps*, where a model is mapped to a set of cube projections, with different volumes of space mapping to different cubes.

Other projector functions are not projections at all, but are an implicit part of surface formation. For example, parametric curved surfaces have a natural set of  $(u, v)$  values as part of their definition. See Figure 6.4. The texture coordinates could also be generated from all sorts of different parameters, such as the view direction, temperature of the surface, or anything else imaginable. The goal of the projector function is to generate texture coordinates. Deriving these as a function of position is just one way to do it.

Noninteractive renderers often call these projector functions as part of the rendering process itself. A single projector function may suffice for the whole model, but often the artist has to use tools to subdivide the model and apply various projector functions separately [983]. See Figure 6.5.

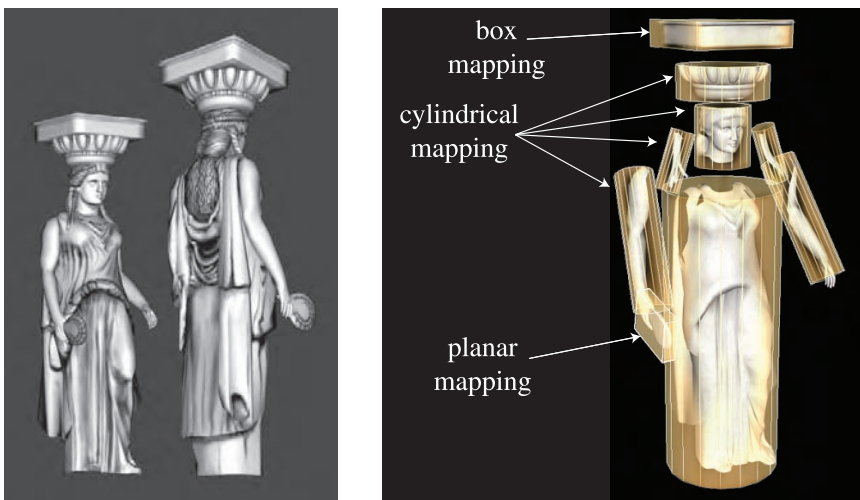


**Figure 6.5.** How various texture projections are used on a single model. (*Images courtesy of Tito Pagán.*)

In real-time work, projector functions are usually applied at the modeling stage, and the results of the projection are stored at the vertices. This is not always the case; sometimes it is advantageous to apply the projection function in the vertex or pixel shader.<sup>2</sup> This enables various effects, including animation (see Section 6.4). Some rendering methods, such as *environment mapping* (see Section 8.4), have specialized projector functions of their own that are evaluated per pixel.

The spherical projection casts points onto an imaginary sphere centered around some point. This projection is the same as used in Blinn and Newell's environment mapping scheme (Section 8.4.1), so Equation 8.25 on page 300 describes this function. This projection method suffers from the same problems of vertex interpolation described in that section.

Cylindrical projection computes the  $u$  texture coordinate the same as spherical projection, with the  $v$  texture coordinate computed as the distance along the cylinder's axis. This projection is useful for objects that have a natural axis, such as surfaces of revolution. Distortion occurs when surfaces are nearperpendicular to the cylinder's axis.

The planar projection is like an x-ray slide projector, projecting along a direction and applying the texture to all surfaces. It uses orthographic projection (Section 4.6.1). This function is commonly used to apply texture

---

<sup>2</sup>This is also possible on fixed-function graphics hardware; for example, OpenGL's fixed-function `glTexGen` routine provides a few different projector functions, including spherical and planar.

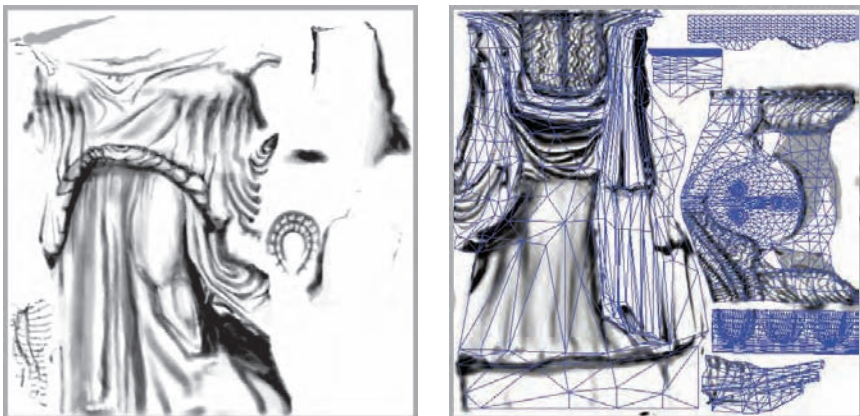


**Figure 6.6.** A number of smaller textures for the statue model, saved in two larger textures. The right figure shows how the polygonal mesh is unwrapped and displayed on the texture to aid in its creation. (*Images courtesy of Tito Pagán.*)

maps to characters, treating the model as if it were a paper doll by gluing separate textures on to its front and rear.

As there is severe distortion for surfaces that are edge-on to the projection direction, the artist often must manually decompose the model into near-planar pieces. There are also tools that help minimize distortion by unwrapping the mesh, or creating a near-optimal set of planar projections, or that otherwise aid this process. The goal is to have each polygon be given a fairer share of a texture's area, while also maintaining as much mesh connectivity as possible. Connectivity is important in that sampling artifacts can appear along the edges of textures, and each split vertex also causes data to be duplicated in the mesh itself. A mesh with a good unwrapping also eases the artist's work [723, 983]. Section 12.2.1 discusses this problem's effect on rendering. Figure 6.6 shows the workspace used to create the statue in Figure 6.5. This unwrapping process is one facet of a larger field of study, *mesh parameterization*. The interested reader is referred to the SIGGRAPH course notes by Hormann et al. [567].

The parameter space is not always a two-dimensional plane; sometimes it is a three-dimensional volume. In this case, the texture coordinates are presented as a three-element vector,  $(u, v, w)$ , with  $w$  being depth along the projection direction. Other systems use up to four coordinates, often designated  $(s, t, r, q)$  [969];  $q$  is used as the fourth value in a homogeneous coordinate (see Section A.4) and can be used for spotlighting effects [1146]. Another important type of parameter space is directional, where each point in the parameter space represents a direction. One way to visualize such

a space is as points on a unit sphere. The most common type of texture using a directional parameterization is the *cube map* (see Section 6.2.4).

It is also worth noting that one-dimensional texture images and functions have their uses. For example, these include contour lines [475, 969] and coloration determined by altitude (e.g., the lowlands are green; the mountain peaks are white). Lines can also be textured; one use of this is to render rain as a set of long lines textured with a semitransparent image. Such textures are also useful for simply converting from one value to another.

Since multiple textures can be applied to a surface, multiple sets of texture coordinates may need to be defined. However the coordinate values are applied, the idea is the same: These parameter values are interpolated across the surface and used to retrieve texture values. Before being interpolated, however, these parameter values are transformed by corresponder functions.

### 6.1.2 The Corresponder Function

Corresponder functions convert parameter-space coordinates to texture-space locations. They provide flexibility in applying textures to surfaces. One example of a corresponder function is to use the API to select a portion of an existing texture for display; only this subimage will be used in subsequent operations.

Another type of corresponder is a matrix transformation, which can be applied in the vertex or pixel shader.<sup>3</sup> This enables to translating, rotating, scaling, shearing, or projecting the texture on the surface.<sup>4</sup>

Another class of corresponder functions controls the way an image is applied. We know that an image will appear on the surface where  $(u, v)$  are in the  $[0, 1]$  range. But what happens outside of this range? Corresponder functions determine the behavior. In OpenGL, this type of corresponder function is called the “wrapping mode”; in DirectX, it is called the “texture addressing mode.” Common corresponder functions of this type are:

- **wrap** (DirectX), **repeat** (OpenGL), or **tile**—The image repeats itself across the surface; algorithmically, the integer part of the parameter value is dropped. This function is useful for having an image of a material repeatedly cover a surface, and is often the default.

---

<sup>3</sup>This is also possible on fixed-function hardware; the OpenGL fixed-function pipeline supports the use of a  $4 \times 4$  matrix.

<sup>4</sup>As discussed in Section 4.1.5, the order of transforms matters. Surprisingly, the order of transforms for textures must be the reverse of the order one would expect. This is because texture transforms actually affect the space that determines where the image is seen. The image itself is not an object being transformed; the space defining the image’s location is being changed.

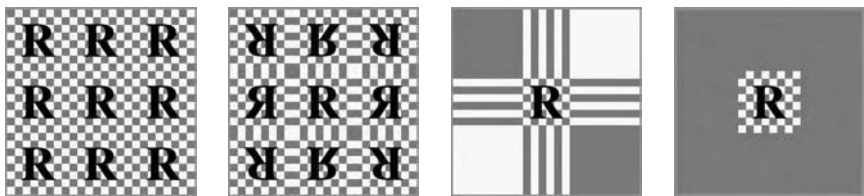


**Figure 6.7.** Image texture repeat, mirror, clamp, and border functions in action.

- **mirror**—The image repeats itself across the surface, but is mirrored (flipped) on every other repetition. For example, the image appears normally going from 0 to 1, then is reversed between 1 and 2, then is normal between 2 and 3, then is reversed, etc. This provides some continuity along the edges of the texture.
- **clamp** (DirectX) or **clamp to edge** (OpenGL)—Values outside the range [0, 1] are clamped to this range. This results in the repetition of the edges of the image texture. This function is useful for avoiding accidentally taking samples from the opposite edge of a texture when bilinear interpolation happens near a texture's edge [969].
- **border** (DirectX) or **clamp to border** (OpenGL)—Parameter values outside [0, 1] are rendered with a separately defined border color. This function can be good for rendering decals onto surfaces, for example, as the edge of the texture will blend smoothly with the border color.

See Figure 6.7. These corresponder functions can be assigned differently for each texture axis, e.g., the texture could repeat along the  $u$ -axis and be clamped on the  $v$ -axis.

Repeated tiling of a texture is an inexpensive way of adding more visual detail to a scene. However, this technique often looks unconvincing after about three repetitions of the texture, as the eye picks out the pattern. A common solution to avoid such *periodicity* problems is to combine the texture values with another, non-tiled, texture. This approach can be considerably extended, as seen in the commercial terrain rendering system described by Andersson [23]. In this system, multiple textures are combined based on terrain type, altitude, slope, and other factors. Texture data is also tied to where geometric models, such as bushes and rocks, are placed within the scene.

Another option to avoid periodicity is to use shader programs to implement specialized corresponder functions that randomly recombine texture patterns or tiles. *Wang tiles* are one example of this approach. A Wang tile set is a small set of square tiles with matching edges. Tiles are selected

randomly during the texturing process [1337]. Lefebvre and Neyret [748] implement a similar type of corresponder function using dependent texture reads and tables to avoid pattern repetition.

For real-time work, the last corresponder function applied is implicit, and is derived from the image's size. A texture is normally applied within the range  $[0, 1]$  for  $u$  and  $v$ . As shown in the brick wall example, by multiplying parameter values in this range by the resolution of the image, one may obtain the pixel location. The advantage of being able to specify  $(u, v)$  values in a range of  $[0, 1]$  is that image textures with different resolutions can be swapped in without having to change the values stored at the vertices of the model.

### 6.1.3 Texture Values

After the corresponder functions are used to produce texture-space coordinates, the coordinates are used to obtain texture values. For image textures, this is done by using the texture to retrieve texel information from the image. This process is dealt with extensively in Section 6.2. Image texturing constitutes the vast majority of texture use in real-time work, but procedural functions are sometimes used. In the case of procedural texturing, the process of obtaining a texture value from a texture-space location does not involve a memory lookup, but rather the computation of a function. Procedural texturing is further described in Section 6.3.

The most straightforward texture value is an RGB triplet that is used to replace or modify the surface colors; similarly, a single grayscale value could be returned. Another type of data to return is  $\text{RGB}\alpha$ , as described in Section 5.7. The  $\alpha$  (alpha) value is normally the opacity of the color, which determines the extent to which the color may affect the pixel. There are many other types of data that can be stored in image textures, as will be seen when bump-mapping is discussed in detail (Section 6.7).

The values returned from the texture are optionally transformed before use. These transformations may be performed in the texturing hardware or in the shader program. One common example is the remapping of data from an unsigned range (0 to 1) to a signed range ( $-1$  to  $1$ ). Another is performing a comparison between the texture values and a reference value, and returning a flag indicating the result of the comparison (often used in shadow mapping—see Section 9.1.4).

## 6.2 Image Texturing

In image texturing, a two-dimensional image is effectively glued onto the surface of a polygon. We have walked through the process of computing

a texture space location; now we will address the issues and algorithms for obtaining a texture value from the image texture, given that location. For the rest of this chapter, the image texture will be referred to simply as the *texture*. In addition, when we refer to a pixel's *cell* here, we mean the screen grid cell surrounding that pixel. As discussed in Section 5.6.1, a *pixel* is actually a displayed color value that can (and should, for better quality) be affected by samples outside of its associated grid cell.

In this section we particularly focus on methods to rapidly sample and filter textured images. Section 5.6.2 discussed the problem of aliasing, especially with respect to rendering edges of objects. Textures can also have sampling problems, but they occur within the interiors of the triangles being rendered.

The texture image size used in GPUs is usually  $2^m \times 2^n$  texels, where  $m$  and  $n$  are nonnegative integers. Modern GPUs can handle textures of arbitrary size, which allows a generated image to then be treated as a texture. Graphics accelerators have different upper limits on texture size. A typical DirectX 9 laptop allows a maximum of  $2048 \times 2048$ , a desktop  $4096^2$ , and a DirectX 10 machine  $8192^2$  texels.

Assume that we have a texture of size  $256 \times 256$  texels and that we want to use it as a texture on a square. As long as the projected square on the screen is roughly the same size as the texture, the texture on the square looks almost like the original image. But what happens if the projected square covers ten times as many pixels as the original image contains (called *magnification*), or if the projected square covers only a small part of the screen (*minification*)? The answer is that it depends on what kind of sampling and filtering methods you use for these two separate cases.

The image sampling and filtering methods discussed in this chapter are applied to the values read from each texture. However, the desired result is to prevent aliasing in the final rendered image, which in theory requires sampling and filtering the final pixel colors. The distinction here is between filtering the inputs to the shading equation, or its output. As long as the inputs and output are linearly related (which is true for inputs such as specular and diffuse colors), then filtering the individual texture values is equivalent to filtering the final colors. However, many shader input values with a nonlinear relationship to the output, such as surface normals and gloss values, are stored in textures. Standard texture filtering methods may not work well for these textures, resulting in aliasing. Improved methods for filtering such textures are discussed in Section 7.8.1.

### 6.2.1 Magnification

In Figure 6.8, a texture of size  $48 \times 48$  texels is textured onto a square, and the square is viewed rather closely with respect to the texture size, so the



**Figure 6.8.** Texture magnification of a  $48 \times 48$  image onto  $320 \times 320$  pixels. Left: nearest neighbor filtering, where the nearest texel is chosen per pixel. Middle: bilinear filtering using a weighted average of the four nearest texels. Right: cubic filtering using a weighted average of the  $5 \times 5$  nearest texels.

underlying graphics system has to magnify the texture. The most common filtering techniques for magnification are *nearest neighbor* (the actual filter is called a box filter—see Section 5.6.1) and *bilinear interpolation*. There is also *cubic convolution*, which uses the weighted sum of a  $4 \times 4$  or  $5 \times 5$  array of texels. This enables much higher magnification quality. Although native hardware support for cubic convolution (also called *bicubic interpolation*) is currently not commonly available, it can be performed in a shader program.

In the left part of Figure 6.8, the nearest neighbor method is used. One characteristic of this magnification technique is that the individual texels may become apparent. This effect is called *pixelation* and occurs because the method takes the value of the nearest texel to each pixel center when magnifying, resulting in a blocky appearance. While the quality of this method is sometimes poor, it requires only one texel to be fetched per pixel.

In the middle part of the same figure, bilinear interpolation (sometimes called *linear interpolation*) is used. For each pixel, this kind of filtering finds the four neighboring texels and linearly interpolates in two dimensions to find a blended value for the pixel. The result is blurrier, and much of the jaggedness from using the nearest neighbor method has disappeared.<sup>5</sup>

To the right in Figure 6.8, a bicubic filter has been used, and the remaining blockiness is removed. It should be noted that bicubic filters are more expensive than bilinear filters.

Returning to the brick texture example on page 150: Without dropping the fractions, we obtained  $(p_u, p_v) = (81.92, 74.24)$ . These fractions are used in computing the bilinear combination of the four closest pixels, which thus range from  $(x_l, y_b) = (81, 74)$  to  $(x_r, y_t) = (82, 75)$ . See Figure 6.9 for

---

<sup>5</sup>Looking at these images with eyes squinted has approximately the same effect as a low-pass filter and reveals the face a bit more.

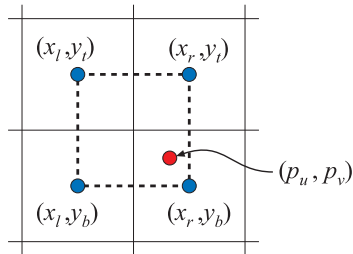


**Figure 6.9.** Notation for bilinear interpolation. The four texels involved are illustrated by the four squares.

notation. First, the decimal part is computed as:  $(u', v') = (p_u - \lfloor p_u \rfloor, p_v - \lfloor p_v \rfloor)$ . This is equal to  $(u', v') = (0.92, 0.24)$  for our example. Assuming we can access the texels' colors in the texture as  $\mathbf{t}(x, y)$ , where  $x$  and  $y$  are integers, the bilinearly interpolated color  $\mathbf{b}$  at  $(p_u, p_v)$  is

$$\begin{aligned} \mathbf{b}(p_u, p_v) = & (1 - u')(1 - v')\mathbf{t}(x_l, y_b) + u'(1 - v')\mathbf{t}(x_r, y_b) \\ & + (1 - u')v'\mathbf{t}(x_l, y_t) + u'v'\mathbf{t}(x_r, y_t). \end{aligned} \quad (6.1)$$

A common solution to the blurriness that accompanies magnification is to use *detail textures*. These are textures that represent fine surface details, from scratches on a cellphone to bushes on terrain. Such detail is overlaid onto the magnified texture as a separate texture, at a different scale. The high-frequency repetitive pattern of the detail texture, combined with the low-frequency magnified texture, has a visual effect similar to the use of a single very high resolution texture.

Bilinear interpolation does just that, interpolates linearly in two directions. However, a linear interpolation is not required. Say a texture consists of black and white pixels in a checkerboard pattern. Using bilinear interpolation gives varying grayscale samples across the texture. By remapping so that, say, all grays lower than 0.4 are black, all grays higher than 0.6 are white, and those in between are stretched to fill the gap, the texture looks more like a checkerboard again, while also giving some blend between texels. See Figure 6.10.

Such remapping is useful in cases where well-defined edges are important, such as text. One method used is to set an alpha value in the pixel shader and use alpha testing to threshold the results. That is, if the alpha value is above a given value, the texture's value is used, else it is not. This is essentially a *cutout texture*, described in Section 6.6. However, higher quality edges can be generated by forming specialized textures made for the task. Called *vector textures*, these store information at a texel describing how the edges cross the grid cell. Qin et al. [1041] discuss previous work and

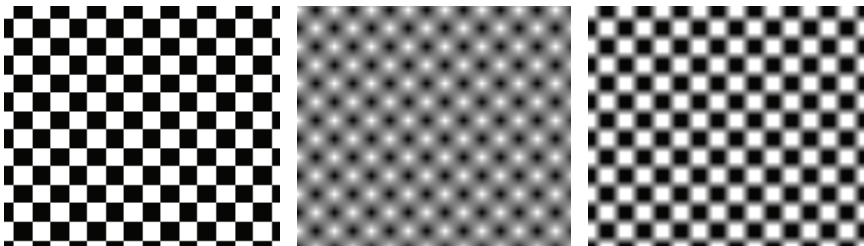


**Figure 6.10.** Nearest neighbor, bilinear interpolation, and part way in between by remapping, using the same  $2 \times 2$  checkerboard texture. Note how nearest neighbor sampling gives slightly different square sizes, since the texture and the image grid do not match perfectly.

propose a method based on computing the distance to the closest cutout boundary. A related method of using a pixel shader to directly evaluate Bézier curves is discussed in Section 13.1.2. Nehab and Hoppe [922] present a fascinating scheme that encodes vector drawings into grid cells and can then render these elements in a resolution-independent way. Each cell contains a “texel program,” a series of rules defining where each element in the cell lies, in back-to-front order. The pixel shader program evaluates each primitive in turn to see its color contribution to the pixel. Such specialized vector texture techniques can represent complex outlines with high accuracy. However, they have high storage or computation costs, as well as other drawbacks (such as not supporting efficient minification) that makes them unsuitable for many real-time applications [883].

Green [439] presents a much simpler, but surprisingly effective technique, used by Valve in *Team Fortress 2*. The technique uses the *sampled distance field* data structure introduced by Frisken et al. [364]. A distance field is a scalar signed field over a space or surface in which an object is embedded. At any point, the distance field has a value with a magnitude equal to the distance to the object’s nearest boundary point. The sign of the value is negative for points inside the object and positive for points outside it. A sampled distance field stores the sampled values of the distance field at a series of points. These values are linearly interpolated for rendering. Since the distance field is nearly linear except in the vicinity of high-curvature boundary areas, this works quite well. Green samples the distance field (scaled and biased to the 0-to-1 range) into an alpha map, and uses the GPU’s built-in support for bilinear linear interpolation and alpha testing to evaluate the distance field, with no pixel shader modifications needed. This method can be seen in general as an improved way to generate alpha maps for alpha test cutouts.

Green also provides simple pixel shader modifications that enable extensions such as antialiased edges, outlines, and drop shadows (see Figure 6.11



**Figure 6.11.** A vector texture used to display crisp text. The original “no trespassing” sign’s data is held in a  $64 \times 64$  distance field. The outline around the text is added by mapping a particular distance range to the outline color [439]. (*Image from “Team Fortress 2” courtesy of Valve Corp.*)

for an example). Sharp corners are smoothed, but optionally can be preserved by encoding a second distance value in a different texture channel.

## 6.2.2 Minification

When a texture is minimized, several texels may cover a pixel’s cell, as shown in Figure 6.12. To get a correct color value for each pixel, you should integrate the effect of the texels influencing the pixel. However, it is difficult to determine precisely the exact influence of all texels near a particular pixel, and it is effectively impossible to do so perfectly in real time.

Because of this limitation, a number of different methods are used in real-time work. One method is to use the nearest neighbor, which works exactly as the corresponding magnification filter does, i.e., it selects the texel that is visible at the very center of the pixel’s cell. This filter may cause severe aliasing problems. In Figure 6.13, nearest neighbor is used in the top figure. Towards the horizon, artifacts appear because only one of the many texels influencing a pixel is chosen to represent the surface. Such artifacts are even more noticeable as the surface moves with respect to the viewer, and are one manifestation of what is called *temporal aliasing*.

Another filter often available is bilinear interpolation, again working exactly as in the magnification filter. This filter is only slightly better than the nearest neighbor approach for minification. It blends four texels instead of using just one, but when a pixel is influenced by more than four texels, the filter soon fails and produces aliasing.

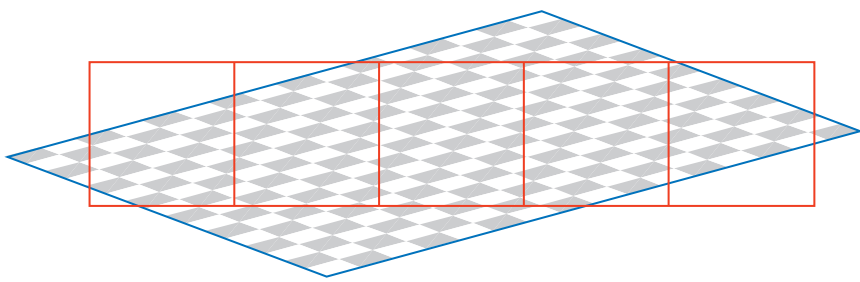


**Figure 6.12.** Minification: A view of a checkerboard-textured polygon through a row of pixel cells, showing roughly how a number of texels affect each pixel.

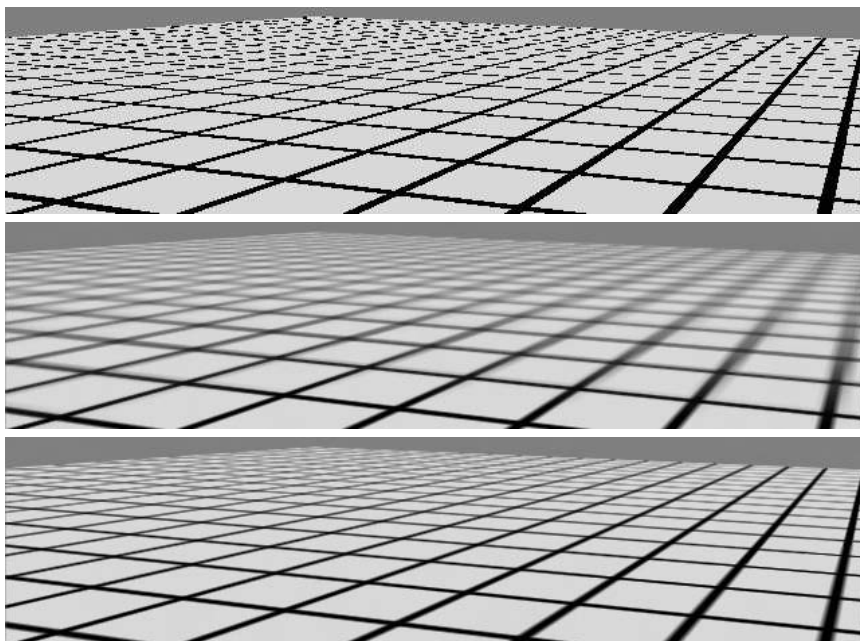


**Figure 6.13.** The top image was rendered with point sampling (nearest neighbor), the center with mipmapping, and the bottom with summed area tables.

Better solutions are possible. As discussed in Section 5.6.1, the problem of aliasing can be addressed by sampling and filtering techniques. The signal frequency of a texture depends upon how closely spaced its texels are on the screen. Due to the Nyquist limit, we need to make sure that the texture’s signal frequency is no greater than half the sample frequency. For example, say an image is composed of alternating black and white lines, a texel apart. The wavelength is then two texels wide (from black line to black line), so the frequency is  $\frac{1}{2}$ . To properly display this texture on a screen, the frequency must then be at least  $2 \times \frac{1}{2}$ , i.e., at least one pixel per texel. So, for textures in general, there should be at most one texel per pixel to avoid aliasing.

To achieve this goal, either the pixel’s sampling frequency has to increase or the texture frequency has to decrease. The antialiasing methods discussed in the previous chapter give ways to increase the pixel sampling rate. However, these give only a limited increase in sampling frequency. To more fully address this problem, various texture minification algorithms have been developed.

The basic idea behind all texture antialiasing algorithms is the same: to preprocess the texture and create data structures that will help compute a quick approximation of the effect of a set of texels on a pixel. For real-time work, these algorithms have the characteristic of using a fixed amount of time and resources for execution. In this way, a fixed number of samples are taken per pixel and combined to compute the effect of a (potentially huge) number of texels.

### Mipmapping

The most popular method of antialiasing for textures is called *mipmapping* [1354]. It is implemented in some form on even the most modest graphics accelerators now produced. “Mip” stands for *multum in parvo*, Latin for “many things in a small place”—a good name for a process in which the original texture is filtered down repeatedly into smaller images.

When the mipmapping minimization filter is used, the original texture is augmented with a set of smaller versions of the texture before the actual rendering takes place. The texture (level zero) is downsampled to a quarter of the original area, with each new texel value often computed as the average of four neighbor texels in the original texture. The new, level-one texture is sometimes called a *subtexture* of the original texture. The reduction is performed recursively until one or both of the dimensions of the texture equals one texel. This process is illustrated in Figure 6.14. The set of images as a whole is often called a *mipmap chain*.

Two important elements in forming high-quality mipmaps are good filtering and gamma correction. The common way to form a mipmap level is to take each  $2 \times 2$  set of texels and average them to get the mip texel value.

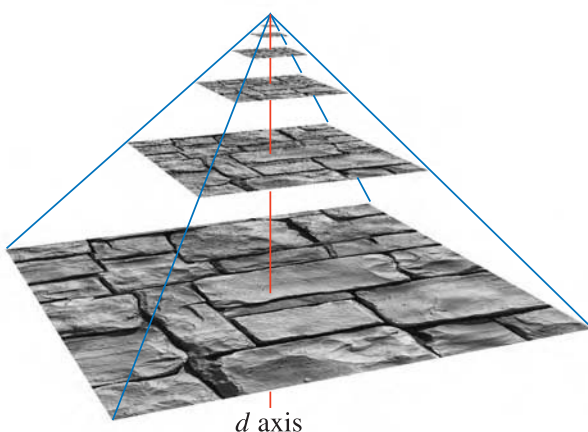


**Figure 6.14.** A mipmap is formed by taking the original image (level 0), at the base of the pyramid, and averaging each  $2 \times 2$  area into a texel value on the next level up. The vertical axis is the third texture coordinate,  $d$ . In this figure,  $d$  is not linear; it is a measure of which two texture levels a sample uses for interpolation.

The filter used is then a box filter, one of the worst filters possible. This can result in poor quality, as it has the effect of blurring low frequencies unnecessarily, while keeping some high frequencies that cause aliasing [120]. It is better to use a Gaussian, Lanczos, Kaiser, or similar filter; fast, free source code exists for the task [120, 1141], and some APIs support better filtering on the GPU itself. Care must be taken filtering near the edges of textures, paying attention to whether the texture repeats or is a single copy. Use of mipmapping on the GPU is why square textures with powers-of-two resolutions are the norm for use on models.

For textures encoded in a nonlinear space (such as most color textures), ignoring gamma correction when filtering will modify the perceived brightness of the mipmap levels [121]. As you get farther away from the object and the uncorrected mipmaps get used, the object can look darker overall, and contrast and details can also be affected. For this reason, it is important to convert such textures into linear space, perform all mipmap filtering in that space, and convert the final results back into nonlinear space for storage.

As mentioned earlier, some textures have a fundamentally nonlinear relationship to the final shaded color. Although this poses a problem for filtering in general, mipmap generation is particularly sensitive to this issue, since many hundred or thousands of pixels are being filtered. Specialized mipmap generation methods are often needed for the best results. Such methods are detailed in Section 7.8.1.

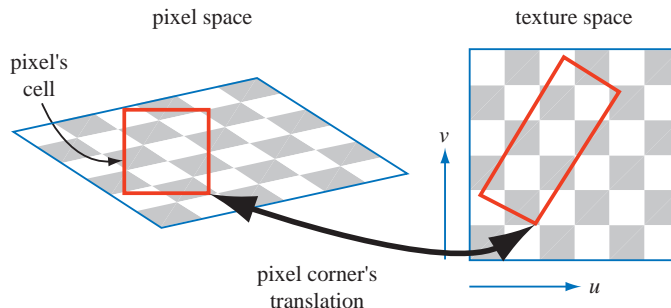


**Figure 6.15.** On the left is a square pixel cell and its view of a texture. On the right is the projection of the pixel cell onto the texture itself.

The basic process of accessing this structure while texturing is straightforward. A screen pixel encloses an area on the texture itself. When the pixel's area is projected onto the texture (Figure 6.15), it includes one or more texels.<sup>6</sup> The goal is to determine roughly how much of the texture influences the pixel. There are two common measures used to compute  $d$  (which OpenGL calls  $\lambda$ , and which is also known as the *level of detail*). One is to use the longer edge of the quadrilateral formed by the pixel's cell to approximate the pixel's coverage [1354]; another is to use as a measure the largest absolute value of the four differentials  $\partial u / \partial x$ ,  $\partial v / \partial x$ ,  $\partial u / \partial y$ , and  $\partial v / \partial y$  [666, 1011]. Each differential is a measure of the amount of change in the texture coordinate with respect to a screen axis. For example,  $\partial u / \partial x$  is the amount of change in the  $u$  texture value along the  $x$ -screen-axis for one pixel. See Williams's original article [1354] or the article by Flavell [345] or Pharr [1011] for more about these equations. McCormack et al. [840] discuss the introduction of aliasing by the largest absolute value method, and they present an alternate formula. Ewins et al. [327] analyze the hardware costs of several algorithms of comparable quality.

These gradient values are available to pixel shader programs using Shader Model 3.0 or newer. Since they are based on the differences between values in adjacent pixels, they are not accessible in sections of the pixel shader affected by dynamic flow control (see Section 3.6). For texture reads to be performed in such a section (e.g., inside a loop), the derivatives must be computed earlier. Note that since vertex shaders cannot access gradient information, the gradients or the level of detail need to be computed in the vertex shader itself and supplied to the GPU when doing vertex texturing.

---

<sup>6</sup>Using the pixel's cell boundaries is not strictly correct, but is used here to simplify the presentation. Texels outside of the cell can influence the pixel's color; see Section 5.6.1.

The intent of computing the coordinate  $d$  is to determine where to sample along the mipmap's pyramid axis (see Figure 6.14). The goal is a pixel-to-texel ratio of at least 1:1 in order to achieve the Nyquist rate. The important principle here is that as the pixel cell comes to include more texels and  $d$  increases, a smaller, blurrier version of the texture is accessed. The  $(u, v, d)$  triplet is used to access the mipmap. The value  $d$  is analogous to a texture level, but instead of an integer value,  $d$  has the fractional value of the distance between levels. The texture level above and the level below the  $d$  location is sampled. The  $(u, v)$  location is used to retrieve a bilinearly interpolated sample from each of these two texture levels. The resulting sample is then linearly interpolated, depending on the distance from each texture level to  $d$ . This entire process is called *trilinear interpolation* and is performed per pixel.

One user control on the  $d$  coordinate is the *level of detail bias (LOD bias)*. This is a value added to  $d$ , and so it affects the relative perceived sharpness of a texture. If we move further up the pyramid to start (increasing  $d$ ), the texture will look blurrier. A good LOD bias for any given texture will vary with the image type and with the way it is used. For example, images that are somewhat blurry to begin with could use a negative bias, while poorly filtered (aliased) synthetic images used for texturing could use a positive bias. The bias can be specified for the texture as a whole, or per-pixel in the pixel shader. For finer control, the  $d$  coordinate or the derivatives used to compute it can be supplied by the user, in any shader stage.

The result of mipmapping is that instead of trying to sum all the texels that affect a pixel individually, precombined sets of texels are accessed and interpolated. This process takes a fixed amount of time, no matter what the amount of minification. However, mipmapping has a number of flaws [345]. A major one is *overblurring*. Imagine a pixel cell that covers a large number of texels in the  $u$  direction and only a few in the  $v$  direction. This case commonly occurs when a viewer looks along a textured surface nearly edge-on. In fact, it is possible to need minification along one axis of the texture and magnification along the other. The effect of accessing the mipmap is that square areas on the texture are retrieved; retrieving rectangular areas is not possible. To avoid aliasing, we choose the largest measure of the approximate coverage of the pixel cell on the texture. This results in the retrieved sample often being relatively blurry. This effect can be seen in the mipmap image in Figure 6.13. The lines moving into the distance on the right show overblurring.

One extension to mipmapping is the *ripmap*. The idea is to extend the mipmap to include downsampled rectangular areas as subtextures that can be accessed [518]. The mipmap is stored  $1 \times 1$ ,  $2 \times 2$ ,  $4 \times 4$ , etc., but all possible rectangles are also stored  $1 \times 2$ ,  $2 \times 4$ ,  $2 \times 1$ ,  $4 \times 1$ ,  $4 \times 2$ , etc.

The  $u$  and  $v$  coverage determines the rectangle's dimensions. While this technique produces better visuals than mipmapping, it comes at a high cost and so normally is avoided in favor of other methods. Instead of adding just one-third storage space, as is needed for mipmapping, the cost is three times additional space beyond the original image.

### Summed-Area Table

Another method to avoid overblurring is the *summed-area table* (SAT) [209]. To use this method, one first creates an array that is the size of the texture but contains more bits of precision for the color stored (e.g., 16 bits or more for each of red, green, and blue). At each location in this array, one must compute and store the sum of all the corresponding texture's texels in the rectangle formed by this location and texel  $(0, 0)$  (the origin). During texturing, the pixel cell's projection onto the texture is bound by a rectangle. The summed-area table is then accessed to determine the average color of this rectangle, which is passed back as the texture's color for the pixel. The average is computed using the texture coordinates of the rectangle shown in Figure 6.16. This is done using the formula given in Equation 6.2:

$$c = \frac{s[x_{ur}, y_{ur}] - s[x_{ur}, y_{ll}] - s[x_{ll}, y_{ur}] + s[x_{ll}, y_{ll}]}{(x_{ur} - x_{ll})(y_{ur} - y_{ll})}. \quad (6.2)$$

Here,  $x$  and  $y$  are the texel coordinates of the rectangle and  $s[x, y]$  is the summed-area value for that texel. This equation works by taking the sum of the entire area from the upper right corner to the origin, then subtracting off areas  $A$  and  $B$  by subtracting the neighboring corners' contributions.

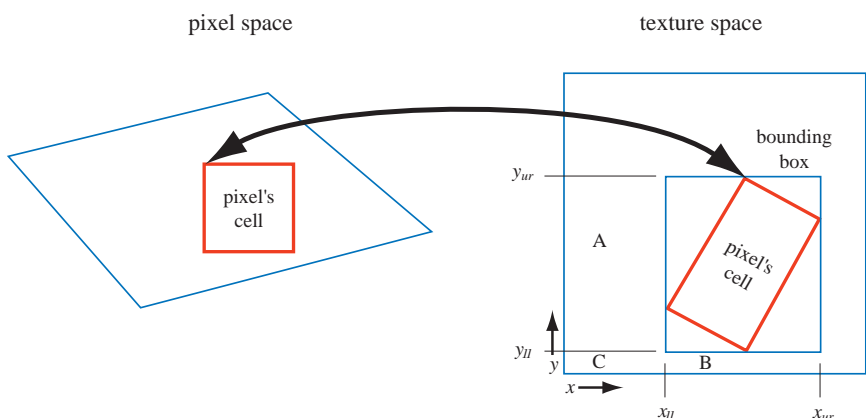


**Figure 6.16.** The pixel cell is back-projected onto the texture, bound by a rectangle; the four corners of the rectangle are used to access the summed-area table.

Area  $C$  has been subtracted twice, so it is added back in by the lower left corner. Note that  $(x_{ll}, y_{ll})$  is the upper right corner of area  $C$ , i.e.,  $(x_{ll} + 1, y_{ll} + 1)$  is the lower left corner of the bounding box.

The results of using a summed-area table are shown in Figure 6.13. The lines going to the horizon are sharper near the right edge, but the diagonally crossing lines in the middle are still overblurred. Similar problems occur with the ripmap scheme. The problem is that when a texture is viewed along its diagonal, a large rectangle is generated, with many of the texels situated nowhere near the pixel being computed. For example, imagine a long, thin rectangle representing the pixel cell's back-projection lying diagonally across the entire texture in Figure 6.16. The whole texture rectangle's average will be returned, rather than just the average within the pixel cell.

Ripmaps and summed-area tables are examples of what are called *anisotropic filtering* algorithms [518]. Such algorithms are schemes that can retrieve texel values over areas that are not square. However, they are able to do this most effectively in primarily horizontal and vertical directions. Both schemes are memory intensive. While a mipmap's subtextures take only an additional third of the memory of the original texture, a ripmap's take an additional three times as much as the original. Summed-area tables take at least two times as much memory for textures of size  $16 \times 16$  or less, with more precision needed for larger textures.

Ripmaps were available in high-end Hewlett-Packard graphics accelerators in the early 1990s. Summed area tables, which give higher quality for lower overall memory costs, can be implemented on modern GPUs [445]. Improved filtering can be critical to the quality of advanced rendering techniques. For example, Hensley et al. [542, 543] provide an efficient implementation and show how summed area sampling improves glossy reflections. Other algorithms in which area sampling is used can be improved by SAT, such as depth of field [445, 543], shadow maps [739], and blurry reflections [542].

### *Unconstrained Anisotropic Filtering*

For current graphics hardware, the most common method to further improve texture filtering is to reuse existing mipmap hardware. The basic idea is that the pixel cell is back-projected, this quadrilateral (quad) on the texture is then sampled a number of times, and the samples are combined. As outlined above, each mipmap sample has a location and a squarish area associated with it. Instead of using a single mipmap sample to approximate this quad's coverage, the algorithm uses a number of squares to cover the quad. The shorter side of the quad can be used to determine  $d$  (unlike in mipmapping, where the longer side is often used); this makes the averaged area smaller (and so less blurred) for each mipmap sample. The quad's

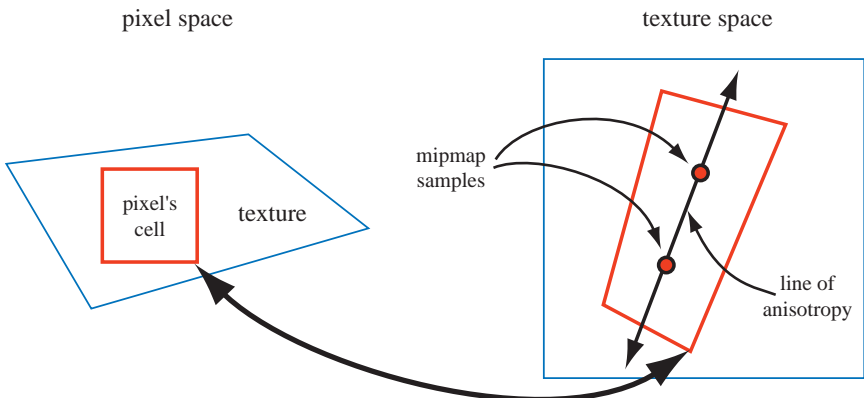


**Figure 6.17.** Anisotropic filtering. The back-projection of the pixel cell creates a quadrilateral. A line of anisotropy is formed between the longer sides.

longer side is used to create a *line of anisotropy* parallel to the longer side and through the middle of the quad. When the amount of anisotropy is between 1:1 and 2:1, two samples are taken along this line (see Figure 6.17). At higher ratios of anisotropy, more samples are taken along the axis.

This scheme allows the line of anisotropy to run in any direction, and so does not have the limitations that ripmaps and summed-area tables had. It also requires no more texture memory than mipmaps do, since it uses the mipmap algorithm to do its sampling. An example of anisotropic filtering is shown in Figure 6.18.

This idea of sampling along an axis was first introduced by Schilling et al. with their Texram dynamic memory device [1123]. Barkans describes the

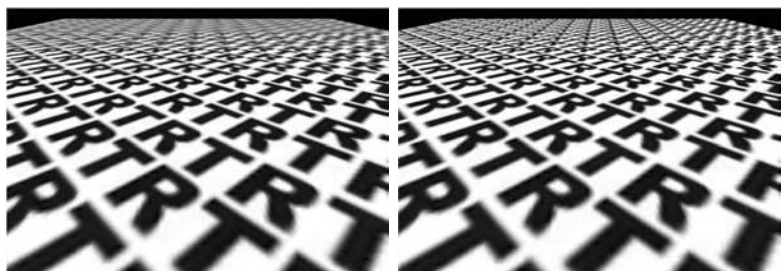


**Figure 6.18.** Mipmap versus anisotropic filtering. Trilinear mipmaping has been done on the left, and 16:1 anisotropic filtering on the right, both at a  $640 \times 450$  resolution, using ATI Radeon hardware. Towards the horizon, anisotropic filtering provides a sharper result, with minimal aliasing.

algorithm's use in the Talisman system [65]. A similar system called *Feline* is presented by McCormack et al. [841]. Texram's original formulation has the samples along the anisotropic axis (also known as *probes*) given equal weights. Talisman gives half weight to the two probes at opposite ends of the axis. Feline uses a Gaussian filter kernel to weight the probes. These algorithms approach the high quality of software sampling algorithms such as the *Elliptical Weighted Average* (EWA) filter, which transforms the pixel's area of influence into an ellipse on the texture and weights the texels inside the ellipse by a filter kernel [518].

### 6.2.3 Volume Textures

A direct extension of image textures is three-dimensional image data that is accessed by  $(u, v, w)$  (or  $(s, t, r)$  values). For example, medical imaging data can be generated as a three-dimensional grid; by moving a polygon through this grid, one may view two-dimensional slices of this data. A related idea is to represent volumetric lights in this form. The illumination on a point on a surface is found by finding the value for its location inside this volume, combined with a direction for the light.

Most GPUs support mipmapping for volume textures. Since filtering inside a single mipmap level of a volume texture involves trilinear interpolation, filtering between mipmap levels requires *quadrilinear interpolation*. Since this involves averaging the results from 16 texels, precision problems may result, which can be solved by using a higher precision volume texture. Sigg and Hadwiger [1180] discuss this and other problems relevant to volume textures and provide efficient methods to perform filtering and other operations.

Although volume textures have significantly higher storage requirements and are more expensive to filter, they do have some unique advantages. The complex process of finding a good two-dimensional parameterization for the three-dimensional mesh can be skipped, since three-dimensional locations can be used directly as texture coordinates. This avoids the distortion and seam problems that commonly occur with two-dimensional parameterizations. A volume texture can also be used to represent the volumetric structure of a material such as wood or marble. A model textured with such a texture will appear to be carved from this material.

Using volume textures for surface texturing is extremely inefficient, since the vast majority of samples are not used. Benson and Davis [81] and DeBry et al. [235] discuss storing texture data in a sparse octree structure. This scheme fits well with interactive three-dimensional painting systems, as the surface does not need explicit texture coordinates assigned to it at the time of creation, and the octree can hold texture detail down to any

level desired. Lefebvre et al. [749] discuss the details of implementing octree textures on the modern GPU. Lefebvre and Hoppe [751] discuss a method of packing sparse volume data into a significantly smaller texture.

### 6.2.4 Cube Maps

Another type of texture is the *cube texture* or *cube map*, which has six square textures, each of which is associated with one face of a cube. A cube map is accessed with a three-component texture coordinate vector that specifies the direction of a ray pointing from the center of the cube outwards. The point where the ray intersects the cube is found as follows. The texture coordinate with the largest magnitude selects the corresponding face (e.g., the vector  $(-3.2, 5.1, -8.4)$  selects the  $-Z$  face). The remaining two coordinates are divided by the absolute value of the largest magnitude coordinate, i.e., 8.4. They now range from  $-1$  to  $1$ , and are simply remapped to  $[0, 1]$  in order to compute the texture coordinates. For example, the coordinates  $(-3.2, 5.1)$  are mapped to  $((-3.2/8.4 + 1)/2, (5.1/8.4 + 1)/2) \approx (0.31, 0.80)$ . Cube maps are useful for representing values which are a function of direction; they are most commonly used for environment mapping (see Section 8.4.3).

Cube maps support bilinear filtering as well as mipmapping, but problems can occur along seams of the map, where the square faces join. Cube maps are supposed to be continuous, but almost all graphics hardware cannot sample across these boundaries when performing bilinear interpolation. Also, the normal implementation for filtering cube maps into mipmap levels is that no data from one cube face affects the other. Another factor that



**Figure 6.19.** Cube map filtering. The leftmost two images use the  $2 \times 2$  and  $4 \times 4$  mipmap levels of a cube map, generated using standard cube map mipmap chain generation. The seams are obvious, making these mipmap levels unusable except for cases of extreme minification. The two rightmost images use mipmap levels at the same resolutions, generated by sampling across cube faces and using angular extents. Due to the lack of seams, these mipmap levels can be used even for objects covering a large screen area. (*Images using CubeMapGen courtesy of ATI Technologies Inc.*)

is usually not taken into account by APIs performing cube map filtering is that the angular size of a texel varies over a cube face. That is, a texel at the center of a cube face represents a greater visual solid angle than a texel at the corner.

Specialized tools to preprocess cube maps, such as ATI's *CubeMapGen*, take these factors into account when filtering. Neighboring samples from other faces are used to create the mipmap chain, and the angular extent of each texel is taken into account. Figure 6.19 shows an example.

### 6.2.5 Texture Caching

A complex application may require a considerable number of textures. The amount of fast texture memory varies from system to system, but the general rule is that it is never enough. There are various techniques for *texture caching*, where a balance is sought between the overhead of uploading textures to memory and the amount of memory taken up by textures at one time. For example, for textured polygons that are initially far away, the application may load only the smaller subtextures in a mipmap, since these are the only levels that will be accessed [1, 118, 359].

Some general advice is to keep the textures small—no larger than is necessary to avoid magnification problems—and to try to keep polygons grouped by their use of texture. Even if all textures are always in memory, such precautions may improve the processor's cache performance.

A *least recently used* (LRU) strategy is one commonly used in texture caching schemes and works as follows. Each texture loaded into the graphics accelerator's memory is given a time stamp for when it was last accessed to render an image. When space is needed to load new textures, the texture with the oldest time stamp is unloaded first. Some APIs also allow a priority to be set for each texture, which is used as a tie-breaker: If the time stamps of two textures are the same, the lower priority texture is unloaded first. Setting priorities can help in avoiding unnecessary texture swapping [1380].

If developing your own texture manager, one useful strategy suggested by Carmack [374] is to check the texture being swapped out. If it was used in the current frame, then thrashing is occurring. LRU is a terrible strategy under these conditions, as every texture will be swapped in during each frame. Under this condition, change to *most recently used* (MRU) until such a time as no textures are swapped out during a frame, then switch back to LRU.

Loading a texture costs a noticeable amount of time, especially on PC where conversions to the hardware native format occur “behind the scenes” as part of the loading process. In a demand-driven system, where a texture is loaded when it is accessed by a polygon in view, the number of textures

loaded in each frame can vary considerably. The need for a large number of textures to be loaded in a single frame makes it difficult to maintain a constant frame rate. One solution is to use *prefetching*, where future needs are anticipated and the texture loading is then spread over a few frames [118].

For flight simulators and geographical information systems, the image datasets can be huge. The traditional approach is to break these images into smaller tiles that hardware can handle. Tanner et al. [899, 1241] present an improved data structure called the *clipmap*. The idea is that the entire dataset is treated as a mipmap, but only a small part of the lower levels of the mipmap is required for any particular view. For example, if the viewer is flying above terrain and looking off into the distance, a large amount of the entire texture may be seen. However, the texture level 0 image is needed for only a small portion of this picture. Since minification will take place, a different portion of the level 1 image is needed further out, level 2 beyond that, and so on. By clipping the mipmap structure by the view, one can identify which parts of the mipmap are needed. An image made using this technique is shown in Figure 6.20. DirectX 10-capable GPUs are able to implement clipmapping [945].



**Figure 6.20.** High resolution terrain mapping accessing a huge image database. Rendered with clipmapping to reduce the amount of data needed at one time. (*Image courtesy of Aechelon Technology, Inc.*)

Cantlay [154] presents a method to automatically determine which mipmap levels are visually significant to an application such as a game. For their terrain engine they found that 80% of the memory used by mipmap textures was never accessed, and so these levels could be discarded. Forsyth [359] also has a good discussion of these issues. Other methods to perform texture caching and improve performance are discussed by Blow [118] and Wright [1380]. Dumont et al. have researched perceptual rules for weighting how textures are cached [284].

## 6.2.6 Texture Compression

One solution that directly attacks memory and bandwidth problems and caching concerns is fixed-rate *texture compression* [79]. By having hardware decode compressed textures on the fly, a texture can require less texture memory and so increase the effective cache size. At least as significant, such textures are more efficient to use, as they consume less memory bandwidth when accessed. There are a variety of image compression methods used in image file formats such as JPEG and PNG [863, 912], but it is costly to implement decoding for these in hardware. S3 developed a scheme called *S3 Texture Compression* (S3TC) [1094], which was chosen as a standard for DirectX and called *DXTC*, and in DirectX 10, *BC* (for Block Compression). It has the advantages of creating a compressed image that is fixed in size, has independently encoded pieces, and is simple (and therefore fast) to decode. Each compressed part of the image can be dealt with independently from the others; there are no shared look-up tables or other dependencies, which also simplifies decoding.

There are five variants of the DXTC/BC compression scheme, and they share some common properties. Encoding is done on  $4 \times 4$  texel blocks, also called *tiles*. Each block is encoded separately. The encoding is based on interpolation; for each encoded quantity, two reference values are stored, and then for each of the 16 texels in the block, an interpolation factor is given to select a value along the line between the two reference values.

The exact encoding varies between the five variants:

- **DXT1** (DirectX 9.0) or **BC1** (DirectX 10.0 and above)—Each block has two 16-bit reference RGB values (5 bits red, 6 green, 5 blue), and each texel has a 2-bit interpolation factor to select from one of the reference values or two intermediate values.<sup>7</sup> This is the most compact variant, taking up 8 bytes for the block, or 4 bits per texel. This represents a 6:1 texture compression ratio, compared to an uncompressed 24-bit RGB texture.

---

<sup>7</sup>An alternate DXT1 mode reserves one of the four possible interpolation factors for transparent pixels, restricting the number of interpolated values to three—the two reference values and their average.

- **DXT3** (DirectX 9.0) or **BC2** (DirectX 10.0 and above)—Each block has RGB data encoded in the same way as a DXT1 block. In addition, each texel has a 4-bit alpha value stored separately (this is the only case where data is stored directly and not in interpolated form). A DXT3 block takes up 16 bytes, or 8 bits per texel. This represents a 4:1 texture compression ratio, compared to an uncompressed 32-bit RGBA texture.<sup>8</sup>
- **DXT5** (DirectX 9.0) or **BC3** (DirectX 10.0 and above)—Each block has RGB data encoded in the same way as a DXT1 block. In addition, alpha data is encoded using two 8-bit reference values, and a per-texel 3-bit interpolation factor. Each texel can select either one of the reference alpha values or one of six intermediate values. A DXT5 block has the same storage requirements as a DXT3 block.<sup>9</sup>
- **ATI1** (ATI-specific extension) or **BC4** (DirectX 10.0 and above)—Each block stores a single color channel of data, encoded in the same way as the alpha data in DXT5. A BC4 block takes up 8 bytes, or 4 bits per texel. This represents a 4:1 texture compression ratio, compared to an uncompressed 8-bit single-channel texture. This format is only supported on newer ATI hardware, or DirectX 10.0 hardware from any vendor.
- **ATI2** (ATI-specific extension, also called **3Dc** [51]) or **BC5** (DirectX 10.0 and above)—Each block stores two color channels of data, each encoded in the same way as a BC4 block or the alpha data in DXT5. A BC5 block takes up 16 bytes, or 8 bits per texel. This represents a 4:1 texture compression ratio, compared to an uncompressed 16-bit two-channel texture. This format is only supported on newer ATI hardware, or DirectX 10.0 hardware from any vendor.

These compression techniques can be applied to cube or volume textures, as well as two-dimensional textures.

The main drawback of these compression schemes is that they are *lossy*. That is, the original image usually cannot be retrieved from the compressed version. Only four or eight interpolated values are used to represent 16 pixels. If a tile has a larger number of distinct values in it, there will be some loss. In practice, these compression schemes generally give acceptable image fidelity if correctly used.

---

<sup>8</sup> Originally two formats (DXT2 and DXT3) were defined. They were encoded identically, but DXT2 textures were intended to contain RGB data that had been premultiplied by alpha. This convention never saw significant use, and today the DXT3 format signifier is commonly used regardless of premultiplied alpha.

<sup>9</sup>DXT4 was defined similarly to DXT2 and was similarly unpopular.

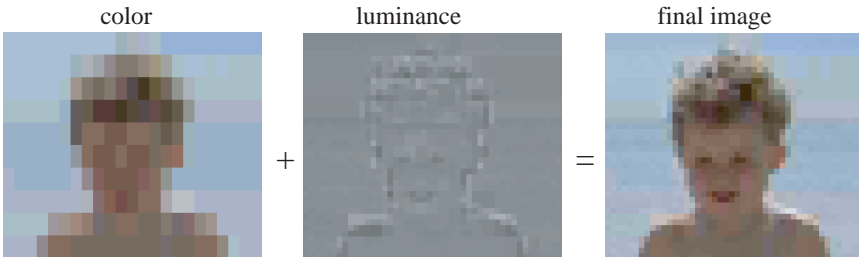


**Figure 6.21.** ETC (Ericsson texture compression) encodes the color of a block of pixels and then modifies the luminance per pixel to create the final texel color.

One of the problems with DXTC is that all the colors used for a block lie on a straight line in RGB space. For example, DXTC cannot represent the colors red, green, and blue in one block. Ivanov and Kuzmin [596] present a similar scheme called *color distribution* that attacks this problem. Essentially, they use the colors from the neighbors' blocks in order to achieve more colors. However, it appears that this scheme needs more memory accesses during decompression, so it is thus slower to unpack, or at least uses more memory bandwidth.

For OpenGL ES, another compression algorithm, called *Ericsson texture compression* (ETC) [1227] was chosen for inclusion in the API. This scheme has the same features as S3TC, namely, fast decoding, random access, no indirect lookups, and fixed rate. It encodes a block of  $4 \times 4$  texels into 64 bits, i.e., four bits per texel are used. The basic idea is illustrated in Figure 6.21. Each  $2 \times 4$  block (or  $4 \times 2$ , depending on which gives best quality) stores a basic color. Each block also selects a set of four constants from a small static lookup table, and each texel in a block can select to add one of the values in the selected lookup table. This basically modifies the luminance per pixel. The image quality is on par with DXTC.

Compression of normal maps (discussed in Section 6.7.2) requires some care. Compressed formats that were designed for RGB colors usually do not work well for normal XYZ data. Most approaches take advantage of the fact that the normal is known to be unit length, and further assume that its  $z$ -component is positive (a reasonable assumption for tangent-space normals). This allows for only storing the  $x$ - and  $y$ -components of a normal. The  $z$ -component is derived on the fly as

$$n_z = \sqrt{1 - n_x^2 - n_y^2}. \quad (6.3)$$

This in itself results in a modest amount of compression, since only two components are stored, instead of three. Since most GPUs do not natively support three-component textures, this also avoids the possibility

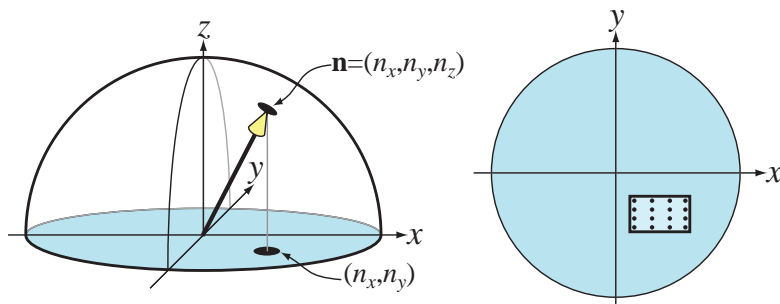


**Figure 6.22.** Left: the unit normal on a sphere only needs to encode the  $x$ - and  $y$ -components. Right: for BC4/3Dc, a box in the  $xy$ -plane encloses the normals, and  $8 \times 8$  normals inside this box can be used per  $4 \times 4$  block of normals (for clarity, only  $4 \times 4$  normals are shown here).

of wasting a component (or having to pack another quantity in the fourth component). Further compression is usually achieved by storing the  $x$ - and  $y$ -components in a BC5/3Dc-format texture (see Figure 6.22). Since the reference values for each block demarcate the minimum and maximum  $x$ - and  $y$ -component values, they can be seen as defining a bounding box on the  $xy$ -plane. The three-bit interpolation factors allow for the selection of eight values on each axis, so the bounding box is divided into an  $8 \times 8$  grid of possible normals.

On hardware that does not support the BC5/3Dc format, a common fallback [887] is to use a DXT5-format texture and store the two components in the green and alpha components (since those are stored with the highest precision). The other two components are unused.

By using unexploited bit combinations in BC5/3Dc, Munkberg et al. [908] propose some extra modes that increase the normal quality at the same bit rate cost. One particularly useful feature is that the aspect ratio of the box determines the layout of the normal inside a block. For example, if the box of the normals is more than twice as wide as high, one can use  $16 \times 4$  normals inside the box instead of  $8 \times 8$  normals. Since this is triggered by the aspect ratio alone, no extra bits are needed to indicate the normal layout per block. Further improvements for normal map compression are also possible. By storing an oriented box and using the aspect ratio trick, even higher normal map quality can be obtained [910].

Several formats for texture compression of high dynamic range images have been suggested, as well. Here, each color component is originally stored using a 16- or 32-bit floating-point number. Most of these schemes start compression of the data after conversion to a luminance-chrominance color space. The reason for this is that the component with high dynamic

range is usually only the luminance, while the chrominances can be compressed more easily. Roimela et al. [1080] present a very fast compressor and decompressor algorithm, where the chrominances are downsampled, and the luminance is stored more accurately. Munkberg et al. [909, 911] store the luminance using a DXTC-inspired variant of the logarithm of the luminance and introduce shape transforms for efficient chrominance encodings. Munkberg et al's algorithm produces compressed HDR textures with better image quality, while Roimela et al's have much simpler hardware for decompression, and compression is also faster. Both these algorithms require new hardware. Wang et al. [1323] take another approach, which reuses the DXTC decompression hardware and stores the content of an HDR texture in two sets of DXTC textures. This gives real-time performance today, but with apparent artifacts in some cases [911].

## 6.3 Procedural Texturing

Performing an image lookup is one way of generating texture values, given a texture-space location. Another is to evaluate a function, thus defining a *procedural texture*.

Although procedural textures are commonly used in offline rendering applications, image textures are far more common in real-time rendering. This is due to the extremely high efficiency of the image texturing hardware in modern GPUs, which can perform many billions of texture accesses in a second. However, GPU architectures are evolving toward cheaper computation and (relatively) more costly memory access. This will make procedural textures more common in real time applications, although they are unlikely to ever replace image textures completely.

Volume textures are a particularly attractive application for procedural texturing, given the high storage costs of volume image textures. Such textures can be synthesized by a variety of techniques. One of the most common is using one or more noise functions to generate values [295, 1003, 1004, 1005]. See Figure 6.23. Because of the cost of evaluating the noise function, the lattice points in the three-dimensional array are often pre-computed and used to interpolate texture values. There are methods that use the accumulation buffer or color buffer blending to generate these arrays [849]. Perlin [1006] presents a rapid, practical method for sampling this noise function and shows some uses. Olano [960] provides noise generation algorithms that permit tradeoffs between storing textures and performing computations. Green [448] gives a higher quality method, but one that is meant more for near-interactive applications, as it uses 50 pixel shader instructions for a single lookup. The original noise function presented by Perlin [1003, 1004, 1005] can be improved upon. Cook and DeRose [197]

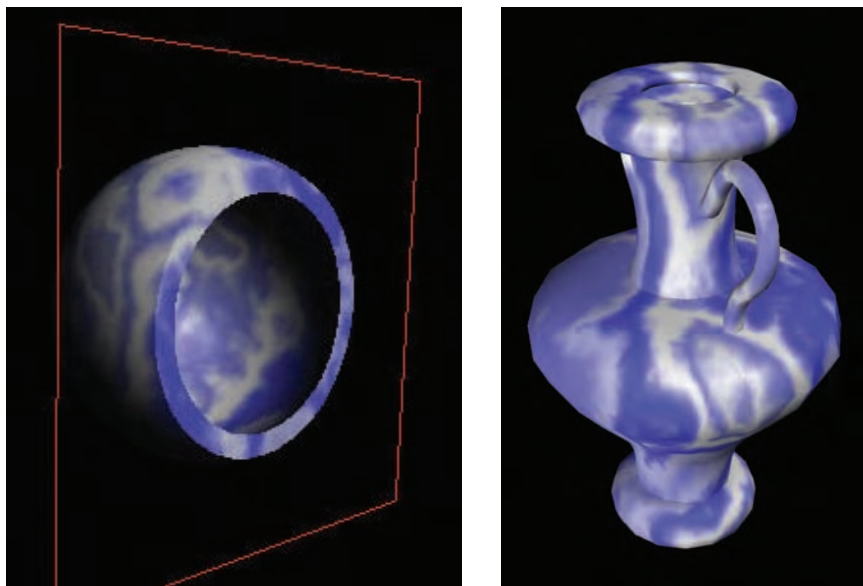


**Figure 6.23.** Two examples of real-time procedural texturing using a volume texture. The marble texture is continuous over the surface, with no mismatches at edges. The object on the left is formed by cutting a pair of spheres with a plane and using the stencil buffer to fill in the gap. (*Images courtesy of Evan Hart, ATI Technologies Inc.*)

present an alternate representation, called wavelet noise, which avoids aliasing problems with only a small increase in evaluation cost.

Other procedural methods are possible. For example, a *cellular texture* is formed by measuring distances from each location to a set of “feature points” scattered through space. Mapping the resulting closest distances in various ways, e.g., changing the color or shading normal, creates patterns that look like cells, flagstones, lizard skin, and other natural textures. Griffiths [456] discusses how to efficiently find the closest neighbors and generate cellular textures on the GPU.

Another type of procedural texture is the result of a physical simulation or some other interactive process, such as water ripples or spreading cracks. In such cases, procedural textures can produce effectively infinite variability in reaction to dynamic conditions.

When generating a procedural two-dimensional texture, parameterization issues can pose even more difficulties than for authored textures, where stretching or seam artifacts can be manually touched up or worked around. One solution is to avoid parameterization completely by synthesizing textures directly onto the surface. Performing this operation on complex sur-

faces is technically challenging and is an active area of research. See Lefebvre and Hoppe [750] for one approach and an overview of past research.

Antialiasing procedural textures is both easier and more difficult than antialiasing image textures. On one hand, precomputation methods such as mipmapping are not available. On the other hand, the procedural texture author has “inside information” about the texture content and so can tailor it to avoid aliasing. This is particularly the case with procedural textures created by summing multiple noise functions—the frequency of each noise function is known, so any frequencies that would cause aliasing can be discarded (actually making the computation cheaper). Various techniques exist for antialiasing other types of procedural textures [457, 1085, 1379].

## 6.4 Texture Animation

The image applied to a surface does not have to be static. For example, a video source can be used as a texture that changes from frame to frame.

The texture coordinates need not be static, either. In fact, for environment mapping, they usually change with each frame because of the way they are computed (see Section 8.4). The application designer can also explicitly change the texture coordinates from frame to frame. Imagine that a waterfall has been modeled and that it has been textured with an image that looks like falling water. Say the  $v$  coordinate is the direction of flow. To make the water move, one must subtract an amount from the  $v$  coordinates on each successive frame. Subtraction from the texture coordinates has the effect of making the texture itself appear to move forward.

More elaborate effects can be created by modifying the texture coordinates in the vertex or pixel shader. Applying a matrix to the texture coordinates<sup>10</sup> allows for linear transformations such as zoom, rotation, and shearing [849, 1377], image warping and morphing transforms [1367], and generalized projections [475]. By performing other computations on the texture coordinates, many more elaborate effects are possible, including waterfalls and animated fire.

By using texture blending techniques, one can realize other animated effects. For example, by starting with a marble texture and fading in a flesh texture, one can make a statue come to life [874].

## 6.5 Material Mapping

A common use of a texture is to modify a material property affecting the shading equation, for example the equation discussed in Chapter 5:

---

<sup>10</sup>This is supported on fixed-function pipelines, as well.

$$L_o(\mathbf{v}) = \left( \frac{\mathbf{c}_{\text{diff}}}{\pi} + \frac{m+8}{8\pi} \overline{\cos}^m \theta_h \mathbf{c}_{\text{spec}} \right) \otimes E_L \overline{\cos} \theta_i. \quad (6.4)$$

In the implementation of this model in Section 5.5 the material parameters were accessed from constants. However, real-world objects usually have material properties that vary over their surface. To simulate such objects, the pixel shader can read values from textures and use them to modify the material parameters before evaluating the shading equation.

The parameter that is most often modified by a texture is the diffuse color  $\mathbf{c}_{\text{diff}}$ ; such a texture is known as a *diffuse color map*. The specular color  $\mathbf{c}_{\text{spec}}$  is also commonly textured, usually as a grayscale value rather than as RGB, since for most real-world materials  $\mathbf{c}_{\text{spec}}$  is uncolored (colored metals such as gold and copper are notable exceptions). A texture that affects  $\mathbf{c}_{\text{spec}}$  is properly called a *specular color map*. Such textures are sometimes referred to as *gloss maps* but this name is more properly applied to textures that modify the surface smoothness parameter  $m$ . The three parameters  $\mathbf{c}_{\text{diff}}$ ,  $\mathbf{c}_{\text{spec}}$ , and  $m$  fully describe the material in this shading model; other shading models may have additional parameters that can similarly be modified by values that are read from textures.

As discussed previously, shading model inputs like  $\mathbf{c}_{\text{diff}}$  and  $\mathbf{c}_{\text{spec}}$  have a linear relationship to the final color output from the shader. Thus, textures containing such inputs can be filtered with standard techniques, and aliasing is avoided. Textures containing nonlinear shading inputs, like  $m$ , require a bit more care to avoid aliasing. Filtering techniques that take account of the shading equation can produce improved results for such textures. These techniques are discussed in Section 7.8.1.

## 6.6 Alpha Mapping

The alpha value can be used for many interesting effects. One texture-related effect is *decaling*. As an example, say you wish to put a picture of a flower on a teapot. You do not want the whole picture, but just the parts where the flower is present. By assigning an alpha of 0 to a texel, you make it transparent, so that it has no effect. So, by properly setting the decal texture's alpha, you can replace or blend the underlying surface with the decal. Typically, a clamp corresponder function is used with a transparent border to apply a single copy of the decal (versus a repeating texture) to the surface.

A similar application of alpha is in making cutouts. Say you make a decal image of a bush and apply it to a polygon in the scene. The principle is the same as for decals, except that instead of being flush with an underlying surface, the bush will be drawn on top of whatever geometry is behind it.

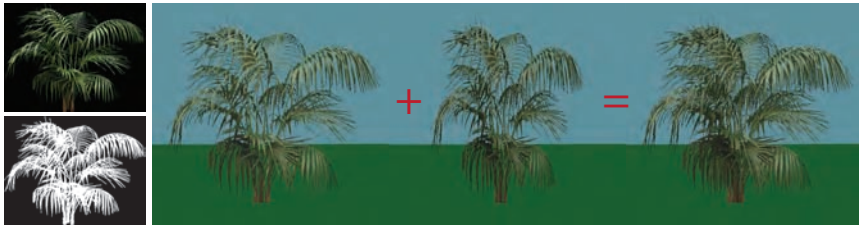


**Figure 6.24.** On the left, the bush texture map and the 1-bit alpha channel map below it. On the right, the bush rendered on a single polygon; by adding a second copy of the polygon rotated 90 degrees, we form an inexpensive three-dimensional bush.

In this way, you can render an object with a complex silhouette, using a single polygon.

In the case of the bush, if you rotate the viewer around it, the illusion fails, since the bush has no thickness. One answer is to copy this bush polygon and rotate it 90 degrees along the trunk. The two polygons form an inexpensive three-dimensional bush, sometimes called a “cross tree” [862], and the illusion is fairly effective when viewed from ground level. See Figure 6.24. Pelzer [1000] discusses a similar configuration using three cutouts to represent grass. In Section 10.6, we discuss a method called *billboarding*, which is used to reduce such rendering to a single polygon.

If the viewer moves above ground level, the illusion breaks down as the bush is seen from above to be two cutouts. See Figure 6.25. To combat this, more cutouts can be added in different ways—slices, branches, layers—to provide a more convincing model. Section 10.7.2 discusses one approach for generating such models. See the images on pages 881 and 882 for more examples.



**Figure 6.25.** Looking at the “cross-tree” bush from a bit off ground level, then further up, where the illusion breaks down.

Combining alpha maps and texture animation can produce convincing special effects, such as flickering torches, plant growth, explosions, atmospheric effects, etc.

There are several options for rendering objects with alpha maps. Alpha blending (see Section 5.7) allows for fractional transparency values, which enables antialiasing the object edges, as well as partially transparent objects. However, alpha blending requires rendering the blended polygons after the opaque ones, and in back-to-front order. In addition, fully transparent pixels are not discarded, so they use merge unit resources and memory bandwidth.

Alpha testing (conditionally discarding pixels with alpha values below a given threshold, in the merge unit or pixel shader) enables polygons to be rendered in any order, and transparent pixels are discarded. However, the quality is low because only two levels of transparency are available. In addition, alpha tested edges do not benefit from multisample antialiasing, since the same alpha value is used for all samples. Alpha testing displays ripple artifacts under magnification, which can be avoided by pre-computing the alpha map as a distance field [439] (see also discussion on page 161).

*Alpha to coverage*, and the similar feature *transparency adaptive anti-aliasing*, take the transparency value of the fragment and convert this into how many samples inside a pixel are covered [914]. This idea is similar to screen-door transparency, described in Section 5.7, but at a subpixel level. Imagine that each pixel has four sample locations, and that a fragment covers a pixel, but is 25% transparent (75% opaque), due to the cutout texture. The alpha to coverage mode makes the fragment become fully opaque but has it cover only three of the four samples. This mode is useful for cutout textures for overlapping grassy fronds, for example [648, 1350]. Since each sample drawn is fully opaque, the closest frond will hide objects behind it in a consistent way along its edges. No sorting is needed to correctly blend semitransparent edge pixels. Alpha to coverage combines some of the advantages of both alpha blending and alpha testing.

## 6.7 Bump Mapping

This section describes a large family of small-scale detail representation techniques that we collectively call *bump mapping*. All of these methods are typically implemented by modifying the per-pixel shading routine. They give a more three-dimensional appearance than texture mapping alone, but less than actual geometry.

Detail on an object can be classified into three scales: macro-features that cover many pixels, meso-features that are a few pixels across, and

micro-features that are substantially smaller than a pixel. These categories are somewhat fluid, since the viewer may observe the same object at many distances during an animation or interactive session.

Macro-geometry is represented by vertices and triangles, or other geometric primitives. When creating a three-dimensional character, the limbs and head are typically modeled at a macroscale. Micro-geometry is encapsulated in the shading model, which is commonly implemented in a pixel shader and uses texture maps as parameters. The shading model used simulates the interaction of a surface's microscopic geometry; e.g., shiny objects are microscopically smooth, and diffuse surfaces are microscopically rough. The skin and clothes of a character appear to have different materials because they use different shaders, or at least different parameters in those shaders.

Meso-geometry describes everything between these two scales. It contains detail that is too complex to efficiently render using individual polygons, but that is large enough for the viewer to distinguish individual changes in surface curvature over a few pixels. The wrinkles on a character's face, musculature details, and folds and seams in his or her clothing, are mesoscale. A family of methods collectively known as *bump mapping techniques* are commonly used for mesoscale modeling. These adjust the shading parameters at the pixel level in such a way that the viewer perceives small perturbations away from the base geometry, which actually remains flat. The main distinctions between the different kinds of bump mapping are how they represent the detail features. Variables include the level of realism and complexity of the detail features.

Blinn introduced the idea of encoding mesoscale detail in a two-dimensional array in 1978 [98]. He observed that a surface appears to have small-scale detail if, during shading, we substitute a slightly perturbed surface normal for the true one. He stored the data describing the perturbation to the surface normal in the array.

So the key idea is that instead of using a texture to change a color component in the illumination equation, we access a texture to modify the surface normal. The geometric normal of the surface remains the same; we merely modify the normal used in the lighting equation. This operation has no physical equivalent; we perform changes on the surface normal, but the surface itself remains smooth in the geometric sense. Just as having a normal per vertex gives the illusion that the surface is smooth between polygons, modifying the normal per pixel changes the perception of the polygon surface itself, without modifying its geometry.

For bump mapping, the normal must change direction with respect to some frame of reference. To do so, a *tangent space basis* is stored at each vertex. This frame of reference is used to transform the lights to a surface location's space (or vice versa) to compute the effect of perturbing the

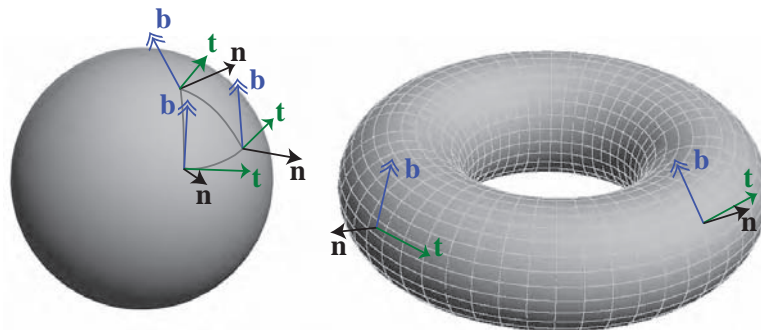


**Figure 6.26.** A spherical triangle is shown, with its tangent space basis shown at each corner. Shapes like a sphere and torus have a natural tangent space basis, as the latitude and longitude lines on the torus show.

normal. With a polygonal surface that has a normal map applied to it, in addition to a vertex normal, we also store what are called the *tangent* and *bitangent vectors*.<sup>11</sup>

The tangent and bitangent vectors represent the axes of the normal map itself in the object's space, since the goal is to transform the light to be relative to the map. See Figure 6.26.

These three vectors, normal  $n$ , tangent  $t$ , and bitangent  $b$ , form a basis matrix:

$$\begin{pmatrix} t_x & t_y & t_z & 0 \\ b_x & b_y & b_z & 0 \\ n_x & n_y & n_z & 0 \\ 0 & 0 & 0 & 1 \end{pmatrix}. \quad (6.5)$$

This matrix transforms a light's direction (for the given vertex) from world space to tangent space. These vectors do not have to truly be perpendicular to each other, since the normal map itself may be distorted to fit the surface. In fact, the tangent and bitangent usually are not perpendicular to each other (though they will be to the normal). One method of saving memory is to store just the tangent and bitangent at the vertex and take their cross product to compute the normal. However, this technique works only if the handedness of the matrix is always the same [886]. Frequently a model is symmetric: an airplane, a human, a file cabinet, and many other objects; just look around. Because textures consume a large amount of memory, they are often mirrored onto symmetric models. Thus, only one side of an object's texture is stored, but the texture mapping places it onto both sides of the model. In this case, the handedness of the

---

<sup>11</sup>The bitangent vector is also, more commonly but less correctly, referred to as the *binormal vector*. We use the better term here.

tangent space will be different on the two sides, and cannot be assumed. It is still possible to avoid storing the normal in this case if an extra bit of information is stored at each vertex to indicate the handedness. A common representation is to store a value of 1 or  $-1$  depending on the handedness; this value is used to scale the cross product of the tangent and bitangent to produce the correct normal.

The idea of tangent space is important for other algorithms. As discussed in the next chapter, many shading equations rely on only the surface's normal direction. However, materials such as brushed aluminum or velvet also need to know the relative direction of the viewer and lighting compared to the surface. The tangent space basis is useful to define the orientation of the material on the surface. Articles by Lengyel [761] and Mittring [886] provide extensive coverage of this area. Schüller [1139] presents a method of computing the tangent space basis on the fly in the pixel shader, with no need to store a precomputed tangent frame per vertex.

### 6.7.1 Blinn's Methods

Blinn's original bump mapping method stores in a texture two signed values,  $b_u$  and  $b_v$ , at each point. These two values correspond to the amount to vary the normal along the  $\mathbf{u}$  and  $\mathbf{v}$  image axes. That is, these texture values, which typically are bilinearly interpolated, are used to scale two vectors that are perpendicular to the normal. These two vectors are added to the normal to change its direction. The two values  $b_u$  and  $b_v$  describe which way the surface faces at the point. See Figure 6.27. This type of bump map texture is called an *offset vector bump map* or *offset map*.

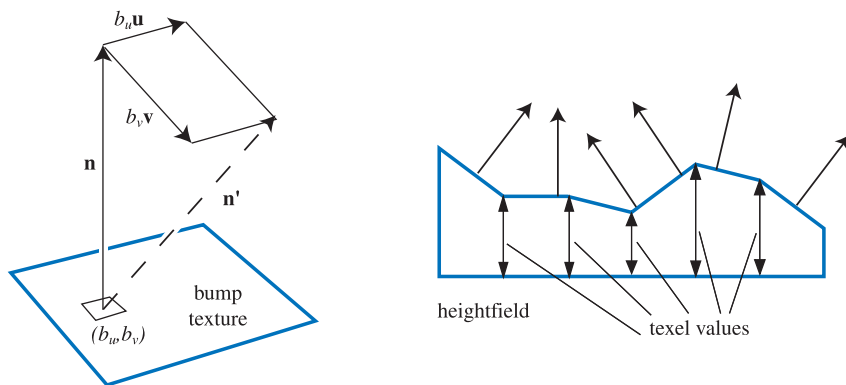


**Figure 6.27.** On the left, a normal vector  $\mathbf{n}$  is modified in the  $\mathbf{u}$  and  $\mathbf{v}$  directions by the  $(b_u, b_v)$  values taken from the bump texture, giving  $\mathbf{n}'$  (which is unnormalized). On the right, a heightfield and its effect on shading normals is shown. These normals could instead be interpolated between heights for a smoother look.

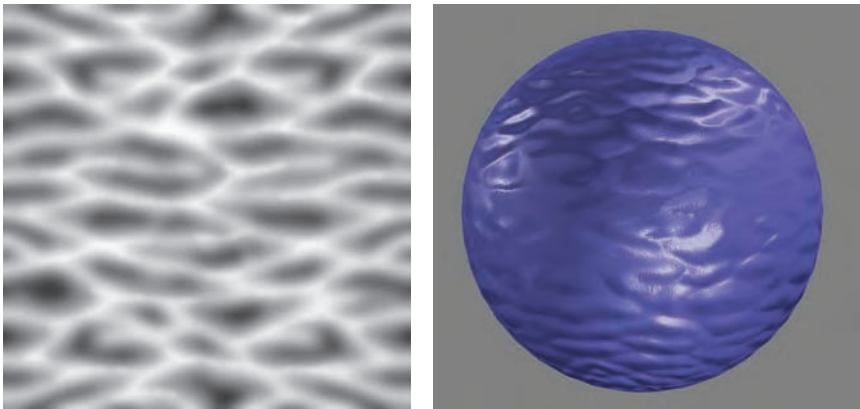


**Figure 6.28.** A wavy heightfield bump image and its use on a sphere, rendered with per-pixel illumination.

Another way to represent bumps is to use a *heightfield* to modify the surface normal's direction. Each monochrome texture value represents a height, so in the texture, white is a high area and black a low one (or vice versa). See Figure 6.28 for an example. This is a common format used when first creating or scanning a bump map and was also introduced by Blinn in 1978. The heightfield is used to derive  $u$  and  $v$  signed values similar to those used in the first method. This is done by taking the differences between neighboring columns to get the slopes for  $u$ , and between neighboring rows for  $v$  [1127]. A variant is to use a Sobel filter, which gives a greater weight to the directly adjacent neighbors [401].

### 6.7.2 Normal Mapping

The preferred implementation of bump mapping for modern graphics cards is to directly store a *normal map*.<sup>12</sup> This is preferred because the storage cost of three components of the perturbed normal versus the two offsets or single bump height is no longer considered prohibitive, and directly storing the perturbed normal reduces the number of computations needed per pixel during shading. The algorithms and results are mathematically identical to bump mapping; only the storage format changes.

The normal map encodes  $(x, y, z)$  mapped to  $[-1, 1]$ , e.g., for an 8-bit texture the  $x$ -axis value 0 represents  $-1.0$  and 255 represents  $1.0$ . An example is shown in Figure 6.29. The color  $[128, 128, 255]$ , a light blue,

<sup>12</sup>In older, fixed-function hardware, this technique is known as *dot product bump mapping*.

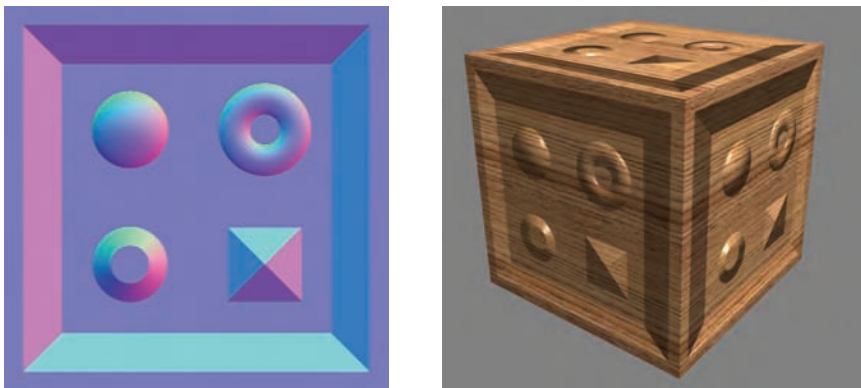


**Figure 6.29.** Bump mapping with a normal map. Each color channel is actually a surface normal coordinate. The red channel is the  $x$  deviation; the more red, the more the normal points to the right. Green is the  $y$  deviation, and blue is  $z$ . At the right is an image produced using the normal map. Note the flattened look on the top of the cube. (*Images courtesy of Manuel M. Oliveira and Fabio Policarpo.*)

would represent a flat surface for the color mapping shown, i.e., a normal of  $[0, 0, 1]$ .

The normal map representation was originally introduced as the world-space normal map [182, 652], which is rarely used in practice. In that case, the perturbation is straightforward: At each pixel, retrieve the normal from the map and use it directly, along with a light's direction, to compute the shade at that location on the surface. This works because the normal map's stored values, where  $+z$  is up, align with how the square happens to be oriented. As soon as the square is rotated to another position, this direct use of the normal map is no longer possible. If the square is not facing up, one solution could be to generate a new normal map, in which all the stored normals were transformed to point using the new orientation. This technique is rarely used, as the same normal map could not then be used on, say, two walls facing different directions. Even if the normal map is used but once, the object it is applied to cannot change orientation or location, or deform in any way.

Normal maps can also be defined in object space. Such normal maps will remain valid as an object undergoes rigid transformations, but not any type of deformation. Such normal maps also usually cannot be reused between different parts of the object, or between objects. Although the light's direction needs to be transformed into object space, this can be done in the application stage and does not add any overhead in the shader.

Usually the perturbed normal is retrieved in tangent space, i.e., relative to the surface itself. This allows for deformation of the surface, as well as

maximal reuse of the normal maps. It is also easier to compress tangent space normal maps, since the sign of the  $z$  component (the one aligned with the unperturbed surface normal) can usually be assumed to be positive. The downside of tangent-space normal maps is that more transformations are required for shading, since the reference frame changes over the surface.

To use illumination within a typical shading model, both the surface and lighting must be in the same space: tangent, object, or world. One method is to transform each light's direction (as viewed from the vertex) into tangent space and interpolate these transformed vectors across the triangle. Other light-related values needed by the shading equation, such as the half vector (see Section 5.5), could also be transformed, or could be computed on the fly. These values are then used with the normal from the normal map to perform shading. It is only the relative direction of the light from the point being shaded that matters, not their absolute positions in space. The idea here is that the light's direction slowly changes, so it can be interpolated across a triangle. For a single light, this is less expensive than transforming the surface's perturbed normal to world space every pixel. This is an example of frequency of computation: The light's transform is computed per vertex, instead of needing a per-pixel normal transform for the surface.

However, if the application uses more than just a few lights, it is more efficient to transform the resulting normal to world space. This is done by using the inverse of Equation 6.5, i.e., its transpose. Instead of interpolating a large number of light directions across a triangle, only a single transform is needed for the normal to go into world space. In addition, as we will see in Chapter 8, some shading models use the normal to generate a reflection direction. In this case, the normal is needed in world space regardless, so there is no advantage in transforming the lights into tangent space. Transforming to world space can also avoid problems due to any tangent space distortion [887]. Normal mapping can be used to good effect to increase realism—see Figure 6.30.

Filtering normal maps is a difficult problem, compared to filtering color textures. In general, the relationship between the normal and the shaded color is not linear, so standard filtering methods may result in objectionable aliasing. Imagine looking at stairs made of blocks of shiny white marble. At some angles, the tops or sides of the stairs catch the light and reflect a bright specular highlight. However, the average normal for the stairs is at, say, a 45-degree angle; it will capture highlights from entirely different directions than the original stairs. When bump maps with sharp specular highlights are rendered without correct filtering, a distracting sparkle effect can occur as highlights wink in and out by the luck of where samples fall.

Lambertian surfaces are a special case where the normal map has an almost linear effect on shading. Lambertian shading is almost entirely a



**Figure 6.30.** An example of normal map bump mapping used in a game scene. The details on the player’s armor, the rusted walkway surface, and the brick surface of the column to the left all show the effects of normal mapping. (*Image from “Crysis” courtesy of Crytek.*)

dot product, which is a linear operation. Averaging a group of normals and performing a dot product with the result is equivalent to averaging individual dot products with the normals:

$$\mathbf{l} \cdot \left( \frac{\sum_{j=1}^n \mathbf{n}_j}{n} \right) = \frac{\sum_{j=1}^n (\mathbf{l} \cdot \mathbf{n}_j)}{n}. \quad (6.6)$$

Note that the average vector is not normalized before use. Equation 6.6 shows that standard filtering and mipmaps *almost* produce the right result for Lambertian surfaces. The result is not quite correct because the Lambertian shading equation is not a dot product; it is a *clamped* dot product— $\max(\mathbf{l} \cdot \mathbf{n}, 0)$ . The clamping operation makes it nonlinear. This will overly darken the surface for glancing light directions, but in practice this is usually not objectionable [652]. One caveat is that some texture compression methods typically used for normal maps (such as reconstructing the  $z$ -component from the other two) do not support non-unit-length normals, so using non-normalized normal maps may pose compression difficulties.

In the case of non-Lambertian surfaces, it is possible to produce better results by filtering the inputs to the shading equation as a group, rather than filtering the normal map in isolation. Techniques for doing so are discussed in Section 7.8.1.

### 6.7.3 Parallax Mapping

A problem with normal mapping is that the bumps never block each other. If you look along a real brick wall, for example, at some angle you will not see the mortar between the bricks. A bump map of the wall will never show this type of occlusion, as it merely varies the normal. It would be better to have the bumps actually affect which location on the surface is rendered at each pixel.

The idea of *parallax mapping* was introduced in 2001 by Kaneko [622] and refined and popularized by Welsh [1338]. *Parallax* refers to the idea that the positions of objects move relative to one another as the observer moves. As the viewer moves, the bumps should occlude each other, i.e., appear to have heights. The key idea of parallax mapping is to take an educated guess of what should be seen in a pixel by examining the height of what was found to be visible.

For parallax mapping, the bumps are stored in a heightfield texture. When viewing the surface at a given pixel, the heightfield value is retrieved at that location and used to shift the texture coordinates to retrieve a different part of the surface. The amount to shift is based on the height retrieved and the angle of the eye to the surface. See Figure 6.31. The heightfield values are either stored in a separate texture, or packed in an unused color or alpha channel of some other texture (care must be taken when packing unrelated textures together, since this can negatively impact compression quality). The heightfield values are scaled and biased before being used to offset the values. The scale determines how high the heightfield is meant to extend above or below the surface, and the bias gives the “sea-level” height at which no shift takes place. Given a location  $\mathbf{p}$ , adjusted heightfield height  $h$ , and a normalized view vector  $\mathbf{v}$  with a height  $v_z$  and horizontal component  $v_{xy}$ , the new parallax-adjusted position  $\mathbf{p}_{adj}$

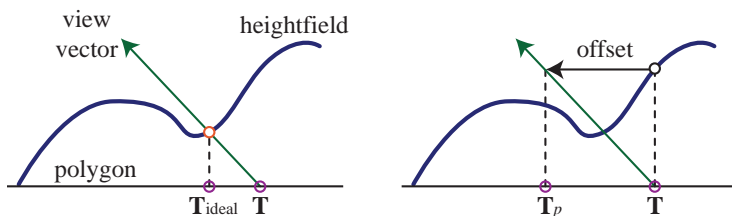


**Figure 6.31.** On the left is the goal: The actual position on the surface is found from where the view vector pierces the heightfield. Parallax mapping does a first-order approximation by taking the height at the location on the polygon and using it to find a new location  $\mathbf{p}_{adj}$ . (After Welsh [1338].)

is

$$\mathbf{p}_{\text{adj}} = \mathbf{p} + \frac{h \cdot \mathbf{v}_{xy}}{v_z}. \quad (6.7)$$

Note that unlike most shading equations, here the space in which the computation is performed matters—the view vector needs to be in tangent space.

Though a simple approximation, this shifting works fairly well in practice if the bump heights change relatively slowly [846]. Nearby neighboring texels then have about the same heights, so the idea of using the original location's height as the new location's height is reasonable. However, this method falls apart at shallow viewing angles. When the view vector is near the surface's horizon, a small height change results in a large texture coordinate shift. The approximation fails, as the new location retrieved has little or no height correlation to the original surface location.

To ameliorate this problem, Welsh [1338] introduced the idea of offset limiting. The idea is to limit the amount of shifting to never be larger than the retrieved height. The equation is then

$$\mathbf{p}'_{\text{adj}} = \mathbf{p} + h \cdot \mathbf{v}_{xy}. \quad (6.8)$$

Note that this equation is faster to compute than the original. Geometrically, the interpretation is that the height defines a radius beyond which the position cannot shift. This is shown in Figure 6.32.

At steep angles, this equation is almost the same as the original, since  $v_z$  is nearly 1. At shallow angles, the offset becomes limited in its effect. Visually, this makes the bumpiness lessen at shallow angles, but this is much better than essentially random sampling of the texture. Problems also remain with texture swimming as the view changes, or for stereo rendering, where the viewer simultaneously perceives two viewpoints that must give consistent depth cues [846].

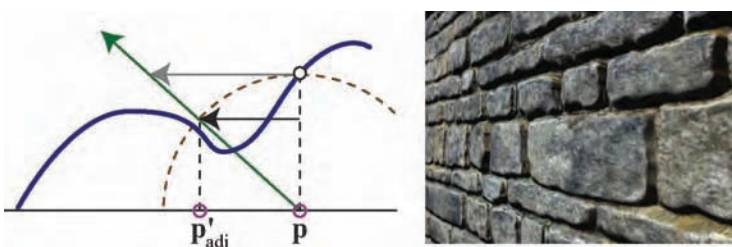


**Figure 6.32.** In parallax offset limiting, the offset moves at most the amount of the height away from the original location, shown as a dashed circular arc. The gray offset shows the original result, the black the limited result. On the right is a wall rendered with the technique. (*Image courtesy of Terry Welsh.*)

Even with these drawbacks, parallax mapping with offset limiting costs just a few additional pixel shader program instructions and gives a considerable image quality improvement over normal mapping. For these reasons, it has seen wide use in games and is today considered the practical standard for bump mapping.

### 6.7.4 Relief Mapping

Bump mapping does not consider the heightfield itself, and so does not modify texture coordinates. Parallax mapping provides a simple approximation of the effect of the heightfield, working on the assumption that the height at one pixel is similar to the height at another. This assumption can quickly break down. Also, where the bias (i.e., the “sea-level”) is set affects how the heightfield is displayed. What we want is what is visible at the pixel, i.e., where the view vector first intersects the heightfield.

Researchers have tackled this problem in a variety of different ways. All methods perform some approximation of ray tracing along the view vector until an intersection point is found. In a traditional ray tracer, the algorithm would walk along the ray through the grid, forming the height field and checking intersection with the relevant geometry in each grid cell encountered. GPU-based approaches usually take a different approach, leveraging the ability of the pixel shader to access texture data.

In computer graphics, just as in other fields, sometimes the time is ripe for a particular idea. With relief mapping, three sets of researchers independently developed the idea at about the same time, each without knowledge of the others’ efforts. Brawley and Tatarchuk [138] presented a straightforward method for finding the intersection, extended later by with improved root finding [1244, 1248]. Policarpo et al. [1020, 1021] and McGuire and McGuire [846] independently discovered and explored similar methods. These algorithms have a variety of names—*parallax occlusion mapping* (POM), *relief mapping*, and *steep parallax mapping*—but take essentially the same approach. For brevity, and to differentiate these ray-tracing related methods from Kaneko and Welsh’s single-shift methods, as a class we will call these “relief mapping” algorithms. What is particularly interesting about this case of parallel development is that the basic algorithm of sampling a texture along a ray had actually been discovered 13 years earlier by Patterson et al. [991], which they call *inverse displacement mapping*.<sup>13</sup> None of the newer researchers had been aware of this work at

---

<sup>13</sup>This problem of multiple names persists today, with “parallax occlusion mapping” and “relief mapping” being the two popular terms. The name “parallax occlusion mapping” was rather long, and the word “occlusion” confuses some readers (it does not refer to shadowing, but to the fact that bumps can occlude each other), so we chose “relief mapping.” Even this name is not ideal, as this term was introduced by Oliveira

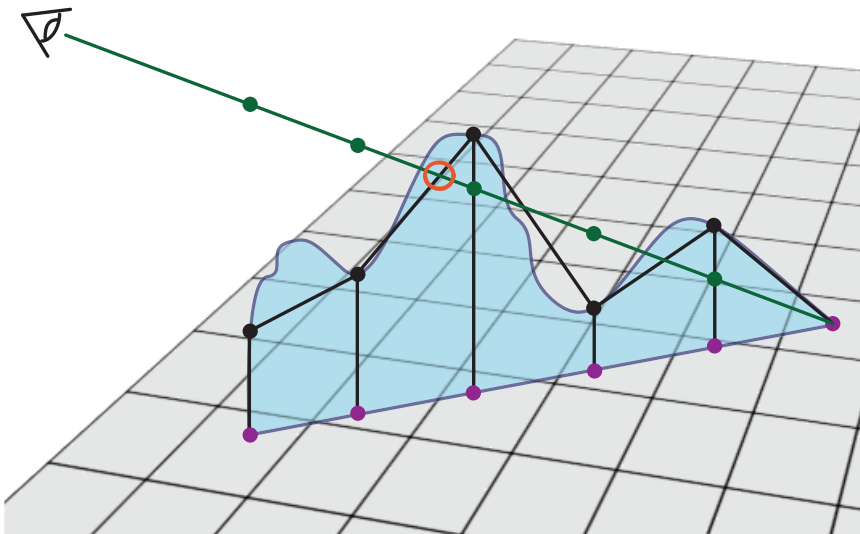


**Figure 6.33.** The green eye ray is projected onto the surface plane, which is sampled at regular intervals (the violet dots) and the heights are retrieved. The algorithm finds the first intersection of the eye ray with the black line segments approximating the curved height field.

the time of their parallel discoveries. There are undoubtedly more little-remembered nuggets of research originally implemented on the CPU that are ripe for GPU implementation.

The key idea is to first test a fixed number of texture samples along the projected vector. More samples are usually generated for view rays at grazing angles, so that the closest intersection point is not missed [1244, 1248]. Each texture location is retrieved and processed to determine if it is above or below the heightfield. Once a sample below the heightfield is found, the amount it is below, and the amount the previous sample is above, are used to find an intersection location. See Figure 6.33. The location is then used to shade the surface, using the attached normal map, color map, etc. Multiple layered heightfields can be used to produce overhangs, independent overlapping surfaces, and two-sided relief-mapped impostors; see Section 10.8.

The heightfield tracing approach can also be used to have the bumpy surface cast shadows onto itself, both hard [1021, 846] and soft [1244, 1248]. See Figure 6.34 for a comparison.

---

et al. [963] to denote a similar effect, though performed in a different way. Given that Oliveira worked on both methods and has no problem with reusing the term, we decided on “relief mapping.”

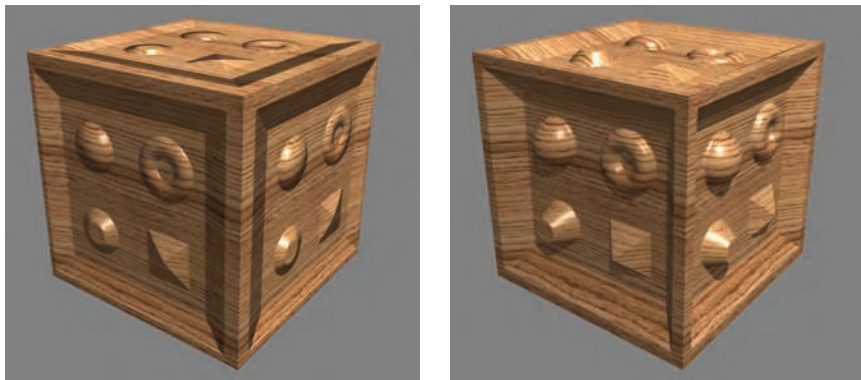


**Figure 6.34.** Parallax mapping compared to relief mapping. On the top of the cube there is flattening with parallax mapping. Relief mapping is also able to provide self-shadowing. (*Images courtesy of Manuel M. Oliveira and Fabio Policarpo.*)

The problem of determining the actual intersection point between the two regular samples is a root-finding problem. In practice the heightfield is treated more as a depthfield, with the polygon’s plane defining the upper limit of the surface. In this way, the initial point on the plane is above the heightfield. After finding the last point above, and first point below, the heightfield’s surface, Tatarchuk [1244, 1248] uses a single step of the secant method to find an approximate solution. Policarpo et al. [1021] use a binary search between the two points found to hone in on a closer intersection. Risser et al. [1068] speed convergence by iterating using a secant method. There is a tradeoff here: Regular sampling can be done in parallel, while iterative methods need fewer overall texture accesses but must wait for results and perform slower dependent texture fetches.

There is critical importance in sampling the heightfield frequently enough. McGuire and McGuire [846] propose biasing the mipmap lookup and using anisotropic mipmaps to ensure correct sampling for high-frequency heightfields, such as those representing spikes or hair. One can also store the heightfield texture at higher resolution than the normal map. Finally, some rendering systems do not even store a normal map, preferring to derive the normal on the fly from the heightfield using a cross filter [23]. Equation 12.2 on page 547 shows the method.

Another approach to increasing both performance and sampling accuracy is to not initially sample the heightfield at a regular interval, but instead to try to skip intervening empty space. Donnelly [271] preprocesses the height field into a set of voxels, storing in each voxel how far away it is from the heightfield surface. In this way, intervening space can be rapidly

skipped, at the cost of higher storage for each heightfield. Wang [1322] uses a five-dimensional displacement mapping scheme to hold distances to the surface from all directions and locations. This allows complex curved surfaces, self-shadowing, and other effects, at the expense of considerably larger amounts of memory. Dummer [283] introduces, and Policarpo and Oliveira [1023] improve upon, the idea of *cone step mapping*. The concept here is to also store for each heightfield location a *cone radius*. This radius defines an interval on the ray in which there is at most one intersection with the heightfield. This property allows rapid skipping along the ray without missing any possible intersections, though at the cost of needing dependent texture reads. Another drawback is the precomputation needed to create the cone step map, making the method unusable for dynamically

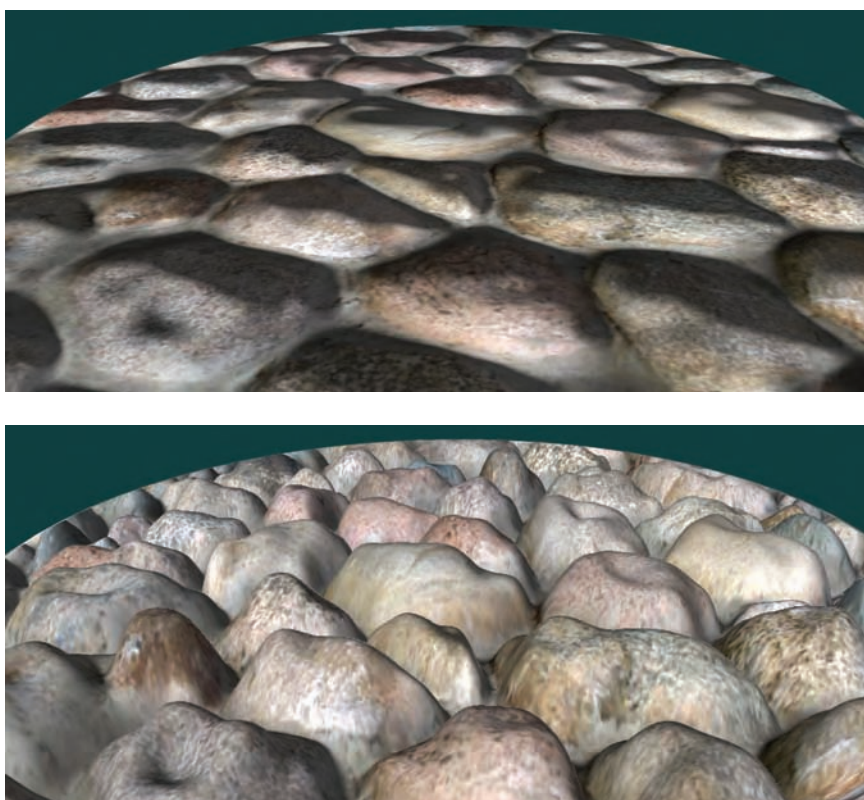


**Figure 6.35.** Normal mapping and relief mapping. No self-occlusion occurs with normal mapping. Relief mapping has problems with silhouettes for repeating textures, as the polygon is more of a view into the heightfield than a true boundary definition. (*Images courtesy of NVIDIA Corporation.*)

changing heightfields. Schroeders and Gulik [1134] present *quadtree relief mapping*, a hierarchical method to skip over volumes during traversal. Tevs et al. [1264] use “maximum mipmaps” to allow skipping while minimizing precomputation costs.

Although this is an active area of research and is highly sensitive to particular GPU architectures, in preliminary testing, one of the most time- and space-efficient methods for relief mapping at the time of printing is Tatarchuk’s [1244] linear ray-marching with single-step secant correction. That said, newer methods, such as cone-stepping and quadtree relief mapping, were not part of this informal survey. Unquestionably, research will continue to improve algorithms in this area.

One problem with relief mapping methods is that the illusion breaks down along the silhouette edges of objects, which will show the original surface’s smooth outlines. See Figure 6.35.

The key idea is that the triangles rendered define which pixels should be evaluated by the pixel shader program, not where the surface actually is located. In addition, for curved surfaces, the problem of silhouettes becomes more involved. One approach is described and developed by Oliveira and Policarpo [964, 1334], which uses a quadratic silhouette approximation technique. Jeschke et al. [610] and Dachsbacher et al. [223] both give a more general and robust method (and review previous work) for dealing with silhouettes and curved surfaces correctly. First explored by Hirche [552], the general idea is to extrude each polygon in the mesh outwards and form a prism. Rendering this prism forces evaluation of all pixels in which the heightfield could possibly appear. This type of approach is called *shell*



**Figure 6.36.** Parallax occlusion mapping, a.k.a. relief mapping, used on a path to make the stones look more realistic. (Image from “Crysis” courtesy of Crytek.)

*mapping*, as the expanded mesh forms a separate shell over the original model. By preserving the nonlinear nature of prisms when intersecting them with rays, artifact-free rendering of heightfields becomes possible, though expensive to compute.

To conclude, an impressive use of this type of technique is shown in Figure 6.36.

### 6.7.5 Heightfield Texturing

One obvious method of rendering bumps is to model the bumps as true geometry, in a very fine mesh. A space-efficient alternative is to use the vertex texture fetch feature (introduced in Shader Model 3.0) to have a flat meshed polygon access a heightfield texture. The height retrieved from the texture is used by the vertex shading program to modify the vertex's location. This method is usually called *displacement mapping*, and the heightfield is therefore called a *displacement texture* in this context. Using a texture allows for faster manipulation of data for wave simulations and other animations to apply to the mesh. These techniques can be expensive in both memory and in processing power, as each vertex in the mesh requires three additional floating-point numbers, all of which must be accessed (the less memory touched, the better). For large expanses (e.g., terrain or ocean rendering [703]), where level of detail techniques can be brought to bear to keep complexity down, such an approach can be suitable. See Section 12.5.2. With the evolution of GPUs towards unified shaders<sup>14</sup> and performing tessellation on the fly, the scale appears to be tipping towards this being the preferred method in general. It is simple to program and on newer GPUs has few drawbacks. We consider it likely that this will be the preferred method once the minimum GPU required for an application supports fast vertex texture access. Szirmay-Kalos and Umenhoffer [1235] have an excellent, thorough survey of relief mapping and displacement methods.

While relief and displacement mapping offer additional realism at a generally reasonable cost, these techniques do have some drawbacks. The fact that the base surface is unperturbed makes collision detection, and therefore object interaction, more challenging. For example, if a displacement map is used to model a rock protruding out of the ground, it will be additional work to have a character's foot properly stop at the correct height at this location. Instead of a simple test against a mesh, the mesh height will also need to be accessed.

Other surfaces than simple quadrilaterals can use displacement mapping. Its use with subdivision surfaces is discussed in Section 13.5.6. In

---

<sup>14</sup>The original vertex texture fetch was slow compared to the pixel shader's. With unified shaders there is no difference.

Section 13.6, we present hardware tessellation where displacement mapping also can be used.

## Further Reading and Resources

Heckbert has written a good survey of the theory of texture mapping [517] and a more in-depth report on the topic [518]; both are available on the web. Wolberg's book [1367] is another older but worthwhile work on textures, particularly in the areas of sampling and filtering. Watt's books [1330, 1331, 1332, 1333] are general texts on computer graphics that have more information about texturing.

Articles by Geiss [386] and Andersson [23] are excellent resources for ideas on using traditional and procedural textures to produce complex surface and terrain effects.

The book *Advanced Graphics Programming Using OpenGL* [849] has extensive coverage of various texturing algorithms. While RenderMan is meant for offline rendering, the *RenderMan Companion* [1283] has some relevant material on texture mapping and on procedural textures. For extensive coverage of three-dimensional procedural textures, see *Texturing and Modeling: A Procedural Approach* [295]. The book *Advanced Game Development with Programmable Graphics Hardware* [1334] has many details about implementing relief mapping techniques, as do Tatarchuk's presentations [1244, 1248].

Visit this book's website, <http://www.realtimerendering.com>, for many other resources.



# Chapter 7

## Advanced Shading

*“Let the form of an object be what it may, light, shade, and perspective will always make it beautiful.”*

—John Constable

The Gouraud shading model was invented in 1971 [435]. Phong’s specular highlighting equation was introduced around 1975 [1014]. The concept of applying textures to surfaces was presented a year later by Blinn and Newell [96]. As part of the standard fixed-function pipeline, these algorithms were the mainstay of graphics accelerators for years. The advent of programmable shaders has vastly increased the available options—modern GPUs can evaluate (almost) arbitrary shading models. This moves the focus from “what is possible?” to “what are the best choices for this application?”

An understanding of the underlying physical and psychological principles pertinent to rendering is important in navigating these choices. The previous chapters presented the technologies for controlling the graphics pipeline and the basic theory behind their use. In this chapter some of the scientific underpinnings of rendering are discussed. Radiometry is presented first, as this is the core field concerned with the physical transmission of light. Our perception of color is a purely psychological phenomenon, and is discussed in the section on colorimetry. A shading model is comprised of two main parts: the light source and the material model. Sections on both describe the various options that are available. The final sections detail methods for the efficient implementation of shading models.

The options covered in this chapter are limited by one basic assumption. Each light source is assumed to illuminate a surface location from one direction only—area, ambient, and environment lighting are not covered. Chapter 8 will describe the theory and practice necessary for the use of more general types of illumination.

## 7.1 Radiometry

The explanation of the example shading model in Chapter 5 included a brief discussion of some concepts from radiometry. Here we will go over those concepts in more depth, and introduce some new ones.

Radiometry deals with the measurement of electromagnetic radiation. Such radiation consists of a flow of *photons*, which behave as either particles or waves, depending on circumstance. Using the mental model of photons as particles works well for the most part. Although some physical phenomena cannot be modeled without accounting for the wave properties of photons,<sup>1</sup> these are usually ignored by even high-quality batch rendering systems [1089].

One wave-related property of photons that cannot be disregarded is the fact that each has an associated frequency or wavelength.<sup>2</sup> This is an important property, because the energy of each photon is proportional to its frequency, which affects interactions between photons and matter. Most importantly, it affects the interaction of photons with sensors such as the rods and cones in the human eye. Different frequencies of photons are perceived as light of different colors (or not perceived at all, if they are outside the limited range of human vision). The relationships between a photon's wavelength  $\lambda$  (in meters), frequency  $\nu$  (in Hertz, or cycles per second) and energy  $Q$  (in joules) are

$$\begin{aligned}\nu &= \frac{c}{\lambda}, \\ \lambda &= \frac{c}{\nu}, \\ Q &= h\nu,\end{aligned}\tag{7.1}$$

where  $c$  is the speed of light ( $2.998 \times 10^8$  meters/second) and  $h$  is Planck's constant ( $6.62620 \times 10^{-34}$  joule-seconds).

Electromagnetic radiation exists in a range of frequencies and energies, from ELF (extremely low frequency) radio waves to gamma rays. Photons with wavelengths between roughly 380 to 780 nanometers are perceptible to the human eye, so only this range, the *visible spectrum*, is typically used for rendering. Figure 7.1 shows the colors perceived for *monochromatic* (single-wavelength) light throughout the visible spectrum. Recall that photon energy is proportional to frequency: “bluer” photons are more energetic; “redder” photons are less energetic.

In this section, we will discuss the various radiometric units and their relationships. Their units are summarized in Table 7.1.

---

<sup>1</sup>These phenomena include polarization, interference, and diffraction.

<sup>2</sup>Quantum theory shows that each photon actually has a range of associated frequencies, but this fact can be ignored for rendering.

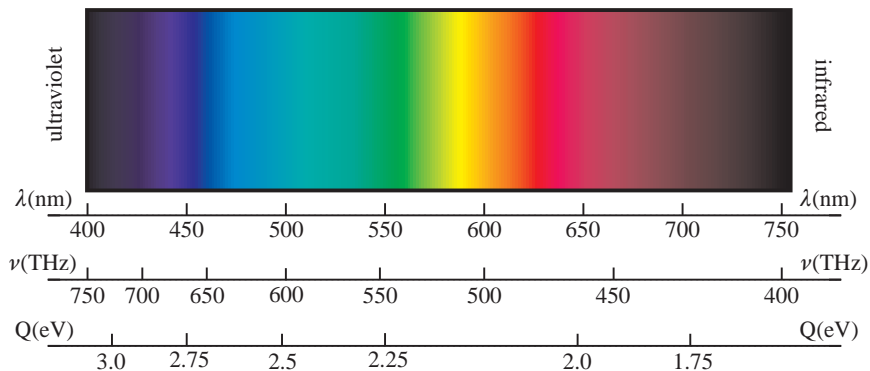


**Figure 7.1.** The visible spectrum. The top scale shows wavelength in nanometers, the middle scale shows frequency in terahertz ( $10^{12}$  Hertz), and the bottom scale shows photon energy in electron-volts (the amount of energy required to move a single electron over an electrical potential difference of one volt).

| Radiometric Quantity: Units                |
|--|
| radiant energy: joule (J)                  |
| radiant flux: watt (W)                     |
| irradiance: $\text{W}/\text{m}^2$          |
| radiant intensity: $\text{W}/\text{sr}$    |
| radiance: $\text{W}/(\text{m}^2\text{sr})$ |

**Table 7.1.** Radiometric quantities and units.

In radiometry, the basic unit is energy or *radiant energy*  $Q$ , measured in *joules* (abbreviated “J”). Each photon has some amount of radiant energy that, as we have seen, is proportional to its frequency. For example, at a wavelength of 550 nm, by Equation 7.1 there are  $2.77 \times 10^{18}$  photons per joule.

The *radiant flux* or *radiant power*,  $\Phi$  or  $P$ , of a light source is equal to the number of joules per second emitted (i.e.,  $dQ/dt$ ). The *watt* (W) is another term for joules per second. In principle, one can measure the radiant flux of a light source by adding up the energies of the photons it emits in a one-second time period. For example, a given light bulb may emit 100 watts of radiant flux (of which only part would be visible)—see the upper-left part of Figure 7.2.

*Irradiance* (briefly discussed in Chapter 5) is the density of radiant flux with respect to area (i.e.,  $d\Phi/dA$ ). Irradiance is defined with respect to a surface, which may be an imaginary surface in space, but is most often

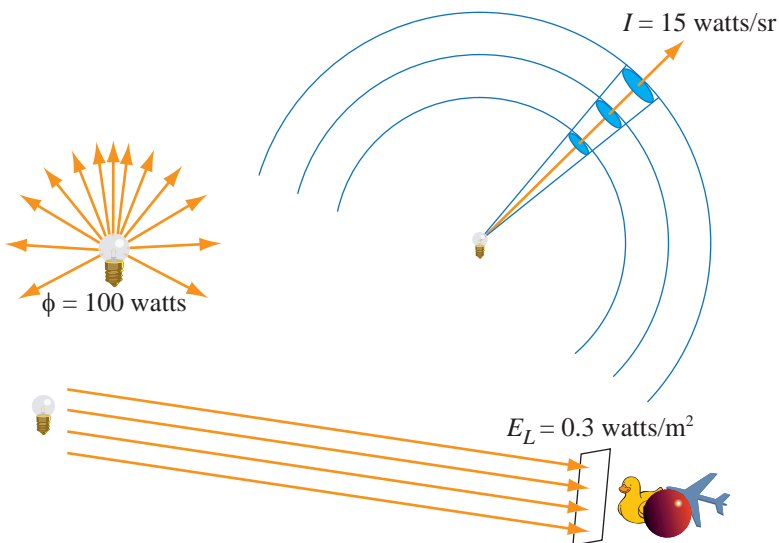


**Figure 7.2.** A light bulb. In the upper-left part of the figure, the light bulb's radiant flux of 100 watts is shown. In the lower part of the figure, the light bulb is illuminating a small scene from a distance, so that its irradiance contribution  $E_L$  (measured in a plane perpendicular to the light direction) is a constant 0.3 watts per square meter over the scene. In the upper-right part of the figure, the intensity of the light bulb is measured in a given direction as 15 watts per steradian.

the surface of an object. In photometry, presented in the next section, the corresponding quantity *illuminance* is what is measured by a light meter. As shown previously, *irradiance*  $E$  is used to measure light flowing into a surface and *exitance*  $M$  (also called *radiosity* or *radiant exitance*) is used to measure light flowing out of a surface. The general term *radiant flux density* is sometimes used to refer to both irradiance and exitance. Chapter 5 showed how to use irradiance to measure the illumination of an ideal directional light source. Such light sources are a useful approximation for situations where the distance to the light is much larger than the extent of the rendered scene—for example, a small pile of toys on the other side of the room from the light bulb (see the bottom part of Figure 7.2). The irradiance from the light bulb  $E_L$  (measured in a plane perpendicular to the light direction) is approximately constant over the scene (in this example, 0.3 watts per square meter—again, only part of this is visible radiation).

For closer light sources (or larger scenes),  $E_L$  varies with distance and cannot be treated as a constant. Imagine concentric spheres around the light bulb, starting at a distance much larger than the size of the bulb (see the upper-right side of Figure 7.2). Since the bulb is relatively small, we

assume that all its light is emitted from a point at its center. We want to examine the light emitted in a particular direction (the orange arrow), so we construct a narrow cone, its axis along this direction and its apex at the center of the bulb. Intersecting this cone with the spheres produces a sequence of patches, increasing in area proportionately to the square of their distance from the light. Since the radiant flux through the patches is the same, irradiance decreases by the same proportion:

$$E_L(r) \propto \frac{1}{r^2}. \quad (7.2)$$

The constant of proportionality in Equation 7.2 is a value that does not change with distance:

$$\begin{aligned} E_L(r) &= \frac{I}{r^2}, \\ I &= E_L(r)r^2. \end{aligned} \quad (7.3)$$

This quantity,  $I$ , is called *intensity* or *radiant intensity*. If the distance  $r$  equals 1, then intensity is the same as irradiance—in other words, intensity is flux density with respect to area on an enclosing radius-1 sphere. The significance of area on a radius-1 sphere can be seen from an analogy with the definition of radians: An angle is a set of directions in a plane, and its size in radians is equal to the length of the arc it intersects on an enclosing radius-1 circle. A *solid angle* is a three-dimensional extension of the concept—a continuous set of directions, measured with *steradians* (abbreviated “sr”), which are defined by patch area on a radius-1 sphere [409] (solid angle is represented by the symbol  $\omega$ ). From this, we can see that intensity is actually flux density with respect to solid angle ( $d\Phi/d\omega$ ), unlike irradiance, which is flux density with respect to area. Intensity is measured in watts per steradian.

The concept of a solid angle is sometimes difficult to grasp, so here is an analogy that may help. Solid angle has the same relationship to direction that surface area has to a surface location. Area is the size of a set of locations, and solid angle is the size of a set of directions.

Most light sources do not emit the same intensity in all directions. The light bulb in Figure 7.2 emits varying intensities of light in different directions, as can be seen from the density of arrows in the upper-left part of the figure. In the upper right, we see that the value of the light bulb’s intensity in the direction represented by the orange arrow is 15 watts per steradian.

In two dimensions, an angle of  $2\pi$  radians covers the whole unit circle. Extending this to three dimensions, a solid angle of  $4\pi$  steradians would cover the whole area of the unit sphere. The size of a solid angle of 1 steradian can be seen in Figure 7.3.

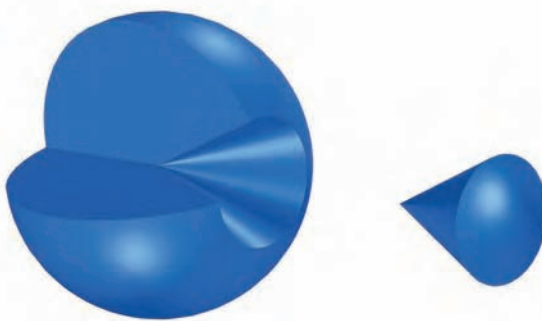


**Figure 7.3.** A cone with a solid angle of one steradian removed from a cutaway view of a sphere. The shape itself is irrelevant to the measurement; the coverage on the sphere’s surface is the key.

In the last few paragraphs, we assumed that the light source could be treated as a point. Light sources that have been approximated in this way are called *point lights*. Just as directional lights are a useful abstraction for lights that are far away compared to the size of the scene, point lights are a useful abstraction for light sources that are far away compared to the size of the light source. Intensity is useful for measuring the illumination of a point light source and how it varies with direction. As we have seen, the irradiance contribution from a point light varies inversely to the square of the distance between the point light and the illuminated surface. When is it reasonable to use this approximation? Lambert’s *Photometria* [716] from 1760 presents the “five-times” rule of thumb. If the distance from the light source is five times or more than that of the light’s width, then the inverse square law is a reasonable approximation and so can be used.

As seen in Section 5.4, radiance  $L$  is what sensors (such as eyes or cameras) measure, so it is of prime importance for rendering. The purpose of evaluating a shading equation is to compute the radiance along a given ray (from the shaded surface point to the camera). Radiance measures the illumination in a single ray of light—it is flux density with respect to both area and solid angle (see the left side of Figure 7.4). The metric units of radiance are watts per square meter per steradian. Radiance is

$$L = \frac{d^2\Phi}{dA_{\text{proj}} d\omega}, \quad (7.4)$$

where  $dA_{\text{proj}}$  refers to  $dA$  projected to the plane perpendicular to the ray.

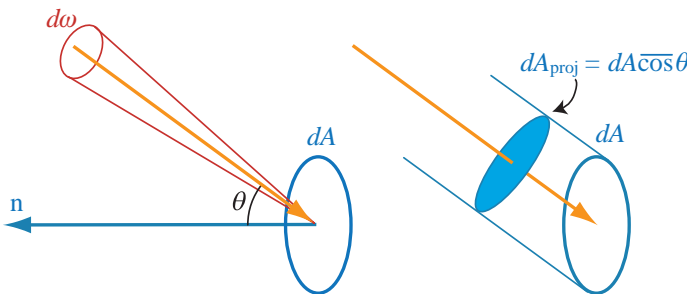


**Figure 7.4.** Radiance is power per unit projected area per unit solid angle.

The relationship between  $dA$  and  $dA_{\text{proj}}$  can be seen in the right side of Figure 7.4, where we see that the projection depends on the cosine of  $\theta$ , the angle between the ray and the surface normal  $\mathbf{n}$ :

$$dA_{\text{proj}} = dA \overline{\cos} \theta. \quad (7.5)$$

Note that Equation 7.5 uses the  $\overline{\cos}$  symbol (defined on page 8), which represents a cosine clamped to zero. Negative cosine values occur when the projected direction is behind the surface, in which case the projected area is 0.

A density with respect to two quantities simultaneously is difficult to visualize. It helps to think of radiance in relation to irradiance or intensity:

$$L = \frac{dI}{dA_{\text{proj}}} = \frac{dE_{\text{proj}}}{d\omega}, \quad (7.6)$$

where  $E_{\text{proj}}$  refers to irradiance measured in the plane perpendicular to the ray. Figure 7.5 illustrates these relationships.

The ray exiting the light bulb in the left side of Figure 7.5 has radiance  $L$ . In the middle of the figure we see the relationship between  $L$  and the irradiance  $E_{\text{proj}}$  from the light bulb (measured at a surface perpendicular to the ray). This irradiance is the flux density per area at a surface point—it represents photons hitting that point from all parts of the light bulb, covering a range of directions represented by the solid angle  $\omega$ . As seen in the right side of Equation 7.6, the radiance  $L$  is the density of  $E$  per solid angle. This is computed for a given direction by looking at only the irradiance contributed by photons arriving from a small solid angle  $d\omega$  around that direction and dividing that irradiance by  $d\omega$ .

On the right side of Figure 7.5 we arrive at radiance “the other way,” starting with intensity  $I$ . Intensity represents all photons from the light bulb going in a certain direction, from all parts of the light bulb, covering a

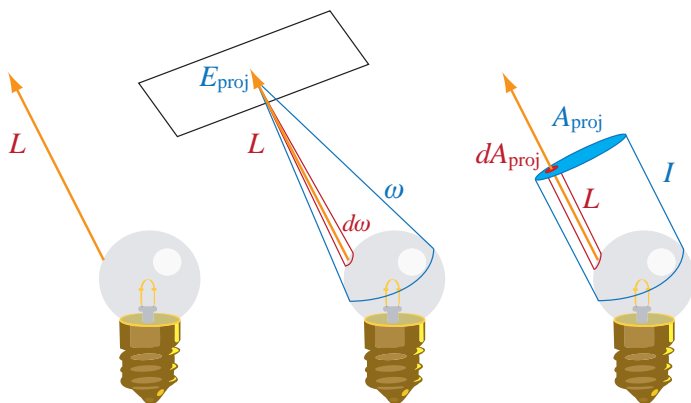


**Figure 7.5.** Radiance, radiance computed from irradiance, and radiance from intensity.

projected area  $A_{proj}$ . As seen in the left side of Equation 7.6, the radiance  $L$  is the density of  $I$  per area. This is computed for a given point by looking at only the intensity contributed by photons passing through a small area  $dA_{proj}$  around the given direction and dividing that irradiance by  $dA_{proj}$ .

The radiance in an environment can be thought of as a function of five variables (or six, including wavelength), called the *radiance distribution* [288]. Three of the variables specify a location, the other two a direction. This function describes all light traveling anywhere in space. One way to think of the rendering process is that the eye and screen define a point and a set of directions (e.g., a ray going through each pixel), and this function is evaluated at the eye for each direction. Image-based rendering, discussed in Section 10.4, uses a related concept, called the *light field*.

An important property of radiance is that it is not affected by distance (ignoring atmospheric effects such as fog). In other words, a surface will have the same radiance regardless of its distance from the viewer. At first blush, this fact is hard to reconcile with the idea that irradiance falls off with the square of the distance. What is happening physically is that the solid angle covered by the light's emitting surface gets smaller as distance increases. For example, imagine a light source that is square, say some fluorescent tubes behind a translucent panel. You are sufficiently far away to use the “five-times” rule. If you double your distance from the light, the number of photons from the light through a unit surface area goes down by a factor of four, the square of the distance. However, the radiance from any point on the light source is the same. It is the fact that the solid angle of the light source has dropped to about one quarter of its previous value, proportional to the overall drop in light level.

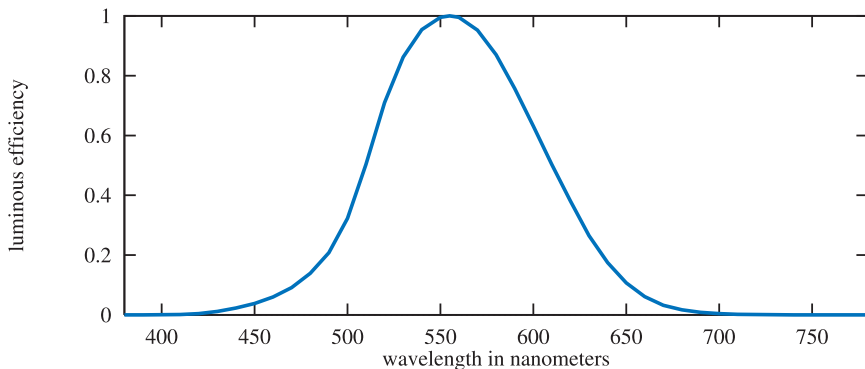


**Figure 7.6.** The photometric curve.

## 7.2 Photometry

Radiometry deals purely with physical quantities, without taking account of human perception. A related field, *photometry*, is like radiometry, except that it weights everything by the sensitivity of the human eye. The results of radiometric computations are converted to photometric units by multiplying by the *CIE photometric curve*,<sup>3</sup> a bell-shaped curve centered around 555 nm that represents the eye's response to various wavelengths of light [40, 409]. See Figure 7.6. There are many other factors—physical, psychological, and physiological—that can affect the eye's response to light, but photometry does not attempt to address these. Photometry is based on the average measured response of the human eye when the observer has adapted to normal indoor lighting conditions. The conversion curve and the units of measurement are the only difference between the theory of photometry and the theory of radiometry.

Photometry does not deal with the perception of color itself, but rather with the perception of brightness from light of various wavelengths. For example, green light appears considerably brighter to the eye than red or blue light.

Each radiometric quantity has an equivalent metric photometric quantity. Table 7.2 shows the names and units of each.

<sup>3</sup>The full and more accurate name is the “CIE photopic spectral luminous efficiency curve.” The word “photopic” refers to lighting conditions brighter than 3.4 candelas per square meter—twilight or brighter. Under these conditions the eye’s cone cells are active. There is a corresponding “scotopic” CIE curve, centered around 507 nm, that is for when the eye has become dark-adapted to below 0.034 candelas per square meter—a moonless night or darker. The eye’s rod cells are active under these conditions.

| <b>Radiometric Quantity: Units</b>        | <b>Photometric Quantity: Units</b>             |
|---|--|
| radiant energy: joule (J)                 | luminous energy: talbot                        |
| radiant flux: watt (W)                    | luminous flux: lumen (lm)                      |
| irradiance: $\text{W}/\text{m}^2$         | illuminance: lux (lx)                          |
| radiant intensity: $\text{W}/\text{sr}$   | luminous intensity: candela (cd)               |
| radiance: $\text{W}/\text{m}^2\text{-sr}$ | luminance: $\text{cd}/\text{m}^2 = \text{nit}$ |

**Table 7.2.** Radiometric and photometric quantities and units.

The units all have the expected relationships (lumens are talbots per second, lux is lumens per square meter, etc.). Although logically the talbot should be the basic unit, historically the candela was defined as a basic unit and the other units were derived from it. In North America, lighting designers measure illuminance using the deprecated Imperial unit of measurement, called the foot-candle (fc), instead of lux. In either case, illuminance is what most light meters measure, and it is important in illumination engineering.

Luminance is often used to describe the brightness of flat surfaces. For example, LCD screens typically range from 150 to 280 nits, and CRT monitors from 50 to 150 nits. In comparison, clear sky has a luminance of about 8000 nits, a 60-watt bulb about 120,000 nits, and the sun at the horizon 600,000 nits [1010].

## 7.3 Colorimetry

Light is perceived in the visible band, from 380 to 780 nanometers (nm). Light from a given direction consists of a set of photons in some distribution of wavelengths. This distribution is called the light's *spectrum*. See Figure 7.7 for an example.

Humans can distinguish about 10 million different colors. For color perception, the eye works by having three different types of cone receptors in the retina, with each type of receptor responding differently to various wavelengths.<sup>4</sup> So for a given spectrum, the brain itself then receives only three different signals from these receptors. This is why just three numbers can be used to precisely represent any spectrum seen [1225].

But what three numbers? A set of standard conditions for measuring color was proposed by the CIE (*Commission Internationale d'Eclairage*),

---

<sup>4</sup>Other animals can have from two to five different color receptors [418].

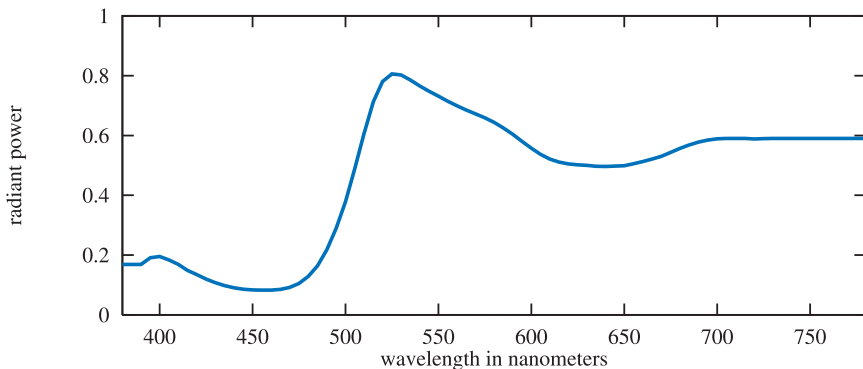


**Figure 7.7.** The spectrum for a ripe brown banana under white light [409].

and color matching experiments were performed using them. In color matching, three colored lights are projected on a white screen so that their colors add together and form a patch. A test color to match is projected next to this patch. The test color patch is of a single wavelength from the spectrum. The observer can then change the three colored lights using knobs calibrated to a range weighted  $[-1, 1]$  until the test color is matched. A negative weight is needed to match some test colors, and such a weight means that the corresponding light is added instead to the wavelength's test color patch. One set of test results for three

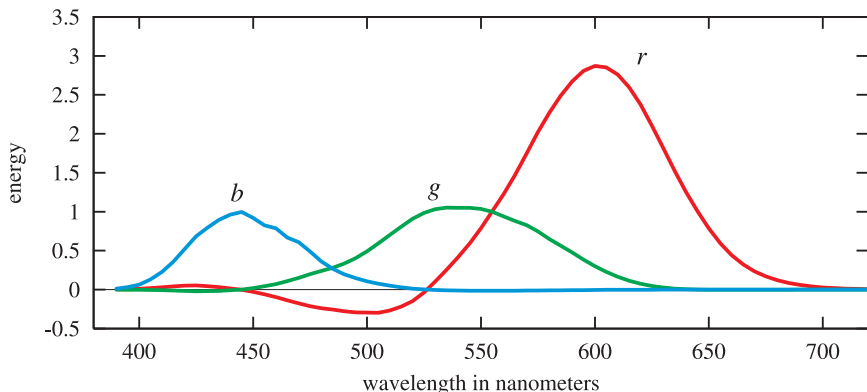


**Figure 7.8.** The  $r$ ,  $g$ , and  $b$  2-degree color matching curves, from Stiles & Burch (1955). Values are shown in terms of energy, not the  $[-1, 1]$  knob range. These color matching curves are not to be confused with the spectral distributions of the light sources used in the color matching experiment.

lights, called  $r$ ,  $g$ , and  $b$ , is shown in Figure 7.8. The lights were almost monochromatic, with the energy distribution of each narrowly clustered around one of the following wavelengths:  $r = 645$  nm,  $g = 526$  nm, and  $b = 444$  nm.

What these curves give is a way to convert a spectrum to three values. Given a single wavelength of light, the three colored light settings can be read off the graph, the knobs set, and lighting conditions created that will give an identical sensation from both patches of light on the screen. Given an arbitrary spectrum, these curves can be multiplied by the spectrum and the area under each resulting curve (i.e., the integral) gives the relative amounts to set the colored lights to match the perceived color produced by the spectrum. Very different spectra can resolve to the same three weights; in other words, they look the same to an observer. Matching spectra are called *metamers*.

The three weighted  $r$ ,  $g$ , and  $b$  values cannot directly represent all visible colors, as their color matching curves have negative weights for various wavelengths. The CIE proposed three different hypothetical light sources that did not use monochromatic light. These color matching curves are denoted  $\bar{x}(\lambda)$ ,  $\bar{y}(\lambda)$ , and  $\bar{z}(\lambda)$ , and their spectra are shown in Figure 7.9. The color matching function  $\bar{y}(\lambda)$  is, in fact, one and the same as the photometric curve (see page 209), as radiance is converted to luminance with this curve. Given a surface reflectance and light source, the product of these two defines a color function  $C(\lambda)$ , i.e., a spectrum. By again multiplying this spectrum by a color matching curve and integrating, a

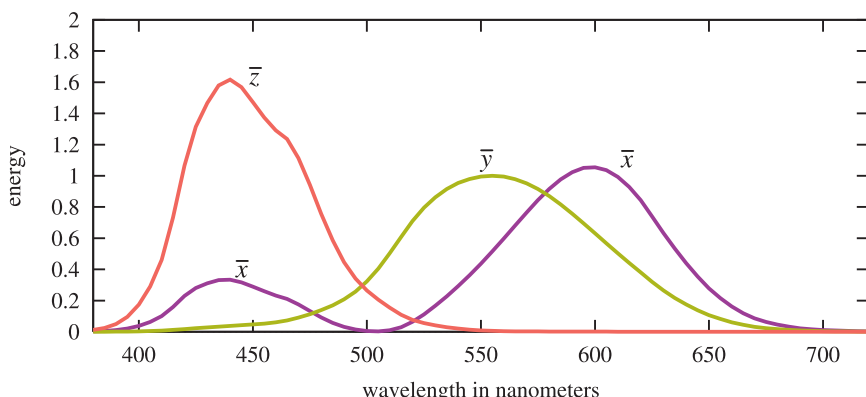


**Figure 7.9.** The Judd-Vos-modified CIE (1978) 2-degree color matching functions. Note that the two  $\bar{x}$ 's are part of the same curve. These color matching curves are not to be confused with the spectral distributions of the light sources used in the color matching experiment.

single value is computed for each curve:

$$\begin{aligned} X &= \int_{380}^{780} C(\lambda) \bar{x}(\lambda) d\lambda, \\ Y &= \int_{380}^{780} C(\lambda) \bar{y}(\lambda) d\lambda, \\ Z &= \int_{380}^{780} C(\lambda) \bar{z}(\lambda) d\lambda. \end{aligned} \quad (7.7)$$

These  $X$ ,  $Y$ , and  $Z$  *tristimulus values* are weights that define a color in CIE XYZ space. This three-dimensional space is awkward to work in, so the plane where  $X + Y + Z = 1$  is used. See Figure 7.10. Coordinates in this space are called  $x$  and  $y$ , and are computed as follows:

$$\begin{aligned} x &= \frac{X}{X + Y + Z}, \\ y &= \frac{Y}{X + Y + Z}, \\ z &= \frac{Z}{X + Y + Z} = 1 - x - y. \end{aligned} \quad (7.8)$$

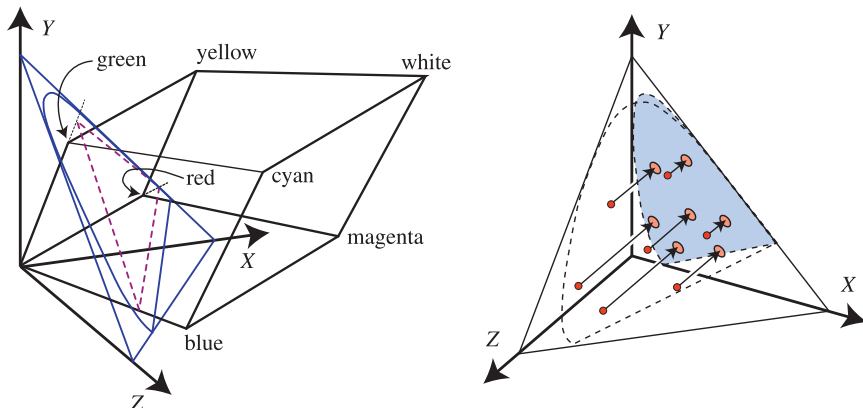


**Figure 7.10.** On the left, the RGB color cube is shown in XYZ space, along with its gamut projection (in violet) and chromaticity diagram (in blue) onto the  $X + Y + Z = 1$  plane. Lines radiating from the origin have a constant chromaticity value, varying only in luminance. On the right, seven points on the plane  $X + Y + Z = 1$ , and so in  $xyz$  coordinates, are projected onto the  $XY$  plane (by dropping the  $z$  value). The chromaticity diagram outline is shown for both planes, with the resulting diagram shown in gray.

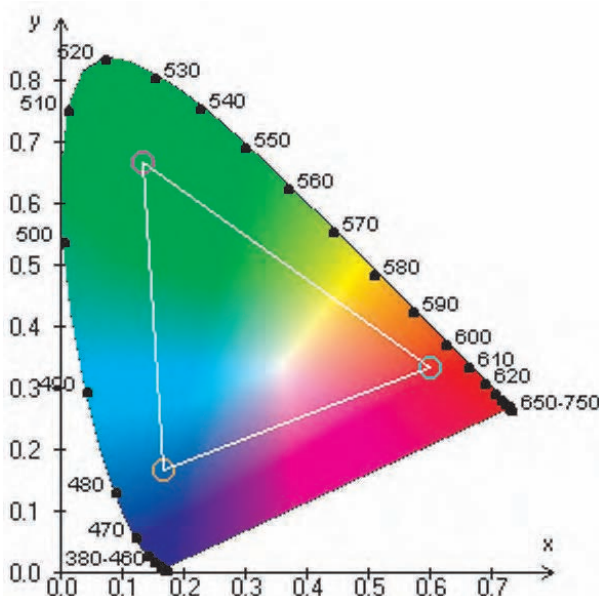


**Figure 7.11.** The chromaticity diagram. The curve is labeled with the corresponding pure wavelength colors, and a typical gamut is shown with the triangle. (Image generated by a Java applet from the Computer Science Department, Rochester Institute of Technology.)

The  $z$  value gives no additional information, so it is normally omitted. The plot of the *chromaticity coordinates*  $x$  and  $y$  values is known as the *CIE chromaticity diagram*. See Figure 7.11. The curved line in the diagram shows where the colors of the spectrum lie, and the straight line connecting the ends of the spectrum is called the *purple line*. Illuminant E, the equal energy spectrum, is often used to define white, at the point  $x = y = z = \frac{1}{3}$ . For a computer monitor, the *white point* is the combination of the three color phosphors at full intensity, i.e., the brightest white.

Given a color point  $(x,y)$ , draw a line from the white point through this point to the spectral line. The relative distance of the color point compared to the distance to the edge of the region is the *saturation* of the color. The point on the region edge defines the *hue* of the color.<sup>5</sup>

The chromaticity diagram describes a plane. The third dimension needed to fully describe a color is the  $Y$  value, luminance. These then define what is called the  $xyY$  coordinate system.

<sup>5</sup> *Saturation* and *hue* are the commonly used terms for these definitions. The proper colorimetric terms are *excitation purity* and *dominant wavelength*, but these are rarely used in graphics.

The chromaticity diagram is important in understanding how color is used in rendering, and the limits of the rendering system. A computer monitor presents colors by using some settings of  $R$ ,  $G$ , and  $B$  color values. Each color channel controls some physical phenomenon, e.g., exciting a phosphor, which in turn emits light in a particular spectrum. By exciting three phosphors, three spectra are emitted, which are added together and create a single spectrum that the viewer perceives. The eye's three types of cones also each have their own color matching functions, i.e., each cone responds to the incoming spectrum and sends a signal to the brain.

The display system is limited in its ability to present different colors by the spectra of its three channels. An obvious limitation is in luminance, as a computer monitor is only so bright, but there are also limits to saturation. As seen earlier, the  $r$ ,  $g$ , and  $b$  color matching system needed to have negative weights for some of the spectrum colors to be matched. These colors with negative weights are colors that could not be displayed by a combination of the three lights. Video displays and printers are limited in a similar fashion.

The triangle in the chromaticity diagram represents the *gamut* of a typical computer monitor. The three corners of the triangle are the most saturated red, green, and blue colors the monitor can display. An important property of the chromaticity diagram is that these limiting colors can be joined by straight lines to show the limits of the monitor as a whole. The straight lines represent the limits of colors that can be displayed by mixing these three primaries. See Stone's book [1224] for more information.

Conversion from  $XYZ$  to  $RGB$  space is linear and can be done with a matrix [287, 349]:

$$\begin{pmatrix} R \\ G \\ B \end{pmatrix} = \begin{pmatrix} 3.240479 & -1.537150 & -0.498535 \\ -0.969256 & 1.875992 & 0.041556 \\ 0.055648 & -0.204043 & 1.057311 \end{pmatrix} \begin{pmatrix} X \\ Y \\ Z \end{pmatrix}. \quad (7.9)$$

This conversion matrix is for a monitor with a D65 white point, a particular definition of the "full on" white color produced by the monitor. Some  $XYZ$  values can transform to  $RGB$  values that are negative or greater than one. These are colors that are out of gamut, not reproducible on the monitor. The inverse  $RGB$  to  $XYZ$  conversion is

$$\begin{pmatrix} X \\ Y \\ Z \end{pmatrix} = \begin{pmatrix} 0.412453 & 0.357580 & 0.180423 \\ 0.212671 & 0.715160 & 0.072169 \\ 0.019334 & 0.119193 & 0.950227 \end{pmatrix} \begin{pmatrix} R \\ G \\ B \end{pmatrix}. \quad (7.10)$$

A common conversion is to transform an  $RGB$  color to a grayscale luminance value, which is simply the middle row of the previous equation:

$$Y = 0.212671R + 0.715160G + 0.072169B. \quad (7.11)$$

A few words are in order about this equation. First, in older texts, it is often given as  $Y = 0.30R + 0.59G + 0.11B$ . Poynton [1028] discusses how this form is based on older NTSC phosphors; the equation given above is based on modern CRT and HDTV phosphors. This brings us full circle to the photometric curve shown on page 209. This curve, representing how a standard observer's eye responds to light of various wavelengths, is multiplied by the spectra of the three phosphors, and each resulting curve is integrated. The three resulting weights are what form the luminance equation above. The reason that a grayscale intensity value is not equal parts red, green, and blue is because the eye has a different sensitivity to various wavelengths of light.

The gamut affects the rendering process in a number of ways. The gamuts and white point locations of monitors vary, both because of the physical makeup and due to the adjustment of brightness and contrast, meaning that how a color looks on one monitor will not be the same as on another. The gamuts of printers differ more still from monitors, so that there are colors that can display well on one printer, but not another. Custom inks can be used to print outside the normal gamut, for both artistic effect and for creating items such as banknotes. Scanners also have a gamut of colors they can record, and so have similar mismatches and limitations. Monitor gamuts are always triangles, by the nature of how they produce colors. Film, print, and other media have gamuts that are roughly triangular, but with curved edges or other irregularities, due to the characteristics of the chemicals or inks used to capture color.

While any given spectrum can be precisely represented by an RGB triplet, it does not follow that using RGB colors for materials and lights is a precise basis for computations. In other words, multiplying two RGB colors to obtain an RGB result is not the same as multiplying two spectra together and then converting the resulting spectrum to RGB. As a simple thought experiment, imagine a light with a spectrum going from 550 to 700 nm, and a material that has a spectral response of 400 nm to 549 nm. Ignoring red and blue, these two spectra will each convert to RGB triplets that both have at least some positive green component. When these two RGB values are multiplied together, the green component in the result will also be positive. However, the spectra themselves, when multiplied together, yield an entirely black spectrum, which would have no green component. That said, while experiments have been done showing differences when spectra are used instead of RGBs, in practice multiplying RGBs together works surprisingly well [111].

The CIE XYZ system is useful for precise description, but there are many other color spaces with different strengths and uses. For example, CIELUV and CIELAB define color spaces that are more perceptually uniform [1225]. Color pairs that are perceptibly different by the same amount

can be up to 20 times different in distance in CIE XYZ space. CIELUV improves upon this, bringing the ratio down to a maximum of four times.

Other color systems common in computer graphics include HSB (*hue, saturation, brightness*) and HLS (*hue, lightness, saturation*) [349]. CMYK (*cyan, magenta, yellow, black*) is for the inks used in standard four-color printing. YUV is the color model used in many video standards, and represents luminance (Y) and two chroma values. YIQ is a similar color space used for NTSC television. Dawson [230] gives a good overview of color display and perception issues concerning real-time applications and television.

Though colorimetry has strong mathematical underpinnings, the basis is the perception of color by some set of observers under controlled conditions. Even under these conditions, observers' genetic, physical, and mental states affect results. In the real world, there are many more variables that affect human perception of a color patch, such as the lighting conditions, the surrounding colors, and past conditions. Some of these perceptual effects can be put to good use. For example, using red lettering on a blue background has long been a way to grab attention, because the blue surrounding color further accentuates the perceived brightness of the red. Another important effect for computer graphics is that of *masking* [341]. A high-frequency, high-contrast pattern laid on an object tends to hide flaws. In other words, a texture such as a Persian rug will help disguise color banding and other shading artifacts, meaning that less rendering effort needs to be expended for such surfaces.

This section has touched on only the basics of color science, primarily to bring an awareness of the relation of spectra to color triplets and to discuss the limitations of devices. Stone's book [1224] is a good place to learn about digital color. Glassner's *Principles of Digital Image Synthesis* [408, 409] discusses color theory and perception. Ferwerda's tutorial discusses vision research relevant to computer graphics [341]. Reinhard's recent book [1060] gives a thorough overview of the whole area of study.

## 7.4 Light Source Types

In real-world scenes, light sources can be natural (like the sun), or artificial. An artificial light source (such as a tungsten filament) is often paired with a housing that shapes the directional distribution of the emitted light (the combination of light source and housing is called a *luminaire*). In rendering it is common to model the luminaire as a light source with a directional distribution that implicitly models the effect of the housing.

Directional light sources were discussed in Chapter 5. Directional lights are the simplest model of a light source—they are fully described by 1 (their

world-space direction vector) and  $E_L$  (their irradiance contribution measured in a plane perpendicular to  $\mathbf{l}$ ). Recall that since  $E_L$  varies for different wavelengths, it is expressed as an RGB vector for rendering purposes.

In Section 7.1 point lights were introduced. Like directional lights, point lights are an approximation to real light sources. However the assumption used (that the distance between the light and the illuminated surfaces is large compared to the size of the light source) is much more likely to be applicable than the assumption underlying directional lights (that the distance between the light and the illuminated surfaces is large compared to the extents of the entire rendered scene). The sun is well modeled as a directional light source, and perhaps some artificial lights might be far enough away from the scene to be appropriately represented with directional lights as well, but most other light sources in a scene will probably be modeled as point lights.

In this chapter we discuss rendering with lights that are variants of directional and point lights. Although we will see many options for varying these lights, there is one thing they all have in common: At a given surface location, each light source illuminates the surface from one direction only. In other words, the light source covers a zero solid angle as seen from the surface point. This is not true for real-world lights, but in most cases the approximation is good enough. In Section 8.2 we will discuss light sources that illuminate a surface location from a range of directions.

### 7.4.1 Omni Lights

Point lights are defined by their position  $\mathbf{p}_L$  and intensity  $I_L$ . In general,  $I_L$  varies as a function of direction. Point lights with a constant value for  $I_L$  are known as *omni lights*. Like  $E_L$ ,  $I_L$  is also expressed as an RGB vector for rendering.

Shading equations (as we saw in Section 5.5) use the light vector  $\mathbf{l}$  and the irradiance contribution of the light  $E_L$  (measured in a plane perpendicular to  $\mathbf{l}$ ). These can be computed from  $I_L$  and  $\mathbf{p}_L$  using the following equations ( $\mathbf{p}_S$  is the surface position):

$$\begin{aligned} r &= \|\mathbf{p}_L - \mathbf{p}_S\|, \\ l &= \frac{\mathbf{p}_L - \mathbf{p}_S}{r}, \\ E_L &= \frac{I_L}{r^2}. \end{aligned} \tag{7.12}$$

Although  $E_L$  decreasing proportionally to  $1/r^2$  is physically correct for a point light, it is often preferable to use a different function to describe how  $E_L$  decreases with distance. Such functions are called *distance falloff*

*functions.* This generalizes the last line in Equation 7.12 to the following:

$$E_L = I_L f_{\text{dist}}(r). \quad (7.13)$$

Various distance falloff functions have been in use in computer graphics for many years. There are various reasons for using a function other than an inverse square falloff. Alternate falloff functions can provide more control for lighting the scene to achieve a particular desired appearance. An inverse square function gets near to 0 with distance, but never quite reaches 0. Falloff functions that reach a value of 0 at a particular distance can enable better performance, since the effect of the light on any objects beyond this distance can be ignored. Unlike inverse square falloff, which gets arbitrarily large when close to the light source, most falloff functions used in graphics have a finite value close to the light source. This avoids the (problematic) need to handle arbitrarily large numbers during shading.

One historically important falloff function is part of the OpenGL and DirectX fixed-function pipelines:

$$f_{\text{dist}}(r) = \frac{1}{s_c + s_l r + s_q r^2}, \quad (7.14)$$

where  $s_c$ ,  $s_l$  and  $s_q$  are properties of the light source. This falloff function was historically not applied to physical values of  $E$  or  $I$ , but to non-physical lighting values (typically limited to a 0 to 1 range). Using this function, physically correct inverse square falloff, as well as other effects, can be achieved. This function does have the drawback of never reaching 0.

A much simpler distance falloff function is often used in games and graphical modeling applications:

$$f_{\text{dist}}(r) = \begin{cases} 1, & \text{where } r \leq r_{\text{start}}, \\ \frac{r_{\text{end}} - r}{r_{\text{end}} - r_{\text{start}}}, & \text{where } r_{\text{start}} < r < r_{\text{end}}, \\ 0, & \text{where } r \geq r_{\text{end}}, \end{cases} \quad (7.15)$$

where  $r_{\text{start}}$  and  $r_{\text{end}}$  are properties of the light source. This falloff function is easy to control and does reach 0 (at  $r_{\text{end}}$ ).

A distance falloff function used by Pixar in film rendering is described in Barzel's 1997 paper [70]:

$$f_{\text{dist}}(r) = \begin{cases} f_{\text{max}} e^{k_0(r/r_c)^{-k_1}}, & \text{where } r \leq r_c, \\ f_c \left(\frac{r_c}{r}\right)^{s_e}, & \text{where } r > r_c. \end{cases} \quad (7.16)$$

This function reaches a desired value  $f_c$  at a specific distance  $r_c$ . At distances closer than  $r_c$  it gradually approaches a maximum value  $f_{\text{max}}$ . The

falloff exponent  $s_e$  controls how gradually the function decreases with distances greater than  $r_c$ . The constants  $k_0$  and  $k_1$  are set to specific values to ensure a continuous derivative at the transition point:  $k_0 = \ln(f_c/f_{\max})$  and  $k_1 = s_e/k_0$ . This falloff function does not reach 0 and is expensive to compute. An interesting note in Barzel's paper [70] is that, in film rendering, ad hoc near and far cutoffs are used more often than falloff functions such as the one in Equation 7.16.

Various other falloff functions are used in real-time rendering applications, motivated by the need for fine control and fast evaluation.

### 7.4.2 Spotlights

Unlike omni lights, real light sources have directional variance in their intensity. Different visual effects can be produced using different functions to describe how  $I_L$  varies with direction. One important type of effect is the *spotlight*. Historically, these have been featured in the OpenGL and DirectX fixed-function pipelines, which use functions based on the cosine of the angle  $\theta_s$  between a vector  $\mathbf{s}$  denoting the direction of the spotlight, and the reversed light vector  $-\mathbf{l}$  to the surface. The light vector needs to be reversed because we define it at the surface as pointing towards the light, and here we need a vector pointing away from the light. See Figure 7.12.

The spotlight function used in the OpenGL fixed-function pipeline is

$$I_L(\mathbf{l}) = \begin{cases} I_{L_{\max}} (\cos \theta_s)^{s_{\text{exp}}}, & \text{where } \theta_s \leq \theta_u, \\ 0, & \text{where } \theta_s > \theta_u. \end{cases} \quad (7.17)$$

The function in Equation 7.17 tapers to 0 as the angle between the light direction and  $\mathbf{s}$  increases. The tightness of the spotlight is controlled by

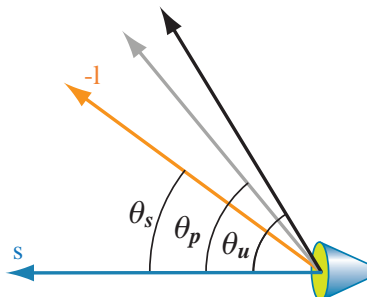


**Figure 7.12.** A spotlight.  $\theta_s$  is the angle from the light's defined direction  $\mathbf{s}$  to the vector  $-\mathbf{l}$ , the direction to the surface.  $\theta_p$  shows the penumbra and  $\theta_u$  the umbra angles defined for the light. Beyond the umbra angle the spotlight has no effect.

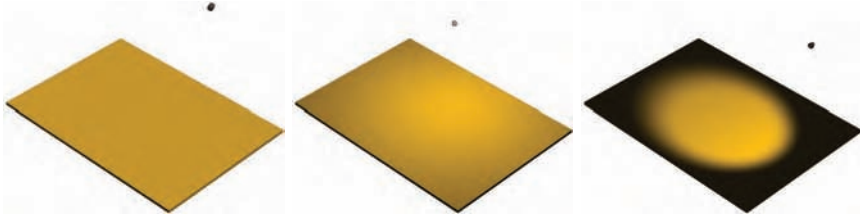


**Figure 7.13.** Some types of lights: directional, omni with no falloff, and spotlight with a smooth transition.

the spotlight's exponent property,  $s_{\text{exp}}$ . An abrupt cutoff can be specified by setting the cutoff angle  $\theta_u$  to be less than  $90^\circ$  (this equation does not allow for values of  $\theta_u$  greater than  $90^\circ$ ).<sup>6</sup> We call  $\theta_u$  the *umbra angle*, the angle at which the intensity reaches 0. The value  $\cos \theta_s$  is computed as  $s \cdot -1$ . Note that unlike most cosines in this chapter, all the cosine factors used in the spotlight equations happen to be unclamped (so cosine is used rather than  $\overline{\cos}$ ).

The exponent and cutoff behavior in the DirectX fixed-function pipeline is more flexible:

$$I_L(l) = \begin{cases} I_{L_{\max}}, & \text{where } \cos \theta_s \geq \cos \theta_p, \\ I_{L_{\max}} \left( \frac{\cos \theta_s - \cos \theta_u}{\cos \theta_p - \cos \theta_u} \right)^{s_{\text{exp}}}, & \text{where } \cos \theta_u < \cos \theta_s < \cos \theta_p, \\ 0, & \text{where } \cos \theta_s \leq \cos \theta_u. \end{cases} \quad (7.18)$$

The angle  $\theta_p$  defines the *penumbra angle* of the spotlight, or the angle at which its intensity starts to decrease. The idea is to create three zones: an inner cone, where the light's intensity is constant; between inner and outer cones, where the intensity drops off in some fashion; and beyond the outer cone, where the light has no effect. Unlike the spotlight function in Equation 7.17, this function allows for umbra and penumbra angles up to  $180^\circ$ , as long as  $\theta_p \leq \theta_u$ . Figure 7.13 shows some light types.

Other spotlight functions can of course be used. For example, the function between the inner and outer cones could be an S-curve, so providing continuity between the two cones. Functions can also vary with radial angle, and can vary over time, e.g., to produce a flickering torch. Real-world lights have more complex curves describing their behavior. An interesting description of a system that measures intensity distributions from real light sources and applies them to rendering can be found in Verbeck and Greenberg's article [1301].

<sup>6</sup>The OpenGL fixed-function pipeline does allow  $\theta_u = 180^\circ$  as a special value that disables spotlight functionality completely.

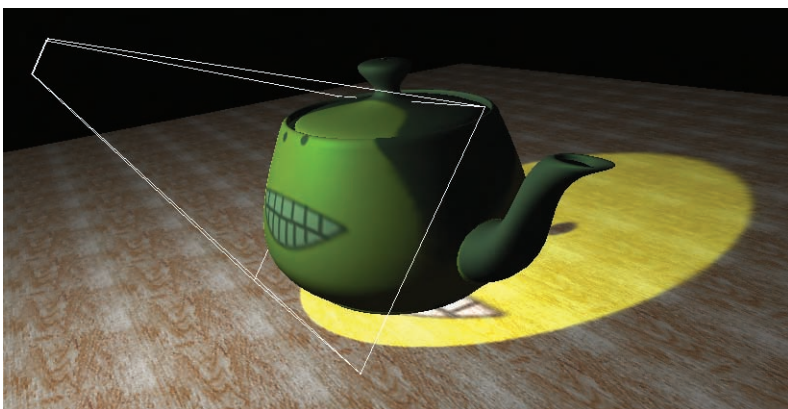


**Figure 7.14.** Projective textured light. The texture is projected onto the teapot and ground plane and used to modulate the light’s contribution within the projection frustum (it is set to 0 outside the frustum). (*Image courtesy of NVIDIA Corporation.*)

### 7.4.3 Textured Lights

Textures can be used to add visual richness to light sources and allow for complex intensity distribution or spotlight functions. For lights that have all their illumination limited to a cone or frustum, projective textures can be used to modulate the light intensity [849, 1146, 1377]. This allows for shaped spotlights, patterned lights, and even “slide projector” effects (Figure 7.14). These lights are often called *gobo* or *cookie* lights, after the terms for the cutouts used in professional theater and film lighting. See Section 9.1.2 for a discussion of projective mapping being used in a similar way to cast shadows.

For lights that are not limited to a frustum but illuminate in all directions, a cube map can be used to modulate the intensity, instead of a two-dimensional projective texture. One-dimensional textures can be used to define arbitrary distance falloff functions. Combined with a two-dimensional angular attenuation map, this can allow for complex volumetric lighting patterns [256]. A more general possibility is to use three-dimensional (volume) textures to control the light’s falloff [256, 401, 849]. This allows for arbitrary volumes of effect, including light beams. This technique is memory intensive (as are all volume textures). If the light’s volume of effect is symmetrical along the three axes, the memory footprint can be reduced eightfold by mirroring the data into each octant.

Textures can be added to any light type to enable additional visual effects. Textured lights allow for easy control of the illumination by artists, who can simply edit the texture used.

## 7.4.4 Other Light Sources

Many other lighting options are possible. As long as the shader has  $\mathbf{l}$  and  $E_L$  values for use in evaluating the shading equation, any method can be used to compute those values. An interesting example of a powerful and flexible light source model used in film rendering is given by Barzel [70]. This light source (called an *uberlight*) is perhaps a bit too costly for most real-time applications, but it shows the variety of useful effects that can be achieved. Pellacini and Vidimče [995] discuss GPU implementations of Barzel’s uberlight, as well as other lighting effects.

# 7.5 BRDF Theory

Section 5.5 described a shading equation for simulating the interaction of light with a surface. This equation is just one of many possible shading equations that can be used. In this section we will explain the theory behind such equations, go over some of the more interesting possibilities, and finally discuss implementation issues.

## 7.5.1 The BRDF

When shading a surface, the outgoing radiance in a given direction is computed, given quantities and directions of incoming light. In radiometry, the function that is used to describe how a surface reflects light is called the *bidirectional reflectance distribution function* (BRDF) [932]. As its name implies, it is a function that describes how light is reflected from a surface given two directions—the incoming light direction  $\mathbf{l}$  and outgoing view direction  $\mathbf{v}$ .

The precise definition of the BRDF is the ratio between differential outgoing radiance and differential irradiance:

$$f(\mathbf{l}, \mathbf{v}) = \frac{dL_o(\mathbf{v})}{dE(\mathbf{l})}. \quad (7.19)$$

To understand what this means, imagine that a surface is illuminated by light incoming from a tiny solid angle (set of directions) around  $\mathbf{l}$ . This illumination is measured at the surface as irradiance  $dE$ . The surface then reflects this light in various directions. In any given outgoing direction  $\mathbf{v}$ , the radiance  $dL_o$  is proportional to the irradiance  $dE$ . The ratio between the two, which depends on  $\mathbf{l}$  and  $\mathbf{v}$ , is the BRDF. The value of the BRDF depends also on wavelength, so for rendering purposes it is represented as an RGB vector.

The discussion in this chapter is restricted to shading with non-area light sources such as point or directional lights. In this case, the BRDF

definition can be expressed in a non-differential form:

$$f(\mathbf{l}, \mathbf{v}) = \frac{L_o(\mathbf{v})}{E_L \cos \theta_i}, \quad (7.20)$$

where  $E_L$  is the irradiance of a light source measured in a plane perpendicular to the light direction vector  $\mathbf{l}$ , and  $L_o(\mathbf{v})$  is the resulting outgoing radiance in the direction of the view vector  $\mathbf{v}$ . The clamped cosine of the angle  $\theta_i$  between  $\mathbf{l}$  and the surface normal  $\mathbf{n}$  converts  $E_L$  to irradiance measured at the surface. It is now straightforward to see how the BRDF fits into a general shading equation with  $n$  non-area lights:

$$L_o(\mathbf{v}) = \sum_{k=1}^n f(\mathbf{l}_k, \mathbf{v}) \otimes E_{L_k} \cos \theta_{i_k}, \quad (7.21)$$

where  $k$  is the index for each light.

The  $\otimes$  symbol (piecewise vector multiply) is used, since both the BRDF and irradiance are RGB vectors. Since the incoming and outgoing directions each have two degrees of freedom (a common parameterization is to use two angles: elevation  $\theta$  relative to the surface normal and rotation  $\phi$  about the normal), the BRDF is a function of four scalar variables in the general case. *Isotropic* BRDFs are an important special case. Such BRDFs remain the same when the incoming and outgoing direction are rotated around the surface normal (keeping the same relative angles between them). Isotropic BRDFs are functions of three scalar variables. Figure 7.15 shows the variables used in both cases.

The BRDF is defined as radiance (power/(area  $\times$  solid angle)) divided by irradiance (power/area), so its units are inverse solid angle, or steradians $^{-1}$ . Intuitively, the BRDF value is the relative amount of energy reflected in the outgoing direction, given the incoming direction.

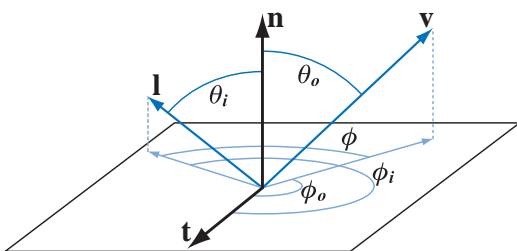


**Figure 7.15.** The BRDF. Azimuth angles  $\phi_i$  and  $\phi_o$  are given with respect to a given tangent vector  $\mathbf{t}$ . The relative azimuth angle  $\phi$  (used for isotropic BRDFs instead of  $\phi_i$  and  $\phi_o$ ) does not require a reference tangent vector.

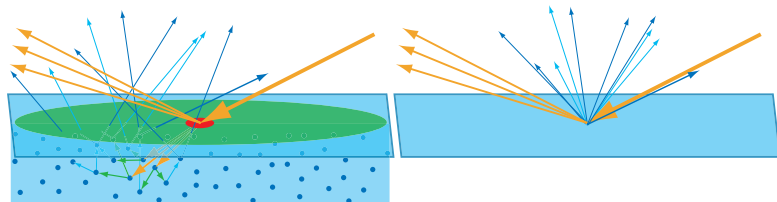


**Figure 7.16.** Light interacting with a surface. On the left, we see the subsurface interactions causing light to be re-emitted away from the entry point. The red and green circles represent the region covered by a pixel at two different scales of observation. On the right, all subsurface scattered light is shown emitting from the entry point—the details of what happens under the surface are ignored.

The BRDF abstracts how light interacts with an object. Section 5.3 discussed the various phenomena that occur: Some light is scattered into the surface (refraction or transmission), and some light is scattered away (reflection). In addition, the light transmitted into the object may undergo absorption and additional scattering, eventually causing some of it to exit the surface—a phenomena called *subsurface scattering*. The left side of Figure 7.16 shows these various types of light-matter interactions.

Figure 7.16 also contains two colored circles that show the areas covered by a pixel in two cases. The red circle represents a case where the area covered by a pixel is small compared to the distance between the entry and exit locations of the subsurface scattered light. In this case, a BRDF cannot be used to describe the subsurface scattering; instead a more general equation must be used. This equation is the *bidirectional surface scattering reflectance distribution function* (BSSRDF) [932]. The general BSSRDF encompasses large-scale subsurface scattering by adding incoming and outgoing locations as inputs to the function. The BSSRDF describes the relative amount of light that travels along the incoming direction, then from one point to the other of the surface, then along the outgoing direction. Techniques for rendering objects that exhibit large-scale subsurface scattering will be discussed in Section 9.7.

The green circle in the left side of Figure 7.16 represents a case where each pixel covers a larger area (perhaps the camera is farther away). In this case, the pixel coverage is large, compared to the scale at which the subsurface scattering occurs. At this scale reflection, refraction and subsurface scattering can be approximated as happening at a single point, as seen in the right side of the figure.

This approximation enables modeling all the light interaction—including subsurface scattering—with a BRDF. Whether a BRDF can be used depends both on the surface material (for example, subsurface scattering occurs over larger distances in wax than in marble) and on the scale of ob-

servation (for example, rendering a close-up of the face of a marble statue versus a long shot of the entire statue). The original derivation of the BRDF as an approximation of the BSSRDF [932] defined the BRDF as a property of uniform surfaces, where the BRDF was assumed to be the same over the surface. Objects in the real world (and in rendered scenes) rarely have uniform material properties over their surface; even an object that is composed of a single material (e.g., a solid gold statue) will have variations in surface roughness, corroded and dirty spots, etc., which will cause its visual properties to change from one surface point to the next. A function that captures BRDF variation based on spatial location is called a *spatially varying BRDF* (SVBRDF) or *spatial BRDF* (SBRDF). Even the general BSSRDF, as complex as it is, still omits variables that can be important in the physical world, such as the polarization of the light [1089]. Also, transmission of light through a surface is not handled, only reflection [409]. To handle transmission, two BRDFs and two BTDFs (“T” for “transmittance”) are defined for the surface, one for each side, and so make up the BSDF (“S” for “scattering”). In practice, these more complex functions are rarely needed, and a BRDF or SVBRDF is sufficient to model most surface behavior.

### *BRDF Characteristics*

The laws of physics impose two constraints on any BRDF. The first constraint is *Helmholtz reciprocity*, which means that the input and output angles can be switched and the function value will be the same:

$$f(\mathbf{l}, \mathbf{v}) = f(\mathbf{v}, \mathbf{l}). \quad (7.22)$$

In practice, BRDFs used in rendering often violate Helmholtz reciprocity without noticeable artifacts. However, it is a useful tool to use when determining if a BRDF is physically plausible.

The second constraint is conservation of energy—the outgoing energy cannot be greater than the incoming energy (not counting glowing surfaces that emit light, which are handled as a special case). Certain offline rendering algorithms (e.g., some kinds of ray tracing) require energy conservation. For real-time rendering, strict energy conservation is not necessary, but approximate energy conservation is desirable. A surface rendered with a BRDF that grossly violates energy conservation might look much too bright, decreasing realism.

The *directional-hemispherical reflectance*  $R(\mathbf{l})$  is a function related to the BRDF. It can be used to measure to what degree a BRDF is energy-conserving. Despite its somewhat daunting name, the directional-hemispherical reflectance is a simple concept. It measures the amount of light coming from a given direction that is reflected at all, regardless of outgoing direction. Essentially, it measures energy loss for a given incoming

direction. The input to this function is the incoming direction vector  $\mathbf{l}$ , and its definition is the ratio between differential exitance and differential irradiance, as shown in Equation 7.23:

$$R(\mathbf{l}) = \frac{dB}{dE(\mathbf{l})}. \quad (7.23)$$

Since the discussion is restricted to non-area light sources in this chapter, a simpler, non-differential definition can be used:

$$R(\mathbf{l}) = \frac{M}{E_L \cos \theta_i}, \quad (7.24)$$

where  $E_L$  is the irradiance of a light source measured in a plane perpendicular to the light direction vector  $\mathbf{l}$ , and  $M$  is the resulting exitance (recall that exitance is the same as irradiance, but for outgoing light).

The value of the directional-hemispherical reflectance  $R(\mathbf{l})$  must always be between 0 and 1 (as a result of energy conservation). A reflectance value of 0 represents a case where all the incoming light is absorbed or otherwise lost. If all of the light is reflected, the reflectance will be 1. In most cases it will be somewhere between these two values. Like the BRDF, the values of  $R(\mathbf{l})$  vary with wavelength, so it is represented as an RGB vector for rendering purposes. Since each component (R, G and B) is restricted to lie between 0 and 1, a value of  $R(\mathbf{l})$  can be thought of as a regular color. Note that this restriction does not apply to the values of the BRDF! As a distribution function, the BRDF can have arbitrarily high values in certain directions (such as the center of a highlight) if the distribution it describes is highly non-uniform.

The directional-hemispherical reflectance is closely related to the BRDF. The relationship between them is presented in Equation 7.25:

$$R(\mathbf{l}) = \int_{\Omega} f(\mathbf{l}, \mathbf{v}) \cos \theta_o d\omega_o. \quad (7.25)$$

The  $\Omega$  subscript on the integral sign means that the integral is performed over the hemisphere above the surface (centered on the surface normal  $\mathbf{n}$ ). Equation 7.25 says that the directional-hemispherical reflectance for a given incoming direction  $\mathbf{l}$  is equal to the BRDF times the cosine of the angle between  $\mathbf{n}$  and  $\mathbf{v}$ , integrated over all possible outgoing directions in the hemisphere. Clamping the cosine to positive values is not necessary here, since the integration is only performed over the region where the cosine is positive. Section 8.1 contains further discussion of hemispherical integrals.

The requirement for a BRDF to be energy conserving is simply that  $R(\mathbf{l})$  be no greater than one for all possible values of  $\mathbf{l}$ .

The simplest possible BRDF is Lambertian. The Lambertian BRDF has a constant value (the cosine factor that distinguishes Lambertian shading is

not part of the BRDF—see Equation 7.21). Lambertian BRDFs are often used (usually in conjunction with other BRDF terms) in real-time rendering to represent subsurface scattering. The directional-hemispherical reflectance of a Lambertian surface is also a constant. Evaluating Equation 7.25 for a constant value of  $f(\mathbf{l}, \mathbf{v})$  gives us the following constant value for the directional-hemispherical reflectance as a function of the BRDF:

$$R(\mathbf{l}) = \pi f(\mathbf{l}, \mathbf{v}). \quad (7.26)$$

The constant reflectance value of a Lambertian BRDF is commonly referred to as the *diffuse color*  $\mathbf{c}_{\text{diff}}$ . Isolating the BRDF from Equation 7.26 gives us the following result:

$$f(\mathbf{l}, \mathbf{v}) = \frac{\mathbf{c}_{\text{diff}}}{\pi}. \quad (7.27)$$

The  $1/\pi$  factor results from the fact that integrating a cosine factor over the hemisphere yields a value of  $\pi$ . Such factors are common in BRDFs. Note that if we plug the Lambertian BRDF into the shading equation shown in Equation 7.21, we get

$$L_o(\mathbf{v}) = \frac{\mathbf{c}_{\text{diff}}}{\pi} \otimes \sum_{k=1}^n E_{L_k} \overline{\cos} \theta_{i_k}. \quad (7.28)$$

The version of this equation typically used in real-time rendering applications lacks the  $1/\pi$  term. This is because real-time applications typically factor this term into the light's irradiance (effectively using  $E_{L_k}/\pi$  as the light property indicating color and brightness, instead of  $E_{L_k}$ ). This has the dual advantages of moving the divide operation out of the shader and making the shading equation simpler to read. However, this means that care must be taken when adapting BRDFs from academic papers for use in real-time shading equations—usually the BRDF will need to be multiplied by  $\pi$  before use.

One way to understand a BRDF is to visualize it with the input direction held constant. See Figure 7.17. For a given direction of incoming light, the BRDFs values are displayed for all outgoing directions. The spherical part around the point of intersection is the diffuse component, since outgoing radiance has an equal chance of reflecting in any direction. The ellipsoidal piece is a *reflectance lobe*, and is from the specular component. Naturally, such lobes are in the reflection direction from the incoming light, with the thickness of the lobe corresponding to the fuzziness of the reflection. By the principle of reciprocity, these same visualizations can also be thought of as how much each different incoming light direction contributes to a single outgoing direction.

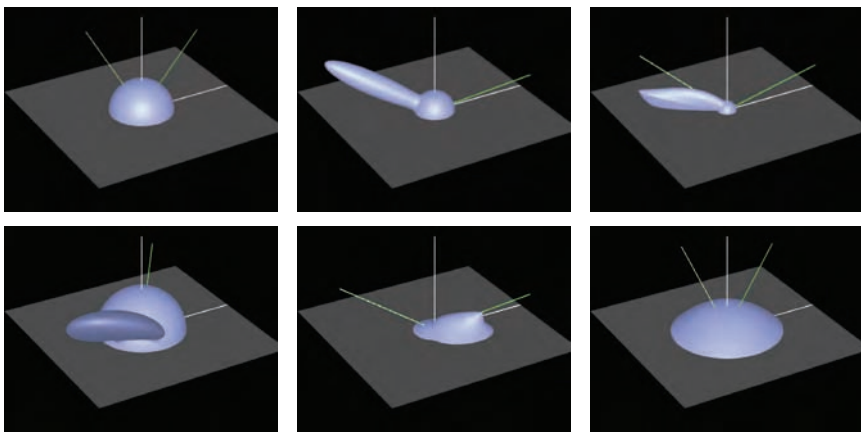


**Figure 7.17.** Example BRDFs. The solid green line coming from the right of each figure is the incoming light direction, and the dashed green and white line is the ideal reflection direction. In the top row, the left figure shows a Lambertian BRDF (a simple hemisphere). The middle figure shows Blinn-Phong highlighting added to the Lambertian term. The right figure shows the Cook-Torrance BRDF [192, 1270]. Note how the specular highlight is not strongest in the reflection direction. In the bottom row, the left figure shows a close-up of Ward’s anisotropic model. In this case, the effect is to tilt the specular lobe. The middle figure shows the Hapke/Lommel-Seeliger “lunar surface” BRDF [501], which has strong retroreflection. The right figure shows Lommel-Seeliger scattering, in which dusty surfaces scatter light toward grazing angles. (*Images courtesy of Szymon Rusinkiewicz, from his “bv” BRDF browser.*)

## 7.5.2 Surface and Body Reflectance

To choose BRDFs for rendering, it is useful to understand the behavior of light when interacting with real-world objects. To have a clear mental model of this interaction, it is important to differentiate between the phenomena that occur at the object’s infinitely thin surface, and those occurring under the surface, in the object’s interior (this distinction was briefly discussed in Section 5.3). When using BRDF representations, surface phenomena are simulated as *surface reflectance*, and interior phenomena are modeled as *body reflectance* (the term *volume reflectance* is also sometimes used). The surface is an optical discontinuity, and as such scatters light (causes it to change direction) but does not absorb any; all incoming light is either reflected or transmitted. The object’s interior contains matter, which may absorb some of the light. It may also contain additional optical discontinuities that will further scatter the light (subsurface scattering).<sup>7</sup>

---

<sup>7</sup>Note that although optical discontinuities require matter, the converse is not true; a liquid or solid with perfectly uniform density contains no optical discontinuities. Light travels through such an object without undergoing any scattering, although absorption may occur.

This is why it is meaningful to talk about surface transmission and refraction even in highly absorptive materials. Absorption occurs under the surface, perhaps very close to it, but never at the surface itself. Surface reflectance is typically modeled with specular BRDF terms—body reflectance is modeled with diffuse terms.

### 7.5.3 Fresnel Reflectance

An object’s surface is an interface between two different substances: air and the object’s substance. The interaction of light with a planar interface between two substances follows the *Fresnel equations* developed by Augustin-Jean Fresnel (pronounced freh-nel) in the 19th century. In theory, the Fresnel equations require a perfect plane, which of course is not possible in a real surface. Even if the surface is perfectly flat at the atomic level (very difficult to achieve!) the atoms themselves form “bumps.” In practice, any irregularities much smaller than the smallest light wavelength (about 400 nanometers in the case of visible light) have no effect on the light, so a surface that possesses only such irregularities can be considered a perfect plane for optical purposes. In Section 7.5.6 we will see how to apply Fresnel reflectance to rougher surfaces. Note that Fresnel reflectance is strictly a surface reflectance phenomenon, independent of any body reflectance phenomena such as absorption.

Recall that optical discontinuities cause light to scatter, or change direction. An optically planar interface between two substances is a special case, which scatters each ray of incoming light into exactly two directions: the ideal reflection direction and the ideal refraction direction (see the left side of Figure 7.18).

Note that the ideal reflection direction (indicated by the vector  $\mathbf{r}_i$ ) forms the same angle ( $\theta_i$ ) with the surface normal  $\mathbf{n}$  as the incoming direction  $\mathbf{l}$ . The ideal refraction or transmission vector  $\mathbf{t}$  forms a different angle ( $\theta_t$ ) with the negated surface normal  $-\mathbf{n}$ . All these vectors are in the same plane. The amount of light reflected is described by the *Fresnel reflectance*  $R_F$ , which depends on the incoming angle  $\theta_i$ . Due to conservation of energy, any light not reflected is transmitted, so the proportion of transmitted flux to incoming flux is  $1 - R_F$ . The proportion of transmitted-to-incident *radiance*, however, is different. Due to differences in projected area and solid angle between the incident and transmitted rays, the relationship between the incident and transmitted radiance is

$$L_t = (1 - R_F(\theta_i)) \frac{\sin^2 \theta_i}{\sin^2 \theta_t} L_i. \quad (7.29)$$

The reflection vector  $\mathbf{r}_i$  can be computed from  $\mathbf{n}$  and  $\mathbf{l}$ :

$$\mathbf{r}_i = 2(\mathbf{n} \cdot \mathbf{l})\mathbf{n} - \mathbf{l}. \quad (7.30)$$

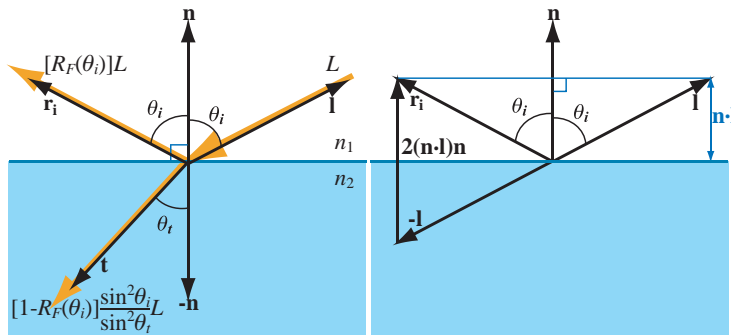


**Figure 7.18.** Reflection and refraction at a planar surface. The left side shows the indices of refraction  $n_1$  and  $n_2$  of the two substances, as well as the radiance and direction of the incoming, reflected, and refracted rays. The right side shows how the light vector  $I$  is reflected around the normal  $n$  in order to generate  $r_i$ . First,  $I$  is projected onto  $n$ , and we get a scaled version of the normal:  $(n \cdot I)n$ . Then  $I$  is negated, and if we add two times the projected vector, the reflection vector is obtained:  $r_i = 2(n \cdot I)n - I$ .

The right side of Figure 7.18 shows a geometrical construction that explains Equation 7.30.

Both the Fresnel reflectance  $R_F$  and the transmission angle  $\theta_t$  depend not only on the incoming angle  $\theta_i$ , but also on an optical property of the two substances called the *refractive index* or *index of refraction*. The symbol  $n$  is commonly used to denote refractive index. In this case  $n_1$  is the refractive index of the substance “above” the interface (where the light is initially propagating) and  $n_2$  is the refractive index of the substance “below” the interface (where the refracted light propagates). The dependence of  $\theta_t$  on  $\theta_i$ ,  $n_1$ , and  $n_2$  obeys a simple equation, known as Snell’s Law:

$$n_1 \sin(\theta_i) = n_2 \sin(\theta_t). \quad (7.31)$$

The vector  $t$  is used in global refraction effects, which are outside the scope of this chapter; the use of Snell’s Law to efficiently compute  $t$  will be shown in Section 9.5.

Snell’s Law combined with Equation 7.29 yields a different form for transmitted radiance:

$$L_t = (1 - R_F(\theta_i)) \frac{n_2^2}{n_1^2} L_i. \quad (7.32)$$

The Fresnel equations describe the dependence of  $R_F$  on  $\theta_i$ ,  $n_1$ , and  $n_2$ . Rather than present the equations themselves (which are quite complicated), we will describe their important characteristics.<sup>8</sup>

<sup>8</sup>The equations can be found in any optics textbook—a good introductory text is *Introduction to Modern Optics* by Fowles [361].

### External Reflection

*External reflection* is the case where light reflects from an object's external surface; in other words, light is in transition from air to the object's substance (the opposite transition, from object to air, is called *internal reflection* and is discussed later).

For a given substance, the Fresnel equations can be interpreted as defining a reflectance function  $R_F(\theta_i)$ , dependent only on incoming light angle. In principle, the value of  $R_F(\theta_i)$  varies continuously over the visible spectrum. For rendering purposes its value is treated as an RGB vector. The function  $R_F(\theta_i)$  has the following characteristics:

- When  $\theta_i = 0^\circ$  (light perpendicular to the surface, or  $\mathbf{l} = \mathbf{n}$ )  $R_F(\theta_i)$  has a value that is a property of the substance. This value,  $R_F(0^\circ)$ , can be thought of as the characteristic specular color of the substance. The case when  $\theta_i = 0^\circ$  is sometimes called *normal incidence*,
- As  $\theta_i$  increases (the surface is viewed at increasingly glancing angles), the value of  $R_F(\theta_i)$  will tend to increase, reaching a value of 1 for all frequencies (white) at  $\theta_i = 90^\circ$ .

Figure 7.19 shows  $R_F(\theta_i)$  curves for external reflection from a variety of substances. The curves are highly nonlinear—they barely change until  $\theta_i = 60^\circ$  or so, and then quickly go to 1. The increase from  $R_F(0^\circ)$  to 1 is mostly monotonic, though some of the substances (most notably aluminum) do show a slight dip just before going to white.

This increase in reflectance at glancing angles is sometimes called the *Fresnel effect* in rendering.<sup>9</sup> You can see the Fresnel effect for yourself with a short experiment. Take a plastic CD case and sit in front of a bright area like a computer monitor. First hold the CD case close to your chest, look down at it, and angle it slightly so that it reflects the monitor. There should be a relatively weak reflection of the monitor on the plastic, and the CD or cover image should be clearly visible under it. This is because the characteristic, normal-incidence reflectance of plastic is quite low. Now raise the CD case up so that it is roughly between your eyes and the monitor, and again angle it to reflect the monitor. Now the reflection of the monitor should be much stronger, obscuring whatever is under the plastic.

Besides their complexity, the Fresnel equations have other properties that make their direct use in rendering difficult. They require (possibly complex) refractive index values sampled over the visible spectrum. The equations are evaluated for all the sampled frequencies and converted into RGB values using the methods detailed in Section 7.3.

---

<sup>9</sup>Outside rendering, the term has a different meaning relating to transmission of radio waves.

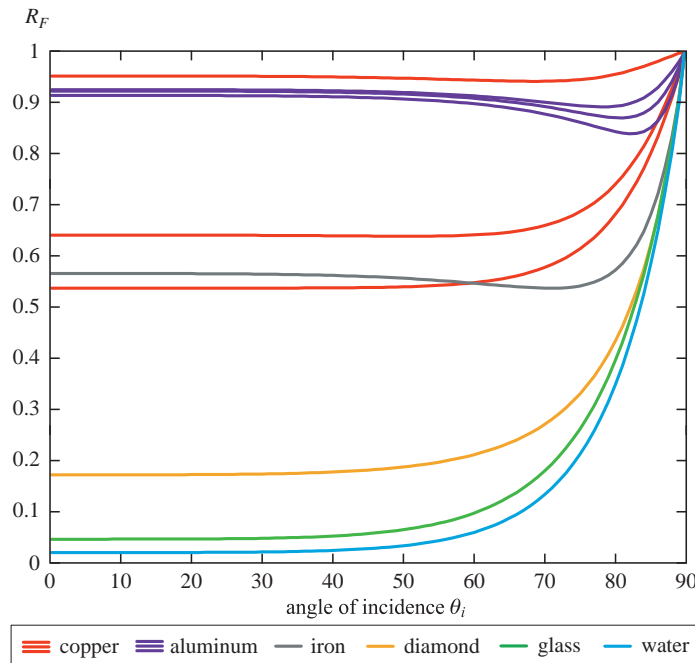


**Figure 7.19.** Fresnel reflectance for external reflection from a variety of substances. Since copper and aluminum have significant variation in their reflectance over the visible spectrum, their reflectance is shown as three separate curves for R, G, and B. Copper’s R curve is highest, followed by G, and finally B (thus its reddish color). Aluminum’s B curve is highest, followed by G, and finally R. Aluminum has a faint bluish tint that is most noticeable at an incidence angle of about 80°.

The curves in Figure 7.19 suggest a simpler approach based on the characteristic specular color  $R_F(0^\circ)$ . Schlick [1128] gives an approximation of Fresnel reflectance that is fairly accurate for most substances:

$$R_F(\theta_i) \approx R_F(0^\circ) + (1 - R_F(0^\circ))(1 - \overline{\cos} \theta_i)^5. \quad (7.33)$$

This is a simple RGB interpolation between white and  $R_F(0^\circ)$ . Despite this, the approximation is reasonably accurate for most materials, as can be seen in Figure 7.20. Sometimes this equation is modified in practice to raise the final term to powers other than 5 (4, or even 2). Although this may reduce accuracy, it is sometimes done for artistic reasons (to modify the material appearance) or for performance reasons (to simplify the pixel shader). The Schlick approximation performs less well with substances that exhibit a noticeable “dip” just before going to white, such as aluminum and iron. If it is important to precisely capture the color shifts of such materials,

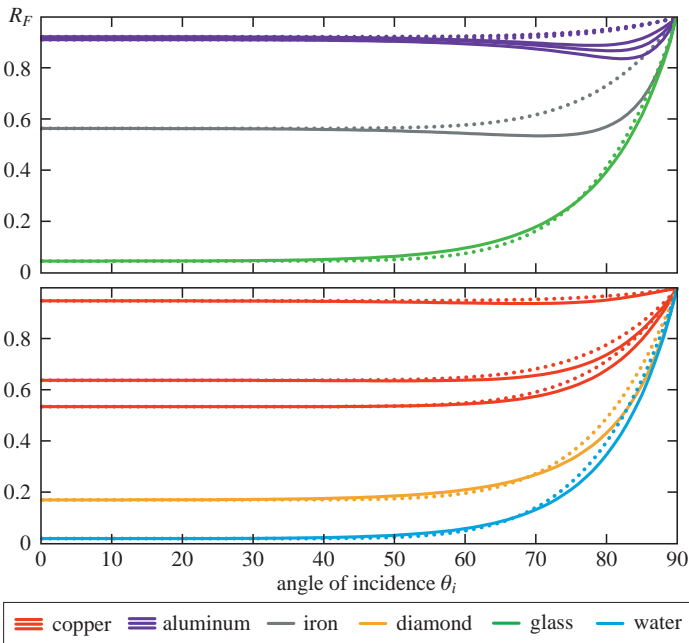


**Figure 7.20.** Schlick’s approximation to Fresnel reflectance compared to the correct values for external reflection from a variety of substances (separated into two graphs for clarity). The solid lines were computed from the full Fresnel equations (in the case of copper and aluminum, this computation was performed at a dense sampling of frequencies and the resulting spectral distribution was converted to RGB values). The dotted lines are the result of Schlick’s approximation (computed separately for R, G, and B in the case of copper and aluminum).

a good course of action may be to precompute  $R_F(\theta_i)$  values for various angles into a one-dimensional lookup texture.

When using the Schlick approximation,  $R_F(0^\circ)$  is the only parameter that controls Fresnel reflectance. This is convenient since  $R_F(0^\circ)$  has a well-defined range of valid values (between 0 and 1), is easy to set with standard color-picking interfaces, and can be textured using texture formats designed for colors. In addition, reference values for  $R_F(0^\circ)$  are available for many real-world materials. The refractive index can also be used to compute  $R_F(0^\circ)$ . It is common to assume that  $n_1 = 1$  (a close approximation for the refractive index of air), and to simply use  $n$  instead of  $n_2$  for the refractive index of the object. This gives the following equation:

$$R_F(0^\circ) = \left( \frac{n - 1}{n + 1} \right)^2. \quad (7.34)$$

This equation works even with complex-valued refractive indices if the magnitude of the (complex) result is used. Note that if the refractive indices vary significantly over the visible spectrum, the spectral distribution of  $R_F(0^\circ)$  needs to be computed and converted into an RGB vector using the methods described in Section 7.3.

### *Typical Fresnel Reflectance Values*

Different types of substances will have different ranges of values for  $R_F(0^\circ)$ . Substances are divided into three main groups with respect to their optical properties: insulators (also called *dielectrics*); metals (conductors); and semiconductors, which have properties somewhere in between the first two groups. Since semiconductors are rarely found in rendered scenes, we will not discuss them further and will focus on insulators and metals.

Most commonly encountered materials are insulators—water,<sup>10</sup> glass, skin, wood, hair, leather, plastic, stone, concrete, etc. Insulators have fairly low values for  $R_F(0^\circ)$ —usually 0.05 or lower. This low reflectance at normal incidence makes the Fresnel effect particularly visible for insulators. The optical properties of insulators rarely vary much over the visible spectrum, resulting in colorless reflectance values. The  $R_F(0^\circ)$  values for several common insulators are shown in Table 7.3, which includes RGB values in both linear and sRGB space.<sup>11</sup> The  $R_F(0^\circ)$  values for other insulators can be inferred by looking at similar substances in the table. For unknown insulators, 0.05 is a good default working value. Most substances of biological origin are close to this value, as well as many others.

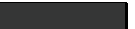
Once the light is transmitted into the insulating substance, it may be further scattered or absorbed. This process is discussed in more detail in Section 7.5.4. If the material is transparent, the light will continue until it hits an object surface “from the inside,” which is detailed later under “Internal Reflection.”

Metals have high values of  $R_F(0^\circ)$ —almost always 0.5 or above. Some metals have optical properties that vary over the visible spectrum, resulting in colored reflectance values. The  $R_F(0^\circ)$  values for several common metals are shown in Table 7.4. The  $R_F(0^\circ)$  values for other metals can be inferred by looking at similar substances in the table.

---

<sup>10</sup>Pure water has very low conductivity, although most water encountered outside the laboratory has numerous impurities that cause it to become conductive. These are usually not present in sufficient quantities to significantly alter the water’s optical properties.

<sup>11</sup>When colors such as  $R_F(0^\circ)$  are set in digital content creation applications, it is often convenient to author them in a nonlinear display space such as sRGB and convert them to linear space before use. This ensures that the colors seen in the color-selection interface match the colors seen when shading. If such colors are stored in textures, encoding them nonlinearly also helps maximize bit precision (see Section 5.8 for details).

| Insulator             | $R_F(0^\circ)$ (Linear) | $R_F(0^\circ)$ (sRGB) | Color   |
|-----------------------|-------------------------|-----------------------|---|
| Water                 | 0.02,0.02,0.02          | 0.15,0.15,0.15        |  |
| Plastic / Glass (Low) | 0.03,0.03,0.03          | 0.21,0.21,0.21        |  |
| Plastic High          | 0.05,0.05,0.05          | 0.24,0.24,0.24        |  |
| Glass (High) / Ruby   | 0.08,0.08,0.08          | 0.31,0.31,0.31        |  |
| Diamond               | 0.17,0.17,0.17          | 0.45,0.45,0.45        |  |

**Table 7.3.** Values of  $R_F(0^\circ)$  for external reflection from various insulators. Various types of plastic have values ranging from 0.03 to 0.05. There is a greater variance among different types of glass, ranging from 0.03 to as high as 0.08. Most common insulators have values close to 0.05—diamond has an unusually high value of  $R_F(0^\circ)$  and is not typical. Recall that these are *specular* colors; for example, ruby’s red color results from absorption inside the substance and is unrelated to its Fresnel reflectance.

| Metal    | $R_F(0^\circ)$ (Linear) | $R_F(0^\circ)$ (sRGB) | Color   |
|----------|-------------------------|-----------------------|---|
| Gold     | 1.00,0.71,0.29          | 1.00,0.86,0.57        |  |
| Silver   | 0.95,0.93,0.88          | 0.98,0.97,0.95        |  |
| Copper   | 0.95,0.64,0.54          | 0.98,0.82,0.76        |  |
| Iron     | 0.56,0.57,0.58          | 0.77,0.78,0.78        |  |
| Aluminum | 0.91,0.92,0.92          | 0.96,0.96,0.97        |  |

**Table 7.4.** Values of  $R_F(0^\circ)$  for external reflection from various metals. Note that the actual value for gold is slightly outside the sRGB gamut; the RGB value shown is after gamut mapping.

Metals immediately absorb any transmitted light, so they do not exhibit any subsurface scattering or transparency [192, 193].

Since reflectance depends on the refractive indices of the substances on both sides of the interface, objects will have lower reflectance when viewed under water (water has a higher refractive index than air), so they will appear slightly darker. Other factors also contribute to the darkening of wet materials both above and under water [605].

### Internal Reflection

Although external reflection is the most commonly encountered case in rendering, *internal reflection* is sometimes important as well. Internal reflection occurs when light is traveling in the interior of a transparent object and encounters the object’s surface “from the inside” (see Figure 7.21).

The differences between internal and external reflection are due to the fact that the refractive index for the object’s interior is higher than that

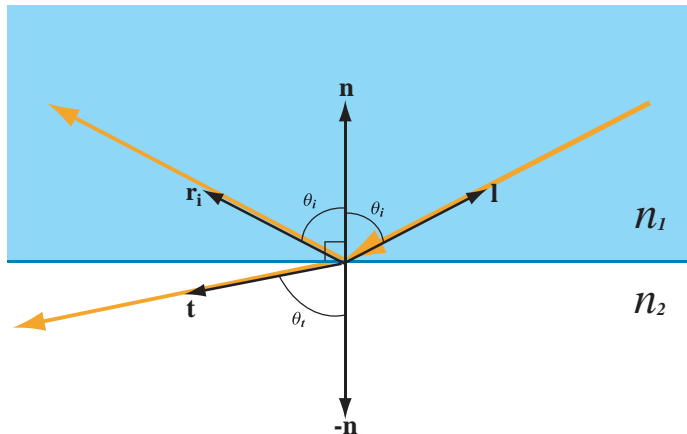


**Figure 7.21.** Internal reflection at a planar surface.

of air. External reflection is a transition from a low refractive index to a higher one; internal reflection is the opposite case. Snell's Law indicates that in the case of internal reflection that  $\sin \theta_t > \sin \theta_i$  (since they are both between  $0^\circ$  and  $90^\circ$ , this also implies  $\theta_t > \theta_i$ , as seen in Figure 7.21). In the case of external reflection the opposite is true—compare to Figure 7.18 on page 231. This is key to understanding the differences between internal and external reflection. In external reflection, a valid (smaller) value of  $\sin \theta_t$  exists for every possible value of  $\sin \theta_i$  between 0 and 1. The same is not true for internal reflection. For values of  $\theta_i$  greater than a *critical angle*  $\theta_c$ , Snell's Law implies that  $\sin \theta_t > 1$ , which is impossible. What happens in reality is that there *is* no  $\theta_t$ —when  $\theta_i > \theta_c$ , no transmission occurs, and all the incoming light is reflected. This phenomenon is known as *total internal reflection*.

The Fresnel equations are symmetrical, in the sense that the incoming and transmission vectors can be switched and the reflectance remains the same. In combination with Snell's Law, this implies that the  $R_F(\theta_i)$  curve for internal reflection will resemble a “compressed” version of the curve for external reflection. The value of  $R_F(0^\circ)$  is the same for both cases, and the internal reflection curve reaches perfect reflectance at  $\theta_c$  instead of at  $90^\circ$  (see Figure 7.22).

Figure 7.22 shows that on average, reflectance is higher in the case of internal reflection. This is why (for example) air bubbles seen underwater have a highly reflective, silvery appearance.

Since internal reflection only occurs in insulators (metals and semiconductors quickly absorb any light propagating inside them [192, 193]), and

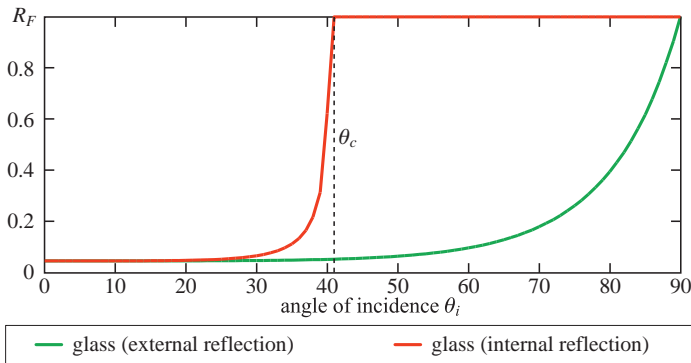


**Figure 7.22.** Comparison of internal and external reflectance curves at a glass-air interface.

insulators have real-valued refractive indices, computation of the critical angle from the refractive indices or from  $R_F(0^\circ)$  is straightforward:

$$\sin \theta_c = \frac{n_2}{n_1} = \frac{1 - \sqrt{R_F(0^\circ)}}{1 + \sqrt{R_F(0^\circ)}} \quad (7.35)$$

The Schlick approximation shown in Equation 7.33 is correct for external reflection. It can be used for internal reflection if the transmission angle  $\theta_t$  is substituted for  $\theta_i$ . If the transmission direction vector  $\mathbf{t}$  has been computed (e.g., for rendering refractions—see Section 9.5), it can be used for finding  $\theta_t$ . Otherwise Snell’s law could be used to compute  $\theta_t$  from  $\theta_i$ , but that is expensive and requires the index of refraction, which may not be available. Another option is to modify the Schlick approximation for use with internal reflection.

### 7.5.4 Local Subsurface Scattering

Metals and semiconductors quickly absorb any transmitted light, so body reflectance is not present, and surface reflectance is sufficient to describe the interaction of light with the object [192, 193]. For insulators, rendering needs to take account of body reflectance as well.

If the insulator is *homogeneous*—with few internal discontinuities to scatter light—then it is transparent.<sup>12</sup> Common examples are glass, gem-

<sup>12</sup>Of course, no real material can be perfectly homogeneous—at the very least, its constituent atoms will cause discontinuities. In practice, any inhomogeneities much smaller than the smallest visible light wavelength (about 400 nanometers) can be ignored. A material possessing only such inhomogeneities can be considered to be optically homogeneous and will not scatter light traveling through it.

stones, crystals, and clear liquids such as water, oil, and wine. Such substances can partially absorb light traveling through them, but do not change its direction.<sup>13</sup> Transmitted light continues on a straight line through such objects until it undergoes internal reflection and transmission out of the object. Techniques for rendering such substances are discussed in Sections 5.7, 9.4, 9.5, and 10.16.

Most insulators (including common substances such as wood, stone, snow, earth, skin, and opaque plastic—any opaque non-metal) are *heterogeneous*—they contain numerous discontinuities, such as air bubbles, foreign particles, density variations, and structural changes. These will cause light to scatter inside the substance. As the light travels through the substance, it may be partially or completely absorbed. Eventually, any light not absorbed is re-emitted from the surface. To model the reflectance with a BRDF, it is necessary to assume that the light is re-emitted from the same point at which it entered. We will call this case *local subsurface scattering*. Methods for rendering in cases where this assumption cannot be made (*global subsurface scattering*) are discussed in Section 9.7.

The *scattering albedo*  $\rho$  of a heterogeneous insulator is the ratio between the energy of the light that escapes a surface compared to the energy of the light entering into the interior of the material. The value of  $\rho$  is between 0 (all light is absorbed) and 1 (no light is absorbed) and can depend on wavelength, so  $\rho$  is modeled as an RGB vector for rendering. One way of thinking about scattering albedo is as the result of a “race” between absorption and scattering—will the light be absorbed before it has had a chance to be scattered back out of the object? This is why foam on a liquid is much brighter than the liquid itself. The process of frothing does not change the absorptiveness of the liquid, but the addition of numerous air-liquid interfaces greatly increases the amount of scattering. This causes most of the incoming light to be scattered before it has been absorbed, resulting in a high scattering albedo and bright appearance. Fresh snow is another example of high scattering albedo; there is a lot of scattering in the interfaces between snow granules and air, but very little absorption, leading to a scattering albedo of 0.8 or more across the visible spectrum. White paint is slightly less—about 0.7. Many common substances, such as concrete, stone, and soil, average between 0.15 and 0.4. Coal is an example of very low scattering albedo, close to 0.0.

Since insulators transmit most incoming light rather than reflecting it at the surface, the scattering albedo  $\rho$  is usually more visually important than the Fresnel reflectance  $R_F(\theta_i)$ . Since it results from a completely different physical process than the specular color (absorption in the inte-

---

<sup>13</sup>Although we have seen that light may change its direction when entering or exiting these substances, it does not change within the substance itself.

rior instead of Fresnel reflectance at the surface),  $\rho$  can have a completely different spectral distribution (and thus RGB color) than  $R_F(\theta_i)$ . For example, colored plastic is composed of a clear, transparent substrate with pigment particles embedded in its interior. Light reflecting specularly will be uncolored, while light reflecting diffusely will be colored from absorption by the pigment particles.

Local subsurface scattering is most often modeled as a Lambertian diffuse term in the BRDF. In this case the directional-hemispherical reflectance of the diffuse term  $R_{\text{diff}}$  is set to a constant value, referred to as the *diffuse color*  $\mathbf{c}_{\text{diff}}$ , yielding the following diffuse BRDF term:

$$f_{\text{diff}}(\mathbf{l}, \mathbf{v}) = \frac{\mathbf{c}_{\text{diff}}}{\pi}. \quad (7.36)$$

What value to choose for  $\mathbf{c}_{\text{diff}}$ ? It could be set to  $\rho$ , but this does not account for the fact that only light that is not reflected at the surface is available to undergo subsurface scattering, so there is an energy tradeoff between the surface (specular) and body (diffuse) reflectance terms. If the directional-hemispherical reflectance  $R_{\text{spec}}$  of the BRDF's specular term happens to have a constant value  $\mathbf{c}_{\text{spec}}$ , then it makes sense to set  $\mathbf{c}_{\text{diff}} = (1 - \mathbf{c}_{\text{spec}})\rho$ .

The Fresnel effect implies that the surface-body reflectance tradeoff mentioned above changes with incoming light angle  $\theta_i$ . As the specular reflectance increases at glancing angles, the diffuse reflectance will decrease. A simple way to account for this is to use the following diffuse term [1169]:

$$f_{\text{diff}}(\mathbf{l}, \mathbf{v}) = (1 - R_F(\theta_i)) \frac{\rho}{\pi}. \quad (7.37)$$

Equation 7.37 results in a uniform distribution of outgoing light; the BRDF value does not depend on the outgoing direction  $\mathbf{v}$ . This makes some sense, since light will typically undergo multiple scattering events before it is re-emitted, so its outgoing direction will be randomized. However, there are two reasons to suspect that the outgoing light is not distributed perfectly uniformly. First, since the diffuse BRDF term in Equation 7.37 varies by incoming direction, Helmholtz reciprocity implies that it must change by outgoing direction as well. Second, the light must undergo Fresnel reflectance on the way out (internal reflection and transmission), which will impose some directional preference on the outgoing light.

Shirley proposed a diffuse term that addresses the Fresnel effect and the surface-body reflectance tradeoff, while supporting both energy conservation and Helmholtz reciprocity [1170]. The derivation assumes that the Schlick approximation [1128] (Equation 7.33) is used for Fresnel reflectance:

$$f_{\text{diff}}(\mathbf{l}, \mathbf{v}) = \frac{21}{20\pi(1 - R_F(0^\circ))} (1 - (1 - \overline{\cos} \theta_i)^5) (1 - (1 - \overline{\cos} \theta_o)^5) \rho. \quad (7.38)$$

Equation 7.38 only applies to optically flat surfaces. A generalized version that can be used to compute a reciprocal, energy-conserving diffuse term to match any specular term was proposed by Ashikhmin and Shirley [42]:

$$f_{\text{diff}}(\mathbf{l}, \mathbf{v}) = k_{\text{norm}}(1 - R_{\text{spec}}(\mathbf{l}))(1 - R_{\text{spec}}(\mathbf{v}))\rho, \quad (7.39)$$

where  $k_{\text{norm}}$  is a constant computed to ensure energy conservation. Given a specular BRDF term, using Equation 7.39 to derive a matching diffuse term is not trivial since in general  $R_{\text{spec}}()$  does not have a closed form. Computation of the normalization constant  $k_{\text{norm}}$  can also be an involved process (BRDF term normalization is further discussed in Section 7.6). The derivation of the diffuse term of the Ashikhmin-Shirley BRDF [42] is an example of the application of Equation 7.39. Kelemen and Szirmay-Kalos [640] also derived a diffuse term for their BRDF using Equation 7.39; rather than attempting to derive a closed form for  $R_{\text{spec}}()$ , their implementation used precomputed lookup tables.

Theoretical considerations aside, the simple Lambertian term shown in Equation 7.36 is the most commonly used diffuse term in practice.

### 7.5.5 Microgeometry

The previous sections discussed material properties relating to the composition or internal structure of the object, with the surface assumed to be optically flat. Most real surfaces exhibit some roughness or structure that affects how light reflects from them. Surface detail modeled by a BRDF is *microscale*—smaller than the visible scale or, in other words, smaller than a single pixel. Larger details are typically modeled with textures or geometry, not with BRDFs. As we discussed in Section 5.3, whether surface structures are considered to be microscale depends on the scale of observation as much as on the size of the structures themselves.

Since such *microgeometry* is too small to be seen directly, its effect is expressed statistically in the way light scatters from the surface. The microscale structures or irregularities are assumed to be significantly larger than visible light wavelengths (approximately 400 to 800 nanometers). This is because structures have no effect on the light if they are much smaller than visible light wavelengths. If the size is on the same order as the wavelength, various wave optics effects come into play [44, 515, 1213, 1345, 1346]. Surface detail on this scale is both difficult to model and relatively rare in rendered scenes, so it will not be further discussed here.

The most important visual effect of the microgeometry is due to the fact that many surface normals are present at each visible surface point, rather than a single macroscopic surface normal. Since the reflected light direction is dependent on the surface normal (recall Equation 7.30), this

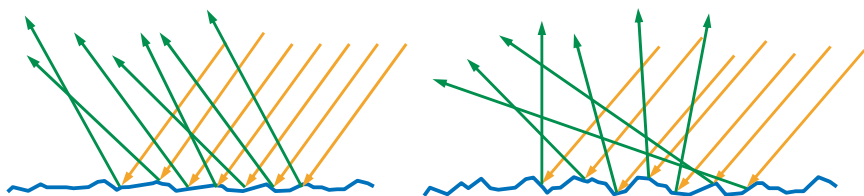


**Figure 7.23.** Light reflecting from two surfaces: a slightly rough surface on the left and a considerably rougher surface on the right.

causes every incoming light ray to be reflected into many directions; see Figure 7.23.

Since we cannot see that the microgeometry surface normals and their directions are somewhat random, it makes sense to model them statistically, as a distribution. For most surfaces, the distribution of microgeometry surface normals is a continuous distribution with a strong peak at the macroscopic surface normal. The “tightness” of this distribution is determined by surface smoothness. On the right side of Figure 7.23, we see light reflecting from a surface that is rougher (and thus has its microgeometry normals clustered less tightly around the overall surface normal) than the surface on the left side of the figure. Note that the wider distribution of normals causes the reflected light to “spread” in a wider range of directions.

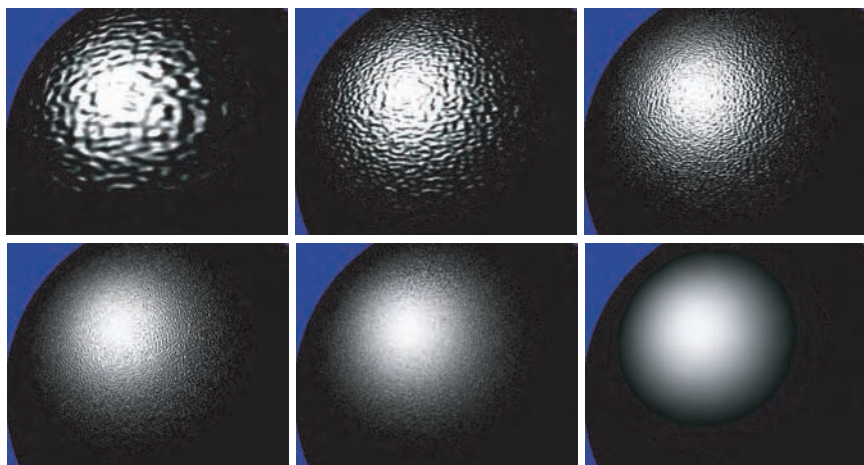


**Figure 7.24.** Gradual transition from visible detail to microscale. The sequence of images goes top row left to right, then bottom row left to right. The surface shape and lighting are constant; only the scale of the surface detail changes.

The visible effect of increasing microscale roughness is greater blurring of reflected environmental detail. In the case of small, bright light sources, this blurring results in broader and dimmer specular highlights (highlights from rougher surfaces are dimmer because the light energy is spread into a wider cone of directions). This can be seen in the photographs in Figure 5.8 on page 106.

Figure 7.24 shows how visible reflectance results from the aggregate reflections of the individual microscale surface details. The series of images shows a curved surface lit by a single light, with bumps that steadily decrease in scale until in the last image the bumps are all smaller than a single pixel. It can be seen that statistical patterns in the many small highlights eventually become details in the shape of the resulting aggregate highlight. For example, the relative sparsity of individual bump highlights in the periphery becomes the relative darkness of the aggregate highlight away from its center.

For most surfaces, the distribution of the microscale surface normals is *isotropic*—rotationally symmetrical, or lacking any inherent directionality. However, some surfaces have microscale structure that is *anisotropic*. This results in anisotropic surface normal distributions, and directional blurring of reflections and highlights (see Figure 7.25).

Some surfaces have highly structured microgeometry, resulting in interesting microscale normal distributions and surface appearance. Fabrics are a commonly encountered example—the unique appearance of velvet and satin is due to the structure of their microgeometry [41].

Although multiple surface normals are the primary effect of microgeometry on reflectance, other effects can also be important. *Shadowing* refers to occlusion of the light source by microscale surface detail, as shown on the



**Figure 7.25.** On the left, an anisotropic surface (brushed metal). Note the directional blurring of reflections. On the right, a photomicrograph showing a similar surface. Note the directionality of the detail. (*Photomicrograph courtesy of the Program of Computer Graphics, Cornell University.*)

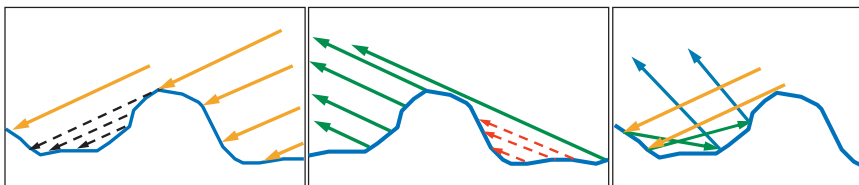


**Figure 7.26.** Geometrical effects of microscale structure. On the left, the black dashed arrows indicate an area that is shadowed (occluded from the light) by other microgeometry. In the center, the red dashed arrows indicate an area that is masked (occluded from view) by other microgeometry. On the right, interreflection of light between the microscale structures is shown.

left side of Figure 7.26. *Masking* (visibility occlusion of microscale surface detail) is shown in the center of the figure.

If there is a correlation between the microgeometry height and the surface normal, then shadowing and masking can effectively change the normal distribution. For example, imagine a surface where the raised parts have been smoothed by weathering or other processes, and the lower parts remain rough. At glancing angles, the lower parts of the surface will tend to be shadowed or masked, resulting in an effectively smoother surface. See Figure 7.27. In addition, the effective size of the surface irregularities is reduced as the incoming angle  $\theta_i$  increases. At extremely glanc-

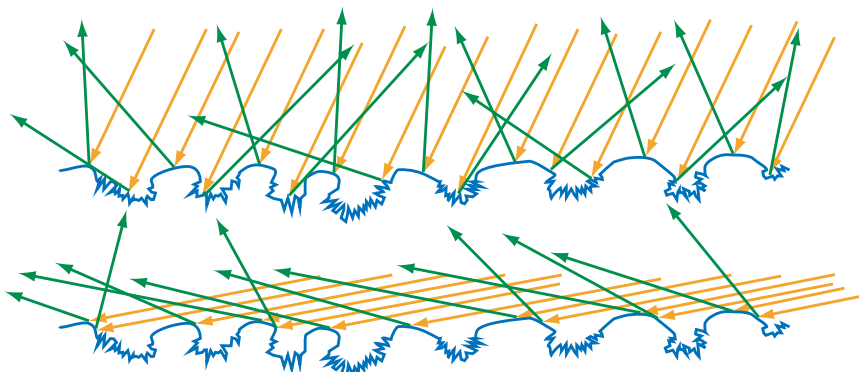


**Figure 7.27.** Microgeometry with a strong correlation between height and surface normal (raised areas are smooth, lower areas are rough). In the top image, the surface is illuminated from an angle close to the macroscopic surface normal. At this angle, the rough pits are accessible to many of the incoming light rays, and many of them are scattered in different directions. In the bottom image, the surface is illuminated from a glancing angle. Shadowing blocks most of the pits, so few light rays hit them, and most rays are reflected from the smooth parts of the surface. In this case, the apparent roughness depends strongly on the angle of illumination.

ing angles, this can decrease the effective size of the irregularities to be shorter than the light's wavelength, making the surface optically smooth. These two effects combine with the Fresnel effect to make surfaces appear highly reflective and mirror-like as the viewing and lighting angles approach  $90^\circ$  [44, 1345, 1346]. Confirm this for yourself: Put a sheet of non-shiny paper nearly edge on to your eye, looking off it toward a computer screen. Hold a pen with a dark surface along the far edge, so that it points out from the paper. At a very shallow angle you will see a reflection of the pen in the paper. The angle has to be extremely close to  $90^\circ$  to see the effect.

Light that was occluded by microscale surface detail does not disappear—it is reflected, possibly onto other microgeometry. Light may undergo multiple bounces in this way before it reaches the eye. Such interreflections are shown on the right side of Figure 7.26. Since the light is being attenuated by the Fresnel reflectance at each bounce, interreflections tend not to be noticeable in insulators. In metals, multiple-bounce reflection is the source of any visible diffuse reflection (since metals lack subsurface scattering). Note that multiple-bounce reflections from colored metals are more deeply colored than the primary reflection, since they are the result of light interacting with the surface multiple times.

So far we have discussed the effects of microgeometry on specular, or surface reflectance. In certain cases, microscale surface detail can affect body reflectance, as well. If the scale of the microgeometry is large relative to the scale of subsurface scattering (the distances between the entry and exit points of subsurface-scattered light), then shadowing and masking can cause a *retro-reflection* effect, where light is preferentially reflected back toward the incoming direction. This is because shadowing and masking will occlude lit areas when the viewing and lighting directions differ greatly (see Figure 7.28).

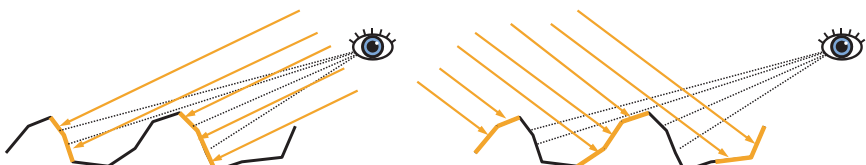


**Figure 7.28.** Retro-reflection due to microscale roughness. Both sides show a rough surface with low Fresnel reflectance and high scattering albedo (so body reflectance is visually important). On the left, the viewing and lighting directions are similar. The parts of the microgeometry that are brightly lit are also the ones that are highly visible, leading to a bright appearance. On the right, the viewing and lighting directions differ greatly. In this case, the brightly lit areas are occluded from view and the visible areas are shadowed. This leads to a darker appearance.



**Figure 7.29.** Photographs of two objects exhibiting non-Lambertian, retro-reflective behavior due to microscale surface roughness. (Photograph on the right courtesy of Peter-Pike Sloan.)

This retro-reflection effect will tend to give rough surfaces a flat appearance (this is why the moon appears as a flat disc and does not look like a Lambert-shaded sphere). Figure 7.29 shows photographs of two objects exhibiting this behavior.

### 7.5.6 Microfacet Theory

Many BRDF models are based on a mathematical analysis of the effects of microgeometry on reflectance called *microfacet theory*. Microfacet theory was developed in its modern form by Torrance and Sparrow [1270] and was introduced to computer graphics in 1977 by Blinn [97] and again in 1981 by Cook and Torrance [192, 193]. This theory is based on the modeling of microgeometry as a collection of *microfacets*. Each microfacet is a tiny, flat Fresnel mirror on the surface. In microfacet theory, a surface is characterized by the distribution of the microfacet surface normals. This distribution is defined by the surface's *normal distribution function*, or NDF. We will use  $p()$  to refer to the NDF in equations. The NDF is defined as the probability distribution function of the microfacet surface normals. The probability that the surface normal of a given microfacet lies within an infinitesimal solid angle  $d\omega$  surrounding a candidate direction vector  $n_\mu$  is equal to  $p(n_\mu)d\omega$ . For a function to be a valid NDF, it needs to be *normalized* so that it integrates to 1 over the sphere, since the possibility of a microfacet normal pointing *somewhere* is 1. Intuitively, the NDF is similar to a histogram of the microfacet normals; it has high values in directions where the microfacet normals are more likely to be pointing. Most surfaces have NDFs that show a strong peak at the macroscopic surface normal  $n$ . In other words, the microfacets are likely to be oriented similarly to the overall macroscopic surface. Section 7.6 will discuss a few different NDF models used in rendering.

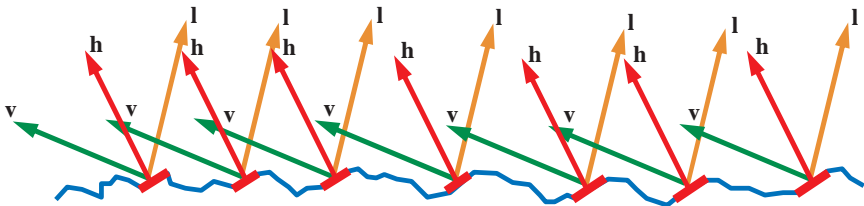


**Figure 7.30.** Surface composed of microfacets. Only the red microfacets, which have their surface normal aligned with the half vector  $\mathbf{h}$ , participate in the reflection of light from the incoming light vector  $\mathbf{l}$  to the view vector  $\mathbf{v}$ .

The NDF does not uniquely define the microgeometry—many different microgeometry configurations can have the same NDF. However, the NDF does capture the most visually important feature of the microgeometry, which is the “spreading” of reflected light due to multiple surface normals at each rendered pixel. Microfacet theory focuses on modeling the first-bounce specular reflection and does not model multiple bounces or body reflectance. For this reason, microfacet-derived BRDF terms are paired with a diffuse (usually Lambertian) term. Shadowing and masking are modeled, but due to the lack of a complete surface representation, this is done in a somewhat ad hoc manner [41, 97, 192, 193, 1270].

Since each microfacet is assumed to be an ideal mirror, it reflects each incoming ray of light in a single reflected direction. When examining reflection of light from a given light vector  $\mathbf{l}$  into a given view vector  $\mathbf{v}$ , it is clear that only those microfacets that happen to be oriented such that they reflect  $\mathbf{l}$  into  $\mathbf{v}$  can participate in the reflection (see Figure 7.30). This means that the participating or active microfacets have their surface normal aligned with a vector pointing exactly halfway between  $\mathbf{l}$  and  $\mathbf{v}$ . This vector is called the *half vector*  $\mathbf{h}$  (see also Figure 5.13 on page 111).

The reflectance will depend on the fraction of the microfacets that are active, i.e., those that participate in the reflection of light from  $\mathbf{l}$  to  $\mathbf{v}$ . This fraction is equal to the NDF evaluated at the half vector, or  $p(\mathbf{h})$ . It will also depend on the Fresnel reflectance of the individual microfacets, which is equal to  $R_F(\alpha_h)$ , where  $\alpha_h$  is the angle between  $\mathbf{l}$  and  $\mathbf{h}$ .<sup>14</sup> This value is the incoming light angle for the active microfacets, since their surface normal is equal to  $\mathbf{h}$  by definition. Figure 7.31 shows  $\alpha_h$ , as well as other angles related to the half vector, that sometimes appear in BRDF models. Note that here the Fresnel term is used with  $\alpha_h$  and not  $\theta_i$ , since the reflection is about the microfacet normal  $\mathbf{h}$  and not the macroscopic surface normal  $\mathbf{n}$ . If the Schlick approximation is used, then  $\alpha_h$  must be

---

<sup>14</sup> $\alpha_h$  is also the angle between  $\mathbf{v}$  and  $\mathbf{h}$ .

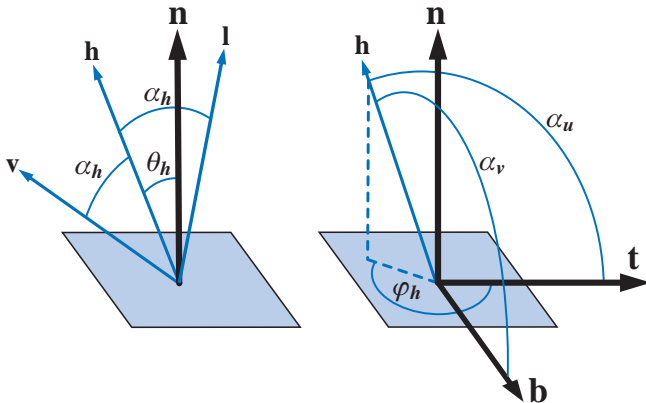


**Figure 7.31.** Angles relating to the half vector. On the left, the half vector  $\mathbf{h}$  lies halfway between  $\mathbf{v}$  and  $\mathbf{l}$ , all in the same plane, and defines  $\alpha_h$ . This is the incidence angle for the microfacets and is used to compute Fresnel reflectance. Here,  $\theta_h$  is the angle between  $\mathbf{h}$  and  $\mathbf{n}$  and is used for evaluating NDFs, isotropic ones in particular. On the right,  $\phi_h$ ,  $\alpha_u$ , and  $\alpha_v$  give the orientation of  $\mathbf{h}$  relative to the tangent vector  $\mathbf{t}$  and the bitangent vector  $\mathbf{b}$ . These are used for evaluating anisotropic NDFs.

given as the input angle:

$$R_F(\alpha_h) \approx R_F(0^\circ) + (1 - R_F(0^\circ))(1 - \cos \alpha_h)^5. \quad (7.40)$$

Note that the term  $\cos \alpha_h$  does not need to be clamped, since  $\alpha_h$  can never exceed  $90^\circ$ .

Shadowing and masking are accounted for by introducing a *geometry factor* or *geometrical attenuation factor* [97, 192, 193, 1270]  $G(\mathbf{l}, \mathbf{v})$ . This is a function of the incoming light direction  $\mathbf{l}$  and view direction  $\mathbf{v}$ , with a value between 0 and 1. It represents how much light remains after shadowing and masking are applied. Another way of thinking about it is that the value of  $G(\mathbf{l}, \mathbf{v})$  is equal to the possibility that a ray of light in direction  $\mathbf{l}$  will be reflected into direction  $\mathbf{v}$  without being shadowed or masked. Shadowing and masking are assumed to be uncorrelated with the microfacet orientation, so microgeometries like that shown in Figure 7.27 are not modeled. Some options for modeling  $G(\mathbf{l}, \mathbf{v})$  will be shown in Section 7.6.

There are several detailed derivations of BRDF terms from microfacet theory [41, 640, 1270]; we will use the derivation from the 2000 paper by Ashikhmin et al. [41] due to its accuracy and accessibility. This paper derives the following BRDF term from first principles using microfacet theory:

$$f(\mathbf{l}, \mathbf{v}) = \frac{p(\mathbf{h})G(\mathbf{l}, \mathbf{v})R_F(\alpha_h)}{4k_p \cos \theta_i \cos \theta_o}, \quad (7.41)$$

where  $k_p$  is calculated thus:<sup>15</sup>

$$k_p = \int_{\Omega} p(\mathbf{h}) \cos \theta_h d\omega_h. \quad (7.42)$$

Equation 7.42 shows that any scale factors applied to  $p(\mathbf{h})$  will apply to  $k_p$  as well, so they can be removed without affecting the value of  $p(\mathbf{h})/k_p$ . Because of this, it does not matter whether the NDF  $p()$  used in Equation 7.41 is normalized.

The NDF  $p()$  is usually *isotropic*—rotationally symmetrical about the macroscopic surface normal  $\mathbf{n}$ . In this case, it is a function of just one variable, the angle  $\theta_h$  between  $\mathbf{n}$  and  $\mathbf{h}$ . This simplifies the BRDF slightly by replacing  $p(\mathbf{h})$  with  $p(\theta_h)$ :

$$f(\mathbf{l}, \mathbf{v}) = \frac{p(\theta_h) G(\mathbf{l}, \mathbf{v}) R_F(\alpha_h)}{4k_p \cos \theta_i \cos \theta_o}. \quad (7.43)$$

Most of the BRDF models we will see in the next section are either explicitly derived from microfacet theory or can be interpreted in terms of it.

Another, more complete surface representation is called *height correlation*. This representation gives enough information about the surface microgeometry to model surfaces such as the one shown in Figure 7.27. It also gives enough information to correctly model wave optics effects that occur in microstructures near the scale of light wavelengths [515, 1213]. However, height correlation models are much more complex than microfacet models, so they are rarely used in offline rendering, and never in real-time rendering.

### 7.5.7 Half Vector versus Reflection Vector

The  $p(\theta_h)$  term seen in Equation 7.43 is fairly common, even in BRDFs not explicitly derived from microfacet theory [42, 43, 1326]. Some BRDFs [710, 1014] contain a superficially similar term, which uses the angle  $\alpha_r$  (between the reflection vector  $\mathbf{r}_i$  and the view vector  $\mathbf{v}$ ) instead of  $\theta_h$  (see Figure 7.32). The difference between the two terms is significant. The angle  $\theta_h$  has a clear physical interpretation—it shows to what extent the active microfacet normals diverge from the overall macroscopic surface normal. However,  $\alpha_r$  has no such physical interpretation.

Although the center of the highlight is present at the same location in both types of BRDF ( $\theta_h$  and  $\alpha_r$  are both equal to 0 when  $\mathbf{h} = \mathbf{n}$ ),

---

<sup>15</sup>Details on the meaning of  $k_p$  and the derivation of Equation 7.42 can be found in the paper [41].

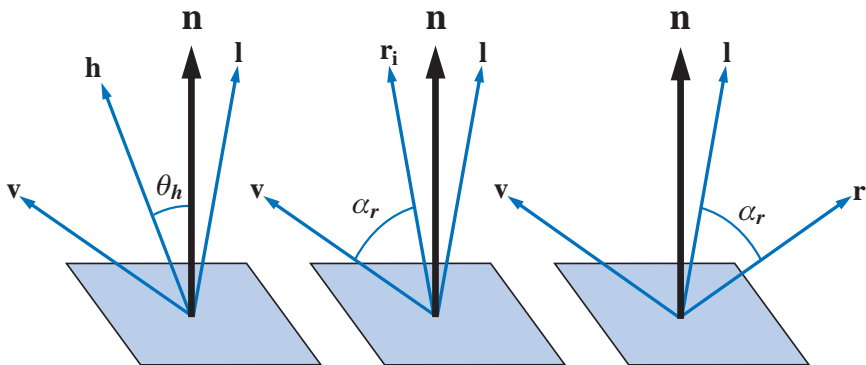


**Figure 7.32.** On the left, the angle  $\theta_h$  between the macroscopic surface normal  $\mathbf{n}$  and the half vector  $\mathbf{h}$  is shown. This angle is used in isotropic microfacet BRDFs. In the middle, the reflection vector  $\mathbf{r}_i$  and view vector  $\mathbf{v}$  define the angle  $\alpha_r$ . This angle is sometimes used in BRDFs instead of  $\theta_h$ . On the right, an alternative definition of  $\alpha_r$ , between the reflected view vector  $\mathbf{r}$  and  $\mathbf{l}$ . Due to symmetry, the same value of  $\alpha_r$  is obtained.

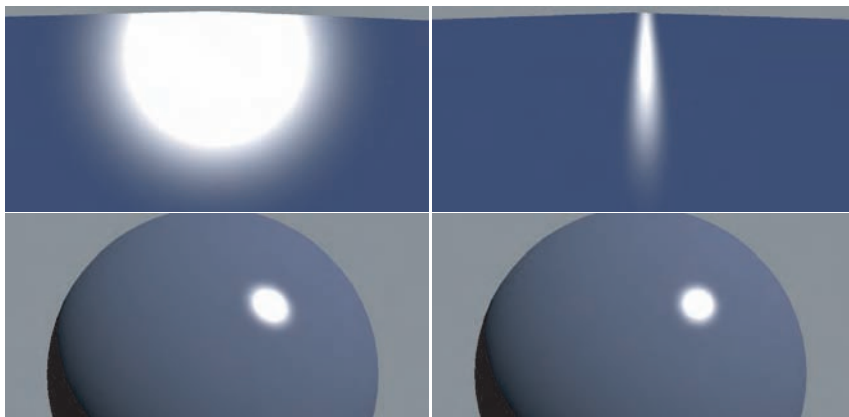


**Figure 7.33.** Renderings of a plane and sphere with both reflection-vector-based (on the left) and half-vector-based (on the right) BRDFs. The top row shows a flat plane with glancing viewing and lighting angles. The left side shows the circular highlight typical of reflection-vector-based BRDFs in this situation; the right side shows the narrow highlight typical of half-vector-based BRDFs. The bottom row shows a sphere; the difference in highlight shape is far more subtle in this case, where the surface curvature is the dominating factor, rather than the BRDF.



**Figure 7.34.** Photographs of surfaces lit and viewed at glancing angles. These surfaces clearly exhibit narrow highlights, which the highlights generated by half-vector-based BRDFs closely resemble. (*Photographs courtesy of Elan Ruskin.*)

the *shape* of the highlight may differ significantly. For highly curved surfaces, there is little difference. For such surfaces, curvature, not BRDF, primarily determines highlight shape. However, on flat surfaces, the shape of the highlight differs greatly between half-vector- and reflection-vector-based BRDFs. Half-vector-based BRDFs have highlights that become increasingly elongated at glancing angles, and reflection-vector-based BRDFs have circular highlights regardless of viewing angle [1124]. Ngan [926, 927] presents an interesting analysis of the reason behind this difference.

The differing behaviors of reflection-vector- and half-vector-based BRDFs can be seen in the rendered images of Figure 7.33. Which of these behaviors is closer to reality? The answer to that question can be seen in Figure 7.34, which shows three photographs of rough, flat surfaces under similar viewing and lighting conditions to the top row of Figure 7.33. The highlight shapes in the photographs clearly resemble the results of the half-vector-based BRDF, and not the reflection-vector-based BRDF. This is not surprising, since the former is based on physical principles, while the latter is not. Aside from the anecdotal evidence of these photographs, quantitative experimental analysis has also found that half-vector-based BRDFs match real-world materials more closely than reflection-vector-based BRDFs [926, 927].

## 7.6 BRDF Models

In most applications BRDFs are represented analytically, as mathematical equations. Many such models have appeared in the computer graphics

literature, and several good surveys are available [44, 926, 1129, 1170, 1345, 1346]. BRDF models fall into two broad groups: those based on physical theory [41, 97, 192, 193, 515, 640, 973, 1027, 1213] and those that are designed to empirically fit a class of surface types [42, 43, 1014, 1326].

Since the empirical BRDF models tend to be simpler, they are more commonly used in real-time rendering. The first such model used in rendering was the Lambertian or constant BRDF. Phong introduced the first specular model to computer graphics in 1975 [1014]. This model is still in common use; however, it has several drawbacks that merit discussion. The form in which the Phong lighting model has historically been used (shown with a single light source for simplicity) is

$$L_o(\mathbf{v}) = \begin{cases} \left( \overline{\cos} \theta_i \mathbf{c}_{\text{diff}} + \overline{\cos}^m \alpha_r \mathbf{c}_{\text{spec}} \right) \otimes B_L, & \text{where } \theta_i > 0, \\ 0, & \text{where } \theta_i \leq 0. \end{cases} \quad (7.44)$$

The use of  $B_L$  rather than  $E_L$  is due to the fact that this form of the shading equation does not use physical illumination quantities, but rather uses ad hoc “brightness” values assigned to light sources. Recall from Section 7.5.4 that effectively  $B_L = E_L/\pi$ . Using this and Equation 7.21, we can transform Equation 7.44 into a BRDF:

$$f(\mathbf{l}, \mathbf{v}) = \begin{cases} \frac{\mathbf{c}_{\text{diff}}}{\pi} + \frac{\mathbf{c}_{\text{spec}} \overline{\cos}^m \alpha_r}{\pi \overline{\cos} \theta_i}, & \text{where } \theta_i > 0, \\ 0, & \text{where } \theta_i \leq 0. \end{cases} \quad (7.45)$$

Comparing this to Equation 7.36 on page 240 shows that  $\mathbf{c}_{\text{diff}}$  is equal to the directional-hemispherical reflectance of the diffuse term. This is fortunate—reflectance values make very good BRDF parameters. As a reflectance value,  $\mathbf{c}_{\text{diff}}$  is restricted to values between 0 and 1, so it can be selected with color-picker interfaces, stored using standard texture formats, etc. The fact that  $\mathbf{c}_{\text{diff}}$  has a clear physical interpretation can also be used to help select appropriate values for it.

It would be useful to ensure that  $\mathbf{c}_{\text{spec}}$  is a reflectance value, as well. To do this, we need to look at the directional-hemispherical reflectance  $R_{\text{spec}}$  of the specular term. However, it turns out that for Equation 7.45,  $R_{\text{spec}}$  is unbounded, increasing to infinity as  $\theta_i$  goes to  $90^\circ$  [769]. This is unfortunate—it means that the BRDF is much too bright at glancing angles. The cause of the problem is the division by  $\overline{\cos} \theta_i$ . Removing this division also allows us to remove the conditional term, resulting in a simpler BRDF:

$$f(\mathbf{l}, \mathbf{v}) = \frac{\mathbf{c}_{\text{diff}}}{\pi} + \frac{\mathbf{c}_{\text{spec}} \overline{\cos}^m \alpha_r}{\pi}. \quad (7.46)$$

This version of the Phong BRDF is more physically plausible in several ways—its reflectance does not go to infinity, it is reciprocal, and it lacks

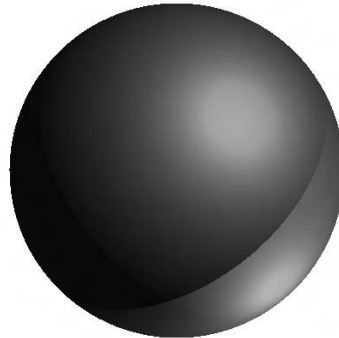


**Figure 7.35.** The cutoff in Equation 7.45 when  $\theta_i = 90^\circ$  can cause artifacts, as seen by the unnatural line towards the bottom right of the figure.

the abrupt cutoff when  $\theta_i = 90^\circ$ . An example of an artifact caused by this cutoff can be seen in Figure 7.35.

The directional-hemispherical reflectance of the specular term in Equation 7.46 can now be calculated. It turns out that when  $\theta_i = 0$ , it reaches a maximum value of  $2\mathbf{c}_{\text{spec}}/(m + 2)$ . If we divide the specular term by  $2/(m + 2)$ , then  $\mathbf{c}_{\text{spec}}$  will be equal to the maximum directional-hemispherical reflectance [586]:

$$f(\mathbf{l}, \mathbf{v}) = \frac{\mathbf{c}_{\text{diff}}}{\pi} + \frac{m + 2}{2\pi} \mathbf{c}_{\text{spec}} \overline{\cos}^m \alpha_r. \quad (7.47)$$

This process of multiplying a BRDF term by a value to ensure that parameters such as  $\mathbf{c}_{\text{spec}}$  are equivalent to reflectance values is called *BRDF normalization*. The value by which the term is divided is called a *normalization factor*, and the resulting BRDF is referred to as a *normalized BRDF*. Normalized BRDFs have many advantages over non-normalized ones. We have already discussed the benefits of color parameters being closely related to reflectance values. In this case  $\mathbf{c}_{\text{spec}}$  is equal to the maximum value of the directional-hemispherical reflectance of the specular term, which in turn is closely related to the Fresnel reflectance at normal incidence  $R_F(0^\circ)$ . Since Equation 7.47 does not account for the Fresnel effect, using  $\mathbf{c}_{\text{spec}} = R_F(0^\circ)$  will probably be too dark. Using a value for  $\mathbf{c}_{\text{spec}}$  that is partway between white and  $R_F(0^\circ)$  may work better. If energy conservation is desired (it can sometimes be a useful guideline to help ensure realism), this can be guaranteed by ensuring that  $\mathbf{c}_{\text{diff}} + \mathbf{c}_{\text{spec}} \leq 1$ .

Another important effect of normalization is that now the  $m$  parameter is independent of reflectance and only controls surface roughness. In

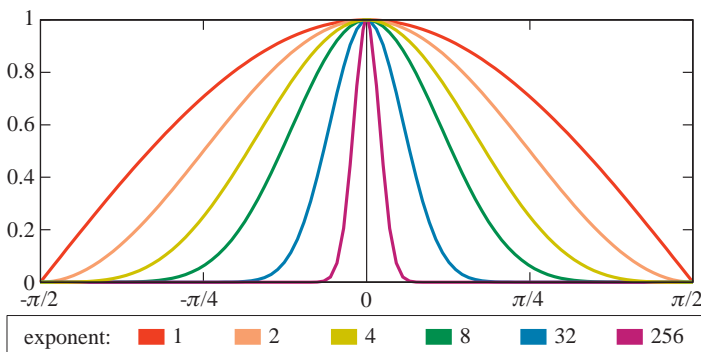


**Figure 7.36.** Graph of unnormalized cosine power term versus angle for various exponents. Increasing the exponent pulls the curve in, making for a tighter highlight. However, the height of the curve remains unchanged. This causes the total specularly reflected energy to decrease.

the non-normalized version of the BRDF, changing  $m$  changed both the amount and distribution of outgoing light. To understand why, see Figure 7.36. With higher exponents, the width of the curve (and thus the size of the rendered highlight) decreases; however the peak of the curve (the brightness at the highlight center) remains the same. The overall energy in the highlight decreases, since it is related to the integral under this curve. This behavior was necessary when graphics hardware could not handle values outside the 0 to 1 range, but, it is avoidable today and is undesirable. With non-normalized BRDFs, adjusting the surface roughness changes the reflectance as a side effect. This is bad because the reflectance defines the *perceived* specular color. This color defines the “look” of gold, copper, glass, etc. independent of surface roughness. For example, with a normalized BRDF an artist can set the overall specular color of a gold statue to the appropriate value (see Table 7.4) and then paint a roughness map with detail to show where the statue is smooth and where it is rough. The rough and smooth areas will both look like gold. If a non-normalized BRDF is used, then to get the correct gold appearance, the artist would need to use a second texture controlling the specular color and painstakingly paint values into it that would compensate for the roughness values. Worse still, depending on the surface roughness, these values could be very small or very large, making it difficult or impossible to store them in a texture.

Compare this graph to Figure 7.37, which shows normalized curves. When the exponent increases (corresponding to a smoother surface), the size of the highlight decreases, but its brightness increases, keeping the total reflectance constant. Recall that although reflectance values such as

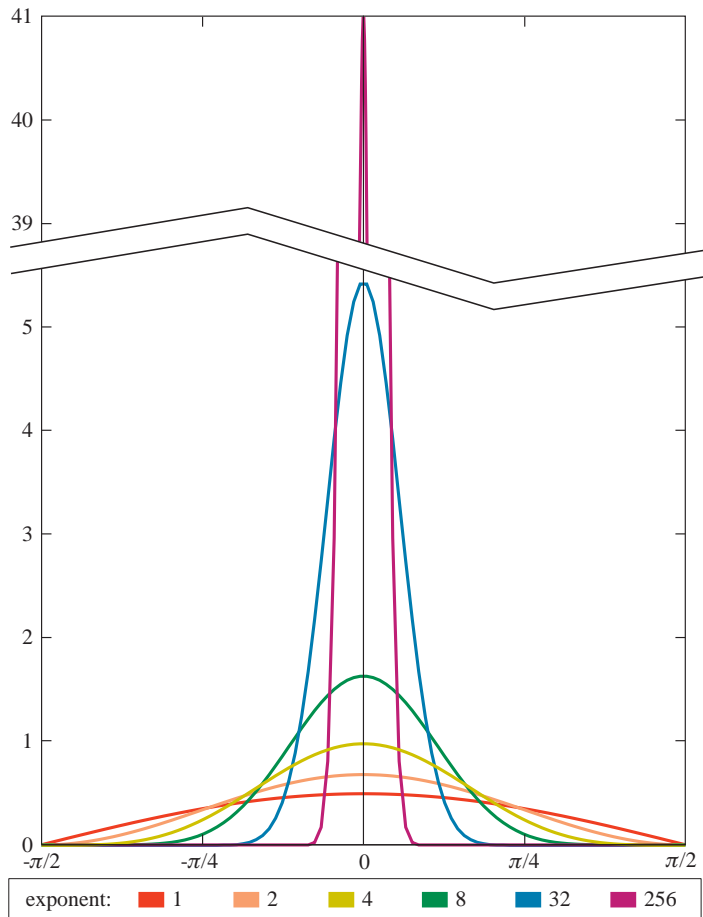


**Figure 7.37.** Graph of normalized cosine power term versus angle for various exponents. Increasing the exponent not only makes the curve narrower, but also higher. This increase in height compensates for the decrease in width, keeping the total reflected energy constant.

$R$  are limited to the 0 to 1 range, BRDF values can (and often do) exceed 1, especially in the case of smooth surfaces.

Figure 7.38 shows a series of spheres rendered with both the original and normalized Phong BRDFs. The intent is to model spheres that are the same except for their smoothness, so the specular and diffuse colors are held constant and  $m$  is varied. The images rendered with the normalized Phong BRDF show the highlight becoming brighter as it narrows, which is both physically correct and visually convincing. The images rendered with

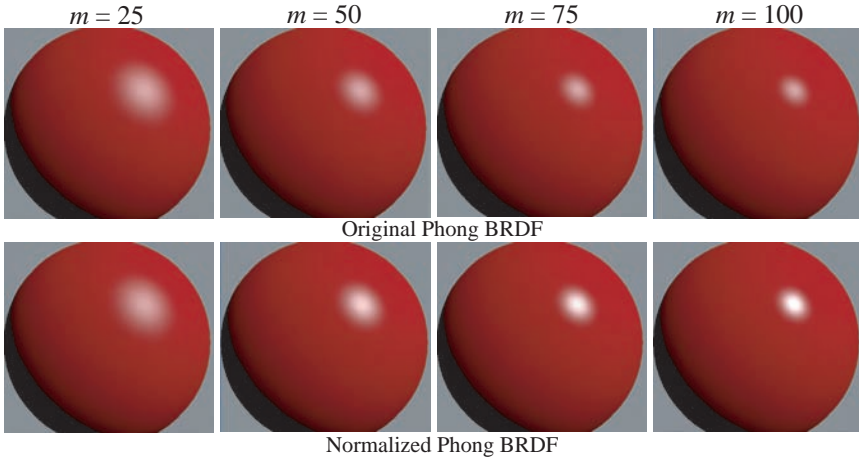


**Figure 7.38.** Rendered images of a red plastic sphere. The bottom row of images was rendered with the normalized Phong BRDF, using  $c_{\text{spec}} = 0.05$  (an appropriate value for plastic). The value of  $c_{\text{diff}}$  was set to  $[0.95, 0, 0]$ , for maximum saturation and brightness without violating energy conservation. The top row of images was rendered with the original (not normalized) Phong BRDF, using values of  $c_{\text{spec}}$  and  $c_{\text{diff}}$  chosen so that the two leftmost images match. The value of the smoothness parameter  $m$  increases from right to left, and the other BRDF parameters are held constant for each row. The intent is to render spheres made of the same substance (red plastic) but of differing surface smoothness. It can be seen that in the bottom row, the highlight grows much brighter as it gets narrower, which is the correct behavior—the outgoing light is concentrated in a narrower cone, so it is brighter. In the top row, the highlight remains equally bright as it gets narrower, so there is a loss of energy and the surface appears to be getting less reflective.

the original Phong BRDF do not have this property. The original Phong BRDF could be used to render the same images as those in the bottom row, but this would require carefully setting  $c_{\text{spec}}$  to values that increase with  $m$ —a highly unintuitive process. As discussed earlier, the authoring problem becomes even worse if values for  $c_{\text{spec}}$  and  $m$  are painted into textures.

Normalized BRDFs yield the ability to intuitively control physically meaningful parameters, enabling easy authoring of realistic materials. The additional rendering cost over a non-normalized version of the same BRDF is very low, so it is recommended to always use the normalized form. Note that physically derived BRDFs do not require normalization, since they have physical parameters by construction.

The normalized version of the Phong BRDF in Equation 7.47 is significantly improved from the original form, but we can do better. The Phong BRDF is reflection-vector-based, which (as noted in Section 7.5.7) is undesirable. Fortunately, a half-vector-based variant was proposed by Blinn

in 1977 [97], commonly referred to as the *Blinn-Phong* BRDF. The BRDF was originally presented in a non-normalized form, but a normalized form was derived<sup>16</sup> by Sloan and Hoffman in 2008 [1191]:

$$f(\mathbf{l}, \mathbf{v}) = \frac{\mathbf{c}_{\text{diff}}}{\pi} + \frac{m+8}{8\pi} \mathbf{c}_{\text{spec}} \overline{\cos}^m \theta_h. \quad (7.48)$$

Note that to get a similar highlight, the value of  $m$  used in the Blinn-Phong BRDF should be about four times that used for the Phong BRDF [344]. The Blinn-Phong BRDF can also be cheaper to evaluate than the Phong BRDF in some cases. If both vectors  $\mathbf{l}$  and  $\mathbf{v}$  are constant,  $\mathbf{h}$  can be computed once and reused. In addition, the computation of  $\mathbf{h}$  requires fewer operations than  $\mathbf{r}_i$ .

Besides the various benefits of half-vector-based BRDFs discussed in Section 7.5.7, another advantage is that the form is similar to a microfacet BRDF. This similarity means that the various expressions can be interpreted using microfacet theory. For example, the cosine power term can be interpreted as a normal distribution function (NDF), which gives a clear physical meaning to the cosine power  $m$ —it is a parameter of the microgeometry NDF. It is also clear that the BRDF can be extended to include the Fresnel effect by simply replacing  $\mathbf{c}_{\text{spec}}$  with  $R_F(\alpha_h)$ . This modification yields a BRDF that has physically meaningful parameters, models the most important phenomena responsible for the visual appearance of most materials, and has reasonably low computation and storage requirements:

$$f(\mathbf{l}, \mathbf{v}) = \frac{\mathbf{c}_{\text{diff}}}{\pi} + \frac{m+8}{8\pi} R_F(\alpha_h) \overline{\cos}^m \theta_h. \quad (7.49)$$

Note that after this modification, the energy conservation condition  $\mathbf{c}_{\text{diff}} + \mathbf{c}_{\text{spec}} \leq 1$  no longer applies, and care needs to be taken when setting parameters if energy conservation is desired. Alternatively, the model could be further extended by replacing the Lambertian diffuse term with one of the diffuse terms discussed in Section 7.5.4.

The BRDF in Equation 7.49 is often sufficient for most real-time rendering needs. However, there are some phenomena it does not model, and sometimes the need for a different BRDF will arise. For example, the “cosine term raised to a power” NDF used in the Blinn-Phong BRDF (sometimes called a *Phong lobe*) causes a certain falloff in intensity from the center of the highlight to its periphery, and sometimes highlights with a different “look” may be desired. The NDF directly controls the appearance of the highlight, so the effects of changing it can be quite visible. It is fairly straightforward to modify the Blinn-Phong BRDF by replacing the cosine power NDF with a different one. The hardest part is computing a new normalization factor for the specular term.

---

<sup>16</sup>See <http://www.realtimerendering.com/blinn-phong-normalization.pdf>.

Various other isotropic NDFs have been proposed in the computer graphics literature [97, 192, 193, 1270], but these are similar visually to the cosine power NDF and are more expensive to compute.<sup>17</sup> Some materials exhibit *multiscale roughness* (different roughnesses at different scales). This results in NDF curves that appear to be combinations of simpler curves, for example a low broad curve and a high narrow one. One simple way to implement such NDFs is to use a sum of appropriately weighted Blinn-Phong lobes.

Anisotropic NDFs can be used as well. Note that unlike isotropic NDFs, anisotropic NDFs cannot be evaluated just with the angle  $\theta_h$ ; additional orientation information is needed. In the general case, the half vector  $\mathbf{h}$  needs to be transformed into the *local frame* defined by the normal, tangent and bitangent vectors (see Figure 7.31 on page 248). The Ward [1326] and Ashikhmin-Shirley [42, 43] BRDFs both include anisotropic NDFs that could be reused in a modified Blinn-Phong BRDF.<sup>18</sup>

A particularly interesting option is to “paint” an arbitrary highlight shape into a bitmap for use as an NDF [632]. This is known as *NDF mapping* and allows for a variety of effects. If care is taken, the result can still be a physically plausible BRDF [41, 46]. NDFs can also be drawn from visual inspection of the highlight shapes of real materials [44]. However, since an NDF map is not a parametric representation, NDF mapping precludes the texturing of NDF parameters, which is useful for modeling spatially variant materials.

Pretty much any function over the hemisphere can be used as an NDF. Usually NDFs are assumed to be normalized so that they integrate to 1 over the hemisphere, but this is not necessary for empirical BRDFs such as Blinn-Phong, since the specular term needs to be renormalized after incorporating a new NDF.

Some surfaces are not modeled well with a Blinn-Phong-style BRDF, regardless of the NDF chosen. For example, extremely anisotropic surfaces like brushed metal and hair are often best modeled as tightly packed one-dimensional lines. Kajiya and Kay developed a simple BRDF model for this case [620], which was given a solid theoretical foundation by Banks [57]. It is alternately known as “the Kajiya-Kay BRDF” and “the Banks BRDF.” The basic concept is based on the observation that a surface composed of one-dimensional lines has an infinite number of normals at any given location, defined by the *normal plane* perpendicular to the tangent vector  $\mathbf{t}$  at that location ( $\mathbf{t}$  represents the direction of the grooves or fur [764]). The

---

<sup>17</sup>It is interesting to note that Blinn [97] proposed the Trowbridge-Reitz NDF as a replacement for the cosine power NDF because it was *cheaper* to compute. It was—in 1977. Changes in hardware have now made the cosine power NDF cheaper.

<sup>18</sup>When implementing the Ward NDF, see the technical report by Walter [1316] that includes a hardware-friendly form using only dot products.

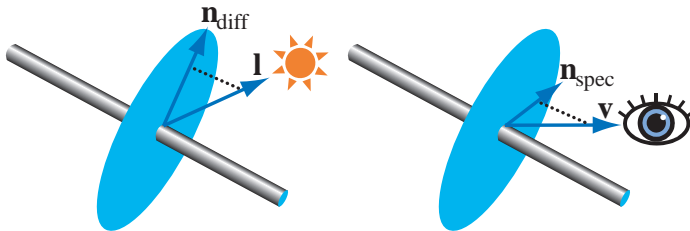


**Figure 7.39.** Shading normals used for the Kajiya-Kay model. A thin fiber is modeled as a cylinder that has an infinite number of surface normals (shown by the light blue circular plane) at each shaded point. On the left, the light vector  $\mathbf{l}$  is projected onto the normal plane, resulting in the vector  $\mathbf{n}_{\text{diff}}$ . This shading normal is used for computing the light projection cosine factor  $\overline{\cos \theta'_i}$ . On the right, the view vector  $\mathbf{v}$  is projected onto the normal plane, resulting in the vector  $\mathbf{n}_{\text{spec}}$ . This shading normal is used for computing the reflection vector  $\mathbf{r}$  used in the specular BRDF term.

Kajiya-Kay BRDF is essentially identical to the original Phong BRDF once a shading normal is selected out of this infinite set. Actually, two different shading normals are used—the diffuse BRDF term uses the projection of the light vector  $\mathbf{l}$  onto the normal plane, and the specular term uses the view vector  $\mathbf{v}$  projected onto the normal plane (see Figure 7.39). One form of these terms is [533, 628]

$$\begin{aligned}\overline{\cos \theta'_i} &= \sqrt{1 - (\mathbf{l} \cdot \mathbf{t})^2}, \\ \overline{\cos \alpha'_r} &= \max \left( \sqrt{1 - (\mathbf{l} \cdot \mathbf{t})^2} \sqrt{1 - (\mathbf{v} \cdot \mathbf{t})^2} - (\mathbf{l} \cdot \mathbf{t})(\mathbf{v} \cdot \mathbf{t}), 0 \right),\end{aligned}\quad (7.50)$$

where  $\overline{\cos \theta'_i}$  and  $\overline{\cos \alpha'_r}$  are the equivalents of  $\overline{\cos \theta_i}$  and  $\overline{\cos \alpha_r}$  in the Phong BRDF, but using the appropriate shading normal, rather than the geometric surface normal  $\mathbf{n}$ . The surface normal  $\mathbf{n}$  is not used, except to simulate self-shadowing by setting the BRDF value to 0 when the angle between  $\mathbf{l}$  and  $\mathbf{n}$  exceeds  $90^\circ$ . Although the Kajiya-Kay model was formulated in terms of the original Phong BRDF, there is no reason that the substitutions from Equation 7.50 could not be performed with the normalized version. Presumably, an anisotropic version of the Blinn-Phong BRDF could be derived using the same principles (most likely projecting the half vector  $\mathbf{h}$ , instead of  $\mathbf{v}$ , onto the normal plane to find the specular shading normal).

It is interesting to interpret the differences between the modified Blinn-Phong BRDF in Equation 7.49 and other empirical BRDFs in terms of the full microfacet BRDF in Equation 7.43 (on page 249). To facilitate this comparison, we will derive a version of the microfacet BRDF that uses a cosine power NDF:

$$f(\mathbf{l}, \mathbf{v}) = \left( \frac{G(\mathbf{l}, \mathbf{v})}{\overline{\cos \theta_i} \overline{\cos \theta_o}} \right) \left( \frac{m+2}{8\pi} \overline{\cos^m \theta_h} \right) R_F(\alpha_h). \quad (7.51)$$

Equation 7.51 shows the microfacet BRDF grouped into logical terms. Here is the specular term of the modified Blinn-Phong BRDF, grouped the same way:

$$f(\mathbf{l}, \mathbf{v}) = \left( \frac{m+8}{8\pi} \cos^m \theta_h \right) R_F(\alpha_h). \quad (7.52)$$

The Fresnel term is identical in both BRDFs. Both BRDFs also have very similar “NDF terms,” each including an exponentiated cosine and a normalization constant. The small difference between the two normalization constants is due to different assumptions in the normalization process. In any case, the difference will be small for all but the roughest surfaces.

The most significant difference between the two BRDFs is the leftmost term in the microfacet BRDF, which is completely missing in the Blinn-Phong BRDF. This term includes the geometry factor divided by two cosine factors. The geometry factor models shadowing and masking, and the cosine factors in the denominator model the foreshortening of the surface with respect to the light or camera. We will refer to the combined term as the *visibility term*.

The modified Blinn-Phong BRDF has the simplest possible visibility term, equal to a constant value of 1. This clearly has advantages in terms of simplicity and evaluation cost—it is worth closer examination to see if there are any disadvantages. A visibility term of 1 can be interpreted to mean that the modified Blinn-Phong BRDF has an implicit geometry factor:

$$G_{BF}(\mathbf{l}, \mathbf{v}) = \overline{\cos} \theta_i \overline{\cos} \theta_o, \quad (7.53)$$

which even makes some sense physically. Geometry factors simulate shadowing and masking effects and tend to decrease at glancing angles. The implicit geometry factor shown in Equation 7.53 does exhibit this behavior. However, this decrease happens rapidly as the light or view vector diverges from the surface normal, and it can be shown that this causes the Blinn-Phong BRDF to appear dark at glancing angles compared to real surfaces, particularly smooth metals [925]. For many applications, this will not be a concern. If it is, then there are several visibility terms proposed in the graphics literature that can be used to mitigate this problem. Since they will be more expensive to compute than the empty visibility term of the modified Blinn-Phong BRDF, they are worth adopting only if they result in some desired visible change.

The visibility term of the Ward BRDF is equal to  $1/(\overline{\cos} \theta_i \overline{\cos} \theta_o)$ ,<sup>19</sup> effectively omitting the geometry factor and ignoring the effects of shadowing and masking [1326]. The Ward BRDF also does not include a Fresnel term

---

<sup>19</sup>Note that the Ward BRDF was originally presented with a different visibility term [1326], but it was changed to  $1/(\overline{\cos} \theta_i \overline{\cos} \theta_o)$  in a later correction by Dür [280]. This correction has also been adopted by Ward, making it official.

(it uses a constant specular color instead). Both omissions are motivated by simplicity and by the fact that these effects tend to work at cross-purposes (shadowing and masking decrease reflectance at glancing angles, and the Fresnel effect increases it). In practice, lack of the Fresnel term causes the Ward BRDF to diverge in appearance from real materials [926]. In addition, the  $1/(\cos \theta_i \cos \theta_o)$  visibility term causes the reflectance to go to infinity at grazing angles, making the surface too bright [925]. For these reasons, we do not recommend adopting the Ward BRDF's visibility term, or its lack of a Fresnel term (although as mentioned above, its NDF is worth considering).

Seeking to find a realistic balance between the “too-dark” effects of no visibility term (Phong and Blinn-Phong BRDFs) and the “too-bright” effects of the  $1/(\cos \theta_i \cos \theta_o)$  visibility term (Ward BRDF), Neumann et al. [925] proposed a new visibility term:  $1/\max(\cos \theta_i, \cos \theta_o)$ . The specular term of the Ashikhmin-Shirley BRDF [42, 43] used a similar visibility term:  $1/(\cos \alpha_h \max(\cos \theta_i, \cos \theta_o))$ . Ashikhmin and Premože [46] propose dropping the  $\cos \alpha_h$  factor, and replacing the Neumann visibility term with a more continuous alternative:  $1/(\cos \theta_i + \cos \theta_o - \cos \theta_i \cos \theta_o)$ .

The visibility terms found in empirical BRDFs are designed primarily to ensure reasonable behavior at glancing angles. Those included in physically based microfacet BRDF models have explicit geometry factors designed to model shadowing and masking, divided by cosine terms to model foreshortening. The most well-known geometry factor was derived by Torrance and Sparrow [1270], and later introduced to computer graphics (re-derived in a greatly simplified form) by Blinn [97]:

$$G_{TS}(\mathbf{l}, \mathbf{v}) = \min \left( 1, \frac{2 \cos \theta_h \cos \theta_o}{\cos \alpha_h}, \frac{2 \cos \theta_h \cos \theta_i}{\cos \alpha_h} \right). \quad (7.54)$$

This same geometry factor was later used by Cook and Torrance in their BRDF model [192, 193]. Kelemen and Szirmay-Kalos derived an approximation to this geometry factor that is numerically more stable and significantly cheaper to evaluate [640]. Instead of approximating the geometry factor by itself, they found a simple approximation to the entire microfacet visibility term:

$$\frac{G_{TS}(\mathbf{l}, \mathbf{v})}{\cos \theta_i \cos \theta_o} \approx \frac{2}{1 + \mathbf{l} \cdot \mathbf{v}} = \frac{4}{\mathbf{h}' \cdot \mathbf{h}'} = \frac{1}{\cos^2 \alpha_h}, \quad (7.55)$$

where  $\mathbf{h}'$  is the non-normalized half vector, or  $\mathbf{l} + \mathbf{v}$ . It is interesting to note that when the rightmost form is used, the complete microfacet BRDF can be factored into two functions, each of which depends on just one variable:  $p(\theta_h)/4k_p$  and  $R_F(\alpha_h)/(\cos^2 \alpha_h)$ .

In reality, shadowing and masking depend heavily on the surface roughness. This has not been accounted for in any of the geometry factors pre-

sented so far. Two roughness-dependent geometry factors from other fields have been used in computer graphics. A geometry factor introduced by Sancer [1102] was used by Stam in his diffraction BRDF [1213], and one introduced by Smith [1193] was used in the HTSG BRDF model [515]. Both of these factors are quite complex and expensive to compute, but a reasonably cheap approximation to the Smith shadowing function was introduced by Schlick [1128]:

$$G_{\text{Smith}}(\mathbf{l}, \mathbf{v}) \approx \left( \frac{\overline{\cos} \theta_i}{\overline{\cos} \theta_i(1-k) + k} \right) \left( \frac{\overline{\cos} \theta_o}{\overline{\cos} \theta_o(1-k) + k} \right), \quad (7.56)$$

where  $k = \sqrt{2m^2/\pi}$ . Here  $m$  is not the cosine power, but rather the root mean square (RMS) slope of a Beckmann NDF—published equivalences between the NDFs [769] can be used to calculate it from the cosine power if needed.

The 2000 paper by Ashikhmin et al. [41] give a method for deriving a geometry factor that matches an arbitrary NDF. Since it is based on integrals that are unlikely to have a closed form in most cases, implementations of this geometry factor will likely be based on lookup tables.

Ashikhmin [44] analyzes the relative importance of the Fresnel, NDF, and visibility terms of various microfacet BRDFs. He finds that the NDF term is by far the most important for determining appearance, followed by the presence or absence of a Fresnel term. The visibility factor is the least important of the three.

A physical phenomenon not modeled by the modified Phong BRDF in Equation 7.49 is the retroreflection seen in certain rough surfaces (as explained in Figure 7.28 on page 245). Blinn described a BRDF intended to model such surfaces [100]. Oren and Nayar [973] proposed a different BRDF targeted at the same problem. The Oren-Nayar BRDF is particularly interesting since it applies microfacet theory to Lambertian facets. A simplified version of this BRDF is given as

$$f(\mathbf{l}, \mathbf{v}) = \frac{c_{\text{diff}}}{\pi} (A + B \overline{\cos}(\phi) \sin(\min(\theta_i, \theta_o)) \tan(\max(\theta_i, \theta_o))), \quad (7.57)$$

where  $\phi$  is the relative azimuth angle between the projections of the incoming light direction  $\mathbf{l}$  and the view direction  $\mathbf{v}$  (see Figure 7.15).  $A$  and  $B$  are defined thus:

$$\begin{aligned} A &= 1 - 0.5 \frac{\sigma^2}{\sigma^2 + 0.33}, \\ B &= 0.45 \frac{\sigma^2}{\sigma^2 + 0.09}. \end{aligned} \quad (7.58)$$

The intermediate values  $A$  and  $B$  are computed from  $\sigma$ , the roughness. The roughness  $\sigma$  is defined as the standard deviation of the angle between

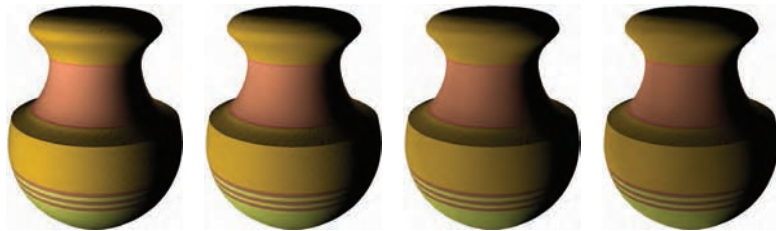


**Figure 7.40.** Simplified Oren-Nayar, with roughness values (going from left to right) of 0 (Lambertian), 0.3 ( $17^\circ$ ), 0.6 ( $34^\circ$ ), and 1.0 ( $57^\circ$ ). (Images courtesy of Michal Valient [1285, 1286].)

the microfacet surface normals and the macroscopic surface normal. It is measured in radians. According to Oren and Nayar, a  $\sigma$  value of 0.52 ( $30^\circ$ ) corresponds to a “very rough surface.” They show graphs and renderings for  $\sigma$  values up to 0.7 ( $40^\circ$ ). See Figure 7.40. A visualization of the various terms is shown in Figure 7.41. When the roughness is zero, the equation devolves to  $\mathbf{c}_{\text{diff}}/\pi$ , the Lambertian BRDF, Equation 7.36. Oren and Nayar note that the 0.33 in the term for  $A$  can be replaced by 0.57 to better approximate surface interreflection.

Valient [1285, 1286] presents techniques to rapidly evaluate this equation on the GPU. For a constant roughness,  $A$  and  $B$  can be precomputed. To compute  $\overline{\cos}(\phi)$ , the light and view vectors are projected to the surface’s tangent plane:

$$\begin{aligned}\mathbf{v}_{\text{proj}} &= \mathbf{v} - \mathbf{n}(\mathbf{n} \cdot \mathbf{v}), \\ \mathbf{l}_{\text{proj}} &= \mathbf{l} - \mathbf{n}(\mathbf{n} \cdot \mathbf{l}).\end{aligned}\tag{7.59}$$

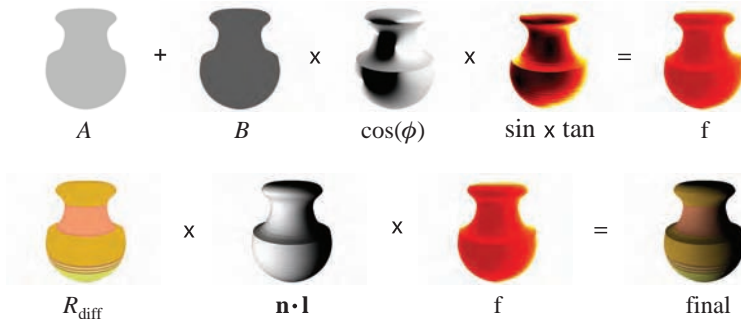


**Figure 7.41.** Visualization of simplified Oren-Nayar shading. The  $\sin \times \tan$  and  $f$  (BRDF) values extend beyond 1 and are visualized using a false-color ramp (black is 0, red is 1, yellow is 2 and white is 3). (Images courtesy of Michal Valient [1285, 1286].)

The resulting vectors are normalized, and the dot product of these vectors is then clamped to be non-negative, so computing the  $\cos$  term. Valient converts the  $\sin \times \tan$  term to a two-dimensional texture lookup, where the texture coordinates are  $\mathbf{n} \cdot \mathbf{l}$  and  $\mathbf{n} \cdot \mathbf{v}$ . Hoxley [314] gives a texture lookup version and a computed version.

In conclusion, although a large variety of analytic BRDF models exist in the literature, for most applications, a simple yet reasonably expressive model such as the one in Equation 7.49 will suffice. In cases where a different BRDF is desired, pieces of models presented here can be added in a “mix-and-match” fashion to produce a new analytic BRDF. The Phong NDF can be extended to a sum of lobes, or an anisotropic NDF can be used [42, 43, 1326]. Alternatively, the Kajiya-Kay modification [620] can be applied to convert an isotropic BRDF into an anisotropic one. The realism of the BRDF can be improved by incorporating visibility terms that change the behavior at glancing angles. The visibility term derived by Kelemen and Szirmay-Kalos [640] is particularly worthy of consideration due to its low cost and physical basis. The Lambertian diffuse term can be replaced with one that models the tradeoff between surface and body reflectance (see Section 7.5.4).

This “mixing and matching” can be extended to pieces represented as lookup tables, since they do not have an analytic closed-form expression. This might be because the values are manually painted for creative reasons. NDF maps are one possibility, but there are others. For example, a one-dimensional lookup table could be used for the Fresnel term, to allow for hand-painted color shifts at glancing angles. In other cases, BRDF terms are derived by computing integrals that may not have closed-form solutions, such as the microfacet geometry term introduced by Ashikhmin et al. [41], or the reciprocal energy-conserving diffuse term introduced by Shirley et al. [640, 1170]. Incorporating such lookup tables can make a BRDF more expressive. However, a lookup table is not something we can modify by a parameter, so it cannot easily be made to vary over a surface.

The field of possible BRDF models and representations is vast. We have endeavored to cover the options of most relevance to real-time rendering, but many others remain. Interested readers are referred to the available surveys [44, 926, 1129, 1170, 1345, 1346], as well as the second volume of Glassner’s *Principles of Digital Image Synthesis* [409] and the more recent *Digital Modeling of Material Appearance* [275] by Dorsey, Rushmeier, and Sillion.

## 7.7 BRDF Acquisition and Representation

In most real-time applications, BRDFs are manually selected and their parameters set to achieve a desired look. However, sometimes BRDFs are

acquired, or measured, directly from actual surfaces. In some cases this is done to closely match rendered objects to real ones (digital doubles in film production, or digital reproductions of cultural artifacts). In others, it may be done to save authoring time. In either case, two problems need to be solved: how to capture the BRDF data, and once captured, how to represent it for later rendering.

### 7.7.1 Acquiring BRDFs

Goniometers, imaging bidirectional reflectometers, and image-based methods have been used to obtain the reflectance measurements over the incoming and outgoing angles. Some of these databases are public and available online, such as those from Cornell University [200], Columbia-Utrecht [190], and MIT [871]. Ward [1326] discusses measurement in depth, Kautz et al. [630] give an overview of acquisition techniques, and Marschner et al. [821] discuss previous work and their own image-based method for measuring BRDFs, which has been since further refined by Matusik [825] and Ngan [926].

While the previously mentioned techniques measure a single BRDF function, the capture of spatially varying BRDFs (SVBRDFs) is of more interest, since real-world objects rarely have uniform reflectance. Acquisition of SVBRDFS [225, 226, 1255] is an active area of research, especially from human faces [232, 369, 388, 1349]. Some SVBRDF capture techniques [232, 377, 495] have been used in commercial applications [2, 1096]. The Columbia-Utrecht database [190] includes some spatially variant measurements, as well as individual BRDFs.

### 7.7.2 Representations for Measured BRDFs

The result of a BRDF capture is a large, densely sampled four-dimensional table (six-dimensional for SVBRDFs). The acquisition process also unavoidably introduces noise into the data. For these reasons, the raw data is unsuitable to be used directly for rendering—it must first be converted into some other representation [1089].

One common method is to select an analytic BRDF and fit its parameters to the measured data. This results in a very compact representation, and rendering is reasonably fast. The results are also easy to edit manually if needed. However, it is not always simple to choose a BRDF for this purpose, and fitting involves a complex and time-consuming optimization process. The error introduced can be quite large and depends on the BRDF model chosen. One way to improve the quality of the results (although further complicating the fitting process) is to use a weighted sum of multiple BRDF terms, such as Ward [1326] or Blinn-Phong [97] lobes.

One model that was designed to be used in a multiple-term fitting process is the Lafourte BRDF [710], which generalizes the calculation of the reflection vector used in the original Phong model [1014]. This generalization enables the modeling of retroreflective and anisotropic surfaces. McAllister et al. used multiple Lafourte terms to render SVBRDFs in real time on a GPU [830, 831].

Ngan et al. [926] perform a detailed analysis of the errors introduced by fitting various measured materials to a selection of analytic BRDF models. For isotropic materials, Ward and Blinn-Phong BRDFs have the highest errors, most likely due to their lack of a Fresnel term (the original form of the Blinn-Phong BRDF was used, which does not have a Fresnel term). The Lafourte BRDF also has fairly high errors, evidently due to the fact that it is derived from a reflection-vector-based BRDF and shares the problems of that class of BRDF models (see Section 7.5.7). The best results are achieved with the HTSG, Cook-Torrance, and Ashikhmin-Shirley BRDFs. About a third of the measured materials gained significant accuracy from the addition of a second lobe of the same type—one lobe was sufficient for the remainder.

Ngan et al. also analyzed several anisotropic materials. Only the Ward [1326] and Poulin-Fournier [1027] BRDFs were used for fitting. Both of them did moderately well on surfaces with simple anisotropic reflectance. Surfaces such as fabrics with complex, periodic microgeometry structure were not modeled well by any of the analytic BRDFs. For those materials, Ngan adopted an interesting semi-analytic fitting approach; an arbitrary microfacet distribution was deduced from the measurements, and then a BRDF was generated from the microfacet distribution, using the method introduced by Ashikhmin et al. [41]. This approach resulted in very good matches to the measured data.

Ashikhmin and Premože propose [46] a distribution-based BRDF model that allows for extremely simple BRDF acquisition. A single image of a sample with known, curved geometry (taken with the light source and camera positions close to each other) can suffice to capture many materials.

Another way to represent BRDFs is to project them onto *orthonormal bases*, such as spherical harmonics [1344], spherical wavelets [180, 715, 1135], or Zernike Polynomials [681]. These techniques are focused on representing the shape of the BRDF as a generic function. Look again at Figure 7.17: For a given incoming direction, a surface is formed that represents the reflectance at any outgoing direction. The BRDF surface is generally changing in a smooth fashion, with few places where it changes rapidly. This implies that a sum of a few low- and high-frequency functions can capture the BRDF shape. Such projections are simpler to perform than fitting to a BRDF or sum of BRDF terms, as no optimization process is needed. However, many terms are usually needed to achieve a reasonable



**Figure 7.42.** Factorization of a BRDF for gold, using the Cook-Torrance surface model [192]. The two textures are accessed with the incoming light and outgoing view directions, respectively, and are multiplied together at each pixel to generate the teapot’s illumination. (*Images courtesy of NVIDIA Corporation.*)

match to the original function (dozens or hundreds), making these methods unsuitable for real-time rendering. Section 8.6.1 discusses basis projection in more detail.

As four-dimensional functions, BRDFs can also be approximated, or *faktored*, into a sum of products of lower-dimensional functions. If these functions are one or two dimensional, they can be stored in textures, making this type of representation amenable to rendering on graphics hardware (although graphics hardware can use volume textures, the storage cost tends to be too high to be reasonable). In practice, it has been found that a single pair of two-dimensional textures is sufficient to give reasonably convincing results for many materials [625]. See Figure 7.42 for an example. The basic factorization algorithm and its implementation are explained thoroughly and clearly by Kautz et al. [631] and Wynn [1389]. We recommend these articles and the related source code to interested readers. McCool et al. [835] present a newer factorization technique with some advantages over the basic factorization algorithm, and also provide code.

The parameterization of the lower-dimensional functions (and thus the set of values used as coordinates to look up the factored textures when rendering) needs to be chosen with care so as to minimize the number of functions needed. A naive parameterization would use the azimuth and elevation angles  $\theta_i$  and  $\phi_i$  of the incoming light direction as the  $u$  and  $v$  coordinates of one texture, and the angles  $\theta_o$  and  $\phi_o$  of the outgoing view direction as the  $u$  and  $v$  coordinates of the second. In practice, such a parameterization would yield a poor factorization, requiring a large number of texture pairs to be summed to approximate the BRDF. Finding a good re-parameterization is not trivial and may depend on the material. Rusinkiewicz suggested a parameterization based on the azimuth and elevation angles of the half vector  $\mathbf{h}$  and the incoming light vector  $\mathbf{l}$  ( $\mathbf{l}$ 's angles measured relatively to  $\mathbf{h}$ ) [1090]. This parameterization is naturally aligned



**Figure 7.43.** Materials rendered using factorization [835], where the BRDF is approximated by pairs of two-dimensional textures. From left to right, the materials are a blue Krylon latex enamel, satin, and a textured velvet body with garnet red paint on the knot shape. The paints and velvet are from measured BRDF data [190, 200], and the satin is computed using the analytic Poulin-Fournier anisotropic reflectance model [1027]. (*Images generated by the “brdfview” program by McCool, Ang, and Ahmad.*)

to the behavior of real-world surfaces and the features of common analytic BRDFs. Other parameterizations (also based on the half vector, but in different ways) are suggested by Stark et al. [1217] and Edwards et al. [298]. If the quantities used as texture coordinates are to be interpolated, this imposes additional conditions on the parameterization. For example, the Rusinkiewicz parameterization does not interpolate well—Kautz et al. [625] suggest several alternatives that do. This is not a concern if the quantities are to be computed in the pixel shader. Once the parameterization has been selected, the measured BRDF data can be factored (a fairly time-consuming process). See Figure 7.43 for some results.

These factorization techniques have two limitations that may be problematic for most applications: They are not suitable for measured SVBRDFS, since a separate factorization process needs to be performed for each location, and the results cannot easily be edited. A recent paper by Lawrence et al. [740] addresses both of these limitations. Their method works directly on captured SVBRDF data, decomposing it into a series of one- or two-dimensional textures. These textures are defined so as to be suitable for editing. A *shade tree* is created to combine the textures and produce the final shaded pixel color. At the top level of the shade tree, weight textures control the mixing of several *basis BRDFs*. Each basis BRDF is decomposed into terms such as specular and diffuse, and each term is further decomposed using Rusinkiewicz’s parameterization [1090]. The bottom level nodes are editable one-dimensional curves or two-dimensional maps. The curves control such aspects of the reflectance as isotropic NDFs and color shifts at glancing angles. The two-dimensional maps are used for anisotropic NDFs. The weight textures can also be edited, changing the spatial distribution of the basis BRDFs. This paper is recommended reading to anyone who needs to render scenes with acquired SVBRDFs.

Basis projections and factorizations have been discussed as representations for measured BRDFs. They could in theory be used for analytic

BRDF models as well, perhaps to save computation. In practice, the falling cost of computation versus the cost of texture lookups on modern hardware, combined with the many advantages of parametric BRDF representations, makes this technique unpopular.

## 7.8 Implementing BRDFs

To incorporate a BRDF model in a rendering system, the BRDF needs to be evaluated as part of a shading equation. The purpose of a shading equation is to compute the outgoing radiance  $L_o$  from a surface location into the view direction  $\mathbf{v}$ . Given a set of  $n$  point or directional light sources, the outgoing radiance is computed thus (repeating Equation 7.21):

$$L_o(\mathbf{v}) = \sum_{k=1}^n f(\mathbf{l}_k, \mathbf{v}) \otimes E_{L_k} \overline{\cos} \theta_{i_k}.$$

The cosine factor is computed as the clamped dot product between the surface normal and the  $k$ th light direction vector:

$$\overline{\cos} \theta_{i_k} = \max(\mathbf{n} \cdot \mathbf{l}_k, 0). \quad (7.61)$$

Various methods for computing the value of  $E_{L_k}$  were discussed in Section 7.4. The computation of the BRDF value  $f(\mathbf{l}_k, \mathbf{v})$  remains in order to complete the evaluation of the shading equation.

As we have seen, most BRDFs contain a  $1/\pi$  factor. In many rendering systems, this factor is folded into  $E_L$  for convenience. When adapting a radiometrically defined BRDF (such as can be found in academic papers, or in Section 7.6 of this book) for use in such a rendering system, care must be taken to multiply the BRDF by  $\pi$ .

The most straightforward way to evaluate any BRDF model that has an analytic expression, as opposed to being represented by a factorization or a sum of basis functions, is to simply evaluate the expression in a shader for each light source (see Equation 7.21 on page 224). Evaluating the full expression in the pixel shader will give the best visual results, but in some cases slowly varying subexpressions can be evaluated in the vertex shader and interpolated. For spatially varying BRDFs, a common approach is to encode BRDF parameters in textures (see Section 6.5), although in some cases it might make sense to store them in vertices instead. Since evaluation of dot products is efficient on graphics hardware, BRDFs intended for real-time use are usually formulated in terms of cosines of angles between vectors such as the incoming light vector  $\mathbf{l}$ , view vector  $\mathbf{v}$ , half vector  $\mathbf{h}$ , surface normal  $\mathbf{n}$ , tangent  $\mathbf{t}$ , or bitangent  $\mathbf{b}$ . If both vectors are of length 1, the dot product is equal to the cosine of the angle between the vectors.

In principle, BRDF equations apply in the *local frame* of the surface defined by the vectors  $\mathbf{n}$ ,  $\mathbf{t}$ , and  $\mathbf{b}$ . In practice, they can be evaluated in any coordinate system (or more than one) as long as care is taken never to perform an operation between vectors in different coordinate systems. Per-pixel BRDF evaluation is often combined with normal mapping. In principle, normal mapping perturbs the entire local frame, not just the normal. Isotropic BRDFs rarely require tangent or bitangent vectors, so perturbing the normal vector is sufficient. When shading with anisotropic BRDFs, it is important to perturb any tangent or bitangent vectors used. Anisotropic BRDFs introduce the possibility of per-pixel modification of the tangent direction—use of textures to perturb both the normal and tangent vectors is called *frame mapping* [618]. Frame mapping can enable effects such as brushed swirls on metal or curly hair.

Some BRDFs are defined as a combination of subexpressions defined analytically and subexpressions defined by values stored in one- or two-dimensional data tables (see Section 7.6). These semi-analytic BRDFs are computed much like fully analytic BRDFs, but with the addition of texture lookups for the tabulated subexpressions.

Even for fully analytically defined BRDFs, there might be a performance benefit in extracting a subexpression that is a function of one or two variables and tabulating its values in a texture for lookup while rendering. In the past, when computation was costly relative to texture lookups, this was a very common practice. Now computation is relatively cheap—a rule of thumb in 2007 was that one texture operation is equivalent to ten arithmetic operations (or more).<sup>20</sup> This number will keep growing as graphics hardware evolves [1400]. Only the most complex subexpressions will benefit from being factored into a texture. To avoid losing the parametric qualities of the BRDF, it is preferable for factored subexpressions to be independent of the BRDF’s parameters.

BRDFs using non-parametric representations are more difficult to render efficiently. In the case of BRDFs defined as an orthonormal expansion of bases such as spherical harmonics, rendering is straightforward—just evaluate the basis functions—but due to the large number of coefficients computation is likely to be expensive. More importantly, if the BRDF is spatially varying, then a very large number of texture reads is needed to read all of the coefficients, further reducing performance.

BRDFs that use factored representations are easier to render, since a relatively small number of textures are read (usually two). Inverse Shade Trees [740] use a larger number of textures (about twenty for the examples given) but most of them are one dimensional. This is still well within the capabilities of modern accelerators, but the large number of texture

---

<sup>20</sup>This holds true for an NVIDIA G80, and it is likely that ATI is similar.

accesses will cause rendering of such BRDFs to be significantly slower than most analytic BRDFs. In addition, note that most of the texture accesses need to be repeated for each light source.

### 7.8.1 Mipmapping BRDF and Normal Maps

In Section 6.2, we discussed a problem with texture filtering: Mechanisms such as bilinear filtering and mipmapping are based on the assumption that the quantity being filtered (which is an input to the shading equation) has a linear relationship to the final color (the output of the shading equation). Although this is true for some quantities, such as diffuse and specular colors, it is not true in general. Artifacts can result from using linear mipmapping methods on normal maps, or on textures containing nonlinear BRDF parameters such as cosine powers. These artifacts can manifest as flickering highlights, or as unexpected changes in surface gloss or brightness with a change in the surface’s distance from the camera.

To understand why these problems occur and how to solve them, it is important to remember that the BRDF is a statistical description of the effects of subpixel surface structure. When the distance between the camera and surface increases, surface structure that previously covered several pixels may be reduced to subpixel size, moving from the realm of bump maps into the realm of the BRDF. This transition is intimately tied to the mipmap chain, which encapsulates the reduction of texture details to subpixel size.

Let us consider how the appearance of an object such as the cylinder in Figure 7.44 is modeled for rendering. Appearance modeling always assumes a certain scale of observation. *Macroscale* (large scale) geometry is modeled as triangles, *mesoscale* (middle scale) geometry is modeled as textures, and *microscale* geometry, smaller than a single pixel, is modeled via the BRDF.



**Figure 7.44.** A shiny, bumpy cylinder, modeled as a cylindrical mesh with a normal map. (Image courtesy of Patrick Conran, ILM.)

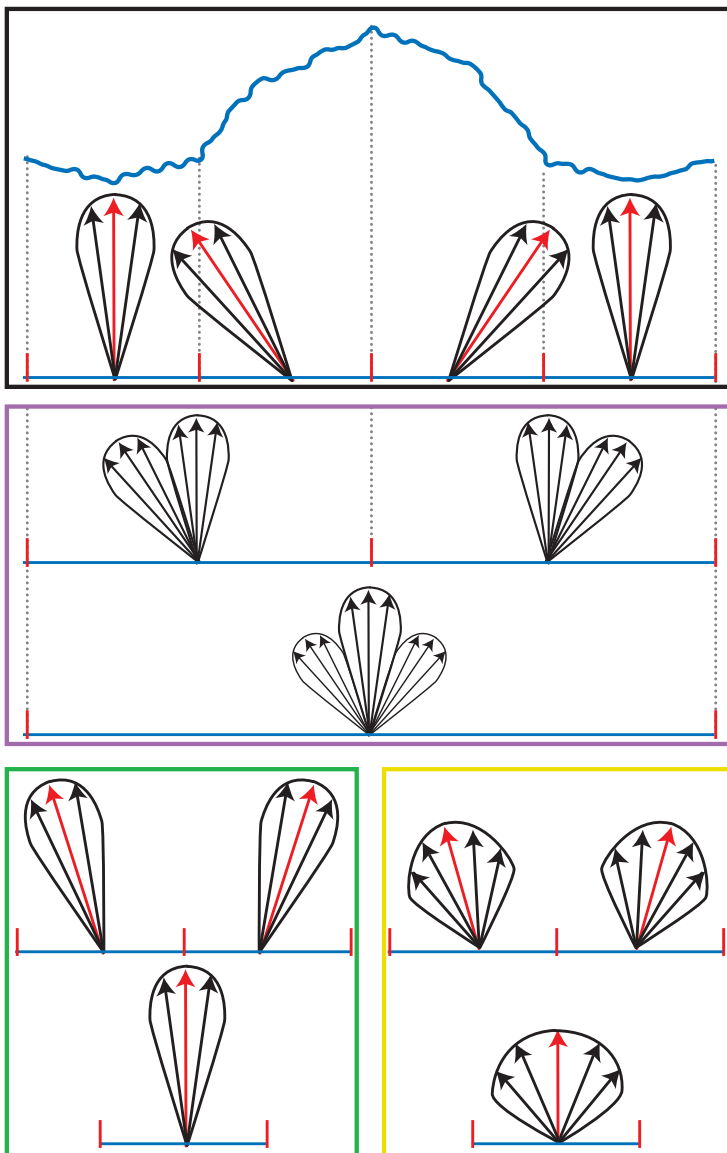


**Figure 7.45.** Part of the surface from Figure 7.44. The top shows the oriented NDFs, as well as the underlying surface geometry they implicitly define. The center shows ideal NDFs collected from the underlying geometry at lower resolutions. The bottom left shows the result of normal averaging, and the bottom right shows the result of cosine lobe fitting.

Given the scale shown in the image, it is appropriate to model the cylinder as a smooth mesh (macroscale), and represent the bumps with a normal map (mesoscale). A Blinn-Phong BRDF with a fixed cosine power is chosen to model the microscale normal distribution function (NDF). This combined representation models the cylinder appearance well at this scale. But what happens when the scale of observation changes?

Study Figure 7.45. The black-framed figure at the top shows a small part of the surface, covered by four normal map texels. For each normal map texel, the normal is shown as a red arrow, surrounded by the cosine lobe NDF, shown in black. The normals and NDF implicitly specify an underlying surface structure, which is shown in cross section. The large hump in the middle is one of the bumps from the normal map, and the small wiggles are the microscale surface structure. Each texel in the normal map, combined with the cosine power, can be seen as collecting the NDF across the surface area covered by the texel.

The ideal representation of this surface at a lower resolution would exactly represent the NDFs collected across larger surface areas. The center of the figure (framed in purple) shows this idealized representation at half and one quarter of the original resolution. The gray dotted lines show which areas of the surface are covered by each texel. This idealized representation, if used for rendering, would most accurately represent the appearance of the surface at these lower resolutions.

In practice, the representation of the surface at low resolutions is the responsibility of the lower mipmap levels in the mipmap chain. At the bottom of the figure, we see two such sets of mipmap levels. On the bottom left (framed in green) we see the result of averaging and renormalizing the normals in the normal map, shown as NDFs oriented to the averaged normals. These NDFs do not resemble the ideal ones—they are pointing in the same direction, but they do not have the same shape. This will lead to the object not having the correct appearance. Worse, since these NDFs are so narrow, they will tend to cause aliasing, in the form of flickering highlights.

We cannot represent the ideal NDFs directly with the Blinn-Phong BRDF. However, if we use a gloss map, the cosine power can be varied from texel to texel. Let us imagine that, for each ideal NDF, we find the rotated cosine lobe that matches it most closely (both in orientation and overall width). We store the center direction of this cosine lobe in the normal map, and its cosine power in the gloss map. The results are shown on the bottom right (framed in yellow). These NDFs are much closer to the ideal ones. With this process, the appearance of the cylinder can be represented much more faithfully than with simple normal averaging, as can be seen in Figure 7.46.

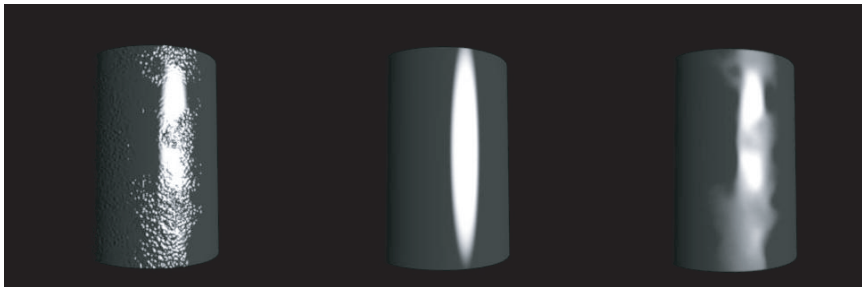


**Figure 7.46.** The cylinder from Figure 7.44. On the left, rendered with the original normal map. In the center, rendered with a much lower-resolution normal map containing averaged and renormalized normals (as shown in the bottom left of Figure 7.45). On the right, the cylinder is rendered with textures at the same low resolution, but containing normal and gloss values fitted to the ideal NDF, as shown in the bottom right of Figure 7.45. The image on the right is a significantly better representation of the original appearance. It will also be less prone to aliasing when rendered at low resolutions. (*Image courtesy of Patrick Conran, ILM.*)

In general, filtering normal maps in isolation will not produce the best results. The ideal is to filter the entire surface appearance, represented by the BRDF, the normal map, and any other maps (gloss map, diffuse color map, specular color map, etc.). Various methods have been developed to approximate this ideal.

Toksvig [1267] makes a clever observation, that if normals are averaged and not renormalized, the length of the averaged normal correlates inversely with the width of the normal distribution. That is, the more the original normals point in different directions, the shorter the normal averaged from them. Assuming that a Blinn-Phong BRDF is used with cosine power  $m$ , Toksvig presents a method to compute a new cosine power  $m'$ . Evaluating the Blinn-Phong BRDF with  $m'$  instead of  $m$  approximates the spreading effect of the filtered normals. The equation for computing  $m'$  is

$$m' = \frac{\|\mathbf{n}_a\| m}{\|\mathbf{n}_a\| + m(1 - \|\mathbf{n}_a\|)}, \quad (7.62)$$

where  $\|\mathbf{n}_a\|$  is the length of the averaged normal. Toksvig's method has the advantage of working with the most straightforward normal mipmapping scheme (linear averaging without normalization). This feature is particularly useful for dynamically generated normal maps (e.g., water ripples), for which mipmap generation must be done on the fly. Note that common methods of compressing normal maps require reconstructing the  $z$ -component from the other two, so they do not allow for non-unit-length normals. For this reason, normal maps used with Toksvig's method may have to remain uncompressed. This issue can be partially compensated for

by the ability to avoid storing a separate gloss map, as the normals in the normal map can be shortened to encode the gloss factor. Toksvig’s method does require a minor modification to the pixel shader to compute a gloss factor from the normal length.

Conran at ILM [191] proposes a process for computing the effect of filtered normal maps on specular response. The resulting representation is referred to as *SpecVar maps*. SpecVar map generation occurs in two stages. In the first stage, the shading equation is evaluated at a high spatial resolution for a number of representative lighting and viewing directions. The result is an array of shaded colors associated with each high-resolution surface location. Each entry of this array is averaged across surface locations, producing an array of shaded colors for each low-resolution texel. In the second stage a fitting process is performed at each low-resolution texel. The goal of the fitting process is to find the shading parameters that produce the closest fit to the array values for the given lighting and viewing directions. These parameters are stored in texture maps, to be used during shading. Although the details of the process are specific to Pixar’s RenderMan renderer, the algorithm can also be used to generate mipmap chains for real-time rendering. SpecVar map generation is computationally expensive, but it produces very high quality results. This method was used at ILM for effects shots in several feature films. Figure 7.46 was also generated using this technique.

Schilling [1124] proposed storing three numbers at each location in the mipmap, to represent the variance of the normals in the  $u$  and  $v$  axes. Unlike the previously discussed methods, this supports extracting anisotropic NDFs from the normal map. Schilling describes an anisotropic variant of the Blinn-Phong BRDF using these three numbers. In later work [1125], this was extended to anisotropic shading with environment maps.

Looking at the ideal lowest-resolution NDF in the middle of Figure 7.45, we see three distinct lobes, which are only somewhat approximated by the single Phong lobe on the bottom right. Such multi-lobe NDFs appear when the normal map contains non-random structure. Several approaches have been proposed to handle such cases.

Tan et al. [1239, 1240] and Han et al. [496] discuss methods to fit a mixture of multiple BRDF lobes to a filtered normal map. They demonstrate significant quality improvement over Toksvig’s method, but at the cost of considerable additional storage and shader computation.

## 7.9 Combining Lights and Materials

Lighting computations occur in two phases. In the *light phase*, the light source properties and surface location are used to compute the light’s di-

rection vector  $\mathbf{l}$  and irradiance contribution (measured in a plane perpendicular to the light source)  $E_L$ . Many different types of light sources can be defined, leading to different ways to compute  $\mathbf{l}$  and  $E_L$ —see Section 7.4. In the *material phase*, the BRDF parameters and surface normal (as well as the tangent and bitangent, in the case of anisotropic materials) are found via interpolation or texturing. These values are used to evaluate the BRDF for  $\mathbf{l}$  and the view vector  $\mathbf{v}$ . The result of the BRDF evaluation is multiplied by a cosine factor and by  $E_L$  to produce the outgoing radiance contributed by the light source. Both phases are repeated for each light source and the results are summed to produce the total outgoing radiance for the fragment.

In many real-time applications, numerous light sources of various types can be applied to surfaces described by a variety of materials. The sheer number of combinations can pose difficulties. Imagine a game that supports just three types of light source (point, directional and spot). Each mesh can be affected by no more than six light sources at once, and can have one of five material types. In this relatively simple case, there are 420 shader combinations.<sup>21</sup> The number of combinations grows rapidly with every addition—just adding a fourth light type (e.g., a projected texture light) increases the number of combinations to 1050.<sup>22</sup> In real applications, the number is even higher. Valve’s *Half-Life 2* has 1920 pixel shader combinations [848].

In addition, the fact that both the light and material phase need to be repeated for each light source affecting the object can lead to great inefficiencies. Imagine a mesh modeling a long hallway, which is lit by twenty spaced light sources. No location is lit by more than two light sources, but if dynamic branches are not employed, then all twenty light sources need to be computed for every pixel.

The most straightforward solution to both problems is to loop over light sources dynamically in the pixel shader. Unfortunately, dynamic branches in the pixel shader perform poorly on many GPUs. Even if branches are reasonably fast, they still introduce some amount of overhead, which may be unpalatable for performance-sensitive applications.

If dynamic branches are not used, then a different shader needs to be generated for each possible combination of lights and material type. Obviously, authoring each combination manually is impractical. A common solution to this problem is to write a single large shader that is compiled

<sup>21</sup>There are four possibilities for each of the six light “slots”—point, directional, spot, and none. This is known in combinatorics as a case of “combinations with repetitions allowed.” In this case, there are 84 possible combinations of lights for each material, for a total of 420 combinations.

<sup>22</sup>As in the previous case, but one more light type increases the number of possible light combinations per material to 210, for a total of 1050 combinations.

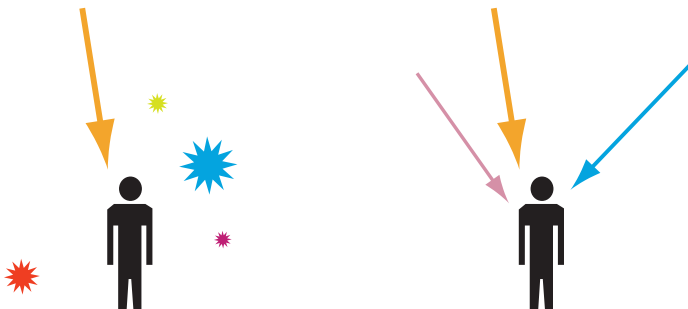


**Figure 7.47.** Lighting a game character. On the left we see the light sources affecting the character. Arrows symbolize directional light sources and stars symbolize point light sources. The size indicates brightness. The character is within the area of effect of one directional light source and four point light sources. On the right we see the approximation enforced by the game’s shaders, which only support up to three directional light sources and do not support point light sources at all. In this case, the two brightest lights (the orange directional light source and the bright blue point light source) map to the first two of the three available slots. The light blue point light source is converted to a directional source. All other lights (the medium red point light and dim green and purple point lights) are approximated by a single directional light (the pink arrow).

multiple times, using language features or code preprocessors to create a different specialized version of the shader each time. This type of shader is called an *ubershader* or *supershader* [845, 1271]. Ideally one compiled shader is produced ahead of time for each possible combination, since “on the fly” compilation may introduce noticeable delays. This is not always possible—in the case of the game *Far Cry*, the number of combinations was too large for an exhaustive compilation. The developers had to find the combinations used during gameplay and compile just those [887].

One tactic commonly used by game developers is to define a fixed, cheap lighting model and approximate the actual lighting environment of each object to fit the model. This reduces the number of combinations and caps the lighting computations required. For example, imagine that a game’s shaders support only one, two, or three directional lights. All other types of lights affecting an object are converted into directional lights by computing  $\mathbf{l}$  and  $E_L$  at the object’s center. The two brightest lights (based on the value of  $E_L$ ) are used to fill the first two available lighting slots, and any remaining lights are combined via a heuristic into a single directional light, which fills the third slot (see Figure 7.47). Such approximations may introduce visual artifacts, since they do not precisely represent the scene lighting. In addition, since the approximation depends on the position of the lit object, large continuous objects such as the hallway mentioned above are problematic. Even if the hallway is chopped up into smaller pieces, the lighting approximation may introduce undesirable discontinuities between

pieces. In addition, if the lights or objects move, then sudden changes in the approximation may cause popping artifacts.

### 7.9.1 Multipass Lighting

Multipass lighting is another solution to the problem of combining lights and materials. Here the idea is to process every light in a separate rendering pass, using the hardware’s additive blending capabilities to sum the results in the frame buffer. The application determines the set of light sources affecting each object. Typically, the light sources have distance attenuation functions that reach 0 at some finite distance. This enables the application to use bounding volume intersection to narrow the list of lights affecting each object. This is an  $O(mn)$  process [503, 691], and performing it efficiently in large scenes is not trivial—relevant techniques are discussed in Chapter 14. After the set of lights is determined, each object is rendered once for each light, with a shader that computes the outgoing radiance contribution for a single light source. Adding a new light source type requires writing one new shader for each material type. In cases where the light source illuminates just part of the object, hardware features such as scissoring, depth bounds, and stencil tests can be used to minimize the number of pixels processed. In theory, the screen could be cleared to black and then the lights rendered additively, but in practice an opaque pass is usually rendered first to lay down an ambient or environment-mapped base value (see Chapter 8 for more details on ambient lighting and environment mapping). The overall number of shaders is lower than in an übershader-type approach. In our example with four direct light source types, up to six lights and five material types, a multipass lighting approach requires 25 shaders (one for each combination of material and light type, including ambient light) instead of 1050.

There are some practical issues with this approach. Multiple blending passes to the frame buffer use a lot of memory bandwidth, which is a scarce resource and is becoming relatively scarcer with time. The trend is that GPU computation resources increase at a much faster rate than available memory bandwidth [981]. Also, the mesh needs to be processed multiple times by the vertex shader, and any pixel shader computations that produce results used by the lighting process (such as texture blending or relief mapping) need to be repeated for each light source. On a GPU that does not perform blending correctly on sRGB frame buffers, lights will be summed in nonlinear space, causing artifacts (see Section 5.8). Nonetheless, many applications (mostly games) have used this technique to good effect.

## 7.9.2 Deferred Shading

The availability of multiple render targets makes *deferred shading* a viable alternative to traditional GPU rendering methods. The basic idea behind deferred shading is to perform all visibility testing before performing any lighting computations. In traditional GPU rendering, the  $Z$ -buffer normally shades as it goes. This process can be inefficient, as a single pixel often contains more than one fragment. Each fragment found to be visible at the moment it is being rendered has its shade computed. If the fragment is completely covered by some later fragment, all the time spent computing its shade is wasted. A rough front-to-back sort of objects can help minimize this problem, but deferred shading completely resolves it and also solves the light/material combination issues.

Deferred shading can be done with a  $Z$ -buffer by performing a rendering pass that stores away the attributes of the closest visible surface. Values saved include the  $z$ -depth, normal, texture coordinates, and material parameters. These values are saved to multiple render targets accessed by the pixel shader program. This is the only rendering pass needed in which the objects themselves are sent through the pipeline. The first pass establishes all geometry and material information for the pixel, so the objects themselves are no longer needed. The stored buffers are commonly called *G-buffers* [1097], short for “geometric buffers.” Such buffers are also sometimes called *deep buffers*, though this term can also mean storing multiple surfaces (fragments) per pixel, so we avoid it here. Figure 7.48 shows typical contents of some G-buffers.

After this point, separate pixel shader programs are used to apply lighting algorithms or decals, or for post-processing effects, such as motion blur or depth of field. A pixel shader program is applied with a viewport-filling quadrilateral (or smaller polygon or object) to drive each computation. By rendering this quadrilateral, each pixel covered has the pixel shader applied to it. Pixel shader programs for lighting read the object attributes from the saved buffers and use these to compute the color of the surface. Multiple shader programs can be applied in this fashion, with the results added to the output color buffer as computed.

One advantage of deferred shading over all the previously discussed approaches has already been mentioned: Fragment shading is done only once per pixel (per shading program) and so has a predictable upper bound on rendering cost. Deferred shading also has many of the advantages of multi-pass lighting and lacks several of its drawbacks. Geometric transformation is done only once, in the initial pass, and any computations needed for lighting are done only once. For example, say that five lights affect a surface, and each light is computed in a separate pass. If the surface has a normal map applied to it, the computations to perturb and transform the normal

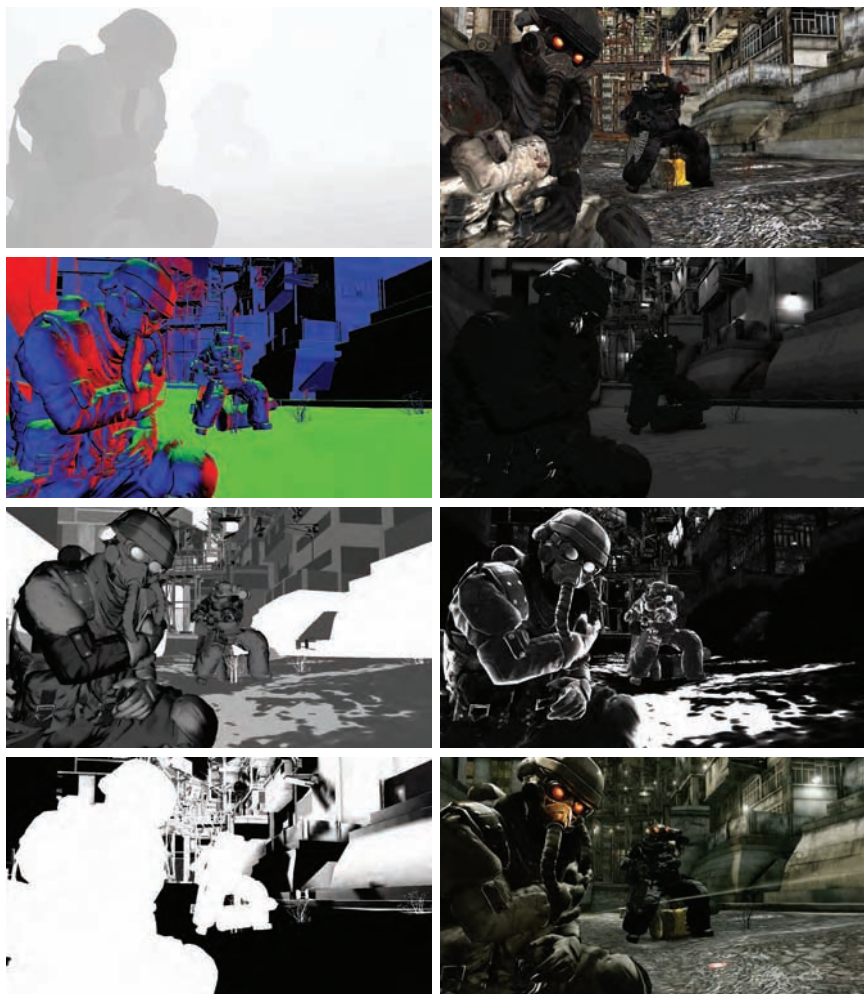


**Figure 7.48.** Geometric buffers for deferred shading, in some cases converted to colors for visualization. Left column: depth map, normal buffer, roughness buffer, sunlight occlusion [1288]. Right column: texture color (a.k.a. *albedo texture*), light intensity, specular intensity, near-final image (without motion blur; see Section 10.14 for the final image). (*Images from “Killzone 2,” courtesy of Guerrilla BV.*)

will be done for each pixel for each light. With deferred shading, such computations are performed once per pixel and stored, then used by each light in turn. This advantage is even greater when relief mapping is used. Deferred shading also takes advantage of the fact that GPUs render faster when objects have the same attributes, e.g., share the same surface shader.

Since the light shader is separate from the surface shader, each shader can be used for a longer string of objects, improving efficiency [1410].

Another important advantage has to do with programming and assets management costs. With the traditional approach, the vertex and pixel shader programs retrieve each light's and material's parameters and compute the effect of one on the other. The deferred shading method of rendering allows a strong separation between lighting and material definition. In our example application, a deferred shading approach would need 11 shaders (one for each material type to compute the effect of the material and store the relevant parameters in the G-buffers, plus one for each light source type) instead of the 25 shaders required by a multipass lighting approach or the 1050 required by an übershader approach. The separation of lighting and material should not be undervalued. This split makes experimentation simple, as instead of numerous combinations, only one new shader needs to be added to the system for a new light or material type [691].

Another advantage of deferred shading is that the time-consuming process of determining exactly which lights affect which objects is avoided. In deferred shading, the model is established in space and lights are applied to it. Shading can be optimized to be computed only in areas where the light source has any possible effect. Local light sources affect only small areas of the screen, and various geometric entities and rendering modes can be used to determine which pixels to shade. For example, point lights can be treated as spheres and spotlights as cones to determine what pixels they affect. Only those pixels where surfaces are inside of the volume of effect need to be shaded [503, 1288]. Even a directional light (e.g., the sun) can be optimized by marking the stencil buffer on the initial draw to shade only pixels affected by it [1174]. Local light sources can be culled based on area of effect or amount of contribution, or can be combined if found to affect similar areas of the screen [1018]. Fifty or more dynamic lights in a scene can easily be handled by deferred shading; a traditional renderer can handle only a fraction of that number at the same frame rate [691].

Deferred shading does have some drawbacks. The video memory requirements and fill rate costs for the G-buffers are significant, especially when programming for consoles.<sup>23</sup> The most significant technical limitations are in the areas of antialiasing and transparency. Antialiasing is not performed and stored for rendered surfaces. To overcome this limitation, Shishkovtsov [1174] uses an edge-detection method for approximating edge coverage computations. Supersampling to perform antialiasing is also possible, but the increase in fill rate makes this approach expensive [1018]. Transparent objects must be drawn using screen-door transparency or ren-

---

<sup>23</sup>For example, the Xbox 360 has 10 megabytes of render-to-texture memory.

dered into the scene after all deferred shading passes are done, since only one object per pixel can be stored in the G-buffer. From an efficiency standpoint, if the lighting computations desired are relatively simple, overall speed can be worse because the costs of writing and reading the render targets outweigh any gains from deferring lighting computations.

Even with these caveats, deferred shading is a practical rendering method used in shipping programs. It can handle large numbers of complex light sources and naturally separates lighting from materials. In deferred shading, the whole process of rendering becomes a series of post-processing effects, once the G-buffers are established.

Variants on the G-buffer approach are possible. One problem with deferred shading is the limitation on what can be stored per pixel. Even with the greater number of render targets available with newer GPUs, there is an imbalance in how much is needed at each pixel. Some surfaces may need only 6 values stored to evaluate their shader formulae, while others could use 20 or more. To compute and store 20 values for all visible surfaces is then a waste of bandwidth. One hybrid approach is to save out some limited set of values, e.g., depth, normal, diffuse, and specular contributions. Apply lighting, then render the geometry in the scene again, this time with shaders that draw upon these common results. In this way, some of the performance increase from deferred shading can be achieved, while also providing a wider range of shader choices.

For more flexibility and little additional rework to existing code, another approach is to perform an *early z pass*. Applications with complex, expensive shaders and high depth complexity can benefit by performing an initial pass and establishing the Z-buffer [484, 946, 1065, 1341]. After the Z-buffer is created, the scene is rendered normally with full shading. In this way, there is only one shader evaluation performed per pixel, for that of the closest surface; no time is wasted evaluating shaders for fragments that are hidden by surfaces rendered later. The cost is that the scene's geometry is rendered an additional time, though the prepass *z*-depth rendering is so simple that it can be extremely rapid. There are some limitations on pixel shaders for this optimization to work. See Section 18.3.6 for details. Obtaining and storing the *z*-depths also turns out to be useful for other rendering techniques [887, 1341]. For example, fog and soft particle techniques, discussed in Chapter 10, use the *z*-depth.

An interesting variant is presented by Zioma [1410]. Instead of first evaluating the geometry, the areas of effect of local light sources are rendered to and stored in buffers. Depth peeling can be used to handle storing the information for overlapping light sources. The scene's geometry is then rendered, using these stored light representations during shading. Similar to traditional deferred shading, efficiency is improved by minimizing switching between shaders. One major advantage that this approach has

over deferred shading is that surface materials are not limited by what is stored in the G-buffers. Also, storing light source descriptions can take considerably less space than storing a full material description, so memory and fill rate costs can be reduced.

## Further Reading and Resources

A valuable reference for information on BRDFs, global illumination methods, color space conversions, and much else is Dutré’s free online *Global Illumination Compendium* [287]. *Advanced Global Illumination* by Dutré et al. [288] provides a strong foundation in radiometry. Glassner’s *Principles of Digital Image Synthesis* [408, 409] discusses the physical aspects of the interaction of light and matter. The book *Color Imaging* by Reinhard et al. [1060] also covers this area, with a focus on the practical use of color in various fields. *Digital Modeling of Material Appearance* [275] by Dorsey, Rushmeier, and Sillion is a comprehensive reference work on all aspects of modeling material appearance for rendering purposes. Although it is older, Hall’s *Illumination and Color in Computer Generated Imagery* is a concise and thorough explanation of illumination and BRDFs in rendering.

Engel’s book [314] gives implementations for a wide range of shading models, including Cook-Torrance, Oren-Nayar, Ashikmin-Shirley, and others. Since shaders draw so heavily on RenderMan, the two books about this scene description language [30, 1283] can still be useful for ideas and inspiration. The book *Real-Time Shading* by Olano et al. [958], while predating true shader programming, discusses some BRDF representations in detail, as well as many other related topics.

Though a relatively new idea, there is already a sizeable literature about using deferred shading in applications. The interested reader should consult Konce [691], Placeres [1018], and Valient [1288] to start; each article has references to earlier presentations and resources. Please check this book’s website, <http://www.realtimerendering.com>, for newer works.

For the reader curious to learn still more about light and color, *Introduction to Modern Optics* by Fowles [361] is a short and accessible introductory text. The colorimetry “bible” is *Color Science* by Wyszecki and Stiles [1390]. *The Physics and Chemistry of Color* by Nassau [921] describes the physical phenomena behind color in great thoroughness and detail.



# Chapter 8

## Area and Environmental Lighting

*“Light makes right.”*

—Andrew Glassner

In Chapter 7 we discussed many aspects of lighting and shading. However, only the effects of point and directional light sources were presented, thus limiting surfaces to receiving light from a handful of discrete directions. This description of lighting is incomplete—in reality, surfaces receive light from *all* incoming directions. Outdoors scenes are not just lit by the sun. If that were true, all surfaces in shadow or facing away from the sun would be black. The sky is an important source of light, caused by sunlight scattering from the atmosphere. The importance of sky light can be seen by looking at a picture of the moon, which lacks sky light because it has no atmosphere (see Figure 8.1).

On overcast days, at dusk, or at dawn, outdoors lighting is *all* sky light. Diffuse, indirect lighting is even more important in indoor scenes. Since directly visible light sources can cause an unpleasant glare, indoor lighting is often engineered to be mostly or completely indirect.

The reader is unlikely to be interested in rendering only moonscapes. For realistic rendering, the effects of indirect and area lights must be taken into account. This is the topic of the current chapter. Until now, a simplified form of the radiometric equations has sufficed, since the restriction of illumination to point and directional lights enabled the conversion of integrals into summations. The topics discussed in this chapter require the full radiometric equations, so we will begin with them. A discussion of ambient and area lights will follow. The chapter will close with techniques for utilizing the most general lighting environments, with arbitrary radiance values incoming from all directions.

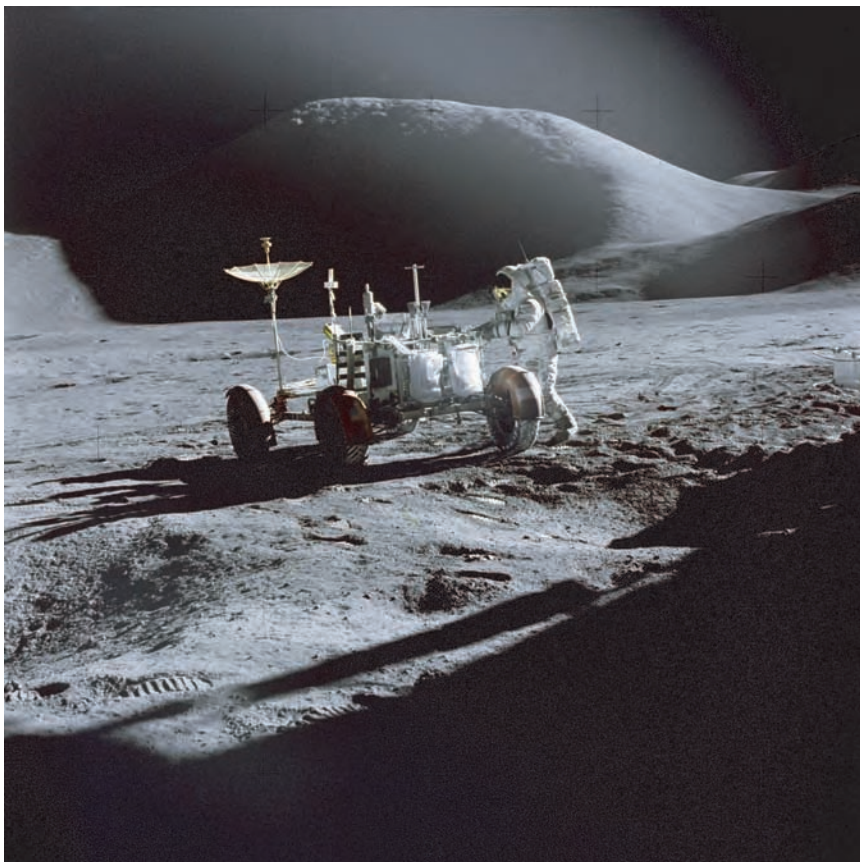


**Figure 8.1.** Scene on the moon, which has no sky light due to the lack of an atmosphere to scatter sunlight. This shows what a scene looks like when it is only lit by a direct light source. Note the pitch-black shadows and lack of any detail on surfaces facing away from the sun. This photograph shows Astronaut James B. Irwin next to the Lunar Roving Vehicle during the Apollo 15 mission. The shadow in the foreground is from the Lunar Module. Photograph taken by Astronaut David R. Scott, Commander. (*Image from NASA's collection.*)

## 8.1 Radiometry for Arbitrary Lighting

In Section 7.1 the various radiometric quantities were discussed. However, some relationships between them were omitted, since they were not important for the discussion of lighting with point and directional light sources.

We will first discuss the relationship between radiance and irradiance. Let us look at a surface point, and how it is illuminated by a tiny patch of incident directions with solid angle  $d\omega_i$  (see Figure 8.2). Since  $d\omega_i$  is

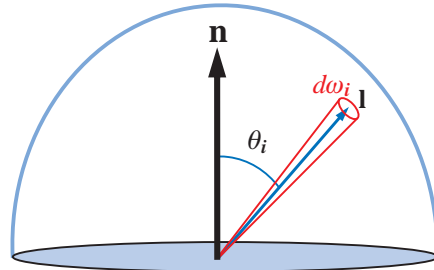


**Figure 8.2.** A surface point illuminated from all directions on the hemisphere. An example light direction  $\mathbf{l}$  and an infinitesimal solid angle  $d\omega_i$  around it are shown.

very small, it can be accurately represented by a single incoming direction  $\mathbf{l}$ , and we can assume that the incoming radiance from all directions in the patch is a constant  $L_i(\mathbf{l})$ .

As discussed in Section 7.1, radiance is a measure of light in a single ray, more precisely defined as the density of light flux (power) with respect to both area (measured on a plane perpendicular to the ray) and solid angle. Irradiance is a measure of light incoming to a surface point from all directions, defined as the density of light flux with respect to area (measured on a plane perpendicular to the surface normal  $\mathbf{n}$ ). It follows from these definitions that

$$L_i(\mathbf{l}) = \frac{dE}{d\omega_i \overline{\cos} \theta_i}, \quad (8.1)$$

where  $\overline{\cos}$  is our notation for a cosine function clamped to non-negative values,  $dE$  is the differential amount of irradiance contributed to the surface by the incoming light from  $d\omega_i$ , and  $\theta_i$  is the angle between the incoming light vector  $\mathbf{l}$  and the surface normal. Isolating  $dE$  results in

$$dE = L_i(\mathbf{l}) d\omega_i \overline{\cos} \theta_i. \quad (8.2)$$

Now that we know how much irradiance is contributed to the surface from the patch of directions  $d\omega_i$  around  $\mathbf{l}$ , we wish to compute the total irradiance at the surface, resulting from light in all directions above the surface. If the hemisphere of directions above the surface (which we will call  $\Omega$ ) is divided up into many tiny solid angles, we can use Equation 8.2 to compute  $dE$  from each and sum the results. This is an integration with respect to  $\mathbf{l}$ , over  $\Omega$ :

$$E = \int_{\Omega} L_i(\mathbf{l}) \cos \theta_i d\omega_i. \quad (8.3)$$

The cosine in Equation 8.3 is not clamped, since the integration is only performed over the region where the cosine is positive. Note that in this

integration,  $\mathbf{l}$  is swept over the entire hemisphere of incoming directions—it is not a specific “light source direction.” The idea is that *any* incoming direction can (and usually will) have some radiance associated with it.

Equation 8.3 describes an important relationship between radiance and irradiance: irradiance is the cosine-weighted integral of radiance over the hemisphere.

When rendering, we are interested in computing the outgoing radiance  $L_o$  in the view direction  $\mathbf{v}$ , since this quantity determines the shaded pixel color. To see how  $L_o$  relates to incoming radiance  $L_i$ , recall the definition of the BRDF:

$$f(\mathbf{l}, \mathbf{v}) = \frac{dL_o(\mathbf{v})}{dE(\mathbf{l})}. \quad (8.4)$$

Combining this with Equation 8.2 and integrating over the hemisphere yields the *reflectance equation*

$$L_o(\mathbf{v}) = \int_{\Omega} f(\mathbf{l}, \mathbf{v}) \otimes L_i(\mathbf{l}) \cos \theta_i d\omega_i, \quad (8.5)$$

where the  $\otimes$  symbol (piecewise vector multiply) is used, since both the BRDF  $f(\mathbf{l}, \mathbf{v})$  and the incoming radiance  $L_i(\mathbf{l})$  vary over the visible spectrum, which in practice for real-time rendering purposes means that they are both RGB vectors. This is the full version of the simplified equation we used in Chapter 7 for point and directional light sources. Equation 8.5 shows that to compute the radiance outgoing in a given direction  $\mathbf{v}$ , the incoming radiance times the BRDF times the cosine of the incoming angle  $\theta_i$  needs to be integrated over the hemisphere above the surface. It is interesting to compare Equation 8.5 to the simplified version used in Chapter 7:

$$L_o(\mathbf{v}) = \sum_{k=1}^n f(\mathbf{l}_k, \mathbf{v}) \otimes E_{L_k} \overline{\cos} \theta_{i_k}. \quad (8.6)$$

The most commonly used parameterization of the hemisphere uses polar coordinates ( $\phi$  and  $\theta$ ). For this parameterization, the differential solid angle  $d\omega$  is equal to  $\sin \theta d\theta d\phi$ . Using this, a double-integral form of Equation 8.5 can be derived, which uses polar coordinates:

$$L(\theta_o, \phi_o) = \int_{\phi_i=0}^{2\pi} \int_{\theta_i=0}^{\pi/2} f(\theta_i, \phi_i, \theta_o, \phi_o) L(\theta_i, \phi_i) \cos \theta_i \sin \theta_i d\theta_i d\phi_i. \quad (8.7)$$

The angles  $\theta_i$ ,  $\phi_i$ ,  $\theta_o$ , and  $\phi_o$  are shown in Figure 7.15 on page 224.

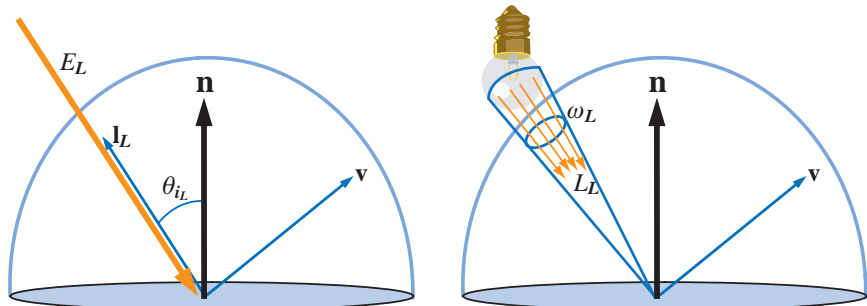


**Figure 8.3.** A surface illuminated by a light source. On the left, the light source is modeled as a point or directional light. On the right, it is modeled as an area light source.

## 8.2 Area Light Sources

Previous chapters have described point or directional light sources. These light sources illuminate a surface point from one direction only. However, real lights illuminate a surface point from a range of directions—they *subtend* (cover) a nonzero solid angle. Figure 8.3 shows a surface that is illuminated by a light source. It is modeled both as a point or directional source and as an *area light source* with a nonzero size. The point or directional light source (on the left) illuminates the surface from a single direction  $\mathbf{l}_L$ ,<sup>1</sup> which forms an angle  $\theta_{i_L}$  with the normal  $\mathbf{n}$ . Its brightness is represented by its irradiance  $E_L$  measured in a plane perpendicular to  $\mathbf{l}_L$ .<sup>2</sup> The point or directional light's contribution to the outgoing radiance  $L_o(\mathbf{v})$  in direction  $\mathbf{v}$  is  $f(\mathbf{l}_L, \mathbf{v}) \otimes E_L \cos \theta_{i_L}$ . On the other hand, the brightness of the area light source (on the right) is represented by its radiance  $L_L$ . The area light subtends a solid angle of  $\omega_L$  from the surface location. Its contribution to the outgoing radiance in direction  $\mathbf{v}$  is the integral of  $f(\mathbf{l}, \mathbf{v}) \otimes L_L \cos \theta_i$  over  $\omega_L$ . The fundamental approximation behind point and directional light sources is expressed in the following equation:

$$L_o(\mathbf{v}) = \int_{\omega_L} f(\mathbf{l}, \mathbf{v}) \otimes L_L \cos \theta_i d\omega_i \approx f(\mathbf{l}_L, \mathbf{v}) \otimes E_L \cos \theta_{i_L}. \quad (8.8)$$

The amount that an area light source contributes to the illumination of a surface location is a function of both its radiance ( $L_L$ ) and its size as seen from that location ( $\omega_L$ ). Point and directional light sources are approx-

<sup>1</sup>Since we are now using  $\mathbf{l}$  to denote a generic incoming direction, specific light source directions will be denoted with subscripts.

<sup>2</sup>As distinguished from the overall irradiance  $E$ , measured in a plane perpendicular to the surface normal  $\mathbf{n}$ .

imations of area light sources—they cannot be realized in practice, since their zero solid angle implies an infinite radiance.

The approximation in Equation 8.8 is much less costly than computing the integral, so it is worth using when possible. Understanding the visual errors that are introduced by the approximation will help to know when to use it, and what approach to take when it cannot be used. These errors will depend on two factors: how large the light source is (measured by the solid angle it covers from the shaded point), and how glossy the surface is. For light sources that subtend a very small solid angle, the error is small. For very rough surfaces, the error is small as well. We will take a closer look at the important special case of Lambertian surfaces.

It turns out that for Lambertian surfaces, the approximation is exact under some circumstances. Recall that for Lambertian surfaces, the outgoing radiance is proportional to the irradiance:

$$L_o(\mathbf{v}) = \frac{\mathbf{c}_{\text{diff}}}{\pi} E, \quad (8.9)$$

where  $\mathbf{c}_{\text{diff}}$  is the diffuse color of the surface.

This lets us use equations for irradiance, which are simpler than the corresponding equations for outgoing radiance. The equivalent of Equation 8.8 for computing irradiance is:

$$E = \int_{\omega_L} L_L \overline{\cos} \theta_i d\omega_i \approx E_L \overline{\cos} \theta_{i_L}. \quad (8.10)$$

To understand how irradiance behaves in the presence of area light sources, the concept of *vector irradiance* is useful. Vector irradiance was introduced by Gershun [392] (who called it the *light vector*) and further described by Arvo [37]. Using vector irradiance, an area light source of arbitrary size and shape can be *accurately* converted into a point or directional light source. There are some caveats, which we will discuss later.

Imagine a distribution of radiance coming into a point  $p$  in space (see Figure 8.4). For now, we assume that the radiance does not vary with wavelength, so that the incoming radiance from each direction can be represented as a scalar, rather than as a spectral distribution or RGB triple. For every infinitesimal solid angle  $d\omega$  centered on an incoming direction  $\mathbf{l}$ , a vector is constructed that is aligned with  $\mathbf{l}$  and has a length equal to the (scalar) radiance incoming from that direction times  $d\omega$ . Finally, all these vectors are summed to produce a total vector  $\mathbf{e}$  (see Figure 8.5). This is the vector irradiance. More formally, the vector irradiance is computed thus:

$$\mathbf{e}(\mathbf{p}) = \int_{\Theta} L_i(\mathbf{p}, \mathbf{l}) \mathbf{l} d\omega_i, \quad (8.11)$$

where  $\Theta$  indicates that the integral is performed over the entire sphere of directions.

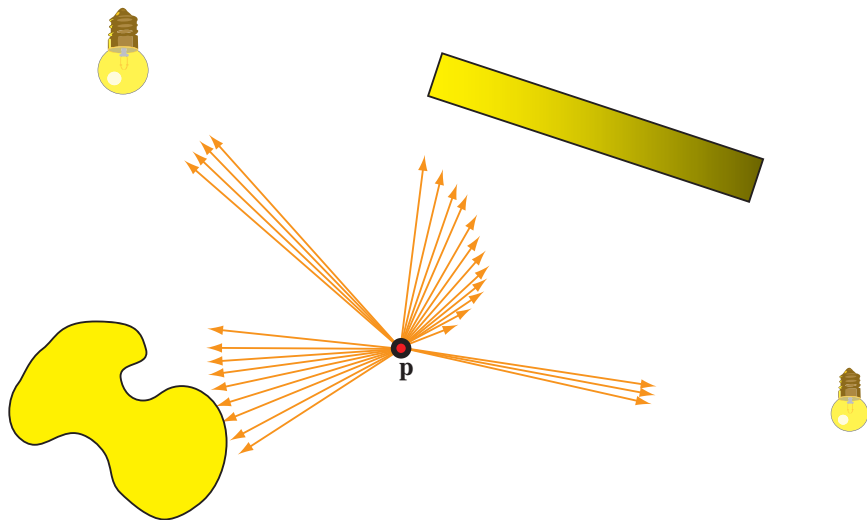


**Figure 8.4.** Computation of vector irradiance. Point  $p$  is surrounded by light sources of various shapes, sizes, and radiance distributions (the brightness of the yellow color indicates the amount of radiance emitted). The orange arrows are vectors pointing in all directions from which there is any incoming radiance, and each length is equal to the amount of radiance coming from that direction times the infinitesimal solid angle covered by the arrow (in principle there should be an infinite number of arrows). The vector irradiance is the sum of all these vectors.

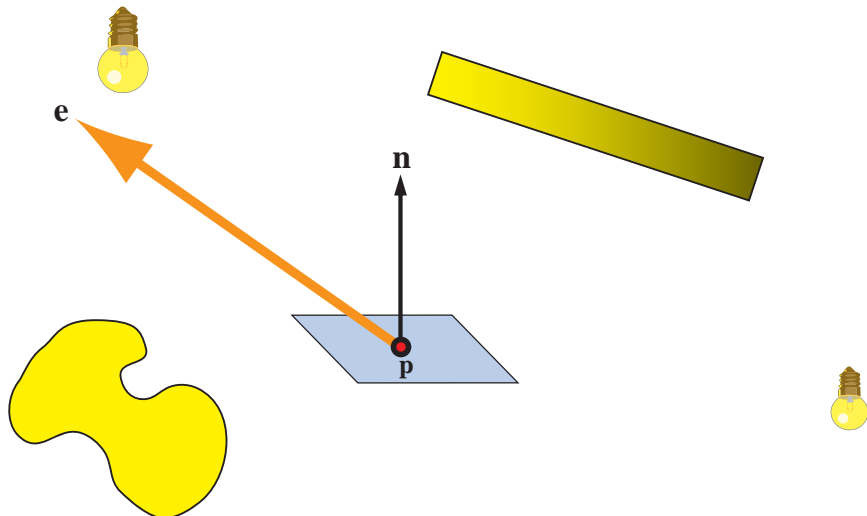


**Figure 8.5.** Vector irradiance. The large orange arrow is the result of summing the small arrows in Figure 8.4. The vector irradiance can be used to compute the *net irradiance* of any plane at point  $p$ .

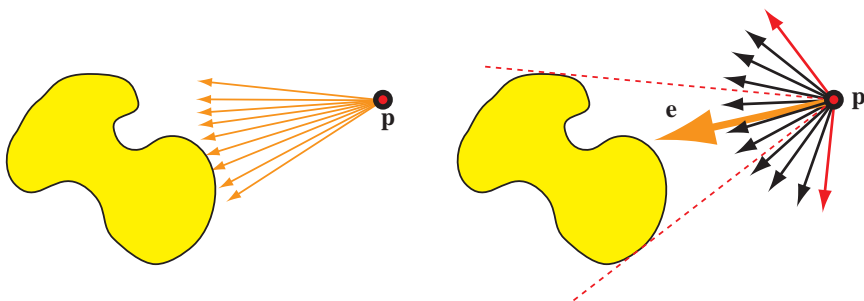


**Figure 8.6.** Vector irradiance of a single area light source. On the left, the arrows represent the vectors used to compute the vector irradiance. On the right, the large orange arrow is the vector irradiance  $e$ . The short black and red vectors represent the range of surface normals for which  $e$  can be used to compute the irradiance from the area light source. The red dashed lines represent the extent of the light source, and the red vectors (which are perpendicular to the red dashed lines) define the limits of the set of surface normals. Normals outside this set will have an angle greater than  $90^\circ$  with some part of the area light source. Such normals cannot use  $e$  to compute their irradiance.

The vector irradiance  $e$  is interesting because, once computed, it can be used to find the net irradiance at  $p$  through a plane of any orientation by performing a dot product (see Figure 8.5):

$$E(\mathbf{p}, \mathbf{n}) - E(\mathbf{p}, -\mathbf{n}) = \mathbf{n} \cdot e(\mathbf{p}), \quad (8.12)$$

where  $\mathbf{n}$  is the normal to the plane. The net irradiance through a plane is the difference between the irradiance flowing through the “positive side” of the plane (defined by the plane normal  $\mathbf{n}$ ) and the irradiance flowing through the “negative side.” By itself, the net irradiance is not useful for shading. But if no radiance is emitted through the “negative side” (in other words, the light distribution being analyzed has no parts for which the angle between  $\mathbf{l}$  and  $\mathbf{n}$  exceeds  $90^\circ$ ), then  $E(\mathbf{p}, -\mathbf{n}) = 0$  and

$$E(\mathbf{p}, \mathbf{n}) = \mathbf{n} \cdot e(\mathbf{p}). \quad (8.13)$$

The vector irradiance of a single area light source can be used with Equation 8.13 to light Lambertian surfaces with any normal  $\mathbf{n}$ , as long as  $\mathbf{n}$  does not face more than  $90^\circ$  away from any part of the area light source (see Figure 8.6).

The vector irradiance is for a single wavelength. Given lights with different colors, the summed vector could be in a different direction for each wavelength. However, if all the light sources have the same spectral distribution, the vectors will all be in the same direction. This allows for a trivial extension to Equation 8.13 for colored lights—just multiply  $\mathbf{n} \cdot e$  by

the light color  $\mathbf{c}_L$ . This results in the same equation used to compute the irradiance from a directional light source, with the following substitutions:

$$\begin{aligned} \mathbf{l} &= \frac{\mathbf{e}(\mathbf{p})}{\|\mathbf{e}(\mathbf{p})\|}, \\ E_L &= \mathbf{c}_L \|\mathbf{e}(\mathbf{p})\|, \end{aligned} \quad (8.14)$$

so we have effectively converted an area light source of arbitrary shape and size to a directional light source—without introducing any error! However, care must be taken only to use normals within the “valid set,” and the directional light source is only equivalent to the area light source for Lambertian surfaces.

This can be solved analytically for simple cases. For example, imagine a spherical light source with a center at  $p_L$  and a radius  $r_L$ . The light emits a constant radiance  $L_L$  from every point on the sphere, in all directions. For such a light source, Equations 8.11 and 8.14 yield the following:

$$\begin{aligned} \mathbf{l} &= \frac{p_L - \mathbf{p}}{\|p_L - \mathbf{p}\|}, \\ E_L &= \pi \frac{r_L^2}{r^2} L_L. \end{aligned} \quad (8.15)$$

This is the same as an omni light (see Section 7.4.1) with  $I_L = \pi r_L^2$  and the standard distance falloff function of  $1/r^2$ . Since it is unclear what the irradiance should be for points *inside* the sphere, it might make sense to cap the falloff function at a value of 1. This is useful, since falloff functions that reach arbitrarily high values can be inconvenient to use. Other practical adjustments could be made to the falloff function (such as scaling and biasing it to make it reach a value of 0 at some finite distance).

We see here that a simplistic light model such as an omni light can actually be a physically accurate description of an area light source. However, this is only true for reflection from Lambertian surfaces, and only as long as no rays to the light source form angles greater than  $90^\circ$  with the surface normal (otherwise  $\mathbf{n} \cdot \mathbf{e} \neq E$ ). Another way to think about this is that no parts of the area light source can be “under the horizon,” or occluded by the surface.

We can generalize the last statement. For Lambertian surfaces, *all* differences between area and point light sources result from occlusion differences. The irradiance from a point light source obeys a cosine law for all normals for which the light is not occluded. Irradiance from an area light source obeys a cosine law (for the cosine of the angle between the vector irradiance  $\mathbf{e}$  and the surface normal  $\mathbf{n}$ ) until some part of the source is occluded. As the area light source continues to descend below the horizon, the irradiance will continue to decrease until the light is 100% occluded,

at which point it will become zero. For point light sources, this happens when the angle between the light source vector  $\mathbf{l}$  and the surface normal  $\mathbf{n}$  reaches  $90^\circ$ —for area light sources this happens at some larger angle when all of the light is “under the horizon.” Snyder derived an analytic expression for a spherical light source, taking occlusion into account [1203]. This expression is quite complex. However, since it depends on only two quantities ( $r/r_L$  and  $\theta_i$ ), it can be pre-computed into a two-dimensional texture. Snyder also gives two functional approximations. The simpler one uses a single cubic polynomial and approximates the original curve fairly well. The second uses two cubic curves, resulting in a curve almost identical to the original. For real-time rendering, the single cubic curve (or perhaps some even simpler curve) is likely to be sufficient.

A less physically based but effective method for modeling the effects of area lights on Lambertian surfaces is to employ *wrap lighting*. In this technique, some simple modification is done to the value of  $\cos \theta_i$  before it is clamped to 0. One form of this is given by Forsyth [358]:

$$E = E_L \max \left( \frac{\cos \theta_i + c_{\text{wrap}}}{1 + c_{\text{wrap}}}, 0 \right), \quad (8.16)$$

where  $c_{\text{wrap}}$  ranges from 0 (for point light sources) to 1 (for area light sources covering the entire hemisphere). Another form that mimics the effect of a large area light source is used by Valve [881]:

$$E = E_L \left( \frac{\cos \theta_i + 1}{2} \right)^2. \quad (8.17)$$

One possible problem with wrap lighting is that shadowing can cancel its effects unless the shadows are reduced in size or softened [139]. Soft shadows are perhaps the most visible effect of area light sources, and will be discussed in Section 9.1.

The effects of area lights on non-Lambertian surfaces are more involved. Snyder derives a solution for spherical light sources [1203], but it is limited to the original reflection-vector Phong BRDF and is extremely complex. The primary visual effect of area lights on glossy surfaces is the shape of the highlight. Instead of a small point, the highlight has a size and shape similar to the area light. The edge of the highlight is blurred according to the roughness of the surface. The effects of area lights on the highlight are particularly important for very smooth surfaces. The highlight from a point light source on such surfaces is a tiny point, which is very unrealistic. In reality, a sharp reflection of the light source appears. One way of approximating this visual effect is to use a texture to define the highlight shape, similarly to NDF mapping (see Section 7.6) or environment mapping (Section 8.4). Another common technique is to threshold the value of the specular highlight [458]—Figure 8.7 shows the result.



**Figure 8.7.** Highlights on smooth objects are sharp reflections of the light source shape. On the left, this appearance has been approximated by thresholding the highlight value of a Blinn-Phong shader. On the right, the same object rendered with an unmodified Blinn-Phong shader for comparison. (*Image courtesy of Larry Gritz.*)

In principle, the reflectance equation does not distinguish between light arriving directly from a light source and indirect light that has been scattered from the sky or objects in the scene. All incoming directions have radiance, and the reflectance equation integrates over them all. However, in practice, direct light is usually distinguished by relatively small solid angles with high radiance values, and indirect light tends to diffusely cover the rest of the hemisphere with moderate to low radiance values. This provides good practical reasons to handle the two separately. This is even true for offline rendering systems—the performance advantages of using separate techniques tailored to direct and indirect light are too great to ignore.

## 8.3 Ambient Light

Ambient light is the simplest model of indirect light, where the indirect radiance does not vary with direction and has a constant value  $L_A$ . Even such a simple model of indirect light improves visual quality significantly. A scene with no indirect light appears highly unrealistic. Objects in shadow or facing away from the light in such a scene would be completely black, which is unlike any scene found in reality. The moonscape in Figure 8.1 comes close, but even in such scenes some indirect light is bouncing from nearby objects.

The exact effects of ambient light will depend on the BRDF. For Lambertian surfaces, the constant radiance  $L_A$  results in a constant contribu-

tion to outgoing radiance, regardless of surface normal  $\mathbf{n}$  or view direction  $\mathbf{v}$ :

$$L_o(\mathbf{v}) = \frac{\mathbf{c}_{\text{diff}}}{\pi} \otimes L_A \int_{\Omega} \cos \theta_i d\omega_i = \mathbf{c}_{\text{diff}} \otimes L_A. \quad (8.18)$$

When shading, this constant outgoing radiance contribution is added to the contributions from direct light sources:

$$L_o(\mathbf{v}) = \frac{\mathbf{c}_{\text{diff}}}{\pi} \otimes \left( \pi L_A + \sum_{k=1}^n E_{L_k} \overline{\cos} \theta_{i_k} \right). \quad (8.19)$$

For arbitrary BRDFs, the equivalent equation is

$$L_o(\mathbf{v}) = L_A \int_{\Omega} f(\mathbf{l}, \mathbf{v}) \cos \theta_i d\omega_i + \sum_{k=1}^n f(\mathbf{l}_k, \mathbf{v}) \otimes E_{L_k} \overline{\cos} \theta_{i_k}. \quad (8.20)$$

We define the *ambient reflectance*  $R_A(\mathbf{v})$  thus:

$$R_A(\mathbf{v}) = \int_{\Omega} f(\mathbf{l}, \mathbf{v}) \cos \theta_i d\omega_i. \quad (8.21)$$

Like any reflectance quantity,  $R_A(\mathbf{v})$  has values between 0 and 1 and may vary over the visible spectrum, so for rendering purposes it is an RGB color. In real-time rendering applications, it is usually assumed to have a view-independent, constant value, referred to as the *ambient color*  $\mathbf{c}_{\text{amb}}$ . For Lambertian surfaces,  $\mathbf{c}_{\text{amb}}$  is equal to the diffuse color  $\mathbf{c}_{\text{diff}}$ . For other surface types,  $\mathbf{c}_{\text{amb}}$  is usually assumed to be a weighted sum of the diffuse and specular colors [192, 193]. This tends to work quite well in practice, although the Fresnel effect implies that some proportion of white should ideally be mixed in, as well. Using a constant ambient color simplifies Equation 8.20, yielding the ambient term in its most commonly used form:

$$L_o(\mathbf{v}) = \mathbf{c}_{\text{amb}} \otimes L_A + \sum_{k=1}^n f(\mathbf{l}_k, \mathbf{v}) \otimes E_{L_k} \overline{\cos} \theta_{i_k}. \quad (8.22)$$

The reflectance equation ignores occlusion—the fact that many surface points will be blocked from “seeing” some of the incoming directions by other objects, or other parts of the same object. This reduces realism in general, but it is particularly noticeable for ambient lighting, which appears extremely flat when occlusion is ignored. Methods for addressing this will be discussed in Sections 9.2 and 9.10.1.

## 8.4 Environment Mapping

Since the full reflectance equation is expensive to compute, real-time rendering tends to utilize simplifying assumptions. In the previous section, we discussed the assumption (constant incoming radiance) behind the ambient light model. In this section, the simplifying assumption relates to the BRDF, rather than the incoming lighting.

An optically flat surface or mirror reflects an incoming ray of light into one direction, the light's reflection direction  $\mathbf{r}_i$  (see Section 7.5.3). Similarly, the outgoing radiance includes incoming radiance from just one direction, the reflected view vector  $\mathbf{r}$ . This vector is computed similarly to  $\mathbf{r}_i$ :

$$\mathbf{r} = 2(\mathbf{n} \cdot \mathbf{v})\mathbf{n} - \mathbf{v}. \quad (8.23)$$

The reflectance equation for mirrors is greatly simplified:

$$L_o(\mathbf{v}) = R_F(\theta_o)L_i(\mathbf{r}), \quad (8.24)$$

where  $R_F$  is the Fresnel term (see Section 7.5.3). Note that unlike the Fresnel terms in half vector-based BRDFs (which use  $\alpha_h$ , the angle between the half vector  $\mathbf{h}$  and  $\mathbf{l}$  or  $\mathbf{v}$ ), the Fresnel term in Equation 8.24 uses the angle  $\theta_o$  between  $\mathbf{v}$  and the surface normal  $\mathbf{n}$ . If the Schlick approximation is used for the Fresnel term, mirror surfaces should use Equation 7.33, rather than Equation 7.40 (substituting  $\theta_o$  for  $\theta_i$ ; the two are equal here).

If the incoming radiance  $L_i$  is only dependent on direction, it can be stored in a two-dimensional table. This enables efficiently lighting a mirror-like surface of any shape with an arbitrary incoming radiance distribution, by simply computing  $\mathbf{r}$  for each point and looking up the radiance in the table. Such a table is called an *environment map*, and its use for rendering is called *environment mapping* (EM). Environment mapping was introduced by Blinn and Newell [96]. Its operation is conceptualized in Figure 8.8.

As mentioned above, the basic assumption behind environment mapping is that the incoming radiance  $L_i$  is only dependent on direction. This requires that the objects and lights being reflected are far away, and that the reflector does not reflect itself. Since the environment map is a two-dimensional table of radiance values, it can be interpreted as an image.

The steps of an EM algorithm are:

- Generate or load a two-dimensional image representing the environment.
- For each pixel that contains a reflective object, compute the normal at the location on the surface of the object.
- Compute the reflected view vector from the view vector and the normal.

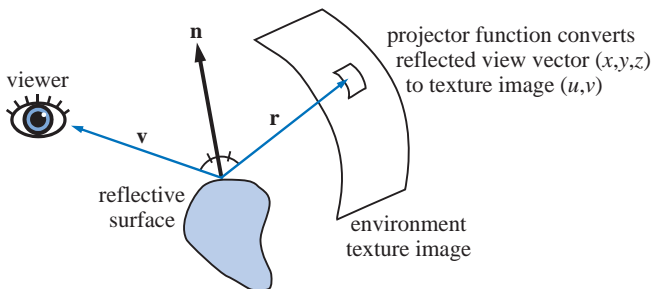


**Figure 8.8.** Environment mapping. The viewer sees an object, and the reflected view vector  $\mathbf{r}$  is computed from  $\mathbf{v}$  and  $\mathbf{n}$ . The reflected view vector accesses the environment's representation. The access information is computed by using some projector function to convert the reflected view vector's  $(x, y, z)$  to (typically) a  $(u, v)$  value, which is used to retrieve texture data.

- Use the reflected view vector to compute an index into the environment map that represents the incoming radiance in the reflected view direction.
- Use the texel data from the environment map as incoming radiance in Equation 8.24.

A potential stumbling block of EM is worth mentioning. Flat surfaces usually do not work well when environment mapping is used. The problem with a flat surface is that the rays that reflect off of it usually do not vary by more than a few degrees. This results in a small part of the EM texture's being mapped onto a relatively large surface. Normally, the individual texels of the texture become visible, unless bilinear interpolation is used; even then, the results do not look good, as a small part of the texture is extremely magnified. We have also been assuming that perspective projection is being used. If orthographic viewing is used, the situation is much worse for flat surfaces. In this case, all the reflected view vectors are the same, and so the surface will get a constant color from some single texel. Other real-time techniques, such as planar reflections (Section 9.3.1), may be of more use for flat surfaces.

The term *reflection mapping* is sometimes used interchangeably with environment mapping. However, this term has a specific meaning. When the surface's material properties are used to modify an existing environment map, a reflection map texture is generated. A simple example: To make a red, shiny sphere, the color red can be multiplied with an environment map to create a reflection map. Reflection mapping techniques are discussed in depth in Section 8.5.



**Figure 8.9.** The character’s armor uses normal mapping combined with environment mapping, giving a shiny, bumpy surface that reflects the environment. (*Image from “Hellgate: London” courtesy of Flagship Studios, Inc.*)

Unlike the colors and shader properties stored in other commonly used textures, the radiance values stored in environment maps have a high dynamic range. Environment maps should usually be stored using high dynamic range texture formats. For this reason, they tend to take up more space than other textures, especially given the difficulty of compressing high dynamic range values (see Section 6.2.6).

The combination of environment mapping with normal mapping is particularly effective, yielding rich visuals (see Figure 8.9). It is also straightforward to implement—the normal used to compute the reflected view vector is simply permuted first by the normal map. This combination of features is also historically important—a restricted form of bumped environment mapping was the first use of a *dependent texture read* in consumer-level graphics hardware, giving rise to this ability as a part of the pixel shader.

There are a variety of projector functions that map the reflected view vector into one or more textures. Blinn and Newell’s algorithm was the first function ever used, and sphere mapping was the first to see use in graphics accelerators. Greene’s cubic environment mapping technique overcomes many of the limitations of these early approaches. To conclude, Heidrich and Seidel’s parabolic mapping method is discussed.

### 8.4.1 Blinn and Newell's Method

In 1976, Blinn and Newell [96] developed the first environment mapping algorithm. The mapping they used is the familiar longitude/latitude system used on a globe of the earth. Instead of being like a globe viewed from the outside, their scheme is like a map of the constellations in the night sky. Just as the information on a globe can be flattened to a Mercator or other<sup>3</sup> projection map, an environment surrounding a point in space can be mapped to a texture. When a reflected view vector is computed for a particular surface location, the vector is converted to spherical coordinates  $(\rho, \phi)$ . Here  $\phi$ , essentially the longitude, varies from 0 to  $2\pi$  radians, and  $\rho$ , essentially the latitude, varies from 0 to  $\pi$  radians. Here,  $(\rho, \phi)$  is computed from Equation 8.25, where  $\mathbf{r} = (r_x, r_y, r_z)$  is the normalized reflected view vector:

$$\begin{aligned}\rho &= \arccos(-r_z), \\ \phi &= \text{atan2}(r_y, r_x).\end{aligned}\quad (8.25)$$

See page 7 for a description of `atan2`. These values are then used to access the environment map and retrieve the color seen in the reflected view direction.

Blinn and Newell's mapping is mentioned here because it was first, and because converting from a vector to polar coordinates is easily

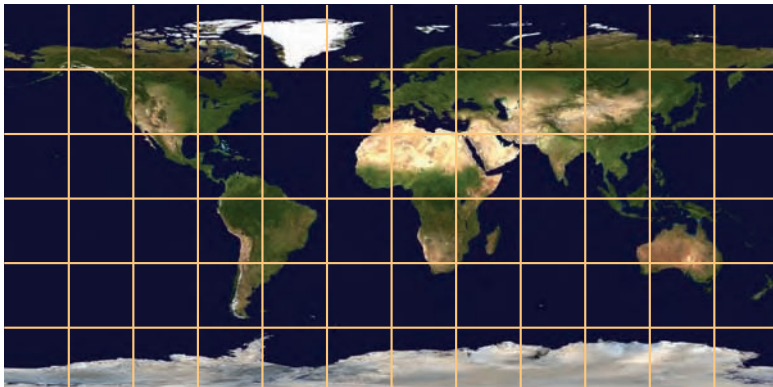


**Figure 8.10.** The earth with equally spaced latitude and longitude lines, versus the traditional Mercator projection. (*Image from NASA's "Blue Marble" collection.*)

---

<sup>3</sup>The Blinn and Newell mapping is not identical to the Mercator projection; theirs keeps the distance between latitude lines constant, while Mercator goes to infinity at the poles.

understood. One problem with this mapping is that the density of information is nowhere near being uniform. As can be seen in Figure 8.10, the areas near the poles receive many more texels than those near the equator. Another problem is the seam where the left and right edges of the mapping join. One fast way to derive the reflected view vector coordinates for a triangle's surface is to compute the texture coordinates for the three corners and interpolate among these. This method will not work for triangles that overlap the seam, without some adjustment. The singularities at the poles also cause problems. The methods that follow attempt to keep projection area representation more balanced, and to avoid mathematical difficulties.

## 8.4.2 Sphere Mapping

Initially mentioned by Williams [1354], and independently developed by Miller and Hoffman [866], this was the first environment mapping technique supported in general commercial graphics hardware. The texture image is derived from the appearance of the environment as viewed orthographically in a perfectly reflective sphere, so this texture is called a *sphere map*. One way to make a sphere map of a real environment is to take a photograph of a shiny sphere, such as a Christmas tree ornament. See Figure 8.11 for an example.

This resulting circular image is also sometimes called a *light probe*, as it captures the lighting situation at the sphere's location [231]. Sphere map textures for synthetic scenes can be generated using ray tracing or by warping the images generated for a cubic environment map [849]. See Figure 8.12 for an example of environment mapping done with sphere maps.

The sphere map has a basis (see Appendix A) that is the frame of reference in which the texture was generated. That is, the image is viewed along some axis  $\mathbf{f}$  in world space, with  $\mathbf{u}$  as the up vector for the image and  $\mathbf{h}$  going horizontally to the right (and all are normalized). This gives a basis matrix:

$$\begin{pmatrix} h_x & h_y & h_z & 0 \\ u_x & u_y & u_z & 0 \\ f_x & f_y & f_z & 0 \\ 0 & 0 & 0 & 1 \end{pmatrix}. \quad (8.26)$$

To access the sphere map, first transform the surface normal  $\mathbf{n}$ , and the view vector  $\mathbf{v}$ , using this matrix. This yields  $\mathbf{n}'$  and  $\mathbf{v}'$  in the sphere map's space. The reflected view vector is then computed to access the sphere map texture:

$$\mathbf{r} = \mathbf{v}' - 2(\mathbf{n}' \cdot \mathbf{v}')\mathbf{n}', \quad (8.27)$$

with  $\mathbf{r}$  being the resulting reflected view vector, in the sphere map's space.



**Figure 8.11.** A light probe image used for sphere mapping, formed by photographing a reflective sphere. This image is of the interior of Grace Cathedral, San Francisco. (*Image courtesy of Paul Debevec, debevec.org.*)



**Figure 8.12.** Specular highlighting. Per-vertex specular is shown on the left, environment mapping with one light in the middle, and environment mapping of the entire surrounding scene on the right. (*Images courtesy of J.L. Mitchell, M. Tatro, and I. Bullard.*)

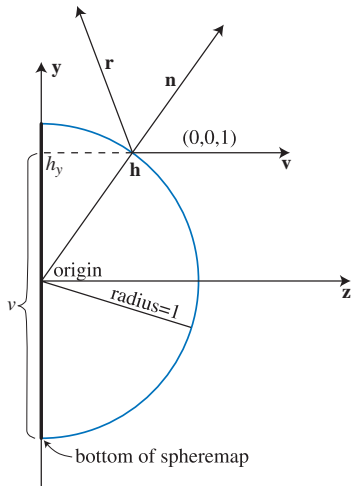


**Figure 8.13.** Given the constant view direction and reflected view vector  $\mathbf{r}$  in the sphere map’s space, the sphere map’s normal  $\mathbf{n}$  is halfway between these two. For a unit sphere at the origin, the intersection point  $\mathbf{h}$  has the same coordinates as the unit normal  $\mathbf{n}$ . Also shown is how  $h_y$  (measured from the origin) and the sphere map texture coordinate  $v$  (not to be confused with the view vector  $\mathbf{v}$ ) are related.

What a reflective sphere does is to show the entire environment on just the front of the sphere. It maps each reflected view direction to a point on the two-dimensional image of this sphere. Say we wanted to go the other direction, that given a point on the sphere map, we would want the reflected view direction. To do this, we would get the surface normal at the sphere at that point, and so generate the reflected view direction. So, to reverse the process and get the location on the sphere from the reflected view vector, we need to derive the surface normal on the sphere, which will then yield the  $(u, v)$  parameters needed to access the sphere map.

The sphere’s normal is the half-angle vector between the reflected view vector  $\mathbf{r}$  and the original view vector  $\mathbf{v}$ , which is  $(0, 0, 1)$  in the sphere map’s space. See Figure 8.13. This normal vector  $\mathbf{n}$  is simply the sum of the original and reflected view vectors, i.e.,  $(r_x, r_y, r_z + 1)$ . Normalizing this vector gives the unit normal:

$$m = \sqrt{r_x^2 + r_y^2 + (r_z + 1)^2}, \quad (8.28)$$

$$\mathbf{n} = \left( \frac{r_x}{m}, \frac{r_y}{m}, \frac{r_z + 1}{m} \right). \quad (8.29)$$

If the sphere is at the origin and its radius is 1, the unit normal’s coordinates are then also the location  $\mathbf{h}$  of the normal on the sphere. We do not need

$h_z$ , as  $(h_x, h_y)$  describes a point on the image of the sphere, with each value in the range  $[-1, 1]$ . To map this coordinate to the range  $[0, 1]$  to access the sphere map, divide each by two and add a half:

$$m = \sqrt{r_x^2 + r_y^2 + (r_z + 1)^2}, \quad (8.30)$$

$$u = \frac{r_x}{2m} + 0.5, \quad (8.31)$$

$$v = \frac{r_y}{2m} + 0.5. \quad (8.32)$$

This equation can even be computed in fixed-function graphics hardware, using the texture matrix [1383].

Sphere mapping is an improvement over Blinn and Newell's method in a number of ways. The projector function is simple to implement. There is no texture seam and only one singularity, located around the edge of the sphere map. While it is still possible to have triangles that interpolate incorrectly and produce artifacts, these occur only at shallow grazing angles, around the silhouette edges of models [849].

There are some other disadvantages to the sphere map. First and foremost, the texture used captures a view of the environment that is valid for only a single view direction. The sphere map does capture the entire environment, so it is possible to compute the EM texture coordinates for the current viewing direction. However, doing so can result in visual artifacts, as small parts of the sphere map become magnified due to the new view, and the singularity around the edge becomes much more noticeable. If the viewer is to be allowed to change view direction, it is better to use a view-independent EM, such as those described next.

### 8.4.3 Cubic Environment Mapping

In 1986, Greene [449] introduced another EM technique. This method is far and away the most popular EM method implemented in modern graphics hardware, due to its speed and flexibility. The *cubic environment map* (a.k.a. *EM cube map*) is obtained by placing the camera in the center of the environment and then projecting the environment onto the sides of a cube positioned with its center at the camera's location. The images of the cube are then used as the environment map. In practice, the scene is rendered six times (one for each cube face) with the camera at the center of the cube, looking at each cube face with a  $90^\circ$  view angle. This type of environment map is shown in Figure 8.14. In Figure 8.15, a typical cubic environment map is shown.

A great strength of Greene's method is that environment maps can be generated relatively easily by any renderer (versus Blinn and Newell's method, which uses a spherical projection), and can be generated in real

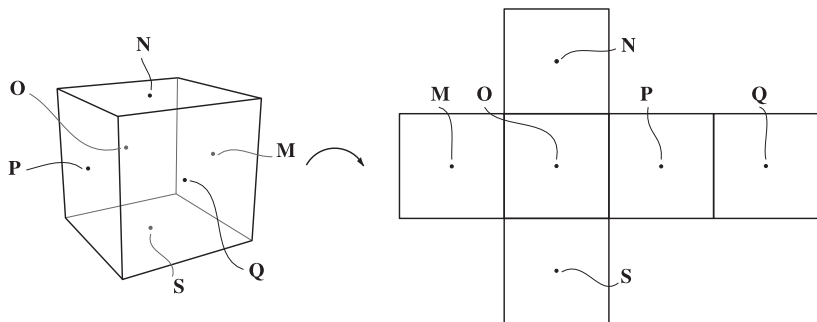


**Figure 8.14.** Illustration of Greene's environment map, with key points shown. The cube on the left is unfolded into the environment map on the right.

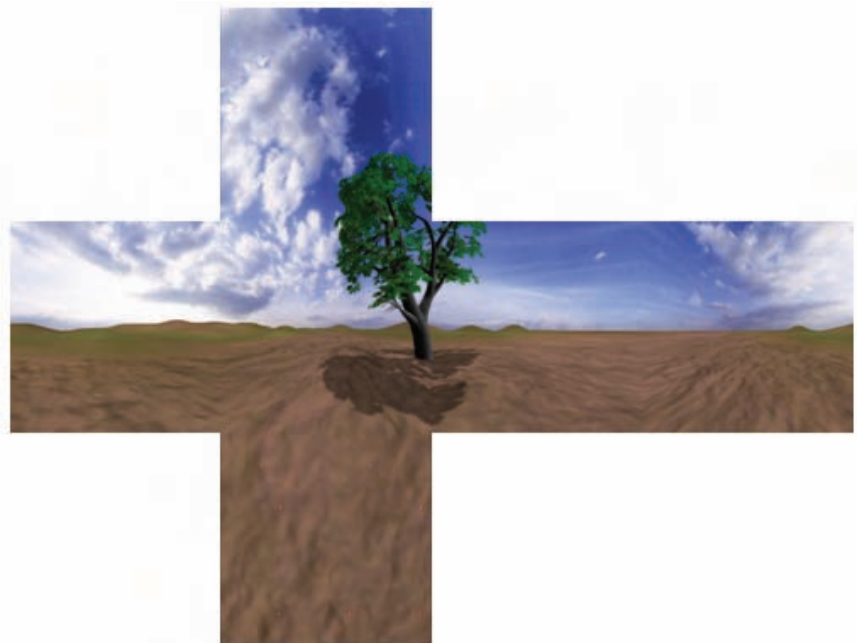


**Figure 8.15.** A typical cubic environment map (one of the first, from 1986 [449]). (Image courtesy of Ned Greene/NYIT.)

time. See Figure 8.16 for an example. Cubic environment mapping is *view independent*, unlike sphere mapping. It also has much more uniform sampling characteristics than Blinn and Newell's method, which oversamples the poles compared to the equator. Uniformity of sampling is important for environment maps, as it helps maintain an equal level of quality of re-



**Figure 8.16.** A still from the Xbox game *Project Gotham Racing*. Glare effects from the headlights make it clear it is nighttime. A cube map of the environment from the car’s location is created, each frame to provide dynamic reflections off the car. (*Image courtesy of Bizarre Creations and Microsoft Corp.*)

flection across a surface. Wan et al. [1317, 1318] present a mapping called the *isocube* that has a lower sampling rate discrepancy than cube mapping and accesses the cube map hardware for rapid display.

For most applications, cube mapping provides acceptably high quality at extremely high speeds. Accessing the cube map is extremely simple—the reflected view vector  $\mathbf{r}$  is used directly as a three-component texture coordinate (it does not even need to be normalized). The only caveat is that  $\mathbf{r}$  must be in the same coordinate system that the environment map is defined in (usually world space).

With the advent of Shader Model 4.0, cube maps can be generated in a single pass using the geometry shader. Instead of having to form six different views and run the geometry through the pipeline six times, the geometry shader replicates incoming data into six separate objects. Each object is transformed using a different view, and the results are sent to different faces stored in a texture array [261].

Note that since environment maps usually contain high dynamic range values, care should be taken when generating them dynamically, so that the right range of values is written into the environment map.

The primary limitation of environment maps is that they only represent distant objects. This can be overcome by using the position of the surface to make the cube map behave more like a local object, instead of an object that is infinitely far away. In this way, as an object moves within a scene, its shading will be more influenced by the part of the environment nearer to it. Bjorke [93] uses a cube with a physical location and extent. He casts a ray from the shaded surface location in the direction of the reflection vector. The vector from the cube center to the ray-cube intersection point is used to look up the cube map. Szirmay-Kalos et al. [1234] store a distance for each texel, allowing more elaborate environments to be reflected realistically.

#### 8.4.4 Parabolic Mapping

Heidrich and Seidel [532, 535] propose using two environment textures to perform parabolic environment mapping. The idea is similar to that of sphere mapping, but instead of generating the texture by recording the reflection of the environment off a sphere, two paraboloids are used. Each paraboloid creates a circular texture similar to a sphere map, with each covering an environment hemisphere. See Figure 8.17.

As with sphere mapping, the reflected view ray is computed with Equation 8.27 in the map's basis (i.e., in its frame of reference). The sign of the  $z$ -component of the reflected view vector is used to decide which of the two

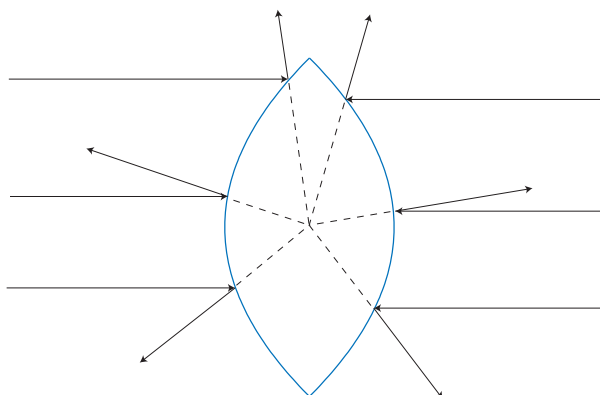


**Figure 8.17.** Two paraboloid mirrors that capture an environment using diametrically opposite views. The reflected view vectors all extend to meet at the center of the object, the foci of both paraboloids.

textures to access. Then the access function is simply

$$u = \frac{r_x}{2(1+r_z)} + 0.5, \quad (8.33)$$

$$v = \frac{r_y}{2(1+r_z)} + 0.5, \quad (8.34)$$

for the front image, and the same, with sign reversals for  $r_z$ , for the back image.

The texture transformation matrix is set and used as follows:

$$\begin{pmatrix} 1 & 0 & 1 & 1 \\ 0 & 1 & 1 & 1 \\ 0 & 0 & 0 & 0 \\ 0 & 0 & 2 & 2 \end{pmatrix} \begin{pmatrix} r_x \\ r_y \\ 1 \\ r_z \end{pmatrix}. \quad (8.35)$$

The authors present an implementation for this method using the OpenGL fixed-function pipeline. The problem of interpolating across the seam between the two textures is handled by accessing both paraboloid textures. If a sample is not on one texture, it is black, and each sample will be on one and only one of the textures. Summing the results (one of which is always zero) gives the environment's contribution.

There is no singularity with the parabolic map, so interpolation can be done between any two reflected view directions. The parabolic map has more uniform texel sampling of the environment compared to the sphere map, and even to the cubical map. Parabolic mapping, like cubic mapping, is view-independent. As with sphere maps, parabolic mapping can be done on any graphics hardware that supports texturing. The main drawback of parabolic mapping is in making the maps themselves. Cubic maps are straightforward to make for synthetic scenes and can be regenerated on the fly, and sphere maps of real environments are relatively simple to photograph, but parabolic maps have neither advantage. Straight edges in world space become curved in parabolic space. Parabolic maps have to be created by tessellating objects, by warping images, or by using ray tracing.

One common use of parabolic mapping is for accessing data stored for a hemisphere of view directions. For this situation only a single parabolic map is needed. Section 7.7.2 gives an example, using parabolic maps to capture angle-dependent surface reflectivity data for factorization.

## 8.5 Glossy Reflections from Environment Maps

While environment mapping was developed as a technique for rendering mirror-like surfaces, it can be extended to glossy reflections as well. To

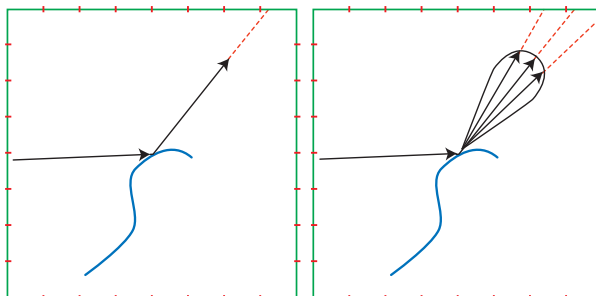


**Figure 8.18.** The left figure shows an eye ray reflecting off an object to retrieve a perfect mirror reflection from an environment texture (a cube map in this case). The right figure shows a reflected view ray’s specular lobe, which is used to sample the environment texture. The green square represents a cross section of the cube map, and the red tick marks denote the boundaries between texels. Although a cube map representation is shown, any environment representation can be used.

simulate surface roughness, the environment’s representation in the texture can be filtered [449]. By blurring the environment map (EM) texture, we can present a rougher-appearing specular reflection. This is sometimes called a *reflection map*, as it combines the reflectance of the surface with the EM. In theory, such blurring should be done in a nonlinear fashion; that is, different parts of the texture should be blurred differently. This is because environment map texture representations have a nonlinear mapping to the ideal spherical space of directions. The angular distance between the centers of two adjacent texels is not constant, nor is the solid angle covered by a single texel. However, the eye tends to be fairly forgiving, because the general effect of the reflection is usually more important than the exact reflection itself. So a lazy way to obtain fuzzy reflections is to just blur the environment maps uniformly in texture space and hope for the best. Care still needs to be taken around the edges of the maps, though. For example, GPUs usually do not automatically filter across cube map faces, so this needs to be addressed when preparing the reflection map. Figure 6.19 on page 171 illustrates this issue.

A more physically realistic method is to use a BRDF lobe such as a cosine power (Phong) or Gaussian lobe to filter the environment map [866], accounting for the distortion introduced by the texture representation. See Figure 8.18. The specular lobe determines which texels on the EM texture to sample and how much to weight each texel’s relative contribution. Heidrich and Seidel [535] use a single reflection map in this way to simulate the blurriness of a surface.

Imagine some light coming in from near a given reflected view direction. Light directly from the reflected view direction will give the largest

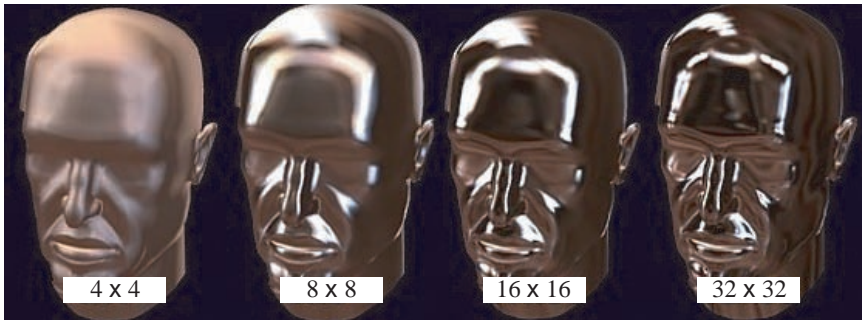


**Figure 8.19.** An example of a cube map mip chain filtered with Gaussian lobes of increasing width. Note that this creates a visual impression of changing surface roughness. (*Images using CubeMapGen courtesy of ATI Technologies Inc.*)

contribution, dropping off as the direction to the incoming light increasingly differs from the reflected view direction. The area of the EM texel multiplied by the texel’s BRDF contribution gives the relative effect of this texel. This weighted contribution is multiplied by the color of the EM texel, and the results are summed to compute  $\mathbf{q}$ . The sum of the weighted contributions,  $s$ , is also computed. The final result,  $\mathbf{q}/s$ , is the overall color integrated over the reflected view direction’s lobe and is stored in the resulting reflection map. When combined with a Fresnel term, such reflection maps work well for glossy surfaces.

For surfaces with spatially varying roughness, an effective approach is to store environment maps filtered with Phong or Gaussian lobes of different widths in the mipmap levels of a single texture (usually a cube map) [443, 830, 831]. This works well, since the blurrier maps are stored in the lower-resolution mipmap levels. ATI’s *CubeMapGen* is an example of a tool that can generate such mip chains. Figure 8.19 shows an example.

When accessing such mip chains, the index of the mipmap level that corresponds to the current filter width can be easily computed in the shader. However, always using this mipmap level may result in aliasing when minification requires lower-resolution mipmap levels to be used. Ashikhmin and Ghosh point out [45] that for best results, the indices of the two candidate mipmap levels (the minification level computed by the texturing hardware and the level corresponding to the current filter width) should be compared, and the index of the lower resolution mipmap level used. When the roughness is constant over a mesh, the texturing hardware can be configured to perform this mipmap level clamping automatically. However, when the roughness varies per pixel, this requires the hardware-computed mipmap index to be accessed in the pixel shader so the comparison can be performed. Since pixel shaders lack the ability to get the mipmap index

that would be used for a given texture access, a common technique is to store the mipmap index in the alpha channel of the texture. The environment map texture is first accessed using a standard texture read operation (which requires the texturing hardware to compute an appropriate mipmap level). The alpha channel of the result is compared to the mipmap index corresponding to the current filter width. The index of the lower resolution mipmap level is used to access the environment map texture again, this time using a texture read operation that allows for specifying the mipmap index directly.

For a view-independent EM representation such as a cubic or parabolic map, the color stored is valid for all mirror reflections in that direction, regardless of the viewer's location. The EM, in fact, stores radiance values of the incoming illumination—it does not matter how this data is accessed. A variety of eye and surface orientations can generate the same reflected view direction, for example. In each case, the radiance in that direction is the same.

However, this same independence does not hold when the EM is filtered to create a reflection map. A single reflection map is sufficient only if all viewing and surface directions that yield the same reflected view direction have the same shaped specular lobe. This is never the case for anything but perfect mirror surfaces. Think about viewing a shiny (not mirror) sphere from in front and nearly behind it. When in front, a ray reflecting from the sphere that goes straight back may have, say, a symmetric Phong lobe. From nearly behind, a ray reflecting the same direction must in reality have a piece of its lobe cut off. See Figure 8.20. The filtering scheme presented earlier assumes that all lobes for a given reflected view direction are the same shape and height. In fact, this means the lobes also have to be radially

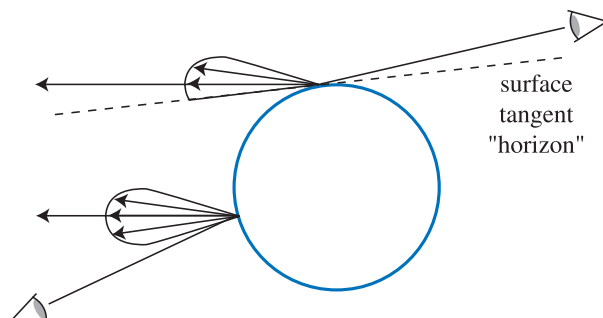


**Figure 8.20.** A shiny sphere is seen by two viewers. Separate locations on the sphere give the same reflected view directions for both viewers. The left viewer's surface reflection samples a symmetric lobe. The right viewer's reflection lobe must be chopped off by the horizon of the surface itself, since light cannot reflect off the surface below its horizon.

symmetric. Beyond the problem at the horizon, most BRDFs do not have uniform, radially symmetric lobes at all angles; at grazing angles the lobes often become sharper and thinner. Also, the lengths of the lobes normally vary with elevation angle.

This effect usually is not noticeable for curved surfaces. However, for flat surfaces such as floors, radially symmetric filters can introduce noticeable errors (see Section 7.5.7 for a detailed explanation).

Kautz and McCool address the problem by approximating the BRDF with multiple lobes, resulting in several reflection maps added together [626]. Their approach requires an array of reflection maps, one for each lobe.

McAllister et al. [830, 831] present a method for representing spatially variant BRDFs (SVBRDFs) with textures containing multiple coefficients for the Lafortune BRDF [710]. Since Lafortune lobes are generalized Phong lobes, a single environment map texture can be used where the mipmap levels are filtered with different Phong cosine exponents. This approach enables rendering a variety of BRDF effects, including anisotropy and retroreflection with environment maps.

Green et al. [443] propose a similar method, which uses Gaussian lobes instead of Phong lobes. Their fitting process is much faster than McAllister's. In addition, their approach can be extended to support directional shadowing of the environment map (see Section 9.10.2).

Colbert and Křivánek [187, 188] describe a high-quality algorithm that supports arbitrary BRDFs. It is quite expensive, requiring 20 to 40 reads from the environment map, but reproduces the effects of integrating over the environment map with the actual BRDF. Colbert and Křivánek's algorithm uses a method called *Monte Carlo quadrature with importance sampling*, which is also used in ray tracing. It is based on the idea that the integral of a function can be approximated by taking random samples, weighted to occur more often in areas where the function is expected to have high values.

Filtering environment maps as a pre-process is straightforward, and tools such as ATI's *CubeMapGen* are available to assist in this process. If the environment maps are dynamically generated, efficient filtering can be difficult. The auto-generated MIP map levels provided by most APIs may be sufficient for some needs, but can result in artifacts. Kautz et al. [627] present a technique for rapidly generating filtered parabolic reflection maps. Hensley et al. [542, 543] present a method to interactively generate summed-area tables (see Section 6.2.2), which are subsequently used for high-quality glossy reflections.

An alternative to regenerating the full environment map is to add the specular highlights from dynamic light sources onto a static base environment map. This technique can be an alternative way to solve the light-

shader combinatorial problem discussed in Section 7.9, since the effect of any number of light sources can simply be handled through the environment map. The added highlights can be prefiltered “blobs” that are added onto a prefiltered base environment map, thus avoiding the need to do any filtering at run time. The limitations are due to the assumptions of environment mapping in general: that lights and reflected objects are distant and so do not change with the location of the object viewed. This means that local light sources cannot easily be used. Using EM often makes it difficult for an object to move among different lighting situations, e.g., from one room to another. Cubic environment maps can be regenerated on the fly from frame to frame (or once every few frames), so swapping in new specular reflection maps is relatively inexpensive.

### 8.5.1 View-Dependent Reflection Maps

The reflection map approaches discussed above are view-independent. View-dependent representations such as sphere maps can also be used for reflection maps. Since sphere maps are defined for a fixed view direction, in principle each point on a sphere map defines not just a reflection direction, but also a surface normal (see Figure 8.13 on page 303). The reflectance equation can be solved for an arbitrary isotropic BRDF and its result stored in a sphere map. This BRDF can include diffuse, specular, retroreflective, and other terms. As long as the illumination and view direction are fixed, the sphere map will be correct. Even a photographic image of a real sphere under real illumination can be used, as long as the BRDF of the sphere is uniform and isotropic.

Although this approach supports more general BRDFs than other filtering approaches, there are some drawbacks. If the view direction ever changes, then the sphere map has to be recomputed. Even for a single frame, the view position changes due to perspective. This may cause errors at grazing angles unless different sphere maps are computed for different parts of the scene or an orthographic projection is used.

Cabral et al. [149] use an image warping approach with multiple sphere maps to get around the limitations of a single sphere map. In their scheme, 20 reflection sphere maps are generated for orthographic views located at the vertices of an icosahedron imposed on the scene. For any given view, the three sphere maps that are closest to the view direction (essentially, the three views at the vertices of the icosahedron face that the view is on) are warped and blended using barycentric coordinates. The resulting sphere map is then used for that view. This method avoids the need to recompute the reflection map when the view changes.

## 8.6 Irradiance Environment Mapping

The previous section discussed using filtered environment maps for glossy specular reflections. Filtered environment maps can be used for diffuse reflections as well [449, 866]. Environment maps for specular reflections have some common properties, whether they are unfiltered and used for mirror reflections, or filtered and used for glossy reflections. In both cases, specular environment maps are indexed with the reflected view vector, and they contain radiance values.<sup>4</sup>

In contrast, environment maps for diffuse reflections are indexed with the surface normal  $\mathbf{n}$ , and they contain *irradiance* values. For this reason they are called *irradiance environment maps* [1045]. Figure 8.20 shows that glossy reflections with environment maps have errors under some conditions due to their inherent ambiguity—the same reflected view vector may correspond to different reflection situations. This is not the case with irradiance environment maps. The surface normal contains all of the relevant information for diffuse reflection. Since irradiance environment maps are extremely blurred compared to the original illumination, they can be stored at significantly lower resolution.

Irradiance environment maps are created by applying a very wide filter (covering an entire hemisphere) to the original environment map. The filter includes the cosine factor (see Figure 8.21). The sphere map in Figure 8.11

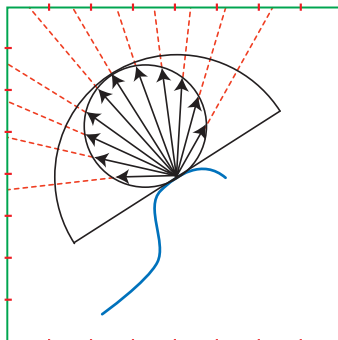


**Figure 8.21.** Computing an irradiance environment map. The cosine weighted hemisphere around the surface normal is sampled from the environment texture (a cube map in this case) and summed to obtain the irradiance, which is view-independent. The green square represents a cross section of the cube map, and the red tick marks denote the boundaries between texels. Although a cube map representation is shown, any environment representation can be used.

<sup>4</sup>Unfiltered environment maps contain incoming radiance values. Filtered environment maps (more properly called *reflection maps*) contain outgoing radiance values.

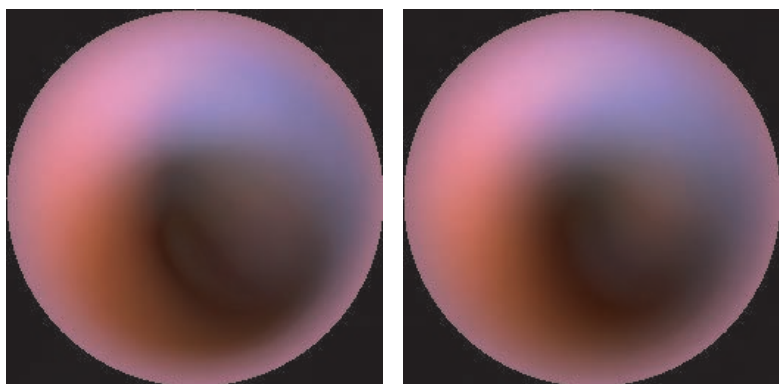


**Figure 8.22.** Irradiance maps formed from the Grace Cathedral sphere map. The left figure is formed by summing the weighted colors in the hemisphere above each pixel. The right figure is generated by deriving a nine-term function approximating this radiance map, then evaluating this function for each pixel. (*Images courtesy of Ravi Ramamoorthi, Computer Graphics Laboratory, Stanford University.*)



**Figure 8.23.** Character lighting performed using an irradiance map. (*Image courtesy of the game "Dead or Alive® 3," Tecmo, Ltd. 2001.*)

on page 302 has a corresponding irradiance map shown in Figure 8.22. Figure 8.23 shows an example of an irradiance map in use.

Irradiance environment maps are stored and accessed separately from the specular environment or reflection map, usually in a view-independent EM representation such as a cube map. See Figure 8.24. Instead of using the reflected view vector, the surface normal is used to access the cube map to retrieve the irradiance. Values retrieved from the irradiance environment map are multiplied by the diffuse reflectance, and values retrieved from the specular environment map are multiplied by the specular reflectance. The Fresnel effect can also be modeled, increasing specular reflectance (and possibly decreasing diffuse reflectance) at glancing angles [535].

Since the irradiance environment maps use extremely wide filters, it is difficult to create them efficiently on the fly. King [660] discusses how to perform convolution on the GPU to create irradiance maps. He was able to generate irradiance maps at rates of more than 300 fps on 2004-era hardware.

If a dynamic environment map is rendered only for the purpose of generating an irradiance environment map, it can have very low resolution. However, any area light sources may “fall between the texels,” causing them to flicker or drop out completely. To avoid this problem, Wiley [1351] proposes representing such light sources by large “cards” when rendering the dynamic environment map.

As in the case of glossy reflections, dynamic light sources can also be added into prefiltered irradiance environment maps. This allows the environment map to react dynamically to moving light sources without filtering

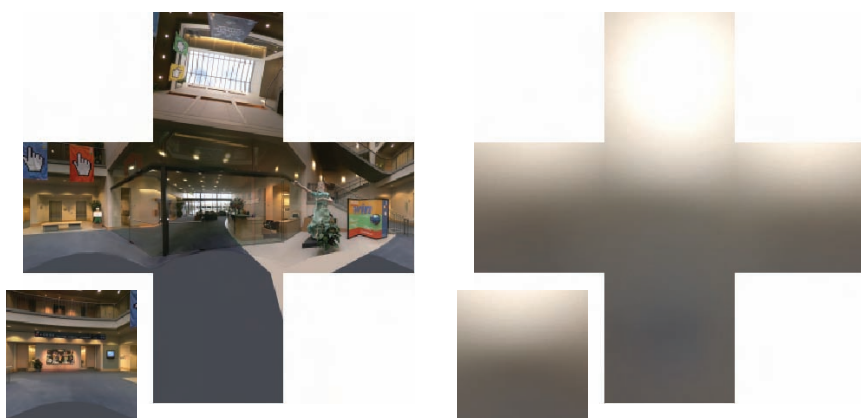


**Figure 8.24.** A cube map and its corresponding filtered irradiance map. (*Reprinted with permission from Microsoft Corporation.*)

the entire environment map. An inexpensive method to do this is given by Brennan [140]. Imagine an irradiance map for a single light source. In the direction of the light, the radiance is at a maximum, as the light hits the surface straight-on. Radiance for a given surface normal direction (i.e., a given texel) falls off with the cosine of the angle to the light, then is zero as the surface faces away from the light. The GPU can be used to rapidly add in this contribution directly to an existing irradiance map. Instead of rendering a point light to a cube map and filtering the map, the filtered appearance of the light is represented by an object. This object can be visualized as a hemisphere centered around the observer, with the pole of the hemisphere along the light’s direction. The hemisphere itself is brightest in this direction, falling off to zero at its edge. Rendering this object directly into the cube map gives an irradiance contribution for that light. In this way, each moving point light in a scene can add its effect to the irradiance map by rendering its corresponding hemisphere.

As with specular environment maps, it is possible to modify how irradiance environment maps are accessed, so that they represent local reflections rather than infinitely far ones. One way to do this is to use a blend of the normal and the direction from the reference location (the “center” of the environment map) to the surface location. This gives some variation with location, while still being affected by the surface normal [947].

### 8.6.1 Spherical Harmonics Irradiance

Although we have only discussed representing irradiance environment maps with textures such as cube maps, other representations are possible. *Spherical harmonics* (SH) have become popular in recent years as an irradiance environment map representation. Spherical harmonics are a set of mathematical functions that can be used to represent functions on the unit sphere such as irradiance.

Spherical harmonics<sup>5</sup> are *basis functions*: a set of functions that can be weighted and summed to approximate some general space of functions. In the case of spherical harmonics, the space is “scalar functions on the unit sphere.” A simple example of this concept is shown in Figure 8.25. Each of the functions is scaled by a weight or *coefficient* such that the sum of the weighted basis functions forms an approximation to the original target function.

Almost any set of functions can form a basis, but some are more convenient to use than others. An *orthogonal set* of basis functions is a set such that the *inner product* of any two different functions from the set is

---

<sup>5</sup>The basis functions we discuss here are more properly called “the real spherical harmonics,” since they represent the real part of the complex-valued spherical harmonic functions.

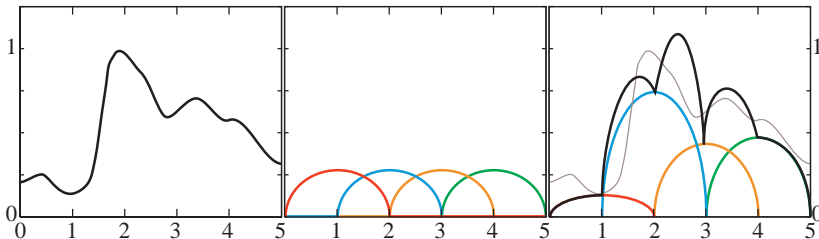


**Figure 8.25.** A simple example of basis functions. In this case, the space is “functions that have values between 0 and 1 for inputs between 0 and 5.” The left side shows an example of such a function. The middle shows a set of basis functions (each color is a different function). The right side shows an approximation to the target function, formed by multiplying each of the basis functions by a weight (the basis functions are shown scaled by their respective weights) and summing them (the black line shows the result of this sum, which is an approximation to the original function, shown in gray for comparison).

zero. The inner product is a more general, but similar, concept to the dot product. The inner product of two vectors is their dot product, and the inner product of two functions is defined as the integral of the two functions multiplied together:

$$\langle f_i(x), f_j(x) \rangle \equiv \int f_i(x) f_j(x) dx, \quad (8.36)$$

where the integration is performed over the relevant domain. For the functions shown in Figure 8.25, the relevant domain is between 0 and 5 on the  $x$ -axis (note that this particular set of functions is *not* orthogonal). For spherical functions the form is slightly different, but the basic concept is the same:

$$\langle f_i(\mathbf{n}), f_j(\mathbf{n}) \rangle \equiv \int_{\Theta} f_i(\mathbf{n}) f_j(\mathbf{n}) d\omega, \quad (8.37)$$

where  $\Theta$  indicates that the integral is performed over the unit sphere.

An *orthonormal set* is an orthogonal set with the additional condition that the inner product of any function in the set with itself is equal to 1. More formally, the condition for a set of functions  $\{f_j()\}$  to be orthonormal is

$$\langle f_i(), f_j() \rangle = \begin{cases} 0, & \text{where } i \neq j, \\ 1, & \text{where } i = j. \end{cases} \quad (8.38)$$

Figure 8.26 shows a similar example to Figure 8.25, where the basis functions are orthonormal.

The advantage of an orthonormal basis is that the process to find the closest approximation to the target function is straightforward. This process is called *basis projection*. The coefficient for each basis function is

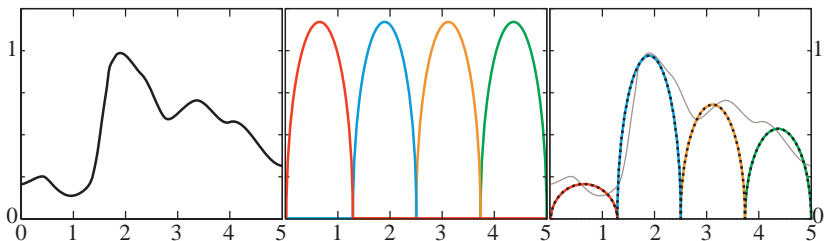


**Figure 8.26.** Orthonormal basis functions. This example uses the same space and target function as Figure 8.25, but the basis functions have been modified to be orthonormal. The left side shows the target function, the middle shows the orthonormal set of basis functions, and the right side shows the scaled basis functions. The resulting approximation to the target function is shown as a dotted black line, and the original function is shown in gray for comparison.

simply the inner product of the target function  $f_{\text{target}}()$  with the appropriate basis function:

$$k_j = \langle f_{\text{target}}(), f_j() \rangle,$$

$$f_{\text{target}}() \approx \sum_{j=1}^n k_j f_j(). \quad (8.39)$$

This is very similar in concept to the “standard basis” introduced in Section 4.2.4. Instead of a function, the target of the standard basis is a point’s location. Instead of a set of functions, the standard basis is composed of three vectors. The standard basis is orthonormal by the same definition used in Equation 8.38. The dot product (which is the inner product for vectors) of every vector in the set with another vector is zero (since they are perpendicular to each other), and the dot product of every vector with itself is one (since they are all unit length). The method of projecting a point onto the standard basis is also the same: The coefficients are the result of dot products between the position vector and the basis vectors. One important difference is that the standard basis *exactly* reproduces every point, and a finite set of basis functions only *approximates* its target functions. This is because the standard basis uses three basis vectors to represent a three-dimensional space. A function space has an infinite number of dimensions, so a finite number of basis functions can only approximate it. A roughly analogous situation would be to try to represent three-dimensional points with just the  $\mathbf{x}$  and  $\mathbf{y}$  vectors. Projecting a three-dimensional point onto such a basis (essentially setting its  $z$ -coordinate to 0) is an approximation roughly similar to the projection of a function onto a finite basis.

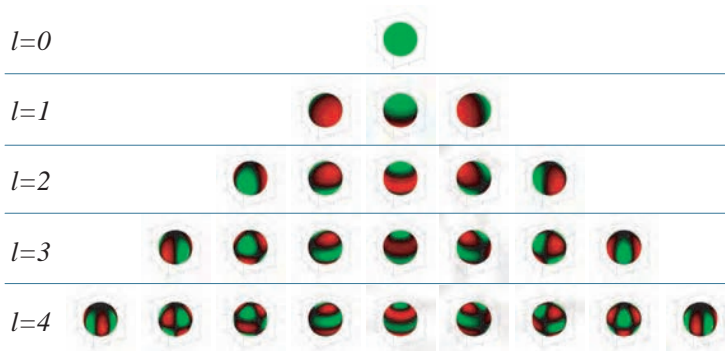


**Figure 8.27.** The first five frequency bands of spherical harmonics. Each spherical harmonic function has areas of positive values (colored green) and areas of negative values (colored red). (*Spherical harmonic visualizations courtesy of Robin Green.*)

Spherical harmonics form an orthonormal basis, and they have several other advantages. They are *rotationally invariant*—the result of rotating the projection of a function is the same as rotating the function and then projecting it. This means that a function approximated with spherical harmonics will not change when rotated.

SH basis functions are inexpensive to evaluate. They are simple polynomials in the  $x$ ,  $y$  and  $z$  coordinates of unit-length vectors (in the case of irradiance environment maps, the coordinates of the surface normal  $\mathbf{n}$ ). The expressions for the basis functions can be found in several references, including a presentation by Sloan [1192]. Sloan’s presentation is noteworthy in that it discusses many practical tips for working with spherical harmonics, including formulae, and in some cases, shader code.

The SH basis functions are arranged in *frequency bands*—the first basis function is constant, the next three are linear functions that change very slowly over the sphere, and the next five represent quadratic functions that change slightly faster, etc. See Figure 8.27. This means that functions that are low-frequency (i.e., change slowly over the sphere), such as irradiance environment maps, are well represented with a relatively small number of SH coefficients. Ramamoorthi and Hanrahan [1045] showed that irradiance environment maps can be represented to an accuracy of about 1% with just the first nine coefficients (note that each coefficient is an RGB vector).

This means that any irradiance environment map can be interpreted as a spherical function  $E(\mathbf{n})$  and projected onto nine RGB coefficients using Equations 8.37 and 8.39. This is a more compact representation than a cubic or parabolic map, and during rendering the irradiance can be reconstructed by evaluating some simple polynomials, instead of accessing a texture.

Ramamoorthi and Hanrahan [1045] also show that the SH coefficients for the incoming radiance function  $L(\mathbf{l})$  can be converted into coefficients for the irradiance function  $E(\mathbf{n})$  by multiplying each coefficient with a constant. This yields a very fast way to filter environment maps into irradiance environment maps: Project them into the SH basis and then multiply each coefficient by a constant. For example, this is how King’s fast irradiance filtering implementation [660] works. The basic concept is that the computation of irradiance from radiance is equivalent to performing an operation called *spherical convolution* between the incoming radiance function  $L(\mathbf{l})$  and the clamped cosine function  $\overline{\cos}(\theta_i)$ . Since the clamped cosine function is rotationally symmetrical about the  $z$ -axis, it has only one nonzero coefficient in each frequency band. The nonzero coefficients correspond to the basis functions in the center column of Figure 8.27, which are also known as the *zonal harmonics*.

The result of performing a spherical convolution between a general spherical function and a rotationally symmetrical one (such as the clamped cosine function) is another function over the sphere. This convolution can be performed directly on the function’s SH coefficients. The SH coefficients of the convolution result is equal to the product (multiplication) of the coefficients of the two functions, scaled by  $\sqrt{4\pi/(2l+1)}$  (where  $l$  is the frequency band index). This means that the SH coefficients of the irradiance function  $E(\mathbf{n})$  are equal to the coefficients of the radiance function  $L(\mathbf{l})$  times those of the clamped cosine function  $\overline{\cos}(\theta_i)$ , scaled by the band constants. The coefficients of  $\overline{\cos}(\theta_i)$  beyond the first nine have small values, which explains why nine coefficients suffice for representing the irradiance function  $E(\mathbf{n})$ . SH irradiance environment maps can be quickly evaluated in this manner. Sloan [1192] describes an efficient GPU implementation.

There is an inherent approximation here, since although the higher-order coefficients of  $E(\mathbf{n})$  are small, they are not zero. The accuracy of the approximation can be seen in Figure 8.28. The approximation is remarkably close, although the “wiggling” of the curve between  $\pi/2$  and  $\pi$ , when it should be zero, is notable. This “wiggling” is called *ringing* in signal processing and typically occurs when a function with a sharp change (like the clamp to zero at  $\pi/2$ ) is approximated with a small number of basis functions. The ringing is not noticeable in most cases, but it can be seen under extreme lighting conditions as color shifts or bright “blobs” on the shadowed sides of objects. If the irradiance environment map is only used to store indirect lighting (as often happens), then ringing is unlikely to be a problem.

Figure 8.22 on page 315 shows how an irradiance map derived directly compares to one synthesized by the nine-term function. This function can be evaluated during rendering with the current surface normal  $\mathbf{n}$  [1045], or

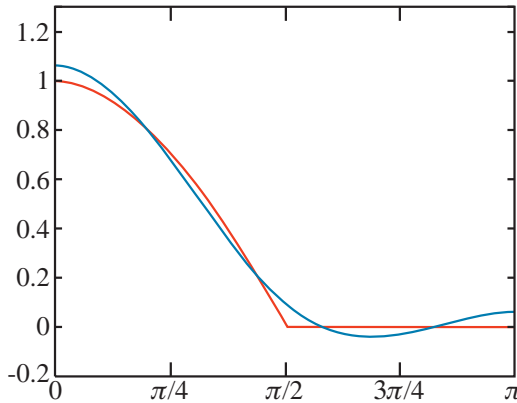


**Figure 8.28.** The clamped cosine function (in red) versus its nine-coefficient spherical harmonic approximation (in blue). The approximation is quite close. Note the slight dip below and the rise above zero between  $\pi/2$  and  $\pi$ .

can be used to rapidly create a cubic or parabolic map for later use. Such lighting is inexpensive and gives visually impressive results.

Dynamically rendered cubic environment maps can be projected onto the SH basis [634, 660, 1045]. Since cubic environment maps are a discrete representation of the incoming radiance function, the integral over the sphere in Equation 8.37 becomes a sum over the cube map texels:

$$k_{Lj} = \sum_t f_j(\mathbf{r}[t]) L[t] d\omega[t], \quad (8.40)$$

where  $t$  is the index of the current cube map texel,  $\mathbf{r}[t]$  is the direction vector pointing to the current texel,  $f_j(\mathbf{r}[t])$  is the  $j$ th SH basis function evaluated at  $\mathbf{r}[t]$ ,  $L[t]$  is the radiance stored in the texel, and  $d\omega[t]$  is the solid angle subtended by the texel. Kautz [634], King [660], and Sloan [1192] describe how to compute  $d\omega[t]$ .

To convert the radiance coefficients  $k_{Lj}$  into irradiance coefficients, they need to be multiplied by the scaled coefficients of the clamped cosine function  $\overline{\cos}(\theta_i)$ :

$$k_{Ej} = k'_{\overline{\cos}_j} k_{Lj} = k'_{\overline{\cos}_j} \sum_t f_j(\mathbf{r}[t]) L[t] d\omega[t], \quad (8.41)$$

where  $k_{Ej}$  is the  $j$ th coefficient of the irradiance function  $E(\mathbf{n})$ ,  $k_{Lj}$  is the  $j$ th coefficient of the incoming radiance function  $L(\mathbf{l})$ , and  $k'_{\overline{\cos}_j}$  is the  $j$ th coefficient of the clamped cosine function  $\overline{\cos}(\theta_i)$  scaled by  $\sqrt{4\pi/(2l+1)}$  ( $l$  is the frequency band index).

Given  $t$  and the cube map resolution, the factor  $k'_{\cos j} f_j(\mathbf{r}[t])d\omega[t]$  is constant for each basis function  $f_j()$ . These basis factors can be precomputed offline and stored in cube maps, which should be of the same resolution as the dynamic environment maps that will be rendered. The number of textures used can be reduced by packing a separate basis factor in each color channel. To compute an irradiance coefficient for the dynamic cube map, the texels of the appropriate basis factor map are multiplied with those of the dynamic cube map and the results summed. King's article [660] on dynamic irradiance cube maps has implementation details on GPU SH projection as well.

Dynamic light sources can be added into an existing SH irradiance environment map, by computing the SH coefficients of the lights' irradiance contributions and adding them to the existing coefficients. This avoids the need to recompute the entire irradiance environment map and is straightforward to do, since simple analytical expressions exist [444, 634, 1192, 1214] for the coefficients of point or circular lights, and summing the coefficients has the same effect as summing the irradiance. Coefficients for light sources with more complex shapes can be computed by drawing them into an image that is then numerically projected onto the SH basis [1214].

Rotation of SH coefficients can be quite expensive. Kautz et al. [633] presented a method to optimize the rotation computations by decomposing them into rotations about the  $x$  and  $z$  axes. Green's white paper [444] discusses this and other rotation methods. Microsoft's DirectX SDK [261] contains various helper functions for projecting cube maps into SH coefficients, rotating spherical harmonics, and other operations.

Ramamoorthi and Hanrahan showed [1045] that nine RGB SH coefficients are needed to accurately represent arbitrary irradiance environment maps. Often, less precision is needed if the irradiance environment maps represent indirect lighting, a common situation in interactive applications. In this case, four coefficients, for the constant basis function and the three linear basis functions, can often produce good results, since indirect illumination tends to be low frequency, i.e., change slowly with the angle.

Annen et al. [25] present a method for computing gradients that describes how the spherical harmonics values vary in space. This can represent somewhat localized lighting, which is not possible with regular irradiance environment maps.

## 8.6.2 Fill Lights

Although irradiance environment maps can represent both direct and indirect lighting, they are often used for indirect lighting only, with light sources being used to represent the direct lighting. Light sources can also be used to represent indirect lighting. This actually has a real-world anal-

ogy in lighting for film and video, where physical *fill lights* are often used to add lighting in shadows. In rendering, fill lights are light sources that are placed in order to simulate the indirect light in the scene. Specular contributions are usually not computed for fill lights, so they can be seen as an irradiance representation. There are several options for the placement of fill lights. When a fill light is attached to the camera location, it is called a *headlight*. Headlights move with the camera and usually do not fall off with distance.

Another option is to have a fill light that follows a character. This is usually done as part of a cinematic *three-point lighting* setup that includes a *key light*, which is the primary light for the character; a fill light to fill in shadowed areas; and a *back light* or *rim light* to add lighting around the outline of the character to make it stand out from the background. Such lights usually affect only the character they follow and do not illuminate other objects. One variant that is sometimes used in real-time rendering applications is to have the fill light direction be exactly opposite from that of the key light. This has the advantage that the cosine factor computed for the key light can be simply negated and used for the fill light, which makes the added cost for the fill light very low [691]. This technique is sometimes referred to as *bidirectional lighting*.

A third option is to place fill lights to simulate specific sources of ambient light in the scene, such as a red fill light placed next to a red wall to simulate light bouncing off the wall. Such lights typically have a distance falloff that restricts their effect to a limited part of the scene.

Fill lights usually look better than simple constant ambient terms—changes in surface orientation affect the lighting, so shadowed areas do not appear flat. Fill lights are an inexpensive and simple, but nonetheless very effective, approach to simulating indirect lighting.

### 8.6.3 Other Irradiance Representations

Although textures and spherical harmonics are the most commonly used representations for irradiance environment maps, other representations can be used. Many irradiance environment maps have two dominant colors—a sky color on the top and a ground color on the bottom. Motivated by this observation, Parker et al. [989] propose a *hemisphere lighting* model that uses just two colors. The upper hemisphere is assumed to emit a uniform radiance  $L_{\text{sky}}$ , and the lower hemisphere is assumed to emit a uniform radiance  $L_{\text{ground}}$ . The irradiance integral for this case is

$$E = \begin{cases} \pi \left( (1 - \frac{1}{2} \sin \theta) L_{\text{sky}} + \frac{1}{2} \sin \theta L_{\text{ground}} \right), & \text{where } \theta < 90^\circ, \\ \pi \left( \frac{1}{2} \sin \theta L_{\text{sky}} + (1 - \frac{1}{2} \sin \theta) L_{\text{ground}} \right), & \text{where } \theta \geq 90^\circ, \end{cases} \quad (8.42)$$

where  $\theta$  is the angle between the surface normal and the sky hemisphere axis. Baker and Boyd propose a cheaper approximation (described by Taylor [1254]):

$$E = \pi \left( \frac{1 + \cos \theta}{2} L_{\text{sky}} + \frac{1 - \cos \theta}{2} L_{\text{ground}} \right), \quad (8.43)$$

which is a linear interpolation between sky and ground using  $(\cos \theta + 1)/2$  as the interpolation factor. The approximation is reasonably close and significantly cheaper, so it is preferable to the full expression for most applications.

Valve uses an *ambient cube* representation for irradiance [848, 881]. This is essentially a weighted blending between six irradiance values specified at the faces of a cube:

$$\begin{aligned} E &= E_x + E_y + E_z, \\ E_x &= (\mathbf{n} \cdot \mathbf{x})^2 \begin{cases} E_{x-}, & \mathbf{n} \cdot \mathbf{x} < 0, \\ E_{x+}, & \mathbf{n} \cdot \mathbf{x} \geq 0, \end{cases} \\ E_y &= (\mathbf{n} \cdot \mathbf{y})^2 \begin{cases} E_{y-}, & \mathbf{n} \cdot \mathbf{y} < 0, \\ E_{y+}, & \mathbf{n} \cdot \mathbf{y} \geq 0, \end{cases} \\ E_z &= (\mathbf{n} \cdot \mathbf{z})^2 \begin{cases} E_{z-}, & \mathbf{n} \cdot \mathbf{z} < 0, \\ E_{z+}, & \mathbf{n} \cdot \mathbf{z} \geq 0, \end{cases} \end{aligned} \quad (8.44)$$

where  $\mathbf{x}$ ,  $\mathbf{y}$ , and  $\mathbf{z}$  are unit-length vectors aligned with the cube axes.

Forsyth [358] presents an inexpensive and flexible lighting model called the *trilight*, which includes directional, bidirectional, hemispherical, and wrap lighting as special cases.

## Further Reading and Resources

A valuable reference for information on the radiometry and mathematics used in this chapter (and much else) is Dutré's free online *Global Illumination Compendium* [287].

The work pioneered by Paul Debevec in the area of image-based lighting is of great interest to anyone who needs to capture environment maps from actual scenes. Much of this work is covered in a SIGGRAPH 2003 course [233], as well as in the book *High Dynamic Range Imaging: Acquisition, Display, and Image-Based Lighting* by Reinhard et al. [1059].

Green's white paper about spherical harmonic lighting [444] gives a very accessible and thorough overview of spherical harmonic theory and practice.



# Chapter 9

## Global Illumination

*“If it looks like computer graphics,  
it is not good computer graphics.”*

—Jeremy Birn

Radiance is the final quantity computed by the rendering process. So far, we have been using the *reflectance equation* to compute it:

$$L_o(\mathbf{p}, \mathbf{v}) = \int_{\Omega} f(\mathbf{l}, \mathbf{v}) \otimes L_i(\mathbf{p}, \mathbf{l}) \cos \theta_i d\omega_i, \quad (9.1)$$

where  $L_o(\mathbf{p}, \mathbf{v})$  is the outgoing radiance from the surface location  $\mathbf{p}$  in the view direction  $\mathbf{v}$ ;  $\Omega$  is the hemisphere of directions above  $\mathbf{p}$ ;  $f(\mathbf{l}, \mathbf{v})$  is the BRDF evaluated for  $\mathbf{v}$  and the current incoming direction  $\mathbf{l}$ ;  $L_i(\mathbf{p}, \mathbf{l})$  is the incoming radiance into  $\mathbf{p}$  from  $\mathbf{l}$ ;  $\otimes$  is the piecewise vector multiplication operator (used because both  $f(\mathbf{l}, \mathbf{v})$  and  $L_i(\mathbf{p}, \mathbf{l})$  vary with wavelength, so are represented as RGB vectors); and  $\theta_i$  is the angle between  $\mathbf{l}$  and the surface normal  $\mathbf{n}$ . The integration is over all possible  $\mathbf{l}$  in  $\Omega$ .

The reflectance equation is a restricted special case of the full *rendering equation*, presented by Kajiya in 1986 [619]. Different forms have been used for the rendering equation. We will use the following one:

$$L_o(\mathbf{p}, \mathbf{v}) = L_e(\mathbf{p}, \mathbf{v}) + \int_{\Omega} f(\mathbf{l}, \mathbf{v}) \otimes L_o(r(\mathbf{p}, \mathbf{l}), -\mathbf{l}) \cos \theta_i d\omega_i, \quad (9.2)$$

where the new elements are  $L_e(\mathbf{p}, \mathbf{v})$  (the emitted radiance from the surface location  $\mathbf{p}$  in direction  $\mathbf{v}$ ), and the following replacement:

$$L_i(\mathbf{p}, \mathbf{l}) = L_o(r(\mathbf{p}, \mathbf{l}), -\mathbf{l}). \quad (9.3)$$

This replacement means that the incoming radiance into location  $\mathbf{p}$  from direction  $\mathbf{l}$  is equal to the *outgoing* radiance from some other point in the opposite direction  $-\mathbf{l}$ . In this case, the “other point” is defined by the *ray casting function*  $r(\mathbf{p}, \mathbf{l})$ . This function returns the location of the first surface point hit by a ray cast from  $\mathbf{p}$  in direction  $\mathbf{l}$  (see Figure 9.1).

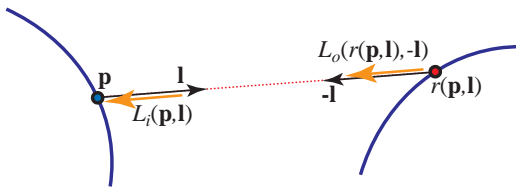


**Figure 9.1.** The shaded surface location  $p$ , lighting direction  $l$ , ray casting function  $r(p, l)$ , and incoming radiance  $L_i(p, l)$ , also represented as  $L_o(r(p, l), -l)$ .

The meaning of the rendering equation is straightforward. To shade a surface location  $p$ , we need to know the outgoing radiance  $L_o$  leaving  $p$  in the view direction  $v$ . This is equal to the emitted radiance  $L_e$  plus the reflected radiance. Emission from light sources has been studied in previous chapters, as has reflectance. Even the ray casting operator is not as unfamiliar as it may seem. The Z-buffer computes it for rays cast from the eye into the scene.

The only new term is  $L_o(r(p, l), -l)$ , which makes explicit the fact that the incoming radiance into one point must be outgoing from another point. Unfortunately, this is a recursive term. That is, it is computed by yet another summation over outgoing radiance from locations  $r(r(p, l), l')$ . These in turn need to compute the outgoing radiance from locations  $r(r(r(p, l), l'), l'')$ , ad infinitum (and it is amazing that the real world can compute all this in real-time).

We know this intuitively, that lights illuminate a scene, and the photons bounce around and at each collision are absorbed, reflected, and refracted in a variety of ways. The rendering equation is significant in that it sums up all possible paths in a simple (looking) equation.

In real-time rendering, using just a local lighting model is the default. That is, only the surface data at the visible point is needed to compute the lighting. This is a strength of the GPU pipeline, that primitives can be generated, processed, and then be discarded. Transparency, reflections, and shadows are examples of *global illumination* algorithms, in that they use information from other objects than the one being illuminated. These effects contribute greatly to increasing the realism in a rendered image, and also provide cues that help the viewer to understand spatial relationships.

One way to think of the problem of illumination is by the paths the photons take. In the local lighting model, photons travel from the light to a surface (ignoring intervening objects), then to the eye. Shadowing techniques take into account these intervening objects' direct effects. With environment mapping, illumination travels from light sources to distant objects, then to local shiny objects, which mirror-reflect this light to the eye. Irradiance maps simulate the photons again, which first travel to distant

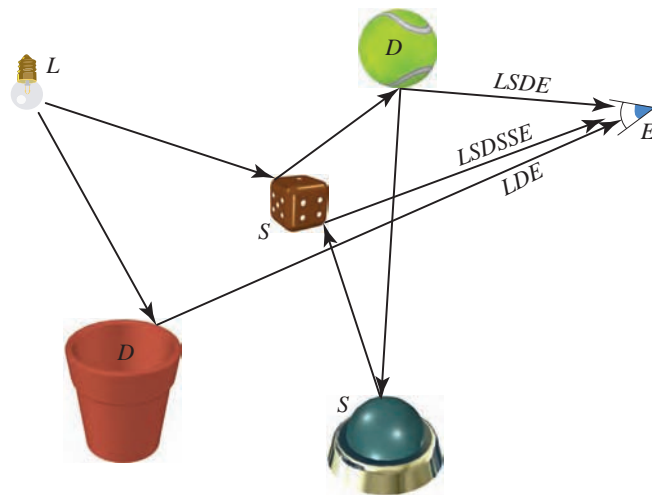


**Figure 9.2.** Some paths and their equivalent notation.

objects, but then light from all these objects is weighted and summed to compute the effect on the diffuse surface, which in turn is seen by the eye.

Thinking about the different types and combinations of light transport paths in a more formal manner is helpful in understanding the various algorithms that exist, and where further research may yield the most benefit. Heckbert [519] has a notational scheme that is useful for describing the paths simulated by a technique. Each interaction of a photon along its trip from the light ( $L$ ) to the eye ( $E$ ) can be labeled as diffuse ( $D$ ) or specular ( $S$ ). Categorization can be taken further by adding other surface types, such as “glossy,” meaning shiny but not mirror-like. Figure 9.2 shows some paths and the equivalent notation. Algorithms can be briefly summarized

| Operator | Description  | Example  | Explanation                              |
|----------|--------------|----------|--|
| *        | zero or more | $S*$     | zero or more specular bounces            |
| +        | one or more  | $D+$     | one or more diffuse bounces              |
| ?        | zero or one  | $S?$     | zero or one specular bounces             |
|          | either/or    | $D SS$   | either a diffuse or two specular bounces |
| ( )      | group        | $(D S)*$ | zero or more of diffuse or specular      |

**Table 9.1.** Regular expression notation.

by regular expressions, showing what types of interactions they simulate. See Table 9.1 for a summary of basic notation.

Photons can take various paths from light to eye. The simplest path is  $LE$ , where a light is seen directly by the eye. A basic Z-buffer is  $L(D|S)E$ , or equivalently,  $LDE|LSE$ . Photons leave the light, reach a diffuse or specular surface, and then arrive at the eye. Note that with a basic rendering system, point lights have no physical representation. Giving lights geometry would yield a system  $L(D|S)?E$ , in which light can also then go directly to the eye.

If environment mapping is added to the renderer, a compact expression is a little less obvious. Though Heckbert's notation reads from light to eye, it is often easier to build up expressions going the other direction. The eye will first see a specular or diffuse surface,  $(S|D)E$ . If the surface is specular, it could also then, optionally, reflect a (distant) specular or diffuse surface that was rendered into the environment map. So there is an additional potential path:  $((S|D)?S|D)E$ . To count in the path where the eye directly sees the light, add in a ? to this central expression to make it optional, and cap with the light itself:  $L((S|D)?S|D)?E$ .<sup>1</sup>

Note that this expression could be expanded to  $LE|LSE|LDE|LSSE|LDSE$ , which shows all the possible paths individually, or the shorter  $L((D|S)?S?E)$ . Each has its uses in understanding relationships and limits. Part of the utility of the notation is in expressing algorithm effects and being able to build off of them. For example,  $L(S|D)$  is what is encoded when an environment map is generated, and  $SE$  is the part that then accesses this map.

As various global algorithms are introduced in this chapter, their notational equivalent will be presented. The rendering equation itself can be summarized by the simple expression  $L(D|S) * E$ , i.e., photons from the light can hit zero to nearly infinite numbers of diffuse or specular surfaces before reaching the eye.

Global illumination research focuses on methods for efficiently computing light transport along some of these paths. Determining whether light reaches a surface is one of the most critical factors, and this chapter begins in this area, discussing shadows and ambient occlusion. A variety of techniques to perform global reflection, refraction, caustics, and subsurface scattering follow. Two basic alternate rendering algorithms, radiosity and ray tracing, are then briefly described.

One of the most common uses of full global illumination algorithms in real-time rendering is to compute various quantities ahead of time, which are later used to accelerate the rendering process or improve its quality.

---

<sup>1</sup>When building up such paths from the eye, it is often easier on the brain to reverse the order of the notation, e.g.,  $E(D|S(S|D)?)?L$ . Either direction is fine; this notation is meant as a tool, not as an exercise in confusion.

The chapter ends with a discussion of the various quantities that can be precomputed and used in this manner.

## 9.1 Shadows

Shadows are important elements in creating realistic images and in providing the user with visual cues about object placement. Here we will present the most important and popular real-time algorithms for dynamic shadows and briefly survey the rest as they apply to the themes developed. Various shadow techniques can usually be mixed as desired in order to maintain quality while still being efficient.

The terminology used throughout this section is illustrated in Figure 9.3, where *occluders* are objects that cast shadows onto *receivers*. Point light sources generate only fully shadowed regions, sometimes called *hard shadows*. If area or volume light sources are used, then soft shadows are produced. Each shadow can then have a fully shadowed region, called the *umbra*, and a partially shadowed region, called the *penumbra*. Soft shadows are recognized by their soft shadow edges. However, it is important to note that they usually cannot be rendered correctly by just blurring the edges of a hard shadow with a low-pass filter. As can be seen in Figure 9.4, a correct soft shadow is sharper the closer the shadow casting geometry is to the receiver. The umbra region of a soft shadow is not equivalent to a hard shadow generated by a point light source. Instead, the umbra region of a soft shadow decreases in size as the light source grows larger, and in fact, it might even disappear, given a large enough light source and a receiver far enough from the occluder. Soft shadows are generally preferable because the soft edges let the viewer know that the shadow is indeed a

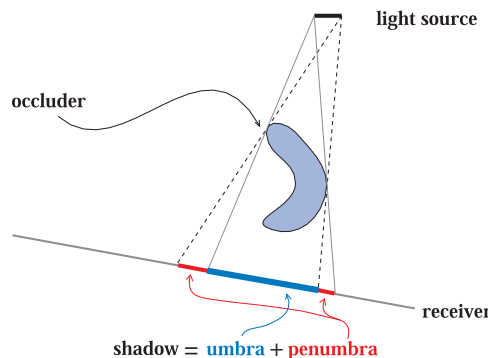


**Figure 9.3.** Shadow terminology: light source, occluder, receiver, shadow, umbra, and penumbra.



**Figure 9.4.** The upper image was rendered with hard shadows, while the lower was rendered with soft shadows. The soft shadow has a smaller umbra region (i.e., area fully in shadow), and the softness increases with the distance from the receiving point (the ground) [916]. (*Images from “Hellgate: London” courtesy of Flagship Studios, Inc.*)

shadow. Hard-edged shadows usually look less realistic and can sometimes be misinterpreted as actual geometric features, such as a crease in a surface.

More important than having a penumbra is having any shadow at all. Without some shadow as a visual cue, scenes are often unconvincing and more difficult to perceive. As Wanger shows [1324], it is usually better to have an inaccurate shadow than none at all, as the eye is fairly forgiving about the shape of the shadow. For example, a blurred black circle applied as a texture on the floor can anchor a person to the ground. A simple black rectangular shape fading off around the edges, perhaps a total of 10 triangles, is often all that is needed for a car's soft shadow.

In the following sections, we will go beyond these simple modeled shadows and present methods that compute shadows automatically in real time from the occluders in a scene. The first section handles the special case of shadows cast on planar surfaces, and the second section covers more general shadow algorithms, i.e., casting shadows onto arbitrary surfaces. Both hard and soft shadows will be covered. To conclude, some optimization techniques are presented that apply to various shadow algorithms.

### 9.1.1 Planar Shadows

A simple case of shadowing occurs when objects cast shadows on planar surfaces. Two kinds of algorithms for planar shadows are presented in this section.

#### *Projection Shadows*

In this scheme, the three-dimensional object is rendered a second time in order to create a shadow. A matrix can be derived that projects the vertices of an object onto a plane [101, 1263]. Consider the situation in Figure 9.5, where the light source is located at  $\mathbf{l}$ , the vertex to be projected is at  $\mathbf{v}$ , and the projected vertex is at  $\mathbf{p}$ . We will derive the projection matrix for the special case where the shadowed plane is  $y = 0$ , then this result will be generalized to work with any plane.

We start by deriving the projection for the  $x$ -coordinate. From the similar triangles in the left part of Figure 9.5, the following equation is obtained:

$$\frac{p_x - l_x}{v_x - l_x} = \frac{l_y}{l_y - v_y} \iff (9.4)$$

$$p_x = \frac{l_y v_x - l_x v_y}{l_y - v_y}.$$

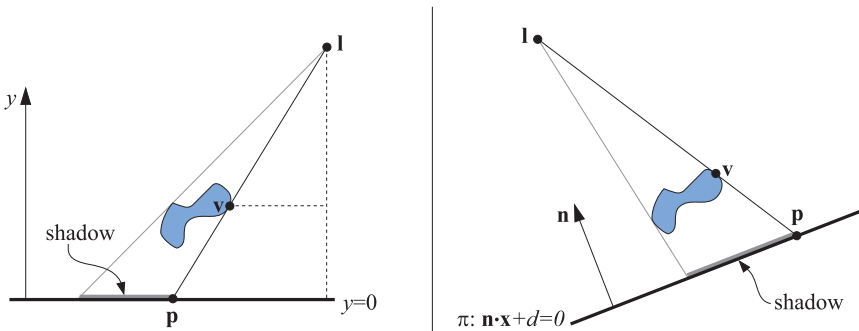


**Figure 9.5.** Left: A light source, located at  $\mathbf{l}$ , casts a shadow onto the plane  $y = 0$ . The vertex  $\mathbf{v}$  is projected onto the plane. The projected point is called  $\mathbf{p}$ . The similar triangles are used for the derivation of the projection matrix. Right: The notation of the left part of this figure is used here. The shadow is being cast onto a plane,  $\pi : \mathbf{n} \cdot \mathbf{x} + d = 0$ .

The  $z$ -coordinate is obtained in the same way:  $p_z = (l_y v_z - l_z v_y) / (l_y - v_y)$ , while the  $y$ -coordinate is zero. Now these equations can be converted into the projection matrix  $\mathbf{M}$ :

$$\mathbf{M} = \begin{pmatrix} l_y & -l_x & 0 & 0 \\ 0 & 0 & 0 & 0 \\ 0 & -l_z & l_y & 0 \\ 0 & -1 & 0 & l_y \end{pmatrix}. \quad (9.5)$$

It is straightforward to verify that  $\mathbf{M}\mathbf{v} = \mathbf{p}$ , which means that  $\mathbf{M}$  is indeed the projection matrix.

In the general case, the plane onto which the shadows should be cast is not the plane  $y = 0$ , but instead  $\pi : \mathbf{n} \cdot \mathbf{x} + d = 0$ . This case is depicted in the right part of Figure 9.5. The goal is again to find a matrix that projects  $\mathbf{v}$  down to  $\mathbf{p}$ . To this end, the ray emanating at  $\mathbf{l}$ , which goes through  $\mathbf{v}$ , is intersected by the plane  $\pi$ . This yields the projected point  $\mathbf{p}$ :

$$\mathbf{p} = \mathbf{l} - \frac{d + \mathbf{n} \cdot \mathbf{l}}{\mathbf{n} \cdot (\mathbf{v} - \mathbf{l})} (\mathbf{v} - \mathbf{l}). \quad (9.6)$$

This equation can also be converted into a projection matrix, shown in Equation 9.7, which satisfies  $\mathbf{M}\mathbf{v} = \mathbf{p}$ :

$$\mathbf{M} = \begin{pmatrix} \mathbf{n} \cdot \mathbf{l} + d - l_x n_x & -l_x n_y & -l_x n_z & -l_x d \\ -l_y n_x & \mathbf{n} \cdot \mathbf{l} + d - l_y n_y & -l_y n_z & -l_y d \\ -l_z n_x & -l_z n_y & \mathbf{n} \cdot \mathbf{l} + d - l_z n_z & -l_z d \\ -n_x & -n_y & -n_z & \mathbf{n} \cdot \mathbf{l} \end{pmatrix}. \quad (9.7)$$

As expected, this matrix turns into the matrix in Equation 9.5 if the plane is  $y = 0$  (that is,  $\mathbf{n} = (0 \ 1 \ 0)^T$  and  $d = 0$ ).

To render the shadow, simply apply this matrix to the objects that should cast shadows on the plane  $\pi$ , and render this projected object with a dark color and no illumination. In practice, you have to take measures to avoid allowing the projected polygons to be rendered beneath the surface receiving them. One method is to add some bias to the plane we project upon, so that the shadow polygons are always rendered in front of the surface. Getting this bias just right is often tricky: too much, and the shadows start to cover the objects and so break the illusion; too little, and the ground plane pokes through the shadows, due to precision error. Biasing solutions are discussed in Section 11.4.

A safer method is to draw the ground plane first, then draw the projected polygons with the  $Z$ -buffer off, then render the rest of the geometry as usual. The projected polygons are then always drawn on top of the ground plane, as no depth comparisons are made.

A flaw with projection shadows is that the projected shadows can fall outside of our plane. To solve this problem, we can use a stencil buffer. First, draw the receiver to the screen and to the stencil buffer. Then, with the  $Z$ -buffer off, draw the projected polygons only where the receiver was drawn, then render the rest of the scene normally.

Projecting the polygons this way works if the shadows are opaque. For semitransparent shadows, where the underlying surface color or texture can be seen, more care is needed. A convex object's shadow is guaranteed to have exactly two (or, by culling backfaces, exactly one) projected polygons covering each shadowed pixel on the plane. Objects with concavities do not have this property, so simply rendering each projected polygon as semi-transparent will give poor results. The stencil buffer can be used to ensure that each pixel is covered at most once. Do this by incrementing the stencil buffer's count by each polygon drawn, allowing only the first projected polygon covering each pixel to be rendered. Alternately, the ground plane could be drawn, the  $Z$ -buffer cleared, and then each successive shadow polygon is drawn increasingly offset (e.g., using `glPolygonOffset`) so that it is further away than the previous polygon. In this way, each shadowed pixel is drawn only once [663]. This works, but the ground plane may need to be redrawn into the  $Z$ -buffer (only) to reestablish the correct  $z$ -depths, if needed.

One way to avoid the problems of rendering multiple projected shadow polygons atop a ground plane is to instead render these polygons to a texture. This texture is then applied to the ground plane. Essentially, this texture is a form of a light map. As will be seen, this idea of rendering the shadow projection to a texture also allows soft shadowing and shadows on

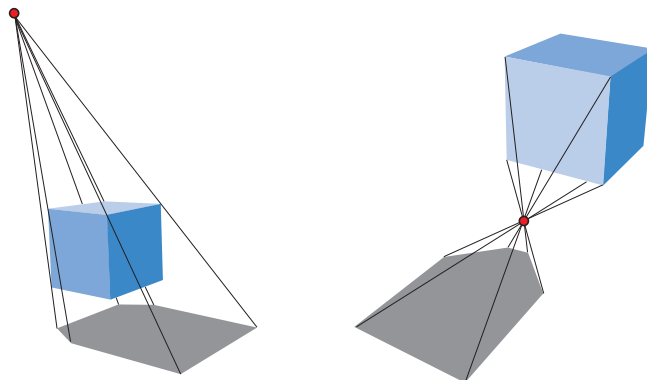


**Figure 9.6.** At the left, a correct shadow is shown, while in the figure on the right, an antishadow appears, since the light source is below the topmost vertex of the object.

curved surfaces. The major drawback of this technique is that the texture can become magnified, with a single texel covering multiple pixels.

If the shadow situation does not change from frame to frame, i.e., the light and shadow casters do not move relative to each other, this texture can be reused. Most shadow techniques can benefit from reusing intermediate computed results from frame to frame.

All shadow casters must be between the light and the ground plane receiver. If the light source is below the topmost point on the object, an *antishadow* [101] is generated, since each vertex is projected through the point of the light source. Correct shadows and antishadows are shown in Figure 9.6. A similar rendering error as that found with planar reflections can occur for this kind of shadow generation. For reflections, errors occur when objects located on the opposite side of the reflector plane are not dealt with properly. In the case of shadow generation, errors occur when we use a shadow-casting object that is on the far side of the receiving plane. This is because an object beyond the shadow receiver does not cast a shadow on it.

It is certainly possible to explicitly cull and trim shadow polygons to avoid such artifacts. A simpler method, presented next, is to use the existing GPU pipeline to perform projection with clipping.

### Soft Shadows

Projective shadows can also be made soft, by using a variety of techniques. Here, we describe an algorithm from Heckbert and Herf [524, 544] that produces soft shadows. The algorithm's goal is to generate a texture on a

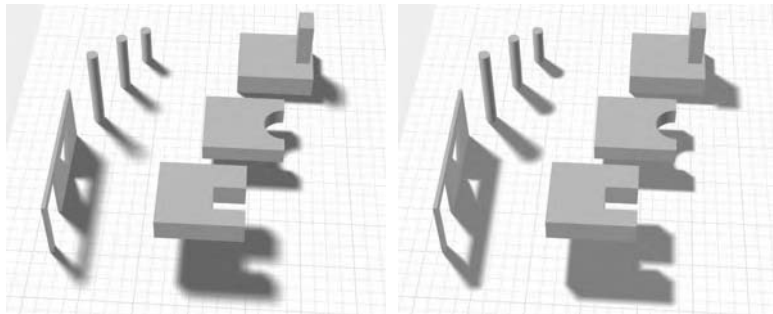


**Figure 9.7.** On the left, a rendering using Heckbert and Herf’s method, using 256 passes. On the right, Haines’ method in one pass. The umbrae are too large with Haines’ method, which is particularly noticeable around the doorway and window.

ground plane that shows a soft shadow.<sup>2</sup> We then describe less accurate, faster methods.

Soft shadows appear whenever a light source has an area. One way to approximate the effect of an area light is to sample it by using a number of point lights placed on its surface. For each of these point light sources, an image is rendered and added to the accumulation buffer. The average of these images is then an image with soft shadows. Note that, in theory, any algorithm that generates hard shadows can be used along with this accumulation technique to produce penumbras. In practice, doing so may be untenable because of execution time or memory constraints.

Heckbert and Herf use a frustum-based method to produce their shadows. The idea is to treat the light as the viewer, and the ground plane forms the far clipping plane of the frustum. The frustum is made wide enough to encompass the ground plane polygon.

A shadow texture for the receiver is generated in the following way. For each sample on the light source, the receiver is first rendered by using this sample as a point light source. Then the projection matrix is used to render all objects inside the pyramid. Since these objects should generate shadows, they are drawn in black (and so Z-buffering, texturing, and lighting can be turned off). All of these images are averaged into the accumulation buffer to produce a shadow texture. See the left side of Figure 9.7.

A problem with the sampled area light method is that it tends to look like what it is: a number of overlapping shadows from point light sources. Instead of varying the location of samples on the light’s surface, Gooch et al. [424] move the receiving plane’s location up and down and the projections cast upon it are averaged. This method has the advantage that the

---

<sup>2</sup>Basic hard shadows can also be generated using this technique.

shadows created are nested, which generally looks better and so requires fewer samples. In addition, a single shadow projection could be generated and reused to create the nested effect. A drawback of Gooch's method is that if the object touches the receiver, the shadow will not be modeled correctly. Darkness will appear to leak out from under the object. Another problem with both of these methods is that the shadows are quantized between a limited number of grayscale shades. For  $n$  shadow passes, only  $n + 1$  distinct shades can be generated. One answer is to fool the eye by applying a color texture to the receiver, as the texture will have a masking effect and hide this quantization [341].

Another approach is to use convolution, i.e., filtering. Soler and Silion [1205] create soft shadows by rendering the hard shadow to a texture and then softening (convolving) it by using a filter in the shape of the area light source. They vary the amount of blurring of the shadow dependent on the occluder silhouette's distance from the receiver, blending between blurred shadow images. This technique gives smooth, soft shadows for objects at a constant distance from the shadow receiver. Similar to Gooch's method, objects touching the ground can cause problems, as the shadow is supposed to be sharp where it touches and become softer as the distance increases. In a similar vein, Pranckevičius [1029] provides a method of smoothly varying the projected shadow's penumbra on the texture. The distance between receiver and occluder at each texel determines the amount of post-process blur to perform.

Haines [487] presents a method that creates soft shadows in a single pass for circular area lights. The idea is to start with a normal projected hard shadow and then paint the silhouette edges with gradients that go from dark in the center to white on the edges to create penumbrae. These gradient areas have a width proportional to the height of the silhouette edge casting

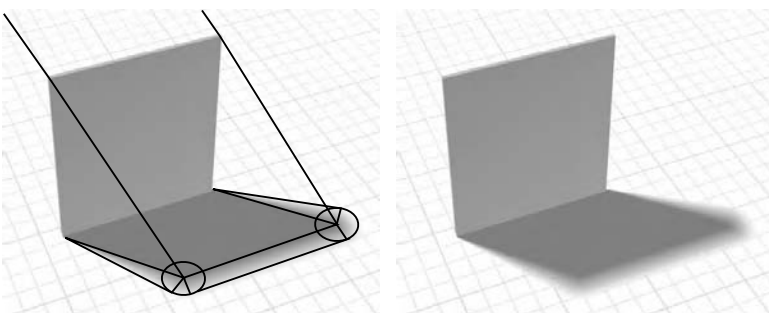


**Figure 9.8.** On the left, a visualization of Haines' method of soft shadowing on a plane. The object casts a hard shadow, and then gradient areas are drawn to simulate the penumbra. On the right is the result.

the shadow. Each silhouette edge casts a quadrilateral gradient area, and each edge endpoint casts a circular gradient area. By using the  $Z$ -buffer and painting these penumbrae objects using three-dimensional primitives such as wedges and cones, the rendered gradient areas are made to properly overlap (see Figure 9.8).

The methods of Gooch et al. and Haines share another problem. They both create umbra regions that are too large, since the projected shadow will always be larger than the object. In reality, if an area light is larger than the width of an occluder, the occluder will cast a smaller or nonexistent umbra region. See Figure 9.7 on page 337 for a comparison between Heckbert and Herf’s method and Haines’.

## 9.1.2 Shadows on Curved Surfaces

One way to extend the idea of planar shadows to curved surfaces is to use a generated shadow image as a projective texture [849, 917, 939, 1146]. Think of shadows from the light’s point of view (literally). Whatever the light sees is illuminated; what it does not see is in shadow. Say the occluder is rendered in black from the light’s viewpoint into an otherwise white texture. This texture can then be projected onto the surfaces that are to receive the shadow. Effectively, each vertex on the receivers has a  $(u, v)$  texture coordinate computed for it and has the texture applied to it. These texture coordinates can be computed explicitly by the application or implicitly using the projective texturing functionality of the graphics hardware. We call this the *shadow texture* technique. It is also occasionally known as the *shadow map* method in the game development community, as it is analogous to light mapping, but for shadows. Because a different technique, covered in Section 9.1.4, is more commonly called “shadow mapping,” we use the term “shadow texture” for the method here.

When forming a shadow texture, only the area of overlap between casters and receivers needs to be rendered. For example, the texture can often be considerably smaller than the area of the potential receivers, since the texture is needed only where the shadows are cast.

When rendered, the shadow texture modifies the receiver surfaces. One example is shown in Figure 9.9. This technique works particularly well for circumstances where the silhouette of the shadowing object does not change shape, so that the texture generated can be reused. Bloom [114] gives a wide range of optimizations that can be performed to minimize the cost of this technique.

There are some serious drawbacks of this method. First, the designer must identify which objects are occluders and which are their receivers. The receiver must be maintained by the program to be further from the light than the occluder, otherwise the shadow is “cast backwards.” Also,



**Figure 9.9.** Shadow projection. On the left is the scene from the light’s view. In the middle is the occluding object rendered as a shadow texture. On the right, the shadow texture has been applied. (*Images courtesy of Hubert Nguyen.*)

occluding objects cannot shadow themselves. The next two sections present algorithms that generate correct shadows without the need for such intervention or limitations.

Note that a variety of lighting patterns can be performed by using pre-built projective textures. A spotlight is simply a square projected texture with a circle inside of it defining the light. A Venetian blinds effect can be created by a projected texture consisting of horizontal lines. Shadows can be made soft by blurring the texture. This type of texture is called a *light attenuation mask*, *cookie texture*, or *gobo map*. A prebuilt pattern can be combined with a projected texture created on the fly by simply multiplying the two textures together. Such lights are discussed further in Section 7.4.3.

### 9.1.3 Shadow Volumes

Presented by Heidmann in 1991 [531], a method based on Crow’s *shadow volumes* [208] can cast shadows onto arbitrary objects by clever use of the stencil buffer. This technique is also sometimes called *volumetric shadows*.

To begin, imagine a point and a triangle. Extending the lines from a point through the vertices of a triangle to infinity yields an infinite pyramid. The part under the triangle, i.e., the part that does not include the point, is a truncated infinite pyramid, and the upper part is simply a pyramid. This is illustrated in Figure 9.10. Now imagine that the point is actually a point light source. Then, any part of an object that is inside the volume of the truncated pyramid (under the triangle) is in shadow. This volume is called a *shadow volume*.

Say we view some scene and follow a ray from the eye through a pixel until the ray hits the object to be displayed on screen. While the ray is on its way to this object, we increment a counter each time it crosses a face

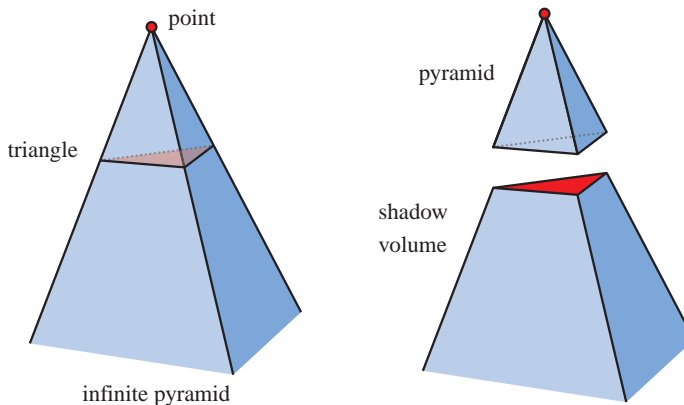


**Figure 9.10.** Left: The lines from a point light are extended through the vertices of a triangle to form an infinite pyramid. Right: The upper part is a pyramid, and the lower part is an infinite truncated pyramid, also called the shadow volume. All geometry that is inside the shadow volume is in shadow.

of the shadow volume that is frontfacing (i.e., facing toward the viewer). Thus, the counter is incremented each time the ray goes into shadow. In the same manner, we decrement the same counter each time the ray crosses a backfacing face of the truncated pyramid. The ray is then going out of a shadow. We proceed, incrementing and decrementing the counter until the ray hits the object that is to be displayed at that pixel. If the counter is greater than zero, then that pixel is in shadow; otherwise it is not. This principle also works when there is more than one triangle that casts shadows. See Figure 9.11.

Doing this geometrically is tedious and time consuming. But there is a much smarter solution [531]: The stencil buffer can do the counting for us. First, the stencil buffer is cleared. Second, the whole scene is drawn into the frame buffer with only ambient and emission components used, in order to get these lighting components in the color buffer and the depth information into the  $Z$ -buffer. Third,  $Z$ -buffer updates and writing to the color buffer are turned off (though  $Z$ -buffer testing is still done), and then the frontfacing polygons of the shadow volumes are drawn. During this process, the stencil operation is set to increment the values in the stencil buffer wherever a polygon is drawn. Fourth, another pass is done with the stencil buffer, this time drawing only the backfacing polygons of the shadow volumes. For this pass, the values in the stencil buffer are decremented when the polygons are drawn. Incrementing and decrementing are done only when the pixels of the rendered shadow-volume face are visible (i.e., not hidden by any real geometry). At this point the stencil

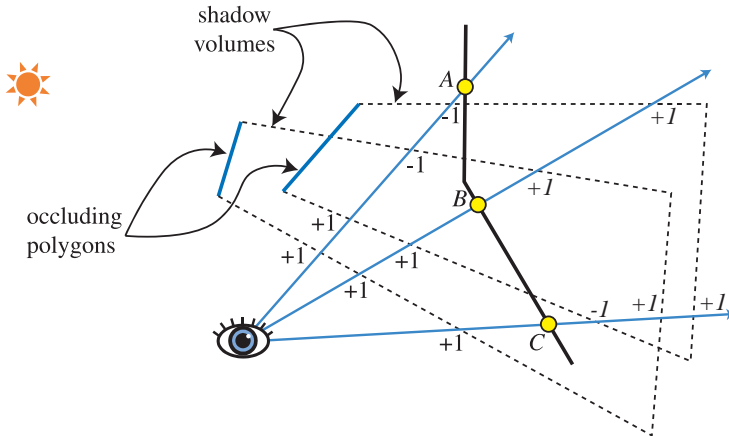


**Figure 9.11.** A two-dimensional side view of counting shadow volume crossings using two different counting methods. In *z*-pass volume counting, the count is incremented as a ray passes through a frontfacing polygon of a shadow volume and decremented on leaving through a backfacing polygon. So at point *A*, the ray enters two shadow volumes for  $+2$ , then leaves two volumes, leaving a net count of zero, so the point is in light. In *z*-fail volume counting, the count starts beyond the surface (these counts are shown in italics). For the ray at point *B*, the *z*-pass method gives a  $+2$  count by passing through two frontfacing polygons, and the *z*-fail gives the same count by passing through two backfacing polygons. Point *C* shows the importance of capping. The ray starting from point *C* first hits a frontfacing polygon, giving  $-1$ . It then exits two shadow volumes (through their endcaps, necessary for this method to work properly), giving a net count of  $+1$ . The count is not zero, so the point is in shadow. Both methods always give the same count results for all points on the viewed surfaces.

buffer holds the state of shadowing for every pixel. Finally, the whole scene is rendered again, this time with only the diffuse and specular components of the materials active, and displayed only where the value in the stencil buffer is 0. A value of 0 indicates that the ray has gone out of shadow as many times as it has gone into a shadow volume—i.e., this location is illuminated by the light.

The stencil buffer itself is not required for this method. Roettger et al. [1075] discuss a number of strategies for using the color and alpha buffers to take the place of the stencil buffer, and they obtain comparable performance. On most GPUs it is possible to do a signed addition to the frame buffer. This allows the separate frontface and backface passes to be performed in a single pass.

The separate frontface and backface passes can also be combined into one pass if shadow volumes are guaranteed to not overlap. In this case, the stencil buffer is toggled on and off for all shadow volume faces rendered. In the final pass, if the stencil bit is on, then the surface is in shadow.

The general algorithm has to be adjusted if the viewer is inside a shadow volume, as this condition throws off the count. In this case, a value of 0 does not mean a point is in the light. For this condition, the stencil buffer should be cleared to the number of shadow volumes the viewer starts inside (instead of 0). Another more serious problem is that the near plane of the viewer's viewing frustum might intersect one or more shadow volume planes. If uncorrected, this case invalidates the count for a portion of the image. This problem cannot be cured by simple count adjustment. The traditional method to solve this problem is to perform some form of *capping* at the near plane [84, 653, 849]. Capping is where additional polygons are drawn so as to make the object appear solid. However, such methods are generally not robust and general.

Bilodeau and Songy [87] were the first to present (and patent) an alternate approach to avoid this near plane clipping problem; Carmack also independently discovered a similar technique [653] (see Hornus et al. [568] for the differences). Nonintuitive as it sounds, the idea is to render the shadow volumes that are obscured by visible surfaces. The first stencil buffer pass becomes: Render the backfacing shadow volume polygons and increment the stencil count when the polygon is equal to *or farther than* the stored  $z$ -depth. In the next stencil pass, render the frontfacing shadow volume polygons and decrement the count when the polygon is, again, equal to *or farther than* the stored  $z$ -depth. Because the shadow volumes are drawn only when the Z-buffer test has failed, they are sometimes called  *$z$ -fail shadow volumes*, versus  *$z$ -pass*. The other passes are done as before. In the original algorithm, a point is in shadow because the number of frontfacing polygons crossed was larger than the number of backfacing polygons; in this version, the object is in shadow if the number of backfacing polygons not seen is larger than the number of frontfacing polygons not seen, something of a logical equivalent. The difference is that now all shadow volume polygons in front of surfaces, including those that could encompass the viewer, are not rendered, so avoiding most viewer location problems. See Figure 9.11.

For the  *$z$* -pass algorithm, the original triangles generating the quadrilaterals do not actually need to be rendered to the stencil buffer. These polygons are always made invisible by the first pass, which will set  $z$ -depths such that these polygons will match and so not be rendered. This is not the case for the  *$z$* -fail algorithm. To properly maintain the count, these originating polygons must be rendered. In addition, the shadow volumes must be closed up at their far ends, and these far endcaps must be inside the far plane. The  *$z$* -fail algorithm has the inverse of the problem that the  *$z$* -pass has. In  *$z$* -pass, it is possible for shadow volumes to penetrate the view frustum's near plane; in  *$z$* -fail, shadow volumes can potentially penetrate the far plane and cause serious shadowing errors. See Figure 9.12.

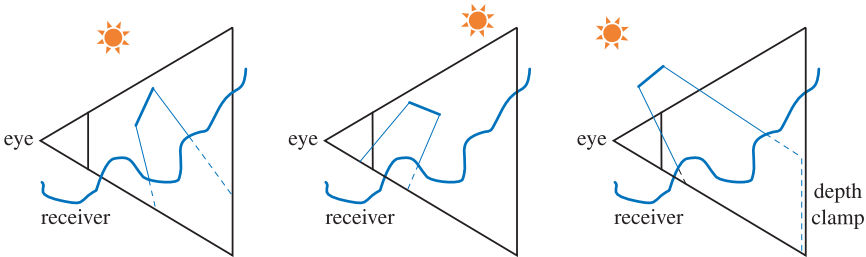


**Figure 9.12.** The *z*-pass and *z*-fail shadow volume methods; *z*-pass is shown as solid lines emanating from the occluder, *z*-fail as dashed lines beyond the receiver. On the left, if the *z*-fail method were used for the case shown, the shadow volume would need to be capped before reaching the far plane. In the middle, *z*-pass would give an incorrect count, as it penetrates the near plane. On the right, neither method can work without some way to avoid the clip by either the near or far plane; depth clamping's effect is shown on *z*-fail.

Everitt and Kilgard [326] present two simple, robust solutions to this problem, one implemented in hardware and the other in software. In hardware, the solution is called *depth clamping*. Beginning with the GeForce3, NVIDIA added the `NV_depth_clamp` extension. What this does is to no longer clip objects to the far view plane, but rather to force all objects that would normally be clipped away by the far plane to instead be drawn on the far plane with a maximum *z*-depth. This extension was introduced specifically to solve the *z*-fail shadow volume capping problem automatically. The edge and capping polygons can be projected out an arbitrarily far distance and will be properly handled by hardware. With this addition, *z*-fail shadow volumes become a simple and robust way to generate hard shadows. The only drawback (besides hardware dependence)<sup>3</sup> is that in some cases, the *z*-pass will fill less pixels overall, so always using *z*-fail with depth clamping may be slower.

Their software solution elegantly uses some of the lesser-known properties of homogeneous coordinates. Normally, positions are represented as  $\mathbf{p} = (p_x, p_y, p_z, 1)$  in homogeneous coordinates. When the fourth component,  $w$ , is 0, the resulting coordinate  $(p_x, p_y, p_z, 0)$  is normally thought of as a vector. See Section A.4. However,  $w = 0$  can also be thought of as a point “at infinity” in a given direction. It is perfectly valid to think of points at infinity in this way, and this is, in fact, used as a matter of course in environment mapping. The assumption in EM is that the environment is far enough away to access with just a vector, and for this to work perfectly, the environment should be infinitely far away.

<sup>3</sup>This functionality might be emulated on non-NVIDIA hardware by using a pixel shader program.

When a shadow is cast by an object, the shadow volume planes extend toward infinity. In practice, they are usually extended some large, finite distance, but this limitation is not necessary. Given a shadow volume edge formed by  $\mathbf{v}_0$  and  $\mathbf{v}_1$  and a light at  $\mathbf{l}$ , the direction vectors  $\mathbf{v}_0 - \mathbf{l}$  and  $\mathbf{v}_1 - \mathbf{l}$  can be treated as the two other points (that is, with  $w = 0$ ) forming a quadrilateral side of the shadow volume. The GPU works with such points just fine, transforming and clipping the object to the view frustum. Similarly, the far cap of the shadow volume for  $z$ -fail can be generated by projecting the triangle out to infinity.

Doing this procedure does not solve anything in and of itself, as the far plane still will clip the shadow volume, and so the  $z$ -fail method will not work. The other, key part of the software solution is to set the far plane itself to infinity. In Section 4.6.2, about projection matrices, the near and far planes are finite, positive numbers. In the limit as the far plane is taken to infinity, Equation 4.68 on page 95 for the projection matrix becomes

$$\mathbf{P}_p = \begin{pmatrix} \frac{2n}{r-l} & 0 & -\frac{r+l}{r-l} & 0 \\ 0 & \frac{2n}{t-b} & -\frac{t+b}{t-b} & 0 \\ 0 & 0 & 1 & -2n \\ 0 & 0 & 1 & 0 \end{pmatrix}. \quad (9.8)$$

Setting the far plane number to infinity loses surprisingly little precision normally. Say the near plane is 1 meter away and the far plane is 20, and these map to  $[-1, 1]$  in  $z$ -depth. Moving the far plane to infinity would map the 1-to-20-meter range to  $[-1, 0.9]$ , with the  $z$ -depth values from 20 meters to infinity mapped to  $[0.9, 1]$ . The amount of numerical range lost between the near plane,  $n$ , and the original far plane,  $f$ , turns out to be only  $n/f$ . In other words, when the distance to the far plane is significantly greater than to the near plane (which is often the case), moving the far plane to infinity has little overall effect on precision.

The  $z$ -fail method will work with the far plane at infinity. The triangle closing the shadow volume at infinity will be properly rendered, and nothing will be clipped against the far plane. For directional lights (i.e., those also “at infinity”) the two quadrilateral points at infinity are even easier to compute: They are always equal to the direction from the light. This has the interesting effect that all the points at infinity from directional lights are the same point. For this case, the side quadrilaterals actually become triangles, and no cap at infinity is necessary. Both Lengyel [759] and McGuire [843] discuss implementation details in depth, as well as a number of other optimizations. Kwoon [705] also has an extremely detailed presentation on the subject.

An example of the shadows that the shadow volume algorithm generates is shown in Figure 9.13. As can be seen in the analysis image, an area of concern is the explosion in the number of polygons rendered, and the corresponding amount of fill rate consumed. Each triangle and each light create three additional quadrilaterals that must be properly extended and rendered into the stencil buffer. For solid occluders, only the set of polygons facing toward (or the set facing away from) the light needs to be used to create shadow volumes. The  $z$ -pass method usually performs faster than  $z$ -fail, so it should be used when the viewer is known to not be in shadow [1220]. Hornus et al. [568] present a method that first efficiently tests where the eye's near plane is in shadow, so it then can properly initialize the state and always use  $z$ -pass.

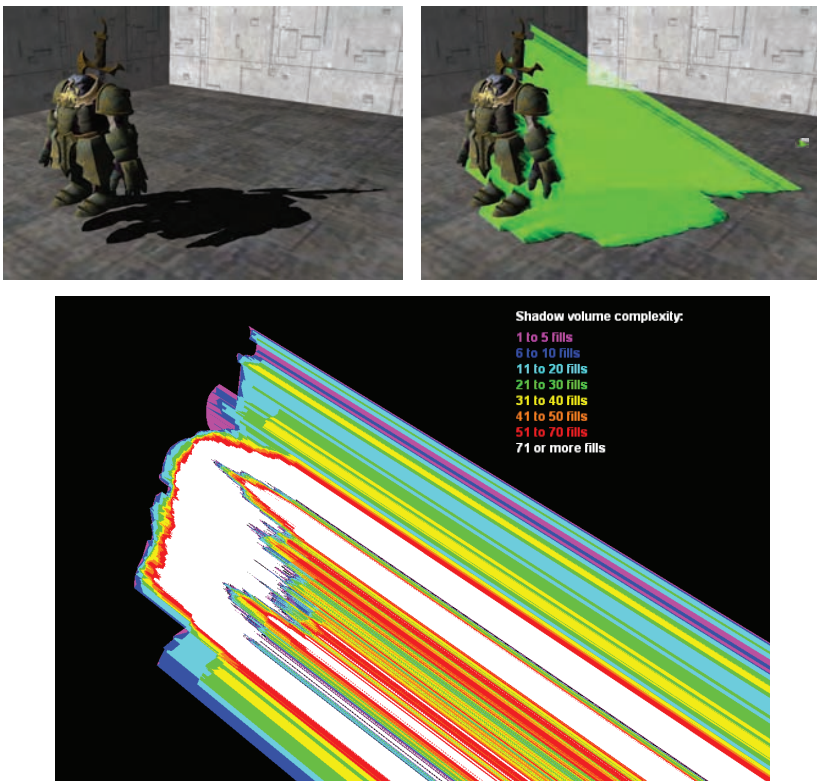


**Figure 9.13.** Shadow volumes. On the left, a character casts a shadow. On the right, the extruded triangles of the model are shown. Below, the number of times a pixel is drawn from the extruded triangles. (*Images from Microsoft SDK [261] sample “ShadowVolume.”*)

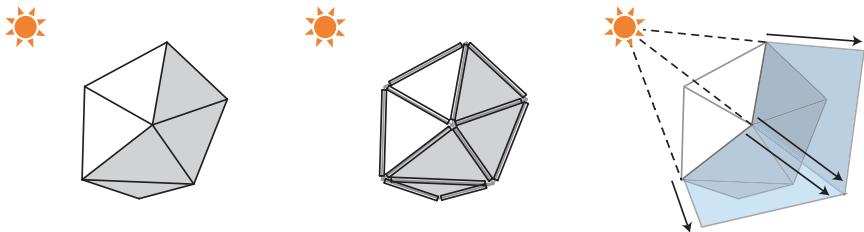


**Figure 9.14.** Forming a shadow volume using the vertex shader. This process is done twice, once for each of the two stencil buffer passes. The occluder is shown in the left figure. In the middle figure, all its edges are sent down as degenerate quadrilaterals, shown schematically here as thin quadrilaterals. On the right, those edges found by the vertex shader to be silhouette edges have two of their vertices projected away from the light, so forming quadrilaterals that define the shadow volume sides. Edges that are not silhouettes render as degenerate (no area) polygons and so cover no pixels.

To drastically cut down on the number of polygons rendered, the silhouette edges of the object could be found. Only the silhouette edges need to generate shadow volume quadrilaterals—a considerable savings. Silhouette edge detection is discussed in detail in Section 11.2.4.

The vertex shader also offers the ability to create shadow volumes on the fly. The idea is to send every edge of the object down the pipeline as a degenerate quadrilateral [137, 141, 506]. The geometric normals of the two triangles that share the edge are sent with it. Specifically, the two vertices of one edge of the degenerate quadrilateral get one face’s surface normal; the other edge’s vertices get the second face’s normal. See Figure 9.14. The vertex shader then checks these normals against the view direction. If the vertex’s stored normal faces toward the light, the vertex is passed through unperturbed. If it faces away from the light, the vertex shader projects the vertex far away along the vector formed by the light’s position to the vertex.

The effect of these two rules is to form silhouette shadow volumes automatically. For edge quadrilaterals that have both triangle neighbors facing the light, the quadrilateral is not moved and so stays degenerate, i.e., never gets displayed. For edge quadrilaterals with both normals facing away, the entire degenerate quadrilateral is moved far away from the light, but stays degenerate and so is never seen. Only for silhouette edges is one edge projected outward and the other remains in place. If a geometry shader is available, these edge quadrilaterals can be created on the fly, thus saving storage and processing overall. Stich et al. [1220] describe this technique in detail, as well as discussing a number of other optimizations and extensions.

The shadow volume algorithm has some advantages. First, it can be used on general-purpose graphics hardware. The only requirement is a

stencil buffer. Second, since it is not image based (unlike the shadow map algorithm described next), it avoids sampling problems and thus produces correct sharp shadows everywhere. This can sometimes be a disadvantage. For example, a character’s clothing may have folds that give thin, sharp shadows that alias badly.

The shadow volume algorithm can be extended to produce visually convincing soft shadows. Assarsson and Akenine-Möller [49] present a method called *penumbra wedges*, in which the projected shadow volume planes are replaced by wedges. A reasonable penumbra value is generated by determining the amount a given location is inside a wedge. Forest et al. [350] improve this algorithm for the case where two separate shadow edges cross, by blending between overlapping wedges.

There are some serious limitations to the shadow volume technique. Semitransparent objects cannot receive shadows properly, because the stencil buffer stores only one object’s shadow state per pixel. It is also difficult to use translucent occluders, e.g., stained glass or other objects that attenuate or change the color of the light. Polygons with cutout textures also cannot easily cast shadows.

A major performance problem is that this algorithm burns fill rate, as shadow volume polygons often cover many pixels many times, and so the rasterizer becomes a bottleneck. Worse yet, this fill rate load is variable and difficult to predict. Silhouette edge computation can cut down on the fill rate, but doing so on the CPU is costly. Lloyd et al. [783] use culling and clamping techniques to lower fill costs. Another problem is that curved surfaces that are created by the hardware, such as N-patches, cannot also generate shadow volumes. These problems, along with the limitation to opaque, watertight models, and the fact that shadows are usually hard-edged, have limited the adoption of shadow volumes. The next method presented is more predictable in cost and can cast shadows from any hardware-generated surface, and so has seen widespread use.

### 9.1.4 Shadow Map

In 1978, Williams [1353] proposed that a common  $Z$ -buffer-based renderer could be used to generate shadows quickly on arbitrary objects. The idea is to render the scene, using the  $Z$ -buffer algorithm, from the position of the light source that is to cast shadows. Note that when the shadow map is generated, only  $Z$ -buffering is required; that is, lighting, texturing, and the writing of color values into the color buffer can be turned off.

When a single  $Z$ -buffer is generated, the light can “look” only in a particular direction. Under these conditions, the light source itself is either a distant directional light such as the sun, which has a single view direction, or some type of spotlight, which has natural limits to its viewing angle.

For a directional light, the light's view is set to encompass the viewing volume that the eye sees, so that every location visible to the eye has a corresponding location in the light's view volume. For local lights, Arvo and Aila [38] provide an optimization that renders a spotlight's view volume to set the image stencil buffer, so that pixels outside the light's view are ignored during shading.

Each pixel in the Z-buffer now contains the  $z$ -depth of the object closest to the light source. We call the entire contents of the Z-buffer the *shadow map*, also sometimes known as the *shadow depth map* or *shadow buffer*. To use the shadow map, the scene is rendered a second time, but this time with respect to the viewer. As each drawing primitive is rendered, its location at each pixel is compared to the shadow map. If a rendered point is farther away from the light source than the corresponding value in the shadow map, that point is in shadow, otherwise it is not. This technique can be

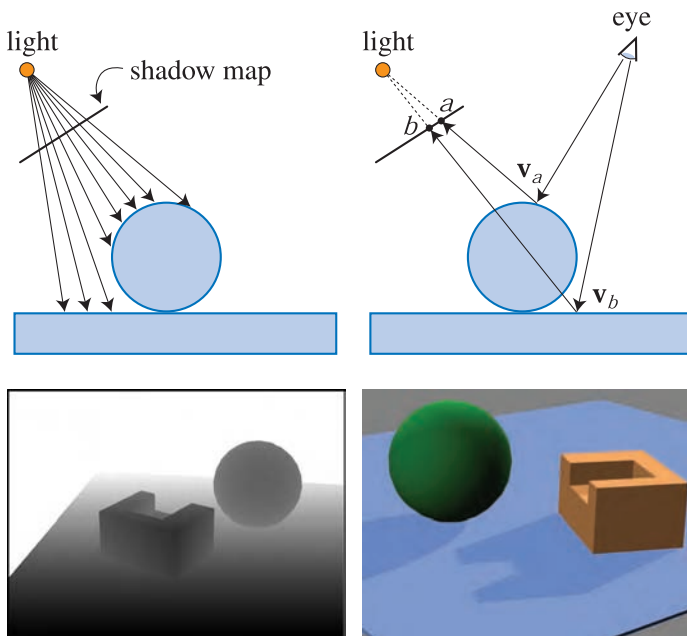


**Figure 9.15.** Shadow mapping. On the top left, a shadow map is formed by storing the depths to the surfaces in view. On the top right, the eye is shown looking at two locations. The sphere is seen at point  $v_a$ , and this point is found to be located at texel  $a$  on the shadow map. The depth stored there is not (much) less than point  $v_a$  is from the light, so the point is illuminated. The rectangle hit at point  $v_b$  is (much) farther away from the light than the depth stored at texel  $b$ , and so is in shadow. On the bottom left is the view of a scene from the light's perspective, with white being further away. On the bottom right is the scene rendered with this shadow map.

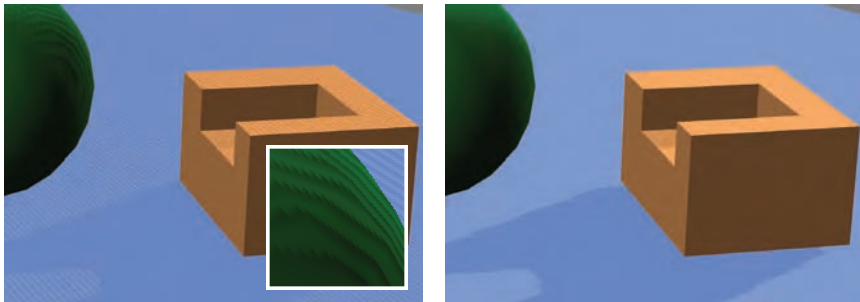


**Figure 9.16.** Shadow mapping problems. On the left there is no bias, so the surface erroneously shadows itself, in this case producing a Moiré pattern. The inset shows a zoom of part of the sphere’s surface. On the right, the bias is set too high, so the shadow creeps out from under the block object, giving the illusion that the block hovers above the surface. The shadow map resolution is also too low, so the texels of the map appear along the shadow edges, giving it a blocky appearance.

implemented by using texture mapping hardware [534, 1146]. Everitt et al. [325] and Kilgard [654] discuss implementation details. See Figure 9.15.

Advantages of this method are that the cost of building the shadow map is linear with the number of rendered primitives, and access time is constant. One disadvantage is that the quality of the shadows depends on the resolution (in pixels) of the shadow map, and also on the numerical precision of the  $Z$ -buffer.

Since the shadow map is sampled during the comparison, the algorithm is susceptible to aliasing problems, especially close to points of contact between objects. A common problem is *self-shadow aliasing*, often called “surface acne,” in which a polygon is incorrectly considered to shadow itself. This problem has two sources. One is simply the numerical limits of precision of the processor. The other source is geometric, from the fact that the value of a point sample is being used to represent an area’s depth. That is, samples generated for the light are almost never at the same locations as the screen samples. When the light’s stored depth value is compared to the viewed surface’s depth, the light’s value may be slightly lower than the surface’s, resulting in self-shadowing. Such errors are shown in Figure 9.16.

Hourcade [570] introduced a different form of shadow mapping that solves the biasing problem by avoiding depth compares entirely. This method stores ID numbers instead of depths. Each object or polygon is given a different ID in the map. When an object is then rendered from the eye’s viewpoint, the ID map is checked and compared at the four neighboring texels. If no ID matches, the object is not visible to the light and so is shadowed. With this algorithm, self-shadowing is not possible: Anything that should shadow itself will never do so, since its ID in the shadowed

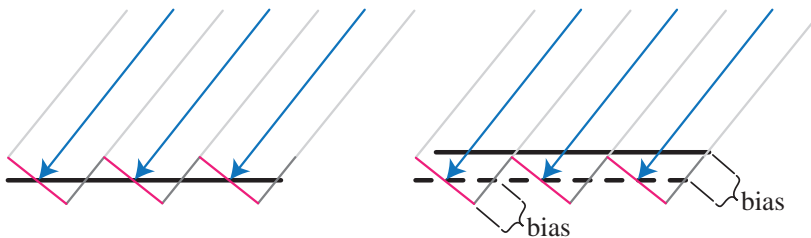


**Figure 9.17.** A shadow map samples a surface at discrete locations, shown by the blue arrows. The gray walls show the shadow map texel boundaries. Within each texel, the red line represents the distance that the shadow map stores for the surface, i.e., where it considers the surface to be located. Where the actual surface is below these red (and dark gray) lines, its distance is greater than the stored depth for that texel, so will be considered, erroneously, to be in shadow. By using a bias to shift the receiver so that it is considered above the red texel depth lines, no self-shadowing occurs. (After Schüller [1138].)

area will match that found in the ID map. Decomposing an object into convex sub-objects solves the problem, but is often impractical. Even with proper convex data, an object can fall through the cracks and not cover any texels, dooming it to always be considered in shadow.

Dietrich [257] and Forsyth [357] describe a hybrid approach with an ID map and depth buffer. The ID map is used for determining object-to-object shadowing, and a low-precision depth buffer stores depths for each object relative to its  $z$ -depth extents and is used only for self-shadowing. Pelzer [999] presents a similar hybrid scheme and provides further implementation details and code.

For depth shadow maps, if the receiver does not itself cast shadows, it does not need to be rendered, and the self-shadowing problem can be avoided. For shadows on occluders, one common method to help renderers avoid (but not always eliminate) this artifact is to introduce a bias factor. When checking the distance found in the shadow map with the distance of the location being tested, a small bias is subtracted from the receiver's distance. See Figure 9.17. This bias could be a constant value [758], but doing so fails when a light is at a shallow angle to the receiver. A more accurate method is to use a bias that is proportional to the angle of the receiver to the light. The more the surface tilts away from the light, the greater the bias grows, to avoid the problem. This type of bias is called *depth-slope scale bias* (or some variant on those words). Schüller [1138, 1140] discusses this problem and some solutions in depth. Because a slope bias solution will not fix all sampling problems for triangles inside concavities, these various bias controls usually have to be hand tweaked for the application; there are no perfect settings.

Too much bias causes a problem called “Peter Panning,” in which the object appears to be slightly above the underlying surface. One method that helps ameliorate this effect is to make sure the light frustum’s near plane is as far away from the light as possible, and that the far plane is as close as possible. Doing so increases the effective precision of the  $Z$ -buffer.

Another method of avoiding self-shadowing problems is to render only the backfaces to the shadow map. Called *second-depth shadow mapping* [1321], this scheme works well for many situations; by default, most surfaces have no chance of shadowing themselves. Or, more precisely, the surfaces that now self-shadow are those that face away from the light, so it does not matter. The problem cases are when objects are two sided or in contact with one another. If an object is a two-sided cutout, e.g., a palm frond or fence, self-shadowing can occur because the backface and the frontface are in the same location. Similarly, if no biasing is performed, problems can occur near silhouette edges or thin objects, since in these areas backfaces are close to frontfaces. Also, solid objects must be “water-tight” (manifold and closed), else the object may not fully cast a shadow.

The other problem with second-depth testing is that light leaks can occur where objects are in contact or interpenetrate. In such cases, the occluding backface’s stored distance is in some places greater than the sampled receiver’s. This problem is in some ways the opposite of self-shadowing. Problems can also occur in concavities in a solid model. Careful rendering (e.g., pushing double-sided objects a bit farther away from the light when building the shadow map), composition (avoiding objects touching as much as possible), modeling (actually building extra occluder polygons inside the shadow object to avoid light leaks), and traditional biasing techniques can give good results. This algorithm is often used in game development, where content and interactions are under full control of the creators.

Woo [1374] proposes a general method of avoiding many biasing and light leak problems by creating an intermediate surface on the fly. Instead of keeping just the closest depth value, the two closest values are tracked in separate buffers. For solid objects that do not intersect in space, frontfaces and backfaces can be rendered to generate the separate buffers. Using two passes of depth peeling is a general way to generate these buffers [76, 324]. These two buffers are averaged into one, which is then used as the shadow map. For a solid object, this technique usually creates a shadowing surface that passes through the middle of the object. For example, a sphere would create a circle passing through its center and facing the light. However, this technique can also have problems, such as light leaks and self-shadowing for thin objects and near silhouette edges. See Figure 9.18. In practice, the problems seen at **j** and **k** are relatively rare and not that noticeable, especially when using multiple shadow map samples per fragment. By

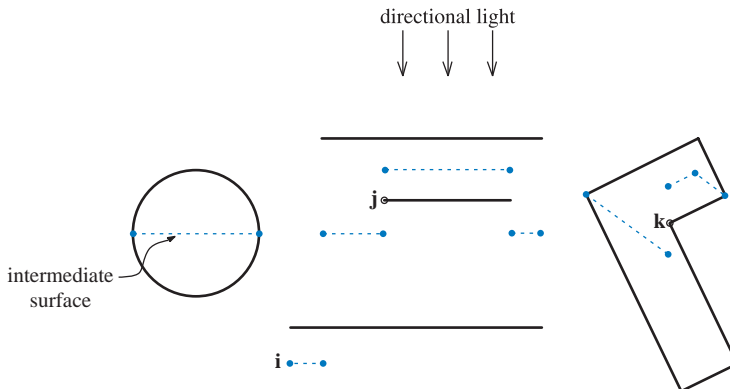


**Figure 9.18.** Woo’s shadow mapping method. A directional light comes from directly above. The depths from each of the two surfaces closest to the light are combined to give an intermediate surface that is stored in the shadow map. This surface is shown as a blue dashed line. The two sets of surfaces on the right have problems due to sampling limitations. A single surface covers area  $i$ , so this intermediate surface is somewhere behind this part of the surface. At location  $j$ , the point may be erroneously found to be in light if the shadow texel to the left of it is sampled, since this intermediate surface is farther from the light. Similarly, point  $k$  may be incorrectly considered to be in light because the intermediate surface to its left is more distant.

creating an intermediate surface, we can eliminate most self-shadowing and light leak problems, at the cost of extra processing.

One other problem that can occur with shadow mapping is that as the viewer moves, the view volume changes size. This causes the shadow map generated to vary its view, which in turn causes the shadows to shift slightly from frame to frame. Koonce [691] and Mittring [887] present the solution of forcing each succeeding directional shadow map generated to maintain the same relative texel beam locations in world space. That is, you can think of the shadow map as imposing a grid frame of reference on the whole world. As you move, the shadow map is generated for a different window onto that world. In other words, the view is snapped to a grid to maintain frame to frame coherence.

### Resolution Enhancement

An example of stair-stepping artifacts is shown in Figure 9.19. The shadow is blocky because each texel of the shadow map covers a large number of pixels. In this case, the projection of each shadow map texel is stretched over the surface because the eye is close to the surface but the light is far away. This type of artifact is called *perspective aliasing*. Texels also are stretched on surfaces that are nearly edge-on to the light, but that directly face the viewer. This problem is called *projective aliasing* [1119, 1216].



**Figure 9.19.** Perspective aliasing stairstepping artifacts due to the shadow map projection being magnified. (*Image from NVIDIA "Hardware Shadow Maps" demo program, courtesy of NVIDIA Corporation.*)

Blockiness can be decreased by increasing the shadow map resolution, but at the cost of additional memory and processing. Another useful technique is to limit the light's view frustum to only those objects in view of the camera [658] and further restrict this frustum to just the shadow-casting objects, since shadow receivers outside this frustum are always in light.

At some point, increasing resolution farther or using other simple optimizations is no longer an option. Similar to how textures are used, ideally we want one shadow map texel to cover about one pixel. If we have a light source located at the same position as the eye, the shadow map perfectly maps one for one with the screen-space pixels (and of course no visible shadows, since the light illuminates exactly what the eye sees). Say the light

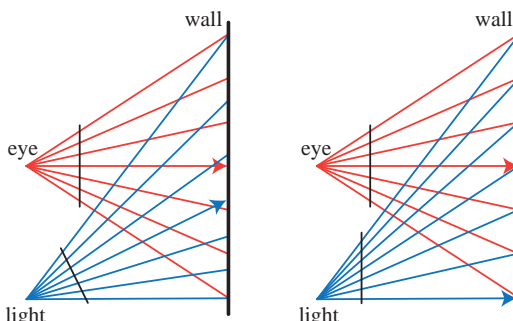


**Figure 9.20.** The light and the eye focus on a wall. On the left, the light has fewer samples at the top of the wall than at the bottom, compared to the eye's even distribution. By shifting the view plane of the light to match that of the eye, the texels again align one for one.

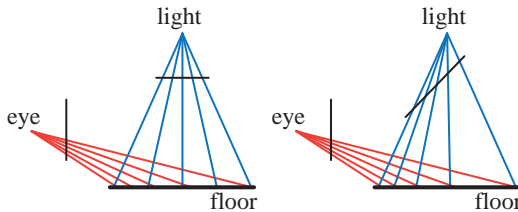


**Figure 9.21.** For an overhead light, on the left the sampling on the floor does not match the eye’s rate. By changing the view direction and projection window, the light’s sampling rate is biased toward having a higher density of texels nearer the eye.

source is a flashlight, held at the chest, pointing at a wall being viewed. See Figure 9.20. The shadow-map-to-pixel correspondence is close, but the top of the wall has shadow map texels that are stretched.

To make the shadow map’s samples match the eye’s, the light’s view and perspective matrices are modified. Specifically, the light’s view vector is made to match the eye’s, and the view window is shifted. Normally, we think of a view as being symmetric, with the view vector in the center of the frustum. However, the view direction merely defines a view plane. The window defining the frustum can be shifted, skewed, or rotated on this plane, creating a quadrilateral that gives a different mapping of world to view. The quadrilateral is still sampled at regular intervals, as this is the nature of a linear transform matrix and its use by the GPU. By varying the view direction and the window’s bounds, the sample density can be changed.

This scheme shows how shifting the view direction and window changes the distribution of samples. The shift shown improves the sampling rate along the wall, but does not address the problem of putting more shadow samples closer to the viewer. Figure 9.21 shows a view shift that creates more shadow map samples near the eye, where they are needed. For specific planar targets such as walls and floors, Chong and Gortler [175] show that it is possible to perfectly match view and light samples. Where the difficulty comes in is when the entire view frustum’s volume is remapped to the light’s space.

As King [658] points out, there are 22 degrees of freedom in mapping the light’s view to the eye’s. Exploration of this solution space has led to a number of different algorithms that attempt to better match the light’s sampling rates to the eye’s over the depth range. Stamminger and Drettaklis first presented *perspective shadow mapping* (PSM) in 2002 [1216]. Their idea is for each light to attempt to fit its view to a post-perspective transform of the scene’s visible objects. Koslov [692] discusses implementation issues and solutions. PSM is a difficult approach to understand and

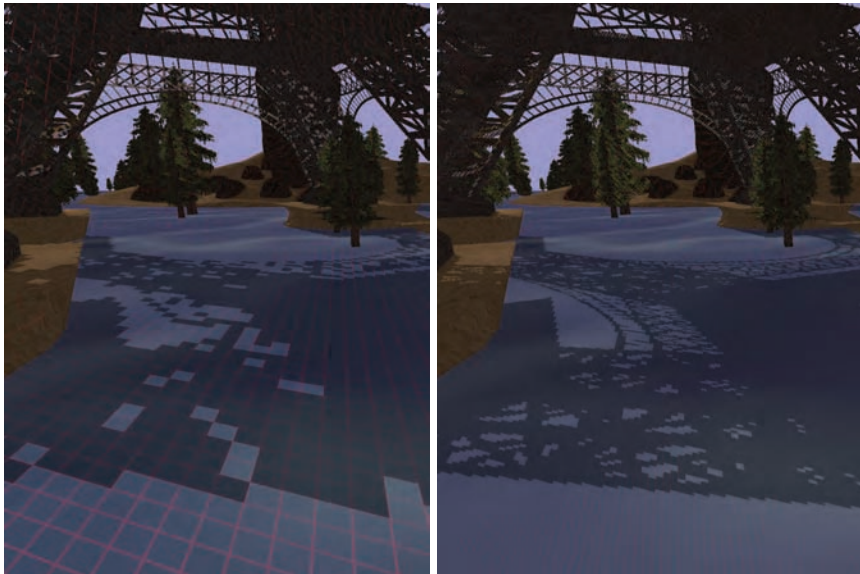


**Figure 9.22.** The image to the left is created using standard shadow mapping; the image to the right using LiSPSM. The projections of each shadow map’s texels are shown. The two shadow maps have the same resolution, the difference being that LiSPSM reforms the light’s matrices to provide a higher sampling rate nearer the viewer. (*Images courtesy of Daniel Scherzer, Vienna University of Technology.*)

implement in a robust fashion [122, 355]. Wimmer et al. [1359, 1361] introduced *light space perspective shadow maps* (LiSPSM or LSPSM), which also modify the light’s matrices. See Figure 9.22. Martin and Tan [823] presented *trapezoidal shadow maps* (TSM), which place a trapezoid around the eye’s frustum and warp it to fit the shadow map. Both LiSPSM and TSM do not use post-perspective space, so they are able to avoid the problems its use engenders. LiSPSM sees more use, due to patent protection on TSM. Hybrid approaches are also possible; Mikkelsen [865] describes how any two schemes can be combined, using the strengths of each. This is done by deriving a separating plane that determines which scheme is best to use for a given location.

An advantage of these matrix warping algorithms is that no additional work is needed beyond modifying the light’s matrices. Each method has its own strengths and weaknesses [355], as each can help match sampling rates for some geometry and lighting situations, while worsening these for others. Biassing to avoid surface acne can become a more serious problem when the matrices are warped. Another problem with these techniques is that they can jump in quality from one frame to the next. As the lighting situation



**Figure 9.23.** On the left, a  $2048 \times 2048$  shadow map rendering of a shadow. In the middle, a  $256 \times 256$  shadow silhouette map provides a considerably better shadow than the  $256 \times 256$  standard shadow map on the right. (*Images courtesy of John Isidoro, ATI Research, Inc.*)

changes, the algorithm to warp the matrix can hit some discontinuity and cause a noticeable shift in the orientation and size of the shadow map texel grid [312]. A number of developers have noted a “nervous,” unstable quality to the shadows produced during camera movement [355, 887].

These schemes work best when the light’s direction is perpendicular to the view’s direction (e.g., overhead), as the perspective transform can then best be shifted to put more samples closer to the eye. One lighting situation where matrix warping techniques fail to help is when a light is in front of the camera and is pointing back at it. This situation is known as *dueling frusta*. What is needed are more shadow map samples nearer the eye, but linear warping can only make the situation worse [1119]. This problem is the major limitation of this class of techniques. Lloyd et al. [784, 785] analyze the equivalences between PSM, TSM, and LiSPSM. This work includes an excellent overview of the sampling and aliasing issues with these approaches.

A number of approaches have been explored to help increase shadow map sampling where it is needed. One concept is to attempt to represent the shadow’s edge more accurately. To this end, Sen et al. [1149] introduce the *shadow silhouette map* algorithm. The shadow map is augmented by silhouette edge information stored as a series of points. In this way, the silhouette itself can be reconstructed more precisely. The main limitation is that only one silhouette point can be stored per shadow texel, so that complex or overlapping silhouette edges cannot be captured. Isidoro [594] discusses optimizing the point-in-triangle test used. An example is shown in Figure 9.23.

In related work, Szécsi [1233] uses geometry maps in a number of ways to produce high-quality hard shadows. Chan and Durand [169] use a shadow map to discover pixels in the image that are near shadow boundaries, then

perform shadow volume computations on only these pixels, to find the exact shadow. Scherzer et al. [1120] explore improving shadow edges of fragments over time by tracking the history of past results.

Fernando et al. [337] first researched the idea of *adaptive shadow maps*, a hierarchical caching scheme combining GPU and CPU, using quadtrees of shadow maps. Giegl and Wimmer [395, 396, 397] explore GPU-only schemes in the same spirit, using a hierarchical grid. Lefohn et al. [752] introduce an improved quadtree scheme for modern GPUs that overcomes a number of earlier limitations.

One class of hierarchical methods that has seen commercial use is *cascaded shadow maps* (CSM). This idea first made a noticeable impact when John Carmack described it at his keynote at Quakecon 2004. Jonathan Blow independently implemented such a system [122]. The idea is simple: Generate a fixed set of shadow maps at different resolutions, covering different areas of the scene. In Blow's scheme, four shadow maps are nested around the viewer. In this way, a high-resolution map is available for nearby objects, with the resolution dropping for those objects far away. Forsyth [354, 357] presents a related idea, generating different shadow maps for different visible sets of objects. The problem of how to handle the transition for objects spanning the border of a shadow map is avoided in his



**Figure 9.24.** On the left, the three shadow maps are shown: animated objects, grid section, and whole level. On the right, a resulting image. (*Images from “Hellgate: London” courtesy of Flagship Studios, Inc.*)

scheme, since each object has one and only one shadow map associated with it.

Flagship Studios developed a system for “Hellgate: London” that blends these two ideas [296]. Three shadow maps are generated. One shadow map adjusts to the view’s focus and frustum and includes just the animated (and/or breakable) objects in the scene. The second map is associated with a grid section of the level, selected by the view position. It covers a much larger area and includes only static objects. Finally, a third map covers the whole level’s static objects. See Figure 9.24.

To access these maps, the object being rendered is checked to see if it fully fits inside the second, grid-based shadow map. If so, this map is used, else the full level map is accessed. In this way, nearby objects will use the map with a higher sampling rate. The first map, of the animated objects, is also accessed, for all objects rendered. Whichever  $z$ -depth result retrieved from the two maps is lower is the one used for shadow determination. One advantage of this system is that by separating out the animated objects to their own map, the grid shadow map is regenerated only when the viewer moves to a new grid section. The level map is generated only once. Nearby animated objects are usually the focus of attention, and by this scheme, these will cast the highest quality shadows.

Lloyd et al. [784, 785] introduce a scheme called *z-partitioning* and show how it can help with shadow sample distribution. Engel [312] and Zhang et al. [1404] independently researched the same idea, which the latter group calls *parallel split shadow mapping*.<sup>4</sup> The idea is to divide the view frustum’s volume into a few pieces by slicing it parallel to the view direction. See Figure 9.25. As depth increases, each successive volume should have about two to three times the depth range of the previous volume [312, 1404]. For each volume, the light source makes a frustum that tightly bounds it and then generates a shadow map. Lloyd et al. discuss how this method can be combined with LiSPSM. By using texture atlases or arrays, the different shadow maps can be treated as one large texture, thus minimizing texture cache access delays [312]. Zhang et al. [1405] give a thorough explanation of how to implement this rendering algorithm efficiently. A comparison of the quality improvement obtained is shown in Figure 9.26. Valient [1289] also provides implementation details and presents a method of avoiding shimmer artifacts as objects transition from one shadow map to another. Deferred shading can be used with CSM, computing the effects of all shadow maps and saving the results in a separate channel for later evaluation [312, 887]. The “sunlight occlusion” buffer in Figure 7.48 on page 280 is an example.

---

<sup>4</sup>Tadamura et al. [1237] introduced the basic idea seven years earlier, but it did not have an impact until these researchers explored its usefulness in 2006.

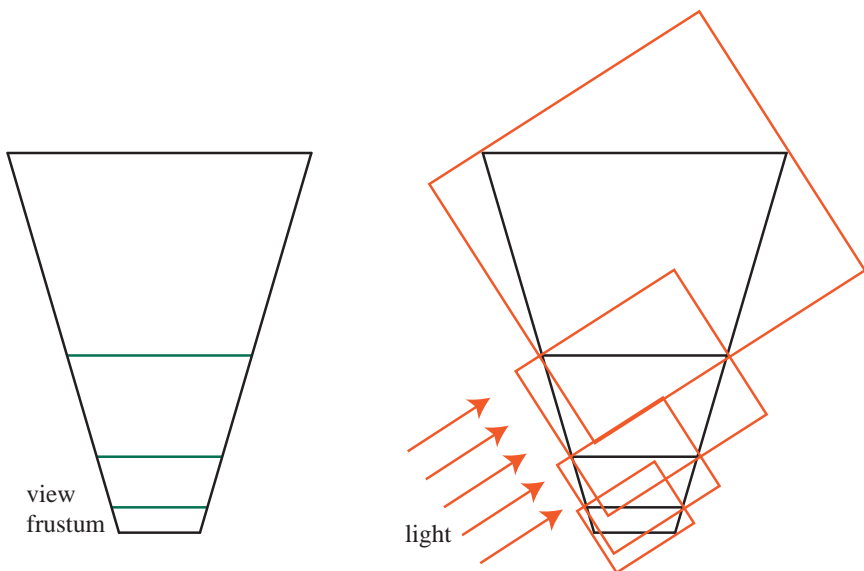


**Figure 9.25.** On the left, the view frustum from the eye is split into four volumes. On the right, bounding boxes are created for the volumes, which determine the volume rendered by each of the four shadow maps for the directional light. (After Engel [312].)



**Figure 9.26.** On the left, the scene's wide viewable area causes a single shadow map at a  $2048 \times 2048$  resolution to exhibit perspective aliasing. On the right, four  $1024 \times 1024$  shadow maps placed along the view axis improve quality considerably [1405]. A zoom of the front corner of the fence is shown in the inset red boxes. (Images courtesy of Fan Zhang, The Chinese University of Hong Kong.)

Overall, this type of algorithm is straightforward to implement, can cover huge scene areas with reasonable results, is trivial to scale by changing the number of slices, and is robust. The dueling frusta problem is addressed by simply sampling closer to the eye, and there are no serious worst-case problems. This method is used in a growing number of applications that render large outdoor environments [887].

A limitation of shadow map methods using a single projection is that the light is assumed to view the scene from somewhere outside of it, something like a spotlight. Positional lights inside a scene can be represented by any structure that captures the parts of the scene needed. The usual approach is to use a six-view cube, similar to cubic environment mapping. These are called *omnidirectional shadow maps*. The main challenge for omnidirectional maps is avoiding artifacts along the seams where two separate maps meet. King and Newhall [659] analyze the problems in depth and provide solutions, and Gerasimov [390] provides some implementation details. Forsyth [355, 357] presents a general multi-frustum partitioning scheme for omnidirectional lights that also provides more shadow map resolution where needed.

Using omni shadows with dual paraboloid mapping creates fewer seams, but normally does not work well, due to non-linear interpolation problems [1174], i.e., straight edges become curves. Osman et al. [976] attack the problem by tessellating objects based on distance from the light.

### Percentage-Closer Filtering

A simple extension of the shadow map technique can provide pseudo-soft shadows. This extension can also help ameliorate resolution problems that cause shadows to look blocky when a single light sample cell covers many screen pixels. The solution is similar to texture magnification (see Section 6.2.1). Instead of a single sample being taken off the shadow map, the four nearest samples are retrieved. The technique does not interpolate between the depths themselves, but rather the results of their comparisons with the surface's depth. That is, the surface's depth is compared separately to the four texel depths, and the point is then determined to be in light or shadow for each shadow map sample. These results are then bilinearly interpolated to calculate how much the light actually contributes to the surface location. This filtering results in an artificially soft shadow. These penumbras change, depending on the shadow map's resolution, and other factors. For example, a higher resolution makes for a narrower softening of the edges. Still, a little penumbra and smoothing, regardless of how nonphysical it is, is better than none at all. Sampling four neighboring texels is a common enough operation that support is built into NVIDIA [145] and ATI [594] GPUs. All GPUs that implement Shader Model 4.0 support shadow map sampling [123].

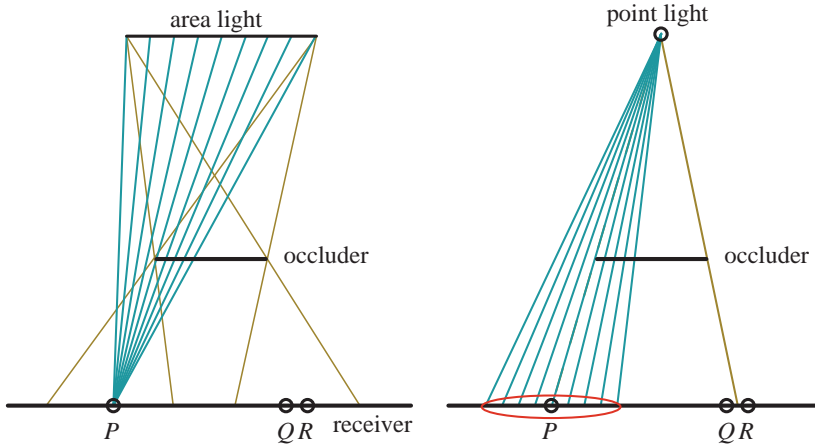


**Figure 9.27.** On the left, the brown lines from the area light source show where penumbrae are formed. For a single point *P* on the receiver, the amount of illumination received could be computed by testing a set of points on the area light’s surface and finding which are not blocked by any occluders. On the right, a point light does not cast a penumbra. PCF approximates the effect of an area light by reversing the process: At a given location, it samples over a comparable area on the shadow map to derive a percentage of how many samples are illuminated. The red ellipse shows the area sampled on the shadow map. Ideally, the width of this disk is proportional to the distance between the receiver and occluder.

This idea of retrieving multiple samples from a shadow map and blending the results is called *percentage-closer filtering* (PCF) [1053]. Soft shadows are produced by area lights. The amount of light reaching a location on a surface is a function of what proportion of the light’s area is visible from the location. PCF attempts to approximate a soft shadow for a point (or directional) light by reversing the process. Instead of finding the light’s visible area from a surface location, it finds the visibility of the point light from a set of surface locations near the original location. See Figure 9.27. The name “percentage-closer filtering” refers to the ultimate goal, to find the percentage of the samples taken that are visible to the light. This percentage is how much light then is used to shade the surface.

In PCF, locations are generated nearby to a surface location, at about the same depth, but at different texel locations on the shadow map. The key idea is that each location must be individually compared with the shadow map to see if it is visible. It is these resulting boolean values, lit or unlit, that are then blended to get a soft shadow. Typical area summation techniques for textures, such as mipmapping or summed area tables, cannot be used directly on shadow maps. Such techniques applied to the shadow map would give an average depth for the occluders over some area, which

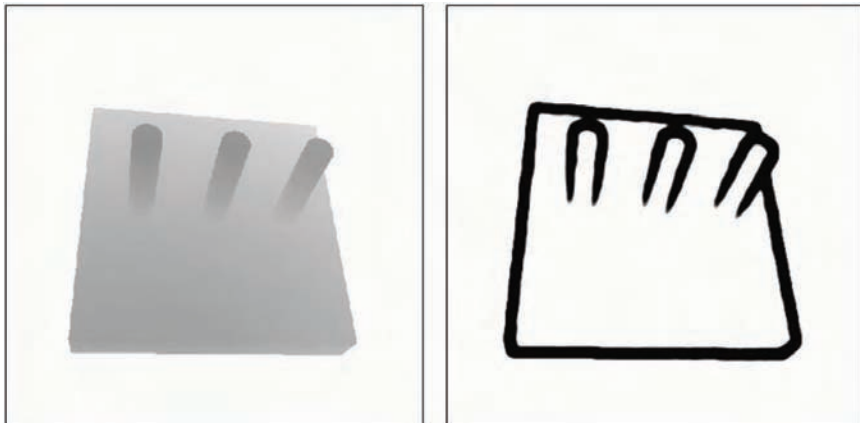


**Figure 9.28.** The depth map on the left has edge detection and dilation applied, to create an edge map, on the right. This map identifies potential penumbra areas. Time is saved by applying PCF to only these areas and using single samples for the rest. (*Images courtesy of John Isidoro, ATI Research, Inc.*)

has little direct correlation to the amount that a receiving point is occluded from the light. We cannot simply average the depths and compare this depth to our location. What this means in practice is that each sample must be evaluated separately (with some potential exceptions, discussed further on).

Sampling a large number of locations on the shadow map per pixel is an expensive proposition. Only points that are in the penumbra benefit from PCF. The problem is knowing which pixels are fully lit or are fully in shadow. Uralsky [1284] takes a few samples, and if they differ, samples more. Isidoro [594, 595] uses image processing techniques on the shadow map to create a bitonal edge map to determine where PCF sampling is likely to be useful. The costs of processing the map are usually outweighed by the savings from performing expensive PCF sampling on just a few locations. See Figure 9.28.

There are numerous variations of how to sample and filter nearby shadow map locations. Variables include how wide an area to sample, how many samples to use, the sampling pattern, and how to weight the results. The width of the area sampled affects how soft the shadow will appear. If the sampling area's width remains constant, shadows will appear uniformly soft, all with the same penumbra width. This may be acceptable under some circumstances, but appears incorrect where there is ground contact between the occluder and receiver. As shown in Figure 9.29, the shadow should be sharp at the point of contact and softer as the distance between occluder and receiver increases.



**Figure 9.29.** Percentage-Closer Filtering. On the left, hard shadows with a little PCF filtering. In the middle, constant width soft shadows. On the right, variable-width soft shadows with proper hardness where objects are in contact with the ground. (*Images courtesy of NVIDIA Corporation.*)

If we could know in advance the distance of the occluder from the receiver, we could set the area to sample accordingly and approximate the effect of an area light. One simple, but incorrect, idea is to examine the shadow map for the occluder location and find the distance between this location and the receiver. The problem with this naive scheme is that if a location is not in shadow for the point light, no further processing will be done. In Figure 9.27, points  $Q$  and  $R$  are in a penumbra. The distance to the occluder from point  $Q$  is a simple lookup. Point  $R$ , however, is fully lit by the basic shadow map—a simple lookup will fail to find the proper sample width for this point.

What is needed is a way to find whether a surface location could be partially affected by any occluder. The distance to the relevant occluder from the location is key in determining the width of the area to sample. Fernando [340, 916] attempts a solution by searching the nearby area on the shadow map and processing the results. The idea is to determine all possible occluders within this sampled area. The average distance of these occluders from the location is used to determine the sample area width:

$$w_{\text{sample}} = w_{\text{light}} \frac{d_r - d_o}{d_r}, \quad (9.9)$$

where  $d_r$  is the distance of the receiver from the light and  $d_o$  the average occluder distance. If there are no occluders found, the location is fully lit and no further processing is necessary. Similarly, if the location is fully occluded, processing can end. Otherwise the area of interest is sampled and the light's approximate contribution is computed. To save on processing costs, the width of the sample area is used to vary the number of samples taken. The drawback of this method is that it needs to always sample an area of the shadow map to find the occluders, if any. Valient and de Boer [1287] present a method of processing the shadow map to create a map in which the distance to the nearest occluder is stored in each texel.

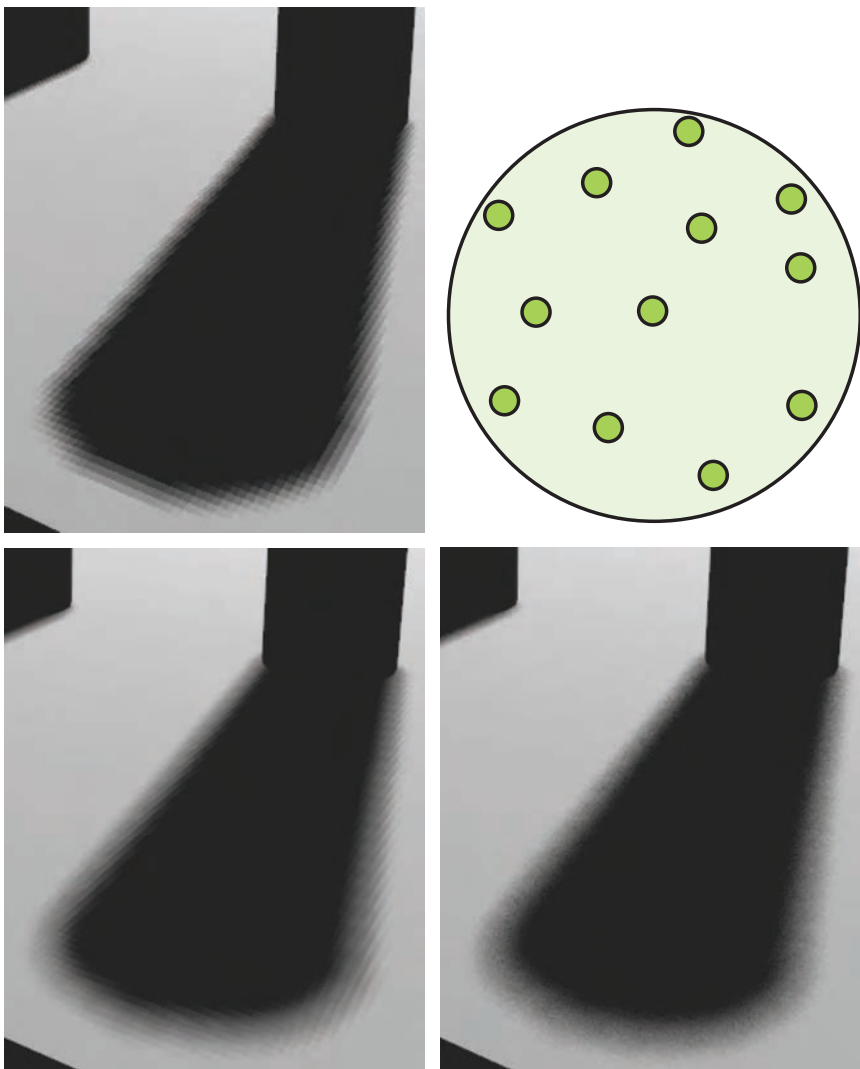


**Figure 9.30.** The upper left shows PCF sampling in a  $4 \times 4$  grid pattern. The upper right shows a 12-tap Poisson sampling pattern on a disk. Using this pattern to sample the shadow map gives the improved result on the lower left, though artifacts are still visible. On the lower right, the sampling pattern is rotated randomly around its center from pixel to pixel. The structured shadow artifacts turn into (much less objectionable) noise. (*Images courtesy of John Isidoro, ATI Research, Inc.*)

Once the width of the area to be sampled is determined, it is important to sample in a way to avoid aliasing artifacts. The typical method is to sample the area using a precomputed Poisson distribution pattern. A Poisson distribution spreads samples out so that they are neither near each other nor in a regular pattern. See Figure 9.30. It is well known that using the same sampling locations for each pixel can result in patterns [195]. One solution is to randomly rotate the sample pattern around its center to turn the aliasing into noise. A separate repeating texture can be used to hold precomputed random rotations that are accessed using the screen pixel location [594]. One problem with this technique is that as the viewer moves the screen sampling patterns cause artifacts by staying in place. Mittering [887] discusses projecting a mipmapped version of the noise pattern into world space to minimize artifacts.

One problem that is exacerbated by using PCF is self-shadowing, i.e., “surface acne.” In addition to the standard problems described earlier, caused by discrete sampling of the light map, other problems can arise. By sampling in a wider area from a single location on a surface, some of the test samples may get blocked by the true surface. Biasing based on slope does not fix this problem. One solution is to add an additional bias factor: Move sample locations closer relative to the distance between the sample and the original location [1287]. See Figure 9.31. Schüller [1140] gives a more involved method based on using the depths retrieved from PCF sampling to determine a better slope gradient.

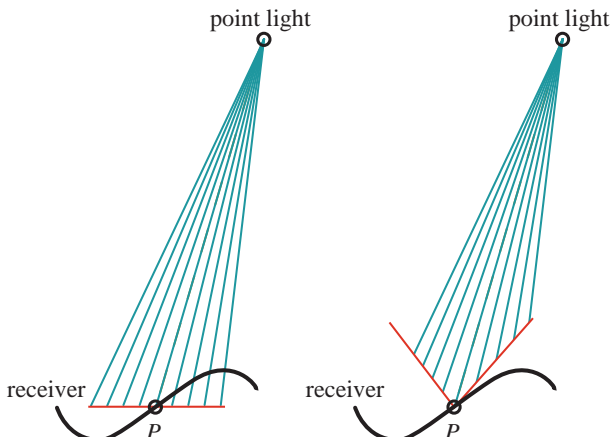


**Figure 9.31.** On the left, the surface sampled with PCF partially shadows itself. On the right, the PCF is sampled in a cone shape to help avoid this problem.

### Variance Shadow Maps

One algorithm that allows filtering of the shadow maps generated is Donnelly and Lauritzen's *variance shadow map* (VSM) [272]. The algorithm stores the depth in one map and the depth squared in another map. MSAA or other antialiasing schemes can be used when generating the maps. These maps can be blurred, mipmapped, put in summed area tables [739], or any other method. The ability to treat these maps as filterable textures is a huge advantage, as the entire array of sampling and filtering techniques can be brought to bear when retrieving data from them. Overall this gives a noticeable increase in quality for the amount of time spent processing, since the GPU's optimized hardware capabilities are used efficiently. For example, while PCF needs more samples (and hence more time) to avoid noise when generating softer shadows, VSM can work with just a single (high-quality) sample to determine the entire sample area's effect and produce a smooth penumbra. This ability means shadows can be made arbitrarily soft at no additional cost, within the limitations of the algorithm.

To begin, for VSM the depth map is sampled (just once) at the receiver's location to return an average depth of the closest light occluder. When this average depth  $M_1$  (also called the *first moment*) is greater than the depth on the shadow receiver  $t$ , the receiver is considered fully in light. When the average depth is less than the receiver's depth, the following equation is used:

$$p_{\max}(t) = \frac{\sigma^2}{\sigma^2 + (t - M_1)^2}. \quad (9.10)$$

where  $p_{\max}$  is the maximum percentage of samples in light,  $\sigma^2$  is the variance,  $t$  is the receiver depth, and  $M_1$  is the average (expected) depth in the shadow map. The depth-squared shadow map's sample  $M_2$  (the *second moment*) is used to compute the variance:

$$\sigma^2 = M_2 - M_1^2. \quad (9.11)$$

The value  $p_{\max}$  is an upper bound on the visibility percentage of the receiver. The actual illumination percentage  $p$  cannot be larger than this value. This upper bound is from Chebychev's inequality, one-tailed version. The equation attempts to estimate, using probability theory, how much of the distribution of occluders at the surface location is beyond the surface's distance from the light. Donnelly and Lauritzen show that for a planar occluder and planar receiver at fixed depths,  $p = p_{\max}$ , so Equation 9.10 can be used as a good approximation of many real shadowing situations.

Myers [915] builds up an intuition as to why this method works. The variance over an area increases at shadow edges. The greater the difference in depths, the greater the variance. The  $(t - M_1)^2$  term is then a significant determinant in the visibility percentage. If this value is just slightly above

zero, this means the average occluder depth is slightly closer to the light than the receiver, and  $p_{\max}$  is then near 1 (fully lit). This would happen along the fully lit edge of the penumbra. Moving into the penumbra, the average occluder depth gets closer to the light, so this term becomes larger and  $p_{\max}$  drops. At the same time the variance itself is changing within the penumbra, going from nearly zero along the edges to the largest variance where the occluders differ in depth and equally share the area. These terms balance out to give a linearly varying shadow across the penumbra. See Figure 9.32 for a comparison with other algorithms.

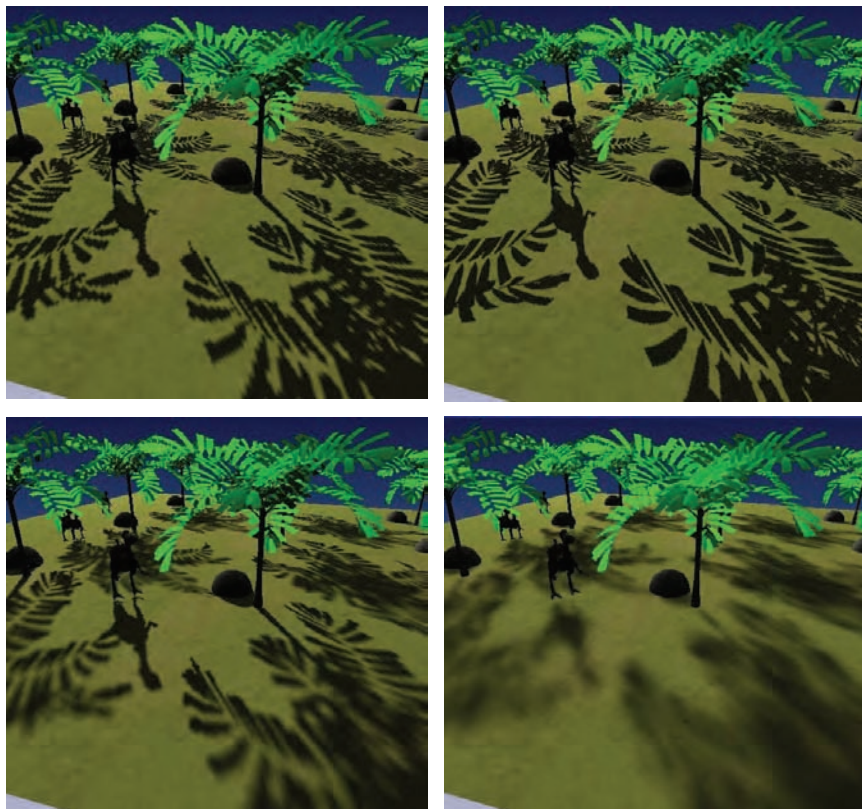


**Figure 9.32.** In the upper left, standard shadow mapping. Upper right, perspective shadow mapping, increasing the density of shadow map texel density near the viewer. Lower left, percentage-closer soft shadows, softening the shadows as the occluder's distance from the receiver increases. Lower right, variance shadow mapping with a constant soft shadow width, each pixel shaded with a single variance map sample. (*Images courtesy of Nico Hempe, Yvonne Jung, and Johannes Behr.*)

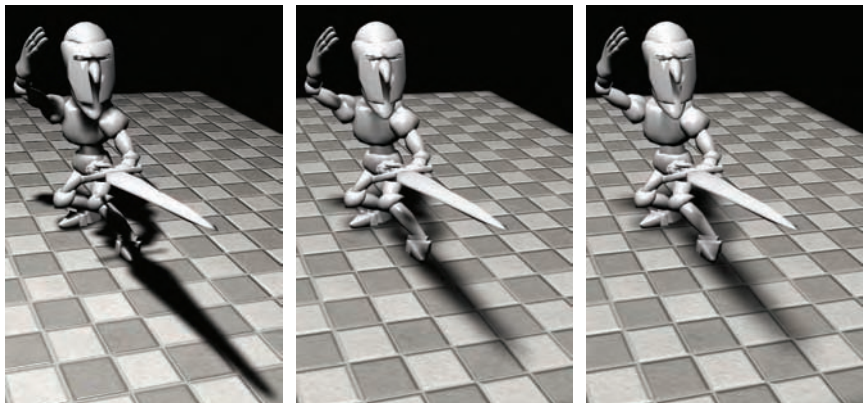


**Figure 9.33.** Variance shadow mapping, varying the light distance. (*Images from the NVIDIA SDK 10 [945] samples courtesy of NVIDIA Corporation.*)

One significant feature of variance shadow mapping is that it can deal with the problem of surface bias problems due to geometry in an elegant fashion. Lauritzen [739] gives a derivation of how the surface's slope is used to modify the value of the second moment. Bias and other problems from numerical stability can be a problem for variance mapping. For example, Equation 9.11 subtracts one large value from another similar value. This type of computation tends to magnify the lack of accuracy of the underlying numerical representation. Using floating point textures helps avoid this problem.

As with PCF, the width of the filtering kernel determines the width of the penumbra. By finding the distance between the receiver and closest occluder, the kernel width can be varied, so giving convincing soft shadows. Mipmapped samples are poor estimators of coverage for a penumbra with a slowly increasing width, creating boxy artifacts. Lauritzen [739] details how to use summed-area tables to give considerably better shadows. An example is shown in Figure 9.33.

One place variance shadow mapping breaks down is along the penumbras areas when two or more occluders cover a receiver and one occluder is close to the receiver. The Chebychev inequality will produce a maximum light value that is not related to the correct light percentage. Essentially, the closest occluder, by only partially hiding the light, throws off the equation's approximation. This results in *light bleeding* (a.k.a. *light leaks*), where areas that are fully occluded still receive light. See Figure 9.34. By taking more samples over smaller areas, this problem can be resolved, which essentially turns variance shadow mapping into PCF. As with PCF, speed and performance trade off, but for scenes with low shadow depth complex-

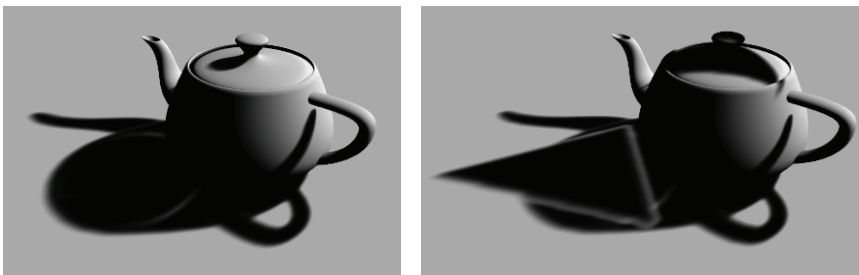


**Figure 9.34.** On the left, variance shadow mapping applied to a teapot. On the right, a triangle (not shown) casts a shadow on the teapot, causing objectionable artifacts in the shadow on the ground. (*Images courtesy of Marco Salvi.*)

ity, variance mapping works well. Lauritzen [739] gives one artist-controlled method to ameliorate the problem, which is to treat low percentages as 0% lit and to remap the rest of the percentage range to 0% to 100%. This approach darkens light bleeds, at the cost of narrowing penumbrae overall. While light bleeding is a serious limitation, VSM is excellent for producing shadows from terrain, since such shadows rarely involve multiple occluders [887].

The promise of being able to use filtering techniques to rapidly produce smooth shadows generated much interest in variance shadow mapping; the main challenge is solving the bleeding problem. Annen et al. [26] introduce the *convolution shadow map*. Extending the idea behind Soler and Sillion’s algorithm for planar receivers [1205], the idea is to portray a shadow’s effect as a set of statistical basis functions based on filtering. As with variance shadow mapping, such maps can be filtered. The method converges to the correct answer, so the light leak problem is avoided. Salvi [1110] discusses saving the exponential of the depth into a buffer. An exponential function approximates the step function that a shadow map performs (i.e., in light or not), so this can work to significantly reduce bleeding artifacts.

Another element that is a problem for shadow map algorithms in general is the non-linear way in which the raw  $z$ -depth value varies with distance from the light. Generating the shadow map so that the values stored vary linearly within the range can also help PCF, but it is particularly important for variance shadow mapping. Setting the near and far planes of the lighting frustum as tight as possible against the scene also helps precision problems [136, 739, 915].

### Related Algorithms

Lokovic and Veach [786] present the concept of *deep shadow maps*, in which each shadow map texel stores a function of how light drops off with depth.



**Figure 9.35.** Hair rendering using deep opacity maps for shadows [1398]. (*Images courtesy of Cem Yuksel, Texas A&M University.*)

This is useful for rendering objects such as hair and clouds, where objects are either small (and cover only part of each texel) or semitransparent. Self-shadowing such objects is critical for realism. St. Amour et al. [1210] use this concept of storing a function to compute penumbras. Kim and Neumann [657] introduce a method they call *opacity shadow maps* that is suited for the GPU. They generate a set of shadow maps at different depths from the light, storing the amount of light received at each texel at each depth. Linear interpolation between the two neighboring depth levels is then used to compute the amount of obscuration at a point. Nguyen and Donnelly [929] give an updated version of this approach, producing images such as Figure 13.1 on page 577. Yuksel and Keyser [1398] improve efficiency and quality by creating opacity maps that more closely follow the shape of the model. Doing so allows them to reduce the number of layers needed, as evaluation of each layer is more significant to the final image. See Figure 9.35. Ward et al. [1327] provide an excellent in-depth survey of hair modeling techniques.

In 2003 Chan and Durand [168] and Wyman [1385] simultaneously presented algorithms that work by using shadow maps and creating additional geometry along silhouette edges to generate perceptually convincing penumbras. The technique of using cones and sheets is similar to that shown on the right in Figure 9.7 on page 337, but it works for receivers at any distance. In their paper, Chan and Durand compare their *smoothies* technique with Wyman's *penumbra maps* method. A major advantage of these algorithms is that a smooth, noiseless penumbra is gen-

erated that looks convincing. However, as with Haines' method [487], the umbra regions are overstated, and rendering artifacts occur wherever two separate shadow edges cross. Arvo et al. [39] and de Boer [234] each take a different approach, finding silhouette edges via edge detection and then using image processing techniques to create plausible penumbrae. By using the depth map to find the distance between occluder and receiver, they grow variable-width silhouette edges via repeated filtering operations. Arvo performs this operation in screen space, de Boer in shadow map space. By using disk sampling to decide whether an edge should cast a penumbra, de Boer is able to avoid artifacts due to crossing edges.

Methods like PCF work by sampling the nearby receiver locations. Ideally we want to determine how much of the area light source is visible from a single receiver location. In 2006 a number of researchers explored *backprojection* using the GPU. The idea is to treat the receiver as a viewer and the area light source as a screen, and project the occluders back onto it. A basic element of these algorithms is the *micropatch*. Each shadow map texel has a given distance and size; this data can literally be treated as a tiny polygon for purposes of backprojection. Both Schwarz and Stamminger [1142] and Guennebaud et al. [465] summarize previous work and offer their own improvements. Bavoil et al. [76] take a different approach, using depth peeling to create a multilayer shadow map.

The challenge is creating a backprojection algorithm that both works efficiently to determine the amount of light covered by micropatches and maintains reasonable quality. One concept that has proven useful is a hierarchical min/max shadow map. While shadow map depths normally cannot be averaged, the minimum and maximum values at each mipmap level can be useful. That is, two mipmaps are formed, one saving the largest  $z$ -depth found, and one the smallest. Given a texel location, depth, and area to be sampled, the mipmaps can be used to rapidly determine fully lit and fully shadowed conditions. For example, if the texel's  $z$ -depth is greater than the maximum  $z$ -depth stored for an area of the mipmap, then the texel must be in shadow—no further samples are needed. This type of shadow map makes the task of determining light visibility much more efficient. In addition, it can be used in place of PCF sampling to create smooth, noiseless penumbra shadows [262].

### 9.1.5 Shadow Optimizations

It has already been noted that shadows add to the level of realism of a rendered image, and that shadows can be used as visual cues to determine spatial relationships. However, shadows may also incur a great cost, both

in terms of performance and in memory usage. Some general optimization strategies for faster shadow generation are presented here.

Since it is fairly difficult to perceive whether a shadow is correct, some shortcuts can be taken. These simplifications can cause inaccuracies in the shadows, but given a high enough frame rate, these are often difficult to notice [114]. One technique is to use a low level of detail model to actually cast the shadow. Whether this method helps performance is dependent on the algorithm and the location of the bottleneck (see Chapter 15). Using a simpler occluder lessens the load on the bus and geometry stage of the pipeline, as fewer vertices are processed.

You yourself are currently in the shadows of billions of light sources around the world. Light reaches you from only a few of these. In real-time rendering, large scenes with multiple lights can become swamped with computation if all lights are active at all times. Various culling strategies can also work for lights. For example, the portal culling technique in Section 14.4 can find which lights affect which cells. Another strategy is to use lights that drop off with distance and that are made inactive when beyond some given distance. Alternately, as the distance from a set of lights increases beyond some value, the lights can be coalesced into a single light source. One of the great strengths of a deferred shading system (see Section 7.9.2) is that it can efficiently handle a large number of lights.

If a light source is inside the view frustum, no object outside this frustum can cast a shadow that is in the view. Thus, objects outside the view frustum need not be processed. Note that this is not true in general. Lights outside the view frustum can have shadows cast by objects outside the frustum and so affect the image. A bounding volume can be formed by using the light's area of effect, and this can then be used to avoid unnecessary shadow generation and rendering by frustum and occlusion culling (see Section 14.2) [114].

Govindaraju et al. [437] present a number of optimization techniques for complex models. They use level of detail methods and combine potentially visible sets with frustum and occlusion culling (see Chapter 14) to save time overall and improve image quality.

## 9.2 Ambient Occlusion

When a light source covers a large solid angle, it casts a soft shadow. Ambient light, which illuminates evenly from all directions (see Section 8.3) casts the softest shadows. Since ambient light lacks any directional variation, shadows are especially important—in their absence, objects appear flat (see left side of Figure 9.36).

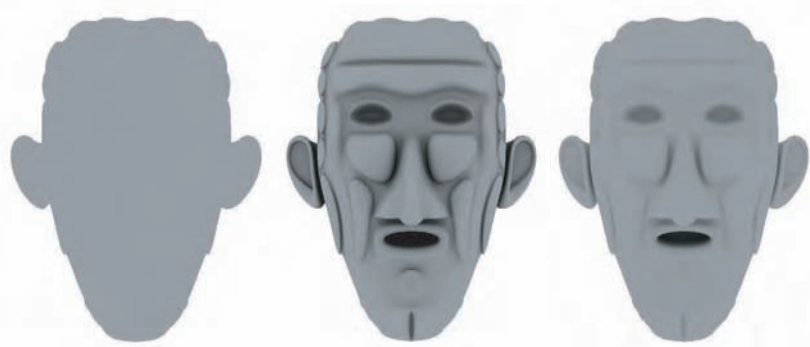


**Figure 9.36.** A diffuse object lit evenly from all directions. On the left, the object is rendered without any shadowing or interreflections. No details are visible, other than the outline. In the center, the object has been rendered with ambient occlusion. The image on the right was generated with a full global illumination simulation. (*Images generated using the Microsoft SDK [261] sample “PRTDemo.”*)

Shadowing of ambient light is referred to as *ambient occlusion*. Unlike other types of shadowing, ambient occlusion does not depend on light direction, so it can be precomputed for static objects. This option will be discussed in more detail in Section 9.10.1. Here we will focus on techniques for computing ambient occlusion dynamically, which is useful for animating scenes or deforming objects.

### 9.2.1 Ambient Occlusion Theory

For simplicity, we will first focus on Lambertian surfaces. The outgoing radiance  $L_o$  from such surfaces is proportional to the surface irradiance  $E$ . Irradiance is the cosine-weighted integral of incoming radiance, and in the general case depends on the surface position  $\mathbf{p}$  and the surface normal  $\mathbf{n}$ . Ambient light is defined as constant incoming radiance  $L_i(\mathbf{l}) = L_A$  for all incoming directions  $\mathbf{l}$ . This results in the following equation for computing irradiance:

$$E(\mathbf{p}, \mathbf{n}) = \int_{\Omega} L_A \cos \theta_i d\omega_i = \pi L_A, \quad (9.12)$$

where the integral is performed over the hemisphere  $\Omega$  of possible incoming directions. It can be seen that Equation 9.12 yields irradiance values unaffected by surface position and orientation, leading to a flat appearance.

Equation 9.12 does not take visibility into account. Some directions will be blocked by other objects in the scene, or by other parts of the same object (see Figure 9.37, for example, point  $\mathbf{p}_2$ ). These directions will have some other incoming radiance, not  $L_A$ . Assuming (for simplicity)

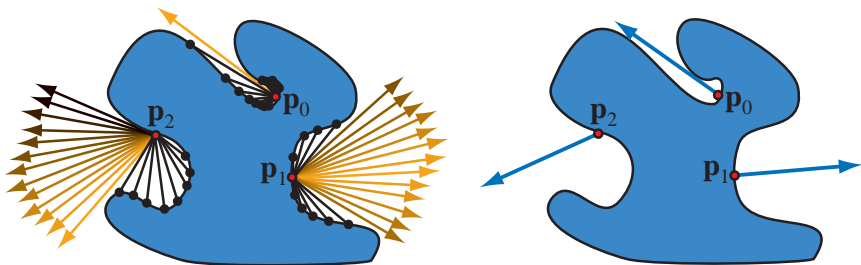


**Figure 9.37.** An object under ambient illumination. Three points ( $p_0$ ,  $p_1$ , and  $p_2$ ) are shown. On the left, blocked directions are shown as black rays ending in intersection points (black circles). Unblocked directions are shown as arrows, colored according to the cosine factor, so arrows closer to the surface normal are lighter. On the right, each blue arrow shows the average unoccluded direction or *bent normal*.

that blocked directions have zero incoming radiance results in the following equation (first proposed by Cook and Torrance [192, 193]):

$$E(\mathbf{p}, \mathbf{n}) = L_A \int_{\Omega} v(\mathbf{p}, \mathbf{l}) \cos \theta_i d\omega_i, \quad (9.13)$$

where  $v(\mathbf{p}, \mathbf{l})$  is a visibility function that equals 0 if a ray cast from  $\mathbf{p}$  in the direction of  $\mathbf{l}$  is blocked, and 1 if it is not. The ambient occlusion value<sup>5</sup>  $k_A$  is defined thus:

$$k_A(\mathbf{p}) = \frac{1}{\pi} \int_{\Omega} v(\mathbf{p}, \mathbf{l}) \cos \theta_i d\omega_i. \quad (9.14)$$

Possible values for  $k_A$  range from 0 (representing a fully occluded surface point, only possible in degenerate cases) to 1 (representing a fully open surface point with no occlusion). Once  $k_A$  is defined, the equation for ambient irradiance in the presence of occlusion is simply

$$E(\mathbf{p}, \mathbf{n}) = k_A(\mathbf{p}) \pi L_A. \quad (9.15)$$

Note that now the irradiance *does* change with surface location, since  $k_A$  does. This leads to much more realistic results, as seen in the middle of Figure 9.36. Surface locations in sharp creases will be dark since their value of  $k_A$  is low—compare surface locations  $p_0$  and  $p_1$  in Figure 9.37. The surface orientation also has an effect, since the visibility function  $v(\mathbf{p}, \mathbf{l})$  is weighted by a cosine factor when integrated. Compare  $p_1$  to  $p_2$  in Figure 9.37. Both have an unoccluded solid angle of about the same size, but most of the unoccluded region of  $p_1$  is around its surface normal, so

<sup>5</sup>Since the value increases with visibility, perhaps it would be more proper to call it *ambient visibility*, but *ambient occlusion* is the commonly used term.

the cosine factor is relatively high (as can be seen by the brightness of the arrows). On the other hand, most of the unoccluded region of  $\mathbf{p}_2$  is off to one side of the surface normal, with correspondingly lower values for the cosine factor. For this reason, the value of  $k_A$  is lower at  $\mathbf{p}_2$ .

From this point, we will cease to explicitly show dependence on the surface location  $\mathbf{p}$ , for brevity.

## 9.2.2 Shading with Ambient Occlusion

Shading with ambient occlusion is best understood in the context of the full shading equation, which includes the effects of both direct and indirect (ambient) light. Similarly to ambient occlusion, shadows for direct light sources use the visibility function  $v(\mathbf{l})$ , but applied directly, rather than in an integral. To help focus on the relevant terms in the (somewhat large) shading equations, the terms under discussion will be shown in red. The shading equation for Lambertian surfaces is

$$L_o(\mathbf{v}) = \frac{\mathbf{c}_{\text{diff}}}{\pi} \otimes \left( k_A \pi L_A + \sum_{k=1}^n v(\mathbf{l}_k) E_{L_k} \overline{\cos} \theta_{i_k} \right), \quad (9.16)$$

where  $\mathbf{l}_k$  is the light direction for the  $k$ th direct light source,  $E_{L_k}$  is the irradiance contribution of that light source (measured in a plane perpendicular to  $\mathbf{l}_k$ ), and  $\theta_{i_k}$  is the angle between  $\mathbf{l}_k$  and the surface normal  $\mathbf{n}$ . The  $\otimes$  symbol (piecewise vector multiply) is used, since both  $\mathbf{c}_{\text{diff}}$  and the lighting values are spectral (RGB). The  $\overline{\cos}$  function represents a cosine clamped to non-negative values.

As we have seen in Section 8.3, non-Lambertian surfaces are shaded with ambient light by defining an *ambient color*  $\mathbf{c}_{\text{amb}}$  that is a blend of the diffuse and specular colors. The equivalent to Equation 9.16 for arbitrary BRDFs is

$$L_o(\mathbf{v}) = k_A \frac{\mathbf{c}_{\text{amb}}}{\pi} \otimes \pi L_A + \sum_{k=1}^n v(\mathbf{l}_k) f(\mathbf{l}_k, \mathbf{v}) \otimes E_{L_k} \overline{\cos} \theta_{i_k}, \quad (9.17)$$

where  $f(\mathbf{l}, \mathbf{v})$  is the BRDF (see Section 7.5).

Ambient occlusion can be used with other types of indirect light besides constant ambient. ILM uses ambient occlusion with irradiance environment maps [728]. In addition to  $k_A$ , ILM also compute an average unoccluded direction or *bent normal* that is used to access the irradiance environment map, instead of the surface normal. The bent normal is computed as a cosine-weighted average of unoccluded light directions:

$$\mathbf{n}_{\text{bent}} = \frac{\int_{\Omega} v(\mathbf{l}) \mathbf{l} \cos \theta_i d\omega_i}{\| \int_{\Omega} v(\mathbf{l}) \mathbf{l} \cos \theta_i d\omega_i \|}. \quad (9.18)$$

The result of the integral is divided by its own length to produce a normalized result (the notation  $\|\mathbf{x}\|$  indicates the length of the vector  $\mathbf{x}$ ). See the right side of Figure 9.37.

The shading equation for applying ambient occlusion to an irradiance environment map is similar to Equation 9.17, except that the environment map irradiance  $E_{\text{env}}(\mathbf{n}_{\text{bent}})$  replaces the ambient irradiance  $\pi L_A$ . We will use the generic notation  $E_{\text{ind}}$  to represent indirect irradiance from either ambient light or an irradiance environment map.

Unlike the use of  $k_A$  to attenuate a constant ambient light (which is exact), accessing an irradiance environment map by the bent normal  $\mathbf{n}_{\text{bent}}$  and attenuating the result by the ambient occlusion factor  $k_A$  is an approximation. However, it produces high-quality results; ILM used it for several feature films. Pharr [1012] presents an alternative that uses the GPU's texture filtering hardware to produce a potentially more accurate result. An area of the original (unfiltered) environment map is dynamically filtered. The center of the filtered area is determined by the direction of the bent normal, and its size depends on the value of  $k_A$ . This technique uses a texture instruction that takes user-supplied derivatives. Unfortunately, on most hardware, this instruction is significantly slower than an ordinary texture access.

ILM [728] sometimes shades direct lights with the bent normal instead of the surface normal, and attenuates the result by the ambient occlusion factor instead of using regular shadowing techniques. Lights treated in this way have some of the visual properties of a large area light.

A similar technique, proposed by Iones et al. [587] is intended to model the indirect contribution of point or directional lights. This is particularly useful in environments with dynamic lighting. Imagine a room that is dark until a character walks in carrying a torch. The direct lighting from the torch is modeled by a point light using a shadowing technique such as shadow maps. However, even areas in shadow or facing away from the torch receive some indirect bounce light from the torch. In the technique proposed by Iones et al., the indirect contributions of light sources are modeled by adding them to the indirect irradiance:

$$L_o(\mathbf{v}) = k_A \frac{\mathbf{c}_{\text{amb}}}{\pi} \otimes \left( E_{\text{ind}} + k_{\text{ind}} \sum_{k=1}^n E_{L_k} \right) + \sum_{k=1}^n v(\mathbf{l}_k) f(\mathbf{l}_k, \mathbf{v}) \otimes E_{L_k} \overline{\cos} \theta_{i_k}, \quad (9.19)$$

where the factor  $k_{\text{ind}}$  is a value between 0 and 1, used to control the relative intensity of the direct and indirect contributions of the lights. Since this model is empirical, the value of  $k_{\text{ind}}$  should be manually set to achieve visually pleasing results. Note that unlike the direct contributions, the indirect contributions of the light sources are unaffected by cosine factors.

If bent normals are available, it is possible to combine the two previous techniques by applying the bent normals to the indirect light contributions:

$$L_o(\mathbf{v}) = k_A \frac{\mathbf{c}_{\text{amb}}}{\pi} \otimes \left( E_{\text{ind}} + k_{\text{ind}} \sum_{k=1}^n E_{L_k} \overline{\cos} \theta'_{i_k} \right) + \sum_{k=1}^n v(\mathbf{l}_k) f(\mathbf{l}_k, \mathbf{v}) \otimes E_{L_k} \overline{\cos} \theta_{i_k}, \quad (9.20)$$

where  $\theta'_{i_k}$  is the angle between  $\mathbf{l}_k$  and the bent normal  $\mathbf{n}_{\text{bent}}$ .

Mittring [887] describes a similar approach used in Crytek's *Crysis*. Instead of a bent normal, Crytek uses a blend of the light direction and the surface normal, and instead of the  $k_{\text{ind}}$  factor, it uses separate intensity, color, and distance falloffs for the direct and indirect contributions of the light source. Otherwise their approach is the same as Equation 9.20.

Although using ambient occlusion to attenuate glossy or specular environment maps is incorrect, Kozlowski and Kautz [695] show that in some cases this can work reasonably well. See Section 9.10.2 for more general approaches to shadowing glossy and specular environment maps.

### 9.2.3 Visibility and Obscurance

The visibility function  $v(\mathbf{l})$  used to compute the ambient occlusion factor  $k_A$  (see Equation 9.14) needs to be carefully defined. For discrete objects, such as characters or vehicles, it is straightforward to define  $v(\mathbf{l})$  based on whether a ray cast from a surface location in direction  $\mathbf{l}$  intersects any other part of the same object. However, this does not account for occlusion by other, nearby objects. Often, the object can be assumed to be placed on a flat plane for lighting purposes. By including this plane in the visibility calculation, more realistic occlusion can be achieved. Another benefit is that the occlusion of the ground plane by the object can be used as a contact shadow [728].

Unfortunately, the visibility function approach fails for enclosed geometry. Imagine a scene consisting of a closed room containing various objects—all surfaces will have a  $k_A$  value of zero! Empirical approaches, which attempt to reproduce the *look* of ambient occlusion without necessarily simulating physical visibility, tend to work better for closed or semi-closed geometry. Some of these approaches were inspired by Miller's concept of *accessibility shading* [867], which models how nooks and crannies in a surface capture dirt or corrosion.

Zhukov et al. [1409] introduced the idea of *obscurance*, which modifies the ambient occlusion computation by replacing the visibility function  $v(\mathbf{l})$  with a distance mapping function  $\rho(\mathbf{l})$ :

$$k_A = \frac{1}{\pi} \int_{\Omega} \rho(\mathbf{l}) \cos \theta_i d\omega_i. \quad (9.21)$$

Unlike  $v(\mathbf{l})$ , which has only two valid values (1 for no intersection and 0 for an intersection),  $\rho(\mathbf{l})$  is a continuous function of intersection distance. The value of  $\rho(\mathbf{l})$  is 0 at an intersection distance of 0 and 1 at intersection distances greater than a specified distance  $d_{\max}$  (or no intersection at all). Intersections beyond  $d_{\max}$  do not need to be tested, which can considerably speed up the computation of  $k_A$ .

Although obscurance is nonphysical (despite attempts to justify it on physical grounds), it is quite effective and practical. One drawback is that the value of  $d_{\max}$  needs to be set by hand to achieve pleasing results.<sup>6</sup> Méndez-Feliu et al. [856, 857] extend obscurance to account for color bleeding as well.

Jones et al. [587] propose a variant of  $\rho(\mathbf{l})$  that asymptotically approaches 1 as the intersection distance goes to infinity. This has a speed disadvantage but does not require manually setting a  $d_{\max}$  parameter.

## 9.2.4 Accounting for Interreflections

Although the results produced by ambient occlusion are darker than those produced by a full global illumination simulation (compare the middle and right images in Figure 9.36 on page 374), they are visually convincing. Computing the value of  $k_A$  is significantly cheaper than performing a full global illumination calculation. This is particularly important for dynamic scenes with deforming objects, where it is preferable to compute  $k_A$  in real time.

The differences between ambient occlusion and global illumination are due to interreflections. Equation 9.14 assumes that the radiance in the blocked directions is zero, while in reality interreflections will introduce a nonzero radiance from those directions. The effect of this can be seen as darkening in the creases and pits of the model in the middle of Figure 9.36 (on page 374), compared to the model on the right. This difference can be addressed by increasing the value of  $k_A$ . Using the obscurance distance mapping function instead of the visibility function (see Section 9.2.3) can also mitigate this problem, since the obscurance function often has values greater than 0 for blocked directions.

Accounting for interreflections in a more accurate manner is expensive, since it requires solving a recursive problem (to shade one point, other points must first be shaded, and so on). Stewart and Langer [1219] propose an inexpensive, but surprisingly accurate, solution. It is based on

---

<sup>6</sup>This is often the case in computer graphics, where a technique has no direct physical basis but is “perceptually convincing.” The goal is usually a plausible image, so such techniques are fine to use. Some advantages of methods based on theory are that they can work automatically and can be improved further by reasoning about how the real world works.

the observation that for Lambertian scenes under diffuse illumination, the surface locations visible from a given location tend to have similar radiance. By assuming that the radiance  $L_i$  from blocked directions is equal to the outgoing radiance  $L_o$  from the currently shaded point, the recursion is broken and an analytical expression can be found:

$$E = \frac{\pi k_A}{1 - \mathbf{c}_{\text{amb}}(1 - k_A)} L_A. \quad (9.22)$$

This is equivalent to replacing the ambient occlusion factor  $k_A$  with a new factor  $k'_A$ :

$$k'_A = \frac{k_A}{1 - \mathbf{c}_{\text{amb}}(1 - k_A)}. \quad (9.23)$$

This equation will tend to brighten the ambient occlusion factor, making it visually closer to the result of a full global illumination solution, including interreflections. The effect is highly dependent on the value of  $\mathbf{c}_{\text{amb}}$ . The underlying approximation assumes that the ambient color is the same over the surface. In cases where the ambient color varies, it should be blurred before use in these equations, so that the results are still somewhat valid. This blurring can also produce an effect somewhat similar to color bleeding. Hoffman and Mitchell [555] use this method to illuminate terrain with sky light.

## 9.2.5 Dynamic Computation of Ambient Occlusion

For static scenes, the ambient occlusion factor  $k_A$  and bent normal  $\mathbf{n}_{\text{bent}}$  can be precomputed (this will be discussed in more detail in Section 9.10.1). However, for dynamic scenes or deforming objects, better results can be achieved by computing these factors dynamically. Methods for doing so can be grouped into those that operate in object space, and those that operate in screen space.

### *Object-Space Methods*

Offline methods for computing ambient occlusion usually involve casting a large number of rays (dozens to hundreds) from each surface point into the scene and checking for intersection. This is a very expensive operation, and real-time methods focus on ways to approximate or avoid much of this computation.

Bunnell [146] computes the ambient occlusion factor  $k_A$  and bent normal  $\mathbf{n}_{\text{bent}}$  by modeling the surface as a collection of disk-shaped elements placed at the mesh vertices. Disks were chosen since the occlusion of one disk by another can be computed analytically, avoiding the need to cast rays. Simply summing the occlusion factors of a disk by all the other

disks leads to overly dark results due to double-shadowing (if one disk is behind another, both will be counted as occluding the surface, even though only the closer of the two should be counted). Bunnell uses a clever two-pass method to avoid double-shadowing. The first pass computes ambient occlusion including double-shadowing. In the second pass, the contribution of each disk is reduced by its occlusion from the first pass. This is an approximation, but in practice, yields results that are quite good.

Computing occlusion between each pair of elements is an order  $O(n^2)$  operation, which is too expensive for all but the simplest scenes. The cost is reduced by using simplified representations for distant surfaces. A hierarchical tree of elements is constructed, where each node is a disk that represents the aggregation of the disks below it in the tree. When performing inter-disk occlusion computations, higher-level nodes are used for more distant surfaces. This reduces the computation to order  $O(n \log n)$ , which is much more reasonable.

Each disk's location, normal, and radius are stored in textures, and the occlusion computations are performed in fragment shaders. This is because at the time the technique was developed (2005), GPUs' fragment shading units possessed significantly higher computation throughput than their vertex shading units. On modern GPUs with unified shader units, vertex shaders may be a better choice for this algorithm, since the lowest-level elements are placed at the vertices.

Bunnell's technique is quite efficient and produces high-quality results—it was even used by ILM when performing renders for the *Pirates of the Caribbean* films [1071].

Hoberock [553] proposes several modifications to Bunnell's algorithm that improve quality at higher computational expense. A distance attenuation factor is also proposed, which yields results similar to the obscurrence factor proposed by Zhukov et al. [1409].

Ren et al. [1062] approximate the occluding geometry as a collection of spheres. The visibility function of a surface point occluded by a single sphere is represented using spherical harmonics. Such visibility functions are simple to project onto the spherical harmonic basis. The aggregate visibility function for occlusion by a group of spheres is the result of multiplying the individual sphere visibility functions. Unfortunately, multiplying spherical harmonic functions is an expensive operation. The key idea is to sum the logarithms of the individual spherical harmonic visibility functions, and exponentiate the result. This produces the same end result as multiplying the visibility functions, but summation of spherical harmonic functions is significantly cheaper than multiplication. The paper shows that with the right approximations, logarithms and exponentiations can be performed quickly, yielding an overall speedup.

Rather than an ambient occlusion factor, a spherical harmonic visibility function is computed. The first (order 0) coefficient can be used as the ambient occlusion factor  $k_A$ , and the next three (order 1) coefficients can be used to compute the bent normal  $\mathbf{n}_{\text{bent}}$ . Higher order coefficients can be used to shadow environment maps or circular light sources. Since geometry is approximated as bounding spheres, occlusion from creases and other small details is not modeled.

Hegeman et al. [530] propose a method that can be used to rapidly approximate ambient occlusion for trees, grass, or other objects that are composed of a group of small elements filling a simple volume such as a sphere, ellipsoid, or slab. The method works by estimating the number of blockers between the occluded point and the outer boundary of the volume, in the direction of the surface normal. The method is inexpensive and produces good results for the limited class of objects for which it was designed.

Evans [322] describes an interesting dynamic ambient occlusion approximation method based on *distance fields*. A distance field is a scalar function of spatial position. Its magnitude is equal to the distance to the closest object boundary, and it is negative for points inside objects and positive for points outside them. Sampled distance fields have many uses in graphics [364, 439]. Evans' method is suited for small volumetric scenes, since the signed distance field is stored in a volume texture that covers the extents of the scene. Although the method is nonphysical, the results are visually pleasing.

### Screen-Space Methods

The expense of object-space methods is dependent on scene complexity. Spatial information from the scene also needs to be collected into some data structure that is amenable for processing. Screen-space methods are independent of scene complexity and use readily available information, such as screen-space depth or normals.

Crytek developed a screen-space dynamic ambient occlusion approach used in *Crysis* [887]. The ambient occlusion is computed in a full-screen pass, using the  $Z$ -buffer as the only input. The ambient occlusion factor  $k_A$  of each pixel is estimated by testing a set of points (distributed in a sphere around the pixel's location) against the  $Z$ -buffer. The value of  $k_A$  is a function of the number of samples that pass the  $Z$ -buffer test (i.e., are in front of the value in the  $Z$ -buffer). A smaller number of passing samples results in a lower value for  $k_A$ —see Figure 9.38. The samples have weights that decrease with distance from the pixel (similarly to the obscurance factor [1409]). Note that since the samples are not weighted by a  $\overline{\cos \theta_i}$

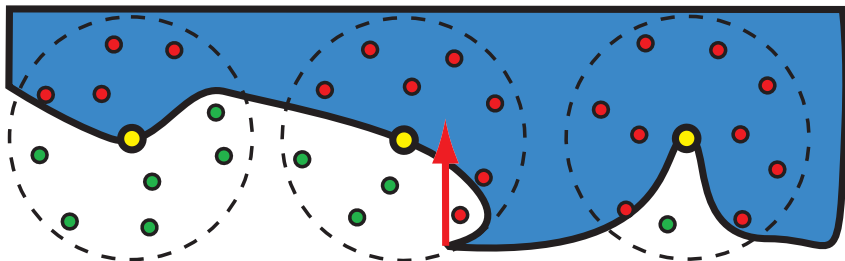


**Figure 9.38.** Crytek’s ambient occlusion method applied to three surface points (the yellow circles). For clarity, the algorithm is shown in two dimensions (up is farther from the camera). In this example, ten samples are distributed over a disk around each surface point (in actuality, they are distributed over a sphere). Samples failing the  $z$ -test (which are behind the  $Z$ -buffer) are shown in red, and passing samples are green. The value of  $k_A$  is a function of the ratio of passing samples to total samples (we ignore the variable sample weights here for simplicity). The point on the left has six passing samples out of 10 total, resulting in a ratio of 0.6, from which  $k_A$  is computed. The middle point has three passing samples (one more is outside the object but fails the  $z$ -test anyway, as shown by the red arrow), so  $k_A$  is determined from the ratio 0.3. The point on the right has one passing sample, so the ratio 0.1 is used to compute  $k_A$ .

factor, the resulting ambient occlusion is incorrect,<sup>7</sup> but the results were deemed by Crytek to be visually pleasing.

To keep performance reasonable, no more than about 16 samples should be taken per pixel. However, experiments indicated that as many as 200 samples are needed for good visual quality. To bridge the gap between these two numbers, the sample pattern is varied for each pixel in a  $4 \times 4$  block of pixels (giving effectively 16 different sample patterns).<sup>8</sup> This converts the banding artifacts caused by the small number of samples into high-frequency noise. This noise is then removed with a  $4 \times 4$ -pixel post-process blur. This technique allows each pixel to be affected by its neighbors, effectively increasing the number of samples. The price paid for this increase in quality is a blurrier result. A “smart blur” is used that does not blur across depth discontinuities, to avoid loss of sharpness on edges. An example using Crytek’s ambient occlusion technique is shown in Figure 9.39.

---

<sup>7</sup>Most notably, samples under the surface are counted when they should not be. This means that a flat surface will be darkened, with edges being brighter than their surroundings. It is hard to avoid this without access to surface normals; one possible modification is to clamp the ratio of passing samples to be no larger than 0.5, multiplying the clamped value by 2.

<sup>8</sup>The variation is implemented by storing a random direction vector in each texel of a  $4 \times 4$  texture that is repeated over the screen. At each pixel, a fixed three-dimensional sample pattern is reflected about the plane, perpendicular to the direction vector.



**Figure 9.39.** The effect of screen-space ambient occlusion is shown in the upper left. The upper right shows the albedo (diffuse color) without ambient occlusion. In the lower left the two are shown combined. Specular shading and shadows are added for the final image, in the lower right. (*Images from “Crysis” courtesy of Crytek.*)



**Figure 9.40.** The Z-buffer unsharp mask technique for approximate ambient occlusion. The image on the left has no ambient occlusion; the image on the right includes an approximate ambient occlusion term generated with the Z-buffer unsharp mask technique. (*Images courtesy of Mike Pan.*)

A simpler (and cheaper) approach that is also based on screen-space analysis of the contents of the  $Z$ -buffer was proposed by Luft et al. [802]. The basic idea is to perform an *unsharp mask* filter on the  $Z$ -buffer. An unsharp mask is a type of high-pass filter that accentuates edges and other discontinuities in an image. It does so by subtracting a blurred version from the original image. This method is inexpensive. The result only superficially resembles ambient occlusion, but with some adjustment of scale factors, a pleasing image can be produced—see Figure 9.40.

Shanmugam and Arikan [1156] describe two approaches in their paper. One generates fine ambient occlusion from small, nearby details. The other generates coarse ambient occlusion from larger objects. The results of the two are combined to produce the final ambient occlusion factor.

Their fine ambient occlusion method uses a full screen pass that accesses the  $Z$ -buffer along with a second buffer containing the surface normals of the visible pixels. For each shaded pixel, nearby pixels are sampled from the  $Z$ -buffer. The sampled pixels are represented as spheres, and an occlusion term is computed for the shaded pixel (taking its normal into account). Double shadowing is not accounted for, so the result is somewhat dark.

Their coarse occlusion method is similar to the object-space method of Ren et al. [1062] (discussed on page 381) in that the occluding geometry is approximated as a collection of spheres. However, Shanmugam and Arikan accumulate occlusion in screen space, using screen-aligned billboards covering the “area of effect” of each occluding sphere. Double shadowing is also not accounted for in the coarse occlusion method either (unlike the method of Ren et al.).

Sloan et al. [1190] propose a technique that combines the spherical harmonic exponentiation of Ren et al. [1062] with the screen-space occlusion approach of Shanmugam and Arikan [1156]. As in the technique by Ren et al., spherical harmonic visibility functions from spherical occluders are accumulated in log space, and the result is exponentiated. As in Shanmugam and Arikan’s technique, these accumulations occur in screen space (in this case by rendering coarsely tessellated spheres rather than billboards). The combined technique by Sloan et al. accounts for double shadowing and can produce not only ambient occlusion factors and bent normals, but also higher-frequency visibility functions that can be used to shadow environment maps and area lights. It can even handle interreflections. However, it is limited to coarse occlusion, since it uses spherical proxies instead of the actual occluding geometry.

One interesting option is to replace Shanmugam and Arikan’s fine occlusion method [1156] with the less expensive Crytek method [887], to improve performance while retaining both coarse and fine occlusion. Alternatively, their coarse method could be replaced with the more accurate one proposed by Sloan et al. [1190], to improve visual quality.

## 9.3 Reflections

Environment mapping techniques for providing reflections of objects at a distance have been covered in Section 8.4 and 8.5, with reflected rays computed using Equation 7.30 on page 230. The limitation of such techniques is that they work on the assumption that the reflected objects are located far from the reflector, so that the same texture can be used by all reflection rays. Generating planar reflections of nearby objects will be presented in this section, along with methods for rendering frosted glass and handling curved reflectors.

### 9.3.1 Planar Reflections

Planar reflection, by which we mean reflection off a flat surface such as a mirror, is a special case of reflection off arbitrary surfaces. As often occurs with special cases, planar reflections are easier to implement and can execute more rapidly than general reflections.

An ideal reflector follows the *law of reflection*, which states that the angle of incidence is equal to the angle of reflection. That is, the angle between the incident ray and the normal is equal to the angle between the reflected ray and the normal. This is depicted in Figure 9.41, which illustrates a simple object that is reflected in a plane. The figure also shows an “image” of the reflected object. Due to the law of reflection, the reflected image of the object is simply the object itself, physically reflected through the plane. That is, instead of following the reflected ray, we could follow the incident ray through the reflector and hit the same point, but

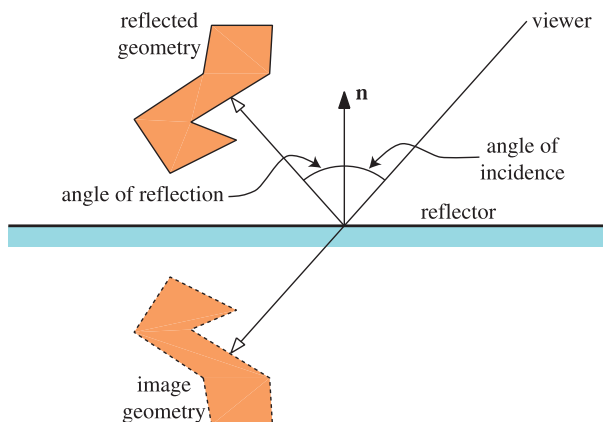


**Figure 9.41.** Reflection in a plane, showing angle of incidence and reflection, the reflected geometry, and the reflector.

on the reflected object. The conclusion that can be drawn from this principle is that a reflection can be rendered by creating a copy of the object, transforming it into the reflected position, and rendering it from there. To achieve correct lighting, light sources have to be reflected in the plane as well, with respect to both position and direction [892, 957].

If for a moment we assume that the reflecting plane has a normal,  $\mathbf{n} = (0, 1, 0)$ , and that it goes through the origin, then the matrix that reflects in this plane is simply this mirror scaling matrix:  $\mathbf{S}(1, -1, 1)$ . For the general case, we derive the reflection matrix  $\mathbf{M}$ , given the normal of the reflector  $\mathbf{n}$  and some point  $\mathbf{p}$  on the reflector plane. Since we know how to reflect in the plane  $y = 0$ , the idea is to transform the plane into  $y = 0$ , then perform the simple scaling, and finally transform back. The concatenation of these matrices yields  $\mathbf{M}$ .

First, we have to translate the plane so that it passes through the origin, which is done with a translation matrix:  $\mathbf{T}(-\mathbf{p})$ . Then the normal of the reflector plane,  $\mathbf{n}$ , is rotated so that it becomes parallel to the  $y$ -axis:  $(0, 1, 0)$ . This can be done with a rotation from  $\mathbf{n}$  to  $(0, 1, 0)$  using  $\mathbf{R}(\mathbf{n}, (0, 1, 0))$  (see Section 4.3.2). The concatenation of these operations is called  $\mathbf{F}$ :

$$\mathbf{F} = \mathbf{R}(\mathbf{n}, (0, 1, 0))\mathbf{T}(-\mathbf{p}). \quad (9.24)$$

After that, the reflector plane has become aligned with the plane  $y = 0$ , and then scaling,  $\mathbf{S}(1, -1, 1)$ , is performed; finally, we transform back with  $\mathbf{F}^{-1}$ . Thus,  $\mathbf{M}$  is constructed as follows:

$$\mathbf{M} = \mathbf{F}^{-1} \mathbf{S}(1, -1, 1)^T \mathbf{F}. \quad (9.25)$$

Note that this matrix has to be recomputed if the position or orientation of the reflector surface changes.

The scene is rendered by first drawing the objects to be reflected (transformed by  $\mathbf{M}$ ), followed by drawing the rest of the scene with the reflector included. An example of the results of this process appear in Figure 9.42. An equivalent method is to instead reflect the viewer's position and orientation through the mirror to the opposite side of the reflector. The advantage of moving the viewer is that none of the geometry has to be manipulated before being sent down to form the reflection [492, 849, 957]. In either case, care must be taken with properly setting backface culling for the reflection pass, as the use of a reflection matrix will normally flip the sense needed. The reflector has to be partially transparent, so that the reflection is visible. As such, the transparency acts like a kind of reflectivity factor; the reflector appears more reflective with increasing transparency.

However, sometimes the reflections can be rendered incorrectly, as in the left part of Figure 9.43. This happens because the reflected geometry can appear at places where there is no reflector geometry. In other words,



**Figure 9.42.** The water reflection is performed by mirroring polygons through the water's surface and blending them with the textured water polygon. The chandelier and some other elements are replaced with sets of textured polygons. (*Image courtesy of Agata and Andrzej Wojaczek [agand@aga3d.com], Advanced Graphics Applications Inc.*)

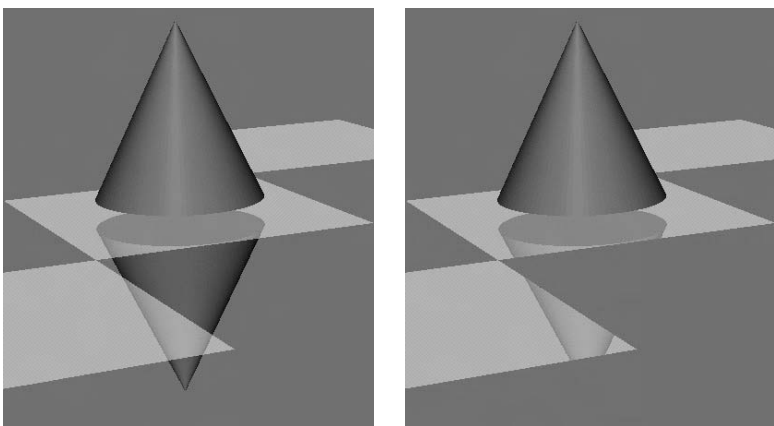


**Figure 9.43.** The left image shows an incorrectly rendered reflection against three mirrored squares. The right image was rendered with the use of the stencil buffer to mask out the part where there is visible reflector geometry, which yields a correct reflection.

the viewer will figure out the trick, seeing that the reflected objects are actually real.

To solve the problem, the reflector is first rendered into the stencil buffer, with the stencil parameters set so that we can write to the screen only where the reflector is present. Then the reflected geometry is rendered with stenciling turned on. In this way, the reflected geometry is rendered only where the stencil buffer is set, i.e., where the reflector exists.

Objects that are on the far side of (i.e., behind) the reflector plane should not be reflected. This problem can be solved by using the reflector's plane equation. The simplest method is to set a user-defined clipping plane. Place the clipping plane so that it coincides with the plane of the reflector [492]. Using such a clipping plane when rendering the reflected objects will clip away all reflected geometry that is on the same side as the viewpoint, i.e., all objects that were originally behind the mirror.

Portal culling methods (Section 14.4) can be used to restrict the amount of reflected geometry that needs to be fully processed. A mirror on a wall can be treated as a different kind of portal, "through the looking-glass." The user-defined clipping plane itself can also help to check if bounding volumes in the scene are entirely culled out, so that parts of the scene do not have to be sent down the pipeline at all.

A number of significant global illumination effects and lighting models are presented by Diefenbach and Badler [253]. We will discuss two here, glossy reflection and frosted glass. A simple way to enhance the illusion that the reflector is truly a mirror is to fog the reflected objects seen in it. This effect is created by having each object fade to black as the distance from the reflector increases. One way to do this is to render the reflected objects with a shader program that fades them to black by their distance from some plane. Another approach is to render the reflected objects to a texture and a  $Z$ -buffer. When the reflector is rendered, its  $z$ -depth is compared to the stored depth. The difference in depths is used to diminish the contribution of the reflected objects. In this way, no modification of the other objects' shader is necessary.

The accumulation and stencil buffers can be used together to produce the effects of fuzzy reflection and frosted glass. The stencil buffer creates the window into the effect, and the accumulation buffer captures the effect from jittering the position of the object. Fogging to black is used for the reflection, fogging to white for the refraction. Examples of these techniques are shown in Figure 9.44.

While conceptually appealing, using an accumulation buffer is expensive, as geometry has to be processed multiple times. A considerably faster way to create a similar effect is to use filtering techniques. The idea is to render the objects beyond the glass to an image that is then used as a texture. When the frosted glass is rendered, its shader program samples

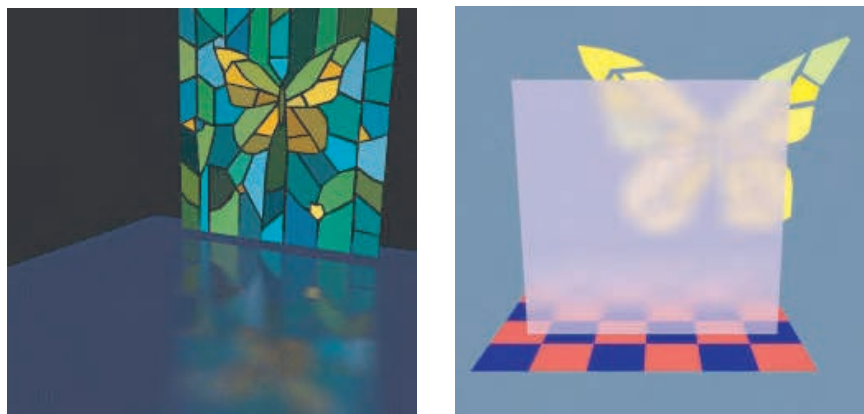


**Figure 9.44.** Fuzzy reflections and refractions, done by using the accumulation and stencil buffers along with fog. (*Images courtesy of Paul Diefenbach, window design by Elsa Schmid.*)



**Figure 9.45.** The upper left and right show the reflection and refraction images generated from the scene. These are then used by the water's surface as environment map textures, in the lower left. The lower right shows a similar shader performing refraction [848]. (*Images courtesy of Valve Corp.*)

this texture in a number of locations, thereby giving a blurred effect. See Section 10.9 for more about such methods.

This idea of having an object (such as the reflector polygon) accessing a previously stored depth or otherwise compute the distance from some surface can be used for many other effects. For example, to simulate translucency, the depth between the front and back faces can be mapped to a one-dimensional texture. Blending and smoothing techniques are needed to avoid artifacts from any tiny folds in the model [947].

One way to provide reflection and refraction effects in a bump-mapped surface is given by McTaggart [848]. The scene is reflected using the technique described earlier in Section 9.3.1. This reflection image is stored for use as a texture. Similarly, the part of the world seen through the surface is stored in a texture. The world in front of the reflector is then rendered normally. The reflector is rendered with a normal map, changing the reflection and refraction directions. These directions then access the corresponding image textures to create the appearance of distorted reflection. See Figure 9.45.

### 9.3.2 Reflections from Curved Reflectors

Ray tracing is the traditional solution for producing general reflections. See Section 9.8.2 for details. A reflection ray starts from the viewed location and picks up and adds in the color in the reflection direction. Ofek and Rappoport [957] present a technique for sharp, true reflections from convex and concave reflectors that can be considerably faster. Their observation is that in a convex reflector (e.g., a sphere), the reflected object is distorted by the surface, but is otherwise unchanged. That is, each reflected vertex is reflected by only one point on the reflector (unlike what can happen with a concave reflector). The curved reflector can be treated like a window into a mirror world, in a similar manner to the planar reflector. The full description of this method is fairly involved and has limitations; the interested reader should see the original paper [957].

Recursive reflections of curved objects in a scene can be performed using environment mapping [253, 849, 933]. For example, imagine a red and a blue mirrored ball some distance from each other. Generate an EM for the red sphere, then generate an EM for the blue while using the red sphere's EM during its creation. The blue sphere now includes a reflection of the red sphere, which in turn reflects the world. This recursion should in theory go on for several steps (until we cannot make out any differences), but this is expensive. A cheaper version of this computes only one environment map per frame using the environment maps from the previous frame [360]. This gives approximate recursive reflections. Figure 9.46 shows some examples using this technique.



**Figure 9.46.** Recursive reflections, done with environment mapping. (*Image courtesy of Kasper Høy Nielsen.*)

Other extensions of the environment mapping technique can enable more general reflections. Hakura et al. [490] show how a set of EMs can be used to capture local interreflections, i.e., when a part of an object is reflected in itself. Such methods are very expensive in terms of texture memory. Rendering a teapot with ray tracing quality required 100 EMs of  $256 \times 256$  resolution. Umenhoffer et al. [1282] describe an extension of environment mapping in which a few of the closest layers of the scene are stored along with their depths and normals per pixel. The idea is like depth peeling, but for forming layers of successive environment maps, which they call *layered distance maps*. This allows objects hidden from view from the center point of the EM to be revealed when reflection rays originate from a different location on the reflector's surface. Accurate multiple reflections and self-reflections are possible. This algorithm is interesting in that it lies in a space between environment mapping, image-based rendering, and ray tracing.

## 9.4 Transmittance

As discussed in Section 5.7, a transparent surface can be treated as a blend color or a filter color. When blending, the transmitter's color is mixed with the incoming color from the objects seen through the transmitter. The

`over` operator uses the  $\alpha$  value as an opacity to blend these two colors. The transmitter color is multiplied by  $\alpha$ , the incoming color by  $1 - \alpha$ , and the two summed. So, for example, a higher opacity means more of the transmitter's color and less of the incoming color affects the pixel. While this gives a visual sense of transparency to a surface [554], it has little physical basis.

Multiplying the incoming color by a transmitter's filter color is more in keeping with how the physical world works. Say a blue-tinted filter is attached to a camera lens. The filter absorbs or reflects light in such a way that its spectrum resolves to a blue color. The exact spectrum is usually unimportant, so using the RGB equivalent color works fairly well in practice. For a thin object like a filter, stained glass, windows, etc., we simply ignore the thickness and assign a filter color.

For objects that vary in thickness, the amount of light absorption can be computed using the Beer-Lambert Law:

$$T = e^{-\alpha' cd}, \quad (9.26)$$

where  $T$  is the transmittance,  $\alpha'$  is the absorption coefficient,  $c$  is the concentration of the absorbing material, and  $d$  is the distance traveled through the glass, i.e., the thickness. The key idea is that the transmitting medium, e.g., the glass, absorbs light relative to  $e^{-d}$ . While  $\alpha'$  and  $c$  are physical values, to make a transmittance filter easy to control, Bavoil [74] sets the value  $c$  to be the least amount of transmittance at some given thickness, defined to be a maximum concentration of 1.0. These settings give

$$T = e^{-\alpha' d_{\text{user}}}, \quad (9.27)$$

so

$$\alpha' = \frac{-\log(T)}{d_{\text{user}}}. \quad (9.28)$$

Note that a transmittance of 0 needs to be handled as a special case. A simple solution is to add some small epsilon, e.g., 0.000001, to each  $T$ . The effect of color filtering is shown in Figure 9.47.

**EXAMPLE: TRANSMITTANCE.** The user decides the darkest transmittance filter color should be (0.3,0.7,0.1) for a thickness of 4.0 inches (the unit type does not matter, as long as it is consistent). The  $\alpha'$  values for these RGB channels are:

$$\begin{aligned} \alpha'_r &= \frac{-\log(0.3)}{4.0} &= 0.3010, \\ \alpha'_g &= \frac{-\log(0.7)}{4.0} &= 0.0892, \\ \alpha'_b &= \frac{-\log(0.1)}{4.0} &= 0.5756. \end{aligned} \quad (9.29)$$

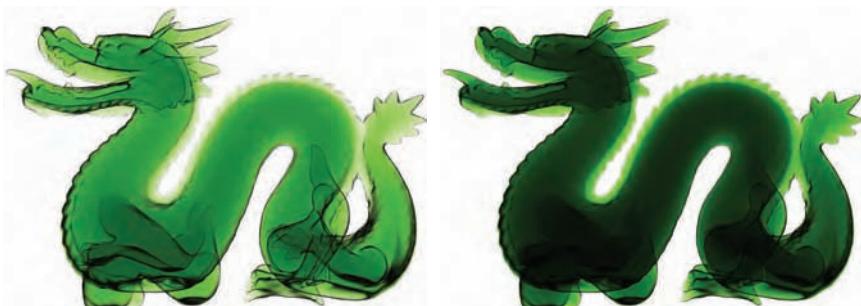


**Figure 9.47.** Translucency with different absorption factors. (*Images courtesy of Louis Bavoil.*)

In creating the material, the artist sets the concentration down to 0.6, letting more light through. During shading, thickness of the transmitter is found to be 1.32 for a fragment. The transmitter filter color is then:

$$\begin{aligned} T_r &= e^{-0.3010 \times 0.6 \times 1.32} = 0.7879, \\ T_g &= e^{-0.0892 \times 0.6 \times 1.32} = 0.9318, \\ T_b &= e^{-0.5756 \times 0.6 \times 1.32} = 0.6339. \end{aligned} \quad (9.30)$$

The color stored in the underlying pixel is then multiplied by this color (0.7879, 0.9318, 0.6339), to get the resulting transmitted color.  $\square$

Varying the transmittance by distance traveled can work as a reasonable approximation for other phenomena. For example, Figure 10.40 on page 500 shows layered fog using the fog's thickness. In this case, the incoming light is attenuated by absorption and by out-scattering, where light bounces off the water particles in the fog in a different direction. In-scattering, where light from elsewhere in the environment bounces off the particles toward the eye, is used to represent the white fog.

Computing the actual thickness of the transmitting medium can be done in any number of ways. A common, general method to use is to first render the surface where the view ray exits the transmitter. This surface could be the backface of a crystal ball, or could be the sea floor (i.e., where the water ends). The  $z$ -depth or location of this surface is stored. Then the transmitter's surface is rendered. In a shader program, the stored  $z$ -depth is accessed and the distance between it and the transmitter's surface location is computed. This distance is then used to compute the amount of transmittance for the incoming light, i.e., for the object behind the transmitter.

This method works if it is guaranteed that the transmitter has one entry and one exit point per pixel, as with a crystal ball or seabed. For more elab-

orate models, e.g., a glass sculpture or other object with concavities, two or more separate spans may absorb incoming light. Using depth peeling, as discussed in Section 5.7, we can render the transmitter surfaces in precise back-to-front order. As each frontface is rendered, the distance through the transmitter is computed and used to compute absorption. Applying each of these in turn gives the proper final transmittance. Note that if all transmitters are made of the same material at the same concentration, the shade could be computed once at the end using the summed distances, if the surface has no reflective component. See Section 10.15 about fog for related techniques.

Most transmitting media have an index of refraction significantly higher than that of air. This will cause light to undergo external reflection when entering the medium, and internal reflection when exiting it. Of the two, internal reflection will attenuate light more strongly. At glancing angles, all the light will bounce back from the interface, and none will be transmitted (*total internal reflection*). Figure 9.48 shows this effect; objects underwater are visible when looking directly into the water, but looking farther out, at a grazing angle, the water's surface mostly hides what is beneath the waves. There are a number of articles on handling reflection, absorption, and refraction for large bodies of water [174, 608, 729]. Section 7.5.3 details how reflectance and transmittance vary with material and angle.



**Figure 9.48.** Water, taking into account the Fresnel effect, where reflectivity increases as the angle to the transmitter's surface becomes shallow. Looking down, reflectivity is low and we can see into the water. Near the horizon the water becomes much more reflective. (Image from “Crysis” courtesy of Crytek.)

## 9.5 Refractions

For simple transmittance, we assume that the incoming light comes from directly beyond the transmitter. This is a reasonable assumption when the front and back surfaces of the transmitter are parallel and the thickness is not great, e.g., for a pane of glass. For other transparent media, the index of refraction plays an important part. Snell's Law, which describes how light changes direction when a transmitter's surface is encountered, is described in Section 7.5.3.

Bec [78] presents an efficient method of computing the refraction vector. For readability (because  $n$  is traditionally used for the index of refraction in Snell's equation), define  $\mathbf{N}$  as the surface normal and  $\mathbf{L}$  as the direction to the light:

$$\mathbf{t} = (w - k)\mathbf{N} - n\mathbf{L}, \quad (9.31)$$

where  $n = n_1/n_2$  is the relative index of refraction, and

$$\begin{aligned} w &= n(\mathbf{L} \cdot \mathbf{N}), \\ k &= \sqrt{1 + (w - n)(w + n)}. \end{aligned} \quad (9.32)$$

The resulting refraction vector  $\mathbf{t}$  is returned normalized.

This evaluation can nonetheless be expensive. Oliveira [962] notes that because the contribution of refraction drops off near the horizon, an approximation for incoming angles near the normal direction is

$$\mathbf{t} = -c\mathbf{N} - \mathbf{L}, \quad (9.33)$$

where  $c$  is somewhere around 1.0 for simulating water. Note that the resulting vector  $\mathbf{t}$  needs to be normalized when using this formula.

The index of refraction varies with wavelength. That is, a transparent medium will bend different colors of light at different angles. This phenomenon is called *dispersion*, and explains why prisms work and why rainbows occur. Dispersion can cause a problem in lenses, called *chromatic aberration*. In photography, this phenomenon is called *purple fringing*, and can be particularly noticeable along high contrast edges in daylight. In computer graphics we normally ignore this effect, as it is usually an artifact to be avoided. Additional computation is needed to properly simulate the effect, as each light ray entering a transparent surface generates a set of light rays that must then be tracked. As such, normally a single refracted ray is used. In practical terms, water has an index of refraction of approximately 1.33, glass typically around 1.5, and air essentially 1.0.

Some techniques for simulating refraction are somewhat comparable to those of reflection. However, for refraction through a planar surface, it is not as straightforward as just moving the viewpoint. Diefenbach [252] discusses this problem in depth, noting that a homogeneous transform matrix



**Figure 9.49.** Refraction and reflection by a glass ball of a cubic environment map, with the map itself used as a skybox background. (*Image courtesy of NVIDIA Corporation.*)

is needed to properly warp an image generated from a refracted viewpoint. In a similar vein, Vlachos [1306] presents the shears necessary to render the refraction effect of a fish tank.

Section 9.3.1 gave some techniques where the scene behind a refractor was used as a limited-angle environment map. A more general way to give an impression of refraction is to generate a cubic environment map from the refracting object’s position. The refracting object is then rendered, accessing this EM by using the refraction direction computed for the front-facing surfaces. An example is shown in Figure 9.49. These techniques give the impression of refraction, but usually bear little resemblance to physical reality. The refraction ray gets redirected when it enters the transparent solid, but the ray never gets bent the second time, when it is supposed to leave this object; this backface never comes into play. This flaw sometimes does not matter, because the eye is forgiving for what the right appearance should be.

Oliveira and Brauwiers [965] improve upon this simple approximation by taking into account refraction by the backfaces. In their scheme, the backfaces are rendered and the depths and normals stored. The frontfaces are then rendered and rays are refracted from these faces. The idea is to find where on the stored backface data these refracted rays fall. Once the



**Figure 9.50.** On the left, the transmitter refracts both nearby objects and the surrounding skybox [1386]. On the right, caustics are generated via hierarchical maps similar in nature to shadow maps [1388]. (*Images courtesy of Chris Wyman, University of Iowa.*)

backface texel is found where the ray exits, the backface’s data at that point properly refracts the ray, which is then used to access the environment map. The hard part is to find this backface pixel. The procedure they use to trace the rays is in the spirit of relief mapping (Section 6.7.4). The backface  $z$ -depths are treated like a heightfield, and each ray walks through this buffer until an intersection is found. Depth peeling can be used for multiple refractions. The main drawback is that total internal reflection cannot be handled. Using Heckbert’s regular expression notation [519], described at the beginning of this chapter, the paths simulated are then  $L(D|S)SSE$ : The eye sees a refractive surface, a backface then also refracts as the ray leaves, and some surface in an environment map is then seen through the transmitter.

Davis and Wyman [229] take this relief mapping approach a step farther, storing both back and frontfaces as separate heightfield textures. Nearby objects behind the transparent object can be converted into color and depth maps so that the refracted rays treat these as local objects. An example is shown in Figure 9.50. In addition, rays can have multiple bounces, and total internal reflection can be handled. This gives a refractive light path of  $L(D|S)S + SE$ . A limitation of all of these image-space refraction schemes is that if a part of the model is rendered offscreen, the clipped data cannot refract (since it does not exist).

Simpler forms of refraction ray tracing can be used directly for basic geometric objects. For example, Vlachos and Mitchell [1303] generate the refraction ray and use ray tracing in a pixel shader program to find which wall of the water’s container is hit. See Figure 9.51.

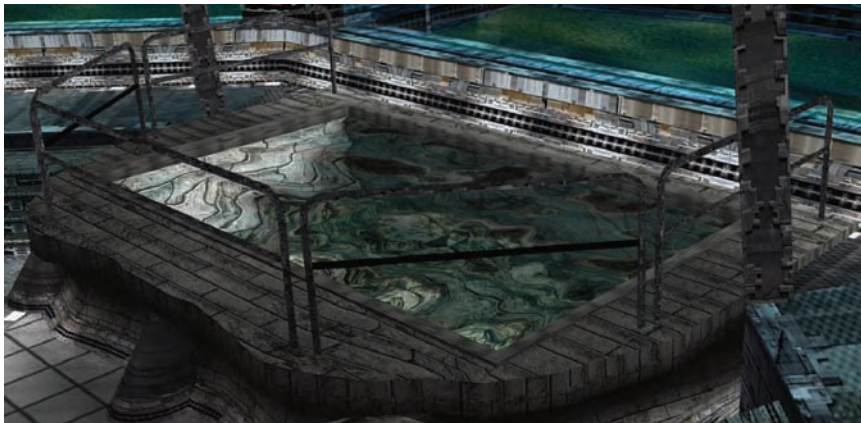


**Figure 9.51.** A pool of water. The walls of the pool appear warped, due to refraction through the water. (*Image courtesy of Alex Vlachos, ATI Technologies Inc.*)

## 9.6 Caustics

The type of refraction discussed in the previous section is that of radiance coming from some surface, traveling through a transmitter, then reaching the eye. In practice, the computation is reversed: The eye sees the surface of the transmitter, then the transmitter's surfaces determine what location and direction are used to sample the radiance. Another phenomenon can occur, called a *caustic*, in which light is focused by reflective or refractive surfaces. A classic example for reflection is the cardioid caustic seen inside a coffee mug. Refractive caustics are often more noticeable: light focused through a crystal ornament, a lens, or a glass of water is an everyday example. See Figure 9.52.

There are two major classes of caustic rendering techniques: image space and object space. The first class uses images to capture the effect of the caustic volume [222, 584, 702, 1153, 1234, 1387]. As an example, Wyman [1388] presents a three-pass algorithm for this approach. In the first, the scene is rendered from the view of the light, similar to shadow mapping. Each texel where a refractive or reflective object is seen will cause the light passing through to be diverted and go elsewhere. This diverted illumination is tracked; once a diffuse object is hit, the texel location is recorded as having received illumination. This image with depth is called the *photon buffer*. The second step is to treat each location that received light as a point object. These points represent where light has accumulated. By treating them as small spheres that drop off in intensity, known as *splats*, these primitives are then transformed with a vertex shader pro-



**Figure 9.52.** Real-world caustics from reflection and refraction.

gram to the eye's viewpoint and rendered to a *caustic map*. This caustic map is then projected onto the scene, along with a shadow map, and is used to illuminate the pixels seen. A problem with this approach is that only so many photons can be tracked and deposited, and results can exhibit serious artifacts due to undersampling. Wyman extends previous techniques by using a mipmap-based approach to treat the photons in a more efficient hierarchical manner. By analyzing the amount of convergence or divergence of the photons, various contributions can be represented by smaller or larger splats on different levels of the caustic's mipmap. The results of this approach can be seen in Figure 9.50.

Ernst et al. [319] provide an object-space algorithm, using the idea of a warped caustic volume. In this approach, objects are tagged as able to receive caustics, and able to generate them (i.e., they are specular or refractive). Each vertex on each generator has a normal. The normal and the light direction are used to compute the refracted (or reflected) ray direction for that vertex. For each triangle in the generator, these three refracted (or reflected) rays will form the sides of a caustic volume. Note that these sides are in general warped, i.e., they are the surface formed by two points from the generating triangle, and the corresponding two points on the “receiver” triangle. This makes the sides of the volume into bilinear patches. The volume represents how the light converges or diverges as a function of the distance from the generating triangle. These caustic volumes will transport the reflected and refracted light.

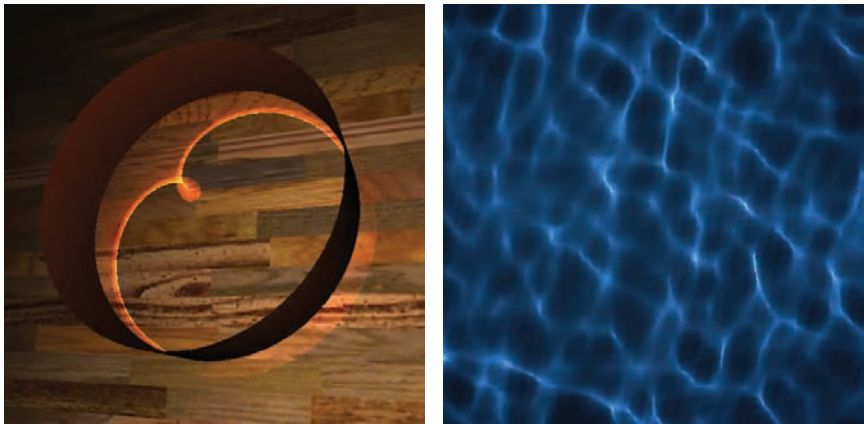


**Figure 9.53.** The caustic volumes technique can generate various types of caustics, such as those from a metallic ring or from the ocean's surface [319].

Caustics are computed in two passes. First the receivers are all rendered to establish a screen-filling texture that holds their world positions. Then each of the caustic volumes is rendered in turn. This rendering process consists of drawing the bounding box for a caustic volume in order to force evaluation of a set of pixels. The bounding box also limits the number of pixels that need to be evaluated. At each pixel, a fragment shader program tests whether the receiver's location is inside the caustic volume. If it is, the caustic's intensity at the point is computed and accumulated. Caustic volumes can converge on a location, giving it a high intensity. This process results in light being added where it focuses.

See Figure 9.53. The right-hand image shows a caustic pattern due to ocean water. Such caustic patterns from large bodies of water are a special case that is often handled by particular shaders tuned for the task. For example, Guardado and Sánchez-Crespo [464] cast a ray from the ocean bottom straight up to the ocean surface. The surface normal is used to generate a refraction ray direction. The more this ray's direction deviates, the less sunlight is assumed to reach the location. This simple shader is not physically correct—it traces rays in the wrong direction and assumes the sun is directly overhead—but rapidly provides plausible results.

## 9.7 Global Subsurface Scattering

When light travels inside a substance, some of it may be absorbed (see Section 9.4). Absorption changes the light's amount (and possibly its spectral

distribution), but not its direction of propagation. Any discontinuities in the substance, such as air bubbles, foreign particles, density variations, or structural changes, may cause the light to be scattered. Unlike absorption, scattering changes the direction, but not the amount, of light. Scattering inside a solid object is called *subsurface scattering*. The visual effect of scattering in air, fog, or smoke is often simply referred to as “fog” in real-time rendering, though the more correct term is *atmospheric scattering*. Atmospheric scattering is discussed in Section 10.15.

In some cases, the scale of scattering is extremely small. Scattered light is re-emitted from the surface very close to its original point of entry. This means that the subsurface scattering can be modeled via a BRDF (see Section 7.5.4). In other cases, the scattering occurs over a distance larger than a pixel, and its global nature is apparent. To render such effects, special methods must be used.

### 9.7.1 Subsurface Scattering Theory

Figure 9.54 shows light being scattered through an object. Scattering causes incoming light to take many different paths through the object. Since it is impractical to simulate each photon separately (even for offline rendering), the problem must be solved probabilistically, by integrating over possible paths, or by approximating such an integral. Besides scatter-

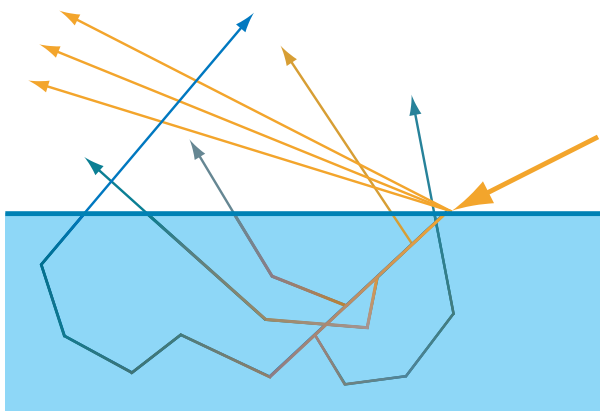


**Figure 9.54.** Light scattering through an object. Initially the light transmitted into the object travels in the refraction direction, but scattering causes it to change direction repeatedly until it leaves the material. The length of the path through the material determines the percentage of light lost to absorption.

ing, light traveling through the material also undergoes absorption. The absorption obeys an exponential decay law with respect to the total travel distance through the material (see Section 9.4). Scattering behaves similarly. The probability of the light *not* being scattered obeys an exponential decay law with distance.

The absorption decay constants are often spectrally variant (have different values for R, G, and B). In contrast, the scattering probability constants usually do not have a strong dependence on wavelength. That said, in certain cases, the discontinuities causing the scattering are on the order of a light wavelength or smaller. In these circumstances, the scattering probability does have a significant dependence on wavelength. Scattering from individual air molecules is an example. Blue light is scattered more than red light, which causes the blue color of the daytime sky. A similar effect causes the blue colors often found in bird feathers.

One important factor that distinguishes the various light paths shown in Figure 9.54 is the number of scattering events. For some paths, the light leaves the material after being scattered once; for others, the light is scattered twice, three times, or more. Scattering paths are commonly grouped into *single scattering* and *multiple scattering* paths. Different rendering techniques are often used for each group.

## 9.7.2 Wrap Lighting

For many solid materials, the distances between scattering events are short enough that single scattering can be approximated via a BRDF. Also, for some materials, single scattering is a relatively weak part of the total scattering effect, and multiple scattering predominates—skin is a notable example. For these reasons, many subsurface scattering rendering techniques focus on simulating multiple scattering.

Perhaps the simplest of these is *wrap lighting* [139]. Wrap lighting was discussed on page 294 as an approximation of area light sources. When used to approximate subsurface scattering, it can be useful to add a color shift [447]. This accounts for the partial absorption of light traveling through the material. For example, when rendering skin, a red color shift could be used.

When used in this way, wrap lighting attempts to model the effect of multiple scattering on the shading of curved surfaces. The “leakage” of light from adjacent points into the currently shaded point softens the transition area from light to dark where the surface curves away from the light source. Kolchin [683] points out that this effect depends on surface curvature, and he derives a physically based version. Although the derived expression is somewhat expensive to evaluate, the ideas behind it are useful.

### 9.7.3 Normal Blurring

Stam [1211] points out that multiple scattering can be modeled as a *diffusion* process. Jensen et al. [607] further develop this idea to derive an analytical BSSRDF model.<sup>9</sup> The diffusion process has a spatial blurring effect on the outgoing radiance.

This blurring affects only diffuse reflectance. Specular reflectance occurs at the material surface and is unaffected by subsurface scattering. Since normal maps often encode small-scale variation, a useful trick for subsurface scattering is to apply normal maps to only the specular reflectance [431]. The smooth, unperturbed normal is used for the diffuse reflectance. Since there is no added cost, it is often worthwhile to apply this technique when using other subsurface scattering methods.

For many materials, multiple scattering occurs over a relatively small distance. Skin is an important example, where most scattering takes place over a distance of a few millimeters. For such materials, the trick of not perturbing the diffuse shading normal may be sufficient by itself. Ma et al. [804] extend this method, based on measured data. They measured reflected light from scattering objects and found that while the specular reflectance is based on the geometric surface normals, subsurface scattering makes diffuse reflectance behave as if it uses blurred surface normals. Furthermore, the amount of blurring can vary over the visible spectrum. They propose a real-time shading technique using independently acquired normal maps for the specular reflectance and for the R, G and B channels of the diffuse reflectance [166]. Since these diffuse normal maps typically resemble blurred versions of the specular map, it is straightforward to modify this technique to use a single normal map, while adjusting the mipmap level. This adjustment should be performed similarly to the adjustment of environment map mipmap levels discussed on page 310.

### 9.7.4 Texture Space Diffusion

Blurring the diffuse normals accounts for some visual effects of multiple scattering, but not for others, such as softened shadow edges. Borshukov and Lewis [128, 129] popularized the concept of *texture space diffusion*.<sup>10</sup> They formalize the idea of multiple scattering as a blurring process. First, the surface irradiance (diffuse lighting) is rendered into a texture. This is done by using texture coordinates as positions for rasterization (the real positions are interpolated separately for use in shading). This texture is blurred, and then used for diffuse shading when rendering. The shape and

---

<sup>9</sup>The BSSRDF is a generalization of the BRDF for the case of global subsurface scattering [932].

<sup>10</sup>This idea was introduced by Lensch et al. [757] as part of a different technique, but the version presented by Borshukov and Lewis has been the most influential.

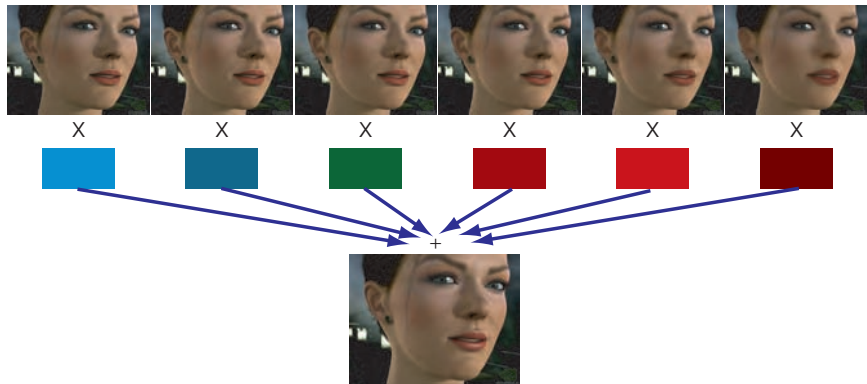


**Figure 9.55.** Texture space multilayer diffusion. Six different blurs are combined using RGB weights. The final image is the result of this linear combination, plus a specular term. (*Images courtesy NVIDIA Corporation.*)

size of the filter depend on the material, and often on the wavelength, as well. For example, for skin, the R channel is filtered with a wider filter than G or B, causing reddening near shadow edges. The correct filter for simulating subsurface scattering in most materials has a narrow spike in the center, and a wide, shallow base. This technique was first presented for use in offline rendering, but real-time GPU implementations were soon proposed by NVIDIA [246, 247, 248, 447] and ATI [431, 432, 593, 1106]. The presentations by d'Eon et al. [246, 247, 248] represent the most complete treatment of this technique so far, including support for complex filters mimicking the effect of multi-layered subsurface structure. Donner and Jensen [273] show that such structures produce the most realistic skin renderings. The full system presented by d'Eon produces excellent results, but is quite expensive, requiring a large number of blurring passes (see Figure 9.55). However, it can easily be scaled back to increase performance, at the cost of some realism.

### 9.7.5 Depth-Map Techniques

The techniques discussed so far model scattering over only relatively small distances. Other techniques are needed for materials exhibiting large-scale scattering. Many of these focus on large-scale single scattering, which is easier to model than large-scale multiple scattering.

The ideal simulation for large-scale single scattering can be seen on the left side of Figure 9.56. The light paths change direction on entering and exiting the object, due to refraction. The effects of all the paths need to be summed to shade a single surface point. Absorption also needs to be taken

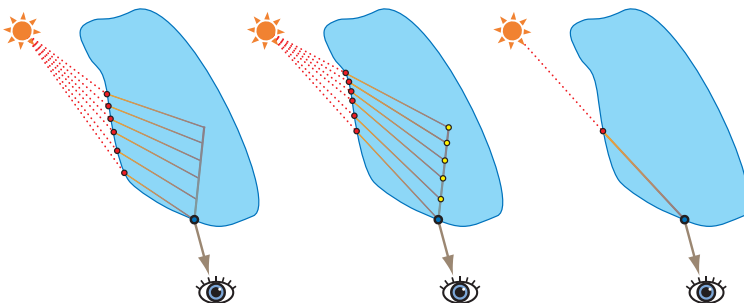


**Figure 9.56.** On the left, the ideal situation, in which light refracts when entering the object, then all scattering contributions that would properly refract upon leaving the object are computed. The middle shows a computationally simpler situation, in which the rays refract only on exit. The right shows a much simpler, and therefore faster, approximation, where only a single ray is considered.

into account—the amount of absorption in a path depends on its length inside the material. Computing all these refracted rays for a single shaded point is expensive even for offline renderers, so the refraction on entering the material is usually ignored, and only the change in direction on exiting the material is taken into account [607]. This approximation is shown in the center of Figure 9.56. Since the rays cast are always in the direction of the light, Hery [547, 548] points out that light space depth maps (typically used for shadowing) can be used instead of ray casting. Multiple points (shown in yellow) on the refracted view ray are sampled, and a lookup into the light space depth map, or shadow map, is performed for each one. The result can be projected to get the position of the red intersection point. The sum of the distances from red to yellow and yellow to blue points is used to determine the absorption. For media that scatter light anisotropically, the scattering angle also affects the amount of scattered light.

Performing depth map lookups is faster than ray casting, but the multiple samples required make Hery’s method too slow for most real-time rendering applications. Green [447] proposes a faster approximation, shown on the right side of Figure 9.56. Instead of multiple samples along the refracted ray, a single depth map lookup is performed at the shaded point. Although this method is somewhat nonphysical, its results can be convincing. One problem is that details on the back side of the object can show through, since every change in object thickness will directly affect the shaded color. Despite this, Green’s approximation is effective enough to be used by Pixar for films such as *Ratatouille* [460]. Pixar refers to this technique as *Gummi Lights*. Another problem (shared with Hery’s implementation, but not Pixar’s) is that the depth map should not contain multiple objects, or highly nonconvex objects. This is because it is

assumed that the entire path between the shaded (blue) point and the red intersection point lies within the object.<sup>11</sup>

Modeling large-scale multiple scattering in real time is quite difficult, since each surface point can be influenced by light incoming from any other surface point. Dachsbaecher and Stamminger [218] propose an extension of the light space depth map method, called *translucent shadow maps*, for modeling multiple scattering. Additional information, such as irradiance and surface normal, is stored in light space textures. Several samples are taken from these textures (as well as from the depth map) and combined to form an estimation of the scattered radiance. A modification of this technique was used in NVIDIA’s skin rendering system [246, 247, 248]. Mertens et al. [859] propose a similar method, but using a texture in screen space, rather than light space.

### 9.7.6 Other Methods

Several techniques assume that the scattering object is rigid and precalculate the proportion of light scattered among different parts of the object [499, 500, 757]. These are similar in principle to *precomputed radiance transfer* techniques (discussed in Section 9.11). Precomputed radiance transfer can be used to model small- or large-scale multiple scattering on rigid objects, under low-frequency distant lighting. Isidoro [593] discusses several practical issues relating to the use of precomputed radiance transfer for subsurface scattering, and also details how to combine it with other subsurface scattering methods, such as texture space diffusion.

Modeling large scale multiple scattering is even more difficult in the case of deforming objects. Mertens et al. [860] present a technique based on a hierarchical surface representation. Scattering factors are dynamically computed between hierarchical elements, based on distance. A GPU implementation is not given. In contrast, Hoberock [553] proposes a GPU-based method derived from Bunnell’s [146] hierarchical disk-based surface model, previously used for dynamic ambient occlusion.

## 9.8 Full Global Illumination

So far, this chapter has presented a “piecemeal” approach to solving the rendering equation. Individual parts or special cases from the rendering equation were solved with specialized algorithms. In this section, we will present algorithms that are designed to solve most or all of the rendering equation. We will refer to these as *full global illumination* algorithms.

---

<sup>11</sup>Pixar gets around this problem by using a type of *deep shadow map*.

In the general case, full global illumination algorithms are too computationally expensive for real-time applications. Why do we discuss them in a book about real-time rendering? The first reason is that in static or partially static scenes, full global illumination algorithms can be run as a pre-process, storing the results for later use during rendering. This is a very popular approach in games, and will be discussed in detail in Sections 9.9, 9.10 and 9.11.

The second reason is that under certain restricted circumstances, full global illumination algorithms can be run at rendering time to produce particular visual effects. This is a growing trend as graphics hardware becomes more powerful and flexible.

Radiosity and ray tracing are the first two algorithms introduced for global illumination in computer graphics, and are still in use today. We will also present some other techniques, including some intended for real time implementation on the GPU.

### 9.8.1 Radiosity

The importance of indirect lighting to the appearance of a scene was discussed in Chapter 8. Multiple bounces of light among surfaces cause a subtle interplay of light and shadow that is key to a realistic appearance. Interreflections also cause *color bleeding*, where the color of an object appears on adjacent objects. For example, walls will have a reddish tint where they are adjacent to a red carpet. See Figure 9.57.

*Radiosity* [427] was the first computer graphics technique developed to simulate bounced light between diffuse surfaces. There have been whole books written on this algorithm [40, 183, 1181], but the basic idea is relatively simple. Light bounces around an environment; you turn a light on



**Figure 9.57.** Color bleeding. The light shines on the beds and carpets, which in turn bounce light not only to the eye but to other surfaces in the room, which pick up their color. (Images generated using the Enlighten SDK courtesy of Geomerics Ltd.)

and the illumination quickly reaches equilibrium. In this stable state, each surface can be considered as a light source in its own right. When light hits a surface, it can be absorbed, diffusely reflected, or reflected in some other fashion (specularly, anisotropically, etc.). Basic radiosity algorithms first make the simplifying assumption that all indirect light is from diffuse surfaces. This assumption fails for places with polished marble floors or large mirrors on the walls, but for most architectural settings this is a reasonable approximation. The BRDF of a diffuse surface is a simple, uniform hemisphere, so the surface's radiance from any direction is proportional purely to the irradiance multiplied by the reflectance of the surface. The outgoing radiance is then

$$L_{\text{surf}} = \frac{rE}{\pi}, \quad (9.34)$$

where  $E$  is the irradiance and  $r$  is the reflectance of the surface. Note that, though the hemisphere covers  $2\pi$  steradians, the integration of the cosine term for surface irradiance brings this divisor down to  $\pi$ .

To begin the process, each surface is represented by a number of patches (e.g., polygons, or texels on a texture). The patches do not have to match one-for-one with the underlying polygons of the rendered surface. There can be fewer patches, as for a mildly curving spline surface, or more patches can be generated during processing, in order to capture features such as shadow edges.

To create a radiosity solution, the basic idea is to create a matrix of *form factors* among all the patches in a scene. Given some point or area on the surface (such as at a vertex or in the patch itself), imagine a hemisphere above it. Similar to environment mapping, the entire scene can be projected onto this hemisphere. The form factor is a purely geometric value denoting the proportion of how much light travels directly from one patch to another. A significant part of the radiosity algorithm is accurately determining the form factors between the receiving patch and each other patch in the scene. The area, distance, and orientations of both patches affect this value.

The basic form of a differential form factor,  $f_{ij}$ , between a surface point with differential area,  $da_i$ , to another surface point with  $da_j$ , is

$$df_{ij} = \frac{\overline{\cos \theta_i} \overline{\cos \theta_j}}{\pi d^2} h_{ij} da_j, \quad (9.35)$$

where  $\theta_i$  and  $\theta_j$  are the angles between the ray connecting the two points and the two surface normals. If the receiving patch faces away from the viewed patch, or vice versa, the form factor is 0, since no light can travel from one to the other. Furthermore,  $h_{ij}$  is a visibility factor, which is either 0 (not visible) or 1 (visible). This value describes whether the two points can “see” each other, and  $d$  is the distance between the two points. See Figure 9.58.

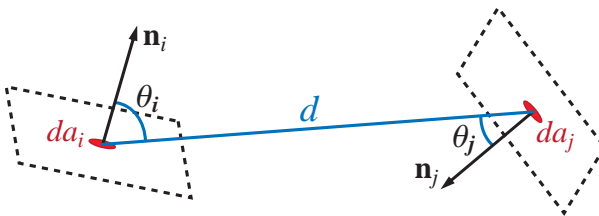


**Figure 9.58.** The form factor between two surface points.

This formula is not practical since the form factor cannot be computed between all points in a scene. Instead, larger areas are used, and so Equation 9.35 has to be integrated. There are a variety of techniques to do so [288]. As the viewed patch nears the horizon of the receiving patch's hemisphere its effect lessens, just the same as how a light's effect on a diffuse surface lessens under the same circumstances.

Another important factor is  $h_{ij}$ , the visibility between two patches. If something else partially or fully blocks two patches from seeing each other, the form factor is correspondingly reduced. Thinking back on the hemisphere, there is only one opaque surface visible in any given direction. Calculating the form factor of a patch for a receiving point is equivalent to finding the area of the patch visible on the hemisphere and then projecting the hemisphere onto the ground plane. The proportion of the circle on the ground plane beneath the hemisphere that the patch covers is the patch's form factor. See Figure 9.59. Called the *Nusselt analog*, this projection effectively folds in the cosine term that affects the importance of the viewed patch to the receiving point.

Given the geometric relations among the various patches, some patches are designated as being emitters (i.e., lights). Energy travels through the system, reaching equilibrium. One way used to compute this equilibrium (in fact, the first way discovered, using heat transfer methods) is to form a square matrix, with each row consisting of the form factors for a given patch times that patch's reflectivity. The *radiosity equation* is then

$$\begin{pmatrix} e_1 \\ e_2 \\ \vdots \\ e_n \end{pmatrix} = \begin{pmatrix} 1 - r_1 f_{11} & -r_1 f_{12} & \cdots & -r_1 f_{1n} \\ -r_2 f_{21} & 1 - r_2 f_{22} & \cdots & -r_2 f_{2n} \\ \vdots & \vdots & \ddots & \vdots \\ -r_n f_{n1} & -r_n f_{n2} & \cdots & 1 - r_n f_{nn} \end{pmatrix} \begin{pmatrix} b_1 \\ b_2 \\ \vdots \\ b_n \end{pmatrix}, \quad (9.36)$$

where  $r_i$  is the reflectance of patch  $i$ ,  $f_{ij}$  the form factor between two patches ( $i$  and  $j$ ),  $e_i$  the initial exitance (i.e., nonzero only for light sources), and  $b_i$  the radiosities to be discovered. Performing Gaussian elimination on this matrix gives the exitance (radiosity) of each patch, so providing the

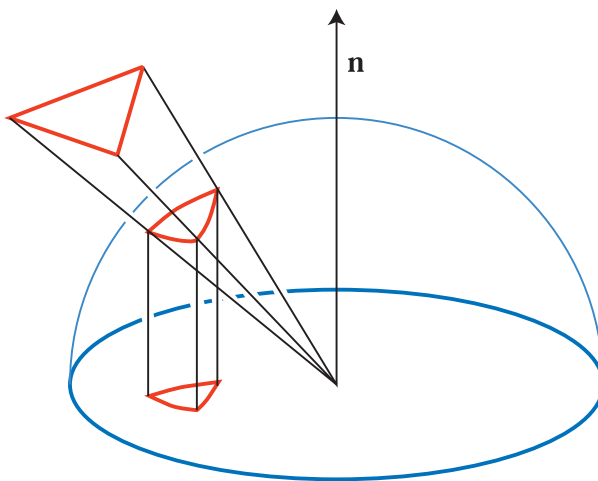


**Figure 9.59.** For a given receiving point, a patch is projected onto the hemisphere, then onto the ground plane to compute the form factor between the two.

radiance of the surface, since the radiance is constant (i.e., independent of view angle) for a diffuse material.

A significant amount of research has focused on simplifying the solution of this matrix. For example, the idea behind the progressive refinement algorithm is to shoot the light out from the light sources and collect it at each patch. The patch receiving the most light is then treated like an emitter, bouncing light back into the environment. The next brightest patch then shoots its light out, possibly starting to refill the first shot patch with new energy to shoot. This process continues until some level of diminishing returns is reached. This algorithm has a number of advantages. Form factors are created for only one column of the radiosity equation for each patch shoot, an  $O(n)$  process. After any given shoot step, a preliminary radiosity solution can be output. This means a usable solution can be rapidly generated and displayed in seconds or less, with the ability to refine the solution over time with unused cycles or separate cores. Figure 9.60 shows an example of an interactive system that takes into account strong indirect sources of light.

Typically, the radiosity process itself is usually performed off-line. Coombe and Harris [198] discuss using the GPU to accelerate computing progressive refinement, but at non-interactive rates. GPUs continue to get faster, but scenes also get more complex. Regardless of how it is computed, the resulting illumination is applied to the surfaces by either storing the amount of light reaching each vertex and interpolating, or by storing a light map for the surface (see Section 9.9.1 for more details). See Fig-



**Figure 9.60.** On the left, the scene is lit only by direction illumination from the lamp. The radiosity lighting on the right is computed once per frame. New lightmaps are computed each frame, containing the diffuse indirect light color along with a vector holding the approximate overall direction of this illumination. This rough lighting vector allows the use of normal maps and low-frequency specular effects. (*Images generated using the Enlighten SDK courtesy of Geomerics Ltd.*)

ure 12.26 on page 567 for an example of a radiosity solution and page 566 for its underlying mesh.

Classical radiosity can compute interreflections and soft shadows from area lights in diffuse environments. Using the notation introduced at the beginning of this chapter, its light transport set is  $LD * E$ . It can follow an effectively unlimited number of diffuse bounces, but it is less well suited to glossy environments and computing sharp reflections and shadows. For those effects, *ray tracing* is typically used, and it is described in the next section.

## 9.8.2 Ray Tracing

Ray tracing is a rendering method in which rays are used to determine the visibility of various elements. The basic mechanism is very simple, and in fact, functional ray tracers have been written that fit on the back of a business card [523]. In classical ray tracing, rays are shot from the eye through the pixel grid into the scene. For each ray, the closest object is found. This intersection point then can be determined to be illuminated or in shadow by shooting a ray from it to each light and finding if any objects are in between. Opaque objects block the light, transparent objects attenuate it.

Other rays can be spawned from an intersection point. If the surface is shiny, a ray is generated in the reflection direction. This ray picks up the color of the first object intersected, which in turn has its intersection point tested for shadows. This reflection process is recursively repeated until a diffuse surface is hit or some maximum depth or contribution is reached. Environment mapping can be thought about as a very simplified version of ray traced reflections; the ray reflects and the radiance coming from

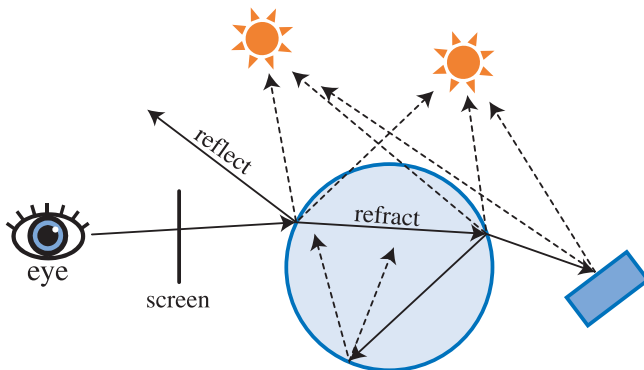


**Figure 9.61.** A single ray traces from the eye through the screen into a scene. It hits a glass sphere and generates four rays; two to the two lights and one reflection and one refraction ray. These rays continue on, possibly spawning yet more rays.

the reflection direction is retrieved. The difference is that, in ray tracing, nearby objects can be intersected by the reflection rays. Note that if these nearby objects are all missed, an environment map could still be used to approximate the rest of the environment.

Rays can also be generated in the direction of refraction for transparent solid objects, again recursively evaluated. When the maximum number of reflections and refractions is reached, a ray tree has been built up. This tree is then evaluated from the deepest reflection and refraction rays on back to the root, so yielding a color for the sample. See Figure 9.61. Using the path transport notation, ray tracing simulates  $LD?S * E$  paths—only one diffuse surface can be part of the light transport path, and if present it must be the first the light illuminates.

Classical ray tracing provides sharp reflection, refraction, and shadow effects. Figure 9.62 shows some examples. Because each sample on the image plane is essentially independent, any point sampling and filtering scheme desired can be used for antialiasing. Another advantage of ray tracing is that true curved surfaces and other untessellated objects can be intersected directly by rays.

In classical ray tracing, rays are spawned in the most significant directions: toward the lights and for mirror reflections and refractions. This handles direct lighting for all surface types and interreflections for purely specular surfaces, but does not handle glossy and diffuse interreflections. *Monte Carlo ray tracing* handles interreflections between surfaces with arbitrary BRDFs by picking a random direction for each reflection or refraction ray. This random direction is influenced by the BRDF. For example, for a glossy surface with a narrow Phong reflection lobe, reflection rays would be much more likely to be spawned near the center of the lobe than



**Figure 9.62.** Three areas where interactive ray tracing can excel. In the upper left image, true reflections and refractions are computed. The free-form surfaces from the model are directly ray traced without having to convert them into triangle meshes, allowing physically precise visualization. In the upper right, volumes are visualized directly via rays, without the need to explicitly find the surfaces before rendering. The lower image shows a scene with 1.5 billion potentially visible triangles. It is very costly because of the many alpha textured leaves. On 16 Opteron cores using untuned code (no SSE) it runs at about 2 fps (one directional light, 640x480). (*Images courtesy of Computer Graphics Group, Saarland University.*)

elsewhere. Weighting the random direction in this way is called *importance sampling*.

In the case of glossy surfaces, importance sampling can drastically reduce the number of rays that need to be cast. The reduction is far more modest in the case of Lambertian surfaces, where the sampling is essentially cosine-weighted. Monte Carlo ray tracing fully solves Kajiya's rendering equation [619], given enough time and rays.

There are two main types of Monte Carlo ray tracing. *Path tracing* takes the approach of having a single ray reflect or refract through the scene, changing direction at each surface intersection. To get a good sampling

of surface illumination, thousands or millions or more rays are shot per pixel. *Distribution ray tracing* shoots many fewer rays through each pixel (perhaps a few dozen), but spawns many random rays from every surface intersection. See the books by Suffern [1228] and Shirley [1171] for more on the theory and practice of classical and Monte Carlo ray tracing.

The main problem with ray tracing is simply speed. One reason GPUs are so fast is that they use coherence efficiently. Each triangle is sent through the pipeline and covers some number of pixels, and all these related computations can be shared when rendering a single triangle. Other sharing occurs at higher levels, such as when a transformed vertex is used to form more than one triangle or a shader configuration is used for rendering more than one primitive. In ray tracing, the ray performs a search to find the closest object. Some caching and sharing of results can be done, but each ray potentially can hit a different object. Much research has been done on making the process of tracing rays as efficient as possible [404].

Interactive ray tracing has been possible on a limited basis for some time. For example, the *demo scene* [1118] has made real-time programs for years that have used ray tracing for some or all of the rendering for simple environments. Because each ray is, by its nature, evaluated independently from the rest, ray tracing is “embarrassingly parallel,” with more processors being thrown at the problem usually giving a nearly linear performance increase. Ray tracing also has another interesting feature, that the time for finding the closest (or for shadows, any) intersection for a ray is typically order  $O(\log n)$  for  $n$  objects, when an efficiency structure is used. For example, bounding volume hierarchies (see Section 14.1 for information on these and other spatial data structures) typically have  $O(\log n)$  search behavior. This compares well with the typical  $O(n)$  performance of the basic  $Z$ -buffer, in which all polygons have to be sent down the pipeline. Techniques such as those discussed in Chapter 10 and 14—hierarchical culling, level of detail, impostors—can be used to speed up the  $Z$ -buffer to give it a more  $O(\log n)$  response. With ray tracing, this performance comes with its efficiency scheme, with minimal user intervention. The problem ray tracing faces is that, while  $O(\log n)$  is better in theory than  $O(n)$ , in practice each of these values is multiplied by a different constant, representing how much time each takes. For example, if ray tracing a single object is 1000 times slower than rendering it with a naive  $Z$ -buffer,  $1000 \log n = n$ , so at  $n = 9119$  objects ray tracing’s time complexity advantage would allow it to start to outperform a simplistic  $Z$ -buffer renderer.

One advantage of the  $Z$ -buffer is its use of coherence, sharing results to generate a set of fragments from a single triangle. As scene complexity rises, this factor loses importance. For this reason ray tracing is a viable alternative for extremely large model visualization. See Figure 14.1 on page 646. As Wald et al. have shown [1312, 1313], by carefully paying

attention to the cache and other architectural features of the CPU, as well as taking advantage of CPU SIMD instructions, interactive and near-interactive rates can be achieved. Rays traveling approximately the same direction can also be bundled in packets and tested together, using a form of box/frustum testing [133].

A few of the techniques discussed in other sections of this book, such as relief mapping and image-based caustic rendering, march along rays and sample the underlying surfaces. These can be thought of as methods of performing ray/object intersection calculations. However, they arise from the desire to leverage the GPU's abilities to rapidly access and interpolate texture data for heightfields. Objects are still rendered one by one, with each passing through the pipeline and the pixel shader, then performing these calculations for visible areas of the surface. A more radical approach is to map ray tracing efficiency structures as a whole to the GPU. Purcell et al. [1038] were the first to describe how to use a graphics accelerator to perform ray tracing. This avenue of exploration has led to other attempts to harness the parallel power of the GPU for ray tracing and other global illumination algorithms. One place to start is with the article by Christen [177], who discusses two implementations in some depth.

Ray tracing has its own limitations to work around. For example, the efficiency structure that reduces the number of ray/object tests needed is critical to performance. When an object moves or deforms, this structure needs to be updated to keep efficiency at a maximum, a task that can be difficult to perform rapidly. There are other issues as well, such as the cache-incoherent nature of reflection rays. See Wald et al. [1314] for a summary of some of the successes and challenges in the field of interactive ray tracing. Friedrich et al. [363] discuss the possibilities of using ray tracing for game rendering.

### 9.8.3 Other Global Illumination Techniques

There are many different global illumination techniques for determining the amount of light reaching a surface and then traveling to the eye. Jensen's book [606] begins with a good technical overview of the subject.

One well-known algorithm is called *irradiance caching* or *photon mapping* [288]. The concept is to follow photons from the light sources and deposit them on surfaces. When the camera then views a surface location, nearby deposits are found and evaluated, to find an approximation of the indirect illumination. Using Heckbert's notation from the beginning of this chapter, creating the photon map computes some paths of  $L(D|S)_{+}$ . Sampling from the camera then completes the paths using traditional rendering methods. Such methods are typically used in offline renderers and produce highly realistic images.

Photon mapping is often used together with ray tracing. Ray tracing is applied in the *final gather* phase, where rays are shot from each rendered location to collect indirect illumination (from the photon maps) and direct illumination (from the light sources).

GPU implementations of these methods have been developed [383, 472, 1039, 1215], but are not yet fast enough to be used in real-time applications. Rather, the motivation is to speed up offline rendering.

An interesting development is the invention of new global illumination algorithms designed specifically for the GPU. One of the earliest of these is “Instant Radiosity” [641], which, despite its name, has little in common with the radiosity algorithm. The basic idea is simple: Rays are cast outward from the light sources. For each place where a ray hits, a light source is placed and rendered with shadows, to represent the indirect illumination from that surface element. This technique was designed to take advantage of fixed-function graphics hardware, but it maps well onto programmable GPUs. Recent extensions [712, 1111, 1147] have been made to this algorithm to improve performance or visuals.

Other techniques have been developed in the same spirit of representing bounce lighting with light sources, where the light sources are stored in textures or splatted on the screen [219, 220, 221, 222].

Another interesting GPU-friendly global illumination algorithm was proposed by Sloan et al. [1190]. This technique was discussed on page 385 in the context of occlusion, but since it models interreflections as well, it should be counted as a full global illumination algorithm.

## 9.9 Precomputed Lighting

The full global illumination algorithms discussed in the previous section are very costly for all but the simplest scenes. For this reason, they are usually not employed during rendering, but for offline computations. The results of these precomputations are then used during rendering.

There are various kinds of data that can be precomputed, but the most common is lighting information. For precomputed lighting or *prelighting* to remain valid, the scene and light sources must remain static. Fortunately, there are many applications where this is at least partially the case, enabling the use of precomputed lighting to good effect. Sometimes the greatest problem is that the static models look much better than the dynamic (changing) ones.

### 9.9.1 Simple Surface Prelighting

The lighting on smooth Lambertian surfaces is fully described by a single RGB value—the irradiance. If the light sources and scene geometry do

not change, the irradiance will be constant and can be precomputed ahead of time. Due to the linear nature of light transport, the effect of any dynamic light sources can simply be added on top of the precomputed irradiance.

In 1997, *Quake II* by id Software was the first commercial interactive application to make use of irradiance values precomputed by a global illumination algorithm. *Quake II* used texture maps that stored irradiance values that were precomputed offline using radiosity. Such textures have historically been called *light maps*, although they are more precisely named *irradiance maps*. Radiosity was a good choice for *Quake II*'s precomputation since it is well suited to the computation of irradiance in Lambertian environments. Also, memory constraints of the time restricted the irradiance maps to be relatively low resolution, which matched well with the blurry, low-frequency shadows typical of radiosity solutions. Born [127] discusses the process of making irradiance map charts using radiosity techniques.

Irradiance values can also be stored in vertices. This works particularly well if the geometry detail is high (so the vertices are close together) or the lighting detail is low. Vertex and texture irradiance can even be used in the same scene, as can be seen in Figure 9.42 on page 388. The castle in this figure is rendered with irradiance values that are stored on vertices over most of the scene. In flat areas with rapid lighting changes (such as the walls behind the torches) the irradiance is stored in texture maps.

Precomputed irradiance values are usually multiplied with diffuse color or albedo maps stored in a separate set of textures. Although the exitance (irradiance times diffuse color) could in theory be stored in a single set of maps, many practical considerations rule out this option in most cases. The color maps are usually quite high frequency and make use of various kinds of tiling and reuse to keep the memory usage reasonable. The irradiance data is usually much lower frequency and cannot easily be reused. The combination of two separate signals consumes much less memory. The low-frequency irradiance changes also tend to mask repetition resulting from tiling the color map. A combination of a diffuse color map and an irradiance map can be seen in Figure 9.63.

Another advantage of storing the irradiance separately from the diffuse color is that the irradiance can then be more easily changed. Multiple irradiance solutions could be stored and reused with the same geometry and diffuse color maps (for example, the same scene seen at night and during the day). Using texture coordinate animation techniques (Section 6.4) or projective texturing (Section 7.4.3), light textures can be made to move on walls—e.g., a moving spotlight effect can be created. Also, light maps can be recalculated on the fly for dynamic lighting.

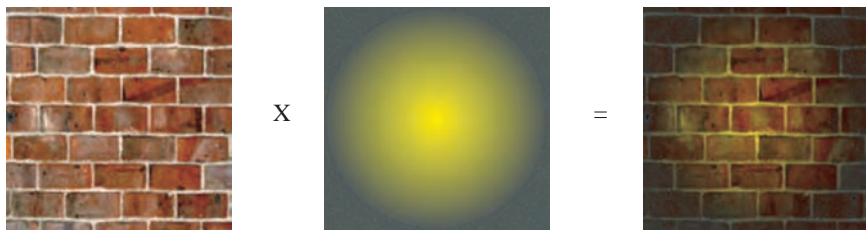


**Figure 9.63.** Irradiance map combined with a diffuse color, or albedo, map. The diffuse color map on the left is multiplied by the irradiance map in the middle to yield the result on the right. (*Images courtesy of J.L. Mitchell, M. Taturo, and I. Bullard.*)

Although additional lights can be added to a precomputed irradiance solution, any change or addition of *geometry* invalidates the solution, at least in theory. In practice, relatively small dynamic objects, such as characters, can be introduced into the scene and their effect on the precomputed solution can be either ignored or approximated, e.g., by attenuating the precomputed irradiance with dynamic shadows or ambient occlusion. The effect of the precomputed solution on the dynamic objects also needs to be addressed—some techniques for doing so will be discussed in Section 9.9.3.

Since irradiance maps have no directionality, they cannot be used with glossy or specular surfaces. Worse still, they also cannot be used with high-frequency normal maps. These limitations have motivated a search for ways to store directional precomputed lighting. In cases where indirect lighting is stored separately, irradiance mapping can still be of interest. Indirect lighting is weakly directional, and the effects of small-scale geometry can be modeled with ambient occlusion.

## 9.9.2 Directional Surface Prelighting

To use low-frequency prelighting information with high-frequency normal maps, irradiance alone will not suffice. Some directional information must be stored, as well. In the case of Lambertian surfaces, this information will represent how the irradiance changes with the surface normal. This is effectively the same as storing an irradiance environment map at each surface location. Since irradiance environment maps can be represented with nine RGB spherical harmonic coefficients, one straightforward approach is to store those in vertex values or texture maps. To save pixel shader cycles, these coefficients can be rotated into the local frame at precomputation time.

Storing nine RGB values at every vertex or texel is very memory intensive. If the spherical harmonics are meant to store only indirect lighting, four coefficients may suffice. Another option is to use a different basis

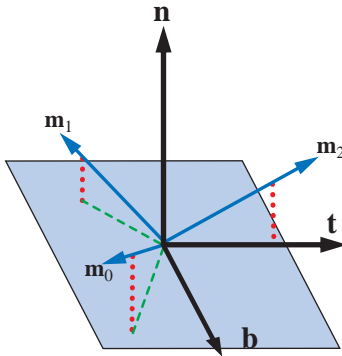


**Figure 9.64.** *Half-Life 2* lighting basis. The three basis vectors have elevation angles of about 26° above the tangent plane, and their projections into that plane are spaced equally (at 120° intervals) around the normal. They are unit length, and each one is perpendicular to the other two.

that is optimized for representing functions on the hemisphere, rather than the sphere. Often normal maps cover only the hemisphere around the unperturbed surface normal. Hemispherical harmonics [382] can represent functions over the hemisphere using a smaller number of coefficients than spherical harmonics. First-order hemispherical harmonics (four coefficients) should in theory have only slightly higher error than second-order spherical harmonics (nine coefficients) for representing functions over the hemisphere.

Valve uses a novel representation [848, 881], which it calls *radiosity normal mapping*, in the *Half-Life 2* series of games. It represents the directional irradiance at each point as three RGB irradiance values, sampled in three directions in tangent space (see Figure 9.64). The coordinates of the three mutually perpendicular basis vectors in tangent space are

$$\begin{aligned} \mathbf{m}_0 &= \left\{ \frac{-1}{\sqrt{6}}, \frac{1}{\sqrt{2}}, \frac{1}{\sqrt{3}} \right\}, \\ \mathbf{m}_1 &= \left\{ \frac{-1}{\sqrt{6}}, \frac{-1}{\sqrt{2}}, \frac{1}{\sqrt{3}} \right\}, \\ \mathbf{m}_2 &= \left\{ \frac{\sqrt{2}}{\sqrt{3}}, 0, \frac{1}{\sqrt{3}} \right\}. \end{aligned} \quad (9.37)$$

At rendering time, the tangent-space normal  $\mathbf{n}$  is read from the normal map and the irradiance is interpolated from the three sampled irradiance

values ( $E_0$ ,  $E_1$ , and  $E_2$ ):<sup>12</sup>

$$E(\mathbf{n}) = \frac{\sum_{k=0}^2 \max(\mathbf{m}_k \cdot \mathbf{n}, 0)^2 E_k}{\sum_{k=0}^2 \max(\mathbf{m}_k \cdot \mathbf{n}, 0)^2}. \quad (9.38)$$

Green [440] points out that shading can be made significantly cheaper if the following three values are stored in the map instead of the tangent-space normal:

$$d_k = \frac{\max(\mathbf{m}_k \cdot \mathbf{n}, 0)^2}{\sum_{k=0}^2 \max(\mathbf{m}_k \cdot \mathbf{n}, 0)^2}, \quad (9.39)$$

for  $k = 0, 1, 2$ . Then Equation 9.38 simplifies to the following:

$$E(\mathbf{n}) = \sum_{k=0}^2 d_k E_k. \quad (9.40)$$

Green describes several other advantages to this representation (some of them are discussed further in Section 9.10.2). However, it should be noted that some of the performance savings are lost if the tangent space normal  $\mathbf{n}$  is needed for other uses, such as specular lighting, since the normal must then be reconstructed in the pixel shader. Also, although the required storage is equivalent in theory to a normal map (both use three numbers), in practice normal maps are easier to compress. For these reasons, the original formulation in Equation 9.38 may be preferable for some applications.

The *Half-Life 2* representation works well for directional irradiance. Sloan [1189] found that this representation produces results superior to low-order hemispherical harmonics.

Another representation of directional irradiance was used by Crytek in the game *Far Cry* [887]. Crytek refers to the maps used in its representation as *dot3 lightmaps*. The Crytek representation consists of an average light direction in tangent space, an average light color, and a scalar directionality factor. The directionality factor expresses to what extent the incoming light varies in direction. It works to weaken the effect of the  $\mathbf{n} \cdot \mathbf{l}$  cosine term when the incoming light is scattered over the hemisphere.

Vector irradiance (discussed in Section 8.2) can also be used as a directional irradiance representation for prelighting. During the prelighting

---

<sup>12</sup>The formulation given in the GDC 2004 presentation [848] is incorrect; the form in Equation 9.38 is from a SIGGRAPH 2007 presentation [440].

phase, the vector irradiance can be computed by integrating over the hemisphere around the unperturbed surface normal. Three separate vectors are computed (one each for R, G and B). During rendering, the perturbed surface normal can be dotted with the three vectors to produce the R, G, and B components of the irradiance. The computed irradiance values may be incorrect due to occlusion effects, but this representation should compare well with the ones previously discussed.

PDI developed an interesting prelighting representation to render indirect illumination in the film *Shrek 2* [1236]. Unlike the previously discussed representations, the PDI representation is designed for prelighting bumped surfaces with arbitrary BRDFs, not just Lambertian surfaces. The PDI representation consists of the surface irradiance  $E$  and three light direction vectors  $\mathbf{l}_R$ ,  $\mathbf{l}_G$ , and  $\mathbf{l}_B$ . These values are sampled in a light gathering phase that is analogous to the prelighting phase for an interactive application. Sampling is performed by shooting many rays over the hemisphere of each sample point and finding the radiance from each intersected surface. No rays are shot to light sources since only indirect lighting is represented. The ray casting results are used to compute the surface irradiance  $E$ . The ray directions, weighted by the radiance's R, G, and B components, are averaged to compute three lighting vectors  $\mathbf{l}_R$ ,  $\mathbf{l}_G$ , and  $\mathbf{l}_B$ :

$$\begin{aligned}\mathbf{l}_R &= \frac{\sum_k L_{k,R} \mathbf{l}_k}{\|\sum_k L_{k,R} \mathbf{l}_k\|}, \\ \mathbf{l}_G &= \frac{\sum_k L_{k,G} \mathbf{l}_k}{\|\sum_k L_{k,G} \mathbf{l}_k\|}, \\ \mathbf{l}_B &= \frac{\sum_k L_{k,B} \mathbf{l}_k}{\|\sum_k L_{k,B} \mathbf{l}_k\|},\end{aligned}\tag{9.41}$$

where  $L_k$  is the radiance from the surface intersected by the  $k$ th ray (and  $L_{k,R}$ ,  $L_{k,G}$ , and  $L_{k,B}$  are its R, G and B components). Also,  $\mathbf{l}_k$  is the  $k$ th ray's direction vector (pointing away from the surface). Each weighted sum of direction vectors is divided by its own length to produce a normalized result (the notation  $\|\mathbf{x}\|$  indicates the length of the vector  $\mathbf{x}$ ).

During final rendering,  $E$ ,  $\mathbf{l}_R$ ,  $\mathbf{l}_G$ , and  $\mathbf{l}_B$  are averaged from nearby sample points (in an interactive application, they would be individually interpolated from vertex or texel values). They are then used to light the surface:

$$L_o(\mathbf{v}) = \sum_{\lambda=R,G,B} f(\mathbf{v}, \mathbf{l}_\lambda) \frac{E_\lambda}{\max(\mathbf{n}_{\text{orig}} \cdot \mathbf{l}_\lambda, 0)} \max(\mathbf{n} \cdot \mathbf{l}_\lambda, 0),\tag{9.42}$$

where  $L_o(\mathbf{v})$  is the outgoing radiance resulting from indirect lighting (PDI computes direct lighting separately). Also,  $f(\mathbf{v}, \mathbf{l}_\lambda)$  is the BRDF evaluated

at the appropriate view and light directions,  $E_\lambda$  is a color component (R, G, or B) of the precomputed irradiance, and  $\mathbf{n}_{\text{orig}}$  is the original unperturbed surface vector (not to be confused with  $\mathbf{n}$ , the perturbed surface vector). If normal mapping is not used, then Equation 9.42 can be simplified somewhat.

A possible lower-cost variant would use just a single lighting direction (in this case luminance should be used for weighting, instead of the radiance R, G, or B color components). Another possibility is to optimize the implementation by scaling the direction vectors by the irradiance and cosine factor in the prelighting phase, to produce three illumination vectors  $\mathbf{i}_R$ ,  $\mathbf{i}_G$ , and  $\mathbf{i}_B$ :

$$\mathbf{i}_\lambda = \frac{E_\lambda}{\max(\mathbf{n}_{\text{orig}} \cdot \mathbf{l}_\lambda, 0)} \mathbf{l}_\lambda, \quad (9.43)$$

for  $\lambda = R, G, B$ . Then Equation 9.42 is simplified to

$$L_o(\mathbf{v}) = \sum_{\lambda=R,G,B} f(\mathbf{v}, \mathbf{l}_\lambda) \max(\mathbf{n} \cdot \mathbf{i}_\lambda, 0), \quad (9.44)$$

where  $\mathbf{l}_\lambda$  is computed by normalizing  $\mathbf{i}_\lambda$ .

Care should be taken when performing this optimization, since the results of interpolating  $\mathbf{i}_R$ ,  $\mathbf{i}_G$ , and  $\mathbf{i}_B$  may not be the same as interpolating  $E$ ,  $\mathbf{l}_R$ ,  $\mathbf{l}_G$ , and  $\mathbf{l}_B$ . This form of the PDI representation is equivalent to the RGB vector irradiance representation suggested earlier. Although in theory this representation is only correct for Lambertian surfaces, PDI reports good results with arbitrary BRDFs, at least for indirect illumination.

As in the case of simple prelighting, all of these prelighting representations can be stored in textures, vertex attributes, or a combination of the two.

### 9.9.3 Volume Prelighting

Many interactive applications (games in particular) feature a static environment in which characters and other dynamic objects move about. Surface prelighting can work well for lighting the static environment, although we need to factor in the occlusion effects of the characters on the environment. However, indirect light from the environment also illuminates the dynamic objects. How can this be precomputed?

Greger et al. [453] proposed the *irradiance volume*, which represents the five-dimensional (three spatial and two directional dimensions) irradiance function with a sparse spatial sampling of irradiance environment maps. That is, there is a three-dimensional grid in space, and at the grid points are irradiance environment maps. Dynamic objects interpolate irradiance values from the closest of these environment maps. Greger et al. used

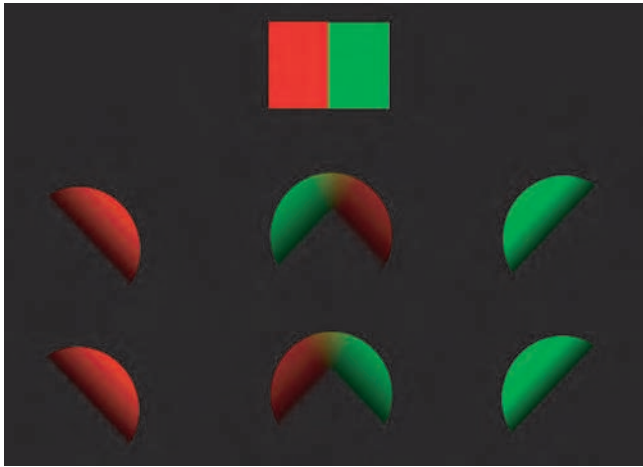


**Figure 9.65.** Interpolation between two spherical harmonic irradiance map samples. In the middle row, simple linear interpolation is performed. The result is clearly wrong with respect to the light source in the top row. In the bottom row, the spherical harmonic gradients are used for a first-order Taylor expansion before interpolation. (Image courtesy of Chris Oat, ATI Research, Inc.)

a two-level adaptive grid for the spatial sampling, but other volume data structures, such as octrees or tetrahedral meshes, could be used. Kontkanen and Laine [687] describe a method for reducing aliasing artifacts when precomputing irradiance volumes.

A variety of representations for irradiance environment maps were described in Section 8.6. Of these, compact representations such as spherical harmonics [1045] and Valve’s ambient cube [848, 881] are best suited for irradiance volumes. Interpolating such representations is straightforward, as it is equivalent to interpolating the individual coefficient values. The use of spherical harmonic gradients [25] can further improve the quality of spherical harmonic irradiance volumes. Oat [952, 953] describes an irradiance volume implementation that uses cubic interpolation of spherical harmonics and spherical harmonic gradients. The gradient is used to improve the quality of the interpolation (see Figure 9.65).

The irradiance volumes in Valve’s *Half-Life 2* are interesting in that no spatial interpolation is performed. The nearest ambient cube to the character is always selected. Popping artifacts are avoided via time averaging.

One way to bypass the need to compute and store an irradiance volume is to use the prelighting on adjacent surfaces. In *Quake III: Arena*, the lightmap value for the floor under the character is used for ambient lighting [558]. A similar approach is described by Hargreaves [502], who uses *radiosity textures* to store the radiosity, or exitance, of the ground plane.

The values beneath the object are then used as ground colors in a hemisphere lighting irradiance representation (see Section 8.6.3 for a description of hemisphere lighting). This technique was used for an outdoor driving game, where it worked quite well.

Evans [322] describes an interesting trick used for the irradiance volumes in *LittleBigPlanet*. Instead of a full irradiance map representation, an average irradiance is stored at each point. An approximate directionality factor is computed from the gradient of the irradiance field (the direction in which the field changes most rapidly). Instead of computing the gradient explicitly, the dot product between the gradient and the surface normal  $\mathbf{n}$  is computed by taking two samples of the irradiance field, one at the surface point  $\mathbf{p}$  and one at a point displaced slightly in the direction of  $\mathbf{n}$ , and subtracting one from the other. This approximate representation is motivated by the fact that the irradiance volumes in *Little Big Planet* are computed dynamically.

Nijasure et al. [938] also compute irradiance volumes dynamically. The irradiance volumes are represented as grids of spherical harmonic irradiance environment maps. Several iteration steps are performed, where the scene geometry lit by the previous iteration is used to compute the next iteration’s irradiance volume. Their method can compute diffuse inter-reflections (similar to those produced by radiosity) at interactive rates for simple scenes.

Little work has been done on volume prelighting for specular and glossy surfaces. Valve’s *Half-Life 2* uses environment maps rendered and stored at artist-determined locations [848, 881]. Objects in the scene use the nearest environment map.

## 9.10 Precomputed Occlusion

Global illumination algorithms can be used to precompute various quantities other than lighting. These quantities can be stored over the surfaces or volumes of the scene, and used during rendering to improve visuals. Some measure of how much some parts of the scene block light from others is often precomputed. These precomputed occlusion quantities can then be applied to changing lighting in the scene, yielding a more dynamic appearance than precomputing the lighting.

### 9.10.1 Precomputed Ambient Occlusion

The ambient occlusion factor and bent normal (both discussed in Section 9.2) are frequently precomputed and stored in textures or vertices. The most common approach to performing this precomputation is to cast

rays over the hemisphere around each surface location or vertex. The cast rays may be restricted to a certain distance, and in some cases the intersection distance may be used in addition to, or instead of, a simple binary hit/miss determination. The computation of obscuration factors is one example where intersection distances are used.

The computation of ambient occlusion or obscuration factors usually includes a cosine weighting factor. The most efficient way to incorporate this factor is by means of *importance sampling*. Instead of casting rays uniformly over the hemisphere and cosine-weighting the results, the distribution of ray directions is cosine-weighted (so rays are more likely to be cast closer to the surface normal). Most commercially available modeling and rendering software packages include an option to precompute ambient occlusion.

Ambient occlusion precomputations can also be accelerated on the GPU, using GPU features such as depth maps [1012] or occlusion queries [362].

Strictly speaking, precomputed ambient occlusion factors are only valid as long as the scene's geometry does not change. For example, ambient occlusion factors can be precomputed over a racetrack, and they will stay valid as the camera moves through the scene. The effect of secondary bounce lighting for light sources moving through the environment can be approximated by applying the ambient occlusion factors to the lights, as discussed in Section 9.2.2. In principle, the introduction of additional objects (such as cars) invalidates the precomputation. In practice, the simple approach of precomputing ambient occlusion factors for the track (without cars), and for each car in isolation, works surprisingly well.

For improved visuals, the ambient occlusion of the track on the cars (and vice versa) can be approximated by placing each car on a large, flat plane when performing its ambient occlusion precomputation. The ambient occlusion factors on the plane can be captured into a texture and projected onto the track underneath the car [728]. This works well because the track is mostly flat and the cars are likely to remain in a fixed relationship to the track surface.

Another reason the simple scheme described above works well is that the cars are rigid objects. For deformable objects (such as human characters) the ambient occlusion solution loses its validity as the character changes pose. Kontkanen and Aila [690] propose a method for precomputing ambient occlusion factors for many reference poses, and for finding a correspondence between these and animation parameters, such as joint angles. At rendering time, they use over 50 coefficients stored at each vertex to compute the ambient occlusion from the parameters of the current pose (the computation is equivalent to performing a dot product between two long vectors). Kirk and Arikan [668] further extend this approach. Both

techniques are rather storage intensive, but the basic idea can probably be used in a more lightweight manner and still produce good results.

Precomputed data can also be used to model the ambient occlusion effects of objects on each other. Kontkanen and Laine [688, 689] store the ambient occlusion effect of an object on its surroundings in a cube map, called an *ambient occlusion field*. Each texel contains seven scalar coefficients (so in practice, two cube maps must be used, since a single cube map can store at most four scalars in a texel). These coefficients, in combination with the distance to the occluding object's center, are used to compute the ambient occlusion.

Malmer et al. [813] show improved results by storing the ambient occlusion factors (and optionally the bent normal) directly in a three-dimensional grid. The computation requirements are lower, since the ambient occlusion factor is read directly. Fewer scalars are stored compared to Kontkanen and Laine's approach, and the textures in both methods have low resolutions, so the overall storage requirements are similar.



**Figure 9.66.** On the top, objects cast shadows on the floor but with no ambient effect. On the bottom, ambient occlusion fields from the objects cause the floor to darken near them. These subtle touches give a richness to the lighting in the scene. (*Images courtesy of Emergent Game Technologies and Third Degree Games.*)

Both methods work for rigid objects and can be extended to articulated objects with small numbers of moving parts. Deformable objects are not discussed, but they could presumably be approximated in many cases as articulated objects. An example of the use of such methods can be seen in Figure 9.66.

### 9.10.2 Precomputed Directional Occlusion

Similar to ambient occlusion, directional shadowing can also benefit from precomputed information. Max [827] introduced the concept of *horizon mapping* to describe self-occlusion of a heightfield surface. In horizon mapping, for each point on the surface, the altitude angle of the horizon is determined for some set of azimuth directions (e.g., eight: north, northeast, east, southeast, etc.). Soft shadowing can also be supported by tracking the angular extents of the light source; see the left side of Figure 9.67. Sloan [1185] describes a horizon mapping implementation on early graphics hardware. Forsyth [353] gives an alternative implementation that is better suited to modern GPUs, using volume textures to store the horizon angles. In the case of a light source (such as the sun) that moves along a predetermined arc, a single pair of horizon angles suffices [555]. In this restricted case, it is also straightforward to extend the horizon map concept to non-heightfield geometry by storing multiple angle intervals [270]; see the right side of Figure 9.67. An example of horizon mapping used for soft shadowing of a terrain heightfield can be seen in Figure 9.68.

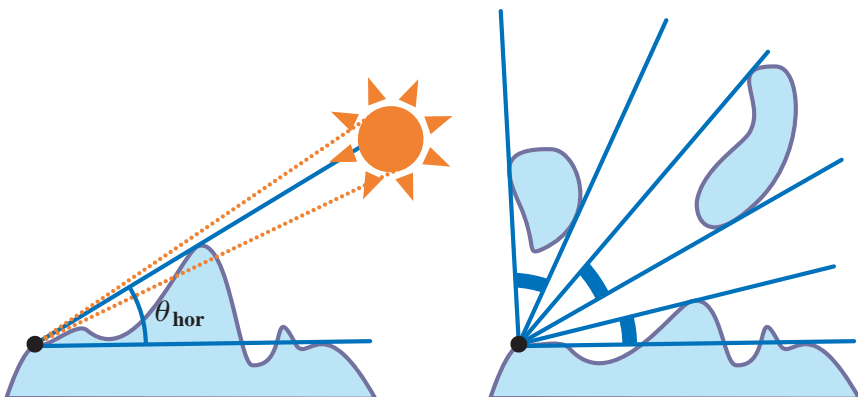


**Figure 9.67.** On the left: The horizon angle in the direction of an area light source is shown in relation to the upper and lower extents of the light source. These values can be used to generate a partial occlusion value for soft shadowing. On the right: Storing a sequence of occluded angle intervals, instead of a single horizon angle, enables modeling non-heightfield geometry.



**Figure 9.68.** A terrain heightfield, lit with normal and horizon mapping. Note the soft shadows.

Instead of storing horizon angles for some given compass directions, the set of unoccluded three-dimensional directions as a whole can be modeled as an elliptical [536, 629] or circular [954, 955] cone (the latter technique is called *ambient aperture lighting*). These techniques have lower storage requirements than horizon maps, but may result in incorrect shadows when the set of unoccluded directions does not resemble an ellipse or circle. For example, a flat plane from which tall spikes protrude at regular intervals has star-shaped, unoccluded direction sets.

Although they can be used for heightfield geometry such as terrain, the most common use of heightfield shadowing techniques is to model self-shadowing of bump maps. In this case, large-scale shadowing by (and on) the geometric meshes must be performed with some other method, such as shadow maps. Handling shadows separately at macroscale and mesoscale can lead to higher performance than attempting to model both with the same approach. The problem with this approach is that it cannot account for some effects. Imagine a column and floor, both with a brick bump map. The column will cast a smooth shadow on the floor, unaffected by the bumps on either object.

The optimized form of the *Half-Life 2* lighting basis shown in Equation 9.39 (on page 421) can be modified to include a directional occlusion factor [440]. If each of the three stored values is attenuated, based on occlusion in the direction of its basis vector, the result is similar to ambient occlusion, but with some directionality. Notably, this is achieved without further modifying the shader or increasing its cost.

Landis [728] describes the concept of *reflection occlusion*, where a ray cast in the direction of the reflected view vector is tested for occlusion against the object or scene. The result is then used to attenuate specular or glossy environment map reflections. Landis does not describe a way to accelerate the ray casts, since the technique was not intended for real time rendering. To compute reflection occlusion in real time, Green et al. [443] propose precomputing directional visibility functions at various surface locations and projecting them into a spherical harmonic basis. The spherical harmonic coefficients are stored in textures or vertices. During rendering, the visibility function is evaluated for the reflection direction. The result is then used to attenuate the environment map. For the precomputed visibility results to remain valid, the object must not deform significantly during rendering. Kozlowski and Kautz [695] found that this type of directional occlusion is the most effective occlusion approach for environment maps, in terms of cost versus perceived realism.

As with lighting, occlusion can also be precomputed over a volume. Zhou et al. [1407] propose storing *shadow fields*—directional visibility sampled on multiple spherical shells—around an object. For low-frequency shadowing effects, their representation consumes about 380 kilobytes of storage per object. Only rigid objects are supported, although the method may be extended to articulated objects by storing a separate shadow field for each rigid part. This method models the shadowing of one object by another, but not self-shadowing. Tamura et al. [1238] propose a more compact representation for the shadow fields, as well as a GPU implementation.

## 9.11 Precomputed Radiance Transfer

Precomputed occlusion models how an object blocks incoming light, but it does not model other global illumination effects, such as interreflection or subsurface scattering. All these effects together comprise the object’s *radiance transfer*. The function that represents the transference of incoming radiance on an object to outgoing radiance is called the *transfer function*.

The idea behind *precomputed radiance transfer* (PRT) is that some representation of the transfer function of the object is computed ahead of time and stored. At rendering time, the transfer function is applied to the incoming radiance to generate the outgoing radiance from the object. It is usually assumed that the scene or object is lit only by distant lighting.<sup>13</sup> The incoming radiance then depends only on incoming direction, and not on position. It is convenient to represent the domain of such functions as

---

<sup>13</sup>This is the same assumption used in environment mapping.

points on the unit sphere. The  $x/y/z$  coordinates of these points are also the coordinates of normalized vectors, which can thus represent directions.

Precomputed radiance transfer techniques require that the incoming radiance be projected into an appropriate basis. For computation and storage reasons, the number of basis functions used must be small. This restricts the possible incoming radiance situations to a low-dimensional space.

The first precomputed radiance transfer technique, proposed by Sloan et al. [1186] used the real spherical harmonics for this purpose (see Section 8.6.1 for more information on this basis). In this technique, the transfer function is represented as a set of spherical harmonic (SH) coefficients. The outgoing radiance from each location is assumed to be the same for all outgoing directions, i.e., the surface is a diffuse reflector, so radiance can be represented by a single value.

For each location, the transfer function SH coefficients describe how much illumination is received, dependent on the incoming light's direction. A more direct way of thinking of this function is to consider each spherical harmonic element as a lighting situation to be evaluated. See Figure 9.69, which shows the computation of the transfer function coefficients. At the top, we see the object for which the transfer function will be computed. Below it are visualizations of the first four spherical harmonic basis functions. We will focus on the leftmost one, which is the simplest spherical harmonic basis function,  $y_0^0$ . This function has a constant value over the sphere. The green color indicates that this value is positive. Light color is ignored for simplicity, so all values shown are scalars (RGB light will be discussed later).

Under this type of lighting situation, equal illumination comes from all directions. Say, by some offline process, we precisely compute the outgoing radiance from each location due to direct illumination, reflection, scattering, etc. The leftmost blue arrow shows the result of this lighting computation, on the bottom left corner of Figure 9.69. We can see that the computed amount varies over the object. This amount is the coefficient, i.e., the multiplier, that says how much light reaches the location and is reflected outward. Locations in crevices are dimmer, and therefore have a lower coefficient, than those fully exposed. This coefficient is similar to the ambient occlusion factor, but it takes the entire radiance transfer process into account, not just occlusion.

Now take the other three spherical harmonic basis functions shown in Figure 9.69, and treat each as a lighting situation. For example, the third basis function from the left ( $y_1^0$ ) can be thought of as lights above and below the object, fading off toward the horizon. Say this lighting situation is then perfectly evaluated for the vertices (or, really, any given set of locations) on the object. The coefficient stored at each location will then perfectly

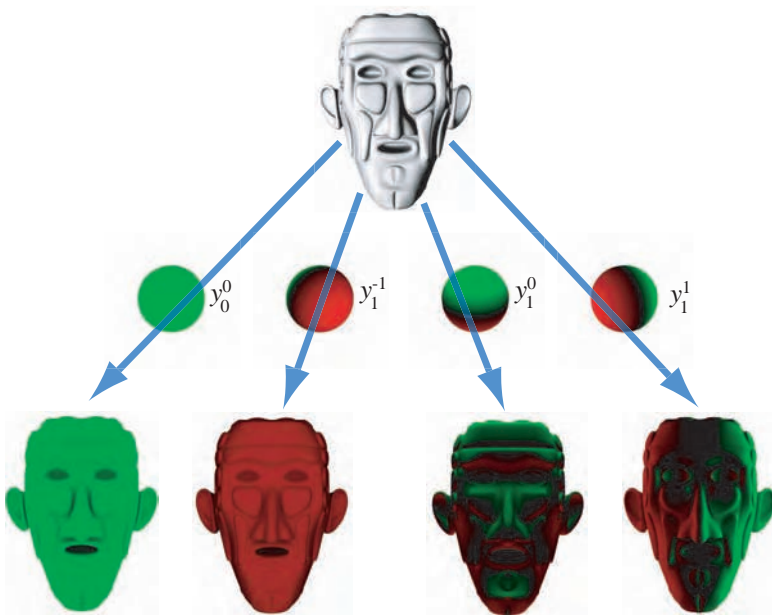


**Figure 9.69.** Computation of spherical harmonic coefficients for the radiance transfer function. The object (at the top) is lit using each of the four basis functions as lighting environments. The results are shown at the bottom. Grayscale lighting is shown—the colors are used to show positive (green) and negative (red) values. (*Images generated using the Microsoft SDK [261] sample “PRTDemo.”*)

represent how much illumination will be reflected back to the viewer, given this lighting situation. The blue arrow going through the  $y_1^0$  basis function shows the resulting coefficients. The parts of the object’s surface that are facing upward are colored bright green. This means that in those areas, the  $y_1^0$  coefficient has a relatively large, positive value.

Note that the directions shown in red on the spherical harmonic basis functions are “negative.” These are treated as negative light for the lighting computations that are carried out. While negative light does not exist in reality, the idea to keep in mind is that we are going to represent the actual lighting in a scene by a sum of weighted spherical harmonic elements, not by a single element. Another way to say this is that the first SH element, the constant sphere, can always be scaled and added to any set of negative lobes to give a lighting description that is non-negative from every direction, in keeping with reality. To continue with the  $y_1^0$  transfer function coefficient, the areas shown in black have coefficient values of 0. These areas are equally lit by the positive and negative lobes. The locations facing toward the bottom have negative coefficients, shown in red.

Given four coefficients for every location on an object, we can perfectly represent any lighting situation that is a combination of the four SH elements shown. It can be mathematically proven that these four elements can reproduce any distant lighting situation with sufficiently low frequencies, i.e., where the radiance changes very slowly as a function of direction. For example, if we wanted to represent a situation where incoming light was symmetrical around the up-down axis and mostly coming from below, we might have the coefficients  $(5.2, 0, -3.0, 0)$ . This would represent a situation where light was coming from the direction of the negative lobe of  $y_1^0$ , since the  $-3.0$  coefficient would make this lobe have a positive effect. The radiance would be at a maximum for light coming in directly from below, dropping gradually to a minimum for light coming directly from above. Four coefficients make for a simple example, but are too few for most applications. Usually, more coefficients would be used (e.g., 16 or 25) so that higher-frequency lighting situations can be represented.

When rendering, we need the spherical harmonic coefficients for the lighting. These are normally not provided and must be derived from the lighting. This is done by projecting the lighting onto the spherical harmonic basis, using the same number of basis functions as the transfer function. See Figure 9.70. The current lighting environment is at the top. It is projected against the four spherical harmonic basis functions, resulting in the four numerical lighting coefficients shown by the blue arrows. Each coefficient gives some information about the lighting situation. The  $y_0^0$  coefficient shows how bright the lighting is on average. The  $y_1^{-1}$  coefficient shows to what extent the lighting from behind the object is brighter than that from the front. Since it is negative, we see that the lighting from the front is slightly brighter. The  $y_1^0$  coefficient shows that the lighting from above is significantly brighter than from below. Finally, the  $y_1^1$  coefficient shows that the lighting from the right is slightly brighter than the lighting from the left.

The final lighting is the result of a dot product between the lighting and transfer coefficients.<sup>14</sup> In our example this dot product combines two vectors, each with 4 elements, but in practice the vectors may have 25 elements or more. As shown in the center rows of Figure 9.70, a dot product means that the precomputed transfer coefficients are multiplied by the corresponding lighting solutions, then summed as shown by the purple arrows. The result is the final lighting solution. Since it should not contain any negative values (if it does, they are clamped), the result is shown in grayscale and not using the green-red visualization.

---

<sup>14</sup>Mathematically, a dot product between the spherical harmonic coefficients of two functions is equivalent to integrating the product of the functions.

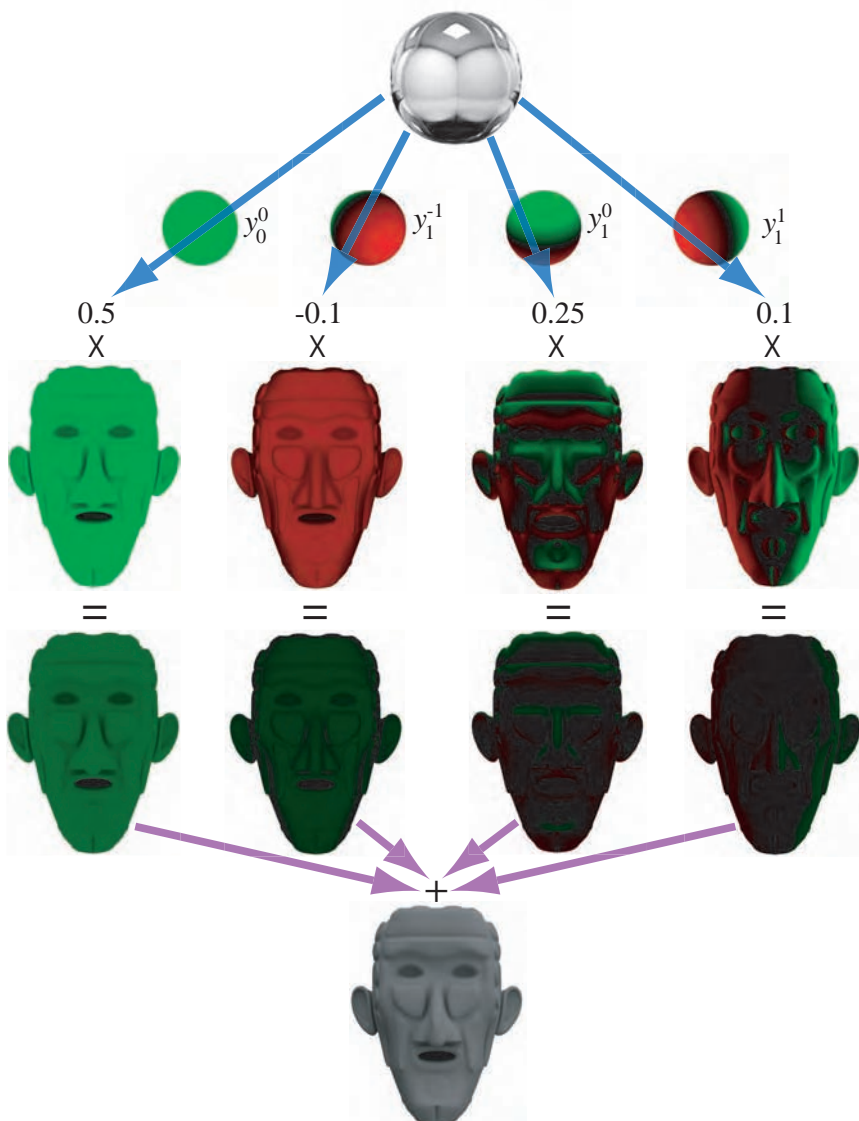


**Figure 9.70.** Using the precomputed radiance transfer function for lighting. The (grayscale) lighting environment shown at the top is projected onto the first four spherical harmonic basis functions (shown in the second row), resulting in the coefficients 0.5, -0.1, 0.25, and 0.1. The lighting at each surface location is the result of a four-element dot product between the lighting and transfer function coefficients. The values of the transfer function coefficients vary over the object. The lighting and transfer functions are both grayscale, so all values are scalars. The convention of showing green for positive and red for negative values is used everywhere except in the top (source lighting) and bottom (final shading) rows, which do not have negative values. (Images generated using the Microsoft SDK [261] sample “PRTDemo.”)

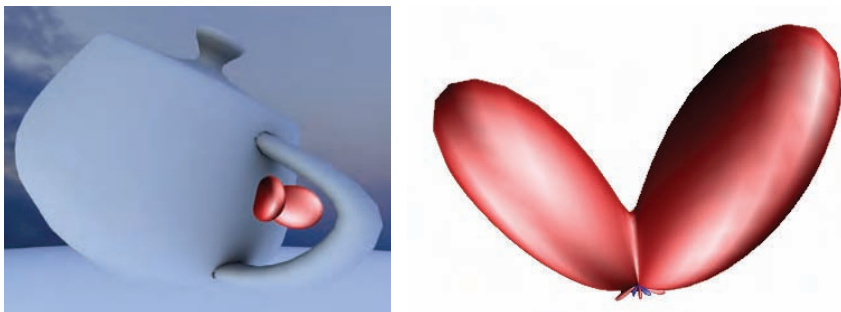


**Figure 9.71.** The spherical harmonic radiance transfer function created for a single point under the handle. The crease is due to occlusion from the handle. (*Courtesy of Chris Oat, ATI Technologies Inc.*)

In this example neither the lighting nor the transfer depended on light wavelength. In the general case, both do. The lighting coefficient for each spherical harmonic basis function is an RGB value, not a scalar. The same is true for the transfer coefficients. However, in many cases scalar transfer coefficients will not introduce a noticeable visual difference, and can save a significant amount of storage.

An alternative way to visualize the transfer function is to look at one point and show it as a function over the sphere, similar to how BRDFs are visualized. Such a visualization can be seen in Figure 9.71. An example of the resulting effects can be seen in Figure 9.72.

This type of precomputed radiance transfer can model any view-independent effect under arbitrary lighting. Lambertian lighting, self-shadowing, interreflections, color bleeding, and subsurface scattering are all examples of effects that can be modeled. However, only distant lighting



**Figure 9.72.** Three renderings of a model from the game *Warhawk* by Incognito Entertainment. The model uses a gray Lambertian material in all three renderings. On the left, the model is rendered with direct lighting and no shadowing. In the center, it is rendered with ambient light and ambient occlusion. On the right, it is rendered with precomputed radiance transfer, with a strong light from the left. (*Images courtesy of Manchor Ko.*)

on rigid objects is supported. Also, any high frequencies in the lighting or transfer will be blurred.

The distant lighting restriction can be relaxed in some cases. The SH lighting coefficients can be varied from location to location to simulate local lighting. However, large-scale effects modeled by the transfer function may be invalidated, especially if the lighting varies too rapidly. As a simple example, imagine precomputed radiance transfer on a statue, which models the shadow cast from the arm onto the body. If a light source moves between the arm and the body, the precomputed radiance transfer will no longer be valid. In short, local lighting can usually be modeled to good effect if some care is taken not to let the light sources get too close to the object.

Green [444] gives various implementation considerations for computing and using the transfer function coefficients, as do Ko et al. [677, 678] and Oat [950]. Isidoro [593] also gives specific considerations for using precomputed radiance transfer with subsurface scattering.

Techniques have been proposed to render glossy reflections with precomputed radiance transfer, using either spherical harmonics [633, 754, 1186] or other bases [442, 782, 1273, 1394]. However, in practice, these techniques are extremely costly in terms of computation, storage, or both, so they are unlikely to be a good fit for most real-time rendering applications.

The basic diffuse precomputed radiance transfer algorithm has been extended or improved in various ways, some of which are of interest for real-time rendering. The storage required by the transfer function can be quite high, including dozens of coefficients sampled over object vertices or texels. Sloan et al. [1187] propose compressing the radiance transfer using *clustered principal components analysis*. This technique speeds up rendering, as well as saving space, but it may result in artifacts.

A later method proposed by Sloan et al. [1188] enables applying precomputed radiance transfer to deformable surfaces, as long as the transfer encodes only local effects. Shadowing and interreflections from small details such as bumps can be modeled, as well as local scattering effects, such as translucency.

Sloan [1189] also discusses different possibilities for combining radiance transfer that has been precomputed at a low spatial resolution with fine-scale normal maps. He investigates projecting the transferred radiance into various bases for this purpose and concludes that the *Half-Life 2* representation produces better results than low-order hemispherical or spherical harmonics.

*Precomputed radiance transfer* usually refers to techniques using environment lighting. However, some methods have been developed for precomputing the response of objects and surfaces to directional or point lights. Malzbender et al. [814] present a method for encoding the directional illumi-

nation of a set of images into a texture consisting of polynomial coefficients that capture bumpiness, self-shadowing, and interreflection effects. Most kinds of view-independent effects can be modeled, as long as they are local (not affected by the large-scale curvature or shape of the surface). The light directions are parameterized in the tangent space of the surface, so these textures can be mapped onto arbitrary objects and tiled. Wong et al. [1368] present a similar technique that uses radial basis functions, rather than polynomials.

The SIGGRAPH 2005 course [635] on precomputed radiance transfer provides a good overview of research in the area. Lehtinen [755, 756] gives a mathematical framework that can be used to analyze the differences between the various algorithms, and to develop new ones.

## Further Reading and Resources

Hasenfratz et al. [508] provide an excellent overview of shadow algorithms developed up through 2003. Diefenbach's thesis [252] discusses and contrasts reflection, refraction, and shadow volume techniques in depth, as well as transparency, light volume filtering, and other techniques. Despite its age, it provides interesting food for thought. Mittring's article on developing graphics algorithms for the game Crysis [887] is a fascinating case study. It discusses implementation of a number of global phenomena and many other graphical elements.

A valuable reference for information on BRDFs, global illumination methods, color space conversions, and much else is Dutré's free online *Global Illumination Compendium* [287]. Pharr and Humphrey's book *Physically Based Rendering* [1010] is an excellent guide to non-interactive global illumination algorithms. What is particularly valuable about their work is that they describe in depth what they found works. Glassner's *Principles of Digital Image Synthesis* [408, 409] discusses the physical aspects of the interaction of light and matter. *Advanced Global Illumination* by Dutré et al. [288] provides a foundation in radiometry and on (primarily offline) methods of solving Kajiya's rendering equation.

Implementing radiosity algorithms is not for the faint of heart. A good practical introduction is Ashdown's book [40], sadly now out of print. Suf-fern's book [1228] is an excellent detailed guide for building a basic ray tracer. Shirley and Morley's book on ray tracing [1171] has less coverage of the basics, and more about advanced algorithms. The ray tracing book by Glassner et al. [404], though old, provides some useful material. The on-line publication *The Ray Tracing News* [479] presents articles and describes resources related to the topic.



# Chapter 10

## Image-Based Effects

*“Landscape painting is really just a box of air with little marks in it telling you how far back in that air things are.”*

—Lennart Anderson

Modeling surfaces with polygons is often the most straightforward way to approach the problem of portraying objects in a scene. Polygons are good only up to a point, however. *Image-based rendering* (IBR) has become a paradigm of its own. As its name proclaims, images are the primary data used for this type of rendering. A great advantage of representing an object with an image is that the rendering cost is proportional to the number of pixels rendered, and not to, say, the number of vertices in a geometrical model. So, one use of image-based rendering is as a more efficient way to render models. However, IBR techniques have a much wider use than this. Many objects, such as clouds and fur, are difficult to represent with polygons. Layered semitransparent images can be used to display such complex surfaces.

In this chapter, image-based rendering is first compared and contrasted with traditional polygon rendering, and an overview of algorithms presented. Commonly used techniques such as sprites, billboards, particles, and impostors are described, along with more experimental methods. Optimizations are described for when the camera and scene are mostly static.

At the same time, there is more involved in making an image than simply portraying objects. We may wish to *post-process* synthesized data in a wide variety of ways. Image processing techniques are explained for performing tone mapping, high dynamic range effects, motion blur, depth of field, and other phenomena. The chapter ends with two related topics, atmospheric effects and using three-dimensional volumetric data for modeling objects.

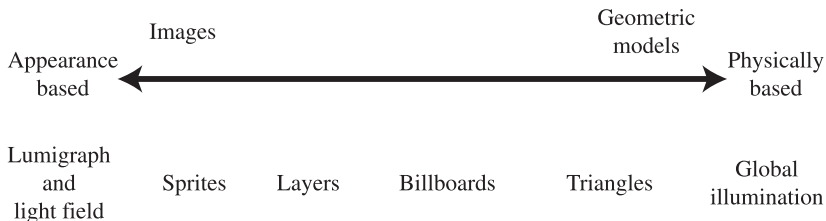


**Figure 10.1.** The rendering spectrum. (After Lengyel [763].)

## 10.1 The Rendering Spectrum

The goal of rendering is to portray an object on the screen; how we attain that goal is our choice. There is no single correct way to render a scene. Each rendering method is an approximation of reality, at least if photorealism is the goal.

Polygons have the advantage of representing the object in a reasonable fashion from any view. As the camera moves, the representation of the object does not have to change. However, to improve quality, we may wish to substitute a more highly detailed model as the viewer gets closer to the object. Conversely, we may wish to use a simplified form of the model if it is off in the distance. These are called *level of detail techniques* (see Section 14.7). Their main purpose is to make the scene display faster.

Other rendering and modeling techniques can come into play as an object recedes from the viewer. Speed can be gained by using images instead of polygons to represent the object. It is often less expensive to represent an object with a single image that can be sent quickly to the screen. One way to represent the continuum of rendering techniques comes from Lengyel [763] and is shown in Figure 10.1. We will first work our way from the left of the spectrum back down to the more familiar territory on the right.

## 10.2 Fixed-View Effects

For complex geometry and shading models, it can be expensive to rerender an entire scene at interactive rates. Various forms of acceleration can be performed by limiting the viewer's ability to move. The most restrictive situation is one where the camera is fixed in position and orientation, i.e., does not move at all. Under such circumstances, much rendering can be done just once.

For example, imagine a pasture with a fence as the static scene, with a horse moving through it. The pasture and fence are rendered once and

the color and  $Z$ -buffers stored away. Each frame, these buffers are copied over to the displayable color and  $Z$ -buffer. The horse itself is then all that needs to be rendered to obtain the final image. If the horse is behind the fence, the  $z$ -depth values stored and copied will obscure the horse. Note that under this scenario, the horse cannot cast a shadow, since the scene is unchanging. Further elaboration can be performed, e.g., the area of effect of the horse’s shadow could be determined, and then only this small area of the static scene would need to be rerendered atop the stored buffers. The key point is that there are no limits on when or how the color gets set in an image to be displayed. For a fixed view, much time can be saved by converting a complex geometric model into a simple set of buffers that can be reused for a number of frames.

It is common in computer-aided design (CAD) applications that all modeled objects are static and the view does not change while the user performs various operations. Once the user has moved to a desired view, the color and  $Z$ -buffers can be stored for immediate reuse, with user interface and highlighted elements then drawn per frame. This allows the user to rapidly annotate, measure, or otherwise interact with a complex static model. By storing additional information in G-buffers, similar to deferred shading (Section 7.9.2), other operations can be performed. For example, a three-dimensional paint program can be implemented by also storing object IDs, normals, and texture coordinates for a given view and converting the user’s interactions into changes to the textures themselves.

A concept related to the static scene is *golden thread* or *adaptive refinement*<sup>1</sup> rendering [83, 1044]. The idea is that while the viewer and scene are not moving, the computer can produce a better and better image as time goes on. Objects in the scene can be made to look more realistic. Such higher-quality renderings can be swapped in abruptly or blended in over a series of frames. This technique is particularly useful in CAD and visualization applications. There are many different types of refinement that can be done. One possibility is to use an accumulation buffer to do anti-aliasing (see Section 5.6.2) and show various accumulated images along the way [894]. Another is to perform slower per-pixel shading (e.g., ray tracing, ambient occlusion, radiosity) off screen and then fade in this improved image.

Some applications take the idea of a fixed view and static geometry a step further in order to allow interactive editing of lighting within a film-quality image. The idea is that the user chooses a view in a scene, then uses this data for offline processing, which in turn produces a representation of the scene as a set of G-buffers or more elaborate structures. Such techniques

---

<sup>1</sup>This idea is also known as “progressive refinement.” We reserve this term for the radiosity algorithm by the same name.

are used in digital film production packages, such as NVIDIA's *Sorbetto*, to allow real-time relighting of highly detailed scenes.

Guenter et al. [466] were one of the first groups to explore this area. They describe a system that allows editing of local lighting model parameters. It automatically optimizes computations for the current parameter, giving an increase in rendering speed of as much as 95 times. Gershbein et al. [391] implement a package that includes BRDF storage and shadow occlusion. Pellacini et al. [997, 998] describe a modern cinematic relighting system that is able to also store indirect illumination from multiple bounces. Ragan-Kelley et al. [1044] present their own package, which keeps shading samples separate from final pixels. This approach allows them to perform motion blur, transparency effects, and antialiasing. They also use adaptive refinement to improve image quality over time. These techniques closely resemble those used in deferred shading approaches (described in Section 7.9.2). The primary difference is that here, the techniques are used to amortize the cost of expensive rendering over multiple frames, and deferred shading uses them to accelerate rendering within a frame.

An important principle, introduced in Section 7.1, is that for a given viewpoint and direction there is an incoming radiance. It does not matter how this radiance is computed or at what distance from the eye it is gener-



**Figure 10.2.** A panorama of the Mission Dolores, used by QuickTime VR to display a wide range of views, with three views below, generated from it. Note how the views themselves are undistorted. (*Images courtesy of Ken Turkowski.*)

ated; the eye does not detect distance, only color. Capturing the radiance in a given direction in the real world can be done by simply<sup>2</sup> snapping a photograph. In the Quicktime VR system [172] a 360-degree panoramic image surrounds the (unmoving) viewer as a cylindrical image. The image is usually created from a set of photographs stitched together. As the camera's orientation changes, the proper part of the image is retrieved, warped, and displayed. Though limited to a single location, this technique has an immersive quality compared to a fixed view, because the viewer's head can turn and tilt. See Figure 10.2. Kim and Hahn [655] and Nielsen [934] discuss efficient use of cylindrical panoramas on the GPU. It is also possible to store the distance or other values of each texel's contents and so allow dynamic objects to interact with the environment.

## 10.3 Skyboxes

Pick up this book and look just past the left or right edge toward what is beyond it. Look with just your right eye, then your left. The shift in the book's edge compared to what is behind it is called the *parallax*. This effect is significant for nearby objects, helping us to perceive relative depths as we move. However, for some group of objects sufficiently far away from the viewer, there is barely any parallax effect when the viewer moves. In other words, a distant mountain itself does not normally look appreciably different if you move a meter, or even a thousand meters. It may be blocked from view by nearby objects as you move, but take away those objects and the mountain itself looks the same.

An environment map represents the incoming radiance for a local volume of space. While such maps are typically used for simulating reflections, they can also be used directly to represent distant objects in the surrounding environment. Any view-independent environment map representation can be used for this purpose; cubic maps are the most common. The environment map is placed on a mesh centered around the viewer, and large enough to encompass the rest of the objects in the scene. The exact shape of the mesh does not matter; a cube is often used. This mesh is called a *skybox*. An example is shown in Figure 9.49 on page 397. The skybox shown in that figure is more like an unconstrained version of a Quicktime VR panorama. The viewer can look in any direction, but any movement would destroy the illusion for this scene, as we would detect no parallax. Environment maps can often contain objects that are relatively close to the reflective object. The effect works because we normally do not

---

<sup>2</sup> "Simply" is a relative term. Factors such as noise, glare, motion, and depth of field can make the process of capturing a high-quality photograph a challenge. Computer graphics has the advantage of full control over these various areas.

detect much inaccuracy in reflections. Parallax is much more obvious when directly viewed. As such, a skybox typically contains only elements such as the sun, sky, distant (unmoving) clouds, and mountains.

For a skybox to look good, the cube map texture resolution has to be sufficient, i.e., a texel per screen pixel [1154]. The formula for the necessary resolution is approximately

$$\text{texture resolution} = \frac{\text{screen resolution}}{\tan(\text{fov}/2)}, \quad (10.1)$$

where  $\text{fov}$  is the field of view. This formula can be derived from observing that the texture of one face of the cube map must cover a field of view (horizontally and vertically) of 90 degrees.

Other shapes than a box surrounding the world are commonly used. For example, Gehling [385] describes a system in which a flattened dome is used to represent the sky. This geometric form was found best for simulating clouds moving overhead. The clouds themselves are represented by combining and animating various two-dimensional noise textures.

## 10.4 Light Field Rendering

Radiance can be captured from different locations and directions, at different times and under changing lighting conditions. In the real world, the burgeoning field of computational photography explores extracting various results from such data [1048]. Some purely image-based representations of an object can be used for modeling. For example, the Lumigraph [429] and light-field rendering [767] techniques attempt to capture a single object from a set of viewpoints. Given a new viewpoint, these techniques perform an interpolation process between stored views in order to create the new view. This is a complex problem, with a very high data requirement (tens of megabytes for even small image sets). Related research on surface light fields [1366] and “Sea of Images” [21] provide useful compression techniques. The concept is akin to holography, where a two-dimensional array of views captures the object. A tantalizing aspect of the Lumigraph and light-field rendering is the ability to capture a real object and be able to redisplay it from any angle. Any object, regardless of surface and lighting complexity, can be displayed at a nearly constant rate [1184]. As with the global illumination end of the rendering spectrum, these techniques currently have limited use in interactive rendering, but they demarcate what is possible in the field of computer graphics as a whole.

## 10.5 Sprites and Layers

One of the simplest image-based rendering primitives is the sprite [384]. A sprite is an image that moves around on the screen, e.g., a mouse cursor. The sprite does not have to have a rectangular shape, since some pixels can be rendered as transparent. For simple sprites, there is a one-to-one mapping with pixels on the screen. Each pixel stored in the sprite will be put in a pixel on the screen. Animation can be generated by displaying a succession of different sprites.

A more general type of sprite is one rendered as an image texture applied to a polygon that always faces the viewer. The image's alpha channel can provide full or partial transparency to the various pixels of the sprite. This type of sprite can have a depth, and so a location in the scene itself, and can smoothly change size and shape. A set of sprites can also be used to represent an object from different views. The illusion is fairly weak for large objects, however, because of the jump when switching from one sprite to another. That said, an image representation for an object from a given view can be valid for a number of frames, if the object's orientation and the view do not change significantly. If the object is small enough on the screen, storing a large set of views, even for animated objects, is a viable strategy [266].

One way to think of a scene is as a series of layers, as is commonly done for two-dimensional cel animation. For example, in Figure 10.3, the tailgate is in front of the chicken, which is in front of the truck's cab, which is in front of the road and trees. This layering holds true for a large set of viewpoints. Each sprite layer has a depth associated with it. By rendering in a back-to-front order, we can build up the scene without need for a  $Z$ -buffer, thereby saving time and resources. Camera zooms just make the object larger, which is simple to handle with the same sprite. Moving the camera in or out actually changes the relative coverage of foreground and background, which can be handled by changing each sprite layer's coverage independently. As the viewer moves perpendicularly to the direction of view, the layers can be moved relative to their depths.

However, as the view changes, the appearance of the object changes. For example, viewing a cube straight-on results in a square. As the view moves, the square appears as a warped quadrilateral. In the same way, a sprite representing an object can also be warped as its relation to the view changes. As the view changes, however, new faces of the cube become visible, invalidating the sprite. At such times, the sprite layer must be regenerated. Determining when to warp and when to regenerate is one of the more difficult aspects of image-based rendering. In addition to surface features appearing and disappearing, specular highlights and shadows

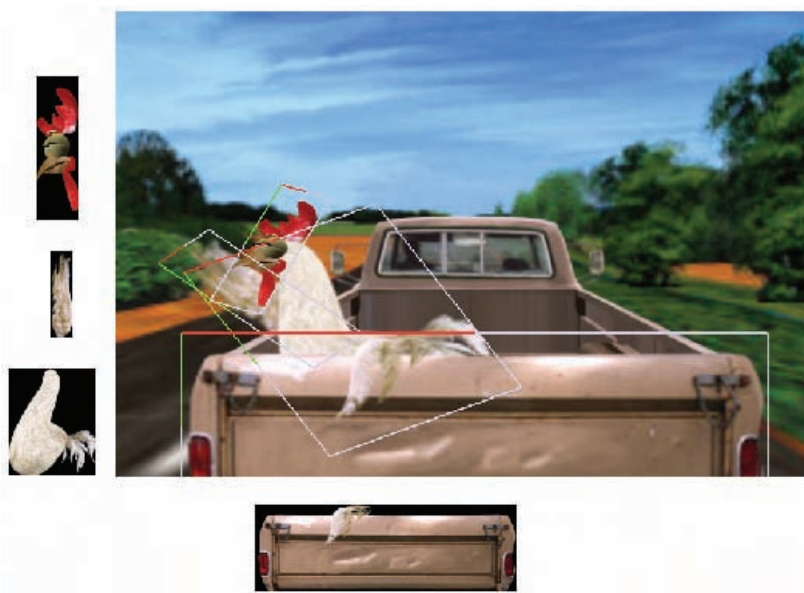


**Figure 10.3.** A still from the animation *Chicken Crossing*, rendered using a Talisman simulator. In this scene, 80 layers of sprites are used, some of which are outlined and shown on the left. Since the chicken wing is partially in front of and behind the tailgate, both were placed in a single sprite. (*Reprinted with permission from Microsoft Corporation.*)

can also change, making a system based purely on sprites difficult to use efficiently.

This layer and image warping process was the basis of the Talisman hardware architecture espoused by Microsoft in the late 1990s [1204, 1268]. Pure image-layer rendering depends on fast, high-quality image warping, filtering, and compositing. While such pure systems have serious drawbacks, the idea of representing a model by one or more image-based representations has been found to be fruitful. Image-based techniques can be combined with polygon-based rendering. The following sections discuss impostors, depth sprites, and other ways of using images to take the place of polygonal content.

## 10.6 Billboardng

Orienting a textured polygon based on the view direction is called *billboarding*, and the polygon is called a *billboard* [849]. As the view changes,

the orientation of the polygon changes. Billboarding, combined with alpha texturing and animation, can be used to represent many phenomena that do not have smooth solid surfaces. Vegetation, especially grass, is an excellent candidate for this type of technique. Smoke, fire, fog, explosions, energy shields, vapor trails, and clouds are just a few of the objects that can be represented by these techniques [849, 1342].

A few popular forms of billboards are described in this section. In each, a surface normal and an up direction are found for orienting the polygon, usually a quadrilateral. These two vectors are sufficient to create an orthonormal basis for the surface. In other words, these two vectors describe the rotation matrix needed to rotate the quadrilateral to its final orientation (see Section 4.2.4). An *anchor location* on the quadrilateral (e.g., its center) is then used to establish its position in space.

Often, the desired surface normal  $\mathbf{n}$  and up vector  $\mathbf{u}$  are not perpendicular. In all billboarding techniques, one of these two vectors is established as being a fixed vector that must be maintained in the given direction. The process is always the same to make the other vector perpendicular to this fixed vector. First, create a “right” vector  $\mathbf{r}$ , a vector pointing toward the right edge of the quadrilateral. This is done by taking the cross product of  $\mathbf{u}$  and  $\mathbf{n}$ . Normalize this vector  $\mathbf{r}$ , as it will be used as an axis of the orthonormal basis for the rotation matrix. If vector  $\mathbf{r}$  is of zero length, then  $\mathbf{u}$  and  $\mathbf{n}$  must be parallel and the technique [576] described in Section 4.2.4 can be used.

The vector that is to be adjusted (i.e., is not fixed), either  $\mathbf{n}$  or  $\mathbf{u}$ , is modified by taking the cross product of the fixed vector and  $\mathbf{r}$ , which creates a vector perpendicular to both. Specifically, if the normal  $\mathbf{n}$  is fixed (as is true for most billboarding techniques), then the new up vector  $\mathbf{u}'$  is

$$\mathbf{u}' = \mathbf{n} \times \mathbf{r}. \quad (10.2)$$

This process is shown in Figure 10.4. If instead, the up direction is fixed (true for axially aligned billboards such as trees on landscape), then the new normal vector  $\mathbf{n}'$  is

$$\mathbf{n}' = \mathbf{r} \times \mathbf{u}. \quad (10.3)$$

The new vector is then normalized and the three vectors are used to form a rotation matrix. For example, for a fixed normal  $\mathbf{n}$  and adjusted up vector  $\mathbf{u}'$  the matrix is

$$\mathbf{M} = ( \mathbf{r}, \mathbf{u}', \mathbf{n} ). \quad (10.4)$$

This matrix transforms a quadrilateral in the  $xy$  plane with  $+y$  pointing toward its top edge, and centered about its anchor position, to the proper orientation. A translation matrix is then applied to move the quadrilateral’s anchor point to the desired location.

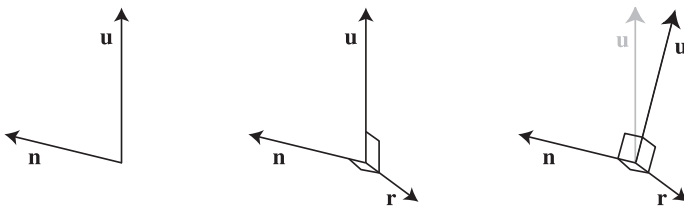


**Figure 10.4.** Given a desired surface normal direction  $\mathbf{n}$  and an approximate up vector direction  $\mathbf{u}$ , we wish to establish a set of three mutually perpendicular vectors to orient the billboard. In the middle figure, the “right” vector  $\mathbf{r}$  is found by taking the cross product of  $\mathbf{u}$  and  $\mathbf{n}$ , and so is perpendicular to both of them. In the right figure, the fixed vector  $\mathbf{n}$  is crossed with  $\mathbf{r}$  to give a mutually perpendicular up vector  $\mathbf{u}'$ .

With these preliminaries in place, the main task that remains is deciding what surface normal and up vector are used to define the billboard’s orientation. A few different methods of constructing these vectors are discussed in the following sections.

### 10.6.1 Screen-Aligned Billboard

The simplest form of billboarding is a *screen-aligned billboard*. This form is similar to a two-dimensional sprite, in that the image is always parallel to the screen and has a constant up vector. For this type of billboard the desired surface normal is the negation of the view plane’s normal. This view direction is a constant vector  $\mathbf{v}_n$  that the camera looks along, in world space. The up vector  $\mathbf{u}$  is from the camera itself. It is a vector in the view plane that defines the camera’s up direction. These two vectors are already perpendicular, so all that is needed is the “right” direction vector  $\mathbf{r}$  to form the rotation matrix for the billboard. Since  $\mathbf{n}$  and  $\mathbf{u}$  are constants for the camera, this rotation matrix is the same for all billboards of this type.

Screen-aligned billboards are useful for information such as annotation text, as the text will always be aligned with the screen itself (hence the name “billboard”).

### 10.6.2 World-Oriented Billboard

The previous billboarding technique can be used for circular sprites such as particles, as the up vector direction actually is irrelevant for these. If the camera rolls, i.e., rotates along its view direction axis, due to symmetry, the appearance of each sprite does not change.

For other sprites, the camera’s up vector is normally not appropriate. If the sprite represents a physical object, it is usually oriented with respect to the world’s up direction, not the camera’s. For such sprites, one way to

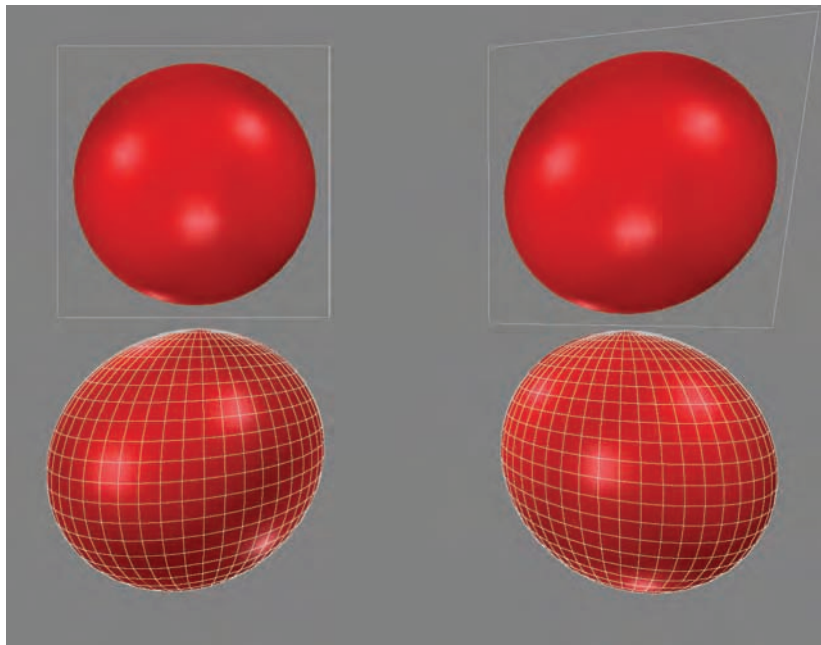


**Figure 10.5.** A view of four spheres, with a wide field of view. The upper left is a billboard texture of a sphere, using view plane alignment. The upper right billboard is viewpoint oriented. The lower row shows two real spheres.

render these by using this world up vector to derive the rotation matrix. In this case, the normal is still the negation of the view plane normal, which is the fixed vector, and a new perpendicular up vector is derived from the world's up vector, as explained previously. As with screen-aligned billboards, this matrix can be reused for all sprites, since these vectors do not change within the rendered scene.

Using the same rotation matrix for all sprites carries a risk. Because of the nature of perspective projection, objects that are away from the view axis are warped. This projection warps objects that are away from the view direction axis. See the bottom two spheres in Figure 10.5. The spheres become elliptical, due to projection onto a plane. This phenomenon is not an error and looks fine if a viewer's eyes are the proper distance and location from the screen. That is, if the virtual camera's field of view matches the eye's actual field of view, then these spheres look unwarped. We usually notice this warping because the real viewing conditions are rarely exactly those portrayed in the two-dimensional image.<sup>3</sup> For example, the field of

---

<sup>3</sup>For centuries, artists have realized this problem and compensated as necessary. Ob-

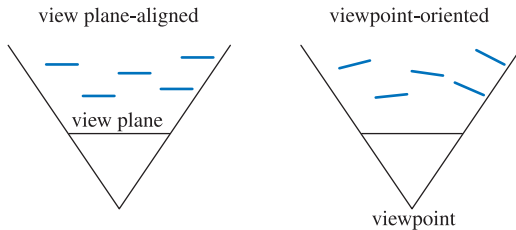


**Figure 10.6.** A top view of the two billboard alignment techniques. The five billboards face differently, depending on the method.

view is often made wider than expected viewing conditions, so that more of the surrounding scene is presented to the user (see Section 4.6.2).

When the field of view and the sprites are small, this warping effect can often be ignored and a single orientation aligned to the view plane used. Otherwise, the desired normal needs to equal the vector from the center of the billboard to the viewer's position. This we call a *viewpoint-oriented* billboard. See Figure 10.6. The effect of using different alignments is shown in Figure 10.5. As can be seen, view plane alignment has the effect of making the billboard have no distortion, regardless of where it is on the screen. Viewpoint orientation distorts the sphere image in the same way in which real spheres are distorted by projecting the scene onto the plane. For impostors, discussed in Section 10.7.1, viewpoint orientation is normally more appropriate. Impostors are meant to simulate geometry in a scene, so the simulation should distort in the same way as real geometry does.

World-oriented billboarding is useful for rendering many different phenomena. Guymon [471] and Nguyen [928] both discuss in depth making convincing flames, smoke, and explosions. One technique is to cluster and overlap animated sprites in a random and chaotic fashion. Doing so helps hide the looping pattern of the animated sequences, while also avoiding making each fire or explosion look the same. Reis [1061] gives a fast method for also approximating the light-scattering properties of smoke, using impostors and relief mapping techniques to achieve more convincing results.

For animating billboards, it is beneficial to store all of the animated frames in the same texture. This reduces the overhead associated with changing textures. One way of doing so is to use a volume texture to store the animation, with the  $z$ -axis essentially acting as time. By changing the  $z$ -axis to a value between two layers, a blend frame between two images can be generated. One drawback to this method is that mipmapping will

---

jects expected to be round, such as the moon, were painted as circular, regardless of their positions on the canvas [477].



**Figure 10.7.** Clouds created by a set of world-oriented impostors. (*Images courtesy of Mark Harris, UNC-Chapel Hill.*)

cause averaging of adjacent frames. Texture arrays (supported by DirectX 10-level hardware) address this problem, although they require two texture lookups to blend between frames. For GPUs without support for texture arrays, a commonly used alternative is to pack the animation frames into a two-dimensional texture as a grid of images.

Dobashi et al. [264] simulate clouds and render them with billboards, and create shafts of light by rendering concentric semitransparent shells. Harris and Lastra [505] also use impostors to simulate clouds. See Figure 10.7. They treat the clouds as three-dimensional objects, in that if a plane is seen flying into a cloud, the impostor is split into two pieces, one behind the plane and one in front. It is worth noting that the world up vector is just one choice for defining an impostor’s orientation. For example, Harris and Lastra use the up vector of the view used to create the impostor originally. Consistency is maintained as long as the same up vector is used frame to frame to orient the impostor.

Wang [1319, 1320] details cloud modeling and rendering techniques used in Microsoft’s flight simulator product. Each cloud is formed from 5 to 400 billboards. Only 16 different base sprite textures are needed, as these can be modified using non-uniform scaling and rotation to form a wide variety of cloud types. Modifying transparency based on distance from the cloud center is used to simulate cloud formation and dissipation. To save on processing, distant clouds are all rendered to a set of eight panorama textures surrounding the scene, similar to a skybox. The artist sets a number of parameters to control shading. For example, there are five different cloud height color levels. The effect of dissipation of light in heavy clouds is approximated by making the lower altitudes darker. The artist also sets colors associated with different sun directions. These determine how clouds look at midday versus sunset.

Billboards are not the only cloud rendering technique possible. For example, Elinas and Stuerzlinger [304] generate clouds using Gardner’s method of rendering sets of nested ellipsoids that become more transparent around the viewing silhouettes. Pallister [985] discusses procedurally generating cloud images and animating these across an overhead sky mesh. Wenzel [1342] uses a series of planes above the viewer for distant clouds.

As discussed in Sections 5.7 and 6.6, overlapping semitransparent billboards should be rendered in sorted order, usually with  $z$ -depth testing on but writing off for semitransparent fragments, to perform compositing correctly. Smoke or fog billboards cause artifacts when they intersect solid objects. See Figure 10.8. The illusion is broken, as what should be a volume is seen to be a set of layers. One solution is to have the pixel shader program check the  $z$ -depth of the underlying objects while processing each billboard. If the underlying object is close to the billboard’s depth at a pixel, then the transparency of the billboard fragment is increased. In this



**Figure 10.8.** On the left, the areas circled show where intersection artifacts occur due to the dust cloud billboards intersecting with objects. On the right, the billboards fade out where they are near objects, avoiding this problem. (*Images from NVIDIA SDK 10 [945] sample “Soft Particles” courtesy of NVIDIA Corporation.*)

way, the billboard is treated more like a volume and the layer artifact disappears. Fading linearly with depth can lead to a discontinuity when the maximum fade distance is reached. An S-curve fadeout function avoids this problem. Lorach [792, 945] provides more information and implementation details. Billboards that have their  $z$ -depths modified in this way are called *soft particles*.

Fadeout using soft particles solves the problem of billboards intersecting solid objects. Another problem can occur when explosions move through scenes or the viewer moves through clouds. In the former case, a billboard could move in front of an object during an animation. This causes a noticeable pop if the billboard moves from entirely invisible to fully visible. Similarly, as the viewer moves through billboards, a billboard can entirely disappear as it moves in front of the near plane, causing a sudden jump in what is seen. Umenhoffer et al. [1280, 1281] introduce the idea of spherical billboards. Essentially, the billboard object is thought of as actually defining a spherical volume in space. The billboard itself is rendered ignoring  $z$ -depth read; the purpose of the billboard is purely to make the pixel shader program execute at locations where the sphere is likely to be. The pixel shader program computes entrance and exit locations on this spherical volume and uses solid objects to change the exit depth as needed and the near clip plane to change the entrance depth. In this way, each billboard’s sphere can be properly faded out.

A slightly different technique was used in *Crysis* [887, 1341], using box-shaped volumes instead of spheres to reduce pixel shader cost. Another

optimization is to have the billboard represent the front of the volume, rather than its back. This enables the use of  $Z$ -buffer testing to skip parts of the volume that are behind solid objects. This optimization is viable only when the sphere is known to be fully in front of the viewer, so that the billboard is not clipped by the near view plane.

### 10.6.3 Axial Billboard

The last common type is called *axial billboarding*. In this scheme the textured object does not normally face straight-on toward the viewer. Instead, it is allowed to rotate around some fixed world space axis and align itself so as to face the viewer as much as possible within this range. This billboarding technique can be used for displaying distant trees. Instead of representing a tree with a solid surface, or even with a pair of tree outlines as described in Section 6.6, a single tree billboard is used. The world's up vector is set as an axis along the trunk of the tree. The tree faces the viewer as the viewer moves, as shown in Figure 10.9. For this form of billboarding, the world up vector is fixed and the viewpoint direction is used as the second, adjustable vector. Once this rotation matrix is formed, the tree is translated to its position.

A problem with the axial billboarding technique is that if the viewer flies over the trees and looks straight down, the illusion is ruined, as the trees will look like the cutouts they are. One workaround is to add a circular, horizontal, cross section texture of the tree (which needs no billboarding) to help ameliorate the problem.

Another technique is to use level of detail techniques to change from an impostor to a three-dimensional model. Automated methods of turning polygonal tree models into sets of billboards are discussed in Section 10.7.2. Meyer et al. [862] give an overview of other real-time tree rendering tech-



**Figure 10.9.** As the viewer moves around the scene, the bush billboard rotates to face forward. In this example the bush is lit from the south so that the changing view makes the overall shade change with rotation.



**Figure 10.10.** Billboard examples. The *heads-up display* (HUD) graphics and star-like projectiles are screen-aligned billboards. The large teardrop explosions in the right image are a viewpoint-oriented billboards. The curved beams are axial billboards made of a number of quadrilaterals. To create a continuous beam, these quadrilaterals are joined at their corners, and so are no longer rectangular. (*Images courtesy of Maxim Garber, Mark Harris, Vincent Scheib, Stephan Sherman, and Andrew Zaferakis, from “BHX: Beamrunner Hypercross.”*)

niques. Kharlamov et al. [648] discuss algorithms used in the commercial *SpeedTree* package.

Just as screen-aligned billboards are good for representing symmetric spherical objects, axial billboards are useful for representing objects with cylindrical symmetry. For example, laser beam effects can be rendered with axial billboards, since their appearance looks the same from any angle around the axis. See Figure 10.10 for an example of this and other billboards. Another example is shown in Figure 3.7 on page 42, using the geometry shader to generate the billboards on the fly.

## 10.7 Particle Systems

A particle system [1052] is a set of separate small objects that are set into motion using some algorithm. Applications include simulating fire, smoke, explosions, water flows, trees, whirling galaxies, and other phenomena. Particle systems are not a form of rendering, but rather a method of animation. The idea is that there are controls for creating, moving, changing, and deleting particles during their lifetimes.

There has been much written on the subject of generating and controlling particle systems [849, 1295, 1331]. What is most relevant here is the way the particles are represented. Representations even simpler than billboards are common—namely, points and lines. Each particle can be a single point rendered on the screen. Particles can also be represented by billboards. As mentioned in Section 10.6.2, if the particle is round, then

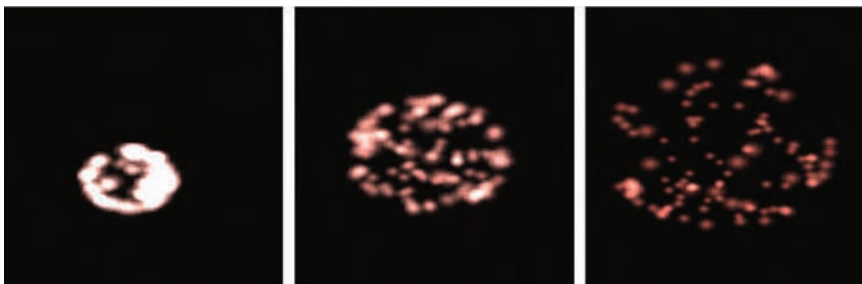


**Figure 10.11.** Fireworks using a single screen-aligned, alpha-textured billboard for each particle, varied in size and shade over time. (*From a DirectX demonstration program, Microsoft.*)

the up vector is irrelevant to its display. In other words, all that is needed is the particle's position to orient it. DirectX supports this by providing a point sprite primitive,<sup>4</sup> thereby eliminating the need for a quadrilateral for each point. Figure 10.11 shows a simple particle system, a fireworks display. In addition to an image texture representing a particle, other textures could be included, such as a normal map. Another rendering technique is to represent a particle by a line segment drawn from the particle's previous location to its current location. Axial billboards can be used to display thicker lines. See Figure 10.43 on page 504 for an example of rain using lines.

LeGrand [753] discusses implementing particle systems with vertex shaders. Modern GPUs can also generate animation paths for sprites and even perform collision detection. A number of researchers use the pixel shader to generate successive locations for the particles, which the vertex shader then accesses to generate sprites [665, 682, 737]. Collision detection with the environment and among particles themselves can also be performed on the GPU.

DirectX 10 further supports particles by using the geometry shader and stream output to control the birth and death of particles. This is done by storing results in a vertex buffer and updating this buffer each frame entirely on the GPU [261, 387]. An example is shown in Figure 10.12.

In addition to animating explosions, waterfalls, rain, froth, and other phenomena, particle systems can also be used for rendering. For example, some trees can be modeled by using particle systems to represent the geometry, with more particles generated and displayed as the viewer comes closer to the model.

---

<sup>4</sup>DirectX 10 eliminated this primitive, since the same functionality (expanding a single vertex into a quadrilateral) is supported by the geometry shader.

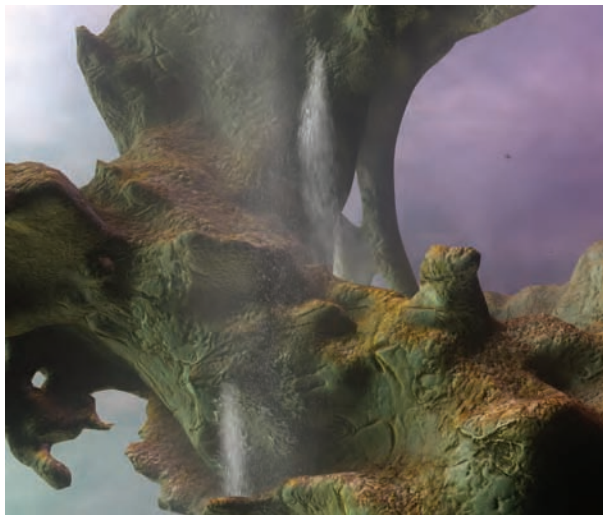


**Figure 10.12.** Particle system used in “Cascades” demo [387]. The water particles have different representations, dependent on state. (*Image courtesy of NVIDIA Corporation.*)

### 10.7.1 Impostors

An impostor<sup>5</sup> is a billboard that is created on the fly by rendering a complex object from the current viewpoint into an image texture, which is mapped onto the billboard. The rendering is therefore proportional to the number of pixels the impostor covers on the screen, instead of the number of vertices or the depth complexity of the object. The impostor can be used for a few instances of the object or a few frames so that a performance increase is obtained. In this section different strategies for updating impostors will be presented.

The impostor image is opaque where the object is present; everywhere else it is totally transparent. Sometimes, impostors are called sprites. One of the best uses for impostors is for collections of small static objects [352]. Impostors are also useful for rendering distant objects rapidly. A different approach is to instead use a very low level of detail model (see Section 14.7). However, such simplified models often lose shape and color information. Impostors do not necessarily have this disadvantage, since a higher quality impostor can be created [20, 1358]. Another advantage is that the texture image can be lowpass filtered to create an out-of-focus image for a depth-of-field effect.

---

<sup>5</sup>Maciel and Shirley [806] identify several different types of impostors in 1995, including the one presented in this section. Since that time, the definition of an impostor has narrowed to the one we use here [352].

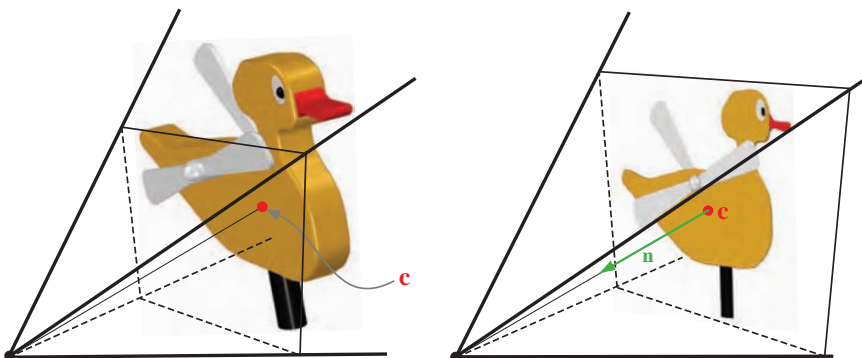


**Figure 10.13.** At the left, an impostor is created of the object viewed from the side by the viewing frustum. The view direction is toward the center,  $c$ , of the object, and an image is rendered and used as an impostor texture. This is shown on the right, where the texture is applied to a quadrilateral. The center of the impostor is equal to the center of the object, and the normal (emanating from the center) points directly toward the viewpoint.

In practice, an impostor should be faster to draw than the object it represents, and it should closely resemble the object. Also of importance is that an impostor should be reused for several viewpoints located close together, and therefore efficiently exploits frame-to-frame coherence. This is usually the case because the movement of the projected image of an object diminishes with an increased distance from the viewer. This means that slowly moving objects that are located far from the viewer are candidates for this method. Another situation in which impostors can be used is for objects located close to the viewer that tend to expose the same side to the viewer as they move [1112].

Before rendering the object to create the impostor image, the viewer is set to view the center of the bounding box of the object, and the impostor polygon is chosen so as to point directly toward the viewpoint (at the left in Figure 10.13). The size of the impostor's quadrilateral is the smallest rectangle containing the projected bounding box of the object.

An impostor of an object is created by first initializing the alpha channel of an offscreen buffer to  $\alpha = 0.0$  (i.e., fully transparent). The object is then drawn into an offscreen image, with the alpha channel set to opaque ( $\alpha = 1.0$ ) where the object is present. The pixels that are not written retain their transparency. Similar to deferred shading, a normal map or other textures could also be generated and used to later render the impostor.

The impostor image is then used as a texture (or textures) on the polygon. Once created, the rendering of the impostor starts with placing the impostor polygon at the center of the bounding box, and orienting the

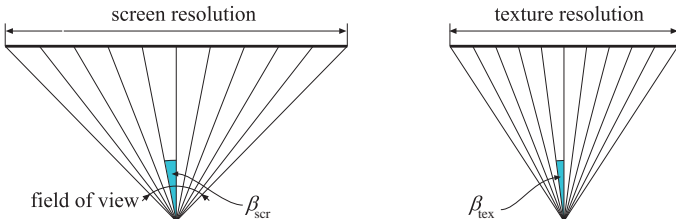


**Figure 10.14.** The angle of a screen pixel is computed as  $\beta_{\text{scr}} = \text{fov}/\text{screenres}$ , and the angle for the texture is computed similarly. Note that these are both approximations as neither of the angles are constant for all pixels/texels.

polygon so its normal points directly to the viewer (see the image on the right in Figure 10.13). This is therefore a viewpoint-oriented billboard.

Mapping the texture onto a polygon facing the viewer does not always give a convincing effect. The problem is that an impostor itself does not have a thickness, so can show problems when combined with real geometry. See Figure 10.17 on page 463. Forsyth suggests instead projecting the texture along the view direction onto the bounding box of the object [352]. This at least gives the impostor a little geometric presence.

The resolution of the texture need not exceed the screen resolution and so can be computed by Equation 10.5 [1112].

$$\text{texres} = \text{screenres} \frac{\text{objsize}}{2 \cdot \text{distance} \cdot \tan(\text{fov}/2)} \quad (10.5)$$

There are many ways in which an impostor may give a bad approximation of the underlying geometry. This happens when some type of change in view or object orientation becomes larger than some threshold, and the impostor is then said to be invalid. One limit to the usefulness of an impostor is its resolution. If a distant impostor comes closer, the individual pixels of the texture may become obvious, and so the illusion breaks down. The angles  $\beta_{\text{scr}}$ , which represents the angle of a pixel, and  $\beta_{\text{tex}}$ , which represents the angle of a texel of the impostor, can be used to determine when the lifetime of an impostor has expired. This is illustrated in Figure 10.14. When  $\beta_{\text{tex}} > \beta_{\text{scr}}$ , there is a possibility that the texels will be clearly visible, requiring the impostor to be regenerated from the current position of both the viewer and the object. In this way, the impostor texture adapts to the screen resolution.

We must also test whether the impostors are valid from the current point of view. Here we present Schaufler's method [1112, 1113]. The first observation is that when only the view direction changes, the impostors need not be updated. The reason is that even though the projection plane

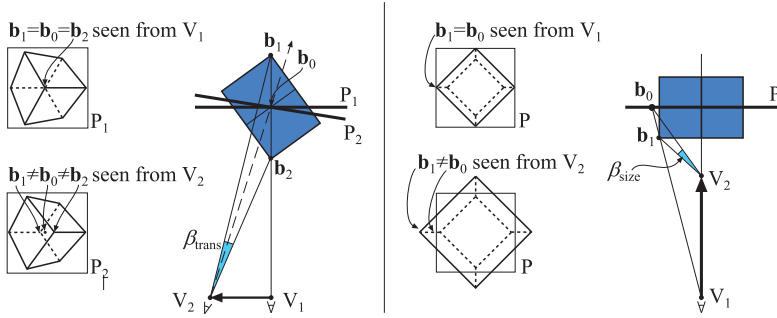


**Figure 10.15.** The left part illustrates the overestimate of the error angle  $\beta_{\text{trans}}$ , and the right part shows the overestimate of  $\beta_{\text{size}}$ . When any of these angles becomes greater than  $\beta_{\text{scr}}$ , the impostor needs to be regenerated. The bounding box of the original object is shown in blue. (Illustration after Schaufler [1112].)

changes as the viewer rotates, the projection itself does not. A viewpoint-oriented billboard always directly faces the viewer, regardless of the view direction.

We need to consider regenerating an impostor only when the viewer moves relative to the impostor. We will look at the two extreme cases, which are shown in Figure 10.15. The left case in this figure shows how to compute an error angle called  $\beta_{\text{trans}}$  that increases as the viewer moves sideways (parallel to the plane of the impostor). The apparent displacement of the object from two such viewpoints is called the *parallax*. The error angle is computed by considering how the extreme points on the object's original bounding box create an angle when the viewer moves. When the viewer has moved sufficiently far, the impostor will need to be updated because  $\beta_{\text{trans}} > \beta_{\text{scr}}$ .

The right case in Figure 10.15 shows the extreme case when the viewer moves toward the impostor. This angle is computed by considering how extreme points on the bounding box project onto the impostor plane when the viewer moves toward the impostor. Both angles  $\beta_{\text{trans}}$  and  $\beta_{\text{size}}$  can be computed with, for example, the law of cosines (see Section B.2). This is a different test than that for  $\beta_{\text{tex}}$ , as it measures the amount of change in perspective effect. In conclusion, an impostor needs to be regenerated every time  $\beta_{\text{tex}}$ ,  $\beta_{\text{trans}}$ , or  $\beta_{\text{size}}$  is greater than  $\beta_{\text{scr}}$ .

Forsyth [352] gives many practical techniques for using impostors in games. He suggests that some heuristic be used to update the texture coordinates (on more complex shapes containing the object) to reduce parallax errors. Also, when impostors are used for dynamic objects, he suggests a preprocessing technique that determines the largest distance,  $d$ , any vertex moves during the entire animation. This distance is divided by the number

of time steps in the animation, so that  $\Delta = d/\text{frames}$ . If an impostor has been used for  $n$  frames without updating, then  $\Delta * n$  is projected onto the image plane. If this distance is larger than a threshold set by the user, the impostor is updated. Other ideas include updating the objects close to the near plane or the mouse cursor more often. For efficient updating of impostors, he suggests rendering a number of them to subregions of a large texture.

Forsyth also uses prediction in an interesting way. Normally, an impostor is created for a certain frame, and it is only correct for that frame. A number of frames later, the impostor is updated again. If some prediction of camera and animation parameters can be done for the frame in between these generation times, then the average quality of the impostor can be improved. However, using impostors for dynamic objects, especially unpredictable ones such as players, is hard. For small objects, such as distant people in crowd scenes, it is possible to store a set of impostors for a wide range of views and in different animated poses using a set of textures. However, the costs can be high, e.g., 1.5 Mb per figure [266]. Often it is best to just render the geometry when an object moves, and switch to impostors when the object is static [352]. Kavan et al. [637] introduce *polypostors*, in which a model of a person is represented by a set of impostors, one for each limb and the trunk. This system tries to strike a balance between pure impostors and pure geometry.

A major advantage of impostors is that they can be used to improve frame rate, sometimes at a reduction in quality. Schaufler [1114] describes a constant-frame-rate algorithm for impostors, which is similar to Funkhouser and Séquin's work [371] presented in Section 14.7.3. Rafferty et al. [1043] present a technique that replaces the geometry seen through a portal with an impostor. They also use image warping to give longer lifetimes to the impostors, as does Schaufler [1116].

Hierarchical image caching is an algorithm that uses impostors arranged in a hierarchy for better performance. This technique was invented independently by Schaufler and Stürzlinger [1113] and Shade et al. [1151]. The basic idea is to partition the scene into a hierarchy of boxes and create an impostor for each box, and also to create impostors for the parents in the partitioning. The impostors are then updated hierarchically. A related area of study, point-based rendering, represent surfaces with a hierarchical arrangements of splats, essentially alpha-blended particles; see Section 14.9.

Meyer et al. [862] use a hierarchy of *bidirectional texture functions* (BTF) to render trees realistically. A BTF is a texture that stores, for each texel, shaded colors for multiple lighting and viewing directions. Another way of thinking about a BTF is as a series of images of an object or surface, one for each combination of viewing and lighting direction. Several such images, evenly located on a sphere, are thus used in a hierarchy to

represent the tree. Nine BTFs are combined to reconstruct the tree for a particular view and light direction. At rendering time, they also use a hierarchy of cube maps to compute shadows on the trees.

### 10.7.2 Billboard Clouds

A problem with impostors is that the rendered image must continue to face the viewer. If the distant object is changing its orientation, the impostor must be recomputed. To model distant objects that are more like the triangle meshes they represent, Décoret et al. [241] present the idea of a *billboard cloud*. A complex model can often be represented by a small collection of overlapping cutout billboards. A real-world analog is a paper cut-out model. Billboard clouds can be considerably more convincing than paper models, as additional information, such as normal or displacement maps and different materials, can be applied to their surfaces. Cracks are handled by projecting polygons along the crack onto both billboards. Décoret et al. present a method of automatically finding and fitting planes to a given model within some given error tolerance.

This idea of finding a set of planes is more general than the paper cut-out analogy might imply. Billboards can intersect, and cutouts can be arbitrarily complex. For example, a number of researchers fit billboards to polygonal tree models [80, 373, 376, 707]. From models with tens of thousands of triangles, they can create convincing billboard clouds consisting of less than a hundred textured quadrilaterals. See Figure 10.16. That said, using billboard clouds can cause a considerable amount of overdraw, costing fill rate, so it is expensive in other ways. Semitransparent pixels can also cause visible problems in some situations if the billboards (and separate objects) are not properly drawn in back-to-front order (for trees, such problems are usually lost in the noise).

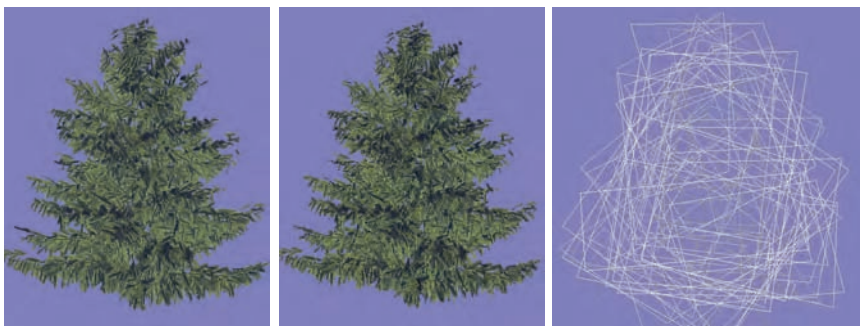


**Figure 10.16.** On the left, a tree model made of 20,610 triangles. In the middle, the tree modeled with 78 billboards. The overlapping billboards are shown on the right. (*Images courtesy of Dylan Lacewell, University of Utah.*)

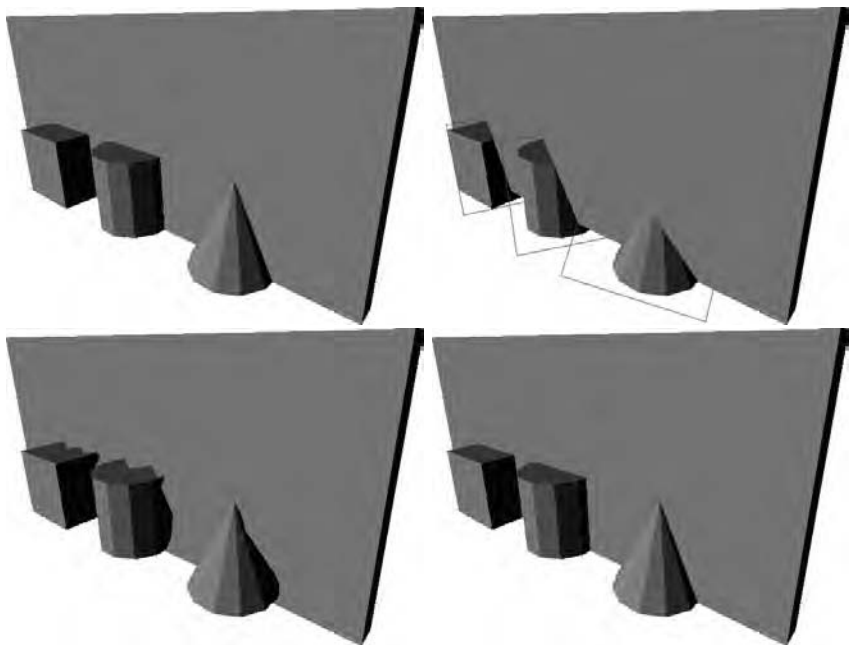


**Figure 10.17.** The upper left image shows a simple scene rendered with geometry. The upper right image shows what happens if impostors are created and used for the cube, the cylinder, and the cone. The bottom image shows the result when depth sprites are used. The depth sprite in the left image uses two bits for depth deviation, while the one on the right uses eight bits. (*Images courtesy of Gernot Schaufler.*)

## 10.8 Displacement Techniques

If the texture of an impostor is augmented with a depth component, this defines a rendering primitive called a *depth sprite* or a *nailboard* [1115]. The texture image is thus an RGB image augmented with a  $\Delta$  parameter for each pixel, forming an  $\text{RGB}\Delta$  texture. The  $\Delta$  stores the deviation from the depth sprite polygon to the correct depth of the geometry that the depth sprite represents. This  $\Delta$  channel is essentially a heightfield in view space. Because depth sprites contain depth information, they are superior to impostors in that they can help avoid visibility problems. This is especially evident when the depth sprite polygon penetrates nearby geometry. Such a case is shown in Figure 10.17. If basic impostors were used, closely located objects would have to be grouped together and treated as one to get a reasonable result [1115].

When a depth sprite is rendered, the depth of the depth sprite polygon is used as an offset for the  $\Delta$ -values. Since depth-difference values are stored in the  $\Delta$ -components, a small number of bits can be used to store

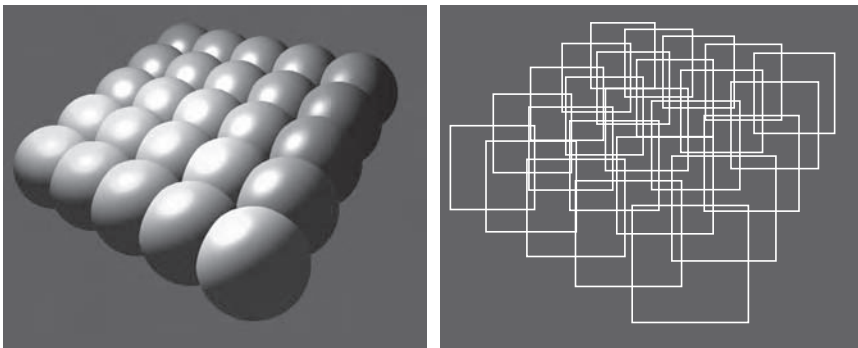


**Figure 10.18.** Each sphere to the left is rendered as one textured quadrilateral with depth. To the right, the wire frame of the scene is shown. (*Images courtesy of NVIDIA Corporation.*)

these. Typically, 8 to 16 fixed-point bits suffice. Schaufler derives a method for transforming between different spaces and so obtains correct depths in the depth buffer [1115]. Pixel shaders are able to perform this algorithm by varying the  $z$ -depth per pixel. See Figure 10.18 for an example.

Shade et al. [1152] also describe a depth sprite primitive, where they use warping to account for new viewpoints. They introduce a primitive called a *layered depth image*, which has several depths per pixel. The reason for multiple depths is to avoid the gaps that are created due to deocclusion (i.e., where hidden areas become visible) during the warping. Related techniques are also presented by Schaufler [1116] and Meyer and Neyret [861]. To control the sampling rate, a hierarchical representation called the *LDI tree* was presented by Chang et al. [171].

Related to depth sprites is *relief texture mapping* introduced by Oliveira et al. [963]. The relief texture is an image with a heightfield that represents the true location of the surface. Unlike a depth sprite, the image is not rendered on a billboard, but rather is oriented on a quadrilateral in world space. An object can be defined by a set of relief textures that match at their seams. In the original CPU-side algorithm, texture warping methods were used to render these sets of textures. Using the GPU, heightfields can be mapped onto surfaces and a form of ray tracing can be used to render them, as discussed at length in Section 6.7.4.

Policarpo and Oliveira [1022] first present a method of displaying relief texture objects on the GPU. A set of textures on a single quadrilateral hold the heightfields, and each is rendered in turn. As a simple analogy, any object formed in an injection molding machine can be formed by two heightfields. Each heightfield represents a half of the mold. More elaborate models can be recreated by additional heightfields. Given a particular view of a model, the number of heightfields needed is equal to the maximum



**Figure 10.19.** Woven surface modeled by applying four heightfield textures to a surface and rendered using relief mapping [1022]. (*Image courtesy of Fabio Policarpo and Manuel M. Oliveira.*)

depth complexity found. Similar to spherical billboards, the main purpose of each underlying quadrilateral is to cause evaluation of the heightfield texture by the pixel shader. This method can also be used to create complex geometric details for surfaces; see Figure 10.19.

One problem with this method is that when the quadrilateral is displayed near edge-on, the heightfield protrudes out beyond the limits of the quadrilateral on the screen. In such an area the heightfield will not be rendered, because the pixels in this area are not evaluated. Risser [1067] solves this problem by using a billboard that faces the viewer and bounds the object. This billboard has its texture coordinates adjusted by using projection to match those of the original quadrilateral when rasterized. In this way, the method decouples the object's bounds from its underlying quadrilateral, with the billboard being more a window through which rays are cast onto the model. The points of intersection are then found using a search similar to relief mapping. Figure 10.20 shows an example using this method.

Another problem with layered heightfields is that texel shading values can be stretched excessively along the displacement direction. That is, a steep heightfield can have single texture value used along its entire height. Baboud and Décoret [52], similarly to the original relief texture mapping

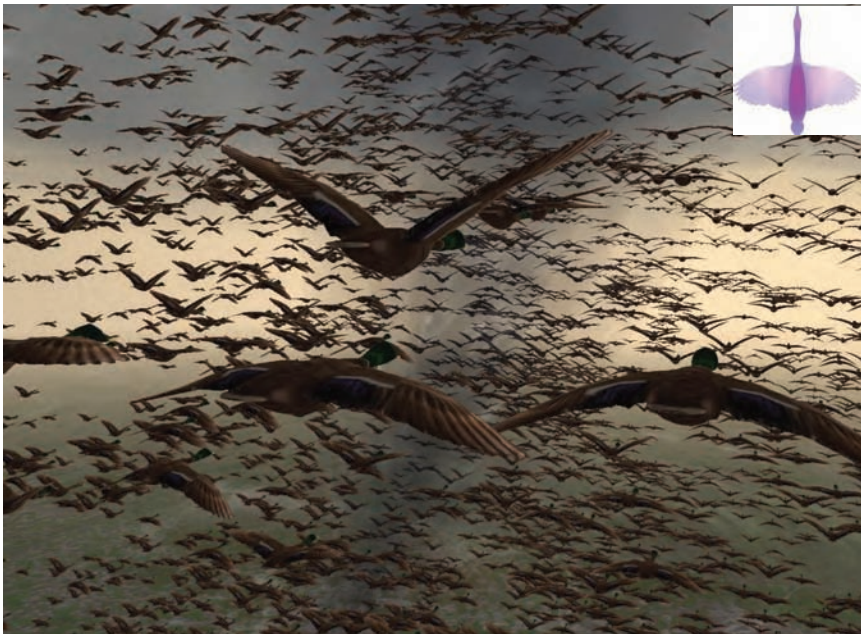


**Figure 10.20.** A scene with 100,000 animated ducks rendered in real time. Each duck is represented by a single quadrilateral. Each quadrilateral renders a model stored as two to four heightfields in a single texture, with additional textures used to add color. Animation is achieved by procedurally warping the input heightfields over time directly in the shader. In the upper right corner are shown the two heightfields, one in each channel, that represent the duck’s body [1069]. (*Images courtesy of Eric Risser, Columbia University.*)

paper, put six heightfields (or, essentially, depthfields) on the surface of a box and use the box to force computation. They also use a distorted texture projection to avoid texel stretching. Andújar et al. [24] generalize the idea of relief impostors by creating an overlapping set of heightfields, each from a different view, that represent the object from any direction. During rendering a few (typically three) of these heightfields are selected and used for display.

Decoret et al. [240] present a taxonomy of rendering errors that may occur when impostors are used, and they also introduce a new impostor, called the *multi-mesh impostor* (MMI). The MMI addresses the different errors by using several meshes per impostor, and by using both pregenerated and dynamically updated impostor images. Aliaga and Lastra [20] develop a constant-frame-rate algorithm, where an automatic preprocessing technique creates layered depth images that are used to replace distant geometry during rendering. Wimmer et al. [1358] develop sampling techniques

in order to accurately create a new type of primitive, called *point-based impostors*.

Sillion et al. [1182] describe an impostor technique suited for urban scenery. Distant geometry is replaced with a texture that is mapped onto a mesh that coarsely follows the geometry it approximates. This type of primitive is called a *textured depth mesh* (TDM). Jeschke and Wimmer [609] describe a process of converting a model or scene to a TDM. Wilson and Manocha [1356] discuss converting complex models into TDMs from different viewpoints, sharing data between these representations to save on processing, memory, and artifacts. Their paper also provides a thorough overview of related work.

Gu et al. [463] introduce the *geometry image*. The idea is to transform an irregular mesh into a square image that holds position values. The image itself represents a regular mesh, i.e., the triangles formed are implicit from the grid locations. That is, four neighboring texels in the image form two triangles. The process of forming this image is difficult and rather involved; what is of interest here is the resulting image that encodes the model. The image can be used to generate a mesh, of course. The interesting feature is that the geometry image can be mipmapped. Different levels of the mipmap pyramid form simpler versions of the model. This blurring of the lines between vertex and texel data, between mesh and image, is a fascinating and tantalizing way to think about modeling.

## 10.9 Image Processing

Graphics accelerators have generally been concerned with creating artificial scenes from geometry and shading descriptions. Image processing is different, taking an input image and analyzing and modifying it in various ways. Some forays were made to create fixed-function hardware to allow graphics accelerators to perform such operations. For example, in the late 1990s some high-end workstations implemented the OpenGL 1.2 image processing extensions. However, these API calls were not implemented in consumer-level graphics hardware. Because of limited die space, IHVs were reluctant to use it for image processing. This desire to avoid custom solutions spurred efforts to create programmable pipeline elements, such as pixel shaders. The combination of programmable shaders and the ability to use an output image as an input texture opened the way to using the GPU for a wide variety of image processing effects. Such effects can be combined with image synthesis: Typically, an image is generated and then one or more image processing operations is performed on it. Performing image processing after rendering is called *post processing*.

There are a few key techniques for post processing using the GPU. A scene is rendered in some form to an offscreen buffer: color image,  $z$ -depth buffer, etc. This resulting image is then treated as a texture. This texture is applied to a screen-filling quadrilateral.<sup>6</sup> Post processing is performed by rendering this quadrilateral, as the pixel shader program will be invoked for every pixel. Most image processing effects rely on retrieving each image texel's information at the corresponding pixel. Depending on system limitations and algorithm, this can be done by retrieving the pixel location from the GPU or by assigning texture coordinates in the range  $[0, 1]$  to the quadrilateral and scaling by the incoming image size.

The stage is now set for the pixel shader to access the image data. All relevant neighboring samples are retrieved and operations are applied to them. The contribution of the neighbor is weighted by a value depending on its relative location from the pixel being evaluated. Some operations, such as edge detection, have a fixed-size neighborhood (for example,  $3 \times 3$  pixels) with different weights (sometimes negative) for each neighbor and the pixel's original value itself. Each texel's value is multiplied by its corresponding weight, the results are summed, and the final result is then output (or processed further).

As discussed in Section 5.6.1, various filter kernels can be used for reconstruction of a signal. In a similar fashion, filter kernels can be used to blur the image. A *rotation-invariant filter kernel* is one that has no dependency on radial angle for the weight assigned to each contributing texel. That is, such filter kernels are described entirely by a texel's distance from the central pixel for the filtering operation. The sinc filter, shown in Equation 5.15 on page 122, is a simple example. The Gaussian filter, the shape of the well-known bell curve, is a commonly used kernel:

$$\text{Gaussian}(x) = \frac{1}{\sigma^2 \sqrt{2\pi}} e^{-\frac{x^2}{2\sigma^2}}, \quad (10.6)$$

where  $x$  is the distance from the texel's center and  $\sigma$  is the standard deviation. A larger standard deviation makes a wider bell curve. The term in front of the  $e$  keeps the area under the continuous curve equal to 1. However, this term is irrelevant when forming a discrete filter kernel. The values computed per texel are summed together over the area, and all values are then divided by this sum, so that the final weights will sum to 1. Because of this normalization process, the constant term serves no purpose, and so often is not shown in filter kernel descriptions. The Gaussian two-dimensional and one-dimensional filters shown in Figure 10.21 are formed this way.

---

<sup>6</sup>It is not always a single quadrilateral. Because of the way caches work, it can be faster to tile the screen.

| (a) |        |        |        |        |        |
|-----|--------|--------|--------|--------|--------|
|     | 0.0030 | 0.0133 | 0.0219 | 0.0133 | 0.0030 |
|     | 0.0133 | 0.0596 | 0.0983 | 0.0596 | 0.0133 |
|     | 0.0219 | 0.0983 | 0.1621 | 0.0983 | 0.0219 |
|     | 0.0133 | 0.0596 | 0.0983 | 0.0596 | 0.0133 |
|     | 0.0030 | 0.0133 | 0.0219 | 0.0133 | 0.0030 |

| (b)    |        |        |        |        |
|--------|--------|--------|--------|--------|
| 0.0545 | 0.2442 | 0.4026 | 0.2442 | 0.0545 |
| 0.0545 | 0.2442 | 0.4026 | 0.2442 | 0.0545 |
| 0.0545 | 0.2442 | 0.4026 | 0.2442 | 0.0545 |
| 0.0545 | 0.2442 | 0.4026 | 0.2442 | 0.0545 |
| 0.0545 | 0.2442 | 0.4026 | 0.2442 | 0.0545 |

| (c)    |        |               |        |        |
|--------|--------|---------------|--------|--------|
| 0.0545 | 0.0545 | <b>0.0545</b> | 0.0545 | 0.0545 |
| 0.2442 | 0.2442 | <b>0.2442</b> | 0.2442 | 0.2442 |
| 0.4026 | 0.4026 | <b>0.4026</b> | 0.4026 | 0.4026 |
| 0.2442 | 0.2442 | <b>0.2442</b> | 0.2442 | 0.2442 |
| 0.0545 | 0.0545 | <b>0.0545</b> | 0.0545 | 0.0545 |

**Figure 10.21.** One way to use a Gaussian blur kernel is to sample a  $5 \times 5$  area, weighting each contribution and summing them. Part (a) of the figure shows these weights for a blur kernel with  $\sigma = 1$ . Using separable filters, two one-dimensional Gaussian blurs, (b) and (c), are performed, with the same net result. The first pass, shown in (b) for 5 separate rows, blurs each pixel horizontally using 5 samples in its row. The second pass, (c), applies a 5-sample vertical blur filter to the resulting image from (b) to give the final result. Multiplying the weights in (b) by those in (c) gives the same weights as in (a), showing that this filter is equivalent and therefore separable. Instead of needing 25 samples, as in (a), each of (b) and (c) effectively each use 5 per pixel, for a total of 10 samples.

A problem with the sinc and Gaussian filters is that the functions go on forever. One expedient is to clamp such filters to a specific diameter or square area and simply treat anything beyond as having a value of zero. A sharp dropoff can sometimes cause problems. Cook [195], in his classic paper on stochastic sampling, presents a truncated Gaussian filter:

$$\text{Cook}(x) = \begin{cases} e^{-\frac{x^2}{2\sigma^2}} - e^{-\frac{w^2}{2\sigma^2}}, & x \leq w, \\ 0, & x > w, \end{cases} \quad (10.7)$$

where  $w$  is the radius of interest.<sup>7</sup> Beyond this radius, the evaluated number would be negative, so it is instead set to zero. This filter kernel has a smoother dropoff than just clamping the Gaussian. Other filtering kernels, such as Mitchell-Netravali [872], are designed for various properties (such as blurring or edge sharpening) while avoiding expensive (on the CPU, less so on a modern GPU) power functions. Bjorke [95], Mitchell et al. [877], and Rost [1084] each provide some common rotation-invariant filters and much other information on image processing on the GPU.

The trend for GPUs is that reading texels is the most expensive shader operation (due to bandwidth costs) and that computations drop in relative cost as time progresses. One advantage of using the GPU is that built-in interpolation and mipmapping hardware can be used to help minimize the number of texels accessed. For example, say the goal is to use a box filter, i.e., to take the average of the nine texels forming a  $3 \times 3$  grid around a given texel and display this blurred result. These nine texture samples would then be weighted and summed together by the pixel shader, which would then output the blurred result to the pixel.

Nine samples are unnecessary, however. By using bilinear filtering of a texture, a single texture access can retrieve the weighted sum of up to four neighboring texels. So the  $3 \times 3$  grid could be sampled with just four texture accesses. See Figure 10.22. For a box filter, where the weights are equal, a single sample could be placed midway among four texels, obtaining the average of the four. For a filter such as the Gaussian, where the weights differ in such a way that bilinear interpolation between four samples can be inaccurate, each sample can still be placed between two texels, but offset closer to one than the other. For instance, imagine one texel's weight was 0.01 and its neighbor was 0.04. The sample could be put so that it was a distance of 0.8 from the first, and so 0.2 from the neighbor, and the sample weight would be 0.05. Alternatively, the Gaussian could be approximated by using a bilinear interpolated sample for every four texels, finding the offset that gives the closest approximation to the ideal weights.

---

<sup>7</sup>As discussed in the previous paragraph, the unused constant scale factor is not shown.

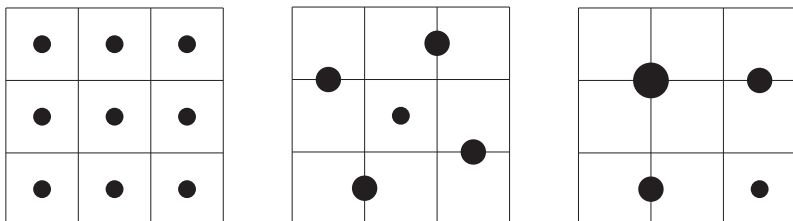


**Figure 10.22.** On the left, a box filter is applied by performing nine texture samples and averaging the contributions together. In the middle, a symmetric pattern of five samples is used, with the outside samples each representing two texels, and so each is given twice the weight of the center sample. This type of pattern can be useful for other filter kernels, where by moving the outside samples between their two texels, the relative contribution of each texel can be changed. On the right, a more efficient four sample pattern is used instead. The sample on the upper left interpolates between four texels' values. The ones on the upper right and lower left each interpolate the values of two texels. Each sample is given a weight proportional to the number of texels it represents.

Some filtering kernels are *separable*. Two examples are the Gaussian and box filters. This means that they can be applied in two separate one-dimensional blurs. Doing so results in considerably less texel access being needed overall. The cost goes from  $d^2$  to  $2d$ , where  $d$  is the kernel diameter or *support* [602, 877, 941]. For example, say the box filter is to be applied in a  $5 \times 5$  area at each pixel in an image. First the image could be filtered horizontally: The two neighboring texels to the left and two to the right of each pixel, along with the pixel's value itself, are equally weighted by 0.2 and summed together. The resulting image is then blurred vertically, with the two neighboring texels above and below averaged with the central pixel. Instead of having to access 25 texels in a single pass, a total of 10 texels are accessed in two passes. See Figure 10.21. Using the bilinear filtering technique for sampling, this can be reduced to three texel accesses per pixel per pass, for a total of six accesses, versus nine for a single-pass area interpolated approach.

Downsampling is another GPU-related technique commonly used for blurring. The idea is to make a smaller version of the image to be manipulated, for example halving the resolution along both axes to make a quarter-screen image. Depending on the input data and the algorithm's requirements, the original image may be filtered down in size or simply sampled or created at this lower resolution. When this image is accessed to blend into the final, full resolution image, magnification of the texture will use bilinear interpolation to blend between samples. This gives a further blurring effect. Performing manipulations on a smaller version of the original image considerably decreases the overall number of texels accessed. Also, any filters applied to this smaller image have the net effect of increas-

ing the relative size of the filter kernel. For example, applying a kernel with a width of five (i.e., two texels to each side of the central pixel) to the smaller image is similar in effect to applying a kernel with a width of nine to the original image. Quality will be lower, but for blurring large areas of similar color, a common case for many glare effects and other phenomena, most artifacts will be minimal. The main problem is flickering during animation [602].

One last process is worth mentioning: *ping-pong buffers* [951]. This term is commonly used in GPU image processing. It is simply the idea of applying operations between two offscreen buffers, each used to hold intermediate or final results. For the first pass, the first buffer is the input texture and the second buffer is where output is sent. In the next pass the roles are reversed, with the second now acting as the input texture and the first getting reused for output. In this second pass the first buffer's original contents are overwritten—it is just being reused as temporary storage for a processing pass.

The field of animation is beyond the scope of this volume, but it should be noted that the GPU can also assist in performing texture animation via image processing. For example, James [600] first showed how a variety of animated effects can be done by modifying textures on the GPU from frame to frame. That is, a texture image can be modified by a pixel shader and the result rendered on a surface. Then in the next frame, the result is modified again by the same pixel shader and rendered. Using one- and two-dimensional cellular automata rules, effects such as fire, smoke, and interactive rippling water can be created on a surface. Textures created can be used to modify the surface color, shading normal, heightfield, or any other attributes. Many articles have been written about performing fluid flow animation on the GPU; see Sanders et al. [1108] for a summary of past work in this area, along with a presentation of their own optimization technique. Tatarchuk's article on simulating rain [1246] is noteworthy for its innovative use of a wide range of techniques. Crane et al. [205] discuss three-dimensional fluid flow, a topic touched upon later in Section 10.16 on volume rendering.

A type of filter that has seen much recent use in graphics and related fields is the *bilateral filter*. This filter uses not only the distance between the texel and central pixel for weighting, but the difference in their values as well. This results in a “smart blur” that preserves sharp edges. The recent SIGGRAPH course on the subject [988] is a good overview of the bilateral filter and its applications.

Pixel shaders can be used in post processing to imitate thermal imaging [549], reproduce film grain [928], perform edge detection [95, 370, 877], generate heat shimmer [928] and ripples [28], posterize an image [28], render clouds [55], simulate VCR playback and rewind [254], and for a huge num-



**Figure 10.23.** Image processing using pixel shaders. The original image in the upper left is processed in various ways. The upper right shows a Gaussian difference operation, the lower left edge shows detection, and lower right a composite of the edge detection blended with the original image. (*Images courtesy of NVIDIA Corporation.*)

ber of other operations [95, 600, 875, 876, 941]. See Figure 10.23. These examples use a color image as the only input. Synthesized images also come with a  $Z$ -buffer, and this data can also be used in post processing, as well as any other buffers the user cares to generate. For example, the stencil buffer can be used to perform screen dissolves and other video-like effects [693].

Rather than continue with an exhaustive (and exhausting) litany of all possible effects, the sections that follow cover some of the common uses for image processing on the GPU, along with related areas such as high dynamic range images.

## 10.10 Color Correction

Color correction<sup>8</sup> is the process of taking an existing image and using some function to convert each color to some other color (or not converting at all). There are many reasons to color correct images or film, e.g., to mimic the appearance of a specific kind of film stock, provide a coherent look among elements, or to portray a particular mood or style. Color correction typically consists of taking a single pixel's RGB value as the input and applying an algorithm to it to produce a new RGB. Another use is to accelerate decoding video from, for example, the YUV color space to RGB. More complex functions that rely on screen position or neighboring pixels are possible [1148], but most operators use the color of each pixel as the sole input. Some color correction functions treat each color separately, i.e., the value of the red input is the only variable that affects the red output channel. Others use all three channels as inputs that can affect each output. The RGB to luminance conversion, Equation 7.11 on page 215, is an example of the latter: All three inputs affect each output channel. In this case, the output value is the same for all three outputs.

For a simple conversion such as luminance, a pixel shader program can be applied with a screen-filling quadrilateral and the equation evaluated directly. Simple formulae can perform basic operations such as scaling the brightness or modifying saturation [476]. However, color correction functions can be anything: complex mathematical functions or user-generated tweaks and modifications. In addition, these functions can be mixed or used multiple times. The final correction function can therefore be arbitrarily complex and so be expensive to apply in an interactive setting. On the GPU, the normal solution for evaluating complex functions is to use a *look-up table* (LUT). For a color correction function that has only one input channel, the table can be one-dimensional. The input acts as the index into the array, and the output value for that input is stored in the array. In this way, any arbitrarily complex function for a single channel is reduced to a constant-time lookup. Implementing this on the GPU is a matter of storing the array in a texture. Given, say, 256 possible values for the input color, a  $1 \times 256$  texture is created to hold the output values. A texture read is then used to access this array to perform the conversion [94].

When a color conversion uses three inputs, a three-dimensional LUT of size  $256^3$  (more than 16 million texels) is usually out of the question. If the color conversion function does not change rapidly between neighboring values, a much smaller LUT array can be used, e.g., a cube of say  $32^3$  values. The resolution of the volume depends on the transform's linearity. The GPU's texture sampling functionality can be used to perform

---

<sup>8</sup>In film production, often called *color grading* or *color timing*.



**Figure 10.24.** Color correction is performed on the scene on the left to create the effect on the right. By dimming and desaturating the colors, a nighttime effect is produced. A volume texture is used to transform the colors of the original image [881]. (*Images from “Day of Defeat: Source” courtesy of Valve Corp.*)

trilinear interpolation among the neighboring values. Usually such tables will need to have higher precision than eight bits to avoid banding artifacts. An example from Valve’s color correction system [881] is shown in Figure 10.24. Selan’s article [1148] provides a good description of color conversion techniques for the GPU.

## 10.11 Tone Mapping

A computer screen has a certain useful luminance range, while a real image has a potentially huge luminance range. *Tone mapping* (also called *tone reproduction*) is the process of fitting a wide range of illumination levels to within the screen’s limited gamut [286, 1274]. The fact that the eye takes time to adjust to rapidly changing lighting conditions, called *light adaptation*, can be simulated in real-time rendering by artificially changing the perception of light. For example, for a person coming out of a tunnel in a virtual world, the scene could be made to appear bright and washed out for a second and then fade to normal light and color levels. This would mimic the perceived feeling of coming out of a real tunnel into the light [990].

There are many other cases where tone reproduction and the eye’s response play a part. As a demonstration, take a CD jewel case and look down on it. Aim it to reflect a fluorescent light source (i.e., a light source that is not painful to view directly). By the Fresnel effect, the reflection

from the CD case is only about 4% the power of the light itself. Our eyes rapidly adjust when shifting from the CD to the light, and so we barely notice this wide disparity.

Older interactive computer rendering systems could not handle color values outside the 0.0 to 1.0 range. This limited the inputs, as well as the outputs, of the shading equation to this range. The limitation on input values was the more restrictive of the two. The fact that any quantity could not exceed 1 meant that any product of two quantities was always darker than either. For example, diffuse lighting could darken the diffuse color texture but never brighten it. These limitations meant that all quantities had to be carefully tweaked to a narrow brightness range, leading to washed-out scenes with low contrast and little detail in shadowed regions. This not only reduced realism, but also made the resulting images less visually appealing.

Modern GPUs can handle almost arbitrarily high shading values, allowing for realistic lighting and high contrast images. Since output devices are still limited in their supported range and precision (8 bits per channel is typical)<sup>9</sup> some form of tone mapping needs to be done on the shaded values. This mapping can be performed on the fly (as the objects are rendered) or in a separate full-screen pass. An advantage of tone mapping on the fly is that low-precision color buffers can be used. However, there are two disadvantages to on-the-fly tone mapping. One is that in scenes with high overdraw, the tone mapping step will be performed multiple times per pixel, which is particularly troublesome if the operator is costly. The other drawback has to do with alpha-blended objects. Tone mapping should properly be performed after blending, and doing it on the fly may result in objectionable artifacts. Performing tone mapping in a separate pass solves these issues, but does require a high-precision color buffer. Such color buffers use more memory bandwidth, an increasingly precious resource.

The simplest “tone mapping operator” is to simply clamp the output values to the displayable range. In many applications where the lighting and camera are predictable, this can work surprisingly well. An extra degree of control can be added via an exposure setting that scales the output colors before they are clamped. Such controls can be set by the application designers or artists for best visual effect.

In applications where the lighting is not predictable, adaptive tone mapping techniques that react to the overall illumination in the scene can produce better results. For first-person games in particular, such mimicry of the human visual system can lead to a more immersive experience. The simplest adaptive tone mapping operator is *maximum to white* [1010]. The

---

<sup>9</sup>Displays with a greater effective contrast and brightness range are available. This subject is touched upon in Section 18.1.1.

largest luminance value found is used to scale the results to a displayable range. One major drawback of this method is that a single exceptionally bright pixel in the scene will make the rest of the results all scale to be extremely dark.

What our eyes most notice are differences in contrast in the area currently being viewed. Tone mapping operators use each pixel's computed luminance value to determine the RGB displayed. Such operators can be global or local in nature. A global algorithm, such as "maximum to white," applies the same mapping to all parts of the image. A local algorithm analyzes each pixel with respect to its neighbors. If a neighbor is extremely different in luminance value, its effect on the pixel's mapping is minimized, as only those pixels that are close in luminance are the ones most noticeable for maintaining contrast. Local tone mapping operators can be quite effective, but are not often implemented in interactive applications. Goodnight et al. [426] present a system that implements both global and local tone operators using pixel shaders.

Global tone mapping operators are less costly in general. There are effectively two steps: Sample the computed image to determine luminance levels, then use this information to remap the image as desired. For example, the "maximum to white" method examines every pixel for the largest luminance, then scales all pixels by this maximum value. Running through all pixels in an image can be costly. One method is to perform a number of passes. The first pass renders a screen-filling quad to a smaller image, using numerous texture samples to downsize and average the luminance. The succeeding passes sample this small image to reduce it further, eventually to a single pixel holding the average luminance [152, 1206]. A variant is to make a direct rendering of a smaller version of the scene, i.e., a quarter size or smaller, then average this. This smaller image is useful for post processing to produce a bloom or glow effect for the brighter pixels in the image, as discussed in Section 10.12. Other sampling schemes are possible, such as sampling over fewer pixels or sampling using some conversion other than the luminance equation [261].

Another approach is to create a *histogram* of the rendered result's luminance and use it to create a mapping. A histogram is an array of bins and is commonly represented as a bar graph, with each bar's height showing the number of pixels of a given luminance value or range of values. Histograms can also be created for individual RGB channels. One simple mapping is *histogram equalization* [422], which remaps the histogram so that each display luminance level has a number of bins assigned to it. The goal is to have each display level have approximately the same number of pixels associated with it. The effect is to increase contrast among the more common luminance levels. One problem with this approach is that contrast can be over-exaggerated. Scheuermann and Hensley [159, 1122] provide an

efficient method of generating histograms with the GPU by using vertex texture fetches or rendering to a vertex buffer. They also give an overview of previous work and alternate methods, as well as implementation details for histogram equalization and tone mapping operators that avoid contrast exaggeration.

Valve [881] uses GPU occlusion queries to count the pixels that fall in a given range of luminance values, building up the luminance histogram over several frames (time averaging is used to smooth out high-frequency variations in the results). Systems such as CUDA, which enable writing from the GPU to different memory locations, can enable the generation of luminance histograms on the fly, without additional passes.

If the range of input values from the image is relatively low, i.e., it does not encompass many magnitudes of difference, a simple averaging and rescaling can work fine to map the image to a displayable range [1206]. Normally, taking the straight average of the luminance values for high dynamic range images is inadequate for reasonable tone mapping operations, since a few extremely large values can dominate the average computed. As summarized by Reinhard et al. [1058], when summing up the pixel values, it is usually better to take the logarithm of the luminance and average these values, then convert back, i.e.,

$$\bar{L}_w = \exp \left( \frac{1}{N} \sum_{x,y} \log(\delta + L_w(x,y)) \right). \quad (10.8)$$

$\bar{L}_w$  is the log-average luminance and  $L_w(x,y)$  is the luminance at pixel  $(x,y)$ . The  $\delta$  is some tiny value, e.g., 0.0001, just so the logarithm of 0 (undefined) is never attempted for black pixels.

The effect of light adaptation can be applied at this point, if desired. One method is to use the previous frame's log-average luminance along with this frame's [261]:

$$\bar{L}'_w = \bar{L}_w^{\text{prev}} + c(\bar{L}_w - \bar{L}_w^{\text{prev}}). \quad (10.9)$$

Setting  $c$  to, say, 0.04 has the effect of taking 4% of the difference between the current luminance and the previous luminance and adapting by this much for the frame.<sup>10</sup> The resulting luminance  $\bar{L}'_w$  is then used as the previous luminance in the next frame. This is a simple hack with little physical basis; other equations are certainly possible [159, 1206]. Such blending based on previous results can also have the desirable effect of damping out any statistical noise from one frame to the next. The slowly changing nature can, in turn, be used to reduce the number of samples

---

<sup>10</sup>This equation assumes a constant frame rate. In practice, a term such as  $1 - \text{pow}(c, t/30)$  should be used in place of  $c$ , where  $t$  is time in seconds and 30 is the fps.



**Figure 10.25.** The effect of varying light level [881]. The brighter images also have a post-process bloom effect applied to them. (*Images from “Half-Life 2: Lost Coast” courtesy of Valve Corp.*)

needed to compute a good approximation of the current frame’s average luminance.

Once this log-average luminance is computed, a variety of tone operators are possible. For example, one simple mapping is

$$L(x, y) = \frac{a}{L_w} L_w(x, y), \quad (10.10)$$

where  $L(x, y)$  is the resulting luminance. The  $a$  parameter is the *key* of the scene. *High-key* in photography means that contrast and shadows are minimized and all is brightly (but not overly) lit; *low-key* tends to maximize contrast between light and dark. A bride in a white dress against a white background is high-key, a wolf backlit by the moon is low-key. A normal key value is around  $a = 0.18$ , high-key up to 0.72, low-key down to 0.045. Within the area of tone mapping, the key value is similar in effect to the exposure level in a camera, and sometimes the two are used interchangeably. True high-key and low-key photography are functions of the type of lighting in a scene, not the exposure level. An example of the effect of varying the mapping is shown in Figure 10.25.

This equation tends to compress both the high and low luminance values. However, normal and low luminance values often hold more visual detail, so an improved equation is

$$L_d(x, y) = \frac{L(x, y)}{1 + L(x, y)}. \quad (10.11)$$

This adjustment compresses high luminance values to approach a value of 1, while low luminance values are nearly untouched.

Some luminance values can be extremely bright in an image, e.g., the sun. One solution is to choose a maximum luminance,  $L_{\text{white}}$ , and use the variant equation

$$L'_d(x, y) = \frac{L(x, y) \left(1 + \frac{L(x, y)}{L_{\text{white}}^2}\right)}{1 + L(x, y)}, \quad (10.12)$$

which blends between the previous equation and a linear mapping.

While the process of tone mapping sounds complex and time consuming, the overall effect can cost as little as 1% of total rendering time [1174]. One caveat with non-linear tone mapping (i.e., using any function more complex than rescaling) is that it can cause problems similar to those discussed in Section 5.8 on gamma correction. In particular, roping artifacts along antialiased edges will be more noticeable, and mipmap generation of textures will not take into account the tone mapping operator used. Persson [1008] discusses how to correct this problem in DirectX 10 by tone mapping the multisample buffer and then resolving it to the final image.

This section has covered some of the more popular global tone operators used in interactive applications. The field itself has considerably more research done in the area of local tone operators, for example. See the books by Reinhard et al. [1059] and Pharr and Humphreys [1010] for more information about tone mapping.

### 10.11.1 High Dynamic Range Imaging and Lighting

Tone mapping is used at the end of the rendering process, when lighting calculations are done. Lighting calculations themselves can suffer if the precision of the light source data is not high enough. One problem with using environment mapping to portray lighting is that the dynamic range of the light captured is often limited to eight bits per color channel [231]. Directly visible light sources are usually hundreds to thousands of times brighter than the indirect illumination (bounced light from walls, ceilings, and other objects in the environment), so eight bits are not enough to simultaneously capture the full range of incident illumination. For example, suppose a highly specular object (say a brass candlestick, reflecting 70% of the light) and a darker specular object (say an ebony statue, reflecting 5% of the light) use the same environment map (EM). If the EM contains just the lights in the room, the statue will look good and the candlestick will not; if the EM contains all the objects in the room, the opposite is true. This is because the statue is only shiny enough to visibly reflect direct light sources and little else, while the candlestick will reflect a nearly mirror-like image of the environment. Even if a single image is used and scaled in some fashion, the lack of precision will often show up as color banding artifacts.

The solution is, at least in theory, simple enough: Use higher precision environment maps. The acquisition of real-world environment data can be done with specialized photographic methods and equipment. For example, a camera might take three photos of the same scene at different exposures, which are then combined into a single high dynamic range image. The process of capturing such images is called *high dynamic range imaging* (HDRI).

Tone mapping is intimately connected with HDRI, since an HDR image is not displayable without mapping its values to the display in some fashion. Tone-mapped images can have a rich visual quality, as detail can be exposed in areas that might normally be too dark or overexposed. An example is of a photo taken inside a room, looking out a window. Overall indoor illumination is normally considerably less than that found outside. Using HDRI acquisition and tone mapping gives a resulting image that shows both environments simultaneously. Reinhard et al. [1059] discuss capture and use of HDR images in computer graphics in their comprehensive book.

Most image file formats store pixel values ranging from 0 to 255. When performing physically accurate simulations, results are computed in floating point radiance values and then tone mapped and gamma-corrected for display. Ward [1325] developed the RGBE format to store the computed values, instead of those finally displayed. RGBE retains the floating-point accuracy of results by using three 8-bit mantissas for RGB and an 8-bit exponent for all three values. In this way, the original radiance computations can be stored at higher precision at little additional cost, just 32 bits versus the usual 24. DirectX 10 adds a variant format, R9G9B9E5, which offers greater color precision with a reduced exponent range (5 bits). This shared-exponent format type is normally used only as an input (texture) format, due to the difficulty in rapidly determining a good exponent that works for all three channels. A DirectX 10 compact HDR format that is supported for output is the R11G11B10\_FLOAT format, where  $R$  and  $G$  each have 6 bits of mantissa and  $B$  has 5, and each channel has a separate 5-bit exponent [123].

In 2003, Industrial Light and Magic released code for its OpenEXR format [617, 968]. This is a high dynamic range file format that supports a number of pixel depth formats, including a 16-bit half-precision floating point format (per channel) that is supported by graphics accelerators.

The term *HDR lighting* is also loosely used to refer to a wider range of effects beyond higher precision images. For example, the term is often used to also mean the glow effect that is created using image post processing. The section that follows describes a variety of phenomena and their simulation that provide the viewer with visual cues that some part of the scene is bright.

## 10.12 Lens Flare and Bloom

*Lens flare* is a phenomenon that is caused by the lens of the eye or camera when directed at bright light. It consists of a halo and a ciliary corona. The halo is caused by the radial fibers of the crystalline structure of the lens. It looks like a ring around the light, with its outside edge tinged with red, and its inside with violet. The halo has a constant apparent size, regardless of the distance of the source. The ciliary corona comes from density fluctuations in the lens, and appears as rays radiating from a point, which may extend beyond the halo [1208].

Camera lenses can also create secondary effects when parts of the lens reflect or refract light internally. For example, hexagonal patterns can appear due to the lens's aperture blades. Streaks of light can also be seen to smear across a windshield, due to small grooves in the glass [951]. Bloom is caused by scattering in the lens and other parts of the eye, creating a glow around the light and dimming contrast elsewhere in the scene. In video production, the camera captures an image by converting photons to charge using a *charge-coupled device* (CCD). Bloom occurs in a video camera when a charge site in the CCD gets saturated and overflows into neighboring sites. As a class, halos, coronae, and bloom are called *glare effects*.

In reality, most such artifacts are less and less commonly seen as camera technology improves. However, these effects are now routinely added digitally to real photos to denote brightness. Similarly, there are limits to the light intensity produced by the computer monitor, so to give the impression of increased brightness in a scene or objects, these types of effects are explicitly rendered. The bloom effect and lens flare are almost interactive computer graphics clichés, due to their common use. Nonetheless, when skillfully employed, such effects can give strong visual cues to the viewer; for example, see Figure 8.16 on page 306.

Figure 10.26 shows a typical lens flare. It is produced by using a set of textures for the glare effects. Each texture is applied to a square that is made to face the viewer, so forming a billboard. The texture is treated as an alpha map that determines how much of the square to blend into the scene. Because it is the square itself that is being displayed, the square can be given a color (typically a pure red, green, or blue) for prismatic effects for the ciliary corona. Where they overlap, these sprites are blended using an additive effect to get other colors. Furthermore, by animating the ciliary corona, we create a sparkle effect [649].

To provide a convincing effect, the lens flare should change with the position of the light source. King [662] creates a set of squares with different textures to represent the lens flare. These are then oriented on a line going from the light source position on screen through the screen's center. When

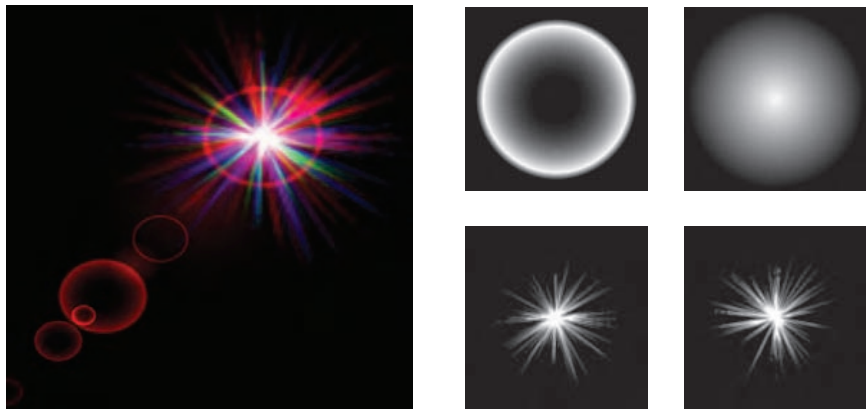


**Figure 10.26.** A lens flare and its constituent textures. On the right, a halo and a bloom are shown above, and two sparkle textures below. These textures are given color when rendered. (*Images from a Microsoft DirectX SDK program.*)

the light is far from the center of the screen, the sprites are small and more transparent, becoming larger and more opaque as the light moves inwards. Maughan [826] varies the brightness of a lens flare by using only the GPU to compute the occlusion of an onscreen area light source. He generates a single-pixel intensity texture that is then used to attenuate the brightness of the effect. Sekulic [1145] renders the light source as a single polygon, using the occlusion query hardware to give a pixel count of the area visible (see Section 14.6.1). To avoid GPU stalls from waiting for the query to return a value to the CPU, the result is used in the *next* frame to determine the amount of attenuation. This idea of gathering information and computing a result for use in the next frame is important, and can be used with most of the techniques discussed in this section.

Streaks from bright objects or lights in a scene can be performed in a similar fashion by either drawing semitransparent billboards or performing post-processing filtering on the bright pixels themselves. Oat [951] discusses using a *steerable filter* to produce the streak effect. Instead of filtering symmetrically over an area, this type of filter is given a direction. Texel values along this direction are summed together, which produces a streak effect. Using an image downsampled to one quarter of the width and height, and two passes using ping-pong buffers, gives a convincing streak effect. Figure 10.27 shows an example of this technique.

The bloom effect, where an extremely bright area spills over into adjoining pixels, is performed by combining a number of techniques already presented. The main idea is to create a bloom image consisting only of the bright objects that are to be “overexposed,” blur this, then composite it

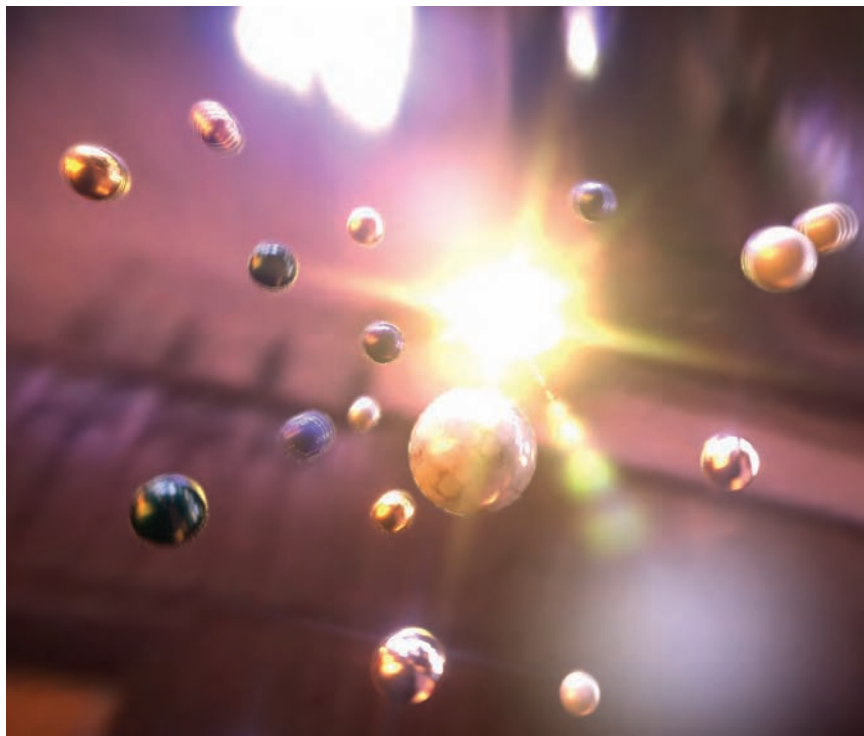


**Figure 10.27.** Lens flare, star glare, and bloom effects, along with depth of field and motion blur [261]. (*Image from “Rthdribl,” by Masaki Kawase.*)

back into the normal image. One approach is to identify bright objects and render just these to the bloom image to be blurred [602]. Another more common method is to *bright-pass filter*: any bright pixels are retained, and all dim pixels are made black, possibly with some blend or scaling at the transition point [1161, 1206].

This bloom image can be rendered at a low resolution, e.g., anywhere from one-half the width by one-half the height to one-eighth by one-eighth of the original. Doing so both saves time and helps increase the effect of filtering; after blurring, bilinear interpolation will increase the area of the blur when this image is magnified and combined with the original. This image is then blurred and combined with the original image. The blur process is done using a separable Gaussian filter in two one-dimensional passes to save on processing costs, as discussed in Section 10.9. Because the goal is an image that looks overexposed where it is bright, this image’s colors are scaled as desired and added to the original image. Additive

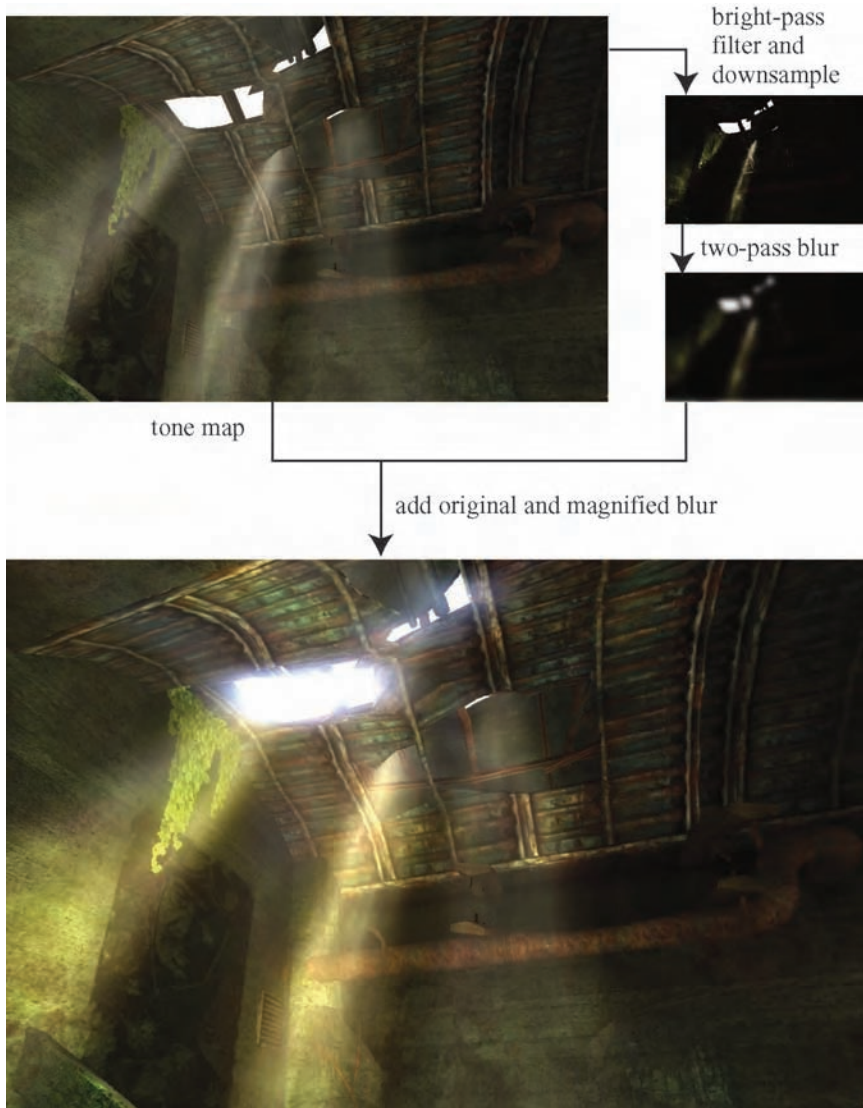


**Figure 10.28.** High-dynamic range tone mapping and bloom. The lower image is produced by using tone mapping on, and adding a post-process bloom to, the original image [1340]. (*Image from Far Cry courtesy of Ubisoft.*)

blending usually saturates a color and goes to white, which is just what is desired. An example is shown in Figure 10.28. Variants are possible, e.g., the previous frame’s results can also be added to the current frame, giving animated objects a streaking glow [602].

## 10.13 Depth of Field

Within the field of photography there is a range where objects are in focus. Objects outside of this range are blurry, the further outside the blurrier. In photography, this blurriness is caused by the ratio of the aperture to the relative distance of the object from the camera. Reducing the aperture size increases the depth of field, but decreases the amount of light forming the image. A photo taken in an outdoor daytime scene typically has a very large depth of field because the amount of light is sufficient to allow a small aperture size. Depth of field narrows considerably inside a poorly lit room. So one way to control depth of field is to have it tied to tone mapping, making out-of-focus objects blurrier as the light level decreases. Another is to permit manual artistic control, changing focus and increasing depth of field for dramatic effect as desired.

The accumulation buffer can be used to simulate depth of field [474]. See Figure 10.29. By varying the view and keeping the point of focus fixed, objects will be rendered blurrier relative to their distance from this focal point. However, as with most accumulation buffer effects, this method comes at a high cost of multiple renderings per image. That said, it does converge to the correct answer. The rest of this section discusses faster image-based techniques, though by their nature these methods can reach only a certain level of realism before their limits are reached.

The accumulation buffer technique of shifting the view location provides a reasonable mental model of what should be recorded at each pixel. Surfaces can be classified into three zones: those at the distance of the focal point, those beyond, and those closer. For surfaces at the focal distance, each pixel shows an area in sharp focus, as all the accumulated images have approximately the same result. A pixel “viewing” surfaces out of focus is a blend of all surfaces seen in the different views.

One limited solution to this problem is to create separate image layers. Render one image of just the objects in focus, one of the objects beyond, and one of the objects closer. This can be done by simply moving the near/far clipping plane locations. The two out-of-focus images are blurred, and then all three images are composited together in back-to-front order [947]. This *2.5 dimensional* approach, so called because two-dimensional images are given depths and combined, provides a reasonable result under some circumstances. The method breaks down when

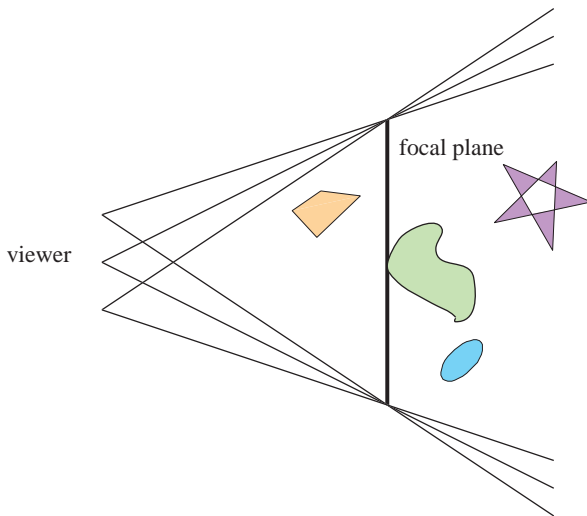


**Figure 10.29.** Depth of field via accumulation. The viewer’s location is moved a small amount, keeping the view direction pointing at the focal point, and the images are accumulated.

objects span multiple images, going abruptly from blurry to in focus. Also, all blurry objects have a uniform blurriness, without variation with distance [245].

Another way to view the process is to think of how depth of field affects a single location on a surface. Imagine a tiny dot on a surface. When the surface is in focus, the dot is seen through a single pixel. If the surface is out of focus, the dot will appear in nearby pixels, depending on the different views. At the limit, the dot will define a filled circle on the pixel grid. This is termed the *circle of confusion*. In photography it is called *bokeh*, and the shape of the circle is related to the aperture blades. An inexpensive lens will produce blurs that have a hexagonal shape rather than perfect circles.

One way to compute the depth-of-field effect is to take each location on a surface and scatter its shading value to its neighbors inside this circle. Sprites are used to represent the circles. The averaged sum of all of the overlapping sprites for the visible surface at a pixel is the color to display. This technique is used by batch (non-interactive) rendering systems to compute depth-of-field effects and is sometimes referred to as a *forward mapping* technique [245].

One problem with using scattering is that it does not map well to pixel shader capabilities. Pixel shaders can operate in parallel because they do not spread their results to neighbors. That said, the geometry shader can be used for generating sprites that, by being rendered, scatter results to

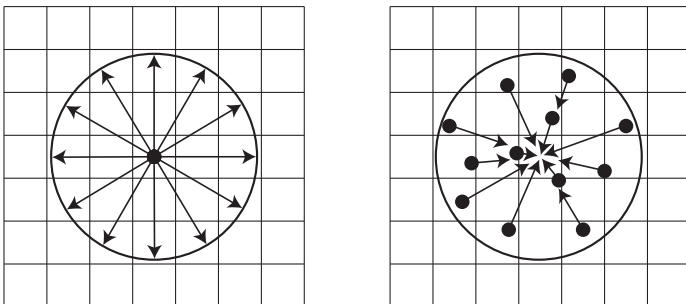


**Figure 10.30.** A scatter operation takes a pixel’s value and spreads it to the neighboring area, for example by rendering a circular sprite. In a gather, the neighboring values are sampled and used to affect a pixel. The GPU’s pixel shader is optimized to perform gather operations via texture sampling.

other pixels. This functionality can be used to aid in computing depth of field [1025].

Another way to think about circles of confusion is to make the assumption that the local neighborhood around a pixel has about the same depth. With this assumption in place, a gather operation can be done. Pixel shaders are optimized for gathering results from previous computations. See Figure 10.30. So, one way to perform depth-of-field effects is to blur the surface at each pixel based on its depth [1204]. The depth defines a circle of confusion, which is how wide an area should be sampled. Wloka [1364] gives one scheme to perform this task. The scene is rendered normally, with no special operations other than storing in the alpha channel the radius of the circle of confusion. The scene image is post-processed using filtering techniques to blur it, and blur it again, resulting in a total of three images: sharp, blurry, and blurrier. Then a pixel shader is used to access the blur factor and interpolate among the three textures for each pixel. Multiple textures are needed because of limitations on the ability of the GPU to access mip levels in mipmaps [245].

The idea behind this technique to use the blur factor to vary the filtering kernel’s size. With modern GPUs, mipmaps or summed-area tables [445, 543] can be used for sampling an area of the image texture. Another approach is to interpolate between the image and a small, blurry version of it. The filter kernel size increases with the blurriness, and the blurred image is given more weight. Sampling artifacts are minimized by using a Poisson-disk pattern [1121] (see Figure 9.30 on page 365). Gillham [400] discusses implementation details on newer GPUs. Such gather approaches are also called *backwards mapping* or *reverse mapping* methods. Figure 10.31 shows an example.



**Figure 10.31.** Depth of field using backwards mapping. (*Image from “Toy” demo courtesy of NVIDIA Corporation.*)

Scattering and gathering techniques both can have problems with occlusion, i.e., one object hiding another. These problems occur at silhouette edges of objects. A major problem is that objects in the foreground should have blurred edges. However, only the pixels covered by the foreground object will be blurred. For example, if a foreground object is in front of an object in focus, the sample radius will drop to zero when crossing the silhouette edge on the original image onto the object in focus. This will cause the foreground object to have an abrupt dropoff, resulting in a sharp silhouette. Hammon [488] present a scheme that blurs the radius of the circle of confusion selectively along silhouettes to avoid the sharp dropoff, while minimizing other artifacts.

A related problem occurs when a sharp silhouette edge from an object in focus is next to a distant, blurred object. In this case the blurred pixels near the silhouette edge will gather samples from the object in focus, causing a halo effect around the silhouette. Scheuermann and Tatarchuk [1121] use the difference in depths between the pixel and the samples retrieved to look for this condition. Samples taken that are in focus and are closer than the pixel’s depth are given lower weights, thereby minimizing this artifact. Kraus and Strengert [696] present a GPU implementation of a sub-image blurring technique that avoids many of these edge rendering artifacts.

For further in-depth discussion of depth-of-field algorithms, we refer the reader to articles by Demers [245], Scheuermann and Tatarchuk [1121], and Kraus and Strengert [696].

## 10.14 Motion Blur

For interactive applications, to render convincing images it is important to have both a steady (unvarying) frame rate that is also high enough. Smooth and continuous motion is preferable, and too low a frame rate is experienced as jerky motion. Films display at 24 fps, but theaters are dark and the temporal response of the eye is less sensitive to flicker in the dark. Also, movie projectors change the image at 24 fps but reduce flickering by redisplaying each image 2–4 times before displaying the next image. Perhaps most important, each film frame normally contains a motion-blurred image; by default, interactive graphics images are not.

In a movie, motion blur comes from the movement of an object across the screen during a frame. The effect comes from the time a camera's shutter is open for 1/40 to 1/60 of a second during the 1/24 of a second spent on that frame. We are used to seeing this blur in films and consider it normal, so we expect to also see it in videogames. The hyperkinetic effect, seen in films such as *Gladiator* and *Saving Private Ryan*, is created by having the shutter be open for 1/500 of a second or less.

Rapidly moving objects appear jerky without motion blur, “jumping” by many pixels between frames. This can be thought of as a type of aliasing, similar to jaggies, but temporal, rather than spatial in nature. In this sense, motion blur is a form of temporal antialiasing. Just as increasing display resolution can reduce jaggies but not eliminate them, increasing frame rate does not eliminate the need for motion blur. Video games in particular are characterized by rapid motion of the camera and objects, so motion blur can significantly improve their visuals. In fact, 30 fps with motion blur often looks better than 60 fps without [316, 446]. Motion blur can also be overemphasized for dramatic effect.

Motion blur depends on relative motion. If an object moves from left to right across the screen, it is blurred horizontally on the screen. If the camera is tracking a moving object, the object does not blur—the background does. There are a number of approaches to producing motion blur in computer rendering. One straightforward, but limited, method is to model and render the blur itself. This is the rationale for drawing lines to represent moving particles (see Section 10.7). This concept can be extended.

Imagine a sword slicing through the air. Before and behind the blade, two polygons are added along its edge. These could be modeled or generated on the fly by a geometry shader. These polygons use an alpha opacity per vertex, so that where a polygon meets the sword, it is fully opaque, and at the outer edge of the polygon, the alpha is fully transparent. The idea is that the model has transparency to it in the direction of movement, simulating blur. Textures on the object can also be blurred by using techniques discussed later in this section. Figure 10.32 shows an example.



**Figure 10.32.** Motion blur done by adding geometry to before and behind objects as they move. Alpha to coverage is used to perform order-independent transparency to avoid alpha-blending artifacts. (*Images from Microsoft SDK [261] sample “MotionBlur10.”*)



**Figure 10.33.** Motion blur done using the accumulation buffer. Note the ghosting on the arms and legs due to undersampling. Accumulating more images would result in a smoother blur.

The accumulation buffer provides a way to create blur by averaging a series of images [474]. The object is moved to some set of the positions it occupies during the frame, and the resulting images are blended together. The final result gives a blurred image. See Figure 10.33 for an example. For real-time rendering such a process is normally counterproductive, as it lowers the frame rate considerably. Also, if objects move rapidly, artifacts are visible whenever the individual images become discernable. However, it does converge to a perfectly correct solution, so is useful for creating reference images for comparison with other techniques.

If what is desired is the suggestion of movement instead of pure realism, the accumulation buffer concept can be used in a clever way that is not as costly. Imagine that eight frames of a model in motion have been generated and stored in an accumulation buffer, then displayed. On the ninth frame, the model is rendered again and accumulated, but also at this time the first frame is rendered again and subtracted from the accumulation buffer. The buffer now has eight frames of a blurred model, frames 2 through 9. On the next frame, we subtract frame 2 and add in frame 10, giving eight frames, 3 through 10. In this way, only two renderings per frame are needed to continue to obtain the blur effect [849].

An efficient technique that has seen wide adoption is creation and use of a *velocity buffer* [446]. To create this buffer, interpolate the screen-space velocity at each vertex across the model's triangles. The velocity can be computed by having two modeling matrices applied to the model, one for the last frame and one for the current. The vertex shader program computes the difference in positions and transforms this vector to relative screen-space coordinates. Figure 10.34 shows a velocity buffer and its results.

Once the velocity buffer is formed, the speed of each object at each pixel is known. The unblurred image is also rendered. The speed and direction at a pixel are then used for sampling this image to blur the object. For example, imagine the velocity of the pixel is left to right (or right to left, which is equivalent) and that we will take eight samples to compute the blur. In this case we would take four samples to the left and four to the right of the pixel, equally spaced. Doing so over the entire object will have the effect of blurring it horizontally. Such directional blurring is called *line integral convolution* (LIC) [148, 534], and it is commonly used for visualizing fluid flow.

The main problem with using LIC occurs along edges of objects. Samples should not be taken from areas of the image that are not part of the object. The interior of the object is correctly blurred, and near the edge of the object, the background correctly gets blended in. Past the object's sharp edge in the velocity buffer there is just the (unmoving) background, which has no blurring. This transition from blurring to no blurring gives a

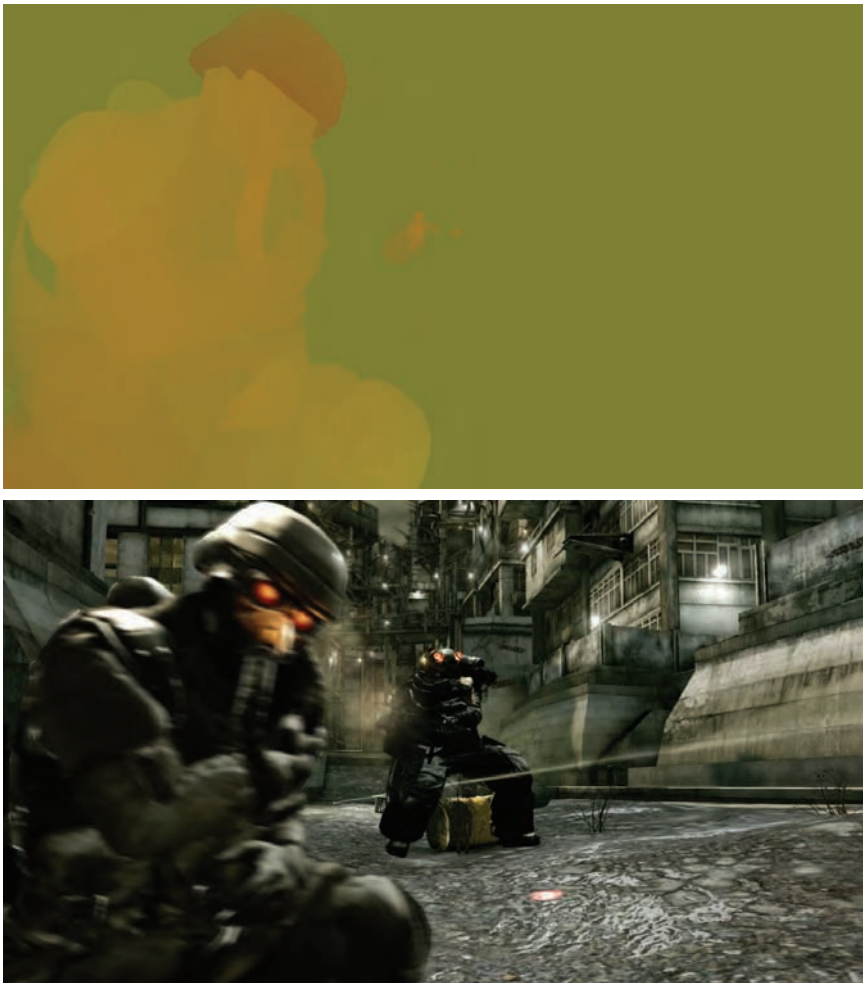


**Figure 10.34.** The top image is a visualization of the velocity buffer, showing the screen-space speed of each object at each pixel, using the red and green channels. The bottom image shows the effect of blurring using the buffer’s results. (*Images from “Killzone 2,” courtesy of Guerrilla BV.*)

sharp, unrealistic discontinuity. A visualization is shown in Figure 10.35. Some blur near the edges is better than none, but eliminating all discontinuities would be better still.

Green [446] and Shimizu et al. [1167] ameliorate this problem by stretching the object. Green uses an idea from Wloka to ensure that blurring happens beyond the boundaries of the object. Wloka’s idea [1364] is to

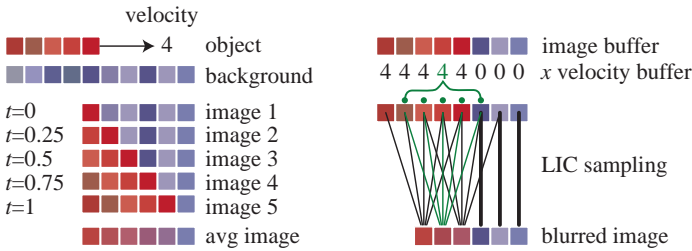


**Figure 10.35.** On the left an accumulation buffer rendering is visualized. The red set of pixels represents an object moving four pixels to the right over a single frame. The results for six pixels over the five frames are averaged to get the final, correct result at the bottom. On the right, an image and  $x$  direction velocity buffer are generated at time 0.5 (the  $y$  velocity buffer values are all zeroes, since there is no vertical movement). The velocity buffer is then used to determine how the image buffer is sampled. For example, the green annotations show how the velocity buffer speed of 4 causes the sampling kernel to be four pixels wide. For simplicity of visualization, five samples, one per pixel, are taken and averaged. In reality, the samples usually do not align on pixel centers, but rather are taken at equal intervals along the width of the kernel. Note how the three background pixels with a velocity of 0 will take all five samples from the same location.

provide motion blur by stretching the model itself. For example, imagine a ball moving across the screen. A blurred version of the ball will look like a cylinder with two round caps [1243]. To create this type of object, triangle vertices facing along the velocity vector (i.e., where the vertex normal and velocity vector dot product is greater than zero) are moved half a frame forward, and vertices facing away are moved half a frame backward. This effectively cuts the ball into two hemispheres, with stretched triangles joining the two halves, so forming the “blurred” object representation.

The stretched representation itself does not form a high-quality blurred image, especially when the object is textured. However, a velocity buffer built using this model has the effect of permitting sampling off the edges of the object in a smooth fashion. Unfortunately, there is a side effect that causes a different artifact: Now the background near the object is blurred, even though it is not moving. Ideally we want to have just the object blurred and the background remain steady.

This problem is similar to the depth-of-field artifacts discussed in the previous section, in which per pixel blurring caused different depths’ results to intermingle incorrectly. One solution is also similar: Compute the object’s motion blur separately. The idea is to perform the same process, but against a black background with a fully transparent alpha channel. Alpha is also sampled by LIC when generating the blurred object. The resulting image is a blurred object with soft, semitransparent edges. This image is then composited into the scene, where the semitransparent blur of the object will be blended with the sharp background. This technique is used



**Figure 10.36.** Radial blurring to enhance the feeling of motion. (*Image from “Assassin’s Creed” courtesy of Ubisoft.*)

in the DirectX 10 version of *Lost Planet*, for example [1025]. Note that no alpha storage is needed for making background objects blurry [402].

Motion blur is simpler for static objects that are blurring due to camera motion, as no explicit velocity buffer is necessary. Rosado [1082] describes using the previous frame’s camera view matrices to compute velocity on the fly. The idea is to transform a pixel’s screen space and depth back to a world space location, then transform this world point using the previous frame’s camera to a screen location. The difference between these screen-space locations is the velocity vector, which is used to blur the image for that pixel. If what is desired is the suggestion of motion as the camera moves, a fixed effect such as a radial blur can be applied to any image. Figure 10.36 shows an example.

There are various optimizations and improvements that can be done for motion blur computations. Hargreaves [504] presents a method of motion blurring textures by using sets of preblurred images. Mitchell [880] discusses motion-blurring cubic environment maps for a given direction of motion. Loviscach [261, 798] uses the GPU’s anisotropic texture sampling

hardware to compute LICs efficiently. Composed objects can be rendered at quarter-screen size, both to save on pixel processing and to filter out sampling noise [1025].

## 10.15 Fog

Within the fixed-function pipeline, *fog* is a simple atmospheric effect that is performed at the end of the rendering pipeline, affecting the fragment just before it is sent to the screen. Shader programs can perform more elaborate atmospheric effects. Fog can be used for several purposes. First, it increases the level of realism and drama; see Figure 10.37. Second, since the fog effect increases with the distance from the viewer, it helps the viewer of a scene determine how far away objects are located. For this reason, the effect is sometimes called *depth cueing*. Third, it can be used in conjunction with culling objects by the far view plane. If the fog is set up so that objects located near the far plane are not visible due to thick fog, then objects that go out of the view frustum through the far plane appear to fade away into the fog. Without fog, the objects would be seen to be sliced by the far plane.

The color of the fog is denoted  $\mathbf{c}_f$  (which the user selects), and the *fog factor* is called  $f \in [0, 1]$ , which decreases with the distance from the viewer. Assume that the color of a shaded surface is  $\mathbf{c}_s$ ; then the final color



**Figure 10.37.** Fog used to accentuate a mood. (*Image courtesy of NVIDIA Corporation.*)

of the pixel,  $\mathbf{c}_p$ , is determined by

$$\mathbf{c}_p = f\mathbf{c}_s + (1 - f)\mathbf{c}_f. \quad (10.13)$$

Note that  $f$  is somewhat nonintuitive in this presentation; as  $f$  decreases, the effect of the fog increases. This is how OpenGL and DirectX present the equation, but another way to describe it is with  $f' = 1 - f$ . The main advantage of the approach presented here is that the various equations used to generate  $f$  are simplified. These equations follow.

*Linear fog* has a fog factor that decreases linearly with the depth from the viewer. For this purpose, there are two user-defined scalars,  $z_{\text{start}}$  and  $z_{\text{end}}$ , that determine where the fog is to start and end (i.e., become fully foggy) along the viewer's  $z$ -axis. If  $z_p$  is the  $z$ -value (depth from the viewer) of the pixel where fog is to be computed, then the linear fog factor is

$$f = \frac{z_{\text{end}} - z_p}{z_{\text{end}} - z_{\text{start}}}. \quad (10.14)$$

There are also two sorts of fog that fall off exponentially, as shown in Equations 10.15 and 10.16. These are called *exponential fog*:

$$f = e^{-d_f z_p}, \quad (10.15)$$

and *squared exponential fog*:

$$f = e^{-(d_f z_p)^2}. \quad (10.16)$$

The scalar  $d_f$  is a parameter that is used to control the density of the fog. After the fog factor,  $f$ , has been computed, it is clamped to  $[0, 1]$ , and Equation 10.13 is applied to calculate the final value of the pixel. Examples of what the fog fall-off curves look like for linear fog and for the

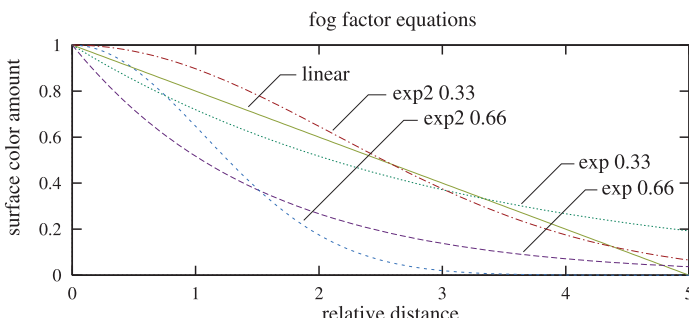


**Figure 10.38.** Curves for fog fall-off: linear, exponential, and squared-exponential, using various densities.

two exponential fog factors appear in Figure 10.38. Of these functions, the exponential fall-off is physically justifiable, as it is derived from the Beer-Lambert Law, presented in Section 9.4. Also known as Beer's Law, it states that the intensity of the outgoing light is diminished exponentially with distance.

A table (typically stored as a one-dimensional texture) is sometimes used in implementing these fog functions in GPUs. That is, for each depth, a fog factor  $f$  is computed and stored in advance. When the fog factor at a given depth is needed, the fog factor is read from the table (or linearly interpolated from the two nearest table entries). Any values can be put into the fog table, not just those in the equations above. This allows interesting rendering styles in which the fog effect can vary in any manner desired [256].

In theory, that is all there is to the fog effect: The color of a pixel is changed as a function of its depth. However, there are a few simplifying assumptions that are used in some real-time systems that can affect the quality of the output.

First, fog can be applied on a vertex level or a pixel level [261]. Applying it on the vertex level means that the fog effect is computed as part of the illumination equation and the computed color is interpolated across the polygon. Pixel-level fog is computed using the depth stored at each pixel. Pixel-level fog usually gives a better result, though at the cost of extra computation overall.

The fog factor equations use a value along the viewer's  $z$ -axis to compute their effect. For a perspective view, the  $z$ -values are computed in a nonlinear fashion (see Section 18.1.2). Using these  $z$ -values directly in the fog-factor equations gives results that do not follow the actual intent of the equations. Using the  $z$ -depth and converting back to a distance in linear space gives a more physically correct result.

Another simplifying assumption is that the  $z$ -depth is used as the depth for computing the fog effect. This is called *plane-based fog*. Using the  $z$ -

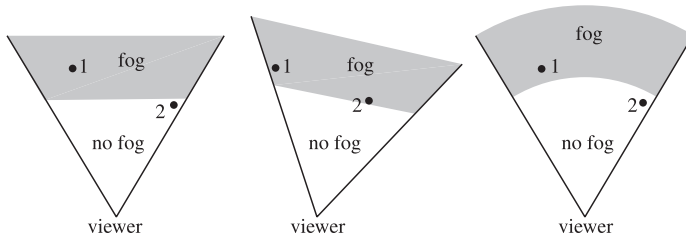


**Figure 10.39.** Use of  $z$ -depth versus radial fog. On the left is one view of two objects, using view-axis-based fog. In the middle, the view has simply been rotated, but in the rotation, the fog now encompasses object 2. On the right, we see the effect of radial fog, which will not vary when the viewer rotates.

depth can cause the unusual effect that the user can see farther into the fog along the edges of the screen than in the center. A more accurate way to compute fog is to use the true distance from the viewer to the object. This is called *radial fog*, *range-based fog*, or *Euclidean distance fog* [534]. Figure 10.39 shows what happens when radial fog is not used. The highest-quality fog is generated by using pixel-level radial fog.

The traditional fog factor described here is actually an approximation to scattering and absorption of light in the atmosphere. The depth cue effect caused by atmospheric scattering is called *aerial perspective* and includes many visual effects not modeled by the somewhat simplistic traditional fog model. The color and intensity of scattered light change with viewing angle, sun position, and distance in subtle ways. The color of the sky is a result of the same phenomena as aerial perspective, and can be thought of as a limit case.

Hoffman and Preetham [556, 557] cover the physics of atmospheric scattering in detail. They present a model with the simplifying assumption of constant density of the atmosphere, allowing for a closed-form solution of the scattering equations and a unified model for sky color and aerial perspective. This closed form solution enables rapid computation on the GPU for a variety of atmospheric conditions. Although their model produces good results for aerial perspective, the resulting sky colors are unrealistic, due to the simplified atmosphere model [1209].

Spörl [1209] presents a GPU implementation of empirical skylight and aerial perspective models proposed by Preetham et al. [1032]. Compared to Hoffman and Preetham's model, the sky colors were found to be significantly more realistic, for about double the computation cost. However, only clear skies can be simulated. Although the aerial perspective model is considerably more costly than Hoffman and Preetham's model, the visual results are similar, so Spörl suggests combining his skylight implementation with Hoffman and Preetham's aerial perspective model.

O'Neil [967] implements a physically based skylight model proposed by Nishita et al. [937] which takes the shape of the earth and variation in atmospheric density into account. The same model is implemented by Wenzel [1341, 1342]. Since the full Nishita model is very expensive, the computation is done onto a low-resolution sky dome texture and distributed over many frames. For aerial perspective, Wenzel uses a simpler model that is quicker to compute.

Mitchell [885] and Rohleder & Jamrozik [1073] present image-processing methods using radial blur to create a beams-of-light effect for backlit objects (e.g., a skyline with the sun in view).

The atmospheric scattering methods discussed so far handle scattering of light from only directional light sources. Sun et al. [1229] propose an analytical model for the more difficult case of a local point light source



**Figure 10.40.** Layered fog. The fog is produced by measuring the distance from a plane at a given height and using it to attenuate the color of the underlying object. (*Image courtesy of Eric Lengyel.*)

and give a GPU implementation. The effects of atmospheric scattering on reflected surface highlights is also handled. Zhou et al. [1408] extend this approach to inhomogeneous media.

An area where the medium strongly affects rendering is when viewing objects underwater. The transparency of coastal water has a transmission of about (30%, 73%, 63%) in RGB per linear meter [174]. An early, impressive system of using scattering, absorption, and other effects is presented by Jensen and Golias [608]. They create realistic ocean water effects in real time by using a variety of techniques, including the Fresnel term, environment mapping to vary the water color dependent on viewing angle, normal mapping for the water’s surface, caustics from projecting the surface of the water to the ocean bottom, simplified volume rendering for godrays, textured foam, and spray using a particle system. Lanza [729] uses a more involved approach for godrays that generates and renders shafts of light, a topic discussed further on in this section.

Other types of fog effects are certainly possible, and many methods have been explored. Fog can be a localized phenomenon: Swirling wisps of fog can present their own shape, for example. Such fog can be produced by overlaying sets of semitransparent billboard images, similar to how clouds and dust can be represented.

Nuebel [942] provides shader programs for layered fog effects. Lengyel presents an efficient and robust pixel shader for layered fog [762]. An example is shown in Figure 10.40. Wenzel [1341, 1342] shows how other volumes of space can be used and discusses other fog and atmospheric effects.

The idea behind these volumetric fog techniques is to compute how much of some volume of space is between the object seen and the viewer, and then use this amount to change the object’s color by the fog color [294]. In effect, a ray-object intersection is performed at each pixel, from the eye to the level where the fog begins. The distance from this intersection to the underlying surface beyond it, or to where the fog itself ends, is used to compute the fog effect.

For volumes of space such as a beam of fog illuminated by a headlight, one idea is to render the volume so as to record the maximum and minimum depths at each pixel. These depths are then retrieved and used to compute the fog’s thickness. James [601] gives a more general technique, using additive blending to sum the depths for objects with concavities. The backfaces add to one buffer, the frontfaces to another, and the difference between the two sums is the thickness of the fog. The fog volume must be watertight, where each pixel will be covered by the same number of frontfacing and backfacing triangles. For objects in the fog, which can hide backfaces, a shader is used to record the object’s depth instead. While there are some limitations to this technique, it is fast and practical for many situations.

There are other related methods. Grün and Spoerl [461] present an efficient method that computes entry and exit points for the fog volume at the vertices of the backfaces of a containing mesh and interpolates these values. Oat and Scheuermann [956] give a clever single-pass method of computing both the closest entry point and farthest exit point in a volume. They save the distance,  $d$ , to a surface in one channel, and  $1 - d$  in another channel. By setting the alpha blending mode to save the minimum value found, after the volume is rendered, the first channel will have the closest value and the second channel will have the farthest value, encoded as  $1 - d$ .

It is also possible to have the fog itself be affected by light and shadow. That is, the fog itself is made of droplets that can catch and reflect the light. James [603] uses shadow volumes and depth peeling to compute the thickness of each layer of fog that is illuminated. Tatarchuk [1246] simulates volumetric lighting by using a noise texture on the surface of a cone light’s extents, which fades off along the silhouette.

There are some limitations to using the computed thickness to render shafts of light. Complex shadowing can be expensive to compute, the density of the fog must be uniform, and effects such as illumination from stained glass are difficult to reproduce. Dobashi et al. [265] present a method of rendering atmospheric effects using a series of sampling planes of this volume. These sampling planes are perpendicular to the view direction and are rendered from back to front. The shaft of light is rendered where it overlaps each plane. These slices blend to form a volume. A variant of this

technique is used in the game *Crysis*. Mitchell [878] also uses a volume-rendering approach to fog. This type of approach allows different falloff patterns, complex gobo light projection shapes, and the use of shadow maps. Rendering of the fog volume is performed by using a layered set of textures, and this approach is described in the next section.

## 10.16 Volume Rendering

Volume rendering is concerned with rendering data that is represented by *voxels*. “Voxel” is short for “volumetric pixel,” and each voxel represents a regular volume of space. For example, creating clinical diagnostic images (such as CT or MRI scans) of a person’s head may create a data set of  $256 \times 256 \times 256$  voxels, each location holding one or more values. This voxel data can be used to form a three-dimensional image. Voxel rendering can show a solid model, or make various materials (e.g., the skin and skull) partially or fully transparent. Cutting planes can be used to show only parts of the model. In addition to its use for visualization in such diverse fields as medicine and oil prospecting, volume rendering can also produce photorealistic imagery. For example, Fedkiw et al. [336] simulate the appearance and movement of smoke by using volume rendering techniques.

There are a wide variety of voxel rendering techniques. For solid objects, implicit surface techniques can be used to turn voxel samples into polygonal surfaces [117]. The surface formed by locations with the same value is called an *isosurface*. See Section 13.3. For semitransparency, one method that can be used is *splatting* [738, 1347]. Each voxel is treated as a volume of space that is represented by an alpha-blended circular object, called a *splat*, that drops off in opacity at its fringe. The idea is that a surface or volume can be represented by screen-aligned geometry or sprites, that when rendered together, form a surface [469]. This method of rendering solid surfaces is discussed further in Section 14.9.

Lacroute and Levoy [709] present a method of treating the voxel data as a set of two-dimensional image slices, then shearing and warping these and compositing the resulting images. A common method for volume rendering makes direct use of the texturing and compositing capabilities of the GPU by rendering volume slices directly as textured quadrilaterals [585, 849, 879]. The volume dataset is sampled by a set of equally spaced slices in layers perpendicular to the view direction. These slice images are then rendered in sorted order so that alpha compositing works properly to form the image. OpenGL Volumizer [971] uses this technique for GPU volume rendering. Figure 10.41 shows a schematic of how this works, and Figure 10.42 shows examples. Ikits et al. [585] discuss this technique and related matters in depth. As mentioned in the previous

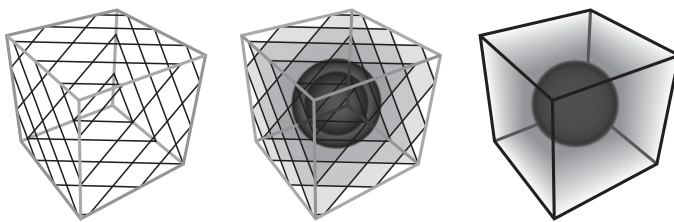


**Figure 10.41.** A volume is rendered by a series of slices parallel to the view plane. Some slices and their intersection with the volume are shown on the left. The middle shows the result of rendering just these slices. On the right the result is shown when a large series of slices are rendered and blended. (*Figures courtesy of Christof Rezk-Salama, University of Siegen, Germany.*)

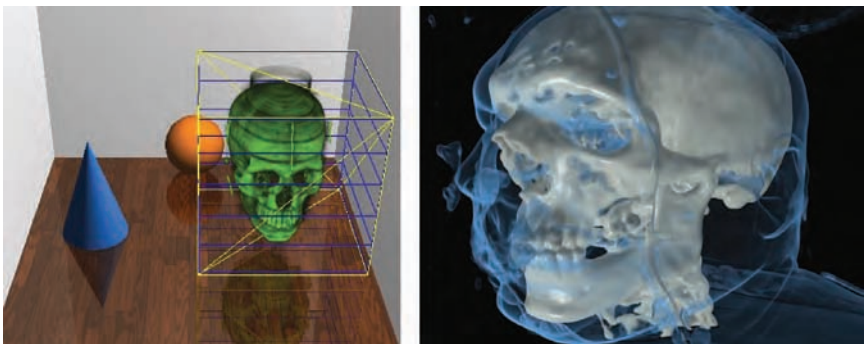


**Figure 10.42.** On the left, volume visualization mixed with the slicing technique, done with OpenGL Volumizer using layered textures. Note the reflection of the voxel-based skull in the floor. On the right, volume visualization done using a ray casting technique on the GPU. (*Left image courtesy of Robert Grzeszczuk, SGI. Right image courtesy of Natalya Tatarchuk, Game Computing Applications Group, Advanced Micro Devices, Inc.*)

section, this method is used to render shafts of light using complex volumes [878]. The main drawback is that many slices can be necessary to avoid banding artifacts, with corresponding costs in terms of fill rate.

Instead of slices, Krüger and Westermann [701] developed the idea of casting rays through the volume using the GPU. Tatarchuk and Shopf [1250] perform medical imaging with this algorithm; see Figure 10.42. Crane et al. [205] use this technique for rendering smoke, fire, and water. The basic idea is that at each pixel, a ray is generated that passes through the volume, gathering color and transparency information from the volume at regular intervals along its length. More examples using this technique are shown in Figure 10.43.



**Figure 10.43.** Fog and water rendered using volume rendering techniques in conjunction with fluid simulation on the GPU. (*Image on left from “Hellgate: London” courtesy of Flagship Studios, Inc., image on right courtesy of NVIDIA Corporation [205].*)

### 10.16.1 Related Work

A concept related to using layers of textures for volume rendering method is *volumetric textures*, which are volume descriptions that are represented by layers of two-dimensional, semitransparent textures [861]. Like two-dimensional textures, volumetric textures can be made to flow along the surface. They are good for complex surfaces, such as landscape details, organic tissues, and fuzzy or hairy objects.

For example, Lengyel [764, 765] uses a set of eight textures to represent fur on a surface. Each texture represents a slice through a set of hairs at a given distance from the surface. The model is rendered eight times, with a vertex shader program moving each triangle slightly outwards along its vertex normals each time. In this way, each successive model depicts a different height above the surface. Nested models created this way are called *shells*. This rendering technique falls apart along the silhouette edges, as the hairs break up into dots as the layers spread out. To hide this artifact, the fur is also represented by a different hair texture applied on *fins* generated along the silhouette edges. See Figure 10.44. Also see Figure 14.22 on page 682 and Figure 15.1 on page 699.

The idea of silhouette fin extrusion can be used to create visual complexity for other types of models. For example, Kharlamov et al. [648] use fins and relief mapping to provide simple tree meshes with complex silhouettes.

The introduction of the geometry shader made it possible to actually extrude shaded polyline hair for surfaces with fur. This technique was used in *Lost Planet* [1025]. A surface is rendered and values are saved at each pixel: fur color, length, and angle. The geometry shader then processes

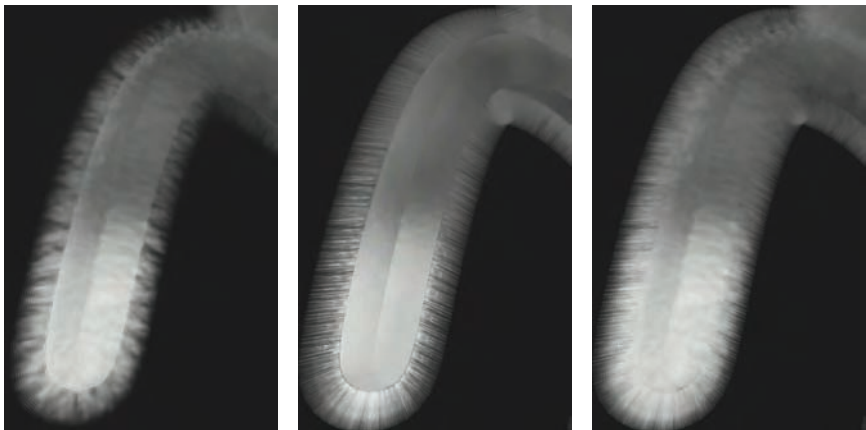


**Figure 10.44.** Fur using volumetric texturing. The model is rendered eight times, with the surface expanding outwards a small amount each pass. On the left is the result of the eight passes. Note the hair breakup along the silhouettes. In the middle, fin rendering is shown. On the right is the final rendering, using both fins and shells. (*Images from NVIDIA SDK 10 [945] sample “Fur—Shells and Fins” courtesy of NVIDIA Corporation*)

this image, turning each pixel into a semitransparent polyline. By creating one hair per pixel covered, level of detail is automatically maintained. The fur is rendered in two passes: Fur pointing down in screen space is rendered first, sorted from the bottom to the top of the screen. In this way, blending is performed correctly, back to front. In the second pass, the rest of the fur pointing up is rendered top to bottom, again blending correctly. As the GPU evolves, new techniques become possible and profitable.

## Further Reading and Resources

For an overview of early, seminal image-based rendering research, see Lengyel’s article [763], available on the web. The book *Advanced Graphics Programming Using OpenGL* [849] provides more details on the use of sprites and billboards, as well as volume rendering techniques. For a comprehensive guide to the field of volume rendering, see *Real-Time Volume Graphics* by Engel et al. [305].

There are many articles on rendering natural phenomena using image-based techniques. The Virtual Terrain Project [1302] has solid summaries of research and resources for modeling and rendering many types of natural objects and phenomena, including clouds and trees. Tatarchuk’s presentation [1246] is a *tour de force*, a detailed case study focused on simulating rain and its many related effects.



# Chapter 11

## Non-Photorealistic Rendering

*“Using a term like ‘nonlinear science’ is like referring to the bulk of zoology as ‘the study of nonelephant animals.’”*

—Stanislaw Ulam

Photorealistic rendering attempts to make an image indistinguishable from a photograph. *Non-photorealistic rendering* (NPR), also called *stylistic rendering*, has a wide range of goals. One objective of some forms of NPR is to create images similar to technical illustrations. Only those details relevant to the goal of the particular application are the ones that should be displayed. For example, a photograph of a shiny Ferrari engine may be



**Figure 11.1.** A variety of non-photorealistic rendering styles applied to a coffee grinder. (Generated using LiveArt from Viewpoint DataLabs.)

useful in selling the car to a customer, but to repair the engine, a simplified line drawing with the relevant parts highlighted may be more meaningful (as well as cheaper to print).

Another area of NPR is in the simulation of painterly styles and natural media, e.g., pen and ink, charcoal, watercolor, etc. This is a huge field that lends itself to an equally huge variety of algorithms that attempt to capture the feel of various media. Some examples are shown in Figure 11.1. Two different books give thorough coverage of technical and painterly NPR algorithms [425, 1226]. Our goal here is to give a flavor of some algorithms used for NPR in real time. This chapter opens with a detailed discussion of ways to implement a cartoon rendering style, then discusses other themes within the field of NPR. The chapter ends with a variety of line rendering techniques.

## 11.1 Toon Shading

Just as varying the font gives a different feel to the text, different styles of rendering have their own mood, meaning, and vocabulary. There has been a large amount of attention given to one particular form of NPR, *cel* or *toon rendering*. Since this style is identified with cartoons, it has strong connotations of fantasy and (in the West, at least) childhood. At its simplest, objects are drawn with solid lines separating areas of different solid colors. One reason this style is popular is what McCloud, in his classic book *Understanding Comics* [834], calls “amplification through simplification.” By simplifying and stripping out clutter, one can amplify the effect of information relevant to the presentation. For cartoon characters, a wider audience will identify with those drawn in a simple style.

The toon rendering style has been used in computer graphics for well over a decade to integrate three-dimensional models with two-dimensional cel animation. It lends itself well to automatic generation by computer because it is easily defined, compared to other NPR styles. Games such as *Okami* and *Cel Damage* have used it to good effect. See Figure 11.2.

There are a number of different approaches to toon rendering. For models with textures and no lighting, a solid-fill cartoon style can be approximated by quantizing the textures [720]. For shading, the two most common methods are to fill the polygonal areas with solid (unlit) color or to use a two-tone approach, representing lit and shadowed areas. Solid shading is trivial, and the two-tone approach, sometimes called *hard shading*, can be performed by remapping traditional lighting equation elements to different color palettes. This approach is related to the lighting model work by Gooch et al. [155, 423, 424] for NPR technical illustration. Also, silhouettes are often rendered in a black color, which amplifies the cartoon look. Silhouette finding and rendering is dealt with in the next section.



**Figure 11.2.** An example of real-time NPR rendering from the game *Okami*. (Image courtesy of Capcom Entertainment, Inc.)

Lake et al. [713, 714] and Lander [721] both present the idea of computing the diffuse shading dot product  $\mathbf{n} \cdot \mathbf{l}$  for each vertex and using this value as a texture coordinate to access a one-dimensional texture map. This can be done on the CPU or implemented as a simple vertex shader [714, 725]. The texture map itself contains only the two shades, light and dark. So, as the surface faces toward the light, the lighter shade in the texture is accessed. The standard use of the diffuse term is that  $\mathbf{n} \cdot \mathbf{l} < 0$  means the surface is facing away from the light and so is in shadow. However, this term can be used and remapped to any other values as desired. For example, in Figure 11.3, the two-tone rendering uses a threshold value of 0.5. Similarly, simple one-dimensional textures can be used to remap the effect of specular highlights. Card and Mitchell [155] describe how to perform this shading algorithm efficiently on the GPU. Barla et al. [66] add view-dependent effects by using two-dimensional maps in place of one-dimensional shade textures. The second dimension is accessed by the depth or orientation of the surface. This allows objects to smoothly soften in contrast when in the distance or moving rapidly, for example. Rusinkiewicz et al. [1092] present an interesting alternate shading model that goes the

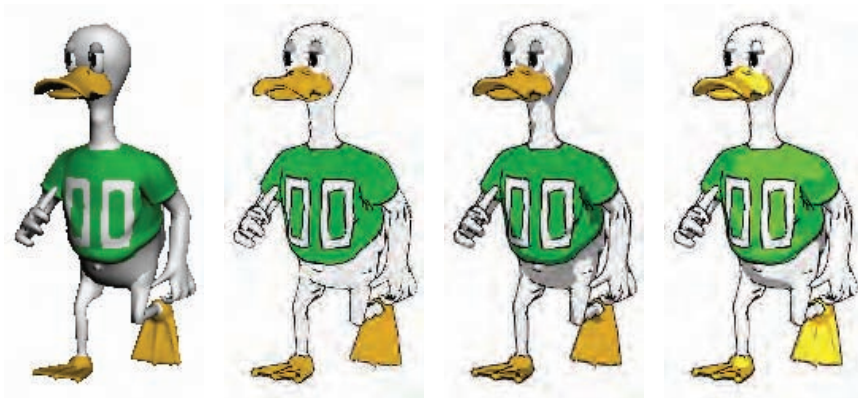


**Figure 11.3.** On the left, a Gouraud-shaded duck. The rest of the ducks have silhouettes rendered, with solid shading, diffuse two-tone shading, and specular/diffuse three-tone shading. (Reprinted by permission of Adam Lake and Carl Marshall, Intel Corporation, copyright Intel Corporation 2002.)

opposite direction, giving a high-contrast, hyperreal feel to surface shading by adjusting the effective light position.

## 11.2 Silhouette Edge Rendering

Algorithms used for cel edge rendering reflect some of the major themes and techniques of NPR. Isenberg et al. [589] present a thorough survey of this topic. Our goal here is to present algorithms that give a flavor of the field in general. Silhouette methods used can be roughly categorized as based on surface angle, procedural geometry, image processing, vector edge detection, or a hybrid of these.

There are a number of different types of edges that can be used in toon rendering:

- A *boundary* or *border edge* is one not shared by two polygons, e.g., the edge of a sheet of paper. A solid object typically has no boundary edges.
- A *crease*, *hard*, or *feature edge* is one that is shared by two polygons, and the angle between the two polygons (called the *dihedral angle*) is greater than some predefined value. A good default crease angle is 60 degrees [726]. Alternately, a crease edge is one in which the vertex normals differ between the two neighboring polygons. For example,

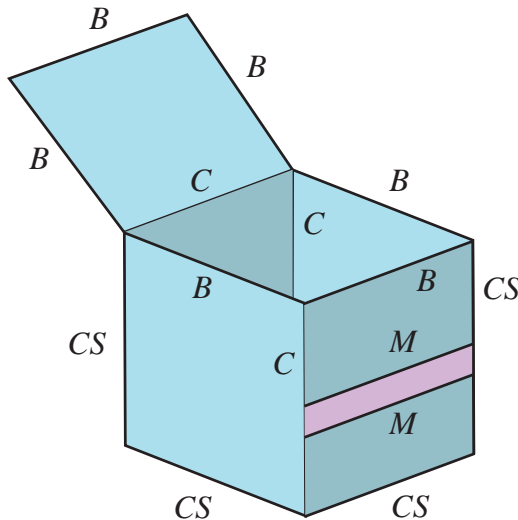


**Figure 11.4.** A box open on the top, with a stripe on the front. The boundary ( $B$ ), crease ( $C$ ), material ( $M$ ), and silhouette ( $S$ ) edges are shown.

a cube has crease edges. Crease edges can be further subcategorized into *ridge* and *valley* edges.

- A *material edge* appears when the two triangles sharing it differ in material or otherwise cause a change in shading. It also can be an edge that the artist wishes to always have displayed, e.g., forehead lines or a line to separate the same colored pants and shirt.
- A *silhouette edge* is one in which the two neighboring triangles face in different directions compared to some direction vector, typically one from the eye.

See Figure 11.4. This categorization is based on common usage within the literature, but there are some variations, e.g., what we call crease and material edges are sometimes called boundary edges elsewhere. While our focus here is toon rendering, there has been research on drawing lines that represent contours, ridges, and valleys on the surface [236, 616] or highlights from illumination [237].

For toon rendering, the direction used to define silhouette edges is the vector from the eye to some point on the edge. In other words, silhouette edges are those for which one neighboring triangle is frontfacing and the other is backfacing. Note that this computer graphics definition is a little different than what is commonly meant by a silhouette, i.e., the outer

boundary of an object. For example, in a side view of a head, the computer graphics definition includes the edges of the ears.

The definition of silhouette edges can also sometimes include boundary edges, which can be thought of as joining the front and back faces of the same triangle (and so in a sense are always silhouette edges). We define silhouette edges here specifically to not include boundary edges. Section 12.3 discusses processing polygon data to create connected meshes with a consistent facing and determining the boundary, crease, and material edges.

### 11.2.1 Surface Angle Silhouetting

In a similar fashion to the surface shader in Section 11.1, the dot product between the direction to the viewpoint and the surface normal can be used to give a silhouette edge [424]. If this value is near zero, then the surface is nearly edge-on to the eye and so is likely to be near a silhouette edge. The technique is equivalent to shading the surface using a spherical environment map (EM) with a black ring around the edge. See Figure 11.5. In practice, a one-dimensional texture can be used in place of the environment map. Marshall [822] performs this silhouetting method by using a vertex shader. Instead of computing the reflection direction to access the EM, he uses the dot product of the view ray and vertex normal to access the one-dimensional texture. Everitt [323] uses the mipmap pyramid to perform the process, coloring the topmost layers with black. As a surface becomes edge-on, it accesses these top layers and so is shaded black. Since no vertex interpolation is done, the edge is sharper. These methods are extremely fast, since the accelerator does all the work in a single pass, and the texture filtering can help antialias the edges.

This type of technique can work for some models, in which the assumption that there is a relationship between the surface normal and the silhouette edge holds true. For a model such as a cube, this method fails, as the silhouette edges will usually not be caught. However, by explicitly drawing the crease edges, such sharp features will be rendered properly, though with a different style than the silhouette edges. A feature or draw-back of this method is that silhouette lines are drawn with variable width, depending on the curvature of the surface. Large, flat polygons will turn entirely black when nearly edge-on, which is usually not the effect desired. In experiments, Wu found that for the game *Cel Damage* this technique gave excellent results for one quarter of the models, but failed on the rest [1382].

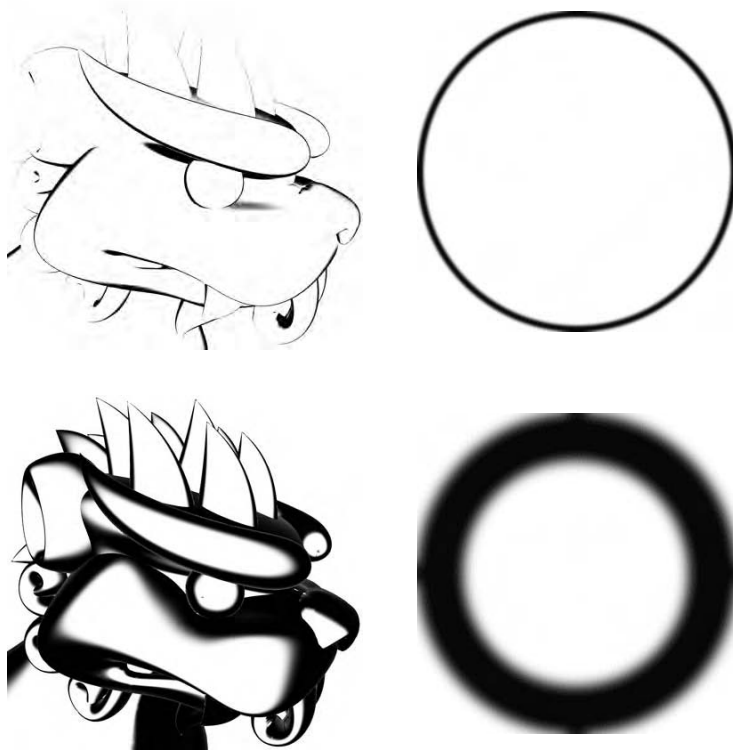


**Figure 11.5.** Silhouettes rendered by using a spheremap. By widening the circle along the edge of the spheremap, a thicker silhouette edge is displayed. (*Images courtesy of Kenny Hoff.*)

### 11.2.2 Procedural Geometry Silhouetting

One of the first techniques for real-time silhouette rendering was presented by Rossignac and van Emmerik [1083], and later refined by Raskar and Cohen [1046]. The basic idea is to render the frontfaces normally, then render the backfaces in a way as to make their silhouette edges visible. There are a number of methods of rendering these backfaces, each with its own strengths and weaknesses. Each method has as its first step that the frontfaces are drawn. Then frontface culling is turned on and backface culling turned off, so that only backfaces are displayed.

One method to render the silhouette edges is to draw only the edges (not the faces) of the backfaces. Using biasing or other techniques (see Section 11.4) ensures that these lines are drawn just in front of the frontfaces. In this way, all lines except the silhouette edges are hidden [720, 1083].

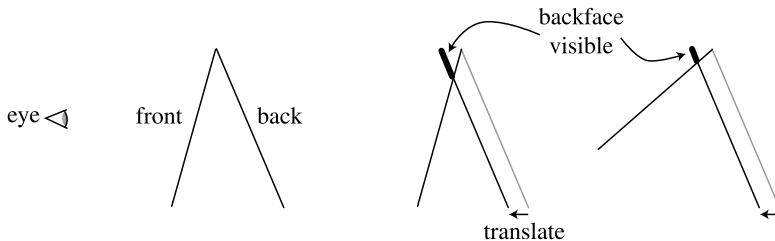


**Figure 11.6.** The  $z$ -bias method of silhouetting, done by translating the backface forward. If the frontface is at a different angle, as shown on the right, a different amount of the backface is visible. (*Illustration after Raskar and Cohen [1046].*)

One way to make wider lines is to render the backfaces themselves in black. Without any bias, these backfaces would remain invisible. So, what is done is to move the backfaces forward in screen  $Z$  by biasing them. In this way, only the edges of the backfacing triangles are visible. Raskar and Cohen give a number of biasing methods, such as translating by a fixed amount, or by an amount that compensates for the nonlinear nature of the  $z$ -depths, or using a depth-slope bias call such as `glPolygonOffset`. Lengyel [758] discusses how to provide finer depth control by modifying the perspective matrix. A problem with all these methods is that they do not create lines with a uniform width. To do so, the amount to move forward depends not only on the backface, but also on the neighboring frontface(s). See Figure 11.6. The slope of the backface can be used to bias the polygon forward, but the thickness of the line will also depend on the angle of the frontface.

Raskar and Cohen [1046] solve this neighbor dependency problem by instead fattening each backface triangle out along its edges by the amount needed to see a consistently thick line. That is, the slope of the triangle and the distance from the viewer determine how much the triangle is expanded.

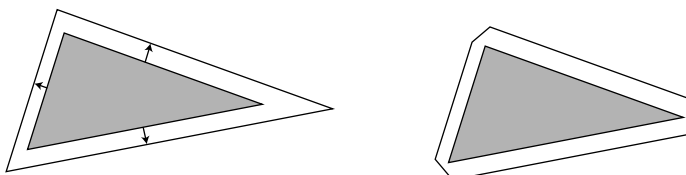


**Figure 11.7.** Triangle fattening. On the left, a backface triangle is expanded along its plane. Each edge moves a different amount in world space to make the resulting edge the same thickness in screen space. For thin triangles, this technique falls apart, as one corner becomes elongated. On the right, the triangle edges are expanded and joined to form mitered corners to avoid this problem.

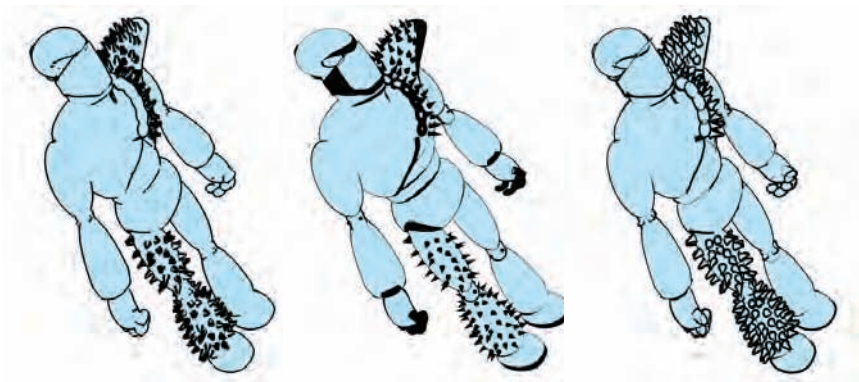


**Figure 11.8.** Silhouettes rendered with backfacing edge drawing with thick lines,  $z$ -bias, and fattened triangle algorithms. The backface edge technique gives poor joins between lines and nonuniform lines due to biasing problems on small features. The  $z$ -bias technique gives nonuniform edge width because of the dependence on the angles of the frontfaces. (*Images courtesy of Raskar and Cohen [1046].*)

One method is to expand the three vertices of each triangle outwards along its plane. A safer method of rendering the triangle is to move each edge of the triangle outwards and connect the edges. Doing so avoids having the vertices stick far away from the original triangle. See Figure 11.7. Note that no biasing is needed with this method, as the backfaces expand beyond the edges of the frontfaces. See Figure 11.8 for results from the three methods. An improved way of computing the edge expansion factors is presented in a later paper by Raskar [1047].

In the method just given, the backface triangles are expanded along their original planes. Another method is to move the backfaces outwards by shifting their vertices along the shared vertex normals, by an amount

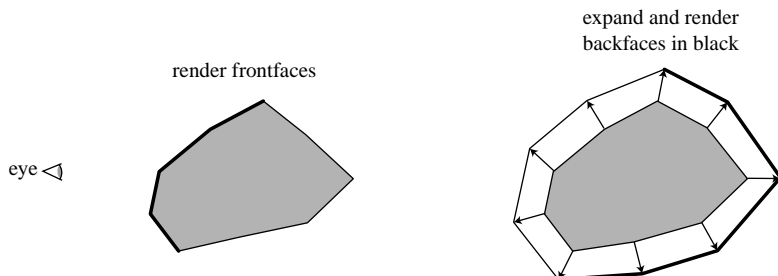


**Figure 11.9.** The triangle shell technique creates a second surface by shifting the surface along its vertex normals.

proportional to their  $z$ -distance from the eye [506]. This is referred to as the shell or halo method, as the shifted backfaces form a shell around the original object. Imagine a sphere. Render the sphere normally, then expand the sphere by a radius that is 5 pixels wide with respect to the sphere's center. That is, if moving the sphere's center one pixel is equivalent to moving it in world space by 3 millimeters, then increase the radius of the sphere by 15 millimeters. Render only this expanded version's backfaces in black.<sup>1</sup> The silhouette edge will be 5 pixels wide. See Figure 11.9. This method has some advantages when performed on the GPU. Moving vertices outwards along their normals is a perfect task for a vertex shader, so the accelerator can create silhouettes without any help from the CPU. This type of expansion is sometimes called shell mapping. Vertex information is shared and so entire meshes can be rendered, instead of individual polygons. The method is simple to implement, efficient, robust, and gives steady performance. It is the technique used by the game *Cel Damage* [1382] for example. See Figure 11.10.

This shell technique has a number of potential pitfalls. Imagine looking head-on at a cube so that only one face is visible. Each of the four backfaces



**Figure 11.10.** An example of real-time toon-style rendering from the game *Cel Damage*, using backface shell expansion to form silhouettes. (Image courtesy of Pseudo Interactive Inc.)

<sup>1</sup>A forcefield or halo effect can be made by expanding further and shading these backfaces dependent on their angle.

forming the silhouette edge will move in the direction of its corresponding cube face, so leaving gaps at the corners. This occurs because while there is a single vertex at each corner, each face has a different vertex normal. The problem is that the expanded cube does not truly form a shell, because each corner vertex is expanding in a different direction. One solution is to force vertices in the same location to share a single, new, average vertex normal. Another technique is to create degenerate geometry at the creases that then gets expanded into polygons with area [1382].

Shell and fattening techniques waste some fill, since all the backfaces are rendered. Fattening techniques cannot currently be performed on curved surfaces generated by the accelerator. Shell techniques can work with curved surfaces, as long as the surface representation can be displaced outwards along the surface normals. The  $z$ -bias technique works with all curved surfaces, since the only modification is a shift in  $z$ -depth. Other limitations of all of these techniques is that there is little control over the edge appearance, semitransparent surfaces are difficult to render with silhouettes, and without some form of antialiasing the edges look fairly poor [1382].

One worthwhile feature of this entire class of geometric techniques is that no connectivity information or edge lists are needed. Each polygon is processed independently from the rest, so such techniques lend themselves to hardware implementation [1047]. However, as with all the methods discussed here, each mesh should be preprocessed so that the faces are consistent (see Section 12.3).

This class of algorithms renders only the silhouette edges. Other edges (boundary, crease, and material) have to be rendered in some other fashion. These can be drawn using one of the line drawing techniques in Section 11.4. For deformable objects, the crease lines can change over time. Raskar [1047] gives a clever solution for drawing ridge lines without having to create and access an edge connectivity data structure. The idea is to generate an additional polygon along each edge of the triangle being rendered. These edge polygons are bent away from the triangle's plane by the user-defined critical dihedral angle that determines when a crease should be visible. Now if two adjoining triangles are at greater than this crease angle, the edge polygons will be visible, else they will be hidden by the triangles. For valley edges, this technique can be performed by using the stencil buffer and up to three passes.

### 11.2.3 Silhouetting by Image Processing

The algorithms in the previous section are sometimes classified as image-based, as the screen resolution determines how they are performed. Another type of algorithm is more directly image-based, in that it operates

entirely on data stored in buffers and does not modify (or even know about) the geometry in the scene.

Saito and Takahashi [1097] first introduced this G-buffer, concept, which is also used for deferred shading (Section 7.9.2). Decaudin [238] extended the use of G-buffers to perform toon rendering. The basic idea is simple: NPR can be done by performing image processing techniques on various buffers of information. By looking for discontinuities in neighboring  $Z$ -buffer values, most silhouette edge locations can be found. Discontinuities in neighboring surface normal values signal the location of boundary (and often silhouette) edges. Rendering the scene in ambient colors can also be used to detect edges that the other two techniques may miss.

Card and Mitchell [155] perform these image processing operations in real time by first using vertex shaders to render the world space normals and  $z$ -depths of a scene to a texture. The normals are written as a normal map to the color channels and the most significant byte of  $z$ -depths as the alpha channel.

Once this image is created, the next step is to find the silhouette, boundary, and crease edges. The idea is to render a screen-filling quadrilateral with the normal map and the  $z$ -depth map (in the alpha channel) and detect edge discontinuities [876]. The idea is to sample the same texture six times in a single pass and implement a Sobel edge detection filter [422]. The texture is sampled six times by sending six pairs of texture coordinates down with the quadrilateral. This filter is actually applied twice to the texture, once along each axis, and the two resulting images are composited. One other feature is that the thickness of the edges generated can be expanded or eroded by using further image processing techniques [155]. See Figure 11.11 for some results.

This algorithm has a number of advantages. The method handles all primitives, even curved surfaces, unlike most other techniques. Meshes do not have to be connected or even consistent, since the method is image-based. From a performance standpoint, the CPU is not involved in creating and traversing edge lists.

There are relatively few flaws with the technique. For nearly edge-on surfaces, the  $z$ -depth comparison filter can falsely detect a silhouette edge pixel across the surface. Another problem with  $z$ -depth comparison is that if the differences are minimal, then the silhouette edge can be missed. For example, a sheet of paper on a desk will usually have its edges missed. Similarly, the normal map filter will miss the edges of this piece of paper, since the normals are identical. One way to detect this case is to add a filter on an ambient or object ID color rendering of the scene [238]. This is still not foolproof; for example, a piece of paper folded onto itself will still create undetectable edges where the edges overlap [546].

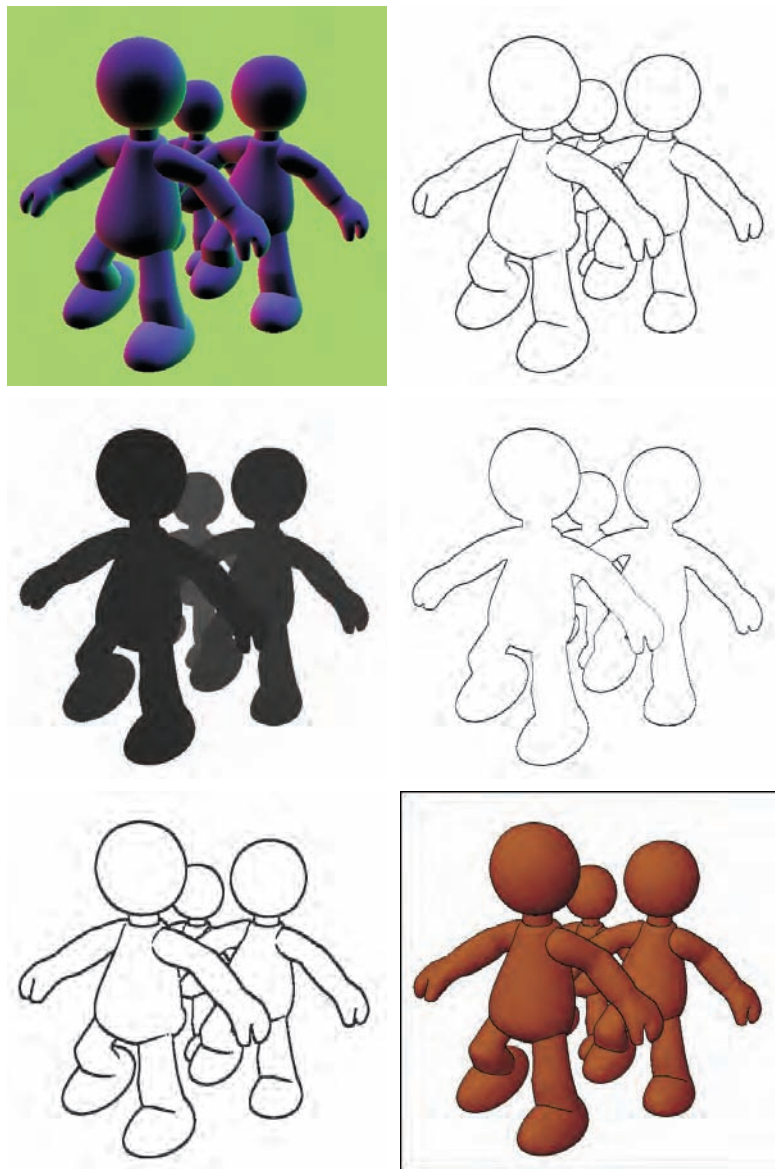


**Figure 11.11.** The normal map (upper left) and depth map (middle left) have edge detection applied to their values. The upper right shows edges found by processing the normal map, the middle right from the  $z$ -depth map. The image on the lower left is a thickened composite. The final rendering in the lower right is made by shading the image with Gooch shading and compositing in the edges. (*Images courtesy of Drew Card and Jason L. Mitchell, ATI Technologies Inc.*)

With the  $z$ -depth information being only the most significant byte, thicker features than a sheet of paper can also be missed, especially in large scenes where the  $z$ -depth range is spread. Higher precision depth information can be used to avoid this problem.

### 11.2.4 Silhouette Edge Detection

Most of the techniques described so far have the disadvantage of needing two passes to render the silhouette. For procedural geometry methods, the second, backfacing pass typically tests many more pixels than it actually shades. Also, various problems arise with thicker edges, and there is little control of the style in which these are rendered. Image methods have similar problems with creating thick lines. Another approach is to detect the silhouette edges and render them directly. This form of silhouette edge rendering allows more fine control of how the lines are rendered. Since the edges are independent of the model, it is possible to create effects such as having the silhouette jump in surprise while the mesh is frozen in shock [1382].

A silhouette edge is one in which one of the two neighboring triangles faces toward the viewer and the other faces away. The test is

$$(\mathbf{n}_0 \cdot \mathbf{v} > 0) \neq (\mathbf{n}_1 \cdot \mathbf{v} > 0), \quad (11.1)$$

where  $\mathbf{n}_0$  and  $\mathbf{n}_1$  are the two triangle normals and  $\mathbf{v}$  is the view direction from the eye to the edge (i.e., to either endpoint). For this test to work correctly, the surface must be consistently oriented (see Section 12.3).

The standard method for finding the silhouette edges in a model is to loop through the list of edges and perform this test [822]. Lander [726] notes that a worthwhile technique is to cull out edges that are inside planar polygons. That is, given a connected triangle mesh, if the two neighboring triangles for an edge lie in the same plane, do not add this edge to the list of edges to test for being a silhouette edge. Implementing this test on a simple clock model dropped the edge count from 444 edges to 256.

There are other ways to improve efficiency of silhouette edge searching. Buchanan and Sousa [144] avoid the need for doing separate dot product tests for each edge by reusing the dot product test for each individual face. Markosian et al. [819] start with a set of silhouette loops and uses a randomized search algorithm to update this set. For static scenes, Aila and Miettinen [4] take a different approach, associating a valid distance with each edge. This distance is how far the viewer can move and still have the silhouette or interior edge maintain its state. By careful caching, silhouette recomputation can be minimized.

In any model each silhouette always consists of a single closed curve, called a *silhouette loop*. It follows that each silhouette vertex must have

an even number of silhouette edges [12]. Note that there can be more than one silhouette curve on a surface. Similarly, a silhouette edge can belong to only one curve. This does not necessarily mean that each vertex on the silhouette curve has only two incoming silhouette edges. For example, a curve shaped like a figure eight has a center vertex with four edges. Once an edge has been found in each silhouette, this edge's neighbors are tested to see whether they are silhouette edges as well. This is done repeatedly until the entire silhouette is traced out.

If the camera view and the objects move little from frame to frame, it is reasonable to assume that the silhouette edges from previous frames might still be valid silhouette edges. Therefore, a fraction of these can be tested to find starting silhouette edges for the next frame. Silhouette loops are also created and destroyed as the model changes orientation. Hall [493] discusses detection of these, along with copious implementation details. Compared to the brute-force algorithm, Hall reported as much as a seven times performance increase. The main disadvantage is that new silhouette loops can be missed for a frame or more if the search does not find them. The algorithm can be biased toward better speed or quality.

Once the silhouettes are found, the lines are drawn. An advantage of explicitly finding the edges is that they can be rendered with line drawing, textured impostors (see Section 10.7.1), or any other method desired. Biassing of some sort is needed to ensure that the lines are properly drawn in front of the surfaces. If thick edges are drawn, these can also be properly capped and joined without gaps. This can be done by drawing a screen-aligned circle at each silhouette vertex [424].

One flaw of silhouette edge drawing is that it accentuates the polygonal nature of the models. That is, it becomes more noticeable that the model's silhouette is made of straight lines. Lake et al. [713] give a technique for drawing curved silhouette edges. The idea is to use different textured strokes depending on the nature of the silhouette edge. This technique works only when the objects themselves are given a color identical to the background; otherwise the strokes may form a mismatch with the filled areas. A related flaw of silhouette edge detection is that it does not work for vertex blended, N-patch, or other accelerator-generated surfaces, since the polygons are not available on the CPU.

Another disadvantage of explicit edge detection is that it is CPU intensive. A major problem is the potentially nonsequential memory access. It is difficult, if not impossible, to order faces, edges, and vertices simultaneously in a manner that is cache friendly [1382]. To avoid CPU processing each frame, Card and Mitchell [155] use the vertex shader to detect and render silhouette edges. The idea is to send every edge of the model down the pipeline as a degenerate quadrilateral, with the two adjoining triangle normals attached to each vertex. When an edge is found to be

part of the silhouette, the quadrilateral's points are moved so that it is no longer degenerate (i.e., is made visible). This results in a thin quadrilateral “fin,” representing the edge, being drawn. This technique is based on the same idea as the vertex shader for shadow volume creation, described on page 347. Boundary edges, which have only one neighboring triangle, can also be handled by passing in a second normal that is the negation of this triangle's normal. In this way, the boundary edge will always be flagged as one to be rendered. The main drawbacks to this technique are a large increase in the number of polygons sent to through the pipeline, and that it does not perform well if the mesh undergoes nonlinear transforms [1382]. McGuire and Hughes [844] present work to provide higher-quality fin lines with endcaps.

If the geometry shader is a part of the pipeline, these additional fin polygons do not need to be generated on the CPU and stored in a mesh. The geometry shader itself can generate the fin quadrilaterals as needed.

Other silhouette finding methods exist. For example, Gooch et al. [423] use Gauss maps for determining silhouette edges. In the last part of Section 14.2.1, hierarchical methods for quickly categorizing sets of polygons as front or back facing are discussed. See Hertzman's article [546] or either NPR book [425, 1226] for more on this subject.

### 11.2.5 Hybrid Silhouetting

Northrup and Markosian [940] use a silhouette rendering approach that has both image and geometric elements. Their method first finds a list of silhouette edges. They then render all the object's triangles and silhouette edges, assigning each a different ID number (i.e., giving each a unique color). This ID buffer is read back and the visible silhouette edges are determined from it. These visible segments are then checked for overlaps and linked together to form smooth stroke paths. Stylized strokes are then rendered along these reconstructed paths. The strokes themselves can be stylized in many different ways, including effects of taper, flare, wiggle, and fading, as well as depth and distance cues. An example is shown in Figure 11.12.

Kalnins et al. [621] use this method in their work, which attacks an important area of research in NPR: *temporal coherence*. Obtaining a silhouette is, in one respect, just the beginning. As the object and viewer move, the silhouette edge changes. With stroke extraction techniques some coherence is available by tracking the separate silhouette loops. However, when two loops merge, corrective measures need to be taken or a noticeable jump from one frame to the next will be visible. A pixel search and “vote” algorithm is used to attempt to maintain silhouette coherence from frame to frame.

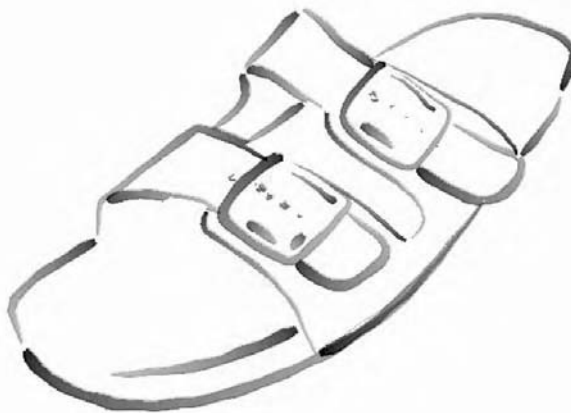


**Figure 11.12.** An image produced using Northrup and Markosian’s hybrid technique, whereby silhouette edges are found, built into chains, and rendered as strokes. (*Image courtesy of Lee Markosian.*)

### 11.3 Other Styles

While toon rendering is a popular style to attempt to simulate, there is an infinite variety of other styles. NPR effects can range from modifying realistic textures [670, 720, 727] to having the algorithm procedurally generate geometric ornamentation from frame to frame [623, 820]. In this section, we briefly survey techniques relevant to real-time rendering.

In addition to toon rendering, Lake et al. [713] discuss using the diffuse shading term to select which texture is used on a surface. As the diffuse term gets darker, a texture with a darker impression is used. The texture is applied with screen-space coordinates to give a hand-drawn look. A paper texture is also applied in screen space to all surfaces to further enhance the sketched look. As objects are animated, they “swim” through the texture, since the texture is applied in screen space. It could be applied in world space for a different effect. See Figure 11.13. Lander [722] discusses doing this process with multitexturing. One problem with this type of algorithm is the *shower door effect*, where the objects look like they are viewed through patterned glass during animation. The problem arises from the textures being accessed by pixel location instead of by surface coordinates—objects then look somewhat detached from these textures, since indeed that is the case.

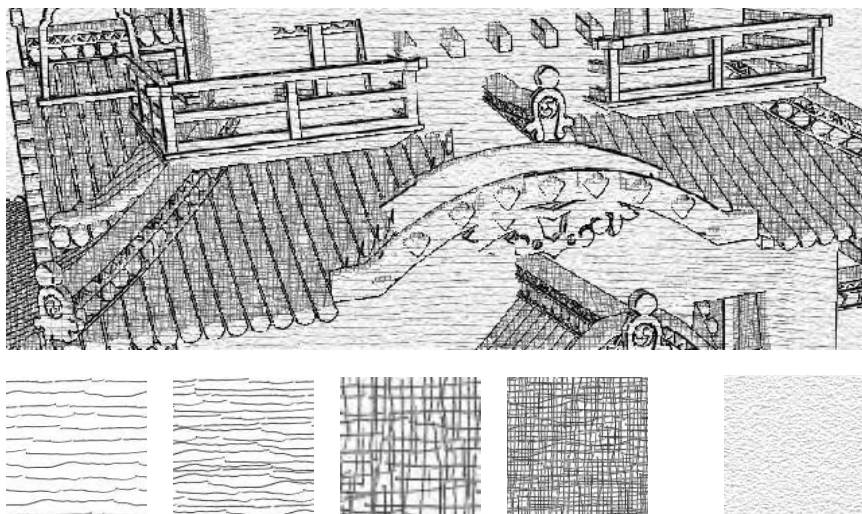


**Figure 11.13.** An image generated by using a palette of textures, a paper texture, and silhouette edge rendering. (Reprinted by permission of Adam Lake and Carl Marshall, Intel Corporation, copyright Intel Corporation 2002.)

One solution is obvious: Use texture coordinates on the surface. The challenge is that stroke-based textures need to maintain a relatively uniform stroke thickness and density to look convincing. If the texture is magnified, the strokes appear too thick; if it is minified, the strokes are either blurred away or are thin and noisy (depending on whether mipmapping is used). Praun et al. [1031] present a real-time method of generating stroke-textured mipmaps and applying these to surfaces in a smooth fashion. Doing so maintains the stroke density on the screen as the object's distance changes. The first step is to form the textures to be used, called *tonal art maps* (TAMs). This is done by drawing strokes into the mipmap levels.<sup>2</sup> See Figure 11.14. Care must be taken to avoid having strokes clump together. With these textures in place, the model is rendered by interpolating between the tones needed at each vertex. Applying this technique to surfaces with a lapped texture parameterization [1030] results in images with a hand-drawn feel. See Figure 11.15.

Card and Mitchell [155] give an efficient implementation of this technique by using pixel shaders. Instead of interpolating the vertex weights, they compute the diffuse term and interpolate this per pixel. This is then used as a texture coordinate into two one-dimensional maps, which yields per-pixel TAM weights. This gives better results when shading large poly-

<sup>2</sup>Klein et al. [670] use a related idea in their “art maps” to maintain stroke size for NPR textures.

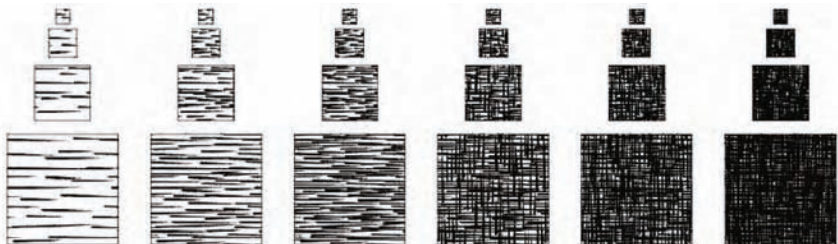


**Figure 11.14.** *Tonal art maps (TAMs).* Strokes are drawn into the mipmap levels. Each mipmap level contains all the strokes from the textures to the left and above it. In this way, interpolation between mip levels and adjoining textures is smooth. (*Images courtesy of Emil Praun, Princeton University.*)

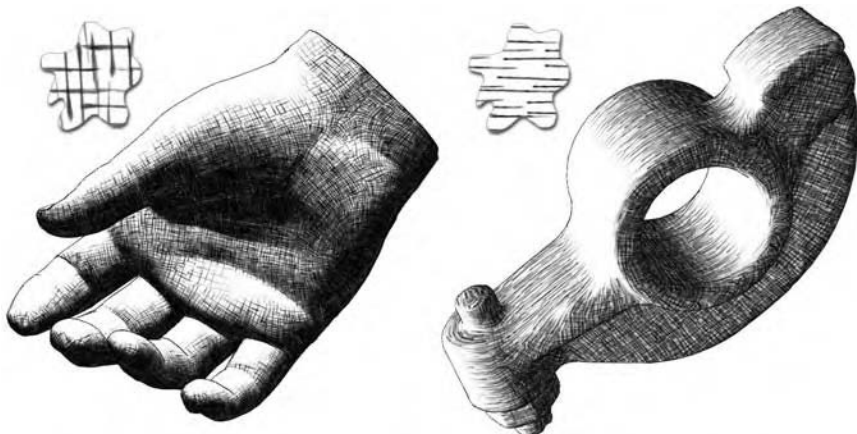


**Figure 11.15.** Two models rendered using *tonal art maps (TAMs)*. The swatches show the lapped texture pattern used to render each. (*Images courtesy of Emil Praun, Princeton University.*)

gons. Webb et al. [1335] present two extensions to TAMs that give better results, one using a volume texture, which allows the use of color, the other using a thresholding scheme, which improves antialiasing. Nuebel [943] gives a related method of performing charcoal rendering. He uses a noise texture that also goes from dark to light along one axis. The intensity value accesses the texture along this axis. Lee et al. [747] use TAMs and a number of other interesting techniques to generate impressive images that appear drawn by pencil.

With regard to strokes, many other operations are possible than those already discussed. To give a sketched effect, edges can be jittered [215, 726,

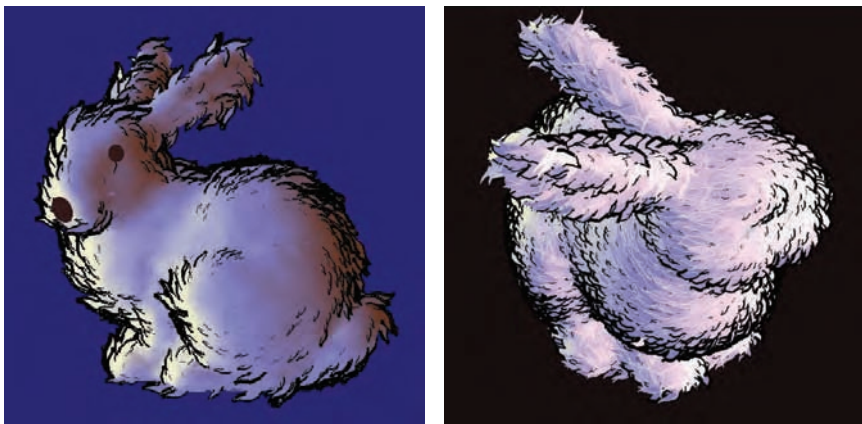


**Figure 11.16.** Two different graftal styles render the Stanford bunny. (*Images courtesy of Bruce Gooch and Matt Kaplan, University of Utah.*)

747] or extended beyond their original locations, as seen in the upper right and lower middle images in Figure 11.1 on page 507.

Girshick et al. [403] discuss rendering strokes along the principal curve direction lines on a surface. That is, from any given point on a surface, there is a *first principal direction* tangent vector that points in the direction of maximum curvature. The *second principal direction* is the tangent vector perpendicular to this first vector and gives the direction in which the surface is least curved. These direction lines are important in the perception of a curved surface. They also have the advantage of needing to be generated only once for static models, since such strokes are independent of lighting and shading.

Mohr and Gleicher [888] intercept OpenGL calls and perform NPR effects upon the low-level primitives, creating a variety of drawing styles. By making a system that replaces OpenGL, existing applications can instantly be given a different look.

The idea of *graftals* [623, 820] is that geometry or decal textures can be added as needed to a surface to produce a particular effect. They can be controlled by the level of detail needed, by the surface's orientation to the eye, or by other factors. These can also be used to simulate pen or brush strokes. An example is shown in Figure 11.16. Geometric graftals are a form of procedural modeling [295].

This section has only barely touched on a few of the directions NPR research has taken. See the “Further Reading and Resources” section at the end of this chapter for where to go for more information. To conclude this chapter, we will turn our attention to the basic line.

## 11.4 Lines

Rendering of simple lines is often considered relatively uninteresting. However, they are important in fields such as CAD for seeing the underlying model facets and discerning the object's shape. They are also useful in highlighting a selected object and in areas such as technical illustration. In addition, some of the techniques involved are applicable to other problems. We cover a few useful techniques here; more are covered by McReynolds and Blythe [849]. Antialiased lines are briefly discussed in Section 5.6.2.

### 11.4.1 Edge Highlighting

Edge highlighting is a fixed-view technique useful for rapid interaction with large models (see Section 10.2). To highlight an object, we draw its edges in a different color, without having to redraw the whole scene. This is an extremely fast form of highlighting, since no polygons are rendered. For example, imagine a blue polygon with gray edges. As the cursor passes over the polygon, we highlight it by drawing the edges in red, then drawing gray edges again when the cursor leaves. Since the view is not moving, the whole scene never has to be redrawn; only the red highlight edges are drawn on top of the existing image. The idea is that the original gray edges were drawn properly, so that when a red edge is drawn using the same geometric description, it should perfectly replace the gray edge.

### 11.4.2 Polygon Edge Rendering

Correctly rendering edges on top of filled polygons is more difficult than it first appears. If a line is at exactly the same location as a polygon, how do we ensure that the line is always rendered in front? One simple solution is to render all lines with a fixed bias [545]. That is, each line is rendered slightly closer than it should truly be, so that it will be above the surface. In practice, the underlying polygon is usually biased away from the viewer.

This works much of the time, but there are problems with this naive approach. For example, Figure 6.26 on page 185 shows a torus that has some edge dropouts due to biasing problems. If the fixed bias is too large, parts of edges that should be hidden appear, spoiling the effect. If polygons are near edge-on to the viewer, a fixed bias is not enough. Current APIs provide a separate factor that makes the bias also vary with the slope of the polygon rendered, thereby helping avoid this particular problem. If API support is not available, other techniques include changing the projection matrix: The viewport near and far values could be adjusted [833], or the  $z$ -scale factor could be modified directly [758, 833]. These techniques can often require hand adjustment to look good.

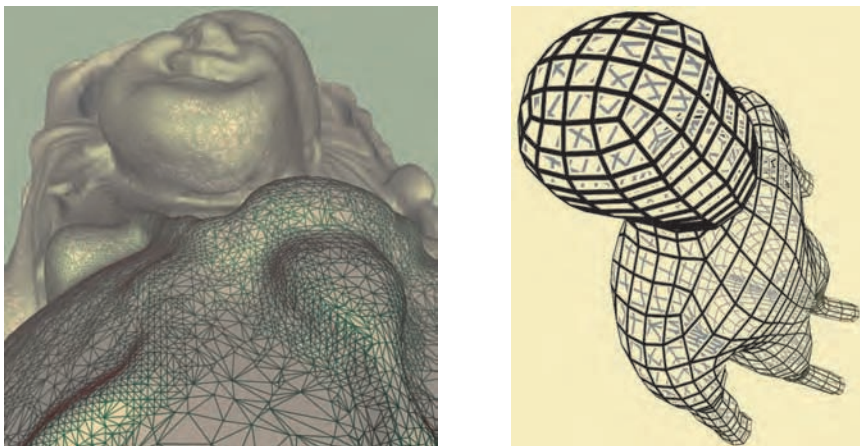


**Figure 11.17.** Pixel-shader-generated lines. On the left are antialiased single-pixel width edges; on the right are variable thickness lines with haloing. (*Images courtesy of J. Andreas Bærentzen.*)

Herrell et al. [545] present a scheme that avoids biasing altogether. It uses a series of steps to mark and clear a stencil buffer, so that edges draw atop polygons correctly. The drawback of using this method on modern GPUs is that each polygon must be drawn separately, hindering overall performance considerably.

Bærentzen et al. [54, 949] present a method that maps well to graphics hardware. They use a pixel shader that uses the triangle's barycentric coordinates to determine the distance to the closest edge. If the pixel is close to an edge, it is drawn with the edge color. Edge thickness can be any value desired and can be affected by distance. See Figure 11.17. This method has the further advantage that lines can be antialiased and haloed (see Section 11.4.4). The main drawback is that silhouette edges are not antialiased and are drawn half as thick as interior lines.

### 11.4.3 Hidden-Line Rendering

In normal wireframe drawing, all edges of a model are visible. Hidden-line rendering treats the model as solid and so draws only the visible lines. The straightforward way to perform this operation is simply to render the polygons with a solid fill color the same as the background's and also render the edges, using a technique from the previous section. Thus the polygons are painted over the hidden lines. A potentially faster method is to draw all the filled polygons to the  $Z$ -buffer, but not the color buffer, then draw the edges [849]. This second method avoids unnecessary color fills.

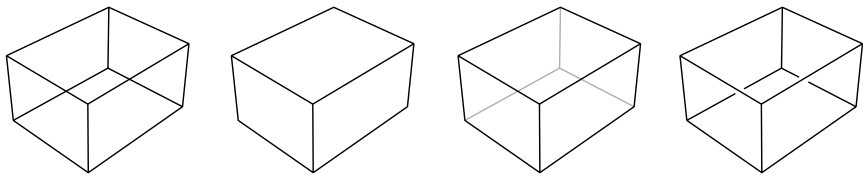


**Figure 11.18.** Four line rendering styles. From left to right: wireframe, hidden-line, obscured-line, and haloed line.

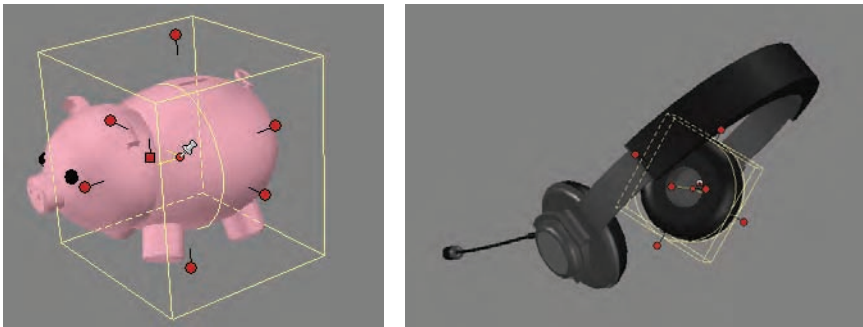


**Figure 11.19.** Dashed lines are drawn only where the  $Z$ -buffer hides the lines.

Lines can also be drawn as partially obscured instead of fully hidden. For example, hidden lines could appear in light gray instead of not being drawn at all. To do this, first draw all the edges in the obscured style desired. Now draw the filled polygons to the  $Z$ -buffer only. In this way, the  $Z$ -buffer protects the hidden lines from being drawn upon. Finally, draw the edges again in the style desired for visible lines.

The method just described has the property that the obscured lines are rendered overlapped correctly by the visible lines. If this feature is not necessary, there are other ways to perform the task that are normally more efficient. One technique is to first draw the surfaces to the  $Z$ -buffer. Next, draw all lines in the visible style. Now reverse the sense of the  $Z$ -buffer, so that only lines that are *beyond* the current pixel  $z$ -depth are drawn. Also turn off  $Z$ -buffer modification, so that these lines drawn do not change any depth values. Draw the lines again in the obscured style. This method performs fewer pixel operations, as visible lines are not drawn twice, and obscured lines do not modify the  $Z$ -buffer.

Figure 11.18 shows results for some of the different line rendering methods discussed here. Figure 11.19 show dashed lines rendered as part of the user interface.

### 11.4.4 Haloing

When two lines cross, a common convention is to erase a part of the more distant line, making the ordering obvious. In computer graphics, this can be accomplished relatively easily by drawing each line twice, once with a halo. This method erases the overlap by drawing over it in the background color. Assume the lines are black and the background white. For each line, first draw a thick version in the background color, then draw the line itself normally. A bias or other method will have to be used to ensure that the thin black line lies atop the thick white background line.

As with hidden-line rendering, this technique can be made more efficient by first drawing all the white halo lines only to the Z-buffer, then drawing the black lines normally [849].

A potential problem with haloing is that lines near each other can get obscured unnecessarily by one line's halo. For example, in Figure 11.18, if the haloing lines extend all the way to the corners, then near the corners, the closer lines may halo the lines further away. One solution is to shorten the lines creating the halos. Because haloing is a technical illustration convention and not a physical phenomenon, it is difficult to automate perfectly.

## Further Reading and Resources

For inspiration about non-photorealistic and toon rendering, read Scott McCloud's *Understanding Comics* [834]. The book by the Gooch's [425] is a fine guide to NPR algorithms in general, though a little dated. Newer research can be found in the proceedings of the *International Symposium on Non-Photorealistic Animation and Rendering (NPAR)*. The book *Advanced Graphics Programming Using OpenGL* [849] has chapters on a wide range of technical illustration and scientific visualization techniques.

This chapter focused on a few methods commonly used for silhouette edge detection and rendering. A comprehensive, wide-ranging survey of silhouette edge algorithms is provided by Isenberg et al. [589]. In this same issue is a survey by Hertzmann [590] of stroke-based rendering techniques. While this field tends toward methods to aid artists, and to algorithms that process static images or models, some techniques are applicable to interactive rendering.

Mitchell et al. [882] provide a case study about how engineers and artists collaborated to give a distinctive graphic style to the game *Team Fortress 2*.

This book's website at <http://www.realtimerendering.com> has pointers to a number of worthwhile websites, tutorials, demonstration programs, and code related to NPR.

# Chapter 12

## Polygonal Techniques

*“It is indeed wonderful that so simple a figure as the triangle is so inexhaustible.”*

—Leopold Crelle

Up to this point, we have assumed that the model we rendered is available in exactly the format we need, and with just the right amount of detail. In reality, we are rarely so lucky. Modelers and data capture devices have their own particular quirks and limitations, giving rise to ambiguities and errors within the data set, and so within renderings. This chapter discusses a variety of problems that are encountered within polygonal data sets, along with some of the fixes and workarounds for these problems. In addition, techniques to efficiently render polygonal models are presented.

The overarching goals for polygonal representation (or any other representation, for that matter) in computer graphics are visual accuracy and speed. “Accuracy” is a term that depends upon the context: For a machine part, it may mean that the model displayed falls within some tolerance range; for an aircraft simulation game, what is important is the overall impression. The way a model is used is a key differentiator. An engineer wants to control and position a part in real time and wants every bevel and chamfer on the machine part visible at every moment. Compare this to a game, where if the frame rate is high enough, minor errors or inaccuracies in a given frame are allowable, since they may not occur where attention is focused, or may disappear in the next frame. In interactive graphics work it is important to know what the boundaries are to the problem being solved, since these determine what sorts of techniques can be applied.

The main topics covered in this chapter are *tessellation*, *consolidation*, *optimization*, and *simplification*. Polygons can arrive in many different forms and may have to be split into more tractable primitives, such as triangles or quadrilaterals; this process is called *triangulation* or, more generally, *tessellation*.<sup>1</sup> *Consolidation* is our term for the process that encompasses

---

<sup>1</sup> “Tessellation” is probably the most frequently misspelled word in computer graphics,

merging and linking polygonal data, as well as deriving new data, such as normals, for surface shading. *Optimization* means grouping and ordering the polygonal data so it will render more rapidly. *Simplification* is taking such linked data and attempting to remove unnecessary or insignificant features within it.

Triangulation ensures that data is displayable and displayed correctly. Consolidation further improves data display and often increases speed, by allowing computations to be shared. Optimization techniques can increase speed still further. Simplification can provide even more speed by removing unneeded polygons.

## 12.1 Sources of Three-Dimensional Data

There are a number of ways a model can be created or generated:

- Directly typing in the geometric description.
- Writing programs that create such data, (this is called *procedural modeling*).
- Transforming data found in other forms into surfaces or volumes, e.g., taking protein data and converting it into spheres, cylinders, etc.
- Using modeling programs.
- Sampling a real model at various points, using a three-dimensional digitizer.
- Reconstruction from one or more photographs of the same object (called *photogrammetry*; using a pair of photos is called *stereophotogrammetry*).
- Using three-dimensional scanning technologies.
- Using some combination of these techniques.

Our focus is on polygonal data generated by these methods. One common thread of most of these techniques is that they can represent their models in polygonal form. Knowing what data sources will be used in an application is important in determining what sort of data can be expected, and so in knowing what techniques are applicable.

In the modeling world, there are two main types of modelers: solid-based and surface-based. Solid-based modelers are usually seen in the area

---

and “frustum” is a close second.

of computer aided design (CAD), and often emphasize modeling tools that correspond to actual machining processes, such as cutting, drilling, etc. Internally, they will have a computational engine that rigorously manipulates the underlying topological boundaries of the objects. For display and analysis, such modelers have *faceters*. A faceter is software that turns the internal model representation into polygons that can then be displayed. For example, a model that appears as a sphere internally may be represented by a center point and a radius, and the faceter could turn it into any number of triangles or quadrilaterals in order to represent it. Sometimes the best rendering speedup is the simplest: Turning down the visual accuracy required when the faceter is employed can increase speed and save storage space by generating fewer polygons.

An important consideration within CAD work is whether the faceter being used is designed for graphical rendering. For example, there are faceters for the *finite element method* (FEM), which aim to split the surface into nearly equal-area triangles; such tessellations are strong candidates for consolidation and simplification, as they contain much graphically useless data, while also providing no vertex normals. Similarly, some faceters produce sets of triangles that are ideal for creating actual physical objects using stereolithography, but that lack vertex normals and are often ill suited for fast graphical display.

Surface-based modelers do not have a built-in concept of solidity; instead, all objects are thought of in terms of their surfaces. Like solid modelers, they may use internal representations and faceters to display objects such as spline or subdivision surfaces (see Chapter 13). They may also allow direct manipulation of surfaces, such as adding or deleting polygons or vertices. This sort of tool can be used to lower the polygon count of a model.

There are other types of modelers, such as implicit surface (including “blobby” metaball) creation systems [117], which work with concepts such as blends, weights, and fields. These modelers can create impressive organic effects by generating surfaces that are defined by the solution to some function  $f(x, y, z) = 0$ . Polygonalization techniques are then used to create sets of polygons for display. See Section 13.3.

Data can also be generated from satellite imagery, by laser scanning, air-borne LIDAR (light detection and ranging) [571], or other three-dimensional scanners, by various medical scanning devices (in which image slices are generated and recombined), and by photogrammetry and computational photography techniques [1048]. Meshes produced are strong candidates for simplification techniques, as the data is often sampled at regular intervals, and many samples have a negligible effect on the visual perception of the data. Some of these techniques generate nothing more than *point clouds*, with no inherent connectivity between the points. Reconstructing meshes

from these samples can be difficult, so alternate rendering techniques such as point rendering may be used instead (see Section 14.9).

There are many other ways in which polygonal data is generated for surface representation. The key is to understand how that data was created, and for what purpose. Often, the data is not generated specifically for graphical display, or even if it is, various assumptions made by the designers about the renderer may no longer hold. There are many different three-dimensional data file formats in existence [912, 1087], and translating between any two is often not a lossless operation. Understanding what sorts of limitations and problems may be encountered with incoming data is a major theme of this chapter.

## 12.2 Tessellation and Triangulation

Tessellation is the process of splitting a surface into a set of polygons. Here, we focus on tessellating polygonal surfaces; curved surface tessellation is discussed in Section 13.6. Polygonal tessellation can be undertaken for a variety of reasons. The most common is that almost all graphics APIs and hardware are optimized for triangles. Triangles are almost like atoms, in that any surface can be made out of them and rendered. Converting a complex polygon into triangles is called triangulation. There are other reasons to tessellate polygons. The renderer may handle only convex polygons (such tessellation is called convex partitioning). The surface may need to be subdivided (meshed) in order to store at each vertex the effect of shadows or interreflections using radiance transfer techniques [288]. Figure 12.1 shows examples of these different types of tessellation. Nongraphical reasons for tessellation include requirements such as having no polygon be larger than some given area, or for triangles to have angles at their vertices all be larger than some minimum angle. While angle restrictions are normally a part of nongraphical applications such as finite element analysis, these can also serve to improve the appearance of a surface. Long,

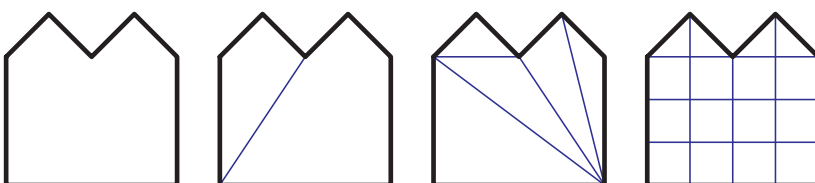


**Figure 12.1.** Various types of tessellation. The leftmost polygon is not tessellated, the next is partitioned into convex regions, the next is triangulated, and the rightmost is uniformly meshed.



**Figure 12.2.** Warped quadrilateral viewed edge-on, forming an ill-defined bowtie or hourglass figure, along with the two possible triangulations.

thin triangles are worth avoiding, if possible, as different shades among the vertices will be interpolated over a long distance.

One of the first processes a surface tessellator normally needs to perform is to determine how best to project a three-dimensional polygon into two dimensions. This is done to simplify the problem and so simplify the algorithms needed. One method is to determine which one of the  $xyz$  coordinates to discard in order to leave just two; this is equivalent to projecting the polygon onto one of three planes, the  $xy$ , the  $yz$ , or the  $xz$ . The best plane is usually the one in which the polygon has the largest projected area (this same technique is used in Section 16.9 for point-in-polygon testing). This plane can be determined by computing the area on each projection plane, or by simply throwing away the coordinates corresponding to the coordinate of greatest magnitude in the polygon's normal. For example, given the polygon normal  $(-5, 2, 4)$ , we would throw away the  $x$  coordinates because  $-5$  has the greatest magnitude.

The projected area test and polygon normal test are not always equivalent, depending on the way in which the normal is computed and whether the polygon is flat. Some modelers create polygon facets that can be badly warped. A common case of this problem is the warped quadrilateral that is viewed nearly edge-on; this may form what is referred to as an *hourglass* or a *bowtie* quadrilateral. Figure 12.2 shows a bowtie quadrilateral. While this figure can be triangulated simply by creating a diagonal edge, more complex warped polygons cannot be so easily managed. Casting these onto the  $xy$ ,  $xz$ , or  $yz$  plane that gives the largest projected area will eliminate most, but not all, self-intersection problems. If using this plane leads to self-intersection (in which a polygon's edge crosses itself), we may consider casting upon the average plane of the polygon itself. The average plane is computed by taking the three projected areas and using these to form the normal [1077]. That is, the area on the  $yz$  plane forms the  $x$  component,  $xz$  the  $y$ , and  $xy$  the  $z$ . This method of computing an average normal is called *Newell's formula*. If self-intersection is a possibility, then a laborious comparison among the polygon's edges and splitting is required. If the polygon has a large number of edges, then a *plane sweep* can be used so as to limit the amount of edge/edge testing that is done [82]. See Section 16.16 for efficient methods for performing the intersection test itself.

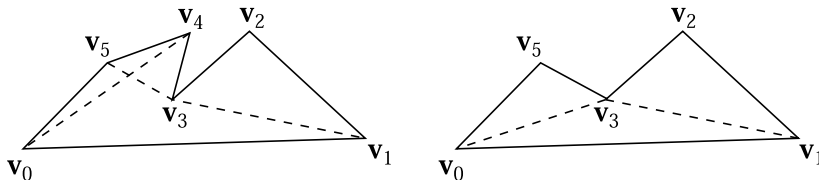


**Figure 12.3.** Ear clipping. A polygon with potential ears at  $v_2$ ,  $v_4$ , and  $v_5$  shown. On the right, the ear at  $v_4$  is removed. The neighboring vertices  $v_3$  and  $v_5$  are reexamined to see if they now form ears;  $v_5$  does.

Schneider and Eberly [1131], Held [540], O'Rourke [975], and de Berg et al. [82] each give an overview of a variety of triangulation methods. The most basic triangulation algorithm is to examine each line segment between any two given points on a polygon and see if it intersects or overlaps any edge of the polygon. If it does, the line segment cannot be used to split the polygon, so examine the next possible pair of points; else split the polygon into two parts by this segment and triangulate these new polygons by the same method. This method is extremely inefficient, at  $O(n^3)$ . A more efficient method is *ear clipping*, which is  $O(n^2)$  when done as two processes. First, a pass is made over the polygon to find the ears, that is, to look at all triangles with vertex indices  $i, (i + 1), (i + 2)$  (modulo  $n$ ) and check if the line segment  $i, (i + 2)$  does not intersect any polygon edges. If so, then triangle  $(i + 1)$  forms an ear. See Figure 12.3. Each ear available is removed from the polygon in turn, and the triangles at vertices  $i$  and  $(i + 2)$  are reexamined to see if they are ears or not. Eventually all ears are removed and the polygon is triangulated. Other, more complex methods of triangulation are  $O(n \log n)$  and some are effectively  $O(n)$  for typical cases. Pseudocode for ear clipping and other, faster triangulation methods is given by Schneider and Eberly [1131].

Partitioning a polygon into convex regions can be more efficient in terms of storage and further computation than triangulating it. Convex polygons

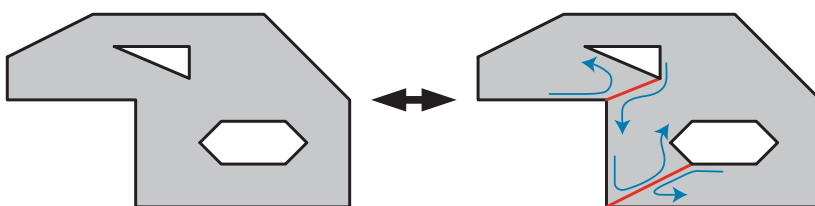


**Figure 12.4.** A polygon with three outlines converted to a single-outline polygon. Join edges are shown in red. Arrows inside the polygon show the order in which vertices are visited to make a single loop.

can easily be represented by fans or strips of triangles, as discussed in Section 12.4, which makes for faster rendering. Code for a robust convexity test is given by Schorn and Fisher [1133]. Some concave polygons can be treated as fans (such polygons are called star-shaped), but detecting these requires more work [975, 1033]. Schneider and Eberly [1131] give two convex partitioning methods, a quick and dirty method and an optimal one.

Polygons are not always made of a single outline. Figure 12.4 shows a polygon made of three outlines (also called loops or contours). Such descriptions can always be converted to a single-outline polygon by carefully generating join edges (also called keyholed or bridge edges) between loops. This conversion process can also be reversed in order to retrieve the separate loops.

Tessellation and triangulation algorithms are an area of computational geometry that has been well explored and documented [82, 920, 975, 1131]. That said, writing a robust and general tessellator is a difficult undertaking. Various subtle bugs, pathological cases, and precision problems make foolproof code surprisingly tricky to create.

One way to finesse the triangulation problem is to use the graphics accelerator itself to directly render a complex polygon. The polygon is rendered as a triangle fan to the stencil buffer. By doing so, the areas that actually should be filled are drawn an odd number of times, the concavities and holes drawn an even number. By using the invert mode for the stencil buffer, only the filled areas are marked at the end of this first pass. In the second pass the triangle fan is rendered again, using the stencil buffer to allow only the filled area to be drawn [969]. The advantage of this method is that it entirely avoids the problem of developing a robust triangulator. The problem with it is that each polygon has to be rendered using two passes and stencil buffer clears every frame.

### 12.2.1 Shading Problems

Often data will arrive as quadrilateral meshes and must be converted into triangles for display, both to avoid bowtie problems and to provide proper input to the renderer. Once in a great while, a quadrilateral will be concave, in which case there is only one way to triangulate it (without adding new vertices); otherwise, we may choose either of the two diagonals to split it. Spending a little time picking the better diagonal can sometimes give significantly better visual results.

There are a few different ways to determine how to split a quadrilateral. The basic idea is to minimize differences. For a flat quadrilateral with no additional data at the vertices, it is often best to choose the shortest diagonal. For radiosity solutions or prelit quadrilaterals (see Section 15.4.4)

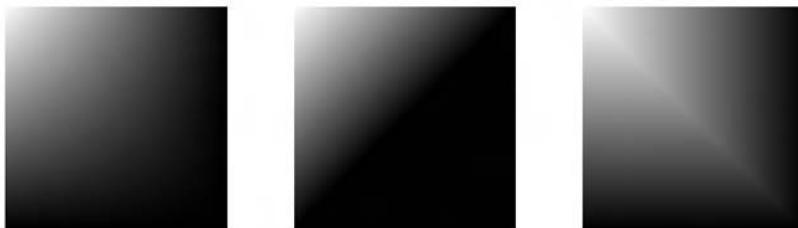


**Figure 12.5.** The left figure is rendered as a quadrilateral; the middle is two triangles with upper-right and lower-left corners connected; the right shows what happens when the other diagonal is used. The middle figure is better visually than the right one.

that have a diffuse color per vertex, choose the diagonal which has the smaller difference between the colors [5]. An example of this technique is shown in Figure 12.5. A drawback of such schemes is that they will ruin the regular nature of the data.

There are cases where triangles cannot properly capture the intent of the designer. If a texture is applied to a warped quadrilateral, neither triangulation preserves the intent; that said, neither does interpolation over the non-triangulated quadrilateral (i.e., interpolating from the left to the right edge). Figure 12.6 shows the problem. This problem arises because

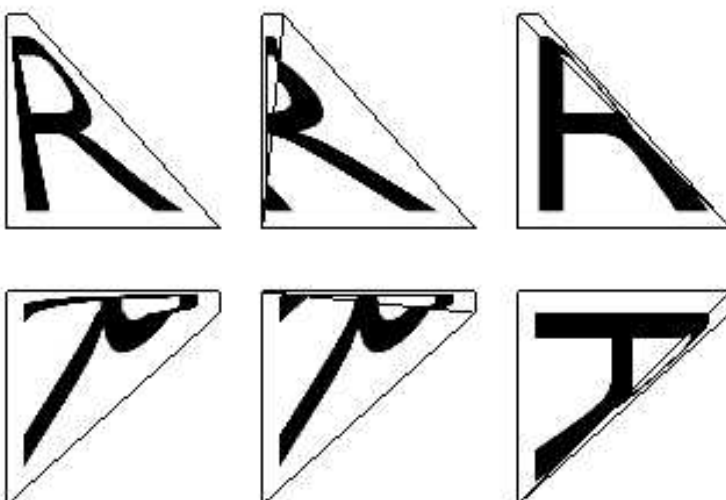


**Figure 12.6.** The top left shows the intent of the designer, a distorted quadrilateral with a square texture map of an “R.” The two images on the right show the two triangulations and how they differ. The bottom row rotates all of the polygons; the non-triangulated quadrilateral changes its appearance.

the image being applied to the surface is to be warped when displayed. A triangle has only three texture coordinates, so it can establish an affine transformation, but not a warp. At most, a basic  $(u, v)$  texture on a triangle can be sheared, not warped. Woo et al. [1375] discuss this problem further. A number of solutions are possible:

- Warp the texture in advance and reapply this new image.
- Tessellate the surface to a finer mesh; this only lessens the problem.
- Use projective texturing to warp the texture on the fly [518]; this has the undesirable effect of nonuniform spacing of the texture on the surface.
- Use a bilinear mapping scheme [518]; this is achievable with additional data per vertex.

While texture distortion sounds like a pathological case, it happens to some extent any time the texture data applied does not match the proportions of the underlying quadrilateral. One extreme case occurs with a common primitive: the cone. When a texture is applied to the cone and the cone is faceted, the triangle vertices at the tip of the cone have different normals. These vertex normals are not shared by the neighboring triangles, so shading discontinuities occur [485].

Figure 12.6 also shows why rendering using only triangles is usually better than interpolation across the original polygon: The quadrilateral's rendering is not rotation-invariant. Such shading will shift around when animated; triangles' shading and textures at least do not move. Interpolation on a triangle is, in fact, equivalent to interpolating across the surface using a triangle's barycentric coordinates (see Section 16.8).

### 12.2.2 Edge Cracking and T-Vertices

Curved surfaces, discussed in detail in Chapter 13, are usually tessellated into meshes for rendering. This tessellation is done by stepping along the spline curves defining the surface and so computing vertex locations and normals. When we use a simple stepping method, problems can occur where spline surfaces meet. At the shared edge, the points for both surfaces need to coincide. Sometimes this may happen, due to the nature of the model, but often the points generated for one spline curve will not match those generated by its neighbor. This effect is called *edge cracking*, and it can lead to disturbing visual artifacts as the viewer peeks through the surface. Even if the viewer cannot see through the cracks, the seam is often visible because of differences in the way the shading is interpolated.

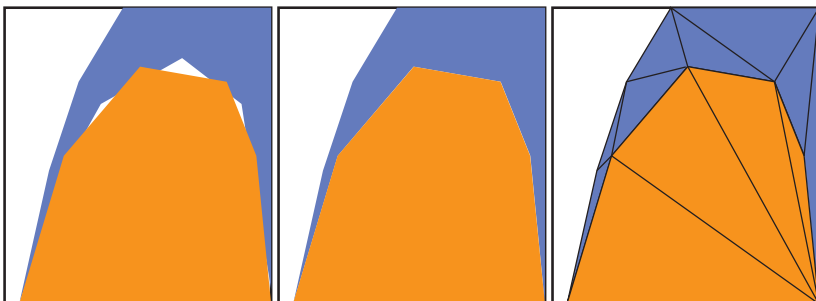


**Figure 12.7.** The left figure shows cracking where the two surfaces meet. The middle shows the cracking fixed by matching up edge points. The right shows the corrected mesh.

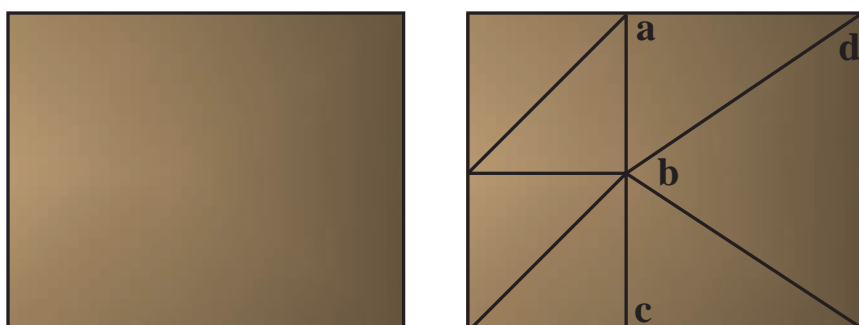
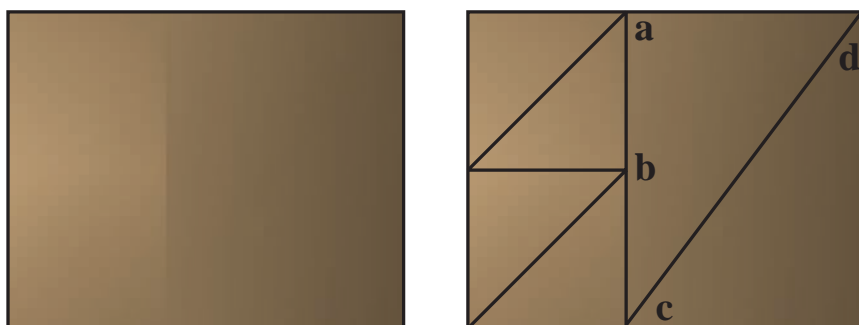


**Figure 12.8.** In the top row, the underlying mesh of a surface shows a shading discontinuity. Vertex **b** is a T-vertex, as it belongs to the polygons to the left of it, but is not a part of the triangle **acd**. One solution is to add this T-vertex to this triangle and create triangles **abd** and **bcd** (not shown). Long and thin triangles are more likely to cause other shading problems, so retriangulating is often a better solution, shown in the bottom row.

The process of fixing these cracks is called *edge stitching*. The goal is to make sure that all vertices along the shared edge are shared by both spline surfaces, so that no cracks appear. See Figure 12.7. Section 13.6.4 discusses using adaptive tessellation to avoid cracking for spline surfaces.

A related problem encountered when joining flat surfaces is that of *T-vertices*. This sort of problem can appear whenever two models' edges meet, but do not share all vertices along them. Even though the edges should theoretically meet perfectly, if the renderer does not have enough precision in representing vertex locations on the screen, cracks can appear. Modern graphics hardware uses subpixel addressing [736], which mostly solves the problem, though gaps can still occur. More obvious are the shading artifacts that can appear [73]. Figure 12.8 shows the problem, which can be fixed by finding such edges and making sure to share common vertices with bordering faces. Lengyel [760] discusses how to find such vertices and provides code to properly triangulate convex polygons. For example, in the figure, if the quadrilateral **abcd** had been triangulated into triangles **abc** and **acd**, the T-vertex problem would not be solved. Cignoni et al. [178] describe a method to avoid creating degenerate (zero-area) triangles when the T-vertices' locations are known. Their algorithm is  $O(n)$  and is guaranteed to produce at most one triangle strip and fan.

## 12.3 Consolidation

Once a model has passed through any tessellation algorithms needed, we are left with a set of polygons to render. There are a few operations that may be useful for displaying this data. The simplest is checking whether the polygon itself is properly formed, that it does not have identical vertices next to each other in its vertex list, and that it has at least three unique vertices. A more elaborate operation is *merging*, which finds shared vertices among faces. Another common operation is called *orientation*, where all polygons forming a surface are made to face the same direction. Once orientation is performed, checking whether a mesh forms a solid surface is important for its use by a number of different algorithms. Feature edge detection can be done to enhance data by finding graphically significant edges. Related to this operation is *vertex normal generation*, where surfaces are made to look smooth. We call these types of techniques *consolidation* algorithms.

### 12.3.1 Merging

Some data comes in the form of disconnected polygons, often termed a *polygon soup*. Storing separate polygons wastes memory, and displaying

separate polygons is extremely inefficient. For these reasons separate polygons are usually merged into a *polygon mesh*. At its simplest, a polygon mesh consists of a list of vertices and a set of outlines. Each vertex contains a position and other additional data, such as diffuse and specular colors, shading normal, texture coordinates, etc. Each polygon outline has a list of integer indices. Each index is a number from 0 to  $n - 1$ , where  $n$  is the number of vertices and so points to a vertex in the list. In this way, each vertex can be stored just once and shared by any number of polygons. A *triangle mesh* is simply a polygon mesh that contains only triangles.

Given a set of disconnected polygons, merging can be done in any number of ways. One simple method is to use hashing. Initialize the current vertex index to zero. For each polygon, attempt to add each of its vertices in turn to a hash table. If a vertex is not already in the table, store it there, along with the current vertex index, which is then incremented; also store the vertex in the final vertex list. If instead the vertex is found in the hash table, retrieve its stored index. Save the polygon with the indices used to point to the vertices. Once all polygons are processed, the vertex and index lists are complete.

Model data sometimes comes in with separate polygons' vertices being extremely close, but not identical. The process of merging such vertices is called *welding*. See Glassner's article [407] for one method of welding vertices.

There are more elaborate polygon mesh data structures possible. For example, a cube has 8 vertex positions and 6 face normals. If each necessary vertex position/normal is stored separately, 24 separate vertices are needed (4 per face). An alternate way to store this data is to keep two separate lists, one of positions, one of normals. Then each polygon outline stores two indices per vertex, selecting the position and normal. Hoppe [562] discusses memory-efficient ways to share vertex-face information while retaining surface-surface connectivity.

### 12.3.2 Orientation

One quality-related problem with model data is face orientation. Some model data comes in oriented properly, with surface normals either explicitly or implicitly pointing in the correct directions. For example, in CAD work, the standard is that the vertices in the polygon outline proceed in a counterclockwise direction when the frontface is viewed. This is called a right-handed orientation (which is independent of the left-handed or right-handed viewing or modeling orientation used): Think of the fingers of your right hand wrapping around the polygon's vertices in counterclockwise order. Your thumb then points in the direction of the polygon's normal.

There are a number of conditions necessary to ensure that a surface can be successfully oriented. Each polygon edge should be shared by at most two polygons in the mesh. For example, if two cubes touched along an edge and were a part of the same mesh, that edge would be shared by four polygons. This makes simple orientation computation more difficult. Also, one-sided objects such as Möbius strips will of course not be able to be oriented.

Given a reasonable model, here is one approach to orient a polygonal mesh:

1. Form edge-face structures for all polygons.
2. Sort or hash the edges to find which edges match.
3. Find groups of polygons that touch each other.
4. For each group, flip faces to obtain consistency.

The first step is to create a set of *half-edge* objects. A half-edge is an edge of a polygon, with a pointer to its associated face (polygon). Since an edge is normally shared by two polygons, this data structure is called a half-edge. Create each half-edge with its first vertex stored before the second vertex, using sorting order. One vertex comes before another in sorting order if its  $x$ -coordinate value is smaller. If the  $x$ -coordinates are equal, then the  $y$ -value is used; if these match, then  $z$  is used. For example, vertex  $(-3, 5, 2)$  comes before vertex  $(-3, 6, -8)$ ; the  $-3$ s match, but  $5 < 6$ .

The goal is to find which edges are identical. Since each edge is stored such that the first vertex is less than the second, comparing edges is simply a matter of comparing first to first and second to second vertices; no permutations such as comparing one edge's first vertex to another's second vertex are needed. A hash table can be used to find matching edges [8, 407]. If all vertices have previously been merged, so that half-edges use the same vertex indices, then each half-edge can be matched by putting it on a temporary list associated with its first vertex index. A vertex has an average of 6 edges attached to it, making edge matching extremely rapid [1063].

Once the edges are matched, connections among neighboring polygons are known, forming an *adjacency graph*. For a triangle mesh, an adjacency graph can be represented as a list of (up to) three triangle indices associated with each triangle, its neighbors. Boundary edges can be determined from adjacency: Any edge that does not have two neighboring polygons is a boundary edge. The set of polygons that touch each other forms a continuous group. A single data set can have more than one continuous group. For example, a teapot can have two groups, the pot and the lid.

The next step is to give the mesh orientation consistency, e.g., we may want all polygons to have counterclockwise outlines. For each continuous

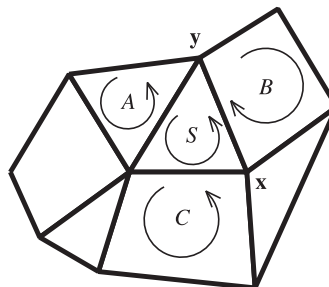


**Figure 12.9.** A starting polygon  $S$  is chosen and its neighbors are checked. Because the vertices in the edge shared by  $S$  and  $B$  are traversed in the same order (from  $x$  to  $y$ ), the outline for  $B$  needs to be reversed.

group of polygons, choose an arbitrary starting polygon. Check each of its neighboring polygons and determine whether the orientation is consistent. Orientation checking is simple: If the direction of traversal for the edge is the same for both polygons, then the neighboring polygon must be flipped. See Figure 12.9. Recursively check the neighbors of these neighbors, until all polygons in a continuous group are tested once.

Although all the faces are properly oriented at this point, they could all be oriented inward. In most cases we want them facing outward. The test for whether all faces should be flipped is to take the signed volume of the group and check the sign; if it is negative, reverse all the loops and normals.

The way to get the signed volume is as follows. First, get the center point of the group's bounding box. Then compute the signed volume of each volume formed by joining the center point to each polygon (e.g., for a triangle and a point, a tetrahedron is formed). The volume is equal to one-third the distance of the center point from the polygon's plane, times the polygon's area. The  $1/3$  term can be dropped, since we need only the sign of the summed volume. The calculation of the area of a triangle is given in Appendix A.

This method is not foolproof. If the object is not solid, but simply a surface description, it is certainly possible for the orientation still to be incorrect. Human intervention is needed in such cases. Even solids can be oriented incorrectly in special cases. For example, if the object is a room, the user wants its normals to face inward toward the camera.

### 12.3.3 Solidity

Informally, a mesh forms a solid if it is oriented and all the polygons visible from the outside have the same orientation. In other words, only one

side of the mesh is visible. Such polygonal meshes are called *closed* or *watertight*.

Knowing an object is solid means backface culling can be used to improve display efficiency, as discussed in Section 14.2. Solidity is also a critical property for objects casting shadow volumes (Section 9.1.3) and for a number of other algorithms. Stereolithography is the process of taking a computer-generated model and creating a physical prototype, and there, models without solidity are unusable.

The simplest test for solidity is to check if every polygon edge in the mesh is shared by exactly two polygons. This test is sufficient for most data sets. Such a surface is loosely referred to as being *manifold*, specifically, *two-manifold*. Technically, a manifold surface is one without any topological inconsistencies, such as having three or more polygons sharing an edge or two or more corners touching each other. A continuous surface forming a solid is a manifold without boundaries.

#### 12.3.4 Normal Smoothing and Crease Edges

Some polygon meshes form curved surfaces, but the polygon vertices do not have normal vectors, so they cannot be rendered with the illusion of curvature. See Figure 12.10.

Many model formats do not provide surface edge information. See Section 11.2 for the various types of edges. These edges are important for a

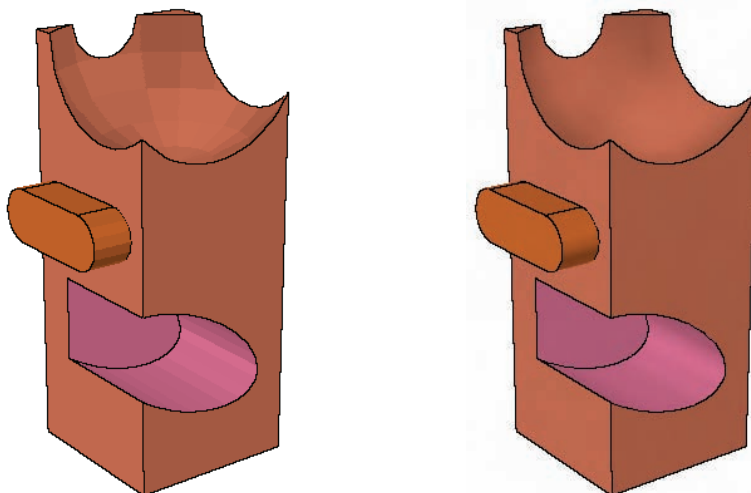


**Figure 12.10.** The object on the left does not have normals per vertex; the one on the right does.

number of reasons. They can highlight an area of the model made of a set of polygons or can help in creating a nonphotorealistic rendering. Because they provide important visual cues, such edges are often favored to avoid being simplified by progressive mesh algorithms (see Section 12.5). Figure 12.10 shows surfaces with crease edges displayed.

Reasonable crease edges and vertex normals can usually be derived with some success from an oriented mesh. Once the orientation is consistent and the adjacency graph is derived, vertex normals can be generated by *smoothing techniques*. Smoothing information is something that the model's format may provide by specifying smoothing groups for the polygons, or by providing a crease angle. Smoothing group values are used to explicitly define which polygons in a group belong together to make up a curved surface. A crease angle is used when there is no smoothing group information. In this case, if two polygons' dihedral angle is found to be within the specified angle, then these two polygons are made to share vertex normals along their common edge. If the dihedral angle between the polygons is greater than the crease angle, then the edge between the polygons is made a crease edge. This technique is sometimes called *edge preservation*.

Once a smoothing group is found, vertex normals can be computed. The standard textbook solution for finding the vertex normal is to average the surface normals of the polygons sharing the vertex [406, 407]. However, this method can lead to inconsistent and poorly weighted results. Thürmer and Wüthrich [1266] present an alternate method, in which each polygon normal's contribution is weighted by the angle it forms at the vertex. This method has the desirable property of giving the same result whether a polygon sharing a vertex is triangulated or not. If the tessellated polygon turned into, say, two triangles sharing the vertex, the equal weight method would then give twice the weight to the two triangles as it would to the original polygon. See Figure 12.11.

Max [828] gives a different weighting method, based on the assumption that long edges form polygons that should affect the normal less. This type of smoothing may be superior when using simplification techniques, as larger polygons formed will be less likely to follow the surface's curvature. The algorithm is

$$\mathbf{n} = \sum_{i=0}^{n-1} \frac{\mathbf{e}_i \times \mathbf{e}_{i+1}}{\|\mathbf{e}_i\|^2 \|\mathbf{e}_{i+1}\|^2} \quad (12.1)$$

for  $n$  counterclockwise-oriented polygons sharing a vertex. The  $\mathbf{e}_i$  vectors are formed by the edges from the center vertex location  $\mathbf{v}$ , e.g.,  $\mathbf{e}_2$  is equal to  $\mathbf{v}_2 - \mathbf{v}$ . Modulo arithmetic is used for the edge vertices, i.e., if  $i+1$  equals  $n$ , use 0. The numerator computes the normal for each pair of edges, and

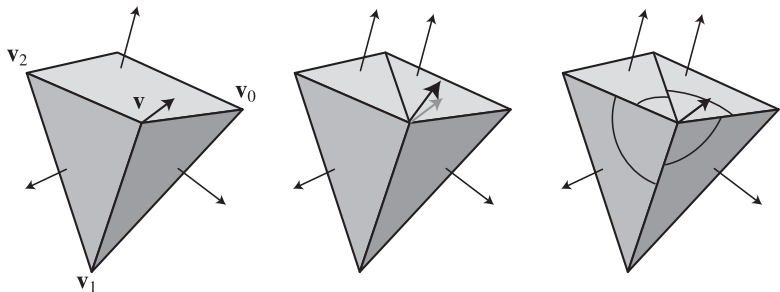


**Figure 12.11.** On the left, the surface normals of a rectangle and two triangles are averaged to give a vertex normal. In the middle, the square has been triangulated. This results in the average normal shifting, since each polygon’s normal is weighted equally. On the right, Thürmer and Wüthrich’s method weights each normal’s contribution by its angle between the pair of edges forming it, so triangulation does not shift the normal.

the squared length terms in the denominator make this normal’s effect less for larger polygons. The resulting normal  $\mathbf{n}$  is then normalized.

For heightfields, Shankel [1155] shows how taking the difference in heights of the neighbors along each axis can be used to rapidly approximate smoothing using the angle-weighted method. For a given point  $\mathbf{p}$  and four neighboring points,  $\mathbf{p}^{X-1}$  and  $\mathbf{p}^{X+1}$  on the  $X$ -axis of the heightfield,  $\mathbf{p}^{Y-1}$  and  $\mathbf{p}^{Y+1}$  on the  $Y$ , a close approximation of the (unnormalized) normal at  $\mathbf{p}$  is

$$\begin{aligned} n_x &= p_x^{X+1} - p_x^{X-1}, \\ n_y &= p_y^{Y+1} - p_y^{Y-1}, \\ n_z &= 2. \end{aligned} \quad (12.2)$$

Using a smoothing angle can sometimes give an improper amount of smoothing, rounding edges that should be creased, or vice versa. However, even smoothing groups can have their own problems. Imagine the curved surface of a cone made of polygons. All the polygons are in the same smoothing group. But at the tip of the cone, there should actually be many normals at a single vertex. Simply smoothing gives the peculiar result that the tip has one normal pointing directly out along the cone’s axis. The cone tip is a singularity; either the faceter has to provide the vertex normals, or the modeler sometimes cuts off the very tip, thereby providing separate vertices to receive these normals properly.

## 12.4 Triangle Fans, Strips, and Meshes

A standard way to increase graphics performance is to send groups of triangles that share vertices to the graphics pipeline. The benefits of this are

quite obvious: fewer points and normals need to be transformed, fewer line clips need to be performed, less lighting needs to be computed, etc. However, if the bottleneck of an application is the fill rate (i.e., the number of pixels that can be filled per second), little or no performance gain is to be expected from such savings. A variety of methods that share data, namely triangle fans, strips, and meshes, are described in this section.

### 12.4.1 Fans

Figure 12.12 shows a *triangle fan*. This type of data structure shows how we can form triangles and have each use an average of less than three vertices.

The vertex shared by all triangles is called the *center vertex* and is vertex 0 in the figure. For the starting triangle 0, send vertices 0, 1, and 2 (in that order). For subsequent triangles, the center vertex (number 0) is always used together with the previously sent vertex and the vertex currently being sent. Triangle 1 is formed merely by sending vertex 3, thereby creating a triangle defined by vertices 0 (always included), 2 (the previously sent vertex), and 3. Further on, triangle 2 is constructed by sending vertex 4. Subsequent triangles are formed in the same manner.

A triangle fan of  $n$  vertices is defined as an ordered vertex list

$$\{\mathbf{v}_0, \mathbf{v}_1, \dots, \mathbf{v}_{n-1}\} \quad (12.3)$$

(where  $\mathbf{v}_0$  is the center vertex), with a structure imposed upon the list indicating that triangle  $i$  is

$$\triangle \mathbf{v}_0 \mathbf{v}_{i+1} \mathbf{v}_{i+2}, \quad (12.4)$$

where  $0 \leq i < n - 2$ .

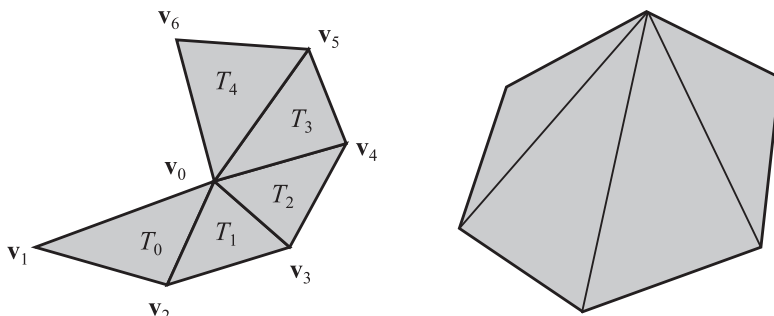


**Figure 12.12.** The left figure illustrates the concept of a triangle fan. Triangle  $T_0$  sends vertices  $\mathbf{v}_0$  (the center vertex),  $\mathbf{v}_1$ , and  $\mathbf{v}_2$ . The subsequent triangles,  $T_i$  ( $i > 0$ ), send only vertex  $\mathbf{v}_{i+2}$ . The right figure shows a convex polygon, which can always be turned into one triangle fan.

If a triangle fan consists of  $m$  triangles, then three vertices are sent for the first one, followed by one more for each of the remaining  $m-1$  triangles. This means that the average number of vertices,  $v_a$ , sent for a sequential triangle strip of length  $m$ , can be expressed as

$$v_a = \frac{3 + (m - 1)}{m} = 1 + \frac{2}{m}. \quad (12.5)$$

As can easily be seen,  $v_a \rightarrow 1$  as  $m \rightarrow \infty$ . This might not seem to have much relevance for real-world cases, but consider a more reasonable value. If  $m = 5$ , then  $v_a = 1.4$ , which means that, on average, only 1.4 vertices are sent per triangle.

Fans are a basic primitive in a number of terrain rendering algorithms [1074, 1132]. A general convex polygon<sup>2</sup> is trivial to represent as a triangle fan. Any triangle fan can be converted into a triangle strip, but not vice versa.

## 12.4.2 Strips

*Triangle strips* are like triangle fans, in that vertices in previous triangles are reused. Instead of a single center point and previous vertex getting reused, it is the vertices of the previous triangle that help form the next triangle. Consider Figure 12.13, in which connected triangles are shown. If these are treated as a triangle strip, then a more compact way of sending them to the rendering pipeline is possible. For the first triangle (denoted  $T_0$ ), all three vertices (denoted  $\mathbf{v}_0$ ,  $\mathbf{v}_1$ , and  $\mathbf{v}_2$ ) are sent in that order.

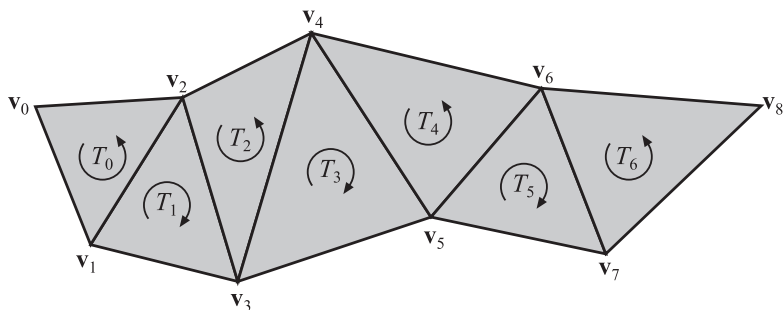


**Figure 12.13.** A sequence of triangles that can be represented as one triangle strip. Note that the orientation changes from triangle to triangle in the strip, and that the first triangle in the strip sets the orientation of all triangles. Internally, counterclockwise order is kept consistent by traversing vertices 0-1-2, 1-3-2, 2-3-4, 3-5-4, and so on.

---

<sup>2</sup>Convexity testing is discussed, and code is given, by Schorn and Fisher [1133].

For subsequent triangles in this strip, only one vertex has to be sent, since the other two have already been sent with the previous triangle. For example, sending triangle  $T_0$ , only vertex  $\mathbf{v}_3$  is sent, and the vertices  $\mathbf{v}_1$  and  $\mathbf{v}_2$  from triangle  $T_0$  are used to form triangle  $T_1$ . For triangle  $T_2$ , only vertex  $\mathbf{v}_4$  is sent, and so on through the rest of the strip.

A sequential triangle strip of  $n$  vertices is defined as an ordered vertex list

$$\{\mathbf{v}_0, \mathbf{v}_1, \dots, \mathbf{v}_{n-1}\}, \quad (12.6)$$

with a structure imposed upon it indicating that triangle  $i$  is

$$\Delta\mathbf{v}_i\mathbf{v}_{i+1}\mathbf{v}_{i+2}, \quad (12.7)$$

where  $0 \leq i < n - 2$ . This sort of strip is called *sequential* because the vertices are sent in the above mentioned sequence. The definition implies that a sequential triangle strip of  $n$  vertices has  $n - 2$  triangles; we call it a triangle strip of length  $n - 2$ .

The analysis of the average number of vertices for a triangle strip of length  $m$  (i.e., consisting of  $m$  triangles), also denoted  $v_a$ , is the same as for triangle fans (see Equation 12.5), since they have the same start-up phase and then send only one vertex per new triangle. Similarly, when  $m \rightarrow \infty$ ,  $v_a$  for triangle strips naturally also tends toward one vertex per triangle. For  $m = 20$ ,  $v_a = 1.1$ , which is much better than 3 and is close to the limit of 1.0. As with triangle fans, the start-up cost for the first triangle (always costing three vertices) is amortized over the subsequent triangles.

The attractiveness of triangle strips stems from this fact. Depending on where the bottleneck is located in the rendering pipeline, there is a potential for saving two-thirds of the time spent rendering without sequential triangle strips. The speedup is due to avoiding redundant operations, i.e., sending each vertex twice to the graphics hardware, then performing matrix transformations, lighting calculations, clipping, etc. on each.

By not imposing a strict sequence on the triangles, as was done for the sequential triangle strips, one can create longer, and thus more efficient, strips. These are called *generalized triangle strips* [242]. To be able to use such strips, there must be some kind of vertex cache on the graphics card that holds transformed and lit vertices. This is called the *post-transform cache*.<sup>3</sup> The vertices in this cache can be accessed and replaced by sending short bit codes. As will be seen in the next section, this idea has been generalized to allow the efficient processing of triangle meshes.

A way to generalize sequential triangle strips a bit is to introduce a *swap* operation, which swaps the order of the two latest vertices. In Iris GL [588],

---

<sup>3</sup>Vertex caches are also occasionally called *vertex buffers* in the literature. We avoid this term here, as *vertex buffer* is used in DirectX to mean a primitive consisting of a set of vertices.

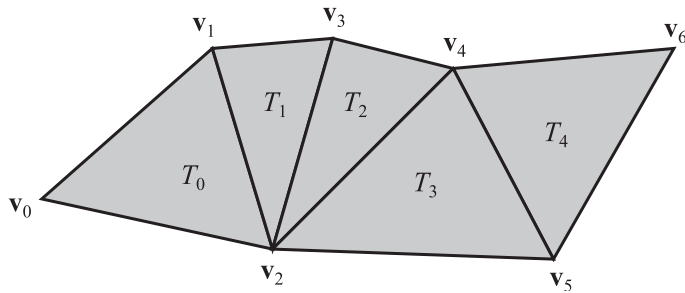


**Figure 12.14.** We would have to send  $(v_0, v_1, v_2, v_3, v_2, v_4, v_5, v_6)$  to the graphics pipeline to use these triangles as a strip. As can be seen, a swap has been implemented by including  $v_2$  twice in the list.

there is an actual command for doing a swap, but in OpenGL [969] and DirectX, a swap command must be implemented by resending a vertex, and thus there is a penalty of one vertex per swap. This implementation of a swap results in a triangle with no area. Since starting a new triangle strip costs two additional vertices, accepting the penalty imposed by a swap is still better than restarting. A triangle strip wanting to send the vertices  $(v_0, v_1, v_2, v_3, \text{swap}, v_4, v_5, v_6)$  could be implemented as  $(v_0, v_1, v_2, v_3, v_2, v_4, v_5, v_6)$ , where the swap has been implemented by resending vertex  $v_2$ . This is shown in Figure 12.14. Starting in DirectX 10, a special “ $-1$ ” restart index is available. This has the same effect as resending two vertices, but costs only one.

Even with the advantages of data sharing afforded by strips, it is important to avoid the *small batch problem* [1054]. The nature of this problem is described further in Section 15.4.2. The basic idea is that there is overhead associated with each separate API draw call, so it is important to

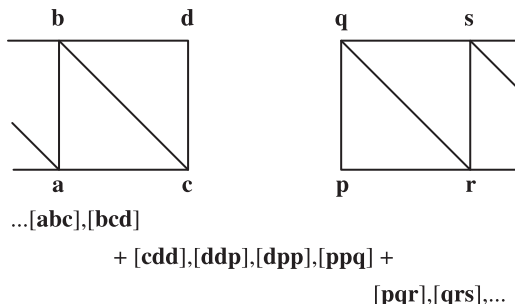


**Figure 12.15.** Two triangle strips are joined by replicating the end vertex  $d$  and beginning vertex  $p$ , forming four degenerate triangles. (Illustration after Huddy [573].)

minimize the number of calls overall. Putting as many triangles as possible in a single buffer is recommended [261]. Normally, no single triangle strip can hold all triangles. So to connect two strips, what is done is to double the last vertex of one strip and the first vertex of the next strip. Doing so has the effect of creating four degenerate triangles that are never seen (except in wireframe). See Figure 12.15. Hardware is efficient at detecting and deleting these degenerate triangles [351].

### 12.4.3 Creating Strips

Given an arbitrary triangle mesh, it can be useful to decompose it efficiently into triangle strips. A visualization of the triangle strips of a model is shown in Figure 12.16. There are free software packages for performing this task, e.g., *OpenSG* [972] and *NvTriStrip*, but it is informative to understand the principles behind these algorithms.

Obtaining optimal triangle strips has been shown to be an NP-complete problem [33], and therefore, we have to be satisfied with heuristic methods that come close to the lower bound on the number of strips. This section will present one greedy method for constructing sequential triangle strips. First, some background information is in order.

Every triangle strip creation algorithm starts by creating an adjacency graph, with each triangle knowing its neighbors. The number of neighbors of a polygon is called its *degree* and is an integer between zero and the number of vertices of the polygon. A *dual graph* is a visualization of an adjacency graph, where each triangle is treated as a node and each shared edge defines a line segment connecting two nodes. See Figure 12.17. Using the dual graph permits stripification to be thought of in terms of graph traversal.

The goal of stripification algorithms is to minimize the total number of strips generated, not to form the longest strips. For example, imagine a

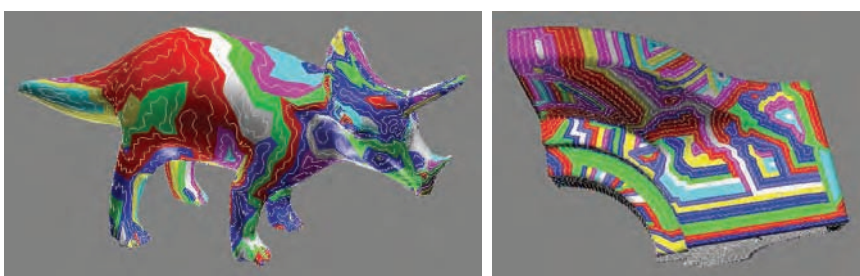


**Figure 12.16.** Triangle strips formed on various surfaces. (*Images from Martin Isenburg's triangle strip compression program.*)

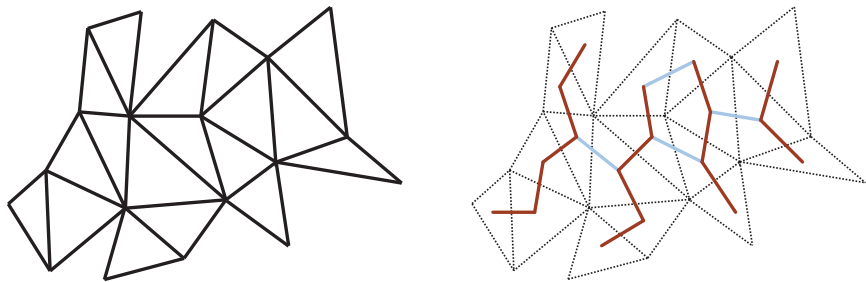


**Figure 12.17.** Left: a triangle mesh. Right: the dual graph (brown and blue lines) of the mesh to the left. Connected brown lines indicate the four different triangle strips in this example.

mesh consists of 100 triangles. One strip of 95 triangles with 5 separate triangles left over gives a total of 112 vertices to transfer. Five strips of 20 triangles each gives 110 vertices total. For this reason, one useful strategy is to begin with a low-degree triangle and grow its strip among the lower-degree candidates [8, 1063]. The SGI algorithm was one of the first strip creation algorithms, and we present it here because of its relative simplicity.

### Improved SGI Stripping Algorithm

*Greedy algorithms* are optimization methods that make choices that are locally optimal; they choose what looks best at the moment [201]. The SGI algorithm [8] is greedy, in the sense that the beginning triangle it chooses always has the lowest degree (lowest number of neighbors). With some improvements [176], the SGI algorithm works like this:

1. Choose a starting triangle.
2. Build three different triangle strips: one for each edge of the triangle.
3. Extend these triangle strips in the opposite direction.
4. Choose the longest of these three strips; discard the others.
5. Repeat Step 1 until all triangles are included in a strip.

In Step 1, the original SGI algorithm picks any triangle of lowest degree (greater than zero, since degree-zero triangles are unconnected to others). If there is a tie—that is, if there is more than one triangle with the same lowest degree—then the algorithm looks at the neighbors' neighbors for their degrees. If again there is no unambiguous way to make a selection, a triangle is arbitrarily selected. Finally, the strip is extended as much as possible in both its start and end directions, making each strip potentially

longer. The idea behind this method is to catch any low-degree triangles, so that they do not become isolated.

A linear time algorithm can be implemented by using a priority queue for finding the starting triangle of each new strip [8]. However, Chow reports that choosing any arbitrary triangle works almost as well [176]. Gumhold and Straßer report the same for their related geometry compression algorithm [468]. Steps 2 through 4 guarantee that the longest strip in the current mesh containing the starting triangle is found.

Xiang et al. [1393] present search algorithms of the dual graph, using dynamic programming. Reuter et al. [1063] present a variation of the STRIPE algorithm [321]. By paying careful attention to data locality and neighbor finding, their results were comparable in quality to software from Xiang et al. [1393] and about three times as fast to compute. Lord and Brown [794] provide a good overview of research to date, while also exploring genetic algorithms for solving the problem.

#### 12.4.4 Triangle Meshes

Triangle fans and strips have their uses, but the trend is to use triangle meshes as much as possible. Strips and fans allow some data sharing, but meshes allow full sharing.

The *Euler-Poincaré formula* for connected planar graphs [82], which is shown in Equation 12.8, helps in determining the average number of vertices that form a closed mesh:

$$v - e + f + 2g = 2. \quad (12.8)$$

Here  $v$  is the number of vertices,  $e$  is the number of edges,  $f$  is the number of faces,<sup>4</sup> and  $g$  is the genus. The *genus* is the number of holes in the object. As an example, a sphere has genus 0 and a torus has genus 1. Since every edge has two faces, and every face has at least three edges (exactly three for triangles),  $2e \geq 3f$  holds. Inserting this fact into the formula and simplifying yields  $f \leq 2v - 4$ . If all faces are triangles, then  $2e = 3f \Rightarrow f = 2v - 4$ .

For large closed triangle meshes, the rule of thumb then is that the number of triangles is about equal to twice the number of vertices. Similarly, each vertex is connected to an average of nearly six triangles (and, therefore, six edges). What is interesting is that the actual network of the mesh is irrelevant; a randomly connected triangle mesh has the same average characteristics as a regular grid of triangles, though the variance differs. Since the average number of vertices per triangle in a strip approaches one, every vertex has to be sent twice (on average) if a large mesh

---

<sup>4</sup>Each face is assumed to have one loop. If faces can have multiple loops, the formula becomes  $v - e + 2f - l + 2g = 2$ , where  $l$  is the number of loops.

is represented by sequential triangle strips. Furthermore, this implies that triangle meshes (Section 12.4.4) can be, at most, twice as efficient as sequential triangle strips. At the limit, triangle meshes can store 0.5 vertices per triangle.

Note that this analysis holds for only closed meshes. As soon as there are *boundary edges* (edges not shared between two polygons), the ratio of triangles to vertices falls. The Euler-Poincaré formula still holds, but the outer boundary of the mesh has to be considered a separate (unused) face bordering all exterior edges.

This is the theory. In practice, vertices are transformed by the GPU and put in a *first-in, first-out* (FIFO) cache. This FIFO cache is limited in size, typically holding between 12 and 24 vertices, though it can range from 4 to 32. For example, the PLAYSTATION® 3 system holds about 24 vertices, depending on the number of bytes per vertex (see Section 18.4.2). If an incoming vertex is already in this cache, the cached results can be used, providing a significant performance increase. However, if the triangles in a triangle mesh are sent down in random order, the cache is unlikely to be useful. Basic triangle strip algorithms essentially optimize for a cache size of two, i.e., the last two vertices used. Deering and Nelson [243] first explored the idea of storing vertex data in a larger FIFO cache by using additional data to determine which vertices to add to the cache.

Hoppe [564] gives an approach that optimizes the ordering of the triangles and their vertices for a given cache size. The idea is to create triangle strips that link together and so optimize cache reuse, then explore local perturbations of the resulting order for greater efficiency.

This work introduces an important measurement of cache reuse, the *average cache miss ratio* (ACMR). This is the average number of vertices that need to be processed per triangle. It can range from 3 (every vertex for every triangle has to be reprocessed each time) to 0.5 (perfect reuse on a large closed mesh; no vertex is reprocessed). If the cache size is as large as the mesh itself, the ACMR is identical to the vertex per triangle computations described earlier. For a given cache size and mesh ordering, the ACMR can be computed precisely, so describing the efficiency of any given approach for that cache size.

A limitation of Hoppe’s method is that the cache size has to be known in advance. If the assumed cache size is larger than the actual cache size, the resulting mesh can have significantly less benefit.

Sander et al. [1109] use the idea of a minimum cache size to their advantage. As discussed in Section 12.4.4, a vertex will have on average about six neighboring vertices, for a total of vertices. Modern GPUs can hold at least seven vertices in the cache at the same time. In other words, this cluster of six triangles can be rendered in any order, since all the vertices will fit in the cache. This freedom to choose the ordering allows them to

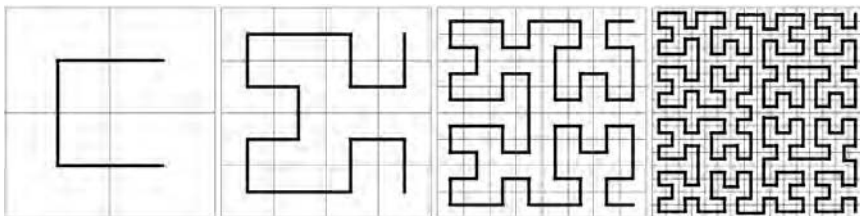


**Figure 12.18.** An illustration of four generations of Hilbert curves. The thin lines represent the grid, and the bold lines the Hilbert curve. As can be seen, the curve visits every grid cell, and it is self-similar at all scales. A nice property is that the Hilbert curve visits every grid cell within  $2 \times 2$  cells, then within  $4 \times 4$  cells, then within  $8 \times 8$  cells, and so on.

explore nearby triangles as the fan attached to a vertex is being output. The algorithm is more involved than will be explained here, but is fairly straightforward to implement and is linear time in execution. Another interesting element of their algorithm is that they attempt to order polygons essentially from the outside in. By doing so, the object draws faster, as triangles drawn later are more likely to be hidden by those drawn earlier.

### Cache-Oblivious Mesh Layouts

The ideal order for triangles in a mesh is one in which the vertex cache use is maximized. Solving for different-sized caches may yield different optimal orderings. For when the target cache size is unknown, *cache-oblivious* mesh layout algorithms have been developed that yield orderings that work well, regardless of size. Such an ordering is sometimes called a *universal* index sequence.

An important idea behind this type of algorithm, as well as other related algorithms, is the concept of a *space-filling curve*. A space-filling curve is a single, continuous curve that, without intersecting itself, fills a square or rectangle containing a uniform grid by visiting every grid cell once. One example is the Hilbert curve, which is shown in Figure 12.18, and another is the Peano curve. A space-filling curve can have good spatial coherence, which means that when walking along the curve, you stay close to the previously visited points, at all scales. The Hilbert curve is an example of a curve with good spatial coherence. See Sagan's book [1095] or Voorhies' article [1309] for more information on this topic.

If a space-filling curve is used to visit the triangles on a triangle mesh, then one can expect a high hit ratio in the vertex cache. Inspired by this, Bogomjakov and Gotsman [125] propose two algorithms, *recursive cuts* and *minimum linear arrangement*, for generating good index sequences for triangle meshes. For cache sizes from about ten and up, these algorithms consistently outperform Xiang's triangle strip method [1393].

Yoon et al. [1395] develop a fast, approximate metric for whether a local permutation of the triangle ordering would reduce the number of cache misses. With this formula in hand, they use a multilevel algorithm to optimize the mesh. They first coarsen the mesh by clustering groups of five nearby vertices into a single node. The coarsened adjacency graph is clustered again, recursively, until five or less vertices are produced. They then evaluate all possible orderings on these vertices, choosing the best. Coarsening is then reversed, with each subset of five vertices exhaustively searched for the best local permutation. Their algorithm works well with large, out-of-core meshes of hundreds of millions of triangles. There is also an open source package called *OpenCCL* that computes cache-oblivious mesh layouts using algorithms by Yoon et al.

Forsyth [356] and Lin and Yu [777] provide extremely rapid greedy algorithms that use similar principles. In Forsyth's method, a vertex-triangle connectivity map is used throughout, which is faster and simpler to generate than an edge-based adjacency graph. Vertices are given scores based on their positions in the cache and by the number of unprocessed triangles attached to them. The triangle with the highest combined vertex score is processed next. By scoring the three most recently used vertices a little lower, the algorithm avoids simply making triangle strips and instead creates patterns similar to a Hilbert curve. By giving higher scores to vertices with fewer triangles still attached, the algorithm tends to avoid leaving isolated triangles behind. The average cache miss ratios achieved are comparable to those of more costly and complex algorithms. Lin and Yu's method is a little more complex but uses related ideas. For a cache size of 12, the average ACMR for a set of 30 unoptimized models was 1.522; after optimization, the average dropped below 0.64. This average was lower than those produced by either Bogomjakov & Gotsman's or Hoppe's algorithms.

Given that the best possible ACMR for an infinitely long triangle strip is 1.0, universal rendering sequences can almost always outperform pure triangle strip creation algorithms when it comes to vertex cache reuse. However, there are other factors that can come into play when deciding on which data format to use. The next section discusses the data structures most commonly used on modern GPUs.

### 12.4.5 Vertex and Index Buffers/Arrays

One efficient way to provide a modern graphics accelerator with model data is by using what OpenGL calls *vertex buffer objects* and DirectX calls *vertex buffers*. We will go with the DirectX terminology in this section; most of the concepts map to OpenGL.

The idea of a vertex buffer is to store model data in a contiguous chunk of memory. A vertex buffer is an array of vertex data in a particular for-

mat. The format specifies whether a vertex contains diffuse or specular colors, a normal, texture coordinates, etc. The size in bytes of a vertex is called its *stride*. Alternately, a set of *vertex streams* can be used. For example, one stream could hold an array of positions  $\mathbf{p}_0\mathbf{p}_1\mathbf{p}_2\dots$  and another a separate array of normals  $\mathbf{n}_0\mathbf{n}_1\mathbf{n}_2\dots$ . In practice, a single buffer containing all data for each vertex is generally more efficient on modern GPUs, but not so much that multiple streams should be avoided [1065]. Multiple streams can help save storage and transfer time. For example, six house models with different lighting due to their surroundings could be represented by six meshes with a different set of illumination colors at each mesh vertex, merged with a single mesh with positions, normals, and texture coordinates.

How the vertex buffer is accessed is up to the device's `DrawPrimitive` method. The data can be treated as:

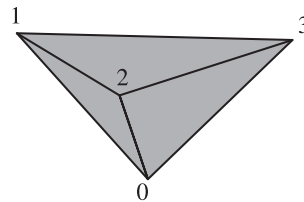
1. A list of individual points.
2. A list of unconnected line segments, i.e., pairs of vertices.
3. A single polyline.
4. A triangle list, where each group of three vertices forms a triangle, e.g., vertices  $[0, 1, 2]$  form one,  $[3, 4, 5]$  form the next, etc.
5. A triangle fan, where the first vertex forms a triangle with each successive pair of vertices, e.g.,  $[0, 1, 2], [0, 2, 3], [0, 3, 4]$ .
6. A triangle strip, where every group of three contiguous vertices forms a triangle, e.g.,  $[0, 1, 2], [1, 2, 3], [2, 3, 4]$ .

In DirectX 10, triangles and triangle strips can also include adjacent triangle vertices, for use by the geometry shader (see Section 3.5).

The indices in an index buffer point to vertices in a vertex buffer. The combination of an index buffer and vertex buffer is used to display the same types of draw primitives as a "raw" vertex buffer. The difference is that each vertex in the index/vertex buffer combination needs to be stored only once in its vertex buffer, versus repetition that can occur in a vertex buffer without indexing. For example, the triangle mesh structure can be represented by an index buffer; the first three indices stored in the index buffer specify the first triangle, the next three the second, etc. See Figure 12.19 for examples of vertex and index buffer structures.

Which structure to use is dictated by the primitives and the program. Displaying a simple rectangle is easily done with a vertex buffer using four vertices as a two-triangle tristrip. One advantage of the index buffer is data sharing. In the previous section the post-transform cache was explained,

Three triangles, made of vertex positions  $\mathbf{p}_0$  through  $\mathbf{p}_3$ , and normals  $\mathbf{n}_0$  through  $\mathbf{n}_3$



The triangles could be rendered through a series of individual calls: begin,  $\mathbf{p}_0$ ,  $\mathbf{n}_0$ ,  $\mathbf{p}_1$ ,  $\mathbf{n}_1$ ,  $\mathbf{p}_2$ ,  $\mathbf{n}_2$ , end, begin,  $\mathbf{p}_1$ ,  $\mathbf{n}_1$ ,  $\mathbf{p}_3$ ,  $\mathbf{n}_3$ ,  $\mathbf{p}_2$ ,  $\mathbf{n}_2$ , end, begin,  $\mathbf{p}_2$ ,  $\mathbf{n}_2$ ,  $\mathbf{p}_3$ ,  $\mathbf{n}_3$ ,  $\mathbf{p}_0$ ,  $\mathbf{n}_0$ , end.

The positions and normals could be put into two separate lists. These two arrays get treated as a list of triangles, so that each separate trio in the array is a triangle:

|  |                    |
|--|--------------------|
| $\boxed{\mathbf{p}_0 \ \mathbf{p}_1 \ \mathbf{p}_2 \ \mathbf{p}_1 \ \mathbf{p}_3 \ \mathbf{p}_2 \ \mathbf{p}_2 \ \mathbf{p}_3 \ \mathbf{p}_0}$ | array of positions |
| $\boxed{\mathbf{n}_0 \ \mathbf{n}_1 \ \mathbf{n}_2 \ \mathbf{n}_1 \ \mathbf{n}_3 \ \mathbf{n}_2 \ \mathbf{n}_2 \ \mathbf{n}_3 \ \mathbf{n}_0}$ | array of normals   |

The positions and normals could be put in arrays and every trio define a triangle:

|  |                    |
|--|--------------------|
| $\boxed{\mathbf{p}_0 \ \mathbf{p}_1 \ \mathbf{p}_2 \ \mathbf{p}_3 \ \mathbf{p}_0}$ | array of positions |
| $\boxed{\mathbf{n}_0 \ \mathbf{n}_1 \ \mathbf{n}_2 \ \mathbf{n}_3 \ \mathbf{n}_0}$ | array of normals   |

Each vertex could be put in a single interleaved array, with each separate trio or every trio (i.e., a tristrip) making a triangle. Here is the array for the tristrip:

|   |                   |
|---|-------------------|
| $\boxed{\mathbf{p}_0 \ \mathbf{n}_0 \ \mathbf{p}_1 \ \mathbf{n}_1 \ \mathbf{p}_2 \ \mathbf{n}_2 \ \mathbf{p}_3 \ \mathbf{n}_3 \ \mathbf{p}_0 \ \mathbf{n}_0}$ | array of vertices |
|---|-------------------|

Each vertex could be in a single array, with an index list giving separate triangles:

|   |                   |
|---|-------------------|
| $\boxed{\mathbf{p}_0 \ \mathbf{n}_0 \ \mathbf{p}_1 \ \mathbf{n}_1 \ \mathbf{p}_2 \ \mathbf{n}_2 \ \mathbf{p}_3 \ \mathbf{n}_3}$ | array of vertices |
| $\boxed{0 \ 1 \ 2 \ 1 \ 3 \ 2 \ 2 \ 3 \ 0}$   | index array       |

Each vertex could be in a single array, with an index list defining the triangle strip:

|   |                   |
|---|-------------------|
| $\boxed{\mathbf{p}_0 \ \mathbf{n}_0 \ \mathbf{p}_1 \ \mathbf{n}_1 \ \mathbf{p}_2 \ \mathbf{n}_2 \ \mathbf{p}_3 \ \mathbf{n}_3}$ | array of vertices |
| $\boxed{0 \ 1 \ 2 \ 3 \ 0}$   | index array       |

**Figure 12.19.** Different ways of defining primitives: separate triangles, or as a vertex triangle list or triangle strip, or an indexed vertex list or strip.

and ways to best use it were described. This vertex cache is available only when rendering index buffers. See Section 18.4.2 for more about vertex caches.

Index buffers also avoid the small batch problem, where the API overhead of processing a single mesh is considerably less than processing a number of triangle strips. However, separate triangle strips can be stitched together into larger vertex buffers by duplicating vertices, as discussed in Section 12.4.

Lastly, the amount of data that needs to be transferred and stored on the GPU is often smaller when an index buffer is used. The small overhead of including an indexed array is far outweighed by the savings achieved by sharing vertices. The index buffer can contain separate triangles or tristrips stitched together by duplicating vertices. One strategy for saving space is to find a cache-efficient ordering for the triangle set, then determine which structure is more space efficient by examining how many tristrips the ordering forms. The rule is that a set of tristrips with an average of two triangles or more will take less storage than using an indexed triangle list. With the DirectX 10 restart index form, this average drops to 1.5 triangles per tristrip.

An index and vertex buffer provide a way of describing a polygonal mesh. However, the data is typically stored with the goal of rendering efficiency, not compact storage. For example, one way to store a cube is to save its eight corner locations in one array, and its six different normals in another, along with the six four-index loops that define its faces. This compact representation is used in many model file formats, such as Wavefront OBJ and VRML. On the GPU, a vertex buffer would be expanded out and store 24 different vertices, as each corner location has three separate normals, depending on the face. The index buffer would store indices (as triplets or in strips) defining the 12 triangles forming the surface. More compact schemes are possible by storing the mesh in texture maps and using the vertex shader's texture fetch mechanism [151], but such usage is not common.

There are higher-level methods for allocating and using vertex and index buffers to achieve greater efficiency. For example, a buffer can be stored on the GPU for use each frame, and multiple instances and variations of an object can be generated from the same buffer. Section 15.4.2 discusses such techniques in depth.

Shader Model 4.0 and its ability to output processed vertices to a new buffer allow more malleable ways to treat vertex buffers. For example, a vertex buffer describing a triangle mesh could be treated as a simple set of points in an initial pass. The vertex shader could be used to perform per-vertex computations as desired, with the results sent to a new vertex buffer using stream out. On a subsequent pass, this new vertex buffer could

be paired with the original index buffer describing the mesh's connectivity, to further process and display the resulting mesh.

## 12.5 Simplification

Research into simplification and alternate model descriptions is an active and wide-ranging field. One area of interest is algorithms to convert surface features into bump maps [182, 1104]. Sander et al. [1103] use bump maps and a coarse mesh for the model, but create a higher precision silhouette. Impostors [806], described in Section 10.7.1, are another form of alternate rendering of the same model. Sprites and layered depth images can replace geometry in scenes (see Sections 10.5 and 10.7.1).

*Mesh simplification*, also known as *data reduction* or *decimation*, is the process of taking a detailed model and reducing its polygon count while attempting to preserve its appearance. For real-time work normally this process is done to reduce the number of vertices stored and sent down the pipeline. This can be important in making the application scalable, as older machines may need to display lower numbers of polygons [984]. Model

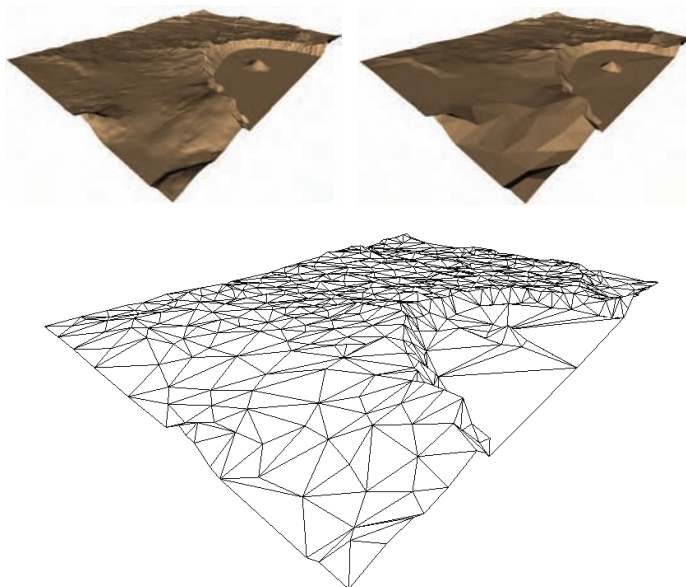


**Figure 12.20.** On the left is a heightfield of Crater Lake rendered with 200,000 triangles. The right figure shows this model simplified down to 1000 triangles. The underlying simplified mesh is shown below. (*Images courtesy of Michael Garland.*)

data may also be received with more tessellation than is necessary for a reasonable representation. Figure 12.20 gives a sense of how the number of stored triangles can be reduced by data reduction techniques.

Luebke [800, 801] identifies three types of polygonal simplification: static, dynamic, and view-dependent. Static simplification is the idea of creating separate level of detail (LOD) models before rendering begins, and the renderer chooses among these. This form is covered in Section 14.7. Batch simplification can also be useful for other tasks, such as providing coarse meshes for subdivision surfaces to refine [745, 746]. Dynamic simplification gives a continuous spectrum of LOD models instead of a few discrete models, and so such methods are referred to as *continuous level of detail* (CLOD) algorithms. View-dependent techniques are meant for models where the level of detail varies within the model. Specifically, terrain rendering is a case in which the nearby areas in view need detailed representation while those in the distance are at a lower level of detail. These two types of simplification are discussed in this section.

### 12.5.1 Dynamic Simplification

One method of reducing the polygon count is to use an *edge collapse* operation. In this operation, an edge is removed by moving its two vertices to one spot. See Figure 12.21 for an example of this operation in action. For a solid model, an edge collapse removes a total of two triangles, three edges, and one vertex. So a closed model with 3000 triangles would have 1500 edge collapses applied to it to reduce it to zero faces. The rule of thumb is that a closed triangle mesh with  $v$  vertices has about  $2v$  faces and  $3v$  edges. This rule can be derived using the Euler-Poincaré formula that  $f - e + v = 2$  for a solid's surface. See Section 12.4.4.

The edge collapse process is reversible. By storing the edge collapses in order, we can start with the simplified model and reconstruct the complex model from it. This characteristic is useful for network transmission of models, in that the edge-collapsed version of the database can be sent in an efficiently compressed form and progressively built up and displayed as the model is received [560, 1253]. Because of this feature, this simplification process is often referred to as *view-independent progressive meshing* (VIPM).

In Figure 12.21, **u** was collapsed into the location of **v**, but **v** could have been collapsed into **u**. A simplification system limited to just these two possibilities is using a *subset placement* strategy. An advantage of this strategy is that, if we limit the possibilities, we may implicitly encode the choice actually made [380, 560]. This strategy is faster because fewer possibilities need to be examined, but it also can yield lower-quality approximations because a smaller solution space is examined. The DirectX

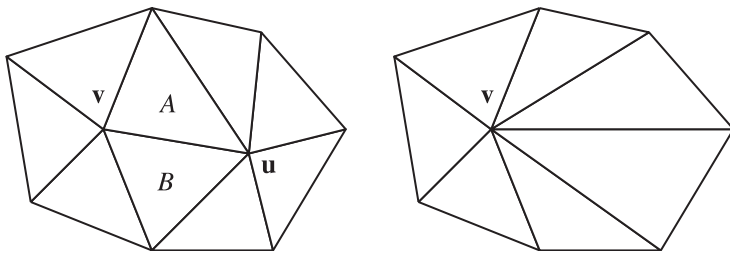


**Figure 12.21.** On the left is the figure before the  $uv$  edge collapse occurs; the right figure shows point  $u$  collapsed into point  $v$ , thereby removing triangles  $A$  and  $B$  and edge  $uv$ .

utility library uses this strategy [351], as do most other systems, such as Melax's [852].

By using an *optimal placement* strategy, we examine a wider range of possibilities. Instead of collapsing one vertex into another, both vertices for an edge are contracted to a new location. Hoppe [560] examines the case in which  $u$  and  $v$  both move to some location on the edge; he notes that in order to improve compression of the final data representation the search can be limited to checking the midpoint. Another strategy is to limit the new placement point to anywhere on the edge. Garland and Heckbert [380] solve a quadratic equation to find an optimal position (which may be located off of the edge). The advantage of optimal placement strategies is that they tend to give higher-quality meshes. The disadvantages are extra processing, code, and memory for recording this wider range of possible placements.

To determine the best point placement, we perform an analysis on the local neighborhood. This locality is an important and useful feature for a number of reasons. If the cost of an edge collapse depends on just a few local variables (e.g., edge length and face normals near the edge), the cost function is easy to compute, and each collapse affects only a few of its neighbors. For example, say a model has 3000 possible edge collapses that are computed at the start. The edge collapse with the lowest cost-function value is performed. Because it influences only a few nearby triangles and their edges, only those edge collapse possibilities whose cost functions are affected by these changes need to be recomputed (say 10 instead of 3000), and the list requires only a minor bit of resorting. Because an edge-collapse affects only a few other edge-collapse cost values, a good choice for maintaining this list of cost values is a heap or other priority queue [1183].

The collapse operation itself is an edit of the model's database. Data structures for storing these collapses are well-documented [112, 351, 562, 852, 1232]. Each edge collapse is analyzed with a cost function, and the one with the smallest cost value is performed next. An open research problem

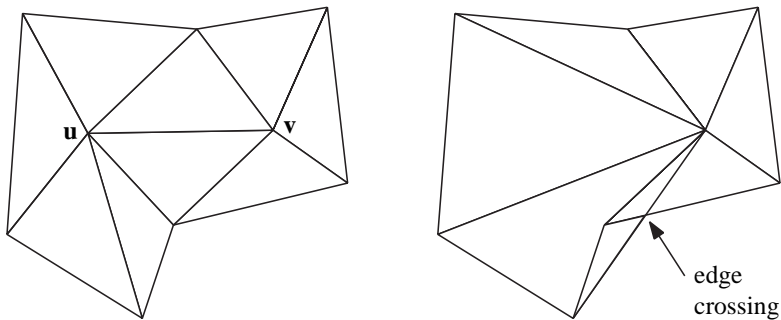


**Figure 12.22.** Example of a bad collapse. On the left is a mesh before collapsing vertex  $u$  into  $v$ . On the right is the mesh after the collapse, showing how edges now cross.

is finding the best cost function under various conditions [801]. Depending on the problem being solved, the cost function may make trade-offs among speed, quality, robustness, and simplicity. It may also be tailored to maintain surface boundaries, material locations, lighting effect, texture placement, volume, or other constraints.

Garland and Heckbert [379] introduced the idea that any pair of vertices, not just edge vertices, can form a pair and be contracted into one vertex. To limit the numbers of pairs to test, only those vertices within some distance  $t$  of each other can form a pair. This concept of pair contraction is useful in joining together separate surfaces that may be close to each other, but are not precisely joined.

Some contractions must be avoided regardless of cost; see the example in Figure 12.22. These can be detected by checking whether a neighboring polygon flips its normal direction due to a collapse.

We will present Garland and Heckbert's cost function [379, 380] in order to give a sense of how such functions work. Because of its efficiency and reasonable results, it is the cost function used in the DirectX utility library and a number of other simplification libraries. For a given vertex there is a set of triangles that share it, and each triangle has a plane equation associated with it. The cost function for moving a vertex is the sum of the squared distances between each of these planes and the new location. More formally,

$$c(\mathbf{v}) = \sum_{i=1}^m (\mathbf{n}_i \cdot \mathbf{v} + d_i)^2$$

is the cost function for new location  $\mathbf{v}$  and  $m$  planes, where  $\mathbf{n}$  is the plane's normal and  $d$  its offset from the origin.

An example of two possible contractions for the same edge is shown in Figure 12.23. Say the cube is two units long. The cost function for

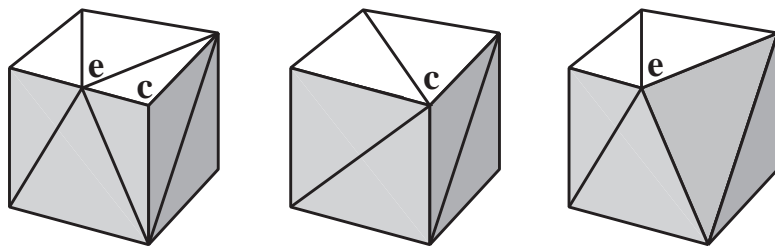


**Figure 12.23.** The left figure shows a cube with an extra point along one edge. The middle figure shows what happens if this point  $e$  is collapsed to corner  $c$ . The right figure shows  $c$  collapsed to  $e$ .

collapsing  $e$  into  $c$  ( $e \rightarrow c$ ) will be 0, because the point  $e$  does not move off of the planes it shares when it goes to  $c$ . The cost function for  $c \rightarrow e$  will be 1, because  $c$  moves away from the plane of the right face of the cube by a squared distance of 1. Because it has a lower cost, the  $e \rightarrow c$  collapse would be preferred over  $c \rightarrow e$ .

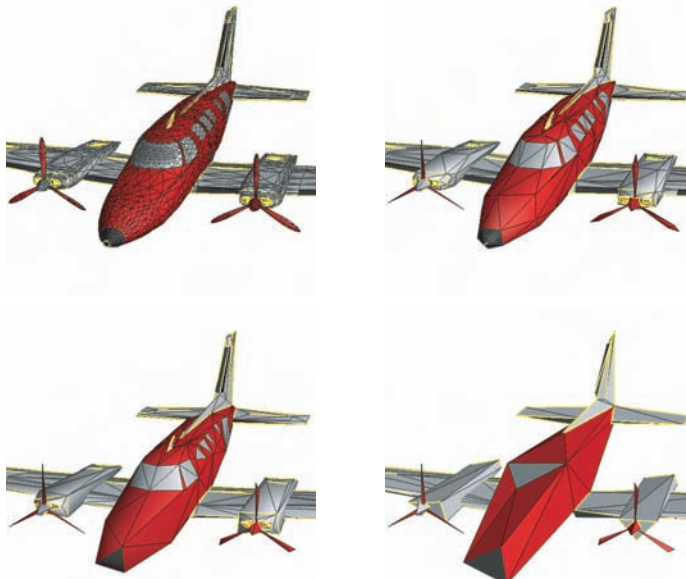


**Figure 12.24.** Mesh simplification. Upper left shows the original mesh of 13,546 faces, upper right is simplified to 1,000 faces, lower left to 500 faces, lower right to 150 faces. (Images courtesy of Hugues Hoppe, Microsoft Research.)

This cost function can be modified in various ways. Imagine two triangles that share an edge that form a very sharp edge, e.g., they are part of a fish's fin or turbine blade. The cost function for collapsing a vertex on this edge is low, because a point sliding along one triangle does not move far from the other triangle's plane. The basic function's cost value is related to the volume change of removing the feature, but is not a good indicator of its visual importance. One way to maintain an edge with a sharp crease is to add an extra plane that includes the edge and has a normal that is the average of the two triangle normals. Now vertices that move far from this edge will have a higher cost function [381]. A variation is to weight the cost function by the change in the areas of the triangles [112].

Another type of extension is to use a cost function based on maintaining other surface features. For example, the crease and boundary edges of a model are important in portraying it, so these should be made less likely to be modified. See Figure 12.24. Other surface features worth preserving are locations where there are material changes, texture map edges, and color-per-vertex changes [565]. Radiosity solutions use color per vertex to record the illumination on a meshed surface and so are excellent candidates for reduction techniques [560]. The underlying meshes are shown in Figure 12.25, a comparison of results in Figure 12.26.

The best edge to collapse is the one that makes the least perceptible change in the resulting image. Lindstrom and Turk [780] use this idea to produce an image-driven collapse function. Images of the original model are created from a set of different view directions, say 20 in all. Then all potential edge collapses are tried for a model and for each one a set of

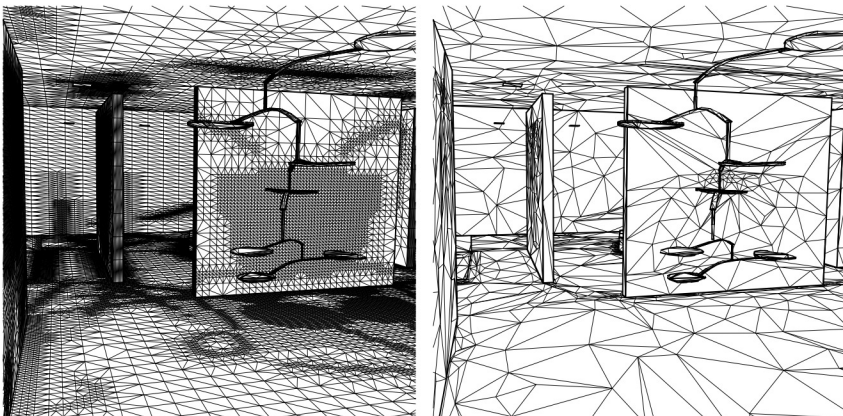


**Figure 12.25.** Simplification of radiosity solution. Left is the original mesh (150,983 faces); right is simplified mesh (10,000 faces). (*Images courtesy of Hugues Hoppe, Microsoft Research.*)



**Figure 12.26.** Simplification of a radiosity solution, shaded results. (*Images courtesy of Hugues Hoppe, Microsoft Research.*)

images is generated and compared to the original. The edge with the least visual difference is collapsed. This cost function is expensive to compute, and is certainly not a technique that can be done on the fly. However, simplification is a process that can be precomputed for later use. The advantage of the scheme is that it directly evaluates the visual effect of each collapse, versus the approximations provided by simpler functions.

One serious problem that occurs with most simplification algorithms is that textures often deviate in a noticeable way from their original appearance [801]. As edges are collapsed, the underlying mapping of the texture to the surface can become distorted. A related concept is the idea of turning a surface's original geometry into a normal map for bump mapping. Sander et al. [1104] discuss previous work in this area and provide a solution. Their idea is to split the mesh into reasonable submeshes, each of which is to give a local texture parameterization. The goal is to treat the surface position separately from the color and bump information.

Edge-collapse simplification can produce a large number of *level of detail* (LOD) models (see Section 14.7) from a single complex model. A problem found in using LOD models is that the transition can sometimes be seen if one model instantly replaces another between one frame and the next [371]. This problem is called “popping.” One solution is to use *geomorphs* [560] to increase or decrease the level of detail. Since we know how the vertices in the more complex model map to the simple model, it is possible to create a smooth transition. See Section 14.7.1 for more details.

One advantage of using VIPM is that a single vertex buffer can be created once and shared among copies of the same model at different levels of detail [1232]. However, under the basic scheme, a separate index buffer



**Figure 12.27.** Symmetry problem. The cylinder on the left has 10 flat faces (including top and bottom). The middle cylinder has 9 flat faces after 1 face is eliminated by automatic reduction. The right cylinder has 9 flat faces after being regenerated by the modeler’s faceter.

needs to be made for each copy. Another problem is efficiency. Static LOD models can undergo stripification to improve their display speeds. For dynamic models, basic VIPM does not take into account the underlying accelerator hardware. Because the order of collapses determines the triangle display order, vertex cache coherency is poor. Bloom [113] and Forsyth [351] discuss a number of practical solutions to improve efficiency when forming and sharing index buffers.

DeCoro and Tatarchuk [239] present a method of performing simplification itself using the GPU pipeline, obtaining a 15–22× increase in performance over the GPU.

Polygon reduction techniques can be useful, but they are not a panacea. A talented model maker can create low-polygon-count objects that are better in quality than those generated by automated procedures. One reason for this is that most reduction techniques know nothing about visually important elements or symmetry. For example, the eyes and mouth are the most important part of the face [852]. A naive algorithm will smooth these away as inconsequential. The problem of maintaining symmetry is shown in Figure 12.27.

### 12.5.2 View-Dependent Simplification

One type of model with unique properties is terrain. The data typically is represented by uniform heightfield grids. View-independent methods of simplification can be used on this data, as seen in Figure 12.20 on page 561. The model is simplified until some limiting criterion is met [378]. Small surface details can be captured by color or bump map textures. The resulting static mesh, often called a *triangulated irregular network* (TIN), is

a useful representation when the terrain area is small and relatively flat in various areas [1302].

For other outdoor scenes, continuous level of detail techniques can be used to minimize the number of vertices that must be processed. The idea is that terrain that is in view and close to the viewer should be shown with a greater level of detail. One type of algorithm is to use edge collapses and geomorphing, as described in the previous section, but with a cost function based on the view [561, 563]. The entire terrain is not represented as a single mesh, but rather as smaller tiles. This allows techniques such as frustum culling and potential visible sets to be used to quickly remove tiles from further consideration.

Another class of algorithms is based on using the underlying structure of the heightfield grid itself. The method by Lindstrom et al. [779], and the ROAM scheme by Duchaineau et al. [278, 1278] are two pioneering papers in this area. While these schemes are relatively inefficient on modern GPUs, many of the concepts presented are relevant to most terrain rendering systems.

The idea is to impose a hierarchical structure on the data, then evaluate this hierarchy and render only the level of complexity needed to sufficiently represent the terrain. A commonly used hierarchical structure introduced in ROAM is the *triangle bintree* (*bintree*). Starting with a large right triangle, with vertices at the corners of the heightfield tile, this triangle can be subdivided by connecting its centerpoint along the diagonal to the opposite corner. This splitting process can be done on down to the limit of the heightfield data. See Figure 12.28. In the ROAM algorithm, an error bound is created for each triangle. This error bound represents the maximum amount that the associated terrain heightfield varies from the plane formed by the triangle. In other words, three points on the heightfield define a triangle, and all the heightfield samples covered by this triangle are compared to the triangle's plane and the absolute value of the maximum difference is the error bound. The vertical error bound and the triangle

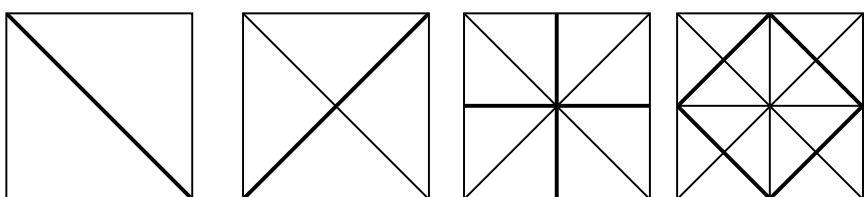


**Figure 12.28.** The triangle bintree. On the left, the heightfield is represented by two triangles at the topmost level. At each successive level, every triangle is split into two, with splits shown by the thick lines.

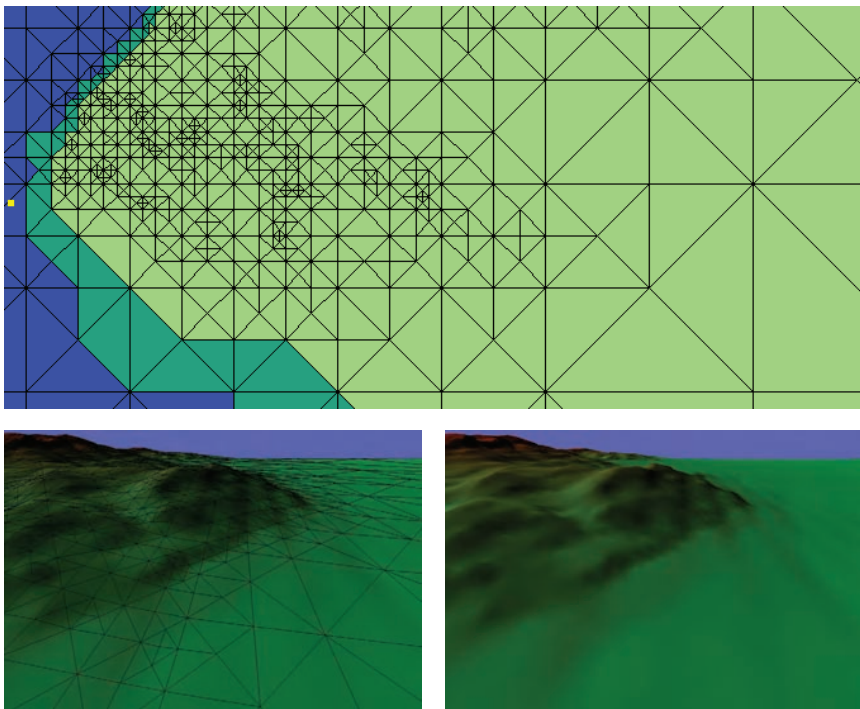


**Figure 12.29.** A ROAM view-dependent subdivision of the terrain. At top, the yellow dot on the left is the viewer. The blue areas are outside the view frustum, the light green are inside, and the dark green overlap the frustum's edges. (*Images courtesy of Mark Duchaineau, LLNL.*)

together define a pie-shaped wedge of space that contains all the terrain associated with that triangle.

During run-time, these error bounds are projected on to the view plane and evaluated for their effect on the rendering. For example, looking edge-on through a wedge means that the silhouette of the terrain is visible through that wedge, so a highly tessellated version of the terrain is needed. Looking top down through the triangular part of the wedge means the geometry itself is not critical. Due to projection, a distant wedge will have a smaller projected error, and so will be tessellated less. Blow [119] discusses improved error metrics for ROAM.

Once the subdivision level of each visible triangle is computed, tessellation can occur. Crack avoidance and repair is a major part of any terrain rendering algorithm. That is, if one triangle is highly subdivided and its neighbors are not, cracks or T-vertices can develop between the levels. The bintree structure lends itself to avoiding such splits. See Figure 12.29.

There are some useful advantages to the ROAM algorithm. The effect of each triangle wedge can be used to prioritize which triangles to split first. This lets a limit be set for the number of triangles rendered. If the view is slowly and smoothly changing, the previous frame's tessellation can be used as a starting point to create the current frame, thereby saving traversal time. Because priority queues are used and the maximum number of triangles can be specified, the frame rate can be guaranteed. See Section 14.7.3 for more on the concept of a guaranteed frame rate.

A problem with ROAM is that it tends to work on creating small sets of triangles for rendering. Hwa et al. [579] describe parts of "ROAM 2.0," an algorithm that is a hybrid of the pure CLOD scheme of ROAM mixed with a discrete LOD system. It takes advantage of the fact that modern GPUs render more rapidly by having a large number of triangles processed in a single API call. See Section 15.4.2. A number of schemes focus on creating tiles and rendering these. One approach is that the heightfield array is broken up into tiles of, say,  $17 \times 17$  vertices each. For a highly detailed view, a single tile can be rendered instead of sending individual triangles or small fans to the GPU. A tile can have multiple levels of detail. For example, by using only every other vertex in each direction, a  $9 \times 9$  tile can be formed. Using every fourth vertex gives a  $5 \times 5$  tile, every eighth a  $2 \times 2$ , and finally the four corners a  $1 \times 1$  tile of two triangles. Note that the original  $17 \times 17$  vertex buffer can be stored on the GPU and reused; only a different index buffer needs to be provided to change the number of triangles rendered.

Heuristics similar to those used in ROAM can be used to determine the level of detail used for each tile. The main challenge for a tiling scheme is crack repair. For example, if one tile is at  $33 \times 33$  and its neighbor is at  $9 \times 9$ , there will be cracking along the edge where they meet. One corrective measure is to remove the highly detailed triangles along the edge and then form sets of triangles that properly bridge the gap between the two tiles [227, 1201]. Bloom [112] gives a number of general techniques of welding splits between terrain tiles.

Andersson [23] uses a restricted quadtree to bridge the gaps and lower the total number of draw calls needed for large terrains. Instead of a uniform grid of tiles rendered at different resolutions, he uses a quadtree of tiles. Each tile has the same base resolution of  $33 \times 33$ , but each can cover a different amount of area. The idea of a restricted quadtree is that each tile's neighbors can be no more than one level of detail different. See Figure 12.30. This restriction means that there are a limited number of situations in which the resolution of the neighboring tile differs. Instead of creating gaps and having additional index buffers rendered to fill these gaps, the idea is to store all the possible permutations of index buffers that create a tile that also includes the gap transition triangles. Each index buffer is

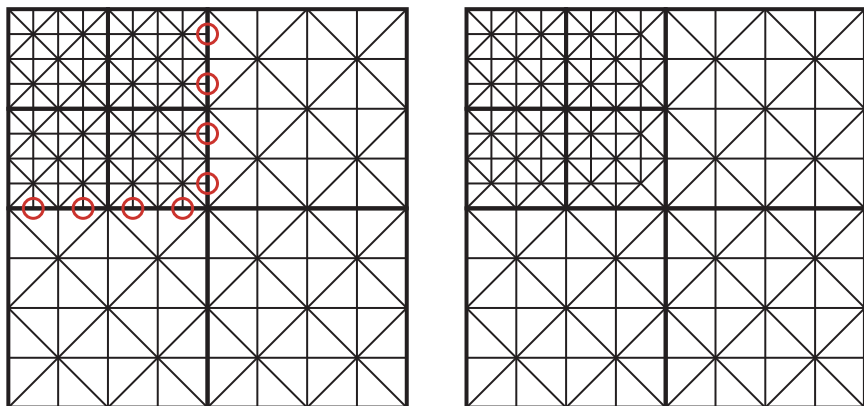


**Figure 12.30.** A restricted quadtree of terrain tiles, in which each tile can neighbor tiles at most one level higher or lower in level of detail. On the left, there are vertices on one tile but not the other, which would result in cracking. On the right, three of the more detailed tiles have modified edges to avoid the problem. Each tile is rendered in a single draw call. In practice, all tiles use  $33 \times 33$  vertices; they are simplified here for visibility. (After Andersson [23].)



**Figure 12.31.** Terrain rendering at many levels of detail in action. (Image from the Frostbite engine courtesy of DICE.)

formed by full resolution edges (33 vertices on an edge) and lower level of detail edges (17 vertices only, since the quadtree is restricted). Because the quadtree is restricted, only up to two neighboring edges are ever a lower level of detail. This limitation results in a total of nine different index buffers to represent all the types of tiles needed. An example of modern terrain rendering is shown in Figure 12.31.

Research continues in the area of terrain rendering. The Virtual Terrain Project [1302] has found that Roettger’s approach and implementation [1074] is superior to other CLOD algorithms tested. Bloom [112] uses VIPM techniques with tiles. Schneider and Westermann [1132] use a compressed format that is decoded by the vertex shader and explore geomorphing between levels of detail, while maximizing cache coherency. Losasso and Hoppe [796] present geometry clipmaps for fast rendering of large terrains, and Asirvatham and Hoppe [47] use this geometry clipmap technique with GPU vertex texture support to create rings of levels of detail for terrain meshes. Pangerl [987] and Torchelsen et al. [1269] give related methods for geometry clipmaps that fit well with the GPU’s capabilities.

## Further Reading and Resources

Schneider and Eberly [1131] present a wide variety of algorithms concerning polygons and triangles, along with pseudocode. The OpenGL Utility Library [969] includes a robust triangulator; this standalone utility library can be used even if you do not use OpenGL itself.

For translating three-dimensional file formats, the best book is Rule’s *3D Graphics File Formats: A Programmer’s Reference* [1087], which includes a file translator with source code. Murray and VanRyper’s *Encyclopedia of Graphics File Formats* [912] includes some information on three-dimensional file format layout. Open source code such as *Blender* import and export a variety of formats.

For more on determining polygon properties such as convexity and area, see Farin and Hansford’s *Practical Linear Algebra* [333]. Schorn and Fisher’s convexity test code [1133] is robust and fast, and available on the web.

Tools such as NVIDIA’s *NvTriStrip* can help in forming efficient triangle strips and index buffers, though they can be slow for extremely large meshes [1063]. DirectX includes a utility, *D3DXOptimizeFaces*, for optimizing indices, based on Hoppe’s work [564]. The triangle strip creator in *OpenSG* [972] was created by Reuter et al. [1063]. There are a number of other free optimizers and stripifiers available on the web; see this book’s website at <http://www.realtimerendering.com> for current links.

Luebke’s practical survey [800] is a worthwhile guide to simplification algorithms. The course notes by Hormann et al. [567] provide an introduc-

tion to the complex area of mesh parameterization operations, which are useful in a number of different fields, including simplification.

The book *Level of Detail for 3D Graphics* [801] covers simplification and related topics in depth. Eberly's *3D Game Engine Design* book [294] provides detailed information on his implementation of view-independent progressive meshing and terrain rendering algorithms. Svarovsky [1232] also presents a nuts and bolts guide to implementing a VIPM system. Garland distributes source code for his simplification algorithm [380]. Forsyth [351] discusses using VIPM techniques efficiently with index buffers. The Virtual Terrain Project [1302] has an excellent summary of research, and pointers to many related resources, as well as source code available on request. Andersson [23] presents a detailed case study of modeling, texturing, and rendering techniques used for a terrain system.

# Chapter 13

## Curves and Curved Surfaces

*“Where there is matter, there is geometry.”*

—Johannes Kepler

The triangle is a basic atomic rendering primitive. It is what graphics hardware is tuned to rapidly turn into lit and textured fragments and put into the frame buffer. However, objects and animation paths that are created in modeling systems can have many different underlying geometric descriptions. Curves and curved surfaces can be described precisely by equations. These equations are evaluated and sets of triangles are then created and sent down the pipeline to be rendered.

The beauty of using curves and curved surfaces is at least fourfold: (1) they have a more compact representation than a set of polygons, (2) they provide scalable geometric primitives, (3) they provide smoother and more continuous primitives than straight lines and planar polygons, and (4) animation and collision detection may become simpler and faster.

Compact curve representation offers a number of advantages for real-time rendering. First, there is a savings in memory for model storage (and so some gain in memory cache efficiency). This is especially useful for game consoles, which typically have little memory compared to a PC. Transforming curved surfaces generally involves fewer matrix multiplications than transforming a mesh representing the surface. If the graphics hardware can accept such curved surface descriptions directly, the amount of data the host CPU has to send to the graphics hardware is usually much less than sending a polygon mesh.

Curved model descriptions such as N-patches and subdivision surfaces have the interesting property that a model with few polygons can be made more convincing and realistic. The individual polygons are treated as curved surfaces, so creating more vertices on the surface. The result of a higher vertex density is better lighting of the surface and silhouette edges with higher quality.

Another major advantage of curved surfaces is that they are scalable. A curved surface description could be turned into 2 triangles or 2000. Curved

surfaces are a natural form of on the fly level of detail modeling: When the curved object is close, generate more triangles from its equations. Also, if an application is found to have a bottleneck in the rasterizer, then turning up the level of detail may increase quality while not hurting performance. Alternately, if the transform and lighting stage is the bottleneck, the tessellation rate can be turned down to increase the frame rate. However, with a unified shader architecture, such as the Xbox 360 (Section 18.4.1), these types of optimizations do not apply.

In terms of animation, curved surfaces have the advantage that a much smaller number of points needs to be animated. These points can then be used to form a curved surface and a smooth surface can be generated. Also, collision detection can potentially be more efficient and more accurate [699, 700].

The topic of curves and curved surfaces has been the subject of entire books [332, 569, 905, 1072, 1328]. Our goal here is to cover curves and surfaces that are finding common use in real-time rendering. In particular, a number of surface types are likely to become or have become a part of graphics APIs and have direct accelerator support.

Curves and surfaces have the potential for making real-time computer graphics applications faster, simpler to code, and last longer (i.e., survive a number of generations of graphics hardware). With the advent of geometry shaders, the programmer even gets control of deriving new primitives in the shader. A possible problem with using this type of shader can be that some CPU-side algorithms rely on knowing the exact geometry. For example, the shadow volume method (Section 9.1.3) needs to use the silhouette edge of a model in order to generate projected quadrilaterals. If the CPU is creating these quadrilaterals, a curve description has to also be evaluated on the CPU to find the silhouette edges. Even with such limitations, the potential quality and speed improvements offered by curved surface descriptions makes them useful today, and future graphics hardware promises to be more powerful and flexible.

## 13.1 Parametric Curves

In this section we will introduce parametric curves. These are used in many different contexts and are implemented using a great many different methods. For real-time graphics, parametric curves are often used to move the viewer or some object along a predefined path. This may involve changing both the position and the orientation; however, in this chapter, we consider only positional paths. See Section 4.3.2 on page 77 for information on orientation interpolation. Another use could be to render hair, as seen in Figure 13.1.



**Figure 13.1.** Hair rendering using tessellated cubic curves [929]. (*Image from “Nalu” demo courtesy of NVIDIA Corporation.*)

Say you want to move the camera from one point to another in a certain amount of time, independent of the performance of the underlying hardware. As an example, assume that the camera should move between these points in one second, and that the rendering of one frame takes 50 ms. This means that we will be able to render 20 frames along the way during that second. On a faster computer, one frame might take only 25 ms, which would be equal to 40 frames per second, and so we would want to move the camera to 40 different locations. Finding either set of points is possible to do with parametric curves.

A parametric curve describes points using some formula as a function of a parameter  $t$ . Mathematically, we write this as  $\mathbf{p}(t)$ , which means that this function delivers a point for each value of  $t$ . The parameter  $t$  may belong to some interval, called the *domain*, e.g.,  $t \in [a, b]$ . The generated points are continuous, that is, as  $\epsilon \rightarrow 0$  then  $\mathbf{p}(t + \epsilon) \rightarrow \mathbf{p}(t)$ . Loosely speaking, this means that if  $\epsilon$  is a very small number, then  $\mathbf{p}(t)$  and  $\mathbf{p}(t + \epsilon)$  are two points very close to each other.

In the next section, we will start with an intuitive and geometrical description of Bézier curves, a common form of parametric curves, and

then put this into a mathematical setting. Then we discuss how to use piecewise Bézier curves and explain the concept of continuity for curves. In Section 13.1.4 and 13.1.5, we will present two other useful curves, namely cubic hermites and Kochanek-Bartels splines. Finally, we cover rendering of Bézier curves using the GPU in Section 13.1.2.

### 13.1.1 Bézier Curves

Linear interpolation traces out a path, which is a straight line, between two points,  $\mathbf{p}_0$  and  $\mathbf{p}_1$ . This is as simple as it gets. See the left illustration in Figure 13.2. Given these points, the following function describes a linearly interpolated point  $\mathbf{p}(t)$ , where  $t$  is the curve parameter, and  $t \in [0, 1]$ :

$$\mathbf{p}(t) = \mathbf{p}_0 + t(\mathbf{p}_1 - \mathbf{p}_0) = (1 - t)\mathbf{p}_0 + t\mathbf{p}_1. \quad (13.1)$$

The parameter  $t$  controls where on the line the point  $\mathbf{p}(t)$  will land;  $\mathbf{p}(0) = \mathbf{p}_0$ ,  $\mathbf{p}(1) = \mathbf{p}_1$ , and  $0 < t < 1$  gives us a point on the straight line between  $\mathbf{p}_0$  and  $\mathbf{p}_1$ . So if we would like to move the camera from  $\mathbf{p}_0$  to  $\mathbf{p}_1$  linearly in 20 steps during 1 second, then we would use  $t_i = i/(20 - 1)$ , where  $i$  is the frame number (starting from 0).

When you are interpolating between only two points, linear interpolation may suffice, but for more points on a path, it often does not. For example, when several points are interpolated, the sudden changes at the points (also called joints) that connect two segments become unacceptable. This is shown at the right of Figure 13.2.

To solve this, we take the approach of linear interpolation one step further, and linearly interpolate repeatedly. By doing this, we arrive at

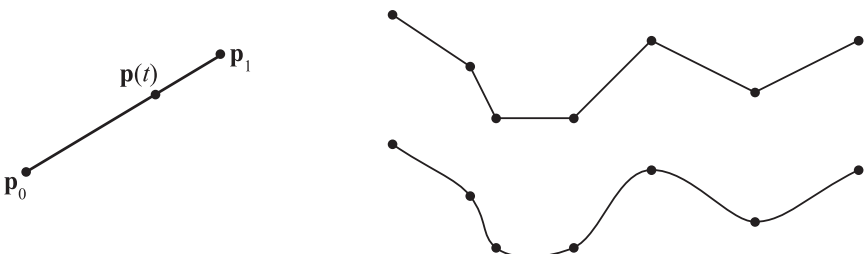


**Figure 13.2.** Linear interpolation between two points is the path on a straight line (left). For seven points, linear interpolation is shown at the upper right, and some sort of smoother interpolation is shown at the lower right. What is most objectionable about using linear interpolation are the discontinuous changes (sudden jerks) at the joints between the linear segments.

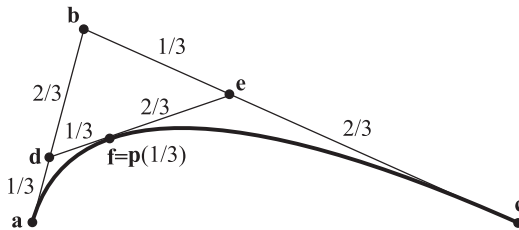


**Figure 13.3.** Repeated linear interpolation gives a Bézier curve. This curve is defined by three control points,  $\mathbf{a}$ ,  $\mathbf{b}$ , and  $\mathbf{c}$ . Assuming we want to find the point on the curve for the parameter  $t = 1/3$ , we first linearly interpolate between  $\mathbf{a}$  and  $\mathbf{b}$  to get  $\mathbf{d}$ . Next,  $\mathbf{e}$  is interpolated from  $\mathbf{b}$  and  $\mathbf{c}$ . The final point,  $\mathbf{p}(1/3) = \mathbf{f}$  is found by interpolating between  $\mathbf{d}$  and  $\mathbf{e}$ .

the geometrical construction of the Bézier (pronounced *beh-zee-eh*) curve.<sup>1</sup> First, to be able to repeat the interpolation, we have to add more points. For example, three points,  $\mathbf{a}$ ,  $\mathbf{b}$ , and  $\mathbf{c}$ , called the *control points*, could be used. Say we want to find  $\mathbf{p}(1/3)$ , that is, the point on the curve for  $t = 1/3$ . We compute two new points  $\mathbf{d}$  and  $\mathbf{e}$  by linear interpolation from  $\mathbf{a} \& \mathbf{b}$  and  $\mathbf{b} \& \mathbf{c}$  using  $t = 1/3$ . See Figure 13.3. Finally, we compute  $\mathbf{f}$  by linear interpolation from  $\mathbf{d}$  and  $\mathbf{e}$  again using  $t = 1/3$ . We define  $\mathbf{p}(t) = \mathbf{f}$ . Using this technique, we get the following relationship:

$$\begin{aligned}\mathbf{p}(t) &= (1 - t)\mathbf{d} + t\mathbf{e} \\ &= (1 - t)[(1 - t)\mathbf{a} + t\mathbf{b}] + t[(1 - t)\mathbf{b} + t\mathbf{c}] \\ &= (1 - t)^2\mathbf{a} + 2(1 - t)t\mathbf{b} + t^2\mathbf{c},\end{aligned}\quad (13.2)$$

which is a parabola since the maximum degree of  $t$  is two (quadratic). In fact, given  $n + 1$  control points, it turns out that the degree of the curve is  $n$ . This means that more control points gives more degrees of freedom for the curve. A second degree curve is also called a *quadratic*, a third degree curve is called a *cubic*, a fourth degree curve is called a *quartic*, and so on.

This kind of repeated or recursive linear interpolation is often referred to as the *de Casteljau algorithm* [332, 569]. An example of what this looks like when using five control points is shown in Figure 13.4. To generalize, instead of using points  $\mathbf{a} \& \mathbf{f}$ , as in this example, the following notation is used. The control points are denoted  $\mathbf{p}_i$ , so in the example,  $\mathbf{p}_0 = \mathbf{a}$ ,  $\mathbf{p}_1 = \mathbf{b}$ , and  $\mathbf{p}_2 = \mathbf{c}$ . Then, after linear interpolation has been applied  $k$  times, intermediate control points  $\mathbf{p}_i^k$  are obtained. In our example, we have  $\mathbf{p}_0^1 = \mathbf{d}$ ,  $\mathbf{p}_1^1 = \mathbf{e}$ , and  $\mathbf{p}_0^2 = \mathbf{f}$ . The Bézier curve for  $n + 1$  control points

<sup>1</sup>As a historical note, the Bézier curves were developed independently by Paul de Casteljau and Pierre Bézier for use in the French car industry. They are called *Bézier* curves because Bézier was able to make his research publicly available before de Casteljau, even though de Casteljau wrote his technical report before Bézier [332].

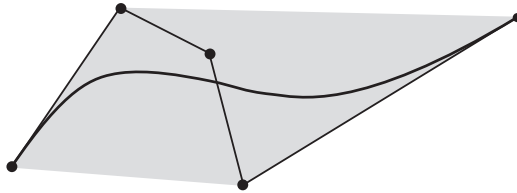


**Figure 13.4.** Repeated linear interpolation from five points gives a fourth degree (quartic) Bézier curve. The curve is inside the convex hull (gray region), of the control points, marked by black dots. Also, at the first point, the curve is tangent to the line between the first and second point. The same also holds for the other end of the curve.

can be described with the recursion formula shown below, where  $\mathbf{p}_i^0 = \mathbf{p}_i$  are the initial control points:

$$\mathbf{p}_i^k(t) = (1-t)\mathbf{p}_i^{k-1}(t) + t\mathbf{p}_{i+1}^{k-1}(t), \quad \begin{cases} k = 1 \dots n, \\ i = 0 \dots n - k. \end{cases} \quad (13.3)$$

Note that a point on the curve is described by  $\mathbf{p}(t) = \mathbf{p}_0^n(t)$ . This is not as complicated as it looks. Consider again what happens when we construct a Bézier curve from three points;  $\mathbf{p}_0$ ,  $\mathbf{p}_1$ , and  $\mathbf{p}_2$ , which are equivalent to  $\mathbf{p}_0^0$ ,  $\mathbf{p}_1^0$ , and  $\mathbf{p}_2^0$ . Three controls points means that  $n = 2$ . To shorten the formulae, sometimes “(t)” is dropped from the  $\mathbf{p}$ ’s. In the first step  $k = 1$ , which gives  $\mathbf{p}_0^1 = (1-t)\mathbf{p}_0 + t\mathbf{p}_1$ , and  $\mathbf{p}_1^1 = (1-t)\mathbf{p}_1 + t\mathbf{p}_2$ . Finally, for  $k = 2$ , we get  $\mathbf{p}_0^2 = (1-t)\mathbf{p}_0^1 + t\mathbf{p}_1^1$ , which is the same as sought for  $\mathbf{p}(t)$ . An illustration of how this works in general is shown in Figure 13.5.

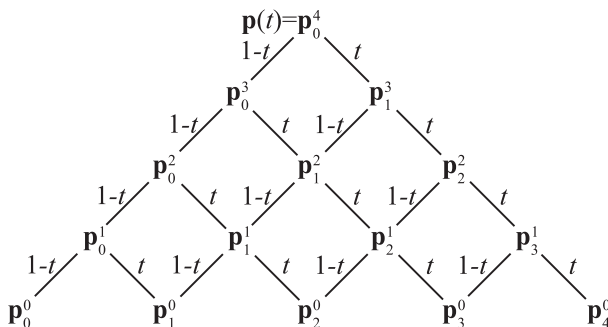


**Figure 13.5.** An illustration of how repeated linear interpolation works for Bézier curves. In this example, the interpolation of a quartic curve is shown. This means there are five control points,  $\mathbf{p}_i^0$ ,  $i = 0, 1, 2, 3, 4$ , shown at the bottom. The diagram should be read from the bottom up, that is,  $\mathbf{p}_1^0$  is formed from weighting  $\mathbf{p}_0^0$  with weight  $1-t$  and adding that with  $\mathbf{p}_1^0$  weighted by  $t$ . This goes on until the point of the curve  $\mathbf{p}(t)$  is obtained at the top. (Illustration after Goldman [413].)

Now that we have the basics in place on how Bézier curves work, we can take a look at a more mathematical description of the same curves.

### Bézier Curves Using Bernstein Polynomials

As seen in Equation 13.2, the quadratic Bézier curve could be described using an algebraic formula. It turns out that every Bézier curve can be described with such an algebraic formula, which means that you do not need to do the repeated interpolation. This is shown below in Equation 13.4, which yields the same curve as described by Equation 13.3. This description of the Bézier curve is called the *Bernstein form*:

$$\mathbf{p}(t) = \sum_{i=0}^n B_i^n(t) \mathbf{p}_i. \quad (13.4)$$

This function contains the Bernstein polynomials,<sup>2</sup>

$$B_i^n(t) = \binom{n}{i} t^i (1-t)^{n-i} = \frac{n!}{i!(n-i)!} t^i (1-t)^{n-i}. \quad (13.5)$$

The first term, the binomial coefficient, in this equation is defined in Equation 1.5 in Chapter 1. Two basic properties of the Bernstein polynomial are the following:

$$\begin{aligned} B_i^n(t) &\in [0, 1], \text{ when } t \in [0, 1], \\ \sum_{i=0}^n B_i^n(t) &= 1. \end{aligned} \quad (13.6)$$

The first formula means that the Bernstein polynomials are in the interval between 0 to 1 when  $t$  also is from 0 to 1. The second formula means that all the Bernstein polynomial terms in Equation 13.4 sum to one for all different degrees of the curve (this can be seen in Figure 13.6). Loosely speaking, this means that the curve will stay “close” to the control points,  $\mathbf{p}_i$ . In fact, the entire Bézier curve will be located in the convex hull (see Section A.5.3) of the control points, which follows from Equations 13.4 and 13.6. This is a useful property when computing a bounding area or volume for the curve. See Figure 13.4 for an example.

In Figure 13.6 the Bernstein polynomials for  $n = 1$ ,  $n = 2$ , and  $n = 3$  are shown. These are also called *blending functions*. The case when  $n = 1$  (linear interpolation) is illustrative, in the sense that it shows the curves  $y = 1 - t$  and  $y = t$ . This implies that when  $t = 0$ , then  $\mathbf{p}(0) = \mathbf{p}_0$ , and when  $t$  increases, the blending weight for  $\mathbf{p}_0$  decreases, while the blending weight for  $\mathbf{p}_1$  increases by the same amount, keeping the sum of the weights

---

<sup>2</sup>The Bernstein polynomials are sometimes called Bézier basis functions.

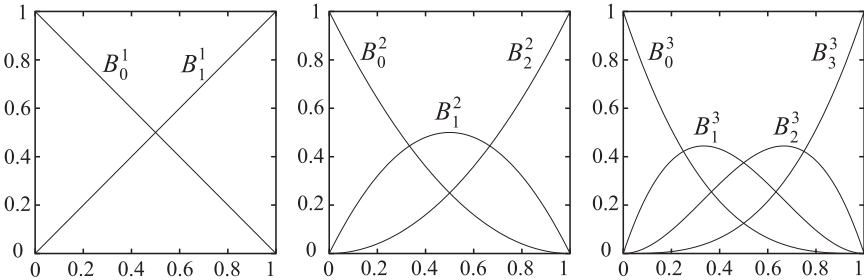


**Figure 13.6.** Bernstein polynomials for  $n = 1$ ,  $n = 2$ , and  $n = 3$  (left to right). The left figure shows linear interpolation, the middle quadratic interpolation, and the right cubic interpolation. These are the blending functions used in the Bernstein form of Bézier curves. So, to evaluate a quadratic curve (middle diagram) at a certain  $t$ -value, just find the  $t$ -value on the  $x$ -axis, and then go vertically until the three curves are encountered, which gives the weights for the three control points. Note that  $B_i^n(t) \geq 0$ , when  $t \in [0, 1]$ , and the symmetry of these blending functions:  $B_i^n(t) = B_{n-i}^n(1-t)$ .

equal to 1. Finally, when  $t = 1$ ,  $\mathbf{p}(1) = \mathbf{p}_1$ . In general, it holds for all Bézier curves that  $\mathbf{p}(0) = \mathbf{p}_0$  and  $\mathbf{p}(1) = \mathbf{p}_n$ , that is, the endpoints are interpolated (i.e., are on the curve). It is also true that the curve is tangent to the vector  $\mathbf{p}_1 - \mathbf{p}_0$  at  $t = 0$ , and to  $\mathbf{p}_n - \mathbf{p}_{n-1}$  at  $t = 1$ . Another interesting property is that instead of computing points on a Bézier curve, and then rotating the curve, the control points can first be rotated, and then the points on the curve can be computed. This is a nice property that most curves and surfaces have, and it means that a program can rotate the control points (which are few) and then generate the points on the rotated curve. This is much faster than doing the opposite.

As an example on how the Bernstein version of the Bézier curve works, assume that  $n = 2$ , i.e., a quadratic curve. Equation 13.4 is then

$$\begin{aligned} \mathbf{p}(t) &= B_0^2 \mathbf{p}_0 + B_1^2 \mathbf{p}_1 + B_2^2 \mathbf{p}_2 \\ &= \binom{2}{0} t^0 (1-t)^2 \mathbf{p}_0 + \binom{2}{1} t^1 (1-t)^1 \mathbf{p}_1 + \binom{2}{2} t^2 (1-t)^0 \mathbf{p}_2 \quad (13.7) \\ &= (1-t)^2 \mathbf{p}_0 + 2t(1-t) \mathbf{p}_1 + t^2 \mathbf{p}_2, \end{aligned}$$

which is the same as Equation 13.2. Note that the blending functions above,  $(1-t)^2$ ,  $2t(1-t)$ , and  $t^2$ , are the functions displayed in the middle of Figure 13.6. In the same manner, a cubic curve is simplified into the formula below:

$$\mathbf{p}(t) = (1-t)^3 \mathbf{p}_0 + 3t(1-t)^2 \mathbf{p}_1 + 3t^2(1-t) \mathbf{p}_2 + t^3 \mathbf{p}_3. \quad (13.8)$$

This equation can be rewritten in matrix form as

$$\mathbf{p}(t) = \begin{pmatrix} 1 & t & t^2 & t^3 \end{pmatrix} \begin{pmatrix} 1 & 0 & 0 & 0 \\ -3 & 3 & 0 & 0 \\ 3 & -6 & 3 & 0 \\ -1 & 3 & -3 & 1 \end{pmatrix} \begin{pmatrix} \mathbf{p}_0 \\ \mathbf{p}_1 \\ \mathbf{p}_2 \\ \mathbf{p}_3 \end{pmatrix}, \quad (13.9)$$

and since it involves dot products (rather than scalar operations, as in Equation 13.8), it may be more efficient when implementing on a GPU. Similarly, Wyatt [1384] argues that B-spline curves can be implemented in a similar way (just a different matrix), but with many advantages, such as the natural continuity of that type of curve, among other things. We will not cover B-splines in this text, other than to say they offer local control. Any Bézier curve can be converted to a B-spline, and any B-spline can be converted to one or more Bézier curves. Shene's website [1165] and Andersson's article online [22] give easily accessible overviews of B-splines and other related curves and surfaces. See *Further Reading and Resources* at the end of this chapter for more sources of information.

By collecting terms of the form  $t^k$  in Equation 13.4, it can be seen that every Bézier curve can be written in the following form, where the  $\mathbf{c}_i$  are points that fall out by collecting terms:

$$\mathbf{p}(t) = \sum_{i=0}^n t^i \mathbf{c}_i. \quad (13.10)$$

It is straightforward to differentiate Equation 13.4, in order to get the derivative of the Bézier curve. The result, after reorganizing and collecting terms, is shown below [332]:

$$\frac{d}{dt} \mathbf{p}(t) = n \sum_{i=0}^{n-1} B_i^{n-1}(t) (\mathbf{p}_{i+1} - \mathbf{p}_i). \quad (13.11)$$

The derivative is, in fact, also a Bézier curve, but with one degree lower than  $\mathbf{p}(t)$ .

One downside of Bézier curves is that they do not pass through all the control points (except the endpoints). Another problem is that the degree increases with the number of control points, making evaluation more and more expensive. A solution to this is to use a simple, low-degree curve between each pair of subsequent control points, and see to it that this kind of piecewise interpolation has a high enough degree of continuity. This is the topic of Sections 13.1.3–13.1.5.

### Rational Bézier Curves

While Bézier curves can be used for many things, they do not have that many degrees of freedom—only the position of the control points can be

chosen freely. Also, not every curve can be described by Bézier curves. For example, the circle is normally considered a very simple shape, but it cannot be described by one or a collection of Bézier curves. One alternative is the *rational Bézier curve*. This type of curve is described by the formula shown in Equation 13.12:

$$\mathbf{p}(t) = \frac{\sum_{i=0}^n w_i B_i^n(t) \mathbf{p}_i}{\sum_{i=0}^n w_i B_i^n(t)}. \quad (13.12)$$

The denominator is a weighted sum of the Bernstein polynomials, while the numerator is a weighted version of the standard Bézier curve (Equation 13.4). For this type of curve, the user has the weights,  $w_i$ , as additional degrees of freedom. More about these curves can be found in Hoschek and Lasser's [569] and in Farin's book [332]. Farin also describes how a circle can be described by three rational Bézier curves.

### 13.1.2 Bounded Bézier Curves on the GPU

A method for rendering Bézier curves on the GPU will be presented [788, 791]. Specifically, the target is “bounded Bézier curves,” where the region between the curve and the straight line between the first and last control points is filled. There is a surprisingly simple way to do this by rendering a triangle with a specialized pixel shader.

We use a quadratic, i.e., degree two, Bézier curve, with control points  $\mathbf{p}_0$ ,  $\mathbf{p}_1$ , and  $\mathbf{p}_2$ . See Section 13.1.1. If we set the texture coordinates at these vertices to  $\mathbf{t}_0 = (0, 0)$ ,  $\mathbf{t}_1 = (0.5, 0)$ , and  $\mathbf{t}_2 = (1, 1)$ , the texture coordinates will be interpolated as usual during rendering of the triangle  $\Delta \mathbf{p}_0 \mathbf{p}_1 \mathbf{p}_2$ . We also evaluate the following scalar function inside the triangle

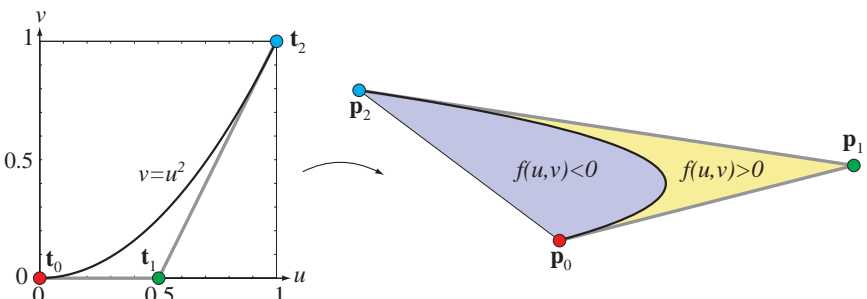


**Figure 13.7.** Bounded Bézier curve rendering. Left: The curve is shown in canonical texture space. Right: The curve is rendered in screenspace. If the condition  $f(u, v) \geq 0$  is used to kill pixels, then the light blue region will result from the rendering.

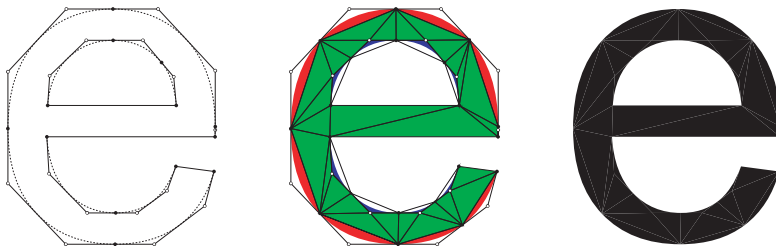


**Figure 13.8.** An *e* is represented by a number of straight lines and quadratic Bézier curves (left). In the middle, this representation has been “tessellated” into a number of bounded Bézier curves (red and blue), and triangles (green). The final letter is shown to the right. (Reprinted with permission from Microsoft Corporation.)

for each pixel, where  $u$  and  $v$  are interpolated texture coordinates:

$$f(u, v) = u^2 - v. \quad (13.13)$$

The pixel shader then determines whether the pixel is inside ( $f(u, v) < 0$ ), or otherwise outside. This is illustrated in Figure 13.7. When rendering a perspective-projected triangle with this pixel shader, we will get the corresponding projected Bézier curve. A proof of this is given by Loop and Blinn [788, 791].

This type of technique can be used to render TrueType fonts, for example. This is illustrated in Figure 13.8. Loop and Blinn also show how to render rational quadratic curves and cubic curves, and how do to anti-aliasing using this representation.

### 13.1.3 Continuity and Piecewise Bézier Curves

Assume that we have two Bézier curves that are cubic, that is, defined by four control points each. The first curve is defined by  $\mathbf{q}_i$ , and the second by  $\mathbf{r}_i$ ,  $i = 0, 1, 2, 3$ . To join the curves, we could set  $\mathbf{q}_3 = \mathbf{r}_0$ . This point is called a *joint*. However, as shown in Figure 13.9, the joint will not be smooth using this simple technique. The composite curve formed from several curve pieces (in this case two) is called a *piecewise Bézier curve*, and is denoted  $\mathbf{p}(t)$  here. Further, assume we want  $\mathbf{p}(0) = \mathbf{q}_0$ ,  $\mathbf{p}(1) = \mathbf{q}_3 = \mathbf{r}_0$ , and  $\mathbf{p}(3) = \mathbf{r}_3$ . Thus, the times for when we reach  $\mathbf{q}_0$ ,  $\mathbf{q}_3 = \mathbf{r}_0$ , and  $\mathbf{r}_3$ , are  $t_0 = 0.0$ ,  $t_1 = 1.0$ , and  $t_2 = 3.0$ . See Figure 13.9 for notation. From the previous section we know that a Bézier curve is defined for  $t \in [0, 1]$ , so this works out fine for the first curve segment defined by the  $\mathbf{q}_i$ 's, since the time at  $\mathbf{q}_0$  is 0.0, and the time at  $\mathbf{q}_3$  is 1.0. But what happens when  $1.0 < t \leq 3.0$ ? The answer is simple: We must use the second curve segment, and then translate and scale the parameter interval from  $[t_1, t_2]$

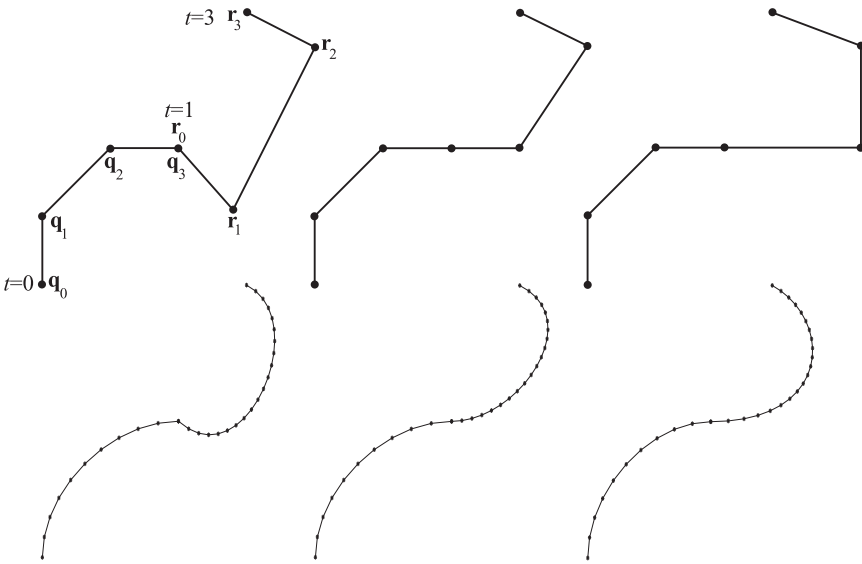


**Figure 13.9.** This figure shows from left to right  $C^0$ ,  $G^1$ , and  $C^1$  continuity between two cubic Bézier curves (four control points each). The top row shows the control points, and the bottom row the curves, with 10 sample points for the left curve, and 20 for the right. The following time-point pairs are used for this example:  $(0.0, \mathbf{q}_0)$ ,  $(1.0, \mathbf{q}_3)$ , and  $(3.0, \mathbf{r}_3)$ . With  $C^0$  continuity, there is a sudden jerk at the join (where  $\mathbf{q}^3 = \mathbf{r}_0$ ). This is improved with  $G^1$  by making the tangents at the join parallel (and equal in length). Though, since  $3.0 - 1.0 \neq 1.0 - 0.0$ , this does not give  $C^1$  continuity. This can be seen at the join where there is a sudden acceleration of the sample points. To achieve  $C^1$ , the right tangent at the join has to be twice as long as the left tangent.

to  $[0, 1]$ . This is done using the formula below:

$$t' = \frac{t - t_1}{t_2 - t_1}. \quad (13.14)$$

Hence, it is the  $t'$  that is fed into the Bézier curve segment defined by the  $\mathbf{r}_i$ 's. This is simple to generalize to stitching several Bézier curves together.

A better way to join the curves is to use the fact that at the first control point of a Bézier curve the tangent is parallel to  $\mathbf{q}_1 - \mathbf{q}_0$  (see Section 13.1.1). Similarly, at the last control point the cubic curve is tangent to  $\mathbf{q}_3 - \mathbf{q}_2$ . This behavior can be seen in Figure 13.4. So, to make the two curves join tangentially at the joint, the tangent for the first and the second curve should be parallel there. Put more formally, the following should hold:

$$(\mathbf{r}_1 - \mathbf{r}_0) = c(\mathbf{q}_3 - \mathbf{q}_2) \quad \text{for } c > 0. \quad (13.15)$$

This simply means that the incoming tangent,  $\mathbf{q}_3 - \mathbf{q}_2$ , at the joint should have the same direction as the outgoing tangent,  $\mathbf{r}_1 - \mathbf{r}_0$ .

It is possible to achieve even better continuity than that, using in Equation 13.15 the  $c$  defined by Equation 13.16 [332]:

$$c = \frac{t_2 - t_1}{t_1 - t_0}. \quad (13.16)$$

This is also shown in Figure 13.9. If we instead set  $t_2 = 2.0$ , then  $c = 1.0$ , so when the time intervals on each curve segment are equal, then the incoming and outgoing tangent vectors should be identical. However, this does not work when  $t_2 = 3.0$ . The curves will look identical, but the speed at which  $\mathbf{p}(t)$  moves on the composite curve will not be smooth. The constant  $c$  in Equation 13.16 takes care of this.

Some advantages of using piecewise curves are that lower degree curves can be used, and that the resulting curves will go through a set of points. In the example above, a degree of three, i.e., a cubic, was used for each of the two curve segments. Cubic curves are often used for this, as those are the lowest-degree curves that can describe an *S-shaped* curve, called an *inflection*. The resulting curve  $\mathbf{p}(t)$  interpolates, i.e., goes through, the points  $\mathbf{q}_0$ ,  $\mathbf{q}_3 = \mathbf{r}_0$ , and  $\mathbf{r}_3$ .

At this point, two important continuity measures have been introduced by example. A slightly more mathematical presentation of the continuity concept for curves follows. For curves in general, we use the  $C^n$  notation to differentiate between different kinds of continuity at the joints. This means that all the  $n$ :th first derivatives should be continuous and nonzero all over the curve. Continuity of  $C^0$  means that the segment should join at the same point, so linear interpolation fulfills this condition. This was the case for the first example in this section. Continuity of  $C^1$  means that if we derive once at any point on the curve (including joints), the result should also be continuous. This was the case for the third example in this section, where Equation 13.16 was used.

There is also a measure that is denoted  $G^n$ . Let us look at  $G^1$  (geometrical) continuity as an example. For this, the tangent vectors from the curve segments that meet at a joint should be parallel and have the same direction, but nothing about the lengths is assumed. In other words,  $G^1$  is a weaker continuity than  $C^1$ , and a curve that is  $C^1$  is always  $G^1$  except when the velocities of two curves go to zero at the point where the curves join and they have different tangents just before the join [349]. The concept of geometrical continuity can be extended to higher dimensions. The middle illustration in Figure 13.9 shows  $G^1$ -continuity.

### 13.1.4 Cubic Hermite Interpolation

Bézier curves are very useful in describing the theory behind the construction of smooth curves, but their use is not always intuitive. In this section,

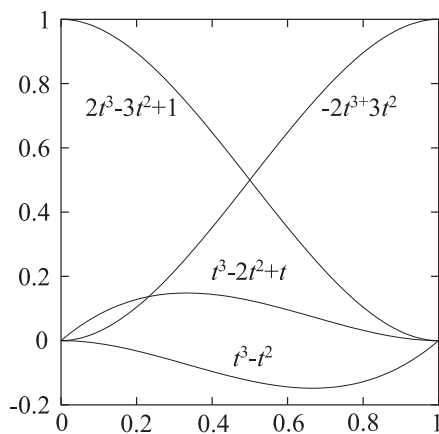


**Figure 13.10.** Blending functions for Hermite cubic interpolation. Note the asymmetry of the blending functions for the tangents. Negating the blending function  $t^3 - t^2$  and  $\mathbf{m}_1$  in Equation 13.17 would give a symmetrical look.

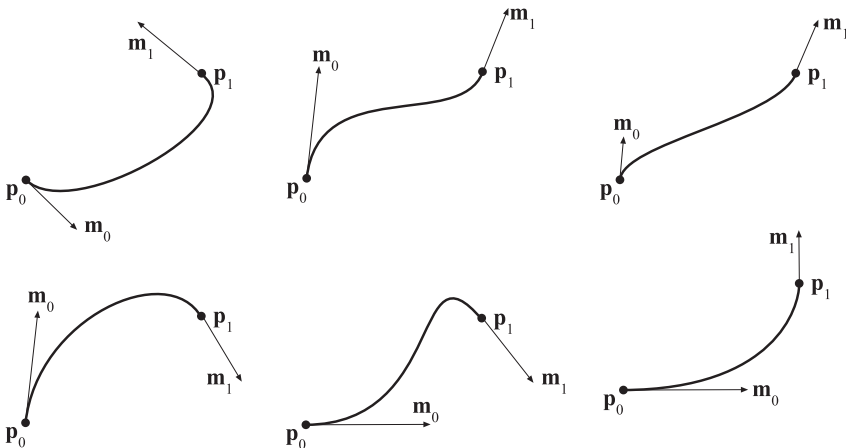


**Figure 13.11.** Hermite interpolation. A curve is defined by two points,  $\mathbf{p}_0$  and  $\mathbf{p}_1$ , and a tangent,  $\mathbf{m}_0$  and  $\mathbf{m}_1$ , at each point.

we will present cubic Hermite interpolation, and these curves tend to be simpler to control. The reason is that instead of giving four control points to describe a cubic Bézier curve, the cubic Hermite curve is defined by starting and ending points,  $\mathbf{p}_0$  and  $\mathbf{p}_1$ , and starting and ending tangents,  $\mathbf{m}_0$  and  $\mathbf{m}_1$ . The Hermite interpolant,  $\mathbf{p}(t)$ , where  $t \in [0, 1]$ , is

$$\mathbf{p}(t) = (2t^3 - 3t^2 + 1)\mathbf{p}_0 + (t^3 - 2t^2 + t)\mathbf{m}_0 + (t^3 - t^2)\mathbf{m}_1 + (-2t^3 + 3t^2)\mathbf{p}_1. \quad (13.17)$$

We also call  $\mathbf{p}(t)$  a Hermite curve segment or a cubic spline segment. This is a cubic interpolant, since  $t^3$  is the highest exponent in the blending functions in the above formula. The following holds for this curve:

$$\mathbf{p}(0) = \mathbf{p}_0, \quad \mathbf{p}(1) = \mathbf{p}_1, \quad \frac{\partial \mathbf{p}}{\partial t}(0) = \mathbf{m}_0, \quad \frac{\partial \mathbf{p}}{\partial t}(1) = \mathbf{m}_1. \quad (13.18)$$

This means that the Hermite curve interpolates  $\mathbf{p}_0$  and  $\mathbf{p}_1$ , and the tangents at these points are  $\mathbf{m}_0$  and  $\mathbf{m}_1$ . The blending functions in Equation 13.17 are shown in Figure 13.10, and they can be derived from Equations 13.4 and 13.18. Some examples of cubic Hermite interpolation can be seen in Figure 13.11. All these examples interpolate the same points, but have different tangents. Note also that different lengths of the tangents give different results; longer tangents have a greater impact on the overall shape.

Note that cubic hermite interpolation was used to render the hair in the Nalu demo [929] (see Figure 13.1), where a coarse control hair was used for animation and collision detection. Then tangents were computed, and cubic curves tessellated and rendered.

### 13.1.5 Kochanek-Bartels Curves

When interpolating between more than two points using Hermite curves, a way is needed to control the shared tangents. Here, we will present one way to compute such tangents, called Kochanek-Bartels curves. Assume that we have  $n$  points,  $\mathbf{p}_0, \dots, \mathbf{p}_{n-1}$ , which should be interpolated with  $n - 1$  Hermite curve segments. We assume that there is only one tangent at each point, and we start to look at the “inner” tangents,  $\mathbf{m}_1, \dots, \mathbf{m}_{n-2}$ . A tangent at  $\mathbf{p}_i$  can be computed as a combination of the two chords [680]:  $\mathbf{p}_i - \mathbf{p}_{i-1}$ , and  $\mathbf{p}_{i+1} - \mathbf{p}_i$ , as shown at the left in Figure 13.12.

First, a tension parameter,  $a$ , is introduced that modifies the length of the tangent vector. This controls how sharp the curve is going to be at the joint. The tangent is computed as

$$\mathbf{m}_i = \frac{1-a}{2}((\mathbf{p}_i - \mathbf{p}_{i-1}) + (\mathbf{p}_{i+1} - \mathbf{p}_i)). \quad (13.19)$$

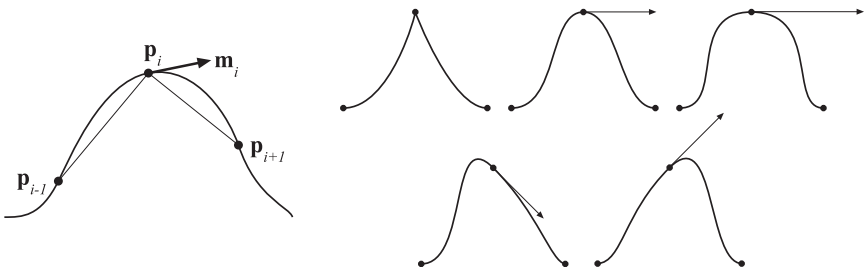


**Figure 13.12.** One method of computing the tangents is to use a combination of the chords (left). The upper row at the right shows three curves with different tension parameters ( $a$ ). The left curve has  $a \approx 1$ , which means high tension; the middle curve has  $a \approx 0$ , which is default tension; and the right curve has  $a \approx -1$ , which is low tension. The bottom row of two curves at the right shows different bias parameters. The curve on the left has a negative bias, and the right curve has a positive bias.

The top row at the right in Figure 13.12 shows different tension parameters. The default value is  $a = 0$ ; higher values give sharper bends (if  $a > 1$ , there will be a loop at the joint), and negative values give less taut curves near the joints. Second, a bias parameter,  $b$ , is introduced that influences the direction of the tangent (and also, indirectly, the length of the tangent). If we ignore the tension ( $a = 0$ ) for a while, then the tangent is computed as below:

$$\mathbf{m}_i = \frac{1+b}{2}(\mathbf{p}_i - \mathbf{p}_{i-1}) + \frac{1-b}{2}(\mathbf{p}_{i+1} - \mathbf{p}_i). \quad (13.20)$$

The default value is  $b = 0$ . A positive bias gives a bend that is more directed toward the chord  $\mathbf{p}_i - \mathbf{p}_{i-1}$ , and a negative bias gives a bend that is more directed toward the other chord:  $\mathbf{p}_{i+1} - \mathbf{p}_i$ . This is shown in the bottom row on the right in Figure 13.12. Combining the tension and the bias gives

$$\mathbf{m}_i = \frac{(1-a)(1+b)}{2}(\mathbf{p}_i - \mathbf{p}_{i-1}) + \frac{(1-a)(1-b)}{2}(\mathbf{p}_{i+1} - \mathbf{p}_i). \quad (13.21)$$

The user can either set the tension and bias parameters or let them have their default values, which gives a Catmull-Rom spline [160]. The tangents at the first and the last points can also be computed with these formulae; one of the chords is simply set to a length of zero.

Yet another parameter that controls the behavior at the joints can be incorporated into the tangent equation [349, 680]. However, this requires the introduction of two tangents at each joint, one incoming, denoted  $\mathbf{s}_i$  (for source) and one outgoing, denoted  $\mathbf{d}_i$  (for destination). See Figure 13.13. Note that the curve segment between  $\mathbf{p}_i$  and  $\mathbf{p}_{i+1}$  uses the tangents  $\mathbf{d}_i$

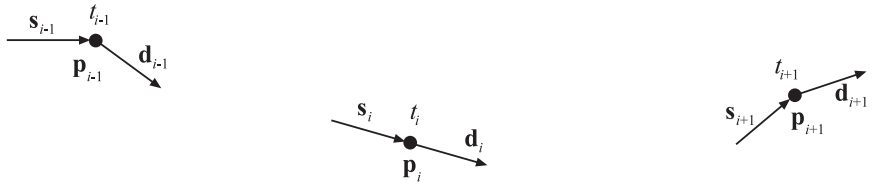


**Figure 13.13.** Incoming and outgoing tangents for Kochanek-Bartels curves. At each control point  $\mathbf{p}_i$ , its time  $t_i$  is also shown, where  $t_i > t_{i-1}$ , for all  $i$ .

and  $\mathbf{s}_{i+1}$ . The tangents are computed as below, where  $c$  is the *continuity* parameter:

$$\begin{aligned}\mathbf{s}_i &= \frac{1-c}{2}(\mathbf{p}_i - \mathbf{p}_{i-1}) + \frac{1+c}{2}(\mathbf{p}_{i+1} - \mathbf{p}_i), \\ \mathbf{d}_i &= \frac{1+c}{2}(\mathbf{p}_i - \mathbf{p}_{i-1}) + \frac{1-c}{2}(\mathbf{p}_{i+1} - \mathbf{p}_i).\end{aligned}\quad (13.22)$$

Again,  $c = 0$  is the default value, which makes  $\mathbf{s}_i = \mathbf{d}_i$ . Setting  $c = -1$  gives  $\mathbf{s}_i = \mathbf{p}_i - \mathbf{p}_{i-1}$ , and  $\mathbf{d}_i = \mathbf{p}_{i+1} - \mathbf{p}_i$ , producing a sharp corner at the joint, which is only  $C^0$ . Increasing the value of  $c$  makes  $\mathbf{s}_i$  and  $\mathbf{d}_i$  more and more alike. For  $c = 0$ , then  $\mathbf{s}_i = \mathbf{d}_i$ . When  $c = 1$  is reached, we get  $\mathbf{s}_i = \mathbf{p}_{i+1} - \mathbf{p}_i$ , and  $\mathbf{d}_i = \mathbf{p}_i - \mathbf{p}_{i-1}$ . Thus, the continuity parameter  $c$  is another way to give even more control to the user, and it makes it possible to get sharp corners at the joints, if desired.

The combination of tension, bias, and continuity, where the default parameter values are  $a = b = c = 0$ , is

$$\begin{aligned}\mathbf{s}_i &= \frac{(1-a)(1+b)(1-c)}{2}(\mathbf{p}_i - \mathbf{p}_{i-1}) + \frac{(1-a)(1-b)(1+c)}{2}(\mathbf{p}_{i+1} - \mathbf{p}_i), \\ \mathbf{d}_i &= \frac{(1-a)(1+b)(1+c)}{2}(\mathbf{p}_i - \mathbf{p}_{i-1}) + \frac{(1-a)(1-b)(1-c)}{2}(\mathbf{p}_{i+1} - \mathbf{p}_i).\end{aligned}\quad (13.23)$$

Both Equations 13.21 and 13.23 work only when all curve segments are using the same time interval length. To account for different time length of the curve segments, the tangents have to be adjusted, similar to what was done in Section 13.1.3. The adjusted tangents, denoted  $\mathbf{s}'_i$  and  $\mathbf{d}'_i$ , are shown below:

$$\begin{aligned}\mathbf{s}'_i &= \mathbf{s}_i \frac{2\Delta_i}{\Delta_{i-1} + \Delta_i}, \\ \mathbf{d}'_i &= \mathbf{d}_i \frac{2\Delta_{i-1}}{\Delta_{i-1} + \Delta_i},\end{aligned}\quad (13.24)$$

where  $\Delta_i = t_{i+1} - t_i$ . This concludes the presentation of Kochanek-Bartels splines, which gives the user three intuitive parameters, bias, tension, and continuity, with which to design curves.

## 13.2 Parametric Curved Surfaces

A natural extension of parametric curves (Section 13.1) is parametric surfaces. An analogy is that a triangle or polygon is an extension of a line segment, in which we go from one to two dimensions. Parametric surfaces can be used to model objects with curved surfaces. A parametric surface is defined by a small number of control points. Tessellation of a parametric surface is the process of evaluating the surface representation at a number of positions, and connecting these to form triangles that approximate the true surface. This is done because graphics hardware can efficiently render triangles. At runtime, the surface can then be tessellated into as many triangles as desired. Thus, parametric surfaces are perfect for making a tradeoff between quality and speed; more triangles take more time to render, but give better shading and silhouettes. Another advantage of parametric surfaces is that the control points can be animated and then the surface can be tessellated. This is in contrast to animating a large triangle mesh directly, which can be more expensive.

This section starts by introducing *Bézier patches*, which are curved surfaces with rectangular domains. These are also called *tensor-product Bézier surfaces*. Then *Bézier triangles* are presented, which have triangular domains. An *N-patch* is a triangular Bézier surface that can replace each triangle in a triangle mesh. Using N-patches can improve the silhouette and shading of a coarse mesh. They are presented in Section 13.2.3. Finally, the topic of continuity is briefly treated in Section 13.2.4.

### 13.2.1 Bézier Patches

The concept of Bézier curves, introduced in Section 13.1.1, can be extended from using one parameter to using two parameters, thus forming surfaces instead of curves. Let us start with extending linear interpolation to *bilinear interpolation*. Now, instead of just using two points, we use four points, called **a**, **b**, **c**, and **d**, as shown in Figure 13.14. Instead of using one parameter called  $t$ , we now use two parameters  $(u, v)$ . Using  $u$  to linearly interpolate **a** & **b** and **c** & **d** gives **e** and **f**:

$$\begin{aligned}\mathbf{e} &= (1 - u)\mathbf{a} + u\mathbf{b}, \\ \mathbf{f} &= (1 - u)\mathbf{c} + u\mathbf{d}.\end{aligned}\tag{13.25}$$

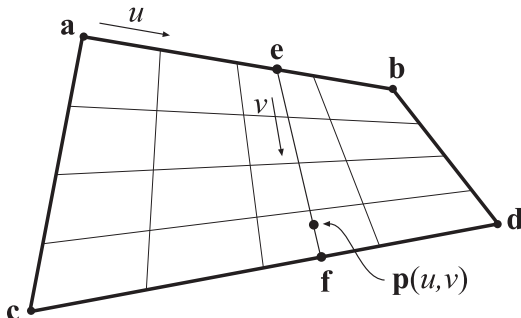


**Figure 13.14.** Bilinear interpolation using four points.

Next, the linearly interpolated points, **e** and **f**, are linearly interpolated in the other direction, using  $v$ . This yields bilinear interpolation:

$$\begin{aligned} \mathbf{p}(u, v) &= (1 - v)\mathbf{e} + v\mathbf{f} \\ &= (1 - u)(1 - v)\mathbf{a} + u(1 - v)\mathbf{b} + (1 - u)v\mathbf{c} + uv\mathbf{d}. \end{aligned} \quad (13.26)$$

Equation 13.26 describes the simplest nonplanar parametric surface, where different points on the surface are generated using different values of  $(u, v)$ . The domain, i.e., the set of valid values, is  $(u, v) \in [0, 1] \times [0, 1]$ , which means that both  $u$  and  $v$  should belong to  $[0, 1]$ . When the domain is rectangular, the resulting surface is often called a *patch*.

To extend a Bézier curve from linear interpolation, more points were added and the interpolation repeated. The same strategy can be used for patches. Assume nine points, arranged in a  $3 \times 3$  grid, are used. This is shown in Figure 13.15, where the notation is shown as well. To form

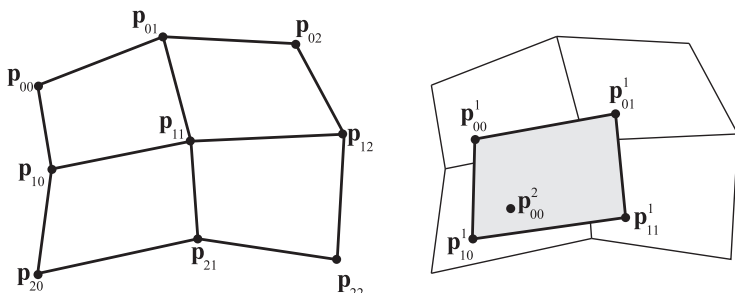


**Figure 13.15.** Left: a biquadratic Bézier surface, defined by nine control points,  $\mathbf{p}_{ij}$ . Right: To generate a point on the Bézier surface, four points  $\mathbf{p}_{ij}^1$  are first created using bilinear interpolation from the nearest control points. Finally, the point  $\mathbf{p}(u, v) = \mathbf{p}_{00}^2$  is bilinearly interpolated from these created points.

a biquadratic Bézier patch from these points, we first need to bilinearly interpolate four times to create four intermediate points, also shown in Figure 13.15. Next, the final point on the surface is bilinearly interpolated from the previously created points.

The repeated bilinear interpolation described above is the extension of de Casteljau's algorithm to patches. At this point we need to define some notation. The degree of the surface is  $n$ . The control points are  $\mathbf{p}_{i,j}$ , where  $i$  and  $j$  belong to  $[0 \dots n]$ . Thus,  $(n+1)^2$  control points are used for a patch of degree  $n$ . Note that the control points should be superscripted with a zero, i.e.,  $\mathbf{p}_{i,j}^0$ , but this is often omitted, and sometimes we use the subscript  $_{ij}$  instead of  $_{i,j}$  when there can be no confusion. The Bézier patch using de Casteljau's algorithm is described in the equation that follows:

**de Casteljau [patches]:**

$$\begin{aligned}\mathbf{p}_{i,j}^k(u, v) &= (1-u)(1-v)\mathbf{p}_{i,j}^{k-1} + u(1-v)\mathbf{p}_{i,j+1}^{k-1} + (1-u)v\mathbf{p}_{i+1,j}^{k-1} + uv\mathbf{p}_{i+1,j+1}^{k-1}, \\ k &= 1 \dots n, \quad i = 0 \dots n-k, \quad j = 0 \dots n-k.\end{aligned}\tag{13.27}$$

Similar to the Bézier curve, the point at  $(u, v)$  on the Bézier patch is  $\mathbf{p}_{0,0}^n(u, v)$ . The Bézier patch can also be described in Bernstein form using Bernstein polynomials, as shown in Equation 13.28:

**Bernstein [patches]:**

$$\begin{aligned}\mathbf{p}(u, v) &= \sum_{i=0}^m B_i^m(u) \sum_{j=0}^n B_j^n(v) \mathbf{p}_{i,j} = \sum_{i=0}^m \sum_{j=0}^n B_i^m(u) B_j^n(v) \mathbf{p}_{i,j}, \\ &= \sum_{i=0}^m \sum_{j=0}^n \binom{m}{i} \binom{n}{j} u^i (1-u)^{m-i} v^j (1-v)^{n-j} \mathbf{p}_{i,j}.\end{aligned}\tag{13.28}$$

Note that in Equation 13.28, there are two parameters,  $m$  and  $n$ , for the degree of the surface. The “compound” degree is sometimes denoted  $m \times n$ . Most often  $m = n$ , which simplifies the implementation a bit. The consequence of, say,  $m > n$  is to first bilinearly interpolate  $n$  times, and then linearly interpolate  $m - n$  times. This is shown in Figure 13.16. An interesting interpretation of Equation 13.28 is found by rewriting it as

$$\begin{aligned}\mathbf{p}(u, v) &= \sum_{i=0}^m B_i^m(u) \sum_{j=0}^n B_j^n(v) \mathbf{p}_{i,j} \\ &= \sum_{i=0}^m B_i^m(u) \mathbf{q}_i(v).\end{aligned}\tag{13.29}$$

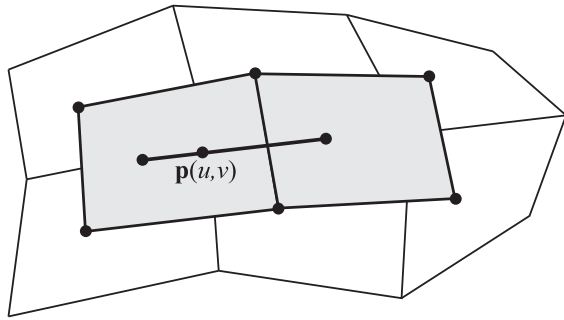


**Figure 13.16.** Different degrees in different directions.

Here,  $\mathbf{q}_i(v) = \sum_{j=0}^n B_j^n(v) \mathbf{p}_{i,j}$  for  $i = 0 \dots m$ . As can be seen in the bottom row in Equation 13.29, this is just a Bézier curve when we fix a  $v$ -value. Assuming  $v = 0.35$ , the points  $\mathbf{q}_i(0.35)$  can be computed from a Bézier curve, and then Equation 13.29 describes a Bézier curve on the Bézier surface, for  $v = 0.35$ .

Next, some useful properties of Bézier patches will be presented. By setting  $(u, v) = (0, 0)$ ,  $(u, v) = (0, 1)$ ,  $(u, v) = (1, 0)$ , and  $(u, v) = (1, 1)$  in Equation 13.28, it is simple to prove that a Bézier patch interpolates, that is, goes through, the corner control points,  $\mathbf{p}_{0,0}$ ,  $\mathbf{p}_{0,n}$ ,  $\mathbf{p}_{n,0}$ , and  $\mathbf{p}_{n,n}$ . Also, each boundary of the patch is described by a Bézier curve of degree  $n$  formed by the control points on the boundary. Therefore, the tangents at the corner control points are defined by these boundary Bézier curves. Each corner control point has two tangents, one in each of the  $u$  and  $v$  directions. As was the case for Bézier curves, the patch also lies within the convex hull of its control points, and

$$\sum_{i=0}^m \sum_{j=0}^n B_i^m(u) B_j^n(v) = 1$$

for  $(u, v) \in [0, 1] \times [0, 1]$ . Finally, rotating the control points and then generating points on the patch is the same mathematically as (though usually faster than) generating points on the patch and then rotating these. Partially differentiating Equation 13.28 gives [332] the equations below:

**Derivatives [patches]:**

$$\begin{aligned} \frac{\partial \mathbf{p}(u, v)}{\partial u} &= m \sum_{j=0}^n \sum_{i=0}^{m-1} B_i^{m-1}(u) B_j^n(v) [\mathbf{p}_{i+1,j} - \mathbf{p}_{i,j}], \\ \frac{\partial \mathbf{p}(u, v)}{\partial v} &= n \sum_{i=0}^m \sum_{j=0}^{n-1} B_i^m(u) B_j^{n-1}(v) [\mathbf{p}_{i,j+1} - \mathbf{p}_{i,j}]. \end{aligned} \tag{13.30}$$

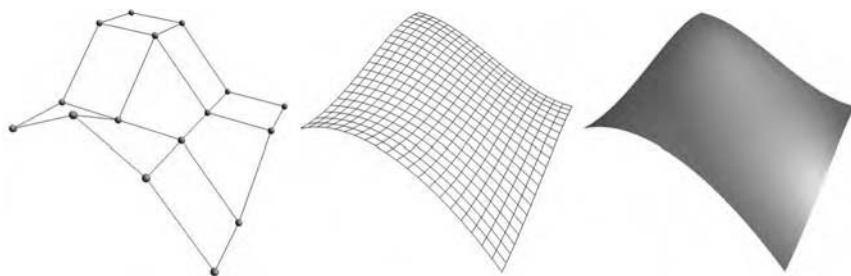


**Figure 13.17.** Left: control mesh of a  $4 \times 4$  degree Bézier patch. Middle: the actual quadrilaterals that were generated on the surface. Right: shaded Bézier patch.

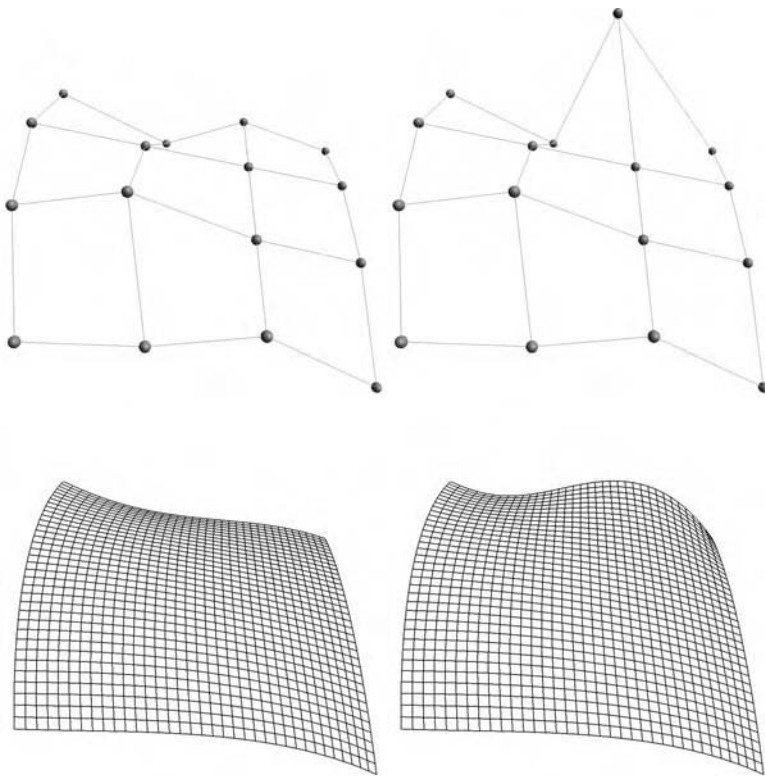


**Figure 13.18.** This set of images shows what happens to a Bézier patch when one vertex is moved. Most of the change is near the moved control point.

As can be seen, the degree of the patch is reduced by one in the direction that is differentiated. The unnormalized normal vector is then formed as

$$\mathbf{n}(u, v) = \frac{\partial \mathbf{p}(u, v)}{\partial u} \times \frac{\partial \mathbf{p}(u, v)}{\partial v}. \quad (13.31)$$

In Figure 13.17, the control mesh together with the actual Bézier patch is shown. The effect of moving a control point is shown in Figure 13.18.

### Rational Bézier Patches

Just as the Bézier curve could be extended into a rational Bézier curve (Section 13.1.1), and thus introduce more degrees of freedom, so can the Bézier patch be extended into a rational Bézier patch:

$$\mathbf{p}(u, v) = \frac{\sum_{i=0}^m \sum_{j=0}^n w_{i,j} B_i^m(u) B_j^n(v) \mathbf{p}_{i,j}}{\sum_{i=0}^m \sum_{j=0}^n w_{i,j} B_i^m(u) B_j^n(v)}. \quad (13.32)$$

Consult Farin's book [332] and Hockek and Lasser's book [569] for information about this type of patch. Similarly, the rational Bézier triangle is an extension of the Bézier triangle, treated next.

## 13.2.2 Bézier Triangles

Even though the triangle often is considered a simpler geometric primitive than the rectangle, this is not the case when it comes to Bézier surfaces: Bézier triangles are not as straightforward as Bézier patches. This type of patch is worth presenting as it is used in forming N-patches, which are supported directly on some GPUs. N-patches are discussed in the section after this.

The control points are located in a triangular grid, as shown in Figure 13.19. The degree of the Bézier triangle is  $n$ , and this implies that there are  $n + 1$  control points per side. These control points are denoted

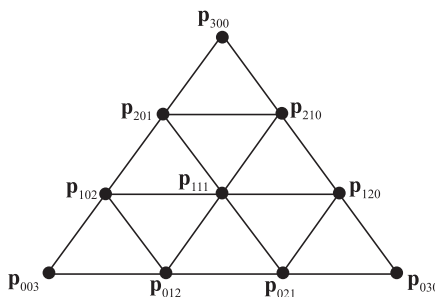


**Figure 13.19.** The control points of a Bézier triangle with degree three (cubic).

$\mathbf{p}_{i,j,k}^0$  and sometimes abbreviated to  $\mathbf{p}_{ijk}$ . Note that  $i + j + k = n$ , and  $i, j, k \geq 0$  for all control points. Thus, the total number of control points is

$$\sum_{x=1}^{n+1} x = \frac{(n+1)(n+2)}{2}.$$

It should come as no surprise that Bézier triangles also are based on repeated interpolation. However, due to the triangular shape of the domain, barycentric coordinates (see Section 16.8) must be used for the interpolation. Recall that a point within a triangle  $\Delta\mathbf{p}_0\mathbf{p}_1\mathbf{p}_2$ , can be described as  $\mathbf{p}(u, v) = \mathbf{p}_0 + u(\mathbf{p}_1 - \mathbf{p}_0) + v(\mathbf{p}_2 - \mathbf{p}_0) = (1 - u - v)\mathbf{p}_0 + u\mathbf{p}_1 + v\mathbf{p}_2$ , where  $(u, v)$  are the barycentric coordinates. For points inside the triangle the following must hold:  $u \geq 0$ ,  $v \geq 0$ , and  $1 - (u + v) \geq 0 \Leftrightarrow u + v \leq 1$ . Based on this, the de Casteljau algorithm for Bézier triangles is

**de Casteljau [triangles]:**

$$\begin{aligned} \mathbf{p}_{i,j,k}^l(u, v) &= u\mathbf{p}_{i+1,j,k}^{l-1} + v\mathbf{p}_{i,j+1,k}^{l-1} + (1 - u - v)\mathbf{p}_{i,j,k+1}^{l-1}, \\ l &= 1 \dots n, \quad i + j + k = n - l. \end{aligned} \quad (13.33)$$

The final point on the Bézier triangle at  $(u, v)$  is  $\mathbf{p}_{000}^n(u, v)$ . The Bézier triangle in Bernstein form is

**Bernstein [triangles]:**

$$\mathbf{p}(u, v) = \sum_{i+j+k=n} B_{ijk}^n(u, v) \mathbf{p}_{ijk}. \quad (13.34)$$

The Bernstein polynomials now depend on both  $u$  and  $v$ , and are therefore computed differently, as shown below:

$$B_{ijk}^n(u, v) = \frac{n!}{i!j!k!} u^i v^j (1 - u - v)^k, \quad i + j + k = n. \quad (13.35)$$

The partial derivatives are [332]:

**Derivatives [triangles]:**

$$\begin{aligned} \frac{\partial \mathbf{p}(u, v)}{\partial u} &= \sum_{i+j+k=n-1} B_{ijk}^{n-1}(u, v) \mathbf{p}_{i+1,j,k}, \\ \frac{\partial \mathbf{p}(u, v)}{\partial v} &= \sum_{i+j+k=n-1} B_{ijk}^{n-1}(u, v) \mathbf{p}_{i,j+1,k}. \end{aligned} \quad (13.36)$$

Some unsurprising properties of Bézier triangles are that they interpolate (pass through) the three corner control points, and that each boundary

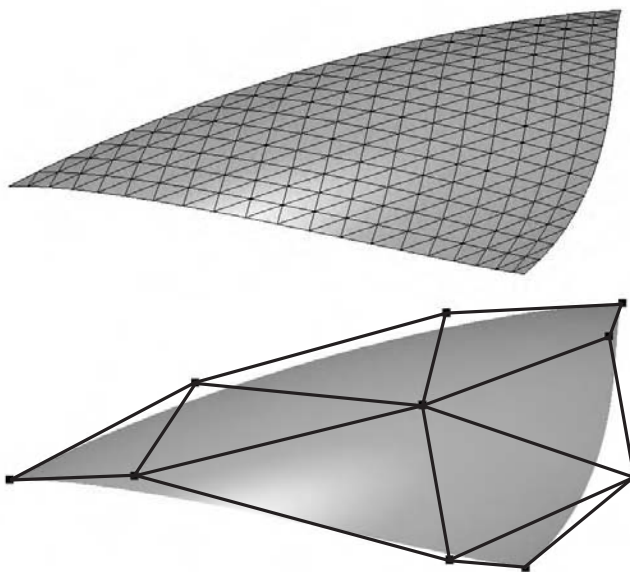


**Figure 13.20.** Top: wireframe of a Bézier triangle. Bottom: shaded surface together with control points.

is a Bézier curve described by the control points on that boundary. Also, the surfaces lies in the convex hull of the control points. A Bézier triangle is shown in Figure 13.20.

Next, we will discuss a direct application of Bézier triangles.

### 13.2.3 N-Patches

Given an input triangle mesh with normals at each vertex, the goal of the *N-patches* scheme by Vlachos et al. [1304] is to construct a better looking surface on a triangle basis. The term “N-patches” is short for “normal patches,” and these patches are also called *PN triangles*. This scheme attempts to improve the triangle mesh’s shading and silhouette by creating a curved surface to replace each triangle. Hardware is able to make each surface on the fly because the tessellation is generated from each triangle’s points and normals, with no neighbor information needed. API changes are minimal; all that is needed is a flag telling whether to generate N-patches, and a level of tessellation. See Figure 13.21 for an example. The algorithm presented here builds upon work by van Overveld and Wyvill [1298].

Assume we have a triangle with vertices  $\mathbf{p}_{300}$ ,  $\mathbf{p}_{030}$ , and  $\mathbf{p}_{003}$  with normals  $\mathbf{n}_{200}$ ,  $\mathbf{n}_{020}$ , and  $\mathbf{n}_{002}$ . The basic idea is to use this information

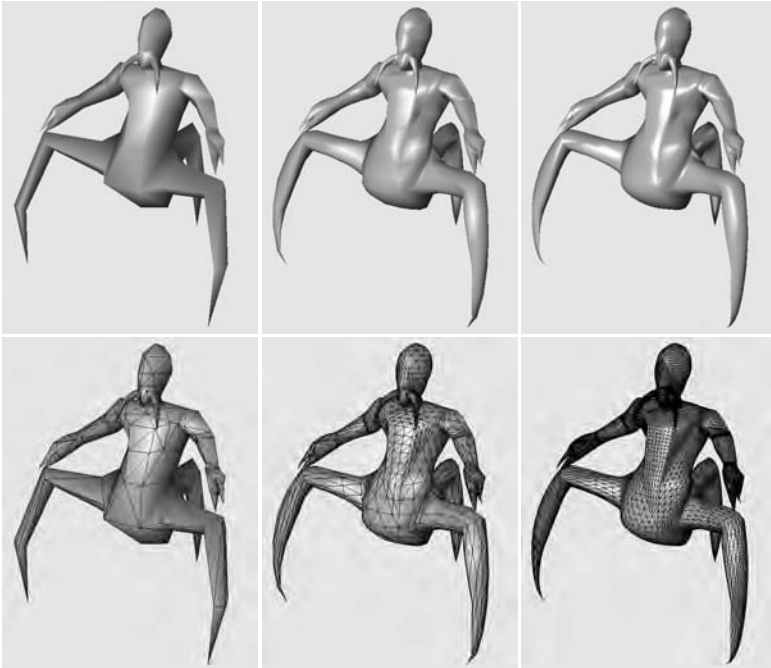


**Figure 13.21.** The columns show different levels of detail of the same model. The original triangle data, consisting of 414 triangles, is shown on the left. The middle model has 3,726 triangles, while the right has 20,286 triangles, all generated with the presented algorithm. Note how the silhouette and the shading improve. The bottom rows show the models in wireframe, which reveals that each original triangle generates the same amount of subtriangles. (*Model courtesy of id Software. Images from ATI Technologies Inc. demo.*)

to create a cubic Bézier triangle for each original triangle, and generate as many triangles as we wish from the Bézier triangle.

To shorten notation,  $w = 1 - u - v$  will be used. A cubic Bézier triangle (see Figure 13.19) is given by

$$\begin{aligned}
 \mathbf{p}(u, v) &= \sum_{i+j+k=3} B_{ijk}^3(u, v) \mathbf{p}_{ijk} \\
 &= u^3 \mathbf{p}_{300} + v^3 \mathbf{p}_{030} + w^3 \mathbf{p}_{003} + 3u^2v\mathbf{p}_{210} + 3u^2w\mathbf{p}_{201} \\
 &\quad + 3uv^2\mathbf{p}_{120} + 3v^2w\mathbf{p}_{021} + 3vw^2\mathbf{p}_{012} + 3uw^2\mathbf{p}_{102} + 6uvw\mathbf{p}_{111}.
 \end{aligned} \tag{13.37}$$

To ensure  $C^0$  continuity at the borders between two N-patch triangles, the control points on the edge can be determined from the corner control points and the normals at the respective control point (assuming that

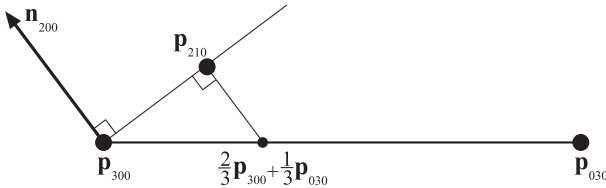


**Figure 13.22.** How the Bézier point  $\mathbf{p}_{210}$  is computed using the normal  $\mathbf{n}_{200}$  at  $\mathbf{p}_{300}$ , and the two corner points  $\mathbf{p}_{300}$  and  $\mathbf{p}_{030}$ .

normals are shared between adjacent triangles). Also, to get reasonable behavior of the surface at the control points, the normals there should be normals of the surface in Equation 13.37. Therefore, the following strategy is adopted to compute the six different control points for the borders.

Say that we want to compute  $\mathbf{p}_{210}$  using the control points  $\mathbf{p}_{300}$ ,  $\mathbf{p}_{030}$  and the normal  $\mathbf{n}_{200}$  at  $\mathbf{p}_{300}$ , as illustrated in Figure 13.22. Simply take the point  $\frac{2}{3}\mathbf{p}_{300} + \frac{1}{3}\mathbf{p}_{030}$  and project it in the direction of the normal,  $\mathbf{p}_{200}$ , onto the tangent plane defined by  $\mathbf{p}_{300}$  and  $\mathbf{n}_{200}$  [331, 332, 1304]. Assuming normalized normals, the point  $\mathbf{p}_{210}$  is computed as

$$\mathbf{p}_{210} = \frac{1}{3} (2\mathbf{p}_{300} + \mathbf{p}_{030} - (\mathbf{n}_{200} \cdot (\mathbf{p}_{030} - \mathbf{p}_{300}))\mathbf{n}_{200}). \quad (13.38)$$

The other border control points can be computed similarly, so it only remains to compute the interior control point,  $\mathbf{p}_{111}$ . This is done as shown in Equation 13.39, and this choice follows a quadratic polynomial [331, 332]:

$$\mathbf{p}_{111} = \frac{1}{4}(\mathbf{p}_{210} + \mathbf{p}_{120} + \mathbf{p}_{102} + \mathbf{p}_{201} + \mathbf{p}_{021} + \mathbf{p}_{012}) - \frac{1}{6}(\mathbf{p}_{300} + \mathbf{p}_{030} + \mathbf{p}_{003}). \quad (13.39)$$

Instead of using Equation 13.36 to compute the two tangents on the surface, and subsequently the normal, Vlachos et al. [1304] choose to interpolate the normal using a quadratic scheme, as shown below:

$$\begin{aligned} \mathbf{n}(u, v) &= \sum_{i+j+k=2} B_{ijk}^2(u, v) \mathbf{n}_{ijk} \\ &= u^2 \mathbf{n}_{200} + v^2 \mathbf{n}_{020} + w^2 \mathbf{n}_{002} + uv \mathbf{n}_{110} + uw \mathbf{n}_{101} + vw \mathbf{n}_{011}. \end{aligned} \quad (13.40)$$

This can be thought of as a Bézier triangle of degree two, where the control points are six different normals. In Equation 13.40, the choice of the degree, i.e., quadratic, is quite natural, since the derivatives are

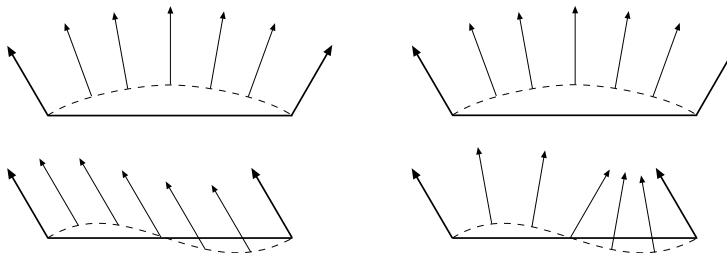


**Figure 13.23.** This figure illustrates why quadratic interpolation of normals is needed, and why linear interpolation is not sufficient. The left column shows what happens when linear interpolation of normals is used. This works fine when the normals describe a convex surface (top), but breaks down when the surface has an inflection (bottom). The right column illustrates quadratic interpolation. (*Illustration after van Overveld and Wyvill [1297].*)

of one degree lower than the actual Bézier triangle, and because linear interpolation of the normals cannot describe an inflection. See Figure 13.23.

To be able to use Equation 13.40, the normal control points  $\mathbf{n}_{110}$ ,  $\mathbf{n}_{101}$ , and  $\mathbf{n}_{011}$  need to be computed. One intuitive, but flawed, solution is to use the average of  $\mathbf{n}_{200}$  and  $\mathbf{n}_{020}$  (normals at the vertices of the original triangle) to compute  $\mathbf{n}_{110}$ . However, when  $\mathbf{n}_{200} = \mathbf{n}_{020}$ , then the problem shown at the lower left in Figure 13.23 will once again be encountered. Instead,  $\mathbf{n}_{110}$  is constructed by taking the average of  $\mathbf{n}_{200}$  and  $\mathbf{n}_{020}$ . Then this normal is reflected in the plane  $\pi$ , which is shown in Figure 13.24. This plane has a normal parallel to the difference between the endpoints  $\mathbf{p}_{300}$  and  $\mathbf{p}_{030}$ . The plane  $\pi$  is passing through the origin, since direction vectors are reflected, and these are independent of the position on the plane. Also, note that each normal should be normalized. Mathematically,

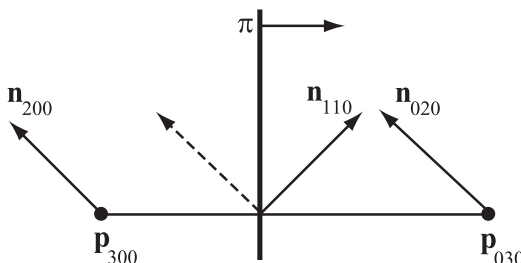


**Figure 13.24.** Construction of  $\mathbf{n}_{110}$  for N-patches. The dashed normal is the average of  $\mathbf{n}_{200}$  and  $\mathbf{n}_{020}$ , and  $\mathbf{n}_{110}$  is this normal reflected in the plane  $\pi$ . The plane  $\pi$  has a normal that is parallel to  $\mathbf{p}_{030} - \mathbf{p}_{300}$ .

the unnormalized version of  $\mathbf{n}_{110}$  is expressed as [1304]

$$\mathbf{n}'_{110} = \mathbf{n}_{200} + \mathbf{n}_{020} - 2 \frac{(\mathbf{p}_{030} - \mathbf{p}_{300}) \cdot (\mathbf{n}_{200} + \mathbf{n}_{020})}{(\mathbf{p}_{030} - \mathbf{p}_{300}) \cdot (\mathbf{p}_{030} - \mathbf{p}_{300})}. \quad (13.41)$$

Originally, van Overveld and Wyvill used a factor of  $3/2$  instead of the  $2$  in this equation. Which value is best is hard to judge from looking at images, but using  $2$  gives the nice interpretation of a true reflection in the plane.

At this point, all Bézier points of the cubic Bézier triangle and all the normal vectors for quadratic interpolation have been computed. It only remains to create triangles on the Bézier triangle so these can be rendered. Advantages of this approach are that the surface gets a better silhouette and shape relatively cheaply, and that only minor modifications must be made to existing code to make it work. All that is needed is that tessellation should be done (instead of rendering as usual), down to some *level of detail* (*LOD*). A hardware implementation is pretty straightforward.

One way to specify LODs is the following. The original triangle data is LOD 0. The LOD number then increases with the number of newly introduced vertices on a triangle edge. So LOD 1 introduces one new vertex per edge, and so creates four subtriangles on the Bézier triangle, and LOD 2 introduces two new vertices per edge, generating nine triangles. In general, LOD  $n$  generates  $(n + 1)^2$  triangles. To prevent cracking between Bézier triangles, each triangle in the mesh must be tessellated with the same LOD. This is a big disadvantage, since a tiny triangle will be tessellated as much as a large triangle. Techniques such as *adaptive tessellation* (Section 13.6.4) and *fractional tessellation* (Section 13.6.2) can be used to avoid these problems, and these are getting more and more widespread support.

One problem with N-patches is that creases are hard to control, and often one needs to insert extra triangles near the desired crease. The continuity between Bézier triangles is only  $C^0$ , but they still look acceptable in many cases. This is mainly because the normals are continuous across triangles, so that a set of N-patches mimics a  $G^1$  surface. A better solution is suggested by Boubekeur et al. [131], where a vertex can have two normals, and two such connected vertices generate a crease. Note that to get good-looking texturing,  $C^1$  continuity is required across borders between triangles (or patches). Also worth knowing is that cracks will appear if two adjacent triangles do not share the same normals. A technique to further improve the quality of the continuity across N-patches is described by Grün [462]. Dyken and Reimers [289] present a technique inspired by N-patches, where only the silhouettes as seen from the viewer are tessellated, and hence, the silhouettes become more curved. These silhouette curves are derived in similar ways as the N-patches curves. To get smooth transitions, they blend between coarse silhouettes and tessellated silhouettes.

### 13.2.4 Continuity

When constructing an interesting object from Bézier surfaces, one often wants to stitch together several different Bézier surfaces to form one composite surface. To get a good-looking result, care must be taken to ensure that reasonable continuity is obtained across the surfaces. This is in the same spirit as for curves, in Section 13.1.3.

Assume two bicubic Bézier patches should be pieced together. These have  $4 \times 4$  control points each. This is illustrated in Figure 13.25, where the left patch has control points,  $\mathbf{a}_{ij}$ , and the right has control points,  $\mathbf{b}_{ij}$ , for  $0 \leq i, j \leq 3$ . To ensure  $C^0$  continuity, the patches must share the same control points at the border, that is,  $\mathbf{a}_{3j} = \mathbf{b}_{0j}$ .

However, this is not sufficient to get a nice looking composite surface. Instead, a simple technique will be presented that gives  $C^1$  continuity [332]. To achieve this we must constrain the position of the two rows of control points closest to the shared control points. These rows are  $\mathbf{a}_{2j}$  and  $\mathbf{b}_{1j}$ . For each  $j$ , the points  $\mathbf{a}_{2j}$ ,  $\mathbf{b}_{0j}$ , and  $\mathbf{b}_{1j}$  must be collinear, that is, they must lie on a line. Moreover, they must have the same ratio, which means that  $\|\mathbf{a}_{2j} - \mathbf{b}_{0j}\| = k\|\mathbf{b}_{0j} - \mathbf{b}_{1j}\|$ . Here,  $k$  is a constant, and it must be the same for all  $j$ . Examples are shown in Figure 13.25 and 13.26.

This sort of construction uses up many degrees of freedom of setting the control points. This can be seen even more clearly when stitching together four patches, sharing one common corner. The construction is visualized in Figure 13.27. The result is shown to the right in this figure, where the locations of the eight control points around the shared control point are shown. These nine points must all lie in the same plane, and they must form a bilinear patch, as shown in Figure 13.14. If one is satisfied with

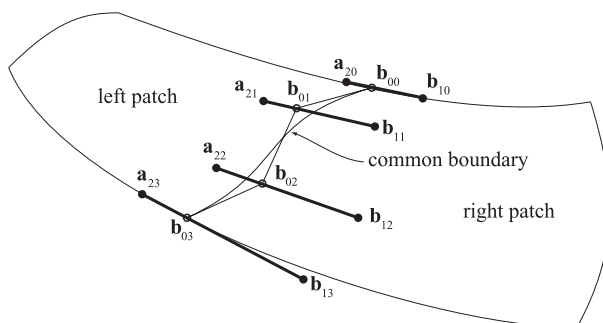


**Figure 13.25.** How to stitch together two Bézier patches with  $C^1$  continuity. All control points on bold lines must be collinear, and they must have the same ratio between the two segment lengths. Note that  $\mathbf{a}_{3j} = \mathbf{b}_{0j}$  to get a shared boundary between patches. This can also be seen to the right in Figure 13.26.

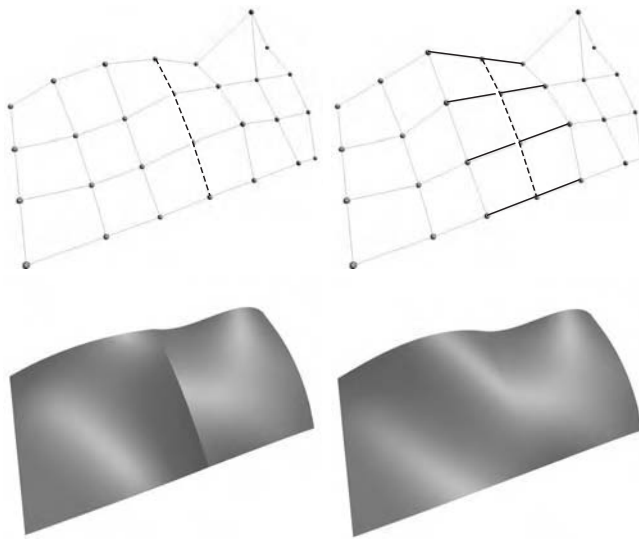


**Figure 13.26.** The left column shows two Bézier patches joined with only  $C^0$  continuity. Clearly, there is a shading discontinuity between the patches. The right column shows similar patches joined with  $C^1$  continuity, which looks better. In the top row, the dashed lines indicate the border between the two joined patches. To the upper right, the black lines show the collinearity of the control points of the joining patches.

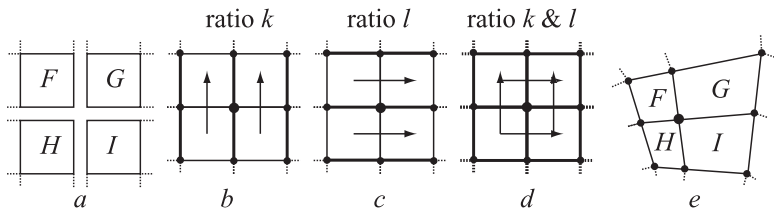


**Figure 13.27.** a) Four patches,  $F$ ,  $G$ ,  $H$ , and  $I$ , are to be stitched together, where all patches share one corner. b) In the vertical direction, the three sets of three points (on each bold line) must use the same ratio,  $k$ . This relationship is not shown here; see the rightmost figure. A similar process is done for c), where, in the horizontal direction, both patches must use the same ratio,  $l$ . d) When stitched together, all four patches must use ratio  $k$  vertically, and  $l$  horizontally. e) The result is shown, in which the ratios are correctly computed for the nine control points closest to (and including) the shared control point.

$G^1$  continuity at the corners (and only there), it suffices to make the nine points coplanar. This uses fewer degrees of freedom.

Continuity for Bézier triangles is generally more complex, as well as the  $G^1$  conditions for both Bézier patches and triangles [332, 569]. When constructing a complex object of many Bézier surfaces, it is often hard to

see to it that reasonable continuity is obtained across all borders. One solution to this is to turn to subdivision surfaces, treated in Section 13.5.

Note that  $C^1$  continuity is required for good-looking texturing across borders. For reflections and shading, a reasonable result is obtained with  $G^1$  continuity.  $C^1$  or higher gives even better results. An example is shown in Figure 13.26.

## 13.3 Implicit Surfaces

To this point, only parametric curves and surfaces have been discussed. However, another interesting and useful class of surfaces are *implicit surfaces*. Instead of using some parameters, say  $u$  and  $v$ , to explicitly describe a point on the surface, the following form, called the implicit function, is used:

$$f(x, y, z) = f(\mathbf{p}) = 0. \quad (13.42)$$

This is interpreted as follows: A point  $\mathbf{p}$  is on the implicit surface if the result is zero when the point is inserted into the implicit function  $f$ . Implicit surfaces are often used in intersection testing with rays (see Sections 16.6–16.9), as they can be simpler to intersect than the corresponding (if any) parametric surface. Another advantage of implicit surfaces is that *constructive solid geometry* algorithms can be applied easily to them, that is, objects can be subtracted from each other, logically **and**:ed or **or**:ed with each other. Also, objects can be easily blended and deformed.

A simple example is the unit sphere, which has  $f(x, y, z) = x^2 + y^2 + z^2 - 1$  as its implicit function. Sometimes it is also useful to use *isosurfaces* of an implicit function. An isosurface is  $f(x, y, z) = c$ , where  $c$  is a scalar function. So, for the unit sphere,  $f(x, y, z) = 3$  describes an isosurface that is a sphere centered around the origin with a radius of two.

The normal of an implicit surface is described by the partial derivatives, called the gradient and denoted  $\nabla f$ :

$$\nabla f(x, y, z) = \left( \frac{\partial f}{\partial x}, \frac{\partial f}{\partial y}, \frac{\partial f}{\partial z} \right). \quad (13.43)$$

To be able to evaluate it, Equation 13.43 must be differentiable, and thus also continuous.

Blending of implicit surfaces is a nice feature that can be used in what is often referred to as blobby modeling [99], soft objects, or metaballs [117]. See Figure 13.28 for a simple example. The basic idea is to use several simple primitives, such as spheres or ellipsoids, and blend these smoothly. Each sphere can be seen as an atom, and after blending the molecule of

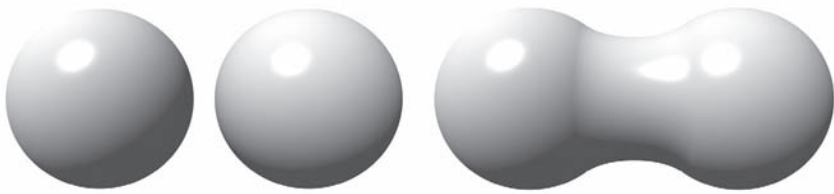


**Figure 13.28.** The two spheres on the left are blended together into the shape on the right.

the atoms is obtained. More mathematically, the blended surface is described by

$$f(\mathbf{p}) = \sum_{i=0}^{n-1} h(r_i). \quad (13.44)$$

In Equation 13.44, we assume that there are  $n$  primitive objects (atoms), and for each atom a distance  $r_i$  is computed. The  $r_i$  is often the distance from  $\mathbf{p}$  to the center of the sphere, or some other distance. Finally, the blending function  $h$  describes the region of influence of the atom  $i$ . Therefore,  $h(0) = 1$ , and  $h(r) = 0$  for  $r \geq R$ , where  $R$  defines where the region of influence ends. As an example, the following blending function by Wyvill [117] gives second-order continuity:

$$h(r) = \left(1 - \frac{r^2}{R^2}\right)^3, \quad h(r) = 0, \quad r \geq R. \quad (13.45)$$

Wyvill also recommends using  $c = 1/2$ , that is, use the implicit surface defined by  $f(\mathbf{p}) = 1/2$ .

Every implicit surface can also be turned into a surface consisting of triangles. There are a number of algorithms available for performing this operation [115, 117, 624, 1299]. One well-known example is the *marching cubes* algorithm [795]. This algorithm places a three-dimensional grid over the entire surface, and samples the implicit function at each grid point. Each point is either inside or outside the implicit surface. Because a cube has 8 grid points for corners, there are 256 different combinations. Each combination then generates from zero to four triangles inside the cube to represent the implicit surface.

See Karkanis and Stewart's article for a review of past work on triangulation of implicit surfaces [624]. Code for performing polygonalization using algorithms by Wyvill and Bloomenthal is available on the web [116]. Tatarchuk and Shopf [1250] describe a technique they call *marching tetrahedra*, in which the GPU can be used to find isosurfaces in a three-dimensional

data set. Figure 3.7 on page 42 shows an example of isosurface extraction using the geometry shader.

## 13.4 Subdivision Curves

Subdivision techniques are a relatively new way for creating curves and surfaces. One reason why they are interesting is that they bridge the gap between discrete surfaces (triangle meshes) and continuous surfaces (e.g., a collection of Bézier patches). Here, we will first describe how subdivision curves work, and then discuss the more interesting subdivision surface schemes.

Subdivision curves are best explained by an example that uses *corner cutting*. See Figure 13.29. The corners of the leftmost polygon are cut off, creating a new polygon with twice as many vertices. Then the corners of this new polygon are cut off, and so on to infinity (or more practically: until we cannot see any difference). The resulting curve, called the *limit curve*, is smooth since all corners are cut off.<sup>3</sup> This is often written as  $P_0 \rightarrow P_1 \rightarrow P_2 \dots \rightarrow P_\infty$ , where  $P_0$  is the starting polygon, and  $P_\infty$  is the limit curve.

This subdivision process can be done in many different ways, and each is characterized by a subdivision scheme. The one shown in Figure 13.29 is called Chaikin's scheme [167] and works as follows. Assume the  $n$  vertices of a polygon are  $P_0 = \{\mathbf{p}_0^0, \dots, \mathbf{p}_{n-1}^0\}$ , where the superscript denotes the level

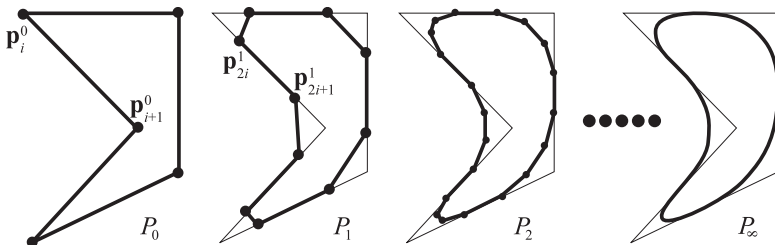


**Figure 13.29.** Chaikin's subdivision scheme in action. The initial polygon  $P_0$  is subdivided once into  $P_1$ , and then again into  $P_2$ . As can be seen, the corners of each polygon,  $P_i$ , are cut off during subdivision. After infinitely many subdivisions, the limit curve  $P_\infty$  is obtained. This is an approximating scheme as the curve does not go through the initial points.

---

<sup>3</sup>This process can also be thought of as a lowpass filter since all sharp corners (high frequency) are removed.

of subdivision. Chaikin's scheme creates two new vertices between each subsequent pair of vertices, say  $\mathbf{p}_i^k$  and  $\mathbf{p}_{i+1}^k$ , of the original polygon as

$$\begin{aligned}\mathbf{p}_{2i}^{k+1} &= \frac{3}{4}\mathbf{p}_i^k + \frac{1}{4}\mathbf{p}_{i+1}^k, \\ \mathbf{p}_{2i+1}^{k+1} &= \frac{1}{4}\mathbf{p}_i^k + \frac{3}{4}\mathbf{p}_{i+1}^k.\end{aligned}\tag{13.46}$$

As can be seen, the superscript changes from  $k$  to  $k+1$ , which means that we go from one subdivision level to the next, i.e.,  $P_k \rightarrow P_{k+1}$ . After such a subdivision step is performed, the original vertices are discarded and the new points are reconnected. This kind of behavior can be seen in Figure 13.29, where new points are created  $1/4$  away from the original vertices toward neighboring vertices. The beauty of subdivision schemes comes from the simplicity of rapidly generating smooth curves. However, you do not immediately have a parametric form of the curve as in Section 13.1, though it can be shown that Chaikin's algorithm generates a quadratic B-spline [68, 332, 569, 1328].<sup>4</sup> So far, the presented scheme works for (closed) polygons, but most schemes can be extended to work for open polylines as well. In the case of Chaikin, the only difference is that the two endpoints of the polyline are kept in each subdivision step (instead of being discarded). This makes the curve go through the endpoints.

There are two different classes of subdivision schemes, namely *approximating* and *interpolating*. Chaikin's scheme is approximating, as the limit curve, in general, does not lie on the vertices of the initial polygon. This is because the vertices are discarded (or updated, for some schemes). In contrast, an interpolating scheme keeps all the points from the previous subdivision step, and so the limit curve  $P_\infty$  goes through all the points of  $P_0, P_1, P_2$ , and so on. This means that the scheme interpolates the initial polygon. An example, using the same polygon as in Figure 13.29, is shown in Figure 13.30. This scheme uses the four nearest points to create a new point [290]:

$$\begin{aligned}\mathbf{p}_{2i}^{k+1} &= \mathbf{p}_i^k, \\ \mathbf{p}_{2i+1}^{k+1} &= \left(\frac{1}{2} + w\right)(\mathbf{p}_i^k + \mathbf{p}_{i+1}^k) - w(\mathbf{p}_{i-1}^k + \mathbf{p}_{i+2}^k).\end{aligned}\tag{13.47}$$

The first line in Equation 13.47 simply means that we keep the points from the previous step without changing them (i.e., interpolating), and the second line is for creating a new point in between  $\mathbf{p}_i^k$  and  $\mathbf{p}_{i+1}^k$ . The weight  $w$  is called a *tension parameter*. When  $w = 0$ , linear interpolation

---

<sup>4</sup>A type of curve that we do not cover in this book.

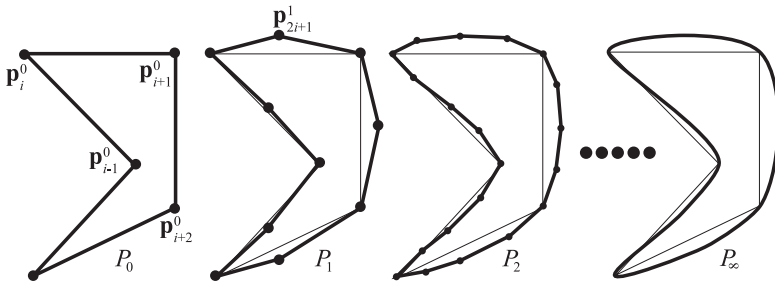


**Figure 13.30.** The 4-point subdivision scheme in action. This is an interpolating scheme as the curve goes through the initial points, and in general curve  $P_{i+1}$  goes through the points of  $P_i$ . Note that the same control polygon is used in Figure 13.29.

is the result, but when  $w = 1/16$ , we get the kind of behavior shown in Figure 13.30. It can be shown [290] that the resulting curve is  $C^1$  when  $0 < w < 1/8$ . For open polylines we run into problems at the endpoints because we need two points on both sides of the new point, and we only have one. This can be solved if the point next to the endpoint is reflected across the endpoint. So, for the start of the polyline,  $\mathbf{p}_1$  is reflected across  $\mathbf{p}_0$  to obtain  $\mathbf{p}_{-1}$ . This point is then used in the subdivision process. The creation of  $\mathbf{p}_{-1}$  is shown in Figure 13.31.

Another interesting approximating scheme uses the following subdivision rules:

$$\begin{aligned}\mathbf{p}_{2i}^{k+1} &= \frac{3}{4}\mathbf{p}_i^k + \frac{1}{8}(\mathbf{p}_{i-1}^k + \mathbf{p}_{i+1}^k), \\ \mathbf{p}_{2i+1}^{k+1} &= \frac{1}{2}(\mathbf{p}_i^k + \mathbf{p}_{i+1}^k).\end{aligned}\tag{13.48}$$

The first line updates the existing points, and the second computes the midpoint on the line segment between two neighboring points. This scheme generates a cubic B-spline curve. Consult the SIGGRAPH course on subdivision [1415], the Killer B's book [68], Warren and Weimer's subdivision book [1328], or Farin's CAGD book [332] for more about these curves.

Given a point  $\mathbf{p}$  and its neighboring points, it is possible to directly “push” that point to the limit curve, i.e., determine what the coordinates

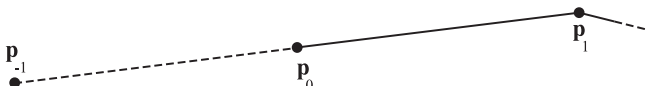


**Figure 13.31.** The creation of a reflection point,  $\mathbf{p}_{-1}$ , for open polylines. The reflection point is computed as:  $\mathbf{p}_{-1} = \mathbf{p}_0 - (\mathbf{p}_1 - \mathbf{p}_0) = 2\mathbf{p}_0 - \mathbf{p}_1$ .

of  $\mathbf{p}$  would be on  $P_\infty$ . This is also possible for tangents. See, for example, Joy's online introduction to this topic [615].

The topic of subdivision curves has only been touched upon, but it is sufficient for the presentation of subdivision surfaces that follows in the next section. See the Further Reading and Resources section at the end of this chapter for more references and information.

## 13.5 Subdivision Surfaces

Subdivision surfaces are a powerful paradigm in defining smooth, continuous, crackless surfaces from meshes with arbitrary topology. As with all other surfaces in this chapter, subdivision surfaces also provide infinite level of detail. That is, you can generate as many triangles or polygons as you

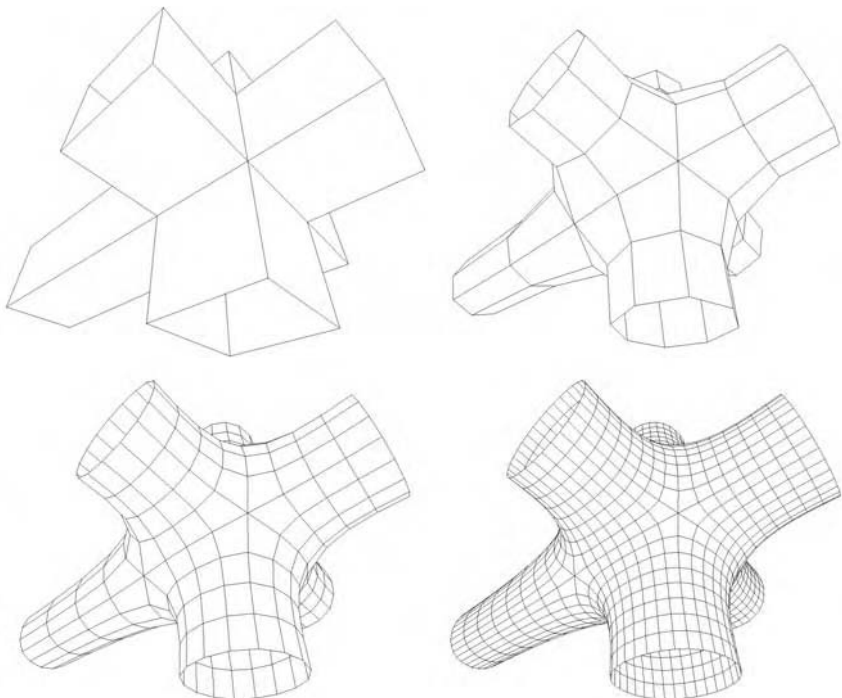


**Figure 13.32.** The top left image shows the control mesh, i.e., that original mesh, which is the only geometrical data that describes the resulting subdivision surface. The following images are subdivided one, two, and three times. As can be seen, more and more polygons are generated and the surface gets smoother and smoother. The scheme used here is the Catmull-Clark scheme, described in Section 13.5.4.

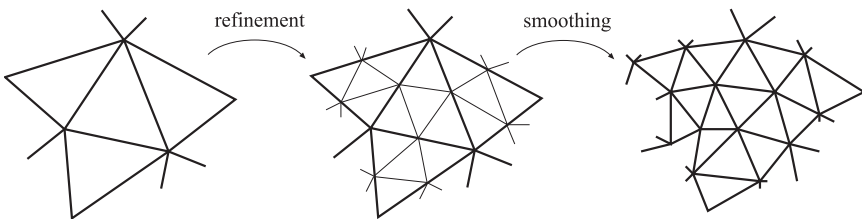


**Figure 13.33.** Subdivision as refinement and smoothing. The refinement phase creates new vertices and reconnects to create new triangles, and the smoothing phase computes new positions for the vertices.

wish, and the original surface representation is compact. An example of a surface being subdivided is shown in Figure 13.32. Another advantage is that subdivision rules are simple and easily implemented. A disadvantage is that the analysis of surface continuity often is very mathematically involved. However, this sort of analysis is often only of interest to those who wish to create new subdivision schemes, and is out of the scope of this book—for such details, consult Warren and Weimer’s book [1328] and the SIGGRAPH course on subdivision [1415].

In general, the subdivision of surfaces (and curves) can be thought of as a two-phase process [679]. Starting with a polygonal mesh, called the *control mesh*, the first phase, called the *refinement phase*, creates new vertices and reconnects to create new, smaller triangles. The second, called the *smoothing phase*, typically computes new positions for some or all vertices in the mesh. This is illustrated in Figure 13.33. It is the details of these two phases that characterize a subdivision scheme. In the first phase, a polygon can be split in different ways, and in the second phase, the choice of subdivision rules give different characteristics such as the level of continuity, and whether the surface is approximating or interpolating.

A subdivision scheme can be characterized by whether it is *stationary*, whether it is *uniform*, and whether it is *triangle-based* or *polygon-based*. A stationary scheme uses the same subdivision rules at every subdivision step, while a nonstationary may change the rules depending on which step currently is being processed. The schemes treated below are all stationary. A uniform scheme uses the same rules for every vertex or edge, while a nonuniform scheme may use different rules for different vertices or edges. As an example, a different set of rules is often used for edges that are on the boundaries of a surface. A triangle-based scheme only operates on triangles, and thus only generates triangles, while a polygon-based scheme operates on arbitrary polygons. We will mostly present triangle-based schemes here because that is what graphics hardware is targeted for, but we will also briefly cover some well-known polygon-based schemes.

Several different subdivision schemes are presented next. Following these, two techniques are presented that extend the use of subdivision surfaces, along with methods for subdividing normals, texture coordinates, and colors. Finally, some practical algorithms for subdivision and rendering are presented.

### 13.5.1 Loop Subdivision

Loop's subdivision scheme [787]<sup>5</sup> was the first subdivision scheme for triangles. It is similar to the last scheme in Section 13.4 in that it is approximating, and that it updates each existing vertex and creates a new vertex for each edge. The connectivity for this scheme is shown in Figure 13.34. As can be seen, each triangle is subdivided into four new triangles, so after  $n$  subdivision steps, a triangle has been subdivided into  $4^n$  triangles.

First, let us focus on an existing vertex  $\mathbf{p}^k$ , where  $k$  is the number of subdivision steps. This means that  $\mathbf{p}^0$  is the vertex of the control mesh.

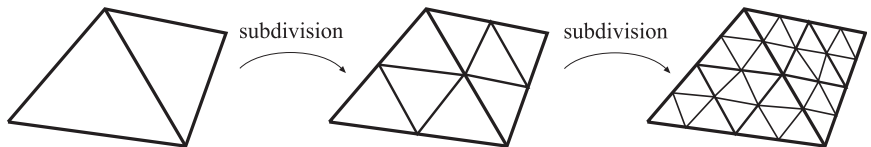


**Figure 13.34.** The connectivity of two subdivision steps for schemes such as Loop's and the modified butterfly scheme (see Section 13.5.2). Each triangle generates four new triangles.

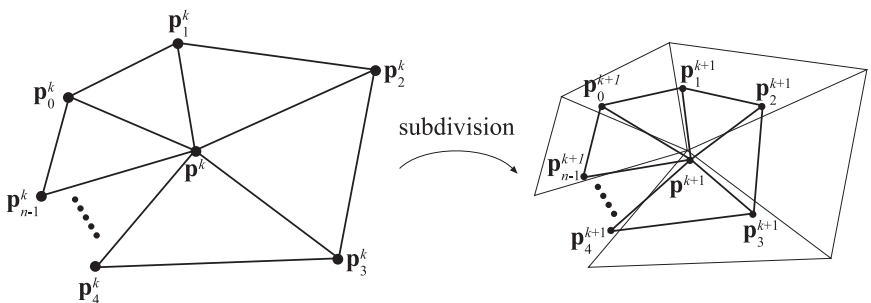


**Figure 13.35.** The notation used for Loop's subdivision scheme. The left neighborhood is subdivided into the neighborhood to the right. The center point  $\mathbf{p}^k$  is updated and replaced by  $\mathbf{p}^{k+1}$ , and for each edge between  $\mathbf{p}^k$  and  $\mathbf{p}_i^k$ , a new point is created ( $\mathbf{p}_i^{k+1}$ ,  $i \in 1, \dots, n$ ).

---

<sup>5</sup> A brief overview of Loop's subdivision scheme is also presented by Hoppe et al. [559].

After one subdivision step,  $\mathbf{p}^0$  turns into  $\mathbf{p}^1$ . In general,  $\mathbf{p}^0 \rightarrow \mathbf{p}^1 \rightarrow \mathbf{p}^2 \rightarrow \dots \rightarrow \mathbf{p}^\infty$ , where  $\mathbf{p}^\infty$  is the limit point. If the *valence* of  $\mathbf{p}^k$  is  $n$ , then  $\mathbf{p}^k$  has  $n$  neighboring vertices,  $\mathbf{p}_i^k$ ,  $i \in \{0, 1, \dots, n - 1\}$ . See Figure 13.35 for the notation described above. Also, a vertex that has valence 6 is called *regular* or *ordinary*; otherwise it is called *irregular* or *extraordinary*.

Below, the subdivision rules for Loop's scheme are given, where the first formula is the rule for updating an existing vertex  $\mathbf{p}^k$  into  $\mathbf{p}^{k+1}$ , and the second formula is for creating a new vertex,  $\mathbf{p}_i^{k+1}$ , between  $\mathbf{p}^k$  and each of the  $\mathbf{p}_i^k$ . Again,  $n$  is the valence of  $\mathbf{p}^k$ :

$$\begin{aligned}\mathbf{p}^{k+1} &= (1 - n\beta)\mathbf{p}^k + \beta(\mathbf{p}_0^k + \dots + \mathbf{p}_{n-1}^k), \\ \mathbf{p}_i^{k+1} &= \frac{3\mathbf{p}^k + 3\mathbf{p}_i^k + \mathbf{p}_{i-1}^k + \mathbf{p}_{i+1}^k}{8}, \quad i = 0 \dots n - 1.\end{aligned}\tag{13.49}$$

Note that we assume that the indices are computed modulo  $n$ , so that if  $i = n - 1$ , then for  $i + 1$ , we use index 0, and likewise when  $i = 0$ , then for  $i - 1$ , we use index  $n - 1$ . These subdivision rules can easily be visualized as masks, also called stencils; see Figure 13.36. The major use of these is that they communicate almost an entire subdivision scheme using only a simple illustration. Note that the weights sum to one for both masks. This is a characteristic that is true for all subdivision schemes, and the rationale for this is that a new point should lie in the neighborhood of the weighted points. In Equation 13.49, the constant  $\beta$  is actually a function of  $n$ , and is given by

$$\beta(n) = \frac{1}{n} \left( \frac{5}{8} - \frac{(3 + 2 \cos(2\pi/n))^2}{64} \right).\tag{13.50}$$

Loop's suggestion [787] for the  $\beta$ -function gives a surface of  $C^2$  continuity at every regular vertex, and  $C^1$  elsewhere [1413], that is, at all irregular vertices. As only regular vertices are created during subdivision, the surface is only  $C^1$  at the places where we had irregular vertices in the control

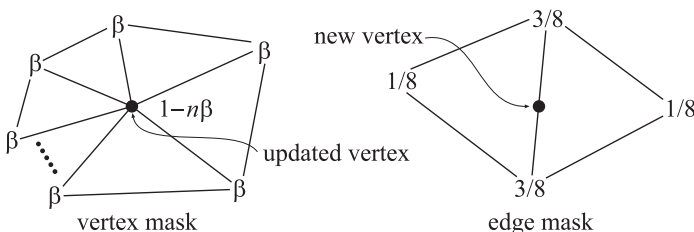


**Figure 13.36.** The masks for Loop's subdivision scheme (black circles indicate which vertex is updated/generated). A mask shows the weights for each involved vertex. For example, when updating an existing vertex, the weight  $1 - n\beta$  is used for the existing vertex, and the weight  $\beta$  is used for all the neighboring vertices, called the 1-ring.

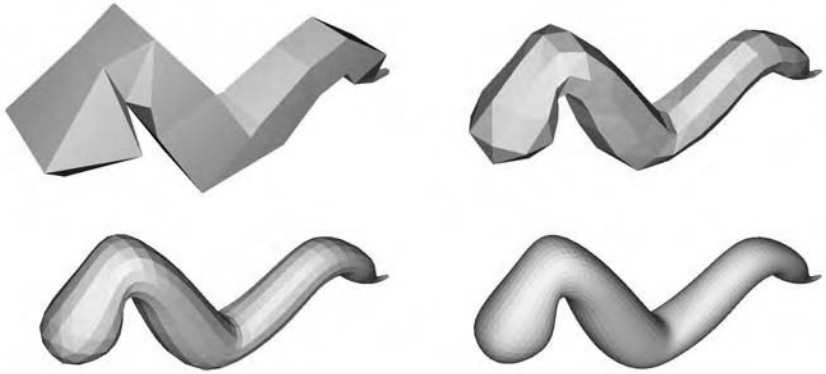


**Figure 13.37.** A worm subdivided three times with Loop’s subdivision scheme.

mesh. See Figure 13.37 for an example of a mesh subdivided with Loop’s scheme. A variant of Equation 13.50, which avoids trigonometric functions, is given by Warren and Weimer [1328]:

$$\beta(n) = \frac{3}{n(n+2)}. \quad (13.51)$$

For regular valences, this gives a  $C^2$  surface, and  $C^1$  elsewhere. The resulting surface is hard to distinguish from a regular Loop surface. For a mesh that is not closed, we cannot use the presented subdivision rules. Instead, special rules have to be used for such boundaries. For Loop’s scheme, the reflection rules of Equation 13.48 can be used. This is also treated in Section 13.5.5.

The surface after infinitely many subdivision steps is called the limit surface. Limit surface points and limit tangents can be computed using closed form expressions. The limit position of a vertex is computed [559, 1415] using the formula on the first row in Equation 13.49, by replacing  $\beta(n)$  with

$$\gamma(n) = \frac{1}{n + \frac{3}{8\beta(n)}}. \quad (13.52)$$

Two limit tangents for a vertex  $\mathbf{p}^k$  can be computed by weighting the immediate neighboring vertices, called the *1-ring* or *1-neighborhood*, as shown below [559, 787]:

$$\mathbf{t}_u = \sum_{i=0}^{n-1} \cos(2\pi i/n) \mathbf{p}_i^k, \quad \mathbf{t}_v = \sum_{i=0}^{n-1} \sin(2\pi i/n) \mathbf{p}_i^k. \quad (13.53)$$

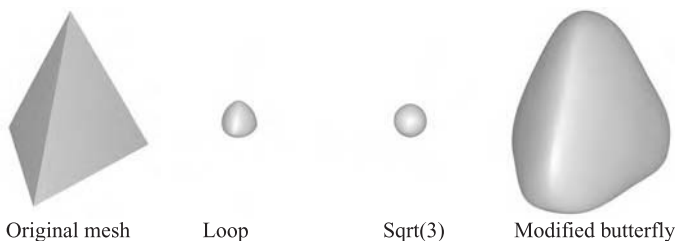


**Figure 13.38.** A tetrahedron is subdivided five times with Loop's, the  $\sqrt{3}$ , and the modified butterfly (MB) scheme. Loop's and the  $\sqrt{3}$ -scheme are both approximating, while MB is interpolating.

The normal is then  $\mathbf{n} = \mathbf{t}_u \times \mathbf{t}_v$ . Note that this often is less expensive [1415] than the methods described in Section 12.3, which need to compute the normals of the neighboring triangles. More importantly, this gives the exact normal at the point.

A major advantage of approximating subdivision schemes is that the resulting surface tends to get very fair. *Fairness* is, loosely speaking, related to how smoothly a curve or surface bends [903]. A higher degree of fairness implies a smoother curve or surface. Another advantage is that approximating schemes converge faster than interpolating schemes. However, this means that the shapes often shrink. This is most notable for small, convex meshes, such as the tetrahedron shown in Figure 13.38. One way to decrease this effect is to use more vertices in the control mesh. i.e., care must be taken while modeling the control mesh. Maillot and Stam present a framework for combining subdivision schemes so that the shrinking can be controlled [809]. A characteristic that can be used to great advantage at times is that a Loop surface is contained inside the convex hull of the original control points [1413].

The Loop subdivision scheme generates a generalized three-directional quartic box spline.<sup>6</sup> So, for a mesh consisting only of regular vertices, we could actually describe the surface as a type of spline surface. However, this description is not possible for irregular settings. Being able to generate smooth surfaces from any mesh of vertices is one of the great strengths of subdivision schemes. See also Sections 13.5.5 and 13.5.6 for different extensions to subdivision surfaces that use Loop's scheme.

### 13.5.2 Modified Butterfly Subdivision

Here we will present the subdivision scheme by Zorin et al. [1411, 1413], which is a modification of the butterfly scheme by Dyn et al. [291], and

<sup>6</sup>These spline surfaces are out of the scope of this book. Consult Warren's book [1328], the SIGGRAPH course [1415], or Loop's thesis [787].



**Figure 13.39.** To the left is a simple three-dimensional star mesh. The middle image shows the resulting surface using Loop's subdivision scheme, which is approximating. The right image shows the result using the modified butterfly scheme, which is interpolating. An advantage of using interpolating schemes is that they often resemble the control mesh more than approximating schemes do. However, for detailed meshes the difference is not as distinct as shown here.

therefore often referred to as the *modified butterfly* (MB) scheme. This scheme is nonuniform, both because it uses different rules at the boundaries, and because different rules are used depending on the valence of the vertices. The main difference from Loop subdivision, however, is that it is interpolating, rather than approximating. An interpolating scheme means that once a vertex exists in the mesh, its location cannot change. Therefore, this scheme never modifies, but only generates new vertices for the edges. See Figure 13.39 for an example between interpolating and approximating schemes. The connectivity is the same as for Loop's scheme, shown in Figure 13.34.

The MB scheme uses four different subdivision rules for creating new vertices between two existing vertices. These are all described below, and the corresponding masks are shown in Figure 13.40.

1. *Regular setting.* Assume that we want to generate a new vertex between two existing vertices,  $\mathbf{v}$  and  $\mathbf{w}$ , that each has valence 6. These vertices are called regular or ordinary, and we call the situation a *regular setting*. The mask for this situation is shown to the left in Figure 13.40.
2. *Semiregular setting.* A *semiregular* setting occurs when one vertex is regular ( $n = 6$ ), and another is irregular ( $n \neq 6$ ), also called extraordinary, and we want to generate a new vertex between these vertices. The following formula computes the new vertex, where  $n$  is the valence of the irregular vertex:

$$\begin{aligned} n = 3 : \quad & w_0 = 5/12, \quad w_1 = -1/12, \quad w_2 = -1/12, \\ n = 4 : \quad & w_0 = 3/8, \quad w_1 = 0, \quad w_2 = -1/8, \quad w_3 = 0, \\ n \geq 5 : \quad & w_j = \frac{0.25 + \cos(2\pi j/n) + 0.5 \cos(4\pi j/n)}{n}. \end{aligned} \tag{13.54}$$

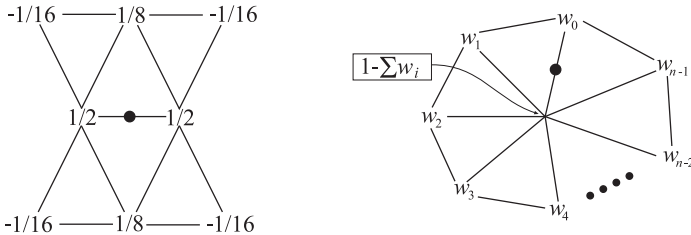


**Figure 13.40.** The mask to the left is the “butterfly” mask, which is used when generating a new vertex between two regular vertices (those with weights  $1/2$ ). The mask to the right shows the weights when one vertex is irregular (the one with weight  $1 - \sum w_i$ ), and one vertex is regular (with weight  $w_0$ ). Note that black circles indicate which vertex is generated. (Illustration after Zorin et al. [1415].)

Note that we used only the immediate neighborhood of the irregular vertex to compute the new vertex, as shown in the mask in Figure 13.40.

3. *Irregular setting.* When an edge connects two vertices, where both vertices are irregular ( $n \neq 6$ ), we temporarily compute a new vertex for each of these two vertices using the formula for the semiregular setting (2). The average of these two vertices is used as the new vertex. This can happen at only the first subdivision step, because after that there will be only regular and semiregular settings in the mesh. Therefore the continuity of this choice does not affect the limit surface. Zorin et al. [1411] note that this rule generates shapes with better fairness.
4. *Boundaries.* At boundaries, where an edge in the triangle mesh has only one triangle connected to it, the interpolating scheme [290] with  $w = 1/16$ , described in Section 13.4 (see Figure 13.30 and Equation 13.47) is used. More types of boundary cases exist—consult the SIGGRAPH course for more about this [1415]. Implementation details are discussed by Sharp [1160]. Since this scheme is interpolating, limit positions of the vertices are the vertices themselves. Limit tangents are more complex to compute. For extraordinary vertices ( $n \neq 6$ ), the tangents can be calculated using Equation 13.53, that is, the same formulae as for Loop [1413]. For ordinary vertices ( $n = 6$ ), the *2-ring* (also called the *2-neighborhood*) is used. The 1-ring and the 2-ring of an ordinary vertex,  $\mathbf{p}$ , is shown in Figure 13.41. The tangent vectors,  $\mathbf{t}_u$  and  $\mathbf{t}_v$ , are then computed as

$$\begin{aligned}\mathbf{t}_u &= \mathbf{u} \cdot \mathbf{r}, \\ \mathbf{t}_v &= \mathbf{v} \cdot \mathbf{r},\end{aligned}\tag{13.55}$$

where  $\mathbf{r}$  is a vector of the difference vectors  $\mathbf{p}_i - \mathbf{p}$  of the entire 2-ring,

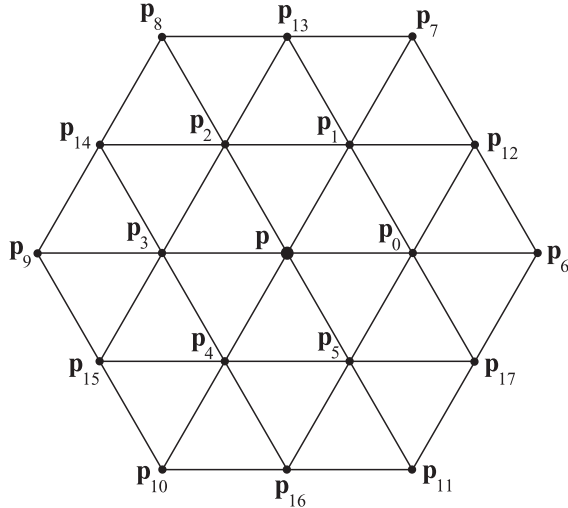


**Figure 13.41.** An ordinary vertex,  $\mathbf{p}$ , with its 1-ring ( $\mathbf{p}_0, \dots, \mathbf{p}_5$ ), and its 2-ring ( $\mathbf{p}_6, \dots, \mathbf{p}_{17}$ ).

and  $\mathbf{u}$  and  $\mathbf{v}$  are vectors of scalars:

$$\begin{aligned}
 \mathbf{r} &= (\mathbf{p}_0 - \mathbf{p}, \mathbf{p}_1 - \mathbf{p}, \mathbf{p}_2 - \mathbf{p}, \dots, \mathbf{p}_{16} - \mathbf{p}, \mathbf{p}_{17} - \mathbf{p}), \\
 \mathbf{u} &= (16, -8, -8, 16, -8, -8, -\frac{8}{\sqrt{3}}, \frac{4}{\sqrt{3}}, \frac{4}{\sqrt{3}}, -\frac{8}{\sqrt{3}}, \frac{4}{\sqrt{3}}, \frac{4}{\sqrt{3}}, \\
 &\quad 1, -\frac{1}{2}, -\frac{1}{2}, 1, -\frac{1}{2}, -\frac{1}{2}), \\
 \mathbf{v} &= (0, 8, -8, 0, 8, -8, 0, -\frac{4}{\sqrt{3}}, \frac{4}{\sqrt{3}}, 0, -\frac{4}{\sqrt{3}}, \frac{4}{\sqrt{3}}, \\
 &\quad 0, \frac{1}{2}, -\frac{1}{2}, 0, \frac{1}{2}, -\frac{1}{2}).
 \end{aligned} \tag{13.56}$$

This means that, for example,  $\mathbf{t}_u$  is computed as

$$\mathbf{t}_u = 16(\mathbf{p}_0 - \mathbf{p}) - 8(\mathbf{p}_1 - \mathbf{p}) - \dots - 0.5(\mathbf{p}_{17} - \mathbf{p}). \tag{13.57}$$

After computing both  $\mathbf{t}_u$  and  $\mathbf{t}_v$ , the normal is  $\mathbf{n} = \mathbf{t}_u \times \mathbf{t}_v$ .

When an interpolating scheme is desired, the MB scheme is a good choice. An interpolating scheme will generate a surface that is more like the control mesh. This is most notable when using meshes with few triangles. For larger meshes, the differences disappear. However, the interpolating characteristics come at the cost that the scheme may generate weird shapes with “unnatural” undulations, and thus, less fairness. This is common

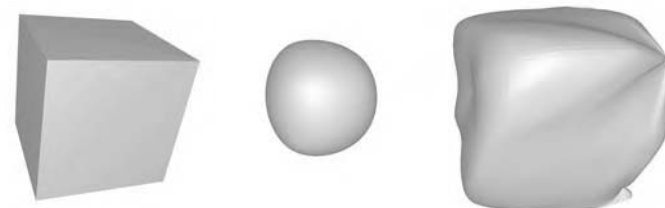


**Figure 13.42.** The cube on the left is subdivided using Loop’s scheme (middle), and the modified butterfly scheme (right). Each face on the cube consists of two triangles. Note the “unnatural” undulations on the right surface. This is because it is much harder to interpolate a given set of vertices.

for all interpolating schemes. See Figure 13.42 for a nasty example. Another disadvantage is that the masks are bigger than those used for Loop’s scheme and the  $\sqrt{3}$ -scheme presented in Section 13.5.3, and thus it is more expensive to evaluate.

Despite these disadvantages, interpolating schemes such as MB can be well-suited for real-time rendering work. Meshes for real-time work are normally not finely tessellated, so an interpolated surface is usually more intuitive, as it more closely matches the location of the control mesh. The tradeoff is that fairness problems can occur, but in many cases, minor adjustments to the underlying mesh can smooth out rippling [1159]. The MB scheme is  $C^1$ -continuous all over the surface, even at irregular vertices [1413]. See Figure 13.38 on page 616, and Figure 13.43 for two examples. More about this scheme can be found in Zorin’s Ph.D. thesis [1413] and in Sharp’s articles [1159, 1160].

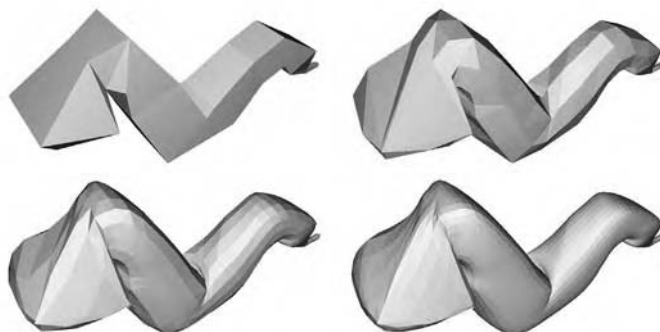


**Figure 13.43.** A worm is subdivided three times with the modified butterfly scheme. Notice that the vertices are interpolated at each subdivision step.

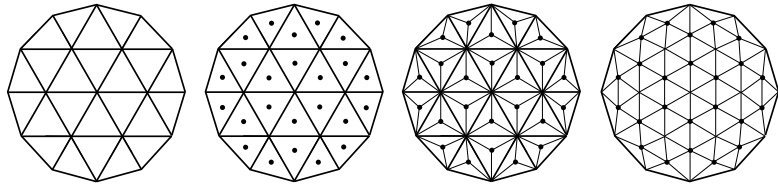


**Figure 13.44.** Illustration of the  $\sqrt{3}$ -subdivision scheme. A 1-to-3 split is performed instead of a 1-to-4 split as for Loop's and the modified butterfly schemes. First, a new vertex is generated at the center of each triangle. Then, this vertex is connected to the triangle's three vertices. Finally, the old edges are flipped. (*Illustration after Kobbelt [679].*)

### 13.5.3 $\sqrt{3}$ -Subdivision

Both Loop's and the MB schemes split each triangle into four new ones, and so create triangles at a rate of  $4^n m$ , where  $m$  is the number of triangles in the control mesh, and  $n$  is the number of subdivision steps. A feature of Kobbelt's  $\sqrt{3}$ -scheme [679] is that it creates only three new triangles per subdivision step.<sup>7</sup> The trick is to create a new vertex (here called *mid-vertex*) in the middle of each triangle, instead of one new vertex per edge. This is shown in Figure 13.44. To get more uniformly shaped triangles, each old edge is flipped so that it connects two neighboring midvertices. In the subsequent subdivision step (and in every second subdivision step thereafter), the shapes of the triangles more resemble the initial triangle configuration due to this edge flip.

The subdivision rules are shown in Equation 13.58, where  $\mathbf{p}_m$  denotes the midvertex, computed as the average of the triangle vertices:  $\mathbf{p}_a$ ,  $\mathbf{p}_b$ , and  $\mathbf{p}_c$ . Each of the old vertices,  $\mathbf{p}^k$ , are updated using the formula in the second line, where  $\mathbf{p}_i^k$  ( $i = 0 \dots n - 1$ ) denotes the immediate neighbors of  $\mathbf{p}^k$ , and  $n$  is the valence of  $\mathbf{p}^k$ . The subdivision step is denoted by  $k$  as before:

$$\begin{aligned}\mathbf{p}_m^{k+1} &= (\mathbf{p}_a^k + \mathbf{p}_b^k + \mathbf{p}_c^k)/3, \\ \mathbf{p}^{k+1} &= (1 - n\beta)\mathbf{p}^k + \beta \sum_{i=0}^{n-1} \mathbf{p}_i^k.\end{aligned}\tag{13.58}$$

Again,  $\beta$  is a function of the valence  $n$ , and the following choice of  $\beta(n)$  generates a surface that is  $C^2$  continuous everywhere except at irregular

---

<sup>7</sup>The name stems from the fact that while Loop's and the MB schemes divide each edge into two new edges per subdivision step, Kobbelt's scheme creates three new edges per two subdivision steps. Thus the name  $\sqrt{3}$ -subdivision.

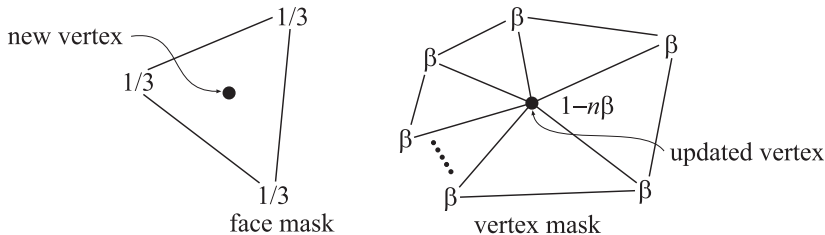


**Figure 13.45.** The masks for the  $\sqrt{3}$ -subdivision scheme. As can be seen, the face mask gives minimal support, since it uses only the three vertices of the triangle. The vertex mask uses all the vertices in the ring, called the 1-ring, around the vertex.

vertices ( $n \neq 6$ ), where the continuity is at least  $C^1$  [679]:

$$\beta(n) = \frac{4 - 2 \cos(2\pi/n)}{9n} \quad (13.59)$$

The masks, which are of minimum size, for the  $\sqrt{3}$ -scheme are shown in Figure 13.45.

The major advantage of this scheme is that it supports adaptive subdivision in a simpler way, since no extra triangles are needed to avoid cracks. See Kobbelt's paper [679] for details. Some other advantages of this scheme are smaller masks, and slower triangle growth rate than Loop's and the MB scheme. The continuity of this scheme is the same as Loop's. Disadvantages include that the edge flip introduces a little complexity, and that the first subdivision step sometimes generates nonintuitive shapes due to the flip. In Figure 13.46, a worm is subdivided with the  $\sqrt{3}$ -scheme, and in Figure 13.38 on page 616, a tetrahedron is subdivided.

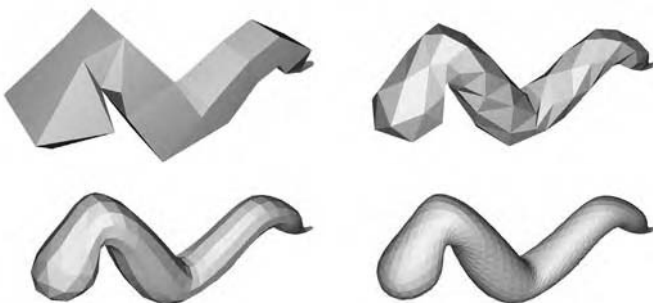


**Figure 13.46.** A worm is subdivided three times with the  $\sqrt{3}$ -subdivision scheme.

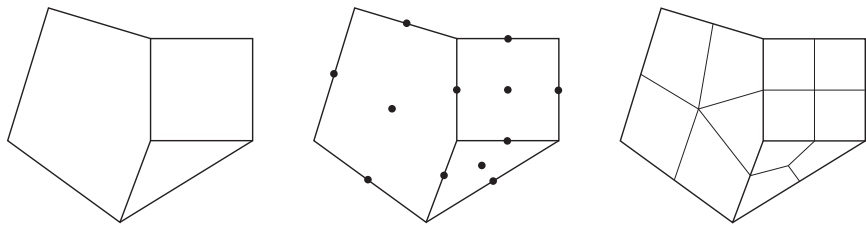


**Figure 13.47.** The basic idea of Catmull-Clark subdivision. Each polygon generates a new point, and each edge generates a new point. These are then connected as shown to the right. Weighting of the original points is not shown here.

### 13.5.4 Catmull-Clark Subdivision

The two most famous subdivision schemes that can handle polygonal meshes (rather than just triangles) are Catmull-Clark [163] and Doo-Sabin [274].<sup>8</sup> Here, we will only briefly present the former. Catmull-Clark surfaces have been used in Pixar’s short film *Geri’s Game* [250] and in *Toy Story 2*, and in all subsequent feature films from Pixar. This subdivision scheme is also commonly used for making models for games, and is probably the most popular one. As pointed out by DeRose et al. [250], Catmull-Clark surfaces tend to generate more symmetrical surfaces. For example, an oblong box results in a symmetrical ellipsoid-like surface, which agrees with intuition.

The basic idea for Catmull-Clark surfaces is shown in Figure 13.47, and an actual example of Catmull-Clark subdivision is shown in Figure 13.32 on page 611. As can be seen, this scheme only generates faces with four vertices. In fact, after the first subdivision step, only vertices of valence 4 are generated, thus such vertices are called ordinary or regular (compared to valence 6 for triangular schemes).

Following the notation from Halstead et al. [494] (see Figure 13.48), let us focus on a vertex  $\mathbf{v}^k$  with  $n$  surrounding edge points  $\mathbf{e}_i^k$ , where  $i = 0 \dots n - 1$ . Now, for each face, a new face point  $\mathbf{f}^{k+1}$  is computed as the face centroid, i.e., the mean of the points of the face. Given this, the subdivision rules are [163, 494, 1415]

$$\begin{aligned}\mathbf{v}^{k+1} &= \frac{n-2}{n} \mathbf{v}^k + \frac{1}{n^2} \sum_{j=0}^{n-1} \mathbf{e}_j^k + \frac{1}{n^2} \sum_{j=0}^{n-1} \mathbf{f}_j^{k+1}, \\ \mathbf{e}_j^{k+1} &= \frac{\mathbf{v}^k + \mathbf{e}_j^k + \mathbf{f}_{j-1}^{k+1} + \mathbf{f}_j^{k+1}}{4}.\end{aligned}\tag{13.60}$$

---

<sup>8</sup>Incidentally, both were presented in the same issue of the same journal.

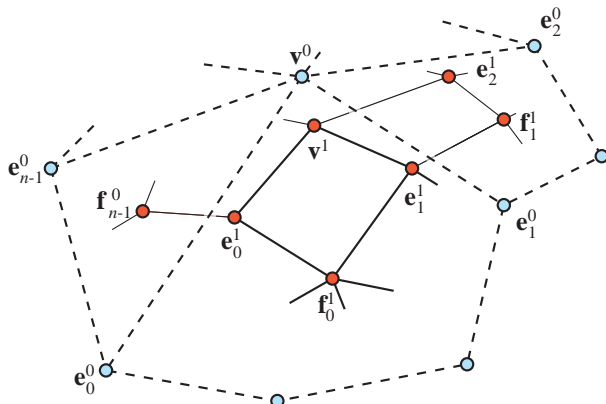


**Figure 13.48.** Before subdivision, we have the blue vertices and corresponding edges and faces. After one step of Catmull-Clark subdivision, we obtain the red vertices, and all new faces are quadrilaterals. (Illustration after Halstead et al. [494].)

As can be seen, new edge points are computed by the average of the considered vertex, the edge point, and the two newly created face points that have the edge as a neighbor. On the other hand, the vertex is computed as weighting of the considered vertex, the average of the edge points, and the average of the newly created face points.

The Catmull-Clark surface describes a generalized bicubic B-spline surface. So, for a mesh consisting only of regular vertices we could actually describe the surface as a B-spline surface.<sup>9</sup> However, this is not possible for irregular settings, and being able to do this using subdivision surfaces is one of the scheme's strengths. Limit positions and tangents are also possible to compute [494]. See Section 13.6.5 for an efficient technique on how to render Catmull-Clark subdivision surfaces on graphics hardware with tessellation shaders.

### 13.5.5 Piecewise Smooth Subdivision

In a sense, curved surfaces may be considered boring because they lack detail. Two ways to improve such surfaces are to use bump or displacement maps (Section 13.5.6). A third approach, *piecewise smooth subdivision*, is described here. The basic idea is to change the subdivision rules so that *darts*, *corners*, and *creases* can be used. This increases the range of different surfaces that can be modeled and represented. Hoppe et al. [559] first described this for Loop's subdivision surfaces. See Figure 13.49 for a

<sup>9</sup>See the SIGGRAPH course notes for more on this topic [1415].

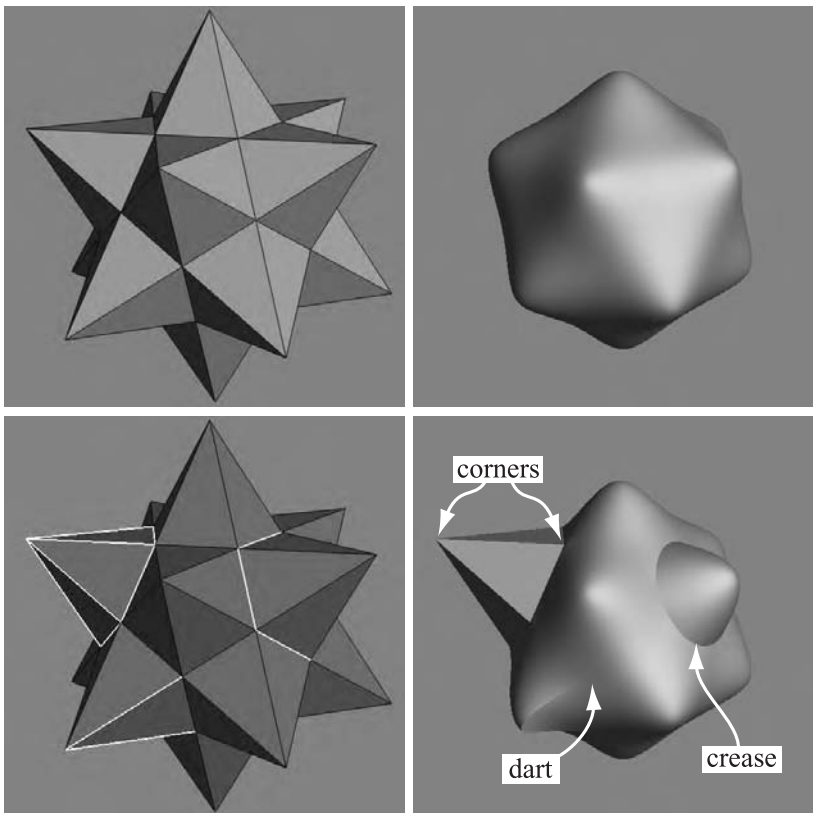


**Figure 13.49.** The top row shows a control mesh, and the limit surface using the standard Loop subdivision scheme. The bottom row shows piecewise smooth subdivision with Loop’s scheme. The lower left image shows the control mesh with tagged edges (sharp) shown in a light gray. The resulting surface is shown to the lower right, with corners, darts, and creases marked. (*Image courtesy of Hugues Hoppe.*)

comparison of a standard Loop subdivision surface, and one with piecewise smooth subdivision.

To actually be able to use such features on the surface the edges that we want to be sharp are first tagged, so we know where to subdivide differently. The number of sharp edges coming in at a vertex is denoted  $s$ . Then the vertices are classified into: smooth ( $s = 0$ ), dart ( $s = 1$ ), crease ( $s = 2$ ), and corner ( $s > 2$ ). Therefore, a crease is a smooth curve on the surface, where the continuity across the curve is  $C^0$ . A dart is a nonboundary vertex where a crease ends and smoothly blends into the surface. Finally, a corner is a vertex where three or more creases come together. Boundaries can be defined by marking each boundary edge as sharp.

After classifying the various vertex types, Hoppe et al. use a table to determine which mask to use for the various combinations. They also show how to compute limit surface points and limit tangents. Biermann et al. [86] present several improved subdivision rules. For example, when extraordinary vertices are located on a boundary, the previous rules could result in gaps. This is avoided with the new rules. Also, their rules make it possible to specify a normal at a vertex, and the resulting surface will adapt to get that normal at that point. DeRose et al. [250] present a technique for creating soft creases. Basically, they allow an edge to first be subdivided as sharp a number of times (including fractions), and after that, standard subdivision is used.

### 13.5.6 Displaced Subdivision

Bump mapping (Section 6.7) is one way to add detail to otherwise smooth surfaces. However, this is just an illusionary trick that changes the normal or local occlusion at each pixel. The silhouette of an object looks the same with or without bump mapping. The natural extension of bump mapping is *displacement mapping* [194], where the surface is displaced. This is usually done along the direction of the normal. So, if the point of the surface is  $\mathbf{p}$ , and its normalized normal is  $\mathbf{n}$ , then the point on the displaced surface is

$$\mathbf{s} = \mathbf{p} + d\mathbf{n}. \quad (13.61)$$

The scalar  $d$  is the displacement at the point  $\mathbf{p}$ . The displacement could also be vector-valued [698].

In this section, the *displaced subdivision surface* [745] will be presented. The general idea is to describe a displaced surface as a coarse control mesh that is subdivided into a smooth surface that is then displaced along its normals using a scalar field. In the context of displaced subdivision surfaces,  $\mathbf{p}$  in Equation 13.61 is the limit point on the subdivision surface (of the coarse control mesh), and  $\mathbf{n}$  is the normalized normal at  $\mathbf{p}$ , computed as

$$\begin{aligned} \mathbf{n}' &= \mathbf{p}_u \times \mathbf{p}_v, \\ \mathbf{n} &= \frac{\mathbf{n}'}{\|\mathbf{n}'\|}. \end{aligned} \quad (13.62)$$

In Equation 13.62,  $\mathbf{p}_u$  and  $\mathbf{p}_v$  are the first-order derivative of the subdivision surface. Thus, they describe two tangents at  $\mathbf{p}$ . Lee et al. [745] use a Loop subdivision surface for the coarse control mesh, and its tangents can be computed using Equation 13.53. Note that the notation is slightly different here; we use  $\mathbf{p}_u$  and  $\mathbf{p}_v$  instead of  $\mathbf{t}_u$  and  $\mathbf{t}_v$ . Equation 13.61 describes the displaced position of the resulting surface, but we also need

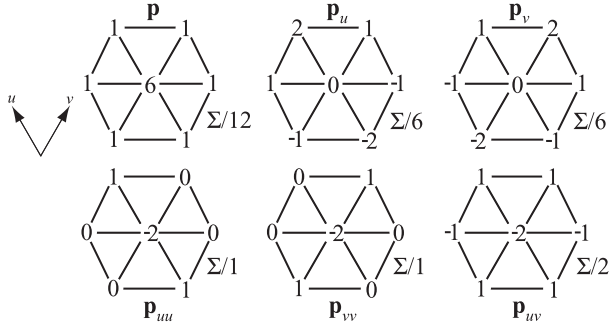


**Figure 13.50.** The masks for an ordinary vertex in Loop’s subdivision scheme. Note that after using these masks, the resulting sum should be divided as shown. (Illustration after Lee et al. [745].)

a normal,  $\mathbf{n}_s$ , on the displaced subdivision surface in order to render it correctly. It is computed analytically as shown below [745]:

$$\begin{aligned} \mathbf{s}_u &= \frac{\partial \mathbf{s}}{\partial u} = \mathbf{p}_u + d_u \mathbf{n} + d \mathbf{n}_u, \\ \mathbf{s}_v &= \frac{\partial \mathbf{s}}{\partial v} = \mathbf{p}_v + d_v \mathbf{n} + d \mathbf{n}_v, \\ \mathbf{n}_s &= \mathbf{s}_u \times \mathbf{s}_v. \end{aligned} \quad (13.63)$$

To simplify computations, Blinn [98] suggests that the third term can be ignored if the displacements are small. Otherwise, the following expressions can be used to compute  $\mathbf{n}_u$  (and similarly  $\mathbf{n}_v$ ) [745]:

$$\begin{aligned} \bar{\mathbf{n}}_u &= \mathbf{p}_{uu} \times \mathbf{p}_v + \mathbf{p}_u \times \mathbf{p}_{uv}, \\ \mathbf{n}_u &= \frac{\bar{\mathbf{n}}_u - (\bar{\mathbf{n}}_u \cdot \mathbf{n})\mathbf{n}}{||\mathbf{n}'||}. \end{aligned} \quad (13.64)$$

Note that  $\bar{\mathbf{n}}_u$  is not any new notation, it is merely a “temporary” variable in the computations. For an ordinary vertex (valence  $n = 6$ ), the first and second order derivatives are particularly simple. Their masks are shown in Figure 13.50. For an extraordinary vertex (valence  $n \neq 6$ ), the third term in rows one and two in Equation 13.63 is omitted.

The displacement map for one triangle in the coarse mesh is a scalar field, that is, a heightfield. The storage requirements for one triangle is one half of  $(2^k + 1) \times (2^k + 1)$ , where  $k$  is the number of subdivisions that the displacement map should be able to handle, which depends on the desired accuracy. The displacement map uses the same parameterization as the underlying subdivision mesh. So, for example, when one triangle is subdivided, three new points are created. Displacements for these three



**Figure 13.51.** To the left is a coarse mesh. In the middle, it is subdivided using Loop’s subdivision scheme. The right image shows the displaced subdivision surface. (*Image courtesy Aaron Lee, Henry Moreton, and Hugues Hoppe.*)

points are retrieved from the displacement map. This is done for  $k$  subdivision levels. If subdivision continues past this maximum of  $k$  levels, the displacement map is subdivided as well, using Loop’s subdivision scheme. The subdivided displacement,  $d$ , is added using Equation 13.61. When the object is farther away, the displacement map is pushed to the limit points, and a mipmap pyramid of displacements is built as a preprocess and used. The resulting displaced subdivision surface is  $C^1$  everywhere, except at extraordinary vertices, where it is  $C^0$ . Remember that after sufficiently many subdivision steps, there is only a small fraction of vertices that are extraordinary. An example is shown in Figure 13.51.

When a displaced surface is far away from the viewer, standard bump mapping could be used to give the illusion of this displacement. Doing so saves on geometry processing. Some bump mapping schemes need a tangent space coordinate system at the vertex, and the following can be used for that:  $(\mathbf{b}, \mathbf{t}, \mathbf{n})$ , where  $\mathbf{t} = \mathbf{p}_u / \|\mathbf{p}_u\|$  and  $\mathbf{b} = \mathbf{n} \times \mathbf{t}$ .

Lee et al. [745] also present how adaptive tessellation and backpatch culling can be used to accelerate rendering. More importantly, they present algorithms to derive the control mesh and the displacement field from a detailed polygon mesh.

### 13.5.7 Normal, Texture, and Color Interpolation

In this section, we will present different strategies for dealing with normals, texture coordinates and color per vertex.

As shown for Loop’s scheme in Section 13.5.1, and the MB scheme in Section 13.5.2, limit tangents, and thus, limit normals can be computed explicitly. This involves trigonometric functions that may be expensive to evaluate. An approximating technique for the normals of Catmull-Clark

surfaces is mentioned in Section 13.6.5, where it can be seen that the normal field is a higher degree “surface” than the actual surface itself. This implies that merely computing limit normals (which are exact) at the vertices of the control mesh, and then use the same subdivision scheme used for the vertices to subdivide the normals is not likely to produce a normal field with good quality. In addition, such a technique would increase storage, and it is not obvious whether this is faster.

Assume that each vertex in a mesh has a texture coordinate and a color. To be able to use these for subdivision surfaces, we also have to create colors and texture coordinates for each newly generated vertex, too. The most obvious way to do this is to use the same subdivision scheme as we used for subdividing the polygon mesh. For example, you can treat the colors as four-dimensional vectors (RGBA), and subdivide these to create new colors for the new vertices [1160]. This is a reasonable way to do it, since the color will have a continuous derivative (assuming the subdivision scheme is at least  $C^1$ ), and thus abrupt changes in colors are avoided over the surface. The same can certainly be done for texture coordinates [250]. However, care must be taken when there are boundaries in texture space. For example, assume we have two patches sharing an edge but with different texture coordinates along this edge. The geometry should be subdivided with the surface rules as usual, but the texture coordinates should be subdivided using boundary rules in this case.

A sophisticated scheme for texturing subdivision surfaces is given by Piponi and Borshukov [1017].

## 13.6 Efficient Tessellation

To display a curved surface in a real-time rendering context, we usually need to create a triangle mesh representation of the surface. This process is known as *tessellation*. The simplest form of tessellation is called *uniform tessellation*. Assume that we have a parametric Bézier patch,  $\mathbf{p}(u, v)$ , as described in Equation 13.28. We want to tessellate this patch by computing 11 points per patch side, resulting in  $10 \times 10 \times 2 = 200$  triangles. The simplest way to do this is to sample the  $uv$ -space *uniformly*. Thus, we evaluate  $\mathbf{p}(u, v)$  for all  $(u_k, v_l) = (0.1k, 0.1l)$ , where both  $k$  and  $l$  can be any integer from 0 to 10. This can be done with two nested **for**-loops. Two triangles can be created for the four surface points  $\mathbf{p}(u_k, v_l)$ ,  $\mathbf{p}(u_{k+1}, v_l)$ ,  $\mathbf{p}(u_k, v_{l+1})$ , and  $\mathbf{p}(u_{k+1}, v_{l+1})$ .

While this certainly is straightforward, there are faster ways to do it. Instead of sending tessellated surfaces, consisting of many triangles, over the bus from the CPU to the GPU, it makes more sense to send the curved surface representation to the GPU and let it handle the data expansion.

In the following five subsections, we will describe tessellation hardware, fractional tessellation, the evaluation shader, and how to render Catmull-Clark surfaces and displacement mapped surfaces with such hardware. This type of tessellation is supported by the ATI Radeon HD 2000 series and beyond, and also by the Xbox 360. Techniques for adaptive tessellation are described in Section 13.6.4.

### 13.6.1 Hardware Tessellation Pipeline

An efficient way of providing inexpensive data expansion of geometry is to send higher-order surfaces to the GPU and let it tessellate the surface. This can be done with a rather small, but important, change in the rendering pipeline. This is illustrated in Figure 13.52.

The tessellator uses a fractional tessellation technique, which is described in the subsequent section. This basically tessellates a triangle or a quadrilateral to many smaller triangles or quadrilaterals. Independent fractional tessellation factors on the sides of a parametric surface can also be used. Such factors allow a continuous level of detail of these surfaces, and hence avoid popping artifacts. Once the tessellation is done, the vertices are forwarded to the vertex shader. This pipeline gives the programmer a very fast way of producing triangles, and letting a programmable shader compute the exact position of a vertex. This shader is described in Section 13.6.3. As an example, the vertex shader can evaluate the formulae for a Bézier triangle in order to create a smooth, curved surface.

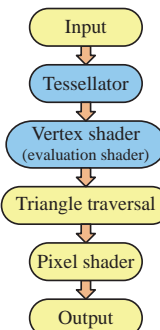


**Figure 13.52.** Pipeline with hardware tessellator. The new parts are in blue, where the geometrical primitives, e.g., triangles, are tessellated into many smaller primitives in the tessellator. These generated vertices are sent to the vertex shader, which is basically a standard vertex shader, except that it also knows the parametric coordinates of the vertex inside the primitive. This makes it possible to compute the three-dimensional position and normal of the vertex within the vertex shader.

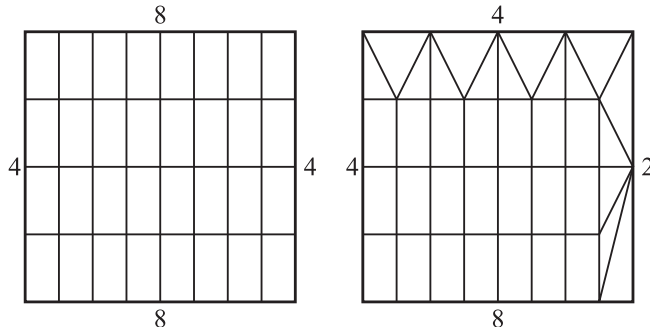


**Figure 13.53.** Left: normal tessellation—one factor is used for the rows, and another for the columns. Right: independent tessellation factors on all four edges. (*Illustration after Moreton [904].*)

### 13.6.2 Fractional Tessellation

To obtain smoother level of detail for parametric surfaces, Moreton introduced *fractional tessellation factors* [904]. These factors enable a limited form of adaptive tessellation, since different tessellation factors can be used on different sides of the parametric surface. Here, an overview of how these techniques work will be presented.

In Figure 13.53, constant tessellation factors for rows and columns are shown to the left, and independent tessellation factors for all four edges to the right. Note that the tessellation factor of an edge is the number of points generated on that edge, minus one. In the patch on the right, the greater of the top and bottom factors is used for both of these edges, and similarly the greater of the left and right factors is used for those. Thus, the basic tessellation rate is  $4 \times 8$ . For the sides with smaller factors, triangles are filled in along the edges. Moreton [904] describes this process in more detail.

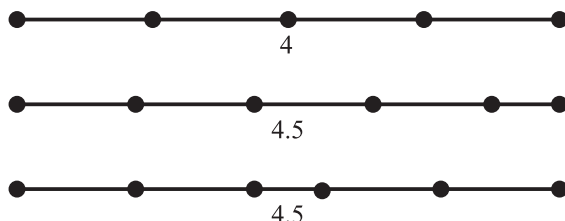


**Figure 13.54.** Top: integer tessellation. Middle: fractional tessellation, with the fraction to the right. Bottom: fractional tessellation with the fraction in the middle. This configuration avoids cracks between adjacent patches.

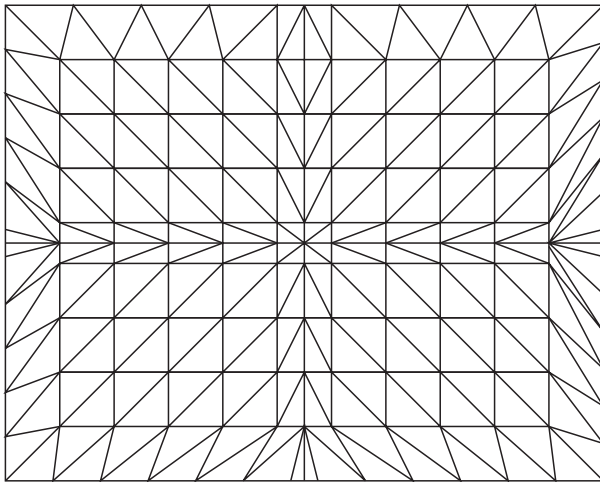


**Figure 13.55.** A patch with the rectangular domain fractionally tessellated. (*Illustration after Moreton [904].*)

The concept of fractional tessellation factors is shown for an edge in Figure 13.54. For an integer tessellation factor of  $n$ ,  $n + 1$  points are generated at  $k/n$ , where  $k = 0, \dots, n$ . For a fractional tessellation factor,  $r$ ,  $\lceil r \rceil$  points are generated at  $k/r$ , where  $k = 0, \dots, \lfloor r \rfloor$ . Here,  $\lceil r \rceil$  computes the *ceil* of  $r$ , which is the closest integer toward  $-\infty$ , and  $\lfloor r \rfloor$  computes the *floor*, which is the closest integer toward  $+\infty$ . Then, the rightmost point is just “snapped” to the rightmost endpoint. As can be seen in the middle illustration in Figure 13.54, this pattern is not symmetric. This leads to problems, since an adjacent patch may generate the points in the other direction, and so give cracks between the surfaces. Moreton solves this by creating a symmetric pattern of points, as shown at the bottom of Figure 13.54. See also Figure 13.55 for an example.

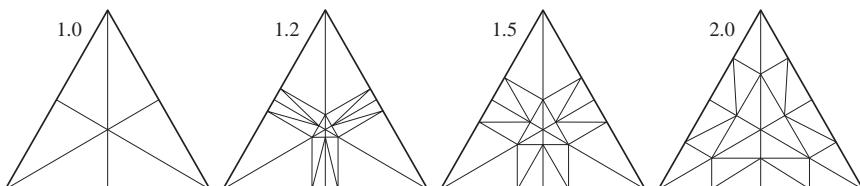


**Figure 13.56.** Fractional tessellation of a triangle, with tessellation factors shown. Note that the tessellation factors may not correspond exactly to those produced by actual tessellation hardware. (*After Tatarchuk [1252].*)

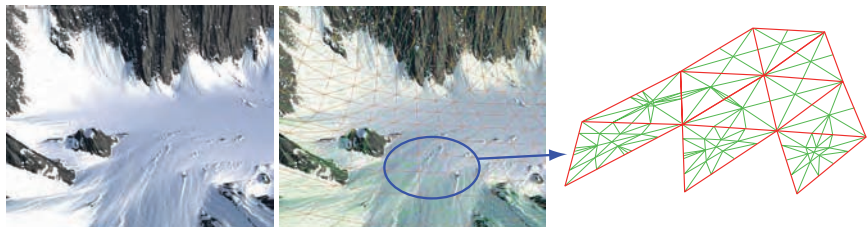


**Figure 13.57.** Displaced terrain rendering using adaptive fractional tessellation. As can be seen in the zoomed-in mesh to the right, independent fractional tessellation rates are used for the edges of the red triangles, which gives us adaptive tessellation. (*Images courtesy of Game Computing Applications Group, Advanced Micro Devices, Inc.*)

So far, we have seen methods for tessellating surfaces with a rectangular domain, e.g., Bézier patches. However, triangles can also be tessellated using fractions [1252], as shown in Figure 13.56. Similar to the quadrilaterals, it is also possible to specify an independent fractional tessellation rate per triangle edge. As mentioned, this enables adaptive tessellation, as illustrated in Figure 13.57, where displaced mapped terrain is rendered. Once triangles or quadrilaterals have been created, they can be forwarded to the next step in the pipeline, which is treated in the next subsection.

### 13.6.3 Vertex + Evaluation Shader

At this point, the tessellation hardware has created new triangles and vertices, and each such vertex is forwarded to the vertex shader. However, the vertex shader now also functions as an *evaluation shader*. This means that its task is to compute each vertex position, which may be located on a curved surface. An example would be to evaluate an N-patch, which is a Bézier triangle, or to evaluate a Catmull-Clark surface. To make it possible to evaluate these using tessellation hardware with evaluation shaders, the subdivision surface must be converted into a representation that does not require neighboring triangles or quadrilaterals. Such a technique is described in Section 13.6.5. Another technique is to use *displacement mapping*, where each vertex is offset from its tessellated position. This is often done in direction of the normal, and hence, only a single scalar value is needed. Such displacements can be done by using a texture fetch in the vertex shader, or using procedural computations (using noise, for example), or some other function (e.g., Gerstner waves to create realistic water). An example is shown in Figure 13.58.

The vertex shader must somehow get information on which surface location it is about to evaluate. The solution here is simple: The hardware tessellator simply forwards the parametric coordinates to the vertex shader.



**Figure 13.58.** Left: wireframe of a ninja model. Middle: The model to the left has now been tessellated with fractional rates on the triangle sides. Right: After tessellation, each vertex has been displaced. (*Images courtesy Game Computing Applications Group, Advanced Micro Devices, Inc.*)

For quadrilaterals, you get a pair of coordinates,  $(u, v)$ , and in the case of triangles, this corresponds to the barycentric coordinates of the vertex inside the original triangle. The barycentric coordinates are  $(u, v, w)$ , where  $w = 1 - u - v$ .

For the future, the most logical evolution of the pipeline is to add yet another type of shader just before the hardware tessellator [134]. This would be a *control point shader*, and its task would be to compute the position of the control points of a curved surface before hardware tessellation. Without this stage, the control points of, say, a Bézier triangle would have to be computed on the CPU. Another idea is to do the animation of the low-resolution mesh in a first pass, and output the resulting mesh to a texture of vertices. In the following pass, the animated model is tessellated. With a control point shader, you can also add simple animation of the curved surface.

### 13.6.4 Adaptive Tessellation

Uniform tessellation gives good results if the sampling rate is high enough. However, in some regions on a surface there may not be as great a need for high tessellation as in other regions. This may be because the surface bends more rapidly in some area and therefore may need higher tessellation there, while other parts of the surface are almost flat, and only a few triangles are needed to approximate them. A solution to the problem of generating unnecessary triangles is *adaptive tessellation*, which refers to

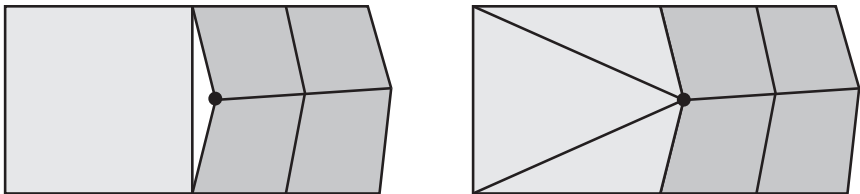


**Figure 13.59.** To the left, a crack is visible between the two regions. This is because the right has a higher tessellation rate than the left. The problem lies in that the right region has evaluated the surface where there is a black circle, and the left region has not. The standard solution is shown to the right.

algorithms that adapt the tessellation rate depending on some measure (for example curvature, triangle edge length, or some screen size measure). Care must be taken to avoid cracks that can appear between different tessellated regions. See Figure 13.59. In this section, we will first describe a three-pass algorithm for computing adaptive tessellation using tessellation hardware, fractional rates, and evaluation shaders. Furthermore, we present some general techniques that can be used to compute fractional tessellation rates or decide when to terminate further tessellation.

### A Three-Pass Technique for Adaptive Tessellation

Tatarchuk [1252] describes a technique for computing the fractional tessellation factors, and how to instruct the hardware to render tessellated surfaces using these factors.

In the first pass, the vertices of the original mesh are first displaced (if such a technique is used). Then, these are transformed into camera space, rendered out as points into a two-dimensional texture. Here, it is assumed that each vertex has a unique vertex ID, and the position of the vertex in the texture is computed from this ID. It is important that each base triangle here outputs all three vertices, i.e., you cannot use indexed primitives. The reasons for this will be clear later on. Note that the result of this pass is only a two-dimensional texture containing the vertices in camera space.

The second pass computes the fractional tessellation factors, and outputs them to a two-dimensional texture as well. This pass sends all the vertices of the original mesh through the pipeline, and we use the vertex ID to access the transformed vertex in the texture from the first pass. Now, assume that each vertex shall compute a fractional tessellation factor as well. The vertices of a triangle,  $\Delta v_0 v_1 v_2$ , will be fed to the vertex shader in order. For the first vertex,  $v_0$ , we want to compute a tessellation factor,  $f_0$ , based on  $v_0$  and  $v_1$ . Similarly,  $f_1$  should be based on  $v_1$  and  $v_2$ , and  $f_2$  should be derived from  $v_2$  and  $v_0$ . Since we are using non-indexed prim-

itives, we can easily find the transformed edge vertices from the texture from the first pass by using the vertex ID. When this is done, we compute a fractional tessellation factor,  $f_i$ , and write it out to a two-dimensional texture as well. Techniques for this are described in the next subsection, called *Terminating Adaptive Tessellation*. Note that since a tessellation factor is computed based solely on the edge's two vertices, and because fractional tessellation is symmetric, there cannot be any cracks with this technique. The entire system has been designed to avoid such issues. However, the developer has to take care that edges always are treated with the same vertex order, because floating-point imprecision may create cracks if the same order is not preserved.

In the final pass, we use the two textures from the first and second passes as input data to the tessellation hardware, which automatically uses on each edge the correct fractional tessellation factor, computed in the previous pass. After tessellation, the vertex shader program evaluates the curved surface, possibly with displacement as well, and then the triangles are rendered. An example of the results is shown in Figure 13.57.

### *Terminating Adaptive Tessellation*

To provide adaptive tessellation, we need to determine when to stop the tessellation, or equivalently how to compute fractional tessellation factors. Either you can use only the information of an edge to determine if tessellation should be terminated, or use information from an entire triangle, or a combination.

It should also be noted that with adaptive tessellation, one can get swimming or popping artifacts from frame to frame if the tessellation factors for a certain edge change too much from one frame to the next. This may be a factor to take into consideration when computing tessellation factors as well.

Given an edge,  $(\mathbf{a}, \mathbf{b})$ , with an associated curve, we can try to estimate how flat the curve is between  $\mathbf{a}$  and  $\mathbf{b}$ . See Figure 13.60. The midpoint,  $\mathbf{m}$ , in parametric space between  $\mathbf{a}$  and  $\mathbf{b}$ , is found, and its three-dimensional counterpart,  $\mathbf{c}$ , is computed. Finally, the length,  $l$ , between  $\mathbf{c}$  and its projection,  $\mathbf{d}$ , onto the line between  $\mathbf{a}$  and  $\mathbf{b}$ , is computed. This length,

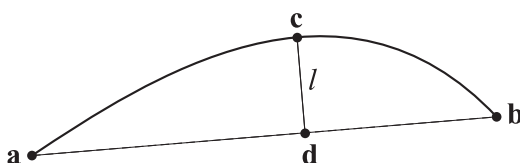


**Figure 13.60.** The points  $\mathbf{a}$  and  $\mathbf{b}$  have already been generated on this surface. The question is: Should a new point, that is  $\mathbf{c}$ , be generated on the surface?

$l$ , is used to determine whether the curve segment on that edge is flat enough. If  $l$  is small enough, it is considered flat. Note that this method may falsely consider an S-shaped curve segment to be flat. A solution to this is to randomly perturb the parametric sample point [343] or even to use multiple randomly perturbed sample points [1300]. An alternative to using just  $l$  is to use the ratio  $l/\|\mathbf{a} - \mathbf{b}\|$  [294]. Note that this technique can be extended to consider a triangle as well: Just compute the surface point in the middle of the triangle and use the distance from that point to the triangle's plane. To be certain that this type of algorithm terminates, it is common to set some upper limit on how many subdivisions can be made. When that limit is reached, the subdivision ends. For fractional tessellation, the vector from  $\mathbf{c}$  to  $\mathbf{d}$  can be projected onto the screen, and its (scaled) length used as a tessellation rate.

So far we have discussed how to determine the tessellation rate from only the shape of the surface. Other factors that typically are used for on-the-fly tessellation include whether the local neighborhood of a vertex is [561, 1392]:

1. Inside the view frustum,
2. Frontfacing,
3. Occupying a large area in screen space,
4. Close to the silhouette of the object, and
5. Illuminated by a significant amount of specular lighting.

These factors will be discussed in turn here. For view frustum culling, one can place a sphere to enclose the edge. This sphere is then tested against the view frustum. If it is outside, we do not subdivide that edge further.

For face culling, the normals at  $\mathbf{a}$ ,  $\mathbf{b}$ , and possibly  $\mathbf{c}$  can be computed from the surface description. These normals, together with  $\mathbf{a}$ ,  $\mathbf{b}$ , and  $\mathbf{c}$ , define three planes. If all are backfacing, it is likely that no further subdivision is needed for that edge.

There are many different ways to implement screen-space coverage (see also Section 14.7.2). All methods project some simple object onto the screen and estimate the length or area in screen space. A large area or length implies that tessellation should proceed. A fast estimation of the screen-space projection of a line segment from  $\mathbf{a}$  to  $\mathbf{b}$  is shown in Figure 13.61. First, the line segment is translated so that its midpoint is on the view ray. Then, the line segment is assumed to be parallel to the near plane,  $n$ , and the screen-space projection,  $s$ , is computed from this line

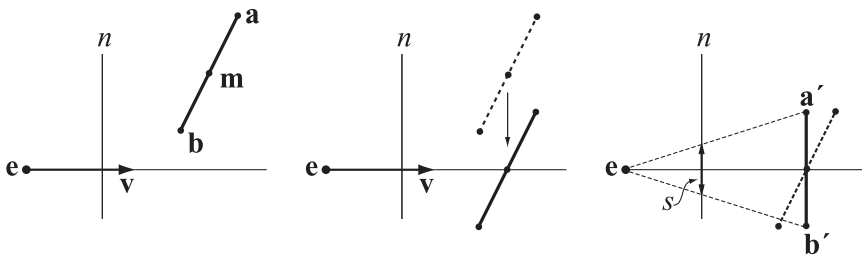


**Figure 13.61.** Estimation of the screen-space projection,  $s$ , of the line segment.

segment. Using the points of the line segment  $\mathbf{a}'$  and  $\mathbf{b}'$  to the right in the illustration, the screen-space projection is then

$$s = \frac{\sqrt{(\mathbf{a}' - \mathbf{b}') \cdot (\mathbf{a}' - \mathbf{b}')}}{\mathbf{v} \cdot (\mathbf{a}' - \mathbf{e})}. \quad (13.65)$$

The numerator simply the length of the line segment. This is divided by the distance from the eye,  $\mathbf{e}$ , to the line segment's midpoint. The computed screen-space projection,  $s$ , is then compared to a threshold,  $t$ , representing the maximum edge length in screen space. Rewriting the previous equation to avoid computing the square root, if the following condition is true, the tessellation should continue:

$$s > t \iff (\mathbf{a}' - \mathbf{b}') \cdot (\mathbf{a}' - \mathbf{b}') > t^2(\mathbf{v} \cdot (\mathbf{a}' - \mathbf{e})). \quad (13.66)$$

Note that  $t^2$  is a constant and so can be precomputed. For fractional tessellation,  $s$  from Equation 13.65 can be used as tessellation rate, possibly with a scaling factor applied.

Increasing the tessellation rate for the silhouettes is important, since they play an important role for the perceived quality of the object. Finding if a triangle is near the silhouette edge can be done by testing whether the dot product between the normal at  $\mathbf{a}$  and the vector from the eye to  $\mathbf{a}$  is close to zero. If this is true for any of  $\mathbf{a}$ ,  $\mathbf{b}$ , or  $\mathbf{c}$ , further tessellation should be done.

Specular illumination changes rapidly on a surface, and so shading artifacts appear most frequently with it (see Figure 5.17 on page 116). Therefore, it makes sense to increase the tessellation in regions where the specular highlight appears. Test if the dot product between the light vector reflected around the normal at a point and the vector from the point to the eye is close to one. If so, then the specular highlight is strong at that point and the tessellation should continue there. This could again be done for points  $\mathbf{a}$ ,  $\mathbf{b}$ , and  $\mathbf{c}$ .

It is hard to say what methods will work in all applications. The best advice is to test several of the presented heuristics, and combinations of them.

Another more common method for adaptive tessellation is to do it on a quad basis. Assume that a rectangular patch is used. Then start a recursive routine with the entire parametric domain, i.e., the square from  $(0, 0)$  to  $(1, 1)$ . Using the subdivision criteria just described, test whether the surface is tessellated enough. If it is, then terminate tessellation. Otherwise, split this domain into four different equally large squares and call the routine recursively for each of the four subsquares. Continue recursively until the surface is tessellated enough or a predefined recursion level is reached. The nature of this algorithm implies that a quadtree is recursively created during tessellation. However, this will give cracks if adjacent subsquares are tessellated to different levels. The standard solution is to ensure that two adjacent subsquares only differ in one level at most. This is called a *restricted quadtree*. Then the technique shown to the right in Figure 13.59 is used to fill in the cracks. The disadvantage with this method is that the bookkeeping is more involved.

Lindstrom et al. [779] and Sharp [1158] present different variations of algorithms for avoiding cracks. Bookkeeping in these algorithms is more involved. Also, Lindstrom [779] presents a geometric screen-space flatness test for heightfields, which Hoppe [561] generalizes to arbitrary geometry. Both these tests are designed for mesh simplification. Eberly describes many different flatness tests, both for curves and surfaces [294]. Chhugani and Kumar [173] present an algorithm for adaptive tessellation of spline surfaces, where tessellation is view-dependent.

### 13.6.5 Catmull-Clark Surfaces with Hardware Tessellation

Catmull-Clark surfaces (Section 13.5.4) are frequently used in modeling software and in feature film rendering, and hence it would be attractive to be able to render these efficiently using graphics hardware as well. Loop and Schaefer [790] present a technique to convert Catmull-Clark surfaces into a representation that can be forwarded to the hardware tessellator, and with a fast evaluation in the vertex shader (without the need to know the polygons' neighbors). Their method will be described in this section, as it is likely to have a large impact on real-time rendering of high-quality surfaces.

As mentioned in Section 13.5.4, the Catmull-Clark surface can be described as many small B-spline surfaces when all vertices are ordinary. Loop and Schaefer convert a quadrilateral (quad) polygon in the original Catmull-Clark subdivision mesh to a bi-cubic Bézier surface (see Sec-

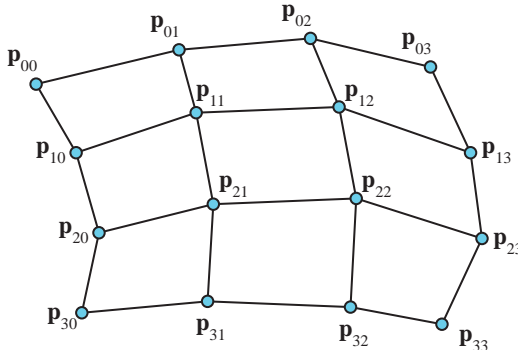


**Figure 13.62.** A bicubic Bézier patch with  $4 \times 4$  control points.

tion 13.2.1). This is not possible for non-quadrilaterals, and so we assume that there are no such polygons (recall that after the first step of subdivision there are only quadrilateral polygons). When a vertex has a valence different from four, it is not possible to create a bicubic Bézier patch that is identical to the Catmull-Clark surface. Hence, an approximative representation is proposed, which is exact for quads with valence-four vertices, and very close to the Catmull-Clark surface elsewhere. To this end, both *geometry patches* and *tangent patches* are used, which will be described next.

The geometry patch is simply a bicubic Bézier patch, as illustrated in Figure 13.62, with  $4 \times 4$  control points. We will describe how these control points are computed. Once this is done, the patch can be tessellated and the vertex shader can evaluate the Bézier patch quickly at any parametric coordinate  $(u, v)$ . So, assuming we have a mesh consisting of only quads with vertices of valence four, we want to compute the control points of the corresponding Bézier patch for a certain quad in the mesh. To that end, the neighborhood around the quad is needed. The standard way of doing this is illustrated in Figure 13.63, where three different masks are shown. These can be rotated and reflected in order to create all the 16 control points. Note that in an implementation the weights for the masks should sum to one; that process is omitted here for clarity.

The above technique computes a Bézier patch for the ordinary case. When there is at least one extraordinary vertex, we compute an extraordinary patch [790]. The masks for this are shown in Figure 13.64, where the lower left vertex in the gray quad is an extraordinary vertex.

Note that this results in a patch that approximates the Catmull-Clark subdivision surface, and, it is only  $C^0$  along edges with an extraordinary vertex. This often looks distracting when shading is added, and hence a

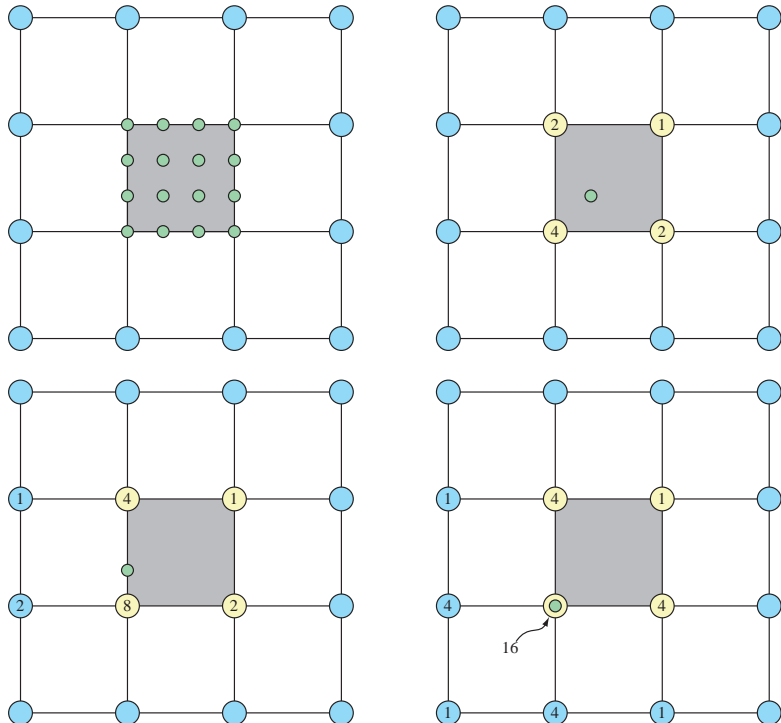


**Figure 13.63.** Top left: part of a quad mesh, where we want to compute a Bézier patch for the gray quad. Note that the gray quad only has vertices with valence four. The blue vertices are neighboring quads' vertices, and the green circles are the control points of the Bézier patch. The following three illustrations show the different masks used to compute the green control points. For example, to compute one of the inner control points, the upper right mask is used, and the vertices of the quad are weighted with the weight shown in the mask.

similar trick as used for N-patches (Section 13.2.3) is suggested. However, to reduce the computational complexity, two tangent patches are derived: one in the  $u$ -direction, and one the  $v$ -direction. The normal is then found as the cross-product between those vectors. In general, the derivatives of a Bézier patch are computed using Equation 13.30. However, since the derived Bézier patches approximate the Catmull-Clark surface, the tangent patches will not form a continuous normal field. Consult Loop and Schaefer's paper [790] on how to overcome these problems. Figure 13.65 shows an example of the types of artifacts that can occur. With an early implementation, this method was able to produce over 100 million polygons/second on an Xbox 360 [790].

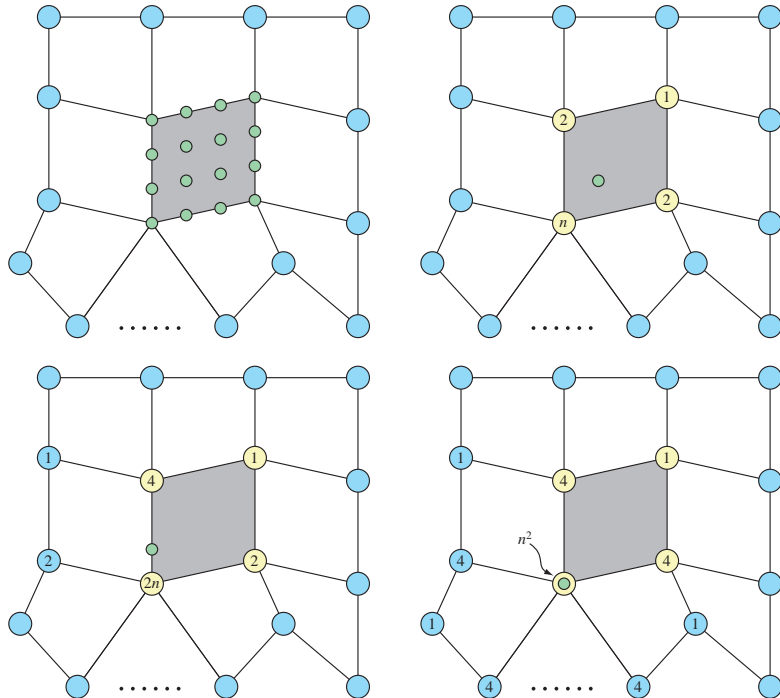


**Figure 13.64.** Top left: part of a quad mesh, where we want to compute a Bézier patch for the gray quad. The lower left vertex in the gray quad is extraordinary, since its valence is  $n \neq 4$ . The blue vertices are neighboring quads' vertices, and the green circles are the control points of the Bézier patch. The following three illustrations show the different masks used to compute the green control points.

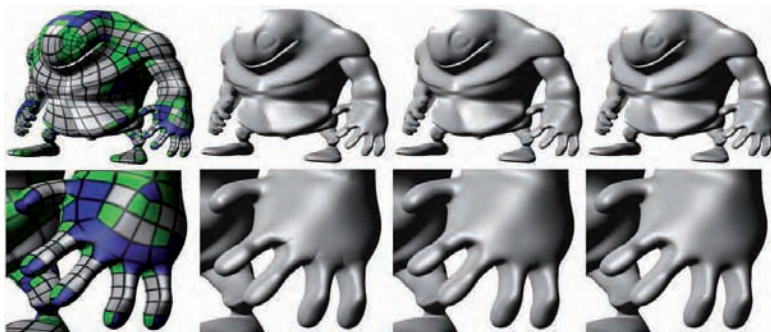


**Figure 13.65.** Left: quad structure of a mesh. White quads are ordinary, green have one extraordinary vertex, and blue have more than one. Mid-left: geometry path approximation. Mid-right: geometry patches with tangent patches. Note that the obvious shading artifacts disappeared. Right: true Catmull-Clark surface. (Image courtesy of Charles Loop and Scott Schaefer, reprinted with permission from Microsoft Corporation.)

## Further Reading and Resources

The topic of curves and surfaces is huge, and for more information, it is best to consult the books that focus solely on this topic. Mortenson’s book [905] serves as a good general introduction to geometric modeling. Books by Farin [332, 335], and by Hoschek and Lasser [569] are general and treat many aspects of *Computer Aided Geometric Design* (CAGD). For implicit surfaces, consult the excellent book by Bloomenthal et al. [117]. For much more information on subdivision surfaces, consult Warren and Heimer’s book [1328], and the SIGGRAPH course notes on “Subdivision for Modeling and Animation” [1415] by Zorin et al.

For spline interpolation, we refer the interested reader to Watt and Watt [1330], Rogers [1076], and the Killer-B’s book [68]. Many properties of Bernstein polynomials, both for curves and surfaces, are given by Goldman [416]. Almost everything about triangular Bézier surfaces can be found in Farin’s article [331]. Another class of rational curves and surfaces is the Non-Uniform Rational B-Splines (NURBS) [334, 1015, 1078].

An easy-to-read article on how to implement a subdivision algorithm is given by Sharp [1160], which is a follow-up to his article on subdivision surface theory [1159]. While Kobbelt’s  $\sqrt{3}$ -scheme is approximating, there is also an interpolating  $\sqrt{3}$ -scheme [706]. Proposals for implementing Loop’s subdivision scheme in hardware have been presented by various researchers [88, 1036]. Biermann et al. [86] present schemes that have normal control, i.e., that a normal can be set at a vertex and a tangent-plane continuous surface generated. Many good presentations on continuity analysis on subdivision surfaces are available [679, 1056, 1328, 1412, 1414, 1415]. See also Stam’s paper [1212] on how to evaluate Catmull-Clark surfaces at arbitrary parameter values using explicit formulae.

There are some different techniques for performing repeated subdivision or tessellation on the GPU [147, 1175]. Most of these render out vertices to two-dimensional textures and perform subdivision repeatedly until some convergence criterion is fulfilled. Loop and Blinn use the GPU to render piecewise algebraic surfaces, i.e., without any tessellation [789]. This looks convincing, but on current GPUs, this disables  $Z$ -culling (Section 18.3.7) and any early- $Z$  test.



# Chapter 14

## Acceleration Algorithms

*“Now here, you see, it takes all the running you can do to keep in the same place. If you want to get somewhere else, you must run at least twice as fast as that!”*

—Lewis Carroll

One of the great myths concerning computers is that one day we will have enough processing power. Even in a relatively simple application like word processing, we find that additional power can be applied to all sorts of features, such as on-the-fly spell and grammar checking, antialiased text display, voice recognition and dictation, etc.

In real-time rendering, we have at least four performance goals: more frames per second, higher resolution and sampling rates, more realistic materials and lighting, and increased complexity. A speed of 60–85 frames per second is generally considered a fast enough frame rate; see the Introduction for more on this topic. Even with motion blurring (Section 10.14), which can lower the frame rate needed for image quality, a fast rate is still needed to minimize latency when interacting with a scene [1329].

IBM’s T221 LCD display offers  $3840 \times 2400$  resolution, with 200 dots per inch (dpi) [1329]. A resolution of 1200 dpi, 36 times the T221’s density, is offered by many printer companies today. A problem with the T221 is that it is difficult to update this many pixels at interactive rates. Perhaps  $1600 \times 1200$  is enough resolution for a while. Even with a limit on screen resolution, antialiasing and motion blur increase the number of samples needed for generating high-quality images. As discussed in Section 18.1.1, the number of bits per color channel can also be increased, which drives the need for higher precision (and therefore more costly) computations.

As previous chapters have shown, describing and evaluating an object’s material can be computationally complex. Modeling the interplay of light



**Figure 14.1.** A “reduced” Boeing model with a mere 350 million triangles rendered with ray tracing. Sectioning is performed by using a user-defined clipping plane. This model can be rendered at 15 fps without shadows on 16 Opteron cores, using more flexible but untuned OpenRT ray tracing code. It can also be rendered at about 4 fps at  $640 \times 480$  with shadows, on heavily tuned code on a dual processor. Once camera movement stops, the image can be progressively enhanced with antialiasing and soft shadowing. (*Image courtesy of Computer Graphics Group, Saarland University. Source 3D data provided by and used with permission of the Boeing Company.*)

and surface can absorb an arbitrarily high amount of computing power. This is true because an image should ultimately be formed by the contributions of light traveling down a limitless number of paths from an illumination source to the eye.

Frame rate, resolution, and shading can always be made more complex, but there is some sense of diminishing returns to increasing any of these. There is no real upper limit on scene complexity. The rendering of a Boeing 777 includes 132,500 unique parts and over 3,000,000 fasteners, which would yield a polygonal model with over 500,000,000 polygons [206]. See Figure 14.1. Even if most of those objects are not seen due to size or position, some work must be done to determine that this is the case. Neither Z-buffering nor ray tracing can handle such models without the use of techniques to reduce the sheer number of computations needed. Our conclusion: Acceleration algorithms will always be needed.

In this chapter, a smörgåsbord of algorithms for accelerating computer graphics rendering, in particular the rendering of large amounts of geometry, will be presented and explained. The core of many such algorithms is based on *spatial data structures*, which are described in the next section. Based on that knowledge, we then continue with *culling techniques*. These are algorithms that try to find out which objects are at all visible and need to be treated further. *Level of detail* techniques reduce the complexity of rendering the remaining objects. Finally, systems for rendering very large models, and point rendering algorithms, are briefly discussed.

## 14.1 Spatial Data Structures

A spatial data structure is one that organizes geometry in some  $n$ -dimensional space. Only two- and three-dimensional structures are used in this book, but the concepts can often easily be extended to higher dimensions. These data structures can be used to accelerate queries about whether geometric entities overlap. Such queries are used in a wide variety of operations, such as culling algorithms, during intersection testing and ray tracing, and for collision detection.

The organization of spatial data structures is usually hierarchical. This means, loosely speaking, that the topmost level encloses the level below it, which encloses the level below that level, and so on. Thus, the structure is nested and of recursive nature. The main reason for using a hierarchy is that different types of queries get significantly faster, typically an improvement from  $O(n)$  to  $O(\log n)$ . It should also be noted that the construction of most spatial data structures is expensive and is often done as a preprocess. Lazy evaluation and incremental updates are possible in real time.

Some common types of spatial data structures are *bounding volume hierarchies* (BVHs), variants of *binary space partitioning* (BSP) trees, quadtrees, and octrees. BSP trees and octrees are data structures based on *space subdivision*. This means that the entire space of the scene is subdivided and encoded in the data structure. For example, the union of the space of all the leaf nodes is equal to the entire space of the scene. Normally the leaf nodes' volumes do not overlap, with the exception of less common structures such as loose octrees. Most variants of BSP trees are *irregular*, which loosely means that the space can be subdivided more arbitrarily. The octree is *regular*, meaning that space is split in a uniform fashion. Though more restrictive, this uniformity can often be a source of efficiency. A bounding volume hierarchy, on the other hand, is not a space subdivision structure. Rather, it encloses the regions of the space surrounding geometrical objects, and thus the BVH need not enclose all space.

BVHs, BSP trees, and octrees are all described in the following sections, along with the *scene graph*, which is a data structure more concerned with model relationships than with efficient rendering.

### 14.1.1 Bounding Volume Hierarchies

A *bounding volume* (BV) is a volume that encloses a set of objects. The point of a BV is that it should be a much simpler geometrical shape than the contained objects, so that doing tests using a BV can be done much faster than using the objects themselves. Examples of BVs are spheres, *axis-aligned bounding boxes* (AABBs), *oriented bounding boxes* (OBBs),

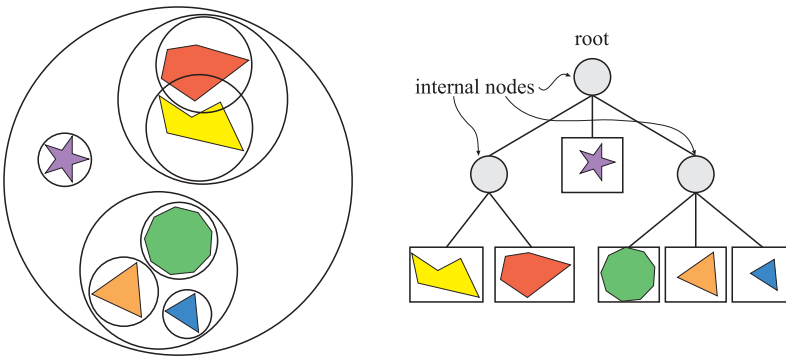


**Figure 14.2.** The left part shows a simple scene with six objects, each enclosed by a bounding sphere. The bounding spheres are then grouped together into larger bounding spheres, until all objects are enclosed by the largest sphere. The right part shows the bounding volume hierarchy (tree) that is used to represent the object hierarchy on the left. The BV of the root encloses all objects in the scene.

and  $k$ -DOPs (see Section 16.2 for definitions). A BV does not contribute visually to the rendered image. Instead, it is used as a *proxy* in place of the bounded objects, to speed up rendering, selection, and other computations and queries.

For real-time rendering of three-dimensional scenes, the bounding volume hierarchy (BVH) is often used for hierarchical view frustum culling (see Section 14.3). The scene is organized in a hierarchical tree structure, consisting of a root, internal nodes, and leaves. The topmost node is the *root*, which has no parents. A *leaf node* holds the actual geometry to be rendered, and it does not have any children. In contrast, an *internal node* has pointers to its children. The root is thus an internal node, unless it is the only node in the tree. Each node, including leaf nodes, in the tree has a bounding volume that encloses the geometry in its entire subtree—thus the name *bounding volume hierarchy*. This means that the root has a BV that contains the entire scene. An example of a BVH is shown in Figure 14.2.

The underlying structure of a BVH is a tree, and in the field of computer science the literature on tree data structures is vast. Here, only a few important results will be mentioned. For more information, see, for example, the book *Introduction to Algorithms* by Cormen et al. [201].

Consider a  $k$ -ary tree, that is, a tree where each internal node has  $k$  children. A tree with only one node (the root) is said to be of height 0. A leaf node of the root is at height 1, and so on. A balanced tree is a tree in which all leaf nodes either are at height  $h$  or  $h - 1$ . In general, the

height,  $h$ , of a balanced tree is  $\lfloor \log_k n \rfloor$ , where  $n$  is the total number of nodes (internal and leaves) in the tree.

A full tree is one where all leaf nodes are at the same height,  $h$ . Some properties of (only) full trees follow. The total number of nodes can be computed as a geometric sum:

$$n = k^0 + k^1 + \dots + k^{h-1} + k^h = \frac{k^{h+1} - 1}{k - 1}. \quad (14.1)$$

Thus, the number of leaf nodes,  $l$ , is  $l = k^h$ , and the number of internal nodes,  $i$ , is  $i = n - l = \frac{k^h - 1}{k - 1}$ . Assuming that only the number of leaf nodes,  $l$ , is known, then the total number of nodes is  $n = i + l = \frac{kl - 1}{k - 1}$ . For a binary tree, where  $k = 2$ , this gives  $n = 2l - 1$ . Note that a higher  $k$  gives a tree with a lower height, which means that it takes fewer steps to traverse the tree, but it also requires more work at each node. The binary tree is often the simplest choice, and one that gives good performance. However, there is evidence that a higher  $k$  (e.g.,  $k = 4$  or  $k = 8$ ) gives slightly better performance for some applications [731]. Using  $k = 2$ ,  $k = 4$ , or  $k = 8$  makes it simple to construct trees; just subdivide along the longest axis for  $k = 2$ , and for the two longest axes for  $k = 4$ , and for all axes for  $k = 8$ . It is much more difficult to form optimal trees for other values of  $k$ .

BVHs are also excellent for performing various queries. For example, assume that a ray should be intersected with a scene, and the first intersection found should be returned. To use a BVH for this, testing starts at the root. If the ray misses its BV, then the ray misses all geometry contained in the BVH. Otherwise, testing continues recursively, that is, the BVs of the children of the root are tested. As soon as a BV is missed by the ray, testing can terminate on that subtree of the BVH. If the ray hits a leaf node's BV, the ray is tested against the geometry at this node. The performance gains come partly from the fact that testing the ray with the BV is fast. This is why simple objects such as spheres and boxes are used as BVs. The other reason is the nesting of BVs, which allows us to avoid testing large regions of space due to early termination in the tree.

Often the closest intersection, not the first found, is what is desired. The only additional data needed are the distance and identity of the closest object found while traversing the tree. The current closest distance is also used to cull the tree during traversal. If a BV is intersected, but its distance is beyond the closest distance found so far, then the BV can be discarded. Normally we do not know which child of a BV is closest without testing, so we must test all children in arbitrary order. As will be seen, a BSP tree has an advantage over normal BVHs in that it can guarantee front-to-back ordering. However, binary BVHs can also achieve this advantage by keeping track of the axis used to split the set of objects into the two children [132].

BVHs can be used for dynamic scenes as well [1050]. When an object contained in a BV has moved, simply check whether it is still contained in its parent's BV. If it is, then the BVH is still valid. Otherwise, the object node is removed and the parent's BV recomputed. The node is then recursively inserted back into the tree from the root. Another method is to grow the parent's BV to hold the child recursively up the tree as needed. With either method, the tree can become unbalanced and inefficient as more and more edits are performed. Another approach is to put a BV around the limits of movement of the object over some period of time. This is called a *temporal bounding volume* [4]. For example, a pendulum could have a bounding box that enclosed the entire volume swept out by its motion.

To create a BVH, one must first be able to compute a tight BV around a set of objects. This topic is treated in Section 16.3 on page 732. Then, the actual hierarchy of BVs must be created. Strategies for this are treated in Section 17.3.1 on page 802.

### 14.1.2 BSP Trees

Binary space partitioning trees, or BSP trees for short, exist as two noticeably different variants in computer graphics, which we call *axis-aligned* and *polygon-aligned*. The trees are created by using a plane to divide the space in two, and then sorting the geometry into these two spaces. This division is done recursively. One interesting property that these trees have is that if the trees are traversed in a certain way, the geometrical contents of the tree can be sorted front-to-back from any point of view. This sorting is approximate for axis-aligned and exact for polygon-aligned BSPs. This is in contrast to BVHs, which usually do not include any type of sorting.

#### *Axis-Aligned BSP Trees*

An axis-aligned BSP tree<sup>1</sup> is created as follows. First, the whole scene is enclosed in an *axis-aligned bounding box* (AABB). The idea is then to recursively subdivide that box into smaller boxes. Now, consider a box at any recursion level. One axis of the box is chosen, and a perpendicular plane is generated that divides the space into two boxes. Some schemes fix this partitioning plane so that it divides the box exactly in half; others allow the plane to vary in position.

An object intersecting the plane can be treated in any number of ways. For example, it could be stored at this level of the tree, or made a member of both child boxes, or truly split by the plane into two separate objects.

---

<sup>1</sup>A BSP tree that is not polygon-aligned may split the space in any way it wishes. However, we focus on axis-aligned BSP trees here because this is the most commonly used variant, and the most practical.

Storing at the tree level has the advantage that there is only one copy of the object in the tree, making object deletion straightforward. However, small objects intersected by the splitting plane become lodged in the upper levels of the tree, which tends to be inefficient. Placing intersected objects into both children can give tighter bounds to larger objects, as all objects percolate down to one or more leaf nodes, but only those they overlap. A *mailbox scheme* (also called *timestamping*) is then used to mark the object when it is first encountered when rendering a frame, e.g., with the number of the frame. When the object is encountered again in another leaf node, its mailbox is checked and the object ignored if it has already been sent to the screen for this frame. One disadvantage here is that large objects could be duplicated into many leaf nodes, costing time and memory. However, a more important, though subtle, problem is that every object's timestamp must be both read and written. Doing so can cause the memory cache to be invalidated and so cause significant slowdowns [864].

Each child box contains some number of objects, and this plane-splitting procedure is repeated, subdividing each AABB recursively until some criterion is fulfilled to halt the process. See Figure 14.3 for an example of an axis-aligned BSP tree.

The axis and placement of the splitting plane is important for maximizing efficiency. One strategy for splitting a node's box is to cycle through the axes. That is, at the root, the box is always split along the  $x$ -axis, its children are split along  $y$ , the grandchildren along  $z$ , then the cycle repeats. BSP trees using this strategy are sometimes called *k-d trees* [1099]. An-

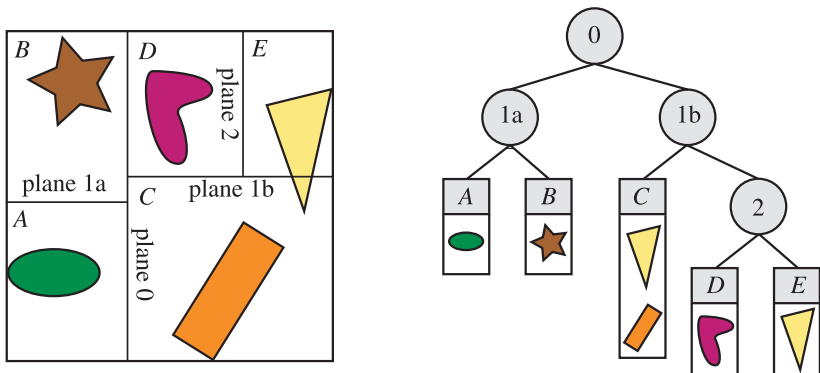


**Figure 14.3.** Axis-aligned BSP tree. In this example, the space partitions are allowed to be anywhere along the axis, not just at its midpoint. The spatial volumes formed are labeled A through E. The tree on the right shows the underlying BSP data structure. Each leaf node represents an area, with that area's contents shown beneath it. Note that the triangle is in the object list for two areas, C and E, because it overlaps both.

other strategy is to find the largest side of the box and split the box along this direction. For example, say the box is largest in the  $y$ -direction; then splitting occurs at some plane,  $y = d$ , where  $d$  is a scalar constant. Geometric probability theory (see Section 16.4) is also useful in determining a near-optimal axis and split location. The idea is to avoid splitting objects as much as possible, along with finding two child nodes that together minimize the number of objects in a child multiplied by surface area or mean width of that child.

Aila and Miettinen [4] present an efficient BSP management scheme for large scenes. The system performs lazy evaluation, subdividing only those nodes that are visible. This can save work by avoiding computing splits for parts of the world that are never viewed. It also spreads out the cost of subdivision over a number of frames. Only those objects that are smaller than the current node are pushed further down the hierarchy; larger objects (judged by their diagonal length) remain as direct children of the node. If the number of small objects in a BSP node is 10 or greater, the node is subdivided. Geometric probability theory is used to determine a near-optimal split axis and location. Mailboxing is used to allow an object cut by a split plane to be in multiple nodes. This approach avoids small objects getting lodged in the upper levels of the BSP tree, while also terminating subdivision when it is unlikely to help further.

Rough front-to-back sorting is an example of how axis-aligned BSP trees can be used. This is useful for occlusion culling algorithms (see Section 14.6 and 18.3.6), as well as for generally reducing pixel shader costs by minimizing pixel overdraw (see Section 15.4.5). Assume that a node called  $N$  is currently traversed. Here,  $N$  is the root at the start of traversal. The splitting plane of  $N$  is examined, and tree traversal continues recursively on the side of the plane where the viewer is located. Thus, it is only when the entire half of the tree has been traversed that we can start to traverse the other side. This traversal does not give exact front-to-back sorting, since the contents of the leaf nodes are not sorted, and because objects may be in many nodes of the tree. However, it gives a rough sorting, which often is useful. By starting traversal on the other side of a node's plane when compared to the viewer's position, rough back-to-front sorting can be obtained. This is useful for transparency sorting (see Section 5.7). This traversal can also be used to test a ray against the scene geometry. The ray's origin is simply exchanged for the viewer's location. Another use is in view frustum culling (Section 14.3).

### Polygon-Aligned BSP Trees

The other type of BSP tree is the polygon-aligned form [1, 366, 367, 428]. This data structure is particularly useful for rendering static or rigid geometry in an exact sorted order. This algorithm was popular for games like

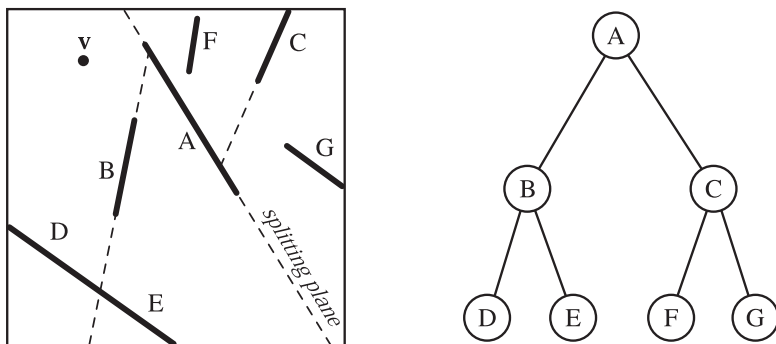


**Figure 14.4.** Polygon-aligned BSP tree. Polygons A through G are shown from above. Space is first split by polygon A, then each half-space is split separately by B and C. The splitting plane formed by polygon B intersects the polygon in the lower left corner, splitting it into separate polygons D and E. The BSP tree formed is shown on the right.

*Doom*, back when there was no hardware Z-buffer. It still has occasional use, such as for collision detection (see Section 17.2).

In this scheme, a polygon is chosen as the divider, splitting space into two halves. That is, at the root, a polygon is selected. The plane in which the polygon lies is used to divide the rest of the polygons in the scene into two sets. Any polygon that is intersected by the dividing plane is broken into two separate pieces along the intersection line. Now in each half-space of the dividing plane, another polygon is chosen as a divider, which divides only the polygons in its half-space. This is done recursively until all polygons are in the BSP tree. Creating an efficient polygon-aligned BSP tree is a time-consuming process, and such trees are normally computed once and stored for reuse. This type of BSP tree is shown in Figure 14.4.

It is generally best to form a balanced tree, i.e., one where the depth of each leaf node is the same, or at most off by one. A totally unbalanced tree is inefficient. An example would be a tree where each selected splitting polygon divides the space into one empty space, and the other space contains the rest of the polygons. There are many different strategies for finding a polygon used for splitting that gives a good tree. One simple strategy is the *least-crossed criterion* [366]. First, a number of candidate polygons are randomly selected. The polygon whose plane splits the fewest other polygons is used. For a test scene of 1,000 polygons, James [597] provides empirical evidence that only five polygons need to be tested per split operation in order to get a good tree. James gives a review of a wide range of other strategies, as well as providing a new one of his own.

The polygon-aligned BSP tree has some useful properties. One is that, for a given view, the structure can be traversed strictly from back to front

(or front to back). This is in comparison to the axis-aligned BSP tree, which normally gives only a rough sorted order. Determine on which side of the root plane the camera is located. The set of polygons on the far side of this plane is then beyond the near side's set. Now with the far side's set, take the next level's dividing plane and determine which side the camera is on. The subset on the far side is again the subset farthest away from the camera. By continuing recursively, this process establishes a strict back-to-front order, and a *painter's algorithm* can be used to render the scene. The painter's algorithm does not need a Z-buffer; if all objects are drawn in a back-to-front order, each closer object is drawn in front of whatever is behind it, and so no  $z$ -depth comparisons are required.

For example, consider what is seen by a viewer  $\mathbf{v}$  in Figure 14.4. Regardless of the viewing direction and frustum,  $\mathbf{v}$  is to the left of the splitting plane formed by A. So C, F, and G are behind B, D, and E. Comparing  $\mathbf{v}$  to the splitting plane of C, we find G to be on the opposite side of this plane, so it is displayed first. A test of B's plane determines that E should be displayed before D. The back-to-front order is then G, C, F, A, E, B, D. Note that this order does not guarantee that one object is closer to the viewer than another; rather it provides a strict occlusion order, a subtle difference. For example, polygon F is closer to  $\mathbf{v}$  than polygon E, even though it is farther back in occlusion order.

Other uses for polygon-aligned BSP trees are intersection testing (see Chapter 16), and collision detection (see Section 17.2).

### 14.1.3 Octrees

The octree is similar to the axis-aligned BSP tree. A box is split simultaneously along all three axes, and the split point must be the center of the box. This creates eight new boxes—hence the name *octree*. This makes the structure regular, which can make some queries more efficient.

An octree is constructed by enclosing the entire scene in a minimal axis-aligned box. The rest of the procedure is recursive in nature and ends when a stopping criterion is fulfilled. As with axis-aligned BSP trees, these criteria can include reaching a maximum recursion depth, or obtaining a certain number of primitives in a box [1098, 1099]. If a criterion is met, the algorithm binds the primitives to the box and terminates the recursion. Otherwise, it subdivides the box along its main axes using three planes, thereby forming eight equal-sized boxes. Each new box is tested and possibly subdivided again into  $2 \times 2 \times 2$  smaller boxes. This is illustrated in two dimensions, where the data structure is called a *quadtree*, in Figure 14.5. Quadtrees are the two-dimensional equivalent of octrees, with a third axis being ignored. They can be useful in situations where there is little advantage to categorizing the data along all three axes.

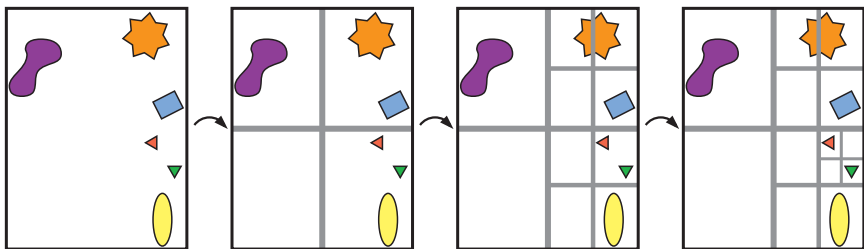


**Figure 14.5.** The construction of a quadtree. The construction starts from the left by enclosing all objects in a bounding box. Then the boxes are recursively divided into four equal-sized boxes until each box (in this case) is empty or contains one object.

Octrees can be used in the same manner as axis-aligned BSP trees, and thus, can handle the same types of queries. They are also used in occlusion culling algorithms (see Section 14.6.2). A BSP tree can, in fact, give the same partitioning of space as an octree. If a cell is first split along the middle of, say, the  $X$ -axis, then the two children are split along the middle of, say,  $Y$ , and finally those children are split in the middle along  $Z$ , eight equal-sized cells are formed that are the same as those created by one application of an octree division. One source of efficiency for the octree is that it does not need to store information needed by more flexible BSP tree structures. For example, the splitting plane locations are known and so do not have to be described explicitly. This more compact storage scheme also saves time by accessing fewer memory locations during traversal. Axis-aligned BSP trees can still be more efficient, as the additional memory cost and traversal time due to the need for retrieving the splitting plane's location can be outweighed by the savings from better plane placement. There is no overall best efficiency scheme; it depends on the nature of the underlying geometry, the use pattern of how the structure is accessed, and the architecture of the hardware running the code, to name a few factors. Often the locality and level of cache-friendliness of the memory layout is the most important factor. This is the focus of the next section.

In the above description, objects are always stored in leaf nodes; therefore, certain objects have to be stored in more than one leaf node. Another option is to place the object in the box that is the smallest that contains the entire object. For example, the star-shaped object in the figure should be placed in the upper right box in the second illustration from the left. This has a significant disadvantage in that, for example, a (small) object that is located at the center of the octree will be placed in the topmost (largest) node. This is not efficient, since a tiny object is then bounded by the box that encloses the entire scene. One solution is to split the objects,

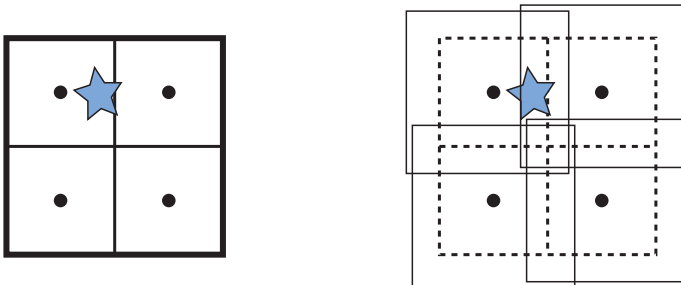


**Figure 14.6.** An ordinary octree compared to a loose octree. The dots indicate the center points of the boxes (in the first subdivision). To the left, the star pierces through one splitting plane of the ordinary octree. Thus, one choice is to put the star in the largest box (that of the root). To the right, a loose octree with  $k = 1.5$  (that is, boxes are 50% larger) is shown. The boxes are slightly displaced, so that they can be discerned. The star can now be placed fully in the upper left box.

but that introduces more primitives. Another is to put a pointer to the object in each leaf box it is in, losing efficiency and making octree editing more difficult.

Ulrich presents a third solution, *loose octrees* [1279]. The basic idea of loose octrees is the same as for ordinary octrees, but the choice of the size of each box is relaxed. If the side length of an ordinary box is  $l$ , then  $kl$  is used instead, where  $k > 1$ . This is illustrated for  $k = 1.5$ , and compared to an ordinary octree, in Figure 14.6. Note that the boxes' center points are the same. By using larger boxes, the number of objects that cross a splitting plane is reduced, so that the object can be placed deeper down in the octree. An object is always inserted into only one octree node, so deletion from the octree is trivial. Some advantages accrue by using  $k = 2$ . First, insertion and deletion of objects is  $O(1)$ . Knowing the object's size means immediately knowing the level of the octree it can successfully be inserted in, fully fitting into one loose box.<sup>2</sup> The object's centroid determines into which loose octree box it is put. Because of these properties, this structure lends itself well to bounding dynamic objects, at the expense of some BV efficiency, and the loss of a strong sort order when traversing the structure. Also, often an object moves only slightly from frame to frame, so that the previous box still is valid in the next frame. Therefore, only a fraction of animated objects in the octree need updating each frame.

<sup>2</sup>In practice it is sometimes possible to push the object to a deeper box in the octree. Also, if  $k < 2$ , the object may have to be pushed up the tree if it does not fit.

### 14.1.4 Cache-Oblivious and Cache-Aware Representations

Since the gap between the bandwidth of the memory system and the computing power of CPUs increases every year, it is very important to design algorithms and spatial data structure representations with caching in mind. In this section, we will give an introduction to cache-aware (or cache-conscious) and cache-oblivious spatial data structures. A cache-aware representation assumes that the size of cache blocks is known, and hence we optimize for a particular architecture. In contrast, a cache-oblivious algorithm is designed to work well for all types of cache sizes, and are hence platform-independent.

To create a cache-aware data structure, you must first find out what the size of a cache block is for your architecture. This may be 64 bytes, for example. Then try to minimize the size of your data structure. For example, Ericson [315] shows how it is sufficient to use only 32 bits for a  $k$ -d tree node. This is done in part by appropriating the two least significant bits of the node's 32-bit value. These two bits can represent four types: a leaf node, or the internal node split on one of the three axes. For leaf nodes, the upper 30 bits hold a pointer to a list of objects; for internal nodes, these represent a (slightly lower precision) floating point split value. Hence, it is possible to store a four-level deep binary tree of 15 nodes in a single cache block of 64 bytes (the sixteenth node indicates which children exist and where they are located). See his book for details. The key concept is that data access is considerably improved by ensuring that structures pack cleanly to cache boundaries.

One popular and simple cache-oblivious ordering for trees is the van Emde Boas layout [32, 315, 1296]. Assume we have a tree,  $\mathcal{T}$ , with height  $h$ . The goal is to compute a cache-oblivious layout, or ordering, of the nodes in the tree. Let us denote the van Emde Boas layout of  $\mathcal{T}$  as  $v(\mathcal{T})$ . This structure is defined recursively, and the layout of a single node in a tree is just the node itself. If there are more than one node in  $\mathcal{T}$ , the tree is split at half the height,  $\lfloor h/2 \rfloor$ . The topmost  $\lfloor h/2 \rfloor$  levels are put in a tree denoted  $\mathcal{T}_0$ , and the children subtree starting at the leaf nodes of  $\mathcal{T}_0$  are denoted  $\mathcal{T}_1, \dots, \mathcal{T}_n$ . The recursive nature of the tree is described as follows:

$$v(\mathcal{T}) = \begin{cases} \{\mathcal{T}\} & , \text{if there is single node in } \mathcal{T}, \\ \{\mathcal{T}_0, \mathcal{T}_1, \dots, \mathcal{T}_n\} & , \text{else.} \end{cases} \quad (14.2)$$

Note that all of the subtrees  $\mathcal{T}_i$ ,  $0 \leq i \leq n$ , are also defined by the recursion above. This means, for example, that  $\mathcal{T}_1$  has to be split at half its height, and so on. See Figure 14.7 for an example.

In general, creating a cache-oblivious layout consists of two steps: clustering and ordering of the clusters. For the van Emde Boas layout, the

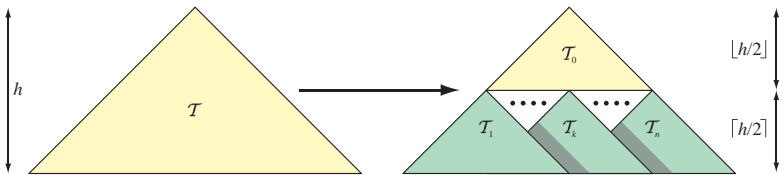


**Figure 14.7.** The van Emde Boas layout of a tree,  $\mathcal{T}$ , is created by splitting the height,  $h$ , of the tree in two. This creates the subtrees,  $\mathcal{T}_0, \mathcal{T}_1, \dots, \mathcal{T}_n$ , and each subtree is split recursively in the same manner until only one node per subtree remains.

clustering is given by the subtrees, and the ordering is implicit in the creation order. Yoon et al. [1395, 1396] develop techniques that are specifically designed for efficient bounding volume hierarchies and BSP trees. They develop a probabilistic model that takes into account both the locality between a parent and its children, and the spatial locality. The idea is to minimize cache misses when a parent has been accessed, by making sure that the children are inexpensive to access. Furthermore, nodes that are close to each other are grouped closer together in the ordering. A greedy algorithm is developed that clusters nodes with the highest probabilities. Generous increases in performance are obtained without altering the underlying algorithm—it is only the ordering of the nodes in the BVH that is different.

### 14.1.5 Scene Graphs

BVHs, BSP trees, and octrees all use some sort of tree as their basic data structure; it is in how they partition the space and store the geometry that they differ. They also store geometrical objects, and nothing else, in a hierarchical fashion. However, rendering a three-dimensional scene is about so much more than just geometry. Control of animation, visibility, and other elements are usually performed using a *scene graph*. This is a user-oriented tree structure that is augmented with textures, transforms, levels of detail, render states (material properties, for example), light sources, and whatever else is found suitable. It is represented by a tree, and this tree is traversed in depth-first order to render the scene. For example, a light source can be put at an internal node, which affects only the contents of its subtree. Another example is when a material is encountered in the tree. The material can be applied to all the geometry in that node's subtree, or possibly be overridden by a child's settings. See also Figure 14.26 on page 688 on how different levels of detail can be supported in a scene graph. In a sense, every graphics application uses some form of scene graph, even if the graph is just a root node with a list of children to display.

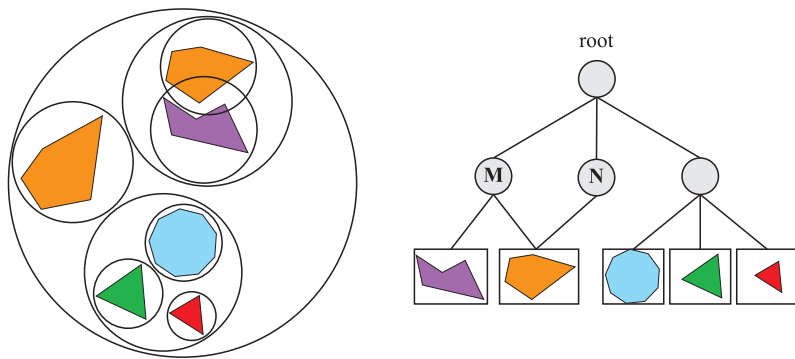


**Figure 14.8.** A scene graph with different transforms  $M$  and  $N$  applied to internal nodes, and their respective subtrees. Note that these two internal nodes also point to the same object, but since they have different transforms, two different objects appear (one is rotated and scaled).

One way of animating objects is to vary transforms in internal nodes in the tree. Scene graph implementations then transform the entire contents of that node’s subtree. Since a transform can be put in any internal node, hierarchical animation can be done. For example, the wheels of a car can spin, and the car as a whole can move forward.

When several nodes may point to the same child node, the tree structure is called a *directed acyclic graph* (DAG) [201]. The term *acyclic* means that it must not contain any loops or cycles. By *directed*, we mean that as two nodes are connected by an edge, they are also connected in a certain order, e.g., from parent to child. Scene graphs are often DAGs because they allow for instantiation, i.e., when we want to make several copies (instances) of an object without replicating its geometry. An example is shown in Figure 14.8, where two internal nodes have different transforms applied to their subtrees. Using instances saves memory, and GPUs can render multiple copies of an instance rapidly via API calls (see Section 15.4.2).

When objects are to move in the scene, the scene graph has to be updated. This can be done with a recursive call on the tree structure. Transforms are updated on the way from the root toward the leaves. The matrices are multiplied in this traversal and stored in relevant nodes. However, when transforms have been updated, the BVs are obsolete. Therefore, the BVs are updated on the way back from the leaves toward the root. A too-relaxed tree structure complicates these tasks enormously, so DAGs are often avoided, or a limited form of DAGs is used, where only the leaf nodes are shared. See Eberly’s book [294] for more information on this topic.

Scene graphs themselves can be used to provide some computational efficiency. A node in the scene graph often has a *bounding volume* (BV), and is thus quite similar to a BVH. A leaf in the scene graph stores geometry. However, one often allows this geometry to be encoded in any spatial data structure that is desired. So, a leaf may hold an entire BSP tree that stores the geometry of, say, a car.

It is important to realize that entirely unrelated efficiency schemes can be used alongside a scene graph. This is the idea of *spatialization*, in which the user's scene graph is augmented with a separate data structure (e.g., BSP tree, BVH, etc.) created for a different task, such as faster culling or picking. The leaf nodes, where most models are located, are shared, so the expense of an additional spatial efficiency structure is relatively low.

Another idea related to scene graphs is the idea of a *display list*. In OpenGL, objects are put into a special display list structure in order to precompile them into a form more efficient to render. Objects in one node in a scene graph can be put into a display list for convenience and speed.

## 14.2 Culling Techniques

To *cull* means to “remove from a flock,” and in the context of computer graphics, this is exactly what *culling techniques* do. The flock is the whole scene that we want to render, and the removal is limited to those portions of the scene that are not considered to contribute to the final image. The rest of the scene is sent through the rendering pipeline. Thus, the term *visibility culling* is also often used in the context of rendering. However, culling can also be done for other parts of a program. Examples include collision detection (by doing less accurate computations for offscreen or hidden objects), physics computations, and AI. Here, only culling techniques related to rendering will be presented. Examples of such techniques are *backface culling*, *view frustum culling*, and *occlusion culling*. These are illustrated in Figure 14.9. Backface culling eliminates polygons facing away from the viewer. This is a simple technique that operates on only a single polygon at a time. View frustum culling eliminates groups of polygons outside the view frustum. As such, it is a little more complex. Occlusion culling eliminates objects hidden by groups of other objects. It is the most complex culling technique, as it requires computing how objects affect each other.

The actual culling can theoretically take place at any stage of the rendering pipeline, and for some occlusion culling algorithms, it can even be precomputed. For culling algorithms that are implemented in hardware, we can sometimes only enable/disable, or set some parameters for, the culling function. For full control, the programmer can implement the algorithm in

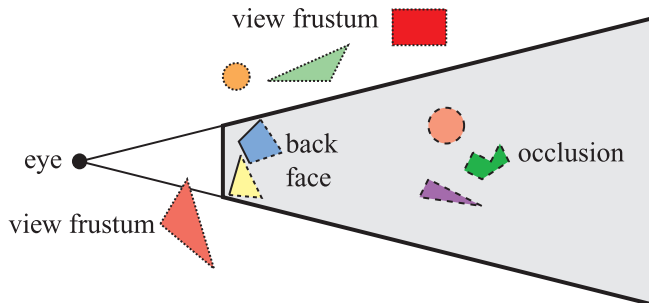


**Figure 14.9.** Different culling techniques. Culled geometry is dashed. (*Illustration after Cohen-Or et al. [185].*)

the application stage (on the CPU). Assuming the bottleneck is not on the CPU, the fastest polygon to render is the one never sent down the accelerator’s pipeline. Culling is often achieved by using geometric calculations, but is in no way limited to these. For example, an algorithm may also use the contents of the frame buffer.

The ideal culling algorithm would send only the *exact visible set* (EVS) of primitives through the pipeline. In this book, the EVS is defined as all primitives that are partially or fully visible. One such data structure that allows for ideal culling is the *aspect graph*, from which the EVS can be extracted, given any point of view [398]. Creating such data structures is possible in theory, but not really in practice, since worst-time complexity can be as bad as  $O(n^9)$  [185]. Instead, practical algorithms attempt to find a set, called the *potentially visible set* (PVS), that is a prediction of the EVS. If the PVS fully includes the EVS, so that only invisible geometry is discarded, the PVS is said to be *conservative*. A PVS may also be *approximate*, in which the EVS is not fully included. This type of PVS may therefore generate incorrect images. The goal is to make these errors as small as possible. Since a conservative PVS always generates correct images, it is often considered more useful. By overestimating or approximating the EVS, the idea is that the PVS can be computed much faster. The difficulty lies in how these estimations should be done to gain overall performance. For example, an algorithm may treat geometry at different granularities, i.e., polygons, whole objects, or groups of objects. When a PVS has been found, it is rendered using the  $Z$ -buffer, which resolves the final per-pixel visibility [185].

In the following sections, we treat backface and clustered backface culling, hierarchical view frustum culling, portal culling, detail culling, and occlusion culling.

### 14.2.1 Backface Culling

Imagine that you are looking at an opaque sphere in a scene. Approximately half of the sphere will not be visible. The obvious conclusion from this observation is that what is invisible need not be rendered since it does not contribute to the image. Therefore, the back side of the sphere need not be processed, and that is the idea behind backface culling. This type of culling can also be done for whole groups at a time, and so is called clustered backface culling.

All backfacing polygons that are part of a solid opaque object can be culled away from further processing, assuming the camera is outside of, and does not penetrate (i.e., near clip into), the object. A consistently oriented polygon (see Section 12.3) is backfacing if the projected polygon is known to be oriented in, say, a counterclockwise fashion in screen space. This test can be implemented by computing the normal of the projected polygon in two-dimensional screen space:  $\mathbf{n} = (\mathbf{v}_1 - \mathbf{v}_0) \times (\mathbf{v}_2 - \mathbf{v}_0)$ . This normal will either be  $(0, 0, a)$  or  $(0, 0, -a)$ , where  $a > 0$ . If the negative  $z$ -axis is pointing into the screen, the first result indicates a frontfacing polygon. This test can also be formulated as a computation of the signed area of the polygon (see Section A.5.4). Either culling test can be implemented immediately after the screen-mapping procedure has taken place (in the geometry stage). Backface culling decreases the load on the rasterizer since we do not have to scan convert the backfacing polygons. But the load on the geometry stage might increase because the backface computations are done there.

Another way to determine whether a polygon is backfacing is to create a vector from an arbitrary point on the plane in which the polygon lies (one of the vertices is the simplest choice) to the viewer's position.<sup>3</sup> Compute the dot product of this vector and the polygon's normal. A negative dot product means that the angle between the two vectors is greater than  $\pi/2$  radians, so the polygon is not facing the viewer. This test is equivalent to computing the signed distance from the viewer's position to the plane of the polygon (see Section A.5.2). If the sign is positive, the polygon is frontfacing. Note that the distance is obtained only if the normal is normalized, but this is unimportant here, as only the sign is of interest. These culling techniques are illustrated in Figure 14.10.

In the article “Backface Culling Snags” [105], Blinn points out that these two tests are geometrically the same. Both compute the dot product between the normal and the vector from a point on the polygon to the eye. In the test that is done in screen space, the eye has been transformed to  $(0, 0, \infty)$ , and the dot product is thus only the  $z$ -component of the polygon

---

<sup>3</sup>For orthographic projections, the vector to the eye position is replaced with the negative view direction, which is constant for the scene.

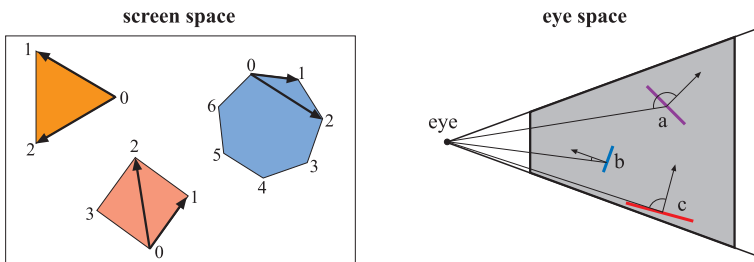


**Figure 14.10.** Two different tests for determining whether a polygon is backfacing. The left figure shows how the test is done in screen space. The triangle and the quadrilateral are frontfacing, while the seven-sided polygon is backfacing and can be omitted from rasterization. The right figure shows how the backface test is done in eye space. Polygon A is backfacing, while B and C are frontfacing.

vector in screen space. In theory, what differentiates these tests is the space where the tests are computed—nothing else. In practice, the screen-space test is often safer, because edge-on polygons that appear to face slightly backward in eye space can become slightly forward in screen space. This happens because the eye-space coordinates get rounded off to screen-space integer pixel or subpixel coordinates.

Using an API such as OpenGL or DirectX, backface culling is normally controlled with a few functions that either enable backface or frontface culling or disable all culling. Be aware that a mirroring transform (i.e., a negative scaling operation) turns backfacing polygons into frontfacing ones and vice versa [105] (see Section 4.1.3). Finally, it is worth noting that DirectX Shader Model 3.0 introduces a register that lets pixel shader programs know which side of a triangle is visible. Prior to this addition the main way to display two-sided objects properly was to render them twice, first culling backfaces then culling frontfaces and reversing the normals.

A common misconception about standard backface culling is that it cuts the number of polygons rendered by about half. While backface culling will remove about half of the polygons in many objects, it will provide little gain for some types of models. For example, the walls, floor, and ceiling of interior scenes are usually facing the viewer, so there are relatively few backfaces of these types to cull in such scenes. Similarly, with terrain rendering often most of the polygons are visible, only those on the back sides of hills or ravines benefit from this technique.

While backface culling is a simple technique for avoiding rasterizing individual polygons, it would be even faster if the CPU could decide with a single test if a whole set of polygons should be sent through the entire

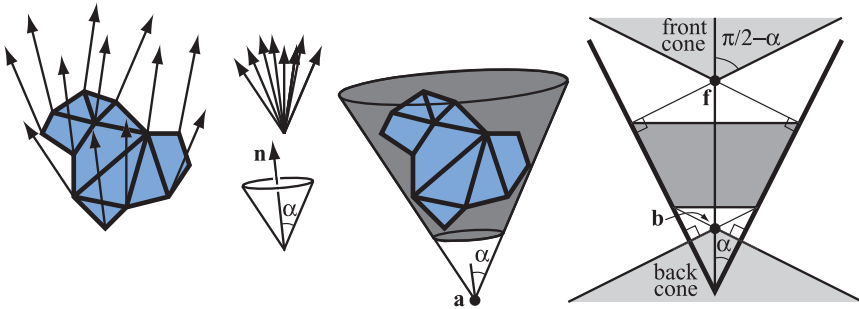


**Figure 14.11.** Left: a set of polygons and their normals. Middle-left: the normals are collected (top), and a minimal cone (bottom), defined by one normal  $\mathbf{n}$ , and a half-angle,  $\alpha$ , is constructed. Middle-right: the cone is anchored at a point  $\mathbf{a}$ , and truncated so that it also contains all points on the polygons. Right: a cross section of a truncated cone. The light gray region on the top is the frontfacing cone, and the light gray region at the bottom is the backfacing cone. The points  $\mathbf{f}$  and  $\mathbf{b}$  are respectively the apexes of the front and backfacing cones.

pipeline or not. Such techniques are called *clustered backface culling* algorithms. The basic concept that many such algorithms use is the *normal cone* [1173]. For some section of a surface, a truncated cone is created that contains all the normal directions and all the points. See Figure 14.11 for an example. As can be seen, a cone is defined by a normal,  $\mathbf{n}$ , and half-angle,  $\alpha$ , and an anchor point,  $\mathbf{a}$ , and some offset distances along the normal that truncates the cone. In the right part of Figure 14.11, a cross section of a normal cone is shown. Shirman and Abi-Ezzi [1173] prove that if the viewer is located in the frontfacing cone, then all faces in the cone are frontfacing, and similarly for the backfacing cone. There has been further work in this field by a number of researchers [612, 704, 1103]. Such techniques are less useful on modern GPUs, where a model is usually represented by a few complex meshes versus smaller patches. It can be useful in some situations, such as culling entire backfacing terrain tiles.

### 14.3 Hierarchical View Frustum Culling

As seen in Section 2.3.4, only primitives that are totally or partially inside the view frustum need to be rendered. One way to speed up the rendering process is to compare the bounding volume (BV) of each object to the view frustum. If the BV is outside the frustum, then the geometry it encloses can be omitted from rendering. Since these computations are done within the CPU, this means that the geometry inside the BV does not need to go through the geometry and the rasterizer stages in the pipeline.

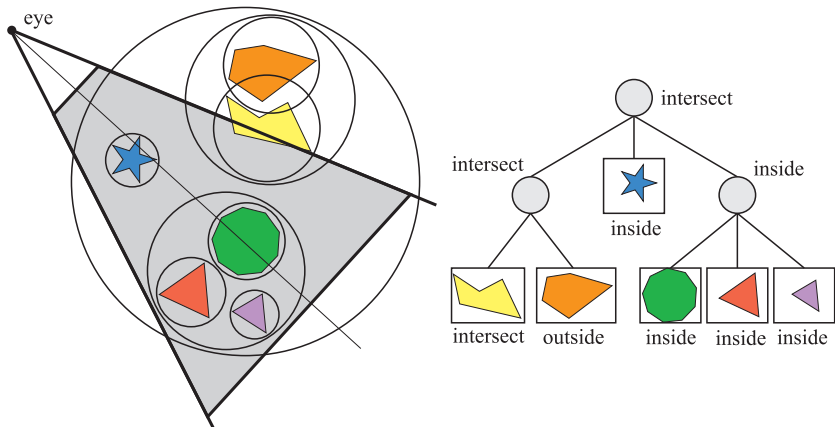


**Figure 14.12.** A set of geometry and its bounding volumes (spheres) are shown on the left. This scene is rendered with view frustum culling from the point of the eye. The BVH is shown on the right. The BV of the root intersects the frustum, and the traversal continues with testing its children's BVs. The BV of the left subtree intersects, and one of that subtree's children intersects (and thus is rendered), and the BV of the other child is outside and therefore is not sent through the pipeline. The BV of the middle subtree of the root is totally inside and is rendered immediately. The BV of the right subtree of the root is also fully inside, and the entire subtree can therefore be rendered without further tests.

If instead the BV is inside or intersecting the frustum, then the contents of that BV may be visible and must be sent through the rendering pipeline. See Section 16.14 for methods of testing for intersection between various bounding volumes and the view frustum.

By using a spatial data structure, this kind of culling can be applied hierarchically [179]. For a bounding volume hierarchy (BVH), a preorder traversal [201] from the root does the job. Each node with a BV is tested against the frustum. If the BV of the node is outside the frustum, then that node is not processed further. The tree is pruned, since the BV's contents and children are outside the view.

If the BV is fully inside the frustum, its contents must all be inside the frustum. Traversal continues, but no further frustum testing is needed for the rest of such a subtree. If the BV intersects the frustum, then the traversal continues and its children are tested. When a leaf node is found to intersect, its contents (i.e., its geometry) is sent through the pipeline. The primitives of the leaf are not guaranteed to be inside the view frustum. An example of view frustum culling is shown in Figure 14.12. It is also possible to use multiple BV tests for an object or cell. For example, if a sphere BV around a cell is found to overlap the frustum, it may be worthwhile to also

perform the more accurate (though more expensive) box/frustum test if this box is known to be much smaller than the sphere [1145].

A useful optimization for the “intersects frustum” case is to keep track of which frustum planes the BV is fully inside [89]. This information, usually stored as a bitmask, can then be passed with the intersector for testing children of this BV. Only those planes that intersected the BV need to be tested against the children. In this way, the root BV will be tested against 6 frustum planes, but as BVs come into view the number of plane/BV tests done at each child will go down.

View frustum culling operates in the application stage (CPU), which means that the load on the GPU can often be dramatically reduced. For large scenes or certain camera views, only a fraction of the scene might be visible, and it is only this fraction that needs to be sent through the rendering pipeline. In such cases a large gain in speed can be expected. View frustum culling techniques exploit the spatial coherence in a scene, since objects that are located near each other can be enclosed in a BV, and nearby BVs may be clustered hierarchically.

Other spatial data structures than the BVH can also be used for view frustum culling. This includes octrees and *Binary Space Partitioning* (BSP) trees [1099]. These methods are usually not flexible enough when it comes to rendering dynamic scenes. That is, it takes too long to update the corresponding data structures when an object stored in the structure moves (an exception is loose octrees). But for static scenes, these methods can perform better than BVHs. Hybrid methods can also be used, e.g., using BVs to tightly bound the contents of octree nodes. Another approach is to keep separate structures for static versus dynamic objects.

Polygon-aligned BSP trees are simple to use for view frustum culling. If the box containing the scene is visible, then the root node’s splitting plane is tested. If the plane intersects the frustum (i.e., if two corners on the frustum are found to be on opposite sides of the plane [see Section 16.10]), then both branches of the BSP tree are traversed. If instead, the view frustum is fully on one side of the plane, then whatever is on the other side of the plane is culled. Axis-aligned BSP trees and octrees are also simple to use. Traverse the tree from the root, and test each box in the tree during traversal. If a box is outside the frustum, traversal for that branch is terminated.

For view frustum culling, there is a simple technique for exploiting frame-to-frame coherency.<sup>4</sup> If a BV is found to be outside a certain plane of the frustum in one frame, then (assuming that the viewer does not move too quickly) it will probably be outside that plane in the next frame too. So if a BV was outside a certain plane, then an index to this plane is stored

---

<sup>4</sup>This is also called temporal coherency.

(cached) with the BV. In the next frame in which this BV is encountered during traversal, the cached plane is tested first, and on average a speedup can be expected [48].

If the viewer is constrained to only translation or rotation around one axis at a time from frame to frame, then this can also be exploited for faster frustum culling. When a BV is found to be outside a plane of the frustum, then the distance from that plane to the BV is stored with the BV. Now, if the viewer only, say, translates, then the distance to the BV can be updated quickly by knowing how much the viewer has translated. This can provide a generous speedup in comparison to a naive view frustum culler [48].

## 14.4 Portal Culling

For architectural models, there is a set of algorithms that goes under the name of *portal culling*. The first of these were introduced by Airey [5, 6] in 1990. Later, Teller and Séquin [1258, 1259] and Teller and Hanrahan [1260] constructed more efficient and more complex algorithms for portal culling. The rationale for all portal-culling algorithms is that walls often act as large occluders in indoor scenes. Portal culling is thus a type of occlusion culling, discussed in the next section. We treat portal culling here because of its importance. This occlusion algorithm uses a view frustum culling mechanism through each portal (e.g., door or window). When traversing a portal, the frustum is diminished to fit closely around the portal. Therefore, this algorithm can be seen as an extension of view frustum culling. Portals that are outside the view frustum are discarded.

Portal-culling methods preprocess the scene in some way. The scene is divided into *cells* that usually correspond to rooms and hallways in a building. The doors and windows that connect adjacent rooms are called *portals*. Every object in a cell and the walls of the cell are stored in a data structure that is associated with the cell. We also store information on adjacent cells and the portals that connect them in an adjacency graph. Teller presents algorithms for computing this graph [1259]. While this technique worked back in 1992 when it was introduced, for modern complex scenes automating the process is extremely difficult. For that reason defining cells and creating the graph is currently done by hand.

Luebke and Georges [799] use a simple method that requires only a small amount of preprocessing. The only information that is needed is the data structure associated with each cell, as described above. Rendering such a scene is accomplished through the following steps:

1. Locate the cell  $V$  where the viewer (eye) is positioned.

2. Initialize a two-dimensional bounding box  $P$  to the rectangle of the screen.
3. Render the geometry of the cell  $V$  using view frustum culling for the frustum that emanates from the viewer and goes through the rectangle  $P$  (initially the whole screen).
4. Recurse on portals of the cells neighboring  $V$ . For each visible portal of the current cell, project the portal onto the screen and find the two-dimensional axis-aligned *bounding box* (BB) of that projection. Compute the logical intersection of  $P$  and the BB of the portal (which is done with a few comparisons).
5. For each intersection: If it is empty, then the cell that is connected via that portal is invisible from the current point of view, and that cell can be omitted from further processing. If the intersection is not empty, then the contents of that neighbor cell can be culled against the frustum that emanates from the viewer and goes though the (rectangular) intersection.
6. If the intersection was not empty, then the neighboring cells of that neighbor may be visible, and so we recurse to Step 3 with  $P$  being the intersection BB. Each object may be tagged when it has been rendered in order to avoid rendering objects more than once.

An optimization that can well be worth implementing is to use the stencil buffer for more accurate culling. Since the portals are overestimated with an AABB, the real portal will most likely be smaller. The stencil buffer can be used to mask away rasterization (e.g., texturing and depth test) outside that real portal. Similarly, a scissor rectangle around the portal can be set for the accelerator to increase performance [4]. Stencil and scissor are particularly useful when dealing with a transparent object seen through multiple portals. The object should be rendered only once per portal in order to perform transparency correctly; multiple renderings of the same object in a portal will give an incorrect result.

The portal culling algorithm is illustrated in Figure 14.13 with an example. The viewer or eye is located in cell  $E$  and therefore rendered together with its contents. The neighboring cells are  $C$ ,  $D$ , and  $F$ . The original frustum cannot see the portal to cell  $D$  and is therefore omitted from further processing. Cell  $F$  is visible, and the view frustum is therefore diminished so that it goes through the portal that connects to  $F$ . The contents of  $F$  are then rendered with that diminished frustum. Then, the neighboring cells of  $F$  are examined— $G$  is not visible from the diminished frustum and so is omitted, while  $H$  is visible. Again, the frustum is diminished with the portal of  $H$ , and thereafter the contents of  $H$  are rendered.  $H$  does

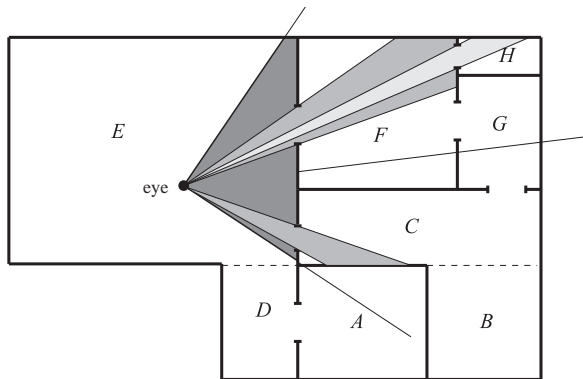


**Figure 14.13.** Portal culling: Cells are enumerated from  $A$  to  $H$ , and portals are openings that connect the cells. Only geometry seen through the portals is rendered.

not have any neighbors that have not been visited, so traversal ends there. Now, recursion falls back to the portal into cell  $C$ . The frustum is diminished to fit the portal of  $C$ , and then rendering of the objects in  $C$  follows, with frustum culling. No more portals are visible, so rendering is complete.

See Figure 14.14 for another view of the use of portals. This form of portal culling can also be used to trim content for planar reflections (see Section 9.3). The left image of the plate shows a building viewed from the top; the white lines indicate the way in which the frustum is diminished with each portal. The red lines are created by reflecting the frustum at a mirror. The actual view is shown in the image on the right side of the



**Figure 14.14.** Portal culling. The left image is an overhead view of the Brooks House. The right image is a view from the master bedroom. Cull boxes for portals are in white and for mirrors are in red. (*Images courtesy of David Luebke and Chris Georges, UNC-Chapel Hill.*)

same plate, where the white rectangles are the portals and the mirror is red. Note that it is only the objects inside any of the frustums that are rendered.

There are many other uses for portals. Mirror reflections can be created efficiently by transforming the viewer when the contents of a cell seen through a portal are about to be rendered. That is, if the viewer looks at a portal, then the viewer's position and direction can be reflected in the plane of that portal (see Section 9.3.1). Other transformations can be used to create other effects, such as simple refractions.

## 14.5 Detail Culling

*Detail culling* is a technique that sacrifices quality for speed. The rationale for detail culling is that small details in the scene contribute little or nothing to the rendered images when the viewer is in motion. When the viewer stops, detail culling is usually disabled. Consider an object with a bounding volume, and project this BV onto the projection plane. The area of the projection is then estimated in pixels, and if the number of pixels is below a user-defined threshold, the object is omitted from further processing. For this reason, detail culling is sometimes called *screen-size culling*. Detail culling can also be done hierarchically on a scene graph. The geometry and rasterizer stages both gain from this algorithm. Note that this could be implemented as a simplified LOD technique (see Section 14.7), where one LOD is the entire model, and the other LOD is an empty object.

## 14.6 Occlusion Culling

As we have seen, visibility may be solved via a hardware construction called the *Z-buffer* (see Section 2.4). Even though it may solve visibility correctly, the *Z-buffer* is not a very smart mechanism in all respects. For example, imagine that the viewer is looking along a line where 10 spheres are placed. This is illustrated in Figure 14.15. An image rendered from this viewpoint will show but one sphere, even though all 10 spheres will be rasterized and compared to the *Z-buffer*, and then potentially written to the color buffer and *Z-buffer*. The middle part of Figure 14.15 shows the depth complexity for this scene from the given viewpoint. Depth complexity refers to how many times each pixel is overwritten. In the case of the 10 spheres, the depth complexity is 10 for the pixel in the middle as 10 spheres are rendered there (assuming backface culling was on), and this means that 9 writes to the pixel are unnecessary. This uninteresting scene is not likely to be found in reality, but it describes (from the given viewpoint) a densely populated

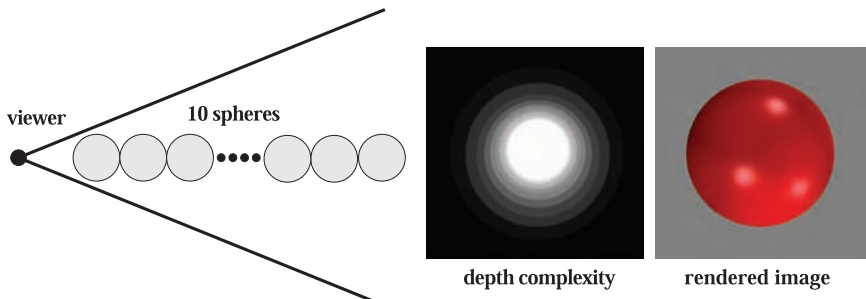


**Figure 14.15.** An illustration of how occlusion culling can be useful. Ten spheres are placed in a line, and the viewer is looking along this line (left). The depth complexity image in the middle shows that some pixels are written to several times, even though the final image (on the right) only shows one sphere.

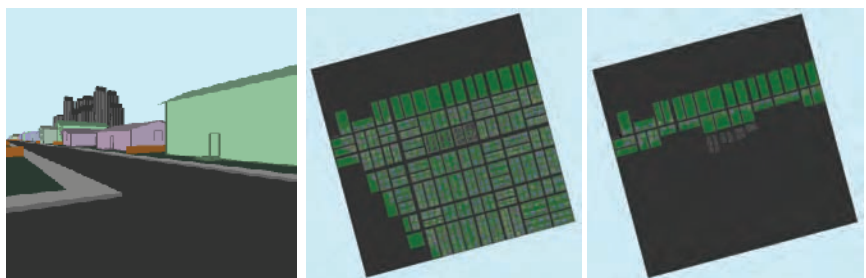


**Figure 14.16.** A simple city example, with a bird's eye view to show the effect of culling. The middle image shows view frustum culling, while the right shows occlusion culling and view frustum culling [277].

model. These sorts of configurations are found in real scenes such as those of a rain forest, an engine, a city, and the inside of a skyscraper. An example of a Manhattan-style city is shown in Figure 14.16.

Given the examples in the previous paragraph, it seems plausible that an algorithmic approach to avoid this kind of inefficiency may pay off in terms of speed. Such approaches go under the name of *occlusion culling algorithms*, since they try to cull away (avoid drawing) objects that are occluded, that is, hidden by other objects in the scene. The optimal occlusion culling algorithm would select only the objects that are visible. In a sense, the  $Z$ -buffer selects and renders only those objects that are visible, but not without having to send all objects inside the view frustum through most of the pipeline. The idea behind efficient occlusion culling algorithms

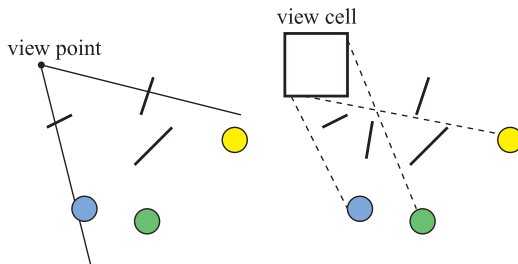


**Figure 14.17.** The left figure shows point-based visibility, while the right shows cell-based visibility, where the cell is a box. As can be seen, the circles are occluded to the left from the viewpoint. To the right, however, the circles are visible, since rays can be drawn from somewhere within the cell to the circles without intersecting any occluder.

is to perform some simple tests early on to cull sets of hidden objects. In a sense, backface culling is a simple form of occlusion culling. If we know in advance that an object is solid and is opaque, then the backfaces are occluded by the frontfaces and so do not need to be rendered.

There are two major forms of occlusion culling algorithms, namely point-based and cell-based. These are illustrated in Figure 14.17. Point-based visibility is just what is normally used in rendering, that is, what is seen from a single viewing location. Cell-based visibility, on the other hand, is done for a cell, which is a region of the space, normally a box or a sphere. An invisible object in cell-based visibility must be invisible from all points within the cell. The advantage of cell-based visibility is that once it is computed for a cell, it can usually be used for a few frames, as long as the viewer is inside the cell. However, it is usually more time consuming to compute than point-based visibility. Therefore, it is often done as a preprocessing step. Note that point-based and cell-based visibility often are compared to point and area light sources. For an object to be invisible, it has to be in the umbra region, i.e., fully occluded.

One can also categorize occlusion culling algorithms into those that operate in *image space*, *object space*, or *ray space*. Image-space algorithms do visibility testing in two dimensions after some projection, while object-space algorithms use the original three-dimensional objects. Ray space [90, 91, 685] methods perform their tests in a dual space. Each point (often two dimensional) of interest is converted to a ray in this dual space. The idea is that testing is simpler, more exact, or more efficient in this space.

Pseudocode for one type of occlusion culling algorithm is shown in Figure 14.18, where the function `isOccluded`, often called the *visibility test*, checks whether an object is occluded.  $G$  is the set of geometrical objects to be rendered,  $O_R$  is the occlusion representation, and  $P$  is a set of potential occluders that can be merged with  $O_R$ . Depending on the particular

```

1:   OcclusionCullingAlgorithm( $G$ )
2:    $O_R = \text{empty}$ 
3:    $P = \text{empty}$ 
4:   for each object  $g \in G$ 
5:     if(isOccluded( $g, O_R$ ))
6:       Skip( $g$ )
7:     else
8:       Render( $g$ )
9:       Add( $g, P$ )
10:      if(LargeEnough( $P$ ))
11:        Update( $O_R, P$ )
12:         $P = \text{empty}$ 
13:      end
14:    end
15:  end

```

**Figure 14.18.** Pseudocode for a general occlusion culling algorithm.  $G$  contains all the objects in the scene, and  $O_R$  is the occlusion representation.  $P$  is a set of potential occluders, that are merged into  $O_R$  when it contains sufficiently many objects. (After Zhang [1403].)

algorithm,  $O_R$  represents some kind of occlusion information.  $O_R$  is set to be empty at the beginning. After that, all objects (that pass the view frustum culling test) are processed.

Consider a particular object. First, we test whether the object is occluded with respect to the occlusion representation  $O_R$ . If it is occluded, then it is not processed further, since we then know that it will not contribute to the image. If the object cannot be determined to be occluded, then that object has to be rendered, since it probably contributes to the image (at that point in the rendering). Then the object is added to  $P$ , and if the number of objects in  $P$  is large enough, then we can afford to merge the *occluding power* of these objects into  $O_R$ . Each object in  $P$  can thus be used as an *occluder*.

Note that for the majority of occlusion culling algorithms, the performance is dependent on the order in which objects are drawn. As an example, consider a car with a motor inside it. If the hood of the car is drawn first, then the motor will (probably) be culled away. On the other hand, if the motor is drawn first, then nothing will be culled. Therefore, performance can be improved by techniques such as rough front-to-back sorting of the objects by their approximate distance from the viewer and rendering in this order. Also, it is worth noting that small objects potentially can be excellent occluders, since the distance to the occluder determines how

much it can occlude. As an example, a matchbox can occlude the Golden Gate Bridge if the viewer is sufficiently close to the matchbox.

### 14.6.1 Hardware Occlusion Queries

Modern GPUs support occlusion culling by using a special rendering mode.<sup>5</sup> Simply put, the user can query the hardware to find out whether a set of polygons is visible when compared to the current contents of the  $Z$ -buffer. These polygons most often form the bounding volume (for example, a box or  $k$ -DOP) of a more complex object. If none of these polygons are visible, then the object can be culled. The implementation in hardware rasterizes the polygons of the query and compares their depths to the  $Z$ -buffer. A count of the number of pixels  $n$  in which these polygons are visible is generated, though no pixels are actually modified. If  $n$  is zero, all polygons are occluded (or clipped). Therefore, the occlusion queries operate in image space. Similar queries are used by the hierarchical  $Z$ -buffer algorithm (Section 14.6.2).

If the pixel count  $n = 0$ , and the camera’s position is not inside the bounding volume,<sup>6</sup> then the entire bounding volume is completely occluded, and the contained objects can safely be discarded. If  $n > 0$ , then a fraction of the pixels failed the test. If  $n$  is smaller than a threshold number of pixels, the object could be discarded as being unlikely to contribute much to the final image [1360]. In this way, speed can be traded for possible loss of quality. Another use is to let  $n$  help determine the LOD (see Section 14.7) of an object. If  $n$  is small, then a smaller fraction of the object is (potentially) visible, and so a less detailed LOD can be used.

When the bounding volume is found to be obscured, we gain performance by avoiding sending the complex object through the rendering pipeline. However, if the test fails, we actually lose a bit of performance as we spent additional time testing this bounding volume to no benefit.

With such techniques, performance has been reported to be up to twice as fast as rendering that does not use any occlusion culling [1143]. For large city scenes or building interiors, gains could be even higher.

The latency of a query is often a relatively long time; often, hundreds or thousands of polygons can be rendered within this time (see Section 18.3.5

<sup>5</sup>This type of hardware support was first implemented on a Kubota Pacific Titan 3000 computer with Denali GB graphics hardware [450].

<sup>6</sup>More precisely, no part of the camera frustum’s visible near plane should be inside the bounding volume. For orthographic views, used in CAD applications, the camera is normally fully outside of all objects, so this is not a problem. For perspective viewing, this near-plane case is important. One solution is to be conservative, never testing such bounding volumes for occlusion.

for more on latency). Hence, this GPU-based occlusion culling method is worthwhile when the bounding boxes contain a large number of objects and a relatively large amount of occlusion is occurring.

On HP's VISUALIZE fx hardware (circa 2000), bounding boxes are created automatically and queried for sufficiently long display lists [213]. It has been shown that using tighter bounding volumes can speed up rendering. Bartz et al. [69] achieved a 50 percent increase in frame rate using  $k$ -DOPs (26-DOPs) for mechanical CAD models (where the interiors of the objects often are complex).

The GPU's occlusion query has been used as the basic building block for a number of algorithms. Meißner et al. [851] use occlusion queries in a hierarchical setting. The scene is represented in a hierarchical data structure, such as a BVH or octree. First, view frustum culling is used to find nodes not fully outside the view frustum. These are sorted, based on a node's center point (for example, the center of a bounding box), in front-to-back order. The nearest leaf node is rendered without occlusion testing to the frame buffer. Using the occlusion query, the BVs of subsequent objects are tested. If a BV is visible, its contents are tested recursively, or rendered. Kłosowski and Silva have developed a constant-frame-rate algorithm using an occlusion culling algorithm, called the *prioritized-layered projection* algorithm [674]. However, at first this was not a conservative algorithm, i.e., it sacrificed image quality in order to keep a constant frame rate. Later, they developed a conservative version of the algorithm, using occlusion queries [675].

The research just described was done with graphics hardware that had a serious limitation: When an occlusion query was made (which was limited to a boolean), the CPU's execution was stalled until the query result was returned. Modern GPUs have adopted a model in which the CPU can send off any number of queries to the GPU, then periodically check to see if any results are available. For its part, the GPU performs each query and puts the result in a queue. The queue check by the CPU is extremely fast, and the CPU can continue to send down queries or actual renderable objects without having to stall.

How to effectively use this model of a queue of queries is an active area of research. The problem is that a query must be done after some actual geometry has been rendered to the screen, so that the bounding box tested is more likely to be occluded, but not so late in the rendering process that the CPU is left waiting for the results of the query. Among other optimizations, Sekulic [1145] recommends taking advantage of temporal coherence. Objects are tested for occlusion, but the results are not checked until the next frame. If an object was found to be occluded in the previous frame, it is not rendered this frame, but it is tested for occlusion again. This gives an approximate occlusion test, since an object could be visible

but not rendered for a frame, but with a high frame rate, the problem is not that serious.

Objects that were visible in the previous frame are handled in a clever way. First, the object itself is used for the query: The object is rendered normally, while also issuing a query for visibility. This technique avoids having to render the test bounding box itself. Next, visible objects do not need to all issue queries every frame. By having a visible object tested for occlusion every few frames, fewer occlusion queries need to be dealt with each frame, at the small cost of occasionally rendering an object that could have been found to be occluded.

Bittner and Wimmer [92, 1360] wish to avoid any errors from temporal coherence, while reaping its benefits. Their approach starts with traversing a hierarchical efficiency structure, rendering objects in a front-to-back order. Only leaf nodes hold objects in their scheme. Leaf nodes and previously hidden internal nodes are tested for occlusion. Visibility states from frame to frame are compared, with changes potentially causing further hierarchy updates and leaf node renderings. Despite the fact that internal nodes are also sometimes queried using this approach, the authors' approach guarantees that the total number of queries will never be greater than the number of leaf nodes. The major benefit of their technique is that much rendering time can be saved when internal nodes are found to be occluded.

The number of queries that are worth performing in a frame is limited, and each query costs some time. As such, queries should be performed on objects most likely to be occluded. Kovalčík and Sochor [694] collect running statistics on queries over a number of frames for each object while the application is running. The number of frames in which an object was found to be hidden affects how often it is tested for occlusion in the future. That is, objects that are visible are likely to stay visible, and so can be tested less frequently. Hidden objects get tested every frame, if possible, since these objects are most likely to benefit from occlusion queries. Guthe et al. [470] likewise explore performing a running statistical analysis, and their system adapts to the underlying GPU.

The schemes discussed here give a flavor of the potential and problems with occlusion culling methods. When to use occlusion queries, or most occlusion schemes in general, is not often clear. If everything is visible, an occlusion algorithm can only cost additional time, never save it. Rapidly determining that the algorithm is not helping, and so cutting back on its fruitless attempts to save time, is one challenge. Another problem is deciding what set of objects to use as occluders. The first objects rendered that are inside the frustum must be visible, so spending queries on these is wasteful. This problem of choosing occluders is a challenge for most of the algorithms in this section.

Nonetheless, hardware occlusion query systems have proven to be useful, especially when depth complexity is high. Statistical methods track whether and when occlusion testing is likely to be effective, so they have good adaptive properties. Systems based on this basic building block of the occlusion query are by far the most commonly used occlusion culling schemes used with modern GPUs. The rest of this section will therefore be limited to discussion of one algorithm that has been important in its effect on the GPU’s architecture, with a brief survey of the rest.

### 14.6.2 Hierarchical $Z$ -Buffering

*Hierarchical Z-buffering* (HZB), an algorithm developed by Greene et al., [450, 452] has had a significant influence on occlusion culling research. Though the CPU-side form presented here is rarely used, the algorithm is the basis for the GPU hardware method of  $Z$ -culling (Section 18.3.7).

The algorithm maintains the scene model in an octree, and a frame’s  $Z$ -buffer as an image pyramid, which we call a  $Z$ -pyramid—the algorithm thus operates in image space. The octree enables hierarchical culling of occluded regions of the scene, and the  $Z$ -pyramid enables hierarchical  $Z$ -buffering of individual primitives and bounding volumes. The  $Z$ -pyramid is thus the occlusion representation of this algorithm. Examples of these data structures are shown in Figure 14.19. Any method can be employed for organizing scene primitives in an octree, although Greene et al. [450] recommend a specific algorithm that avoids assigning small primitives to large octree nodes.

Now we will describe how the  $Z$ -pyramid is maintained and how it is used to accelerate culling. The finest (highest-resolution) level of the  $Z$ -pyramid is simply a standard  $Z$ -buffer. At all other levels, each  $z$ -value is the farthest  $z$  in the corresponding  $2 \times 2$  window of the adjacent finer level. Therefore, each  $z$ -value represents the farthest  $z$  for a square region of the screen. Whenever a  $z$ -value is overwritten in the  $Z$ -buffer, it is propagated through the coarser levels of the  $Z$ -pyramid. This is done recursively until the top of the image pyramid is reached, where only one  $z$ -value remains. Pyramid formation is illustrated in Figure 14.20.

Hierarchical culling of octree nodes is done as follows. Traverse the octree nodes in a rough front-to-back order. A bounding box of the octree is tested against the  $Z$ -pyramid using an extended occlusion query (Section 14.6.1). We begin testing at the coarsest  $Z$ -pyramid cell that encloses the box’s screen projection. The box’s nearest depth within the cell ( $z_{near}$ ) is then compared to the  $Z$ -pyramid value, and if  $z_{near}$  is farther, the box is known to be occluded. This testing continues recursively down the  $Z$ -pyramid until the box is found to be occluded, or until the bottom level of the  $Z$ -pyramid is reached, at which point the box is known to be visible.

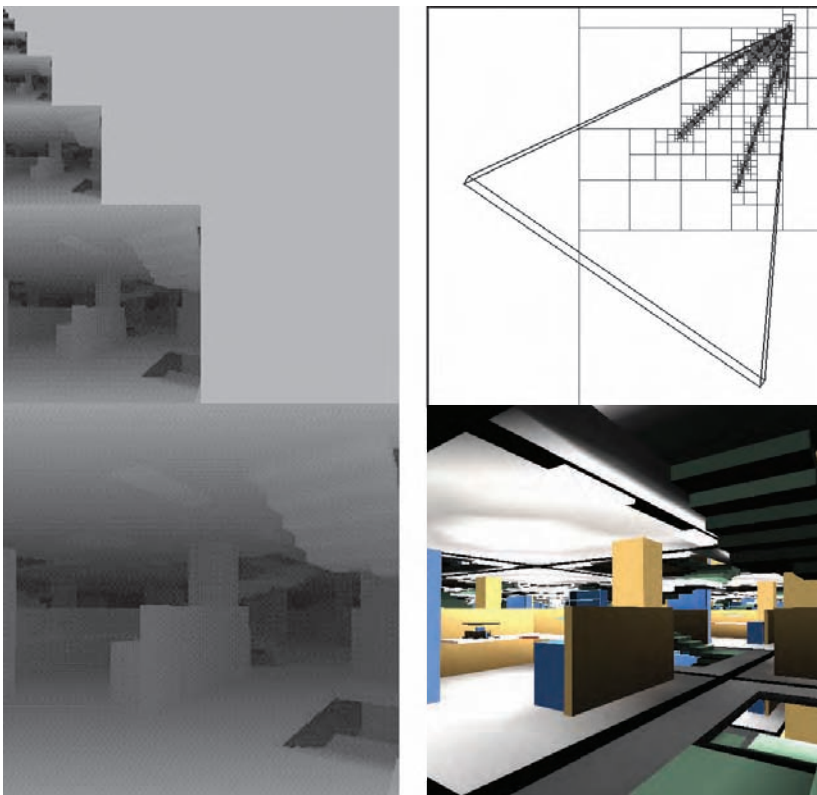


**Figure 14.19.** Example of occlusion culling with the HZB algorithm [450, 452], showing a complex scene (lower right) with the corresponding Z-pyramid (on the left), and octree subdivision (upper right). By traversing the octree from front-to-back and culling occluded octree nodes as they are encountered, this algorithm visits only visible octree nodes and their children (the nodes portrayed at the upper right) and renders only the polygons in visible boxes. In this example, culling of occluded octree nodes reduces the depth complexity from 84 to 2.5. (*Image courtesy of Ned Greene/Apple Computer.*)

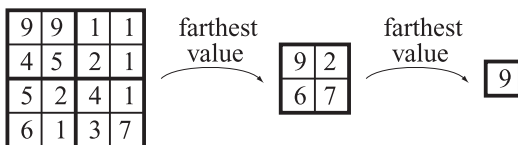


**Figure 14.20.** On the left, a  $4 \times 4$  piece of the Z-buffer is shown. The numerical values are the actual  $z$ -values. This is downsampled to a  $2 \times 2$  region where each value is the farthest (largest) of the four  $2 \times 2$  regions on the left. Finally, the farthest value of the remaining four  $z$ -values is computed. These three maps compose an image pyramid that is called the hierarchical Z-buffer.

For visible octree boxes, testing continues recursively down in the octree, and finally potentially visible geometry is rendered into the hierarchical Z-buffer. This is done so that subsequent tests can use the occluding power of previously rendered objects.

### 14.6.3 Other Occlusion Culling Techniques

There has been a large body of work on occlusion culling techniques. Much of it has fallen out of favor, due to the performance of GPUs outpacing CPUs. As such, a brief tour of some schemes are presented here. These are worth at least some passing knowledge because architectures are constantly evolving. With the rise of multicore systems, the CPU-side has additional resources that are difficult to bring directly to bear on rendering itself. Using one or more cores to perform cell-based visibility testing or other schemes is certainly conceivable.

The *hierarchical occlusion map* (HOM) algorithm [1402, 1403], like hierarchical Z-buffering, is a way of enabling hierarchical image-space culling. It differs from HZB in that it offers the ability to use approximate occlusion culling. Each frame a hierarchical depth buffer is built up for occlusion testing. An opacity threshold is used at each level to determine if enough of the object about to be drawn is visible. If only a small portion of the object is potentially visible then the object is culled. As a CPU-driven system, this algorithm has fallen out of favor.

The idea of *occlusion horizons* has been used in computer games since at least 1995 [864]. Wonka and Schmalstieg [1369] and Downs et al. [277] discuss two variants. This type of algorithm was often used for efficiently rendering urban environments, that is, cities and villages. By rendering such scenes front to back, the horizon drawn can be tracked. Any object found to be both behind and below the current horizon can then be culled. While its use for cities is dated, Fiedler [342] presents a horizon-based occlusion culling scheme for mountainous scenes in a GPU-based terrain rendering system.

The occlusion horizon algorithm is point-based. Cell-based visibility is sometimes preferable, but is in general much more complex to compute than point-based visibility. *Occluder shrinking* is a technique developed by Wonka et al. [1370] that can use a point-based occlusion algorithm to generate cell-based visibility. The idea is to extend the validity of point visibility by shrinking all occluders in the scene by a given amount. They also present *frustum growing* [1371, 1372], which is often used in conjunction with occluder shrinking. Given that the viewer can move and change orientation at certain speeds, a grown frustum is created that includes all possible changes in view position and orientation.

Schaufler et al. [1117] uses shafts (Section 16.15) for occlusion culling. It has been used for visibility preprocessing for walkthroughs in city scenes. Like occluder shrinking, it is designed to be cell-based, and uses interesting techniques to fuse occluders. By determining what cells are fully occluded, a large number of cells and their geometry can quickly be culled away.

An algorithm called “instant visibility” uses occluder shrinking and frustum growing to compute visibility on the fly, simultaneous to rendering done on another machine [1371]. The basic idea is to calculate visibility in parallel to the rendering pipeline on a visibility server, possibly a distinct computer communicating with the display host over a local network. In the resulting system, the display host continues rendering new frames while the visibility server calculates visibility for future frames. Therefore, a visibility solution is always ready at the start of each frame, and no additional latency is introduced to the rendering pipeline. With today’s multicore architectures such lookahead schemes become more useful. Allotting more than one rendering frame to visibility calculations allows for improved visibility solutions. The instant visibility system combines the advantages of online visibility processing and cell-based visibility by decoupling visibility calculations and rendering. Another algorithm for cell-based visibility is presented by Koltun et al. [684], where they notice that the fusion of several occluders can be replaced by a much simpler occluder that covers almost as much. Such a replacement is called a *virtual occluder*.

Aila and Miettinen [3, 4] implement what they call *incremental occlusion maps* (IOM) by combining several different existing algorithms with new techniques. Their implementation can handle dynamic scenes at impressive rates. However, it is a complex system to implement.

## 14.7 Level of Detail

The basic idea of *levels of detail* (LODs) is to use simpler versions of an object as it makes less and less of a contribution to the rendered image. For example, consider a detailed car that may consist of a million triangles. This representation can be used when the viewer is close to the car. When the object is farther away, say covering only 200 pixels, we do not need all one million triangles. Instead, we can use a simplified model that has only, say, 1000 triangles. Due to the distance, the simplified version looks approximately the same as the more detailed version. In this way, a significant performance increase can be expected.

Fog, described in Section 10.15, is often used together with LODs. This allows us to completely skip the rendering of an object as it enters opaque fog. Also, the fogging mechanism can be used to implement time-critical rendering (see Section 14.7.3). By moving the far plane closer to the viewer,

objects can be culled earlier, and more rapid rendering can be achieved to keep the frame rate up.

Some objects, such as spheres, Bézier surfaces, and subdivision surfaces, have levels of detail as part of their geometrical description. The underlying geometry is curved, and a separate LOD control determines how it is tessellated into displayable polygons. In this section we describe some common methods for using such LODs. See Section 13.6.4 for algorithms that adapt the quality of tessellations for parametric surfaces and subdivision surfaces.

In general, LOD algorithms consist of three major parts, namely, *generation*, *selection*, and *switching*. LOD generation is the part where different representations of a model are generated with different detail. The simplification methods discussed in Section 12.5 can be used to generate the desired number of LODs. Another approach is to make models with different numbers of triangles by hand. The selection mechanism chooses a level of detail model based on some criteria, such as estimated area on the screen. Finally, we need to change from one level of detail to another, and this process is termed *LOD switching*. Different LOD switching and selection mechanisms are presented in this section.

While the focus in this section is on choosing among different geometric representations, the ideas behind LODs can also be applied to other aspects of the model, or even to the rendering method used. Lower level of detail models can also use lower quality textures and shaders, thereby further saving memory and computation time [164]. Shaders themselves can be simplified depending on distance, importance, or other factors [959, 996]. Kajiya [618] presents a hierarchy of scale showing how surface lighting models overlap texture mapping methods, which in turn overlap geometric details. Another technique is that fewer bones can be used for skinning operations for distance objects.

When static objects are relatively far away, impostors (Section 10.7.1) are a natural way to represent them at little cost [806]. Other surface rendering methods, such as bump or relief mapping, can be used to simplify the representation of a model. Figure 14.21 gives an example. Teixeira [1257] discusses how to bake normal maps onto surfaces using the GPU. The most noticeable flaw with this simplification technique is that the silhouettes lose their curvature. Loviscach [797] presents a method of extruding fins along silhouette edges to create curved silhouettes.

An example of the range of techniques that can be used to represent an object is from Lengyel et al. [764, 765]. In this research, fur is represented by geometry when extremely close up, by alpha blended polylines when further away, then by a blend with volume texture “shells,” finally becoming a texture map when far away. See Figure 14.22. Knowing when and how best to switch from one set of modeling and rendering techniques to another in



**Figure 14.21.** On the left, the original model consists of 1.5 million triangles. On the right, the model has 1100 triangles, with surface details stored as heightfield textures and rendered using relief mapping. (*Image courtesy of Natalya Tatarchuk, ATI Research, Inc.*)



**Figure 14.22.** From a distance, the bunny's fur is rendered with volumetric textures. When the bunny comes closer, the hair is rendered with alpha blended polylines. When close up, the fur along the silhouette is rendered with graftal fins. (*Image courtesy of Jed Lengyel and Michael Cohen, Microsoft Research.*)

order to maximize frame rate and quality is still an art and an open area for exploration.

### 14.7.1 LOD Switching

When switching from one LOD to another, an abrupt model substitution is often noticeable and distracting. This difference is called *popping*. Several different ways to perform this switching will be described here, and they all have different popping traits.

#### Discrete Geometry LODs

In the simplest type of LOD algorithm, the different representations are models of the same object containing different numbers of primitives. This algorithm is well-suited for modern graphics hardware [801], because these separate static meshes can be stored in GPU memory and reused (see Section 18.3.4 and Section 12.4.5). A more detailed LOD has a higher number of primitives. An example of three LODs of an object is shown in Figure 14.23. This figure also shows the different LODs at different distances from the viewer. The switching from one LOD to another just

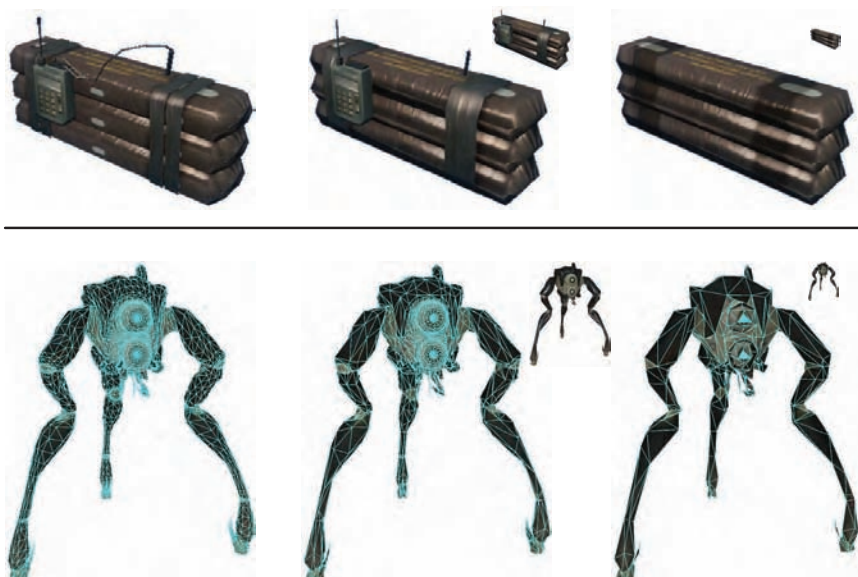


**Figure 14.23.** Here, we show three different levels of detail for models of C4 explosives and a Hunter. Elements are simplified or removed altogether at lower levels of detail. The small inset images show the simplified models at the relative sizes they might be used. (*Upper row of images courtesy of Crytek; lower row courtesy of Valve Corp.*)

happens, that is, on the current frame a certain LOD is used. Then on the next frame, the selection mechanism selects another LOD, and immediately uses that for rendering. Popping is typically the worst for this type of LOD method. Better alternatives are described next.

### *Blend LODs*

Conceptually, an obvious way to switch is to do a linear blend between the two LODs over a short period of time. Doing so will certainly make for a smoother switch. Rendering two LODs for one object is naturally more expensive than just rendering one LOD, so this somewhat defeats the purpose of LODs. However, LOD switching usually takes place during only a short amount of time, and often not for all objects in a scene at the same time, so the quality improvement may very well be worth the cost.

Assume a transition between two LODs—say LOD1 and LOD2—is desired, and that LOD1 is the current LOD being rendered. The problem is in how to render and blend both LODs in a reasonable fashion. Making both LODs semitransparent will result in a semitransparent (though somewhat more opaque) object being rendered to the screen. Writing separate offscreen targets and blending these is expensive and has its own problems.

Giegl and Wimmer [394] propose a blending method that works well in practice and is simple to implement. First draw LOD1 opaquely to the frame buffer (both color and  $Z$ ). Then fade in LOD2 by increasing its alpha value from 0 to 1 and using the “over” blend mode, described in Section 5.7. When LOD2 has faded so it is completely opaque, it is turned into the current LOD, and LOD1 is then faded out. The LOD that is being faded (in or out) should be rendered with the  $z$ -test enabled and  $z$ -writes disabled. To avoid distant objects that are drawn later drawing over the results of rendering the faded LOD, simply draw all faded LODs in sorted order after all opaque content, as is normally done for transparent objects. Note that in the middle of the transition, both LODs are rendered opaquely, one on top of the other. This technique works best if the transition intervals are kept short, which also helps keep the rendering overhead small. Mittring [887] discusses a similar method, except that screen-door transparency (potentially at the subpixel level) is used to dissolve between versions.

### *Alpha LODs*

A simple method that avoids popping altogether is to use what we call alpha LODs. This technique can be used by itself or combined with other LOD switching techniques. It is used on the original model or the simplest visible LOD. As the metric used for LOD selection (e.g., distance to this object) increases the overall transparency of the object is increased ( $\alpha$  is

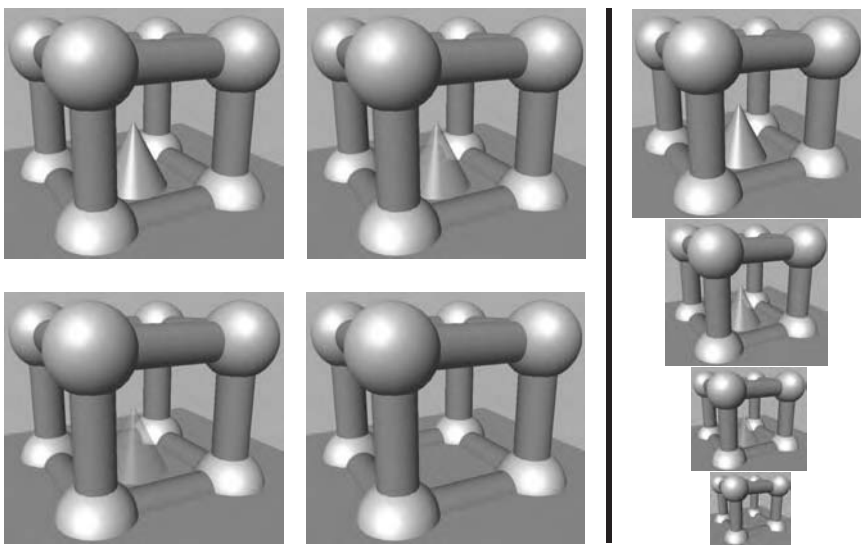


**Figure 14.24.** The cone in the middle is rendered using an alpha LOD. The transparency of the cone is increased when the distance to it increases, and it finally disappears. The images on the left are shown from the same distance for viewing purposes, while the images to the right of the line are shown at different sizes.

decreased), and the object finally disappears when it reaches full transparency ( $\alpha = 0.0$ ). This happens when the metric value is larger than a user-defined invisibility threshold. There is also another threshold that determines when an object shall start to become transparent. When the invisibility threshold has been reached, the object need not be sent through the rendering pipeline at all as long as the metric value remains above the threshold. When an object has been invisible and its metric falls below the invisibility threshold, then it decreases its transparency and starts to be visible again.

The advantage of using this technique standalone is that it is experienced as much more continuous than the discrete geometry LOD method, and so avoids popping. Also, since the object finally disappears altogether and need not be rendered, a significant speedup can be expected. The disadvantage is that the object entirely disappears, and it is only at this point that a performance increase is obtained. Figure 14.24 shows an example of alpha LODs.

One problem with using alpha transparency is that sorting by depth needs to be done to ensure transparency blends correctly. To fade out distant vegetation, Whatley [1350] discusses how a noise texture can be used for screen-door transparency. This has the effect of a dissolve, with more texels on the object disappearing as the distance increases. While

the quality is not as good as a true alpha fade, screen-door transparency means that no sorting is necessary.

### CLODs and Geomorph LODs

The process of mesh simplification can be used to create various LOD models from a single complex object. Algorithms for performing this simplification are discussed in Section 12.5.1. One approach is to create a set of discrete LODs and use these as discussed previously. However, edge collapse methods have an interesting property that allows other ways of making a transition between LODs.

A model has two fewer polygons after each edge collapse operation is performed. What happens in an edge collapse is that an edge is shrunk until its two endpoints meet and it disappears. If this process is animated, a smooth transition occurs between the original model and its slightly simplified version. For each edge collapse, a single vertex is joined with another. Over a series of edge collapses, a set of vertices move to join other vertices. By storing the series of edge collapses, this process can be reversed, so that a simplified model can be made more complex over time. The reversal of an edge collapse is called a *vertex split*. So one way to change the level of detail of an object is to precisely base the number of polygons visible on the LOD selection value. At 100 meters away, the model might consist of 1000 polygons, and moving to 101 meters, it might drop to 998 polygons. Such a scheme is called a *continuous level of detail* (CLOD) technique. There is not, then, a discrete set of models, but rather a huge set of models available for display, each one with two less polygons than its more complex neighbor. While appealing, using such a scheme in practice has some drawbacks. Not all models in the CLOD stream look good. Polygonal meshes, which can be rendered much more rapidly than single triangles, are more difficult to use with CLOD techniques than with static models. If there are a number of the same objects in the scene, then each CLOD object needs to specify its own specific set of triangles, since it does not match any others. Bloom [113] and Forsyth [351] discuss solutions to these and other problems.

In a vertex split, one vertex becomes two. What this means is that every vertex on a complex model comes from some vertex on a simpler version. *Geomorph LODs* [560] are a set of discrete models created by simplification, with the connectivity between vertices maintained. When switching from a complex model to a simple one, the complex model's vertices are interpolated between their original positions and those of the simpler version. When the transition is complete, the simpler level of detail model is used to represent the object. See Figure 14.25 for an example of a transition. There are a number of advantages to geomorphs. The individual static models can be selected in advance to be of high quality, and easily



**Figure 14.25.** The left and right images show a low detail model and a higher detail model. The image in the middle shows a geomorph model interpolated approximately halfway between the left and right models. Note that the cow in the middle has equally many vertices and triangles as the model to the right. (*Images generated using Melax’s “Polychop” simplification demo [852].*)

can be turned into polygonal meshes. Like CLOD, popping is also avoided by smooth transitions. The main drawback is that each vertex needs to be interpolated; CLOD techniques usually do not use interpolation, so the set of vertex positions themselves never changes. Another drawback is that the objects always appear to be changing, which may be distracting. This is especially true for textured objects. Sander and Mitchell [1107] describe a system in which geomorphing is used in conjunction with static, GPU-resident vertex and index buffers.

A related idea called fractional tessellation has been finding its way onto hardware. In such schemes, the tessellation factor for a curved surface can be set to any floating point number, and so a popping can be avoided. Fractional tessellation has been used for Bézier patches, and displacement mapping primitives. See Section 13.6.2 for more on these techniques.

### 14.7.2 LOD Selection

Given that different levels of detail of an object exist, a choice must be made for which one of them to render, or which ones to blend. This is the task of LOD selection, and a few different techniques for this will be presented here. These techniques can also be used to select good occluders for occlusion culling algorithms.

In general, a metric, also called the benefit function, is evaluated for the current viewpoint and the location of the object, and the value of this metric picks an appropriate LOD. This metric may be based on, for example, the projected area of the bounding volume (BV) of the object or the distance from the viewpoint to the object. The value of the benefit function is denoted  $r$  here. See also Section 13.6.4 on how to rapidly estimate the projection of a line onto the screen.

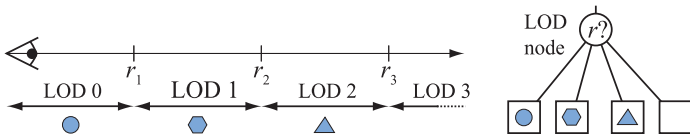


**Figure 14.26.** The left part of this illustration shows how range-based LODs work. Note that the fourth LOD is an empty object, so when the object is farther away than  $r_3$ , nothing is drawn, because the object is not contributing enough to the image to be worth the effort. The right part shows a LOD node in a scene graph. Only one of the children of a LOD node is descended based on  $r$ .

### Range-Based

A common way of selecting a LOD is to associate the different LODs of an object with different ranges. The most detailed LOD has a range from zero to some user-defined value  $r_1$ , which means that this LOD is visible when the distance to the object is less than  $r_1$ . The next LOD has a range from  $r_1$  to  $r_2$  where  $r_2 > r_1$ . If the distance to the object is greater than or equal to  $r_1$  and less than  $r_2$ , then this LOD is used, and so on. Examples of four different LODs with their ranges, and their corresponding LOD node used in a scene graph are illustrated in Figure 14.26.

### Projected Area-Based

Another common metric for LOD selection is the projected area of the bounding volume (or an estimation of it). Here, we will show how the number of pixels of that area, called the *screen-space coverage*, can be estimated for spheres and boxes with perspective viewing, and then present how the solid angle of a polygon can be efficiently approximated.

Starting with spheres, the estimation is based on the fact that the size of the projection of an object diminishes with the distance from the viewer along the view direction. This is shown in Figure 14.27, which illustrates how the size of the projection is halved if the distance from the viewer is doubled. We define a sphere by its center point  $\mathbf{c}$  and a radius  $r$ . The viewer is located at  $\mathbf{v}$  looking along the normalized direction vector  $\mathbf{d}$ . The distance from the view direction is simply the projection of the sphere's center onto the view vector:  $\mathbf{d} \cdot (\mathbf{c} - \mathbf{v})$ . We also assume that the distance from the viewer to the near plane of the view frustum is  $n$ . The near plane is used in the estimation so that an object that is located on the near plane returns its original size. The estimation of the radius of the projected sphere is then

$$p = \frac{nr}{\mathbf{d} \cdot (\mathbf{c} - \mathbf{v})}. \quad (14.3)$$

The area of the projection is thus  $\pi p^2$ . A higher value selects a more detailed LOD.

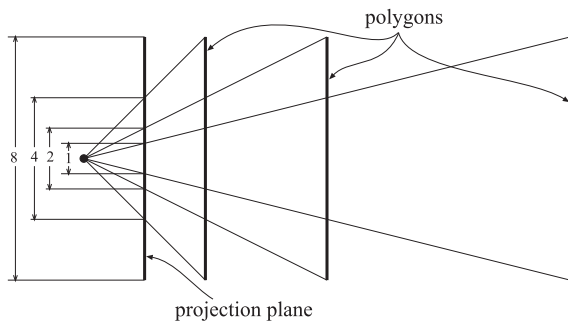


**Figure 14.27.** This illustration shows how the size of the projection of objects is halved when the distance is doubled.

It is common practice to simply use a bounding sphere around an object's bounding box. Thin or flat objects can vary considerably in the amount of projected area actually covered. Schmalstieg and Tobler have developed a rapid routine for calculating the projected area of a box [1130]. The idea is to classify the viewpoint of the camera with respect to the box, and use this classification to determine which projected vertices are included in the silhouette of the projected box. This process is done via a *look-up table* (LUT). Using these vertices, the area can be computed using the technique presented on page 910. The classification is categorized into three major cases, shown in Figure 14.28. Practically, this classification is done by determining on which side of the planes of the bounding box the viewpoint is located. For efficiency, the viewpoint is transformed into the coordinate system of the box, so that only comparisons are needed for classification. The result of the comparisons are put into a bitmask, which is used as an index into a LUT. This LUT determines how many vertices there are in the silhouette as seen from the viewpoint. Then, an-

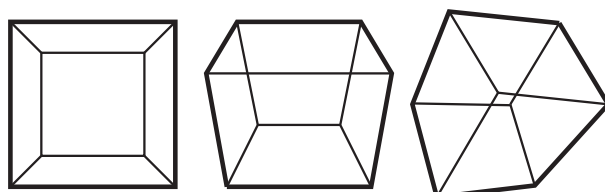


**Figure 14.28.** Three cases of projection of a cube, showing one, two, and three frontfaces. (Illustration after Schmalstieg and Tobler [1130].)

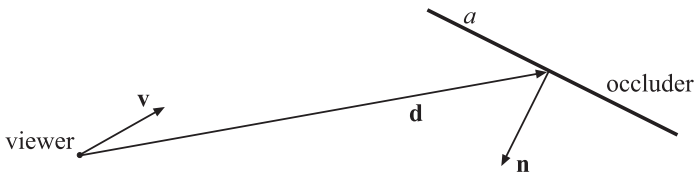


**Figure 14.29.** The geometry involved in the estimation of the solid angle.

other lookup is used to actually find the silhouette vertices. After they have been projected to the screen, the area is computed. Source code is available on the web.

To select a good occluder, Coorg and Teller [199] estimate the solid angle that a polygon subtends. This can also be used for LOD selection. Their approximation is

$$r = -\frac{a(\mathbf{n} \cdot \mathbf{v})}{\mathbf{d} \cdot \mathbf{d}}. \quad (14.4)$$

Here,  $a$  is the area of the polygon,  $\mathbf{n}$  is the normal of the polygon,  $\mathbf{v}$  is the view direction vector, and  $\mathbf{d}$  is the vector from the viewpoint to the center of the polygon. Both  $\mathbf{v}$  and  $\mathbf{n}$  are assumed to be normalized. The geometry involved is shown in Figure 14.29. The higher the value of  $r$ , the higher benefit. The solid angle approximation estimates the benefit because the larger the area, the larger the value, and the value is inversely proportional to the distance to the polygon. Also, the maximum value is reached when the viewer looks at a polygon “head-on,” and the value decreases with an increasing angle between the polygon normal and the view direction [199]. However, this property is mostly useful for occluder selection and not for LOD selection.

### Hysteresis

Unnecessary popping can occur if the metric used to determine which LOD to use varies from frame to frame around some value,  $r_i$ . A rapid cycling back and forth between levels can occur. This can be solved by introduc-

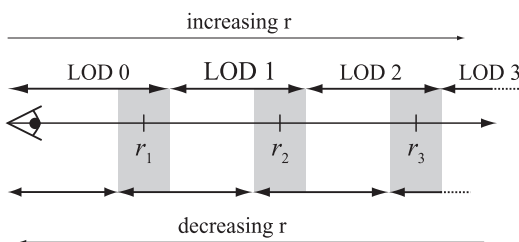


**Figure 14.30.** The gray areas illustrate the hysteresis regions for the LOD technique.

ing some hysteresis around the  $r_i$  value [661, 1079]. This is illustrated in Figure 14.30 for a range-based LOD, but applies to any type. Here, the upper row of LOD ranges are used only when  $r$  is increasing. When  $r$  is decreasing, the bottom row of ranges is used.

### Other Selection Methods

Range-based and projected area-based LOD selection are typically the most common metrics used. However, many other are possible, and some will be mentioned here. Besides projected area, Funkhouser and Séquin [371] also suggest using the importance of an object (e.g., walls are more important than a clock on the wall), motion, hysteresis (when switching LOD the benefit is lowered), and focus. The viewer’s focus of attention can be an important factor. For example, in a sports game, the figure controlling the ball is where the user will be paying the most attention, so the other characters can have relatively lower levels of detail [661].

Depending on the application, other strategies may be fruitful. Overall visibility can be used, e.g., a nearby object seen through dense foliage can be rendered with a lower LOD. More global metrics are possible, such as limiting the overall number of highly detailed LODs used in order to stay within a given polygon budget [661]. See the next section for more on this topic. Other factors are visibility, colors, and textures. Perceptual metrics can also be used to choose a LOD [1051].

### 14.7.3 Time-Critical LOD Rendering

It is often a desirable feature of a rendering system to have a constant frame rate. In fact, this is what often is referred to as “hard real time” or time-critical. Such a system is given a specific amount of time, say 30 ms, and must complete its task (e.g., render the image) within that time. When time is up, the system has to stop processing. A hard real-time rendering algorithm can be achieved if the objects in a scene are represented by, for example, LODs.

Funkhouser and Séquin [371] have presented a heuristic algorithm that adapts the selection of the level of detail for all visible objects in a scene to meet the requirement of constant frame rate. This algorithm is *predictive* in the sense that it selects the LOD of the visible objects based on desired frame rate and on which objects are visible. Such an algorithm contrasts with a *reactive* algorithm, which bases its selection on the time it took to render the previous frame.

An object is called  $O$  and is rendered at a level of detail called  $L$ , which gives  $(O, L)$  for each LOD of an object. Two heuristics are then defined. One heuristic estimates the cost of rendering an object at a certain level of detail:  $\text{Cost}(O, L)$ . Another estimates the benefit of an object rendered at

a certain level of detail:  $\text{Benefit}(O, L)$ . The benefit function estimates the contribution to the image of an object at a certain LOD.

Assume the objects inside or intersecting the view frustum are called  $S$ . The main idea behind the algorithm is then to optimize the selection of the LODs for the objects  $S$  using the heuristically chosen functions. Specifically, we want to maximize

$$\sum_S \text{Benefit}(O, L) \quad (14.5)$$

under the constraint

$$\sum_S \text{Cost}(O, L) \leq \text{TargetFrameTime}. \quad (14.6)$$

In other words, we want to select the level of detail for the objects that gives us “the best image” within the desired frame rate. Next we describe how the cost and benefit functions can be estimated, and then we present an optimization algorithm for the above equations.

Both the cost function and the benefit function are hard to define so that they work under all circumstances. The cost function can be estimated by timing the rendering of a LOD several times with different viewing parameters. See Section 14.7.2 for different benefit functions. In practice, the projected area of the BV of the object often suffices as a benefit function.

Finally, we will discuss how to choose the level of detail for the objects in a scene. First, we note the following: For some viewpoints, a scene may be too complex to be able to keep up with the desired frame rate. To solve this, we can define a LOD for each object at its lowest detail level, which is simply an object with no primitives—i.e., we avoid rendering the object [371]. Using this trick, we render only the most important objects and skip the unimportant ones.

To select the “best” LODs for a scene, Equation 14.5 has to be optimized under the constraint shown in Equation 14.6. This is an NP-complete problem, which means that to solve it correctly, the only thing to do is to test *all* different combinations and select the best. This is clearly infeasible for any kind of algorithm. A simpler, more feasible approach is to use a greedy algorithm that tries to maximize the  $\text{Value} = \text{Benefit}(O, L)/\text{Cost}(O, L)$  for each object. This algorithm treats all the objects inside the view frustum and chooses to render the objects in descending order, i.e., the one with the highest value first. If an object has the same value for more than one LOD, then the LOD with the highest benefit is selected and rendered. This approach gives the most “bang for the buck.” For  $n$  objects inside the view frustum, the algorithm runs in  $O(n \log n)$  time, and it produces a solution that is at least half as good as the best [371, 372]. Funkhouser and Séquin

also exploit frame-to-frame coherence for speeding up the sorting of the values.

More information about LOD management and the combination of LOD management and portal culling can be found in Funkhouser's Ph.D. thesis [372]. Maciel and Shirley [806] combine LODs with impostors and present an approximately constant-time algorithm for rendering outdoor scenes. The general idea is that a hierarchy of different representations (some LODs, hierarchical impostors, etc.) of an object is used. Then the tree is traversed in some fashion to give the best image given a certain amount of time. Mason and Blake [824] present an incremental hierarchical LOD selection algorithm. Again, the different representations of an object can be arbitrary. Eriksson et al. [317] present hierarchical level of details (HLODs). Using these, a scene can be rendered with constant frame rate as well, or rendered such that the rendering error is bounded. Wimmer and Schmalstieg present analytic formulae for selecting balanced choices of the polygon count for continuous levels of detail [1357]. They use Lagrange multipliers to solve the same problem Funkhouser and Séquin solved for managing static LODs [371].

## 14.8 Large Model Rendering

So far it has been implied that the model that is rendered fits into the main memory of the computer. This may not always be the case. One example is to render a model of the earth. This is a complex topic, and so we only point to some relevant literature. Very briefly, several nested data structures are used. Often a quadtree-like data structure is used to cover the surface of the earth [228, 330]. Inside each leaf node different data structures can be used, depending on its contents. Also, in order to maintain a reasonable frame rate, areas that are about to come into view are paged in from disk just before they are needed. The quadtree is used for that as well. The combination of different acceleration algorithms is nontrivial. Aliaga et al. [17, 18, 19] have combined several algorithms for extremely large scenes. Section 6.2.5 discusses *clip-mapping*, a related technique for managing large textures. Dietrich et al. [255] provide an excellent overview of work in this field as a whole.

## 14.9 Point Rendering

In 1985, Levoy and Whitted wrote a pioneering technical report [766] where they suggested the use of points as a new primitive used to render everything. The general idea is to represent a surface using a large set of points



**Figure 14.31.** These models were rendered with point-based rendering, using circular splats. The left image shows the full model of an angel named Lucy, with 10 million vertices. However, only about 3 million splats were used in the rendering. The middle and right images zoom in on the head. The middle image used about 40,000 splats during rendering. When the viewer stopped moving, the result converged to the image shown to the right, with 600,000 splats. (*Images generated by the QSplat program by Szymon Rusinkiewicz. The model of Lucy was created by the Stanford Graphics Laboratory.*)

and render these. In a subsequent pass, Gaussian filtering is performed in order to fill in gaps between rendered points. The radius of the Gaussian filter depends on the density of points on the surface, and the projected density on the screen. Levoy and Whitted implemented this system on a VAX-11/780. However, it was not until about 15 years later that point-based rendering again became of interest. Two reasons for this resurgence are that computing power reached a level where point-based rendering truly made sense, and that extremely large models obtained from laser range scanners became available [768]. Such models are initially represented as unconnected three-dimensional points. Rusinkiewicz and Levoy present a system called *QSplat* [1091], which uses a hierarchy of spheres to represent the model. This hierarchy is used for hierarchical backface and view frustum culling, and level of detail rendering. The nodes in this tree are compressed in order to be able to render scenes consisting of several hundred million points. A point is rendered as a shape with a radius, called a splat. Different splat shapes that can be used are squares, opaque circles, and fuzzy circles. See Figure 14.31 for an example. Rendering may stop at any level in the tree. The nodes at that level are rendered as splats with the same radius as the node's sphere. Therefore, the bounding sphere hierarchy is constructed so that no holes are visible at all levels. Since traversal of the tree can stop at any level, interactive frame rates can be obtained by stopping the traversal at an appropriate level. When the user stops moving around, the quality of the rendering can be refined repeatedly until the leaves of the hierarchy are reached. Pfister et al. [1009] present the *surfel*—

a surface element. A surfel is also a point-based primitive. An octree is used to store the sampled surfels (position, normal, filtered texels). During rendering, the surfels are projected onto the screen, and subsequently, a visibility splatting algorithm is used to fill in any holes created.

Bærentzen [53] discusses using point-based models as substitutes for objects in the distance. When triangles in a model each cover a pixel or less, points can be faster to render as there is no triangle setup or interpolation. Botsch et al. [130] use deferred shading techniques along with an elliptical weighted average (EWA) filter to efficiently provide high quality.

## Further Reading and Resources

*The Inventor Mentor* [1343] discusses the way scene graphs operate. Abrash's (now free) book [1] offers a thorough treatment of the use of polygon-based BSP trees and their application in games such as *Doom* and *Quake*. A thorough treatment of BSP trees and their history is also given by James [597]. Though the focus is collision detection, Ericson's book [315] has relevant material about forming and using various space subdivision schemes. A number of different view frustum culling optimizations (and their combinations) are presented by Assarsson and Möller [48].

There is a wealth of literature about occlusion culling. Two good starting places for early work on algorithms are the visibility surveys by Cohen-Or et al. [185] and Durand [285]. Aila and Miettinen [4] describe the architecture of a commercial, state-of-the-art culling system. An excellent resource for information on levels of detail is the book *Level of Detail for 3D Graphics* by Luebke et al. [801]. A recent overview of research in the area of rendering massive models is presented by Dietrich et al. [255].



# Chapter 15

## Pipeline Optimization

*“We should forget about small efficiencies, say about 97% of the time: Premature optimization is the root of all evil.”*

—Donald Knuth

As we saw in Chapter 2, the process of rendering an image is based on a pipelined architecture with three conceptual stages: *application*, *geometry*, and *rasterizer*. At any given moment, one of these stages, or the communication path between them, will *always* be the bottleneck—the slowest stage in the pipeline. This implies that the bottleneck stage sets the limit for the throughput, i.e., the total rendering performance, and so is a prime candidate for *optimization*.

Optimizing the performance of the rendering pipeline resembles the process of optimizing a pipelined processor (CPU) [541] in that it consists mainly of two steps. First, the bottleneck of the pipeline is located. Second, that stage is optimized in some way; and after that, step one is repeated if the performance goals have not been met. Note that the bottleneck may or may not be located at the same place after the optimization step. It is a good idea to put only enough effort into optimizing the bottleneck stage so that the bottleneck moves to another stage. Several other stages may have to be optimized before this stage becomes the bottleneck again. For this reason, effort should not be wasted on over-optimizing a stage.

The location of the bottleneck may change within a frame. At one moment the geometry stage may be the bottleneck because many tiny triangles are rendered. Later in the frame the rasterizer could be the bottleneck because triangles covering large parts of the screen are rendered. So, when we talk about, say, the rasterizer stage being the bottleneck, we mean it is the bottleneck most of the time during that frame.

Another way to capitalize on the pipelined construction is to recognize that when the slowest stage cannot be optimized further, the other stages can be made to work just as much as the slowest stage. This will not change performance, since the speed of the slowest stage will not be altered, but the

extra processing can be used to improve image quality. For example, say that the bottleneck is in the application stage, which takes 50 milliseconds (ms) to produce a frame, while the others each take 25 ms. This means that without changing the speed of the rendering pipeline (50 ms equals 20 frames per second), the geometry and the rasterizer stages could also do their work in 50 ms. For example, we could use a more sophisticated lighting model or increase the level of realism with shadows and reflections, assuming that this does not increase the workload on the application stage.

Pipeline optimization is a process in which we first maximize the rendering speed, then allow the stages that are not bottlenecks to consume as much time as the bottleneck. That said, this idea does not apply for newer architectures such as the Xbox 360, which automatically load-balance computational resources (more on this in a moment).

This exception is an excellent example of a key principle. When reading this chapter, the dictum

#### *KNOW YOUR ARCHITECTURE*

should always be in the back of your mind, since optimization techniques vary greatly for different architectures. A related dictum is, simply, “Measure.”

## 15.1 Profiling Tools

There are a number of worthwhile tools available for profiling use of the graphics accelerator and CPU. Such tools are useful both for locating bottlenecks and for optimizing. Examples include *PIX* for Windows (for DirectX), *gDEBugger* (for OpenGL), NVIDIA’s *NVPerfKit* suite of tools, ATI’s *GPU PerfStudio* [1401], and Apple’s *OpenGL Profiler*.

As an example, PIX for Windows provides real-time performance evaluation by providing counters for a wide variety of data, such as the number of draw calls, state changes, texture and shader calls, CPU and GPU idle time, locks on various resources, read and write I/O, the amount of memory used, etc. This data can be displayed overlaid on the application itself. Figure 15.1 was rendered with this technique.

PIX can capture all the DirectX calls made within a given frame for later analysis or playback. Examining this stream can show whether and where unnecessary API calls are being made. PIX can also be used for pixel debugging, showing the frame buffer history for a single pixel.

While these tools can provide developers with most of the information they need, sometimes other data is needed that does not fit the mold. Pelzer [1001] presents a number of useful techniques to display debugging information.

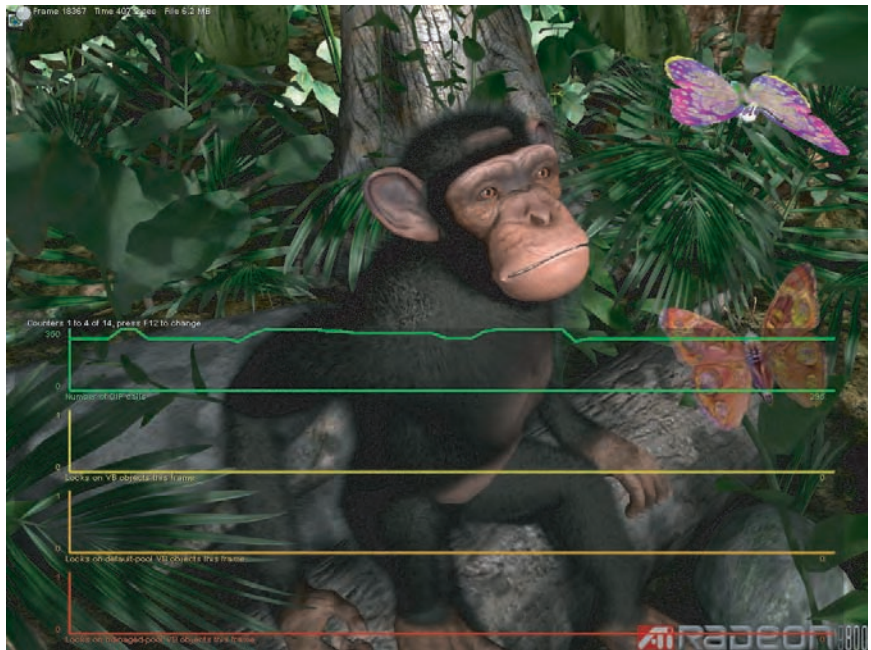


**Figure 15.1.** PIX run atop a DirectX program, showing HUD information about the number of draw calls performed. (*Image from ATI's Chimp Demo with Microsoft's PIX overlaid.*)

## 15.2 Locating the Bottleneck

The first step in optimizing a pipeline is to locate the bottleneck. One way of finding bottlenecks is to set up a number of tests, where each test decreases the amount of work a particular stage performs. If one of these tests causes the frames per second to increase, the bottleneck stage has been found. A related way of testing a stage is to reduce the workload on the other stages without reducing the workload on the stage being tested. If performance does not change, the bottleneck is the stage where the workload was not altered. Performance tools can provide detailed information on what API calls are expensive, but do not necessarily pinpoint exactly what stage in the pipeline is slowing down the rest. Even when they do, such as the “simplified experiments” provided by *NVPerfAPI*, it is important to understand the idea behind each test.

What follows is a brief discussion of some of the ideas used to test the various stages, to give a flavor of how such testing is done. There are a number of documents available that discuss testing and optimizations for specific architectures and features [164, 946, 1065, 1400]. A per-

fect example of the importance of understanding the underlying hardware comes with the advent of the *unified shader architecture*. The Xbox 360 (see Section 18.4.1) uses this architecture, and it forms the basis of high-end cards from the end of 2006 on. The idea is that vertex, pixel, and geometry shaders all use the same functional units. The GPU takes care of load balancing, changing the proportion of units assigned to vertex versus pixel shading. As an example, if a large quadrilateral is rendered, only a few shader units could be assigned to vertex transformation, while the bulk are given the task of fragment processing. For this architecture, pinpointing whether the bottleneck is in the vertex or pixel shader stage is moot [1400]. Either this combined set of stages or another stage will still be the bottleneck, however, so we discuss each possibility in turn.

### 15.2.1 Testing the Application Stage

If the platform being used is supplied with a utility for measuring the workload on the processor(s), that utility can be used to see if your program uses 100 percent (or near that) of the CPU processing power. For Windows there is the *Task Manager*, and for Macs, there is the *Activity Monitor*. For Unix systems, there are usually programs called `top` or `osview` that show the process workload on the CPU(s). If the CPU is in constant use, your program is *CPU-limited*. This is not always foolproof, since you may be waiting for the hardware to complete a frame, and this wait operation is sometimes implemented as a busy-wait. Using a code profiler to determine where the time is spent is better. AMD has a tool called *CodeAnalyst* for analyzing and optimizing the code run on their line of CPUs, and Intel has a similar tool called *VTune* that can analyze where the time is spent in the application or in a driver. There are other places where time can go, e.g., the *D3D runtime* sits between the application and the driver. This element converts API calls to device-independent commands, which are stored in a command buffer. The runtime sends the driver these commands in batches, for efficiency.

A smarter way to test for CPU limits is to send down data that causes the other stages to do little or no work. For some systems this can be accomplished by simply using a null driver (a driver that accepts calls but does nothing) instead of a real driver [946]. This effectively sets an upper limit on how fast you can get the entire program to run, because you do not use the graphics hardware, and thus, the CPU is always the bottleneck. By doing this test, you get an idea on how much room for improvement there is for the stages not run in the application stage. That said, be aware that using a null driver can also hide any bottleneck due to driver processing itself and communication between stages.

Another more direct method is to underclock the CPU, if possible [164, 946]. If performance drops in direct proportion to the CPU rate, the application is CPU-bound. Finally, the process of elimination can be used: If none of the GPU stages are the bottleneck, the CPU must be. This same underclocking approach can be done for many GPUs for various stages with programs such as *Coolbits* or EnTech's *PowerStrip*. These underclocking methods can help identify a bottleneck, but can sometimes cause a stage that was not a bottleneck before to become one. The other option is to overclock, but you did not read that here.

### 15.2.2 Testing the Geometry Stage

The geometry stage is the most difficult stage to test. This is because if the workload on this stage is changed, then the workload on one or both of the other stages is often changed as well. To avoid this problem, Cebenoyan [164] gives a series of tests working from the rasterizer stages back up the pipeline.

There are two main areas where a bottleneck can occur in the geometry stage: vertex fetching and processing. To see if the bottleneck is due to object data transfer is to increase the size of the vertex format. This can be done by sending several extra texture coordinates per vertex, for example. If performance falls, this area is the bottleneck.

Vertex processing is done by the vertex shader or the fixed-function pipeline's transform and lighting functionality. For the vertex shader bottleneck, testing consists of making the shader program longer. Some care has to be taken to make sure the compiler is not optimizing away these additional instructions. For the fixed-function pipeline, processing load can be increased by turning on additional functionality such as specular highlighting, or by changing light sources to more complex forms (e.g., spotlights).

### 15.2.3 Testing the Rasterizer Stage

This stage consists of three separate substages: triangle setup, the pixel shader program, and raster operations. Triangle setup is almost never the bottleneck, as it simply joins vertices into triangles [1400]. The simplest way to test if raster operations are the bottleneck is by reducing the bit depth of color output from 32 (or 24) bit to 16 bit. The bottleneck is found if the frame rate increases considerably.

Once raster operations are ruled out, the pixel shader program's effect can be tested by changing the screen resolution. If a lower screen resolution causes the frame rate to rise appreciably, the pixel shader is the bottleneck, at least some of the time. Care has to be taken if a level-of-detail system

is in place. A smaller screen is likely to also simplify the models displayed, lessening the load on the geometry stage.

Another approach is the same as that taken with vertex shader programs, to add more instructions to see the effect on execution speed. Again, it is important to determine that these additional instructions were not optimized away by the compiler.

## 15.3 Performance Measurements

Before delving into different ways of optimizing the performance of the graphics pipeline, a brief presentation of performance measurements will be given. One way to express the performance of the geometry stage is in terms of *vertices per second*. As in the geometry stage, one way to express the fill rate of the rasterizer stage is in terms of *pixels per second* (or sometimes *texels per second*).

Note that graphics hardware manufacturers often present peak rates, which are at best hard to reach. Also, since we are dealing with a pipelined system, true performance is not as simple as listing these kinds of numbers. This is because the location of the bottleneck may move from one time to another, and the different pipeline stages interact in different ways during execution. It is educational to find out what the peak rates represent, and try to duplicate them: Usually you will find the bus getting in the way, but the exercise is guaranteed to generate insights into the architecture like nothing else can.

When it comes to measuring performance for CPUs, the trend has been to avoid IPS (*instructions per second*), FLOPS (*floating point operations per second*), gigahertz, and simple short benchmarks. Instead, the preferred method is to use clock cycle counters [1], or to measure wall clock times for a range of different, real programs [541], and then compare the running times for these. Following this trend, most independent benchmarks instead measure the actual frame rate in fps for a number of given scenes, and for a number of different screen resolutions, antialiasing settings, etc. Many graphics-heavy games include a benchmarking mode or have one created by a third party, and these benchmarks are commonly used in comparing GPUs.

To be able to see the potential effects of pipeline optimization, it is important to measure the total rendering time per frame with double buffering disabled, i.e., in single-buffer mode. This is because with double buffering turned on, swapping of the buffers occurs only in synchronization with the frequency of the monitor, as explained in the example in Section 2.1. Other benchmarking tips and numerous optimizations are provided in NVIDIA’s [946] and ATI’s guides [1400].

## 15.4 Optimization

Once a bottleneck has been located, we want to optimize that stage to boost the performance. Optimizing techniques for the application, geometry, and rasterizer stages are presented next. Some of these optimizations trade off quality for speed, and some are just clever tricks for making the execution of a certain stage faster.

### 15.4.1 Application Stage

The application stage is optimized by making the code faster and the memory accesses of the program faster or fewer. Detailed code optimization is out of the scope of this book, and optimization techniques usually differ from one CPU manufacturer to another.

One of the first steps to take is to turn on the optimization flags for the compiler. There are usually a number of different flags, and you will have to check which of these apply to your code. Make few assumptions about what optimization options to use. For example, setting the compiler to “minimize code size” instead of “optimizing for speed” may result in faster code because memory caching performance is improved. Also, if possible, try different compilers, as these are optimized in different ways, and some are markedly superior.

For code optimization, it is crucial to locate the place in the code where most of the time is spent. A good code profiler is key in finding these code hot spots, where most time is spent. Optimization efforts are then made in these places. Such locations in the program are often *inner loops*, pieces of the code that are executed many times each frame.

The basic rule of optimization is to try a variety of tactics: Reexamine algorithms, assumptions, and code syntax, trying as many variants as possible. CPU architecture and compiler performance often limit the user’s ability to form an intuition about how to write the fastest code, so question your assumptions and keep an open mind. For example, Booth [126] shows a piece of code in which a seemingly useless array access actually feeds the cache and speeds the overall routine by 25 percent.

A cache is a small fast-memory area that exists because there is usually much coherence in a program, which the cache can exploit. That is, nearby locations in memory tend to be accessed one after another (spatial locality), and code is often accessed sequentially. Also, memory locations tend to be accessed repeatedly (temporal locality), which the cache also exploits [282]. Processor caches are fast to access, second only to registers for speed. Many fast algorithms work to access data as locally (and as little) as possible.

Registers and local caches form one end of the *memory hierarchy*, which extends next to dynamic random access memory (DRAM), then to storage

on hard disks. At the one end are small amounts of very expensive and very fast memory, at the other are large amounts of slow and cheap storage. Between each level of the hierarchy the speed drops by some noticeable factor. For example, processor registers are usually accessed in one clock cycle, while L1 cache memory is accessed in a few cycles. Each change in level has an increase in latency in this way. The one level change to be avoided if at all possible is accessing the hard disk, which can have hundreds of thousands of cycles of latency. Sometimes latency can be hidden by the architecture. Section 18.4.2 describes this technique for the PLAYSTATION® 3 system, but it is always a factor that must be taken into account.

Below we address memory issues and then present tricks and methods for writing fast code. These considerations apply to most pipelined CPUs with a memory hierarchy and a cache at the topmost level(s). The rules are constantly changing, though, so it helps to know your target architecture well. Also, keep in mind that the hardware will change, so some optimizations made now may eventually become useless or counterproductive.

### *Memory Issues*

The memory hierarchy can be a major source of slowdown on CPU architectures, much more than inefficiency in computation. Years ago the number of arithmetic instructions was the key measure of an algorithm's efficiency; now the key is memory access patterns. Below is a list of pointers that should be kept in consideration when programming.

- Assume nothing when it comes to the system memory routines (or anything else, for that matter). For example, if you know the direction of a copy, or that no overlap of source and destination occurs, an assembly loop using the largest registers available is the quickest way to do a copy. This is not necessarily what the system's memory routines provide.
- Data that is accessed sequentially in the code should also be stored sequentially in memory. For example, when rendering a triangle mesh, store texture coordinate #0, normal #0, color #0, vertex #0, texture coordinate #1, normal #1, etc., sequentially in memory if they are accessed in that order.
- Avoid pointer indirection, jumps, and function calls, as these may significantly decrease the performance of the cache. You get pointer indirection when you follow a pointer to another pointer and so on. This is typical for linked lists and tree structures; use arrays instead, as possible. McVoy and Staelin [850] show a code example that follows a linked list through pointers. This causes cache misses for data

both before and after, and their example stalls the CPU more than 100 times longer than it takes to follow the pointer (if the cache could provide the address of the pointer). Smits [1200] notes how flattening a pointer-based tree into a list with skip pointers considerably improves hierarchy traversal. Using a van Emde Boas layout is another way to help avoid cache misses—see Section 14.1.4.

- The default memory allocation and deletion functions may be slow on some systems, so it is often better to allocate a large pool of memory at start-up for objects of the same size, and then use your own allocation and free routines for handling the memory of that pool [72, 550]. Libraries such as *Boost* provide pool allocation. That said, for languages with garbage collection, such as C# and Java, pools can actually reduce performance.
- Better yet, try to avoid allocating or freeing memory altogether within the rendering loop, e.g., allocate scratch space once, and have stacks, arrays, and other structures only grow (using a variable or flags to note which elements should be treated as deleted).
- On PCs, aligning frequently used data structures to multiples of exactly 32 bytes can noticeably improve overall performance by using cache lines optimally [1144]. Check the cache line size on your computer; on Pentium IVs, the L1 (level 1) cache line size is 64 bytes, and the L2 (level 2) cache line size is 128 bytes; so for these, it is better to align to either 64 or 128 bytes. On an AMD Athlon, the cache line size is 64 bytes for both L1 and L2. Compiler options can help, but it helps to design your data structures with alignment, called *padding*, in mind. Tools such as *VTune* and *CodeAnalyst* for Windows and Linux and the open-source *Valgrind* for Linux can help identify caching bottlenecks.
- Try different organizations of data structures. For example, Hecker [525] shows how a surprisingly large amount of time was saved by testing a variety of matrix structures for a simple matrix multiplier. An array of structures,

```
struct Vertex {float x,y,z;}  
Vertex myvertices[1000];
```

or a structure of arrays,

```
struct VertexChunk {float x[1000],y[1000],z[1000];}  
VertexChunk myvertices;
```

may work better for a given architecture. This second structure is better for using SIMD commands, but as the number of vertices goes up, the chance of a cache miss increases. As the array size increases, a hybrid scheme,

```
struct Vertex4 {float x[4],y[4],z[4];}
Vertex4 myvertices[250];
```

may be the best choice that works well with existing code.

### *Code Issues*

The list that follows gives some techniques for writing fast code that are particularly relevant to computer graphics. Such methods vary with the compiler and the evolving CPU, but most of the following have held for some years.

- Single Instruction Multiple Data (SIMD) instruction sets, such as Intel's SSE series, AMD's 3DNow! series, and the AIM Alliance's AltiVec, could be used in many situations with great performance gains. Typically, 2–4 elements can be computed in parallel, which is perfect for vector operations. Alternately, four tests can be done in parallel. For example, Ericson [315] provides SIMD tests for comparing four separate pairs of objects simultaneously for overlap.
- Using **float-to-long** conversion is slow on Pentiums, due to compliance with the C ANSI standard. A custom assembly language routine can save significant time (while sacrificing ANSI compliance) [251, 664]. Intel added SSE instructions for integer truncation and other operations to improve performance [347].
- Avoid using division as much as possible. Such instructions can take 2.5 or more times longer to execute than multiplying [591]. For example, take normalizing a three-dimensional vector. Conceptually, this is done by dividing all elements in the vector by the length of the vector. Instead of dividing three times, it is faster to compute  $1/d$ , where  $d$  is the length of the vector, and then multiply all elements by this factor.
- Math functions such as sin, cos, tan, exp, arcsin, etc., are expensive and should be used with care. If lower precision is acceptable, develop or use approximate routines (possibly using SIMD instructions) where only the first few terms in the MacLaurin or Taylor series (see Equation B.2) are used. Since memory accesses can be expensive on modern CPUs, this is strongly preferred over using lookup tables.

- Conditional branches are often expensive, though most processors have branch prediction, which means as long as the branches can be consistently predicted, the cost can be low. However, a mispredicted branch is often very expensive on some architectures, especially those with deep pipelines.
- Unroll small loops in order to get rid of the loop overhead. However, this makes the code larger and thus may degrade cache performance. Also, branch prediction usually works well on loops. Sometimes the compiler can do the loop unrolling for you.
- Use inline code for small functions that are called frequently.
- Lessen floating-point precision when reasonable. For example, on an Intel Pentium, floating-point division normally takes 39 cycles at 80 bits of precision, but only 19 cycles at 32 bits (however, at any precision, division by a power of 2 takes around 8 cycles) [126]. When choosing `float` instead of `double`, remember to attach an `f` at the end of constants. Otherwise, they, and whole expressions, may be cast to `double`. So `float x=2.42f;` may be faster than `float x=2.42;`.
- Lower precision is also better because less data is then sent down the graphics pipeline. Graphics computations are often fairly forgiving. If a normal vector is stored as three 32-bit floats, it has enough accuracy to point from Earth to a rock on Mars with sub-centimeter precision [1207]. This level of precision is usually a bit more than is needed.
- Virtual methods, dynamic casting, (inherited) constructors, and passing structs by value have some efficiency penalties. In one case reported to us, 40% of the time spent in a frame was used on the virtual inheritance hierarchy that managed models. Blinn [109] presents techniques for avoiding overhead for evaluating vector expressions in C++.

### 15.4.2 API Calls

Throughout this book we have given advice based on general trends in hardware. For example, indexed vertex buffers (in OpenGL, vertex buffer objects) are usually the fastest way to provide the accelerator with geometric data (see Section 12.4.5). This section deals with some of the features of the API and how to use them to best effect.

One problem touched upon in Section 12.4.2 that we would like to revisit here is the small batch problem. This is by far the most significant factor

affecting performance in modern APIs. DirectX 10 had specific changes in its design to combat this bottleneck, improving performance by a factor of  $2\times$  [1066], but its effect is still significant. Simply put, a few large meshes are much more efficient to render than many small ones. This is because there is a fixed-cost overhead associated with each API call, a cost paid for processing a primitive, regardless of size. For example, Wloka [1365] shows that drawing two (relatively small) triangles per batch was a factor of  $375\times$  away from the maximum throughput for the GPU tested. Instead of 150 million triangles per second, the rate was 0.4 million, for a 2.7 GHz CPU. This rate dropped to 0.1 million,  $1500\times$  slower, for a 1.0 GHz CPU. For a scene rendered consisting of many small and simple objects, each with only a few triangles, performance is entirely CPU-bound by the API; the GPU has no ability to increase it. That is, the processing time on the CPU for the draw call is greater than the amount of time the GPU takes to actually draw the mesh, so the GPU is starved.

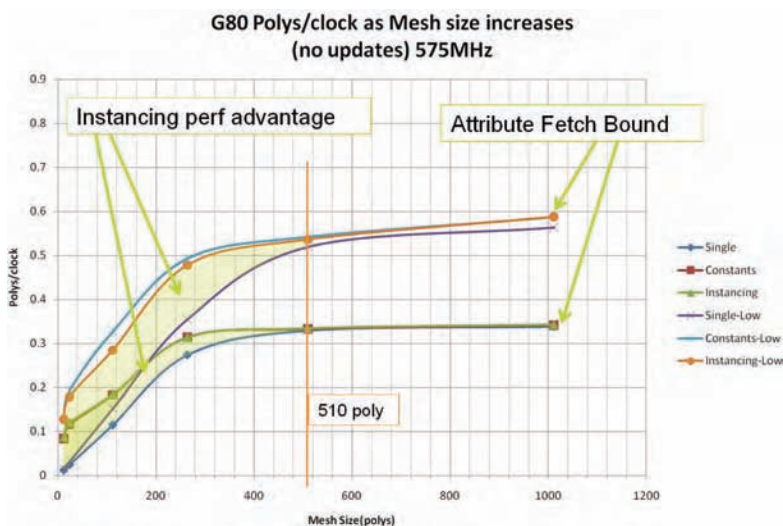


**Figure 15.2.** Batching performance benchmarks for an Intel Core 2 Duo 2.66 GHz CPU using an NVIDIA G80 GPU, running DirectX 10. Batches of varying size were run and timed under different conditions. The “Low” conditions are for triangles with just the position and a constant-color pixel shader; the other set of tests is for reasonable meshes and shading. “Single” is rendering a single batch many times. “Instancing” reuses the mesh data and puts the per-instance data in a separate stream. “Constants” is a DirectX 10 method where instance data is put in constant memory. As can be seen, small batches hurt all methods, but instancing gives proportionally much faster performance. At a few hundred polygons, performance levels out, as the bottleneck becomes how fast vertices are retrieved from the vertex buffer and caches. (*Graph courtesy of NVIDIA Corporation.*)

Back in 2003, the breakpoint where the API was the bottleneck was about 130 triangles per object. The breakpoint for NVIDIA's GeForce 6 and 7 series with typical CPUs is about 200 triangles per draw call [75]. In other words, when batches have 200 triangles or less (and the triangles are not large or shaded in a complex fashion), the bottleneck is the API on the CPU side; an infinitely fast GPU would not change this performance, since the GPU is not the bottleneck under these conditions. A slower GPU would of course make this breakpoint lower. See Figure 15.2 for more recent tests.

Wloka's rule of thumb, borne out by others, is that "You get  $X$  batches per frame." and that  $X$  depends on the CPU speed. This is a maximum number of batches given the performance of just the CPU; batches with a large number of polygons or expensive rasterization, making the GPU the bottleneck, lower this number. This idea is encapsulated in his formula:

$$X = \frac{BCU}{F}, \quad (15.1)$$

where  $B$  is the number of batches per second for a 1 GHz CPU,  $C$  is GHz rating of the current CPU,  $U$  is the amount of the CPU that is dedicated to calling the object API,  $F$  is the target frame rate in fps, and  $X$  is the computed number of batches callable per frame. Wloka gives  $B$  as a constant of 25,000 batches per second for a 1 GHz CPU at 100% usage. This formula is approximate, and some API and driver improvements can be done to lower the impact of the CPU on the pipeline (which may increase  $B$ ). However, with GPUs increasing in speed faster than CPUs (about 3.0 – 3.7× for GPUs versus 2.2× for CPUs over an eighteen month span), the trend is toward each batch containing more triangles, not less. That said, a few thousand polygons per mesh is enough to avoid the API being the bottleneck and keep the GPU busy.

**EXAMPLE: BATCHES PER FRAME.** For a 3.7 GHz CPU, a budget of 40% of the CPU's time spent purely on object API calls, and a 60 fps frame rate, the formula evaluates to

$$X = \frac{25000 \text{ batches/GHz} \times 3.7 \text{ GHz} \times 0.40 \text{ usage}}{60 \text{ fps}} = 616 \text{ batches/frame}.$$

For this configuration, usage budget, and goals, the CPU limits the application to roughly 600 batches that can be sent to the GPU each frame. □

There are a number of ways of ameliorating the small batch problem, and they all have the same goal: fewer API calls. The basic idea of *batching* is to combine a number of objects into a single object, so needing only one API call to render the set.



**Figure 15.3.** Vegetation instancing. All objects the same color in the lower image are rendered in a single draw call [1340]. (*Image from CryEngine1 courtesy of Crytek.*)

Combining can be done one time and the buffer reused each frame for sets of objects that are static. For dynamic objects, a single buffer can be filled with a number of meshes. The limitation of this basic approach is that all objects in a mesh need to use the same set of shader programs, i.e., the same material. However, it is possible to merge objects with different colors, for example, by tagging each object's vertices with an identifier. This identifier is used by a shader program to look up what color is used to shade the object. This same idea can be extended to other surface attributes. Similarly, textures attached to surfaces can also hold identifiers as to which material to use. Light maps of separate objects need to be combined into texture atlases or arrays [961].

However, such practices can be taken too far. Adding branches and different shading models to a single pixel shader program can be costly. Sets of fragments are processed in parallel. If all fragments do not take the same branch, then both branches must be evaluated for all fragments. Care has to be taken to avoid making pixel shader programs that use an excessive number of registers. The number of registers used influences the number of fragments that a pixel shader can handle at the same time in parallel. See Section 18.4.2.

The other approach to minimize API calls is to use some form of *instancing*. Most APIs support the idea of having an object and drawing it a number of times in a single call. So instead of making a separate API call for each tree in a forest, you make one call that renders many copies of the tree model. This is typically done by specifying a base model and providing a separate data structure that holds information about each specific instance desired. Beyond position and orientation, other attributes could be specified per instance, such as leaf colors or curvature due to the wind, or anything else that could be used by shader programs to affect the model. Lush jungle scenes can be created by liberal use of instancing. See Figure 15.3. Crowd scenes are a good fit for instancing, with each character appearing unique by having different body parts from a set of choices. Further variation can be added by random coloring and decals [430]. Instancing can also be combined with level of detail techniques [158, 279, 810, 811]. See Figure 15.4 for an example.

In theory, the geometry shader could be used for instancing, as it can create duplicate data of an incoming mesh. In practice, this method is often slower than using instancing API commands. The intent of the geometry shader is to perform local, small scale amplification of data [1311].

Another way for the application to improve performance is to minimize state changes by grouping objects with a similar rendering state (vertex and pixel shader, texture, material, lighting, transparency, etc.) and rendering them sequentially. When changing the state, there is sometimes a need to wholly or partially flush the pipeline. For this reason, changing shader



**Figure 15.4.** Crowd scene. Using instancing minimizes the number of draw calls needed. Level of detail techniques are also used, such as rendering impostors for distant models [810, 811]. (*Image courtesy of Jonathan Maim, Barbara Yersin, Mireille Clavien, and Daniel Thalmann.*)

programs or material parameters can be very expensive [849, 946, 1400]. Nodes with a shared material could be grouped for better performance. Rendering polygons with a shared texture minimizes texture cache thrashing [873, 1380]. A way to minimize texture binding changes is to put several texture images into one large texture or texture array (see Section 6.2.5).

Understanding object buffer allocation and storage is also important when rendering. For a system with a CPU and GPU, each has its own memory. The graphics driver is usually in control of where objects reside, but it can be given hints of where best to store them. A common classification is static versus dynamic buffers. If an object is not deforming, or the deformations can be carried out entirely by shader programs (e.g., skinning), then it is profitable to store the data for the object in GPU memory. The unchanging nature of this object can be signalled by storing it as a static buffer. In this way, it does not have to be sent across the bus for every frame rendered, so avoiding any bottleneck at this stage of the pipeline. For example, memory bandwidth on a GPU in 2006 was in excess of 50 GB/sec, versus no more than 4 GB/sec from the CPU using PCI Express [123]. If the data is changing each frame, using a dynamic buffer, which requires no permanent storage space on the GPU, is preferable.

### 15.4.3 Geometry Stage

The geometry stage is responsible for transforms, lighting, clipping, projection, and screen mapping. Transforms and lighting are processes that can be optimized relatively easily; the rest are difficult or impossible to optimize. Transform, lighting, projection, clipping, and screen-mapping operations can also all gain from using lower precision data when feasible.

The previous chapters discussed ways to reduce the number of vertices and drawing primitives that have to pass through the (entire) pipeline. Simplifying the models so they have fewer vertices lowers transfer and vertex transform costs. Techniques such as frustum and occlusion culling avoid sending the full primitive itself down the pipeline. Adding such large-scale techniques can entirely change performance characteristics of the application and so are worth trying early on in development.

There are further optimizations that can be done for those objects that are visible and need a certain level of resolution. As discussed in Section 12.4.5, using index and vertex buffers is usually more space efficient than storing single triangles or triangle strips. Doing so saves space and memory, and bus transfer time. Section 12.4.4 has an extensive discussion of cache-oblivious layout algorithms, where the vertices are ordered in a fashion that maximizes cache reuse, so saving processing time.

To save both memory and time spent accessing it, choose as low a precision as possible (without rendering artifacts) on vertices, normals, colors, and other shading parameters. There is sometimes a choice between half, single, and double floating-point precision. Note also that some formats may be faster than others because of what is used internally in the hardware—use a native format.

Another way to decrease memory use is to store the vertex data in a compressed form. Deering [243] discusses such techniques in depth. Calver [150] presents a variety of schemes that use the vertex shader for decompression. Zarge [1400] notes that data compression can also help align vertex formats to cache lines. Purnomo et al. [1040] combine simplification and vertex quantization techniques, and optimize the mesh for a given target mesh size, using an image-space metric.

### 15.4.4 Lighting

The effect of elements of lighting can be computed per vertex, per pixel, or both. Lighting computations can be optimized in several ways. First, the types of light sources being used should be considered. Is lighting needed for all polygons? Sometimes a model only requires texturing, or texturing with colors at the vertices, or simply colors at the vertices. If light sources are static with respect to geometry, then the diffuse and ambient lighting can be

precomputed and stored as colors at the vertices. Doing so is often referred to as “baking” on the lighting. A more elaborate form of prelighting is to use radiosity methods to precompute the diffuse global illumination in a scene (see Section 9.8.1). Such illumination can be stored as colors at the vertices or as light maps (see Section 9.9.1).

The number of light sources influences the performance of the geometry stage. More light sources mean less speed. Also, two-sided lighting may be more expensive than one-sided lighting. When using fixed-function distance attenuation on the light sources, it is useful, and hardly noticeable, to turn off/on light sources on a per-object basis, depending on the distance from the object to the light sources. When the distance is great enough, turn off the light source. A common optimization is to cull based on distance from the light, rendering only those objects affected by the local light source. Another way to lessen work is to disable lighting and instead use an environment map (see Section 8.5). With a large number of light sources, deferred shading techniques can help limit computations and avoid state changes (see Section 7.9.2).

### 15.4.5 Rasterizer Stage

The rasterizer stage can be optimized in a variety of ways. For closed (solid) objects and for objects that will never show their backfaces (for example, the back side of a wall in a room), backface culling should be turned on (see Section 14.2.1). For a closed object, this reduces the number of triangles to be rasterized by approximately 50 percent.

Another technique is to turn off  $Z$ -buffering at certain times. For example, after the frame buffer has been cleared, any background image can be drawn without the need for depth testing. If every pixel on the screen is guaranteed to be covered by some object (e.g., the scene is indoors, or a background sky image is in use), the color buffer does not need to be cleared. Similarly, make sure to enable blend modes only when useful. If the  $Z$ -buffer is being used, on some systems it costs no additional time to also access the stencil buffer. This is because the 8-bit stencil buffer value is stored in the same word as the 24-bit  $z$ -depth value [651].

Remember to use native texture and pixel formats, i.e., use the formats that the graphics accelerator uses internally to avoid a possible expensive transform from one format to another [186]. Another technique commonly used is texture compression. Such textures are faster to send to texture memory if they are compressed before they are sent to the graphics hardware, and faster to send over the bus from memory to the GPU. Another advantage of compressed textures is that they improve cache usage since they use less memory. This gives better performance. See also Section 6.2.5.

One useful technique is to use different pixel shader programs, depending on the distance of the object from the viewer. For example, with three



**Figure 15.5.** The depth complexity of the scene on the left is shown on the right. (*Images created using NVPerfHUD from NVIDIA Corporation.*)

flying saucer models in a scene, the closest might have an elaborate bump map for surface details that the two further away do not need. In addition, the farthest saucer might have specular highlighting simplified or removed altogether, both to simplify computations and to reduce speckling artifacts from undersampling.

To understand the behavior of a program, and especially the load on the rasterizer, it is useful to visualize the depth complexity, which is the number of times a pixel is touched. Figure 15.5 shows an example. One simple method of generating a depth complexity image is to use a call like OpenGL’s `glBlendFunc(GL_ONE,GL_ONE)`, with  $Z$ -buffering disabled. First, the image is cleared to black. All objects in the scene are then rendered with the color  $(0, 0, 1)$ . The effect of the blend function setting is that for each primitive rendered, the values of the written pixels will increase by  $(0, 0, 1)$ . A pixel with a depth complexity of 0 is then black and a pixel of depth complexity 255 is full blue  $(0, 0, 255)$ .

A two-pass approach can be used to count the number of pixels that pass or fail the  $Z$ -buffer depth tests. In the first pass, enable  $Z$ -buffering and use the method above to count the pixels that have passed the depth test. To count the number of pixels that fail the depth test, increment the stencil buffer upon depth buffer failure. Alternately, render with  $Z$ -buffering off to obtain the depth complexity, and then subtract the first-pass results.

These methods can serve to determine the average, minimum, and maximum depth complexity in a scene; the number of pixels per primitive (assuming that the number of primitives that have made it to the scene is known); and the number of pixels that pass and fail the depth tests. These numbers are useful for understanding the behavior of a real-time graphics application and determining where further optimization may be worthwhile.

Depth complexity tells how many surfaces cover each pixel. The amount of *pixel overdraw* is related to how many surfaces actually were rendered. Say two polygons cover a pixel, so the depth complexity is two. If the farther polygon is drawn first, the nearer polygon overdraws it, and the amount of overdraw is one. If the nearer is drawn first, the farther polygon fails the depth test and is not drawn, so there is no overdraw. For a random set of opaque polygons covering a pixel, the average number of draws is the *harmonic series* [203]:

$$H(n) = 1 + \frac{1}{2} + \frac{1}{3} + \dots + \frac{1}{n}. \quad (15.2)$$

The logic behind this is that the first polygon rendered is one draw. The second polygon is either in front or behind the first, a 50/50 chance. The third polygon can have one of three positions compared to the first two, giving one chance in three of it being frontmost. As  $n$  goes to infinity,

$$\lim_{n \rightarrow \infty} H(n) = \ln(n) + \gamma, \quad (15.3)$$

where  $\gamma = 0.57721\dots$  is the Euler-Mascheroni constant. Overdraw rises rapidly when depth complexity is low, but quickly tapers off. For example, a depth complexity of 4 gives an average of 2.08 draws, 11 gives 3.02 draws, but it takes a depth complexity of 12,367 to reach an average of 10.00 draws.

There is a performance gain in roughly sorting and then drawing the scene in front-to-back order (near to far) [164]. This is because the occluded objects that are drawn later will not write to the color or  $Z$ -buffers (i.e., overdraw is reduced). Also, the pixel fragment can be rejected by occlusion culling hardware before even reaching the pixel shader program (see Section 18.3.6).

Another technique is useful for surfaces with complex pixel shader programs. The “early z pass” technique renders the  $Z$ -buffer first, then the whole scene is rendered normally. This method can be useful for avoiding unnecessary pixel shader evaluation, since only the visible surface has its pixel shader evaluated. However, drawing in a rough front-to-back order, as provided by a BSP tree traversal or explicit sort, can provide much of the same benefit without the need for this extra pass. This technique is discussed further in Section 7.9.2.

## 15.5 Multiprocessing

Multiprocessor computers can be broadly classified into *message-passing* architectures and *shared memory multiprocessors*. In message-passing designs, each processor has its own memory area, and messages are sent

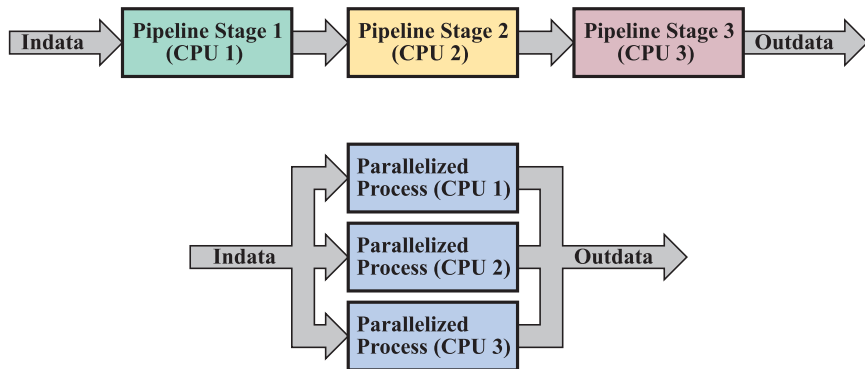


**Figure 15.6.** Two different ways of utilizing multiple processors. At the top we show how three processors (CPUs) are used in a *multiprocessor pipeline*, and at the bottom we show *parallel* execution on three CPUs. One of the differences between these two implementations is that lower latency can be achieved if the configuration at the bottom is used. On the other hand, it may be easier to use a multiprocessor pipeline. The ideal speedup for both of these configurations is linear, i.e., using  $n$  CPUs would give a speedup of  $n$  times.

between the processors to communicate results. Shared memory multiprocessors are just as they sound; all processors share a logical address space of memory among themselves. Most popular multiprocessor systems use shared memory, and most of these have a *symmetric multiprocessing* (SMP) design. SMP means that all the processors are identical. A multicore PC system is an example of a symmetric multiprocessing architecture.

Here, we will present two methods for utilizing multiple processors for real-time graphics. The first method—*multiprocessor pipelining*, also called temporal parallelism—will be covered in more detail than the second—*parallel processing*, also called spatial parallelism. These two methods are illustrated in Figure 15.6. Multiprocessor pipelining and parallel processing can also be combined, but little research has been done in this area. For this discussion, we assume that a multiprocessor computer is available, but do not go into details about different types of multiprocessors.

### 15.5.1 Multiprocessor Pipelining

As we have seen, pipelining is a method for speeding up execution by dividing a job into certain pipeline stages that are executed in parallel. The result from one pipeline stage is passed on to the next. The ideal speedup is  $n$  times for  $n$  pipeline stages, and the slowest stage (the bottleneck) determines the actual speedup. Up to this point, we have seen pipelining used to run the application, geometry processing, and rasterization in parallel for a single-CPU system. This technique can also be used when

multiple processors are available on the host, and in these cases, it is called *multiprocess pipeline* or *software pipelining*.

We assume there is only one graphics accelerator available to the system, and that only one processor thread can access it. This leaves the application stage to be pipelined. Therefore, the application stage is divided into three stages [1079]: APP, CULL, and DRAW. This is very coarse-grained pipelining, which means that each stage is relatively long. The APP stage is the first stage in the pipeline and therefore controls the others. It is in this stage that the application programmer can put in additional code that does, for example, collision detection. This stage also updates the viewpoint. The CULL stage can perform:

- Traversal and hierarchical view frustum culling on a scene graph (see Section 14.3).
- Level of detail selection (see Section 14.7).
- State sorting—geometry with similar state is sorted into bins in order to minimize state changes. For example, all transparent objects are sorted into one bin, which minimizes the need to change the blend state. These objects could also be sorted in a rough back-to-front order for correct rendering (see Section 5.7).
- Finally (and always performed), generation of a simple list of all objects that should be rendered.

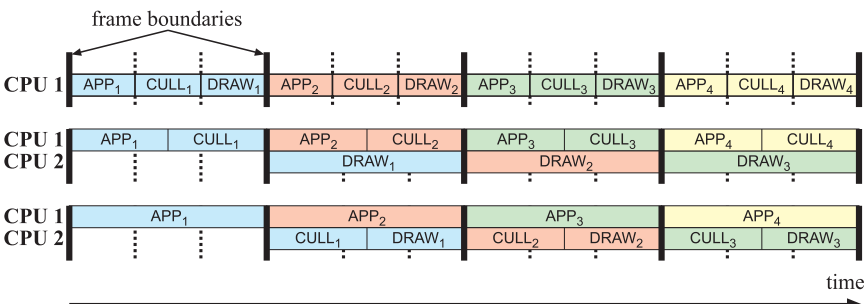


**Figure 15.7.** Different configurations for a multiprocessor pipeline. The thick lines represent synchronization between the stages, and the subscripts represent the frame number. At the top, a single CPU pipeline is shown. In the middle and at the bottom are shown two different pipeline subdivisions using two CPUs. The middle has one pipeline stage for APP and CULL and one pipeline stage for DRAW. This is a suitable subdivision if DRAW has much more work to do than the others. At the bottom, APP has one pipeline stage and the other two have another. This is suitable if APP has much more work than the others. Note that the bottom two configurations have more time for the APP, CULL, and DRAW stages.

The DRAW stage takes the list from the CULL stage and issues all graphics calls in this list. This means that it simply walks through the list and feeds the geometry stage, which in turn feeds the rasterizer stage. Figure 15.7 shows some examples of how this pipeline can be used.

If one processor is available, then all three stages are run on that CPU. If two CPUs are available, then APP and CULL can be executed on one CPU and DRAW on the other. Another configuration would be to execute APP on one processor and CULL and DRAW on the other. Which is the best depends on the workloads for the different stages. Finally, if the host has three CPUs, then each stage can be executed on a separate CPU. This possibility is shown in Figure 15.8.

The advantage of this technique is that the throughput, i.e., the rendering speed, increases. The downside is that, compared to parallel processing, the latency is greater. Latency, or temporal delay, is the time it takes from the polling of the user's actions to the final image [1329]. This should not be confused with frame rate, which is the number of frames displayed per second. For example, say the user is using a head-mounted display. The determination of the head's position may take 50 milliseconds to reach the CPU, then it takes 15 milliseconds to render the frame. The latency is then 65 milliseconds from initial input to display. Even though the frame rate is 66.7 Hz (1/0.015 seconds), interactivity will feel sluggish because of the delay in sending the position changes to the CPU. Ignoring any delay due to user interaction (which is a constant under both systems), multiprocessing has more latency than parallel processing because it uses a pipeline. As is discussed in detail in the next section, parallel processing breaks up the frame's work into pieces that are run concurrently.

In comparison to using a single CPU on the host, multiprocessor pipelining gives a higher frame rate and the latency is about the same or a little greater due to the cost of synchronization. The latency increases with

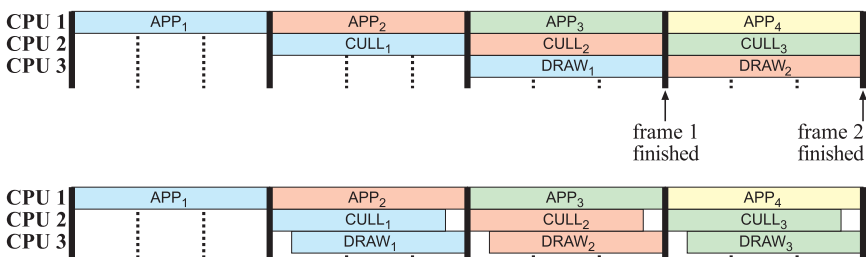


**Figure 15.8.** At the top, a three-stage pipeline is shown. In comparison to the configurations in Figure 15.7, this configuration has more time for each pipeline stage. The bottom illustration shows a way to reduce the latency: The CULL and the DRAW are overlapped with FIFO buffering in between.

the number of stages in the pipeline. For a well-balanced application the speedup is  $n$  times for  $n$  CPUs.

One technique for reducing the latency is to update the viewpoint and other latency-critical parameters at the end of the APP stage [1079]. This reduces the latency by (approximately) one frame. Another way to reduce latency is to execute CULL and DRAW overlapped. This means that the result from CULL is sent over to DRAW as soon as anything is ready for rendering. For this to work, there has to be some buffering, typically a FIFO, between those stages. The stages are stalled on empty and full conditions; i.e., when the buffer is full, then CULL has to stall, and when the buffer is empty, DRAW has to stall. The disadvantage is that techniques such as state sorting cannot be used to the same extent, since primitives have to be rendered as soon as they have been processed by CULL. This latency reduction technique is visualized in Figure 15.8.

The pipeline in this figure uses a maximum of three CPUs, and the stages have certain tasks. However, this technique is in no way limited to this configuration—rather, you can use any number of CPUs and divide the work in any way you want. The key is to make a smart division of the entire job to be done so that the pipeline tends to be balanced. For example, multiprocessor pipelining has been used to speed up the occlusion culling algorithm in Section 14.6 using a different pipeline stage division than the one presented here [1403]. Multiprocessor pipelining has also been used by Funkhouser [372] to speed up LOD management (see Section 14.7.3) and portal culling (Section 14.4).

The multiprocessor pipelining technique requires a minimum of synchronization in that it needs to synchronize only when switching frames. In all kinds of multiprocessing systems, there are many factors to consider when it comes to data sharing, data exclusion, multibuffering, and more. Details on these topics can be found in Rohlf and Helman’s paper [1079].

### 15.5.2 Parallel Processing

The most apparent disadvantage of using a multiprocessor pipeline technique is that the latency tends to increase. For some applications, such as flight simulators, first person shooters, etc., this is not acceptable. When moving the viewpoint, you usually want instant (next-frame) response, but when the latency is long this will not happen. That said, it all depends: If multiprocessing raised the frame rate from 30 fps with 1 frame latency to 60 fps with 2 frames latency, the extra frame delay would then cause no additional latency.

If multiple processors are available, one can try to parallelize the code instead, which may result in shorter latency. To do this, the program must possess the characteristics of *parallelism*. This means that, for a

program with no or a small amount of parallelism, there is no gain in parallelizing the program—a parallel version may even become slower due to the overhead involved in extra synchronization, etc. However, many programs and algorithms do have a large amount of parallelism and can therefore benefit.

There are several different methods for parallelizing an algorithm. Assume that  $n$  processors are available. Using static assignment [212], the total work package, such as the traversal of an acceleration structure, is divided into  $n$  work packages. Each processor then takes care of a work package, and all processors execute their work packages in parallel. When all processors have completed their work packages, it may be necessary to merge the results from the processors. For this to work, the workload must be highly predictable. When that is not the case, dynamic assignment algorithms that adapt to different workloads may be used [212]. These use one or more work pools. When jobs are generated, they are put into the work pools. CPUs can then fetch one or more jobs from the queue when they have finished their current job. Care must be taken so that only one CPU can fetch a particular job, and so that the overhead in maintaining the queue does not damage performance. Larger jobs mean that the overhead for maintaining the queue becomes less of a problem, but, on the other hand, if the jobs are too big, then performance may degrade due to imbalance in the system—i.e., one or more CPUs may starve.

As for the multiprocessor pipeline, the ideal speedup for a parallel program running on  $n$  processors would be  $n$  times. This is called *linear speedup*. Even though linear speedup rarely happens, actual results can sometimes be very close to it.

In Figure 15.6 on page 717, both a multiprocessor pipeline and a parallel processing system with three CPUs are shown. Temporarily assume that these should do the same amount of work for each frame and that both configurations achieve linear speedup. This means that the execution will run three times faster in comparison to serial execution (i.e., on a single CPU). Furthermore, we assume that the total amount of work per frame takes 30 ms, which would mean that the maximum frame rate on a single CPU would be  $1/0.03 \approx 33$  frames per second.

The multiprocessor pipeline would (ideally) divide the work into three equal-sized work packages and let each of the CPUs be responsible for one work package. Each work package should then take 10 ms to complete. If we follow the work flow through the pipeline, we will see that the first CPU in the pipeline does work for 10 ms (i.e., one-third of the job) and then sends it on to the next CPU. The first CPU then starts working on the first part of the next frame. When a frame is finally finished, it has taken 30 ms for it to complete, but since the work has been done in parallel in the pipeline, one frame will be finished every 10 ms. So the latency is

30 ms, and the speedup is a factor of three (30/10), resulting in 100 frames per second.

Now, a parallel version of the same program would also divide the jobs into three work packages, but these three packages will execute at the same time on the three CPUs. This means that the latency will be 10 ms, and the work for one frame will also take 10 ms. The conclusion is that the latency is much shorter when using parallel processing than when using a multiprocessor pipeline. However, parallel processing often does not map to hardware constraints. For example, DirectX 10 and earlier allow only one thread to access the GPU at a time, so parallel processing for the DRAW stage is more difficult [1057].

**EXAMPLE: VALVE'S GAME ENGINE PIPELINE.** Valve reworked their engine to take advantage of multicore systems. They found a mix of coarse and fine-grained threading worked well. Coarse-grained threading is where an entire subsystem, such as artificial intelligence or sound, is handled by a core. Fine-grained uses parallel processing to split a single task among a set of cores. For the tasks related to rendering, their new pipeline acts as follows [1057]:

1. Construct scene rendering lists for multiple scenes in parallel (world, water reflections, and TV monitors).
2. Overlap graphics simulations (particles, ropes).
3. Compute character skeletal transformations for all characters in all scenes in parallel.
4. Compute shadows for all characters in parallel.
5. Allow multiple threads to draw in parallel (which required a rewrite of low-level graphics libraries). □

## Further Reading and Resources

Though a little dated, Cebenoyan's article [164] gives an overview of how to find the bottleneck and techniques to improve efficiency. NVIDIA's extensive guide [946] covers a wide range of topics, and ATI's newer presentation [1400] provides a number of insights into some of the subtleties of various architectures. Some of the better optimization guides for C++ are Fog's [347] and Isensee's [591], free on the web.

There are a number of tools that make the task of performance tuning and debugging much simpler. These include Microsoft's *PIX*, NVIDIA's *NVPerfHUD*, ATI's *GPU PerfStudio*, and *gDEBugger* for OpenGL. See <http://www.realtimerendering.com> for a current list. Zarge et al. [1401]

discusses *GPU PerfStudio* and optimizing performance specifically for DirectX 10. Futuremark's *3DMark* benchmarking suites provides information about the capabilities of your PC system, while also being entertaining to watch.

Issues that arise in the design of a parallel graphics API are treated by Igehy et al. [581]. See the book *Parallel Computer Architecture: A Hardware/Software Approach* [212] for more information on parallel programming.



# Chapter 16

## Intersection Test Methods

*"I'll sit and see if that small sailing cloud  
Will hit or miss the moon."*

—Robert Frost

Intersection testing is often used in computer graphics. We may wish to click the mouse on an object, or to determine whether two objects collide, or to make sure we maintain a constant height off the floor for our viewer as we navigate a building. All of these operations can be performed with intersection tests. In this chapter, we cover the most common ray/object and object/object intersection tests.

In interactive computer graphics applications, it is often desirable to let the user select a certain object by *picking* (clicking) on it with the mouse or any other input device. Naturally, the performance of such an operation needs to be high. One picking method, supported by OpenGL, is to render all objects into a tiny pick window. All the objects that overlap the window are returned in a list, along with the minimum and maximum *z*-depth found for each object. This sort of system usually has the added advantage of being able to pick on lines and vertices in addition to surfaces. This pick method is always implemented entirely on the host processor and does not use the graphics accelerator. Some other picking methods do use the graphics hardware, and are covered in Section 16.1.

Intersection testing offers some benefits that OpenGL's picking method does not. Comparing a ray against a triangle is normally faster than sending the triangle through OpenGL, having it clipped against a pick window, then inquiring whether the triangle was picked. Intersection testing methods can compute the location, normal vector, texture coordinates, and other surface data. Such methods are also independent of API support (or lack thereof).

The picking problem can be solved efficiently by using a bounding volume hierarchy (see Section 14.1.1). First, we compute the ray from the camera's position through the pixel that the user picked. Then, we recursively test whether this ray hits a bounding volume of the hierarchy. If at

any time the ray misses a bounding volume (BV), then that subtree can be discarded from further tests, since the ray will not hit any of its contents. However, if the ray hits a BV, its children's BVs must be tested as well. Finally, the recursion may end in a leaf that contains geometry, in which case the ray must be tested against each primitive in the geometry node.

As we have seen in Section 14.3, view frustum culling is a means for efficiently discarding geometry that is outside the view frustum. Tests that decide whether a bounding volume is totally outside, totally inside, or partially inside a frustum are needed to use this method.

In collision detection algorithms (see Chapter 17), which are also built upon hierarchies, the system must decide whether or not two primitive objects collide. These primitive objects include triangles, spheres, *axis-aligned bounding boxes* (AABBs), *oriented bounding boxes* (OBBs), and *discrete oriented polytopes* ( $k$ -DOPs).

In all of these cases, we have encountered a certain class of problems that require *intersection tests*. An intersection test determines whether two objects,  $A$  and  $B$ , intersect, which may mean that  $A$  is totally inside  $B$  (or vice versa), that the boundaries of  $A$  and  $B$  intersect, or that they are totally disjoint. However, sometimes more information may be needed, such as the closest intersection point, the distance to this intersection point, etc.

In this chapter, a set of fast intersection test methods is identified and studied thoroughly. We not only present the basic algorithms, but also give advice on how to construct new and efficient intersection test methods. Naturally, the methods presented in this chapter are also of use in offline computer graphics applications. For example, the algorithms presented in Sections 16.6 through 16.9 can be used in ray tracing and global illumination programs.

After briefly covering hardware-accelerated picking methods, this chapter continues with some useful definitions, followed by algorithms for forming bounding volumes around primitives. Rules of thumb for constructing efficient intersection test methods are presented next. Finally, the bulk of the chapter is made up of a cookbook of intersection test methods.

## 16.1 Hardware-Accelerated Picking

There are a few hardware-accelerated picking methods worth mentioning. One method was first presented by Hanrahan and Haeberli [497]. To support picking, the scene is rendered with each polygon having a unique color value that is used as an identifier. The image formed is stored offscreen and is then used for extremely rapid picking. When the user clicks on a pixel, the color identifier is looked up in this image and the polygon is immediately identified. The major disadvantage of this method is that the entire

scene must be rendered in a separate pass to support this sort of picking. This method was originally presented in the context of a three-dimensional paint system. In this sort of application, the amount of picking per view is extremely high, so the cost of forming the buffer once for the view becomes inconsequential.

It is also possible to find the relative location of a point inside a triangle using the color buffer [724]. Each triangle is rendered using Gouraud shading, where the colors of the triangle vertices are red (255, 0, 0), green (0, 255, 0), and blue (0, 0, 255). Say that the color of the picked pixel is (23, 192, 40). This means that the red vertex contributes with a factor 23/255, the green with 192/255, and the red with 40/255. This information can be used to find out the actual coordinates on the triangle, the  $(u, v)$  coordinates of the picked point, and for normal interpolation. The values are barycentric coordinates, which are discussed further in Section 16.8.1. In the same manner, the normals of the vertices can be directly encoded into RGB colors. The interval  $[-1, 1]$  per normal component has to be transformed to the interval  $[0, 1]$  so it can be rendered. Alternatively, rendering can be done directly to a floating-point buffer without the transform. After rendering the triangles using Gouraud shading, the normal at any point can be read from the color buffer.

The possibilities for using the GPU to accelerate selection directly increase considerably with newer hardware and APIs. Features such as the geometry shader, stream out, and triangle identifiers being available to shader programs open up new ways to generate selection sets and know what is in a pick window.

## 16.2 Definitions and Tools

This section introduces notation and definitions useful for this entire chapter.

A ray,  $\mathbf{r}(t)$ , is defined by an origin point,  $\mathbf{o}$ , and a direction vector,  $\mathbf{d}$  (which, for convenience, is usually normalized, so  $\|\mathbf{d}\| = 1$ ). Its mathematical formula is shown in Equation 16.1, and an illustration of a ray is shown in Figure 16.1:

$$\mathbf{r}(t) = \mathbf{o} + t\mathbf{d}. \quad (16.1)$$

The scalar  $t$  is a variable that is used to generate different points on the ray, where  $t$ -values of less than zero are said to lie behind the ray origin (and so are not part of the ray), and the positive  $t$ -values lie in front of it. Also, since the ray direction is normalized, a  $t$ -value generates a point on the ray that is situated  $t$  distance units from the ray origin.

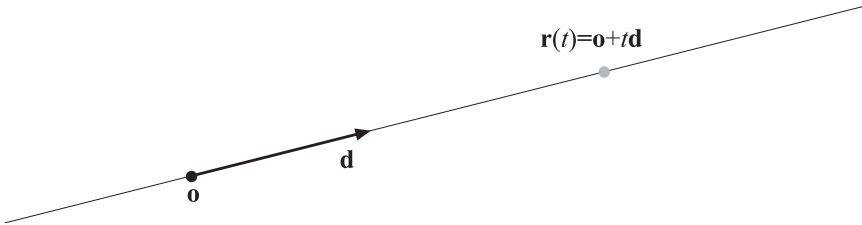


**Figure 16.1.** A simple ray and its parameters:  $\mathbf{o}$  (the ray origin),  $\mathbf{d}$  (the ray direction), and  $t$ , which generates different points on the ray,  $\mathbf{r}(t) = \mathbf{o} + t\mathbf{d}$ .

In practice, we often also store a current distance  $l$ , which is the maximum distance we want to search along the ray. For example, while picking, we usually want the closest intersection along the ray; objects beyond this intersection can be safely ignored. The distance  $l$  starts at  $\infty$ . As objects are successfully intersected,  $l$  is updated with the intersection distance. In the ray/object intersection tests we will be discussing, we will normally not include  $l$  in the discussion. If you wish to use  $l$ , all you have to do is perform the ordinary ray/object test, then check  $l$  against the intersection distance computed and take the appropriate action.

When talking about surfaces, we distinguish *implicit* surfaces from *explicit* surfaces. An implicit surface is defined by Equation 16.2:

$$f(\mathbf{p}) = f(p_x, p_y, p_z) = 0. \quad (16.2)$$

Here,  $\mathbf{p}$  is any point on the surface. This means that if you have a point that lies on the surface and you plug this point into  $f$ , then the result will be 0. Otherwise, the result from  $f$  will be nonzero. An example of an implicit surface is  $p_x^2 + p_y^2 + p_z^2 = r^2$ , which describes a sphere located at the origin with radius  $r$ . It is easily seen that this can be rewritten as  $f(\mathbf{p}) = p_x^2 + p_y^2 + p_z^2 - r^2 = 0$ , which means that it is indeed implicit. Implicit surfaces are briefly covered in Section 13.3, while modeling and rendering with a wide variety of implicit surface types is well covered in Bloomenthal et al. [117].

An explicit surface, on the other hand, is defined by a vector function  $\mathbf{f}$  and some parameters  $(\rho, \phi)$ , rather than a point on the surface. These parameters yield points,  $\mathbf{p}$ , on the surface. Equation 16.3 below shows the general idea:

$$\mathbf{p} = \begin{pmatrix} p_x \\ p_y \\ p_z \end{pmatrix} = \mathbf{f}(\rho, \phi) = \begin{pmatrix} f_x(\rho, \phi) \\ f_y(\rho, \phi) \\ f_z(\rho, \phi) \end{pmatrix}. \quad (16.3)$$

An example of an explicit surface is again the sphere, this time expressed in spherical coordinates, where  $\rho$  is the latitude and  $\phi$  longitude, as shown

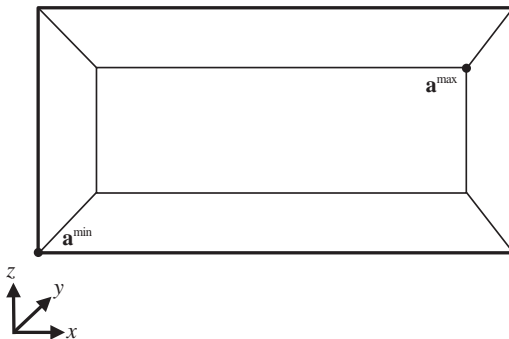


**Figure 16.2.** A three-dimensional AABB,  $A$ , with its extreme points,  $\mathbf{a}^{\min}$  and  $\mathbf{a}^{\max}$ , and the axes of the standard basis.

in Equation 16.4:

$$\mathbf{f}(\rho, \phi) = \begin{pmatrix} r \sin \rho \cos \phi \\ r \sin \rho \sin \phi \\ r \cos \rho \end{pmatrix} \quad (16.4)$$

As another example, a triangle,  $\Delta \mathbf{v}_0 \mathbf{v}_1 \mathbf{v}_2$ , can be described in explicit form like this:  $\mathbf{t}(u, v) = (1 - u - v)\mathbf{v}_0 + u\mathbf{v}_1 + v\mathbf{v}_2$ , where  $u \geq 0$ ,  $v \geq 0$  and  $u + v \leq 1$  must hold.

Finally, we shall give definitions of three bounding volumes, namely the AABB, the OBB, and the  $k$ -DOP, used extensively in this and the next chapter.

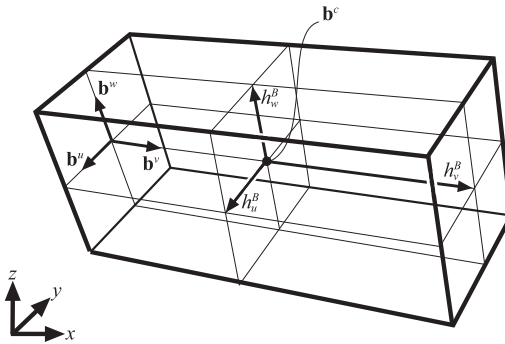
**Definition.** An *axis-aligned bounding box*<sup>1</sup> (also called a *rectangular box*), AABB for short, is a box whose faces have normals that coincide with the standard basis axes. For example, an AABB  $A$  is described by two diagonally opposite points,  $\mathbf{a}^{\min}$  and  $\mathbf{a}^{\max}$ , where  $\mathbf{a}_i^{\min} \leq \mathbf{a}_i^{\max}, \forall i \in \{x, y, z\}$ .

Figure 16.2 contains an illustration of a three-dimensional AABB together with notation.

**Definition.** An *oriented bounding box*, OBB for short, is a box whose faces have normals that are all pairwise orthogonal—i.e., it is an AABB that is arbitrarily rotated. An OBB,  $B$ , can be described by the center point of the box,  $\mathbf{b}^c$ , and three normalized vectors,  $\mathbf{b}^u$ ,  $\mathbf{b}^v$ , and  $\mathbf{b}^w$ , that describe the side directions of the box. Their respective positive half-lengths are denoted  $h_u^B$ ,  $h_v^B$ , and  $h_w^B$ , which is the distance from  $\mathbf{b}^c$  to the center of the respective face.

---

<sup>1</sup>In fact, neither the AABB nor OBB needs to be used as a BV, but can act as a pure geometric box. However, these names are widely accepted.



**Figure 16.3.** A three-dimensional OBB,  $B$ , with its center point,  $\mathbf{b}^c$ , and its normalized, positively oriented side vectors,  $\mathbf{b}^u$ ,  $\mathbf{b}^v$ , and  $\mathbf{b}^w$ . The half-lengths of the sides,  $h_u^B$ ,  $h_v^B$ , and  $h_w^B$ , are the distances from the center of the box to the center of the faces, as shown.

A three-dimensional OBB and its notation are depicted in Figure 16.3.

**Definition.** A  $k$ -DOP (*discrete oriented polytope*) is defined by  $k/2$  (where  $k$  is even) normalized normals (orientations),  $\mathbf{n}_i$ ,  $1 \leq i \leq k/2$ , and with each  $\mathbf{n}_i$  two associated scalar values  $d_i^{\min}$  and  $d_i^{\max}$ , where  $d_i^{\min} < d_i^{\max}$ . Each triple  $(\mathbf{n}_i, d_i^{\min}, d_i^{\max})$  describes a slab,  $S_i$ , which is the volume between the two planes,  $\pi_i^{\min} : \mathbf{n}_i \cdot \mathbf{x} + d_i^{\min} = 0$  and  $\pi_i^{\max} : \mathbf{n}_i \cdot \mathbf{x} + d_i^{\max} = 0$ , and where the intersection of all slabs,  $\bigcap_{1 \leq l \leq k/2} S_l$ , is the actual  $k$ -DOP volume. The  $k$ -DOP is defined as the tightest set of slabs that bound the object [315].

Figure 16.4 depicts an 8-DOP in two dimensions.

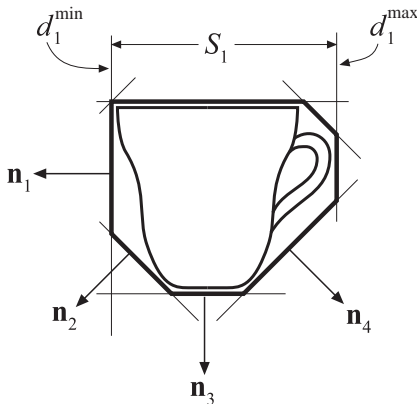


**Figure 16.4.** An example of a two-dimensional 8-DOP for a tea cup, with all normals,  $\mathbf{n}_i$ , shown along with the zero'th slab,  $S_1$ , and the “size” of the slab:  $d_1^{\min}$  and  $d_1^{\max}$ .

A *separating axis* specifies a line in which two objects that do not overlap (are disjoint) have projections onto that line that also do not overlap. Similarly, where a plane can be inserted between two three-dimensional objects, that plane's normal defines a separating axis. An important tool for intersection testing [433, 451] follows, one that works for convex polyhedra such as AABBs, OBBs, and  $k$ -DOPs. It is an aspect of the *separating hyperplane theorem* [135].<sup>2</sup>

**Separating Axis Test (SAT).** For any two arbitrary, convex, disjoint polyhedra,  $A$  and  $B$ , there exists at least one separating axis where the projections of the polyhedra, which form intervals on the axis, are also disjoint. This does not hold if one object is concave. For example, the walls of a well and a bucket inside may not touch, but no plane can divide them. Furthermore, if  $A$  and  $B$  are disjoint, then they can be separated by an axis that is orthogonal (i.e., by a plane that is parallel) to either

1. A face of  $A$ ,
2. A face of  $B$ , or
3. An edge from each polyhedron (e.g., cross product).

This test is illustrated for two boxes in Figure 16.21 on page 768. Note that the definition of a convex polyhedron is very liberal here. A line segment and a convex polygon such as a triangle are also convex polyhedra (though degenerate, since they enclose no volume). A line segment  $A$  does not have a face, so the first test disappears. This test is used in deriving the box/line segment overlap test in Section 16.7.2, the triangle/box overlap test in Section 16.12, and the OBB/OBB overlap test in Section 16.13.5.

To return to the discussion of methods that can be brought to bear, a common technique for optimizing intersection tests is to make some simple calculations early on that can determine whether the ray or object totally misses the other object. Such a test is called a *rejection test*, and if the test succeeds, the intersection is said to be *rejected*.

Another approach often used in this chapter is to project the three-dimensional objects onto the “best” orthogonal plane ( $xy$ ,  $xz$ , or  $yz$ ), and solve the problem in two dimensions instead.

Finally, due to numerical imprecision, we often use a very small number in the intersection tests. This number is denoted  $\epsilon$  (epsilon), and its value will vary from test to test. However, often an epsilon is chosen that works for the programmer's problem cases (what Press et al. [1034] call a “convenient fiction”), as opposed to doing careful roundoff error analysis

---

<sup>2</sup>This test is sometimes known as the “separating axis theorem” in computer graphics, a misnomer we helped promulgate in previous editions. It is not a theorem itself, but is rather a special case of the separating hyperplane theorem.

and epsilon adjustment. Such code used in another setting may well break because of differing conditions. Ericson’s book [315] discusses the area of numerical robustness in depth in the context of geometric computation. This caveat firmly in place, we sometimes do attempt to provide epsilons that are at least reasonable starting values for “normal” data, small scale (say less than 100, more than 0.1) and near the origin.

## 16.3 Bounding Volume Creation

Given a collection of objects, finding a tight fitting bounding volume is important to minimizing intersection costs. The chance that an arbitrary ray will hit any convex object is proportional to that object’s surface area (see Section 16.4). Minimizing this area increases the efficiency of any intersection algorithm, as a rejection is never slower to compute than an intersection. In contrast, it is often better to minimize the volume of each BV for collision detection algorithms. This section briefly covers methods of finding optimal or near-optimal bounding volumes given a collection of polygons.

### *AABB and k-DOP Creation*

The simplest bounding volumes to create is an AABB. Take the minimum and maximum extents of the set of polygon vertices along each axis and the AABB is formed. The *k*-DOP is an extension of the AABB: Project the vertices onto each normal,  $\mathbf{n}_i$ , of the *k*-DOP, and the extreme values ( $\min, \max$ ) of these projections are stored in  $d_{\min}^i$  and  $d_{\max}^i$ . These two values define the tightest slab for that direction. Together, all such values define a minimal *k*-DOP.

### *Sphere Creation*

Bounding sphere formation is not as straightforward as determining slab extents. There are a number of algorithms that perform this task, and these have speed versus quality tradeoffs. A fast, constant-time single pass algorithm is to form an AABB for the polygon set and then use the center and the diagonal of this box to form the sphere. This sometimes gives a poor fit, and the fit can often be improved by another quick pass: Starting with the center of the AABB as the center of the sphere BV, go through all vertices once again and find the one that is farthest from this center (comparing against the square of the distance so as to avoid taking the square root). This is then the new radius.

Ritter [1070] presents a simple algorithm that creates a near-optimal bounding sphere. The idea is to find the vertex that is at the minimum and the vertex at the maximum along each of the  $x$ ,  $y$ , and  $z$  axes. For

these three pairs of vertices, find the pair with the largest distance between them. Use this pair to form a sphere with its center at the midpoint between them and a radius equal to the distance to them. Go through all the other vertices and check their distance  $d$  to the center of the sphere. If the vertex is outside the sphere's radius  $r$ , move the sphere's center toward the vertex by  $(d - r)/2$ , set the radius to  $(d + r)/2$ , and continue. This step has the effect of enclosing the vertex and the existing sphere in a new sphere. After this second time through the list, the bounding sphere is guaranteed to enclose all vertices. Code is available on the web.

Welzl [1339] presents a more complex algorithm, which is implemented by Eberly [294, 1131] and Ericson [315], with code on the web. This algorithm is expected to be linear for a randomized list of vertices (randomization helps find a good sphere quickly on average). The idea is to find a supporting set of points defining a sphere. A sphere can be defined by a set of two, three, or four points on its surface. When a vertex is found to be outside the current sphere, its location is added to the supporting set (and possibly old support vertices removed from the set), the new sphere is computed, and the entire list is run through again. This process repeats until the sphere contains all vertices. While more complex than the previous methods, this algorithm guarantees that an optimal bounding sphere is found.

### OBB Creation

OBB formation, with its arbitrary basis orientation, is even more involved than finding a reasonable bounding sphere. One method by Gottschalk [434] will be presented, followed by a brief explanation of another method by Eberly [294].

It has been shown that a tight-fitting OBB enclosing an object can be found by computing an orientation from the triangles of the convex hull [433, 434]. The convex hull is used because it avoids using points in the interior of the object that should not affect the orientation of the box. Also, an integration is performed over each triangle of the convex hull. This is done since using the vertices of the convex hull can make for bad-fitting boxes, if, for example, several vertices clump in a small region. Here, we will present the formulae for computing a good-fit OBB using a statistical method. The derivation is found in Gottschalk's Ph.D. thesis [434].

First, the convex hull of an object must be computed. This can be done with, for example, the *Quickhull* algorithm [62]. This gives us, say,  $n$  triangles defined as  $\Delta \mathbf{p}^k \mathbf{q}^k \mathbf{r}^k$ , where  $\mathbf{p}^k$ ,  $\mathbf{q}^k$ , and  $\mathbf{r}^k$  are the vertices of triangle  $k$ ,  $0 \leq k < n$ . We also denote the area of triangle  $k$  as  $a^k$ , and the total area of the convex hull as  $a^H = \sum_{k=0}^{n-1} a^k$ . Furthermore, the centroid of triangle  $i$  is  $\mathbf{m}^i = (\mathbf{p}^i + \mathbf{q}^i + \mathbf{r}^i)/3$ , that is, the mean of the vertices. The centroid of the whole convex hull,  $\mathbf{m}^H$ , is the weighted mean of the

triangle centroids, as shown in Equation 16.5:

$$\mathbf{m}^H = \frac{1}{a^H} \sum_{k=0}^{n-1} a^k \mathbf{m}^k. \quad (16.5)$$

With the use of these definitions, we will present a formula that computes a  $3 \times 3$  covariance matrix,  $\mathbf{C}$ , whose eigenvectors (see Section A.3.1 on how to compute the eigenvectors) are the direction vectors for a good-fit box:

$$\mathbf{C} = [c_{ij}] = \left[ \left( \frac{1}{a^H} \sum_{k=0}^{n-1} \frac{a^k}{12} (9m_i^k m_j^k + p_i^k p_j^k + q_i^k q_j^k + r_i^k r_j^k) \right) - m_i^H m_j^H \right], \\ 0 \leq i, j < 3. \quad (16.6)$$

After computing  $\mathbf{C}$ , the eigenvectors are computed and normalized. These vectors are the direction vectors,  $\mathbf{a}^u$ ,  $\mathbf{a}^v$ , and  $\mathbf{a}^w$ , of the OBB. We must next find the center and the half-lengths of the OBB. This is done by projecting the points of the convex hull onto the direction vectors and finding the minimum and maximum along each direction. These will determine the size and position of the box, i.e., will fully specify the OBB according to its definition (see Section 16.2).

When computing the OBB, the most demanding operation is the convex hull computation, which takes  $O(n \log n)$  time, where  $n$  is the number of primitives of the object. The basis calculation takes, at most, linear time, and the eigenvector computation takes constant time, which means that computing an OBB for a set of  $n$  triangles takes  $O(n \log n)$  time.

Eberly [294] presents a method for computing a minimum-volume OBB using a minimization technique. An advantage is that the convex hull need not be computed. This is an iterative algorithm, and so the initial guess of the box determines how fast the solution converges to the minimum box. For a box with the axes  $\mathbf{a}^u$ ,  $\mathbf{a}^v$ , and  $\mathbf{a}^w$ , the points are projection onto these axes. The min,  $k_{\min}^u$ , and max,  $k_{\max}^u$ , along  $\mathbf{a}^u$  are found. Then  $k_{\min}^v$ ,  $k_{\max}^v$ ,  $k_{\min}^w$ , and  $k_{\max}^w$  are computed similarly. The center of this box is then

$$\mathbf{a}^c = \frac{k_{\min}^u + k_{\max}^u}{2} \mathbf{a}^u + \frac{k_{\min}^v + k_{\max}^v}{2} \mathbf{a}^v + \frac{k_{\min}^w + k_{\max}^w}{2} \mathbf{a}^w. \quad (16.7)$$

The half-lengths of the sides of the box are then  $h_l = (k_{\max}^l - k_{\min}^l)/2$ , for  $l \in \{u, v, w\}$ . Eberly samples the set of possible directions of the box, and uses the axes whose box is smallest as a starting point for the numeric minimizer. Then Powell's direction set method [1034] is used to find the minimum volume box. Eberly has code for this operation on the web [294].

## 16.4 Geometric Probability

Common geometric operations include whether a plane or ray intersects an object, and whether a point is inside it. A related question is what is the relative probability that a point, ray, or plane intersects an object. The relative probability of a random point in space being inside an object is fairly obvious: It is directly proportional to the volume of the object. So a  $1 \times 2 \times 3$  box is 6 times as likely to contain a randomly chosen point as is a  $1 \times 1 \times 1$  box.

For an arbitrary ray in space, what is the relative chance of it intersecting one object versus another? This question is related to another question: What is the average number of pixels covered by an object when using an orthographic projection? An orthographic projection can be thought of as a set of parallel rays in the view volume, with a ray traveling through each pixel. Given a randomly oriented object, the number of pixels covered is equal to the number of rays intersecting the object.

An informal solution by Nienhuys [935] for convex objects is as follows:

1. Imagine an equilateral triangle being randomly oriented and then projected onto a plane a huge number of times. The ratio of the triangle's average projection area divided by its actual surface area is some constant (though unknown) value  $f$ .
2. All triangles, at the limit,<sup>3</sup> can be tessellated into equilateral triangles of varying size, so  $f$  is the same ratio for all shapes of triangles.
3. All convex objects can be tessellated into triangles, at the limit.
4. All (non-degenerate) convex objects have a depth complexity of 2 from any angle.
5. A sphere is a convex object, and its surface area is  $4\pi r^2$ .
6. A sphere's orthographic projection is always a circle with area  $\pi r^2$ .

So a sphere's projected area is always  $\frac{1}{4}$  of its surface area. That is,  $f = \frac{1}{4}$  for a sphere, and also for any convex object, by the reasoning in the steps presented.

A sphere has a depth complexity of 2, so there are always two points on the sphere projected to one point on the projected circle. This allows us to know what  $f$  for a triangle is:  $\frac{1}{4}$  times a depth complexity of 2, i.e.,  $f = \frac{1}{2}$ . This means that any polygon projects an average surface area equal to  $\frac{1}{2}$  of its actual surface area.

---

<sup>3</sup>Meaning that an infinite number of equilateral triangles can be used to tessellate an arbitrary triangle.

So for our original question, a  $1 \times 1 \times 1$  box has a surface area of 6 and the  $1 \times 2 \times 3$  box has a surface area of 22. Therefore, the second box is  $22/6 \approx 3.67$  times as likely to be hit by an arbitrary ray as the first box.

This metric is referred to as the *surface area heuristic* (SAH) [35, 805, 1314] in the ray tracing literature, as it is important in forming efficient visibility structures for data sets. One use is in comparing bounding volume efficiency. For example, a sphere has a relative probability of  $1.57 (\pi/2)$  of being hit by a ray, compared to an inscribed cube (i.e., a cube with its corners touching the sphere). Similarly, a cube has a relative probability of 1.91 ( $6/\pi$ ) of being hit, versus a sphere inscribed inside it.

This type of probability measurement can be useful in areas such as level of detail computation. For example, imagine a long and thin object that covers many fewer pixels than a rounder object, yet both have the same bounding sphere size. Knowing this in advance from the area of its bounding box, the long and thin object may be assigned a different screen area for when it changes its level of detail.

It may also be useful to know the relative probability of a plane intersecting one convex object versus another. Similar to surface area, the chance of a plane intersecting a box is directly proportional to the sum of the extents of the box in three dimensions [1136]. This sum is called the object's *mean width*. For example, a cube with an edge length of 1 has a mean width of  $1 + 1 + 1 = 3$ . A box's mean width is proportional to its chance of being hit by a plane. So a  $1 \times 1 \times 1$  box has a measure of 3, and a  $1 \times 2 \times 3$  box a measure of 6, meaning that the second box is twice as likely to be intersected by an arbitrary plane.

However, this sum is larger than the true geometric mean width, which is the average projected length of an object along a fixed axis over the set of all possible orientations. There is no easy relationship (such as surface area) among different convex object types for mean width computation. A sphere of diameter  $d$  has a geometric mean width of  $d$ , since the sphere spans this same length for any orientation. We will leave this topic by simply stating that multiplying the sum of a box's dimensions (i.e., its mean width) by 0.5 gives its geometric mean width, which can be compared directly to a sphere's diameter. So the  $1 \times 1 \times 1$  box with measure 3 has a geometric mean width of  $3 \times 0.5 = 1.5$ . A sphere bounding this box has a diameter of  $\sqrt{3} = 1.732$ . Therefore a sphere surrounding a cube is  $1.732/1.5 = 1.155$  times as likely to be intersected by an arbitrary plane. It is worth noting that the best-fitting sphere around an object can in some cases be smaller than the sphere whose surface encloses all the object's bounding box corners.

These relationships are useful for determining the benefits of various algorithms. Frustum culling is a prime candidate, as it involves intersecting planes with bounding volumes. The relative benefits of using a sphere

versus a box for a bounding volume can be computed. Another use is for determining whether and where to best split a BSP node containing objects, so that frustum culling performance becomes better (see Section 14.1.2).

## 16.5 Rules of Thumb

Before we begin studying the specific intersection methods, here are some rules of thumb that can lead to faster, more robust, and more exact intersection tests. These should be kept in mind when designing, inventing, and implementing an intersection routine:

- Perform computations and comparisons early on that might trivially *reject* or *accept* various types of intersections to obtain an early escape from further computations.
- If possible, exploit the results from previous tests.
- If more than one rejection or acceptance test is used, then try changing their internal order (if possible), since a more efficient test may result. Do not assume that what appears to be a minor change will have no effect.
- Postpone expensive calculations (especially trigonometric functions, square roots, and divisions) until they are truly needed (see Section 16.8 for an example of delaying an expensive division).
- The intersection problem can often be simplified considerably by *reducing the dimension* of the problem (for example, from three dimensions to two dimensions or even to one dimension). See Section 16.9 for an example.
- If a single ray or object is being compared to many other objects at a time, look for precalculations that can be done just once before the testing begins.
- Whenever an intersection test is expensive, it is often good to start with a sphere or other simple BV around the object to give a first level of quick rejection.
- Make it a habit always to perform timing comparisons on your computer, and use real data and testing situations for the timings.
- Finally, try to make your code *robust*. This means it should work for all special cases and that it will be insensitive to as many floating point precision errors as possible. Be aware of any limitations it

may have. For more information about numerical and geometrical robustness, we refer to Ericson's book [315].

Finally, we emphasize on the fact that it is hard to determine whether there is a “best” algorithm for a particular test. For evaluation, random data with a set of different, predetermined hit rates are often used, but this shows only part of the truth. However, the algorithm will get used in real scenarios, e.g., in a game, and it is best evaluated in that context, and the more test scenes, the better understanding of performance issues you get. Furthermore, algorithms tend to behave differently on different CPU architectures, and that is also something that needs to be examined if the algorithm should work well over several platforms.

## 16.6 Ray/Sphere Intersection

Let us start with a mathematically simple intersection test—namely, that between a ray and a sphere. As we will see later, the straightforward mathematical solution can be made faster if we begin thinking in terms of the geometry involved [480].

### 16.6.1 Mathematical Solution

A sphere can be defined by a center point,  $\mathbf{c}$ , and a radius,  $r$ . A more compact implicit formula (compared to the one previously introduced) for the sphere is then

$$f(\mathbf{p}) = \|\mathbf{p} - \mathbf{c}\| - r = 0, \quad (16.8)$$

where  $\mathbf{p}$  is any point on the sphere's surface. To solve for the intersections between a ray and a sphere, the ray  $\mathbf{r}(t)$  simply replaces  $\mathbf{p}$  in Equation 16.8 to yield

$$f(\mathbf{r}(t)) = \|\mathbf{r}(t) - \mathbf{c}\| - r = 0. \quad (16.9)$$

Using Equation 16.1, that  $\mathbf{r}(t) = \mathbf{o} + t\mathbf{d}$ , Equation 16.9 is simplified as follows:

$$\begin{aligned} & \|\mathbf{r}(t) - \mathbf{c}\| - r = 0 \\ \iff & \|\mathbf{o} + t\mathbf{d} - \mathbf{c}\| = r \\ \iff & (\mathbf{o} + t\mathbf{d} - \mathbf{c}) \cdot (\mathbf{o} + t\mathbf{d} - \mathbf{c}) = r^2 \\ \iff & t^2(\mathbf{d} \cdot \mathbf{d}) + 2t(\mathbf{d} \cdot (\mathbf{o} - \mathbf{c})) + (\mathbf{o} - \mathbf{c}) \cdot (\mathbf{o} - \mathbf{c}) - r^2 = 0 \\ \iff & t^2 + 2t(\mathbf{d} \cdot (\mathbf{o} - \mathbf{c})) + (\mathbf{o} - \mathbf{c}) \cdot (\mathbf{o} - \mathbf{c}) - r^2 = 0. \end{aligned} \quad (16.10)$$

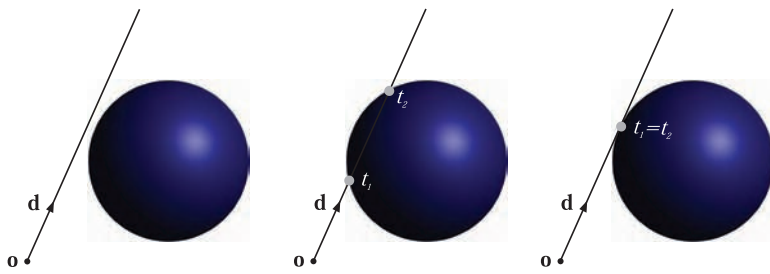


**Figure 16.5.** The left image shows a ray that misses a sphere and consequently  $b^2 - c < 0$ . The middle image shows a ray that intersects a sphere at two points ( $b^2 - c > 0$ ) determined by the scalars  $t_1$  and  $t_2$ . The right image illustrates the case where  $b^2 - c = 0$ , which means that the two intersection points coincide.

The last step comes from the fact that  $\mathbf{d}$  is assumed to be normalized, i.e.,  $\mathbf{d} \cdot \mathbf{d} = \|\mathbf{d}\|^2 = 1$ . Not surprisingly, the resulting equation is a polynomial of the second order, which means that if the ray intersects the sphere, it does so at up to two points (see Figure 16.5). If the solutions to the equation are imaginary, then the ray misses the sphere. If not, the two solutions  $t_1$  and  $t_2$  can be inserted into the ray equation to compute the intersection points on the sphere.

The resulting Equation 16.10 can be written as a quadratic equation:

$$t^2 + 2tb + c = 0, \quad (16.11)$$

where  $b = \mathbf{d} \cdot (\mathbf{o} - \mathbf{c})$  and  $c = (\mathbf{o} - \mathbf{c}) \cdot (\mathbf{o} - \mathbf{c}) - r^2$ . The solutions of the second-order equation are shown below:

$$t = -b \pm \sqrt{b^2 - c}. \quad (16.12)$$

Note that if  $b^2 - c < 0$ , then the ray misses the sphere and the intersection can be rejected and calculations avoided (e.g., the square root and some additions). If this test is passed, both  $t_0 = -b - \sqrt{b^2 - c}$  and  $t_1 = -b + \sqrt{b^2 - c}$  can be computed. To find the smallest positive value of  $t_0$  and  $t_1$ , an additional comparison needs to be executed.

If these computations are instead viewed from a geometric point of view, then better rejection tests can be discovered. The next subsection describes such a routine.

For the other quadrics, e.g., the cylinder, ellipsoid, cone, and hyperboloid, the mathematical solutions to their intersection problems are almost as straightforward as for the sphere. Sometimes, however, it is necessary to bound a surface (for example, usually you do not want a cylinder to be infinite, so caps must be added to its ends), which can add some complexity to the code.

## 16.6.2 Optimized Solution

For the ray/sphere intersection problem, we begin by observing that intersections behind the ray origin are not needed (this is normally the case in picking, etc.). Therefore, a vector  $\mathbf{l} = \mathbf{c} - \mathbf{o}$ , which is the vector from the ray origin to the center of the sphere, is computed. All notation that is used is depicted in Figure 16.6. Also, the squared length of this vector is computed,  $l^2 = \mathbf{l} \cdot \mathbf{l}$ . Now if  $l^2 < r^2$ , this implies that the ray origin is inside the sphere, which, in turn, means that the ray is guaranteed to hit the sphere and we can exit if we want to detect only whether or not the ray hits the sphere; otherwise, we proceed. Next, the projection of  $\mathbf{l}$  onto the ray direction,  $\mathbf{d}$ , is computed:  $s = \mathbf{l} \cdot \mathbf{d}$ . Now, here comes the first rejection test: If  $s < 0$  and the ray origin is outside the sphere, then the sphere is behind the ray origin and we can reject the intersection. Otherwise, the squared distance from the sphere center to the projection is computed using the Pythagorean theorem (Equation B.6):  $m^2 = l^2 - s^2$ . The second rejection test is even simpler than the first: If  $m^2 > r^2$  the ray will definitely miss the sphere and the rest of the calculations can safely be omitted. If the sphere and ray pass this last test, then the ray is guaranteed to hit the sphere and we can exit if that was all we were interested in finding out.

To find the real intersection points, a little more work has to be done. First, the squared distance  $q^2 = r^2 - m^2$  (see Figure 16.6) is calculated.<sup>4</sup> Since  $m^2 \leq r^2$ ,  $q^2$  is greater than or equal to zero, and this means that  $q = \sqrt{q^2}$  can be computed. Finally, the distances to the intersections are  $t = s \pm q$ , whose solution is quite similar to that of the second-order

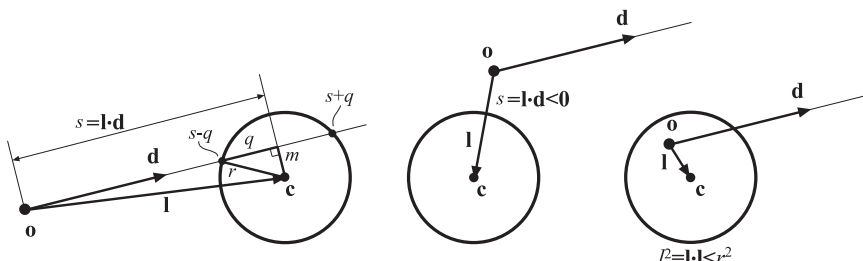


**Figure 16.6.** The notation for the geometry of the optimized ray/sphere intersection. In the left figure, the ray intersects the sphere in two points, where the distances are  $t = s \pm q$  along the ray. The middle case demonstrates a rejection made when the sphere is behind the ray origin. Finally, at the right, the ray origin is inside the sphere, in which case the ray always hits the sphere.

<sup>4</sup>The scalar  $r^2$  could be computed once and stored within the data structure of the sphere in an attempt to gain further efficiency. In practice such an “optimization” may be slower, as more memory is then accessed, a major factor for algorithm performance.

equation obtained in the previous mathematical solution section. If we are interested in only the first, positive intersection point, then we should use  $t_1 = s - q$  for the case where the ray origin is outside the sphere and  $t_2 = s + q$  when the ray origin is inside. The true intersection point(s) are found by inserting the  $t$ -value(s) into the ray equation (Equation 16.1).

Pseudocode for the optimized version is shown in the box below. The routine returns a boolean value that is REJECT if the ray misses the sphere and INTERSECT otherwise. If the ray intersects the sphere, then the distance,  $t$ , from the ray origin to the intersection point along with the intersection point,  $\mathbf{p}$ , are also returned.

```

RaySphereIntersect( $\mathbf{o}, \mathbf{d}, \mathbf{c}, r$ )
  returns ({REJECT, INTERSECT},  $t$ ,  $\mathbf{p}$ )
  1 :    $\mathbf{l} = \mathbf{c} - \mathbf{o}$ 
  2 :    $s = \mathbf{l} \cdot \mathbf{d}$ 
  3 :    $l^2 = \mathbf{l} \cdot \mathbf{l}$ 
  4 :   if( $s < 0$  and  $l^2 > r^2$ ) return (REJECT, 0,  $\mathbf{0}$ );
  5 :    $m^2 = l^2 - s^2$ 
  6 :   if( $m^2 > r^2$ ) return (REJECT, 0,  $\mathbf{0}$ );
  7 :    $q = \sqrt{r^2 - m^2}$ 
  8 :   if( $l^2 > r^2$ )  $t = s - q$ 
  9 :   else  $t = s + q$ 
 10 :  return (INTERSECT,  $t$ ,  $\mathbf{o} + t\mathbf{d}$ );

```

Note that after line 3, we can test whether  $\mathbf{p}$  is inside the sphere and, if all we want to know is whether the ray and sphere intersect, the routine can terminate if they do so. Also, after line 6, the ray is guaranteed to hit the sphere. If we do an operation count (counting adds, multiplies, compares, etc.), we find that the geometric solution, *when followed to completion*, is approximately equivalent to the algebraic solution presented earlier. The important difference is that the rejection tests are done much earlier in the process, making the overall cost of this algorithm lower on average.

Optimized geometric algorithms exist for computing the intersection between a ray and some other quadrics and hybrid objects. For example, there are methods for the cylinder [216, 539, 1163], cone [539, 1164], ellipsoid, capsule (a cylinder with spherical caps), and lozenge (a box with cylindrical sides and spherical corners) [294].

## 16.7 Ray/Box Intersection

Three methods for determining whether a ray intersects a solid box are given below. The first handles both AABBs and OBBs. The second is

often faster, but deal with only the simpler AABB. The third is based on the separating axis test on page 731, and handles only line segments versus AABBs. Here, we use the definitions and notation of the BVs from Section 16.2.

### 16.7.1 Slabs Method

One scheme for ray/AABB intersection is based on Kay and Kajiya's slab method [480, 639], which in turn is inspired by the Cyrus-Beck line clipping algorithm [217].

We extend this scheme to handle the more general OBB volume. It returns the closest positive  $t$ -value (i.e., the distance from the ray origin  $\mathbf{o}$  to the point of intersection, if any exists). Optimizations for the AABB will be treated after we present the general case. The problem is approached by computing all  $t$ -values for the ray and all planes belonging to the faces of the OBB. The box is considered as a set of three slabs,<sup>5</sup> as illustrated in two dimensions in the left part of Figure 16.7. For each slab, there is a minimum and a maximum  $t$ -value, and these are called  $t_i^{\min}$  and  $t_i^{\max}$ ,  $\forall i \in \{u, v, w\}$ . The next step is to compute the variables in Equation 16.14:

$$\begin{aligned} t^{\min} &= \max(t_u^{\min}, t_v^{\min}, t_w^{\min}) \\ t^{\max} &= \min(t_u^{\max}, t_v^{\max}, t_w^{\max}) \end{aligned} \quad (16.14)$$

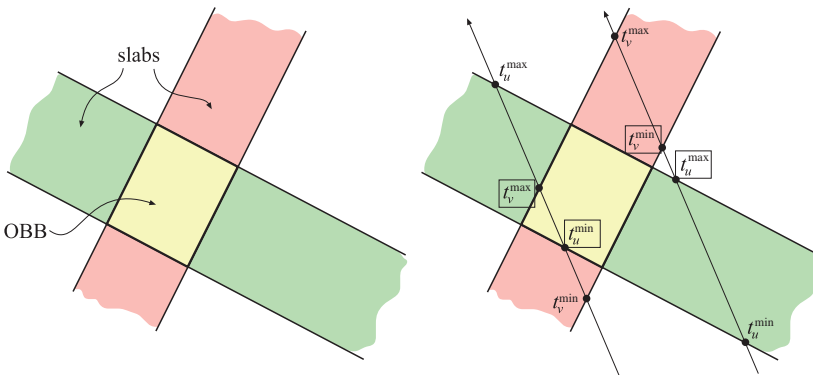


**Figure 16.7.** The left figure shows a two-dimensional OBB (*oriented bounding box*) formed by two slabs, while the right shows two rays that are tested for intersection with the OBB. All  $t$ -values are shown, and they are subscripted with  $u$  for the green slab and with  $v$  for the other. The extreme  $t$ -values are marked with boxes. The left ray hits the OBB since  $t^{\min} < t^{\max}$ , and the right ray misses since  $t^{\max} < t^{\min}$ .

<sup>5</sup>A slab is two parallel planes, which are grouped for faster computations.

Now, the clever test: If  $t^{\min} \leq t^{\max}$ , then the ray intersects the box; otherwise it misses. The reader should convince himself of this by inspecting the illustration on the right side of Figure 16.7.

Pseudocode for the ray/OBB intersection test, between an OBB ( $A$ ) and a ray (described by Equation 16.1) follows. The code returns a boolean indicating whether or not the ray intersects the OBB (INTERSECT or REJECT), and the distance to the intersection point (if it exists). Recall that for an OBB  $A$ , the center is denoted  $\mathbf{a}^c$ , and  $\mathbf{a}^u$ ,  $\mathbf{a}^v$ , and  $\mathbf{a}^w$  are the normalized side directions of the box;  $h_u$ ,  $h_v$ , and  $h_w$  are the positive half-lengths (from the center to a box face).

```

RayOBBIntersect( $\mathbf{o}, \mathbf{d}, A$ )
    returns ({REJECT, INTERSECT},  $t$ );
1 :    $t^{\min} = -\infty$ 
2 :    $t^{\max} = \infty$ 
3 :    $\mathbf{p} = \mathbf{a}^c - \mathbf{o}$ 
4 :   for each  $i \in \{u, v, w\}$ 
5 :      $e = \mathbf{a}^i \cdot \mathbf{p}$ 
6 :      $f = \mathbf{a}^i \cdot \mathbf{d}$ 
7 :     if( $|f| > \epsilon$ )
8 :        $t_1 = (e + h_i)/f$ 
9 :        $t_2 = (e - h_i)/f$ 
10 :      if( $t_1 > t_2$ ) swap( $t_1, t_2$ );
11 :      if( $t_1 > t^{\min}$ )  $t^{\min} = t_1$ 
12 :      if( $t_2 < t^{\max}$ )  $t^{\max} = t_2$ 
13 :      if( $t^{\min} > t^{\max}$ ) return (REJECT, 0);
14 :      if( $t^{\max} < 0$ ) return (REJECT, 0);
15 :      else if( $-e - h_i > 0$  or  $-e + h_i < 0$ ) return (REJECT, 0);
16 :      if( $t^{\min} > 0$ ) return (INTERSECT,  $t^{\min}$ );
17 :      else return (INTERSECT,  $t^{\max}$ );

```

Line 7 checks whether the ray direction is not perpendicular to the normal direction of the slab currently being tested. In other words, it tests whether the ray is not parallel to the slab planes and so can intersect them. Note that  $\epsilon$  is a very small number here, on the order of  $10^{-20}$ , simply to avoid overflow when the division occurs. Lines 8 and 9 show a division by  $f$ ; in practice, it is usually faster to compute  $1/f$  once and multiply by this value, since division is often expensive. Line 10 ensures that the minimum of  $t_1$  and  $t_2$  is stored in  $t_1$ , and consequently, the maximum of these is stored in  $t_2$ . In practice, the swap does not have to be made; instead lines 11 and 12 can be repeated for the branch, and  $t_1$  and  $t_2$  can change positions there. Should line 13 return, then the ray misses the box, and similarly, if line 14

returns, then the box is behind the ray origin. line 15 is executed if the ray is parallel to the slab (and so cannot intersect it); it tests if the ray is outside the slab. If so, then the ray misses the box and the test terminates. For even faster code, Haines discusses a way of unwrapping the loop and thereby avoiding some code [480].

There is an additional test not shown in the pseudocode that is worth adding in actual code. As mentioned when we defined the ray, we usually want to find the closest object. So after line 15, we could also test whether  $t^{\min} \geq l$ , where  $l$  is the current ray length. If the new intersection is not closer, the intersection is rejected. This test could be deferred until after the entire ray/OBB test has been completed, but it is usually more efficient to try for an early rejection inside the loop.

There are other optimizations for the special case of an OBB that is an AABB. Lines 5 and 6 change to  $e = p_i$  and  $f = d_i$ , which makes the test faster. Normally the  $\mathbf{a}^{\min}$  and  $\mathbf{a}^{\max}$  corners of the AABB are used on lines 8 and 9, so the addition and subtraction is avoided. Kay and Kajiya [639] and Smits [1200] note that line 7 can be avoided by allowing division by 0 and interpreting the processor's results correctly. Williams et al. [1352] provide implementation details to handle division by 0 correctly, along with other optimizations. Woo [1373] introduced an optimization where only three candidate planes are identified and tested against.

A generalization of the slabs method can be used to compute the intersection of a ray with a  $k$ -DOP, frustum, or any convex polyhedron; code is available on the web [481].

### 16.7.2 Line Segment/Box Overlap Test

In this section, it will be shown that the separating axis test on page 731 can be used to determine whether a line segment overlaps an AABB [454]. The line segment has finite length in contrast to a ray. Assume the line segment is defined by a center (mean of the two endpoints)  $\mathbf{c}$  and a half vector  $\mathbf{w}$ . Furthermore, both the AABB, denoted  $B$ , and the line segment have been translated so the AABB's origin is  $(0, 0, 0)$ . Also, the size of the box is  $(2h_x, 2h_y, 2h_z)$ , i.e.,  $\mathbf{h}$  is the half vector of the box. This is shown in Figure 16.8.

It is normally most effective to first test against an axis that is orthogonal to a face of both objects to be tested. Since the line segment does not have a face, it does not generate any test. The box generates three axes to test:  $(1, 0, 0)$ ,  $(0, 1, 0)$ , and  $(0, 0, 1)$ . Finally, the axes formed from the cross product between line segment direction and the box axes should be tested.

The test for the axis  $(1, 0, 0)$  is shown below, and Figure 16.8 shows this as well. The other two axes are similar:

$$|c_x| > |w_x| + h_x. \quad (16.16)$$

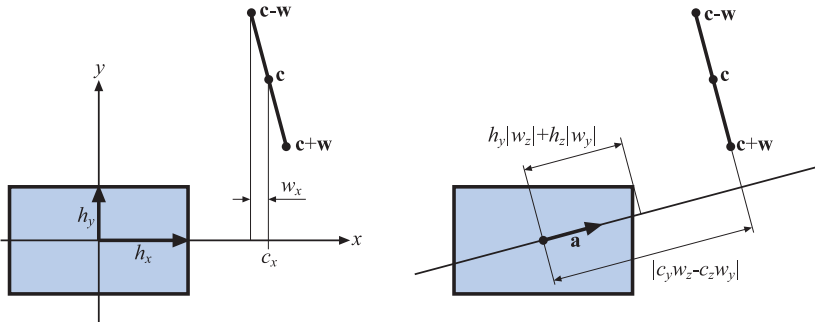


**Figure 16.8.** Left: The  $x$ -axis is tested for overlap between the box and the line segment. Right: The  $\mathbf{a}$ -axis is tested. Note that  $h_y|w_z| + h_z|w_y|$  and  $|c_y w_z - c_z w_y|$  are shown in this illustration as if  $\mathbf{w}$  is normalized. When this is not the case, then both the shown values should be scaled with  $\|\mathbf{w}\|$ . See text for notation.

If this test is true then the line segment and the box do not overlap.

The cross product axis  $\mathbf{a} = \mathbf{w} \times (1, 0, 0) = (0, w_z, -w_y)$  is tested as follows. The extent of the box projected onto  $\mathbf{a}$  is  $h_y|w_z| + h_z|w_y|$ . Next we need to find the projected length of the line segment, and the projection of the line segment center. The projection of the line segment direction  $\mathbf{w}$  onto  $\mathbf{a}$  is zero, since  $\mathbf{w} \cdot (\mathbf{w} \times (1, 0, 0)) = 0$ . The projection of  $\mathbf{c}$  onto  $\mathbf{a}$  is  $\mathbf{c} \cdot \mathbf{a} = \mathbf{c} \cdot (0, w_z, -w_y) = c_y w_z - c_z w_y$ . Thus, the test becomes

$$|c_y w_z - c_z w_y| > h_y|w_z| + h_z|w_y|. \quad (16.17)$$

Again, if this test is true, then there is no overlap. The other two cross product axes are similar.

The routine is summarized below:

```

RayAABBOverlap(c, w, B)
  returns ({OVERLAP, DISJOINT});

1 :  vx = |wx|
2 :  vy = |wy|
3 :  vz = |wz|
4 :  if(|cx| > vx + hx) return DISJOINT;
5 :  if(|cy| > vy + hy) return DISJOINT;
6 :  if(|cz| > vz + hz) return DISJOINT;
7 :  if(|cywz - czwy| > hyvz + hzvy) return DISJOINT;
8 :  if(|cxwz - czwx| > hxvz + hzvx) return DISJOINT;
9 :  if(|cxwy - cywx| > hxvy + hyvx) return DISJOINT;
10 : return OVERLAP;

```

In terms of code, this routine is fast, but it has the disadvantage of not being able to return the intersection distance.

### 16.7.3 Ray Slope Method

In 2007 Eisemann et al. [301] presented a method of intersecting boxes that appears to be faster than previous methods. Instead of a three-dimensional test, the ray is tested against three projections of the box in two dimensions. The key idea is that for each two-dimensional test, there are two box corners that define the extreme extents of what the ray “sees,” akin to the silhouette edges of a model. To intersect this projection of the box, the slope of the ray must be between the two slopes defined by the ray’s origin and these two points. If this test passes for all three projections, the ray must hit the box. The method is extremely fast because some of the comparison terms rely entirely on the ray’s values. By computing these terms once, the ray can then efficiently be compared against a large number of boxes. This method can return just whether the box was hit, or can also return the intersection distance, at a little additional cost.

## 16.8 Ray/Triangle Intersection

In real-time graphics libraries and APIs, triangle geometry is usually stored as a set of vertices with associated normals, and each triangle is defined by three such vertices. The normal of the plane in which the triangle lies is often not stored, in which case it must be computed if needed. There exist many different ray/triangle intersection tests, and many of them first compute the intersection point between the ray and the triangle’s plane. Thereafter, the intersection point and the triangle vertices are projected on the axis-aligned plane ( $xy$ ,  $yz$ , or  $xz$ ) where the area of the triangle is maximized. By doing this, we reduce the problem to two dimensions, and we need only decide whether the (two-dimensional) point is inside the (two-dimensional) triangle. Several such methods exist, and they have been reviewed and compared by Haines [482], with code available on the web. See Section 16.9 for one popular algorithm using this technique. A wealth of algorithms have been evaluated for different CPU architectures, compilers, and hit ratios [803], and it could not be concluded that there is a single best test in all cases.

Here, the focus will be on an algorithm that does not presume that normals are precomputed. For triangle meshes, this can amount to significant memory savings, and for dynamic geometry, we do not need to recompute any extra data, such as the plane equation of the triangle every frame. This algorithm, along with optimizations, was discussed by Möller and Trum-

bore [890], and their presentation is used here. It is also worth noting that Kensler and Shirley [644] noted that most ray-triangle tests operating directly in three dimensions<sup>6</sup> are computationally equivalent. They develop new tests using SSE to test four rays against a triangle, and use a genetic algorithm to find the best order of the operations in this equivalent test. Code for the best-performing test is in the paper.

The ray from Equation 16.1 is used to test for intersection with a triangle defined by three vertices,  $\mathbf{p}_1$ ,  $\mathbf{p}_2$ , and  $\mathbf{p}_3$ —i.e.,  $\triangle \mathbf{p}_1 \mathbf{p}_2 \mathbf{p}_3$ .

### 16.8.1 Intersection Algorithm

A point,  $\mathbf{f}(u, v)$ , on a triangle is given by the explicit formula

$$\mathbf{f}(u, v) = (1 - u - v)\mathbf{p}_0 + u\mathbf{p}_1 + v\mathbf{p}_2, \quad (16.19)$$

where  $(u, v)$  are two of the *barycentric coordinates*, which must fulfill  $u \geq 0$ ,  $v \geq 0$ , and  $u + v \leq 1$ . Note that  $(u, v)$  can be used for texture mapping, normal interpolation, color interpolation, etc. That is,  $u$  and  $v$  are the amounts by which to weight each vertex's contribution to a particular location, with  $w = (1 - u - v)$  being the third weight.<sup>7</sup> See Figure 16.9.

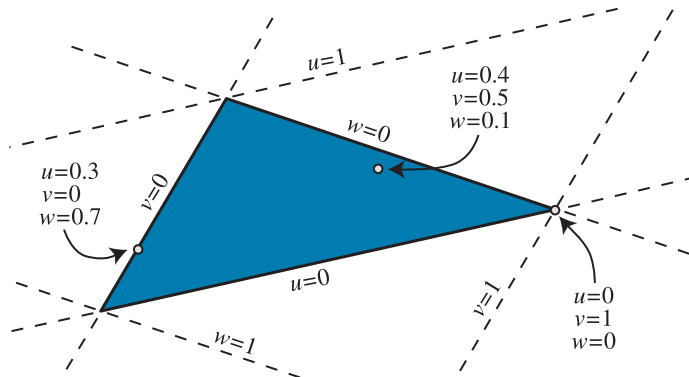


**Figure 16.9.** Barycentric coordinates for a triangle, along with example point values. The values  $u$ ,  $v$ , and  $w$  all vary from 0 to 1 inside the triangle, and the sum of these three is always 1 over the entire plane. These values can be used as weights for how data at each of the three vertices influence any point on the triangle. Note how at each vertex, one value is 1 and the others 0, and along edges, one value is always 0.

<sup>6</sup>As opposed to first computing the intersection between the ray and the plane, and then performing a two-dimensional inside test.

<sup>7</sup>These coordinates are often denoted  $\alpha$ ,  $\beta$ , and  $\gamma$ . We use  $u$ ,  $v$ , and  $w$  here for readability and consistency of notation.

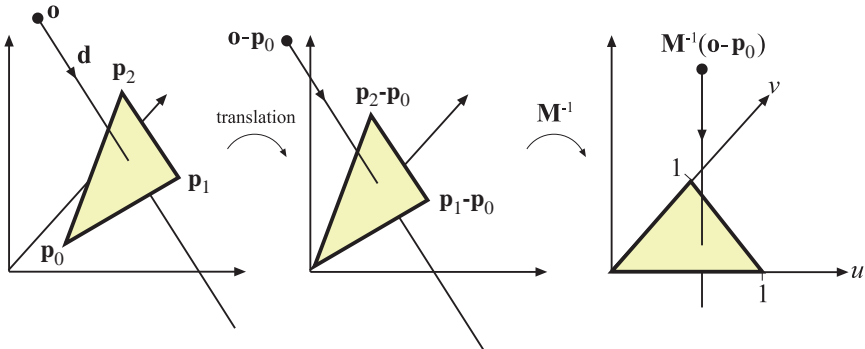


**Figure 16.10.** Translation and change of base of the ray origin.

Computing the intersection between the ray,  $\mathbf{r}(t)$ , and the triangle,  $\mathbf{f}(u, v)$ , is equivalent to  $\mathbf{r}(t) = \mathbf{f}(u, v)$ , which yields

$$\mathbf{o} + t\mathbf{d} = (1 - u - v)\mathbf{p}_0 + u\mathbf{p}_1 + v\mathbf{p}_2. \quad (16.20)$$

Rearranging the terms gives

$$\begin{pmatrix} -\mathbf{d} & \mathbf{p}_1 - \mathbf{p}_0 & \mathbf{p}_2 - \mathbf{p}_0 \end{pmatrix} \begin{pmatrix} t \\ u \\ v \end{pmatrix} = \mathbf{o} - \mathbf{p}_0. \quad (16.21)$$

This means the barycentric coordinates  $(u, v)$  and the distance  $t$  from the ray origin to the intersection point can be found by solving this linear system of equations.

This manipulation can be thought of geometrically as translating the triangle to the origin and transforming it to a unit triangle in  $y$  and  $z$  with the ray direction aligned with  $x$ . This is illustrated in Figure 16.10. If  $\mathbf{M} = (-\mathbf{d} \ \mathbf{p}_1 - \mathbf{p}_0 \ \mathbf{p}_2 - \mathbf{p}_0)$  is the matrix in Equation 16.21, then the solution is found by multiplying Equation 16.21 with  $\mathbf{M}^{-1}$ .

Denoting  $\mathbf{e}_1 = \mathbf{p}_1 - \mathbf{p}_0$ ,  $\mathbf{e}_2 = \mathbf{p}_2 - \mathbf{p}_0$ , and  $\mathbf{s} = \mathbf{o} - \mathbf{p}_0$ , the solution to Equation 16.21 is obtained by using Cramer's rule:

$$\begin{pmatrix} t \\ u \\ v \end{pmatrix} = \frac{1}{\det(-\mathbf{d}, \mathbf{e}_1, \mathbf{e}_2)} \begin{pmatrix} \det(\mathbf{s}, \mathbf{e}_1, \mathbf{e}_2) \\ \det(-\mathbf{d}, \mathbf{s}, \mathbf{e}_2) \\ \det(-\mathbf{d}, \mathbf{e}_1, \mathbf{s}) \end{pmatrix}. \quad (16.22)$$

From linear algebra, we know that  $\det(\mathbf{a}, \mathbf{b}, \mathbf{c}) = |\mathbf{a} \mathbf{b} \mathbf{c}| = -(\mathbf{a} \times \mathbf{c}) \cdot \mathbf{b} = -(\mathbf{c} \times \mathbf{b}) \cdot \mathbf{a}$ . Equation 16.22 can therefore be rewritten as

$$\begin{pmatrix} t \\ u \\ v \end{pmatrix} = \frac{1}{(\mathbf{d} \times \mathbf{e}_2) \cdot \mathbf{e}_1} \begin{pmatrix} (\mathbf{s} \times \mathbf{e}_1) \cdot \mathbf{e}_2 \\ (\mathbf{d} \times \mathbf{e}_2) \cdot \mathbf{s} \\ (\mathbf{s} \times \mathbf{e}_1) \cdot \mathbf{d} \end{pmatrix} = \frac{1}{\mathbf{q} \cdot \mathbf{e}_1} \begin{pmatrix} \mathbf{r} \cdot \mathbf{e}_2 \\ \mathbf{q} \cdot \mathbf{s} \\ \mathbf{r} \cdot \mathbf{d} \end{pmatrix}, \quad (16.23)$$

where  $\mathbf{q} = \mathbf{d} \times \mathbf{e}_2$  and  $\mathbf{r} = \mathbf{s} \times \mathbf{e}_1$ . These factors can be used to speed up the computations.

If you can afford some extra storage, this test can be reformulated in order to reduce the number of computations. Equation 16.23 can be rewritten as

$$\begin{aligned} \begin{pmatrix} t \\ u \\ v \end{pmatrix} &= \frac{1}{(\mathbf{d} \times \mathbf{e}_2) \cdot \mathbf{e}_1} \begin{pmatrix} (\mathbf{s} \times \mathbf{e}_1) \cdot \mathbf{e}_2 \\ (\mathbf{d} \times \mathbf{e}_2) \cdot \mathbf{s} \\ (\mathbf{s} \times \mathbf{e}_1) \cdot \mathbf{d} \end{pmatrix} \\ &= \frac{1}{-(\mathbf{e}_1 \times \mathbf{e}_2) \cdot \mathbf{d}} \begin{pmatrix} (\mathbf{e}_1 \times \mathbf{e}_2) \cdot \mathbf{s} \\ (\mathbf{s} \times \mathbf{d}) \cdot \mathbf{e}_2 \\ -(\mathbf{s} \times \mathbf{d}) \cdot \mathbf{e}_1 \end{pmatrix} \\ &= \frac{1}{-\mathbf{n} \cdot \mathbf{d}} \begin{pmatrix} \mathbf{n} \cdot \mathbf{s} \\ \mathbf{m} \cdot \mathbf{e}_2 \\ -\mathbf{m} \cdot \mathbf{e}_1 \end{pmatrix}, \end{aligned} \quad (16.24)$$

where  $\mathbf{n} = \mathbf{e}_1 \times \mathbf{e}_2$  is the unnormalized normal of the triangle, and hence constant (for static geometry), and  $\mathbf{m} = \mathbf{s} \times \mathbf{d}$ . If we store  $\mathbf{p}_0$ ,  $\mathbf{e}_1$ ,  $\mathbf{e}_2$ , and  $\mathbf{n}$  for each triangle, we can avoid many ray triangle intersection computations. Most of the gain comes from avoiding a cross product. It should be noted that this defies the original idea of the algorithm, namely to store minimal information with the triangle. However, if speed is of utmost concern, this may a reasonable alternative. The tradeoff is whether the savings in computation is outweighed by the additional memory accesses. Only careful testing can ultimately show what is fastest.

## 16.8.2 Implementation

The algorithm is summarized in the pseudocode below. Besides returning whether or not the ray intersects the triangle, the algorithm also returns the previously-described triple  $(u, v, t)$ . The code does not cull backfacing triangles, and it returns intersections for negative  $t$ -values, but these can be culled too, if desired.

```

RayTriIntersect( $\mathbf{o}, \mathbf{d}, \mathbf{p}_0, \mathbf{p}_1, \mathbf{p}_2$ )
  returns (REJECT, INTERSECT),  $u, v, t$ );

1 :    $\mathbf{e}_1 = \mathbf{p}_1 - \mathbf{p}_0$ 
2 :    $\mathbf{e}_2 = \mathbf{p}_2 - \mathbf{p}_0$ 
3 :    $\mathbf{q} = \mathbf{d} \times \mathbf{e}_2$ 
4 :    $a = \mathbf{e}_1 \cdot \mathbf{q}$ 
5 :   if( $a > -\epsilon$  and  $a < \epsilon$ ) return (REJECT, 0, 0, 0);
6 :    $f = 1/a$ 
7 :    $\mathbf{s} = \mathbf{o} - \mathbf{p}_0$ 
8 :    $u = f(\mathbf{s} \cdot \mathbf{q})$ 
9 :   if( $u < 0.0$ ) return (REJECT, 0, 0, 0);
10 :   $\mathbf{r} = \mathbf{s} \times \mathbf{e}_1$ 
11 :   $v = f(\mathbf{d} \cdot \mathbf{r})$ 
12 :  if( $v < 0.0$  or  $u + v > 1.0$ ) return (REJECT, 0, 0, 0);
13 :   $t = f(\mathbf{e}_2 \cdot \mathbf{r})$ 
14 :  return (INTERSECT,  $u, v, t$ );

```

A few lines may require some explanation. Line 4 computes  $a$ , which is the determinant of the matrix  $\mathbf{M}$ . This is followed by a test that avoids determinants close to zero. With a properly adjusted value of  $\epsilon$ , this algorithm is extremely robust.<sup>8</sup> In line 9, the value of  $u$  is compared to an edge of the triangle ( $u = 0$ ).

C-code for this algorithm, including both culling and nonculling versions, is available on the web [890]. The C-code has two branches: one that efficiently culls all backfacing triangles, and one that performs intersection tests on two-sided triangles. All computations are delayed until they are required. For example, the value of  $v$  is not computed until the value of  $u$  is found to be within the allowable range (this can be seen in the pseudocode as well).

The one-sided intersection routine eliminates all triangles where the value of the determinant is negative. This procedure allows the routine's only division operation to be delayed until an intersection has been confirmed.

## 16.9 Ray/Polygon Intersection

Even though triangles are the most common rendering primitive, a routine that computes the intersection between a ray and a polygon is useful to have. A polygon of  $n$  vertices is defined by an ordered vertex list  $\{\mathbf{v}_0, \mathbf{v}_1, \dots, \mathbf{v}_{n-1}\}$ , where vertex  $\mathbf{v}_i$  forms an edge with  $\mathbf{v}_{i+1}$  for  $0 \leq i <$

---

<sup>8</sup>For floating point precision and “normal” conditions,  $\epsilon = 10^{-5}$  works fine.

$n - 1$  and the polygon is closed by the edge from  $\mathbf{v}_{n-1}$  to  $\mathbf{v}_0$ . The plane of the polygon<sup>9</sup> is denoted  $\pi_p : \mathbf{n}_p \cdot \mathbf{x} + d_p = 0$ .

We first compute the intersection between the ray (Equation 16.1) and  $\pi_p$ , which is easily done by replacing  $\mathbf{x}$  by the ray. The solution is presented below:

$$\begin{aligned} \mathbf{n}_p \cdot (\mathbf{o} + t\mathbf{d}) + d_p &= 0 \\ \iff t &= \frac{-d_p - \mathbf{n}_p \cdot \mathbf{o}}{\mathbf{n}_p \cdot \mathbf{d}}. \end{aligned} \quad (16.26)$$

If the denominator  $|\mathbf{n}_p \cdot \mathbf{d}| < \epsilon$ , where  $\epsilon$  is a very small number,<sup>10</sup> then the ray is considered parallel to the polygon plane and no intersection occurs.<sup>11</sup> Otherwise, the intersection point,  $\mathbf{p}$ , of the ray and the polygon plane is computed:  $\mathbf{p} = \mathbf{o} + t\mathbf{d}$ , where the  $t$ -value is that from Equation 16.26. Thereafter, the problem of deciding whether  $\mathbf{p}$  is inside the polygon is reduced from three to two dimensions. This is done by projecting all vertices and  $\mathbf{p}$  to one of the  $xy$ -,  $xz$ -, or  $yz$ -planes where the area of the projected polygon is maximized. In other words, the coordinate component that corresponds to  $\max(|n_{p,x}|, |n_{p,y}|, |n_{p,z}|)$  can be skipped and the others kept as two-dimensional coordinates. For example, given a normal  $(0.6, -0.692, 0.4)$ , the  $y$  component has the largest magnitude, so all  $y$  coordinates are ignored. Note that this component information could be precomputed once and stored within the polygon for efficiency. The topology of the polygon and the intersection point is conserved during this projection (assuming the polygon is indeed flat; see Section 12.2 for more on this topic). The projection procedure is shown in Figure 16.11.

The question left is whether the two-dimensional ray/plane intersection point  $\mathbf{p}$  is contained in the two-dimensional polygon. Here, we will review just one of the more useful algorithms—the “crossings” test. Haines [482] and Schneider and Eberly [1131] provide extensive surveys of two-dimensional, point-in-polygon strategies. A more formal treatment can be found in the computational geometry literature [82, 975, 1033]. Lagae and Dutré [711] provide a fast method for ray/quadrilateral intersection based on the Möller and Trumbore ray/triangle test. Walker [1315] provides a method for rapid testing of polygons with more than 10 vertices. Nishita et al. [936] discuss point inclusion testing for shapes with curved edges.

<sup>9</sup>This plane can be computed from the vertices on the fly or stored with the polygon, whichever is most convenient. It is sometimes called the supporting plane of the polygon.

<sup>10</sup>An epsilon of  $10^{-20}$  or smaller can work, as the goal is to avoid overflowing when dividing.

<sup>11</sup>We ignore the case where the ray is in the polygon’s plane.

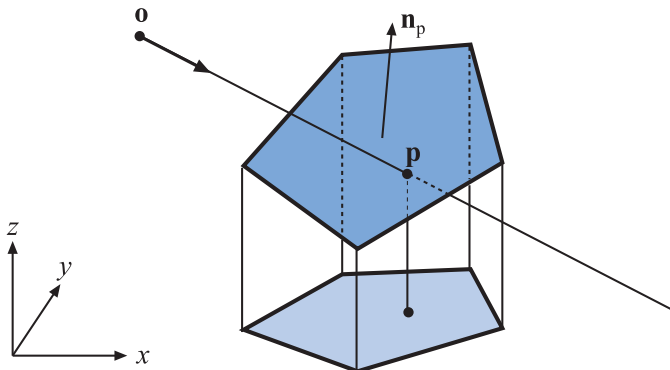


**Figure 16.11.** Orthographic projection of polygon vertices and intersection point  $p$  onto the  $xy$ -plane, where the area of the projected polygon is maximized. This is an example of using dimension reduction to obtain simpler calculations.

### 16.9.1 The Crossings Test

The crossings test is based on the *Jordan Curve Theorem*, a result from topology. From it, a point is inside a polygon if a ray from this point in an arbitrary direction in the plane crosses an odd number of polygon edges. The Jordan Curve Theorem actually limits itself to non-self-intersecting loops. For self-intersecting loops, this ray test causes some areas visibly

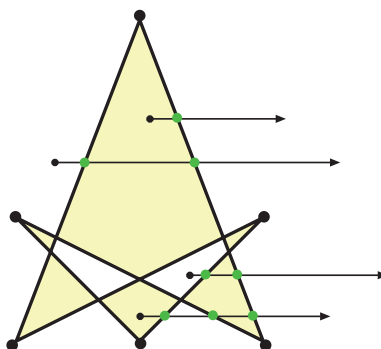


**Figure 16.12.** A general polygon that is self-intersecting and concave, yet all of its enclosed areas are not considered inside (only yellow areas are inside). Vertices are marked with large, black dots. Three points being tested are shown, along with their test rays. According to the Jordan Curve Theorem, a point is inside if the number of crossings with the edges of the polygon is odd. Therefore, the uppermost and the bottommost points are inside (one and three crossings, respectively). The two middle points each cross two edges and are thus, because of self-intersection, considered outside the polygon.

inside the polygon to be considered outside. This is shown in Figure 16.12. This test is also known as the parity or the even-odd test.

The crossings algorithm is the fastest test that does not use preprocessing. It works by shooting a ray from the projection of the point  $\mathbf{p}$  along the positive  $x$ -axis. Then the number of crossings between the polygon edges and this ray is computed. As the Jordan Curve Theorem proves, an odd number of crossings indicates that the point is inside the polygon.

The test point  $\mathbf{p}$  can also be thought of as being at the origin, and the (translated) edges may be tested against the positive  $x$ -axis instead. This option is depicted in Figure 16.13. If the  $y$ -coordinates of a polygon edge have the same sign, then that edge cannot cross the  $x$ -axis. Otherwise, it can, and then the  $x$ -coordinates are checked. If both are positive, then the number of crossings is incremented. If they differ in sign, the  $x$ -coordinate of the intersection between the edge and the  $x$ -axis must be computed, and if it is positive, the number of crossings is again incremented.

These enclosed areas could be included as well. This variant test finds the *winding number*, the number of times the polygon loop goes around the test point. See Haines [482] for treatment.

Problems might occur when the test ray intersects a vertex, since two crossings might be detected. These problems are solved by setting the ver-

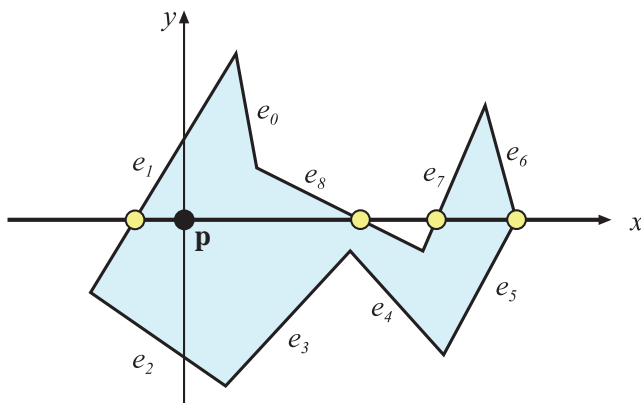


**Figure 16.13.** The polygon has been translated by  $-\mathbf{p}$  ( $\mathbf{p}$  is the point to be tested for containment in the polygon), and so the number of crossings with the positive  $x$ -axis determines whether  $\mathbf{p}$  is inside the polygon. Edges  $e_0$ ,  $e_2$ ,  $e_3$ , and  $e_4$  do not cross the  $x$ -axis. The intersection between edge  $e_1$  and the  $x$ -axis must be computed, but will not yield a crossing, since the intersection has a negative  $x$ -component. Edges  $e_7$  and  $e_8$  will each increase the number of crossings, since the vertices of these edges have positive  $x$ -components and one negative and one positive  $y$ -component. Finally, the edges  $e_5$  and  $e_6$  share a vertex where  $y = 0$  and  $x > 0$ , and they will together increase the number of crossings by one. By considering vertices on the  $x$ -axis as above the ray,  $e_5$  is classified as crossing the ray,  $e_6$  as above the ray.

tex infinitesimally above the ray, which, in practice, is done by interpreting the vertices with  $y \geq 0$  as lying above the  $x$ -axis (the ray). The code becomes simpler and speedier, and no vertices will be intersected [480].

The pseudocode for an efficient form of the crossings test follows. It was inspired by the work of Joseph Samosky [1101] and Mark Haigh-Hutchinson, and the code is available on the web [482]. A two-dimensional test point  $\mathbf{t}$  and polygon  $P$  with vertices  $\mathbf{v}_0$  through  $\mathbf{v}_{n-1}$  are compared.

```

bool PointInPolygon( $\mathbf{t}, P$ )
returns ({TRUE, FALSE});
1 : bool inside = FALSE
2 :  $\mathbf{e}_0 = \mathbf{v}_{n-1}$ 
3 : bool  $y_0 = (e_{0y} \geq t_y)$ 
4 : for  $i = 0$  to  $n - 1$ 
5 :    $\mathbf{e}_1 = \mathbf{v}_i$ 
6 :   bool  $y_1 = (e_{1y} \geq t_y)$ 
7 :   if( $y_0 \neq y_1$ )
8 :     if(( $(e_{1y} - t_y)(e_{0x} - e_{1x}) \geq (e_{1x} - t_x)(e_{0y} - e_{1y})$ ) ==  $y_1$ )
9 :       inside =  $\neg$ inside
10 :       $y_0 = y_1$ 
11 :       $\mathbf{e}_0 = \mathbf{e}_1$ 
12 : return inside;

```

Line 4 checks whether the  $y$ -value of the last vertex in the polygon is greater than or equal to the  $y$ -value of the test point  $\mathbf{t}$ , and stores the result in the boolean  $y_0$ . In other words, it tests whether the first endpoint of the first edge we will test is above or below the  $x$ -axis. Line 7 tests whether the endpoints  $e_0$  and  $e_1$  are on different sides of the  $x$ -axis formed by the test point. If so, then line 8 tests whether the  $x$ -intercept is positive. Actually, it is a bit trickier than that: To avoid the divide normally needed for computing the intercept, we perform a sign-canceling operation here. By inverting  $inside$ , line 9 records that a crossing took place. Lines 10 to 12 move on to the next vertex.

In the pseudocode we do not perform a test after line 7 to see whether both endpoints have larger or smaller  $x$ -coordinates compared to the test point. Although we presented the algorithm with using a quick accept or reject of these types of edges, code based on the pseudocode presented often runs faster without this test. A major factor is the number of vertices in the polygons tested. In testing, checking the signs of the  $x$ -coordinate differences begins to pay off when testing polygons with more than 10 to 30 vertices, as there are then enough edges that benefit from early rejection or acceptance and fewer that require the full test on line 8. That said, the overall increase in speed seen for 1000 vertex polygons was at most 16%.

The advantages of the crossings test is that it is relatively fast and robust, and requires no additional information or preprocessing for the polygon. A disadvantage of this method is that it does not yield anything beyond the indication of whether a point is inside or outside the polygon. Other methods, such as the ray/triangle test in Section 16.8.1, can also compute barycentric coordinates that can be used to interpolate additional information about the test point [482]. Note that barycentric coordinates can be extended to handle convex and concave polygons with more than three vertices [346, 566].

## 16.10 Plane/Box Intersection Detection

One way to determine whether a box intersects a plane,  $\pi : \mathbf{n} \cdot \mathbf{x} + d = 0$ , is to insert all the vertices of the box into the plane equation. If both a positive and a negative result (or a zero) is obtained, then vertices are located on both sides of (or on) the plane, and therefore, an intersection has been detected. There are smarter, faster ways to do this test, which are presented in the next two sections, one for the AABB, and one for the OBB.

The idea behind both methods is that only two points need to be inserted into the plane equation. For an arbitrarily-oriented box, intersecting a plane or not, there are two diagonally opposite corners on the box that are the maximum distance apart, when measured along the plane's normal. Every box has four diagonals, formed by its corners. Taking the dot product of each diagonal's direction with the plane's normal, the largest value identifies the diagonal with these two furthest points. By testing just these two corners, the box as a whole is tested against a plane.

### 16.10.1 AABB

Assume we have an AABB,  $B$ , defined by a center point,  $\mathbf{c}$ , and a positive half diagonal vector,  $\mathbf{h}$ . Note that  $\mathbf{c}$  and  $\mathbf{h}$  can easily be derived from the minimum and maximum corners,  $\mathbf{b}^{\min}$  and  $\mathbf{b}^{\max}$  of  $B$ , that is,  $\mathbf{c} = (\mathbf{b}^{\max} + \mathbf{b}^{\min})/2$ , and  $\mathbf{h} = (\mathbf{b}^{\max} - \mathbf{b}^{\min})/2$ .

Now, we want to test  $B$  against a plane  $\mathbf{n} \cdot \mathbf{x} + d = 0$ . There is a surprisingly fast way of performing this test, and the idea is to compute the “extent,” here denoted  $e$ , of the box when projected onto the plane normal,  $\mathbf{n}$ . In theory, this can be done by projecting all the eight different half diagonals of the box onto the normal, and picking the longest one. In practice, however, this can be implemented very rapidly as

$$e = h_x|n_x| + h_y|n_y| + h_z|n_z|. \quad (16.28)$$

Why is this equivalent to finding the maximum of the eight different half diagonals projections? These eight half diagonals are the combinations:  $\mathbf{g}^i = (\pm h_x, \pm h_y, \pm h_z)$ , and we want to compute  $\mathbf{g}^i \cdot \mathbf{n}$  for all eight  $i$ . The dot product  $\mathbf{g}^i \cdot \mathbf{n}$  will reach its maximum when each term in the dot product is positive. For the  $x$ -term, this will happen when  $n_x$  has the same sign as  $h_x^i$ , but since we know that  $h_x$  is positive already, we can compute the max term as  $h_x |n_x|$ . Doing this for  $y$  and  $z$  as well gives us Equation 16.28.

Next, we compute the signed distance,  $s$ , from the center point,  $\mathbf{c}$ , to the plane. This is done with:  $s = \mathbf{c} \cdot \mathbf{n} + d$ . Both  $s$  and  $e$  are illustrated in Figure 16.14. Assuming that the “outside” of the plane is the positive half-space, we can simply test if  $s - e > 0$ , which then indicates that the box is fully outside the plane. Similarly,  $s + e < 0$  indicates that the box is fully inside. Otherwise, the box intersects the plane. This technique is based on ideas by Ville Miettinen and his clever implementation [864]. Pseudo code is below:

```

PlaneAABBIntersect( $B, \pi$ )
    returns({OUTSIDE, INSIDE, INTERSECTING});
1 :    $\mathbf{c} = (\mathbf{b}^{\max} + \mathbf{b}^{\min})/2$ 
2 :    $\mathbf{h} = (\mathbf{b}^{\max} - \mathbf{b}^{\min})/2$ 
3 :    $e = h_x |n_x| + h_y |n_y| + h_z |n_z|$ 
4 :    $s = \mathbf{c} \cdot \mathbf{n} + d$ 
5 :   if( $s - e > 0$ ) return (OUTSIDE);
9 :   if( $s + e < 0$ ) return (INSIDE);
10 :  return (INTERSECTING);

```

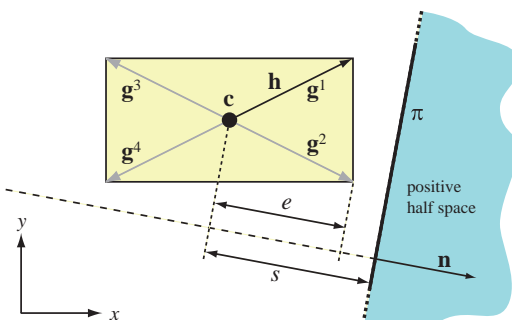


**Figure 16.14.** An axis-aligned box with center,  $\mathbf{c}$ , and positive half diagonal,  $\mathbf{h}$ , is tested against a plane,  $\pi$ . The idea is to compute the signed distance,  $s$ , from the center of the box to the plane, and compare that to the “extent,”  $e$ , of the box. The vectors  $\mathbf{g}^i$  are the different possible diagonals of the two-dimensional box, where  $\mathbf{h}$  is equal to  $\mathbf{g}^1$  in this example. Note also that the signed distance  $s$  is negative, and its magnitude is larger than  $e$ , indicating that the box is inside the plane ( $s + e < 0$ ).

## 16.10.2 OBB

Testing an OBB against a plane differs only slightly from the AABB/plane test from the previous section. It is only the computation of the “extent” of the box that needs to be changed, which is done as

$$e = h_u^B |\mathbf{n} \cdot \mathbf{b}^u| + h_v^B |\mathbf{n} \cdot \mathbf{b}^v| + h_w^B |\mathbf{n} \cdot \mathbf{b}^w|. \quad (16.30)$$

Recall that  $(\mathbf{b}^u, \mathbf{b}^v, \mathbf{b}^w)$  are the coordinate system axes (see the definition of the OBB in Section 16.2) of the OBB, and  $(h_u^B, h_v^B, h_w^B)$  are the lengths of the box along these axes.

## 16.11 Triangle/Triangle Intersection

Since graphics hardware uses the triangle as its most important (and optimized) drawing primitive, it is only natural to perform collision detection tests on this kind of data as well. So, the deepest levels of a collision detection algorithm typically have a routine that determines whether or not two triangles intersect.

The problem is: Given two triangles,  $T_1 = \Delta \mathbf{p}_1 \mathbf{q}_1 \mathbf{r}_1$  and  $T_2 = \Delta \mathbf{p}_2 \mathbf{q}_2 \mathbf{r}_2$  (which lie in the planes  $\pi_1$  and  $\pi_2$ , respectively), determine whether or not they intersect.

Note that the separating axis test (see page 731) can be used to derive a triangle/triangle overlap test. However, here we will present a method called the *interval overlap method*, introduced by Möller [891], because it is faster than using SAT. We will then present a further optimization by Guigue and Devillers [467], which also makes the algorithm more robust. Other algorithms exist for performing triangle-triangle intersection, including a similar test by Shen et al. [1162], and one by Held [539]. Architectural and compiler differences, as well as variation in expected hit ratios, make it difficult to single out a single algorithm that always performs best.

From a high level, the interval overlap method starts by checking whether  $T_1$  intersects with  $\pi_2$ , and whether  $T_2$  intersects with  $\pi_1$ . If both these tests fail, there can be no intersection. Assuming the triangles are not coplanar, we know that the intersection of the planes,  $\pi_1$  and  $\pi_2$ , will be a line,  $L$ . This is illustrated in Figure 16.15. From the figure, it can be concluded that if the triangles intersect, their intersections on  $L$  will also have to overlap. Otherwise, there will be no intersection. There are different ways to implement this, and in the following, we will present the method by Guigue and Devillers [467].

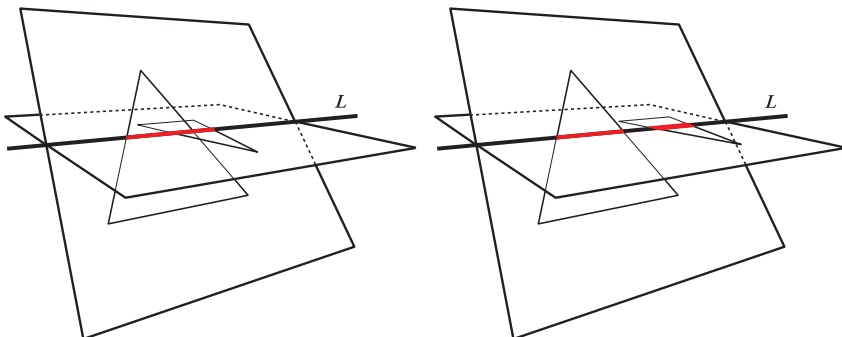


**Figure 16.15.** Triangles and the planes in which they lie. Intersection intervals are marked in red in both figures. Left: The intervals along the line  $L$  overlap, as well as the triangles. Right: There is no intersection; the two intervals do not overlap.

In this implementation, there is heavy use of  $4 \times 4$  determinants from four three-dimensional vectors,  $\mathbf{a}$ ,  $\mathbf{b}$ ,  $\mathbf{c}$ , and  $\mathbf{d}$ :

$$[\mathbf{a}, \mathbf{b}, \mathbf{c}, \mathbf{d}] = - \begin{vmatrix} a_x & b_x & c_x & d_x \\ a_y & b_y & c_y & d_y \\ a_z & b_z & c_z & d_z \\ 1 & 1 & 1 & 1 \end{vmatrix} = (\mathbf{d} - \mathbf{a}) \cdot ((\mathbf{b} - \mathbf{a}) \times (\mathbf{c} - \mathbf{a})). \quad (16.31)$$

Note that we do not use the standard notation for determinants (Section A.3.1), because the vectors are three dimensional, but the determinant is  $4 \times 4$ . Geometrically, Equation 16.31 has an intuitive interpretation. The cross product,  $(\mathbf{b} - \mathbf{a}) \times (\mathbf{c} - \mathbf{a})$ , can be seen as computing the normal of a triangle,  $\Delta \mathbf{abc}$ . By taking the dot product between this normal and the vector from  $\mathbf{a}$  to  $\mathbf{d}$ , we get a value that is positive if  $\mathbf{d}$  is in the positive half space of the triangle's plane,  $\Delta \mathbf{abc}$ . An alternative interpretation is that the sign of the determinant tells us whether a screw in the direction of  $\mathbf{b} - \mathbf{a}$  turns in the same direction as indicated by  $\mathbf{d} - \mathbf{c}$ . This is illustrated in Figure 16.16.

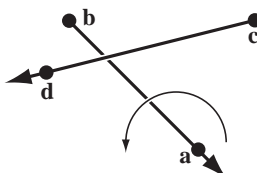


**Figure 16.16.** Illustration of the screw a vector  $\mathbf{b} - \mathbf{a}$  in the direction of  $\mathbf{d} - \mathbf{c}$ .

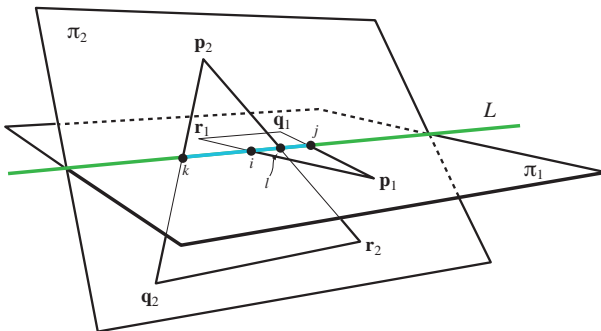


**Figure 16.17.** Two intersecting triangles with their intersection shown on the line of intersection,  $L$ . The intervals on  $L$  are also shown and are represented by  $i$ ,  $j$ ,  $k$ , and  $l$ .

Now, with interval overlap methods, we first test whether  $T_1$  intersects with  $\pi_2$ , and vice versa. This can be done using the specialized determinants from Equation 16.31 by evaluating  $[\mathbf{p}_2, \mathbf{q}_2, \mathbf{r}_2, \mathbf{p}_1]$ ,  $[\mathbf{p}_2, \mathbf{q}_2, \mathbf{r}_2, \mathbf{q}_1]$ , and  $[\mathbf{p}_2, \mathbf{q}_2, \mathbf{r}_2, \mathbf{r}_1]$ . The first test is equivalent to computing the normal of  $T_2$ , and then testing which half-space the point  $\mathbf{p}_1$  is in. If the signs of these determinants are the same and non-zero, there can be no intersection, and the test ends. If all are zero, the triangles are coplanar, and a separate test is performed to handle this case. Otherwise, we continue testing whether  $T_2$  intersects with  $\pi_1$ , using the same type of test.

Guigue and Devillers assume that no triangle vertex or edge is exactly on the plane of the other triangle. If this occurs, they perturb the vertices in such a way that the intersection with  $L$  is preserved. The algorithm then proceeds by changing the order of the triangle vertices so that  $\mathbf{p}_1$  ( $\mathbf{p}_2$ ) is the only vertex that lies in that half space. At the same time, the other vertices ( $\mathbf{q}_2$  and  $\mathbf{r}_2$ ) are swapped so that  $\mathbf{p}_1$  “sees” the vertices  $\mathbf{p}_2$ ,  $\mathbf{q}_2$ , and  $\mathbf{r}_2$  in counterclockwise order (and similarly for  $\mathbf{p}_2$ ). The vertex order has been arranged in this way in Figure 16.17. Let us denote the scalar intersections on  $L$  with  $i$ ,  $j$ ,  $k$ , and  $l$ , for the edges  $\mathbf{p}_1\mathbf{q}_1$ ,  $\mathbf{p}_1\mathbf{r}_1$ ,  $\mathbf{p}_2\mathbf{q}_2$ , and  $\mathbf{p}_2\mathbf{r}_2$ . This is also shown in Figure 16.17. These scalars form two intervals,  $I_1 = [i, j]$  and  $I_2 = [k, l]$ , on  $L$ . If  $I_1$  overlaps with  $I_2$ , then the two triangles intersect, and this occurs only if  $k \leq j$  and  $i \leq l$ . To implement  $k \leq j$ , we can use the sign test of the determinant (Equation 16.31), and note that  $j$  is derived from  $\mathbf{p}_1\mathbf{r}_1$ , and  $k$  from  $\mathbf{p}_2\mathbf{q}_2$ . Using the interpretation of the “screw test” of the determinant computation, we can conclude that  $k \leq j$  if  $[\mathbf{p}_1, \mathbf{q}_1, \mathbf{p}_2, \mathbf{q}_2] \leq 0$ . The final test then becomes

$$[\mathbf{p}_1, \mathbf{q}_1, \mathbf{p}_2, \mathbf{q}_2] \leq 0 \text{ and } [\mathbf{p}_1, \mathbf{r}_1, \mathbf{r}_2, \mathbf{p}_2] \leq 0. \quad (16.32)$$

The entire test starts with six determinant tests, and the first three share the first arguments, so there is a lot to gain in terms of shared computations. In principle, the determinant can be computed using many smaller  $2 \times 2$  subdeterminants (see Section A.3.1), and when these occur in more than one  $4 \times 4$  determinant, the computations can be shared. There is code on the web for this test [467], and it is also possible to augment the code to compute the actual line segment of intersection.

If the triangles are coplanar, they are projected onto the axis-aligned plane where the areas of the triangles are maximized (see Section 16.9). Then, a simple two-dimensional triangle-triangle overlap test is performed. First, test all closed edges (i.e., including endpoints) of  $T_1$  for intersection with the closed edges of  $T_2$ . If any intersection is found, the triangles intersect. Otherwise, we must test whether  $T_1$  is totally contained in  $T_2$  or vice versa. This can be done by performing a point-in-triangle test (see Section 16.8) for one vertex of  $T_1$  against  $T_2$ , and vice versa.

Robustness problems may arise when the triangles are nearly coplanar or when an edge is nearly coplanar to the other triangle (especially when the edge is close to an edge of the other triangle). To handle these cases in a reasonable way, a user-defined constant,  $\text{EPSILON}(\epsilon)$ , can be used.<sup>12</sup> For example, if  $\|[\mathbf{p}_2, \mathbf{q}_2, \mathbf{r}_2, \mathbf{p}_1]\| < \epsilon$ , then we move  $\mathbf{p}_1$  so that  $[\mathbf{p}_2, \mathbf{q}_2, \mathbf{r}_2, \mathbf{p}_1] = 0$ . Geometrically, this means that if a point is “close enough” to the other triangle’s plane, it is considered to be on the plane. The same is done for the points of the other triangle, as well. The source code does not handle degenerate triangles (i.e., lines and points). To do so, those cases should be detected first and then handled as special cases.

## 16.12 Triangle/Box Overlap

This section presents an algorithm for determining whether a triangle intersects an axis-aligned box. Such a test can be used to build voxel-spaces, test triangles against boxes in collision detection, and test polygons against canonical view volumes (see Section 4.6), and thus potentially eliminate the need for calls to clipping and lighting routines, etc.

Green and Hatch [441] present an algorithm that can determine whether an arbitrary polygon overlaps a box. Akenine-Möller [11] developed a faster method that is based on the separating axis test (page 731), and which we present here.

We focus on testing an axis-aligned bounding box (AABB), defined by a center  $\mathbf{c}$ , and a vector of half lengths,  $\mathbf{h}$ , against a triangle  $\Delta\mathbf{u}_0\mathbf{u}_1\mathbf{u}_2$ . To simplify the tests, we first move the box and the triangle so that the box is centered around the origin, i.e.,  $\mathbf{v}_i = \mathbf{u}_i - \mathbf{c}$ ,  $i \in \{0, 1, 2\}$ . This

---

<sup>12</sup>For floating point precision,  $\epsilon = 10^{-6}$  works for “normal” data.

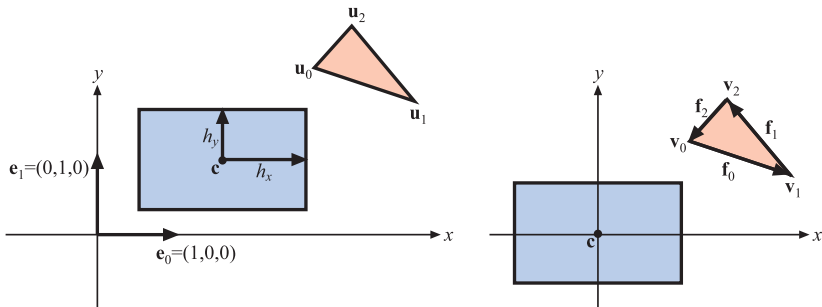


**Figure 16.18.** Notation used for the triangle-box overlap test. To the left, the initial position of the box and the triangle is shown, while to the right, the box and the triangle have been translated so that the box center coincides with the origin.

translation and the notation used is shown in Figure 16.18. To test against an oriented box, we would first rotate the triangle vertices by the inverse box transform, then use the test here.

Based on the separating axis test (SAT), we test the following 13 axes:

1. [3 tests]  $\mathbf{e}_0 = (1, 0, 0)$ ,  $\mathbf{e}_1 = (0, 1, 0)$ ,  $\mathbf{e}_2 = (0, 0, 1)$  (the normals of the AABB). In other words, test the AABB against the minimal AABB around the triangle.
2. [1 test]  $\mathbf{n}$ , the normal of  $\Delta \mathbf{u}_0 \mathbf{u}_1 \mathbf{u}_2$ . We use a fast plane/AABB overlap test (see Section 16.10.1), which tests only the two vertices of the box diagonal whose direction is most closely aligned to the normal of the triangle.
3. [9 tests]  $\mathbf{a}_{ij} = \mathbf{e}_i \times \mathbf{f}_j$ ,  $i, j \in \{0, 1, 2\}$ , where  $\mathbf{f}_0 = \mathbf{v}_1 - \mathbf{v}_0$ ,  $\mathbf{f}_1 = \mathbf{v}_2 - \mathbf{v}_1$ , and  $\mathbf{f}_2 = \mathbf{v}_0 - \mathbf{v}_2$ , i.e., edge vectors. These tests are very similar and we will only show the derivation of the case where  $i = 0$  and  $j = 0$  (see below).

As soon as a separating axis is found the algorithm terminates and returns “no overlap.” If all tests pass, i.e., there is no separating axis, then the triangle overlaps the box.

Here we derive one of the nine tests, where  $i = 0$  and  $j = 0$ , in Step 3. This means that  $\mathbf{a}_{00} = \mathbf{e}_0 \times \mathbf{f}_0 = (0, -f_{0z}, f_{0y})$ . So, now we need to project the triangle vertices onto  $\mathbf{a}_{00}$  (hereafter called  $\mathbf{a}$ ):

$$\begin{aligned} p_0 &= \mathbf{a} \cdot \mathbf{v}_0 = (0, -f_{0z}, f_{0y}) \cdot \mathbf{v}_0 = v_{0z}v_{1y} - v_{0y}v_{1z}, \\ p_1 &= \mathbf{a} \cdot \mathbf{v}_1 = (0, -f_{0z}, f_{0y}) \cdot \mathbf{v}_1 = v_{0z}v_{1y} - v_{0y}v_{1z} = p_0, \\ p_2 &= \mathbf{a} \cdot \mathbf{v}_2 = (0, -f_{0z}, f_{0y}) \cdot \mathbf{v}_2 = (v_{1y} - v_{0y})v_{2z} - (v_{1z} - v_{0z})v_{2y}. \end{aligned} \quad (16.33)$$

Normally, we would have had to find  $\min(p_0, p_1, p_2)$  and  $\max(p_0, p_1, p_2)$ , but fortunately  $p_0 = p_1$ , which simplifies the computations. Now we only need to find  $\min(p_0, p_2)$  and  $\max(p_0, p_2)$ , which is significantly faster because conditional statements are expensive on modern CPUs.

After the projection of the triangle onto  $\mathbf{a}$ , we need to project the box onto  $\mathbf{a}$  as well. We compute a “radius,”  $r$ , of the box projected on  $\mathbf{a}$  as

$$r = h_x|a_x| + h_y|a_y| + h_z|a_z| = h_y|a_y| + h_z|a_z|, \quad (16.34)$$

where the last step comes from that  $a_x = 0$  for this particular axis. Then, this axis test becomes

```
if (min(p0, p2) > r or max(p0, p2) < -r) return false;    (16.35)
```

Code is available on the web [11].

## 16.13 BV/BV Intersection Tests

A closed volume that totally contains a set of objects is (in most situations) called a *bounding volume* (BV) for this set. The purpose of a BV is to provide simpler intersection tests and make more efficient rejections. For example, to test whether or not two cars collide, first find their BVs and test if these overlap. If they do not, then the cars are guaranteed not to collide (which we assume is the most common case). We then have avoided testing each primitive of one car against each primitive of the other, thereby saving computation.

Bounding volume hierarchies are often part of the foundation of collision detection algorithms (see Chapter 17). Four bounding volumes that are commonly used for this purpose are the sphere, the *axis-aligned bounding box* (AABB), the *discrete oriented polytope* ( $k$ -DOP), and the *oriented*

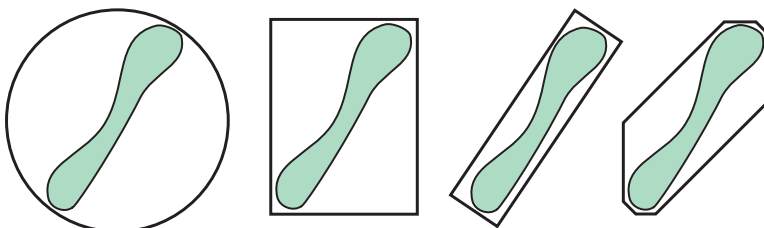


**Figure 16.19.** The efficiency of a bounding volume can be estimated by the “empty” volume; the more empty space, the worse the fit. A sphere (left), an AABB (middle left), an OBB (middle right), and a  $k$ -DOP (right) are shown for an object, where the OBB and the  $k$ -DOP clearly have less empty space than the others.

*bounding box* (OBB). A fundamental operation is to test whether or not two bounding volumes overlap. Methods of testing overlap for the AABB, the  $k$ -DOP, and the OBB are presented in the following sections. See Section 16.3 for algorithms that form BVs around primitives.

The reason for using more complex BVs than the sphere and the AABB is that more complex BVs often have a tighter fit. This is illustrated in Figure 16.19. Other bounding volumes are possible, of course. For example, cylinders, ellipsoids, and capsules are sometimes used as bounding volumes for objects. Also, a number of spheres can be placed to enclose a single object [572, 1137].

### 16.13.1 Sphere/Sphere Intersection

For spheres, the intersection test is simple and quick: Compute the distance between the two spheres' centers and then reject if this distance is greater than the sum of the two spheres' radii. Otherwise, they intersect. In implementing this algorithm the squared distances of the various quantities are used, since all that is desired is the result of the comparison. In this way, computing the square root (an expensive operation) is avoided. Ericson [315] gives SSE code for testing four separate pairs of spheres simultaneously.

```

bool Sphere_intersect(c1, r1, c2, r2)
  returns({OVERLAP, DISJOINT});
1 : h = c1 - c2
2 : d2 = h · h
3 : if(d2 > (r1 + r2)2) return (DISJOINT);
4 : return (OVERLAP);
```

### 16.13.2 Sphere/Box Intersection

An algorithm for testing whether a sphere and an AABB intersect was first presented by Arvo [34] and is surprisingly simple. The idea is to find the point on the AABB that is closest to the sphere's center,  $\mathbf{c}$ . One-dimensional tests are used, one for each of the three axes of the AABB. The sphere's center coordinate for an axis is tested against the bounds of the AABB. If it is outside the bounds, the distance between the sphere center and the box along this axis (a subtraction) is computed and squared. After we have done this along the three axes, the sum of these squared distances is compared to the squared radius,  $r^2$ , of the sphere. If the sum is less than the squared radius, the closest point is inside the sphere, and the box

overlaps. As Arvo shows, this algorithm can be modified to handle hollow boxes and spheres, as well as axis-aligned ellipsoids.

Larsson et al. [734] present some variants of this algorithm, including a considerably faster SSE vectorized version. Their insight is to use simple rejection tests early on, either per axis or all at the start. The rejection test is to see if the center-to-box distance along an axis is greater than the radius. If so, testing can end early, since the sphere then cannot possibly overlap with the box. When the chance of overlap is low, this early rejection method is noticeably faster. What follows is the QRI (quick rejections intertwined) version of their test. The early out tests are at lines 4 and 7, and can be removed if desired.

```

bool SphereAABB_intersect(c, r, A)
returns({OVERLAP, DISJOINT});
1 :   d = 0
2 :   for each i ∈ {x, y, z}
3 :     if ((e = ci − aimin) < 0)
4 :       if (e < −r) return (DISJOINT);
5 :       d = d + e2;
6 :     else if ((e = ci − aimax) > 0)
7 :       if (e > r) return (DISJOINT);
8 :       d = d + e2;
9 :   if (d > r2) return (DISJOINT);
10 :  return (OVERLAP);
```

For a fast vectorized (using SSE) implementation, Larsson et al. propose to eliminate the majority of the branches. The insight is to evaluate lines 3 and 6 simultaneously using the following expression:

$$e = \max(a_i^{\min} - c_i, 0) + \max(c_i - a_i^{\max}). \quad (16.38)$$

Normally, we would then update *d* as *d* = *d* + *e*<sup>2</sup>. However, using SSE, we can evaluate Equation 16.38 for *x*, *y*, and *z* in parallel. Pseudo code for the full test is given below.

```

bool SphereAABB_intersect(c, r, A)
returns({OVERLAP, DISJOINT});
1 :   e = (max(axmin − cx, 0), max(aymin − cy, 0), max(azmin − cz, 0))
2 :   e = e + (max(cx − axmax, 0), max(cy − aymax, 0), max(cz − azmax, 0))
3 :   d = e · e
4 :   if (d > r2) return (DISJOINT);
5 :   return (OVERLAP);
```

Note that lines 1 and 2 can be implemented using a parallel SSE max function. Even though there are no early outs in this test, it is still faster

than the other techniques. This is because branches have been eliminated and parallel computations used.

Another approach to SSE is to vectorize the object pairs. Ericson [315] presents SIMD code to compare four spheres with four AABBs at the same time.

For sphere/OBB intersection, first transform the sphere's center into the OBB's space. That is, use the OBB's normalized axes as the basis for transforming the sphere's center. Now this center point is expressed in terms of the OBB's axes, so the OBB can be treated as an AABB. The sphere/AABB algorithm is then used to test for intersection.

### 16.13.3 AABB/AABB Intersection

An AABB is, as its name implies, a box whose faces are aligned with the main axis directions. Therefore, two points are sufficient to describe such a volume. Here we use the definition of the AABB presented in Section 16.2.

Due to their simplicity, AABBs are commonly employed both in collision detection algorithms and as bounding volumes for the nodes in a scene graph. The test for intersection between two AABBs,  $A$  and  $B$ , is trivial and is summarized below:

```
bool AABB_intersect(A, B)
  returns({OVERLAP, DISJOINT});
1:  for each  $i \in \{x, y, z\}$ 
2:    if( $a_i^{\min} > b_i^{\max}$  or  $b_i^{\min} > a_i^{\max}$ )
3:      return (DISJOINT);
4:  return (OVERLAP);
```

Lines 1 and 2 loop over all three standard axis directions  $x$ ,  $y$ , and  $z$ . Ericson [315] provides SSE code for testing four separate pairs of AABBs simultaneously.

Another approach to SSE is to vectorize the object pairs. Ericson [315] presents SIMD code to compare four spheres with four AABBs at the same time.

### 16.13.4 $k$ -DOP/ $k$ -DOP Intersection

The bounding volume called a *discrete orientation polytope* or  $k$ -DOP was named by Klosowski et al. [672]. A  $k$ -DOP is a convex polytope<sup>13</sup> whose faces are determined by a small, fixed set of  $k$  normals, where the outward half-space of the normals is not considered part of the BV. Kay and Kajiya were the first to introduce this kind of BV, and they used them in the

---

<sup>13</sup>A (convex) polytope is the convex hull of a finite set of points (see Section A.5.3).

context of ray tracing. Also, they called the volume between two oppositely oriented normals on parallel planes a bounding *slab* and used these to keep the intersection cost down (see Section 16.7.1). This technique is used for the  $k$ -DOPs for the same reason. As a result the intersection test consists of only  $k/2$  interval overlap tests. Klosowski et al. [672] have shown that, for moderate values of  $k$ , the overlap test for two  $k$ -DOPs is an order of a magnitude faster than the test for two OBBs. In Figure 16.4 on page 730, a simple two-dimensional  $k$ -DOP is depicted. Note that the AABB is a special case of a 6-DOP where the normals are the positive and negative main axis directions. Also note that as  $k$  increases, the BV increasingly resembles the convex hull, which is the tightest-fitting convex BV.

The intersection test that follows is simple and extremely fast, inexact but conservative. If two  $k$ -DOPs,  $A$  and  $B$  (superscripted with indices  $A$  and  $B$ ), are to be tested for intersection, then test all pairs of slabs ( $S_i^A, S_i^B$ ) for overlap;  $s_i = S_i^A \cap S_i^B$  is a one-dimensional interval overlap test, which is solved with ease.<sup>14</sup> If at any time  $s_i = \emptyset$  (i.e., the empty set), then the BVs are disjoint and the test is terminated. Otherwise, the slab overlap tests continues. If and only if all  $s_i \neq \emptyset, 1 \leq i \leq k/2$ , then the BVs are considered to be overlapping. According to the separating axis test (see Section 16.2), one also needs to test an axis parallel to the cross product of one edge from each  $k$ -DOP. However, these tests are often omitted because they cost more than they give back in performance. Therefore, if the test below returns that the  $k$ -DOPs overlap, then they might actually be disjoint. Here is the pseudocode for the  $k$ -DOP/ $k$ -DOP overlap test:

```

kDOP_intersect( $d_1^{A,\min}, \dots, d_{k/2}^{A,\min},$   

 $d_1^{A,\max}, \dots, d_{k/2}^{A,\max}, d_1^{B,\min}, \dots, d_{k/2}^{B,\min},$   

 $d_1^{B,\max}, \dots, d_{k/2}^{B,\max})$   

returns( $\{\text{OVERLAP}, \text{DISJOINT}\}$ );  

1 : for each  $i \in \{1, \dots, k/2\}$   

2 :     if ( $d_i^{B,\min} > d_i^{A,\max}$  or  $d_i^{A,\min} > d_i^{B,\max}$ )  

3 :         return ( $\text{DISJOINT}$ );  

4 :     return ( $\text{OVERLAP}$ );

```

Note that only  $k$  scalar values need to be stored with each instance of the  $k$ -DOP (the normals,  $\mathbf{n}_i$ , are stored once for all  $k$ -DOPs since they are static). If the  $k$ -DOPs are translated by  $\mathbf{t}^A$  and  $\mathbf{t}^B$ , respectively, the test gets a tiny bit more complicated. Project  $\mathbf{t}^A$  onto the normals,  $\mathbf{n}_i$ , e.g.,  $p_i^A = \mathbf{t}^A \cdot \mathbf{n}_i$  (note that this is independent of any  $k$ -DOP in particular

<sup>14</sup>This is indeed an example of dimension reduction as the rules of thumb recommended. Here, a three-dimensional slab test is simplified into a one-dimensional interval overlap test.

and therefore needs to be computed only once for each  $\mathbf{t}^A$  or  $\mathbf{t}^B$ ) and add  $p_i^A$  to  $d_i^{A,\min}$  and  $d_i^{A,\max}$  in the `if`-statement. The same is done for  $\mathbf{t}^B$ . In other words, a translation changes the distance of the  $k$ -DOP along each normal's direction.

### 16.13.5 OBB/OBB Intersection

In this section, a fast routine by Gottschalk et al. [433, 434] will be derived for testing whether two OBBs,  $A$  and  $B$ , overlap. The algorithm uses the separating axis test, and is about an order of magnitude faster than previous methods, which use closest features or linear programming. The definition of the OBB may be found in Section 16.2.

The test is done in the coordinate system formed by  $A$ 's center and axes. This means that the origin is  $\mathbf{a}^c = (0, 0, 0)$  and that the main axes in this coordinate system are  $\mathbf{a}^u = (1, 0, 0)$ ,  $\mathbf{a}^v = (0, 1, 0)$ , and  $\mathbf{a}^w = (0, 0, 1)$ . Moreover,  $B$  is assumed to be located relative to  $A$ , with a translation  $\mathbf{t}$  and a rotation (matrix)  $\mathbf{R}$ .

According to the separating axis test, it is sufficient to find one axis that separates  $A$  and  $B$  to be sure that they are disjoint (do not overlap). Fifteen axes have to be tested: three from the faces of  $A$ , three from the faces of  $B$ , and  $3 \cdot 3 = 9$  from combinations of edges from  $A$  and  $B$ . This is shown in two dimensions in Figure 16.20. As a consequence of the orthonormality of the matrix  $\mathbf{A} = (\mathbf{a}^u \ \mathbf{a}^v \ \mathbf{a}^w)$ , the potential separating axes that should be orthogonal to the faces of  $A$  are simply the axes  $\mathbf{a}^u$ ,  $\mathbf{a}^v$ , and  $\mathbf{a}^w$ . The same holds for  $B$ . The remaining nine potential axes, formed by one edge each from both  $A$  and  $B$ , are then  $\mathbf{c}^{ij} = \mathbf{a}^i \times \mathbf{b}^j$ ,  $\forall i \in \{u, v, w\}$  and  $\forall j \in \{u, v, w\}$ .

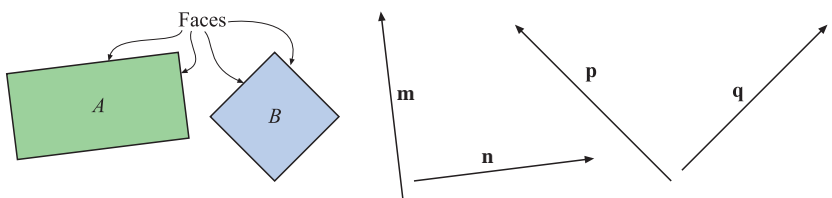


**Figure 16.20.** To determine whether two OBBs  $A$  and  $B$  overlap, the separating axis test can be used. Here, it is shown in two dimensions. The separating axes should be orthogonal to the faces of  $A$  and  $B$ . The axes  $\mathbf{m}$  and  $\mathbf{n}$  are orthogonal to the faces of  $A$ , and  $\mathbf{p}$  and  $\mathbf{q}$  are orthogonal to the faces of  $B$ . The OBBs are then projected onto the axes. If both projections overlap on all axes, then the OBBs overlap; otherwise, they do not. So it is sufficient to find one axis that separates the projections in order to know that the OBBs do not overlap. In this example, the  $\mathbf{n}$  axis is the only axis that separates the projections.

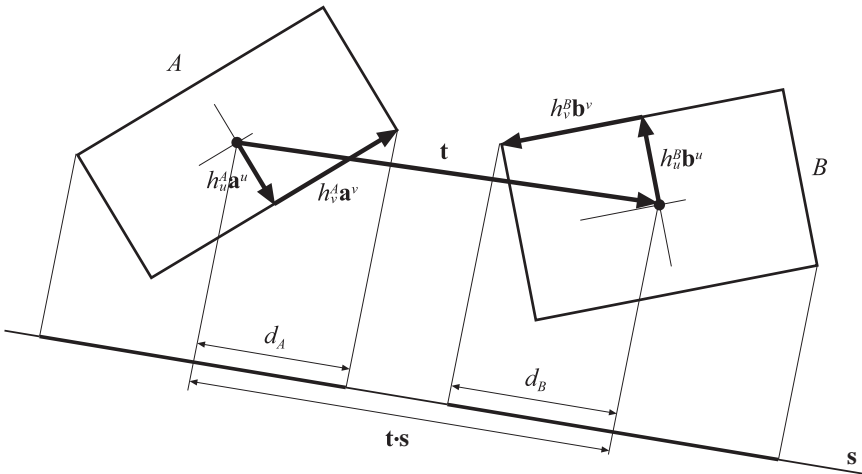


**Figure 16.21.** The separating axis test illustrated. The two OBBs,  $A$  and  $B$ , are disjoint, since the projections of their “radii,”  $d_A$  and  $d_B$ , of the OBBs on the axis determined by  $s$  are not overlapping. (Illustration after Gottschalk et al. [433].)

Assume that a potential separating axis is denoted as  $s$ , and adopt the notation from Figure 16.21. The “radii,”  $d_A$  and  $d_B$ , of the OBBs on the axis,  $s$ , are obtained by simple projections, as expressed in Equation 16.42. Remember that  $h_i^A$  and  $h_i^B$  are always positive, and so their absolute values do not need to be computed:

$$\begin{aligned} d_A &= \sum_{i \in \{u, v, w\}} h_i^A |\mathbf{a}^i \cdot \mathbf{s}|, \\ d_B &= \sum_{i \in \{u, v, w\}} h_i^B |\mathbf{b}^i \cdot \mathbf{s}|. \end{aligned} \quad (16.42)$$

If, and only if,  $s$  is a separating axis, then the intervals on the axis should be disjoint. That is, the following should hold:

$$|\mathbf{t} \cdot \mathbf{s}| > d_A + d_B. \quad (16.43)$$

Derivations and simplifications of Equation 16.43 for three cases follow—one for an edge of  $A$ , one for an edge of  $B$ , and one for a combination of edges from  $A$  and  $B$ .

First, let  $\mathbf{s} = \mathbf{a}^u$ . This gives the expression below:

$$|\mathbf{t} \cdot \mathbf{s}| = |\mathbf{t} \cdot \mathbf{a}^u| = |t_x|. \quad (16.44)$$

The last step comes from the fact that we are operating in the coordinate system of  $A$ , and thus  $\mathbf{a}^u = (1 \ 0 \ 0)^T$ . In Equation 16.45, the expressions

for  $d_A$  and  $d_B$  are simplified:

$$\begin{aligned} d_A &= \sum_{i \in \{u, v, w\}} h_i^A |\mathbf{a}^i \cdot \mathbf{s}| = \sum_{i \in \{u, v, w\}} h_i^A |\mathbf{a}^i \cdot \mathbf{a}^u| = h_u^A, \\ d_B &= \sum_{i \in \{u, v, w\}} h_i^B |\mathbf{b}^i \cdot \mathbf{s}| = \sum_{i \in \{u, v, w\}} h_i^B |\mathbf{b}^i \cdot \mathbf{a}^u| \\ &= h_u^B |b_x^u| + h_v^B |b_x^v| + h_w^B |b_x^w| = h_u^B |r_{00}| + h_v^B |r_{01}| + h_w^B |r_{02}|. \end{aligned} \quad (16.45)$$

The resulting equation for  $d_A$  comes from the orthonormality of  $\mathbf{A}$ , and in the last step in the derivation of  $d_B$ , note that

$$\mathbf{R} = \begin{pmatrix} r_{00} & r_{01} & r_{02} \\ r_{10} & r_{11} & r_{12} \\ r_{20} & r_{21} & r_{22} \end{pmatrix} = (\mathbf{b}^u \ \mathbf{b}^v \ \mathbf{b}^w), \quad (16.46)$$

since  $\mathbf{R}$  is the relative rotation matrix. The disjointedness test for the axis  $\mathbf{l} = \mathbf{a}^u$  becomes

$$|t_x| > h_u^A + h_u^B |r_{00}| + h_v^B |r_{01}| + h_w^B |r_{02}|, \quad (16.47)$$

and if this expression is true, then  $A$  and  $B$  are disjoint. Similar test expressions are derived in the same manner for  $\mathbf{s} = \mathbf{a}^v$  and  $\mathbf{s} = \mathbf{a}^w$ .

Second, let  $\mathbf{s} = \mathbf{b}^u$ , for which the derivation follows:

$$|\mathbf{t} \cdot \mathbf{s}| = |\mathbf{t} \cdot \mathbf{b}^u| = |t_x b_x^u + t_y b_y^u + t_z b_z^u| = |t_x r_{00} + t_y r_{10} + t_z r_{20}|,$$

$$\begin{aligned} d_A &= \sum_{i \in \{u, v, w\}} h_i^A |\mathbf{a}^i \cdot \mathbf{s}| = \sum_{i \in \{u, v, w\}} h_i^A |\mathbf{a}^i \cdot \mathbf{b}^u| \\ &= h_u^A |b_x^u| + h_v^A |b_y^u| + h_w^A |b_z^u| = h_u^A |r_{00}| + h_v^A |r_{10}| + h_w^A |r_{20}|, \end{aligned} \quad (16.48)$$

$$d_B = \sum_{i \in \{u, v, w\}} h_i^B |\mathbf{b}^i \cdot \mathbf{s}| = \sum_{i \in \{u, v, w\}} h_i^B |\mathbf{b}^i \cdot \mathbf{b}^u| = h_u^B.$$

This leads to the disjointedness test in Equation 16.49 for  $\mathbf{s} = \mathbf{b}^u$ :

$$|t_x r_{00} + t_y r_{10} + t_z r_{20}| > h_u^A |r_{00}| + h_v^A |r_{10}| + h_w^A |r_{20}| + h_u^B. \quad (16.49)$$

Again, for the remaining axes,  $\mathbf{b}^v$  and  $\mathbf{b}^w$ , similar tests are derived in the same manner.

Finally, the separating axis could be a combination of an edge from each OBB. As an example, the axis is chosen as  $\mathbf{s} = \mathbf{a}^u \times \mathbf{b}^v$ . This gives

$$\begin{aligned} |\mathbf{t} \cdot \mathbf{s}| &= |\mathbf{t} \cdot (\mathbf{a}^u \times \mathbf{b}^v)| = |\mathbf{t} \cdot (0, -b_z^v, b_y^v)| \\ &= |t_z b_y^v - t_y b_z^v| = |t_z r_{11} - t_y r_{21}|, \end{aligned}$$

$$\begin{aligned} d_A &= \sum_{i \in \{u, v, w\}} h_i^A |\mathbf{a}^i \cdot \mathbf{s}| = \sum_{i \in \{u, v, w\}} h_i^A |\mathbf{a}^i \cdot (\mathbf{a}^u \times \mathbf{b}^v)| \\ &= \sum_{i \in \{u, v, w\}} h_i^A |\mathbf{b}^v \cdot (\mathbf{a}^u \times \mathbf{a}^i)| = h_v^A |\mathbf{b}^v \cdot \mathbf{a}^w| + h_w^A |\mathbf{b}^v \cdot \mathbf{a}^v| \\ &= h_v^A |b_z^v| + h_w^A |b_y^v| = h_v^A |r_{21}| + h_w^A |r_{11}|, \end{aligned} \quad (16.50)$$

$$\begin{aligned} d_B &= \sum_{i \in \{u, v, w\}} h_i^B |\mathbf{b}^i \cdot \mathbf{s}| = \sum_{i \in \{u, v, w\}} h_i^B |\mathbf{b}^i \cdot (\mathbf{a}^u \times \mathbf{b}^v)| \\ &= \sum_{i \in \{u, v, w\}} h_i^B |\mathbf{a}^u \cdot (\mathbf{b}^i \times \mathbf{b}^v)| = h_u^B |\mathbf{a}^u \cdot \mathbf{b}^w| + h_w^B |\mathbf{a}^u \cdot \mathbf{b}^u| \\ &= h_u^B |b_x^w| + h_w^B |b_x^u| = h_u^B |r_{02}| + h_w^B |r_{00}|. \end{aligned}$$

The resulting test becomes

$$|t_z r_{11} - t_y r_{21}| > h_v^A |r_{21}| + h_w^A |r_{11}| + h_u^B |r_{02}| + h_w^B |r_{00}|. \quad (16.51)$$

Disjointedness tests for the remaining axes, formed by  $\mathbf{c}^{ij} = \mathbf{a}^i \times \mathbf{b}^j$ ,  $\forall i \in \{u, v, w\}$  and  $\forall j \in \{u, v, w\}$ , are derived analogously.

Once again, if any of these 15 tests is positive, the OBBs are disjoint ( $A \cap B = \emptyset$ ). The maximum number of operations (reported to be around 180, or 240 if the transform of  $B$  into  $A$ 's coordinate system is included) [434] occurs when the OBBs overlap ( $A \cap B \neq \emptyset$ ). However, in most cases, the routine may terminate earlier because a separating axis has been found. Gottschalk et al. [433] point out that the absolute values of the elements of  $\mathbf{R}$  are used four times and could therefore be computed once and reused for more rapid code.

Note that testing the axes in different orders has an impact on performance. To get a good average result for two OBBs,  $A$  and  $B$ , one should first test the three axes  $\mathbf{a}^u$ ,  $\mathbf{a}^v$ , and  $\mathbf{a}^w$ . The main reasons for this are that they are orthogonal and thus reject the overlap faster, and that they are the simplest tests [1088]. After these have been tested, the axes of  $B$  could be tested, followed by the axes formed from the axes of  $A$  and  $B$ .

Depending on the application, it may be worthwhile to add a quick rejection test before beginning the actual OBB/OBB test. The enclosing

sphere for an OBB is centered at the OBB's center  $\mathbf{b}^c$ , and the sphere's radius is computed from the OBB's half-lengths  $h_u$ ,  $h_v$ , and  $h_w$ . Then the sphere/sphere intersection test (Section 16.13.1) can be used for a possible quick rejection.

## 16.14 View Frustum Intersection

As has been seen in Section 14.3, hierarchical view frustum culling is essential for rapid rendering of a complex scene. One of the few operations called during bounding-volume-hierarchy cull traversal is the intersection test between the view frustum and a bounding volume. These operations are thus critical to fast execution. Ideally, they should determine whether the BV is totally inside (inclusion), totally outside (exclusion), or whether it intersects the frustum.

To review, a view frustum is a pyramid that is truncated by a near and a far plane (which are parallel), making the volume finite. In fact, it becomes a polyhedron. This is shown in Figure 16.22, where the names of the six planes, *near*, *far*, *left*, *right*, *top*, and *bottom* also are marked. The view frustum volume defines the parts of the scene that should be visible and thus rendered (in perspective for a pyramidal frustum).

The most common bounding volumes used for internal nodes in a hierarchy (e.g., a scene graph) and for enclosing geometry are spheres, AABBs, and OBBs. Therefore frustum/sphere and frustum/AABB/OBB tests will be discussed and derived here.

To see why we need the three return results outside/inside/intersect, we will examine what happens when traversing the bounding volume hierarchy. If a BV is found to be totally outside the view frustum, then that

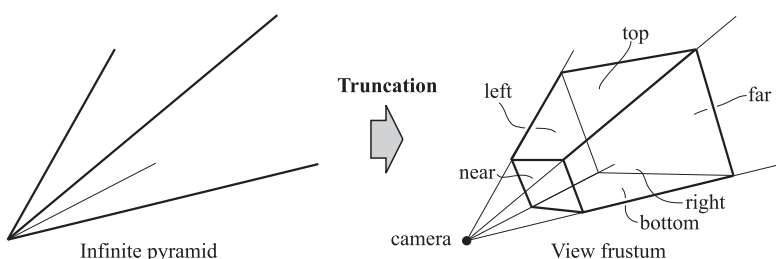


**Figure 16.22.** The illustration on the left is an infinite pyramid, which then is cropped by the parallel near and far planes in order to construct a view frustum. The names of the other planes are also shown, and the position of the camera is at the apex of the pyramid.

BV's subtree will not be traversed further and none of its geometry will be rendered. On the other hand, if the BV is totally inside, then no more frustum/BV tests need to be computed for that subtree and every renderable leaf will be drawn. For a partially visible BV, i.e., one that intersects the frustum, the BV's subtree is tested recursively against the frustum. If the BV is for a leaf, then that leaf must be rendered.

The complete test is called an *exclusion/inclusion/intersection test*. Sometimes the third state, intersection, may be considered too costly to compute. In this case, the BV is classified as “probably-inside.” We call such a simplified algorithm an *exclusion/inclusion test*. If a BV cannot be excluded successfully, there are two choices. One is to treat the “probably-inside” state as an inclusion, meaning that everything inside the BV is rendered. This is often inefficient, as no further culling is performed. The other choice is to test each node in the subtree in turn for exclusion. Such testing is often without benefit, as much of the subtree may indeed be inside the frustum. Because neither choice is particularly good, some attempt at quickly differentiating between intersection and inclusion is often worthwhile, even if the test is imperfect.

It is important to realize that the quick classification tests do not have to be exact for scene-graph culling, just conservative. For differentiating exclusion from inclusion, all that is required is that the test err on the side of inclusion. That is, objects that should actually be excluded can erroneously be included. Such mistakes simply cost extra time. On the other hand, objects that should be included should never be quickly classified as excluded by the tests, otherwise rendering errors will occur. With inclusion versus intersection, either type of incorrect classification is usually legal. If a fully included BV is classified as intersecting, time is wasted testing its subtree for intersection. If an intersected BV is considered fully inside, time is wasted by rendering all objects, some of which could have been culled.

Before we introduce the tests between a frustum and a sphere, AABB, or OBB, we shall describe an intersection test method between a frustum and a general object. This test is illustrated in Figure 16.23. The idea is to transform the test from a BV/frustum test to a point/volume test. First, a point relative to the BV is selected. Then the BV is moved along the outside of the frustum, as closely as possible to it without overlapping. During this movement, the point relative to the BV is traced, and its trace forms a new volume (a polygon with thick edges in Figure 16.23). The fact that the BV was moved as close as possible to the frustum means that if the point relative to the BV (in its original position) lies inside the traced-out volume, then the BV intersects or is inside the frustum. So instead of testing the BV for intersection against a frustum, the point relative to the BV is tested against another new volume, which is traced out by the point.

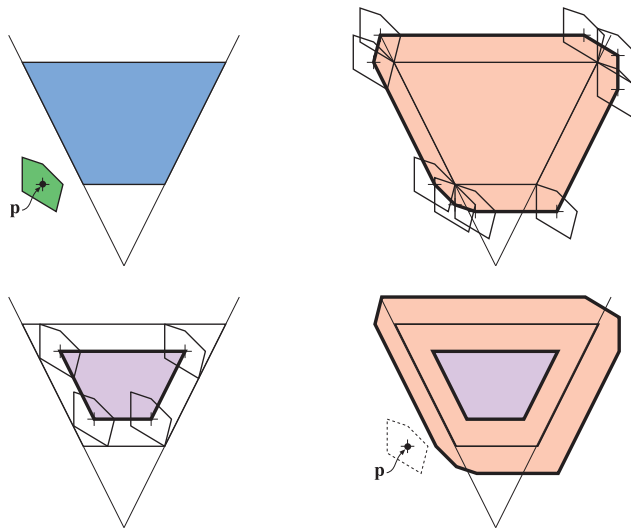


**Figure 16.23.** The upper left image shows a frustum (blue) and a general bounding volume (green), where a point  $\mathbf{p}$  relative to the object has been selected. By tracing the point  $\mathbf{p}$  where the object moves on the outside (upper right) and on the inside (lower left) of the frustum, as close as possible to the frustum, the frustum/BV can be reformulated into testing the point  $\mathbf{p}$  against an outer and an inner volume. This is shown on the lower right. If the point  $\mathbf{p}$  is outside the orange volume, then the BV is outside the frustum. The BV intersects the frustum if  $\mathbf{p}$  is inside the orange area, and the BV is fully inside the frustum if  $\mathbf{p}$  is inside the violet area.

In the same way, the BV can be moved on the inside of the frustum and as close as possible to the frustum. This will trace out a new, smaller frustum with planes parallel to the original frustum [48]. If the point relative to the object is inside this new volume, then the BV is inside the frustum. This technique is used to derive tests in the subsequent sections. Note that the creation of the new volumes is independent of the position of the actual BV—it is dependent solely on the position of the point relative to the BV. This means that a BV with an arbitrary position can be tested against the same volumes.

First, the plane equations of the frustum are derived, since these are needed for these sorts of tests. Frustum/sphere intersection is presented next, followed by an explanation of frustum/box intersection.

### 16.14.1 Frustum Plane Extraction

In order to do view frustum culling, the plane equations for the six different sides of the frustum are needed. Here, a clever and fast way of deriving these

is presented. Assume that the view matrix is  $\mathbf{V}$  and that the projection matrix is  $\mathbf{P}$ . The composite transform is then  $\mathbf{M} = \mathbf{PV}$ . A point  $\mathbf{s}$  (where  $s_w = 1$ ) is transformed into  $\mathbf{t}$  as  $\mathbf{t} = \mathbf{Ms}$ . At this point,  $\mathbf{t}$  may have  $t_w \neq 1$  due to, for example, perspective projection. Therefore, all components in  $\mathbf{t}$  are divided by  $t_w$  in order to obtain a point  $\mathbf{u}$  with  $u_w = 1$ . For points inside the view frustum, it holds that  $-1 \leq u_i \leq 1$ , for  $i \in x, y, z$ , i.e., the point  $\mathbf{u}$  is inside a unit cube.<sup>15</sup> From this equation, the planes of the frustum can be derived, which is shown next.

Focus for a moment on the volume on the right side of the left plane of the unit-cube, for which  $-1 \leq u_x$ . This is expanded below:

$$\begin{aligned} -1 \leq u_x &\iff -1 \leq \frac{t_x}{t_w} \iff t_x + t_w \geq 0 \iff \\ &\iff (\mathbf{m}_0 \cdot \mathbf{s}) + (\mathbf{m}_3 \cdot \mathbf{s}) \geq 0 \iff (\mathbf{m}_0 + \mathbf{m}_3) \cdot \mathbf{s} \geq 0. \end{aligned} \tag{16.52}$$

In the derivation,  $\mathbf{m}_i$  denotes the  $i$ :th row in  $\mathbf{M}$ . The last step  $(\mathbf{m}_0 + \mathbf{m}_3) \cdot \mathbf{s} \geq 0$  is, in fact, denoting a (half) plane equation of the left plane of the view frustum. This is so because the left plane in the unit cube has been transformed back to world coordinates. Also note that  $s_w = 1$ , which makes the equation a plane. To make the normal of the plane point outwards from the frustum, the equation must be negated (as the original equation described the inside of the unit cube). This gives  $-(\mathbf{m}_3 + \mathbf{m}_0) \cdot (x, y, z, 1) = 0$  for the left plane of the frustum (where we use  $(x, y, z, 1)$  instead to use a plane equation of the form:  $ax + by + cz + d = 0$ ). To summarize, all the planes are

$$\begin{aligned} -(\mathbf{m}_3 + \mathbf{m}_0) \cdot (x, y, z, 1) &= 0 && [\text{left}], \\ -(\mathbf{m}_3 - \mathbf{m}_0) \cdot (x, y, z, 1) &= 0 && [\text{right}], \\ -(\mathbf{m}_3 + \mathbf{m}_1) \cdot (x, y, z, 1) &= 0 && [\text{bottom}], \\ -(\mathbf{m}_3 - \mathbf{m}_1) \cdot (x, y, z, 1) &= 0 && [\text{top}], \\ -(\mathbf{m}_3 + \mathbf{m}_2) \cdot (x, y, z, 1) &= 0 && [\text{near}], \\ -(\mathbf{m}_3 - \mathbf{m}_2) \cdot (x, y, z, 1) &= 0 && [\text{far}]. \end{aligned} \tag{16.53}$$

Code for doing this in OpenGL and DirectX is available on the web [455].

### 16.14.2 Frustum/Sphere Intersection

A frustum for an orthographic view is a box, so the overlap test in this case becomes a sphere/OBB intersection and can be solved using the algorithm presented in Section 16.13.2. To further test whether the sphere is entirely inside the box, we treat the box as hollow when we are finding the closest

<sup>15</sup>This is for the OpenGL type of projection matrices (see Section 4.6). For DirectX, the same holds, except that  $0 \leq u_z \leq 1$ .

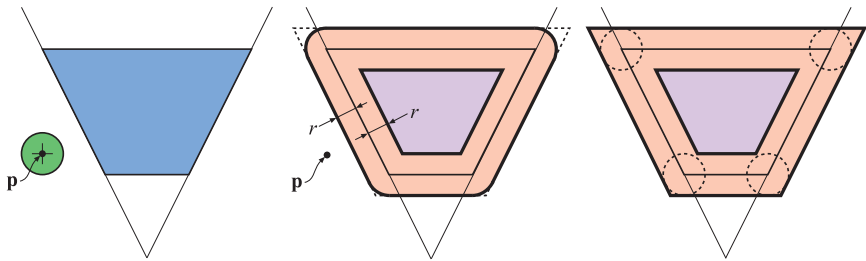


**Figure 16.24.** At the left, a frustum and a sphere are shown. The exact frustum/sphere test can be formulated as testing  $\mathbf{p}$  against the orange and violet volumes in the middle figure. At the right is a reasonable approximation of the volumes in the middle. If the center of the sphere is located outside a rounded corner, but inside all outer planes, it will be incorrectly classified as intersecting, even though it is outside the frustum.

point. For a full presentation of this modified algorithm, along with code, see Arvo [34].

Following the method for deriving a frustum/BV test, we select the origin of the sphere as the point  $\mathbf{p}$  to trace. This is shown in Figure 16.24. If the sphere, with radius  $r$ , is moved along the inside and along the outside of the frustum and as close to the frustum as possible, then the trace of  $\mathbf{p}$  gives us the volumes that are needed to reformulate the frustum/sphere test. The actual volumes are shown in the middle segment of Figure 16.24. As before, if  $\mathbf{p}$  is outside the orange volume, then the sphere is outside the frustum. If  $\mathbf{p}$  is inside the violet area, then the sphere is completely inside the frustum. If the point is inside the orange area, the sphere intersects the frustum sides planes. In this way, the exact test can be done. However, for the sake of efficiency we use the approximation that appears on the right side of Figure 16.24. Here, the orange volume has been extended so as to avoid the more complicated computations that the rounded corners would require. Note that the outer volume consists of the planes of the frustum moved  $r$  distance units outwards in the direction of the frustum plane normal, and that the inner volume can be created by moving the planes of the frustum  $r$  distance units inwards in the direction of the frustum plane normals.

Assume that the plane equations of the frustum are such that the positive half-space is located outside of the frustum. Then, an actual implementation would loop over the six planes of the frustum, and for each frustum plane, compute the signed distance from the sphere's center to the plane. This is done by inserting the sphere center into the plane equation. If the distance is greater than the radius  $r$ , then the sphere is outside the frustum. If the distances to all six planes are less than  $-r$ , then the

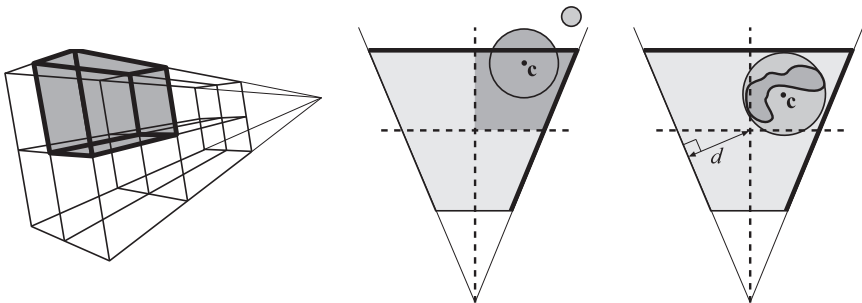


**Figure 16.25.** The left figure shows how a three-dimensional frustum is divided into eight octants. The other figure shows a two-dimensional example, where the sphere center  $c$  is in the upper right octant. The only planes that then need to be considered are the right and the far planes (thick black lines). Note that the small sphere is in the same octant as the large sphere. This technique also works for arbitrary objects, but the following condition must hold: The minimum distance,  $d$ , from the frustum center to the frustum planes must be larger than the radius of a tight bounding sphere around the object. If that condition is fulfilled, then the bounding sphere can be used to find the octant.

sphere is inside the frustum; otherwise the sphere intersects it.<sup>16</sup> To make the test more accurate, it is possible to add extra planes for testing if the sphere is outside. However, for the purposes of quickly culling out scene-graph nodes, occasional false hits simply cause unnecessary testing, not algorithm failure, and this additional testing will cost more time overall.

Most frustums are symmetric around the view direction, meaning that the left plane is the right plane reflected around the view direction. This also holds for the bottom and top planes. To reduce the number of planes that must be tested for a symmetric frustum, an *octant test* can be added to the previous view frustum test [48]. For this test, the frustum is divided into eight octants, much as an octree is subdivided (see Figure 16.25). When that has been done, we need to test against only the three outer planes of the octant that the sphere center is in. This means that we can actually halve the number of planes that need to be tested. While it was found that this test did not improve the performance of a frustum/sphere test, since the sphere/plane test is already so fast, it could be extended and used for arbitrary objects (see the right side of Figure 16.25). As will be seen in the next sections, this test can be used to speed up the frustum tests for AABBs and OBBs.

---

<sup>16</sup>More correctly, we say that the sphere intersects the frustum, but the sphere center may be located in the rounded corners shown in Figure 16.24. This would mean that the sphere is outside the frustum but we report it to be intersecting. Still, this is conservatively correct.

Bishop et al. [89] discuss the following clever optimization for using sphere culling in a game engine. This useful technique can apply to any hierarchical frustum culling scheme, regardless of BV type. If a BV is found to be fully inside a certain frustum plane, then its children are also inside this plane. This means that this plane test can be omitted for all children, which can result in faster overall testing.

### 16.14.3 Frustum/Box Intersection

If the view's projection is orthographic (i.e., the frustum has a box shape), precise testing can be done using OBB/OBB intersection testing (see Section 16.13.5). For general frustum/box intersection testing there is a simple exclusion/inclusion/intersection test that is inexact but conservative. This test is similar to the frustum/sphere test in that the OBB or AABB bounding box is checked against the six view frustum planes. If all corner points of the bounding box are outside of one such plane, the bounding box is guaranteed to be outside the frustum. However, instead of checking all corner points (in the worst case) with each plane equation, we can use the smarter test presented in Section 16.10.

The algorithm tests the box against each of the six frustum planes in turn. If the box is outside one such plane, the box is outside the frustum and the test is terminated. If the box is inside all six planes, then the box is inside the frustum, else it is considered as intersecting the frustum (even though it might actually be slightly outside—see below). Pseudocode for this is shown below, where  $\pi^i$ ,  $i = 0 \dots 5$ , are the six frustum planes and  $B$  is the AABB. As can be seen, the core of this algorithm is the plane/box test from Section 16.10.

```

FrustumAABBIntersect( $\pi^0, \dots, \pi^5, B$ )
  returns({OUTSIDE, INSIDE, INTERSECTING});
1 :  intersecting = false;
2 :  for  $k = 0$  to 5
3 :    result = PlaneAABBIntersect( $B, \pi_k$ )
4 :    if(result == OUTSIDE) return OUTSIDE;
5 :    elseif(result == INTERSECTING) intersecting = true;
6 :    if(intersecting == true) return INTERSECTING;
7 :  else return INSIDE;

```

Similar to the frustum/sphere algorithm, this test suffers from classifying boxes as intersecting that are actually fully outside. Those kinds of errors are shown in Figure 16.26. An exclusion/inclusion approach that does not have this problem is to use the separating axis test (found in Section 16.13) to derive an intersection routine.

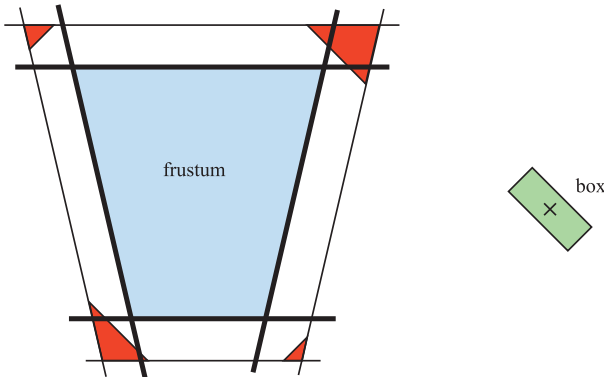


**Figure 16.26.** The bold black lines are the planes of the frustum. When testing the box (left) against the frustum using the presented algorithm, the box can be incorrectly classified as intersecting when it is outside. For the situation in the figure, this happens when the box’s center is located in the red areas.

Since the plane/box test is more expensive than the plane/sphere test, there is often a gain in using the octant test from Section 16.14.2. This test would immediately discard three of the six frustum planes [48]. Alternately, the dot product computations for the near and far planes can be shared, since these planes are parallel. The techniques discussed in the previous section from Bishop [89] for optimizing testing and clipping of bounding spheres apply here as well.

## 16.15 Shaft/Box and Shaft/Sphere Intersection

Sometimes it is important to find what is in between two AABBs. This operation can be useful for occlusion culling, for dynamic intersection testing (see Section 16.18), or for light transport algorithms such as radiosity. The volume between two AABBs, including the AABBs themselves, is called a *shaft*, and the intersection operation is called *shaft culling*. See Figure 16.27.

A shaft is actually defined by a single large AABB and set of  $n$  planes. Each plane trims off some amount of volume from this AABB, and the volume inside the AABB and all the planes is the shaft. In fact, the shaft’s AABB can be thought of as a set of six planes, thereby defining the shaft as purely a set of  $n + 6$  planes. That said, it is important that six of the planes that make a shaft be axis-aligned, as this property ensures that no false hits are generated when testing against another AABB.

The shaft is defined by two initial AABBs, e.g., the bounding boxes for the two objects forming the shaft. The shaft’s AABB is simply the

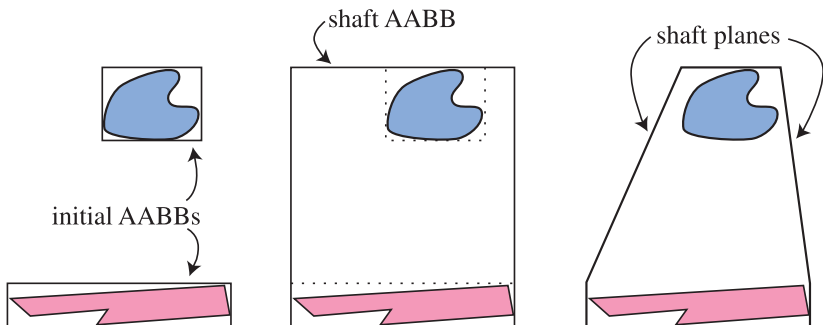


**Figure 16.27.** Two initial AABBs define a shaft. First, the shaft’s AABB is formed to enclose these two AABBs. Then, planes are added to the shaft’s definition to chop off volumes of space that are not between the initial AABBs.

minimal AABB surrounding these two initial AABBs. The next task is computing the set of planes connecting the two initial AABBs. Each plane is associated with, and parallel to, one of the twelve edges of the shaft’s AABB. Each plane generated attaches one of the twelve edges of one of the initial AABBs to the corresponding edge of the other initial AABB.

To determine which edges form planes for the shaft, first, for each of the six faces of the shaft’s AABB, find which of the two initial AABBs it touches. Now examine each edge of the shaft’s AABB: If the two faces bordering this edge touch different initial AABBs, then a plane joining the corresponding edges of these initial AABBs is formed and added to the shaft definition.<sup>17</sup> Up to eight different planes can be added to the shaft in this way (there are twelve shaft AABB edges, but not all edges will form planes). At this point, shaft formation is done. As an example, in Figure 16.27, the upper initial AABB touches the top of the shaft’s AABB, and the lower initial AABB touches the other sides. Planes are generated for only the upper corners’ edges, since these edges adjoin shaft AABB faces that touch different initial AABBs.

To test a shaft against another AABB or a sphere, first the shaft’s AABB and then each plane in turn is tested against the primitive. If the primitive is fully outside the AABB or any plane, then testing is done and the shaft does not intersect the primitive. If the primitive is fully inside all planes, then the primitive is inside the shaft. Otherwise, the primitive overlaps the shaft. Testing against a shaft, then, is simply a series

<sup>17</sup> Another way to think of this process is to imagine the shaft’s AABB. If the first initial AABB touches a face of the shaft’s AABB, paint the shaft AABB’s face red, else paint it blue (because it must be touched by the other initial AABB). Any edge touching a red and a blue face is one for which a shaft plane is formed, which will chop this edge off the shaft’s AABB.

of plane/AABB (Section 16.10) or plane/sphere (Section 16.14.2) tests. While it is possible for false hits to be generated when doing shaft/sphere testing, shaft/box testing is exact.

Haines and Wallace discuss optimizations for shaft formation and culling, and code is available on the web [483, 486].

## 16.16 Line/Line Intersection Tests

In this section, both two- and three-dimensional line/line intersection tests will be derived and examined. Lines, rays, and line segments will be intersected, and methods that are both fast and elegant will be described.

### 16.16.1 Two Dimensions

#### *First Method*

From a theoretical viewpoint, this first method of computing the intersection between a pair of two-dimensional lines is truly beautiful. Consider two lines,  $\mathbf{r}_1(s) = \mathbf{o}_1 + s\mathbf{d}_1$  and  $\mathbf{r}_2(t) = \mathbf{o}_2 + t\mathbf{d}_2$ . Since  $\mathbf{a} \cdot \mathbf{a}^\perp = 0$  (the perp dot product [551] from Section 1.2.1), the intersection calculations between  $\mathbf{r}_1(s)$  and  $\mathbf{r}_2(t)$  become elegant and simple. Note that all vectors are two dimensional in this subsection:

$$\begin{aligned}
 1 : \quad & \mathbf{r}_1(s) = \mathbf{r}_2(t) \\
 & \iff \\
 2 : \quad & \mathbf{o}_1 + s\mathbf{d}_1 = \mathbf{o}_2 + t\mathbf{d}_2 \\
 & \iff \\
 3 : \quad & \begin{cases} s\mathbf{d}_1 \cdot \mathbf{d}_2^\perp = (\mathbf{o}_2 - \mathbf{o}_1) \cdot \mathbf{d}_2^\perp \\ t\mathbf{d}_2 \cdot \mathbf{d}_1^\perp = (\mathbf{o}_1 - \mathbf{o}_2) \cdot \mathbf{d}_1^\perp \end{cases} \\
 & \iff \\
 4 : \quad & \begin{cases} s = \frac{(\mathbf{o}_2 - \mathbf{o}_1) \cdot \mathbf{d}_2^\perp}{\mathbf{d}_1 \cdot \mathbf{d}_2^\perp} \\ t = \frac{(\mathbf{o}_1 - \mathbf{o}_2) \cdot \mathbf{d}_1^\perp}{\mathbf{d}_2 \cdot \mathbf{d}_1^\perp} \end{cases} \tag{16.55}
 \end{aligned}$$

If  $\mathbf{d}_1 \cdot \mathbf{d}_2^\perp = 0$ , then the lines are parallel and no intersection occurs. For lines of infinite length, all values of  $s$  and  $t$  are valid, but for line segments (with normalized directions), say of length  $l_1$  and  $l_2$  (starting at  $s = 0$  and  $t = 0$  and ending at  $s = l_1$  and  $t = l_2$ ), we have a valid intersection if and only if  $0 \leq s \leq l_1$  and  $0 \leq t \leq l_2$ . Or, if you set  $\mathbf{o}_1 = \mathbf{p}_1$  and  $\mathbf{d}_1 = \mathbf{p}_2 - \mathbf{p}_1$  (meaning that the line segment starts at  $\mathbf{p}_1$  and ends at  $\mathbf{p}_2$ ) and do likewise for  $\mathbf{r}_2$  with startpoints and endpoints  $\mathbf{q}_1$  and  $\mathbf{q}_2$ , then a valid intersection occurs if and only if  $0 \leq s \leq 1$  and  $0 \leq t \leq 1$ . For rays with origins, the

valid range is  $s \geq 0$  and  $t \geq 0$ . The point of intersection is obtained either by plugging  $s$  into  $\mathbf{r}_1$  or by plugging  $t$  into  $\mathbf{r}_2$ .

### Second Method

Antonio [29] describes another way of deciding whether two line segments (i.e., of finite length) intersect by doing more compares and early rejections and by avoiding the expensive calculations (divisions) in the previous formulae. This method is therefore faster. The previous notation is used again, i.e., the first line segment goes from  $\mathbf{p}_1$  to  $\mathbf{p}_2$  and the second from  $\mathbf{q}_1$  to  $\mathbf{q}_2$ . This means  $\mathbf{r}_1(s) = \mathbf{p}_1 + s(\mathbf{p}_2 - \mathbf{p}_1)$  and  $\mathbf{r}_2(t) = \mathbf{q}_1 + t(\mathbf{q}_2 - \mathbf{q}_1)$ . The result from Equation 16.55 is used to obtain a solution to  $\mathbf{r}_1(s) = \mathbf{r}_2(t)$ :

$$\left\{ \begin{array}{l} s = \frac{-\mathbf{c} \cdot \mathbf{a}^\perp}{\mathbf{b} \cdot \mathbf{a}^\perp} = \frac{\mathbf{c} \cdot \mathbf{a}^\perp}{\mathbf{a} \cdot \mathbf{b}^\perp} = \frac{d}{f}, \\ t = \frac{\mathbf{c} \cdot \mathbf{b}^\perp}{\mathbf{a} \cdot \mathbf{b}^\perp} = \frac{e}{f}. \end{array} \right. \quad (16.56)$$

In Equation 16.56,  $\mathbf{a} = \mathbf{q}_2 - \mathbf{q}_1$ ,  $\mathbf{b} = \mathbf{p}_2 - \mathbf{p}_1$ ,  $\mathbf{c} = \mathbf{p}_1 - \mathbf{q}_1$ ,  $d = \mathbf{c} \cdot \mathbf{a}^\perp$ ,  $e = \mathbf{c} \cdot \mathbf{b}^\perp$ , and  $f = \mathbf{a} \cdot \mathbf{b}^\perp$ . The simplification step for the factor  $s$  comes from the fact that  $\mathbf{a}^\perp \cdot \mathbf{b} = -\mathbf{b}^\perp \cdot \mathbf{a}$  and  $\mathbf{a} \cdot \mathbf{b}^\perp = \mathbf{b}^\perp \cdot \mathbf{a}$ . If  $\mathbf{a} \cdot \mathbf{b}^\perp = 0$ , then the lines are collinear. Antonio [29] observes that the denominators for both  $s$  and  $t$  are the same, and that, since  $s$  and  $t$  are not needed explicitly, the division operation can be omitted. Define  $s = d/f$  and  $t = e/f$ . To test if  $0 \leq s \leq 1$  the following code is used:

```

1 : if(f > 0)
2 :   if(d < 0 or d > f) return NO_INTERSECTION;
3 : else
4 :   if(d > 0 or d < f) return NO_INTERSECTION;
```

After this test, it is guaranteed that  $0 \leq s \leq 1$ . The same is then done for  $t = e/f$  (by replacing  $d$  by  $e$  in the code). If the routine has not returned after this test, the line segments do intersect, since the  $t$ -value is then also valid.

Source code for an integer version of this routine is available on the web [29], and is easily converted for use with floating point numbers.

## 16.16.2 Three Dimensions

Say we want to compute in three dimensions the intersection between two lines (defined by rays, Equation 16.1). The lines are again called  $\mathbf{r}_1(s) = \mathbf{o}_1 + s\mathbf{d}_1$  and  $\mathbf{r}_2(t) = \mathbf{o}_2 + t\mathbf{d}_2$ , with no limitation on the value of  $t$ . The three-dimensional counterpart of the perp dot product is, in this case, the

cross product, since  $\mathbf{a} \times \mathbf{a} = 0$ , and therefore the derivation of the three-dimensional version is very similar to that of the two-dimensional version. The intersection between two lines is derived below:

$$\begin{aligned}
 1 : \quad & \mathbf{r}_1(s) = \mathbf{r}_2(t) \\
 & \iff \\
 2 : \quad & \mathbf{o}_1 + s\mathbf{d}_1 = \mathbf{o}_2 + t\mathbf{d}_2 \\
 & \iff \\
 3 : \quad & \begin{cases} s\mathbf{d}_1 \times \mathbf{d}_2 = (\mathbf{o}_2 - \mathbf{o}_1) \times \mathbf{d}_2 \\ t\mathbf{d}_2 \times \mathbf{d}_1 = (\mathbf{o}_1 - \mathbf{o}_2) \times \mathbf{d}_1 \end{cases} \\
 & \iff \\
 4 : \quad & \begin{cases} s(\mathbf{d}_1 \times \mathbf{d}_2) \cdot (\mathbf{d}_1 \times \mathbf{d}_2) = ((\mathbf{o}_2 - \mathbf{o}_1) \times \mathbf{d}_2) \cdot (\mathbf{d}_1 \times \mathbf{d}_2) \\ t(\mathbf{d}_2 \times \mathbf{d}_1) \cdot (\mathbf{d}_2 \times \mathbf{d}_1) = ((\mathbf{o}_1 - \mathbf{o}_2) \times \mathbf{d}_1) \cdot (\mathbf{d}_2 \times \mathbf{d}_1) \end{cases} \quad (16.58) \\
 & \iff \\
 5 : \quad & \begin{cases} s = \frac{\det(\mathbf{o}_2 - \mathbf{o}_1, \mathbf{d}_2, \mathbf{d}_1 \times \mathbf{d}_2)}{\|\mathbf{d}_1 \times \mathbf{d}_2\|^2} \\ t = \frac{\det(\mathbf{o}_2 - \mathbf{o}_1, \mathbf{d}_1, \mathbf{d}_1 \times \mathbf{d}_2)}{\|\mathbf{d}_1 \times \mathbf{d}_2\|^2} \end{cases}
 \end{aligned}$$

Step 3 comes from subtracting  $\mathbf{o}_1$  ( $\mathbf{o}_2$ ) from both sides and then cross-ing with  $\mathbf{d}_2$  ( $\mathbf{d}_1$ ), and Step 4 is obtained by dotting with  $\mathbf{d}_1 \times \mathbf{d}_2$  ( $\mathbf{d}_2 \times \mathbf{d}_1$ ). Finally, Step 5, the solution, is found by rewriting the right sides as de-terminants (and changing some signs in the bottom equation) and then by dividing by the term located to the right of  $s$  ( $t$ ).

Goldman [411] notes that if the denominator  $\|\mathbf{d}_1 \times \mathbf{d}_2\|^2$  equals 0, then the lines are parallel. He also observes that if the lines are skew (i.e., they do not share a common plane), then the  $s$  and  $t$  parameters represent the points of closest approach.

If the lines are to be treated like line segments, with lengths  $l_1$  and  $l_2$  (assuming the direction vectors  $\mathbf{d}_1$  and  $\mathbf{d}_2$  are normalized), then check whether  $0 \leq s \leq l_1$  and  $0 \leq t \leq l_2$  both hold. If not, then the intersection is rejected.

Rhodes [1064] gives an in-depth solution to the problem of intersecting two lines or line segments. He gives robust solutions that deal with special cases, and he discusses optimizations and provides source code.

## 16.17 Intersection Between Three Planes

Given three planes, each described by a normalized normal vector,  $\mathbf{n}_i$ , and an arbitrary point on the plane,  $\mathbf{p}_i$ ,  $i = 1, 2$ , and  $3$ , the unique point,  $\mathbf{p}$ , of intersection between those planes is given by Equation 16.59 [410]. Note

that the denominator, the determinant of the three plane normals, is zero if two or more planes are parallel:

$$\mathbf{p} = \frac{(\mathbf{p}_1 \cdot \mathbf{n}_1)(\mathbf{n}_2 \times \mathbf{n}_3) + (\mathbf{p}_2 \cdot \mathbf{n}_2)(\mathbf{n}_3 \times \mathbf{n}_1) + (\mathbf{p}_3 \cdot \mathbf{n}_3)(\mathbf{n}_1 \times \mathbf{n}_2)}{|\mathbf{n}_1 \mathbf{n}_2 \mathbf{n}_3|}. \quad (16.59)$$

This formula can be used to compute the corners of a BV consisting of a set of planes. An example is a  $k$ -DOP, which consists of  $k$  plane equations. Equation 16.59 can calculate the corners of the polytope if it is fed with the right planes.

If, as is usual, the planes are given in implicit form, i.e.,  $\pi_i : \mathbf{n}_i \cdot \mathbf{x} + d_i = 0$ , then we need to find the points  $\mathbf{p}_i$  in order to be able to use the equation. Any arbitrary point on the plane can be chosen. We compute the point closest to the origin, since those calculations are inexpensive. Given a ray from the origin pointing along the plane's normal, intersect this with the plane to get the point closest to the origin:

$$\begin{aligned} \mathbf{r}_i(t) &= t\mathbf{n}_i \\ \mathbf{n}_i \cdot \mathbf{x} + d_i &= 0 \end{aligned} \quad \left. \right\} \Rightarrow$$

$$\begin{aligned} \mathbf{n}_i \cdot \mathbf{r}_i(t) + d_i &= 0 \\ \iff t\mathbf{n}_i \cdot \mathbf{n}_i + d_i &= 0 \\ \iff t &= -d_i \\ \Rightarrow \mathbf{p}_i &= \mathbf{r}_i(-d_i) = -d_i \mathbf{n}_i. \end{aligned} \quad (16.60)$$

This result should not come as a surprise, since  $d_i$  in the plane equation simply holds the perpendicular, negative distance from the origin to the plane (the normal must be of unit length if this is to be true).

## 16.18 Dynamic Intersection Testing

Up until now, only *static* intersection testing has been considered. This means that all objects involved are not moving during testing. However, this is not always a realistic scenario, especially since we render frames at discrete times. For example, discrete testing means that a ball that is on one side of a closed door at time  $t$  might move to the other side at  $t + \Delta t$  (i.e., the next frame), without any collision being noticed by a static intersection test. One solution is to make several tests uniformly spaced between  $t$  and  $t + \Delta t$ . This would increase the computational load, and still the intersection could be missed. A *dynamic* intersection test is designed

to cope with this problem. This section provides an introduction to the topic. More information can be found in Ericson's [315] and Eberly's [294] books.

Methods such as shaft culling (Section 16.15) can be used to aid in intersection testing of moving AABBs. The object moving through space is represented by two AABBs at different times, and these two AABBs are joined by a shaft. However, intersection algorithms usually become simpler and faster if the moving object is contained in a bounding sphere. In fact, it is often worthwhile to use a set of a few spheres to tightly bound and represent the moving object [1137].

One principle that can be applied to dynamic intersection testing situations where only translations (not rotations) take place is the fact that motion is relative. Assume object  $A$  moves with velocity  $\mathbf{v}_A$  and object  $B$  with velocity  $\mathbf{v}_B$ , where the velocity is the amount an object has moved during the frame. To simplify calculations, we instead assume that  $A$  is moving and  $B$  is still. To compensate for  $B$ 's velocity,  $A$ 's velocity is then:  $\mathbf{v} = \mathbf{v}_A - \mathbf{v}_B$ . As such, only one object is given a velocity in the algorithms that follow.

### 16.18.1 Sphere/Plane

Testing a sphere dynamically against a plane is simple. Assume the sphere has its center at  $\mathbf{c}$  and a radius  $r$ . In contrast to the static test, the sphere also has a velocity  $\mathbf{v}$  during the entire frame time  $\Delta t$ . So, in the next frame, the sphere will be located at  $\mathbf{e} = \mathbf{c} + \Delta t \mathbf{v}$ . For simplicity, assume  $\Delta t$  is 1 and that this frame starts at time 0. The question is: Has the sphere collided with a plane  $\pi : \mathbf{n} \cdot \mathbf{x} + d = 0$  during this time?

The signed distance,  $s_c$ , from the sphere's center to the plane is obtained by plugging the sphere center into the plane equation. Subtracting the sphere radius from this distance gives how far (along the plane normal) the sphere can move before reaching the plane. This is illustrated in Figure 16.28. A similar distance,  $s_e$ , is computed for the endpoint  $\mathbf{e}$ . Now, if the sphere centers are on the same side of the plane (tested as  $s_c s_e > 0$ ), and if  $|s_c| > r$  and  $|s_e| > r$ , then an intersection cannot occur, and the sphere can safely be moved to  $\mathbf{e}$ . Otherwise, the sphere position and the exact time when the intersection occurs is obtained as follows [420]. The time when the sphere first touches the plane is  $t$ , where  $t$  is computed as

$$t = \frac{s_c - r}{s_c - s_e}. \quad (16.61)$$

The sphere center is then located at  $\mathbf{c} + t\mathbf{v}$ . A simple collision response at this point would be to reflect the velocity vector  $\mathbf{v}$  around the plane normal, and move the sphere using this vector:  $(1 - t)\mathbf{r}$ , where  $1 - t$  is the

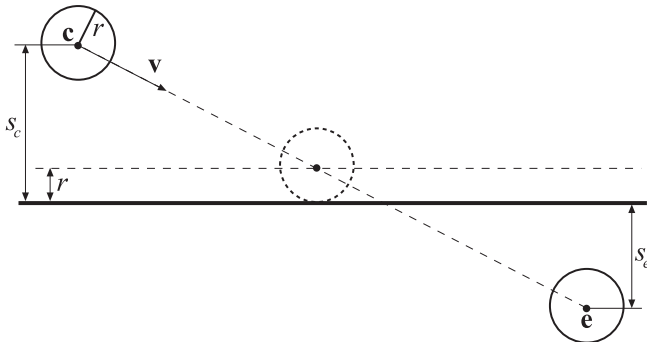


**Figure 16.28.** The notation used in the dynamic sphere/plane intersection test. The middle sphere shows the position of the sphere at the time when collision occurs. Note that  $s_c$  and  $s_e$  are both signed distances.

remaining time to the next frame from the collision, and  $\mathbf{r}$  is the reflection vector.

## 16.18.2 Sphere/Sphere

Testing two moving spheres  $A$  and  $B$  for intersection turns out to be equivalent to testing a ray against a static sphere—a surprising result. This equivalency is shown by performing two steps. First, use the principle of relative motion to make sphere  $B$  become static. Then, a technique is borrowed from the frustum/sphere intersection test (Section 16.14.2). In that test, the sphere was moved along the surface of the frustum to create a larger frustum. By extending the frustum outwards by the radius of the sphere, the sphere itself could be shrunk to a point. Here, moving one sphere over the surface of another sphere results in a new sphere that is the sum of the radii of the two original spheres.<sup>18</sup> So, the radius of sphere  $A$  is added to the radius of  $B$  to give  $B$  a new radius. Now we have the situation where sphere  $B$  is static and is larger, and sphere  $A$  is a point moving along a straight line, i.e., a ray. See Figure 16.29.

As this basic intersection test was already presented in Section 16.6, we will simply present the final result:

$$(\mathbf{v}_{AB} \cdot \mathbf{v}_{AB})t^2 + 2(\mathbf{l} \cdot \mathbf{v}_{AB})t + \mathbf{l} \cdot \mathbf{l} - (r_A + r_B)^2 = 0. \quad (16.62)$$

In this equation,  $\mathbf{v}_{AB} = \mathbf{v}_A - \mathbf{v}_B$ , and  $\mathbf{l} = \mathbf{c}_A - \mathbf{c}_B$ , where  $\mathbf{c}_A$  and  $\mathbf{c}_B$  are the centers of the spheres.

---

<sup>18</sup>This discussion assumes that the spheres do not overlap to start; the intersections computed by the algorithm here computes where the outsides of the two spheres first touch.

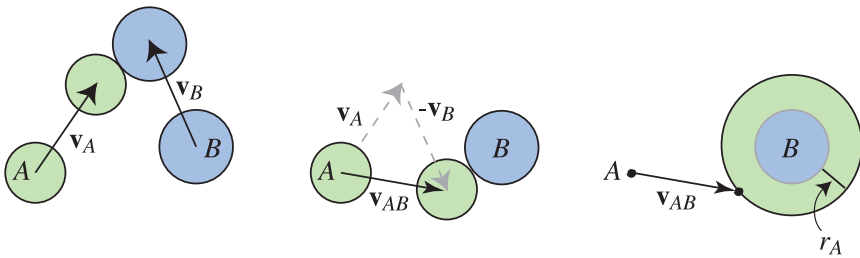


**Figure 16.29.** The left figure shows two spheres moving and colliding. In the center figure, sphere  $B$  has been made static by subtracting its velocity from both spheres. Note that the relative positions of the spheres at the collision point remains the same. On the right, the radius  $r_A$  of sphere  $A$  is added to  $B$  and subtracted from itself, making the moving sphere  $A$  into a ray.

This gives  $a$ ,  $b$ , and  $c$ :

$$\begin{aligned} a &= (\mathbf{v}_{AB} \cdot \mathbf{v}_{AB}), \\ b &= 2(\mathbf{l} \cdot \mathbf{v}_{AB}), \\ c &= \mathbf{l} \cdot \mathbf{l} - (r_A + r_B)^2, \end{aligned} \quad (16.63)$$

which are values used in the quadratic equation

$$at^2 + bt + c = 0. \quad (16.64)$$

The two roots are computed by first computing

$$q = -\frac{1}{2}(b + \text{sign}(b)\sqrt{b^2 - 4ac}). \quad (16.65)$$

Here,  $\text{sign}(b)$  is  $+1$  when  $b \geq 0$ , else  $-1$ . Then the two roots are

$$\begin{aligned} t_0 &= \frac{q}{a}, \\ t_1 &= \frac{c}{q}. \end{aligned} \quad (16.66)$$

This form of solving the quadratic is not what is normally presented in textbooks, but Press et al. note that it is more numerically stable [1034].

The smallest value in the range  $[t_0, t_1]$  that lies within  $[0, 1]$  (the time of the frame) is the time of first intersection. Plugging this  $t$ -value into

$$\begin{aligned} \mathbf{p}_A(t) &= \mathbf{c}_A + t\mathbf{v}_A, \\ \mathbf{p}_B(t) &= \mathbf{c}_B + t\mathbf{v}_B \end{aligned} \quad (16.67)$$

yields the location of each sphere at the time of first contact. The main difference of this test and the ray/sphere test presented earlier is that the ray direction  $\mathbf{v}_{AB}$  is not normalized here.

### 16.18.3 Sphere/Polygon

Dynamic sphere/plane intersection was simple enough to visualize directly. That said, sphere/plane intersection can be converted to another form in a similar fashion as done with sphere/sphere intersection. That is, the moving sphere can be shrunk to a moving point, so forming a ray, and the plane expanded to a slab the thickness of the sphere's diameter. The key idea used in both tests is that of computing what is called the *Minkowski sum* of the two objects. The Minkowski sum of a sphere and a sphere is a larger sphere equal to the radius of both. The sum of a sphere and a plane is a plane thickened in each direction by the sphere's radius. Any two volumes can be added together in this fashion, though sometimes the result is difficult to describe. For dynamic sphere/polygon testing the idea is to test a ray against the Minkowski sum of the sphere and polygon.

Intersecting a moving sphere with a polygon is somewhat more involved than sphere/plane intersection. Schroeder gives a detailed explanation of this algorithm, and provides code on the web [1137]. We follow his presentation here, making corrections as needed, then show how the Minkowski sum helps explain why the method works.

If the sphere never overlaps the plane, then no further testing is done. The sphere/plane test presented previously finds when the sphere first intersects the plane. This intersection point can then be used in performing a point in polygon test (Section 16.9). If this point is inside the polygon, the sphere first hits the polygon there and testing is done.

However, this hit point can be outside the polygon but the sphere's body can still hit a polygon edge or point while moving further along its path. If a sphere collides with the infinite line formed by the edge, the first point of contact  $\mathbf{p}$  on the sphere will be radius  $r$  away from the center:

$$(\mathbf{c}_t - \mathbf{p}) \cdot (\mathbf{c}_t - \mathbf{p}) = r^2, \quad (16.68)$$

where  $\mathbf{c}_t = \mathbf{c} + t\mathbf{v}$ . The initial position of the sphere is  $\mathbf{c}$ , and its velocity is  $\mathbf{v}$ . Also, the vector from the sphere's center to this point will be perpendicular to the edge:

$$(\mathbf{c}_t - \mathbf{p}) \cdot (\mathbf{p}_1 - \mathbf{p}_0) = 0. \quad (16.69)$$

Here,  $\mathbf{p}_0$  and  $\mathbf{p}_1$  are the vertices of the polygon edge. The hit point's location  $\mathbf{p}$  on the edge's line is defined by the parametric equation

$$\mathbf{p} = \mathbf{p}_0 + d(\mathbf{p}_1 - \mathbf{p}_0), \quad (16.70)$$

where  $d$  is a relative distance from  $\mathbf{p}_0$ , and  $d \in [0, 1]$  for points on the edge.

The variables to compute are the time  $t$  of the first intersection with the edge's line and the distance  $d$  along the edge. The valid intersection

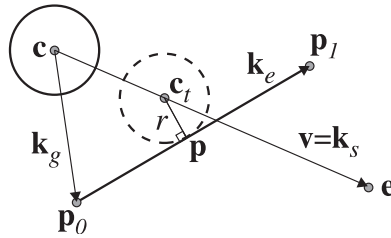


**Figure 16.30.** Notation for the intersection test of a moving sphere and a polygon edge. (After Schroeder [1137].)

range for  $t$  is  $[0, 1]$ , i.e., during this frame's duration. If  $t$  is discovered to be outside this range, the collision does not occur during this frame. The valid range for  $d$  is  $[0, 1]$ , i.e., the hit point must be on the edge itself, not beyond the edge's endpoints. See Figure 16.30.

This set of two equations and two unknowns gives

$$\begin{aligned} a &= k_{ee}k_{ss} - k_{es}^2, \\ b &= 2(k_{eg}k_{es} - k_{ee}k_{gs}), \\ c &= k_{ee}(k_{gg} - r^2) - k_{eg}^2, \end{aligned} \quad (16.71)$$

where

$$\begin{aligned} k_{ee} &= \mathbf{k}_e \cdot \mathbf{k}_e, & k_{eg} &= \mathbf{k}_e \cdot \mathbf{k}_g, \\ k_{es} &= \mathbf{k}_e \cdot \mathbf{k}_s, & k_{gg} &= \mathbf{k}_g \cdot \mathbf{k}_g, \\ k_{gs} &= \mathbf{k}_g \cdot \mathbf{k}_s, & k_{ss} &= \mathbf{k}_s \cdot \mathbf{k}_s, \end{aligned} \quad (16.72)$$

and

$$\begin{aligned} \mathbf{k}_e &= \mathbf{p}_1 - \mathbf{p}_0, \\ \mathbf{k}_g &= \mathbf{p}_0 - \mathbf{c}, \\ \mathbf{k}_s &= \mathbf{e} - \mathbf{c} = \mathbf{v}. \end{aligned} \quad (16.73)$$

Note that  $\mathbf{k}_s = \mathbf{v}$ , the velocity vector for one frame, since  $\mathbf{e}$  is the destination point for the sphere. This gives  $a$ ,  $b$ , and  $c$ , which are the variables of the quadratic equation in Equation 16.64 on page 786, and so solved for  $t_0$  and  $t_1$  in the same fashion.

This test is done for each edge of the polygon, and if the range  $[t_0, t_1]$  overlaps the range  $[0, 1]$ , then the edge's line is intersected by the sphere in this frame at the smallest value in the intersection of these ranges. The sphere's center  $\mathbf{c}_t$  at first intersection time  $t$  is computed and yields a distance

$$d = \frac{(\mathbf{c}_t - \mathbf{p}_0) \cdot \mathbf{k}_e}{k_{ee}}, \quad (16.74)$$

which needs to be in the range  $[0, 1]$ . If  $d$  is not in this range, the edge is considered missed.<sup>19</sup> Using this  $d$  in Equation 16.70 gives the point where the sphere first intersects the edge. Note that if the point of first intersection is needed, then all three edges must be tested against the sphere, as the sphere could hit more than one edge.

The sphere/edge test is computationally complex. One optimization for this test is to put an AABB around the sphere's path for the frame and test the edge as a ray against this box before doing this full test. If the line segment does not overlap the AABB, then the edge cannot intersect the sphere [1137].

If no edge is the first point of intersection for the sphere, further testing is needed. Recall that the sphere is being tested against the *first* point of contact with the polygon. A sphere may eventually hit the interior or an edge of a polygon, but the tests given here check only for first intersection. The third possibility is that the first point of contact is a polygon vertex. So, each vertex in turn is tested against the sphere. Using the concept of relative motion, testing a moving sphere against a static point is exactly equivalent to testing a sphere against a moving point, i.e., a ray. Using the ray/sphere intersection routine in Section 16.6 is then all that is needed. To test the ray  $\mathbf{c}_t = \mathbf{c} + t\mathbf{v}$  against a sphere centered at  $\mathbf{p}_0$  with radius,  $r$ , results can be reused from the previous edge computations to solve  $t$ , as follows:

$$\begin{aligned} a &= k_{ss}, \\ b &= -2k_{gs}, \\ c &= k_{gg} - r^2. \end{aligned} \tag{16.75}$$

Using this form avoids having to normalize the ray direction for ray/sphere intersection. As before, solve the quadratic equation shown in Equation 16.64 and use the lowest valid root to compute when in the frame the sphere first intersects the vertex. The point of intersection is the vertex itself, of course.

In truth, this sphere/polygon test is equivalent to testing a ray (represented by the center of the sphere moving along a line) against the Minkowski sum of the sphere and polygon. This summed surface is one in which the vertices have been turned into spheres of radius  $r$ , the edges into cylinders of radius  $r$ , and the polygon itself raised and lowered by  $r$  to seal off the object. See Figure 16.31 for a visualization of this. This is the same sort of expansion as done for frustum/sphere intersection (Section 16.14.2). So the algorithm presented can be thought of as testing a

---

<sup>19</sup>In fact, the edge could be hit by the sphere, but the hit point computed here would not be where contact is actually made. The sphere will first hit one of the vertex endpoints, and this test follows next.

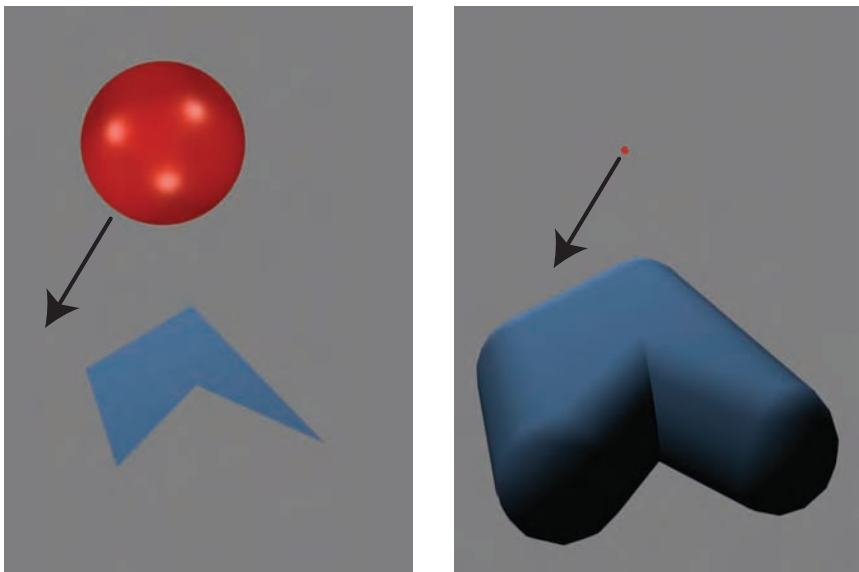


**Figure 16.31.** In the left figure, a sphere moves towards a polygon. In the right figure, a ray shoots at an “inflated” version of the polygon. The two intersection tests are equivalent.

ray against this volume’s parts: First, the polygon facing the ray is tested, then the edge cylinders are tested against the ray, and finally, the vertex spheres are tested.

Thinking about this puffy object gives insight as to why a polygon is most efficiently tested by using the order of area, then edges, then vertices. The polygon in this puffy object that faces the sphere is not covered by the object’s cylinders and spheres, so testing it first will give the closest possible intersection point without further testing. Similarly, the cylinders formed by the edges cover the spheres, but the spheres cover only the insides of the cylinders. Hitting the inside of the cylinder with a ray is equivalent to finding the point where the moving sphere last hits the corresponding edge, a point we do not care about. The closest cylinder exterior intersection (if one exists) will always be closer than the closest sphere intersection. So, finding a closest intersection with a cylinder is sufficient to end testing without needing to check the vertex spheres. It is much easier (at least for us) to think about testing order when dealing with a ray and this puffy object than the original sphere and polygon.

Another insight from this puffy object model is that, for polygons with concavities, a vertex at any concave location does not have to be tested against the moving sphere, as the sphere formed at such a vertex is not

visible from the outside. Efficient dynamic sphere/object intersection tests can be derived by using relative motion and the transformation of a moving sphere into a ray by using Minkowski sums.

### 16.18.4 Dynamic Separating Axis Method

The separating axis test (SAT) on page 731 is very useful in testing convex polyhedrons, e.g., boxes and triangles, against each other. This can be extended quite easily to dynamic queries as well [124, 292, 315, 1131].

Remember that the SAT method tests a set of axes to see whether the projections of the two objects onto these axes overlap. If all projections on all axes overlap, then the objects overlap as well. The key to solving the problem dynamically is to move the projected interval of the moving object with a speed of  $(\mathbf{v} \cdot \mathbf{a})/(\mathbf{a} \cdot \mathbf{a})$  (see Equation A.17) on the axis,  $\mathbf{a}$  [124]. Again, if there is overlap on all tested axes, then the dynamic objects overlap, otherwise they do not. See Figure 16.32 for an illustration of the difference between the stationary SAT and the dynamic SAT.

Eberly [292], using an idea by Ron Levine, also computes the actual time of intersection between  $A$  and  $B$ . This is done by computing times when they just start to overlap,  $t_s$ , and when they stop overlapping (because the intervals have moved “through” each other),  $t_e$ . The hit between  $A$  and  $B$  occurs at the largest of all the  $t_s$ s for all the axes. Likewise, the end of overlapping occurs at the smallest of all the  $t_e$ s. Optimizations include detecting when the intervals are nonoverlapping at  $t = 0$  and also moving apart. Also, if at any time the largest  $t_s$  is greater than the smallest  $t_e$ , then the objects do not overlap, and so the test is terminated. This is similar to the ray/box intersection test in Section 16.7.1. Eberly has code for a wide range of tests between convex polyhedra, including box/box, triangle/box, and triangle/triangle.

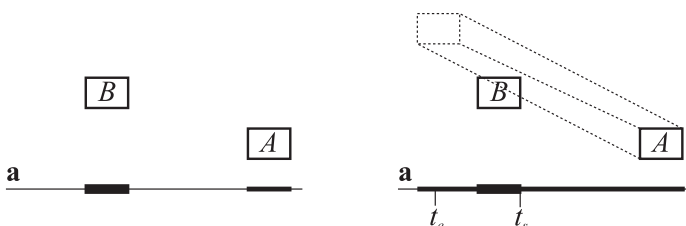


**Figure 16.32.** Left: the stationary SAT illustrated for an axis  $\mathbf{a}$ .  $A$  and  $B$  do not overlap on this axis. Right: the dynamic SAT illustrated.  $A$  moves and the projection of its interval on  $\mathbf{a}$  is tracked during the movement. Here, the two objects overlap on axis  $\mathbf{a}$ .

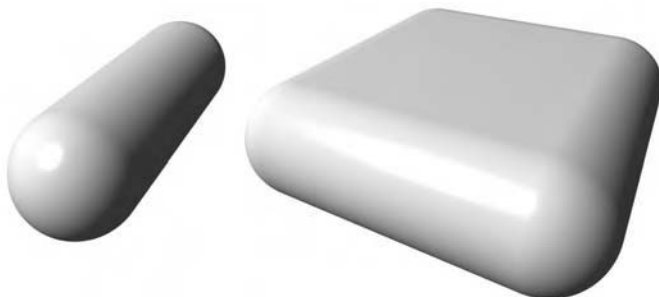


**Figure 16.33.** A *line swept sphere* (LSS) and *rectangle swept sphere* (RSS).

## Further Reading and Resources

Ericson's *Real-Time Collision Detection* [315] and Eberly's *3D Game Engine Design* [294] cover a wide variety of object/object intersection tests, hierarchy traversal methods, and much else, and also include source code. Schneider and Eberly's *Geometric Tools for Computer Graphics* [1131] provides many practical algorithms for two- and three-dimensional geometric intersection testing. *Practical Linear Algebra* [333] is a good source for two-dimensional intersection routines and many other geometric manipulations useful in computer graphics. The *Graphics Gems* series [36, 405, 522, 667, 982] includes many different kinds of intersection routines, and reusable code is available on the web. The free *Maxima* [829] software is good for manipulating equations and deriving formulae. This book's website includes a page, <http://www.realtimerendering.com/int>, summarizing resources available for many object/object intersection tests.

Other bounding volumes of possible interest are *line swept spheres* (LSS) and *rectangle swept spheres* (RSS). These are also called capsules and lozenges, respectively, and are shown in Figure 16.33. For these BVs it is a relatively quick operation to compute the minimum distance. Therefore, they are often used in tolerance verification applications, where one wants to verify that two (or more) objects are at least a certain distance apart. Eberly [294] and Larsen et al. [730] derive formulae and efficient algorithms for these types of bounding volumes.

# Chapter 17

## Collision Detection

*“To knock a thing down, especially if it is cocked at an arrogant angle, is a deep delight to the blood.”*

—George Santayana

*Collision detection* (CD) is a fundamental and important ingredient in many computer graphics applications. Areas where CD plays a vital role include virtual manufacturing, CAD/CAM, computer animation, physically based modeling, games, flight and vehicle simulators, robotics, path and motion planning (tolerance verification), assembly, and almost all virtual reality simulations. Due to its huge number of uses, CD has been and still is a subject of extensive research.

Collision detection is part of what is often referred to as *collision handling*, which can be divided into three major parts: *collision detection*, *collision determination*, and *collision response*. The result of collision detection is a boolean saying whether two or more objects collide, while collision determination finds the actual intersections between objects; finally, collision response determines what actions should be taken in response to the collision of two objects.

In Section 17.1 we discuss simple and extremely fast collision detection techniques. The main idea is to approximate a complex object using a set of lines. These lines are then tested for intersection with the primitives of the environment. This technique is often used in games. Another approximative method is described in Section 17.2, where a BSP tree representation of the environment is used, and a cylinder may be used to describe a character. However, all objects cannot always be approximated with lines or cylinders, and some applications may require more accurate tests.

Imagine, for example, that we want to determine whether a three-dimensional hand collides with (grabs) a three-dimensional cup of tea, where both objects are represented by triangles. How can this be done efficiently? Certainly, each triangle of the hand can be tested for intersection with each triangle of the cup of tea using the triangle/triangle intersection tests from Section 16.11. But in the case where the two objects



**Figure 17.1.** On the left, collision detection and response computed for many barrels colliding against themselves and the environment. On the right, more chaos. (*Image on the left courtesy of Crytek, on the right courtesy of Valve Corp.*)

are far from each other, an algorithm should report this quickly, which would be impossible with such exhaustive testing. Even when the objects are close together, exhaustive testing is not efficient. There is a need for algorithms that handle these cases rapidly. It is easy to think of more complex scenarios for collision detection, and one such example is shown in Figure 17.1.

Section 17.3 deals with a general, hierarchical bounding volume collision detection algorithm. One particular implementation based on OBBs is then presented in Sections 17.4. The following features are characteristics that are desirable for most CD systems.

- They achieve interactive rates with models consisting of a large number of polygons, both when the models are far from each other and when they are in close proximity.
- They handle *polygon soups*, i.e., general polygon models with no restrictions such as convexity or the availability of adjacency information.
- The models can undergo rigid-body motion, i.e., rotation plus translation, or even more general types of deformation.
- They provide efficient *bounding volumes* (BVs), in that they try to create tight fitting volumes for a set of geometry. Small BVs improve the performance of algorithms that determine whether there are collisions between two objects. The creation of the BVs should also be fast.

Since a scenario may contain tens or hundreds of moving objects, a good CD system must be able to cope with such situations as well. If

the scenario contains  $n$  moving objects and  $m$  static objects, then a naive method would perform

$$nm + \binom{n}{2} = nm + n(n - 1)/2 \quad (17.1)$$

object tests for each frame. The first term corresponds to testing the number of static objects against the dynamic (moving) objects, and the last term corresponds to testing the dynamic objects against each other. The naive approach quickly becomes expensive as  $m$  and  $n$  rise. This situation calls for smarter methods, which are the subject of Section 17.5. Such a method typically uses an algorithm that first detects all potential object-to-object collisions, which are then resolved using, for example, the OBBTree algorithm from Section 17.4.

After discussing hierarchical collision detection, brief subsections follow on several miscellaneous topics. *Time-critical collision detection* is a technique for doing approximate collision detection in constant time, and is treated in Section 17.6.1. Sometimes the shortest distance between two objects is desired, and this topic is introduced next, followed by some research on collision detection for deformable objects. Finally, collision response is briefly covered.

It must be pointed out that performance evaluations are extremely difficult in the case of CD, since the algorithms are sensitive to the actual collision scenarios, and there is no algorithm that performs best in all cases [433].

## 17.1 Collision Detection with Rays

In this section, we will present a fast technique that works very well under certain circumstances. Imagine that a car drives upward on an inclined road and that we want to use the information about the road (i.e., the primitives of which the road is built) in order to steer the car upward. This could, of course, be done by testing all primitives of all car wheels against all primitives of the road, using the techniques from Section 17.3. However, for games and some other applications, this kind of detailed collision detection is not always needed. Instead, we can approximate a moving object with a set of *rays*. In the case of the car, we can put one ray at each of the four wheels (see Figure 17.2). This approximation works well in practice, as long as we can assume that the four wheels are the only places of the car that will be in contact with the environment (the road). Assume that the car is standing on a plane at the beginning, and that we place each ray at a wheel so that each origin lies at the place where the wheel is in contact with the environment. The rays at the wheels are then intersection-tested against

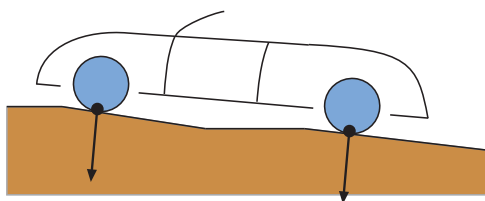


**Figure 17.2.** Instead of computing the collision between the entire car and the environment (the road), we place a ray at each wheel. These rays are then tested for intersection against the environment.

the environment. If the distance from a ray origin to the environment is zero, then that wheel is exactly on the ground. If the distance is greater than zero, then that wheel has no contact with the environment, and a negative distance means that the wheel has penetrated the environment. The application can use these distances for computing a collision response—a negative distance would move the car (at that wheel) upward, while a positive distance would move the car downward (unless the car is flying through the air for a short while). Note that this type of techniques could be harder to adapt to more complicated scenarios. For example, if the car crashes and is set in rotating motion, many more rays in different directions are needed.

To speed up the intersection testing, we can use the same technique we most often use to speed things up in computer graphics—a *hierarchical representation*. The environment can be represented by an axis-aligned BSP tree (which is essentially the same as a  $k$ -d tree). BSP trees are presented in Section 14.1.2, where they were used for view frustum culling algorithms. BSP trees can also be used to speed up intersection testing. Depending on what primitives are used in the environment, different ray-object intersection test methods are needed (see Chapter 16). A BSP tree is not the only representation that can be used to find intersections quickly—e.g., a bounding volume hierarchy is also usable.

Unlike standard ray tracing, where we need the closest object in front of the ray, what is actually desired is the intersection point furthest back along the ray, which can have a negative distance. To avoid having to treat the ray as searching in two directions, the test ray’s origin is essentially moved back until it is outside the bounding box surrounding the environment, and is then tested against the environment. In practice, this just means that, instead of a ray starting at a distance 0, it starts at a negative distance that lets it begin outside the box. To handle a more general setting, such as driving a car through a tunnel and detecting collision against the roof, one would have to search in both directions though.

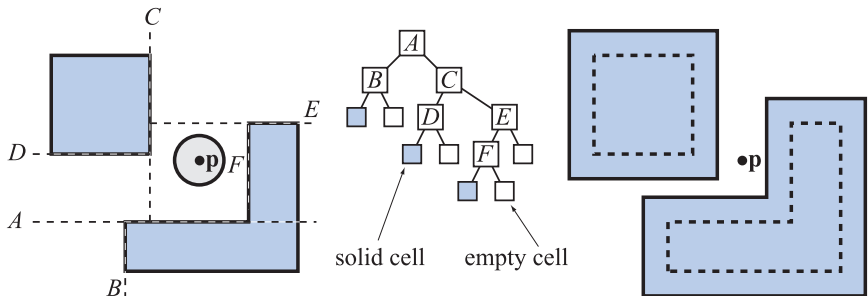


**Figure 17.3.** To the left is some geometry (blue) seen from above. Its BSP tree is shown in the middle. To test this tree against a circle with origin at  $\mathbf{p}$ , the BSP tree is grown outwards with the circle's radius, and then the point  $\mathbf{p}$  can instead be tested against the grown BSP tree. This is shown to the right. Notice that the corners should really be rounded, so this is an approximation that the algorithm introduces.

## 17.2 Dynamic CD using BSP Trees

Here, the collision detection algorithm by Melax [854, 855] will be presented. It determines collisions between the geometry described by a BSP tree (see Section 14.1.2), and a collider that can be either a sphere, a cylinder, or the convex hull of an object. It also allows for dynamic collision detection. For example, if a sphere moves from a position  $\mathbf{p}_0$  at frame  $n$  to  $\mathbf{p}_1$  at frame  $n + 1$ , the algorithm can detect if a collision occurs anywhere along the straight line path from  $\mathbf{p}_0$  to  $\mathbf{p}_1$ . The presented algorithm has been used in commercial games, where a character's geometry was approximated by a cylinder.

The standard BSP tree can be tested against a line segment very efficiently. A line segment can represent a point (particle) that moves from  $\mathbf{p}_0$  to  $\mathbf{p}_1$ . There may be several intersections, but the first one (if any) represents the collision between the point and the geometry represented in the BSP tree. Note that, in this case, the BSP tree is surface aligned, not axis-aligned. That is, each plane in the tree is coincident with a wall, floor, or ceiling in the scene. This is easily extended to handle a sphere, with radius  $r$ , that moves from  $\mathbf{p}_0$  to  $\mathbf{p}_1$  instead of a point. Instead of testing the line segment against the planes in the BSP tree nodes, each plane is moved a distance  $r$  along the plane normal direction (see Section 16.18 for similar ways of recasting intersection tests). This sort of plane adjustment is illustrated in Figure 17.3. This is done for every collision query on the fly, so that one BSP tree can be used for spheres of any size. Assuming a plane is  $\pi : \mathbf{n} \cdot \mathbf{x} + d = 0$ , the adjusted plane is  $\pi' : \mathbf{n} \cdot \mathbf{x} + d \pm r = 0$ , where the sign of  $r$  depends on which side of the plane you continue testing/traversing in search of a collision. Assuming that the character is supposed to be in the

positive half-space of the plane, i.e., where  $\mathbf{n} \cdot \mathbf{x} + d \geq 0$ , we would have to subtract the radius  $r$  from  $d$ . Note then that the negative half-space is considered “solid,” i.e., something that the character cannot step through.

A sphere does not approximate a character in a game very well.<sup>1</sup> The convex hull of the vertices of a character or a cylinder surrounding the character does a better job. In order to use these other bounding volumes,  $d$  in the plane equation has to be adjusted differently. To test a moving convex hull of a set of vertices,  $S$ , against a BSP tree, the scalar value in Equation 17.2 below is added to the  $d$ -value of the plane equation [854]:

$$-\max_{\mathbf{v}_i \in S}(\mathbf{n} \cdot (\mathbf{v}_i - \mathbf{p}_0)). \quad (17.2)$$

The minus sign, again, assumes that characters are in the positive half-space of the planes. The point  $\mathbf{p}_0$  can be any point found suitable to be used as a reference point. For the sphere, the center of the sphere was implicitly chosen. For a character, a point close to the feet may be chosen, or perhaps a point at the navel. Sometimes this choice simplifies equations (as the center of a sphere does). It is this point  $\mathbf{p}_0$  that is tested against the adjusted BSP tree. For a dynamic query, that is, where the character moves from one point to another during one frame, this point  $\mathbf{p}_0$  is used as the starting point of the line segment. Assuming that the character is moved with a vector  $\mathbf{w}$  during one frame, the endpoint of the line segment is  $\mathbf{p}_1 = \mathbf{p}_0 + \mathbf{w}$ .

The cylinder is perhaps even more useful because it is faster to test and still approximates a character in a game fairly well. However, the derivation of the value that adjusts the plane equation is more involved. What we do in general for this algorithm is that we recast the testing of a bounding volume (sphere, convex hull, and cylinder, in this case) against a BSP tree into testing a point,  $\mathbf{p}_0$ , against the adjusted BSP tree. This is basically the same as Minkowski sums (Section 16.18.3 and 17.6.2). Then, to extend this to a moving object, the point  $\mathbf{p}_0$  is replaced by testing with a line segment from  $\mathbf{p}_0$  to the destination point  $\mathbf{p}_1$ .

We derive such a test for a cylinder, whose properties are shown to the top left in Figure 17.4, where the reference point,  $\mathbf{p}_0$ , is at the bottom center of the cylinder. Figure 17.4(b) shows what we want to solve: testing the cylinder against the plane  $\pi$ . In Figure 17.4(c), we move the plane  $\pi$  so that it barely touches the cylinder. The distance,  $e$ , from  $\mathbf{p}_0$  to the moved plane is computed. This distance,  $e$ , is then used in Figure 17.4(d) to move the plane  $\pi$  into its new position  $\pi'$ . Thus, the test has been reduced to testing  $\mathbf{p}_0$  against  $\pi'$ . The  $e$ -value is computed on the fly for each plane each frame. In practice, a vector is first computed from  $\mathbf{p}_0$  to

---

<sup>1</sup>Schroeder notes that a few spheres can work [1137].

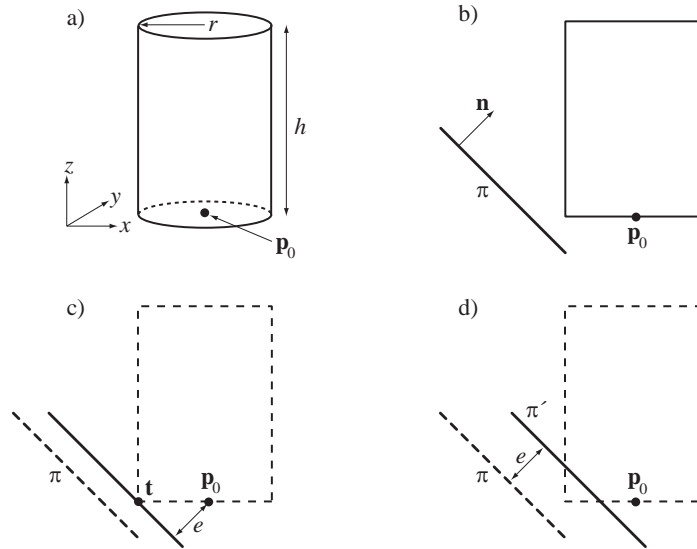


**Figure 17.4.** Figure (a) shows a cylinder with height  $h$ , radius  $r$ , and reference point  $\mathbf{p}_0$ . The sequence (b)-(d) then shows how testing a plane,  $\pi$ , against a cylinder (shown from the side) can be recast into testing a point  $\mathbf{p}_0$  against a new plane  $\pi'$ .

the point  $\mathbf{t}$ , where the moved plane touches the cylinder. This is shown in Figure 17.4(c). Next,  $e$  is computed as

$$e = |\mathbf{n} \cdot (\mathbf{t} - \mathbf{p}_0)|. \quad (17.3)$$

Now all that remains is to compute  $\mathbf{t}$ . The  $z$ -component (i.e., cylinder axis direction) of  $\mathbf{t}$  is simple; if  $n_z > 0$ , then  $t_z = p_{0z}$ , i.e., the  $z$ -component of  $\mathbf{p}_0$ . Else,  $t_z = p_{0z} + h$ . These  $t_z$  values correspond to the bottom and top of the cylinder. If  $n_x$  and  $n_y$  are both zero (e.g., for a floor or ceiling), then we can use any point on the caps of the cylinder. A natural choice is  $(t_x, t_y) = (p_x, p_y)$ , the center of the cylinder cap. Otherwise, for an  $\mathbf{n}$  not vertical, the following choice gives a point on the rim of the cylinder cap:

$$\begin{aligned} t_x &= \frac{-rn_x}{\sqrt{n_x^2 + n_y^2}} + p_x, \\ t_y &= \frac{-rn_y}{\sqrt{n_x^2 + n_y^2}} + p_y. \end{aligned} \quad (17.4)$$

That is, we project the plane normal onto the  $xy$ -plane, normalize it, and then scale by  $r$  to land on the rim of the cylinder.

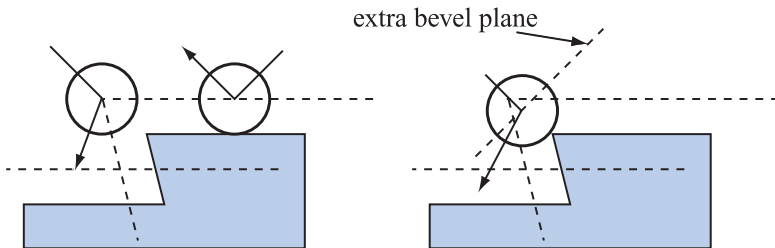


**Figure 17.5.** In the left illustration, the right sphere collides correctly, while the left sphere detects a collision too early. To the right, this is solved by introducing an extra *bevel plane*, which actually does not correspond to any real geometry. As can be seen the collision appears to be more correct using such planes. (*Illustration after Melax [854].*)

Inaccuracies can occur using this method. One case is shown in Figure 17.5. As can be seen, this can be solved by introducing extra *bevel planes*. In practice, the “outer” angle between two neighboring planes are computed, and an extra plane is inserted if the angle is greater than  $90^\circ$ . The idea is to improve the approximation of what should be a rounded corner. In Figure 17.6, the difference between a normal BSP tree and a BSP tree augmented with bevel planes can be seen. The beveling planes certainly improves the accuracy, but it does not remove all errors.

Pseudocode for this collision detection algorithm follows below. It is called with the root  $N$  of the BSP tree, whose children are  $N.\text{negativechild}$  and  $N.\text{positivechild}$ , and the line segment defined by  $\mathbf{p}_0$  and  $\mathbf{p}_1$ . Note that the point of impact (if any) is returned in a global variable called  $\mathbf{p}_{\text{impact}}$ :

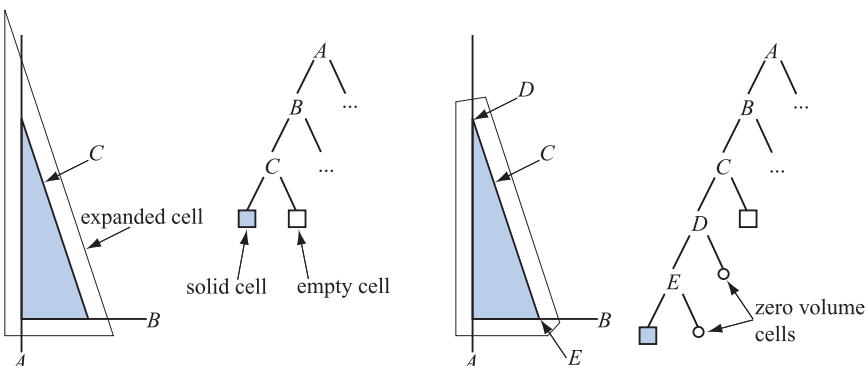


**Figure 17.6.** To the left, a normal cell and its BSP tree is shown. To the right, bevel planes have been added to the cell, and the changes in the BSP tree are shown. (*Illustration after Melax [854].*)

```

HitCheckBSP(N, p0, p1)
  returns ({TRUE, FALSE});
1 :  if(not isSolidCell(N)) return FALSE;
2 :  else if(isSolidCell(N))
3 :    Pimpact = p0
4 :    return TRUE;
5 :  end
6 :  hit = FALSE;
7 :  if(clipLineInside(N shift out, p0, p1, &w0, &w1))
8 :    hit = HitCheckBSP(N.negativechild, w0, w1);
9 :    if(hit) p1 = Pimpact
10:   end
11:  if(clipLineOutside(N shift in, p0, p1, &w0, &w1))
12:    hit |= HitCheckBSP(N.positivechild, w0, w1);
13:  end
14:  return hit;

```

The function `isSolidCell` returns TRUE if we have reached a leaf, and we are on the solid side (as opposed to the empty). See Figure 17.3 for an illustration of empty and solid cells. The function `clipLineInside` returns TRUE if part of the line segment (defined by the movement path  $\mathbf{v}_0$  and  $\mathbf{v}_1$ ) is inside the node's shifted plane, that is, in the negative half-space. It also clips the line against the node's shifted plane, and returns

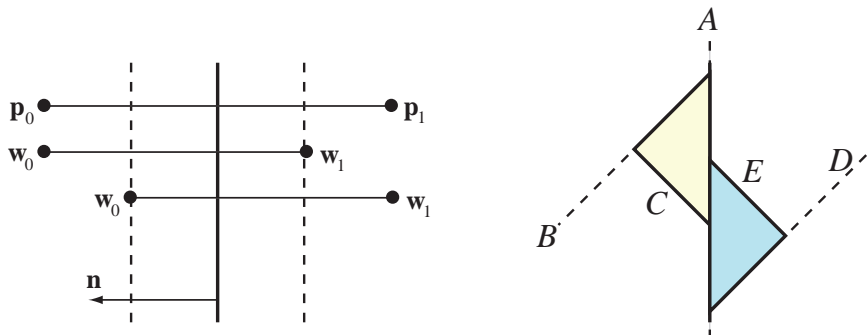


**Figure 17.7.** To the left, the line segment defined by  $\mathbf{p}_0$  and  $\mathbf{p}_1$  is clipped against a plane defined by a normal  $\mathbf{n}$ . The dynamic adjustments of this plane is shown as dashed lines. The functions `clipLineInside` and `clipLineOutside` returns the line segments defined by  $\mathbf{w}_0$  and  $\mathbf{w}_1$ . Note that all three lines should have the same  $y$ -coordinates, but they are shown like this for clarity. To the right, an example is shown that explains why the lines should be clipped as shown to the left. The node  $A$  in the BSP tree belongs to both the triangle on the left and on the right. Therefore, it is necessary to move its plane in both directions.

the resulting line segment in  $\mathbf{w}_0$  and  $\mathbf{w}_1$ . The function `clipLineOutside` is similar. Note also that the line segments returned by `clipLineInside` and `clipLineOutside` overlap each other. The reason for this is shown in Figure 17.7, as well as how the line is clipped. Line 9 sets  $\mathbf{v}_1 = \mathbf{p}_{\text{impact}}$ , and this is simply an optimization. If a hit has been found, and thus a potential impact point,  $\mathbf{p}_{\text{impact}}$ , then nothing beyond this point need to be tested since we want the first point of impact. On Lines 7 and 11,  $N$  is shifted “out” versus “in.” These shifts refer to the adjusted plane equations derived earlier for spheres, convex hulls, and cylinders.

Melax has shown that this algorithm is between 2.5 and 3.5 times more expensive than an algorithm not using dynamically adjusted planes. This is so because there is overhead in computing the proper adjustments, and also the BSP tree gets larger due to the bevel planes. Even though this slowdown may seem serious, Melax points out that it is not so bad in context. A frame typically takes 33,000  $\mu\text{s}$  (giving 30 fps) to compute, and his most expensive collision query takes 66  $\mu\text{s}$ . The advantage of this scheme is that only a single BSP tree is needed to test all characters and objects. The alternative would be to store different BSP trees for each different radius and object type.

## 17.3 General Hierarchical Collision Detection

This section will present some general ideas and methods that are used in collision detection algorithms for detecting collisions between two given models. These algorithms have the four features listed on page 794. Common denominators of these algorithms are:

- They build a representation of each model hierarchically using bounding volumes.
- The high-level code for a collision query is similar, regardless of the kind of BV being used.<sup>2</sup>
- A simple cost function can be used to trim, evaluate, and compare performance.

These points are treated in the following three subsections.

### 17.3.1 Hierarchy Building

Initially, a model is represented by a number of primitives, which in our case are polygon soups, where all polygons with more than three vertices

---

<sup>2</sup>However, BV-BV overlap tests and primitive-primitive overlap tests are different depending on what BVs and primitives are used.

are decomposed into triangles (see Section 12.2). Then, since each model should be represented as a hierarchy of some kind of bounding volumes, methods must be developed that build such hierarchies with the desired properties. A hierarchy that is commonly used in the case of collision detection algorithms is a data structure called a  $k$ -ary tree, where each node may have at most  $k$  children (see Section 14.1). Many algorithms use the simplest instance of the  $k$ -ary tree, namely the binary tree, where  $k = 2$ . At each internal node, there is a BV that encloses all of its children in its volume, and at each leaf are one or more primitives (which in our case are triangles). The bounding volume of an arbitrary node (either an internal node or a leaf),  $A$ , is denoted  $A_{BV}$ , and the set of children belonging to  $A$  is denoted  $A_c$ .

There are three main ways to build a hierarchy: a *bottom-up* method, an *incremental tree-insertion*, or a *top-down* approach. In order to create efficient, tight structures, typically the areas or the volumes of the BVs are minimized wherever possible [63, 417, 672, 966]. For CD, it makes more sense to minimize volume since a BV is tested against another BV. The first of these methods, bottom-up, starts by combining a number of primitives and finding a BV for them. These primitives should be located close together, which can be determined by using the distance between the primitives. Then, either new BVs can be created in the same way, or existing BVs can be grouped with one or more BVs constructed in a similar way, thus yielding a new, larger parent BV. This is repeated until only one BV exists, which then becomes the root of the hierarchy. In this way, closely located primitives are always located near each other in the bounding volume hierarchy. Barequet et al. present BOXTREE [63], a data structure for performing ray tracing and collision detection, where the tree is built from the bottom up.

The incremental tree-insertion method starts with an empty tree. Then all other primitives and their BVs are added one at a time to this tree. This

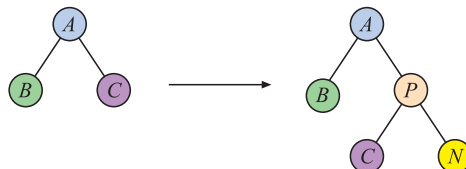


**Figure 17.8.** On the left, a binary tree with three nodes is shown. We assume that only one primitive is stored at each leaf. Now we wish to insert a new node, named  $N$ . This node has a bounding volume (BV) and a primitive that BV encloses. Therefore, the node will be inserted as a leaf node. In this example, say we find that the total tree volume is smaller if we insert  $N$  at the node called  $C$  (rather than at  $B$ ). Then a new parent node  $P$  is created that encloses both  $C$  and the new node  $N$ .

is illustrated in Figure 17.8. To make an efficient tree, an insertion point in the tree must be found. This point should be selected so that the total tree volume increase is minimized. A simple method for doing this is to descend to the child that gives a smaller increase in the tree. This kind of algorithm typically takes  $O(n \log n)$  time. Randomizing the ordering in which primitives are inserted can improve tree formation [417]. For more sophisticated methods, see Omohundro's work [966]. Little is known about incremental tree-insertion in the context of collision detection, but it has been used with good results in ray tracing [417] and in intersection queries [966], so it probably works well for collision detection, too.

The top-down approach, which is used by the majority of hierarchy construction algorithms, starts by finding a BV for all primitives of the model, which then acts as the root of the tree. Then a divide-and-conquer strategy is applied, where the BV is first split into  $k$  or fewer parts. For each such part, all included primitives are found, and then a BV is created in the same manner as for the root, i.e., the hierarchy is created recursively. It is most common to find some axis along which the primitives should be split, and then to find a good split point on this axis. In Section 16.4 geometric probability is discussed, and this can be used when searching for a good split point, which will result in better BVHs. Note that a potential advantage of the top-down approach is that a hierarchy can be created lazily, i.e., on an as-needed basis. This means that we construct the hierarchy only for those parts of the scene where it is actually needed. But since this building process is performed during runtime, whenever a part of the hierarchy is created, the performance may go down significantly. This is not acceptable for applications such as games with real-time requirements, but may be a great time and memory saver for CAD applications or off-line calculations such as path planning, animation, and more.

One challenge for CD algorithms is to find tight-fitting bounding volumes and hierarchy construction methods that create balanced and efficient trees. Note that balanced trees are expected to perform best on average in all cases, since the depth of every leaf is the same (or almost the same). This means that it takes an equal amount of time to traverse the hierarchy down to any leaf (i.e., a primitive), and that the time of a collision query will not vary depending on which leaves are accessed. In this sense, a balanced tree is optimal. However, this does not mean that it is best for all inputs. For example, if part of a model will seldom or never be queried for a collision, then those parts can be located deep in an unbalanced tree, so that the parts that are queried most often are closer to the root [434]. The details of this procedure for an OBB tree is described on page 809.

Note also that several spatial data structures are described in relation to accelerations algorithms in Section 14.1, and that BV creation is treated in Section 16.3.

### 17.3.2 Collision Testing between Hierarchies

Usually there are two different situations that we want to detect at different times. First, we might only be interested in whether or not the two models collide, and then the method may terminate whenever a pair of triangles has been found to overlap. Second, we might want all pairs of overlapping triangles reported. The solution to the first problem is called collision detection, while the solution to the second is called collision determination. Here, pseudocode is given that solves the first problem. The second situation can be solved with small alterations of the given code, and will be discussed later.

$A$  and  $B$  are two nodes in the model hierarchies, which at the first call are the roots of the models.  $A_{BV}$  and  $B_{BV}$  are used to access the BV of the appropriate node. Recall that  $A_c$  is the set of children nodes of  $A$ , and that  $T_A$  is used to denote the triangle of a leaf node (in the pseudocode, only one triangle per node is assumed). The basic idea is, when overlap is detected, to open a (larger) box and recursively test its contents.

```

FindFirstHitCD( $A, B$ )
    returns ({TRUE, FALSE});
1:   if(isLeaf( $A$ ) and isLeaf( $B$ ))
2:     if(overlap( $T_A, T_B$ )) return TRUE;
3:   else if(isNotLeaf( $A$ ) and isNotLeaf( $B$ ))
4:     if(overlap( $A_{BV}, B_{BV}$ ))
5:       if(Volume( $A$ ) > Volume( $B$ ))
6:         for each child  $C \in A_c$ 
7:           FindFirstHitCD( $C, B$ )
8:         else
9:           for each child  $C \in B_c$ 
10:          FindFirstHitCD( $A, C$ )
11:        else if(isLeaf( $A$ ) and isNotLeaf( $B$ ))
12:          if(overlap( $T_A, B_{BV}$ ))
13:            for each child  $C \in B_c$ 
14:              FindFirstHitCD( $C, A$ )
15:            else
16:              if(overlap( $T_B, A_{BV}$ ))
17:                for each child  $C \in A_c$ 
18:                  FindFirstHitCD( $C, B$ )
19:      return FALSE;
```

As can be seen in this pseudocode, there are portions of code that could be shared, but it is presented like this to show how the algorithm works. Some lines deserve some attention. Lines 1–2 take care of the case where both nodes are leaves. Lines 3–10 handle the case where both nodes are in-

ternal nodes. The consequence of the comparison  $\text{Volume}(A) > \text{Volume}(B)$  is that the node with the largest volume is descended. The idea behind such a test is to get the same tree traversal for the calls **FindFirstHitCD**( $A, B$ ) and for **FindFirstHitCD**( $B, A$ ), so that traversal becomes deterministic. This is important if the first collision detected has a special status (early end, collision response, etc.). Perhaps even more important is that this tends to give better performance, as the largest box is traversed first at each step. Another idea is to alternate between descending  $A$  and  $B$ . This avoids the volume computation, and so could be faster. Alternatively, the volume can be precomputed for rigid bodies, but this requires extra memory per node. Also, note for many BVs the actual volume need not be computed, since it suffices with a computation that preserves the “volume order.” As an example, for sphere it suffices to compare the radii.

To find all pairs of triangles that collide, this pseudocode is modified in the following way. The pairs of triangles that the algorithm finds are stored in a global list,  $L$ , which begins empty. Then Line 2 requires modification: If the test is passed, the program should add the triangle pair to  $L$  (instead of returning). When recursion ends, all the collision are found in  $L$ .

### 17.3.3 Cost Function

The function  $t$  in Equation 17.7 below was first introduced (in a slightly different form, without the last term) as a framework for evaluating the performance of hierarchical BV structures in the context of acceleration algorithms for ray tracing [1336]. It has since been used to evaluate the performance of CD algorithms as well [433], and it has been augmented by the last term to include a new cost specific to some systems [672, 699] that might have a significant impact on performance. This cost results from the fact that if a model is undergoing a rigid-body motion, then its BV and parts or all of its hierarchy might have to be recomputed, depending on the motion and the choice of BV:

$$t = n_v c_v + n_p c_p + n_u c_u. \quad (17.7)$$

Here, the parameters are

- $n_v$  : number of BV/BV overlap tests
- $c_v$  : cost for a BV/BV overlap test
- $n_p$  : number of primitive pairs tested for overlap
- $c_p$  : cost for testing whether two primitives overlap
- $n_u$  : number of BVs updated due to the model’s motion
- $c_u$  : cost for updating a BV

Creating a better hierarchical decomposition of a model would result in lower values of  $n_v$ ,  $n_p$ , and  $n_u$ . Creating better methods for determining

whether two BVs or two triangles overlap would lower  $c_v$  and  $c_p$ . However, these are often conflicting goals, because changing the type of BV in order to use a faster overlap test usually means that we get looser-fitting volumes.

Examples of different bounding volumes that have been used in the past are spheres [572], axis-aligned bounding boxes (AABBS) [537, 1290], oriented bounding boxes (OBBs) [433],  $k$ -DOPs (discrete oriented polytopes) [672, 686, 1399], pie slices [63], spherical shells [699, 700] (which provide a good fit for Bézier patches), line swept spheres (LSSs), rectangle swept spheres (RSSs) [730], and QuOSPOs (which combines the advantages of OBBs and  $k$ -DOPs) [514]. Spheres are the fastest to transform, and the overlap test is also fast, but they provide quite a poor fit. AABBS normally provide a better fit and a fast overlap test, and they are a good choice if there is a large amount of axially aligned geometry in a model (as is the case in most architectural models). OBBs have a much better fit, but slower overlap tests. The fit of the  $k$ -DOPs are determined by the parameter  $k$ —higher values of  $k$  give a better fit, slower overlap testing, and poorer transform speed. For more information on  $k$ -DOPTrees, we refer the reader to the work by Klosowski et al. [538, 672, 673].

There are obviously many parameters to fine tune in order to get good performance, and that is the focus of the following section on the OBBTree.

## 17.4 OBBTree

In this section, we will present the OBBTree, first developed by Gottschalk et al. [433], which is a data structure that has influenced the CD field substantially.<sup>3</sup>

The OBBTree was designed to perform especially well if *parallel close proximity*, where two surfaces are very close and nearly parallel, is found during collision detection. These kinds of situations often occur in tolerance analysis and in virtual prototyping.

### *Choice of Bounding Volume*

As the name of the *OBBTree* algorithm implies, the bounding volume used is the oriented bounding box, the OBB. One reason for this choice is that both the AABB (axis-aligned bounding box) and the sphere, which were commonly used in previous CD algorithms, provide quite a poor fit in general. That is, they contain much empty space compared to the geometry they are holding. The convergence of the OBB to the underlying geometry of the models was generally better than that for either AABBs or spheres.

---

<sup>3</sup>In 1981, Ballard [56] did similar work in two dimensions for computing intersections between curves, so his work was a precursor to the OBBTree.

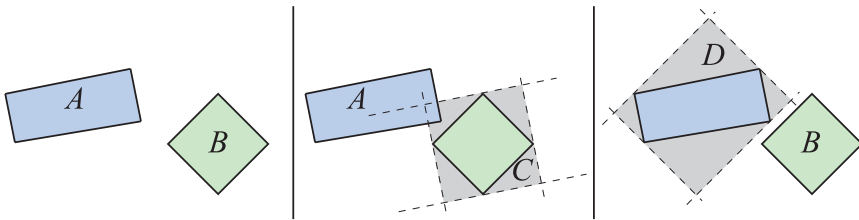


**Figure 17.9.** At the left are two OBBs (*A* and *B*) that are to be tested for overlap with an OBB/OBB overlap test that omits the last nine axis tests. If this is interpreted geometrically, then the OBB/OBB overlap test is approximated with two AABB-AABB overlap tests. The middle illustration shows how *B* is bounded by an AABB in the coordinate system of *A*. *C* and *A* overlap, so the test continues on the right. Here, *A* is enclosed with an AABB in the coordinate system of *B*. *B* and *D* are reported not to overlap. So, testing ends here. However, in three dimensions, *D* and *B* could overlap as well, and still *A* and *B* need not overlap due to the remaining axis tests. In such cases, *A* and *B* would erroneously be reported to overlap.

Another reason is that Gottschalk et al. developed a new method for determining whether two OBBs overlap. This method is about a magnitude faster than previous methods. The speed of this test mainly is because the OBBs are transformed so that one of them becomes an AABB centered around the origin. The actual transform (presented below in Section 17.4) takes 63 operations, and the OBB/OBB test may exit early due to one of the 15 axis tests. After the transformation, an exit after the first axis test takes 17 operations, and an exit after the last axis would take 180 operations.<sup>4</sup> OBB/OBB overlap testing is treated in Section 16.13.5.

In terms of the performance evaluation framework of Section 17.3.3, the preceding reasoning means that  $n_v$  and  $n_p$  are lower for OBBs than for AABBs and spheres.

Van den Bergen has suggested a simple technique for speeding up the overlap test between two OBBs [1290, 1292]: Simply skip the last nine axis tests that correspond to a direction perpendicular to one edge of the first OBB and one edge of the second OBB. This test is often referred to as *SAT lite*. Geometrically, this can be thought of as doing two AABB/AABB tests, where the first test is done in the coordinate system of the first OBB and the other is done in the coordinate system of the other. This is illustrated in Figure 17.9. The shortened OBB/OBB test (which omits the last nine axis tests) will sometimes report two disjoint OBBs as overlapping. In these cases, the recursion in the OBBTree will go deeper than necessary. The reason for using such extensive recursion is that it was found that these last nine axis tests culled away only a small proportion of the overlaps. The net result was that the average performance was improved by skipping

<sup>4</sup>Extra arithmetic error testing would take nine additional operations.

these tests. Van den Bergen's technique has been implemented in a collision detection package called SOLID [1290, 1291, 1292, 1294], which also handles deformable objects.

### Hierarchy Building

The basic data structure is a binary tree with each internal node holding an OBB (see Section 16.2 for a definition) and each external (leaf) node holding only one triangle. The top-down approach developed by Gottschalk et al. for creating the hierarchy is divided into finding a tight-fitting OBB for a polygon soup and then splitting this along one axis of the OBB, which also categorizes the triangles into two groups. For each of these groups, a new OBB is computed. The creation of OBBs is treated in Section 16.3.

After we have computed an OBB for a set of triangles, the volume and the triangles should be split and formed into two new OBBs. Gottschalk et al. use a strategy that takes the longest axis of the box and splits it into two parts of the same length. An illustration of this procedure is shown in Figure 17.10. A plane that contains the center of the box and has the longest box axis for its normal is thus used to partition the triangles into two subgroups. A triangle that crosses this plane is assigned to the group that contains its centroid. If the longest axis cannot be subdivided (in the rare case that all centroids of all triangles are located on the dividing plane or that all centroids are located on the same side of the splitting plane), the other axes are tried in diminishing order.

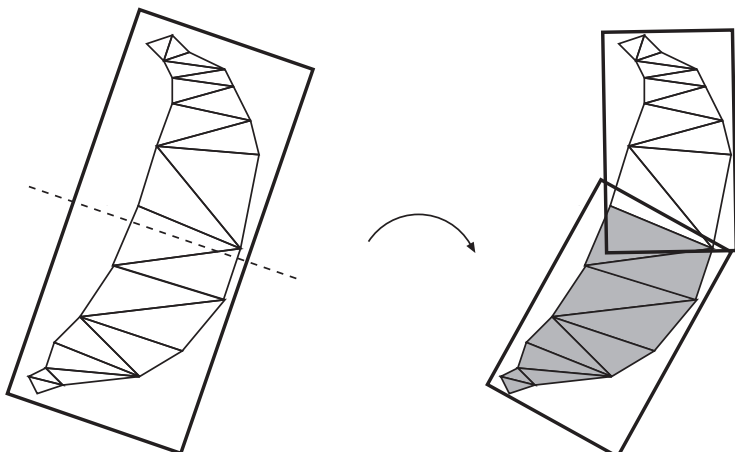


**Figure 17.10.** This figure shows how a set of geometry with its OBB is split along the longest axis of the OBB, at the split point marked by the dashed line. Then the geometry is partitioned into two subgroups, and an OBB is found for each of them. This procedure is repeated recursively in order to build the OBBTree.

For each of the subgroups, the matrix method presented in Section 16.3 is used to compute (sub-) OBBs. If the OBB is instead split at the median center point, then balanced trees are obtained.

Since the computation of the convex hull takes  $O(n \log n)$  and the depth of a binary tree is  $O(\log n)$ , the total running time for the creation of an OBBTree is  $O(n \log^2 n)$ .

### *Handling Rigid-Body Motions*

In the OBBTree hierarchy, each OBB,  $A$ , is stored together with a rigid-body transformation (a rotation matrix  $\mathbf{R}$  and a translation vector  $\mathbf{t}$ ) matrix  $\mathbf{M}_A$ . This matrix holds the relative orientation and position of the OBB with respect to its parent.

Now, assume that we start to test two OBBs,  $A$  and  $B$ , against each other. The overlap test between  $A$  and  $B$  should then be done in the coordinate system of one of the OBBs. Let us say that we decide to do the test in  $A$ 's coordinate system. In this way,  $A$  is an AABB (in its own coordinate system) centered around the origin. The idea is then to transform  $B$  into  $A$ 's coordinate system. This is done with the matrix below, which first transforms  $B$  into its own position and orientation (with  $\mathbf{M}_B$ ) and then into  $A$ 's coordinate system (with the inverse of  $A$ 's transform,  $\mathbf{M}_A^{-1}$ ). Recall that for rigid body transforms, the transpose is the inverse, so little additional computation is needed:

$$\mathbf{T}_{AB} = \mathbf{M}_A^{-1} \mathbf{M}_B. \quad (17.9)$$

The OBB/OBB overlap test takes as input a matrix consisting of a  $3 \times 3$  rotation matrix  $\mathbf{R}$  and a translation vector  $\mathbf{t}$ , which hold the orientation and position of  $B$  with respect to  $A$  (see Section 16.13.5), so  $\mathbf{T}_{AB}$  is decomposed as below:

$$\mathbf{T}_{AB} = \begin{pmatrix} \mathbf{R} & \mathbf{t} \\ \mathbf{0}^T & 0 \end{pmatrix}. \quad (17.10)$$

Now, assume that  $A$  and  $B$  overlap, and that we want to descend into  $A$ 's child called  $C$ . A smart technique for doing this is as follows. We choose to do the test in  $C$ 's coordinate system. The idea is then to transform  $B$  into  $A$ 's coordinate system (with  $\mathbf{T}_{AB}$ ) and then transform that into the coordinate system of  $C$  (using  $\mathbf{M}_C^{-1}$ ). This is done with the following matrix, which is then used as the input to the OBB/OBB overlap test:

$$\mathbf{T}_{CB} = \mathbf{M}_C^{-1} \mathbf{T}_{AB}. \quad (17.11)$$

This procedure is then used recursively to test all OBBs.

### Miscellaneous

The **FindFirstHitCD** pseudocode for collision detection between two hierarchical trees, as presented in Section 17.3.2, can be used on two trees created with the preceding algorithms. All that needs to be exchanged is the `overlap()` function, which should point to a routine that tests two OBBs for overlap.

All algorithms involved in OBBTree have been implemented in a free software package called *RAPID* (Robust and Accurate Polygon Interference Detection) [433].

## 17.5 A Multiple Objects CD System

Consider an old-style clock consisting of springs and cog-wheels. Say this clock is represented as a detailed, three-dimensional model in the computer. Now imagine that the clock's movements are to be simulated using collision detection. The spring is wound and the clock's motion is simulated as collisions are detected and responses are generated. Such a system would require collision detection between possibly hundreds of pairs of objects. The previously described algorithms that detect collisions between only one pair of objects (two-body collision detection). A brute-force search of all possible collision pairs is incredibly inefficient and so is impractical under these circumstances.

Here, we will describe a two-level collision detection system [181, 574, 775] that is targeted at large-scale environments with multiple objects in motion. The first level of this system reports potential collisions among all the objects in the environment. These results are then sent to the second level, which performs exact collision detection between each pair of objects. The OBBTree algorithm from Section 17.4 (or any other method that detects collisions between two objects) can be used for this task.

### 17.5.1 Broad Phase Collision Detection

The goal of the first level is to minimize the number of calls to the second level in the collision detection system. This means that we want to report as few potential object/object collisions as possible. At this level, the testing is done on a higher level (i.e., on the object level), and therefore this is often called *broad phase collision detection*.

Most algorithms for this start by enclosing each object in a BV, and then apply some technique to find all BV/BV pairs that overlap. A simple approach is to use an axis-aligned bounding box (AABB) for each object. To avoid recomputing this AABB for an object undergoing rigid-body motion, the AABB is adjusted to be a *fixed cube* large enough to contain the

object in any arbitrary orientation. The fixed cubes are used to determine rapidly which pairs of objects are totally disjoint in terms of these bounding volumes. Sometimes it may be better to use dynamically resized AABBs.

Instead of fixed cubes, spheres can be used. This is reasonable, since the sphere is the perfect BV with which to enclose an object at any orientation. An algorithm for spheres is presented by Kim et al. [656]. Yet another approach is to use the convex hull or any other convex polyhedron, using for example the Lin-Canny algorithm [773, 774] or the V-clip [870] instead of fixed cubes. In the following, we describe two algorithms for broad phase CD: sweep-and-prune, and using grids. An entirely different method is to use the loose octree presented in Section 14.1.3.

### Sweep-and-Prune

We assume that each object has an enclosing AABB. In the *sweep-and-prune* technique [60, 774, 1363], the *temporal coherence*, which often is present in typical applications, is exploited. Temporal coherence means that objects undergo relatively small (if any) changes in their position and orientation from frame to frame (and so it is also called *frame-to-frame coherence*).

Lin [774] points out that the overlapping bounding box problem in three dimensions can be solved in  $O(n \log^2 n + k)$  time (where  $k$  is the number of pairwise overlaps), but it can be improved upon by exploiting coherence and so can be reduced to  $O(n + k)$ . However, this assumes that the animation has a fair amount of temporal coherence.

If two AABBs overlap, all three one-dimensional intervals (formed by the startpoints and endpoints of AABBs) in each main axis direction must also overlap. Here, we will describe how all overlaps of a number of one-dimensional intervals can be detected efficiently when the frame-to-frame coherency is high (which is what we can expect in a reasonable application). Given that solution, the three-dimensional problem for AABBs is solved by using the one-dimensional algorithm for each of the three main axes.

Assume that  $n$  intervals (along a particular axis) are represented by  $s_i$  and  $e_i$ , where  $s_i < e_i$  and  $0 \leq i < n$ . These values are sorted in one list in increasing order. This list is then swept from start to end. When a startpoint  $s_i$  is encountered, the corresponding interval is put into an active interval list. When an endpoint is encountered, the corresponding interval is removed from the active list. Now, if the startpoint of an interval is encountered while there are intervals in the active list, then the encountered interval overlaps all intervals in the list. This is shown in Figure 17.11.

This procedure would take  $O(n \log n)$  to sort all the intervals, plus  $O(n)$  to sweep the list and  $O(k)$  to report  $k$  overlapping intervals, resulting in an  $O(n \log n + k)$  algorithm. However, due to temporal coherence, the lists are not expected to change very much from frame to frame, and so a *bubble*

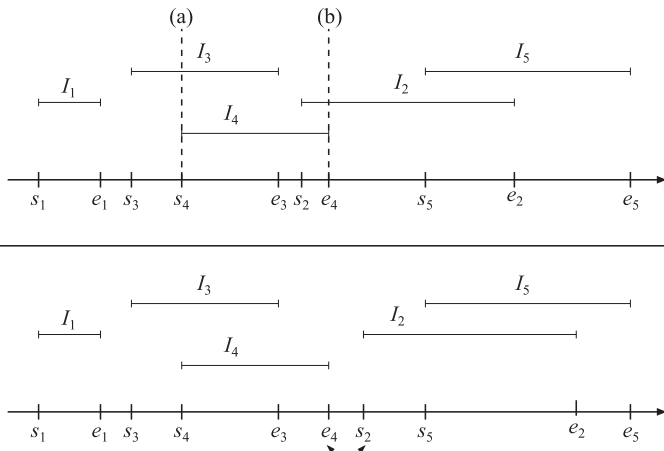


**Figure 17.11.** At the top, the interval  $I_4$  is encountered (at the point marked (a)) when there is only one interval in the active list ( $I_3$ ), so it is concluded that  $I_4$  and  $I_3$  overlap. When  $I_2$  is encountered,  $I_4$  is still in the active list (since  $e_4$  has not been encountered yet), and so  $I_4$  and  $I_2$  also overlap. When  $e_4$  is encountered,  $I_4$  is removed (at the point marked (b)) from the active list. At the bottom,  $I_2$  has moved to the right, and when the insertion sort finds that  $s_2$  and  $e_4$  need to change places, it can also be concluded that  $I_2$  and  $I_4$  do not overlap any longer. (Illustration after Witkin et al. [1363].)

*sort* or *insertion sort* [676] can be used with great efficiency after the first pass has taken place. These sorting algorithms sort nearly-sorted lists in an expected time of  $O(n)$ .

Insertion sort works by building up the sorted sequence incrementally. We start with the first number in the list. If we consider only this entry, then the list is sorted. Next, we add the second entry. If the second entry is smaller than the first, then we change places of the first and the second entries; otherwise, we leave them be. We continue to add entries, and we change the places of the entries, until the list is sorted. This procedure is repeated for all objects that we want to sort, and the result is a sorted list.

To use temporal coherence to our advantage, we keep a boolean for each interval pair. For large models, this may not be practical, as it implies an  $O(n^2)$  storage cost. A specific boolean is **TRUE** if the pair overlaps and **FALSE** otherwise. The values of the booleans are initialized at the first step of the algorithm when the first sorting is done. Assume that a pair of intervals were overlapping in the previous frame, and so their boolean was **TRUE**. Now, if the startpoint of one interval exchanges places with the endpoint of the other interval, then the status of this interval pair is inverted, which in this case means that their boolean is then **FALSE** and they do not overlap anymore. The same goes in the other direction, i.e., if

a boolean was FALSE, then it becomes TRUE when one startpoint changes place with one endpoint. This is also illustrated in Figure 17.11.

So we can create a sorted list of intervals for all three main axes and use the preceding algorithm to find overlapping intervals for each axis. If all three intervals for a pair overlap, their AABBs (which the intervals represent) also overlap; otherwise, they do not. The expected time is linear, which results in an  $O(n + k)$ -expected-time sweep-and-prune algorithm, where, again,  $k$  is the number of pairwise overlaps. This makes for fast overlap detection of the AABBs. Note that this algorithm can deteriorate to the worst of the sorting algorithm, which may be  $O(n^2)$ . This can happen when clumping occurs; a common example is when a large number of objects are lying on a floor, for example. If the  $z$ -axis is pointing in the normal direction of the floor, we get clumping on the  $z$ -axis. One solution would be to skip the  $z$ -axis entirely and only perform the testing on the  $x$ - and  $y$ -axes [315]. In many cases, this works well.

### *Grids*

While grids and hierarchical grids are best known as data structures for ray tracing acceleration, they can also be used for broad phase collision detection [1275]. In its simplest form, a grid is just an  $n$ -dimensional array of non-overlapping grid cells that cover the entire space of the scene. Each cell is therefore a box, where all boxes have the same size. From a high level, broad phase CD with a grid starts with insertion of all the objects' BVs in our scene into the grid. Then, if two objects are associated with the same grid cell, we immediately know that the BVs of these two objects are likely to overlap. Hence, we perform a simple BV/BV overlap test, and if they collide, we can proceed to the second level of the CD system. To the left in Figure 17.12, a two-dimensional grid with four objects is shown.

To obtain good performance, it is important to choose a reasonable grid cell size. This problem is illustrated to the right in Figure 17.12. One idea is to find the largest object in the scene, and make the grid cell size big enough to fit that object at all possible orientations [315]. In this way, all objects will overlap at most eight cells in the case of a three-dimensional grid.

Storing a large grid can be quite wasteful, especially if significant portions of the grid are left unused. Therefore, it has been suggested that spatial hashing should be used instead [315, 1261, 1275]. In general, each grid cell is mapped to an index in a hash table. All objects overlapping with a grid cell are inserted into the hash table, and testing can continue as usual. Without spatial hashing, we need to determine the size of the AABB enclosing the entire scene before memory can be allocated for the grid. We also must limit where objects can move, so they do not leave these bounds. These problems are avoided altogether with spatial hash-

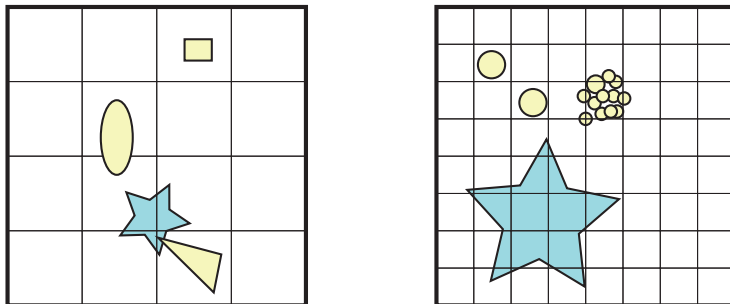


**Figure 17.12.** Left: a low-resolution two-dimensional grid with four objects. Note that since the ellipse and the star overlap a shared grid cell, these objects have to be tested using a BV/BV test. In this case, they do not collide. The triangle and the star also overlap a shared grid cell, and they do in fact collide. Right: a higher-resolution grid. As can be seen, the star overlaps with many grid cells, which can make this procedure expensive. Also note that there are many smaller objects where clumping occurs, and this is another possible source of inefficiency.

ing, as objects can immediately be inserted into the hash table, no matter where they are located.

As illustrated in Figure 17.12, it is not always optimal to use the same grid cell size in the entire grid. Therefore, we can instead turn to hierarchical grids. In this case, several different nested grids with different cell sizes are used, and an object is inserted in only the grid where the object's BV is (just) smaller than the grid cell. If the difference in grid cell size between adjacent levels in the hierarchical grid is exactly two, this structure is quite similar to an octree. There are many details worth knowing about when implementing grids and hierarchical grids for CD, and we refer to the excellent treatment of this topic by Ericson [315].

## 17.5.2 Summary

The outline of the two-level collision detection system is summarized below, and depicted in Figure 17.13.

- First, using the sweep-and-prune algorithm or a grid-based technique, all pairs of objects whose BVs overlap are detected and stored in the pair list.
- Second, the object pairs are sent to exact collision detection algorithms, such as the OBBTree.
- Finally, the results from collision detection are forwarded and taken care of by the application, so that action (collision response) can be taken.

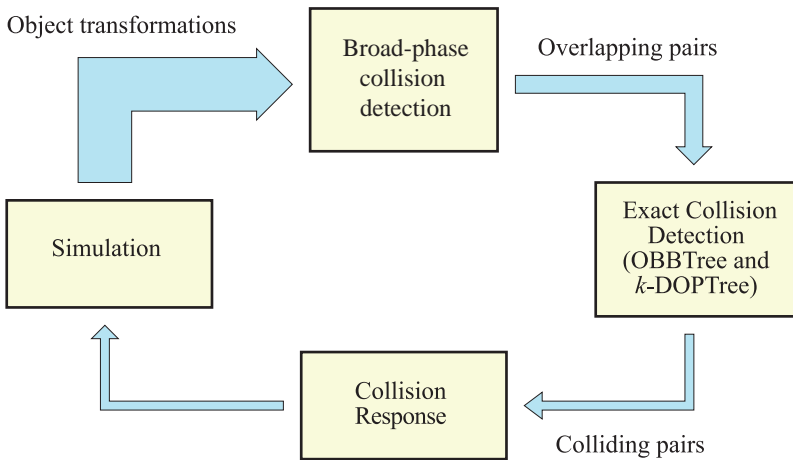


**Figure 17.13.** The outline of the collision detection system. The overlapping object pairs found by the first level broad phase CD algorithm are reported to the exact CD system, which, in turn, reports true collisions to a part of the system that should compute the collision response. Finally, all objects are treated by the simulation, where objects get their transforms, for example. (After Cohen et al. [181].)

## 17.6 Miscellaneous Topics

In this section, short introductions will be given for a number of different topics of interest: time-critical collision detection, distance queries, collision detection of arbitrarily deformable models, and finally, collision response.

### 17.6.1 Time-Critical Collision Detection

Assume that a certain game engine is rendering a scene in 7 ms when the viewer looks at a single wall, but that the rendering takes 15 ms when the viewer is looking down a long corridor. Clearly, this will give very different frame rates, which is usually disturbing to the user. One rendering algorithm that attempts to achieve constant frame rate is presented in Section 14.7.3. Here, another approach, called *time-critical collision detection*, is taken, which can be used if the application uses CD as well. It is called “time-critical” because the CD algorithm is given a certain time frame, say 9 ms, to complete its task, and it must finish within this time. Another reason to use such algorithms for CD is that it is very important for the perceived causality [977, 978], e.g., detecting whether one object causes another to move. So, returning to our example, assume that we set the goal that each frame (including CD) should take at most 20 ms, that is, 50 frames per second. With a time-critical collision detection algorithm,

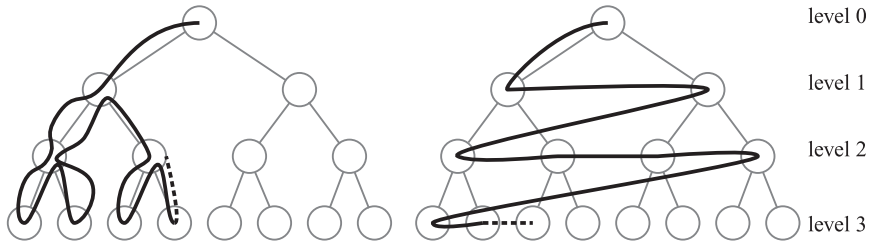


**Figure 17.14.** Depth-first (left) versus breadth-first (right) traversals. Depth-first traversal is often used in collision detection when traversing the bounding volume hierarchies, but for time-critical CD, breadth-first traversal is used.

we can see to it that the collision detection part of the rendering engine uses what time is left, up to 20 ms. For example, if a frame uses 15 ms for rendering, the CD part can use only 5 ms.

The following algorithm was introduced by Hubbard [572]. The idea is to traverse the bounding volume hierarchies in *breadth-first* order. This means that all nodes at one level in the tree are visited before descending to the next level. This is in contrast to *depth-first traversal*, which traverses the shortest way to the leaves (as done in the pseudocode in Section 17.3.2). These two traversals are illustrated in Figure 17.14. The reason for using breadth-first traversal is that both the left and the right subtree of a node are visited, which means that BVs which together enclose the entire object are visited. With depth-first traversal, we might only visit the left subtree because the algorithm might run out of time. When we do not know whether we have time to traverse the whole tree, it is at least better to traverse a little of both subtrees.

The algorithm first finds all pairs of objects whose BVs overlap, using, for example, the algorithm in Section 17.5.1. These pairs are put in a queue, called  $Q$ . The next phase starts by taking out the first BV pair from the queue. Their children BVs are tested against each other and if they overlap, the children pairs are put at the end of the queue. Then the testing continues with the next BV pair in the queue, until either the queue is empty (in which case all of the tree has been traversed) or until we run out of time [572].

Another related approach is to give each BV pair a priority and sort the queue on this priority. This priority can be based on factors such as visibility, eccentricity, distance, etc. Dingliana and O’Sullivan describe algorithms for computing approximate collision response and approximate collision contact determination [259]. This is needed for time-critical CD since the time may run out before the tree traversal has finished. Mendoza and O’Sullivan present a time-critical CD algorithm for deformable objects [858].

## 17.6.2 Distance Queries

In certain applications one wants to test whether an object is at least a certain distance from an environment. For example, when designing new cars, there has to be enough space for different sized passengers to be able to seat themselves comfortably. Therefore, a virtual human of different sizes can be tried against the car seat and the car, to see if he can be seated without bumping into the car. Preferably, the passengers should be able to seat themselves and still be at least, say, 10 cm apart from some of the car's interior elements. This sort of testing is called *tolerance verification*. This can be used for *path planning*, i.e., how an object's collision-free path from one point to another can be determined algorithmically. Given the acceleration and velocity of an object, the minimum distance can be used to estimate a lower bound on the time to impact. In this way, collision detection can be avoided until that time [774]. Another related query is of the penetration depth, that is, finding out how far two objects have moved into each other. This distance can be used to move the objects back just enough so that they do not penetrate any longer, and then an appropriate collision response can be computed at that point.

One of the first practical approaches that compute the minimum distance between convex polyhedra is called *GJK*, after its inventors; Gilbert, Johnson and Keerthi [399]. An overview of this algorithm will be given in this section. This algorithm computes the minimum distance between two convex objects,  $A$  and  $B$ . To do this, the *difference object* (sometimes called the *sum object*) between  $A$  and  $B$  is used [1291]:

$$A - B = \{\mathbf{x} - \mathbf{y} : \mathbf{x} \in A, \mathbf{y} \in B\}. \quad (17.12)$$

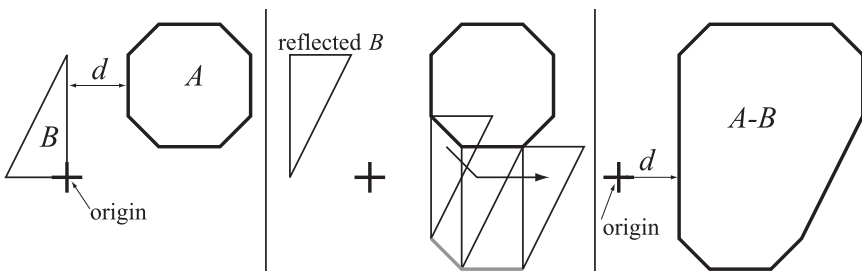


**Figure 17.15.** To the left, two convex objects  $A$  and  $B$  are shown. To construct  $A - B$ , first move  $A$  and  $B$  so that one reference point is at the origin (already done at the left). Then  $B$  is reflected, as shown in the middle, and the chosen reference point on  $B$  is put on the surface of  $A$  and then the reflected  $B$  is swept around  $A$ . This creates  $A - B$ , to the right. The minimum distance,  $d$ , is shown both on the left and the right.

This is also called the *Minkowski sum* of  $A$  and (reflected)  $B$  (see Section 16.18.3). All differences  $\mathbf{x} - \mathbf{y}$  are treated as a point set, which forms a convex object. An example of such a difference is shown in Figure 17.15, which also explains how to mentally build such a difference object.

The idea of GJK is that instead of computing the minimum distance between  $A$  and  $B$ , the minimum distance between  $A - B$  and the origin is computed. These two distances can be shown to be equivalent. The algorithm is visualized in Figure 17.16. Note that if the origin is inside  $A - B$  then  $A$  and  $B$  overlap.

The algorithm starts from an arbitrary simplex in the polyhedron. A simplex is the simplest primitive in the respective dimension, so it is a

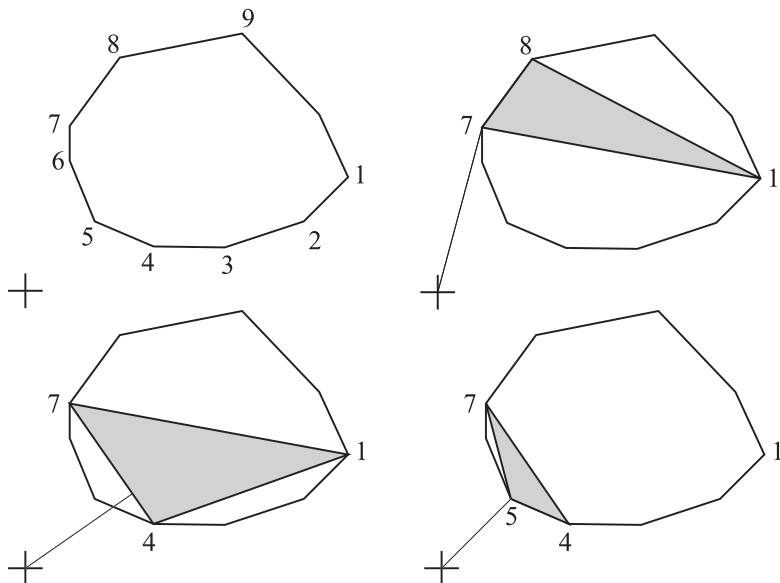


**Figure 17.16.** Upper left: The minimum distance between the origin and the polygon is to be computed. Upper right: An arbitrary triangle is chosen as a starting point for the algorithm, and the minimum distance to that triangle is computed. Vertex 7 is closest. Lower left: In the next step, all vertices are projected onto the line from the origin to vertex 7, and the closest vertex replaces the one in the triangle that is farthest away on this projection. Thus vertex 4 replaces vertex 8. The closest point on this triangle is then found, which is located on the edge from vertex 4 to 7. Lower right: The vertices are projected onto the line from the origin to the closest point from the previous step, and vertex 5 thus replaces vertex 1, which is farthest away on the projection. Vertex 5 is the closest point on this triangle, and when the vertices are projected on the line to vertex 5, we find that vertex 5 is the closest point overall. This completes the iteration. At this time the closest point on the triangle is found, which also happens to be vertex 5. This point is returned. (Illustration after Jiménez et al. [611].)

triangle in two dimensions, and a tetrahedron in three dimensions. Then the point on this simplex closest to the origin is computed. Van den Bergen shows how this can be done by solving a set of linear equations [1291, 1292]. A vector is then formed starting at the origin and ending at the nearest point. All vertices of the polyhedron are projected onto this vector, and the one with the smallest projection distance from the origin is chosen to be a new vertex in the updated simplex. Since a new vertex is added to the simplex, an existing vertex in the simplex must be removed. The one whose projection is farthest away is deleted. At this point, the minimum distance to the updated simplex is computed, and the algorithm iterates through all vertices again until the algorithm cannot update the simplex any longer. The algorithm terminates in a finite number of steps for two polyhedra [399]. The performance of this algorithm can be improved using many techniques, such as incremental computation and caching [1291].

Van den Bergen describes a fast and robust implementation of GJK [1291, 1292]. GJK can also be extended to compute penetration depth [153, 1293]. GJK is not the only algorithm for computing minimum distance; there are many others, such as the Lin-Canny algorithm [773], V-Clip [870], PQP [730] SWIFT [299], and SWIFT++ [300] (which also computes distance between concave rigid bodies).

### 17.6.3 Deformable Models

So far, the main focus of this section has been on either static models or rigid-body animated models. Obviously, there are other sorts of motion, such as waves on the water or a piece of cloth swaying in the wind. This type of motion is generally not possible to describe using rigid bodies, and instead, one can treat each vertex as being an independent vector function over time. Collision detection for such models is generally more expensive, and some initial research is presented here.

Assuming that the mesh connectivity stays the same for an object during deformation, it is possible to design clever algorithms that exploit this property. Such deformation is what would happen to a piece of cloth in the wind (unless it is somehow torn apart). As a preprocess, an initial hierarchical bounding volume (BV) tree is built. Instead of actually rebuilding the tree when deformation has taken place, the bounding volumes are simply refitted to the deformed geometry [731, 1290]. By using AABBs, which are fast to recompute, this operation is pretty efficient (as compared to OBBs). In addition, merging  $k$  children AABBs into a parent AABB is also quick and gives an optimal parent AABB. However, in general, any type of BV can be used. Van den Bergen organizes his tree so that all BVs are allocated and placed in an array, where a node always is placed so that its index is lower than its child nodes [1290, 1292]. In this way, a bottom-

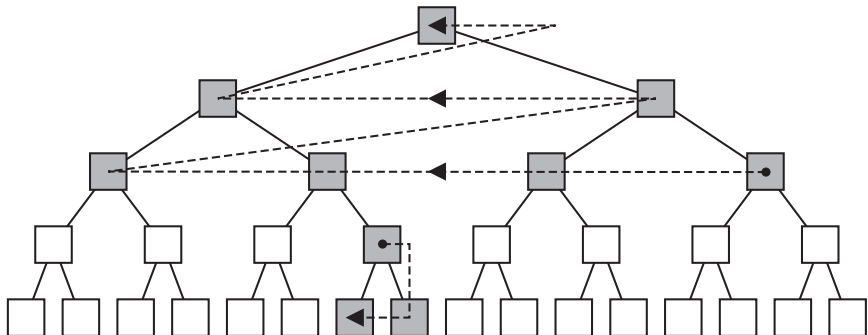


**Figure 17.17.** The hybrid bottom-up/top-down tree update method. The upper levels are updated using a bottom-up strategy, and only those nodes deeper down in the tree that are reached during a tree traversal are updated using a top-down method.

up update can be done by traversing the array from the end backwards, recomputing each BV at each node. This means that the BVs of the leaves are recomputed first, and then their parents' BVs are recomputed using the newly computed BVs, and so on back to the root of the tree. This sort of refit operation is reported to be about ten times as fast as rebuilding the tree from scratch [1290].

However, it has been noted that, in general, few BVs in a tree need to be updated. This is because most of them are not used during a collision query. A hybrid bottom-up/top-down tree update has therefore been proposed [731]. The idea is to use a bottom-up update for the higher levels (including the root), which means that only the upper BVs will be updated each frame. The rationale for this is that the upper levels often prune away most geometry. These updated upper levels are tested for overlap with the other tree (also possibly deforming and updated). For nodes that do not overlap, we can skip the updating of their subtrees, and so save much effort. On the other hand, for nodes that do overlap, a top-down strategy is used for updating nodes in their subtrees as they are needed during a tree traversal. Bottom-up could also be used for these, but top-down was found to be more effective [731]. Good results were achieved when the first  $n/2$  upper levels were updated with a bottom-up method, and the lower  $n/2$  levels with a top-down method. This is shown in Figure 17.17. To update a node top-down, the node records which vertices its entire subtree holds, and this list is traversed and a minimal BV is computed. When using top-down update, overlap testing is done as soon as a BV has been updated, so that the traversal can be terminated if no overlap is found. This, again, gives more efficiency. Initial tests show that this method is four to five times faster than van den Bergen's method [731].

Sometimes, one can create more efficient algorithms when there is some known information about the type of deformation. For example, if a model is deformed using morphing (see Section 4.5), then you can morph (i.e., blend) the BVs in a bounding volume hierarchy in the same way that you morph the actual geometry [732]. This does not create optimal BVs during morphing, but they are guaranteed to always contain the morphed geometry. This update can also be done in a top-down manner, i.e., only where it is needed. This technique can be used for AABBs, k-DOPs, and spheres. Computing a morphed BV from  $k$  different BVs costs  $O(k)$ , but usually  $k$  is very low and can be regarded as a constant. James and Pai [598] present a framework with a reduced deformation model, which is described by a combination of displacement fields. This provides for generous increases in performance. Ladislav and Zara present similar CD techniques for skinned models [708].

However, when the motion is completely unstructured and has breaking objects, these methods do not work. Some recent techniques attempt to track how well a subtree in a BVH fits the underlying geometry, and only rebuilds them as needed using some heuristics [733, 1397].

Another general method for deformable objects first computes minimal AABBs around two objects to be tested for collision [1199]. If they overlap, the overlap AABB region is computed, which simply is the intersection volume of the AABBs. It is only inside this overlap region that a collision can occur. A list of all triangles inside this region is created. An octree (see Section 14.1.3) that surrounds the entire scene is then used. The idea is then to insert triangles into the octree's nodes, and if triangles from both objects are found in a leaf node, then these triangles are tested against each other. Several optimizations are possible. First, the octree does not need to be built explicitly. When a node gets a list of triangles, the triangles are tested against the eight children nodes, and eight new triangle lists are created. This recursion ends at the leaves, where triangle/triangle testing can take place. Second, this recursion can end any time the triangle list has triangles from only one of the objects. To avoid testing a triangle pair more than once, a checklist is kept that tracks the tested pairs. The efficiency of this method may break down when an overlap region is very large, or there are many triangles in an overlap region.

### 17.6.4 Collision Response

Collision response is the action that should be taken to avoid (abnormal) interpenetration of objects. Assume, for example, that a sphere is moving toward a cube. When the sphere first hits the cube, which is determined by collision detection algorithms, we would like the sphere to change its trajectory (e.g., velocity direction), so it appears that they collided. This

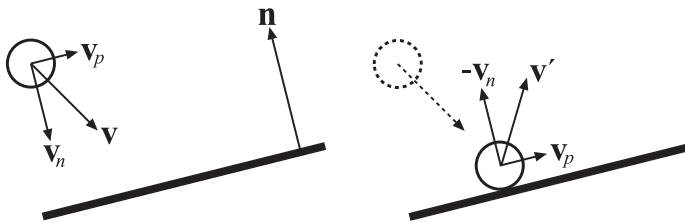


**Figure 17.18.** Collision response for a sphere approaching a plane. To the left the velocity vector  $\mathbf{v}$  is divided into two components,  $\mathbf{v}_n$ , and  $\mathbf{v}_p$ . To the right, perfectly elastic (bouncy) collision is shown, where the new velocity is  $\mathbf{v}' = \mathbf{v}_p - \mathbf{v}_n$ . For a less elastic collision, the length of  $-\mathbf{v}_n$  could be decreased.

is the task of *collision response* techniques, which has been and still is the subject of intensive research [58, 258, 478, 869, 901, 1363]. It is a complex topic, and in this section only the simplest technique will be presented.

In Section 16.18.3, a technique for computing the exact time of collision between a sphere and a plane was presented. Here we will explain what happens to the sphere’s motion at the time of collision.

Assume that a sphere is moving towards a plane. The velocity vector is  $\mathbf{v}$ , and the plane is  $\pi : \mathbf{n} \cdot \mathbf{x} + d = 0$ , where  $\mathbf{n}$  is normalized. This is shown in Figure 17.18. To compute the simplest response, we represent the velocity vector as

$$\begin{aligned}\mathbf{v} &= \mathbf{v}_n + \mathbf{v}_p, \quad \text{where} \\ \mathbf{v}_n &= (\mathbf{v} \cdot \mathbf{n})\mathbf{n}, \\ \mathbf{v}_p &= \mathbf{v} - \mathbf{v}_n.\end{aligned}\tag{17.13}$$

With this representation, the velocity vector,  $\mathbf{v}'$ , after the collision is [718]

$$\mathbf{v}' = \mathbf{v}_p - \mathbf{v}_n.\tag{17.14}$$

Here, we have assumed that the response was totally elastic. This means that no kinetic energy is lost, and thus that the response is “perfectly bouncy” [1363]. Now, normally the ball is deformed slightly at collision, and some energy transformed into heat, so some energy is lost. This is described with a coefficient of *restitution*,  $k$  (often also denoted  $\epsilon$ ). The velocity parallel to the plane,  $\mathbf{v}_p$ , remains unchanged, while  $\mathbf{v}_n$  is damped with  $k \in [0, 1]$ :

$$\mathbf{v}' = \mathbf{v}_p - k\mathbf{v}_n.\tag{17.15}$$

As  $k$  gets smaller, more and more energy is lost, and the collision appears less and less bouncy. At  $k = 0$ , the motion after collision is parallel to the plane, so the ball appears to roll on the plane.

More sophisticated collision response is based on physics, and involves creating a system of equations that is solved using an *ordinary differential equation* (ODE) solver. In such algorithms, a point of collision and a normal at this point is needed. The interested reader should consult the SIGGRAPH course notes by Witkin et al. [1363] and the paper by Dingliana et al. [258]. Also, O’Sullivan and Dingliana present experiments that show that it is hard for a human to judge whether a collision response is correct [977, 978]. This is especially true when more dimensions are involved (i.e., it is easier in one dimension than in three). To produce a real-time algorithm, they found that when there was not time enough to compute an accurate response, a random collision response could be used. These were found to be as believable as more accurate responses.

### 17.6.5 GPU-Based Collision Detection

It has been long known that rasterization can be used to detect collisions [1168]. The major difference between what has been described so far in this chapter is that algorithms based on GPUs are often performed in image space. This is in contrast to the techniques operating directly on the geometry.

There is a wealth of algorithms for performing CD on the GPU, and here we will present only one of the algorithms, called *CULLIDE* [436]. The basic idea is to use occlusion queries (see Section 14.6.1) to perform a test that determines whether an object,  $O$ , is “fully visible” (i.e., not colliding with) another set of objects,  $S$ . Recall that an occlusion query is usually used with a *less-or-equal* depth test. The occlusion query can count the number of fragments that pass the depth test, and if no fragments pass, then we can be certain that the rendered object (or its bounding box) is occluded with respect to the contents of the depth buffer.

For collision detection, we are instead interested in finding objects that definitely do *not* overlap with other objects. Govindaraju et al. suggest that this is done by reversing the depth test, so that we use *greater-or-equal*, and writing to the depth buffer is turned off. If both the front and the back faces of an object are rendered, and no fragment passes the depth test, we can conclude that the object is *fully visible* with respect to the depth buffer. In this way, we test for overlap in the depth direction, and in the image plane.

Next, we describe how this test can be used to implement a broad-phase collision detection algorithm on the GPU. Assume there are  $n$  objects, denoted  $O_i$ ,  $1 \leq i \leq n$ . That  $O_i$  does not collide with any other object simply means that it does not collide with any of the objects,  $O_1, \dots, O_{i-1}$ , nor with any of  $O_{i+1}, \dots, O_n$ . This can be formulated as an efficient rendering algorithm. In a first pass, the objects are rendered in order, and we test

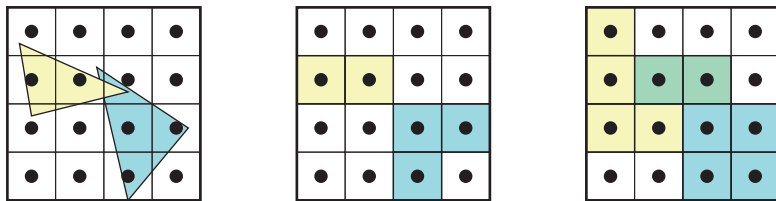


**Figure 17.19.** To the left, two triangles are shown on top of the pixel grid. In the middle, the triangles have been rendered using standard rasterization (with one sample at the center of each pixel), and as can be seen no overlap between the triangles is detected. To the right the triangles have been rasterized conservatively, so that each pixel that overlaps with a triangle is visited. This correctly detects the true geometric overlap.

whether each object is fully visible with respect to the objects already rendered. So, when  $O_i$  is being rendered, this means that we test it against  $O_1, \dots, O_{i-1}$ . In the second pass, we render the objects in reversed order, and this means that  $O_i$  now is tested against  $O_{i+1}, \dots, O_n$ . This type of rendering is done using orthographic projection, and typically it is done once for each axis ( $x$ ,  $y$ , and  $z$ ). In other words, the objects are evaluated from six views. If any pair overlaps from all six it is likely they may collide. The result is a small set of objects that can potentially collide, and this set is often called a *potentially colliding set* (PCS). This test can also be improved by using another object level, i.e., by splitting each object into a set of smaller sub-objects and continue with similar testing there. In the end, the remaining objects or triangles in the PCS are tested for true overlap by the CPU.

It should be noted that the performance and accuracy of these types of image-space algorithms is influenced by the screen resolution, and in the case of CULLIDE, also the accuracy of the depth buffer. In general, with a higher resolution, we will get better accuracy and fewer objects in the PCS, but this will also affect the fill rate requirements, and vice versa. For truly correct results, we also need a conservative rasterizer [509]. The reason for this is that the rasterizer usually only samples the geometry at the center of the pixel. What is needed for collision detection is a rasterizer that visits every pixel that is overlapping (ever so slightly) with the geometry being rendered. An example of when standard rasterization can go wrong is shown in Figure 17.19. Note that this problem can be ameliorated by using a higher resolution, but the problem cannot be completely avoided.

Govindaraju et al. [438] have extended the CULLIDE system so that it also can handle self-collision detection (for deformable objects) using a new visibility testing algorithm. Georgii et al. [389] use depth peeling to detect possible collision in the depth direction, and a mipmap hierarchy of bounding boxes to further prune the PCS. In the end a sparse texture

is packed into smaller representation, and read back to the CPU for exact polygon-polygon testing. Collisions between objects can truly deform the objects simply by painting the colliding areas onto the texture [1381].

## 17.7 Other Work

The OBBTree algorithm has been extended by Eberly to handle dynamic collision detection [294]. This work is briefly described in *IEEE CG&A* [89]. Algorithms for collision detection of extremely large models (millions of triangles) have been presented by Wilson et al. [1355]. They combine BVHs of spheres, AABBs, and OBBs, with a data structure called the overlap graph, lazy creation of BVHs, temporal coherence, and more, into a system called *IMMPACT*. Storing a bounding volume hierarchy may use much memory, and so Gomez presents some methods for compressing an AABB tree [421].

Frisken et al. [365] present a framework for soft bodies, where collisions, impact forces, and contact determination can be computed efficiently. Their framework is based on *adaptively sampled distance fields* (ADFs), which is a relatively new shape representation [364].

Baraff and Witkin [59] and Hughes et al. [575] present collision detection algorithms for objects undergoing polynomial deformation. Another more general system for arbitrary deformable objects is presented by Ganovelli et al. [375]. Related to this are algorithms for response and collision detection for cloth. This is treated by Baraff and Witkin [61], COURSSESNE et al. [202], and Volino and Magnenat-Thalmann [1307, 1308]. Another complex phenomenon is CD of hair. Hadap and Magnenat-Thalmann [473] treat hair as a continuum, which makes it possible to simulate hair relatively quickly.

Distance queries have been extended to handle concave objects by Quinlan [1042], and Ehmann and Lin also handle concave objects by decomposing an object into convex parts [300]. Kawachi and Suzuki present another algorithm for computing the minimum distance between concave parts [638].

## Further Reading and Resources

See this book's website, <http://www.realtimerendering.com>, for the latest information and free software in this rapidly evolving field. One of the best resources for CD is Ericson's book *Real-Time Collision Detection* [315], which also includes much code. The collision detection book by van den Bergen [1294] has a particular focus on GJK and the SOLID CD software system, included with the book. An extensive survey of collision detection

algorithms was presented by Lin and Gottschalk [776] in 1998. More recent surveys are given by Jiménez and Torras [611], and by O’Sullivan et al. [979]. Teschner et al. present a survey of CD algorithms for deformable objects [1262]. Schneider and Eberly present algorithms for computing the distance between many different primitives in their book on geometrical tools [1131].

More information on spatial data structures can be found in Section 14.1. Beyond Ericson’s more approachable book [315], Samet’s books [1098, 1099, 1100] are extremely comprehensive reference works on spatial data structures.

For an overview of dynamic CD, i.e., continuous CD, we refer to Zhang et al.’s paper [1406], which also present a new algorithm based on a conservative Taylor model and temporal culling.

For an overview, Hecker has a set of four theoretical and practical tutorials on collision response and the physics involved [526, 527, 528, 529]. Lander also has a good introduction to the physics of collision response for accurately simulating a pool table [719]. Books by Millington [868], Erleben et al. [318], and Eberly [293] are comprehensive guides to the field.



# Chapter 18

## Graphics Hardware

*“Thermal issues are going to force parallelism extraction into the software domain, and that transition will result in a more homogeneous computing environment. The current strategy of CPU execution separated from GPU execution by DirectX or OpenGL will be replaced by a massive number of similar cores executing an instruction set that works well for a wide variety of applications, including graphics. The question will not be heterogenous versus homogeneous, it will be a question of whose cores win the hearts and minds of software developers.”*

—Gabe Newell, Valve, 2007

Despite the fact that graphics hardware is evolving at a rapid pace, there are some general concepts and architectures that are commonly used in its design. Our goal in this chapter is to give an understanding of the various hardware elements of a graphics system and how they relate to one another. Other parts of the book discuss these in terms of their use with particular algorithms. Here, we discuss hardware on its own terms. We begin by discussing how the contents of the color buffer get displayed on the monitor. The various different buffers that can be a part of a real-time rendering system are then discussed. After that, perspective-correct interpolation is described. We continue with an overview of graphics architecture concepts, followed by three case studies of specific graphics systems.

### 18.1 Buffers and Buffering

In Section 2.4, we saw that the colors of the pixels are located in a color buffer. Visible primitives affect these pixels. Here, we will use a simple model to describe how the contents of the color buffer end up on the monitor. The memory of the frame buffer may be located in the same memory as the CPU uses for its tasks, in dedicated frame-buffer memory, or in *video*

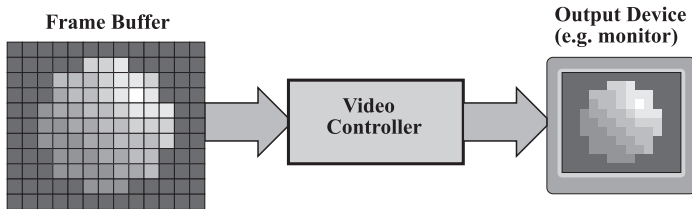


**Figure 18.1.** A simple display system: The color buffer is scanned by the video controller, which fetches the colors of the pixels. These colors are in turn used to control the intensities on the output device.

*memory* that can contain any GPU data but is not directly accessible to the CPU. The color buffer is a part of the frame buffer. It is in some way connected to a *video controller*, that, in turn, is connected to the monitor. This is illustrated in Figure 18.1. The video controller often includes a *digital-to-analog converter* (DAC), since if an analog display device is used, the digital pixel value must be converted to an analog equivalent. Because digital-to-analog conversion operates on every pixel of each frame, this system must be able to deal with high bandwidths. CRT-based displays are analog devices, and hence need analog input. LCD-based displays are digital devices, but can usually take both analog and digital input. Personal computers use the *digital visual interface* (DVI) or *DisplayPort* digital interfaces, while consumer electronics devices such as game systems and televisions commonly use the *high-definition multimedia interface* (HDMI) standard.

The rate at which a cathode ray tube (CRT) monitor updates the image is typically between 60 and 120 times per second (Hertz). The job of the video controller is to scan through the color buffer, scanline by scanline, at the same rate as the monitor, and to do this in synchronization with the beam of the monitor. During a single refresh of the image, the colors of the pixels in the color buffer are used to control the intensities of the monitor beam. Note that the electron beam usually moves in a left-to-right and up-to-down manner. Because of this, the beam does not contribute to the image on the screen when it moves from the right side to the left. This is called the *horizontal retrace*. Related to this is the *line rate* or *horizontal refresh rate*, the amount of time it takes to complete one entire left-right-left cycle. The *vertical retrace* is the movement of the beam from the bottom to the upper left corner, i.e., its return to position to begin the next frame. This is shown in Figure 18.2. The *vertical refresh rate* is the number of times per second the monitor performs this process. Most viewers notice flicker at rates less than 72 Hz (see Section 10.14 for more information on this).

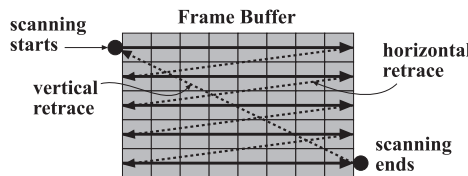


**Figure 18.2.** The horizontal and vertical retraces of a monitor. The color buffer shown here has five scanlines of pixels. The scanning of the lines starts at the upper left corner and proceeds one scanline at a time. At the end of a scanline it stops scanning and moves to the line below the current line. This passage is called horizontal retrace. When the bottom right corner is reached, the scanning ends and moves back to the upper left corner in order to be able to scan the next frame. This movement is called vertical retrace.

A liquid crystal display (LCD) usually updates at 60 Hertz. CRTs need a higher refresh rate because the phosphor begins to dim as soon as the electron beam passes it. LCD cells transmit light continuously, so do not normally require higher refresh rates. They also do not need retrace time. The concept of vertical sync still applies to LCDs, in the sense that the effective update rate is affected by the speed at which frames are generated. See Section 2.1 for how these rates interact.

Related to this topic is interlacing. Computer monitors are typically noninterlaced, or what is commonly known as *progressive scan*. In television, the horizontal lines are interlaced, so that during one vertical refresh, the odd numbered lines are drawn, and during the next one, the even numbered lines are drawn. Filtering computer animation for television is nontrivial [230, 1202].

### 18.1.1 The Color Buffer

The color buffer usually has a few color modes, based on the number of bytes representing the color. These modes include:

- High color: two bytes per pixel, of which 15 or 16 bits are used for the color, giving 32,768 or 65,536 colors, respectively.
- True color or RGB color: three or four bytes per pixel, of which 24 bits are used for the color, giving  $16,777,216 \approx 16.8$  million different colors.

The high color mode has 16 bits of color resolution to use. Typically, this amount is split into at least 5 bits each for red, green, and blue, giving 32 levels of color. This leaves one bit, which is usually given to the green channel, resulting in a 5-6-5 division. The green channel is chosen because it has the largest luminance effect on the eye, and so requires greater precision.



**Figure 18.3.** As the rectangle is shaded from white to black, banding appears. Although each grayscale bar has a solid intensity level, each can appear to be darker on the left and lighter on the right due to Mach banding.

High color has a speed advantage over true color. This is because two bytes of memory per pixel may usually be accessed more quickly than three or four bytes per pixel. That said, the use of high color mode is fading out for desktop graphics. However, some laptop displays use 18 bits for color, i.e., six bits per color component.<sup>1</sup> In addition, mobile devices, such as mobile phones and portable game consoles, also often use 16 or 18 bits for color, but can also use as many as 24 bits per pixel.

With 32 or 64 levels of color in each channel, it is possible to discern differences in adjacent color levels. The human visual system further magnifies the differences due to a perceptual phenomenon called *Mach banding* [408, 491]. See Figure 18.3. Dithering [64, 349] can lessen the effect by trading spatial resolution for increased effective color resolution.

True color uses 24 bits of RGB<sup>2</sup> color, one byte per color channel. Internally, these colors may be stored as 24 or 32 bits. A 32-bit representation can be present for speed purposes, because data access is optimized for groups of four bytes. On some systems the extra 8 bits can also be used to store an alpha channel (see Section 5.7), giving the pixel an RGBA value. The 24-bit color (no alpha) representation is also called the *packed pixel format*, which can save frame buffer memory in comparison to its 32-bit, unpacked counterpart. Using 24 bits of color is almost always acceptable for real-time rendering. It is still possible to see banding of colors, but much less likely than with only 16 bits.

Monitors can have more than 8 bits per channel. For example, BrightSide Technologies, acquired by Dolby in 2007, uses a lower resolution array of LED backlights to enhance their LCD monitors. Doing so gives their display about 10 times the brightness and 100 times the contrast of a typical monitor [1150]. These displays are commercially available, but currently target certain high-end markets, such as medical imaging and film post-production.

<sup>1</sup>The MacBook and MacBook Pro display may be in this class, as in 2007 a lawsuit was brought alleging false claims of displaying 8 bits per channel [930].

<sup>2</sup>On PC systems, the ordering is often reversed to BGR.

## 18.1.2 Z-Buffering

Depth resolution is important because it helps avoid rendering errors. For example, say you modeled a sheet of paper and placed it on a desk, ever so slightly above the desk's surface.<sup>3</sup> With precision limits of the  $z$ -depths computed for the desk and paper, the desk can poke through the paper at various spots. This problem is sometimes called *z-fighting*.

As we saw in Section 2.4, the  $Z$ -buffer (also called the depth buffer) can be used to resolve visibility. This kind of buffer typically has 24 bits per pixel. For orthographic viewing, the corresponding world space distance values are proportional to the  $z$ -value, and so the depth resolution is uniform. For example, say the world space distance between the near and far planes is 100 meters, and the  $Z$ -buffer stores 16 bits per pixel. This means that the distance between any adjacent depth values is the same,  $100 \text{ meters}/2^{16}$ , i.e., about 1.5 millimeters.

However, for perspective viewing, this is not the case; the distribution is non-uniform. After applying the perspective transform (Equations 4.68–4.70), a point  $\mathbf{v} = (v_x, v_y, v_z, v_w)$  is obtained. Next, division by  $v_w$  is done, giving  $(v_x/v_w, v_y/v_w, v_z/v_w, 1)$ . The value  $v_z/v_w$  is mapped from its valid range (e.g.,  $[0, 1]$  for DirectX) to the range  $[0, 2^b - 1]$  and is stored in the  $Z$ -buffer, where  $b$  is the number of bits. The characteristics of the perspective transform matrix result in greater precision for objects closer to the viewer (see page 97). This is especially true when there is a large difference between the near and the far values. When the near value is close to the far value, the precision tends to be uniform over the depth. To return to the paper and desk example, this change in precision can mean that as the viewer moves farther away from the paper, the desk poke-through problem occurs more frequently.

## 18.1.3 Single, Double, and Triple Buffering

In Section 2.4, we mentioned that double buffering is used in order for the viewer not to see the actual rendering of the primitives. Here, we will describe single, double, and even triple buffering.

Assume that we have only a single buffer. This buffer has to be the one that is currently shown to the viewer. As polygons for a frame are drawn, we will see more and more of them as the monitor refreshes—an unconvincing effect. Even if our frame rate is equal to the monitor's update rate, single buffering has problems. If we decide to clear the buffer or draw a large polygon, then we will briefly be able to see the actual partial changes

---

<sup>3</sup>If the paper were placed exactly at the same height as the desk, i.e., the paper and desk were made coplanar, then there would be no right answer without additional information about their relationship. This problem is due to poor modeling and cannot be resolved by better  $z$  precision.

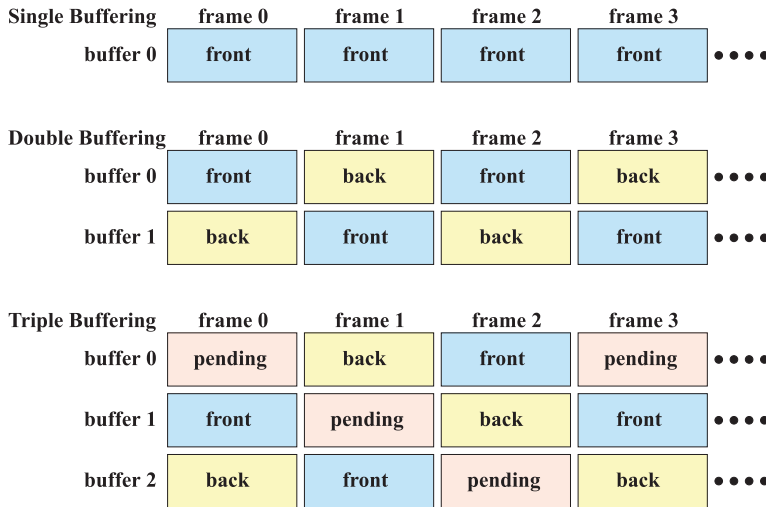


**Figure 18.4.** For single buffering, the front buffer is always shown. For double buffering, buffer 0 is first in front and buffer 1 is in the back. Then they swap from front-to-back and vice versa for each frame. Triple buffering works by having a pending buffer as well. Here, a buffer is first cleared, and rendering to it is begun (pending). Second, the system continues to use the buffer for rendering until the image has been completed (back). Finally, the buffer is shown (front).

to the color buffer as the beam of the monitor passes those areas that are being drawn. Sometimes called tearing, because the image displayed looks as if it were briefly ripped in two, this is not a desirable feature for real-time graphics.<sup>4</sup>

To avoid the visibility problem, double buffering is commonly used. In this scheme, a finished image is shown in the *front buffer*, while an off-screen *back buffer* contains the scene that is currently being drawn. The back buffer and the front buffer are then swapped by the graphics driver, typically during vertical retrace to avoid tearing. The swap does not have to occur during retrace; instantly swapping is useful for benchmarking a rendering system, but is also used in many applications because it maximizes frame rate. Immediately after the swap, the (new) back buffer is then the recipient of graphics commands, and the new front buffer is shown to the user. This process is shown in Figure 18.4. For applications that control the whole screen, the swap is normally implemented using a *color buffer flipping* technique [204], also known as *page flipping*. This means that the front buffer is associated with the address of a special register. This address points to the pixel at the position (0, 0), which may be at the

<sup>4</sup>On some ancient systems, like the old Amiga, you could actually test where the beam was and so avoid drawing there, thus allowing single buffering to work.

lower or upper left corner. When buffers are swapped, the address of the register is changed to the address of the back buffer.

For windowed applications, the common way to implement swapping is to use a technique called *BLT swapping* [204] or, simply, *blitting*.

The double buffer can be augmented with a second back buffer, which we call the *pending buffer*. This is called *triple buffering* [832]. The pending buffer is similar to the back buffer in that it is also offscreen, and in that it can be modified while the front buffer is being displayed. The pending buffer becomes part of a three-buffer cycle. During one frame, the pending buffer can be accessed. At the next swap, it becomes the back buffer, where the rendering is completed. Then it becomes the front buffer and is shown to the viewer. At the next swap, the buffer again turns into a pending buffer. This course of events is visualized at the bottom of Figure 18.4.

Triple buffering has one major advantage over double buffering. Using it, the system can access the pending buffer while waiting for the vertical retrace. With double buffering, a swap can stall the graphics pipeline. While waiting for the vertical retrace so a swap can take place, a double-buffered construction must simply be kept waiting. This is so because the front buffer must be shown to the viewer, and the back buffer must remain unchanged because it has a finished image in it, waiting to be shown. The drawback of triple buffering is that the latency increases up to one entire frame. This increase delays the reaction to user inputs, such as keystrokes and mouse or joystick moves. Control can become sluggish because these user events are deferred after the rendering begins in the pending buffer. Some hardcore game players will even turn off vertical sync and accept tearing in order to minimize latency [1329].

In theory, more than three buffers could be used. If the amount of time to compute a frame varies considerably, more buffers give more balance and an overall higher display rate, at the cost of more potential latency. To generalize, multibuffering can be thought of as a ring structure. There is a rendering pointer and a display pointer, each pointing at a different buffer. The rendering pointer leads the display pointer, moving to the next buffer when the current rendering buffer is done being computed. The only rule is that the display pointer should never be the same as the rendering pointer.

A related method of achieving additional acceleration for PC graphics accelerators is to use *SLI* mode. Back in 1998 3dfx used SLI as an acronym for *scanline interleave*, where two graphics chipsets run in parallel, one handling the odd scanlines, the other the even. NVIDIA (who bought 3dfx's assets) uses this abbreviation for an entirely different way of connecting two (or more) graphics cards, called *scalable link interface*. ATI/AMD calls it CrossFire X. This form of parallelism divides the work by either splitting the screen into two (or more) horizontal sections, one per card, or by having

each card fully render its own frame, alternating output. There is also a mode that allows the cards to accelerate antialiasing of the same frame. The most common use is having each GPU render a separate frame, called *alternate frame rendering* (AFR). While this scheme sounds as if it should increase latency, it can often have little or no effect. Say a single GPU system renders at 10 frames per second (fps). If the GPU is the bottleneck, two GPUs using AFR could render at 20 fps, or even four at 40 fps. Each GPU takes the same amount of time to render its frame, so latency does not necessarily change.

### 18.1.4 Stereo and Multi-View Graphics

In stereo rendering, two images are used in order to make objects look more three dimensional. With two eyes, the visual system takes two views, and in combining them, retrieves depth information. This ability is called *stereopsis*, *stereo vision* [349, 408], or *binocular parallax*. The idea behind stereo vision is to render two images, one for the left eye and one for the right eye (as shown in Figure 18.5), and then use some technique that ensures that the human viewer experiences a depth in the rendered image. These two images are called the *stereo pair*. One common method for creating stereo vision is to generate two images, one in red and one in green (or cyan, by rendering to both the blue and green channels), composite these images, then view the result with red-green glasses. In this case, only a normal single display buffer is needed, but display of color is problematic. For color images, the solution can be as simple as having two small screens, one in

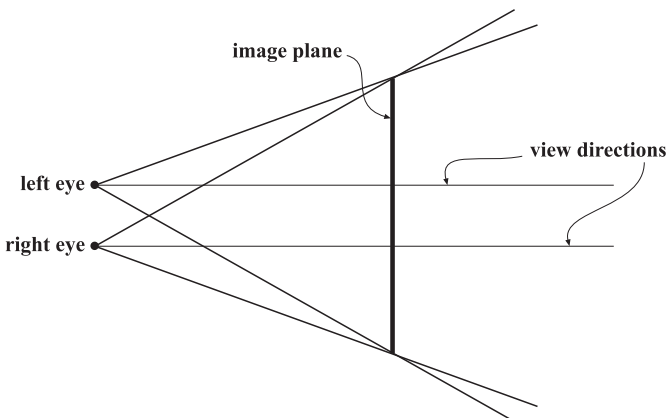


**Figure 18.5.** Stereo rendering. Note that the image plane is shared between the two frustums, and that the frustums are asymmetric. Such rendering would be used on, for example, a stereo monitor. Shutter glasses could use separate image planes for each eye.

front of each (human) eye, in a head-mounted display. Another hardware solution is the use of shutter glasses, in which only one eye is allowed to view the screen at a time. Two different views can be displayed by rapidly alternating between eyes and synchronizing with the monitor [210].

For these latter forms of stereography, two separate display buffers are needed. When viewing is to take place in real time, double buffering is used in conjunction with stereo rendering. In this case, there have to be two front and two back buffers (one set for each eye), so the color buffer memory requirement doubles.

Other technologies that provide full color without the need for glasses are possible. Such displays are therefore often called *autostereoscopic* [267]. The basic idea is to modify the display surface in some way. One technique is covering the LCD with a plastic sheet of vertical (or near vertical) lenses (half cylinders) or prisms that refract the light so that alternating pixel columns are directed toward the left and right eyes. These displays are called *lenticular displays*. Another mechanism is to place black vertical stripes (which may be implemented as another LCD) a small distance in front of the LCD to mask out alternating columns from each eye. These are called *parallax barrier displays*.

So far, only stereo rendering have been considered, where two *views* are displayed. However, it is possible to build displays with many more views as well. There are commercial displays with nine views, and research displays with more than 80 views. In general, these displays are often called *multi-view displays*. The idea is that such displays also can provide another type of depth cue called *motion parallax*. This means that the human viewer can move the head to, say, the left, in order to look “around a corner.” In addition, it makes it easier for more than one person to look at the display.

Systems for three-dimensional TV and video have been built, and standardization work is proceeding for defining how TV and video signals will be sent for a wide variety of displays. The transition from black-and-white TVs to color was a large step forward for TV, and it may be that the transition to three-dimensional TV could be as large. When rendering to these displays, it is simple to use brute force techniques: Either just render each image in sequence, or put a number of graphics cards into the computer, and let each render one image. However, there is clearly a lot of coherency among these images, and by rendering a triangle to all views simultaneously and using a sorted traversal order, texture cache content can be exploited to a great extent, which speeds up rendering [512].

### 18.1.5 Buffer Memory

Here, a simple example will be given on how much memory is needed for the different buffers in a graphics system. Assume that we have a

color buffer of  $1280 \times 1024$  pixels with true colors, i.e., 8 bits per color channel. With 32 bits per color, this would require  $1280 \times 1024 \times 4 = 5$  megabytes (MB). Using double buffering doubles this value to 10 MB. Also, let us say that the  $Z$ -buffer has 24 bits per pixel and a stencil buffer of 8 bits per (these usually are paired to form a 32 bit word). The  $Z$ -buffer and stencil buffer would then need 5 MB of memory. This system would therefore require  $10 + 5 = 15$  MB of memory for this fairly minimal set of buffers. Stereo buffers would double the color buffer size. Note that under all circumstances, only one  $Z$ -buffer and stencil buffer are needed, since at any moment they are always paired with one color buffer active for rendering. When using supersampling or multisampling techniques to improve quality, the amount of buffer memory increases further. Using, say, four samples per pixel increases most buffers by a factor of four.

## 18.2 Perspective-Correct Interpolation

The fundamentals of how perspective-correct interpolation is done in a rasterizer will briefly be described here. This is important, as it forms the basis of how rasterization is done so that textures look and behave correctly on primitives. As we have seen, each primitive vertex,  $\mathbf{v}$ , is perspective projected using any of Equations 4.68-4.70. A projected vertex,  $\mathbf{p} = (p_x w, p_y w, p_z w, w)$ , is obtained. We use  $w = p_w$  here to simplify the presentation. After division by  $w$  we obtain  $(p_x, p_y, p_z, 1)$ . Recall that  $-1 \leq p_z \leq 1$  for the OpenGL perspective transform. However, the stored  $z$ -value in the  $Z$ -buffer is in  $[0, 2^b - 1]$ , where  $b$  is the number of bits in the  $Z$ -buffer. This is achieved with a simple translation and scale of  $p_z$ . Also, each vertex may have a set of other parameters associated with it, e.g., texture coordinates  $(u, v)$ , fog, and color,  $\mathbf{c}$ .

The screen position  $(p_x, p_y, p_z)$  can be correctly interpolated linearly over the triangle, with no need for adjustment. In practice, this is often done by computing delta slopes:  $\frac{\Delta z}{\Delta x}$  and  $\frac{\Delta z}{\Delta y}$ . These slopes represent how much the  $p_z$  value differs between two adjacent pixels in the  $x$ - and  $y$ -directions, respectively. Only a simple addition is needed to update the  $p_z$  value when moving from one pixel to its neighbor. However, it is important to realize that the colors and especially texture coordinates cannot normally be linearly interpolated. The result is that improper foreshortening due to the perspective effect will be achieved. See Figure 18.6 for a comparison. To solve this, Heckbert and Moreton [521] and Blinn [103] show that  $1/w$  and  $(u/w, v/w)$  can be linearly interpolated. Then the interpolated texture coordinates are divided by the interpolated  $1/w$  to get the correct texture location. That is,  $(u/w, v/w)/(1/w) = (u, v)$ . This type of interpolation is called *hyperbolic interpolation*, because a graph of the

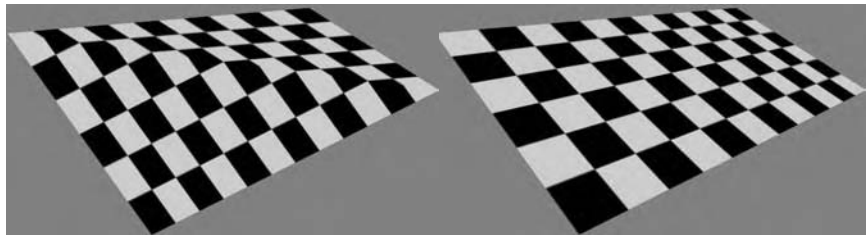


**Figure 18.6.** A textured quadrilateral consists of two triangles. To the left, linear interpolation is used over each triangle, and to the right, perspective-correct interpolation is used. Notice how linear interpolation ruins the three-dimensional effect.

interpolated value versus position forms a hyperbola. It is also called *ratio-linear linear interpolation*, because a numerator and denominator are linearly interpolated.

As an example, assume a triangle should be rasterized, and that each vertex is

$$\mathbf{r}_i = \left[ \mathbf{p}_i, \frac{1}{w_i}, \frac{u_i}{w_i}, \frac{v_i}{w_i} \right]. \quad (18.1)$$

Here,  $\mathbf{p}_i = (p_{ix}, p_{iy}, p_{iz})$  is the point after projection and division by its  $w$ -component, which is denoted  $w_i$ . The  $(u_i, v_i)$  are texture coordinates at the vertices. This is shown in Figure 18.7. To find the coordinates of a pixel on the horizontal scanline shown in gray, one must first linearly interpolate  $\mathbf{r}_0$  and  $\mathbf{r}_1$  to get  $\mathbf{r}_3$ , and also linearly interpolate  $\mathbf{r}_2$  and  $\mathbf{r}_1$  to get  $\mathbf{r}_4$ . Then linear interpolation of  $\mathbf{r}_3$  and  $\mathbf{r}_4$  can be used to find a  $\mathbf{r}$  vertex for each pixel on the gray scanline. The interpolated  $\mathbf{p}$ -values are correct as is. The other interpolated surface values  $(u/w, v/w)$  are multiplied by a computed value  $w$  to obtain  $(u, v)$ . To obtain  $w$  itself the linearly interpolated value  $1/w$  is used, with a division done per pixel to compute  $w = 1/(1/w)$ .

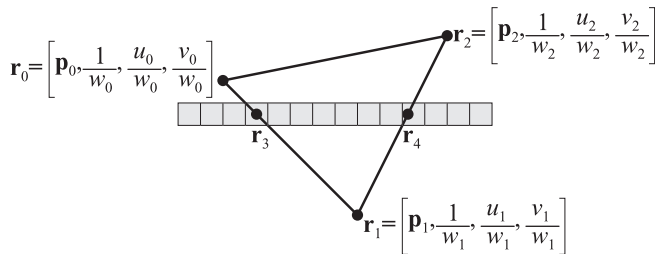


**Figure 18.7.** A triangle being rasterized. The vectors  $\mathbf{r}_i$  are linearly interpolated over the triangle.

This implementation of the interpolation is only one choice. Another possibility is to compute delta slopes for texture interpolation:  $\Delta(u/w)/\Delta x$ ,  $\Delta(u/w)/\Delta y$ ,  $\Delta(v/w)/\Delta x$ ,  $\Delta(v/w)/\Delta y$ ,  $\Delta(1/w)/\Delta x$ , and  $\Delta(1/w)/\Delta y$ . Again, the  $u/w$ ,  $v/w$ , and  $1/w$  values can be updated with only additions between neighboring pixels, and then the texture coordinates  $(u, v)$  are computed as before.

An in-depth discussion of perspective-correct interpolation is provided by Blinn [103, 105, 108]. It should be noted that in current GPUs, edge functions [1016] are often used to determine whether a sample is inside a triangle. An edge function is simply the equation of a two-dimensional line on implicit form (see Equation A.47 on page 907). As an interesting side effect, perspective-correct interpolation can also be done by using the evaluated edge functions [836].

## 18.3 Architecture

In this section we will first present a general architecture for a real-time computer graphics system. The geometry and rasterizer stages, as well as a texture cache mechanism, will also be discussed here. Bandwidth, memory, ports, and buses are important components in a graphics architecture, as is latency. These topics are discussed in Sections 18.3.2–18.3.5. To reduce bandwidth requirements, buffers can be compressed and occlusion culling can be performed. Such algorithms are treated in Sections 18.3.6 and 18.3.7. Section 18.3.8 describes the *programmable culling unit*, a hardware construction for culling unnecessary instructions in the fragment shader.

### 18.3.1 General

Graphics accelerators have generally evolved from the end of the pipeline backward. For example, the first PC accelerators did little more than draw interpolated or textured spans of pixels rapidly. Triangle setup was then added in 1998 by the 3Dfx Voodoo 2. NVIDIA introduced geometry stage acceleration, known as hardware *transform and lighting* (T&L), with the GeForce 256 in 1999 [360]. However, the fixed-function implementation limited the usefulness of this hardware stage. With the introduction of vertex and pixel shaders in 2000, graphics hardware has both the speed and programmability needed to overcome purely CPU-based renderers in essentially all areas. The modern accelerator is often called a *graphics processing unit* (GPU) because of these capabilities.

The host is the computer system without any graphics hardware, i.e., it is a system with CPU(s), memory, buses, etc. Applications run on the

host, i.e., on the CPU(s). The interface between the application and the graphics hardware is called a *driver*.

The GPU is often thought of in different terms than the CPU. A GPU is not a serial processor like the CPU, but is rather a *dataflow* or *stream processor*. It is the appearance of data at the beginning of the pipeline that causes computation to occur, and a limited set of inputs is needed to perform the computation. This different processing model lends itself in particular to problems where each datum is affected by only nearby data. One active area of research is how to apply the GPU to non-rendering problems of this type, such as fluid flow computation and collision detection. This form of computation is called *general purpose* computation on the GPU, abbreviated as *GPGPU*. AMD's *CTM* [994] and NVIDIA's *CUDA* [211] are toolkits that aid the programmer in using the GPU for non-graphical applications, as well as alternative rendering methods such as ray tracing. Other architectures, such as Intel's *Larrabee* [1221], aim to provide graphics acceleration using CPU-centric processors with texture samplers. The Larrabee architecture is expected to be able to attack a wider range of problems that can benefit from parallelization.

### Pipelining and Parallelization

Two ways to achieve faster processing in graphics hardware are *pipelining* and *parallelism*. These techniques are most often used in conjunction with each other. See Section 2.1 for the basics of pipelining. When discussing pipelining in this section, we do not mean the conceptual or the functional stages, but rather the physical pipeline stages, i.e., the actual blocks built in silicon that are executed in parallel. It is worth repeating that dividing a certain function (for example, the lighting computation of a vertex) into  $n$  pipeline stages ideally gives a performance increase of  $n$ . In general, graphics hardware for polygon rendering is much simpler to pipeline than a CPU. For example, the Intel Pentium IV has 20 pipeline stages, which should be compared to NVIDIA's GeForce3, which has 600–800 stages (depending on which path is taken). The reasons for this are many, including that the CPU is operation-driven, while most of the GPU is data-driven, that pixels are rendered independent of each other, and that some parts of the GPU are highly specialized and fixed-function (not programmable).

The clock frequency of a CPU is often much higher than that of a graphics accelerator, but this hardly touches the huge advantage that modern accelerators have over the CPU when used correctly. CPUs typically have much higher clock frequencies because, among other reasons, CPU designers spend much more time on optimizing the blocks. One reason for this is because CPUs have tens of pipeline stages, compared to hundreds or thousands for GPUs. Also, for GPUs, the clock frequency is most often not the

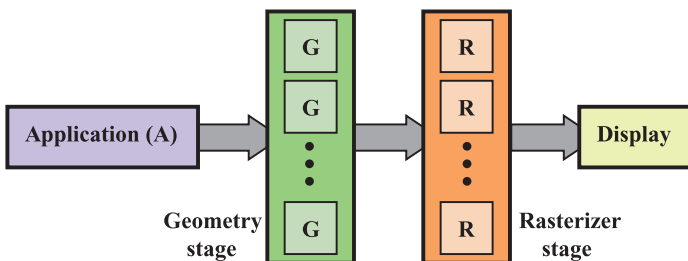


**Figure 18.8.** The general architecture for a high-performance, parallel computer graphics architecture. Each geometry unit (G) processes (i.e., transforms, projects, etc.) a portion of the geometry to be rendered, and each rasterizer unit (R) takes care of a portion of the pixel calculations.

bottleneck—rather, memory bandwidth is.<sup>5</sup> Another reason why graphics algorithms can run fast in hardware is that it is relatively simple to predict what memory accesses will be done, and so efficient memory prefetching can be achieved. The majority of memory accesses are reads, which also simplifies and improves performance. Also note that a CPU cannot tolerate long latencies (when an instruction is executed, the result is usually desired immediately), whereas a graphics accelerator can tolerate longer latencies, as long as sufficiently many primitives can be rendered per second. In addition, in the beginning of the 21st century, the most complex GPUs surpassed the most complex PC CPUs in terms of number of transistors. In conclusion, if the same chip area is used to build a dedicated graphics accelerator as a standard CPU, hardware rendering is at least 100 times faster than using software rendering with the CPU [816].

The other way of achieving faster graphics is to parallelize, and this can be done in both the geometry and the rasterizer stages. The idea is to compute multiple results simultaneously and then merge these at a later stage. In general, a parallel graphics architecture has the appearance shown in Figure 18.8. The result of the graphics database traversal is sent to a number of *geometry units* (G's) that work in parallel. Together, these geometry units do the geometry-stage work of the rendering pipeline (see Section 2.3), and forward their results to a set of *rasterizer units* (R's), which together implement the rasterizer stage in the rendering pipeline.

However, since multiple results are computed in parallel, some kind of sorting must be done, so that the parallel units together render the image that the user intended. Specifically, the sorting needed is from model space to screen space (see Section 2.3.1 and 2.4). It should be noted that the

<sup>5</sup>In fact, memory bandwidth is most often the bottleneck for CPUs as well. However, CPU company marketing departments have found that a high clock frequency number is what sells best.

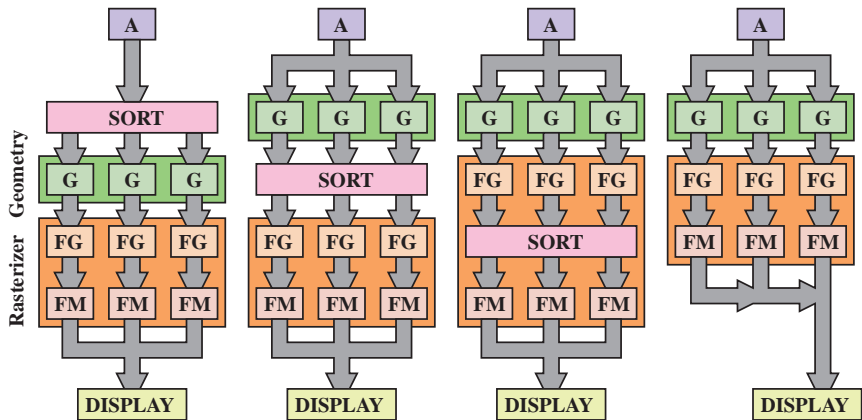


**Figure 18.9.** Taxonomy of parallel graphics architectures. A is the application, G is the geometry stage, then follows the rasterizer comprised of FG, which is *fragment generation*, and FM, which is *fragment merging*. The architectures are (left to right): sort-first, sort-middle, sort-last fragment, and sort-last image. (*Illustration after Eldridge et al. [302].*)

G's and R's may be identical units, i.e., unified shader cores, capable of executing both geometry and per-pixel processing, and switching between these. See Section 18.4.1 on how the Xbox 360 uses unified shaders. Even if this is the case, it is important to understand where this sorting takes place.

Molnar et al. [896] present a taxonomy for parallel architectures, based on where in the parallel rendering pipeline the sort occurs. Eldridge et al. [302] present a slight variation of this taxonomy, and we follow their notation here. The sort can occur anywhere in the pipeline, which gives rise to four different classes of parallel architectures, as shown in Figure 18.9. These are called *sort-first*, *sort-middle*, *sort-last fragment*, and *sort-last image*. The rasterizer stage is comprised of two internal stages, namely, *fragment generation* (FG) and *fragment merge* (FM). FG generates the actual locations inside a primitive, and forwards these to FM, which merges the result, using the Z-buffer. Shading is not shown, but is, in general, done either at the end of FG, or in the beginning of FM. Also note that there may be, for example, twice as many FGs as there are geometry units. Any configuration is possible.

A sort-first-based architecture sorts primitives before the geometry stage. The strategy is to divide the screen into a set of regions, and the primitives inside a region are sent to a complete pipeline that “owns” that region. See Figure 18.10. A primitive is initially processed enough to know which region(s) it needs to be sent—this is the sorting step. Sort-first

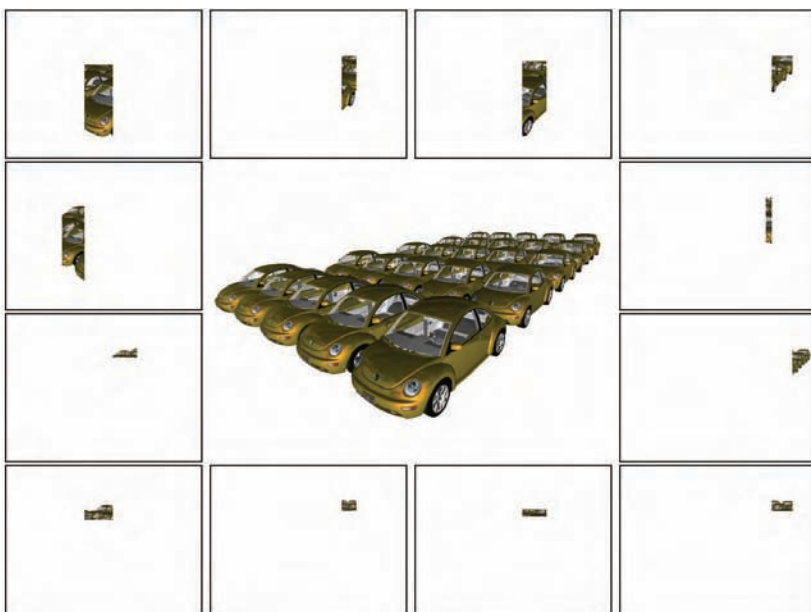


**Figure 18.10.** Sort-first splits the screen into separate tiles and assigns a processor to each tile, as shown here. A primitive is then sent to the processors whose tiles they overlap. This is in contrast to sort-middle architecture, which needs to sort *all* triangles after geometry processing has occurred. Only after all triangles have been sorted can per-pixel rasterization start. (*Images courtesy of Marcus Roth and Dirk Reiners.*)

is the least explored architecture for a single machine [303, 896]. It is a scheme that does see use when driving a system with multiple screens or projectors forming a large display, as a single computer is dedicated to each screen [1086]. A system called Chromium [577] has been developed, which can implement any type of parallel rendering algorithm using a cluster of workstations. For example, sort-first and sort-last can be implemented with high rendering performance.

The Mali 200 (Section 18.4.3) is a sort-middle architecture. Geometry processors are given arbitrary sets of primitives, with the goal of load-balancing the work. Also, each rasterizer unit is responsible for a screen-space region, here called a *tile*. This may be a rectangular region of pixels, or a set of scanlines, or some other interleaved pattern (e.g., every eighth pixel). Once a primitive is transformed to screen coordinates, sorting occurs to route the processing of this primitive to the rasterizer units (FGs and FMs) that are responsible for that tile of the screen. Note that a transformed triangle or mesh may be sent to several rasterizer units if it overlaps more than one tile. One limitation of these tiling architectures

is the difficulty of using various post-processing effects such as blurs or glows, as these require communication between neighboring pixels, and so neighboring tiles, of computed results. If the maximum neighborhood of the filter is known in advance, each tile can be enlarged by this amount to capture the data needed and so avoid the problem, at the cost of redundant computation along the seams.

The sort-last fragment architecture sorts the fragments after fragment generation (FG) and before fragment merge (FM). An example is the GPU of the PLAYSTATION® 3 system described in Section 18.4.2. Just as with sort-middle, primitives are spread as evenly as possible across the geometry units. One advantage with sort-last fragment is that there will not be any overlap, meaning that a generated fragment is sent to only one FM, which is optimal. However, it may be hard to balance fragment generation work. For example, assume that a set of large polygons happens to be sent down to one FG unit. The FG unit will have to generate all the fragments on these polygons, but the fragments are then sorted to the FM units responsible for the respective pixels. Therefore, imbalance is likely to occur for such cases [303].



**Figure 18.11.** In sort-last image, different objects in the scene are sent to different processors. Transparency is difficult to deal with when compositing separate rendered images, so transparent objects are usually sent to all nodes. (*Images courtesy of Marcus Roth and Dirk Reiners.*)

Finally, the sort-last image architecture sorts after the entire rasterizer stage (FG and FM). A visualization is shown in Figure 18.11. PixelFlow [328, 895] is one such example. This architecture can be seen as a set of independent pipelines. The primitives are spread across the pipelines, and each pipeline renders an image with depth. In a final composition stage, all the images are merged with respect to its Z-buffers. The PixelFlow architecture is also interesting because it used deferred shading, meaning that it textured and shaded only visible fragments. It should be noted that sort-last image cannot fully implement an API such as OpenGL, because OpenGL requires that primitives be rendered in the order they are sent.

One problem with a pure sort-last scheme for large tiled display systems is the sheer amount of image and depth data that needs to be transferred between rendering nodes. Roth and Reiners [1086] optimize data transfer and composition costs by using the screen and depth bounds of each processor’s results.

Eldridge et al. [302, 303] present “Pomegranate,” a sort-everywhere architecture. Briefly, it inserts sort stages between the geometry stage and the fragment generators (FGs), between FGs and fragment mergers (FMs), and between FMs and the display. The work is therefore kept more balanced as the system scales (i.e., as more pipelines are added). The sorting stages are implemented as a high-speed network with point-to-point links. Simulations showed a nearly linear performance increase as more pipelines are added.

All the components in a graphics system (host, geometry processing, and rasterization) connected together give us a multiprocesssing system. For such systems there are two problems that are well-known, and almost always associated with multiprocesssing: *load balancing* and *communications* [204]. FIFO (first-in, first-out) queues are often inserted into many different places in the pipeline, so that jobs can be queued in order to avoid stalling parts of the pipeline. For example, it is possible to put a FIFO between the geometry and the rasterizer stage. The different sort architectures described have different load balancing advantages and disadvantages. Consult Eldridge’s Ph.D. thesis [303] or the paper by Molnar et al. [896] for more on these. The programmer can also affect the load balance; techniques for doing so are discussed in Chapter 15. Communications can be a problem if the bandwidth of the buses is too low, or is used unwisely. Therefore, it is of extreme importance to design a graphics system so that the bottleneck does not occur in any of the buses, e.g., the bus from the host to the graphics hardware. Bandwidth is discussed in Section 18.3.4.

One significant development in commercial GPUs introduced in 2006 is the unified shader model. See Section 15.2 for a short description, and Section 18.4.1, which describes the unified shader architecture of the Xbox 360.

### Texture Access

The performance increase in terms of pure computations has grown exponentially for many years. While processors have continued to increase in speed at a rate in keeping with Moore's Law, and graphics pipelines have actually exceeded this rate [735], memory bandwidth and memory latency have not kept up. Bandwidth is the rate at which data can be transferred, and latency is the time between request and retrieval. While the capability of a processor has been going up 71% per year, DRAM bandwidth is improving about 25%, and latency a mere 5% [981]. For NVIDIA's 8800 architecture [948], you can do about 14 floating-point operations per texel access.<sup>6</sup> Chip density rises faster than available bandwidth, so this ratio will only increase [1400]. In addition, the trend is to use more and more textures per primitive. Reading from texture memory is often the main consumer of bandwidth [10]. Therefore, when reading out texels from memory, care must be taken to reduce the bandwidth used and to hide latency.

To save bandwidth, most architectures use caches at various places in the pipeline, and to hide latency, a technique called *prefetching* is often used. Caching is implemented with a small on-chip memory (a few kilobytes) where the result of recent texture reads are stored, and access is very fast [489, 582, 583]. This memory is shared among all textures currently in use. If neighboring pixels need to access the same or closely located texels, they are likely to find these in the cache. This is what is done for standard CPUs, as well. However, reading texels into the cache takes time, and most often entire cache blocks (e.g., 32 bytes) are read in at once.

So, if a texel is not in the cache, it may take relatively long before it can be found there. One solution employed by GPUs today to hide this latency is to keep many fragments in flight at a time. Say the shader program is about to execute a texture lookup instruction. If only one fragment is kept in flight, we need to wait until the texels are available in the texture cache, and this will keep the pipeline idle. However, assume that we can keep 100 fragments in flight at a time. First, fragment 0 will request a texture access. However, since it will take many clock cycles before the requested data is in the cache, the GPU executes the same texture lookup instruction for fragment 1, and so on for all 100 fragments. When these 100 texture lookup instructions have been executed, we are back at processing fragment 0. Say a dot product instruction, using the texture lookup as an argument, follows. At this time, it is very likely that the requested data is in the cache, and processing can continue immediately. This is a common way of hiding latency in GPUs. This is also the reason why a GPU has many registers. See the Xbox 360 description in Section 18.4.1 for an example.

---

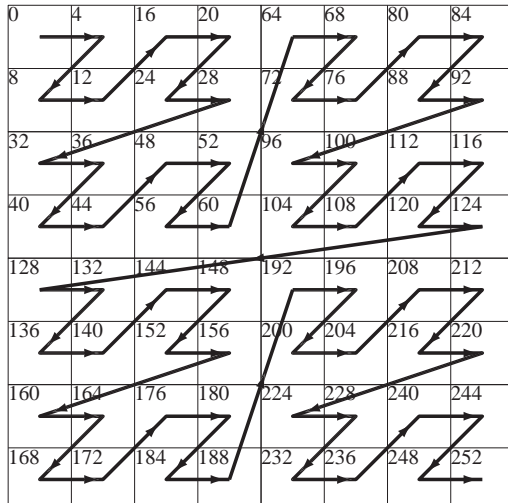
<sup>6</sup>This ratio was obtained using 520 GFLOPS as the computing power, and 38.4 billion texel accesses per second. It should be noted that these are peak performance numbers.

Mipmapping (see Section 6.2.2) is important for texture cache coherence, since it enforces a maximum texel-pixel ratio. When traversing the triangle, each new pixel represents a step in texture space of one texel at most. Mipmapping is one of the few cases in rendering where a technique improves both visuals and performance. There are other ways in which the cache coherence of texture access can be improved. *Texture swizzling* is a technique that can be used to improve the texture cache performance and page locality. There are various methods of texture swizzling employed by different GPU manufacturers, but all have the same goal: to maximize texture cache locality regardless of the angle of access. We will describe a swizzle pattern commonly used by NVIDIA GPUs—it is representative of the patterns used.

Assume that the texture coordinates have been transformed to fixed point numbers:  $(u, v)$ , where each of  $u$  and  $v$  have  $n$  bits. The bit with number  $i$  of  $u$  is denoted  $u_i$ . Then the remapping of  $(u, v)$  to a swizzled texture address is

$$\begin{aligned} \text{texaddr}(u, v) = & \text{texbaseaddr} \\ & + (v_{n-1}u_{n-1}v_{n-2}u_{n-2} \dots v_2u_2v_1u_1v_0u_0) * \text{texelsize}. \end{aligned} \quad (18.2)$$

Here,  $\text{texelsize}$  is the number of bytes occupied by one texel. The advantage of this remapping is that it gives rise to the texel order shown in



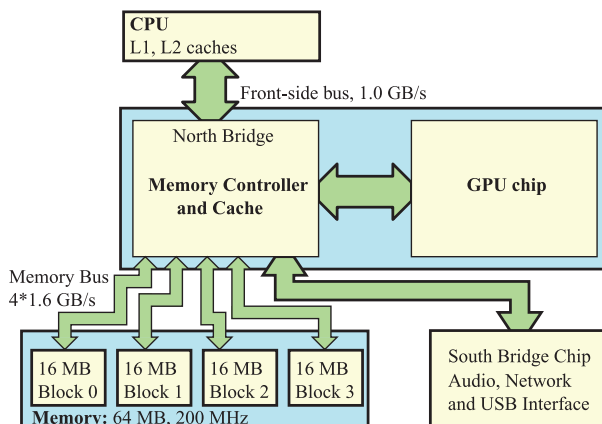
**Figure 18.12.** Texture swizzling increases coherency of texel memory accesses. Note that texel size here is four bytes, and that the texel address is shown in each texel's upper left corner.

Figure 18.12. As can be seen, this is a space-filling curve, called a *Morton sequence* [906], and these are known to improve coherency. In this case, the curve is two dimensional, since textures normally are, too. See Section 12.4.4 for more on space-filling curves.

### 18.3.2 Memory Architecture

Here, we will mention a few different architectures that have been used for memory layout. The Xbox, i.e., the first game console from Microsoft, uses a *unified memory architecture* (UMA), which means that the graphics accelerator can use any part of the host memory for textures and different kinds of buffers [650]. An example of UMA is shown in Figure 18.13. As can be seen, both the CPU and the graphics accelerator use the same memory, and thus also the same bus.

The Xbox 360 (Section 18.4.1) has a different memory architecture, as shown in Figure 18.15 on page 860. The CPU and the GPU share the same bus and interface to the system memory, which the GPU uses mainly for textures. However, for the different kinds of buffers (color, stencil, Z, etc.), the Xbox 360 has separate memory (eDRAM) that only the GPU can access. This GPU-exclusive memory is often called *video memory* or *local memory*. Access to this memory is usually much faster than letting the GPU access system memory over a bus. As an example, on a typical PC in 2006 local memory bandwidth was greater than 50 GB/sec, compared to at most 4 GB/sec between CPU and GPU using PCI Express [123]. Using a small video memory (e.g., 32 MB) and then accessing system memory



**Figure 18.13.** The memory architecture of the first Xbox, which is an example of a unified memory architecture (UMA).

using the GPU is called *TurboCache* by NVIDIA and *HyperMemory* by ATI/AMD.

Another somewhat less unified layout is to have dedicated memory for the GPU, which can then be used for textures and buffers in any way desired, but cannot be used directly by the CPU. This is the approach taken by the architecture of the PLAYSTATION® 3 system (Section 18.4.2), which uses a local memory for scene data and for textures.

### 18.3.3 Ports and Buses

A port is a channel for sending data between two devices, and a bus is a shared channel for sending data among more than two devices. Bandwidth is the term used to describe throughput of data over the port or bus, and is measured in bytes per second,  $b/s$ . Ports and buses are important in computer graphics architecture because, simply put, they glue together different building blocks. Also important is that bandwidth is a scarce resource, and so a careful design and analysis must be done before building a graphics system. An example of a port is one that connects the CPU with the graphics accelerator, such as PCI Express (PCIe) used in PCs. Since ports and buses both provide data transfer capabilities, ports are often referred to as buses, a convention we will follow here.

Many objects in a scene do not appreciably change shape from frame to frame. Even a human character is typically rendered with a set of unchanging meshes that use GPU-side vertex blending at the joints. For this type of data, animated purely by modeling matrices and vertex shader programs, it is common to use *static* vertex buffers, which are placed in video memory (sometimes called local memory), i.e., dedicated graphics memory. Doing so makes for fast access by the GPU. For vertices that are updated by the CPU each frame, *dynamic* vertex buffers are used, and these are placed in system memory that can be accessed over a bus, such as PCI Express. This is the main reason why vertex buffers are so fast. Another nice property of PCI Express is that queries can be pipelined, so that several queries can be requested before results return.

### 18.3.4 Memory Bandwidth

Next, we will present a simplified view of memory bandwidth usage between the CPU and the GPU, and the bandwidth usage for a single fragment. We say simplified, because there are many factors, such as caching and DMA, that are hard to take into account.

To begin, let us discuss a theoretical model for the bandwidth used by a single fragment on its way through the pixel pipeline. Let us assume that the bandwidth usage consists of three terms, namely,  $B_c$ , which is the

bandwidth usage to the color buffer,  $B_z$ , which is the bandwidth usage to the depth buffer ( $Z$ -buffer), and  $B_t$ , which is bandwidth usage to textures. The total bandwidth usage,  $B$ , is then

$$B = B_c + B_z + B_t. \quad (18.3)$$

Recall that the average depth complexity, here denoted  $d$ , is the number of times a pixel is covered by. The average overdraw, here denoted  $o(d)$ , is the number of times a pixel has its contents written. Both depth complexity and overdraw are covered in Section 15.4.5. The average overdraw can be modeled as a Harmonic series, as shown in Equation 15.2, and this equation is repeated here for clarity:

$$o(d) = 1 + \frac{1}{2} + \frac{1}{3} + \cdots + \frac{1}{d}. \quad (18.4)$$

The interesting thing is that if there are  $d$  triangles covering a pixel, then one will write to  $o(d)$  of these. In terms of depth buffer bandwidth,  $B_z$ , this means that there will  $d$  depth buffer reads (costing  $Z_r$  bytes each), but only  $o(d)$  depth buffer writes (costing  $Z_w$  bytes each). This can be summarized as

$$B_z = d \times Z_r + o(d) \times Z_w. \quad (18.5)$$

For blending operations, one may also need to read the color buffer ( $C_r$ ), but we assume this is not part of the common case. However, there will be as many color buffer writes as depth buffer writes, so  $B_c = o(d) \times C_w$ , where  $C_w$  is the cost (in bytes) of writing the color of a single pixel. Since most scenes are textured, one or more *texture reads* ( $T_r$ ) may also occur. Some architectures may perform texturing before the depth test, which means  $B_t = d \times T_r$ . However, in the following, we assume that texture reads are done after the depth test, which means that  $B_t = o(d) \times T_r$ . Together, the total bandwidth cost is then [13]

$$B = d \times Z_r + o(d) \times (Z_w + C_w + T_r). \quad (18.6)$$

With trilinear mipmapping, each  $T_r$  may cost  $8 \times 4 = 32$ , i.e., eight texel accesses costing four bytes each. If we assume that four textures are accessed per pixel, then  $T_r = 128$  bytes. We also assume  $C_w$ ,  $Z_r$ , and  $Z_w$  each cost four bytes. Assuming a target depth complexity of  $d = 6$  gives  $o(d) \approx 2.45$ , which means a pixel costs

$$b = 6 \times 4 + 2.45 \times (4 + 4 + 128) \approx 357 \text{ bytes per pixel.} \quad (18.7)$$

However, we can also take a texture cache (Section 18.3.1) into account, and this reduces the  $B_t$ -cost quite a bit. With a texture cache miss rate

$m$ , Equation 18.6 is refined to

$$\begin{aligned}
 b &= d \times Z_r + o(d) \times (Z_w + C_w + m \times T_r) \\
 &= \underbrace{d \times Z_r + o(d) \times Z_w}_{\text{depth buffer, } B_z} + \underbrace{o(d) \times C_w}_{\text{color buffer, } B_c} + \underbrace{o(d) \times m \times T_r}_{\text{texture read, } B_t} \\
 &= B_d + B_c + B_t.
 \end{aligned} \tag{18.8}$$

This equation is what we call the *rasterization equation*. Hakura and Gupta uses  $m = 0.25$ , which means that on every fourth texel access, we get a miss in the cache. Now, let us use this formula for an example where, again,  $d = 6$  and  $o \approx 2.45$ . This gives  $B_c = 2.45 \times 4 = 9.8$  bytes, and  $B_z = 6 \times 4 + 2.45 \times 4 = 33.8$  bytes. The texture bandwidth usage becomes:  $B_t = 2.45 \times 4 \times 8 \times 4 \times 0.25 = 78.4$  bytes. This sums to  $b = 33.8 + 9.8 + 78.4 = 122$  bytes, which is a drastic reduction compared to the previous example (357 bytes).

A cost of 122 bytes per pixel may seem small, but put in a real context, it is not. Assume that we render at 72 frames per second at  $1920 \times 1200$  resolution. This gives

$$72 \times 1920 \times 1200 \times 122 \text{ bytes/s} \approx 18.8 \text{ Gbytes/s.} \tag{18.9}$$

Next, assume that the clock of the memory system is running at 500 MHz. Also, assume that a type of memory called DDRAM is used. Now, 256 bits can be accessed per clock from DDRAM, as opposed to 128 bits for SDRAM. Using DDRAM gives

$$500\text{Mhz} \times \frac{256}{8} \approx 15.6 \text{ Gbytes/s.} \tag{18.10}$$

As can be seen here, the available memory bandwidth (15.6 GB/s) is almost sufficient for this case, where the per-pixel bandwidth usage is 18.8 GB/s. However, the figure of 18.8 GB/s is not truly realistic either. The depth complexity could be higher, and buffers with more bits per component can be used (i.e., floating-point buffers, etc.). In addition, the screen resolution could be increased, even more textures could be accessed, better texture filtering (which costs more memory accesses) could be used, multisampling or supersampling may be used, etc. Furthermore, we have only looked at memory bandwidth usage for fragment processing. Reading vertices and vertex attributes into the GPU also uses up bandwidth resources.

On top of that, the usage of bandwidth is never 100% in a real system. It should now be clear that memory bandwidth is extremely important in a computer graphics system, and that care must be taken when designing the memory subsystem. However, it is not as bad as it sounds. There are

many techniques for reducing the number of memory accesses, including a texture cache with prefetching, texture compression, and the techniques in Sections 18.3.6 and 18.3.7. Another technique often used is to put several memory banks that can be accessed in parallel. This also increases the bandwidth delivered by the memory system.

Let us take a look at the bus bandwidth from the CPU to the GPU. Assume that a vertex needs 56 bytes ( $3 \times 4$  for position,  $3 \times 4$  for normal, and  $4 \times 2 \times 4$  for texture coordinates). Then, using an indexed vertex array, an additional 6 bytes per triangle are needed to index into the vertices. For large closed triangle meshes, the number of triangles is about twice the number of vertices (see Equation 12.8 on page 554). This gives  $(56 + 6 \times 2)/2 = 34$  bytes per triangle. Assuming a goal of 300 million triangles per second, a rate of 10.2 Gbytes per second is needed just for sending the triangles from the CPU to the graphics hardware. Compare this to PCI Express 1.1 with 16 lanes of data (a commonly used version in 2007), which can provide a peak (and essentially unreachable) rate of 4.0 GBytes/sec in one direction.

These numbers imply that the memory system of a GPU and the corresponding algorithms should be designed with great care. Furthermore, the needed bus bandwidth in a graphics system is huge, and one should design the buses with the target performance in mind.

### 18.3.5 Latency

In general, the latency is the time between making the query and receiving the result. As an example, one may ask for the value at a certain address in memory, and the time it takes from the query to getting the result is the latency. In a pipelined system with  $n$  pipeline stages, it takes at least  $n$  clock cycles to get through the entire pipeline, and the latency is thus  $n$  clock cycles. This type of latency is a relatively minor problem. As an example, we will examine an older GPU, where variables such as the effect of shader program length are less irrelevant. The GeForce3 accelerator has 600–800 pipeline stages and is clocked at 233 MHz. For simplicity, assume that 700 pipeline stages are used on average, and that one can get through the entire pipeline in 700 clock cycles (which is ideal). This gives  $700/(233 \cdot 10^6) \approx 3 \cdot 10^{-6}$  seconds = 3 microseconds ( $\mu$ s). Now assume that we want to render the scene at 50 Hz. This gives  $1/50$  seconds = 20 milliseconds (ms) per frame. Since  $3 \mu$ s is much smaller than 20 ms (about four magnitudes), it is possible to pass through the entire pipeline many times per frame. More importantly, due to the pipelined design, results will be generated every clock cycle, that is, 233 million times per second. On top of that, as we have seen, the architectures are often parallelized. So, in terms of rendering, this sort of latency is not often much of a problem. There is also

the latency when requesting access to texel data. One technique for hiding this type of latency is described on page 847.

A different type of latency is that from reading back data from GPU to CPU. A good mental model is to think of the GPU and CPU as separate computers working asynchronously, with communication between the two taking some effort. Latency from changing the direction of the flow of information can seriously hurt performance. When data is read back from the accelerator, the pipeline often has to be flushed before the read. During this time, the CPU is idle. An example of a read-back mechanism that does not produce a stall is the occlusion query. See Section 14.6.1. For occlusion testing, the mechanism is to perform the query and then occasionally check the GPU to see if the results of the query are available. While waiting for the results, other work can then be done on both the CPU and GPU.

### 18.3.6 Buffer Compression

As can be seen in Equation 18.8, there are several components adding up to the bandwidth traffic. To obtain an efficient GPU architecture, one needs to work on all fronts to reduce bandwidth usage. Even for occluded triangles, there is still a substantial amount of  $Z$ -buffer bandwidth ( $d \times Z_r$ ). In addition, it would be advantageous to reduce the bandwidth traffic to other buffers, such as color and stencil, as well. In this section, we will present techniques to compress and decompress these types of buffers on the fly, i.e., as images are being rendered. This includes algorithms for rapidly clearing the contents of the buffers. Automatic GPU occlusion culling (called  $Z$ -*culling*), compression and decompression of buffers, and rapid clears are typically implemented in the same subsystem in hardware, since they share some parts of the implementation. For clarity, we present buffer compression and fast clears together with the system first, and then discuss  $Z$ -culling.

Central to these algorithms is on-chip storage or a cache, which we call the *tile table*, with additional information stored for each tile, i.e., rectangle, of pixels in the buffer. A block diagram of this algorithm is shown in Figure 18.14, where we consider only  $Z$ -buffer compression, for simplicity. However, this general architecture applies to other buffers, such as color and stencil, as well. Each element in the tile table stores the status of, say, an  $8 \times 8$  tile of pixels in the frame buffer. This includes a state and the maximum  $z$ -value,  $z_{\max}$  (and possibly  $z_{\min}$  as well—more about that in Section 18.3.7), for the tile. As will be seen later, the  $z_{\max}$  can be used for occlusion culling. The state of each tile can be either *compressed*, *uncompressed*, or *cleared*. In general there could also be different types of compressed blocks. For example, one compressed mode might compress down to 25% and another to 50%. These modes are used to implement a

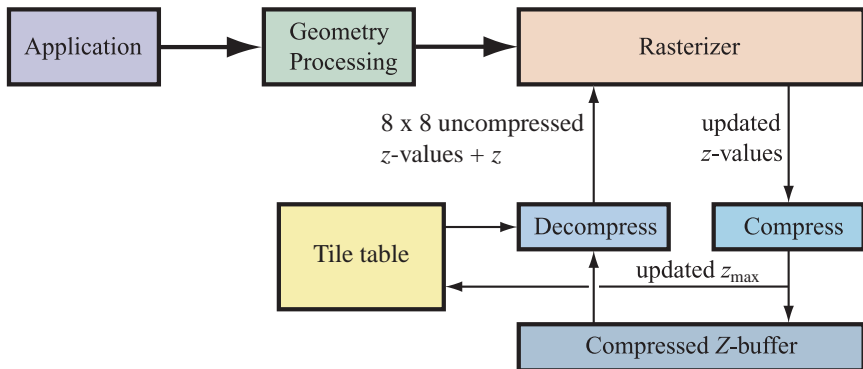


**Figure 18.14.** Block diagram of hardware techniques for fast clear of the  $Z$ -buffer, compression of  $Z$ -buffer, and  $Z$ -culling. Applies to other types of buffers too.

fast clear and compression of the buffer. When the system issues a clear of the buffer, the state of each tile is set to *cleared*, and the frame buffer proper is not touched. When the rasterizer needs to read the cleared buffer, the *decompressor* unit first checks the state, sees that the tile is cleared, and so can send a buffer tile with all values set to the clear value for that buffer (e.g.,  $z_{\text{far}}$  for the  $Z$ -buffer) without reading and uncompressing the actual buffer. In this way, access to the buffer itself is minimized during clears, so saving bandwidth. If the state is not cleared, then the buffer for that tile has to be read. When the rasterizer has finished writing new values to the tile, it is sent to the *compressor*, where an attempt is made at compressing it. If there are two compression modes, both could be tried, and the one that can compress that tile with smallest amount of bits is used. Since we usually need lossless buffer compression, a fallback to using uncompressed data is needed if all compression techniques fail. This also implies that lossless buffer compression never can reduce memory usage in the actual buffer—such techniques only reduce memory bandwidth usage. In addition, for the  $Z$ -buffer, a new  $z_{\text{max}}$  is also computed. This  $z_{\text{max}}$  is sent to the tile table. If compression succeeded, the tile's state is set to *compressed* and the data is sent in a compressed form. Otherwise, it is sent uncompressed and the state is set to *uncompressed*.

The ATI Radeon cards from 2000 used a *differential pulse code modulation* (DPCM) scheme for compressing the  $8 \times 8$  tiles [902]. This type of algorithm is good when there is a great deal of coherence in the data to be compressed. This is often the case for the contents of the  $Z$ -buffer, as a triangle tends to cover many pixels, and objects consist of adjacent triangles. In addition to a new algorithm for depth buffer compression, a survey of existing depth buffer compression patents is given by Hasselgren

and Akenine-Möller [511]. For color buffer compression, there is a similar survey by Rasmusson et al. [1049], who also suggest that lossy compression can be used for color buffer compression if the error is kept under strict control. This may be reasonable in cases where reducing bandwidth is extremely important, such as for a mobile phone.

### 18.3.7 Z-Culling and Early-Z

Testing the  $z$ -depth is a raster operation that is often done after almost all the rest of the pipeline has done its work. Automatically killing a fragment in a tile, before the pixel shader itself is accessed, is a useful optimization performed by essentially all modern GPUs. This optimization is called *hierarchical Z-culling*, or simply *Z-culling*. There are two variants, called  $Z_{\max}$ -culling and  $Z_{\min}$ -culling. These techniques are automatically used by the GPU if the pixel shader is analyzed and found not to modify the  $z$ -depth of the fragment [1065]. Doing so saves on pixel shader program execution costs. In the next section an alternative culling technique is described that can also be used for pixel shaders modifying the  $z$ -depth, among other situations.

We start by describing  $Z_{\max}$ -culling. This is basically the same idea as the hierarchical  $z$ -buffering algorithm (Section 14.6.2), with the exception that each triangle is not tested for occlusion, and with the restriction that the entire  $Z$ -pyramid is not used; instead only a few levels are used. To perform occlusion culling, the rasterizer fetches the  $z_{\max}$  for each tile of pixels it processes, and it uses this value to exit the pipeline early for occluded pixels. The size of the tiles may vary from architecture to architecture, but  $8 \times 8$  pixels is a common size [902]. For these techniques, the triangle traversal visits a tile at a time. Imagine a triangle being rasterized, and that a particular tile is visited. In order to test whether the triangle is occluded inside this tile, we need to compute the minimum  $z$ -value,  $z_{\min}^{\text{tri}}$ , on the triangle. If  $z_{\min}^{\text{tri}} > z_{\max}$ , it is guaranteed that the triangle is occluded by previously rendered geometry in that tile, and all pixel shader processing can be avoided. In practice, we cannot afford to compute the exact value of  $z_{\min}^{\text{tri}}$ , so instead, a conservative estimate is computed. Several different ways to compute  $z_{\min}^{\text{tri}}$  are possible, each with its own advantages and disadvantages:

1. The minimum  $z$ -value of the three vertices of a triangle can be used to test against the  $z_{\max}$ . This is not very accurate, but has little overhead.
2. Evaluate the  $z$ -value at the four corners of a tile using the plane equation of the triangle, and use the minimum of those.

Best culling performance is obtained if these two strategies are combined. This is done by taking the larger of the two  $z_{\min}$ -values. Using  $Z_{\max}$ -culling means that both pixel shader processing and testing against the  $Z$ -buffer can be avoided for most occluded pixels on rasterized primitives, and so a significant performance boost can be expected. If the tile or pixel is determined not to be occluded, then processing continues as normal. It should be noted that the description here use a hierarchical  $Z$ -buffer with only two levels (the real  $Z$ -buffer, and the level at, say,  $8 \times 8$  pixel tiles). However, it is likely that GPUs are using hierarchical  $Z$ -buffers with more than two levels.

The other technique is called  $Z_{\min}$ -culling, and the idea is to store  $z_{\min}$  of all the pixels in a tile [13]. There are two uses for this. First, it can be used to support different depth tests. For the  $Z_{\max}$ -culling method, we assumed a “less than” depth test. However, it would be beneficial if culling could be used with other depth tests as well, and if  $z_{\min}$  and  $z_{\max}$  are both available, all depth tests can be supported in this culling process. Second, it can be used to avoid  $Z$ -buffer reads. If a triangle being rendered is definitely in front of all previously rendered geometry, per-pixel depth testing is unnecessary. In some cases,  $Z$ -buffer reads can be completely avoided, which further boosts performance.

ATI’s implementation of this type of occlusion culling is called *HyperZ* [1065], NVIDIA’s is called the *Lightspeed Memory Architecture* (LMA). As always, occlusion culling benefits from rendering front to back.

This occlusion culling hardware can be of great benefit to multipass algorithms (see Section 7.9.1). The first pass establishes the  $z$ -values and the corresponding  $z_{\max}$ -values. Succeeding passes use all the  $z_{\max}$ -values, which gives almost perfect occlusion culling for hidden triangles. Given that pixel shaders are often expensive to evaluate, it can be profitable to render an extra pass at the beginning purely to establish the  $Z$ -buffer and  $z_{\max}$ -values in advance.

If a tile survives  $Z$ -culling, there is still another test that a GPU can apply per fragment, called *early-Z* [879, 1108]. The pixel shader program is analyzed in the same way as for  $Z$ -culling. If it does not modify the  $z$ -depth, and the rendering state is set for a typical  $Z$ -buffer test, then early- $Z$  can be performed. Before the execution of the pixel shader program, the fragment’s precise  $z$ -depth value is computed and compared to the  $Z$ -buffer’s stored value. If the fragment is occluded, it is discarded at this point. This process thus avoids unnecessary execution of the pixel shader program hardware. The early- $Z$  test is often confused with  $Z$ -culling, but it is performed by entirely separate hardware; either technique can be used without the other.

Another technique with a similar name, and similar intent, is the “early z pass” method. This is a software technique, the idea being to render geometry once and establish the Z-buffer depths. See Section 7.9.2.

### 18.3.8 PCU: Programmable Culling Unit

As seen in the previous section,  $Z$ -culling has to be disabled by the hardware if the fragment shader writes out a custom depth per pixel. Rendering algorithms such as relief mapping and evaluating the sphere equation inside a quad are two examples where the shader modifies the  $z$ -depth. Blythe [123] mentions that getting good performance relies on being able to predict the shader output (on a tile basis). One reason why a fully programmable output merger, i.e., blending, depth testing, stencil testing, etc, was not included in DirectX 10 is that  $Z$ -culling is disabled when the shader writes to the depth, for example.

The programmable culling unit (PCU) [513] solves this problem, but is more general than that. The core idea is to run parts of the fragment shader over an entire tile of pixels, and determine, for example, a lower bound on the  $z$ -values, i.e.,  $z_{\min}^{\text{tri}}$  (Section 18.3.7). In this example, the lower bound can be used for  $Z$ -culling. Another example would be to determine if all the pixels in a tile are completely in shadow, i.e., totally black. If this is true, then the GPU can avoid executing large parts (or sometimes the entire) fragment shader program for the current tile.

To compute these conservative bounds (e.g.,  $z_{\min}^{\text{tri}}$ ), the fragment shader instructions are executed using interval arithmetic instead of floating-point numbers. An interval,  $\hat{a} = [\underline{a}, \bar{a}]$ , is simply an interval of numbers, starting from  $\underline{a}$  to  $\bar{a}$ . An example is  $\hat{a} = [-1, 2]$ , which is the entire set of numbers from  $-1$  to  $2$ . Arithmetic operations can also be defined to operate on intervals [900]. Addition of two intervals results in an interval including all possible combinations from the two interval operands. This can be expressed as:  $\hat{a} + \hat{b} = [\underline{a} + b, \bar{a} + \bar{b}]$ . As an example,  $[-1, 2] + [4, 5] = [3, 7]$ .

If the fragment shader program contains a KIL instruction, all instructions that depend on this KIL are extracted into a *cull shader program*, which will be executed once for the entire tile. All arithmetic operations work on intervals in this cull shader, and all varying operands are intervals as well. When the interval operand of the KIL instruction has been computed, it is known whether all fragments in the tile can be killed without executing the fragment shader for each fragment in the tile. Before starting the execution of the cull shader, the varying input has to be converted into intervals, and this is done using techniques similar to the one used for computing  $z_{\min}^{\text{tri}}$  in the previous section.

As a simple example, imagine that the shader program computes diffuse shading as  $d = \mathbf{l} \cdot \mathbf{n}$ . It then tests this dot product to see if it is less than

zero (facing away from the light). If so, the program sends a KIL command, which terminates the fragment if the dot product is less than zero. Assume that the interval result of the dot product is  $[-1.2, -0.3]$ . This means that all possible combinations of the light vectors,  $\mathbf{l}$ , and the normals,  $\mathbf{n}$ , for the fragments in the current tile evaluate to a negative dot product. The tile is then culled because the diffuse shading is guaranteed to be zero.

Assume that the tile size is  $8 \times 8$  pixels, and that the cull shader program uses four<sup>7</sup> times [513] as many instructions as the fragment shader program. This is so because evaluating the cull shader is done using interval arithmetic, which is more costly than using plain floating-point arithmetic. In this case, it is possible to get a  $16 \times$  speedup (in theory) for tiles that can be culled, since the cull shader is only evaluated once for a tile and then ends the execution. For tiles that cannot be culled, there is actually a slight slowdown, since you need to execute the PCU's cull shader program once, and then the normal  $8 \times 8$  pixel shader programs. Overall the performance gains are significant, with a 1.4–2.1 times speedup. Currently there are no commercial implementations available, but the PCU solves an important problem. It allows programmers to use more general shader programs (e.g., modified  $z$ -depth) while maintaining performance. A research implementation shows that the size of a simple fragment shader unit increases by less than 10% in terms of gates. It should be straightforward to add PCU hardware to a unified shader architecture.

## 18.4 Case Studies

In this section, three different graphics hardware architectures will be presented. The Xbox 360 is described first, followed by the PLAYSTATION® 3 system architecture. Finally, an architecture that targets mobile devices, called *Mali*, is presented.

### 18.4.1 Case Study: Xbox 360

The Xbox 360 is a game console built by Microsoft with a graphics hardware solution by ATI/AMD [268]. It is built around the memory architecture illustrated in Figure 18.15. The main GPU chip also acts as a memory controller (often called the *north bridge*), so the CPU accesses the system memory through the GPU chip. So, in a sense this is a kind of a unified memory architecture (UMA). However, as can be seen, there is also memory that only the GPU can access.

---

<sup>7</sup>The exact number is somewhere between two and four per instruction. However, the cull shader program is often shorter than the actual fragment shader program.

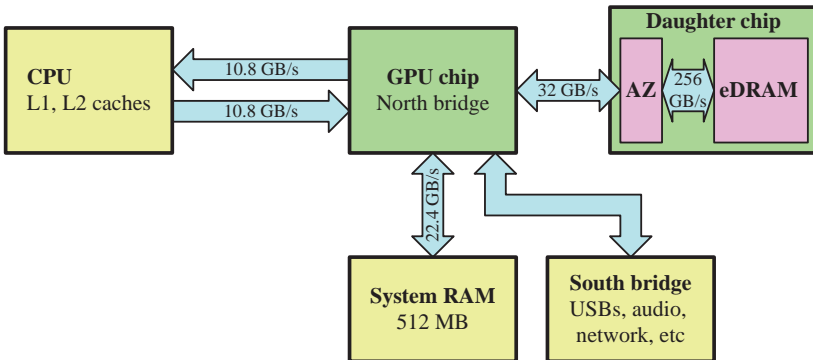


**Figure 18.15.** Xbox 360 memory architecture.

In this overview of the Xbox 360 architecture, we will focus on the GPU and its daughter chip. One design choice in the Xbox 360 was to use *embedded DRAM* (eDRAM) for the frame buffers, and this memory is embedded in a separate daughter chip. The main point of this design is that the daughter chip also has some extra logic, here called *AZ*, which takes care of all alpha and depth testing, and related operations. Hence, eDRAM is sometimes called “intelligent” RAM, because it can actually do something more than just store content. Instead of accessing the frame buffer from main memory, this is accessed through the eDRAM with AZ logic, and this gives high performance at a low cost. The eDRAM has  $10 \times 1024^2$  bytes, i.e., 10 MB of storage. In addition, the Xbox 360 is designed around the concept of a unified shader architecture, which will be described later.

A block diagram of the Xbox 360 GPU can be found in Figure 18.16. Rendering commences when the *command processor* starts reading commands from the main memory. This can be either the start of a rendering batch, or state changes. Drawing commands are then forwarded to the *vertex grouper and tessellator* (VGT) unit. This unit may receive a stream of vertex indices, which it groups into primitives (e.g., triangles or lines). This unit also acts as a vertex cache after transforms, and hence already-transformed vertices may be reused. In addition, tessellation can be performed here, as described in Section 13.6.

The instruction set for the Xbox is a superset of SM 3.0 (not a full SM 4.0), and its vertex and pixel shader languages have converged, i.e., they share the same common core. For this reason, a single shader element can be designed and implemented that can execute both vertex and pixel shader programs. This is the main idea of a *unified shader architecture*. In the Xbox 360, shader execution is always done on vectors of 64 vertices

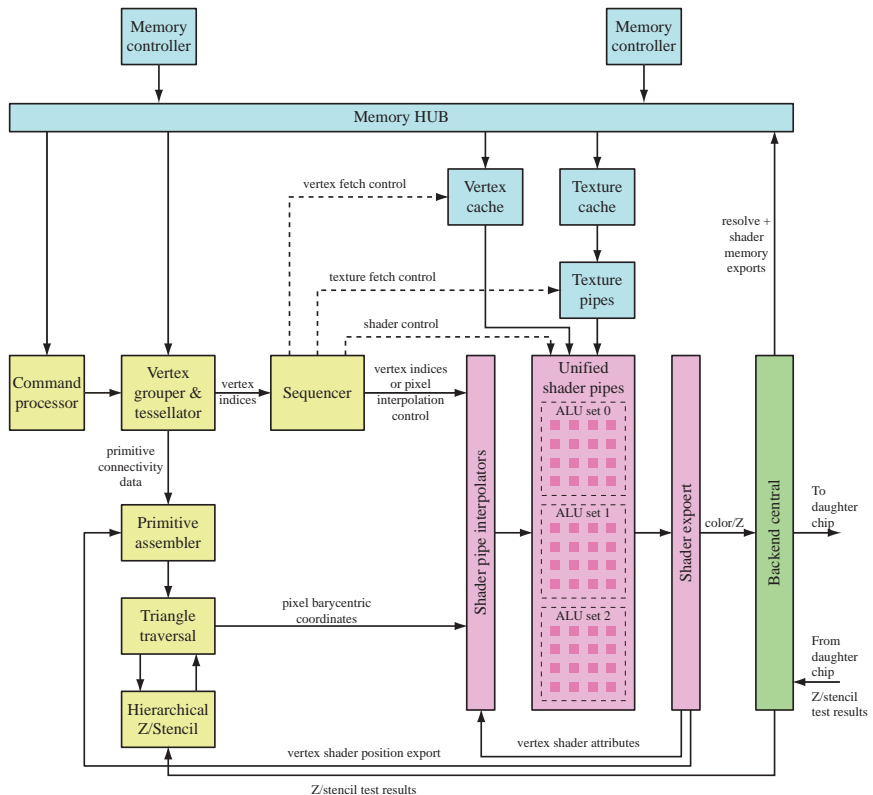


**Figure 18.16.** Block diagram of the Xbox 360 graphics processor.

or pixels. Each such vector is executed as a *thread*, and up to 32 vertex threads or 64 pixel threads can be active at a time. So while a thread is waiting for, say, a texture fetch from memory, another thread can be scheduled for execution on the unified shader pipes. When the requested memory content is available, the previous thread can be switched back to active, and execution can continue. This greatly helps to hide latency, and it also provides for much better load balancing than previous non-unified architectures. As an example of this, consider a typical GPGPU application that renders a screen-size quad with long pixel shader programs. In this case, few shader cores will be used for vertex computations in the beginning, and then all shader cores will be used for per-pixel computations. Note also that all execution is performed on 32-bit floating point numbers, and that all threads share a very large register file containing registers for the shader computations. For the Xbox 360, there are 24,576 registers. In general, the more registers a shader needs, the fewer threads can be in flight at a

time. This concept will be discussed in detail in the next case study, on the PLAYSTATION® 3 system.

The *sequencer* (Figure 18.16) receives vertex indices from the VGT. Its core task is to schedule threads for execution. Depending on what needs to be processed, this is done by sending vertex and pixel vectors to units such as the vertex cache, the texture pipes, or the unified shader pipes.

In the unified shader pipes unit, there are three sets of *ALUs* (*arithmetic logic units*), each consisting of 16 small shader cores. One such set of cores can execute one operation on a vertex vector (64 entries) or pixel vector (64 entries) over four clock cycles. Each shader core can execute one vector operation and one scalar operation per cycle.

After a vertex or pixel shader program has been executed, the results are forwarded to the *shader export*. If a vertex shader has been executed, all the outputs, such as transformed vertex coordinates and texture coordinates, are “exported” back into the *primitive assembler*. The primitive assembler obtains how a triangle is connected from the VGT (through a deep FIFO), and “imports” the transformed vertices from the shader export unit. Note that FIFO buffers are there to avoid stalls during operations with long latency. Then it performs triangle setup, clipping, and viewport culling. The remaining information is then forwarded to the *triangle traversal* unit, which operates on  $8 \times 8$  tiles. The reason to work with tiles is that texture caching is more efficient, and buffer compression and various Z-culling techniques can be used. Tiles are sent to the *hierarchical Z/stencil* unit, where Z-culling (see Section 18.3.7) and early stencil rejection are done. This unit stores 11 bits for depth ( $z_{\max}$ ) and one bit for stencil per 16 samples in the depth buffer. Each quad is tested against the  $z_{\max}$  for occlusion, and up to 16 quads can be accepted/rejected per cycle. Surviving  $2 \times 2$  pixels quads are sent back to the triangle traversal unit. Since the ALU sets can handle a vector of 64 pixels at a time, the triangle traversal unit packs 16 quads (i.e.,  $16 \times 2 \times 2$ ) into a vector. Note that there can be quads from different primitives in a vector. A similar process is used in the PLAYSTATION® 3 system, and will be explained further in that section.

A vector of quad fragments with their barycentric coordinates is then sent to the *shader pipe interpolators*, which perform all vertex attribute interpolation, and place these values into the register file of the unified shader.

The texture cache is a 32 kB four-way set associative cache that stores uncompressed texture data. The *texture pipes* retrieve texels from the texture cache, and can compute 16 bilinear filtered samples per cycle. So, trilinear mipmapping then runs at half the speed, but this still amounts to eight trilinear filtered samples per clock. Adaptive anisotropic filtering is also handled here.

When the unified shaders have executed a pixel shader program for a 64 entry vector, it “exports” the pixel shader outputs, which typically consist of color. Two quads ( $2 \times 2 \times 2$  pixels) can be handled per cycle. Depth can also be exported (but this is seldom done), which costs an extra cycle. The *backend central* groups pixel quads and reorders them to best utilize the eDRAM bandwidth. Note that at this point, we have “looped through” the entire architecture. The execution starts when triangles are read from memory, and the unified shader pipes executes a vertex shader program for the vertices. Then, the resulting information is rerouted back to the setup units and then injected into the unified shader pipes, in order to execute a pixel shader program. Finally, pixel output (color + depth) is ready to be sent to the frame buffer.

The daughter chip of the Xbox 360 performs merging operations, and the available bandwidth is 32 GB/s. Eight pixels, each with four samples, can be sent per clock cycle. A sample stores a representation of a 32-bit color and uses lossless Z-compression for depth. Alternatively, 16 pixels can be handled if only depth is used. This can be useful for shadow volumes and when rendering out depth only, e.g., for shadow mapping or as a pre-pass for deferred shading. In the daughter chip, there is extra logic (called “AZ” in Figure 18.15) for handling alpha blending, stencil testing, and depth testing. When this has been done, there are 256 GB/s available directly to the DRAM memory in the daughter chip.

As an example of the great advantage of this design, we consider alpha blending. Usually, one first needs to read the colors from the color buffer, then blend the current color (generated by a pixel shader), and then send it back to the color buffer. With the Xbox 360 architecture, the generated color is sent to the daughter chip, and the rest of the communication is handled inside that chip. Since depth compression also is used and performed in the daughter chip, similar advantages accrue.

When a frame has been rendered, all the samples of the pixels reside in the eDRAM in the daughter chip. The back buffer needs to be sent to main memory, so it can be displayed onscreen. For multi-sampled buffers, the downsampling is done by the AZ unit in the daughter chip, before it is sent over the bus to main memory.

## 18.4.2 Case Study: The PLAYSTATION<sup>®</sup> 3 System

The PLAYSTATION 3 system<sup>8</sup> is a game system built by Sony Computer Entertainment. The architecture of the PLAYSTATION 3 system can be seen in Figure 18.17. The Cell Broadband Engine<sup>TM</sup> was developed by

---

<sup>8</sup>“PlayStation,” “PLAYSTATION,” and the “PS” Family logo are registered trademarks and “Cell Broadband Engine” is a trademark of Sony Computer Entertainment Inc. The “Blu-ray Disc” name and logo are trademarks.

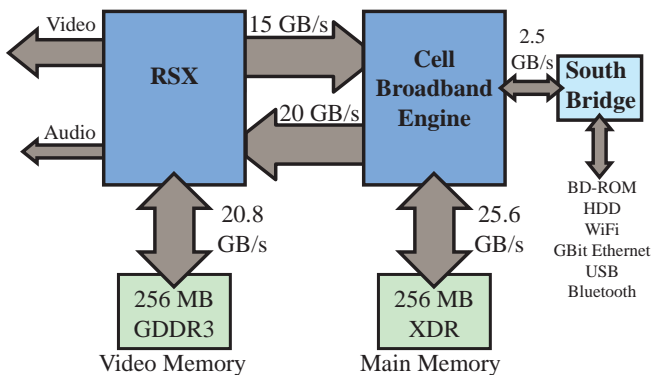


**Figure 18.17.** PLAYSTATION 3 architecture. (*Illustration after Perthuis [1002].*)

Sony Computer Entertainment in partnership with IBM and Toshiba, and is the CPU (central processing unit) of the system. The RSX<sup>®</sup>, developed by NVIDIA, serves as the GPU (graphics processing unit).

As can be seen, the memory of the PLAYSTATION 3 system is split into two separate pools. Main memory consists of 256MB of Rambus-developed XDR memory, connected to the Cell Broadband Engine. The RSX has its own pool of 256 MB of GDDR3 memory. Although the GDDR3 memory operates at a higher frequency, the XDR memory operates at a higher bandwidth due to its ability to transfer eight bits over each pin in a clock cycle (as opposed to two bits for GDDR3). The Cell Broadband Engine and RSX can access each other's memory over the FlexIO<sup>TM</sup> interface (also developed by Rambus) connecting the two, although the full bandwidth can only be used when the RSX is accessing main memory. The Cell Broadband Engine accesses video memory at lower data rates, especially when reading from video memory. For this reason, PLAYSTATION 3 application developers try to have the Cell Broadband Engine read from video memory as little as possible. The south bridge chip, also connected to the Cell Broadband Engine via FlexIO, is used to access a variety of I/O devices. These include Blu-Ray Disc and magnetic drives, wireless game controllers, and network access devices. Video and audio outputs are connected to the RSX.

### *The PLAYSTATION 3<sup>®</sup> GPU: The RSX<sup>®</sup>*

We will start with a description of the GPU. The RSX is essentially a modified GeForce 7800. The block diagram of the GPU is shown in Figure 18.18.

The geometry stage of the PLAYSTATION 3 system, located on the top half of Figure 18.18, supports programmable vertex shaders. It has

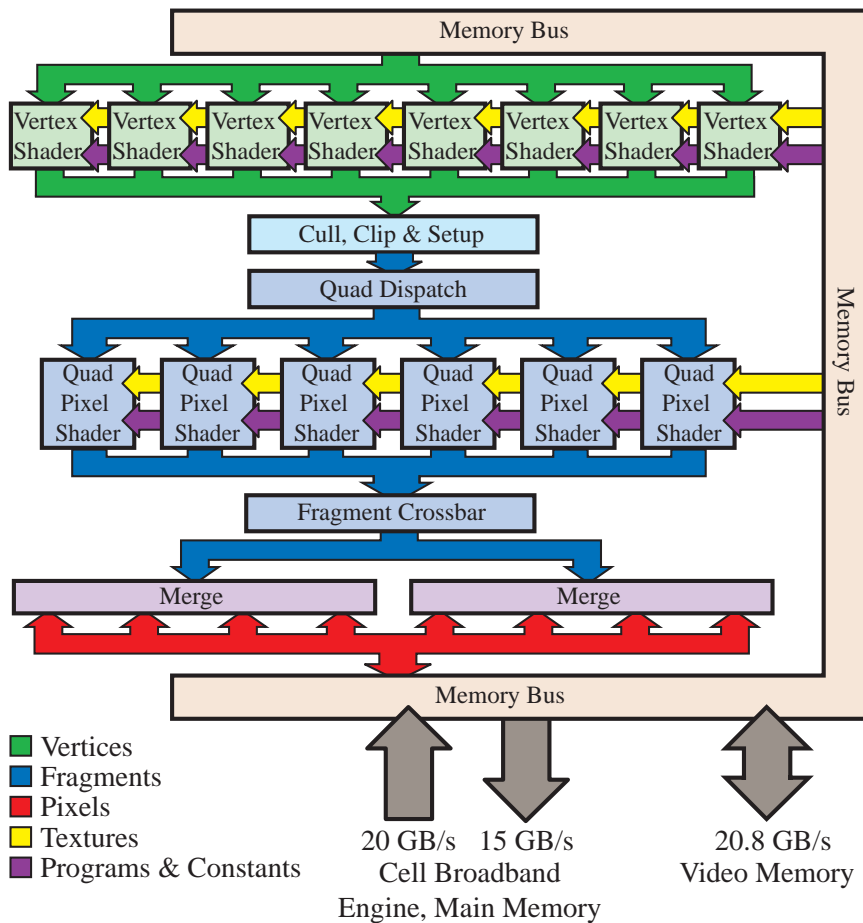


Figure 18.18. RSX architecture.

eight vertex shader (geometry) units that execute programs in parallel on multiple vertices, enabling a throughput of eight instructions (including compound multiply-add instructions) per clock. These units support vertex shader model 3.0 (see Section 3.3.1), and have access to the same constants and textures.

There are four caches in the geometry stage, one for textures and three for vertices. The vertex shader units share a small (2 kilobytes) L1 texture cache. Any misses go to the L2 texture cache, which is shared between the vertex and pixel shader units. The vertex cache before the vertex shader units is called *Pre T&L* (*transform and lighting*), and the one immediately after the vertex shader units is called *Post T&L*. Pre T&L has 4 kilobytes of

storage, and Post T&L has, in practice, storage for roughly 24 vertices. The task of the Pre T&L vertex cache is to avoid redundant memory fetches. When a vertex that is needed for a triangle can be found in the Pre T&L vertex cache, the memory fetch for that vertex data can be avoided. The Post T&L vertex cache, on the other hand, is there to avoid processing the same vertex with the vertex shader more than once. This can happen because a vertex is, on average, shared by six other triangles. Both these caches can improve performance tremendously.

Due to the memory requirements of a shaded vertex located in the Post T&L vertex cache, it may take quite some time to fetch it from that cache. Therefore, a *Primitive Assembly* cache is inserted after the Post T&L vertex cache. This cache can store only four fully shaded vertices, and its task is to avoid fetches from the Post T&L vertex cache. For example, when rendering a triangle strip, two vertices from the previous triangle are used, along with another new vertex, to create a new triangle. If those two vertices already are located in the Primitive Assembly cache, only one vertex is fetched from the Post T&L. It should be noted, however, that as with all caches, the hit rate is not perfect, so when the desired data is not in the cache, it needs to be fetched or recomputed.

When all the vertices for a triangle have been assembled in the Primitive Assembly cache, they are forwarded to the cull, clip, and setup block. This block implements clipping, triangle setup, and triangle traversal, so it can be seen as straddling the boundary between the geometry and rasterization stages. In addition, the cull, clip, and setup block also implements two types of culling: backface culling (discussed in Section 14.2), and Z-culling (described in Section 18.3.7). Since this block generates all the fragments that are inside a triangle, the PLAYSTATION 3 system can be seen as a sort-last fragment architecture when only the GPU is taken into consideration. As we shall see, usage of the Cell Broadband Engine can introduce another level of sorting, making the PLAYSTATION 3 system a hybrid of sort-first and sort-last fragment.

Fragments are always generated in  $2 \times 2$ -pixel units called *quads*. All the pixels in a quad must belong to the same triangle. Each quad is sent to one of six quad pixel shader (rasterizer) units. Each of these units processes all the pixels in a quad simultaneously, so these units can be thought of as comprising 24 pixel shader units in total. However, in practice, many of the quads will have some invalid pixels (pixels that are outside the triangle), especially in scenes composed of many small triangles. These invalid pixels are still processed by the quad pixel shader units, and their shading results are discarded. In the extreme case where each quad has one valid pixel, this inefficiency can decrease pixel shader throughput by a factor of four. See McCormack et al.'s paper [842] for different rasterization strategies.

The pixel shader microcode is arranged into *passes*, each of which contains a set of computations that can be performed by a quad pixel shader unit in one clock cycle. A pixel shader will execute some number of passes, proportional to the shader program length. A quad pixel shader unit contains a texture processor that can do one texture read operation (for the four pixels in a quad), as well as two arithmetic processors, each of which can perform up to two vector operations (totaling a maximum vector width of four) or one scalar operation. Possible vector operations include multiply, add, multiply-add, and dot product. Scalar operations tend to be more complex, like reciprocal square root, exponent, and logarithm. There is also a branch processor that can perform one branch operation. Since there are many scheduling and dependency restrictions, it is not to be expected that each pass will fully utilize all the processors.

The pixel shader is run over a batch of quads. This is handled by the quad dispatch unit, which sends the quads through the quad pixel shader units, processing the first pixel shader pass for all the quads in a batch. Then the second pass is processed for all quads, and so on, until the pixel shader is completed. This arrangement has the dual advantages of allowing very long pixel shaders to be executed, and hiding the very long latencies common to texture read operations. Latency is hidden because the result of a texture read for a given quad will not be required until the next pass, by which time hundreds of quads will have been processed, giving the texture read time to complete.

The quad's state is held in a buffer. Since the state includes the values of temporary variables, the number of quads in a batch is inversely proportional to the memory required to store the state of the temporary registers. This will depend on the number and precision of the registers, which can be specified as 32-floats or 16-bit half floats.

Batches are typically several hundred pixels in size. This can cause problems with dynamic flow control. If the conditional branches do not go the same way for all the pixels in the batch, performance can degrade significantly. This means that dynamic conditional branching is only efficient if the condition remains constant over large portions of the screen. As discussed in Section 3.6, processing pixels in quads also enables the computation of derivatives, which has many applications.

Each quad pixel shader unit has a 4 kilobyte L1 texture cache that is used to provide texel data for texture read operations. Misses go to the L2 texture cache, which is shared between the vertex and pixel shader units. The L2 texture cache is divided into 96 kilobytes for textures in main memory, and 48 kilobytes for textures in video memory. Texture reads from main memory go through the Cell Broadband Engine, resulting in higher latency. This latency is why more L2 cache space is allocated for main memory. The RSX<sup>®</sup> also supports texture swizzling to improve cache

coherence, using the pattern shown in Figure 18.12. See Section 18.3.1 for more information on texture caching.

After the pixel shader is run, the final color of each fragment is sent to the fragment crossbar, where the fragments are sorted and distributed to the merge units, whose task it is to merge the fragment color and depth with the pixel values in the color and Z-buffer. Thus it is here that alpha blending, depth testing, stencil testing, alpha testing, and writing to the color buffer and the Z-buffer occur. The merge units in the RSX can be configured to support up to  $4 \times$  multisampling, in which case the color and Z-buffers will contain multiple values for each pixel (one per sample).

The merge units also handle Z-compression and decompression. Both the color buffer and Z-buffer can be configured to have a tiled memory architecture. Either buffer can be in video or main memory, but in practice, most games put them in video memory. Tiling is roughly similar to texture swizzling, in that memory ordering is modified to improve coherence of memory accesses. However, the reordering is done on a coarser scale. The exact size of a tile depends on the buffer format and whether it is in video or main memory, but it is on the order of  $32 \times 32$  pixels.

### *The PLAYSTATION® 3 CPU: The Cell Broadband Engine™*

While the RSX® is fundamentally similar to GPUs found in other systems, the Cell Broadband Engine is more unusual and is perhaps a sign of future developments in rendering systems. The architecture of the Cell Broadband Engine can be seen in Figure 18.19.

Besides a conventional PowerPC processor (the *PowerPC Processor Element*, or *PPE*), the Cell Broadband Engine contains eight additional *Syn-*

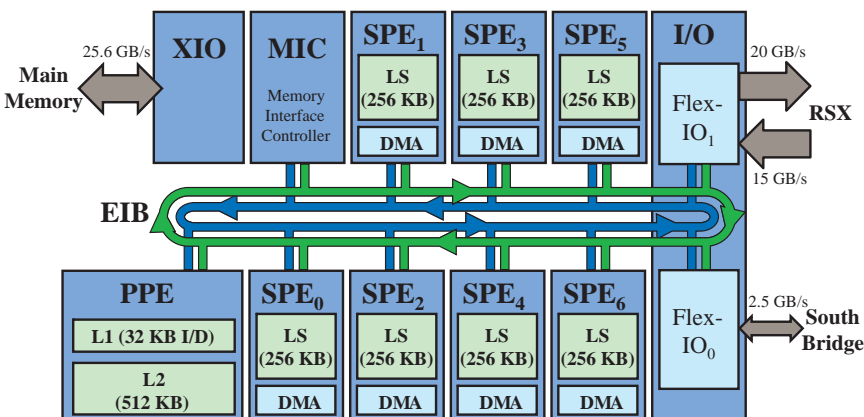


**Figure 18.19.** Cell Broadband Engine architecture. (*Illustration after Perthuis [1002].*)

*ergistic Processor Element (SPE)* cores. Each SPE contains a memory controller and *Synergistic Processor Unit (SPU)*. The SPE is commonly referred to as an SPU, but this acronym properly refers only to the computational core of the SPE. In the Cell Broadband Engine processors used in the PLAYSTATION 3 system, one of the SPEs has been disabled, so only seven can be used.<sup>9</sup> The SPEs are different from processors that are designed to run general-purpose code. Each SPE has 256 kilobytes of local storage that is directly addressed by the processor. Main memory, video memory, or the local storage of other SPEs cannot be directly addressed by the SPE. The only way for an SPE to process data stored at such locations is to transfer it into its local storage via *DMA (direct memory access)*. Each SPE is a “pure SIMD” processor. All registers are 16 bytes in width; there are no scalar registers or scalar instruction variants. All memory accesses are 16 bytes wide and must be to addresses that are aligned to 16 bytes. Smaller or unaligned accesses are emulated via multiple instructions.

The SPEs were designed in this way because their role is not to run general-purpose code—that is the role of the PPE. The SPEs are intended to be used for computation-intensive tasks while the PPE performs more general code and orchestrates the activities of the SPEs. An SPE can access all of its local storage at full speed without any cache misses (there is no cache) or other penalties. A new memory access can be initiated at a throughput of one per clock cycle, with its results available five clock cycles later. An SPE can also perform multiple DMA transfers concurrently with processing. This enables an SPE to efficiently perform localized computations on large data sets by working on subsets of data. While the current subset is being processed, the next subset is being transferred in, and the results of processing the previous subset are being transferred out.

The SPE can issue two instructions per clock, one of which is an arithmetic instruction, while the other is a “support” instruction such as load, store, branch, data shuffle, etc. The execution of all instructions (except double-precision floating point operations) is fully pipelined, so a similar instruction can be issued again on the next clock. To enable operation at high frequencies, the execution units are highly pipelined, so that many commonly used instructions have six-clock latencies. However, the large register file (128 registers) means that techniques such as loop unrolling and software pipelining can be used extensively to hide these latencies. In

---

<sup>9</sup>This is a common maneuver to improve yield in high-volume chips. The advantage is that if any one of the eight SPEs has a defect, the chip is still viable. Unfortunately, for compatibility reasons, this means that even a Cell Broadband Engine with no defects must have one of its SPEs disabled to be used in the PLAYSTATION 3 system. It should be noted that one additional SPE is reserved for the use of the operating system, leaving six for application use.

practice, highly efficient operation can be achieved for most computation-intensive tasks.

A common use for the SPEs in PLAYSTATION 3 games is to perform rendering-related tasks. For example, Sony Computer Entertainment's EDGE library performs triangle culling and vertex skinning. Other vertex operations are often offloaded from the RSX® onto the SPEs. The SPEs are not restricted by the "one vertex at a time" model of the vertex shader on the RSX, so it can perform other types of processing. This can include computations similar to those performed by a GPU geometry shader, as well as more general processing. For this reason, the SPEs can be seen as implementing part of the geometry stage. The results of these computations will need to be sorted to keep them in the original order, which makes the PLAYSTATION 3 system a hybrid sort-first (for the SPEs) / sort-last fragment (for the RSX) architecture.

The *EIB* (Element Interconnect Bus) is a ring bus that connects the PPE, the SPEs, and the memory and I/O controllers. It is an extremely fast bus, capable of sustaining over 200 gigabytes per second in bandwidth.

The PLAYSTATION 3 system is an interesting case because of the inclusion of the Cell Broadband Engine. GPUs have been becoming more "CPU-like" for several years, as programmable shaders have become more general. The Cell Broadband Engine is an example of a CPU that is somewhat "GPU-like" due to its inclusion of heterogeneous processing units optimized for localized computations.

The Game Developers Conference 2005 presentation by Mallinson and DeLoura [812] contains additional interesting information about the Cell Broadband Engine processor. Full Cell Broadband Engine documentation is available on IBM's website [165].

### 18.4.3 Case Study: Mali 200

In this section, the Mali 200 architecture from ARM will be described. This architecture is different from the Xbox 360 and the PLAYSTATION® 3 system in two major ways. First, the target is not desktop PCs nor game consoles, but rather *mobile* devices, such as mobile phones or *portable* game consoles. Since these are powered by batteries, and you want long use time on the battery, it is important to design an energy-efficient architecture, rather than just one with high performance. In the mobile context, the focus is therefore both on energy efficiency and on performance. Second, this architecture is what we call a *tiling* architecture, and this has certain important implications for the mobile context. The mobile phone is now one of the most widespread devices with rendering capabilities [13], and the potential impact of graphics on these is therefore huge. The Mali 200 architecture is fully compliant with the OpenGL ES 2.0 API, which has

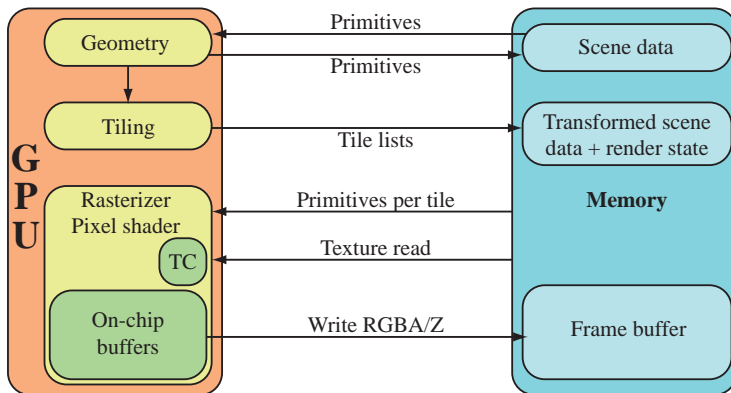


**Figure 18.20.** Overview of the Mali 200 tiling architecture, targeted toward mobile devices. The TC block is the texture cache.

been designed specifically for handheld devices. This API supports both programmable vertex and pixel shaders using GLSL (OpenGL Shading Language).

A tile in this case is simply a  $16 \times 16$  pixel region<sup>10</sup> of the frame buffer. The major difference with this type of architecture is that a per-pixel processing unit (including rasterizer, pixel shaders, blending, etc.) works on only a single tile at a time, and when this tile is finished, it will never be touched again during the current frame. While this may sound awkward, it actually gives several advantages, as explained later. The first tiling architecture was *Pixel-Planes 5* [368], and that system has some high-level similarities to the Mali 200. Other tiling architectures include the PowerVR-based KYRO II and MBX/SGX GPUs from Imagination Technologies.

The core idea of tiling architectures is to first perform all geometry processing, so that the screen-space position of each rendering primitive is found. At the same time, a *tile list*, containing pointers to all the primitives overlapping a tile, is built for each tile in the frame buffer. When this sorting has been done, the set of primitives overlapping a tile is known, and therefore, one can render all the primitives in a tile and output the result to an external frame buffer. Then the next tile is rasterized, and so on, until the entire frame has been rendered. Conceptually, this is how every tiling architecture works, and hence, these are sort-middle architectures.

An outline of the architecture is presented in Figure 18.20. As can be seen, the rendering primitives are first read from memory, and geometry processing with programmable vertex shaders commences. In most GPUs,

<sup>10</sup>Other tile sizes may be used in other tiling architectures.

the output from the vertex shader is forwarded to the rasterizer stage. With the Mali 200, this output is written back to memory. The vertex processing unit is heavily pipelined, and this pipeline is single-threaded, allowing that processing of one vertex to start every cycle.

The *Tiling* unit (Figure 18.20) performs backface and viewport culling first, then determines which tiles a primitive overlaps. It stores pointers to these primitives in each corresponding tile list. The reason it is possible to process one tile at a time is that all primitives in the scene need to be known before rasterization can begin. This may be signaled by requesting that the front and back buffers be swapped. When this occurs for a tiling architecture, all geometry processing is basically done, and the results are stored in external memory. The next step is to start per-pixel processing of the triangles in each tile list, and while this is done, the geometry processing can commence working on the next frame. This processing model implies that there is more latency in a tiling architecture.

At this point, fragment processing is performed, and this includes triangle traversal (finding which pixels/samples are inside a triangle), and pixel shader execution, blending, and other per-pixel operations. The single most important feature of a tiling architecture is that the frame buffer (including color, depth, and stencil, for example) for a single tile can be stored in very fast on-chip memory, here called the *on-chip tile buffer*. This is affordable because the tiles are small ( $16 \times 16$  pixels). Bigger tile sizes make the chip larger, and hence less suitable for mobile phones. When all rendering has finished to a tile, the desired output (usually color, and possibly depth) of the tile is copied to an off-chip frame buffer (in external memory) of the same size as the screen. This means that all accesses to the frame buffer during per-pixel processing is essentially for free. Avoiding using the external buses is highly desirable, because this use comes with a high cost in terms of energy [13]. This design also means that buffer compression techniques, such as the ones described in Section 18.3.6, are of no relevance here.

To find which pixels or samples are inside a triangle, the Mali 200 employs a hierarchical testing scheme. Since the triangle is known to overlap with the  $16 \times 16$  pixel tile, testing starts against the four  $8 \times 8$  pixel subtiles. If the triangle is found not to overlap with a subtitle, no further testing, nor any processing, is done there. Otherwise, the testing continues down until the size of a subtitle is  $2 \times 2$  pixels. At this scale, it is possible to compute approximations of the derivatives on any variable in the fragment shader. This is done by simply subtracting in the  $x$ - and  $y$ -directions. The Mali 200 architecture also performs hierarchical depth testing, similar to the  $Z$ -max culling technique described in Section 18.3.7, during this hierarchical triangle traversal. At the same time, hierarchical stencil culling and alpha culling are done. If a tile survives  $Z$ -culling, Mali computes individ-

ual fragment  $z$ -depths and performs early- $Z$  testing as possible to avoid unnecessary fragment processing.

The next step is to start with per-fragment processing, and the Mali 200 can have 128 fragments in flight at the same time. This is a common technique to hide the latency in the system. For example, when fragment 0 requests a texel, it will take awhile before that data is available in the texture cache, but in the meantime, another 127 pixels can request access to other texels, as well. When it is time to continue processing fragment 0, the texel data should be available.

To reduce texture bandwidth, there is a texture cache with hardware decompression units for ETC [1227] (see Section 6.2.6), which is a texture compression algorithm. ETC is part of OpenGL ES 2.0. Also, as another cost-efficient technique, compressed textures are actually stored in compressed form in the cache, as opposed to decompressing them and then putting the texels in the cache. This means that when a request for a texel is made, the hardware reads out the block from the cache and then decompresses it on the fly. Most other architectures appear to store the texels in uncompressed form in the cache.

The Mali 200 architecture was designed from the ground up with screen-space antialiasing in mind, and it implements the rotated-grid supersampling (RGSS) scheme described on page 128, using four samples per pixel. This means that the native mode for is  $4\times$  antialiasing. Another important consequence of a tiling architecture is that screen-space antialiasing is more affordable. This is because filtering is done just before the tile leaves the GPU and is sent out to the external memory. Hence, the frame buffer in external memory needs to store only a single color per pixel. A standard architecture would need a frame buffer to be four times as large (which gives you less memory for textures, etc.). For a tiling architecture, you need to increase only the on-chip tile buffer by four times, or effectively use smaller display tiles (half the width and height of a processing tile).

The Mali 200 can also selectively choose to use either multisampling or supersampling on a batch of rendering primitives. This means that the more expensive supersampling approach, where you execute the pixel shader for each sample, can be used when it is really needed. An example would be rendering a textured tree with alpha mapping (see Section 6.6), where you need high quality sampling to avoid disturbing artifacts. For these primitives, supersampling could be enabled. When this complex situation ends and simpler objects are to be rendered, one can switch back to using the less expensive multisampling approach. In addition, there is a  $16\times$  antialiasing mode as well, where the contents of  $2\times 2$  pixels, each with four samples, are filtered down into a single color before they are written to the external frame buffer. See Figure 18.21 for an example of an antialiased rendering using the Mali 200 architecture.



**Figure 18.21.** Two images rendered using the Mali 200 architecture for mobile devices, using the OpenGL ES 2.0 API. Rotated-grid supersampling (with four samples per pixel) is used to increase the image quality, and the antialiasing effect can be seen in the zoomed inset in the left image. The planet was rendered using pixel shader programs implementing a variety of techniques, including parallax mapping, environment mapping, and a full lighting equation. (*Images courtesy of ARM.*)

When all triangles have been rasterized, and per-pixel processing has finished for a tile, the desired content (color and possibly depth) of the on-chip tile buffer is copied out to the frame buffer in external memory. The Mali 200 has two on-chip tile buffers, so once rendering has finished into on-chip tile buffer 1, processing of the next tile into on-chip tile buffer 2 can start, while the content of tile buffer 1 is written to external memory.

Low-level power saving techniques, such as clock gating, are also heavily used in this architecture. This basically means that unused or inactive parts of the pipeline are shut down in order to preserve energy.

As we have seen here, the Mali 200 is not designed as a unified shader architecture. Keeping the size of the hardware down is another important design factor for mobile graphics hardware, and the Mali 200 hardware designers found that their vertex shader unit occupies less than 30% of the gates, as compared to a fragment shader unit. Hence, if you can keep the vertex shader and fragment shader units reasonably busy, you have a very cost-effective architecture.

An advantage of the tiling architecture, in general, is that it is inherently designed for rendering in parallel. For example, more fragment-processing units could be added, where each unit is responsible for independently rendering to a single tile at a time. A disadvantage of tiling architectures is that the entire scene data needs to be sent to the graphics hardware and stored in local memory. This places an upper limit on how large a scene can be rendered. Note that more complex scenes can be rendered with a multipass approach. Assume that in the first pass, 30,000 triangles are

rendered, and the  $Z$ -buffer is saved out to the local memory. Now, in the second pass, another 30,000 triangles are rendered. Before the per-pixel processing of a tile starts, the  $Z$ -buffer, and possibly the color buffer (and stencil) for that tile, is read into the on-chip tile buffer external memory. This multipass method comes at a cost of more bandwidth usage, and so there is an associated performance hit. Performance could also drop in some pathological cases. For example, say there are many different and long pixel shader programs for small triangles that are to be executed inside a tile. Switching long shader programs often comes with a significant cost. Such situations seldom happen with normal content.

More and more mobile phones are being equipped with special-purpose hardware for three-dimensional graphics. Energy-efficient architectures such as the one described here will continue to be important, since even with a “miracle” battery (lasting long), the heat has to dissipate through the cover of the phone. Too much heat will be inconvenient for the user. This suggests that there is much research to be done for mobile graphics, and that fundamental changes in the core architecture should be investigated.

#### 18.4.4 Other Architectures

There are many other three-dimensional graphics architectures that have been proposed and built over the years. Two major systems, *Pixel-Planes* and *PixelFlow*, have been designed and built by the graphics group at the University of North Carolina, Chapel Hill. *Pixel-Planes* was built in the late 1980s [368] and was a sort-middle architecture with tile-based rendering. *PixelFlow* [328, 895, 897] was an example of a sort-last image architecture with deferred shading and programmable shading. Recently, the group at UNC also has developed the *WarpEngine* [1024], which is a rendering architecture for image-based rendering. The primitives used are images with depth. Owens et al. describe a stream architecture for polygon rendering, where the pipeline work is divided in time, and each stage is run in sequence using a single processor [980]. This architecture can be software programmed at all pipeline stages, giving high flexibility. The *SHARP* architecture developed at Stanford uses ray tracing as its rendering algorithm [10].

The REYES software rendering architecture [196] used in RenderMan has used stochastic rasterization for a long time now. This technique is more efficient for motion blur and depth-of-field rendering, among other advantages. Stochastic rasterization is not trivial to simply move over to the GPU. However, some research on a new architecture to perform this algorithm has been done, with some of the problems solved [14]. See Figure 18.22 for an example of motion blur rendering. One of the con-

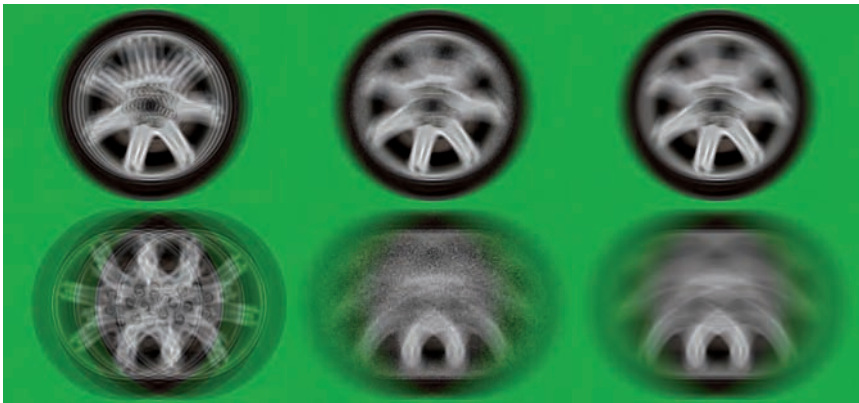


**Figure 18.22.** The top row shows a slowly rotating and translating wheel, while the bottom row shows a faster-moving wheel. The left column was rendered by accumulating four different images. The middle column was rendered with four samples using a new stochastic rasterizer targeting new GPU hardware, and the right column is a reference rendering with 64 jittered samples.

clusions was that new hardware modifications are necessary in order to obtain high performance. In addition, since the pixel shader writes out custom depth,  $Z$ -culling (Section 18.3.7) must be disabled, unless the PCU (Section 18.3.8) is implemented on top. Algorithms for stochastic lookups in shadow maps and cube maps were also presented. This gives blurred shadows and reflections for moving objects.

In terms of newer GPU architectures, the GeForce 8800 GTX architecture from NVIDIA [948] is the next generation after that used in the PLAYSTATION<sup>®</sup> 3 system. This is a unified shader architecture with 128 stream processors running at 1.35 GHz, so there are similarities with the Xbox 360 GPU. Each stream processor works on scalars, which was a design choice made to further increase efficiency. For example, not all instructions in the code may need all four components ( $x$ ,  $y$ ,  $z$ , and  $w$ ). The efficiency can thus be higher when using stream processors based on scalar execution. The GeForce 8800 can issue both a MAD and a MUL instruction each clock cycle. Note also that a consequence of the unified architecture is that the number of pipeline stages is reduced drastically. The GPU supports thousands of execution threads for better load balancing, and is DirectX 10-compatible.

There has also been considerable research done on new hardware specifically for ray tracing, where the most recent work is on a ray processing unit [1378], i.e., an RPU. This work includes, among other things, a fully programmable shader unit, and custom traversal units for quickly accessing a scene described by a  $k$ -d tree. Similar to the unified shader architecture

for GPUs, the RPU also works on executing threads, and may switch between these quickly to hide latency, etc.

## Further Reading and Resources

A great resource is the set of course notes on computer graphics architectures by Akeley and Hanrahan [10] and Hwu and Kirk [580]. Owens [981] discusses trends in hardware properties and how they affect architecture. The annual *SIGGRAPH/Eurographics Workshop on Graphics Hardware* and *SIGGRAPH* conference proceedings are good sources for more information. The book *Advanced Graphics Programming Using OpenGL* [849] discusses ways of creating stereo pairs. The book *Mobile 3D Graphics* by Pulli et al. [1037] thoroughly covers programming in OpenGL ES and M3G, a graphics API for Java ME. A survey on GPUs for handhelds [15] also describes some trends in the mobile field, as well as differences and similarities between desktop GPUs and mobile GPUs.

Check this book's website, <http://www.realtimerendering.com>, for information on benchmarking tests and results, as well as other hardware-related links.



# Chapter 19

## The Future

*“Pretty soon, computers will be fast.”*

—Billy Zelnack

*“Prediction is difficult, especially of the future.”*

—Niels Bohr or Yogi Berra

*“The best way to predict the future is to create it.”*

—Alan Kay

*“I program my home computer,  
beam myself into the future.”*

—Kraftwerk

There are two parts to the future: you and everything else. This chapter is about both. First, we will make some predictions, a few of which may even come true. More important is the second part of this chapter, about where you could go next. It is something of an extended Further Reading and Resources section, but it also discusses ways to proceed from here—sources of information, conferences, programming tools, etc.

### 19.1 Everything Else

One yardstick of progress is how closely interactive applications can approach offline rendered images. Films such as Pixar’s *Ratatouille* and PDI’s *Shrek* series use render farms chock full of racks of CPUs, around 3100 cores in all, each with access to 16 GB of memory. For example, for *Ratatouille*, a single frame took an average of 6.5 hours, though complex shots could take tens of hours. One constraint is the number of primitives. Scenes with swarms of rats have hundreds of millions of hairs in them [1093]. All the assets—models, textures, shaders, precomputed lighting—totaled 5 terabytes, all of which had to be available to the network at all times. At one

point, network traffic was a major bottleneck for the film *Cars*, not CPU processing power [613].

Going from 300+ minutes per frame to 30 frames per second is a challenge. On one level, current games can claim levels of visual complexity near that of *Toy Story*. This perhaps is not quite true, as the texture detail, geometry tessellation, and amount of sampling per pixel is higher in *Toy Story* than in any game. RenderMan is a microgeometry renderer at heart, with each surface chopped into polygons smaller than a pixel [31, 196]. Such fine tessellations are rarely used in interactive applications because of the cost. Effective resolution, in terms of total number of samples taken per pixel multiplied by total number of pixels, is a magnitude or two higher in films than at playable frame rates for video games. That said, a case can be made that for some shots, at relatively low resolution (so that antialiasing can be used), *Toy Story* complexity has been achieved.

Say that with the latest GPUs we are only a factor of 100 away from achieving a decent frame rate at a fine level of detail and shading for most scenes. Moore's Law gives an acceleration rate of 2 times every 1.5 years, or, more usefully, about 10 times every 5 years [1198]. So by this measure, we are only a decade away from achieving this goal. Unfortunately, it does not appear that processor speed will be the main constraint on computing in the future. Bandwidth is increasing by only around 25% per year, a rise of a little more than 3 times every 5 years. This makes a hundred-fold increase take about 20 years instead of 10, as long as some other bottleneck does not appear. Also, the goal line has moved: *Ratatouille* took 420 times the computing resources that *Toy Story* did [613]. On one level, it is incredible to see what has been done in the area of interactive rendering, such as Figures 19.1 and 19.2. On another, there is still a lot more processing that can be done.

Graphics helps sell games, and games help sell chips. One of the best features of real-time rendering from a chipmaker's marketing perspective is that graphics eats huge amounts of processing power and other resources. As discussed at the beginning of Chapter 14, hardware constraints such as frame rate, resolution, and color depth all can grow to some extent. The direction that is essentially unbounded is complexity. By complexity, we mean both the number of objects in a scene and the way these objects are rendered. Ignoring all other directions for growth, this single factor makes graphics a bottomless pit for processing power to fill. The depth complexity of scenes will rise, primitives will get smaller, illumination models will become more complex, and so on. First, build a model of the place where you are right now, down to the tiniest details, and then create shaders that create a photorealistic rendering of that environment. Add shadows, then glossy reflections. Now, model the surroundings with the same detail.



**Figure 19.1.** Realistic and artistic interactive renderings. (Image above from “Crysis,” courtesy of Crytek [887, 1342], image below from “Okami,” courtesy of Capcom Entertainment, Inc.)



**Figure 19.2.** How many effects can you identify? (© 2008 EA Digital Illusions CE AB [23].)

Then, add additional light transport paths for indirect lighting. Soon, any real-time rendering system will be a nonreal-time system.

So, we promised some predictions. “Faster and better” is a simple one to make. One simple possibility is that the Z-buffer triangle rasterization pipeline will continue to rule the roost. All but the simplest games use the GPU for rendering. Even if tomorrow some incredible technique supplanted the current pipeline, one that was a hundred times faster and that consisted

of downloading a system patch, it could still take years for the industry to move to this new technology. The catch would be whether the new technology could use exactly the same APIs as the existing ones. If not, adoption could take awhile. A complex game costs tens of millions of dollars and takes years to make. The target platforms are chosen, which informs decisions about everything from the algorithms and shaders used, to the size and complexity of artwork produced. Beyond that, the tools needed to work with or produce these elements need to be made. The momentum that the current pipeline has behind it gives it a number of years of life, even with a miracle occurring.

The way in which special purpose features are added to peripheral hardware, which then later gets folded into the main CPU, is referred to as the *wheel of reincarnation* [913]. The interesting question is whether the GPU pipeline will evolve to perform more general algorithms by itself, will continue to complement the CPU's capabilities, or will evolve in some other direction entirely. There are a few foreseeable paths, along with any hybrids among them.

If the wheel of reincarnation turns, a possible future is something along the lines of AMD's *Fusion* and Intel's *Nehalem* projects [1222]. ATI and AMD merged in the latter half of 2006. Their *Fusion* project and Intel's *Nehalem* look to be aimed at putting one or more CPU cores and a GPU on the same chip. CPUs and GPUs are comparable in size, so replacing one CPU core with a GPU makes sense. Such a design has a number of advantages, such as lower latency and overall lower power consumption. However, it seems aimed more at the mobile market, where small size and lower wattage matter more.

Intel's *Larrabee* project is thought to be aimed more squarely at high performance, along with broader GPGPU-type computational functionality [1221, 1256]. Larrabee appears to be a GPU with more of the feel of a CPU that has access to texture samplers. Larrabee products may have from 16 to 24 cores and attach to a main processor via a second generation PCI Express bus.

Back in 2006, Intel promised 80 cores on a chip by 2011 [697]. Whether they reach this goal or not is irrelevant. The key is that the number of cores is only going to rise, and they will be used in interesting new ways, as the preceding projects attest. Another Intel initiative (and AMD certainly is aiming the same direction) is what they call *terascale computing* [1221, 1256], using multicore to provide a teraflop of performance and a terabyte of bandwidth on computationally intensive problems. The GPU already has elements that are massively parallel. One algorithm that immediately comes to mind when the words "massive parallelism" are spoken is ray tracing. GPGPU languages such as AMD's *CTM* [994] and NVIDIA's *CUDA* [211] make writing a ray tracer that takes advantage of the GPU

much easier. NVIDIA, Intel, IBM, and others are actively researching ray tracing. Intel considers ray tracing a key computational area [1221, 1256].

The major advantages and drawbacks of ray tracing are discussed in Section 9.8.2. Ray tracing does scale well, at least for 8 or even 16 cores, but nothing is as simple as it seems. Currently, ray tracing can outperform the  $Z$ -buffer for some very large models, but such rendering is a relatively small niche, compared to the computer games industry. Ray tracing is also radically different than established APIs in a number of areas, so it faces a serious delay in adoption, even if proven to be superior.

As GPUs and CPUs continue on their convergence collision course, GPGPU (which was primarily distinguished by the use of GPUs for non-graphical applications) has come full circle, with the GPU being used to perform graphics computations in ways that do not resemble the traditional pipeline. New techniques for illumination and rendering are continually being developed, which take advantage of the GPU’s parallel processing power. One recent example is the  $k$ -buffer [74, 75, 77], proposed by Bavoil et al. for efficient order-independent rendering of translucent objects.

Somewhere in between the evolutionary path of yet more  $Z$ -buffered triangles and the revolutionary options of ray tracing or some as-yet unknown algorithm, the micropolygon-based REYES rendering system [31, 196] (first used for Pixar’s RenderMan) occupies an intriguing middle ground. It has many commonalities with the current GPU pipeline. For example, both use a  $Z$ -buffer for visibility. Micropolygons have the potential to be more efficient than triangle rasterization in scenes where most of the triangles are under one pixel in size. Like ray tracing, REYES is also “embarrassingly parallel,” but in an entirely different way. It treats each object separately, dices it into grids of micropolygons, then shades and merges these [31, 196]. It uses stochastic rasterization, a technique that can be performed by graphics hardware (Section 18.4.4). Ray tracing is performed only when no other option will work. This system is battle-tested, having been used for the majority of film rendering over the last twenty years. Other studios have implemented essentially the same algorithm. It is almost as ubiquitous for film rendering as  $Z$ -buffered triangles are for games. At the current speed of around 0.0006 fps, five orders of magnitude are needed to have it perform at 60 fps. In making an estimation, let’s say that the speed gains already achieved by GPUs are balanced out by the slower memory bandwidth growth rate. In other words, ignore reality, so that we can use our Moore’s Law yardstick. Using the 5 years per factor of 10 rule for Moore’s Law, this puts us at 2033 for interactive *Ratatouille*. And there will also be colonies on Mars, underwater cities, and personal jet packs. And cake.

## 19.2 You

So, while you and your children’s children are waiting for the next big thing to take over the world, what do you do in the meantime? Program, of course: discover new algorithms, create applications, design new hardware, or whatever else you enjoy doing. In this section, we cover various resources we have found to be useful in keeping on top of the field of real-time rendering.

This book does not exist in a vacuum; it draws upon a huge number of sources of information. If you are interested in a particular algorithm, track down the original sources. Journal and conference articles in computer graphics are usually not utterly mysterious, especially now that you have read this book. Go and get them. Most articles are available for download from the authors, and services such as the *ACM Digital Library* have a huge amount of new and older information available at reasonable subscription rates.

There are many resources that can help you keep abreast of the field. In the area of research, the *SIGGRAPH* annual conference is a premier venue for new ideas, but hardly the only one. Other technical gatherings, such as the various *Eurographics* conferences and workshops, the *Symposium on Interactive 3D Graphics and Games*, and the *Graphics Interface* conference, publish a significant amount of material relevant to real-time rendering. Particularly noteworthy are the *Eurographics Symposium on Rendering* and the *Eurographics/SIGGRAPH Graphics Hardware* forum. Of course, one of the best ways to stay in touch is actually to attend these conferences. There are also many excellent field-specific conferences, such as the *Game Developers Conference* (GDC). Meeting people and exchanging ideas face to face is rewarding on many levels.

There are a number of journals that publish technical articles, such as *IEEE Computer Graphics and Applications*, the *Journal of graphics tools*, *ACM Transactions on Graphics* (which now includes the SIGGRAPH proceedings as an issue), and *IEEE Transactions on Visualization and Computer Graphics*, to mention a few.

The most significant trend in the past few years has been the proliferation of books in the area of interactive rendering. Beyond some excellent texts in various fields, edited collections of articles have appeared. Prime examples are the *GPU Gems* series [339, 931, 1013] and the *ShaderX* series [306, 307, 308, 309, 310, 311, 313]. Also noteworthy are the *Game Programming Gems* series [249], though in recent years this series truly has become more about game programming as a whole. All these books allow game developers to present their algorithms without having to write a formal conference paper. They also allow academics to discuss technical details about their work that do not fit into a research paper. For a pro-

fessional developer, an hour saved working out some implementation detail found in an article more than pays back the cost of the entire book.

When all is said and done, code needs to be written. There are code samples that accompany many of the books mentioned. Researchers also often provide code on their websites, or may offer it if you show an interest. There are plenty of demos with source to be found on the web. Some of the highest concentrations of code are from those who offer and implement the APIs. The Microsoft SDK [261] has numerous code samples. ATI/AMD and NVIDIA offer excellent free systems for exploring shaders, such as RenderMonkey and FX Composer 2, and many other tools.

We refer you one last time to our website for links to online resources at <http://www.realtimerendering.com>. There you will find many other resources, such as lists of recommended and new books, as well as pointers to frequently asked questions pages, developer forums, and mailing lists. Some information on the web is available nowhere else, and there is a huge amount of useful material out there.

Our last words of advice are to go and learn and do. The field of real-time computer graphics is continually evolving, and new ideas and features are appearing at an increasing rate. The wide array of techniques



**Figure 19.3.** LittleBigPlanet has a unique rendering style, designed to look like a video of a real-world miniature set. The developers took care to choose techniques that fit the game's art style and constraints [322], combining them in unusual ways to achieve stunning results. (*LittleBigPlanet* ©2007 Sony Computer Entertainment Europe. Developed by Media Molecule. *LittleBigPlanet* is a trademark of Sony Computer Entertainment Europe.)

employed can seem daunting, but you do not need to implement a laundry list of buzzwords-du-jour to get good results. Cleverly combining a small number of techniques, based on the constraints and visual style of your application, can result in amazing visuals (see Figure 19.3).

Even areas that seem old and well established are worth revisiting; computer architectures change, and what worked (or did not work) a few years ago may no longer apply. What makes real-time rendering a qualitatively different field from other areas of computer graphics is that it provides different tools and has different goals. Today, hardware-accelerated shading, filtering, stencil buffering, and other operations change the relative costs of algorithms, and so change our ways of doing things.

This edition comes 34 years after one of the milestone papers in the field of computer graphics, “A Characterization of Ten Hidden-Surface Algorithms” by Sutherland, Sproull, and Schumacker, published in 1974 [1231]. Their 55-page paper is an incredibly thorough comparison of ten different algorithms. What is interesting is that the algorithm described as “ridiculously expensive,” the brute-force technique not even dignified with



What do you want to do next? (*Image from “Assassin’s Creed,” courtesy of Ubisoft.*)

a researcher's name, and mentioned only in the appendices, is what is now called the *Z-buffer*.<sup>1</sup> This eleventh hidden surface technique won out because it was easy to implement in hardware and because memory densities went up and costs went down. The research done by Sutherland et al. was perfectly valid for its time. As conditions change, so do the algorithms. It will be exciting to see what happens in the years to come. How will it feel when we look back on this current era of rendering technology? No one knows, and each person can have a significant effect on the way the future turns out. There is no one future, no course that must occur. You create it.

---

<sup>1</sup>In fairness, Sutherland was the advisor of the inventor of the *Z-buffer*, Ed Catmull, whose thesis discussing this concept would be published a few months later [161].

# Appendix A

## Some Linear Algebra

### *BOOK I. DEFINITIONS.*

*A point is that which has no part.*

*A line is a breadthless length.*

*The extremities of a line are points.*

*A straight line is a line which lies evenly with the points on itself.*

—The first four definitions from *Elements* by Euclid [320]

This appendix deals with the fundamental concepts of linear algebra that are of greatest use for computer graphics. Our presentation will not be as mathematically abstract and general as these kinds of descriptions often are, but will rather concentrate on what is most relevant. For the inexperienced reader, it can be seen as a short introduction to the topic, and for the more experienced one, it may serve as a review.

We will start with an introduction to the Euclidean spaces. This may feel abstract at first, but in the section that follows, these concepts are connected to geometry, bases, and matrices. So bite the bullet during the first section, and reap the rewards in the rest of the appendix and in many of the other chapters of this book.

If you are uncertain about the notation used in this book, take a look at Section 1.2.

### A.1 Euclidean Space

The  $n$ -dimensional real Euclidean space is denoted  $\mathbb{R}^n$ . A vector  $\mathbf{v}$  in this space is an  $n$ -tuple, that is, an ordered list of real numbers:<sup>1</sup>

---

<sup>1</sup>Note that the subscripts start at 0 and end at  $n - 1$ , a numbering system that follows the indexing of arrays in many programming languages, such as C and C++. This makes it easier to convert from formula to code. Some computer graphics books and linear algebra books start at 1 and end at  $n$ .

$$\mathbf{v} \in \mathbb{R}^n \iff \mathbf{v} = \begin{pmatrix} v_0 \\ v_1 \\ \vdots \\ v_{n-1} \end{pmatrix} \text{ with } v_i \in \mathbb{R}, i = 0, \dots, n-1. \quad (\text{A.1})$$

The vector can also be presented as a row vector, but most computer graphics book use column vectors, in what is called the column-major form. We call  $v_0, \dots, v_{n-1}$  the elements, the coefficients, or the components of the vector  $\mathbf{v}$ . All bold lowercase letters are vectors that belong to  $\mathbb{R}^n$ , and italicized lowercase letters are scalars that belong to  $\mathbb{R}$ . As an example, a two-dimensional vector is  $\mathbf{v} = (v_0, v_1)^T \in \mathbb{R}^2$ . For vectors in a Euclidean space there exist two operators, *addition* and *multiplication by a scalar*, which work as might be expected:

$$\mathbf{u} + \mathbf{v} = \begin{pmatrix} u_0 \\ u_1 \\ \vdots \\ u_{n-1} \end{pmatrix} + \begin{pmatrix} v_0 \\ v_1 \\ \vdots \\ v_{n-1} \end{pmatrix} = \begin{pmatrix} u_0 + v_0 \\ u_1 + v_1 \\ \vdots \\ u_{n-1} + v_{n-1} \end{pmatrix} \in \mathbb{R}^n \quad (\text{addition}) \quad (\text{A.2})$$

and

$$a\mathbf{u} = \begin{pmatrix} au_0 \\ au_1 \\ \vdots \\ au_{n-1} \end{pmatrix} \in \mathbb{R}^n \quad (\text{multiplication by a scalar}). \quad (\text{A.3})$$

The “ $\in \mathbb{R}^n$ ” simply means that addition and multiplication by a scalar yields vectors of the same space. As can be seen, addition is done componentwise, and multiplication is done by multiplying all elements in the vector with the scalar  $a$ .

A series of rules hold for Euclidean space.<sup>2</sup> Addition of vectors in a Euclidean space also works as might be expected:

$$(i) \quad (\mathbf{u} + \mathbf{v}) + \mathbf{w} = \mathbf{u} + (\mathbf{v} + \mathbf{w}) \quad (\text{associativity}) \quad (\text{A.4})$$

$$(ii) \quad \mathbf{u} + \mathbf{v} = \mathbf{v} + \mathbf{u} \quad (\text{commutativity}).$$

There is a unique vector, called the zero vector, which is  $\mathbf{0} = (0, 0, \dots, 0)$  with  $n$  zeros, such that

$$(iii) \quad \mathbf{0} + \mathbf{v} = \mathbf{v} \quad (\text{zero identity}). \quad (\text{A.5})$$

---

<sup>2</sup>Actually, these are the definition of Euclidean space.

There is also a unique vector  $-\mathbf{v} = (-v_0, -v_1, \dots, -v_{n-1})$  such that

$$(iv) \quad \mathbf{v} + (-\mathbf{v}) = \mathbf{0} \quad (\text{additive inverse}). \quad (\text{A.6})$$

Rules for multiplication by a scalar work as follows:

- (i)  $(ab)\mathbf{u} = a(b\mathbf{u})$
  - (ii)  $(a+b)\mathbf{u} = a\mathbf{u} + b\mathbf{u} \quad (\text{distributive law})$
  - (iii)  $a(\mathbf{u} + \mathbf{v}) = a\mathbf{u} + a\mathbf{v} \quad (\text{distributive law})$
  - (iv)  $1\mathbf{u} = \mathbf{u}.$
- (A.7)

For a Euclidean space we may also compute the *dot product*<sup>3</sup> of two vectors  $\mathbf{u}$  and  $\mathbf{v}$ . The dot product is denoted  $\mathbf{u} \cdot \mathbf{v}$ , and its definition is shown below:

$$\mathbf{u} \cdot \mathbf{v} = \sum_{i=0}^{n-1} u_i v_i \quad (\text{dot product}). \quad (\text{A.8})$$

For the dot product we have the rules:

- (i)  $\mathbf{u} \cdot \mathbf{u} \geq 0$ , with  $\mathbf{u} \cdot \mathbf{u} = 0$  if and only if  $\mathbf{u} = (0, 0, \dots, 0) = \mathbf{0}$
  - (ii)  $(\mathbf{u} + \mathbf{v}) \cdot \mathbf{w} = \mathbf{u} \cdot \mathbf{w} + \mathbf{v} \cdot \mathbf{w}$
  - (iii)  $(a\mathbf{u}) \cdot \mathbf{v} = a(\mathbf{u} \cdot \mathbf{v})$
  - (iv)  $\mathbf{u} \cdot \mathbf{v} = \mathbf{v} \cdot \mathbf{u} \quad (\text{commutativity})$
  - (v)  $\mathbf{u} \cdot \mathbf{v} = 0 \iff \mathbf{u} \perp \mathbf{v}.$
- (A.9)

The last formula means that if the dot product is zero then the vectors are orthogonal (perpendicular). The norm of a vector, denoted  $\|\mathbf{u}\|$ , is a nonnegative number that can be expressed using the dot product:

$$\|\mathbf{u}\| = \sqrt{\mathbf{u} \cdot \mathbf{u}} = \sqrt{\left( \sum_{i=0}^{n-1} u_i^2 \right)} \quad (\text{norm}). \quad (\text{A.10})$$

---

<sup>3</sup>Also called *inner (dot) product* or *scalar product*.

The following rules hold for the norm:

- (i)  $\|\mathbf{u}\| = 0 \iff \mathbf{u} = (0, 0, \dots, 0) = \mathbf{0}$
  - (ii)  $\|a\mathbf{u}\| = |a| \|\mathbf{u}\|$
  - (iii)  $\|\mathbf{u} + \mathbf{v}\| \leq \|\mathbf{u}\| + \|\mathbf{v}\|$  (triangle inequality)
  - (iv)  $|\mathbf{u} \cdot \mathbf{v}| \leq \|\mathbf{u}\| \|\mathbf{v}\|$  (Cauchy–Schwartz inequality).
- (A.11)

The next section shows how we can use the theory in this section by interpreting everything geometrically.

## A.2 Geometrical Interpretation

Here, we will interpret the vectors (from the previous section) geometrically. For this, we first need to introduce the concepts of *linear independence* and the *basis*.<sup>4</sup>

If the only scalars to satisfy Equation A.12 below are  $v_0 = v_1 = \dots = v_{n-1} = 0$ , then the vectors,  $\mathbf{u}_0, \dots, \mathbf{u}_{n-1}$ , are said to be linearly independent. Otherwise, the vectors are linearly dependent:

$$v_0 \mathbf{u}_0 + \dots + v_{n-1} \mathbf{u}_{n-1} = 0 \quad (\text{A.12})$$

For example, the vectors  $\mathbf{u}_0 = (4, 3)$  and  $\mathbf{u}_1 = (8, 6)$  are *not* linearly independent, since  $v_0 = 2$  and  $v_1 = -1$  (among others) satisfy Equation A.12. Only vectors that are parallel are linearly dependent.

If a set of  $n$  vectors,  $\mathbf{u}_0, \dots, \mathbf{u}_{n-1} \in \mathbb{R}^n$ , is linearly independent and any vector  $\mathbf{v} \in \mathbb{R}^n$  can be written as

$$\mathbf{v} = \sum_{i=0}^{n-1} v_i \mathbf{u}_i, \quad (\text{A.13})$$

then the vectors  $\mathbf{u}_0, \dots, \mathbf{u}_{n-1}$  are said to span Euclidean space  $\mathbb{R}^n$ . If, in addition,  $v_0, \dots, v_{n-1}$  are uniquely determined by  $\mathbf{v}$  for all  $\mathbf{v} \in \mathbb{R}^n$ , then  $\mathbf{u}_0, \dots, \mathbf{u}_{n-1}$  is called a basis of  $\mathbb{R}^n$ . What this means is that every vector can be described uniquely by  $n$  scalars ( $v_0, v_1, \dots, v_{n-1}$ ) and the basis vectors  $\mathbf{u}_0, \dots, \mathbf{u}_{n-1}$ . The dimension of the space is  $n$ , if  $n$  is the largest number of linearly independent vectors in the space.

---

<sup>4</sup>Note that the concepts of linear independence and the basis can be used without any geometry.

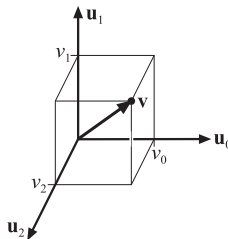


**Figure A.1.** A three-dimensional vector  $\mathbf{v} = (v_0, v_1, v_2)$  expressed in the basis formed by  $\mathbf{u}_0, \mathbf{u}_1, \mathbf{u}_2$  in  $\mathbb{R}^3$ . Note that this is a right-handed system.

An example of a linearly independent basis is  $\mathbf{u}_0 = (4, 3)$  and  $\mathbf{u}_1 = (2, 6)$ . This spans  $\mathbb{R}^2$ , as any vector can be expressed as a unique combination of these two vectors. For example,  $(-5, -6)$  is described by  $v_0 = -1$  and  $v_1 = -0.5$  and no other combinations of  $v_0$  and  $v_1$ .

To completely describe a vector,  $\mathbf{v}$ , one should use Equation A.13, that is, using both the vector components,  $v_i$  and the basis vectors,  $\mathbf{u}_i$ . That often becomes impractical, and therefore the basis vectors are often omitted in mathematical manipulation when the same basis is used for all vectors. If that is the case, then  $\mathbf{v}$  can be described as

$$\mathbf{v} = \begin{pmatrix} v_0 \\ v_1 \\ \vdots \\ v_{n-1} \end{pmatrix}, \quad (\text{A.14})$$

which is exactly the same vector description as in Expression A.1, and so this is the one-to-one mapping of the vectors in Section A.1 onto geometrical vectors.<sup>5</sup> An illustration of a three-dimensional vector is shown in Figure A.1. A vector  $\mathbf{v}$  can either be interpreted as a point in space or as a directed line segment (i.e., a direction vector). All rules from Section A.1 apply in the geometrical sense, too. For example, the addition and the scaling operators from Equation A.2 are visualized in Figure A.2. A basis can also have different “handedness.” A three-dimensional, right-handed basis is one in which the  $x$ -axis is along the thumb, the  $y$ -axis is along index-finger, and the  $z$ -axis is along the middle finger. If this is done with the left hand, a left-handed basis is obtained. See page 901 for a more formal definition of “handedness.”

The norm of a vector (see Equation A.10) can be thought of as the length of the vector. For example, the length of a two-dimensional vector,

---

<sup>5</sup>In mathematics, this is called an isomorphism.

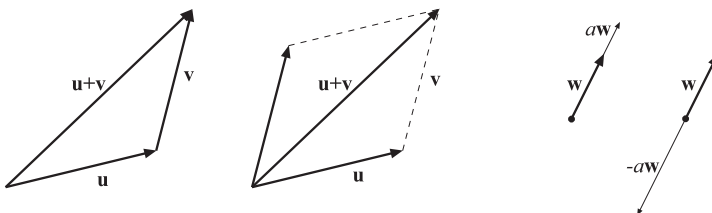


**Figure A.2.** Vector-vector addition is shown in the two figures on the left. They are called the head-to-tail axiom and the parallelogram rule. The two rightmost figures show scalar-vector multiplication for a positive and a negative scalar,  $a$  and  $-a$ , respectively.

$\mathbf{u}$ , is  $\|\mathbf{u}\| = \sqrt{u_0^2 + u_1^2}$ , which is basically the Pythagorean theorem. To create a vector of unit length, i.e., of length one, the vector has to be normalized. This can be done by dividing by the length of the vector:  $\mathbf{q} = \frac{1}{\|\mathbf{p}\|} \mathbf{p}$ , where  $\mathbf{q}$  is the normalized vector, which also is called a unit vector.

For  $\mathbb{R}^2$  and  $\mathbb{R}^3$ , or two- and three-dimensional space, the dot product can also be expressed as below, which is equivalent to Expression A.8:

$$\mathbf{u} \cdot \mathbf{v} = \|\mathbf{u}\| \|\mathbf{v}\| \cos \phi \quad (\text{dot product}) \quad (\text{A.15})$$

Here,  $\phi$  (shown at the left in Figure A.3) is the smallest angle between  $\mathbf{u}$  and  $\mathbf{v}$ . Several conclusions can be drawn from the sign of the dot product, assuming that both vectors have non-zero length. First,  $\mathbf{u} \cdot \mathbf{v} = 0 \Leftrightarrow \mathbf{u} \perp \mathbf{v}$ , i.e.,  $\mathbf{u}$  and  $\mathbf{v}$  are orthogonal (perpendicular) if their dot product is zero. Second, if  $\mathbf{u} \cdot \mathbf{v} > 0$ , then it can be seen that  $0 \leq \phi < \frac{\pi}{2}$ , and likewise if  $\mathbf{u} \cdot \mathbf{v} < 0$  then  $\frac{\pi}{2} < \phi \leq \pi$ .

Now we will go back to the study of basis for a while, and introduce a special kind of basis that is said to be *orthonormal*. For such a basis, consisting of the basis vectors  $\mathbf{u}_0, \dots, \mathbf{u}_{n-1}$ , the following must hold:

$$\mathbf{u}_i \cdot \mathbf{u}_j = \begin{cases} 0, & i \neq j, \\ 1, & i = j. \end{cases} \quad (\text{A.16})$$

This means that every basis vector must have a length of one, i.e.,  $\|\mathbf{u}_i\| = 1$ , and also that each pair of basis vectors must be orthogonal, i.e., the angle between them must be  $\pi/2$  radians ( $90^\circ$ ). In this book, we mostly use two- and three-dimensional orthonormal bases. If the basis vectors are mutually perpendicular, but not of unit length, then the basis is called *orthogonal*. Orthonormal bases do not have to consist of simple vectors. For example, in precomputed radiance transfer techniques the bases often are either spherical harmonics or wavelets. In general, the vectors are

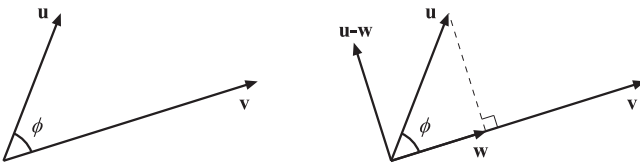


**Figure A.3.** The left figure shows the notation and geometric situation for the dot product. In the rightmost figure, orthographic projection is shown. The vector  $\mathbf{u}$  is orthogonally (perpendicularly) projected onto  $\mathbf{v}$  to yield  $\mathbf{w}$ .

exchanged for functions, and the dot product is augmented to work on these functions. Once that is done, the concept of orthonormality applies as above. See Section 8.6.1 for more information about this.

Let  $\mathbf{p} = (p_0, \dots, p_{n-1})$ , then for an orthonormal basis it can also be shown that  $p_i = \mathbf{p} \cdot \mathbf{u}_i$ . This means that if you have a vector  $\mathbf{p}$  and a basis (with the basis vectors  $\mathbf{u}_0, \dots, \mathbf{u}_{n-1}$ ), then you can easily get the elements of that vector in that basis by taking the dot product between the vector and each of the basis vectors. The most common basis is called the standard basis, where the basis vectors are denoted  $\mathbf{e}_i$ . The  $i$ th basis vector has zeroes everywhere except in position  $i$ , which holds a one. For three dimensions, this means  $\mathbf{e}_0 = (1, 0, 0)$ ,  $\mathbf{e}_1 = (0, 1, 0)$ , and  $\mathbf{e}_2 = (0, 0, 1)$ . We also denote these vectors  $\mathbf{e}_x$ ,  $\mathbf{e}_y$ , and  $\mathbf{e}_z$ , since they are what we normally call the  $x$ -, the  $y$ -, and the  $z$ -axes.

A very useful property of the dot product is that it can be used to project a vector orthogonally onto another vector. This orthogonal projection (vector),  $\mathbf{w}$ , of a vector  $\mathbf{u}$  onto a vector  $\mathbf{v}$  is depicted on the right in Figure A.3.

For arbitrary vectors  $\mathbf{u}$  and  $\mathbf{v}$ ,  $\mathbf{w}$  is determined by

$$\mathbf{w} = \left( \frac{\mathbf{u} \cdot \mathbf{v}}{\|\mathbf{v}\|^2} \right) \mathbf{v} = \left( \frac{\mathbf{u} \cdot \mathbf{v}}{\mathbf{v} \cdot \mathbf{v}} \right) \mathbf{v} = t\mathbf{v}, \quad (\text{A.17})$$

where  $t$  is a scalar. The reader is encouraged to verify that Expression A.17 is indeed correct, which is done by inspection and the use of Equation A.15. The projection also gives us an orthogonal decomposition of  $\mathbf{u}$ , which is divided into two parts,  $\mathbf{w}$  and  $(\mathbf{u} - \mathbf{w})$ . It can be shown that  $\mathbf{w} \perp (\mathbf{u} - \mathbf{w})$ , and of course  $\mathbf{u} = \mathbf{w} + (\mathbf{u} - \mathbf{w})$  holds. An additional observation is that if  $\mathbf{v}$  is normalized, then the projection is  $\mathbf{w} = (\mathbf{u} \cdot \mathbf{v})\mathbf{v}$ . This means that  $\|\mathbf{w}\| = |\mathbf{u} \cdot \mathbf{v}|$ , i.e., the length of  $\mathbf{w}$  is the absolute value of the dot product between  $\mathbf{u}$  and  $\mathbf{v}$ .

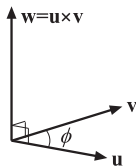


**Figure A.4.** The geometry involved in the cross product.

### Cross Product

The cross product, also called the vector product, and the previously introduced dot product are two very important operations on vectors.

The cross product in  $\mathbb{R}^3$  of two vectors,  $\mathbf{u}$  and  $\mathbf{v}$ , denoted by  $\mathbf{w} = \mathbf{u} \times \mathbf{v}$ , is defined by a unique vector  $\mathbf{w}$  with the following properties:

- $||\mathbf{w}|| = ||\mathbf{u} \times \mathbf{v}|| = ||\mathbf{u}|| ||\mathbf{v}|| \sin \phi$ , where  $\phi$  is, again, the smallest angle between  $\mathbf{u}$  and  $\mathbf{v}$ . See Figure A.4.
- $\mathbf{w} \perp \mathbf{u}$  and  $\mathbf{w} \perp \mathbf{v}$ .
- $\mathbf{u}, \mathbf{v}, \mathbf{w}$  form a right-handed system.

From this definition, it is deduced that  $\mathbf{u} \times \mathbf{v} = \mathbf{0}$  if and only if  $\mathbf{u} \parallel \mathbf{v}$  (i.e.,  $\mathbf{u}$  and  $\mathbf{v}$  are parallel), since then  $\sin \phi = 0$ . The cross product also comes equipped with the following laws of calculation, among others:

$$\begin{aligned}
 \mathbf{u} \times \mathbf{v} &= -\mathbf{v} \times \mathbf{u} && \text{(anti-commutativity)} \\
 (\mathbf{au} + \mathbf{bv}) \times \mathbf{w} &= a(\mathbf{u} \times \mathbf{w}) + b(\mathbf{v} \times \mathbf{w}) && \text{(linearity)} \\
 \left. \begin{aligned}
 (\mathbf{u} \times \mathbf{v}) \cdot \mathbf{w} &= (\mathbf{v} \times \mathbf{w}) \cdot \mathbf{u} \\
 = (\mathbf{w} \times \mathbf{u}) \cdot \mathbf{v} &= -(\mathbf{v} \times \mathbf{u}) \cdot \mathbf{w} \\
 = -(\mathbf{u} \times \mathbf{w}) \cdot \mathbf{v} &= -(\mathbf{w} \times \mathbf{v}) \cdot \mathbf{u}
 \end{aligned} \right\} && \text{(scalar triple product)} \\
 \mathbf{u} \times (\mathbf{v} \times \mathbf{w}) &= (\mathbf{u} \cdot \mathbf{w})\mathbf{v} - (\mathbf{u} \cdot \mathbf{v})\mathbf{w} && \text{(vector triple product)}
 \end{aligned} \tag{A.18}$$

From these laws, it is obvious that the order of the operands is crucial in getting correct results from the calculations.

For three-dimensional vectors,  $\mathbf{u}$  and  $\mathbf{v}$ , in an orthonormal basis, the cross product is computed according to Equation A.19:

$$\mathbf{w} = \begin{pmatrix} w_x \\ w_y \\ w_z \end{pmatrix} = \mathbf{u} \times \mathbf{v} = \begin{pmatrix} u_y v_z - u_z v_y \\ u_z v_x - u_x v_z \\ u_x v_y - u_y v_x \end{pmatrix}. \tag{A.19}$$

A method called Sarrus's scheme, which is simple to remember, can be used to derive this formula:

$$\begin{array}{ccc}
 + & + & + \\
 \searrow & \searrow & \searrow \\
 \mathbf{e}_x & \mathbf{e}_y & \mathbf{e}_z & \mathbf{e}_x & \mathbf{e}_y & \mathbf{e}_z \\
 u_x & u_y & u_z & u_x & u_y & u_z \\
 v_x & v_y & v_z & v_x & v_y & v_z
 \end{array} \quad (\text{A.20})$$

To use the scheme, follow the diagonal arrows, and for each arrow, generate a term by multiplying the elements along the direction of the arrow and giving the product the sign associated with that arrow. The result is shown below and it is exactly the same formula as in Equation A.19, as expected:

$$\mathbf{u} \times \mathbf{v} = +\mathbf{e}_x(u_y v_z) + \mathbf{e}_y(u_z v_x) + \mathbf{e}_z(u_x v_y) - \mathbf{e}_x(u_z v_y) - \mathbf{e}_y(u_x v_z) - \mathbf{e}_z(u_y v_x).$$

## A.3 Matrices

This section presents the definitions concerning matrices and some common, useful operations on them. Even though this presentation is (mostly) for arbitrarily sized matrices, square matrices of the sizes  $2 \times 2$ ,  $3 \times 3$ , and  $4 \times 4$  will be used in the chapters of this book. Note that Chapter 4 deals with transforms represented by matrices.

### A.3.1 Definitions and Operations

A matrix,  $\mathbf{M}$ , can be used as a tool for manipulating vectors and points.  $\mathbf{M}$  is described by  $p \times q$  scalars (complex numbers are an alternative, but not relevant here),  $m_{ij}$ ,  $0 \leq i \leq p-1$ ,  $0 \leq j \leq q-1$ , ordered in a rectangular fashion (with  $p$  rows and  $q$  columns) as shown in Equation A.22:

$$\mathbf{M} = \begin{pmatrix} m_{00} & m_{01} & \cdots & m_{0,q-1} \\ m_{10} & m_{11} & \cdots & m_{1,q-1} \\ \vdots & \vdots & \ddots & \vdots \\ m_{p-1,0} & m_{p-1,1} & \cdots & m_{p-1,q-1} \end{pmatrix} = [m_{ij}]. \quad (\text{A.22})$$

The notation  $[m_{ij}]$  will be used in the equations below and is merely a shorter way of describing a matrix. There is a special matrix called the *unit matrix*,  $\mathbf{I}$ , which is square and contains ones in the diagonal and zeros elsewhere. This is also called the *identity matrix*. Equation A.23 shows

its general appearance. This is the matrix-form counterpart of the scalar number one:

$$\mathbf{I} = \begin{pmatrix} 1 & 0 & 0 & \cdots & 0 & 0 \\ 0 & 1 & 0 & \cdots & 0 & 0 \\ \vdots & \vdots & \vdots & \ddots & \vdots & \vdots \\ 0 & 0 & 0 & \cdots & 1 & 0 \\ 0 & 0 & 0 & \cdots & 0 & 1 \end{pmatrix}. \quad (\text{A.23})$$

Next, the most ordinary operations on matrices will be reviewed.

### *Matrix-Matrix Addition*

Adding two matrices, say  $\mathbf{M}$  and  $\mathbf{N}$ , is possible only for equal-sized matrices and is defined as

$$\mathbf{M} + \mathbf{N} = [m_{ij}] + [n_{ij}] = [m_{ij} + n_{ij}], \quad (\text{A.24})$$

that is, componentwise addition, very similar to vector-vector addition. The resulting matrix is of the same size as the operands. The following operations are valid for matrix-matrix addition: *i*)  $(\mathbf{L} + \mathbf{M}) + \mathbf{N} = \mathbf{L} + (\mathbf{M} + \mathbf{N})$ , *ii*)  $\mathbf{M} + \mathbf{N} = \mathbf{N} + \mathbf{M}$ , *iii*)  $\mathbf{M} + \mathbf{0} = \mathbf{M}$ , *iv*)  $\mathbf{M} - \mathbf{M} = \mathbf{0}$ , which are all very easy to prove. Note that  $\mathbf{0}$  is a matrix containing only zeroes.

### *Scalar-Matrix Multiplication*

A scalar  $a$  and a matrix,  $\mathbf{M}$ , can be multiplied to form a new matrix of the same size as  $\mathbf{M}$ , which is computed by  $\mathbf{T} = a\mathbf{M} = [am_{ij}]$ .  $\mathbf{T}$  and  $\mathbf{M}$  are of the same size, and these trivial rules apply: *i*)  $0\mathbf{M} = \mathbf{0}$ , *ii*)  $1\mathbf{M} = \mathbf{M}$ , *iii*)  $a(b\mathbf{M}) = (ab)\mathbf{M}$ , *iv*)  $a\mathbf{0} = \mathbf{0}$ , *v*)  $(a+b)\mathbf{M} = a\mathbf{M} + b\mathbf{M}$ , *vi*)  $a(\mathbf{M} + \mathbf{N}) = a\mathbf{M} + a\mathbf{N}$ .

### *Transpose of a Matrix*

$\mathbf{M}^T$  is the notation for the transpose of  $\mathbf{M} = [m_{ij}]$ , and the definition is  $\mathbf{M}^T = [m_{ji}]$ , i.e., the columns become rows and the rows become columns. For the transpose operator, we have: *i*)  $(a\mathbf{M})^T = a\mathbf{M}^T$ , *ii*)  $(\mathbf{M} + \mathbf{N})^T = \mathbf{M}^T + \mathbf{N}^T$ , *iii*)  $(\mathbf{M}^T)^T = \mathbf{M}$ , *iv*)  $(\mathbf{MN})^T = \mathbf{N}^T\mathbf{M}^T$ .

### *Trace of a Matrix*

The trace of a matrix, denoted  $\text{tr}(\mathbf{M})$ , is simply the sum of the diagonal elements of a square matrix, as shown below:

$$\text{tr}(\mathbf{M}) = \sum_{i=0}^{n-1} m_{ii}. \quad (\text{A.25})$$

### Matrix-Matrix Multiplication

This operation, denoted  $\mathbf{MN}$  between  $\mathbf{M}$  and  $\mathbf{N}$ , is defined only if  $\mathbf{M}$  is of size  $p \times q$  and  $\mathbf{N}$  is of size  $q \times r$ , in which case the result,  $\mathbf{T}$ , becomes a  $p \times r$  sized matrix. Mathematically, for these matrices the operation is as follows:

$$\begin{aligned} \mathbf{T} = \mathbf{MN} &= \left( \begin{array}{ccc} m_{00} & \cdots & m_{0,q-1} \\ \vdots & \ddots & \vdots \\ m_{p-1,0} & \cdots & m_{p-1,q-1} \end{array} \right) \left( \begin{array}{ccc} n_{00} & \cdots & n_{0,r-1} \\ \vdots & \ddots & \vdots \\ n_{q-1,0} & \cdots & n_{q-1,r-1} \end{array} \right) \\ &= \left( \begin{array}{ccc} \sum_{i=0}^{q-1} m_{0,i} n_{i,0} & \cdots & \sum_{i=0}^{q-1} m_{0,i} n_{i,r-1} \\ \vdots & \ddots & \vdots \\ \sum_{i=0}^{q-1} m_{p-1,i} n_{i,0} & \cdots & \sum_{i=0}^{q-1} m_{p-1,i} n_{i,r-1} \end{array} \right). \end{aligned} \quad (\text{A.26})$$

In other words, each row of  $\mathbf{M}$  and column of  $\mathbf{N}$  are combined using a dot product, and the result placed in the corresponding row and column element. The elements of  $\mathbf{T}$  are computed as  $t_{ij} = \sum_{k=0}^{q-1} m_{i,k} n_{k,j}$ , which can also be expressed as  $t_{ij} = \mathbf{m}_i \cdot \mathbf{n}_{:,j}$ , that is, using the dot product and the matrix-vector indexing from Section 1.2.1. Note also that an  $n \times 1$  matrix,  $\mathbf{S} = (s_{00} \ s_{10} \ \cdots \ s_{n-1,0})^T$ , is basically an  $n$ -tuple vector. If seen as such, then matrix-vector multiplication, between  $\mathbf{M}$  ( $p \times q$ ) and  $\mathbf{v}$  ( $q$ -tuple), can be derived from the definition of matrix-matrix multiplication. This is shown in Equation A.27, resulting in a new vector,  $\mathbf{w}$ :

$$\begin{aligned} \mathbf{w} = \mathbf{Mv} &= \left( \begin{array}{ccc} m_{00} & \cdots & m_{0,q-1} \\ \vdots & \ddots & \vdots \\ m_{p-1,0} & \cdots & m_{p-1,q-1} \end{array} \right) \left( \begin{array}{c} v_0 \\ \vdots \\ v_{q-1} \end{array} \right) \\ &= \left( \begin{array}{c} \sum_{k=0}^{q-1} m_{0,k} v_k \\ \vdots \\ \sum_{k=0}^{q-1} m_{p-1,k} v_k \end{array} \right) = \left( \begin{array}{c} \mathbf{m}_0 \cdot \mathbf{v} \\ \vdots \\ \mathbf{m}_{p-1} \cdot \mathbf{v} \end{array} \right) = \left( \begin{array}{c} w_0 \\ \vdots \\ w_{q-1} \end{array} \right). \end{aligned} \quad (\text{A.27})$$

These three rules hold for the matrix-matrix multiplication: *i)*  $(\mathbf{LM})\mathbf{N} = \mathbf{L}(\mathbf{MN})$ , *ii)*  $(\mathbf{L} + \mathbf{M})\mathbf{N} = \mathbf{LN} + \mathbf{MN}$ , *iii)*  $\mathbf{MI} = \mathbf{IM} = \mathbf{M}$ . If the dimensions of the matrices are the same, then  $\mathbf{MN} \neq \mathbf{NM}$ , in general. This means that some pairs of matrices do commute, but usually they do not.

### Determinant of a Matrix

The determinant is defined only for square matrices, and in the general case, the definition is recursive or defined via permutations [742]. Here, the focus will be on determinants for  $2 \times 2$  and  $3 \times 3$  matrices, since those are the ones most often needed in computer graphics.

The determinant of  $\mathbf{M}$ , written  $|\mathbf{M}|$ , for these matrices appears in Equation A.28 and A.29:

$$|\mathbf{M}| = \begin{vmatrix} m_{00} & m_{01} \\ m_{10} & m_{11} \end{vmatrix} = m_{00}m_{11} - m_{01}m_{10} \quad (\text{A.28})$$

$$\begin{aligned} |\mathbf{M}| &= \begin{vmatrix} m_{00} & m_{01} & m_{02} \\ m_{10} & m_{11} & m_{12} \\ m_{20} & m_{21} & m_{22} \end{vmatrix} \\ &= m_{00}m_{11}m_{22} + m_{01}m_{12}m_{20} + m_{02}m_{10}m_{21} \\ &\quad - m_{02}m_{11}m_{20} - m_{01}m_{10}m_{22} - m_{00}m_{12}m_{21} \end{aligned} \quad (\text{A.29})$$

In these two equations, a certain pattern can be distinguished: The positive terms are the elements multiplied in the diagonals from the top downwards to the right and the negative terms are the elements in the diagonals from the top downwards to the left, where a diagonal continues on the opposite side if an edge is crossed. Note that if the top row in  $\mathbf{M}$  is replaced by  $\mathbf{e}_x \ \mathbf{e}_y \ \mathbf{e}_z$ , the middle row by  $\mathbf{u}_x \ \mathbf{u}_y \ \mathbf{u}_z$ , and the bottom row by  $\mathbf{v}_x \ \mathbf{v}_y \ \mathbf{v}_z$ , the cross product  $\mathbf{u} \times \mathbf{v}$  is obtained according to Sarrus's scheme (see Section A.2 on the cross product).

Another useful way to compute the determinant for  $3 \times 3$  matrices is to use the dot and the cross product as in Equation A.30, which is reminiscent of the column vector indexing introduced in Section 1.2.1:

$$|\mathbf{M}| = |\mathbf{m}_{,0} \ \mathbf{m}_{,1} \ \mathbf{m}_{,2}| = |\mathbf{m}_x \ \mathbf{m}_y \ \mathbf{m}_z| = (\mathbf{m}_x \times \mathbf{m}_y) \cdot \mathbf{m}_z \quad (\text{A.30})$$

The following notation is also used for determinants:

$$|\mathbf{M}| = \det(\mathbf{M}) = \det(\mathbf{m}_x, \mathbf{m}_y, \mathbf{m}_z). \quad (\text{A.31})$$

Observe that the scalar triple product from Equation A.18 can be applied to Equation A.30; that is, if the vectors are rotated, the determinant remains unchanged, but changing the places of two vectors will change the sign of the determinant.

If  $n \times n$  is the size of  $\mathbf{M}$ , then the following apply to determinant calculations: *i)*  $|\mathbf{M}^{-1}| = 1/|\mathbf{M}|$ , *ii)*  $|\mathbf{MN}| = |\mathbf{M}| |\mathbf{N}|$ , *iii)*  $|a\mathbf{M}| = a^n |\mathbf{M}|$ , *iv)*  $|\mathbf{M}^T| = |\mathbf{M}|$ . Also, if all elements of one row (or one column)

are multiplied by a scalar,  $a$ , then  $a|\mathbf{M}|$  is obtained, and if two rows (or columns) coincide (i.e., the cross product between them is zero), then  $|\mathbf{M}| = 0$ . The same result is obtained if any row or column is composed entirely of zeroes.

The orientation of a basis can be determined via determinants. A basis is said to form a right-handed system, also called a positively oriented basis, if its determinant is positive. The standard basis has this property, since  $|\mathbf{e}_x \ \mathbf{e}_y \ \mathbf{e}_z| = (\mathbf{e}_x \times \mathbf{e}_y) \cdot \mathbf{e}_z = (0, 0, 1) \cdot \mathbf{e}_z = \mathbf{e}_z \cdot \mathbf{e}_z = 1 > 0$ . If the determinant is negative, the basis is called negatively oriented or is said to be forming a left-handed system.

Some geometrical interpretations of the determinant are given in Section A.5.

### Adjoints

The adjoint<sup>6</sup> is another form of a matrix that can sometimes be useful. In particular, it is a matrix that is useful for transforming surface normals, as discussed in Section 4.1.7. It is also a first step in computing the inverse of a matrix. We start by defining the subdeterminant (also called cofactor)  $d_{ij}^{\mathbf{M}}$  of an  $n \times n$  matrix  $\mathbf{M}$  as the determinant that is obtained by deleting row  $i$  and column  $j$  and then taking the determinant of the resulting  $(n - 1) \times (n - 1)$  matrix. An example of computing the subdeterminant  $d_{02}^{\mathbf{M}}$  of a  $3 \times 3$  matrix is shown in Equation A.32:

$$d_{02}^{\mathbf{M}} = \begin{vmatrix} m_{10} & m_{11} \\ m_{20} & m_{21} \end{vmatrix}. \quad (\text{A.32})$$

For a  $3 \times 3$  matrix, the adjoint is then

$$\text{adj}(\mathbf{M}) = \begin{pmatrix} d_{00} & -d_{10} & d_{20} \\ -d_{01} & d_{11} & -d_{21} \\ d_{02} & -d_{12} & d_{22} \end{pmatrix}, \quad (\text{A.33})$$

where we have left out the superscript  $\mathbf{M}$  of the subdeterminants for clarity. Note the signs and the order in which the subdeterminants appear. If we want to compute the adjoint  $\mathbf{A}$  of an arbitrary sized matrix  $\mathbf{M}$ , then the component at position  $(i, j)$  is

$$[a_{ij}] = [(-1)^{(i+j)} d_{ji}^{\mathbf{M}}]. \quad (\text{A.34})$$

---

<sup>6</sup>Sometimes the adjoint has another definition than the one presented here, i.e., the adjoint of a matrix  $\mathbf{M} = [m_{ij}]$  is denoted  $\mathbf{M}^* = [\overline{m_{ji}}]$ , where  $\overline{m_{ji}}$  is the complex conjugate.

### Inverse of a Matrix

The multiplicative inverse of a matrix,  $\mathbf{M}$ , denoted  $\mathbf{M}^{-1}$ , which is dealt with here, exists only for square matrices with  $|\mathbf{M}| \neq 0$ . If all elements of the matrix under consideration are real scalars, then it suffices to show that  $\mathbf{MN} = \mathbf{I}$  and  $\mathbf{NM} = \mathbf{I}$ , where then  $\mathbf{N} = \mathbf{M}^{-1}$ . The problem can also be stated thus: If  $\mathbf{u} = \mathbf{Mv}$  and a matrix  $\mathbf{N}$  exists such that  $\mathbf{v} = \mathbf{Nu}$ , then  $\mathbf{N} = \mathbf{M}^{-1}$ .

The inverse of a matrix can be computed either implicitly or explicitly. If the inverse is to be used several times, then it is more economical to compute  $\mathbf{M}^{-1}$  explicitly, i.e., to get a representation of the inverse as an array of  $n \times n$  real numbers. On the other hand, if only a linear system of the type  $\mathbf{u} = \mathbf{Mv}$  needs to be solved (for  $\mathbf{v}$ ), then an implicit method, like *Cramer's rule*, can be used. For a linear system of the type  $\mathbf{Mv} = \mathbf{0}$ ,  $|\mathbf{M}| = 0$  is a requirement if there is to be a solution,  $\mathbf{v}$ .

Using Cramer's rule to solve  $\mathbf{u} = \mathbf{Mv}$  gives  $\mathbf{v} = \mathbf{M}^{-1}\mathbf{u}$ , but not  $\mathbf{M}^{-1}$  explicitly. Equation A.35 shows the general solution for the elements of  $\mathbf{v}$ :

$$v_i = \frac{d_i}{|\mathbf{M}|}, \quad (\text{A.35})$$

$$d_i = |\mathbf{m}_{,0} \ \mathbf{m}_{,1} \ \dots \ \mathbf{m}_{,i-1} \ \mathbf{u} \ \mathbf{m}_{,i+1} \ \dots \ \mathbf{m}_{,n-1}|.$$

The terms  $d_i$  are thus computed as  $|\mathbf{M}|$ , except that column  $i$  is replaced by  $\mathbf{u}$ . For a  $3 \times 3$  system, the solution obtained by Cramer's rule is presented below:

$$\mathbf{v} = \begin{pmatrix} v_x \\ v_y \\ v_z \end{pmatrix} = \frac{1}{|\mathbf{M}|} \begin{pmatrix} \det(\mathbf{u}, \mathbf{m}_y, \mathbf{m}_z) \\ \det(\mathbf{m}_x, \mathbf{u}, \mathbf{m}_z) \\ \det(\mathbf{m}_x, \mathbf{m}_y, \mathbf{u}) \end{pmatrix}. \quad (\text{A.36})$$

Many terms in this equation can be factorized using the scalar triple product rule and then reused for faster calculation. For example, this is done in Section 16.8 when computing the intersection between a ray and a triangle.

For a  $2 \times 2$  matrix,  $\mathbf{M}$ , the explicit solution is given by Equation A.37, and as can be seen, it is very simple to implement, since  $|\mathbf{M}| = m_{00}m_{11} - m_{01}m_{10}$ :

$$\mathbf{M}^{-1} = \frac{1}{|\mathbf{M}|} \begin{pmatrix} m_{11} & -m_{01} \\ -m_{10} & m_{00} \end{pmatrix}. \quad (\text{A.37})$$

For the general case, the adjoint from the previous section can be used:

$$\mathbf{M}^{-1} = \frac{1}{|\mathbf{M}|} \text{adj}(\mathbf{M}). \quad (\text{A.38})$$

In fact, this is Cramer's rule expressed differently to get the inverse matrix explicitly.

However, for larger sizes than  $4 \times 4$ , there are no simple formulae, and Cramer's rule also becomes infeasible for matrices larger than  $4 \times 4$ . Gaussian elimination is then the method of preference, and it can be used to solve for  $\mathbf{u} = \mathbf{M}\mathbf{v} \Rightarrow \mathbf{v} = \mathbf{M}^{-1}\mathbf{u}$ —that is, an implicit solution, as is the case for Cramer's rule. However, Gaussian elimination can also be used to compute the matrix  $\mathbf{M}^{-1}$  explicitly. Consider the system in Equation A.39, where  $\mathbf{u}$  and  $\mathbf{v}$  are arbitrary vectors of the same dimension as  $\mathbf{M}$  and  $\mathbf{I}$  (the identity matrix):

$$\mathbf{Mu} = \mathbf{Iv}. \quad (\text{A.39})$$

Performing Gaussian elimination on this system until  $\mathbf{M}$  has been transformed into the identity matrix  $\mathbf{I}$  means that the right side identity matrix has become the inverse  $\mathbf{M}^{-1}$ . Thus,  $\mathbf{u}$  and  $\mathbf{v}$  are, in fact, not of any particular use; they are merely means for expressing Equation A.39 in a mathematically sound way.

LU decomposition is another method that can be used to compute the inverse efficiently. However, a discussion of Gaussian elimination and LU decomposition is beyond the scope of this text. Virtually any book on linear algebra [741, 742] or numerical methods books, such as the one by Press et al. [1034], describe these methods.

Some important rules of computation for the inverse of matrices are:  
*i)*  $(\mathbf{M}^{-1})^T = (\mathbf{M}^T)^{-1}$ ,   *ii)*  $(\mathbf{MN})^{-1} = \mathbf{N}^{-1}\mathbf{M}^{-1}$ .

### Eigenvalue and Eigenvector Computation

The solution to the *eigenvalue* problem has a large range of uses. For example, one application area is the computation of tight bounding volumes (see Section 17.4). The problem is stated as follows:

$$\mathbf{Ax} = \lambda\mathbf{x}, \quad (\text{A.40})$$

where  $\lambda$  is a scalar.<sup>7</sup> The matrix  $\mathbf{A}$  has to be square (say of size  $n \times n$ ), and  $\mathbf{x} \neq \mathbf{0}$ , then, if  $\mathbf{x}$  fulfills this equation,  $\mathbf{x}$  is said to be an *eigenvector* to  $\mathbf{A}$ , and  $\lambda$  is its belonging *eigenvalue*. Rearranging the terms of Equation A.40 yields Equation A.41:

$$(\lambda\mathbf{I} - \mathbf{A})\mathbf{x} = \mathbf{0}. \quad (\text{A.41})$$

This equation has a solution if and only if  $p_A(\lambda) = \det(\lambda\mathbf{I} - \mathbf{A}) = 0$ , where the function  $p_A(\lambda)$  is called the characteristic polynomial to  $\mathbf{A}$ . The eigenvalues,  $\lambda_0, \dots, \lambda_{n-1}$ , are thus solutions to  $p_A(\lambda) = 0$ . Focus for a while on a particular eigenvalue  $\lambda_i$  to  $\mathbf{A}$ . Then  $\mathbf{x}_i$  is its corresponding eigenvector if  $(\lambda_i\mathbf{I} - \mathbf{A})\mathbf{x}_i = \mathbf{0}$ , which means that once the eigenvalues have been found, the eigenvectors can be found via Gaussian elimination.

---

<sup>7</sup>We use  $\lambda$  (even though this is not consistent with our notation) because that is what most texts use.

Some theoretical results of great use are: *i)*  $\text{tr}(\mathbf{A}) = \sum_{i=0}^{n-1} a_{ii} = \sum_{i=0}^{n-1} \lambda_i$ , *ii)*  $\det(\mathbf{A}) = \prod_{i=0}^{n-1} \lambda_i$ , *iii)* if  $\mathbf{A}$  is real (consists of only real values) and is symmetric, i.e.,  $\mathbf{A} = \mathbf{A}^T$ , then its eigenvalues are real and the different eigenvectors are orthogonal.

### Orthogonal Matrices

Here, we will shed some light on the concept of an orthogonal matrix, its properties, and its characteristics. A square matrix,  $\mathbf{M}$ , with only real elements is orthogonal if and only if  $\mathbf{MM}^T = \mathbf{M}^T\mathbf{M} = \mathbf{I}$ . That is, when multiplied by its transpose, it yields the identity matrix.

The orthogonality of a matrix,  $\mathbf{M}$ , has some significant implications such as: *i)*  $|\mathbf{M}| = \pm 1$ , *ii)*  $\mathbf{M}^{-1} = \mathbf{M}^T$ , *iii)*  $\mathbf{M}^T$  is also orthogonal, *iv)*  $\|\mathbf{Mu}\| = \|\mathbf{u}\|$ , *v)*  $\mathbf{Mu} \perp \mathbf{Mv} \Leftrightarrow \mathbf{u} \perp \mathbf{v}$ , *vi)* if  $\mathbf{M}$  and  $\mathbf{N}$  are orthogonal, so is  $\mathbf{MN}$ .

The standard basis is orthonormal because the basis vectors are mutually orthogonal and of length one. Using the standard basis as a matrix, we can show that the matrix is orthogonal:<sup>8</sup>  $\mathbf{E} = (\mathbf{e}_x \ \mathbf{e}_y \ \mathbf{e}_z) = \mathbf{I}$ , and  $\mathbf{I}^T\mathbf{I} = \mathbf{I}$ .

To clear up some possible confusion, an orthogonal matrix is not the same as an orthogonal vector set (basis). Informally, the difference is that an orthogonal matrix must consist of normalized vectors. A set of vectors may be mutually perpendicular, and so be called an orthogonal vector set. However, if these are inserted into a matrix either as rows or columns, this does not automatically make the matrix orthogonal, if the vectors themselves are not normalized. An orthonormal vector set (basis), on the other hand, always forms an orthogonal matrix if the vectors are inserted into the matrix as a set of rows or columns. A better term for an orthogonal matrix would be an orthonormal matrix, since it is always composed of an orthonormal basis, but even mathematics is not always logical.

### A.3.2 Change of Base

Assume we have a vector,  $\mathbf{v}$ , in the standard basis (see Section 1.2.1), described by the coordinate axes  $\mathbf{e}_x$ ,  $\mathbf{e}_y$ , and  $\mathbf{e}_z$ . Furthermore, we have another coordinate system described by the arbitrary basis vectors  $\mathbf{f}_x$ ,  $\mathbf{f}_y$ , and  $\mathbf{f}_z$  (which must be noncoplanar, i.e.,  $|\mathbf{f}_x \ \mathbf{f}_y \ \mathbf{f}_z| \neq 0$ ). How can  $\mathbf{v}$  be expressed uniquely in the basis described by  $\mathbf{f}_x$ ,  $\mathbf{f}_y$ , and  $\mathbf{f}_z$ ? The solution is given below, where  $\mathbf{w}$  is  $\mathbf{v}$  expressed in the new basis, described by  $\mathbf{F}$  [741]:

$$\begin{aligned} \mathbf{Fw} &= (\mathbf{f}_x \ \mathbf{f}_y \ \mathbf{f}_z) \mathbf{w} = \mathbf{v} \\ &\iff \\ \mathbf{w} &= \mathbf{F}^{-1}\mathbf{v}. \end{aligned} \tag{A.42}$$

---

<sup>8</sup>Note that the basis is orthonormal, but the matrix is orthogonal, though they mean the same thing.

A special situation occurs if the matrix  $\mathbf{F}$  is orthogonal, which implies that the inverse is easily obtained by  $\mathbf{F}^{-1} = \mathbf{F}^T$ . Therefore, Equation A.42 simplifies to Equation A.43:

$$\mathbf{w} = \mathbf{F}^T \mathbf{v} = \begin{pmatrix} \mathbf{f}_x^T \\ \mathbf{f}_y^T \\ \mathbf{f}_z^T \end{pmatrix} \mathbf{v} = \begin{pmatrix} \mathbf{f}_x \cdot \mathbf{v} \\ \mathbf{f}_y \cdot \mathbf{v} \\ \mathbf{f}_z \cdot \mathbf{v} \end{pmatrix}. \quad (\text{A.43})$$

Orthogonal coordinate system changes are the most common ones in the context of computer graphics.

## A.4 Homogeneous Notation

This section is probably the most important in this chapter, since it influences many areas of computer graphics and is almost never treated in a common linear algebra book.

A point describes a location in space, while a vector describes a direction and has no location. Using  $3 \times 3$  matrices (or  $2 \times 2$  for two dimensions), it is possible to perform linear transformations such as rotations, scalings, and shears on coordinates. However, translation cannot be performed using such matrices. This lack is unimportant for vectors, for which translation has no meaning, but translation is meaningful for points.

Homogeneous notation is useful for transforming both vectors and points, and includes the ability to perform translation only on points. It augments  $3 \times 3$  matrices to the size of  $4 \times 4$ , and three-dimensional points and vectors get one more element. So a homogeneous vector is  $\mathbf{p} = (p_x, p_y, p_z, p_w)$ . As will soon be made clear,  $p_w = 1$  for points, and  $p_w = 0$  for vectors. For projections, other values can be used for  $p_w$  (see Section 4.6). When  $p_w \neq 0$  and  $p_w \neq 1$ , then the actual point is obtained through *homogenization*, where all components are divided by  $p_w$ . This means the point  $(p_x/p_w, p_y/p_w, p_z/p_w, 1)$  is obtained.

Equation A.44 shows how a  $3 \times 3$  matrix,  $\mathbf{M}$ , is augmented (in the simplest case) into the homogeneous form:

$$\mathbf{M}_{4 \times 4} = \begin{pmatrix} m_{00} & m_{01} & m_{02} & 0 \\ m_{10} & m_{11} & m_{12} & 0 \\ m_{20} & m_{21} & m_{22} & 0 \\ 0 & 0 & 0 & 1 \end{pmatrix}. \quad (\text{A.44})$$

Rotation, scaling, and shear matrices can replace  $\mathbf{M}$  in this equation, and affect both vectors and points, as they should. A translation, however, uses the additional elements of the augmented matrix to obtain the goal of

the foundation. A typical translation matrix,  $\mathbf{T}$ , which translates a point by a vector,  $\mathbf{t}$ , is shown in Equation A.45:

$$\mathbf{T} = \begin{pmatrix} 1 & 0 & 0 & t_x \\ 0 & 1 & 0 & t_y \\ 0 & 0 & 1 & t_z \\ 0 & 0 & 0 & 1 \end{pmatrix}. \quad (\text{A.45})$$

The combination of a linear transform followed by a translation is called an *affine transform*.

It is quickly verified that a vector  $\mathbf{v} = (v_x, v_y, v_z, 0)$  is unaffected by the  $\mathbf{T}\mathbf{v}$  transform due to the fact that its last element is 0. If the point  $\mathbf{p} = (p_x, p_y, p_z, 1)$  is transformed as  $\mathbf{T}\mathbf{p}$ , the result is  $(p_x + t_x, p_y + t_y, p_z + t_z, 1)$ , i.e.,  $\mathbf{p}$  translated by  $\mathbf{t}$ .

Matrix-matrix multiplications (and thus concatenations of homogeneous matrices) and matrix-vector multiplications are carried out precisely as usual. In Chapter 4, many kinds of different homogeneous transforms will be introduced and thoroughly dissected.

## A.5 Geometry

This section is concerned with presenting some useful geometrical techniques that are used extensively in, for example, Chapter 16.

### A.5.1 Lines

#### *Two-Dimensional Lines*

For two-dimensional lines, there are two main mathematical descriptions: the implicit form and the explicit form. The latter is parametric, and a typical equation for it is Equation A.46:

$$\mathbf{r}(t) = \mathbf{o} + t\mathbf{d}. \quad (\text{A.46})$$

Here,  $\mathbf{o}$  is a point on the line,  $\mathbf{d}$  is the direction vector of the line, and  $t$  is a parameter that can be used to generate different points,  $\mathbf{r}$ , on the line.<sup>9</sup>

The implicit form is different in that it cannot generate points explicitly. Assume, instead, that on our line of interest, called  $L$ , any point can be described by  $\mathbf{p} = (p_x, p_y) = (x, y)$ , where the latter coordinate notation

---

<sup>9</sup>The points are named  $\mathbf{r}$  here because in other chapters the line is usually referred to as a ray.

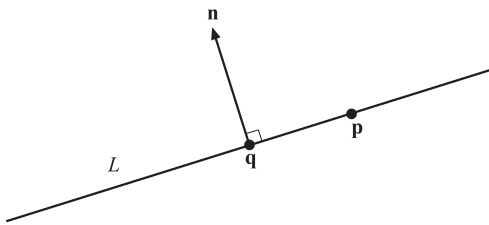


**Figure A.5.** Notation used for the implicit form of a two-dimensional line equation.  $L$  is the line,  $\mathbf{p}$  and  $\mathbf{q}$  are points on the line, and  $\mathbf{n}$  is a vector perpendicular to the direction of  $L$ .

is used only in Equation A.47, because this is the line equation form that most people learn first:

$$ax + by + c = 0. \quad (\text{A.47})$$

For  $\mathbf{p}$  to lie on the line  $L$ , it must fulfill this equation. Now, if the constants  $a$  and  $b$  are combined into a vector  $\mathbf{n} = (n_x, n_y) = (a, b)$ , then Equation A.47 can be expressed using the dot product as

$$\mathbf{n} \cdot \mathbf{p} + c = 0. \quad (\text{A.48})$$

A common task is, naturally, to compute the constants of a line. Looking at Figure A.5 and using its notation, we may see that one way of describing  $L$  would be  $\mathbf{n} \cdot (\mathbf{p} - \mathbf{q}) = 0$ , where  $\mathbf{q}$  is another point on the line. Thus,  $\mathbf{n}$  must be perpendicular to the line direction, i.e.,  $\mathbf{n} = (\mathbf{p} - \mathbf{q})^\perp = (- (p_y - q_y), p_x - q_x) = (a, b)$ , and  $c = -\mathbf{q} \cdot \mathbf{n}$ . Then, given two points on  $L$ ,  $\mathbf{n} = (a, b)$  and  $c$  can be calculated.

Rewriting Equation A.48 as a function,  $f(\mathbf{p}) = \mathbf{n} \cdot \mathbf{p} + c$ , allows some very useful properties to be derived. Nothing is now assumed about  $\mathbf{p}$ ; it can be any point in the two-dimensional plane. First, if again  $\mathbf{q} \in L$ , the following holds:

1.  $f(\mathbf{p}) = 0 \iff \mathbf{p} \in L$ .
2.  $f(\mathbf{p}) > 0 \iff \mathbf{p}$  lies on the same side of the line as the point  $\mathbf{q} + \mathbf{n}$ .
3.  $f(\mathbf{p}) < 0 \iff \mathbf{p}$  lies on the same side of the line as the point  $\mathbf{q} - \mathbf{n}$ .

This test is usually called a *half-plane test* and is used in, for example, some point-in-polygon routines (see Section 16.9). Second,  $f(\mathbf{p})$  happens to be a measure for the perpendicular distance from  $\mathbf{p}$  to  $L$ . In fact, it

turns out that the *signed distance*,  $f_s$ , is found by using Equation A.49:

$$f_s(\mathbf{p}) = \frac{f(\mathbf{p})}{\|\mathbf{n}\|}. \quad (\text{A.49})$$

If  $\|\mathbf{n}\| = 1$ , that is,  $\mathbf{n}$  is normalized, then  $f_s(\mathbf{p}) = f(\mathbf{p})$ .

### Three-Dimensional Lines

In three dimensions, the implicit form of a line is often expressed as the intersection between two nonparallel planes. An explicit form is shown in Equation A.50. This equation is heavily used in computing the intersection between a line (or ray) and a three-dimensional surface:

$$\mathbf{r}(t) = \mathbf{o} + t\mathbf{d}. \quad (\text{A.50})$$

This is exactly the same equation used for the two-dimensional line, except that the points and the direction vector are now three dimensional.

The distance from a point  $\mathbf{p}$  to  $\mathbf{r}(t)$  can be computed by first projecting  $\mathbf{p}$  onto  $\mathbf{r}(t)$ , using Equation A.17. Assuming  $\mathbf{d}$  is normalized, this is done by computing the vector  $\mathbf{w} = ((\mathbf{p} - \mathbf{o}) \cdot \mathbf{d})\mathbf{d}$ . Then the sought-for distance is  $\|(\mathbf{p} - \mathbf{o}) - \mathbf{w}\|$ .

## A.5.2 Planes

Since the three-dimensional plane is a natural extension of the two-dimensional line, it can be expected that the plane has similar properties as the line. In fact, any hyperplane, which is the name for a plane of an arbitrary dimension, has these similar characteristics. Here, the discussion will be limited to the three-dimensional plane.

First, the plane can be described in both explicit and implicit form. Equation A.51 shows the explicit form of the three-dimensional plane:

$$\mathbf{p}(u, v) = \mathbf{o} + u\mathbf{s} + v\mathbf{t}. \quad (\text{A.51})$$

Here,  $\mathbf{o}$  is a point lying on the plane,  $\mathbf{s}$  and  $\mathbf{t}$  are direction vectors that span the plane (i.e., they are noncollinear), and  $u$  and  $v$  are parameters that generate different points on the plane. The normal of this plane is  $\mathbf{s} \times \mathbf{t}$ .

The implicit equation for the plane, called  $\pi$ , shown in Equation A.52, is identical to Equation A.48, with the exception that the plane equation is augmented with an extra dimension, and  $c$  has been renamed to  $d$ :

$$\mathbf{n} \cdot \mathbf{p} + d = 0. \quad (\text{A.52})$$

Again,  $\mathbf{n}$  is the normal of the plane,  $\mathbf{p}$  is any point on the plane, and  $d$  is a constant that determines part of the position of the plane. As was

shown previously, the normal can be computed using two direction vectors, but it can naturally also be obtained from three noncollinear points,  $\mathbf{u}$ ,  $\mathbf{v}$ , and  $\mathbf{w}$ , lying on the plane, as  $\mathbf{n} = (\mathbf{u} - \mathbf{w}) \times (\mathbf{v} - \mathbf{w})$ . Given  $\mathbf{n}$  and a point  $\mathbf{q}$  on the plane, the constant is computed as  $d = -\mathbf{n} \cdot \mathbf{q}$ . The half-plane test is equally valid. By denoting  $f(\mathbf{p}) = \mathbf{n} \cdot \mathbf{p} + d$ , the same conclusions can be drawn as for the two-dimensional line; that is,

1.  $f(\mathbf{p}) = 0 \iff \mathbf{p} \in \pi$ .
2.  $f(\mathbf{p}) > 0 \iff \mathbf{p}$  lies on the same side of the plane as the point  $\mathbf{q} + \mathbf{n}$ .
3.  $f(\mathbf{p}) < 0 \iff \mathbf{p}$  lies on the same side of the plane as the point  $\mathbf{q} - \mathbf{n}$ .

The signed distance from an arbitrary point  $\mathbf{p}$  to  $\pi$  is obtained by exchanging the two-dimensional parts of Equation A.49 for their three-dimensional counterparts for the plane. Also, it is very easy to interpret the meaning of  $d$  using the signed distance formula. This requires inserting the origin,  $\mathbf{0}$ , into that formula;  $f_s(\mathbf{0}) = d$ , which means that  $d$  is the shortest (signed) distance from the origin to the plane.

### A.5.3 Convex Hull

For a set of points, the *convex hull* is defined as the smallest set that satisfies the condition that the straight line between any two points in the set is totally included in the set as well. This holds for any dimension.

In two dimensions, the construction of the convex hull is intuitively illustrated by the rubberband/nail scheme. Imagine that the points are nails in a table, and that a rubber band is held in such a way that its interior includes all nails. The rubber band is then released, and now the

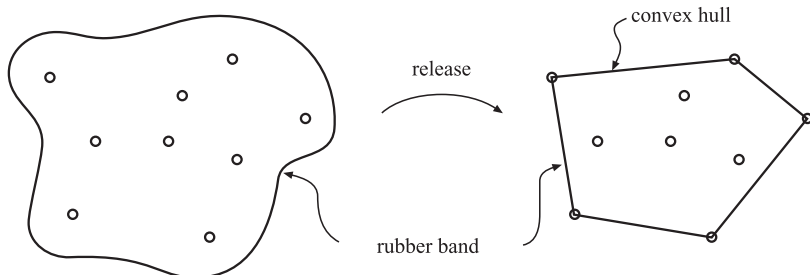


**Figure A.6.** The rubberband/nail scheme in action. The left figure shows the rubber band before it has been released and the right figure shows the result after. Then the rubber band is a representation of the convex hull of the nails.

rubber band is, in fact, the convex hull of the nails. This is illustrated in Figure A.6.

The convex hull has many areas of use; the construction of bounding volumes is one. The convex hull is, by its definition, the smallest convex volume for a set of points, and is therefore attractive for those computations. Algorithms for computing the convex hull in two and three dimensions can be found in, for example, books by de Berg et al. [82] or O'Rourke [975]. A fast algorithm, called *QuickHull*, is presented by Barber et al. [62].

### A.5.4 Miscellaneous

#### *Area Calculation*

A parallelogram defined by two vectors,  $\mathbf{u}$  and  $\mathbf{v}$ , starting at the origin, has the area  $\|\mathbf{u} \times \mathbf{v}\| = \|\mathbf{u}\| \|\mathbf{v}\| \sin \phi$ , as shown in Figure A.7.

If the parallelogram is divided by a line from  $\mathbf{u}$  to  $\mathbf{v}$ , two triangles are formed. This means that the area of each triangle is half the area of the parallelogram. So, if a triangle is given by three points, say  $\mathbf{p}$ ,  $\mathbf{q}$ , and  $\mathbf{r}$ , its area is

$$\text{Area}(\triangle \mathbf{pqr}) = \frac{1}{2} \|(\mathbf{p} - \mathbf{r}) \times (\mathbf{q} - \mathbf{r})\|. \quad (\text{A.53})$$

The signed area of a general two-dimensional polygon can be computed by [975, 1081]

$$\text{Area}(P) = \frac{1}{2} \sum_{i=0}^{n-1} (x_i y_{i+1} - y_i x_{i+1}), \quad (\text{A.54})$$

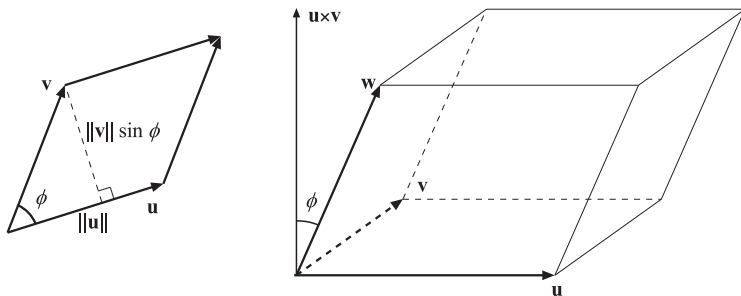


**Figure A.7.** Left figure: a parallelogram whose area is computed by multiplying the length of the base ( $\|\mathbf{u}\|$ ) with the height ( $\|\mathbf{v}\| \sin \phi$ ). Right figure: the volume of a parallelepiped is given by  $(\mathbf{u} \times \mathbf{v}) \cdot \mathbf{w}$ .

where  $n$  is the number of vertices, and where  $i$  is modulo  $n$ , so that  $x_n = x_0$ , etc. This area can be computed with fewer multiplies and potentially more accuracy (though needing a wider range of indices for each term) by the following formula [1230]:

$$\text{Area}(P) = \frac{1}{2} \sum_{i=0}^{n-1} (x_i(y_{i+1} - y_{i-1})). \quad (\text{A.55})$$

The sign of the area is related to the order in which the outline of the polygon is traversed; positive means counterclockwise.

### Volume Calculation

The scalar triple product, from Equation A.18, is sometimes also called the volume formula. Three vectors,  $\mathbf{u}$ ,  $\mathbf{v}$  and  $\mathbf{w}$ , starting at the origin, form a solid, called a parallelepiped, whose volume is given by the equation that follows. The volume and the notation are depicted in Figure A.7:

$$\text{Volume}(\mathbf{u}, \mathbf{v}, \mathbf{w}) = (\mathbf{u} \times \mathbf{v}) \cdot \mathbf{w} = \det(\mathbf{u}, \mathbf{v}, \mathbf{w}) \quad (\text{A.56})$$

This is a positive value only if the vectors form a positively oriented basis. The formula intuitively explains why the determinant of three vectors is zero if the vectors do not span the entire space  $\mathbb{R}^3$ : In that case, the volume is zero, meaning that the vectors must lie in the same plane (or one or more of them may be the zero vector).

## Further Reading and Resources

For a more thorough treatment of linear algebra, the reader is directed to, for example, the books by Lawson [741] and Lax [742]. Hutson and Pym's book [578] gives an in-depth treatment of all kinds of spaces (and more). A lighter read is Farin and Hansford's *Practical Linear Algebra* [333], which builds up a geometric understanding for transforms, eigenvalues, and much else.

The 30th edition of the *CRC Standard Mathematical Tables and Formulas* [1416] is a recent major update of this classic reference. Much of the material in this appendix is included, as well as a huge amount of other mathematical knowledge.



# Appendix B

## Trigonometry

*“Life is good for only two things, discovering mathematics and teaching mathematics.”*

—Siméon Poisson

This appendix is intended to be a reference to some simple laws of trigonometry as well as some more sophisticated ones. The laws of trigonometry are particularly important tools in computer graphics. One example of their usefulness is that they provide ways to simplify equations and thereby to increase speed.

### B.1 Definitions

According to Figure B.1, where  $\mathbf{p} = (p_x, p_y)$  is a unit vector, i.e.,  $\|\mathbf{p}\| = 1$ , the fundamental trigonometric functions, sin, cos, and tan, are defined by Equation B.1.

**Fundamental trigonometric functions :**

$$\begin{aligned}\sin \phi &= p_y \\ \cos \phi &= p_x \\ \tan \phi &= \frac{\sin \phi}{\cos \phi} = \frac{p_y}{p_x}\end{aligned}\tag{B.1}$$

The sin, cos, and tan functions can be expanded into MacLaurin series, as shown in Equation B.2. MacLaurin series are a special case of the more general Taylor series. A Taylor series is an expansion about an arbitrary point, while a MacLaurin series always is developed around  $x = 0$ .

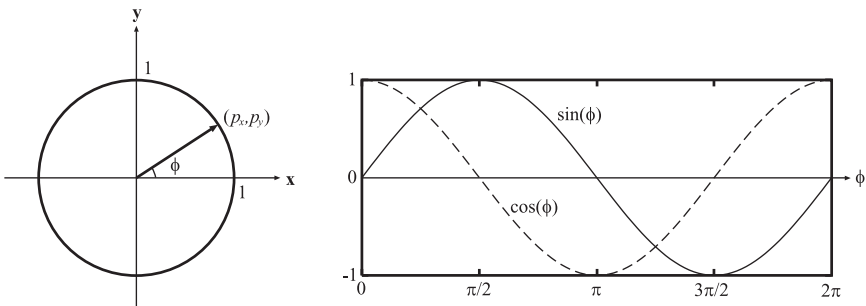


**Figure B.1.** The geometry for the definition of the sin, cos, and tan functions is shown to the left. The right-hand part of the figure shows  $p_x = \cos \phi$  and  $p_y = \sin \phi$ , which together traces out the circle.

MacLaurin series are beneficial because they clarify the origins of some of the derivatives (shown in Equation set B.4).

**MacLaurin series :**

$$\begin{aligned} \sin \phi &= \phi - \frac{\phi^3}{3!} + \frac{\phi^5}{5!} - \frac{\phi^7}{7!} + \cdots + (-1)^n \frac{\phi^{2n+1}}{(2n+1)!} + \dots \\ \cos \phi &= 1 - \frac{\phi^2}{2!} + \frac{\phi^4}{4!} - \frac{\phi^6}{6!} + \cdots + (-1)^n \frac{\phi^{2n}}{(2n)!} + \dots \\ \tan \phi &= \phi + \frac{\phi^3}{3} + \frac{2\phi^5}{15} + \cdots + (-1)^{n-1} \frac{2^{2n}(2^{2n}-1)}{(2n)!} B_{2n} \phi^{2n-1} + \dots \end{aligned} \quad (\text{B.2})$$

The two first series hold for  $-\infty < \phi < \infty$ , the last one for  $-\pi/2 < \phi < \pi/2$  and  $B_n$  is the  $n$ th Bernoulli number.<sup>1</sup>

The inverses of the trigonometric functions, arcsin, arccos, and arctan, are defined as in Equation B.3.

**Inverses of trigonometric functions :**

$$\begin{aligned} p_y = \sin \phi &\Leftrightarrow \phi = \arcsin p_y, \quad -1 \leq p_y \leq 1, \quad -\frac{\pi}{2} \leq \phi \leq \frac{\pi}{2} \\ p_x = \cos \phi &\Leftrightarrow \phi = \arccos p_x, \quad -1 \leq p_x \leq 1, \quad 0 \leq \phi \leq \pi \\ \frac{p_y}{p_x} = \tan \phi &\Leftrightarrow \phi = \arctan \frac{p_y}{p_x}, \quad -\infty \leq \frac{p_y}{p_x} \leq \infty, \quad -\frac{\pi}{2} \leq \phi \leq \frac{\pi}{2} \end{aligned} \quad (\text{B.3})$$

<sup>1</sup>The Bernoulli numbers can be generated with a recursive formula, where  $B_0 = 1$  and then for  $k > 1$ ,  $\sum_{j=0}^{k-1} \binom{k}{j} B_j = 0$ .

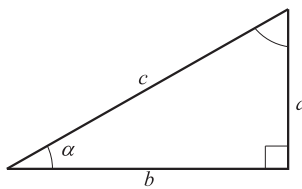


**Figure B.2.** A right triangle and its notation.

The derivatives of the trigonometric functions and their inverses are summarized below.

**Trigonometric derivatives :**

$$\frac{d \sin \phi}{d\phi} = \cos \phi$$

$$\frac{d \cos \phi}{d\phi} = -\sin \phi$$

$$\frac{d \tan \phi}{d\phi} = \frac{1}{\cos^2 \phi} = 1 + \tan^2 \phi$$

(B.4)

$$\frac{d \arcsin t}{dt} = \frac{1}{\sqrt{1-t^2}}$$

$$\frac{d \arccos t}{dt} = -\frac{1}{\sqrt{1-t^2}}$$

$$\frac{d \arctan t}{dt} = \frac{1}{1+t^2}$$

## B.2 Trigonometric Laws and Formulae

We begin with some fundamental laws about right triangles. To use the notation from Figure B.2, the following laws apply:

**Right triangle laws :**

$$\begin{aligned}\sin \alpha &= \frac{a}{c} \\ \cos \alpha &= \frac{b}{c} \\ \tan \alpha &= \frac{\sin \alpha}{\cos \alpha} = \frac{a}{b}\end{aligned}\tag{B.5}$$

**Pythagorean relation :**  $c^2 = a^2 + b^2$  (B.6)

For arbitrarily angled triangles, the following well-known rules are valid, using the notation from Figure B.3.

|  |       |
|--|-------|
| <b>Law of sines :</b> $\frac{\sin \alpha}{a} = \frac{\sin \beta}{b} = \frac{\sin \gamma}{c}$                 |       |
| <b>Law of cosines :</b> $c^2 = a^2 + b^2 - 2ab \cos \gamma$  | (B.7) |
| <b>Law of tangents :</b> $\frac{a+b}{a-b} = \frac{\tan \frac{\alpha+\beta}{2}}{\tan \frac{\alpha-\beta}{2}}$ |       |

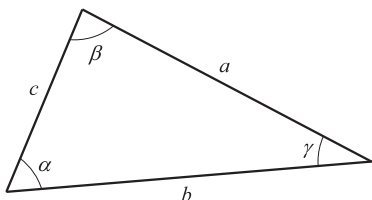


**Figure B.3.** An arbitrarily angled triangle and its notation.

Named after their inventors, the following two formulae are also valid for arbitrarily angled triangles.

$$\text{Newton's formula : } \frac{b+c}{a} = \frac{\cos \frac{\beta-\gamma}{2}}{\sin \frac{\alpha}{2}} \quad (\text{B.8})$$

$$\text{Mollweide's formula : } \frac{b-c}{a} = \frac{\sin \frac{\beta-\gamma}{2}}{\cos \frac{\alpha}{2}}$$

The definition of the trigonometric functions (Equation B.1) together with the Pythagorean relation (Equation B.6) gives the *trigonometric identity*:

$$\boxed{\text{Trigonometric identity : } \cos^2 \phi + \sin^2 \phi = 1} \quad (\text{B.9})$$

Here follow some laws that can be exploited to simplify equations and thereby make their implementation more efficient.

#### Double angle relations :

$$\sin 2\phi = 2 \sin \phi \cos \phi = \frac{2 \tan \phi}{1 + \tan^2 \phi}$$

$$\cos 2\phi = \cos^2 \phi - \sin^2 \phi = 1 - 2 \sin^2 \phi = 2 \cos^2 \phi - 1 = \frac{1 - \tan^2 \phi}{1 + \tan^2 \phi}$$

$$\tan 2\phi = \frac{2 \tan \phi}{1 - \tan^2 \phi}$$

(B.10)

Extensions of these laws are called the *multiple angle relations*, shown below.

#### Multiple angle relations :

$$\sin(n\phi) = 2 \sin((n-1)\phi) \cos \phi - \sin((n-2)\phi)$$

$$\cos(n\phi) = 2 \cos((n-1)\phi) \cos \phi - \cos((n-2)\phi)$$

$$\tan(n\phi) = \frac{\tan((n-1)\phi) + \tan \phi}{1 - \tan((n-1)\phi) \tan \phi}$$

(B.11)

Equations B.12 and B.13 show a collection of laws that we call the *angle sum* and *angle difference relations*.

**Angle sum relations :**

$$\begin{aligned}\sin(\phi + \rho) &= \sin \phi \cos \rho + \cos \phi \sin \rho \\ \cos(\phi + \rho) &= \cos \phi \cos \rho - \sin \phi \sin \rho \\ \tan(\phi + \rho) &= \frac{\tan \phi + \tan \rho}{1 - \tan \phi \tan \rho}\end{aligned}\tag{B.12}$$

**Angle difference relations :**

$$\begin{aligned}\sin(\phi - \rho) &= \sin \phi \cos \rho - \cos \phi \sin \rho \\ \cos(\phi - \rho) &= \cos \phi \cos \rho + \sin \phi \sin \rho \\ \tan(\phi - \rho) &= \frac{\tan \phi - \tan \rho}{1 + \tan \phi \tan \rho}\end{aligned}\tag{B.13}$$

Next follow the *product relations*.

**Product relations :**

$$\begin{aligned}\sin \phi \sin \rho &= \frac{1}{2}(\cos(\phi - \rho) - \cos(\phi + \rho)) \\ \cos \phi \cos \rho &= \frac{1}{2}(\cos(\phi - \rho) + \cos(\phi + \rho)) \\ \sin \phi \cos \rho &= \frac{1}{2}(\sin(\phi - \rho) + \sin(\phi + \rho))\end{aligned}\tag{B.14}$$

The formulae in Equations B.15 and B.16 go under the names *function sums and differences* and *half-angle relations*.

**Function sums and differences :**

$$\sin \phi + \sin \rho = 2 \sin \frac{\phi + \rho}{2} \cos \frac{\phi - \rho}{2}$$

$$\cos \phi + \cos \rho = 2 \cos \frac{\phi + \rho}{2} \cos \frac{\phi - \rho}{2}$$

$$\tan \phi + \tan \rho = \frac{\sin(\phi + \rho)}{\cos \phi \cos \rho} \quad (\text{B.15})$$

$$\sin \phi - \sin \rho = 2 \cos \frac{\phi + \rho}{2} \sin \frac{\phi - \rho}{2}$$

$$\cos \phi - \cos \rho = -2 \sin \frac{\phi + \rho}{2} \sin \frac{\phi - \rho}{2}$$

$$\tan \phi - \tan \rho = \frac{\sin(\phi - \rho)}{\cos \phi \cos \rho}$$

**Half-angle relations :**

$$\sin \frac{\phi}{2} = \pm \sqrt{\frac{1 - \cos \phi}{2}} \quad (\text{B.16})$$

$$\cos \frac{\phi}{2} = \pm \sqrt{\frac{1 + \cos \phi}{2}}$$

$$\tan \frac{\phi}{2} = \pm \sqrt{\frac{1 - \cos \phi}{1 + \cos \phi}} = \frac{1 - \cos \phi}{\sin \phi} = \frac{\sin \phi}{1 + \cos \phi}$$

## Further Reading and Resources

The first chapter of *Graphics Gems* [405] provides other geometric relationships that are useful in computer graphics. The 31st edition of the *CRC Standard Mathematical Tables and Formulas* [1416] includes the formulae in this appendix and much more.



# Bibliography

- [1] Abrash, Michael, *Michael Abrash's Graphics Programming Black Book, Special Edition*, The Coriolis Group, Inc., Scottsdale, Arizona, 1997. Cited on p. 172, 652, 695, 702
- [2] Aguru Images, Inc. website. <http://www.aguruimages.com/> Cited on p. 265
- [3] Aila, T., and V. Miettinen, *Umbra Reference Manual*, Hybrid Holding Ltd., Helsinki, Finland, October 2000. Cited on p. 680
- [4] Aila, Timo, and Ville Miettinen, "dPVS: An Occlusion Culling System for Massive Dynamic Environments," *IEEE Computer Graphics and Applications*, vol. 24, no. 2, pp. 86–97, March 2004. Cited on p. 520, 650, 652, 668, 680, 695
- [5] Airey, John M., John H. Rohlff, and Frederick P. Brooks Jr., "Towards Image Realism with Interactive Update Rates in Complex Virtual Building Environments," *Computer Graphics (1990 Symposium on Interactive 3D Graphics)*, vol. 24, no. 2, pp. 41–50, March 1990. Cited on p. 538, 667
- [6] Airey, John M., *Increasing Update Rates in the Building Walkthrough System with Automatic Model-Space Subdivision and Potentially Visible Set Calculations*, Ph.D. Thesis, Technical Report TR90-027, Department of Computer Science, University of North Carolina at Chapel Hill, July 1990. Cited on p. 667
- [7] Akeley, K., and T. Jermoluk, "High-Performance Polygon Rendering," *Computer Graphics (SIGGRAPH '88 Proceedings)*, pp. 239–246, August 1988. Cited on p. 22
- [8] Akeley, K., P. Haeberli, and D. Burns, `tomesh.c`, a C-program on the *SGI Developer's Toolbox CD*, 1990. Cited on p. 543, 553, 554
- [9] Akeley, Kurt, "RealityEngine Graphics," *Computer Graphics (SIGGRAPH 93 Proceedings)*, pp. 109–116, August 1993. Cited on p. 126
- [10] Akeley, Kurt, and Pat Hanrahan, "Real-Time Graphics Architectures," Course CS448A Notes, Stanford University, Fall 2001. Cited on p. 847, 875, 877
- [11] Akenine-Möller, Tomas, "Fast 3D Triangle-Box Overlap Testing," *journal of graphics tools*, vol. 6, no. 1, pp. 29–33, 2001. Cited on p. 760, 762
- [12] Akenine-Möller, Tomas, and Ulf Assarsson, "On the Degree of Vertices in a Shadow Volume Silhouette," *journal of graphics tools*, vol. 8, no. 4, pp. 21–24, 2003. Cited on p. 521
- [13] Akenine-Möller, Tomas, and Jacob Ström, "Graphics for the Masses: A Hardware Rasterization Architecture for Mobile Phones," *ACM Transactions on Graphics*, vol. 22, no. 3, pp. 801–808, 2003. Cited on p. 133, 851, 857, 870, 872
- [14] Akenine-Möller, Tomas, Jacob Munkberg, and Jon Hasselgren, "Stochastic Rasterization using Time-Continuous Triangles," *Graphics Hardware*, pp. 7–16, August 2007. Cited on p. 875

- [15] Akenine-Möller, Tomas, and Jacob Ström, “Graphics Processing Units for Handhelds,” *Proceedings of the IEEE*, vol. 96, no. 5, pp. 779–789, May 2008. Cited on p. 877
- [16] Alexa, Marc, “Recent Advances in Mesh Morphing,” *Computer Graphics Forum*, vol. 21, no. 2, pp. 173–197, 2002. Cited on p. 85, 97
- [17] Aliaga, D., J. Cohen, H. Zhang, R. Bastos, T. Hudson, and C. Erikson, “Power Plant Walkthrough: An Integrated System for Massive Model Rendering,” Technical Report TR no. 97-018, Computer Science Department, University of North Carolina at Chapel Hill, 1997. Cited on p. 693
- [18] Aliaga, D., J. Cohen, A. Wilson, H. Zhang, C. Erikson, K. Hoff, T. Hudson, W. Stürzlinger, E. Baker, R. Bastos, M. Whitton, F. Brooks Jr., and D. Manocha, “A Framework for the Real-Time Walkthrough of Massive Models,” Technical Report UNC TR no. 98-013, Computer Science Department, University of North Carolina at Chapel Hill, 1998. Cited on p. 693
- [19] Aliaga, D., J. Cohen, A. Wilson, E. Baker, H. Zhang, C. Erikson, K. Hoff, T. Hudson, W. Stürzlinger, R. Bastos, M. Whitton, F. Brooks, and D. Manocha, “MMR: An Interactive Massive Model Rendering System Using Geometric and Image-Based Acceleration,” *Proceedings 1999 Symposium on Interactive 3D Graphics*, pp. 199–206, April 1999. Cited on p. 693
- [20] Aliaga, Daniel G., and Anselmo Lastra, “Automatic Image Placement to Provide A Guaranteed Frame Rate,” *Computer Graphics (SIGGRAPH 1999 Proceedings)*, pp. 307–316, August 1999. Cited on p. 457, 466
- [21] Aliaga, Daniel G., Thomas Funkhouser, Dimah Yanovsky, and Ingrid Carlom, “Sea of Images,” *Proceedings of IEEE Visualization*, pp. 331–338, 2002. Cited on p. 444
- [22] Andersson, Fredrik, “Bezier and B-Spline Technology,” M.Sc. Thesis, Umeå Universitet, 2003. Cited on p. 583
- [23] Andersson, Johan, “Terrain Rendering in Frostbite Using Procedural Shader Splatting,” *SIGGRAPH 2007 Advanced Real-Time Rendering in 3D Graphics and Games course notes*, 2007. Cited on p. 40, 155, 195, 199, 571, 572, 574, 882
- [24] Andújar, Carlos, Javier Boo, Pere Brunet, Marta Fairén, Isabel Navazo, Pere Pau Vázquez, and Àlvar Vinacua, “Omni-directional Relief Impostors,” *Computer Graphics Forum*, vol. 26, no. 3, pp. 553–560, 2007. Cited on p. 466
- [25] Annen, Thomas, Jan Kautz, Frédo Durand, and Hans-Peter Seidel, “Spherical Harmonic Gradients for Mid-Range Illumination,” *Eurographics Symposium on Rendering (2004)*, pp. 331–336, June 2004. Cited on p. 323, 424
- [26] Annen, Thomas, Tom Mertens, Philippe Bekaert, Hans-Peter Seidel, and Jan Kautz, “Convolution Shadow Maps,” *Eurographics Symposium on Rendering (2007)*, 51–60, June 2007. Cited on p. 370
- [27] Ankrum, Dennis R., “Viewing Distance at Computer Workstations,” *WorkPlace Ergonomics*, pp. 10–12, Sept./Oct. 1996. Cited on p. 95
- [28] Ansari, Marwan Y., “Image Effects with DirectX 9 Pixel Shaders,” in Engel, Wolfgang, ed., *ShaderX<sup>2</sup>: Shader Programming Tips and Tricks with DirectX 9*, Wordware, pp. 481–518, 2004. Cited on p. 472
- [29] Antonio, Franklin, “Faster Line Segment Intersection,” in David Kirk, ed., *Graphics Gems III*, Academic Press, pp. 199–202, 1992. Cited on p. 781
- [30] Apodaca, Anthony A., and Larry Gritz, *Advanced RenderMan: Creating CGI for Motion Pictures*, Morgan Kaufmann, 1999. Cited on p. 33, 283

- [31] Apodaca, Anthony A., "How PhotoRealistic RenderMan Works," in *Advanced RenderMan: Creating CGI for Motion Pictures*, Morgan Kaufmann, 1999. Also in *SIGGRAPH 2000 Advanced RenderMan 2: To RI-INFINITY and Beyond course notes*, 2000. Cited on p. 44, 880, 884
- [32] Arge, L., G. S. Brodal, and R. Fagerberg, "Cache-Oblivious Data Structures," Chapter 34 in *Handbook of Data Structures*, CRC Press, 2005. Cited on p. 657
- [33] Arkin, Esther M., Martin Held, Joseph S. B. Mitchell, and Steven S. Skiena, "Hamiltonian Triangulations for Fast Rendering," *The Visual Computer*, vol. 12, no. 9, pp. 429–444, 1996. Cited on p. 552
- [34] Arvo, James, "A Simple Method for Box-Sphere Intersection Testing," in Andrew S. Glassner, ed., *Graphics Gems*, Academic Press, pp. 335–339, 1990. Cited on p. 763, 775
- [35] Arvo, James, "Ray Tracing with Meta-Hierarchies," *SIGGRAPH '90 Advanced Topics in Ray Tracing course notes*, Volume 24, 1990. Cited on p. 736
- [36] Arvo, James, ed., *Graphics Gems II*, Academic Press, 1991. Cited on p. 97, 792
- [37] Arvo, James, "The Irradiance Jacobian for Partially Occluded Polyhedral Sources," *Computer Graphics (SIGGRAPH 94 Proceedings)*, pp. 343–350, July 1994. Cited on p. 290
- [38] Arvo, Jukka, and Timo Aila, "Optimized Shadow Mapping Using the Stencil Buffer," *journal of graphics tools*, vol. 8, no. 3, pp. 23–32, 2003. Also collected in [71]. Cited on p. 349
- [39] Arvo, Jukka, Mika Hirvikorpi, and Joonas Tyystjärvi, "Approximate Soft Shadows Using an Image-Space Flood-Fill Algorithm," *Computer Graphics Forum*, vol. 23, no. 3, pp. 271–280, 2004. Cited on p. 372
- [40] Ashdown, Ian, *Radiosity: A Programmer's Perspective*, John Wiley & Sons, Inc., 1994. Cited on p. 209, 408, 437
- [41] Ashikhmin, Michael, Simon Premože, and Peter Shirley, "A Microfacet-Based BRDF Generator," *Computer Graphics (SIGGRAPH 2000 Proceedings)*, pp. 67–74, July 2000. Cited on p. 243, 247, 248, 249, 252, 258, 262, 264, 266
- [42] Ashikhmin, Michael, and Peter Shirley, "An Anisotropic Phong Light Reflection Model," Technical Report UUCS-00-014, Computer Science Department, University of Utah, June 2000. Cited on p. 241, 249, 252, 258, 261, 264
- [43] Ashikhmin, Michael, Simon Premože, and Peter Shirley, "An Anisotropic Phong BRDF Model," *journal of graphics tools*, vol. 5, no. 2, pp. 25–32, 2000. Cited on p. 249, 252, 258, 261, 264
- [44] Ashikhmin, Michael, "Microfacet-based BRDFs," *SIGGRAPH 2001 State of the Art in Modeling and Measuring of Surface Reflection course notes*, August 2001. Cited on p. 241, 245, 252, 258, 262, 264
- [45] Ashikhmin, Michael, Abhijeet Ghosh, "Simple Blurry Reflections with Environment Maps," *journal of graphics tools*, vol. 7, no. 4, pp. 3–8, 2002. Cited on p. 310
- [46] Ashikhmin, Michael, and Simon Premože, "Distribution-based BRDFs," 2007. <http://www.cs.utah.edu/~premoze/dbrdf> Cited on p. 258, 261, 266
- [47] Asirvatham, Arul, and Hugues Hoppe, "Terrain Rendering Using GPU-Based Geometry Clipmaps," in Matt Pharr, ed., *GPU Gems 2*, Addison-Wesley, pp. 27–45, 2005. Cited on p. 573

- [48] Assarsson, Ulf, and Tomas Möller, “Optimized View Frustum Culling Algorithms for Bounding Boxes,” *journal of graphics tools*, vol. 5, no. 1, pp. 9–22, 2000. Cited on p. 667, 695, 773, 776, 778
- [49] Assarsson, Ulf, and Tomas Akenine-Möller, “A Geometry-based Soft Shadow Volume Algorithm using Graphics Hardware,” *ACM Transactions on Graphics (SIGGRAPH 2003)*, vol. 22, no. 3, pp. 511–520, 2003. Cited on p. 348
- [50] ATI developer website. <http://ati.amd.com/developer/index.html> Cited on p. 50
- [51] ATI, “3Dc White Paper,” ATI website, <http://ati.de/products/radeonx800/3DcWhitePaper.pdf> Cited on p. 175
- [52] Baboud, Lionel, and Xavier Décoret “Rendering Geometry with Relief Textures,” *Graphics Interface 2006*, pp. 195–201, 2006. Cited on p. 465
- [53] Bærentzen, J. Andreas, “Hardware-Accelerated Point Generation and Rendering of Point-Based Impostors,” *journal of graphics tools*, vol. 10, no. 2, pp. 1–12, 2005. Cited on p. 695
- [54] Bærentzen, J. Andreas, Steen L. Nielsen, Mikkel Gjøl, Bent D. Larsen, and Niels Jørgen Christensen, “Single-pass Wireframe Rendering,” *SIGGRAPH 2006 Technical Sketch*, 2006. Cited on p. 528
- [55] Bahnassi, Homam, and Wessam Bahnassi, “Volumetric Clouds and Mega-Particles,” in Engel, Wolfgang, ed., *ShaderX<sup>5</sup>*, Charles River Media, pp. 295–302, 2006. Cited on p. 472
- [56] Ballard, Dana H., “Strip Trees: A Hierarchical Representation for Curves,” *Graphics and Image Processing*, vol. 24, no. 5, pp. 310–321, May 1981. Cited on p. 807
- [57] Banks, David, “Illumination in Diverse Codimensions,” *Computer Graphics (SIGGRAPH 94 Proceedings)*, pp. 327–334, July 1994. Cited on p. 258
- [58] Baraff, D., “Curved Surfaces and Coherence for Non-Penetrating Rigid Body Simulation,” *Computer Graphics (SIGGRAPH '90 Proceedings)*, pp. 19–28, August 1990. Cited on p. 823
- [59] Baraff, D., and A. Witkin, “Dynamic Simulation of Non-Penetrating Flexible Objects,” *Computer Graphics (SIGGRAPH '92 Proceedings)*, pp. 303–308, July 1992. Cited on p. 826
- [60] Baraff, D., *Dynamic Simulation of Non-Penetrating Rigid Bodies*, PhD thesis, Technical Report 92-1275, Computer Science Department, Cornell University, 1992. Cited on p. 812
- [61] Baraff, David, and Andrew Witkin, “Large Steps in Cloth Simulation,” *Computer Graphics (SIGGRAPH 98 Proceedings)*, pp. 43–54, July 1998. Cited on p. 826
- [62] Barber, C.B., D.P. Dobkin, and H. Huhdanpaa, “The Quickhull Algorithm for Convex Hull,” Geometry Center Technical Report GCG53, July 1993. Cited on p. 733, 910
- [63] Barequet, G., B. Chazelle, L.J. Guibas, J.S.B. Mitchell, and A. Tal, “BOXTREE: A Hierarchical Representation for Surfaces in 3D,” *Computer Graphics Forum*, vol. 15, no. 3, pp. 387–396, 1996. Cited on p. 803, 807
- [64] Barkans, Anthony C., “Color Recovery: True-Color 8-Bit Interactive Graphics,” *IEEE Computer Graphics and Applications*, vol. 17, no. 1, pp. 67–77, Jan./Feb. 1997. Cited on p. 832
- [65] Barkans, Anthony C., “High-Quality Rendering Using the Talisman Architecture,” *ACM SIGGRAPH/Eurographics Workshop on Graphics Hardware Los Angeles, CA*, pp. 79–88, August 1997. Cited on p. 170

- [66] Barla, Pascal, Joëlle Thollot, and Lee Markosian, “X-Toon: An extended toon shader,” *International Symposium on Non-Photorealistic Animation and Rendering (NPAR)*, 2006. Cited on p. 509
- [67] Barrett, Sean, “Blend Does Not Distribute Over Lerp,” *Game Developer Magazine*, vol. 11, no. 10, pp. 39–41, November 2004. Cited on p. 140
- [68] Bartels, Richard H., John C. Beatty, and Brian A. Barsky, *An Introduction to Splines for use in Computer Graphics & Geometric Modeling*, Morgan Kaufmann, 1987. Cited on p. 609, 610, 643
- [69] Bartz, Dirk, James T. Klosowski, and Dirk Stanecker, “ $k$ -DOPs as Tighter Bounding Volumes for Better Occlusion Performance,” *Visual Proceedings (SIGGRAPH 2001)*, p. 213, August 2001. Cited on p. 675
- [70] Barzel, Ronen, “Lighting Controls for Computer Cinematography” *journal of graphics tools*, vol. 2, no. 1, pp. 1–20, 1997. Cited on p. 219, 220, 223
- [71] Barzel, Ronen, ed., *Graphics Tools—The jgt Editors’ Choice*, A K Peters Ltd., 2005. Cited on p. 923, 928, 931, 948, 953, 968, 971, 972, 985, 989, 991, 993, 994
- [72] Batov, Vladimir, “A Quick and Simple Memory Allocator,” *Dr. Dobbs’s Portal*, January 1, 1998. Cited on p. 705
- [73] Baum, Daniel R., Stephen Mann, Kevin P. Smith, and James M. Winget, “Making Radiosity Usable: Automatic Preprocessing and Meshing Techniques for the Generation of Accurate Radiosity Solutions,” *Computer Graphics (SIGGRAPH ’91 Proceedings)*, pp. 51–60, July 1991. Cited on p. 541
- [74] Bavoil, Louis, Steven P. Callahan, Aaron Lefohn, João L.D. Comba, and Cláudio T. Silva, “Multi-Fragment Effects on the GPU using the  $k$ -Buffer,” *ACM Symposium on Interactive 3D Graphics and Games (I3D 2007)*, pp. 97–104, 2007. Cited on p. 131, 138, 393, 884
- [75] Bavoil, Louis, “Efficient Multi-Fragment Effects on GPUs,” Masters Thesis, School of Computing, University of Utah, May 2007. Cited on p. 709, 884
- [76] Bavoil, Louis, Steven P. Callahan, and Cláudio T. Silva, “Robust Soft Shadow Mapping with Depth Peeling,” *journal of graphics tools*, vol. 13, no. 1, pp. 16–30, 2008. Cited on p. 352, 372
- [77] Bavoil, Louis, and Kevin Myers, “Deferred Rendering using a Stencil Routed K-Buffer,” in Wolfgang Engel, ed., *ShaderX<sup>6</sup>*, Charles River Media, pp. 189–198, 2008. Cited on p. 131, 884
- [78] Bec, Xavier, “Faster Refraction Formula, and Transmission Color Filtering,” in Eric Haines, ed., *Ray Tracing News*, vol. 10, no. 1, January 1997. Cited on p. 396
- [79] Beers, Andrew C., Maneesh Agrawala, and Navin Chaddha, “Rendering from Compressed Textures,” *Computer Graphics (SIGGRAPH 96 Proceedings)*, pp. 373–378, August 1996. Cited on p. 174
- [80] Behrendt, S., C. Colditz, O. Franzke, J. Kopf, and O. Deussen, “Realistic Real-time Rendering of Landscapes Using Billboard Clouds,” *Computer Graphics Forum*, vol. 24, no. 3, pp. 507–516, 2005. Cited on p. 462
- [81] Benson, David, and Joel Davis, “Octree Textures,” *ACM Transactions on Graphics (SIGGRAPH 2002)*, vol. 21, no. 3, pp. 785–790, July 2002. Cited on p. 170
- [82] de Berg, M., M. van Kreveld, M. Overmars, and O. Schwarzkopf, *Computational Geometry—Algorithms and Applications*, second edition, Springer-Verlag, Berlin, 2000. Cited on p. 535, 536, 537, 554, 751, 910

- [83] Bergman, L. D., H. Fuchs, E. Grant, and S. Spach, "Image Rendering by Adaptive Refinement," *Computer Graphics (SIGGRAPH '86 Proceedings)*, pp. 29–37, August 1986. Cited on p. 133, 441
- [84] Bestimt, Jason, and Bryant Freitag, "Real-Time Shadow Casting Using Shadow Volumes," *Gamasutra*, Nov. 1999. Cited on p. 343
- [85] Bier, Eric A., and Kenneth R. Sloan, Jr., "Two-Part Texture Mapping," *IEEE Computer Graphics and Applications*, vol. 6, no. 9, pp. 40–53, September 1986. Cited on p. 151
- [86] Biermann, Henning, Adi Levin, and Denis Zorin, "Piecewise Smooth Subdivision Surface with Normal Control," *Computer Graphics (SIGGRAPH 2000 Proceedings)*, pp. 113–120, July 2000. Cited on p. 626, 643
- [87] Bilodeau, Bill, with Mike Songy, "Real Time Shadows," *Creativity '99*, Creative Labs Inc. sponsored game developer conferences, Los Angeles, California, and Surrey, England, May 1999. Cited on p. 343
- [88] Bischoff, Stephan, Leif P. Kobbelt, and Hans-Peter Seidel, "Towards Hardware Implementation of Loop Subdivision," *ACM SIGGRAPH/Eurographics Workshop on Graphics Hardware*, pp. 41–50, 2000. Cited on p. 643
- [89] Bishop, L., D. Eberly, T. Whitted, M. Finch, and M. Shantz, "Designing a PC Game Engine," *IEEE Computer Graphics and Applications*, pp. 46–53, Jan./Feb. 1998. Cited on p. 666, 777, 778, 826
- [90] Bittner, Jiří, and Jan Přikryl, "Exact Regional Visibility using Line Space Partitioning," Technical Report TR-186-2-01-06, Institute of Computer Graphics and Algorithms, Vienna University of Technology, March 2001. Cited on p. 672
- [91] Bittner, Jiří, Peter Wonka, and Michael Wimmer, "Visibility Preprocessing for Urban Scenes using Line Space Subdivision," *Pacific Graphics 2001*, pp. 276–284, October 2001. Cited on p. 672
- [92] Bittner, J., M. Wimmer, H. Purgathofer, "Coherent Hierarchical Culling: Hardware Occlusion Queries Made Useful," *Computer Graphics Forum*, vol. 23 no. 3, pp. 615–624, 2004. Cited on p. 676
- [93] Bjarke, Kevin, "Image-Based Lighting," in Randima Fernando, ed., *GPU Gems*, Addison-Wesley, pp. 308–321, 2004. Cited on p. 307
- [94] Bjarke, Kevin, "Color Controls," in Randima Fernando, ed., *GPU Gems*, Addison-Wesley, pp. 363–373, 2004. Cited on p. 474
- [95] Bjarke, Kevin, "High-Quality Filtering," in Randima Fernando, ed., *GPU Gems*, Addison-Wesley, pp. 391–424, 2004. Cited on p. 470, 472, 473
- [96] Blinn, J.F., and M.E. Newell, "Texture and reflection in computer generated images," *Communications of the ACM*, vol. 19, no. 10, pp. 542–547, October 1976. Cited on p. 201, 297, 300
- [97] Blinn, James F., "Models of Light Reflection for Computer Synthesized Pictures," *ACM Computer Graphics (SIGGRAPH '77 Proceedings)*, pp. 192–198, July 1977. Cited on p. 112, 246, 247, 248, 252, 257, 258, 261, 265
- [98] Blinn, James, "Simulation of wrinkled surfaces," *Computer Graphics (SIGGRAPH '78 Proceedings)*, pp. 286–292, August 1978. Cited on p. 184, 627
- [99] Blinn, James F., "A Generalization of Algebraic Surface Drawing," *ACM Transactions on Graphics*, vol. 1, no. 3, pp. 235–256, 1982. Cited on p. 606
- [100] Blinn, James F., "Light Reflection Functions for Simulation of Clouds and Dusty Surfaces," *Computer Graphics (SIGGRAPH '82 Proceedings)*, pp. 21–29, August 1982. Cited on p. 262

- [101] Blinn, Jim, "Me and My (Fake) Shadow," *IEEE Computer Graphics and Applications*, vol. 8, no. 1, pp. 82–86, January 1988. Also collected in [105]. Cited on p. 333, 336
- [102] Blinn, Jim, "A Trip Down the Graphics Pipeline: Line Clipping," *IEEE Computer Graphics and Applications*, vol. 11, no. 1, pp. 98–105, January 1991. Also collected in [105]. Cited on p. 18
- [103] Blinn, Jim, "Hyperbolic Interpolation," *IEEE Computer Graphics and Applications*, vol. 12, no. 4, pp. 89–94, July 1992. Also collected in [105]. Cited on p. 838, 840
- [104] Blinn, Jim, "Image Compositing—Theory," *IEEE Computer Graphics and Applications*, vol. 14, no. 5, pp. 83–87, September 1994. Also collected in [106]. Cited on p. 140
- [105] Blinn, Jim, *Jim Blinn's Corner: A Trip Down the Graphics Pipeline*, Morgan Kaufmann, 1996. Cited on p. 27, 662, 663, 840, 927
- [106] Blinn, Jim, *Jim Blinn's Corner: Dirty Pixels*, Morgan Kaufmann, 1998. Cited on p. 146, 927
- [107] Blinn, Jim, "A Ghost in a Snowstorm," *IEEE Computer Graphics and Applications*, vol. 18, no. 1, pp. 79–84, Jan/Feb 1998. Also collected in [110], Chapter 9. Cited on p. 143, 144
- [108] Blinn, Jim, "W Pleasure, W Fun," *IEEE Computer Graphics and Applications*, vol. 18, no. 3, pp. 78–82, May/June 1998. Also collected in [110], Chapter 10. Cited on p. 840
- [109] Blinn, Jim, "Optimizing C++ Vector Expressions," *IEEE Computer Graphics & Applications*, vol. 20, no. 4, pp. 97–103, 2000. Also collected in [110], Chapter 18. Cited on p. 707
- [110] Blinn, Jim, *Jim Blinn's Corner: Notation, Notation, Notation*, Morgan Kaufmann, 2002. Cited on p. 927
- [111] Blinn, Jim, "What Is a Pixel?" *IEEE Computer Graphics and Applications*, vol. 25, no. 5, pp. 82–87, September/October 2005. Cited on p. 125, 146, 216
- [112] Bloom, Charles, "View Independent Progressive Meshes (VIPM)," June 5, 2000. Cited on p. 563, 566, 571, 573
- [113] Bloom, Charles, "VIPM Advanced Topics," Oct. 30, 2000. Cited on p. 568, 686
- [114] Bloom, Charles, "Advanced Techniques in Shadow Mapping," June 3, 2001. Cited on p. 339, 373
- [115] Bloomenthal, Jules, "Polygonization of Implicit Surfaces," *Computer-Aided Geometric Design*, vol. 5, no. 4, pp. 341–355, 1988. Cited on p. 607
- [116] Bloomenthal, Jules, "An Implicit Surface Polygonizer," in Paul S. Heckbert, ed., *Graphics Gems IV*, Academic Press, pp. 324–349, 1994. Cited on p. 607
- [117] Bloomenthal, Jules, ed., *Introduction to Implicit Surfaces*, Morgan Kaufmann, 1997. Cited on p. 502, 533, 606, 607, 643, 728
- [118] Blow, Jonathan, "Implementing a Texture Caching System," *Game Developer*, vol. 5, no. 4, pp. 46–56, April 1998. Cited on p. 172, 173, 174
- [119] Blow, Jonathan, "Terrain Rendering at High Levels of Detail," *Game Developers Conference*, March 2000. [http://www.bolt-action.com/dl\\_papers.html](http://www.bolt-action.com/dl_papers.html) Cited on p. 570
- [120] Blow, Jonathan, "Mipmapping, Part 1," *Game Developer*, vol. 8, no. 12, pp. 13–17, Dec. 2001. Cited on p. 164

- [121] Blow, Jonathan, "Mipmapping, Part 2," *Game Developer*, vol. 9, no. 1, pp. 16–19, Jan. 2002. Cited on p. 164
- [122] Blow, Jonathan, "Happycake Development Notes: Shadows," article on website. [http://number-none.com/happycake/notes\\_8/index.html](http://number-none.com/happycake/notes_8/index.html) Cited on p. 356, 358
- [123] Blythe, David, "The Direct3D 10 System," *ACM Transactions on Graphics*, vol. 25, no. 3, pp. 724–734, July 2006. Cited on p. 29, 31, 36, 38, 41, 44, 50, 361, 481, 712, 849, 858
- [124] Bobic, Nick, "Advanced Collision Detection Techniques," *Gamasutra*, March 2000. Cited on p. 791
- [125] Bogomjakov, Alexander, and Craig Gotsman, "Universal Rendering Sequences for Transparent Vertex Caching of Progressive Meshes," *Graphics Interface 2001*, Ottawa, Canada, pp. 81–90, June 2001. Cited on p. 556
- [126] Booth, Rick, *Inner Loops*, Addison-Wesley, 1997. Cited on p. 703, 707
- [127] Born, Florian, "Implementing Radiosity for a Light Map Precomputation Tool," in Engel, Wolfgang, ed., *ShaderX<sup>4</sup>*, Charles River Media, pp. 499–512, 2005. Cited on p. 418
- [128] Borshukov, George, and J. P. Lewis, "Realistic Human Face Rendering for 'The Matrix Reloaded,'" *SIGGRAPH 2003 Technical Sketch*, 2003. Cited on p. 404
- [129] Borshukov, George, and J. P. Lewis, "Fast Subsurface Scattering," *SIGGRAPH 2005 Digital Face Cloning course notes*, 2005. Cited on p. 404
- [130] Botsch, Mario, Alexander Hornung, Matthias Zwicker, and Leif Kobbelt, "High-Quality Surface Splatting on Today's GPUs," *Eurographics Symposium on Point-Based Graphics 2005*, pp. 17–24, June 2005. Cited on p. 695
- [131] Boubekeur, Tamy, Patrick Reuter, and Christophe Schlick, "Scalar Tagged PN Triangles," *Eurographics 2005*, short presentation, pp. 17–20, September 2005. Cited on p. 603
- [132] Boulos, Solomon, and Eric Haines, "Ray-Box Sorting," in Eric Haines, ed., *Ray Tracing News*, vol. 19, no. 1, September 2006. Cited on p. 649
- [133] Boulos, Solomon, Dave Edwards, J Dylan Lacewell, Joe Kniss, Jan Kautz, Ingo Wald, and Peter Shirley, "Packet-based Whitted and Distribution Ray Tracing," *Graphics Interface 2007*, pp. 177–184, 2007. Cited on p. 416
- [134] Boyd, Chas, "The Future of DirectX," *Game Developer's Conference*, 2007. Cited on p. 634
- [135] Boyd, Stephen, and Lieven Vandenberghe, *Convex Optimization*, Cambridge University Press, 2004. Freely downloadable. <http://www.stanford.edu/~boyd/cvxbook/> Cited on p. 731
- [136] Brabec, Stefan, Thomas Annen, and Hans-Peter Seidel, "Practical Shadow Mapping," *journal of graphics tools*, vol. 7, no. 4, pp. 9–18, 2002. Also collected in [71]. Cited on p. 370
- [137] Brabec, Stefan, and Hans-Peter Seidel, "Shadow Volumes on Programmable Graphics Hardware," *Computer Graphics Forum*, vol. 22, no. 3, pp. 433–440, Sept. 2003. Cited on p. 347
- [138] Brawley, Zoe, and Natalya Tatarchuk, "Parallax Occlusion Mapping: Self-Shadowing, Perspective-Correct Bump Mapping Using Reverse Height Map Tracing," in Wolfgang Engel, ed., *ShaderX<sup>3</sup>*, Charles River Media, pp. 135–154, November 2004. Cited on p. 193

- [139] Bredow, Rob, "Fur in Stuart Little," *SIGGRAPH 2000 Advanced RenderMan 2: To RLMINITY and Beyond course notes*, July 2000. Cited on p. 294, 403
- [140] Brennan, Chris, "Diffuse Cube Mapping," in Wolfgang Engel, ed., *ShaderX*, Wordware, pp. 287–289, May 2002. Cited on p. 317
- [141] Brennan, Chris, "Shadow Volume Extrusion using a Vertex Shader," in Wolfgang Engel, ed., *ShaderX*, Wordware, pp. 188–194, May 2002. Cited on p. 347
- [142] Bresenham, J.E., "Algorithm for Computer Control of a Digital Plotter," *IBM Systems Journal*, vol. 4, no. 1, pp. 25–30, 1965. Cited on p. 11
- [143] Brinkmann, Ron, *The Art and Science of Digital Compositing*, Morgan Kaufmann, 1999. Cited on p. 135, 139, 140
- [144] Buchanan, J.W., and M.C. Sousa, "The edge buffer: A Data Structure for Easy Silhouette Rendering," *Proceedings of the First International Symposium on Non-photorealistic Animation and Rendering (NPAR)*, pp. 39–42, June 2000. Cited on p. 520
- [145] Bunnell, Michael, and Fabio Pellacini "Shadow Map Antialiasing," in Randima Fernando, ed., *GPU Gems*, Addison-Wesley, pp. 167–183, 2004. Cited on p. 361
- [146] Bunnell, Michael, "Dynamic Ambient Occlusion and Indirect Lighting," in Matt Pharr, ed., *GPU Gems 2*, Addison-Wesley, pp. 223–233, 2005. Cited on p. 380, 407
- [147] Bunnell, Michael, "Adaptive Tessellation of Subdivision Surfaces with Displacement Mapping," in Matt Pharr, ed., *GPU Gems 2*, Addison-Wesley, pp. 109–122, 2005. Cited on p. 643
- [148] Cabral, Brian, and Leith (Casey) Leedom "Imaging Vector Fields Using Line Integral Convolution," *Computer Graphics (SIGGRAPH 93 Proceedings)*, pp. 263–270, August 1993. Cited on p. 492
- [149] Cabral, Brian, Marc Olano, and Phillip Nemec, "Reflection Space Image Based Rendering," *Computer Graphics (SIGGRAPH 99 Proceedings)*, pp. 165–170, August 1999. Cited on p. 313
- [150] Calver, Dean, "Vertex Decompression Using Vertex Shaders," in Wolfgang Engel, ed., *ShaderX*, Wordware, pp. 172–187, May 2002. Cited on p. 713
- [151] Calver, Dean, "Accessing and Modifying Topology on the GPU," in Engel, Wolfgang, ed., *ShaderX<sup>3</sup>*, Charles River Media, pp. 5–19, 2004. Cited on p. 560
- [152] Calver, Dean, "Deferred Lighting on PS 3.0 with High Dynamic Range," in Engel, Wolfgang, ed., *ShaderX<sup>3</sup>*, Charles River Media, pp. 97–105, 2004. Cited on p. 477
- [153] Cameron, S., "Enhancing GJK: Computing Minimum and Penetration Distance Between Convex Polyhedra," *International Conference on Robotics and Automation*, pp. 3112–3117, 1997. Cited on p. 820
- [154] Cantlay, Iain, "Mipmap Level Measurement," in Matt Pharr, ed., *GPU Gems 2*, Addison-Wesley, pp. 437–449, 2005. Cited on p. 174
- [155] Card, Drew, and Jason L. Mitchell, "Non-Photorealistic Rendering with Pixel and Vertex Shaders," in Wolfgang Engel, ed., *ShaderX*, Wordware, pp. 319–333, May 2002. Cited on p. 508, 509, 518, 521, 524
- [156] Carling, Richard, "Matrix Inversion," in Andrew S. Glassner, ed., *Graphics Gems*, Academic Press, pp. 470–471, 1990. Cited on p. 63
- [157] Carpenter, Loren, "The A-buffer, an Antialiased Hidden Surface Method," *Computer Graphics (SIGGRAPH '84 Proceedings)*, pp. 103–108, July 1984. Cited on p. 129

- [158] Carucci, Francesco, “Inside Geometry Instancing,” in Matt Pharr, ed., *GPU Gems 2*, Addison-Wesley, pp. 47–67, 2005. Cited on p. 711
- [159] Carucci, Francesco, “HDR meets Black&White 2,” in Wolfgang Engel, ed., *ShaderX<sup>6</sup>*, Charles River Media, pp. 199–210, 2008. Cited on p. 477, 478
- [160] Catmull, E., and R. Rom, “A Class of Local Interpolating Splines,” *Computer Aided Geometric Design*, edited by R. Barnhill and R. Riesenfeld, Academic Press, pp. 317–326, 1974. Cited on p. 590
- [161] Catmull, E., *A Subdivision Algorithm for Computer Display of Curved Surfaces*, Ph.D. Thesis, University of Utah, December 1974. Cited on p. 888
- [162] Catmull, Edwin, “Computer Display of Curved Surfaces,” *Proceedings of the IEEE Conference on Computer Graphics, Pattern Recognition and Data Structures*, Los Angeles, pp. 11–17, May 1975. Cited on p. 23
- [163] Catmull, E., and J. Clark, “Recursively Generated B-Spline Surfaces on Arbitrary Topological Meshes,” *Computer-Aided Design*, vol. 10, no. 6, pp. 350–355, September 1978. Cited on p. 623
- [164] Cebeboyan, Cem, “Graphics Pipeline Performance,” in Randima Fernando, ed., *GPU Gems*, Addison-Wesley, pp. 473–486, 2004. Cited on p. 681, 699, 701, 716, 722
- [165] “Cell Broadband Engine resource center,” IBM. Cited on p. 870
- [166] Chabert, Charles-Félix, Wan-Chun Ma, Tim Hawkins, Pieter Peers, and Paul Debevec, “Fast Rendering of Realistic Faces with Wavelength Dependent Normal Maps,” Poster at *SIGGRAPH 2007*, 2007. Cited on p. 404
- [167] Chaikin, G., “An Algorithm for High Speed Curve Generation,” *Computer Graphics and Image Processing*, vol. 4, no. 3, 1974. Cited on p. 608
- [168] Chan, Eric, and Frédéric Durand, “Rendering Fake Soft Shadows with Smoothies,” *Eurographics Symposium on Rendering (2003)*, pp. 208–218, June 2003. Cited on p. 371
- [169] Chan, Eric, and Frédéric Durand, “An Efficient Hybrid Shadow Rendering Algorithm,” *Eurographics Symposium on Rendering (2004)*, pp. 185–196, June 2004. Cited on p. 357
- [170] Chan, Eric, and Frédéric Durand, “Fast Prefiltered Lines,” in Matt Pharr, ed., *GPU Gems 2*, Addison-Wesley, pp. 345–359, 2005. Cited on p. 119, 125
- [171] Chang, Chun-Fa, Gary Bishop, Anselmo Lastra, “LDI Tree: A Hierarchical Representation for Image-based Rendering,” *Computer Graphics (SIGGRAPH 99 Proceedings)*, pp. 291–298, August, 1999. Cited on p. 464
- [172] Chen, S. E., “Quicktime VR—An Image-Based Approach to Virtual Environment Navigation,” *Computer Graphics (SIGGRAPH 95 Proceedings)*, pp. 29–38, August 1995. Cited on p. 443
- [173] Chhugani, Jatin, and Subodh Kumar, “View-dependent Adaptive Tessellation of Spline Surfaces,” *Proceedings 2001 Symposium on Interactive 3D Graphics*, pp. 59–62 March 2001. Cited on p. 639
- [174] Chi, Yung-feng, “True-to-Life Real-Time Animation of Shallow Water on Todays GPUs,” in Engel, Wolfgang, ed., *ShaderX<sup>4</sup>*, Charles River Media, pp. 467–480, 2005. Cited on p. 395, 500
- [175] Chong, Hamilton Y. and Steven J. Gortler, “A Lixel for every Pixel,” *Eurographics Symposium on Rendering (2004)*, pp. 167–172, June 2004. Cited on p. 355

- [176] Chow, Mike M., "Using Strips for Higher Game Performance," Presentation at *Meltdown X99*. Cited on p. 553, 554
- [177] Christen, Martin, "Implementing Ray Tracing on the GPU," in Engel, Wolfgang, ed., *ShaderX<sup>4</sup>*, Charles River Media, pp. 409–427, 2005. Cited on p. 416
- [178] Cignoni, P., C. Montani, and R. Scopigno, "Triangulating Convex Polygons Having T-Vertices," *journal of graphics tools*, vol. 1, no. 2, pp. 1–4, 1996. Also collected in [71]. Cited on p. 541
- [179] Clark, James H., "Hierarchical Geometric Models for Visible Surface Algorithms," *Communications of the ACM*, vol. 19, no. 10, pp. 547–554, October 1976. Cited on p. 665
- [180] Claustres, Luc, Loïc Barthe, and Mathias Paulin, "Wavelet Encoding of BRDFs for Real-Time Rendering," *Graphics Interface 2007*, pp. 169–176, 2007. Cited on p. 266
- [181] Cohen, Jonathan D., Ming C. Lin, Dinesh Manocha, and Madhav Ponamgi, "I-COLLIDE: An Interactive and Exact Collision Detection System for Large-Scaled Environments," *Proceedings 1995 Symposium on Interactive 3D Graphics*, pp. 189–196, 1995. Cited on p. 811, 816
- [182] Cohen, Jonathan D., Marc Olano, and Dinesh Manocha, "Appearance-Preserving Simplification," *Computer Graphics (SIGGRAPH 98 Proceedings)*, pp. 115–122, July 1998. Cited on p. 188, 561
- [183] Cohen, Michael F., and John R. Wallace, *Radiosity and Realistic Image Synthesis*, Academic Press Professional, Boston, 1993. Cited on p. 408
- [184] Cohen-Or, Daniel, Yiorgos Chrysanthou, Frédéric Durand, Ned Greene, Vladlen Koltun, and Cláudio T. Silva, "Visibility, Problems, Techniques and Applications," *Course 30 notes at SIGGRAPH 2001*, 2001. Cited on p.
- [185] Cohen-Or, Daniel, Yiorgos Chrysanthou, Cláudio T. Silva, and Frédéric Durand, "A Survey of Visibility for Walkthrough Applications," *IEEE Transactions on Visualization and Computer Graphics*, vol. 9, no. 3, pp. 412–431, July–Sept. 2003. Cited on p. 661, 695
- [186] Cok, Keith, Roger Corron, Bob Kuehne, Thomas True, "Developing Efficient Graphics Software: The Yin and Yang of Graphics," *Course 6 notes at SIGGRAPH 2000*, 2000. Cited on p. 714
- [187] Colbert, Mark, and Jaroslav Křivánek, "GPU-Based Importance Sampling," in Hubert Nguyen, ed., *GPU Gems 3*, Addison-Wesley, pp. 459–475, 2007. Cited on p. 312
- [188] Colbert, Mark, and Jaroslav Křivánek, "Real-time Shading with Filtered Importance Sampling," *SIGGRAPH 2007 Technical Sketch*, 2007. Cited on p. 312
- [189] *Munsell ColorChecker Chart*, X-Rite, Incorporated, Cited on p. 145
- [190] Columbia-Utrecht Reflectance and Texture Database (CUReT). Cited on p. 265, 268
- [191] Conran, Patrick, "SpecVar Maps: Baking Bump Maps into Specular Response," *SIGGRAPH 2005 Technical Sketch*, 2005. Cited on p. 275
- [192] Cook, Robert L., and Kenneth E. Torrance, "A Reflectance Model for Computer Graphics," *Computer Graphics (SIGGRAPH '81 Proceedings)*, pp. 307–316, July 1981. Cited on p. 112, 229, 236, 237, 238, 246, 247, 248, 252, 258, 261, 267, 296, 375

- [193] Cook, Robert L., and Kenneth E. Torrance, “A Reflectance Model for Computer Graphics,” *ACM Transactions on Graphics*, vol. 1, no. 1, pp. 7–24, January 1982. Cited on p. 236, 237, 238, 246, 247, 248, 252, 258, 261, 296, 375
- [194] Cook, Robert L., “Shade Trees,” *Computer Graphics (SIGGRAPH '84 Proceedings)*, pp. 223–231, July 1984. Cited on p. 33, 34, 626
- [195] Cook, Robert L., “Stochastic Sampling in Computer Graphics,” *ACM Transactions on Graphics*, vol. 5, no. 1, pp. 51–72, January 1986. Cited on p. 132, 366, 470
- [196] Cook, Robert L., Loren Carpenter, and Edwin Catmull, “The Reyes Image Rendering Architecture,” *Computer Graphics (SIGGRAPH '87 Proceedings)*, pp. 95–102, July 1987. Cited on p. 26, 875, 880, 884
- [197] Cook, Robert L., and Tony DeRose, “Wavelet Noise,” *ACM Transactions on Graphics (SIGGRAPH 2005)*, vol. 24, no. 3, pp. 803–811, 2005. Cited on p. 178
- [198] Coombe, Greg, and Mark Harris, “Global Illumination using Progressive Refinement Radiosity,” in Matt Pharr, ed., *GPU Gems 2*, Addison-Wesley, pp. 635–647, 2005. Cited on p. 411
- [199] Coorg, S., and S. Teller, “Real-Time Occlusion Culling for Models with Large Occluders,” *Proceedings 1997 Symposium on Interactive 3D Graphics*, pp. 83–90, April 1997. Cited on p. 690
- [200] Cornell University Program of Computer Graphics Measurement Data. Cited on p. 265, 268
- [201] Cormen, T.H., C.E. Leiserson, and R. Rivest, *Introduction to Algorithms*, MIT Press, Inc., Cambridge, Massachusetts, 1990. Cited on p. 553, 648, 659, 665
- [202] Courchesnes, Martin, Pascal Volino, and Nadia Magnenat Thalmann, “Versatile and Efficient Techniques for Simulating Cloth and Other Deformable Objects,” *Computer Graphics (SIGGRAPH 95 Proceedings)*, pp. 137–144, August 1995. Cited on p. 826
- [203] Cox, Michael, and Pat Hanrahan, “Pixel Merging for Object-Parallel Rendering: a Distributed Snooping Algorithm,” *ACM SIGGRAPH Symposium on Parallel Rendering*, pp. 49–56, Nov. 1993. Cited on p. 716
- [204] Cox, Michael, David Sprague, John Danskin, Rich Ehlers, Brian Hook, Bill Lorensen, and Gary Tarolli, “Developing High-Performance Graphics Applications for the PC Platform,” *Course 29 notes at SIGGRAPH 98*, 1998. Cited on p. 834, 835, 846
- [205] Crane, Keenan, Ignacio LLamas, and Sarah Tariq, “Real-Time Simulation and Rendering of 3D Fluids,” in Hubert Nguyen, ed., *GPU Gems 3*, Addison-Wesley, pp. 633–675, 2007. Cited on p. 472, 503, 504
- [206] Cripe, Brian and Thomas Gaskins, “The DirectModel Toolkit: Meeting the 3D Graphics Needs of Technical Applications,” *Hewlett-Packard Journal*, pp. 19–27, May 1998. Cited on p. 646
- [207] Croal, N'Gai, “Geek Out: Xbox Uber-Boss Robbie Bach Takes a Shot At Nintendo's 'Underpowered' Wii. Does He Manage to Score a Bulls-Eye, or Is He Just Shooting Blanks?,” Newsweek's “Level Up” blog. Cited on p. 35
- [208] Crow, Franklin C., “Shadow Algorithms for Computer Graphics,” *Computer Graphics (SIGGRAPH '77 Proceedings)*, pp. 242–248, July 1977. Cited on p. 340
- [209] Crow, Franklin C., “Summed-Area Tables for Texture Mapping,” *Computer Graphics (SIGGRAPH '84 Proceedings)*, pp. 207–212, July 1984. Cited on p. 167

- [210] Cruz-Neira, Carolina, Daniel J. Sandin, and Thomas A. DeFanti, "Surround-screen Projection-based Virtual Reality: The Design and Implementation of the CAVE," *Computer Graphics (SIGGRAPH 93 Proceedings)*, pp. 135–142, August 1993. Cited on p. 94, 837
- [211] "NVIDIA CUDA Homepage," NVIDIA website, 2007. <http://developer.nvidia.com/cuda> Cited on p. 36, 841, 883
- [212] Culler, David E., and Jaswinder Pal Singh, with Anoop Gupta, *Parallel Computer Architecture: A Hardware/Software Approach*, Morgan Kaufmann, 1998. Cited on p. 721, 723
- [213] Cunnif, R., "Visualize fx Graphics Scalable Architecture," *Hot3D Proceedings, ACM SIGGRAPH/Eurographics Workshop on Graphics Hardware*, Switzerland, August 2000. Cited on p. 675
- [214] Cunningham, Steve, "3D Viewing and Rotation using Orthonormal Bases," in Andrew S. Glassner, ed., *Graphics Gems*, Academic Press, pp. 516–521, 1990. Cited on p. 70
- [215] Curtis, Cassidy, "Loose and Sketchy Animation," *SIGGRAPH 98 Technical Sketch*, p. 317, 1998. Cited on p. 526
- [216] Cyphosz, J.M. and W.N. Waggoner Jr., "Intersecting a Ray with a Cylinder," in Paul S. Heckbert, ed., *Graphics Gems IV*, Academic Press, pp. 356–365, 1994. Cited on p. 741
- [217] Cyrus, M., and J. Beck, "Generalized two- and three-dimensional clipping," *Computers and Graphics*, vol. 3, pp. 23–28, 1978. Cited on p. 742
- [218] Dachsbaecher, Carsten, and Marc Stamminger, "Translucent Shadow Maps," *Eurographics Symposium on Rendering (2003)*, pp. 197–201, June 2003. Cited on p. 407
- [219] Dachsbaecher, Carsten, and Marc Stamminger, "Reflective Shadow Maps," *ACM Symposium on Interactive 3D Graphics and Games (I3D 2005)*, pp. 203–231, 2005. Cited on p. 417
- [220] Dachsbaecher, Carsten, and Marc Stamminger, " $I^3$ : Interactive Indirect Illumination," in Engel, Wolfgang, ed., *ShaderX<sup>4</sup>*, Charles River Media, pp. 235–246, 2005. Cited on p. 417
- [221] Dachsbaecher, Carsten, and Marc Stamminger, "Splatting of Indirect Illumination," *ACM Symposium on Interactive 3D Graphics and Games (I3D 2006)*, pp. 93–100, March 2006. Cited on p. 417
- [222] Dachsbaecher, Carsten, and Marc Stamminger, "Splatting of Diffuse and Glossy Indirect Illumination," in Engel, Wolfgang, ed., *ShaderX<sup>5</sup>*, Charles River Media, pp. 373–387, 2006. Cited on p. 399, 417
- [223] Dachsbaecher, C., and N. Tatarchuk, "Prism Parallax Occlusion Mapping with Accurate Silhouette Generation," Poster at *ACM Symposium on Interactive 3D Graphics and Games (I3D 2007)*, 2007. Cited on p. 197
- [224] Dam, Erik B., Martin Koch, and Martin Lillholm, "Quaternions, Interpolation and Animation," Technical Report DIKU-TR-98/5, Department of Computer Science, University of Copenhagen, July 1998. Cited on p. 77
- [225] Dana, Kristin J., Bram van Ginneken, Shree K. Nayar, and Jan J. Koenderink "Reflectance and Texture of Real-World Surfaces," *ACM Transactions on Graphics*, vol. 18, no. 1, pp. 1–34, 1999. Cited on p. 265
- [226] "BRDF/BTF measurement device," in *Proceedings of ICCV 2001*, vol. 2, pp. 460–466, 2001. Cited on p. 265

- [227] Dallaire, Chris, "Binary Triangle Trees for Terrain Tile Index Buffer Generation," *Gamasutra*, December 21, 2006. Cited on p. 571
- [228] Davis, Douglass, William Ribarsky, T.Y. Kiang, Nickolas Faust, and Sean Ho, "Real-Time Visualization of Scalably Large Collections of Heterogeneous Objects," *IEEE Visualization*, pp. 437–440, 1999. Cited on p. 693
- [229] Davis, Scott T., and Chris Wyman, "Interactive Refractions with Total Internal Reflection," *Graphics Interface 2007*, pp. 185–190, 2007. Cited on p. 398
- [230] Dawson, Bruce, "What Happened to My Colours?!?" *Game Developers Conference*, pp. 251–268, March 2001. [http://www.gdconf.com/archives/proceedings/2001/prog\\_papers.html](http://www.gdconf.com/archives/proceedings/2001/prog_papers.html) Cited on p. 217, 831
- [231] Debevec, Paul E., "Rendering Synthetic Objects into Real Scenes: Bridging Traditional and Image-Based Graphics with Global Illumination and High Dynamic Range Photography," *Computer Graphics (SIGGRAPH 98 Proceedings)*, pp. 189–198, July 1998. Cited on p. 301, 480
- [232] Debevec, Paul E., "Acquiring the Reflectance Field of a Human Face," *Computer Graphics (SIGGRAPH 2000 Proceedings)*, pp. 145–156, July 2000. Cited on p. 265
- [233] Debevec, Paul, Rod Bogart, Frank Vitz, and Greg Ward, "HDRI and Image-Based Lighting," *Course 19 notes at SIGGRAPH 2003*, 2003. Cited on p. 325
- [234] de Boer, Willem H., "Smooth Penumbra Transitions with Shadow Maps," *journal of graphics tools*, vol. 11, no. 2, pp. 59–71, 2006. Cited on p. 372
- [235] DeBry, David (grue), Jonathan Gibbs, Devorah DeLeon Petty, and Nate Robins, "Painting and Rendering Textures on Unparameterized Models," *ACM Transactions on Graphics (SIGGRAPH 2002)*, vol. 21, no. 3, pp. 763–768, July 2002. Cited on p. 170
- [236] DeCarlo, Doug, Adam Finkelstein, and Szymon Rusinkiewicz, "Interactive Rendering of Suggestive Contours with Temporal Coherence," *The 3rd International Symposium on Non-Photorealistic Animation and Rendering (NPAR 2004)*, pp. 15–24, June 2004. Cited on p. 511
- [237] DeCarlo, Doug, and Szymon Rusinkiewicz, "Highlight Lines for Conveying Shape," *International Symposium on Non-Photorealistic Animation and Rendering (NPAR)*, August 2007. Cited on p. 511
- [238] Decaudin, Philippe, "Cartoon-Looking Rendering of 3D-Scenes," Technical Report INRIA 2919, Université de Technologie de Compiègne, France, June 1996. Cited on p. 518
- [239] DeCoro, Christopher, and Natalya Tatarchuk, "Implementing Real-Time Mesh Simplification Using the GPU," in Wolfgang Engel, ed., *ShaderX<sup>6</sup>*, Charles River Media, pp. 29–39, 2008. Cited on p. 568
- [240] Décoret, Xavier, Gernot Schaufler, François Sillion, and Julie Dorsey, "Multi-layered Impostors for Accelerated Rendering," *Computer Graphics Forum*, vol. 18, no. 3, pp. 61–72, 1999. Cited on p. 466
- [241] Décoret, Xavier, Frédéric Durand, François Sillion, and Julie Dorsey, "Billboard Clouds for Extreme Model Simplification," *ACM Transactions on Graphics (SIGGRAPH 2003)*, vol. 22, no. 3, pp. 689–696, 2003. Cited on p. 462
- [242] Deering, Michael F., and Scott R. Nelson, "Leo: A System for Cost Effective 3D Shaded Graphics," *Computer Graphics (SIGGRAPH 93 Proceedings)*, pp. 101–108, August 1993. Cited on p. 550

- [243] Deering, Michael, “Geometry Compression.” *Computer Graphics (SIGGRAPH 95 Proceedings)*, pp. 13–20, August 1995. Cited on p. 555, 713
- [244] Deering, Michael, and David Naegle, “The SAGE Graphics Architecture,” *ACM Transactions on Graphics (SIGGRAPH 2002)*, vol. 21, no. 3, pp. 683–692, July 2002. Cited on p. 133
- [245] Demers, Joe, “Depth of Field: A Survey of Techniques,” in Randima Fernando, ed., *GPU Gems*, Addison-Wesley, pp. 375–390, 2004. Cited on p. 487, 488, 489
- [246] d’Eon, Eugene, and David Luebke, “Advanced Techniques for Realistic Real-Time Skin Rendering,” in Hubert Nguyen, ed., *GPU Gems 3*, Addison-Wesley, pp. 293–347, 2007. Cited on p. 405, 407
- [247] d’Eon, Eugene, David Luebke, and Eric Enderton, “Efficient Rendering of Human Skin,” *Eurographics Symposium on Rendering (2007)*, 147–157, June 2007. Cited on p. 405, 407
- [248] d’Eon, Eugene, “NVIDIA Demo Team Secrets—Advanced Skin Rendering.” *Game Developers Conference*, March 2007. <http://developer.nvidia.com/object/gdc-2007.htm> Cited on p. 405, 407
- [249] DeLoura, Mark, ed., *Game Programming Gems*, Charles River Media, 2000. Cited on p. 885
- [250] DeRose, T., M. Kass, and T. Truong, “Subdivision Surfaces in Character Animation,” *Computer Graphics (SIGGRAPH 98 Proceedings)*, pp. 85–94, July 1998. Cited on p. 623, 626, 629
- [251] de Castro Lopo, Erik, *Faster Floating Point to Integer Conversions*, 2001. Cited on p. 706
- [252] Diefenbach, Paul J., “Pipeline Rendering: Interaction and Realism through Hardware-based Multi-pass Rendering,” Ph.D. Thesis, University of Pennsylvania, 1996. Cited on p. 396, 437
- [253] Diefenbach, Paul J., and Norman I. Badler, “Multi-Pass Pipeline Rendering: Realism for Dynamic Environments,” *Proceedings 1997 Symposium on Interactive 3D Graphics*, pp. 59–70, April 1997. Cited on p. 137, 389, 391
- [254] Diepstraten, Joachim, “Simulating the Visual Effects of a Video Recording System,” in Engel, Wolfgang, ed., *ShaderX<sup>4</sup>*, Charles River Media, pp. 269–274, 2005. Cited on p. 472
- [255] Dietrich, Andreas, Enrico Gobbetti, and Sung-Eui Yoon, “Massive-Model Rendering Techniques,” *IEEE Computer Graphics and Applications*, vol. 27, no. 6, pp. 20–34, November/December 2007. Cited on p. 693, 695
- [256] Dietrich, Sim, “Attenuation Maps,” in Mark DeLoura, ed., *Game Programming Gems*, Charles River Media, pp. 543–548, 2000. Cited on p. 222, 498
- [257] Dietrich, D. Sim, Jr., “Practical Priority Buffer Shadows,” in Mark DeLoura, ed., *Game Programming Gems 2*, Charles River Media, pp. 481–487, 2001. Cited on p. 351
- [258] Dingiana, John, and Carol O’Sullivan, “Graceful Degradation of Collision Handling in Physically Based Animation,” *Computer Graphics Forum*, vol. 19, no. 3, pp. 239–247, 2000. Cited on p. 823, 824
- [259] Dingiana, John, and Carol O’Sullivan, “Collisions and Adaptive Level of Detail,” *Visual Proceedings (SIGGRAPH 2001)*, p. 156, August 2001. Cited on p. 817
- [260] Dippé, Mark A. Z., and Erling Henry Wold, “Antialiasing Through Stochastic Sampling,” *Computer Graphics (SIGGRAPH ’85 Proceedings)*, pp. 69–78, July 1985. Cited on p. 132

- [261] “The DirectX Software Development Kit,” Microsoft, November 2007. Cited on p. 31, 37, 38, 43, 45, 51, 306, 323, 346, 374, 432, 434, 456, 477, 478, 484, 491, 495, 498, 552, 886
- [262] Dmitriev, Kirill, and Yury Uralsky, “Soft Shadows Using Hierarchical Min-Max Shadow Maps,” *Game Developers Conference*, March 2007. <http://developer.nvidia.com/object/gdc-2007.htm> Cited on p. 372
- [263] Do Carmo, Manfred P., *Differential Geometry of Curves and Surfaces*, Prentice-Hall, Inc., Englewood Cliffs, New Jersey, 1976. Cited on p. 78
- [264] Dobashi, Yoshinori, Kazufumi Kaneda, Hideo Yamashita, Tsuyoshi Okita, and Tomoyuki Nishita, “A Simple, Efficient Method for Realistic Animation of Clouds,” *Computer Graphics (SIGGRAPH 2000 Proceedings)*, pp. 19–28, July 2000. Cited on p. 452
- [265] Dobashi, Yoshinori, Tsuyoshi Yamamoto, and Tomoyuki Nishita, “Interactive Rendering of Atmospheric Scattering Effects Using Graphics Hardware,” *Graphics Hardware (2002)*, pp. 1–10, 2002. Cited on p. 501
- [266] Simon Dobbyn, John Hamill, Keith O’Conor, and Carol O’Sullivan, “Geopostors: A Real-time Geometry/Impostor Crowd Rendering System,” *ACM SIGGRAPH 2005 Symposium on Interactive 3D Graphics and Games*, pp. 95–102, August 2005. Cited on p. 445, 461
- [267] Dodgson, N. A., “Autostereoscopic 3D Displays,” *IEEE Computer*, vol. 38, no. 8, pp. 31–36, 2005. Cited on p. 837
- [268] Doggett, Michael, “Xenos: Xbox 360 GPU,” *GDC-Europe 2005*, 2005. Cited on p. 859
- [269] Dominé, Sébastien, “OpenGL Multisample,” *Game Developers Conference*, March 2002. [http://developer.nvidia.com/object/gdc\\_ogl\\_multisample.html](http://developer.nvidia.com/object/gdc_ogl_multisample.html) Cited on p. 132
- [270] Donnelly, William, and Joe Demers, “Generating Soft Shadows Using Occlusion Interval Maps,” in Randima Fernando, ed., *GPU Gems*, Addison-Wesley, pp. 205–215, 2004. Cited on p. 428
- [271] Donnelly, William, “Per-Pixel Displacement Mapping with Distance Functions,” in Matt Pharr, ed., *GPU Gems 2*, Addison-Wesley, pp. 123–136, 2005. Cited on p. 195
- [272] Donnelly, William, and Andrew Lauritzen, “Variance Shadow Maps,” *Proceedings 2006 Symposium on Interactive 3D Graphics*, pp. 161–165, 2006. Cited on p. 367
- [273] Donner, Craig, and Henrik Wann Jensen, “Light Diffusion in Multi-Layered Translucent Materials,” *ACM Transactions on Graphics (SIGGRAPH 2005)*, vol. 24, no. 3, pp. 1032–1039, 2005. Cited on p. 405
- [274] Doo, D., and M. Sabin, “Behaviour of Recursive Division Surfaces Near Extraordinary Points,” *Computer-Aided Design*, vol. 10, no. 6, pp. 356–360, September 1978. Cited on p. 623
- [275] Dorsey, Julie, Holly Rushmeier, and François Sillion, *Digital Modeling of Material Appearance*, Morgan Kaufmann, 2007. Cited on p. 264, 283
- [276] Dougan, Carl, “The Parallel Transport Frame,” in Mark DeLoura, ed., *Game Programming Gems 2*, Charles River Media, pp. 215–219, 2001. Cited on p. 97
- [277] Downs, Laura, Tomas Möller, and Carlo Séquin, “Occlusion Horizons for Driving through Urban Scenery,” *Proceedings 2001 Symposium on Interactive 3D Graphics*, pp. 121–124, March 2001. Cited on p. 671, 679

- [278] Duchaineau, Mark A., Murray Wolinsky, David E. Sigeti, Mark C. Miller, Charles Aldrich, and Mark B. Mineev-Weinstein, “ROAMing Terrain: Real-time Optimally Adapting Meshes,” *IEEE Visualization ’97*, pp. 81–88, 1997. Cited on p. 569
- [279] Dudash, Bryan, “Animated Crowd Rendering,” in Hubert Nguyen, ed., *GPU Gems 3*, Addison-Wesley, pp. 39–52, 2007. Cited on p. 711
- [280] Dür, Arne, “An Improved Normalization for the Ward Reflectance Model,” *Journal of graphics tools*, vol. 11, no. 1, pp. 51–59, 2006. Cited on p. 260
- [281] Duff, Tom, “Compositing 3-D Rendered Images,” *Computer Graphics (SIGGRAPH ’85 Proceedings)*, pp. 41–44, July 1985. Cited on p. 135
- [282] Duffy, Joe, “CLR Inside Out,” *MSDN Magazine*, vol. 21, no. 10, September 2006. Cited on p. 703
- [283] Dummer, Jonathan, “Cone Step Mapping: An Iterative Ray-Heightfield Intersection Algorithm,” website, 2006. <http://www.lonesock.net/papers.html> Cited on p. 196
- [284] Dumont, Reynald, Fabio Pellacini, and James A. Ferwerda, “A Perceptually-Based Texture Caching Algorithm for Hardware-Based Rendering,” *12th Eurographics Workshop on Rendering*, pp. 246–253, June 2001. Cited on p. 174
- [285] Durand, Frédéric, *3D Visibility: Analytical Study and Applications*, Ph.D. Thesis, Université Joseph Fourier, Grenoble, July 1999. Cited on p. 695
- [286] Durand, Frédéric, and Julie Dorsey, “Interactive Tone Mapping,” *11th Eurographics Workshop on Rendering*, pp. 219–230, June 2000. Cited on p. 475
- [287] Dutré, Philip, *Global Illumination Compendium*, 1999. Cited on p. 215, 283, 325, 437
- [288] Dutré, Philip, Kavita Bala, and Philippe Bekaert, *Advanced Global Illumination*, second edition, A K Peters Ltd., 2006. Cited on p. 208, 283, 410, 416, 437, 534
- [289] Dyken, C., and M. Reimers, “Real-time Linear Silhouette Enhancement,” *Mathematical Methods for Curves and Surfaces*, pp. 145–156, 2005. Cited on p. 603
- [290] Dyn, Nira, David Levin, and John A. Gregory, “A 4-point Interpolatory Subdivision Scheme for Curve Design,” *Computer Aided Geometric Design*, vol. 4, no. 4, pp. 257–268, 1987. Cited on p. 609, 610, 618
- [291] Dyn, Nira, David Levin, and John A. Gregory, “A Butterfly Subdivision Scheme for Surface Interpolation with Tension Control,” *ACM Transactions on Graphics*, vol. 9, no. 2, pp. 160–169, April 1990. Cited on p. 616
- [292] Eberly, David, “Testing for Intersection of Convex Objects: The Method of Separating Axes,” Technical Report, Magic Software, 2001. <http://www.geometrictools.com> Cited on p. 791
- [293] Eberly, David, *Game Physics*, Morgan Kaufmann, 2003. Cited on p. 827
- [294] Eberly, David, *3D Game Engine Design, Second Edition: A Practical Approach to Real-Time Computer Graphics*, Morgan Kaufmann, 2006. <http://www.geometrictools.com/> Cited on p. 79, 501, 574, 637, 639, 659, 733, 734, 741, 784, 792, 826
- [295] Ebert, David S., John Hart, Bill Mark, F. Kenton Musgrave, Darwyn Peachey, Ken Perlin, and Steven Worley, *Texturing and Modeling: A Procedural Approach*, third edition, Morgan Kaufmann, 2002. Cited on p. 178, 199, 526
- [296] Ebrahimi, Amir. Personal communication, 2008. Cited on p. 359

- [297] Eccles, Allen, "The Diamond Monster 3Dfx Voodoo 1," Gamespy Hall of Fame, 2000. Cited on p. 1
- [298] Edwards, Dave, Solomon Boulos, Jared Johnson, Peter Shirley, Michael Ashikhmin, Michael Stark, and Chris Wyman, "The Halfway Vector Disk for BRDF Modeling," *ACM Transactions on Graphics*, vol. 25, no. 1, pp. 1–18, 2006. Cited on p. 268
- [299] Ehmann, Stephen A., and Ming C. Lin, "Accelerated Proximity Queries Between Convex Polyhedra Using Multi-Level Voronoi Marching," *IEEE/RSJ International Conference on Intelligent Robots and Systems 2000*, pp. 2101–2106, 2000. Cited on p. 820
- [300] Ehmann, Stephen A., and Ming C. Lin, "Accurate and Fast Proximity Queries Between Polyhedra Using Convex Surface Decomposition," *Computer Graphics Forum*, vol. 20, no. 3, pp. C500–C510, 2001. Cited on p. 820, 826
- [301] Eisemann, Martin, Marcus Magnor, Thorsten Grosch, and Stefan Müller, "Fast Ray/Axis-Aligned Bounding Box Overlap Tests using Ray Slopes," *journal of graphics tools*, vol. 12, no. 4, pp. 35–46, 2007. Cited on p. 746
- [302] Eldridge, Matthew, Homan Igehy, and Pat Hanrahan, "Pomegranate: A Fully Scalable Graphics Architecture," *Computer Graphics (SIGGRAPH 2001 Proceedings)*, pp. 443–454, July 2000. vol. 11, no. 6, pp. 290–296, 1995. Cited on p. 843, 846
- [303] Eldridge, Matthew, *Designing Graphics Architectures around Scalability and Communication*, Ph.D. Thesis, Stanford University, June 2001. Cited on p. 844, 845, 846
- [304] Elinas, Pantelis, and Wolfgang Stuerzlinger, "Real-time Rendering of 3D Clouds," *journal of graphics tools*, vol. 5, no. 4, pp. 33–45, 2000. Cited on p. 452
- [305] Engel, Klaus, Markus Hadwiger, Joe M. Kniss, Christof Rezk-Salama, and Daniel Weiskopf, *Real-Time Volume Graphics*, A K Peters Ltd., 2006. Cited on p. 505
- [306] Engel, Wolfgang, ed., *ShaderX*, Wordware, May 2002. Cited on p. xvi, 885
- [307] Engel, Wolfgang, ed., *ShaderX<sup>2</sup>: Introduction & Tutorials with DirectX 9*, Wordware, 2004. Cited on p. xiv, 885
- [308] Engel, Wolfgang, ed., *ShaderX<sup>2</sup>: Shader Programming Tips & Tricks with DirectX 9*, Wordware, 2004. Cited on p. xiv, 885, 949
- [309] Engel, Wolfgang, ed., *ShaderX<sup>3</sup>*, Charles River Media, November 2004. Cited on p. 885, 997
- [310] Engel, Wolfgang, ed., *ShaderX<sup>4</sup>*, Charles River Media, 2005. Cited on p. 885
- [311] Engel, Wolfgang, ed., *ShaderX<sup>5</sup>*, Charles River Media, 2006. Cited on p. 885, 943
- [312] Engel, Wolfgang, "Cascaded Shadow Maps," in Engel, Wolfgang, ed., *ShaderX<sup>5</sup>*, Charles River Media, pp. 197–206, 2006. Cited on p. 357, 359, 360
- [313] Engel, Wolfgang, ed., *ShaderX<sup>6</sup>*, Charles River Media, 2008. Cited on p. 885
- [314] Engel, Wolfgang, ed., *Programming Vertex, Geometry, and Pixel Shaders, Second Edition*, Charles River Media, 2008. Cited on p. 264, 283
- [315] Ericson, Christer, *Real-Time Collision Detection*, Morgan Kaufmann, 2005. Cited on p. 657, 695, 706, 730, 732, 733, 738, 763, 765, 784, 791, 792, 814, 815, 826, 827
- [316] Ericson, Christer, "More Capcom/CEDEC bean-spilling," realtimecollisiondetection.net blog. <http://realtimecollisiondetection.net/blog/?p=35> Cited on p. 490
- [317] Eriksson, Carl, Dinesh Manocha, William V. Baxter III, *Proceedings 2001 Symposium on Interactive 3D Graphics*, pp. 111–120, March 2001. Cited on p. 693

- [318] Erleben, Kenny, Jon Sporring, Knud Henriksen, and Henrik Dohlmann, *Physics Based Animation*, Charles River Media, 2005. Cited on p. 827
- [319] Ernst, Manfred, Tomas Akenine-Möller, and Henrik Wann Jensen, “Interactive Rendering of Caustics Using Interpolated Warped Volumes,” *Graphics Interface 2005*, pp. 87–96, May 2005. Cited on p. 400, 401
- [320] Euclid (original translation by Heiberg, with introduction and commentary by Sir Thomas L. Heath), *The Thirteen Books of EUCLID'S ELEMENTS*, Second Edition, Revised with Additions, Volume I (Books I, II), Dover Publications, Inc., 1956. Cited on p. 889
- [321] Evans, Francine, Steven Skiena, and Amitabh Varshney, “Optimizing Triangle Strips for Fast Rendering,” *IEEE Visualization '96*, pp. 319–326, 1999. Cited on p. 554
- [322] Evans, Alex, “Fast Approximations for Global Illumination on Dynamic Scenes,” *SIGGRAPH 2006 Advanced Real-Time Rendering in 3D Graphics and Games course notes*, 2006. Cited on p. 382, 425, 886
- [323] Everitt, Cass, “One-Pass Silhouette Rendering with GeForce and GeForce2,” NVIDIA White Paper, June 2000. <http://developer.nvidia.com> Cited on p. 512
- [324] Everitt, Cass, “Interactive Order-Independent Transparency,” NVIDIA White Paper, May 2001. <http://developer.nvidia.com> Cited on p. 137, 352
- [325] Everitt, Cass, Ashu Rege, and Cem Cebenoyan, “Hardware Shadow Mapping,” NVIDIA White Paper, December 2001. <http://developer.nvidia.com> Cited on p. 350
- [326] Everitt, Cass, and Mark Kilgard, “Practical and Robust Stenciled Shadow Volumes for Hardware-Accelerated Rendering,” NVIDIA White Paper, March 2002. <http://developer.nvidia.com> Cited on p. 344
- [327] Ewins, Jon P., Marcus D. Waller, Martin White, and Paul F. Lister, “MIP-Map Level Selection for Texture Mapping,” *IEEE Transactions on Visualization and Computer Graphics*, vol. 4, no. 4, pp. 317–329, Oct.–Dec. 1998. Cited on p. 165
- [328] Eyles, J., S. Molnar, J. Poulton, T. Greer, A. Lastra, N. England, and L. Westover, “PixelFlow: The Realization,” *ACM SIGGRAPH/Eurographics Workshop on Graphics Hardware* Los Angeles, CA, pp. 57–68, August 1997. Cited on p. 846, 875
- [329] Fairchild, Mark D. and David R. Wyble, “Colorimetric Characterization of the Apple Studio Display (Flat Panel LCD),” Technical Report, RIT Munsell Color Science Laboratory, July, 1998. Cited on p. 141
- [330] Falby, John S., Michael J. Zyda, David R. Pratt, and Randy L. Mackey, “NPSNET: Hierarchical Data Structures for Real-Time Three-Dimensional Visual Simulation,” *Computers & Graphics*, vol. 17, no. 1, pp. 65–69, 1993. Cited on p. 693
- [331] Farin, Gerald, “Triangular Bernstein-Bézier Patches,” *Computer Aided Geometric Design*, vol. 3, no. 2, pp. 83–127, 1986. Cited on p. 601, 643
- [332] Farin, Gerald, *Curves and Surfaces for Computer Aided Geometric Design—A Practical Guide*, Fourth Edition (First Edition, 1988), Academic Press Inc., 1996. Cited on p. 576, 579, 583, 584, 587, 595, 597, 598, 601, 604, 605, 609, 610, 643
- [333] Farin, Gerald E., and Dianne Hansford, *Practical Linear Algebra: A Geometry Toolbox*, A K Peters Ltd., 2004. Cited on p. 97, 573, 792, 911
- [334] Farin, Gerald E., *NURBS: From Projective Geometry to Practical Use*, 2nd edition, A K Peters Ltd., 1999. Cited on p. 643

- [335] Farin, Gerald, and Dianne Hansford, *The Essentials of CAGD*, A K Peters Ltd., 2000. Cited on p. 643
- [336] Fedkiw, Ronald, Jos Stam, and Henrik Wann Jensen, “Visual Simulation of Smoke,” *Computer Graphics (SIGGRAPH 2001 Proceedings)*, pp. 15–22, August 2001. Cited on p. 502
- [337] Fernando, Randima, Sebastian Fernandez, Kavita Bala, and Donald P. Greenberg, “Adaptive Shadow Maps,” *Computer Graphics (SIGGRAPH 2001 Proceedings)*, pp. 387–390, August 2001. Cited on p. 358
- [338] Fernando, Randima, and Mark J. Kilgard, *The Cg Tutorial: The Definitive Guide to Programmable Real-Time Graphics*, Addison-Wesley, 2003. Cited on p. 31
- [339] Fernando, Randima, ed., *GPU Gems*, Addison-Wesley, 2004. Cited on p. 885
- [340] Fernando, Randima, “Percentage-closer Soft Shadows,” *SIGGRAPH 2005 Technical Sketch*, 2005. Cited on p. 364
- [341] Ferwerda, James, “Elements of Early Vision for Computer Graphics,” *IEEE Computer Graphics and Applications*, vol. 21, no. 5, pp. 22–33, September/October 2001. Cited on p. 217, 338
- [342] Fiedler, Glenn, “Terrain Occlusion Culling with Horizons,” in Andrew Kirmse, ed., *Game Programming Gems 4*, Charles River Media, pp. 515–527, 2004. Cited on p. 679
- [343] de Figueiredo, L.H., “Adaptive Sampling of Parametric Curves,” in Alan Paeth, ed., *Graphics Gems V*, Academic Press, pp. 173–178, 1995. Cited on p. 637
- [344] Fisher, F., and A. Woo, “R.E versus N.H Specular Highlights,” in Paul S. Heckbert, ed., *Graphics Gems IV*, Academic Press, pp. 388–400, 1994. Cited on p. 257
- [345] Flavell, Andrew, “Run Time Mip-Map Filtering,” *Game Developer*, vol. 5, no. 11, pp. 34–43, November 1998. Cited on p. 165, 166
- [346] Floater, Michael, Kai Hormann, and Géza Kós, “A General Construction of Barycentric Coordinates over Convex Polygons,” *Advances in Computational Mathematics*, vol. 24, no. 1–4, pp. 311–331, January 2006. Cited on p. 755
- [347] Fog, Agner, *Optimizing software in C++*, 2007. Cited on p. 706, 722
- [348] Foley, J.D., A. van Dam, S.K. Feiner, J.H. Hughes, and R.L. Philips, *Introduction to Computer Graphics*, Addison-Wesley, 1993. Cited on p. 61, 97
- [349] Foley, J.D., A. van Dam, S.K. Feiner, and J.H. Hughes, *Computer Graphics: Principles and Practice, Second Edition in C*, Addison-Wesley, 1995. Cited on p. 61, 77, 97, 146, 215, 217, 587, 590, 832, 836
- [350] Forest, Vincent, Loïc Barthe, and Mathias Paulin, “Realistic Soft Shadows by Penumbra-Wedges Blending,” *Graphics Hardware (2006)*, pp. 39–48, 2006. Cited on p. 348
- [351] Forsyth, Tom, “Comparison of VIPM Methods,” in Mark DeLoura, ed., *Game Programming Gems 2*, Charles River Media, pp. 363–376, 2001. Cited on p. 552, 563, 568, 574, 686
- [352] Forsyth, Tom, “Impostors: Adding Clutter,” in Mark DeLoura, ed., *Game Programming Gems 2*, Charles River Media, pp. 488–496, 2001. Cited on p. 457, 459, 460, 461
- [353] Forsyth, Tom, “Self-Shadowing Bumpmap Using 3D Texture Hardware,” *journal of graphics tools*, vol. 7, no. 4, pp. 19–26, 2002. Cited on p. 428

- [354] Forsyth, Tom, "Making Shadow Buffers Robust Using Multiple Dynamic Frustums," in Wolfgang Engel, ed., *ShaderX<sup>4</sup>*, Charles River Media, pp. 331–346, 2005. Cited on p. 358
- [355] Forsyth, Tom, "Extremely Practical Shadows," *Game Developers Conference*, March 2006. <http://www.eelpi.gotdns.org/papers/papers.html> Cited on p. 356, 357, 361
- [356] Forsyth, Tom, "Linear-Speed Vertex Cache Optimisation," website, September 2006. <http://www.eelpi.gotdns.org/papers/papers.html> Cited on p. 557
- [357] Forsyth, Tom, "Shadowbuffers," *Game Developers Conference*, March 2007. <http://www.eelpi.gotdns.org/papers/papers.html> Cited on p. 351, 358, 361
- [358] "The Trilight: A Simple General-Purpose Lighting Model for Games," website, March 2007. <http://www.eelpi.gotdns.org/papers/papers.html> Cited on p. 294, 325
- [359] "Knowing Which Mipmap Levels are Needed," website, August 2007. [http://www.eelpi.gotdns.org/blog/wiki.html#\[\[Knowingwhichmipmaplevelsareneeded\]\]](http://www.eelpi.gotdns.org/blog/wiki.html#[[Knowingwhichmipmaplevelsareneeded]]) Cited on p. 172, 174
- [360] Fosner, Ron, "All Aboard Hardware T & L," *Game Developer*, vol. 7, no. 4, pp. 30–41, April 2000. Cited on p. 391, 840
- [361] Fowles, Grant R., *Introduction to Modern Optics, Second Edition*, Holt, Reinhart, and Winston, 1975. Cited on p. 231, 283
- [362] Franklin, Dustin, "Hardware-Based Ambient Occlusion," in Engel, Wolfgang, ed., *ShaderX<sup>4</sup>*, Charles River Media, pp. 91–100, 2005. Cited on p. 426
- [363] Friedrich, Heiko, Johannes Günther, Andreas Dietrich, Michael Scherbaum, Hans-Peter Seidel, and Philipp Slusallek, *Exploring the Use of Ray Tracing for Future Games*, SIGGRAPH Video Game Symposium 2006, 2006. Cited on p. 416
- [364] Frisken, Sarah, Ronald N. Perry, Alyn P. Rockwood, and Thouis R. Jones, "Adaptively Sampled Distance Fields: A General Representation of Shape for Computer Graphics," *Computer Graphics (SIGGRAPH 2000 Proceedings)*, pp. 249–254, July 2000. Cited on p. 160, 382, 826
- [365] Frisken, Sarah, and Ronald N. Perry, "A Computationally Efficient Framework for Modeling Soft Body Impact," *Visual Proceedings (SIGGRAPH 2001)*, p. 160, August 2001. Cited on p. 826
- [366] Fuchs, H., Z.M. Kedem, and B.F. Naylor, "On Visible Surface Generation by A Priori Tree Structures," *Computer Graphics (SIGGRAPH '80 Proceedings)*, pp. 124–133, July 1980. Cited on p. 652, 653
- [367] Fuchs, H., G.D. Abram, and E.D. Grant, "Near Real-Time Shaded Display of Rigid Objects," *Computer Graphics (SIGGRAPH '83 Proceedings)*, pp. 65–72, July 1983. Cited on p. 652
- [368] Fuchs, H., J. Poulton, J. Eyles, T. Greer, J. Goldfeather, D. Ellsworth, S. Molnar, G. Turk, B. Tebbs, and L. Israel, "Pixel-Planes 5: A Heterogeneous Multiprocessor Graphics System Using Processor-Enhanced Memories," *Computer Graphics (SIGGRAPH '89 Proceedings)*, pp. 79–88, July 1989. Cited on p. 8, 871, 875
- [369] Fuchs, Martin, Volker Blanz, Hendrik Lensch, and Hans-Peter Seidel, "Reflectance from Images: A Model-Based Approach for Human Faces," *IEEE Transactions on Visualization and Computer Graphics*, vol. 11, no. 3, pp. 296–305, May–June. 2005. Cited on p. 265
- [370] Fung, James, "Computer Vision on the GPU," in Matt Pharr, ed., *GPU Gems 2*, Addison-Wesley, pp. 649–666, 2005. Cited on p. 472

- [371] Funkhouser, Thomas A., and Carlo H. Séquin, “Adaptive Display Algorithm for Interactive Frame Rates During Visualization of Complex Virtual Environments,” *Computer Graphics (SIGGRAPH 93 Proceedings)*, pp. 247–254, August 1993. Cited on p. 461, 567, 691, 692, 693
- [372] Funkhouser, Thomas A., *Database and Display Algorithms for Interactive Visualization of Architectural Models*, Ph.D. Thesis, University of California, Berkeley, 1993. Cited on p. 692, 693, 720
- [373] Fuhrmann, Anton L., Eike Umlauf, and Stephan Mantler, “Extreme Model Simplification for Forest Rendering,” *Eurographics Workshop on Natural Phenomena (2005)*, pp. 57–66, 2005. Cited on p. 462
- [374] *Game Development Algorithms* mailing list archives. Cited on p. 172
- [375] Ganovelli, Fabio, John Dingiana, and Carol O’Sullivan, “BucketTree: Improving Collision Detection between Deformable Objects,” *Spring Conference in Computer Graphics (SCCG2000)*, pp. 156–163, 2000. Cited on p. 826
- [376] Garcia, Ismael, Mateu Sbert, and Lázló Szirmay-Kalos, “Tree Rendering with Billboard Clouds,” *Third Hungarian Conference on Computer Graphics and Geometry*, pp., 2005. Cited on p. 462
- [377] Gardner, Andrew, Chris Tchou, Tim Hawkins, and Paul Debevec, “Linear Light Source Reflectometry,” *ACM Transactions on Graphics (SIGGRAPH 2003)*, vol. 22, no. 3, pp.749–758, 2003. Cited on p. 265
- [378] Garland, Michael, and Paul S. Heckbert, “Fast Polygonal Approximation of Terrains and Height Fields,” Technical Report CMU-CS-95-181, Carnegie Mellon University, 1995. Cited on p. 568
- [379] Garland, Michael, and Paul S. Heckbert, “Surface Simplification Using Quadric Error Metrics,” *Proceedings of SIGGRAPH 97*, pp. 209–216, August 1997. Cited on p. 564
- [380] Garland, Michael, and Paul S. Heckbert, “Simplifying Surfaces with Color and Texture using Quadric Error Metrics,” *IEEE Visualization 98*, pp. 263–269, July 1998. Cited on p. 562, 563, 564, 574
- [381] Garland, Michael, “Quadric-Based Polygonal Surface Simplification,” Ph.D. thesis, Technical Report CMU-CS-99-105, Carnegie Mellon University, 1999. Cited on p. 566
- [382] Gautron, Pascal, Jaroslav Křivánek, Sumanta Pattanaik, and Kadi Bouatouch, “A Novel Hemispherical Basis for Accurate and Efficient Rendering,” *Eurographics Symposium on Rendering (2004)*, pp. 321–330, June 2004. Cited on p. 420
- [383] Gautron, Pascal, Jaroslav Křivánek, Kadi Bouatouch, and Sumanta Pattanaik, “Radiance Cache Splatting: A GPU-Friendly Global Illumination Algorithm,” *Rendering Techniques 2005: 16th Eurographics Workshop on Rendering*, pp. 55–64, June–July 2005. Cited on p. 417
- [384] Geczy, George, “2D Programming in a 3D World: Developing a 2D Game Engine Using DirectX 8 Direct3D,” *Gamasutra*, June 2001. Cited on p. 445
- [385] Gehling, Michael, “Dynamic Skyscapes,” *Game Developer Magazine*, vol. 13, no. 3, pp. 23–33, March 2006. Cited on p. 444
- [386] Geiss, Ryan, “Generating Complex Procedural Terrains Using the GPU,” in Hubert Nguyen, ed., *GPU Gems 3*, Addison-Wesley, pp. 7–37, 2007. Cited on p. 151, 199
- [387] Geiss, Ryan, and Michael Thompson, “NVIDIA Demo Team Secrets—Cascades,” *Game Developers Conference*, March 2007. <http://developer.nvidia.com/object/gdc-2007.htm> Cited on p. 151, 456, 457

- [388] Georghiades, Athinodoros S., "Recovering 3-D Shape and Reflectance from a Small Number of Photographs," *Eurographics Symposium on Rendering (2003)*, pp. 230–240, June 2003. Cited on p. 265
- [389] Georgii, Joachim, Jens Krüger, and Rüdiger Westermann, "Interactive GPU-based Collision Detection," *Proceedings of IADIS Computer Graphics and Visualization*, pp. 3–10, 2007. Cited on p. 825
- [390] Gerasimov, Philipp, "Omnidirectional Shadow Mapping," in Randima Fernando, ed., *GPU Gems*, Addison-Wesley, pp. 193–203, 2004. Cited on p. 361
- [391] Gershbein, Reid, and Pat Hanrahan, "A Fast Relighting Engine for Interactive Cinematic Lighting Design," *Computer Graphics (SIGGRAPH 2000 Proceedings)*, pp. 353–358, July 2000. Cited on p. 442
- [392] Gershun, Arun, "The Light Field," Moscow, 1936, translated by P. Moon and G. Timoshenko, *Journal of Mathematics and Physics*, vol. 18, no. 2, pp. 51–151, 1939. Cited on p. 290
- [393] Gibson, Steve, "The Origins of Sub-Pixel Font Rendering," web article. <http://www.grc.com/ctwho.htm> Cited on p. 134
- [394] Giegl, Markus, and Michael Wimmer, "Unpopping: Solving the Image-Space Blend Problem for Smooth Discrete LOD Transition," *Computer Graphics Forum*, vol. 26, no. 1, pp. 46–49, March 2007. Cited on p. 684
- [395] Giegl, Markus, and Michael Wimmer, "Queried Virtual Shadow Maps," *ACM Symposium on Interactive 3D Graphics and Games (I3D 2007)*, pp. 65–72, 2007. Similar article in [311]. Cited on p. 358
- [396] Giegl, Markus, and Michael Wimmer, "Fitted Virtual Shadow Maps," *Graphics Interface 2007*, pp. 159–168, 2007. Cited on p. 358
- [397] Giegl, Markus, "Fitted Virtual Shadow Maps and Shadow Fog," in Wolfgang Engel, ed., *ShaderX<sup>6</sup>*, Charles River Media, pp. 275–300, 2008. Cited on p. 358
- [398] Gigus, Z., J. Canny, and R. Seidel, "Efficiently Computing and Representing Aspect Graphs of Polyedral Objects," *IEEE Transactions On Pattern Analysis and Machine Intelligence*, vol. 13, no. 6, pp. 542–551, 1991. Cited on p. 661
- [399] Gilbert, E., D. Johnson, and S. Keerthi, "A Fast Procedure for Computing the Distance between Complex Objects in Three-Dimensional Space," *IEEE Journal of Robotics and Automation*, vol. 4, no. 2, pp. 193–203, April 1988. Cited on p. 818, 820
- [400] Gillham, David, "Real-time Depth-of-Field Implemented with a Postprocessing-Only Technique," in Wolfgang Engel, ed., *ShaderX<sup>5</sup>*, Charles River Media, pp. 163–175, 2006. Cited on p. 488
- [401] Ginsburg, Dan, and Dave Gosselin, "Dynamic Per-Pixel Lighting Techniques," in Mark DeLoura, ed., *Game Programming Gems 2*, Charles River Media, pp. 452–462, 2001. Cited on p. 187, 222
- [402] Ginsburg, Dan, "Ruby: Dangerous Curves," *Game Developers Conference*, March 2005. <http://ati.amd.com/developer/techreports.html> Cited on p. 495
- [403] Girshick, Ahna, Victoria Interrante, Steve Haker, and Todd Lemoine, "Line Direction Matters: An Argument for the Use of Principal Directions in 3D Line Drawings," *Proceedings of the First International Symposium on Non-photorealistic Animation and Rendering (NPAR)*, pp. 43–52, June 2000. Cited on p. 526
- [404] Glassner, Andrew S., ed., *An Introduction to Ray Tracing*, Academic Press Inc., London, 1989. Cited on p. 119, 131, 415, 437

- [405] Glassner, Andrew S., ed., *Graphics Gems*, Academic Press, 1990. Cited on p. 97, 792, 919
- [406] Glassner, Andrew S., “Computing Surface Normals for 3D Models,” in Andrew S. Glassner, ed., *Graphics Gems*, Academic Press, pp. 562–566, 1990. Cited on p. 546
- [407] Glassner, Andrew, “Building Vertex Normals from an Unstructured Polygon List,” in Paul S. Heckbert, ed., *Graphics Gems IV*, Academic Press, pp. 60–73, 1994. Cited on p. 542, 543, 546
- [408] Glassner, Andrew S., *Principles of Digital Image Synthesis*, vol. 1, Morgan Kaufmann, 1995. Cited on p. 217, 283, 437, 832, 836
- [409] Glassner, Andrew S., *Principles of Digital Image Synthesis*, vol. 2, Morgan Kaufmann, 1995. Cited on p. 205, 209, 211, 217, 226, 264, 283, 437
- [410] Goldman, Ronald, “Intersection of Three Planes,” in Andrew S. Glassner, ed., *Graphics Gems*, Academic Press, p. 305, 1990. Cited on p. 782
- [411] Goldman, Ronald, “Intersection of Two Lines in Three-Space,” in Andrew S. Glassner, ed., *Graphics Gems*, Academic Press, p. 304, 1990. Cited on p. 782
- [412] Goldman, Ronald, “Matrices and Transformations,” in Andrew S. Glassner, ed., *Graphics Gems*, Academic Press, pp. 472–475, 1990. Cited on p. 71
- [413] Goldman, Ronald, “Some Properties of Bézier Curves,” in Andrew S. Glassner, ed., *Graphics Gems*, Academic Press, pp. 587–593, 1990. Cited on p. 580
- [414] Goldman, Ronald, “Recovering the Data from the Transformation Matrix,” in James Arvo, ed., *Graphics Gems II*, Academic Press, pp. 324–331, 1991. Cited on p. 70
- [415] Goldman, Ronald, “Decomposing Linear and Affine Transformations,” in David Kirk, ed., *Graphics Gems III*, Academic Press, pp. 108–116, 1992. Cited on p. 70
- [416] Goldman, Ronald, “Identities for the Univariate and Bivariate Bernstein Basis Functions,” in Alan Paeth, ed., *Graphics Gems V*, Academic Press, pp. 149–162, 1995. Cited on p. 643
- [417] Goldsmith, Jeffrey, and John Salmon, “Automatic Creation of Object Hierarchies for Ray Tracing,” *IEEE Computer Graphics and Applications*, vol. 7, no. 5, pp. 14–20, May 1987. Cited on p. 803, 804
- [418] Goldsmith, Timothy H., “What Birds See,” *Scientific American*, pp. 69–75, July 2006. Cited on p. 210
- [419] Golub, Gene, and Charles Van Loan, *Matrix Computations*, Third Edition, Johns Hopkins University Press, 1996. Cited on p. 97
- [420] Gomez, Miguel, “Simple Intersection Tests for Games,” *Gamasutra*, October 1999. Cited on p. 784
- [421] Gomez, Miguel, “Compressed Axis-Aligned Bounding Box Trees,” in Mark DeLoura, ed., *Game Programming Gems 2*, Charles River Media, pp. 388–393, 2001. Cited on p. 826
- [422] Gonzalez, Rafael C., and Richard E. Woods, *Digital Image Processing*, Third Edition, Addison-Wesley, 1992. Cited on p. 117, 477, 518
- [423] Gooch, Amy, Bruce Gooch, Peter Shirley, and Elaine Cohen, “A Non-Photorealistic Lighting Model for Automatic Technical Illustration,” *Computer Graphics (SIGGRAPH 98 Proceedings)*, pp. 447–452, July 1998. Cited on p. 45, 508, 522

- [424] Gooch, Bruce, Peter-Pike J. Sloan, Amy Gooch, Peter Shirley, and Richard Riesenfeld, "Interactive Technical Illustration," *Proceedings 1999 Symposium on Interactive 3D Graphics*, pp. 31–38, April 1999. Cited on p. 337, 508, 512, 521
- [425] Gooch, Bruce or Amy, and Amy or Bruce Gooch, *Non-Photorealistic Rendering*, A K Peters Ltd., 2001. Cited on p. 508, 522, 530
- [426] Goodnight, Nolan, Rui Wang, Cliff Woolley, and Greg Humphreys, "Interactive Time-Dependent Tone Mapping Using Programmable Graphics Hardware," *Eurographics Symposium on Rendering (2003)*, pp. 26–37, June 2003. Cited on p. 477
- [427] Goral, Cindy M., Kenneth E. Torrance, Donald P. Greenberg, and Bennett Battaille, "Modelling the Interaction of Light Between Diffuse Surfaces," *Computer Graphics (SIGGRAPH '84 Proceedings)*, pp. 212–222, July 1984. Cited on p. 408
- [428] Gordon, Dan, and Shuhong Chen, "Front-to-back display of BSP trees," *IEEE Computer Graphics and Applications*, vol. 11, no. 5, pp. 79–85, September 1991. Cited on p. 652
- [429] Gortler, Steven J., Radek Grzeszczuk, Richard Szeliski, and Michael F. Cohen, "The Lumigraph," *Computer Graphics (SIGGRAPH 96 Proceedings)*, pp. 43–54, August, 1996. Cited on p. 444
- [430] Gosselin, David R., Pedro V. Sander, and Jason L. Mitchell, "Drawing a Crowd," in Engel, Wolfgang, ed., *ShaderX<sup>3</sup>*, Charles River Media, pp. 505–517, 2004. Cited on p. 711
- [431] Gosselin, David R., "Real Time Skin Rendering," *Game Developers Conference*, March 2004. [ati.amd.com/developer/gdc/Gosselin\\_skin.pdf](http://ati.amd.com/developer/gdc/Gosselin_skin.pdf) Cited on p. 404, 405
- [432] Gosselin, David R., Pedro V. Sander, and Jason L. Mitchell, "Real-Time Texture-Space Skin Rendering," in Engel, Wolfgang, ed., *ShaderX<sup>3</sup>*, Charles River Media, pp. 171–183, 2004. Cited on p. 405
- [433] Gottschalk, S., M.C. Lin, and D. Manocha, "OBBTree: A Hierarchical Structure for Rapid Interference Detection," *Computer Graphics (SIGGRAPH 96 Proceedings)*, pp. 171–180, August, 1996. Cited on p. 731, 733, 767, 768, 770, 795, 806, 807, 811
- [434] Gottschalk, Stefan, *Collision Queries using Oriented Bounding Boxes*, Ph.D. Thesis, Department of Computer Science, University of North Carolina at Chapel Hill, 1999. Cited on p. 733, 767, 770, 804
- [435] Gouraud, H., "Continuous Shading of Curved Surfaces," *IEEE Transactions on Computers*, vol. C-20, pp. 623–629, June 1971. Cited on p. 115, 201
- [436] Govindaraju, N. K., S. Redon, M. C. Lin, and D. Manocha, "CULLIDE: Interactive Collision Detection between Complex Models in Large Environments using Graphics Hardware," *Graphics Hardware (2003)*, pp. 25–32, 2003. Cited on p. 824
- [437] Govindaraju, Naga K., Brandon Lloyd, Sung-Eui Yoon, Avneesh Sud, and Dinesh Manocha, "Interactive Shadow Generation in Complex Environments," *ACM Transactions on Graphics (SIGGRAPH 2003)*, vol. 22, no. 3, pp. 501–510, 2003. Cited on p. 373
- [438] Govindaraju, N. K., M. C. Lin, and D. Manocha, "Quick-CULLIDE: Fast Inter- and Intra-Object Collision Culling Using Graphics Hardware," *IEEE Virtual Reality*, pp. 59–66, 2005. Cited on p. 825
- [439] Green, Chris, "Improved Alpha-Tested Magnification for Vector Textures and Special Effects," *SIGGRAPH 2007 Advanced Real-Time Rendering in 3D Graphics and Games course notes*, 2007. Cited on p. 160, 161, 183, 382

- [440] Green, Chris, "Efficient Self-Shadowed Radiosity Normal Mapping," *SIGGRAPH 2007 Advanced Real-Time Rendering in 3D Graphics and Games course notes*, 2007. Cited on p. 421, 429
- [441] Green, D., and D. Hatch, "Fast Polygon-Cube Intersection Testing," in Alan Paeth, ed., *Graphics Gems V*, Academic Press, pp. 375–379, 1995. Cited on p. 760
- [442] Green, Paul, Jan Kautz, Wojciech Matusik, and Frédo Durand, "View-Dependent Precomputed Light Transport Using Nonlinear Gaussian Function Approximations," *ACM Symposium on Interactive 3D Graphics and Games (I3D 2006)*, pp. 7–14, March 2006. Cited on p. 436
- [443] Green, Paul, Jan Kautz, and Frédo Durand, "Efficient Reflectance and Visibility Approximations for Environment Map Rendering," *Computer Graphics Forum*, vol. 26, no. 3, pp. 495–502, 2007. Cited on p. 310, 312, 430
- [444] Green, Robin, "Spherical Harmonic Lighting: The Gritty Details," *Game Developers Conference*, March 2003. <http://www.research.scea.com/gdc2003/spherical-harmonic-lighting.pdf> Cited on p. 323, 325, 436
- [445] Green, Simon, "Summed Area Tables using Graphics Hardware," *Game Developers Conference*, March 2003. [http://developer.nvidia.com/object/GDC\\_2003\\_Presentations.html](http://developer.nvidia.com/object/GDC_2003_Presentations.html) Cited on p. 168, 488
- [446] Green, Simon, "Stupid OpenGL Shader Tricks," *Game Developers Conference*, March 2003. [http://developer.nvidia.com/docs/IO/8230/GDC2003\\_OpenGLShaderTricks.pdf](http://developer.nvidia.com/docs/IO/8230/GDC2003_OpenGLShaderTricks.pdf) Cited on p. 490, 492, 493
- [447] Green, Simon, "Real-Time Approximations to Subsurface Scattering," in Randima Fernando, ed., *GPU Gems*, Addison-Wesley, pp. 263–278, 2004. Cited on p. 403, 405, 406
- [448] Green, Simon, "Implementing Improved Perlin Noise," in Matt Pharr, ed., *GPU Gems 2*, Addison-Wesley, pp. 409–416, 2005. Cited on p. 178
- [449] Greene, Ned, "Environment Mapping and Other Applications of World Projections," *IEEE Computer Graphics and Applications*, vol. 6, no. 11, pp. 21–29, November 1986. Cited on p. 304, 305, 309, 314
- [450] Greene, Ned, Michael Kass, and Gavin Miller, "Hierarchical Z-Buffer Visibility," *Computer Graphics (SIGGRAPH 93 Proceedings)*, pp. 231–238, August 1993. Cited on p. 674, 677, 678
- [451] Greene, Ned, "Detecting Intersection of a Rectangular Solid and a Convex Polyhedron," in Paul S. Heckbert, ed., *Graphics Gems IV*, Academic Press, pp. 74–82, 1994. Cited on p. 731
- [452] Greene, Ned, *Hierarchical Rendering of Complex Environments*, Ph.D. Thesis, University of California at Santa Cruz, Report no. UCSC-CRL-95-27, June 1995. Cited on p. 677, 678
- [453] Greger, Gene, Peter Shirley, Philip M. Hubbard, and Donald P. Greenberg, "The Irradiance Volume," *IEEE Computer Graphics and Applications*, vol. 18, no. 2, pp. 32–43, Mar./Apr. 1998. Cited on p. 423
- [454] Gregory, Arthur, Ming C. Lin, Stefan Gottschalk, and Russell Taylor, "H-Collide: A Framework for Fast and Accurate Collision Detection for Haptic Interaction," *Proceedings of Virtual Reality Conference 1999*, pp. 38–45, 1999. Cited on p. 744
- [455] Gribb, Gil, and Klaus Hartmann, "Fast Extraction of Viewing Frustum Planes from the World-View-Projection Matrix," June 2001. Cited on p. 774

- [456] Griffiths, Andrew, “Real-time Cellular Texturing,” in Engel, Wolfgang, ed., *ShaderX<sup>5</sup>*, Charles River Media, pp. 519–532, 2006. Cited on p. 179
- [457] Gritz, Larry, “Shader Antialiasing,” in *Advanced RenderMan: Creating CGI for Motion Pictures*, Morgan Kaufmann, 1999. Also (as “Basic Antialiasing in Shading Language”) in *SIGGRAPH 99 Advanced RenderMan: Beyond the Companion course notes*, 1999. Cited on p. 180
- [458] Gritz, Larry, “The Secret Life of Lights and Surfaces,” in *Advanced RenderMan: Creating CGI for Motion Pictures*, Morgan Kaufmann, 1999. Also in *SIGGRAPH 2000 Advanced RenderMan 2: To RI-INFINITY and Beyond course notes*, 2000. Cited on p. 294
- [459] Gritz, Larry, and Eugene d’Eon, “The Importance of Being Linear,” in Hubert Nguyen, ed., *GPU Gems 3*, Addison-Wesley, pp. 529–542, 2007. Cited on p. 143, 146
- [460] Gronsky, Stefan, “Lighting Food,” *SIGGRAPH 2007 Anyone Can Cook—Inside Ratatouille’s Kitchen course notes*, 2007. Cited on p. 406
- [461] Grün, Holger, and Marco Spoerl, “Ray-Traced Fog Volumes,” in Engel, Wolfgang, ed., *ShaderX<sup>4</sup>*, Charles River Media, pp. 143–155, 2005. Cited on p. 501
- [462] Grün, Holger, “Smoothed N-Patches,” in Engel, Wolfgang, ed., *ShaderX<sup>5</sup>*, Charles River Media, pp. 5–22, 2006. Cited on p. 603
- [463] Gu, Xianfeng, Steven J. Gortler, Hugues Hoppe, “Geometry Images,” *ACM Transactions on Graphics (SIGGRAPH 2002)*, vol. 21, no. 3, pp. 355–361, 2002. Cited on p. 467
- [464] Guardado, Juan, and Daniel Sánchez-Crespo, “Rendering Water Caustics,” in Randima Fernando, ed., *GPU Gems*, Addison-Wesley, pp. 31–62, 2004. Cited on p. 401
- [465] Guennebaud, Gaël, Loïc Barthe, and Mathias Paulin, “High-Quality Adaptive Soft Shadow Mapping,” *Computer Graphics Forum*, vol. 26, no. 3, pp. 525–533, 2007. Cited on p. 372
- [466] Guenter, Brian, Todd Knoblock, and Erik Ruf, “Specializing Shaders,” *Computer Graphics (SIGGRAPH 95 Proceedings)*, pp. 343–350, August 1995. Cited on p. 442
- [467] Guigue, Philippe, and Olivier Devillers, “Fast and Robust Triangle-Triangle Overlap Test using Orientation Predicates,” *journals of graphics tools*, vol. 8, no. 1, pp. 25–42, 2003. Cited on p. 757, 760
- [468] Gumhold, Stefan, and Wolfgang Straßer, “Real Time Compression of Triangle Mesh Connectivity,” *Computer Graphics (SIGGRAPH 98 Proceedings)*, pp. 133–140, August 1998. Cited on p. 554
- [469] Guthe, Stefan, Stefan Roettger, Andreas Schieber, Wolfgang Strasser, Thomas Ertl, “High-Quality Unstructured Volume Rendering on the PC Platform,” *ACM SIGGRAPH/Eurographics Workshop on Graphics Hardware*, pp. 1–8, 2002. Cited on p. 502
- [470] Guthe, Stefan, Ákos Balázs, and Reinhard Klein, “Near Optimal Hierarchical Culling: Performance Driven Use of Hardware Occlusion Queries,” *Eurographics Symposium on Rendering (2006)*, pp. 207–214, June 2006. Cited on p. 676
- [471] Guymon, Mel, “Pyro-Techniques: Playing with Fire,” *Game Developer*, vol. 7, no. 2, pp. 23–27, Feb. 2000. Cited on p. 450
- [472] Hachisuka, Toshiya, “High-Quality Global Illumination Rendering Using Rasterization,” in Matt Pharr, ed., *GPU Gems 2*, Addison-Wesley, pp. 615–633, 2005. Cited on p. 417

- [473] Hadap, Sunil, and Nadia Magnenat-Thalmann, “Modeling Dynamic Hair as a Continuum,” *Computer Graphics Forum*, vol. 20, no. 3, pp. 329–338, 2001. Cited on p. 826
- [474] Haeberli, P., and K. Akeley, “The Accumulation Buffer: Hardware Support for High-Quality Rendering,” *Computer Graphics (SIGGRAPH '90 Proceedings)*, pp. 309–318, August 1990. Cited on p. 24, 126, 486, 492
- [475] Haeberli, Paul, and Mark Segal, “Texture Mapping as a Fundamental Drawing Primitive,” *4th Eurographics Workshop on Rendering*, pp. 259–266, June 1993. Cited on p. 154, 180
- [476] Haeberli, Paul, “Matrix Operations for Image Processing,” Grafica Obscura website, November 1993. <http://www.graficaobscura.com/matrix/index.html> Cited on p. 474
- [477] Hagen, Margaret A., “How to Make a Visually Realistic 3D Display,” *Computer Graphics*, vol. 25, no. 2, pp. 76–81, April 1991. Cited on p. 450
- [478] Hahn, James K., “Realistic Animation of Rigid Bodies,” *Computer Graphics (SIGGRAPH '88 Proceedings)*, pp. 299–308, 1988. Cited on p. 823
- [479] Haines, Eric, ed., *The Ray Tracing News*. Cited on p. 437
- [480] Haines, Eric, “Essential Ray Tracing Algorithms,” Chapter 2 in Andrew Glassner, ed., *An Introduction to Ray Tracing*, Academic Press Inc., London, 1989. Cited on p. 738, 742, 744, 754
- [481] Haines, Eric, “Fast Ray-Convex Polyhedron Intersection,” in James Arvo, ed., *Graphics Gems II*, Academic Press, pp. 247–250, 1991. Cited on p. 744
- [482] Haines, Eric, “Point in Polygon Strategies,” in Paul S. Heckbert, ed., *Graphics Gems IV*, Academic Press, pp. 24–46, 1994. Cited on p. 746, 751, 753, 754, 755
- [483] Haines, Eric, and John Wallace, “Shaft Culling for Efficient Ray-Traced Radiosity,” in P. Brunet and F.W. Jansen, eds., *Photorealistic Rendering in Computer Graphics (Proceedings of the Second Eurographics Workshop on Rendering)*, Springer-Verlag, pp. 122–138, 1994. Cited on p. 780
- [484] Haines, Eric, and Steven Worley, “Fast, Low-Memory Z-buffering when Performing Medium-Quality Rendering,” *journal of graphics tools*, vol. 1, no. 3, pp. 1–6, 1996. Cited on p. 282
- [485] Haines, Eric, “The Curse of the Monkey’s Paw,” in Eric Haines, ed., *Ray Tracing News*, vol. 10, no. 2, June 1997. Cited on p. 539
- [486] Haines, Eric, “A Shaft Culling Tool,” *journal of graphics tools*, vol. 5, no. 1, pp. 23–26, 2000. Also collected in [71]. Cited on p. 780
- [487] Haines, Eric, “Soft Planar Shadows Using Plateaus,” *journal of graphics tools*, vol. 6, no. 1, pp. 19–27, 2001. Also collected in [71]. Cited on p. 338, 372
- [488] Hammon, Earl, Jr., “Practical Post-Process Depth of Field,” in Hubert Nguyen, ed., *GPU Gems 3*, Addison-Wesley, pp. 583–605, 2007. Cited on p. 489
- [489] Hakura, Ziyad S., and Anoop Gupta, “The Design and Analysis of a Cache Architecture for Texture Mapping,” *24th International Symposium of Computer Architecture (ISCA)*, pp. 108–120, June 1997. Cited on p. 847
- [490] Hakura, Ziyad S., John M. Snyder, and Jerome E. Lengyel, “Parameterized Environment Maps,” *Proceedings 2001 Symposium on Interactive 3D Graphics*, pp. 203–208, March 2001. Cited on p. 392
- [491] Hall, Roy, *Illumination and Color in Computer Generated Imagery*, Springer-Verlag, 1989. Cited on p. 832

- [492] Hall, Tim, “A how to for using OpenGL to Render Mirrors,” *comp.graphics.api.opengl* newsgroup, August 1996. Cited on p. 387, 389
- [493] Hall, Tom, “Silhouette Tracking,” website, May 2003. [http://www.geocities.com/tom\\_j\\_hall](http://www.geocities.com/tom_j_hall) Cited on p. 521
- [494] Halstead, Mark, Michal Kass, and Tony DeRose, “Efficient, Fair Interpolation using Catmull-Clark Surfaces,” *Computer Graphics (SIGGRAPH 93 Proceedings)*, pp. 35–44, August 1994. Cited on p. 623, 624
- [495] Han, Jefferson Y., and Ken Perlin, “Measuring Bidirectional Texture Reflectance with a Kaleidoscope,” *ACM Transactions on Graphics (SIGGRAPH 2003)*, vol. 22, no. 3, pp.741–748, 2003. Cited on p. 265
- [496] Han, Charles, Bo Sun, Ravi Ramamoorthi, and Eitan Grinspun, “Frequency Domain Normal Map Filtering,” *ACM Transactions on Graphics (SIGGRAPH 2007)*, vol. 26, no. 3, 28:1–28:11, July, 2007. Cited on p. 275
- [497] Hanrahan, P., and P. Haeberli, “Direct WYSIWYG Painting and Texturing on 3D Shapes,” *Computer Graphics (SIGGRAPH '90 Proceedings)*, pp. 215–223, August 1990. Cited on p. 726
- [498] Hanson, Andrew J., *Visualizing Quaternions*, Morgan Kaufmann, 2006. Cited on p. 97
- [499] Hao, Xuejun, Thomas Baby, and Amitabh Varshney, “Interactive Subsurface Scattering for Translucent Meshes,” *ACM Symposium on Interactive 3D Graphics (I3D 2003)*, pp. 75–82, 2003. Cited on p. 407
- [500] Hao, Xuejun, and Amitabh Varshney, “Real-Time Rendering of Translucent Meshes,” *ACM Transactions on Graphics*, vol. 23, no. 2, pp. 120–142, 2004. Cited on p. 407
- [501] Hapke, B., “A Theoretical Photometric Function for the Lunar Surface,” *J. Geophysical Research*, vol. 68, no. 15, 1 August 1963. Cited on p. 229
- [502] Hargreaves, Shawn, “Hemisphere Lighting With Radiosity Maps,” *Gamasutra*, Aug. 2003. Also collected in [308]. Cited on p. 424
- [503] Hargreaves, Shawn, “Deferred Shading,” *Game Developers Conference*, March 2004. <http://www.talula.demon.co.uk/DeferredShading.pdf> Cited on p. 278, 281
- [504] Hargreaves, Shawn, “Detail Texture Motion Blur,” in Engel, Wolfgang, ed., *ShaderX<sup>3</sup>*, Charles River Media, pp. 205–214, 2004. Cited on p. 495
- [505] Harris, Mark J., and Anselmo Lastra, “Real-Time Cloud Rendering,” *Computer Graphics Forum*, vol. 20, no. 3, pp. 76–84, 2001. Cited on p. 452
- [506] Hart, Evan, Dave Gosselin, and John Isidoro, “Vertex Shading with Direct3D and OpenGL,” *Game Developers Conference*, March 2001. [http://www.ati.com/na/pages/resource\\_centre/dev\\_rel/techpapers.html](http://www.ati.com/na/pages/resource_centre/dev_rel/techpapers.html) Cited on p. 347, 516
- [507] Hart, John C., George K. Francis, and Louis H. Kauffman, “Visualizing Quaternion Rotation,” *ACM Transactions on Graphics*, vol. 13, no. 3, pp. 256–276, 1994. Cited on p. 97
- [508] Hasenfratz, Jean-Marc, Marc Lapierre, Nicolas Holzschuch, François Sillion, “A Survey of Real-time Soft Shadows Algorithms,” *Computer Graphics Forum*, vol. 22, no. 4, pp. 753–774, Dec. 2003. Cited on p. 437
- [509] Hasselgren, J., T. Akenine-Möller, and L. Ohlsson, “Conservative Rasterization,” in Matt Pharr, ed., *GPU Gems 2*, Addison-Wesley, pp. 677–690, 2005. Cited on p. 825

- [510] Hasselgren, J., T. Akenine-Möller, and S. Laine, “A Family of Inexpensive Sampling Schemes,” *Computer Graphics Forum*, vol. 24, no.4, pp. 843–848, 2005. Cited on p. 133
- [511] Hasselgren, J., and T. Akenine-Möller, “Efficient Depth Buffer Compression,” *Graphics Hardware*, pp. 103–110, 2006. Cited on p. 856
- [512] Hasselgren, J., and T. Akenine-Möller, “An Efficient Multi-View Rasterization Architecture,” *Eurographics Symposium on Rendering*, pp. 61–72, June 2006. Cited on p. 837
- [513] Hasselgren, J., and T. Akenine-Möller, “PCU: The Programmable Culling Unit,” *ACM Transactions on Graphics*, vol. 26, no. 3, pp. 92.1–91.20, 2007. Cited on p. 858, 859
- [514] He, Taosong, “Fast Collision Detection Using QuOSPO Trees,” *Proceedings 1999 Symposium on Interactive 3D Graphics*, pp. 55–62, April 1999. Cited on p. 807
- [515] He, Xiao D., Kenneth E. Torrance, François X. Sillion, and Donald P. Greenberg, “A Comprehensive Physical Model for Light Reflection,” *Computer Graphics (SIGGRAPH '91 Proceedings)*, pp. 175–186, July 1991. Cited on p. 241, 249, 252, 262
- [516] Hearn, Donald, and M. Pauline Baker, *Computer Graphics with OpenGL*, Third Edition, Prentice-Hall, Inc., Englewoods Cliffs, New Jersey, 2003. Cited on p. 18, 97
- [517] Heckbert, Paul, “Survey of Texture Mapping,” *IEEE Computer Graphics and Applications*, vol. 6, no. 11, pp. 56–67, November 1986. Cited on p. 199
- [518] Heckbert, Paul S., “Fundamentals of Texture Mapping and Image Warping,” Report no. 516, Computer Science Division, University of California, Berkeley, June 1989. Cited on p. 166, 168, 170, 199, 539
- [519] Heckbert, Paul S., “Adaptive Radiosity Textures for Bidirectional Ray Tracing,” *Computer Graphics (SIGGRAPH '90 Proceedings)*, pp. 145–154, August 1990. Cited on p. 329, 398
- [520] Heckbert, Paul S., “What Are the Coordinates of a Pixel?” in Andrew S. Glassner, ed., *Graphics Gems*, Academic Press, pp. 246–248, 1990. Cited on p. 21
- [521] Heckbert, Paul S., and Henry P. Moreton, “Interpolation for Polygon Texture Mapping and Shading,” *State of the Art in Computer Graphics: Visualization and Modeling*, Springer-Verlag, pp. 101–111, 1991. Cited on p. 838
- [522] Heckbert, Paul S., ed., *Graphics Gems IV*, Academic Press, 1994. Cited on p. 97, 792
- [523] Heckbert, Paul S., “A Minimal Ray Tracer,” in Paul S. Heckbert, ed., *Graphics Gems IV*, Academic Press, pp. 375–381, 1994. Cited on p. 412
- [524] Heckbert, Paul S., and Michael Herf, *Simulating Soft Shadows with Graphics Hardware*, Technical Report CMU-CS-97-104, Carnegie Mellon University, January 1997. Cited on p. 336
- [525] Hecker, Chris, “More Compiler Results, and What To Do About It,” *Game Developer*, pp. 14–21, August/September 1996. Cited on p. 705
- [526] Hecker, Chris, “Physics, The Next Frontier,” *Game Developer*, pp. 12–20, October/November 1996. Cited on p. 827
- [527] Hecker, Chris, “Physics, Part 2: Angular Effects,” *Game Developer*, pp. 14–22, December/January 1997. Cited on p. 827

- [528] Hecker, Chris, "Physics, Part 3: Collision Response," *Game Developer*, pp. 11–18, February/March 1997. Cited on p. 827
- [529] Hecker, Chris, "Physics, Part 4: The Third Dimension," *Game Developer*, pp. 15–26, June 1997. Cited on p. 827
- [530] Hegeman, Kyle, Simon Premoze, Michael Ashikhmin, and George Drettakis, "Approximate Ambient Occlusion for Trees," *ACM Symposium on Interactive 3D Graphics and Games (I3D 2006)*, pp. 41–48, March 2006. Cited on p. 382
- [531] Heidmann, Tim, "Real shadows, real time," *Iris Universe*, no. 18, pp. 23–31, Silicon Graphics Inc., November 1991. Cited on p. 340, 341
- [532] Heidrich, Wolfgang, and Hans-Peter Seidel, "View-independent Environment Maps," *ACM SIGGRAPH/Eurographics Workshop on Graphics Hardware*, pp. 39–45, August 1998. Cited on p. 307
- [533] Heidrich, Wolfgang, and Hans-Peter Seidel, "Efficient Rendering of Anisotropic Surfaces Using Computer Graphics Hardware," *Image and Multi-dimensional Digital Signal Processing Workshop (IMDSP)*, 1998. Cited on p. 259
- [534] Heidrich, Wolfgang, Rüdiger Westermann, Hans-Peter Seidel, and Thomas Ertl, "Applications of Pixel Textures in Visualization and Realistic Image Synthesis," *Proceedings 1999 Symposium on Interactive 3D Graphics*, pp. 127–134, April 1999. Cited on p. 350, 492, 499
- [535] Heidrich, Wolfgang, and Hans-Peter Seidel, "Realistic, Hardware-accelerated Shading and Lighting," *Computer Graphics (SIGGRAPH 99 Proceedings)*, pp. 171–178, August 1999. Cited on p. 307, 309, 316
- [536] Heidrich, Wolfgang, Katja Daubert, Jan Kautz, and Hans-Peter Seidel, "Illuminating Micro Geometry Based on Precomputed Visibility," *Computer Graphics (SIGGRAPH 2000 Proceedings)*, pp. 455–464, July 2000. Cited on p. 429
- [537] Held, M., J.T. Klosowski, and J.S.B. Mitchell, "Evaluation of Collision Detection Methods for Virtual Reality Fly-Throughs," *Proceedings of the 7th Canadian Conference on Computational Geometry*, pp. 205–210, 1995. Cited on p. 807
- [538] Held, M., J.T. Klosowski, and J.S.B. Mitchell, "Real-Time Collision Detection for Motion Simulation within Complex Environments," *Visual Proceedings (SIGGRAPH 96)*, p. 151, August 1996. Cited on p. 807
- [539] Held, Martin, "ERIT—A Collection of Efficient and Reliable Intersection Tests," *journal of graphics tools*, vol. 2, no. 4, pp. 25–44, 1997. Cited on p. 741, 757
- [540] Held, Martin, "FIST: Fast Industrial-Strength Triangulation," submitted for publication, 1998. Cited on p. 536
- [541] Hennessy, John L., and David A. Patterson, *Computer Architecture: A Quantitative Approach*, Second Edition, Morgan Kaufmann, 1996. Cited on p. 12, 697, 702
- [542] Hensley, Justin, and Thorsten Scheuermann, "Dynamic Glossy Environment Reflections Using Summed-Area Tables," in Engel, Wolfgang, ed., *ShaderX<sup>4</sup>*, Charles River Media, pp. 187–200, 2005. Cited on p. 168, 312
- [543] Hensley, Justin, Thorsten Scheuermann, Greg Coombe, Montek Singh, and Anselmo Lastra, "Fast Summed-Area Table Generation and its Applications," *Computer Graphics Forum*, vol. 24, no. 3, pp. 547–555, 2005. Cited on p. 168, 312, 488
- [544] Herf, M., and P.S. Heckbert, "Fast Soft Shadows," *Visual Proceedings (SIGGRAPH 96)*, p. 145, August 1996. Cited on p. 336

- [545] Herrell, Russ, Joe Baldwin, and Chris Wilcox, "High-Quality Polygon Edging," *IEEE Computer Graphics and Applications*, vol. 15, no. 4, pp. 68–74, July 1995. Cited on p. 527, 528
- [546] Hertzmann, Aaron, "Introduction to 3D Non-Photorealistic Rendering: Silhouettes and Outlines," *SIGGRAPH 99 Non-Photorealistic Rendering course notes*, 1999. Cited on p. 518, 522
- [547] Hery, Christophe, "On Shadow Buffers," *Stupid RenderMan/RAT Tricks*, SIGGRAPH 2002 RenderMan Users Group meeting, 2002. Cited on p. 406
- [548] Hery, Christophe, "Implementing a Skin BSSRDF (or Several)," *SIGGRAPH 2003 RenderMan, Theory and Practice course notes*, 2003. Cited on p. 406
- [549] Hicks, Odell, "A Simulation of Thermal Imaging," in Engel, Wolfgang, ed., *ShaderX<sup>3</sup>*, Charles River Media, pp. 169–170, 2004. Cited on p. 472
- [550] Hill, Steve, "A Simple Fast Memory Allocator," in David Kirk, ed., *Graphics Gems III*, Academic Press, pp. 49–50, 1992. Cited on p. 705
- [551] Hill, F.S., Jr., "The Pleasures of 'Perp Dot' Products," in Paul S. Heckbert, ed., *Graphics Gems IV*, Academic Press, pp. 138–148, 1994. Cited on p. 6, 780
- [552] Hirche, Johannes, Alexander Ehlert, Stefan Guthe, and Michael Doggett, "Hardware Accelerated Per-Pixel Displacement Mapping," *Graphics Interface 2000*, pp. 153–158, 2004. Cited on p. 197
- [553] Hoberock, Jared, and Yuntao Jia, "High-Quality Ambient Occlusion," in Hubert Nguyen, ed., *GPU Gems 3*, Addison-Wesley, pp. 257–274, 2007. Cited on p. 381, 407
- [554] Hoffman, Donald D., *Visual Intelligence*, W.W. Norton & Company, 2000. Cited on p. 140, 393
- [555] Hoffman, Naty, and Kenny Mitchell, "Photorealistic Terrain Lighting in Real Time," *Game Developer*, vol. 8, no. 7, pp. 32–41, July 2001. More detailed version in *Game Developers Conference*, pp. 357–367, March 2001. Also collected in [1272]. [http://www.gdconf.com/archives/proceedings/2001/prog\\_papers.html](http://www.gdconf.com/archives/proceedings/2001/prog_papers.html) Cited on p. 380, 428
- [556] Hoffman, Naty, and Arcot J. Preetham, "Rendering Outdoor Light Scattering in Real Time," *Game Developers Conference*, March 2002. <http://ati.amd.com/developer/dx9/ATI-LightScattering.pdf> Cited on p. 499
- [557] Hoffman, Naty, and Arcot J. Preetham, "Real-Time Light Atmosphere Interaction for Outdoor Scenes," in Lander, Jeff, ed., *Graphics Programming Methods*, Charles River Media, pp. 337–352, 2003. Cited on p. 499
- [558] Hook, Brian, "The Quake 3 Arena Rendering Architecture," *Game Developers Conference*, March 1999. [http://www.gamasutra.com/features/index\\_video.htm](http://www.gamasutra.com/features/index_video.htm) Cited on p. 33, 424
- [559] Hoppe, H., T. DeRose, T. Duchamp, M. Halstead, H. Jin, J. McDonald, J. Schweitzer, and W. Stuetzle, "Piecewise Smooth Surface Reconstruction," *Computer Graphics (SIGGRAPH 94 Proceedings)*, pp. 295–302, July 1994. Cited on p. 613, 615, 624
- [560] Hoppe, Hugues, "Progressive Meshes," *Computer Graphics (SIGGRAPH 96 Proceedings)*, pp. 99–108, August 1996. Cited on p. 562, 563, 566, 567, 686
- [561] Hoppe, Hugues, "View-Dependent Refinement of Progressive Meshes," *Computer Graphics (SIGGRAPH 97 Proceedings)*, pp. 189–198, August 1997. Cited on p. 569, 637, 639

- [562] Hoppe, Hugues, “Efficient Implementation of Progressive Meshes,” *Computers and Graphics*, vol. 22, no. 1, pp. 27–36, 1998. Cited on p. 542, 563
- [563] Hoppe, Hugues, “Smooth View-Dependent Level-of-Detail Control and Its Application to Terrain Rendering,” *IEEE Visualization 1998*, pp. 35–42, Oct. 1998. Cited on p. 569
- [564] Hoppe, Hugues, “Optimization of Mesh Locality for Transparent Vertex Caching,” *Computer Graphics (SIGGRAPH 99 Proceedings)*, pp. 269–276, August 1999. Cited on p. 555, 573
- [565] Hoppe, Hugues, “New Quadric Metric for Simplifying Meshes with Appearance Attributes,” *IEEE Visualization 1999*, pp. 59–66, October 1999. Cited on p. 566
- [566] Hormann, K., and M. Floater, ‘Mean Value Coordinates for Arbitrary Planar Polygons,’ *ACM Transactions on Graphics*, vol. 25, no. 4, no. 1424–1441, October 2006. Cited on p. 755
- [567] Hormann, Kai, Bruno Lévy, and Alla Sheffer, “Mesh Parameterization: Theory and Practice,” *Course 2 notes at SIGGRAPH 2007*, 2007. Cited on p. 153, 573
- [568] Hornus, Samuel, Jared Hoberock, Sylvain Lefebvre, and John Hart, “ZP+: Correct Z-pass Stencil Shadows,” *ACM Symposium on Interactive 3D Graphics and Games (I3D 2005)*, pp. 195–202, 2005. Cited on p. 343, 346
- [569] Hoschek, Josef, and Dieter Lasser, *Fundamentals of Computer Aided Geometric Design*, A.K. Peters Ltd., 1993. Cited on p. 576, 579, 584, 597, 605, 609, 643
- [570] Hourcade, J.C., and A. Nicolas, “Algorithms for Antialiased Cast Shadows,” *Computers and Graphics*, vol. 9, no. 3, pp. 259–265, 1985. Cited on p. 350
- [571] Hu, Jinhui, Suya You, and Ulrich Neumann, “Approaches to Large-Scale Urban Modeling,” *IEEE Computer Graphics and Applications*, vol. 23, no. 6, pp. 62–69, November/December 2003. Cited on p. 533
- [572] Hubbard, Philip M., “Approximating Polyhedra with Spheres for Time-Critical Collision Detection,” *ACM Transactions on Graphics*, vol. 15, no. 3, pp. 179–210, 1996. Cited on p. 763, 807, 817
- [573] Huddy, Richard, “The Efficient Use of Vertex Buffers,” NVIDIA White Paper, November 2000. <http://developer.nvidia.com> Cited on p. 551
- [574] Hudson, T., M. Lin, J. Cohen, S. Gottschalk, and D. Manocha, “V-COLLIDE: Accelerated collision detection for VRML,” *Proceedings of VRML ’97*, Monterey, California, February 1997. Cited on p. 811
- [575] Hughes, M., M. Lin, D. Manocha, and C. Dimattia, “Efficient and Accurate Interference Detection for Polynomial Deformation,” *Proceedings of Computer Animation*, Geneva, Switzerland, pp. 155–166, 1996. Cited on p. 826
- [576] Hughes, John F., and Tomas Möller, “Building an Orthonormal Basis from a Unit Vector,” *journal of graphics tools*, vol. 4, no. 4, pp. 33–35, 1999. Also collected in [71]. Cited on p. 71, 447
- [577] Humphreys, Greg, Mike Houston, Ren Ng, Randall Frank, Sean Ahern, Peter D. Kirchner, and James t. Klosowski, “Chromium: A Stream-Processing Framework for Interactive Rendering on Clusters,” *ACM Transactions on Graphics*, vol. 21, no. 3, pp. 693–702, July 2002. Cited on p. 844
- [578] Hutson, V., and J.S. Pym, *Applications of Functional Analysis and Operator Theory*, Academic Press, London, 1980. Cited on p. 911
- [579] Hwa, Lok M., Mark A. Duchaineau, and Kenneth I. Joy, “Adaptive 4-8 Texture Hierarchies,” *Visualization ’04 conference*, pp. 219–226, 2004. Cited on p. 571

- [580] Hwu, Wen-Mei, and David Kirk, "Programming Massively Parallel Processors," Course ECE 498 AL1 Notes, ECE Illinois, Fall 2007. Cited on p. 877
- [581] Igehy, Homan, Gordon Stoll, and Pat Hanrahan, "The Design of a Parallel Graphics Interface," *Computer Graphics (SIGGRAPH 98 Proceedings)*, pp. 141–150, July 1998. Cited on p. 723
- [582] Igehy, Homan, Matthew Eldridge, and Kekoa Proudfoot, "Prefetching in a Texture Cache Architecture," *ACM SIGGRAPH/Eurographics Workshop on Graphics Hardware*, pp. 133–142, August 1998. Cited on p. 847
- [583] Igehy, Homan, Matthew Eldridge, and Pat Hanrahan, "Parallel Texture Caching," *ACM SIGGRAPH/Eurographics Workshop on Graphics Hardware*, pp. 95–106, August 1999. Cited on p. 847
- [584] Ihrke, Ivo, Gernot Ziegler, Art Tevs, Christian Theobalt, Marcus Magnor, and Hans-Peter Seidel, "Eikonal Rendering: Efficient Light Transport in Refractive Objects," *ACM Transactions on Graphics*, vol. 26, no. 3, article 59, 2007. Cited on p. 399
- [585] Ilkits, Milan, Joe Kniss, Aaron Lefohn, and Charles Hansen, "Volume Rendering Techniques," in Randima Fernando, ed., *GPU Gems*, Addison-Wesley, pp. 667–692, 2004. Cited on p. 137, 502
- [586] Immel, David S., Michael F. Cohen, and Donald P. Greenberg, "A Radiosity Method for Non-diffuse Environments," *Computer Graphics (SIGGRAPH '86 Proceedings)*, pp. 133–142, August 1986. Cited on p. 253
- [587] Iones, Andrei, Anton Krupkin, Mateu Sbert, and Sergei Zhukov, "Fast, Realistic Lighting for Video Games," *IEEE Computer Graphics and Applications*, vol. 23, no. 3, pp. 54–64, May 2003. Cited on p. 377, 379
- [588] *Iris Graphics Library Programming Guide*, Silicon Graphics Inc., 1991. Cited on p. 550
- [589] Isenberg, Tobias, Bert Freudenberg, Nick Halper, Stefan Schlechtweg, and Thomas Strothotte, "A Developer's Guide to Silhouette Algorithms for Polygonal Models," *IEEE Computer Graphics and Applications*, vol. 23, no. 4, pp. 28–37, July/August 2003. Cited on p. 510, 530
- [590] Hertzmann, Aaron, "A Survey of Stroke-Based Rendering," *IEEE Computer Graphics and Applications*, vol. 23, no. 4, pp. 70–81, July/August 2003. Cited on p. 530
- [591] Isensee, Pete, "C++ Optimization Strategies and Techniques," 2007. Cited on p. 706, 722
- [592] Isidoro, John, Alex Vlachos, and Chris Brennan, "Rendering Ocean Water," in Wolfgang Engel, ed., *ShaderX*, Wordware, pp. 347–356, May 2002. Cited on p. 40
- [593] Isidoro, John, "Next Generation Skin Rendering," *Game Tech Conference*, 2004. <http://www.game-tech.com/Talks/SkinRendering.pdf> Cited on p. 405, 407, 436
- [594] Isidoro, John, "Shadow Mapping: GPU-based Tips and Techniques," *Game Developers Conference*, March 2006. <http://ati.amd.com/developer/gdc/2006/Isidoro-ShadowMapping.pdf> Cited on p. 357, 361, 363, 366
- [595] Isidoro, John, "Edge Masking and Per-Texel Depth Extent Propagation For Computation Culling During Shadow Mapping," in Wolfgang Engel, ed., *ShaderX<sup>5</sup>*, Charles River Media, pp. 239–248, 2006. Cited on p. 363
- [596] Ivanov, D. V., and Y. P. Kuzmin, "Color Distribution—A New Approach to Texture Compression," *Computer Graphics Forum*, vol. 19, no. 3, pp. 283–289, 2000. Cited on p. 176

- [597] James, Adam, *Binary Space Partitioning for Accelerated Hidden Surface Removal and Rendering of Static Environments*, Ph.D. Thesis, University of East Anglia, August 1999. Cited on p. 653, 695
- [598] James, Doug L., and Dinesh K. Pai, "BD-Tree: Output-Sensitive Collision Detection for Reduced Deformable Models," *ACM Transactions on Graphics*, vol. 23, no. 3, pp. 393–398, August 2004. Cited on p. 822
- [599] James, Doug L., and Christopher D. Twigg, "Skinning Mesh Animations," *ACM Transactions on Graphics (SIGGRAPH 2004)*, vol. 23, no. 3, pp. 399–407, August, 2004. Cited on p. 83
- [600] James, Greg, "Operations for Hardware Accelerated Procedural Texture Animation," in Mark DeLoura, ed., *Game Programming Gems 2*, Charles River Media, pp. 497–509, 2001. Cited on p. 472, 473
- [601] James, Greg, "Rendering Objects as Thick Volumes," in Engel, Wolfgang, ed., *ShaderX<sup>2</sup>: Shader Programming Tips and Tricks with DirectX 9*, Wordware, pp. 89–106, 2004. Cited on p. 501
- [602] James, Greg, and John ORorke, "Real-Time Glow," in Randima Fernando, ed., *GPU Gems*, Addison-Wesley, pp. 343–362, 2004. Cited on p. 471, 472, 484, 486
- [603] James, Robert, "True Volumetric Fog," in Lander, Jeff, ed., *Graphics Programming Methods*, Charles River Media, pp. 353–366, 2003. Cited on p. 501
- [604] Jaquays, Paul, and Brian Hook, *Quake 3: Arena Shader Manual, Revision 12*, December 1999. Cited on p. 33
- [605] Jensen, Henrik Wann, Justin Legakis, and Julie Dorsey, "Rendering of Wet Materials," *10th Eurographics Workshop on Rendering*, pp. 273–282, June 1999. Cited on p. 236
- [606] Jensen, Henrik Wann, *Realistic Image Synthesis Using Photon Mapping*, A.K. Peters Ltd., 2001. Cited on p. 416
- [607] Jensen, Henrik Wann, Stephen R. Marschner, Marc Levoy, and Pat Hanrahan, "A Practical Model for Subsurface Light Transport," *Computer Graphics (SIGGRAPH 2001 Proceedings)*, pp. 511–518, August 2001. Cited on p. 404, 406
- [608] Jensen, Lasse Staff, and Robert Golias, "Deep-Water Animation and Rendering," *Gamasutra*, Sept. 2001. Cited on p. 395, 500
- [609] Jeschke, Stefan, and Michael Wimmer, "Textured Depth Meshes for Real-Time Rendering of Arbitrary Scenes," *13th Eurographics Workshop on Rendering*, pp. 181–190, June 2002. Cited on p. 467
- [610] Jeschke, Stefan, Stephan Mantler, Michael Wimmer, "Interactive Smooth and Curved Shell Mapping," *Eurographics Symposium on Rendering (2007)*, pp. 351–360, June 2007. Cited on p. 197
- [611] Jiménez, P., and Thomas C. Torras, "3D Collision Detection: A Survey," *Computers & Graphics*, vol. 25, pp. 269–285, 2001. Cited on p. 819, 827
- [612] Johannsen, Andreas, and Michael B. Carter, "Clustered Backface Culling," *journal of graphics tools*, vol. 3, no. 1, pp. 1–14, 1998. Cited on p. 664
- [613] Johnson, Carolyn Y., "Making a Rat's Tale," Boston Globe website, July 9, 2007. <http://www.boston.com/business/technology/articles/2007/07/09/making-a-rats-tale/> Cited on p. 880
- [614] Jouppi, Norman P., and Chun-Fa Chang, "Z<sup>3</sup>: An Economical Hardware Technique for High-Quality Antialiasing and Transparency," *ACM SIGGRAPH/Eurographics Workshop on Graphics Hardware*, pp. 85–93, August 1999. Cited on p. 129, 130, 131

- [615] Joy, Kenneth I., *On-Line Geometric Modeling Notes*, Cited on p. 611
- [616] Judd, Tilke, Frédéric Durand, and Edward Adelson, “Apparent Ridges for Line Drawing,” *ACM Transactions on Graphics*, vol. 26, no. 3, article 19, 2007. Cited on p. 511
- [617] Kainz, Florian, Rod Bogart, and Drew Hess, “The OpenEXR File Format,” in Randima Fernando, ed., *GPU Gems*, Addison-Wesley, pp. 425–444, 2004. Cited on p. 481
- [618] Kajiya, James T., “Anisotropic Reflection Models,” *Computer Graphics (SIGGRAPH '85 Proceedings)*, pp. 15–21, July 1985. Cited on p. 270, 681
- [619] Kajiya, James T., “The Rendering Equation,” *Computer Graphics (SIGGRAPH '86 Proceedings)*, pp. 143–150, August 1986. Cited on p. 327, 414
- [620] Kajiya, James T., and Timothy L. Kay, “Rendering Fur with Three Dimensional Textures,” *Computer Graphics (SIGGRAPH '89 Proceedings)*, pp. 271–280, July 1989. Cited on p. 258, 264
- [621] Kalnins, Robert D., Philip L. Davidson, Lee Markosian, and Adam Finkelstein, “Coherent Stylized Silhouettes,” *ACM Transactions on Graphics (SIGGRAPH 2003)*, vol. 22, no. 3, pp. 856–861, 2003. Cited on p. 522
- [622] Kaneko, Tomomichi, Toshiyuki Takahei, Masahiko Inami, Naoki Kawakami, Yasuyuki Yanagida, Taro Maeda, and Susumu Tachi, “Detailed Shape Representation with Parallax Mapping,” *ICAT 2001*, Tokyo, pp. 205–208, Dec. 2001. Cited on p. 191
- [623] Kaplan, Matthew, Bruce Gooch, and Elaine Cohen, “Interactive Artistic Rendering,” *Proceedings of the First International Symposium on Non-photorealistic Animation and Rendering (NPAR)*, pp. 67–74, June 2000. Cited on p. 523, 526
- [624] Karkanis, Tasso, and A. James Stewart, “Curvature-Dependent Triangulation of Implicit Surfaces,” *IEEE Computer Graphics and Applications*, vol. 22, no. 2, pp. 60–69, March 2001. Cited on p. 607
- [625] Kautz, Jan, and M.D. McCool, “Interactive Rendering with Arbitrary BRDFs using Separable Approximations,” *10th Eurographics Workshop on Rendering*, pp. 281–292, June 1999. Cited on p. 267, 268
- [626] Kautz, Jan, and M.D. McCool, “Approximation of Glossy Reflection with Pre-filtered Environment Maps,” *Graphics Interface 2000*, pp. 119–126, May 2000. Cited on p. 312
- [627] Kautz, Jan, P.-P. Vázquez, W. Heidrich, and H.-P. Seidel, “A Unified Approach to Prefiltered Environment Maps,” *11th Eurographics Workshop on Rendering*, pp. 185–196, June 2000. Cited on p. 312
- [628] Kautz, Jan, and Hans-Peter Seidel, “Towards Interactive Bump Mapping with Anisotropic Shift-Variant BRDFs,” *ACM SIGGRAPH/Eurographics Workshop on Graphics Hardware*, pp. 51–58, 2000. Cited on p. 259
- [629] Kautz, Jan, Wolfgang Heidrich, and Katja Daubert, “Bump Map Shadows for OpenGL Rendering,” Technical Report MPII20004-001, Max-Planck-Institut für Informatik, Saarbrücken, Germany, 2000. Cited on p. 429
- [630] Kautz, Jan, Chris Wynn, Jonathan Blow, Chris Blasband, Anis Ahmad, and Michael McCool, “Achieving Real-Time Realistic Reflectance, Part 1” *Game Developer*, vol. 8, no. 1, pp. 32–37, January 2001. Cited on p. 265
- [631] Kautz, Jan, Chris Wynn, Jonathan Blow, Chris Blasband, Anis Ahmad, and Michael McCool, “Achieving Real-Time Realistic Reflectance, Part 2” *Game Developer*, vol. 8, no. 2, pp. 38–44, February 2001. Cited on p. 267

- [632] Kautz, Jan, “Rendering with Handcrafted Shading Models,” in Dante Treglia, ed., *Game Programming Gems 3*, Charles River Media, pp. 477–484, 2002. Cited on p. 258
- [633] Jan, Kautz, Peter-Pike Sloan, and John Snyder, “Fast, Arbitrary BRDF Shading for Low-Frequency Lighting using Spherical Harmonics,” *13th Eurographics Workshop on Rendering*, pp. 291–296, June 2002. Cited on p. 323, 436
- [634] Kautz, Jan, “SH Light Representations,” *SIGGRAPH 2005 Precomputed Radiance Transfer: Theory and Practice course notes*, 2005. Cited on p. 322, 323
- [635] Kautz, Jan, Jaakko Lehtinen, and Peter-Pike Sloan, “Precomputed Radiance Transfer: Theory and Practice,” *Course 18 notes at SIGGRAPH 2005*, 2005. Cited on p. 437
- [636] Kavan, Ladislav, Steven Collins, Jiří Žára, and Carol O’Sullivan, “Skinning with Dual Quaternions,” *ACM Symposium on Interactive 3D Graphics and Games (I3D 2007)*, pp. 39–46, 2007. Cited on p. 85
- [637] Kavan, Ladislav, Simon Dobbyn, Steven Collins, Jiří Žára, Carol O’Sullivan. “Polypostors: 2D Polygonal Impostors for 3D Crowds,” *ACM Symposium on Interactive 3D Graphics and Games (I3D 2008)*, pp. 149–156, February 2008. Cited on p. 461
- [638] Kawachi, Katsuaki, and Hirosama Suzuki, “Distance Computation between Non-convex Polyhedra at Short Range Based on Discrete Voronoi Regions,” *IEEE Geometric Modeling and Processing*, pp. 123–128, April 2000. Cited on p. 826
- [639] Kay, T.L., and J.T. Kajiya, “Ray Tracing Complex Scenes,” *Computer Graphics (SIGGRAPH ’86 Proceedings)*, pp. 269–278, August 1986. Cited on p. 742, 744
- [640] Kelemen, Csaba, and Lázló Szirmay-Kalos, “A Microfacet Based Coupled Specular-Matte BRDF Model with Importance Sampling,” *Eurographics 2001*, short presentation, pp. 25–34, September 2001. Cited on p. 241, 248, 252, 261, 264
- [641] Keller, Alexander, “Instant Radiosity,” *Proceedings of SIGGRAPH 97*, pp. 49–56, August 1997. Cited on p. 417
- [642] Keller, Alexander, and Wolfgang Heidrich, “Interleaved Sampling,” *12th Eurographics Workshop on Rendering*, pp. 266–273, June 2001. Cited on p. 132
- [643] Kelley, Michael, Kirk Gould, Brent Pease, Stephanie Winner, and Alex Yen, “Hardware Accelerated Rendering of CSG and Transparency,” *Computer Graphics (SIGGRAPH 94 Proceedings)*, pp. 177–184, July 1994. Cited on p. 137
- [644] Kensler, Andrew, and Peter Shirley, “Optimizing Ray-Triangle Intersection via Automated Search,” *Symposium on Interactive Ray Tracing*, pp. 33–38, 2006. Cited on p. 747
- [645] Kent, James R., Wayne E. Carlson, and Richard E. Parent, “Shape transformation for polyhedral objects,” *Computer Graphics (SIGGRAPH ’92 Proceedings)*, pp. 47–54, 1992. Cited on p. 85
- [646] Kershaw, Kathleen, *A Generalized Texture-Mapping Pipeline*, M.S. Thesis, Program of Computer Graphics, Cornell University, Ithaca, New York, 1992. Cited on p. 149, 151
- [647] Kessenich, John, Dave Baldwin, and Radi Rost, “The OpenGL Shading Language,” Cited on p. 31, 35
- [648] Kharlamov, Alexander, Iain Cantlay, and Yury Stepanenko, “Next-Generation SpeedTree Rendering,” in Hubert Nguyen, ed., *GPU Gems 3*, Addison-Wesley, pp. 69–92, 2007. Cited on p. 183, 455, 504

- [649] Kilgard, Mark, “Fast OpenGL-rendering of Lens Flares,” Cited on p. 482
- [650] Kilgard, Mark J., “Realizing OpenGL: Two Implementations of One Architecture,” *ACM SIGGRAPH/Eurographics Workshop on Graphics Hardware*, Los Angeles, California, pp. 45–55, August 1997. Cited on p. 849
- [651] Kilgard, Mark J., “Creating Reflections and Shadows Using Stencil Buffers,” *Game Developers Conference*, March 1999. <http://developer.nvidia.com> Cited on p. 714
- [652] Kilgard, Mark J., “A Practical and Robust Bump-mapping Technique for Today’s GPUs,” *Game Developers Conference*, March 2000. <http://developer.nvidia.com> Cited on p. 188, 190
- [653] Kilgard, Mark J., “More Advanced Hardware Rendering Techniques,” *Game Developers Conference*, March 2001. <http://developer.nvidia.com> Cited on p. 343
- [654] Kilgard, Mark J., “Shadow Mapping with Today’s OpenGL Hardware,” *CEDEC*, 2001. Cited on p. 350
- [655] Kim, Dongho, and James K. Hahn, “Hardware-Assisted Rendering of Cylindrical Panoramas,” *Journal of graphics tools*, vol. 7, no. 4, pp. 33–42, 2005. Cited on p. 443
- [656] Kim, Dong-Jin, Leonidas J. Guibas, and Sung-Yong Shin, “Fast Collision Detection Among Multiple Moving Spheres,” *IEEE Transactions on Visualization and Computer Graphics*, vol. 4, no. 3., July/September 1998. Cited on p. 812
- [657] Kim, Tae-Yong, and Ulrich Neumann, “Opacity Shadow Maps,” *Proceedings of Eurographics Rendering Workshop 2001*, pp. 177–182, 2001. Cited on p. 371
- [658] King, Gary, “Shadow Mapping Algorithms,” GPU Jackpot presentation, Oct. 2004. Cited on p. 354, 355
- [659] King, Gary, and William Newhall, “Efficient Omnidirectional Shadow Maps,” in Engel, Wolfgang, ed., *ShaderX<sup>3</sup>*, Charles River Media, pp. 435–448, 2004. Cited on p. 361
- [660] King, Gary, “Real-Time Computation of Dynamic Irradiance Environment Maps,” in Matt Pharr, ed., *GPU Gems 2*, Addison-Wesley, pp. 167–176, 2005. Cited on p. 316, 321, 322, 323
- [661] King, Yossarian, “Never Let ‘Em See You Pop—Issues in Geometric Level of Detail Selection,” in Mark DeLoura, ed., *Game Programming Gems*, Charles River Media, pp. 432–438, 2000. Cited on p. 691
- [662] King, Yossarian, “2D Lens Flare,” in Mark DeLoura, ed., *Game Programming Gems*, Charles River Media, pp. 515–518, 2000. Cited on p. 482
- [663] King, Yossarian, “Ground-Plane Shadows,” in Mark DeLoura, ed., *Game Programming Gems*, Charles River Media, pp. 562–566, 2000. Cited on p. 335
- [664] King, Yossarian, “Floating-Point Tricks: Improving Performance with IEEE Floating Point,” in Mark DeLoura, ed., *Game Programming Gems 2*, Charles River Media, pp. 167–181, 2001. Cited on p. 706
- [665] Kipfer, Peter, Mark Segal, and Rüdiger Westermann, “UberFlow: A GPU-based Particle Engine,” *SIGGRAPH/Eurographics Workshop on Graphics Hardware*, pp. 115–122, 2004. Cited on p. 456
- [666] Kirk, David B., and Douglas Voorhies, “The Rendering Architecture of the DN-10000VS,” *Computer Graphics (SIGGRAPH ’90 Proceedings)*, pp. 299–307, August 1990. Cited on p. 165
- [667] Kirk, David, ed., *Graphics Gems III*, Academic Press, 1992. Cited on p. 97, 792

- [668] Kirk, Adam G., and Okan Arikan, "Real-Time Ambient Occlusion for Dynamic Character Skins," *ACM Symposium on Interactive 3D Graphics and Games (I3D 2007)*, pp. 47–52 , 2007. Cited on p. 426
- [669] Kirmse, Andrew, ed., *Game Programming Gems 4*, Charles River Media, 2004. Cited on p. 990
- [670] Klein, Allison W., Wilmot Li, Michael M. Kazhdan, Wagner T. Corrêa, Adam Finkelstein, and Thomas A. Funkhouser, "Non-Photorealistic Virtual Environments," *Computer Graphics (SIGGRAPH 2000 Proceedings)*, pp. 527–534, July 2000. Cited on p. 523, 524
- [671] Kleinhuis, Christian, "Morph Target Animation Using DirectX," in Engel, Wolfgang, ed., *ShaderX<sup>4</sup>*, Charles River Media, pp. 39–45, 2005. Cited on p. 85
- [672] Klosowski, J.T., M. Held, J.S.B. Mitchell, H. Sowizral, and K. Zikan, "Efficient Collision Detection Using Bounding Volume Hierarchies of k-DOPs," *IEEE Transactions on Visualization and Computer Graphics*, vol. 4, no. 1, 1998. Cited on p. 765, 766, 803, 806, 807
- [673] Klosowski, James T., *Efficient Collision Detection for Interactive 3D Graphics and Virtual Environments*, Ph.D. Thesis, State University of New York at Stony Brook, May 1998. Cited on p. 807
- [674] Klosowski, James T., and Cláudio T. Silva, "The Prioritized-Layered Projection Algorithm for Visible Set Estimation," *IEEE Transactions on Visualization and Computer Graphics*, vol. 6, no. 2, pp. 108–123, April/June 2000. Cited on p. 675
- [675] Klosowski, James T., and Cláudio T. Silva, "Efficient Conservative Visibility Culling Using The Prioritized-Layered Projection Algorithm," *IEEE Transactions on Visualization and Computer Graphics*, vol. 7, no. 4, pp. 365–379, 2001. Cited on p. 675
- [676] Knuth, Donald E., *The Art of Computer Programming: Sorting and Searching*, vol. 3, Second Edition, Addison-Wesley, 1998. Cited on p. 813
- [677] Ko, Jerome, Manchor Ko, and Matthias Zwicker, "Practical Methods for a PRT-based Shader Using Spherical Harmonics," in Wolfgang Engel, ed., *ShaderX<sup>6</sup>*, Charles River Media, pp. 355–381, 2008. Cited on p. 436
- [678] Ko, Manchor, and Jerome Ko, "Practical Methods for a PRT-based Shader Using Spherical Harmonics," *GDC 2008 Core Techniques & Algorithms in Shader Programming tutorial*, 2008. <http://www.coretechniques.info/> Cited on p. 436
- [679] Kobbelt, Leif, " $\sqrt{3}$ -Subdivision," *Computer Graphics (SIGGRAPH 2000 Proceedings)*, pp. 103–112, July 2000. Cited on p. 612, 621, 622, 643
- [680] Kochanek, Doris H.U., and Richard H. Bartels, "Interpolating Splines with Local Tension, Continuity, and Bias Control," *Computer Graphics (SIGGRAPH '84 Proceedings)*, pp. 33–41, July 1984. Cited on p. 589, 590
- [681] Koenderink, Jan J., Andrea J. van Doorn, and Marigo Stavridi, "Bidirectional Reflection Distribution Function Expressed in Terms of Surface Scattering Modes," in *Proceedings of ECCV 2001*, vol. 2, pp. 28–39, 1996. Cited on p. 266
- [682] Kolb, Andreas, Lutz Latta, and Christof Rezk-Salama, "Hardware-based Simulation and Collision Detection for Large Particle Systems," *SIGGRAPH/Eurographics Workshop on Graphics Hardware*, pp. 123–131, 2004. Cited on p. 456
- [683] Kolchin, Konstantin, "Curvature-Based Shading of Translucent Materials, such as Human Skin," *GRAPHITE 2007*, pp. 239–242, 2007. Cited on p. 403

- [684] Koltun, Vladlen, Yiorgos Chrysanthou, and Daniel Cohen-Or, “Virtual Occluders: An Efficient Intermediate PVS representation,” *11th Eurographics Workshop on Rendering*, pp. 59–70, June 2000. Cited on p. 680
- [685] Koltun, Vladlen, Yiorgos Chrysanthou, and Daniel Cohen-Or, “Hardware-Accelerated From-Region Visibility using a Dual Ray Space,” *12th Eurographics Workshop on Rendering*, pp. 204–214, June 2001. Cited on p. 672
- [686] Konečný, Petr, *Bounding Volumes in Computer Graphics*, M.S. Thesis, Faculty of Informatics, Masaryk University, Brno, April 1998. Cited on p. 807
- [687] Kontkanen, Janne, and Samuli Laine, “Sampling Precomputed Volumetric Lighting,” *journal of graphics tools*, vol. 11, no. 3, pp. 1–16, 2006. Cited on p. 424
- [688] Kontkanen, Janne, and Samuli Laine, “Ambient Occlusion Fields,” *ACM Symposium on Interactive 3D Graphics and Games (I3D 2005)*, pp. 41–48, 2005. Cited on p. 427
- [689] Kontkanen, Janne, and Samuli Laine, “Ambient Occlusion Fields,” in Engel, Wolfgang, ed., *ShaderX<sup>4</sup>*, Charles River Media, pp. 101–108, 2005. Cited on p. 427
- [690] Kontkanen, Janne, and Timo Aila, “Ambient Occlusion for Animated Characters,” *Eurographics Symposium on Rendering (2006)*, 343–348, June 2006. Cited on p. 426
- [691] Koonce, Rusty, “Deferred Shading in *Tabula Rasa*” in Hubert Nguyen, ed., *GPU Gems 3*, Addison-Wesley, pp. 429–457, 2007. Cited on p. 278, 281, 283, 324, 353
- [692] Koslov, Simon, “Perspective Shadow Maps: Care and Feeding,” in Randima Fernando, ed., *GPU Gems*, Addison-Wesley, pp. 217–244, 2004. Cited on p. 355
- [693] Kovach, Peter, “Inside Direct3D: Stencil Buffers,” *Gamasutra*, August 2000. Cited on p. 473
- [694] Kovalčík, Vít, and Jiří Sochor, “Occlusion Culling with Statistically Optimized Occlusion Queries,” *WSCG 2005*, 2005. Cited on p. 676
- [695] Kozlowski, Oscar, and Jan Kautz, “Is Accurate Occlusion of Glossy Reflections Necessary?,” *Proceedings of Symposium on Applied Perception in Graphics and Visualization 2007*, pp. 91–98, July 2007. Cited on p. 378, 430
- [696] Kraus, Martin, and Magnus Strengert, “Depth-of-Field Rendering by Pyramidal Image Processing,” *Computer Graphics Forum*, vol. 26, no. 3, pp. 645–654, 2007. Cited on p. 489
- [697] Krazit, Tom, “Intel Pledges 80 Cores in Five Years,” *CNET News.com*, September 26, 2006. <http://www.news.com/Intel-pledges-80-cores-in-five-years/2100-1006-3-6119618.html> Cited on p. 883
- [698] Krishnamurthy, V., and M. Levoy, “Fitting Smooth Surfaces to Dense Polygon Meshes,” *Computer Graphics (SIGGRAPH 96 Proceedings)*, pp. 313–324, August, 1996. Cited on p. 626
- [699] Krishnan, S., A. Pattekar, M.C. Lin, and D. Manocha, “Spherical Shell: A Higher Order Bounding Volume for Fast Proximity Queries,” *Proceedings of Third International Workshop on Algorithmic Foundations of Robotics*, pp. 122–136, 1998. Cited on p. 576, 806, 807
- [700] Krishnan, S., M. Gopi, M. Lin, D. Manocha, and A. Pattekar, “Rapid and Accurate Contact Determination between Spline Models using ShellTrees,” *Computer Graphics Forum*, vol. 17, no. 3, pp. 315–326, 1998. Cited on p. 576, 807
- [701] Krüger, Jens, and Rüdiger Westermann, “Acceleration Techniques for GPU-based Volume Rendering,” *IEEE Visualization 2003*, pp. 287–292, 2003. Cited on p. 503

- [702] Krüger, Jens, Kai Bürger, and Rüdiger Westermann, “Interactive Screen-Space Accurate Photon Tracing on GPUs,” *Eurographics Symposium on Rendering (2006)*, pp. 319–329, June 2006. Cited on p. 399
- [703] Kryachko, Yuri, “Using Vertex Texture Displacement for Realistic Water Rendering,” in Matt Pharr, ed., *GPU Gems 2*, Addison-Wesley, pp. 283–294, 2005. Cited on p. 40, 198
- [704] Kumar, Subodh, and Dinesh Manocha, “Hierarchical Visibility Culling for Spline Models,” *Graphics Interface 96*, Toronto, Canada, pp. 142–150, May 1996. Cited on p. 664
- [705] Kwoon, Hun Yen, “The Theory of Stencil Shadow Volumes,” in Engel, Wolfgang, ed., *Shader X<sup>2</sup>: Introduction & Tutorials with DirectX 9*, Wordware, pp. 197–278, 2004. Cited on p. 345
- [706] Labsik, U., and G. Greiner, “Interpolatory  $\sqrt{3}$ -Subdivision,” *Computer Graphics Forum*, vol. 19, no. 3, pp. 131–138, 2000. Cited on p. 643
- [707] Lacewell, J. Dylan, Dave Edwards, Peter Shirley, and William B. Thompson, “Stochastic Billboard Clouds for Interactive Foliage Rendering,” *journal of graphics tools*, vol. 11, no. 1, pp. 1–12, 2006. Cited on p. 462
- [708] Ladislav, Kavan, and Zara Jiri, “Fast Collision Detection for Skeletally Deformable Models,” *Computer Graphics Forum*, vol. 24, no. 3, p. 363–372, 2005. Cited on p. 822
- [709] Lacroute, Philippe, and Marc Levoy, “Fast Volume Rendering Using a Shear-Warp Factorization of the Viewing Transformation,” *Computer Graphics (SIGGRAPH 94 Proceedings)*, pp. 451–458, July 1994. Cited on p. 502
- [710] Lafortune, Eric P. F., Sing-Choong Foo, Kenneth E. Torrance, and Donald P. Greenberg, “Non-Linear Approximation of Reflectance Functions,” *Computer Graphics (SIGGRAPH 97 Proceedings)*, pp. 117–126, August 1997. Cited on p. 249, 266, 312
- [711] Ares Lagae, Ares, and Philip Dutré “An Efficient Ray-Quadrilateral Intersection Test,” *journal of graphics tools*, vol. 10, no. 4, pp. 23–32, 2005. Cited on p. 751
- [712] Laine, Samuli, Hannu Saransaari, Janne Kontkanen, Jaakko Lehtinen, Timo Aila, “Incremental Instant Radiosity for Real-Time Indirect Illumination,” *Eurographics Symposium on Rendering (2007)*, 277–286, June 2007. Cited on p. 417
- [713] Lake, Adam, Carl Marshall, Mark Harris, and Marc Blackstein, “Stylized Rendering Techniques for Scalable Real-time Animation,” *Proceedings of the First International Symposium on Non-photorealistic Animation and Rendering (NPAR)*, pp. 13–20, June 2000. Cited on p. 509, 521, 523
- [714] Lake, Adam, “Cartoon Rendering Using Texture Mapping and Programmable Vertex Shaders,” in Mark DeLoura, ed., *Game Programming Gems 2*, Charles River Media, pp. 444–451, 2001. Cited on p. 509
- [715] Lalonde, Paul, and Alain Fournier, “A Wavelet Representation of Reflectance Functions,” *IEEE Transactions on Visualization and Computer Graphics*, vol. 3, no. 4, pp. 329–336, Oct. 2003. Cited on p. 266
- [716] Lambert, J. H., *Photometria*, 1760. English translation by D. L. DiLaura, Illuminating Engineering Society of North America, 2001. Cited on p. 206
- [717] Lander, Jeff, “Skin Them Bones: Game Programming for the Web Generation,” *Game Developer*, vol. 5, no. 5, pp. 11–16, May 1998. Cited on p. 82
- [718] Lander, Jeff, “Collision Response: Bouncy, Trouncy, Fun,” *Game Developer*, vol. 6, no. 3, pp. 15–19, March 1999. Cited on p. 823

- [719] Lander, Jeff, "Physics on the Back of a Cocktail Napkin," *Game Developer*, vol. 6, no. 9, pp. 17–21, September 1999. Cited on p. 827
- [720] Lander, Jeff, "Under the Shade of the Rendering Tree," *Game Developer Magazine*, vol. 7, no. 2, pp. 17–21, Feb. 2000. Cited on p. 508, 513, 523
- [721] Lander, Jeff, "Shades of Disney: Opaquing a 3D World," *Game Developer Magazine*, vol. 7, no. 3, pp. 15–20, March 2000. Cited on p. 509
- [722] Lander, Jeff, "Return to Cartoon Central," *Game Developer Magazine*, vol. 7, no. 8, pp. 9–14, August 2000. Cited on p. 523
- [723] Lander, Jeff, "That's a Wrap: Texture Mapping Methods," *Game Developer Magazine*, vol. 7, no. 10, pp. 21–26, October 2000. Cited on p. 151, 153
- [724] Lander, Jeff, "Haunted Trees for Halloween," *Game Developer Magazine*, vol. 7, no. 11, pp. 17–21, November 2000. Cited on p. 727
- [725] Lander, Jeff, "Graphics Programming and the Tower of Babel," *Game Developer*, vol. 8, no. 3, pp. 13–16, March 2001. Cited on p. 509
- [726] Lander, Jeff, "Images from Deep in the Programmer's Cave," *Game Developer*, vol. 8, no. 5, pp. 23–28, May 2001. Cited on p. 510, 520, 526
- [727] Lander, Jeff, "The Era of Post-Photorealism," *Game Developer*, vol. 8, no. 6, pp. 18–22, June 2001. Cited on p. 523
- [728] Landis, Hayden, "Production-Ready Global Illumination," *SIGGRAPH 2002 RenderMan in Production course notes*, July 2002. Cited on p. 376, 377, 378, 426, 430
- [729] Lanza, Stefano, "Animation and Rendering of Underwater God Rays," in Engel, Wolfgang, ed., *ShaderX<sup>5</sup>*, Charles River Media, pp. 315–327, 2006. Cited on p. 395, 500
- [730] Larsen, E., S. Gottschalk, M. Lin, and D. Manocha, "Fast proximity queries with swept sphere volumes," Technical Report TR99-018, Department of Computer Science, University of North Carolina, 1999. Cited on p. 792, 807, 820
- [731] Larsson, Thomas, and Tomas Akenine-Möller, "Collision Detection for Continuously Deforming Bodies," *Eurographics 2001*, short presentation, pp. 325–333, September 2001. Cited on p. 649, 820, 821
- [732] Larsson, Thomas, and Tomas Akenine-Möller, "Efficient Collision Detection for Models Deformed by Morphing," *The Visual Comptuer*, vol. 19, no. 2–3, pp. 164–174, 2003. Cited on p. 822
- [733] Larsson, Thomas, and Tomas Akenine-Möller, "A Dynamic Bounding Volume Hierarchy for Generalized Collision Detection," *Comptuers & Graphics*, vol. 30, no. 3, pp. 451–460, 2006. Cited on p. 822
- [734] Larsson, Thomas, Tomas Akenine-Möller, and Eric Lengyel, "On Faster Sphere-Box Overlap Testing," *journal of graphics tools*, vol. 12, no. 1, pp. 3–8, 2007. Cited on p. 764
- [735] Lastra, Anselmo, "All the Triangles in the World," *Cornell Workshop on Rendering, Perception, and Measurement*, April 1999. Cited on p. 847
- [736] Lathrop, Olin, David Kirk, and Doug Voorhies, "Accurate Rendering by Subpixel Addressing," *IEEE Computer Graphics and Applications*, vol. 10, no. 5, pp. 45–53, September 1990. Cited on p. 541
- [737] Latta, Lutz, "Massively Parallel Particle Systems on the GPU," in Engel, Wolfgang, ed., *ShaderX<sup>3</sup>*, Charles River Media, pp. 119–133, 2004. Cited on p. 456

- [738] Laur, David, and Pat Hanrahan, "Hierarchical Splatting: A Progressive Refinement Algorithm for Volume Rendering," *Computer Graphics (SIGGRAPH '91 Proceedings)*, pp. 285–288, July 1991. Cited on p. 502
- [739] Lauritzen, Andrew, "Summed-Area Variance Shadow Maps," in Hubert Nguyen, ed., *GPU Gems 3*, Addison-Wesley, pp. 157–182, 2007. Cited on p. 168, 367, 369, 370
- [740] Lawrence, Jason, Aner Ben-Artzi, Christopher DeCoro, Wojciech Matusik, Hanspeter Pfister, Ravi Ramamoorthi, and Szymon Rusinkiewicz, "Inverse Shade Trees for Non-Parametric Material Representation and Editing," *ACM Transactions on Graphics*, vol. 25, no. 3, pp. 735–745, July 2006. Cited on p. 268, 270
- [741] Lawson, Terry, *Linear Algebra*, John Wiley & Sons, Inc., 1996. Cited on p. 903, 904, 911
- [742] Lax, Peter D., *Linear Algebra*, John Wiley & Sons, Inc., 1997. Cited on p. 57, 900, 903, 911
- [743] Lazarus, F., and A. Verroust, "Three-Dimensional Metamorphosis: A Survey" *The Visual Computer*, vol. 14, pp. 373–389, 1998. Cited on p. 85, 97
- [744] Lee, Aaron W. F., David Dobkin, Wim Sweldens, and Peter Schröder, "Multiresolution mesh morphing," *Computer Graphics (SIGGRAPH 1999 Proceedings)*, pp. 343–350, 1999. Cited on p. 85
- [745] Lee, Aaron, Henry Moreton, and Hugues Hoppe, "Displaced Subdivision Surfaces," *Computer Graphics (SIGGRAPH 2000 Proceedings)*, pp. 85–94, July 2000. Cited on p. 562, 626, 627, 628
- [746] Lee, Aaron, "Building Your Own Subdivision Surfaces," *Gamasutra*, September 8, 2000. Cited on p. 562
- [747] Lee, Hyunjun, Sungtae Kwon, and Seungyong Lee, "Real-time pencil rendering," *International Symposium on Non-Photorealistic Animation and Rendering (NPRA)*, 2006. Cited on p. 525, 526
- [748] Lefebvre, Sylvain, and Fabrice Neyret, "Pattern Based Procedural Textures," *ACM Symposium on Interactive 3D Graphics (I3D 2003)*, pp. 203–212, 2003. Cited on p. 156
- [749] Lefebvre, Sylvain, Samuel Hornus, and Fabrice Neyret, "Octree Textures on the GPU," in Matt Pharr, ed., *GPU Gems 2*, Addison-Wesley, pp. 595–613, 2005. Cited on p. 171
- [750] Lefebvre, Sylvain, and Hugues Hoppe, "Appearance-Space Texture Synthesis," *ACM Transactions on Graphics*, vol. 25, no. 3, pp. 541–548, July 2006. Cited on p. 180
- [751] Lefebvre, Sylvain, and Hugues Hoppe, "Perfect Spatial Hashing," *ACM Transactions on Graphics*, vol. 25, no. 3, pp. 579–588, July 2006. Cited on p. 171
- [752] Lefohn, Aaron E., Shubhabrata Sengupta, and John D. Owens, "Resolution-matched Shadow Maps," *ACM Transactions on Graphics*, vol. 20, no. 4, pp. 20:1–20:17, October 2007. Cited on p. 358
- [753] LeGrand, Scott, "Compendium of Vertex Shader Tricks," in Wolfgang Engel, ed., *ShaderX*, Wordware, pp. 228–231, May 2002. Cited on p. 456
- [754] Lehtinen, Jaakko, and Jan Kautz, "Matrix Radiance Transfer," *ACM Symposium on Interactive 3D Graphics (I3D 2003)*, pp. 59–64, 2003. Cited on p. 436
- [755] Lehtinen, Jaakko, "Theory and Algorithms for Efficient Physically-Based Illumination," Ph.D. Thesis, Helsinki University of Technology (Espoo, Finland), 2007. Cited on p. 437

- [756] Lehtinen, Jaakko, “A Framework for Precomputed and Captured Light Transport,” *ACM Transactions on Graphics*, vol. 26, no. 4, pp. 13:1–13:22, 2007. Cited on p. 437
- [757] Lensch, Hendrik P. A., Michael Goesele, Philippe Bekaert, Jan Kautz, Marcus A. Magnor, Jochen Lang, and Hans-Peter Seidel, “Interactive Rendering of Translucent Objects,” *Pacific Graphics 2002*, pp. 214–224, October 2002. Cited on p. 404, 407
- [758] Lengyel, Eric, “Tweaking a Vertex’s Projected Depth Value,” in Mark DeLoura, ed., *Game Programming Gems*, Charles River Media, pp. 361–365, 2000. Cited on p. 351, 514, 527
- [759] Lengyel, Eric, “The Mechanics of Robust Stencil Shadows,” *Gamasutra*, October 11, 2002. Cited on p. 345
- [760] Lengyel, Eric, “T-Junction Elimination and Retriangulation,” in Dante Treglia, ed., *Game Programming Gems 3*, Charles River Media, pp. 338–343, 2002. Cited on p. 541
- [761] Lengyel, Eric, *Mathematics for 3D Game Programming and Computer Graphics, Second Edition*, Charles River Media, 2003. Cited on p. 97, 186
- [762] Lengyel, Eric, “Unified Distance Formulas for Halfspace Fog,” *journal of graphics tools*, vol. 12, no. 2, pp. 23–32, 2007. Cited on p. 500
- [763] Lengyel, Jerome, “The Convergence of Graphics and Vision,” *Computer*, pp. 46–53, July 1998. Cited on p. 440, 505
- [764] Lengyel, Jerome, “Real-Time Fur,” *11th Eurographics Workshop on Rendering*, pp. 243–256, June 2000. Cited on p. 258, 504, 681
- [765] Lengyel, Jed, Emil Praun, Adam Finkelstein, and Hugues Hoppe, “Real-Time Fur over Arbitrary Surfaces,” *Proceedings 2001 Symposium on Interactive 3D Graphics*, pp. 59–62 March 2001. Cited on p. 504, 681
- [766] Levoy, Marc, and Turner Whitted, *The Use of Points as a Display Primitive*, Technical Report 85-022, Computer Science Department, University of North Carolina at Chapel Hill, January, 1985. Cited on p. 693
- [767] Levoy, Marc, and Pat Hanrahan, “Light Field Rendering,” *Computer Graphics (SIGGRAPH 96 Proceedings)*, pp. 31–42, August, 1996. Cited on p. 444
- [768] Levoy, Marc, Kari Pulli, Brian Curless, Szymon Rusinkiewicz, David Koller, Lucas Pereira, Matt Ginzton, Sean Anderson, James Davis, Jeremy Ginsberg, and Jonathan Shade, “The Digital Michelangelo Project: 3D scanning of large statues,” *Computer Graphics (SIGGRAPH 2000 Proceedings)*, pp. 131–144, July 2000. Cited on p. 694
- [769] Lewis, Robert R., “Making Shaders More Physically Plausible,” *Computer Graphics Forum*, vol. 13, no. 2, pp. 109–120, 1994. Cited on p. 252, 262
- [770] Lewis, J.P., Matt Cordiner, and Nickson Fong, “Pose Space Deformation: A Unified Approach to Shape Interpolation and Skeleton-Driven Deformation,” *Computer Graphics (SIGGRAPH 2000 Proceedings)*, pp. 165–172, July 2000. Cited on p. 81, 85, 87, 97
- [771] Li, Xin, “To Slerp, or Not to Slerp,” *Game Developer*, vol. 13, no. 7, pp. 17–23, August 2006. Cited on p. 78
- [772] Li, Xin, “iSlerp: An incremental approach of Slerp,” *journal of graphics tools*, vol. 12, no. 1, pp. 1–6, 2007. Cited on p. 78

- [773] Lin, M.C., and J. Canny, "Efficient algorithms for incremental distance computation," *IEEE Conference on Robotics and Automation*, pp. 1008–1014, 1991. Cited on p. 812, 820
- [774] Lin, M.C., *Efficient Collision Detection for Animation and Robotics*, Ph.D. Thesis, University of California, Berkeley, 1993. Cited on p. 812, 818
- [775] Lin, M.C., D. Manocha, J. Cohen, and S. Gottschalk, "Collision Detection: Algorithms and Applications," *Proceedings of Algorithms for Robotics Motion and Manipulation*, Jean-Paul Laumond and M. Overmars, eds., A.K. Peters Ltd., pp. 129–142, 1996. Cited on p. 811
- [776] Lin, M.C., and S. Gottschalk, "Collision Detection between Geometric Models: A Survey," *Proceedings of IMA Conference on Mathematics of Surfaces*, 1998. Cited on p. 827
- [777] Lin, Gang, and Thomas P.-Y. Yu, "An Improved Vertex Caching Scheme for 3D Mesh Rendering," *IEEE Trans. on Visualization and Computer Graphics*, vol. 12, no. 4, pp. 640–648, 2006. Cited on p. 557
- [778] Lindholm, Erik, Mark Kilgard, and Henry Moreton, "A User-Programmable Vertex Engine," *Computer Graphics (SIGGRAPH 2001 Proceedings)*, pp. 149–158, August 2001. Cited on p. 34
- [779] Lindstrom, P., D. Koller, W. Ribarsky, L.F. Hodges, N. Faust, and G.A. Turner, "Real-Time, Continuous Level of Detail Rendering of Height Fields," *Computer Graphics (SIGGRAPH 96 Proceedings)*, pp. 109–118, August 1996. Cited on p. 569, 639
- [780] Lindstrom, Peter, and Greg Turk, "Image-Driven Simplification," *ACM Transactions on Graphics*, vol. 19, no. 3, pp. 204–241, July 2000. Cited on p. 566
- [781] Liu, Baoquan, Li-Yi Wei, Ying-Qing Xu, "Multi-Layer Depth Peeling via Fragment Sort," Technical Report MSR-TR-2006-81, Microsoft Research Asia, 2006. Cited on p. 138
- [782] Liu, Xinguo, Peter-Pike Sloan, Heung-Yeung Shum, and John Snyder, "All-Frequency Precomputed Radiance Transfer for Glossy Objects," *Eurographics Symposium on Rendering (2004)*, pp. 337–344, June 2004. Cited on p. 436
- [783] Lloyd, D. Brandon, Jeremy Wendt, Naga K. Govindaraju, and Dinesh Manocha "CC Shadow Volumes," *Eurographics Symposium on Rendering (2004)*, pp. 197–206, June 2004. Cited on p. 348
- [784] Lloyd, Brandon, David Tuft, Sung-Eui Yoon, and Dinesh Manocha, "Warping and Partitioning for Low Error Shadow Maps," *Eurographics Symposium on Rendering (2006)*, pp. 215–226, June 2006. Cited on p. 357, 359
- [785] Lloyd, Brandon, "Logarithmic Perspective Shadow Maps," Ph.D. Thesis, Dept. of Computer Science, University of North Carolina at Chapel Hill, August 2007. Cited on p. 357, 359
- [786] Lokovic, Tom, and Eric Veach, "Deep Shadow Maps," *Computer Graphics (SIGGRAPH 2000 Proceedings)*, pp. 385–392, July 2000. Cited on p. 370
- [787] Loop, C., *Smooth Subdivision Based on Triangles*, Master's Thesis, Department of Mathematics, University of Utah, August 1987. Cited on p. 613, 614, 615, 616
- [788] Loop, Charles, and Jim Blinn, "Resolution Independent Curve Rendering using Programmable Graphics Hardware," *ACM Transactions on Graphics*, vol. 24, no. 3, pp. 1000–1009, 2005. Cited on p. 584, 585
- [789] Loop, Charles, and Jim Blinn, "Real-Time GPU Rendering Piecewise Algebraic Surfaces," *ACM Transactions on Graphics*, vol. 25, no. 3, pp. 664–670, 2006. Cited on p. 643

- [790] Loop, Charles, and Scott Schaefer, “Approximating Catmull-Clark Subdivision Surfaces with Bicubic Patches,” Microsoft Research Technical Report, MSR-TR-2007-44, 2007. Cited on p. 639, 640, 641
- [791] Loop, Charles, and Jim Blinn, “Rendering Vector Art on the GPU,” in Hubert Nguyen, ed., *GPU Gems 3*, Addison-Wesley, pp. 543–561, 2007. Cited on p. 584, 585
- [792] Lorach, Tristan, “Soft Particles,” NVIDIA White Paper, January 2007. [http://developer.download.nvidia.com/whitepapers/2007/SDK10/SoftParticles\\_hi.pdf](http://developer.download.nvidia.com/whitepapers/2007/SDK10/SoftParticles_hi.pdf) Cited on p. 453
- [793] Lorach, Tristan, “DirectX 10 Blend Shapes: Breaking the Limits,” in Hubert Nguyen, ed., *GPU Gems 3*, Addison-Wesley, pp. 53–67, 2007. Cited on p. 88
- [794] Lord, Kieren, and Ross Brown, “Using Genetic Algorithms to Optimise Triangle Strips,” *GRAPHITE 2005*, pp. 169–176, 2005. Cited on p. 554
- [795] Lorensen, William E., and Harvey E. Cline, “Marching Cubes: A High Resolution 3D Surface Construction Algorithm,” *Computer Graphics (SIGGRAPH '87 Proceedings)*, pp. 163–169, July 1987. Cited on p. 607
- [796] Losasso, F., and H. Hoppe, “Geometry Clipmaps: Terrain Rendering using Nested Regular Grids,” *ACM Transactions on Graphics*, vol. 23, no. 3, pp. 769–776, 2004. Cited on p. 573
- [797] Loviscach, Jörn, “Silhouette Geometry Shaders,” in Engel, Wolfgang, ed., *ShaderX<sup>3</sup>*, Charles River Media, pp. 49–56, 2004. Cited on p. 681
- [798] Loviscach, J., “Motion Blur for Textures by Means of Anisotropic Filtering,” *Eurographics Symposium on Rendering (2005)*, pp. 7–14, June–July 2005. Cited on p. 495
- [799] Luebke, David P., and Chris Georges, “Portals and Mirrors: Simple, Fast Evaluation of Potentially Visible Sets,” *Proceedings 1995 Symposium on Interactive 3D Graphics*, pp. 105–106, April 1995. Cited on p. 667
- [800] Luebke, David P., “A Developer’s Survey of Polygonal Simplification Algorithms,” *IEEE Computer Graphics & Applications*, vol. 21, no. 3, pp. 24–35, May/June 2001. Cited on p. 562, 573
- [801] Luebke, David, *Level of Detail for 3D Graphics*, Morgan Kaufmann, 2002. Cited on p. 562, 564, 567, 574, 683, 695
- [802] Luft, Thomas, Carsten Colditz, and Oliver Deussen, “Image Enhancement by Unsharp Masking the Depth Buffer,” *ACM Transactions on Graphics*, vol. 25, no. 3, pp. 1206–1213, July 2006. Cited on p. 385
- [803] Löfstedt, Marta, and Tomas Akenine-Möller, “An Evaluation Framework for Ray-Triangle Intersection Algorithms,” *journal of graphics tools*, vol. 10, no. 2, pp. 13–26, 2005. Cited on p. 746
- [804] Ma, Wan-Chun, Tim Hawkins, Pieter Peers, Charles-Félix Chabert, Malte Weiss, and Paul Debevec, “Rapid Acquisition of Specular and Diffuse Normal Maps from Polarized Spherical Gradient Illumination,” *Eurographics Symposium on Rendering (2007)*, pp. 183–194, June 2007. Cited on p. 404
- [805] MacDonald, J.D., and K.S. Booth, “Heuristics for Ray Tracing using Space Subdivision,” *Visual Computer*, vol. 6, no. 6, pp. 153–165, 1990. Cited on p. 736
- [806] Maciel, P., and P. Shirley, “Visual Navigation of Large Environments Using Textured Clusters,” *Proceedings 1995 Symposium on Interactive 3D Graphics*, pp. 96–102, 1995. Cited on p. 457, 561, 681, 693

- [807] Magnenat-Thalmann, Nadia, Richard Laperrière, and Daniel Thalmann, “Joint-Dependent Local Deformations for Hand Animation and Object Grasping,” *Graphics Interface '88*, pp. 26–33, June 1988. Cited on p. 81
- [808] Maillot, Patrick-Giles, “Using Quaternions for Coding 3D Transformations,” in Andrew S. Glassner, ed., *Graphics Gems*, Academic Press, pp. 498–515, 1990. Cited on p. 73
- [809] Maillot, Jérôme, and Jos Stam, “A Unified Subdivision Scheme for Polygonal Modeling,” *Computer Graphics Forum*, vol. 20, no. 3, pp. 471–479, 2001. Cited on p. 616
- [810] Maïm, Jonathan, and Daniel Thalmann, “Improved Appearance Variety for Geometry Instancing,” in Wolfgang Engel, ed., *ShaderX<sup>6</sup>*, Charles River Media, pp. 17–28, 2008. Cited on p. 711, 712
- [811] Maïm, Jonathan, Barbara Yersin, and Daniel Thalmann, “Unique Instances for Crowds,” *IEEE Computer Graphics & Applications*, to appear, vol. 9, 2008. Cited on p. 711, 712
- [812] Mallinson, Dominic, and Mark DeLoura, “CELL: A New Platform for Digital Entertainment,” *Game Developers Conference*, March 2005. <http://www.research.seca.com/research/html/CellGDC05/index.html> Cited on p. 870
- [813] Malmer, Mattias, Fredrik Malmer, Ulf Assarsson and Nicolas Holzschuch, “Fast Precomputed Ambient Occlusion for Proximity Shadows,” *journal of graphics tools*, vol. 12, no. 2, pp. 59–71, 2007. Cited on p. 427
- [814] Malzbender, Tom, Dan Gelb, and Hans Wolters, “Polynomial Texture Maps,” *Computer Graphics (SIGGRAPH 2001 Proceedings)*, pp. 519–528, August 2001. Cited on p. 436
- [815] Mammen, Abraham, “Transparency and Antialiasing Algorithms Implemented with the Virtual Pixel Maps Technique,” *IEEE Computer Graphics & Applications*, vol. 9, no. 4, pp. 43–55, July 1989. Cited on p. 126, 137
- [816] Mark, Bill, “Background and Future of Real-Time Procedural Shading,” in *Approaches for Procedural Shading on Graphics Hardware, Course 27 notes at SIGGRAPH 2000*, 2000. Cited on p. 842
- [817] Mark, William R., and Kekoa Proudfoot, “The F-Buffer: A Rasterization-Order FIFO Buffer for Multi-Pass Rendering,” *ACM SIGGRAPH/Eurographics Workshop on Graphics Hardware*, pp. 57–63, August 2001. Cited on p. 137
- [818] Mark, William R., R. Steven Glanville, Kurt Akeley, and Mark J. Kilgard, “Cg: A System for Programming Graphics Hardware in a C-like Language,” *ACM Transactions on Graphics (SIGGRAPH 2003)*, vol. 22, no. 3, pp. 896–907, 2003. Cited on p. 35
- [819] Markosian, Lee, Michael A. Kowalski, Samuel J. Trychin, Lubomir D. Bourdev, Daniel Goldstein, and John F. Hughes, “Real-Time Nonphotorealistic Rendering,” *Computer Graphics (SIGGRAPH 97 Proceedings)*, pp. 415–420, August 1997. Cited on p. 520
- [820] Markosian, Lee, Barbara J. Meier, Michael A. Kowalski, Loring S. Holden, J.D. Northrup, and John F. Hughes, “Art-based Rendering with Continuous Levels of Detail,” *Proceedings of the First International Symposium on Non-photorealistic Animation and Rendering (NPAR)*, pp. 59–66, June 2000. Cited on p. 523, 526
- [821] Marschner, Stephen R., Stephen H. Westin, Eric P.F. Lafortune, and Kenneth E. Torrance, “Image-based Bidirectional Reflectance Distribution Function Measurement,” *Applied Optics*, vol. 39, no. 16, June 2000. Cited on p. 265

- [822] Marshall, Carl S., "Cartoon Rendering: Real-time Silhouette Edge Detection and Rendering," in Mark DeLoura, ed., *Game Programming Gems 2*, Charles River Media, pp. 436–443, 2001. Cited on p. 512, 520
- [823] Martin, Tobias, and Tiow-Seng Tan, "Anti-aliasing and Continuity with Trapezoidal Shadow Maps," *Eurographics Symposium on Rendering (2004)*, pp. 153–160, June 2004. Cited on p. 356
- [824] Mason, Ashton E. W., and Edwin H. Blake, "Automatic Hierarchical Level Of Detail Optimization in Computer Animation," *Computer Graphics Forum*, vol. 16, no. 3, pp. 191–199, 1997. Cited on p. 693
- [825] Matusik, Wojciech, Hanspeter Pfister, Matt Brand, and Leonard McMillan, "A Data-Driven Reflectance Model," *ACM Transactions on Graphics (SIGGRAPH 2003)*, vol. 22, no. 3, pp. 759–769, 2003. Cited on p. 265
- [826] Maughan, Chris, "Texture Masking for Faster Lens Flare," in Mark DeLoura, ed., *Game Programming Gems 2*, Charles River Media, pp. 474–480, 2001. Cited on p. 483
- [827] Max, Nelson L., "Horizon Mapping: Shadows for Bump-Mapped Surfaces," *The Visual Computer*, vol. 4, no. 2, pp. 109–117, 1988. Cited on p. 428
- [828] Max, Nelson L., "Weights for Computing Vertex Normals from Facet Normals," *journal of graphics tools*, vol. 4, no. 2, pp. 1–6, 1999. Also collected in [71]. Cited on p. 546
- [829] "Maxima for Symbolic Computation Program," Cited on p. 792
- [830] McAllister, David K., Anselmo A. Lastra, and Wolfgang Heidrich, "Efficient Rendering of Spatial Bi-directional Reflectance Distribution Functions," *Graphics Hardware (2002)*, pp. 79–88, 2002. Cited on p. 266, 310, 312
- [831] McAllister, David, "Spatial BRDFs," in Randima Fernando, ed., *GPU Gems*, Addison-Wesley, pp. 293–306, 2004. Cited on p. 266, 310, 312
- [832] McCabe, Dan, and John Brothers, "DirectX 6 Texture Map Compression," *Game Developer*, vol. 5, no. 8, pp. 42–46, August 1998. Cited on p. 835
- [833] McClellan, Matt, and Kipp Owens, "Alternatives to Using Z-Bias to Fix Z-Fighting Issues," Intel Corporation website, 2006. <http://softwarecommunity.intel.com/articles/eng/1688.htm> Cited on p. 527
- [834] McCloud, Scott, *Understanding Comics: The Invisible Art*, Harper Perennial, 1994. Cited on p. 508, 530
- [835] McCool, Michael D., Jason Ang, and Anis Ahmad, "Homomorphic Factorization of BRDFs for High-performance Rendering," *Computer Graphics (SIGGRAPH 2001 Proceedings)*, pp. 171–178, August 2001. Cited on p. 267, 268
- [836] McCool, Michael D., Chris Wales, and Kevin Moule, "Incremental and Hierarchical Hilbert Order Edge Equation Polygon Rasterization," *Graphics Hardware*, pp. 65–72, 2001. Cited on p. 840
- [837] McCool, Michael D., Zheng Qin, and Tiberiu S. Popa, "Shader Metaprogramming," *ACM SIGGRAPH/Eurographics Workshop on Graphics Hardware*, pp. 57–68, September 2002. revised version. Cited on p. 35
- [838] McCool, Michael, and Stefanus Du Toit, *Metaprogramming GPUs with Sh*, A K Peters Ltd., 2004. Cited on p. 35
- [839] McCool, Michael D., Stefanus Du Toit, Tiberiu S. Popa, Bryan Chan, and Kevin Moule, "Shader Algebra," *ACM Transactions on Graphics (SIGGRAPH 2004)*, vol. 23, no. 3, pp. 787–795, August, 2004. Cited on p. 35

- [840] McCormack, Joel, Bob McNamara, Christopher Ganos, Larry Seiler, Norman P. Jouppi, Ken Corell, Todd Dutton, and John Zurawski, “Implementing Neon: A 256-Bit Graphics Accelerator,” *IEEE Micro*, vol. 19, no. 2, pp. 58–69, March/April 1999. Cited on p. 165
- [841] McCormack, Joel, Ronald Perry, Keith I. Farkas, and Norman P. Jouppi, “Feline: Fast Elliptical Lines for Anisotropic Texture Mapping,” *Computer Graphics (SIGGRAPH 99 Proceedings)*, pp. 243–250, August 1999. Cited on p. 170
- [842] McCormack, Joel, and Robert McNamara, “Tiled Polygon Traversal Using Half-Plane Edge Functions,” *ACM SIGGRAPH/Eurographics Workshop on Graphics Hardware*, pp. 15–22, 2000. Cited on p. 866
- [843] McGuire, Morgan, “Efficient Shadow Volume Rendering,” in Randima Fernando, ed., *GPU Gems*, Addison-Wesley, pp. 137–166, 2004. Cited on p. 345
- [844] McGuire, Morgan, and John F. Hughes, “Hardware-Determined Feature Edges,” *The 3rd International Symposium on Non-Photorealistic Animation and Rendering (NPAR 2004)*, pp. 35–47, June 2004. Cited on p. 522
- [845] McGuire, Morgan, “The SuperShader,” in Wolfgang Engel, ed., *ShaderX<sup>4</sup>*, Charles River Media, pp. 485–498, 2005. Cited on p. 50, 277
- [846] McGuire, Morgan, and Max McGuire, “Steep Parallax Mapping,” Poster at *ACM Symposium on Interactive 3D Graphics and Games (I3D 2005)*, 2005. Cited on p. 192, 193, 194, 195
- [847] McGuire, Morgan, George Stathis, Hanspeter Pfister, and Shriram Krishnamurthi, “Abstract Shade Trees,” *ACM Symposium on Interactive 3D Graphics and Games (I3D 2006)*, pp. 79–86, March 2006. Cited on p. 36, 50
- [848] McTaggart, Gary, “Half-Life 2/Valve Source Shading,” *Game Developers Conference*, March 2004. [http://www2.ati.com/developer/gdc/D3DTutorial10-Half-Life2\\_Shading.pdf](http://www2.ati.com/developer/gdc/D3DTutorial10-Half-Life2_Shading.pdf) Cited on p. 276, 325, 390, 391, 420, 421, 424, 425
- [849] McReynolds, Tom, and David Blythe, *Advanced Graphics Programming Using OpenGL*, Morgan Kaufmann, 2005. Cited on p. 124, 139, 178, 180, 199, 222, 301, 304, 339, 343, 387, 391, 446, 447, 455, 492, 502, 505, 527, 528, 530, 712, 877
- [850] McVoy, Larry, and Carl Staelin, “lmbench: Portable tools for performance analysis,” *Proceedings of the USENIX 1996 Annual Technical Conference*, San Diego, pp. 120–133, January 1996. Cited on p. 704
- [851] Meißner, Michael, Dirk Bartz, Tobias Hüttner, Gordon Müller, and Jens Einighammer, *Generation of Subdivision Hierarchies for Efficient Occlusion Culling of Large Polygonal Models*, Technical Report WSI-99-13, WSI/GRIS, University of Tbingen, 1999. Cited on p. 675
- [852] Melax, Stan, “A Simple, Fast, and Effective Polygon Reduction Algorithm,” *Game Developer*, vol. 5, no. 11, pp. 44–49, November 1998. Cited on p. 563, 568, 687
- [853] Melax, Stan, “The Shortest Arc Quaternion,” in Mark DeLoura, ed., *Game Programming Gems*, Charles River Media, pp. 214–218, 2000. Cited on p. 79
- [854] Melax, Stan, “Dynamic Plane Shifting BSP Traversal,” *Graphics Interface 2000*, Canada, pp. 213–220, May 2000. Cited on p. 797, 798, 800
- [855] Melax, Stan, “BSP Collision Detection as Used in MDK2 and NeverWinter Nights,” *Gamasutra*, March 2001. Cited on p. 797
- [856] Méndez-Feliu, Àlex, Mateu Sbert, and Jordi Catà, “Real-Time Obscurances with Color Bleeding,” *Spring Conference in Computer Graphics (SCCG2003)*, pp. 171–176, 2003. Cited on p. 379

- [857] Méndez-Feliu, Àlex, Mateu Sbert, Jordi Catà, Nicolau Sunyer, and Sergi Funyané, “Real-Time Obscurances with Color Bleeding,” in Engel, Wolfgang, ed., *ShaderX<sup>4</sup>*, Charles River Media, pp. 121–133, 2005. Cited on p. 379
- [858] Mendoza, Cesar, and Carol O’Sullivan, “Interruptible Collision Detection for Deformable Objects,” *Computer and Graphics*, vol. 30, no 2., pp. 432–438, 2006. Cited on p. 817
- [859] Mertens, Tom, Jan Kautz, Philippe Bekaert, Hans-Peter Seidel, and Frank Van Reeth, “Efficient Rendering of Local Subsurface Scattering,” *Pacific Graphics 2003*, pp. 51–58, October 2003. Cited on p. 407
- [860] Mertens, Tom, Jan Kautz, Philippe Bekaert, Hans-Peter Seidel, and Frank Van Reeth, “Interactive Rendering of Translucent Deformable Objects,” *Eurographics Symposium on Rendering (2003)*, pp. 130–140, June 2003. Cited on p. 407
- [861] Meyer, Alexandre, and Fabrice Neyret, “Interactive Volumetric Textures,” *9th Eurographics Workshop on Rendering*, pp. 157–168, July 1998. Cited on p. 464, 504
- [862] Meyer, Alexandre, Fabrice Neyret, and Pierre Poulin, “Interactive Rendering of Trees with Shading and Shadows,” *12th Eurographics Workshop on Rendering*, pp. 182–195, June 2001. Cited on p. 182, 454, 461
- [863] Miano, John, *Compressed Image File Formats: JPEG, PNG, GIF, XBM, BMP*, Addison-Wesley, 1999. Cited on p. 174
- [864] Miettinen, Ville. Personal communication, 2007. Cited on p. 651, 679, 756
- [865] Mikkelsen, Morten S., “Separating-Plane Perspective Shadow Mapping,” *journal of graphics tools*, vol. 12, no. 3, pp. 43–54, 2007. Cited on p. 356
- [866] Miller, Gene S., and C. Robert Hoffman, “Illumination and Reflection Maps: Simulated Objects in Simulated and Real Environments,” *SIGGRAPH ’84 Advanced Computer Graphics Animation course notes*, 1984. Cited on p. 301, 309, 314
- [867] Miller, Gavin, “Efficient Algorithms for Local and Global Accessibility Shading,” *Computer Graphics (SIGGRAPH 94 Proceedings)*, pp. 319–326, July 1994. Cited on p. 378
- [868] Millington, Ian, *Game Physics Engine Development*, Morgan Kaufmann, 2007. Cited on p. 827
- [869] Mirtich, Brian, and John Canny, “Impulse-Based Simulation of Rigid-Bodies,” *Proceedings 1995 Symposium on Interactive 3D Graphics*, pp. 181–188, 1995. Cited on p. 823
- [870] Mirtich, Brian, “V-Clip: fast and robust polyhedral collision detection,” *ACM Transactions on Graphics*, vol. 17, no. 3, pp. 177–208, July 1998. Cited on p. 812, 820
- [871] MIT Anisotropic BRDF Measurement Data. Cited on p. 265
- [872] Mitchell, D., and A. Netravali, “Reconstruction Filters in Computer Graphics,” *Computer Graphics (SIGGRAPH ’88 Proceedings)*, pp. 239–246, August 1988. Cited on p. 122, 133, 470
- [873] Mitchell, Jason L., “Optimizing Direct3D Applications for Hardware Acceleration,” *Gamasutra*, December 5, 1997. Cited on p. 712
- [874] Mitchell, Jason L., Michael Tatton, and Ian Bullard, “Multitexturing in DirectX 6,” *Game Developer*, vol. 5, no. 9, pp. 33–37, September 1998. Cited on p. 180
- [875] Mitchell, Jason L., “Advanced Vertex and Pixel Shader Techniques,” *European Game Developers Conference*, London, September 2001. <http://www.users.qwest.net/~jlmitchell1> Cited on p. 473

- [876] Mitchell, Jason L. “Image Processing with 1.4 Pixel Shaders in Direct3D,” in Wolfgang Engel, ed., *ShaderX*, Wordware, pp. 258–269, May 2002. Cited on p. 473, 518
- [877] Mitchell, Jason L., Marwan Y. Ansari, and Evan Hart, “Advanced Image Processing with DirectX 9 Pixel Shaders,” in Engel, Wolfgang, ed., *ShaderX<sup>2</sup>: Shader Programming Tips and Tricks with DirectX 9*, Wordware, pp. 439–468, 2004. Cited on p. 470, 471, 472
- [878] Mitchell, Jason L., “Light Shaft Rendering,” in Engel, Wolfgang, ed., *ShaderX<sup>3</sup>*, Charles River Media, pp. 573–588, 2004. Cited on p. 502, 503
- [879] Mitchell, Jason L., and Pedro V. Sander, “Applications of Explicit Early-Z Culling,” *Real-Time Shading Course*, SIGGRAPH 2004, 2004. Cited on p. 502, 857
- [880] Mitchell, Jason, “Motion Blurring Environment Maps,” in Engel, Wolfgang, ed., *ShaderX<sup>4</sup>*, Charles River Media, pp. 263–268, 2005. Cited on p. 495
- [881] Mitchell, Jason, Gary McTaggart, and Chris Green, “Shading in Valve’s Source Engine,” *SIGGRAPH 2006 Advanced Real-Time Rendering in 3D Graphics and Games course notes*, 2006. Cited on p. 294, 325, 420, 424, 425, 475, 478, 479
- [882] Mitchell, Jason L., Moby Francke, and Dhabih Eng, “Illustrative Rendering in Team Fortress 2,” *International Symposium on Non-Photorealistic Animation and Rendering, 2007*, pp. 71–76, 2007. Collected in [1251]. Cited on p. 530
- [883] Mitchell, Jason L., “Graphics Research and the Game Developer,” *I3D 2008 Game Developer RoundTable*, February 2008. Cited on p. 160
- [884] Mitchell, Kenny, “Real-Time Full Scene Anti-Aliasing for PCs and Consoles,” *Game Developers Conference*, pp. 537–543, March 2001. [http://www.gdcconf.com/archives/proceedings/2001/prog\\_papers.html](http://www.gdcconf.com/archives/proceedings/2001/prog_papers.html) Cited on p. 126, 146
- [885] Mitchell, Kenny, “Volumetric Light Scattering as a Post-Process,” in Hubert Nguyen, ed., *GPU Gems 3*, Addison-Wesley, pp. 275–285, 2007. Cited on p. 499
- [886] Mittring, Martin, “Triangle Mesh Tangent Space Calculation,” in Engel, Wolfgang, ed., *ShaderX<sup>4</sup>*, Charles River Media, pp. 77–89, 2005. Cited on p. 185, 186
- [887] Mittring, Martin, “Finding Next Gen–CryEngine 2,” *SIGGRAPH 2007 Advanced Real-Time Rendering in 3D Graphics and Games course notes*, 2007. Cited on p. 40, 50, 177, 189, 277, 282, 353, 357, 359, 361, 366, 370, 378, 382, 385, 421, 437, 453, 684, 881
- [888] Mohr, Alex, and Michael Gleicher, “Non-Invasive, Interactive, Stylized Rendering,” *Proceedings 2001 Symposium on Interactive 3D Graphics*, pp. 59–62 March 2001. Cited on p. 526
- [889] Mohr, Alex, and Michael Gleicher, “Building Efficient, Accurate Character Skins From Examples,” *ACM Transactions on Graphics (SIGGRAPH 2003)*, vol. 22, no. 3, pp. 562–568, 2003. Cited on p. 83
- [890] Möller, Tomas, and Ben Trumbore, “Fast, Minimum Storage Ray-Triangle Intersection,” *journal of graphics tools*, vol. 2, no. 1, pp. 21–28, 1997. Also collected in [71]. Cited on p. 747, 750
- [891] Möller, Tomas, “A Fast Triangle-Triangle Intersection Test,” *journal of graphics tools*, vol. 2, no. 2, pp. 25–30, 1997. Cited on p. 757

- [892] Möller, Tomas, *Real-Time Algorithms and Intersection Test Methods for Computer Graphics*, Ph.D. Thesis, Technology, Technical Report no. 341, Department of Computer Engineering, Chalmers University of Technology, October 1998. Cited on p. 387
- [893] Möller, Tomas, and John F. Hughes, "Efficiently Building a Matrix to Rotate One Vector to Another," *journal of graphics tools*, vol. 4, no. 4, pp. 1–4, 1999. Also collected in [71]. Cited on p. 80
- [894] Molnar, Steven, "Efficient Supersampling Antialiasing for High-Performance Architectures," TR91-023, Department of Computer Science, The University of North Carolina at Chapel Hill, 1991. Cited on p. 132, 441
- [895] Molnar, S., J. Eyles, and J. Poulton, "PixelFlow: High-Speed Rendering Using Image Composition," *Computer Graphics (SIGGRAPH '92 Proceedings)*, pp. 231–240, July 1992. Cited on p. 846, 875
- [896] Molnar, S., M. Cox, D. Ellsworth, and H. Fuchs, "A Sorting Classification of Parallel Rendering," *IEEE Computer Graphics and Applications*, vol. 14, no. 4, pp. 23–32, July 1994. Cited on p. 843, 844, 846
- [897] Molnar, S., "The PixelFlow Texture and Image Subsystem," in the *Proceedings of the 10th Eurographics Workshop on Graphics Hardware*, Maastricht, Netherlands, pp. 3–13, August 28–29, 1995. Cited on p. 875
- [898] Monk, Thomas, "7 Years of Graphics," Acceleration website, 2006. <http://acceleration.com/?ac.id.123.1> Cited on p. 29, 34
- [899] Montrym, J., D. Baum, D. Dignam, and C. Migdal, "InfiniteReality: A Real-Time Graphics System," *Computer Graphics (SIGGRAPH 97 Proceedings)*, pp. 293–302, August 1997. Cited on p. 117, 131, 173
- [900] Moore, R. E., *Interval Analysis*, Prentice-Hall, 1966. Cited on p. 858
- [901] Moore, Matthew, and Jane Wilhelms, "Collision Detection and Response for Computer Animation," *Computer Graphics (SIGGRAPH '88 Proceedings)*, pp. 289–298, August 1988. Cited on p. 823
- [902] Morein, Steve, "ATI Radeon HyperZ Technology," *ACM SIGGRAPH/Eurographics Workshop on Graphics Hardware*, Hot3D Proceedings, Switzerland, August 2000. Cited on p. 855, 856
- [903] Moreton, Henry P., and Carlo H. Séquin, "Functional Optimization for Fair Surface Design," *Computer Graphics (SIGGRAPH '92 Proceedings)*, pp. 167–176, July 1992. Cited on p. 616
- [904] Moreton, Henry, "Watertight Tessellation using Forward Differencing," *ACM SIGGRAPH/Eurographics Workshop on Graphics Hardware*, pp. 25–132, August 2001. Cited on p. 631, 632
- [905] Mortenson, Michael E., *Geometric Modeling*, Second Edition, John Wiley & Sons, 1997. Cited on p. 576, 643
- [906] Morton, G.M., "A Computer Oriented Geodetic Data Base and a New Technique in File Sequencing," Technical Report, IBM, Ottawa, Ontario, March 1, 1966. Cited on p. 849
- [907] Mueller, Carl, "Architectures of Image Generators for Flight Simulators," TR95-015, Department of Computer Science, The University of North Carolina at Chapel Hill, 1995. Cited on p. 135
- [908] Munkberg, Jacob, Tomas Akenine-Möller, and Jacob Ström, "High Quality Normal Map Compression," *Graphics Hardware*, pp. 95–101, 2006. Cited on p. 177

- [909] Munkberg, Jacob, Petrik Clarberg, Jon Hasselgren and Tomas Akenine-Möller, “High Dynamic Range Texture Compression for Graphics Hardware,” *ACM Transactions on Graphics*, vol. 25, no. 3, pp. 698–706, 2006. Cited on p. 178
- [910] Munkberg, Jacob, Ola Olsson, Jacob Ström, and Tomas Akenine-Möller, “Tight Frame Normal Map Compression,” *Graphics Hardware*, pp. 37–40, 2007. Cited on p. 177
- [911] Munkberg, Jacob, Petrik Clarberg, Jon Hasselgren and Tomas Akenine-Möller, “Practical HDR Texture Compression,” to appear in *Computer Graphics Forum*, 2008. Cited on p. 178
- [912] Murray, James D., and William VanRyper, *Encyclopedia of Graphics File Formats*, Second Edition, O’Reilly & Associates, 1996. Cited on p. 140, 174, 534, 573
- [913] Myer, T.H., and I.E. Sutherland, “On the Design of Display Processors,” *Communications of the ACM*, vol. 11, no. 6, pp. 410–414, June 1968. Cited on p. 883
- [914] Myers, Kevin, “Alpha-to-Coverage in Depth,” in Engel, Wolfgang, ed., *ShaderX<sup>5</sup>*, Charles River Media, pp. 69–74, 2006. Cited on p. 183
- [915] Myers, Kevin, “Variance Shadow Mapping,” NVIDIA White Paper, 2007. <http://developer.download.nvidia.com/SDK/10/direct3d/Source/VarianceShadowMapping/Doc/VarianceShadowMapping.pdf> Cited on p. 367, 370
- [916] Myers, Kevin, Randima (Randy) Fernando, and Louis Bavoil, “Integrating Realistic Soft Shadows into Your Game Engine,” NVIDIA White Paper, February 2008. <http://news.developer.nvidia.com/2008/02/integrating-re.html> Cited on p. 332, 364
- [917] Nagy, Gabor, “Real-Time Shadows on Complex Objects,” in Mark DeLoura, ed., *Game Programming Gems*, Charles River Media, pp. 567–580, 2000. Cited on p. 339
- [918] Nagy, Gabor, “Convincing-Looking Glass for Games,” in Mark DeLoura, ed., *Game Programming Gems*, Charles River Media, pp. 586–593, 2000. Cited on p. 137
- [919] Naiman, Avi C., “Jagged edges: when is filtering needed?,” *ACM Transaction on Graphics*, vol. 14, no. 4, pp. 238–258, 1998. Cited on p. 128
- [920] Narkhede, Atul, and Dinesh Manocha, “Fast Polygon Triangulation Based on Seidel’s Algorithm,” in Alan Paeth, ed., *Graphics Gems V*, Academic Press, pp. 394–397, 1995. Improved code at: Cited on p. 537
- [921] Nassau, Kurt, *The Physics and Chemistry of Color: The Fifteen Causes of Color*, second edition, John Wiley & Sons, Inc., 2001. Cited on p. 283
- [922] Nehab, Diego, and Hugues Hoppe, “Texel Programs for Random-Access Antialiased Vector Graphics,” Microsoft Research Technical Report, MSR-TR-2007-95, July 2007. Cited on p. 160
- [923] Nelson, Scott R., “Twelve characteristics of correct antialiased lines,” *journal of graphics tools*, vol. 1, no. 4, pp. 1–20, 1996. Cited on p. 125, 144
- [924] Nelson, Scott R., “High quality hardware line antialiasing,” *journal of graphics tools*, vol. 2, no. 1, pp. 29–46, 1997. Cited on p. 125
- [925] Neumann, Lázló, Attila Neumann, and Lázló Szirmay-Kalos, “Compact Metallic Reflectance Models,” *Computer Graphics Forum*, vol. 18, no. 3, pp. 161–172, 1999. Cited on p. 260, 261

- [926] Ngan, Addy, Frédéric Durand, and Wojciech Matusik, “Experimental Analysis of BRDF Models,” *Eurographics Symposium on Rendering (2005)*, 117–126, June–July 2005. Cited on p. 251, 252, 261, 264, 265, 266
- [927] Ngan, Addy, *Acquisition and Modeling of Material Appearance*, Ph.D. Thesis, Massachusetts Institute of Technology, 2006. Cited on p. 251
- [928] Nguyen, Hubert, “Fire in the ‘Vulcan’ Demo,” in Randima Fernando, ed., *GPU Gems*, Addison-Wesley, pp. 87–105, 2004. Cited on p. 139, 450, 472
- [929] Nguyen, Hubert, and William Donnelly, “Hair Animation and Rendering in the Nalu Demo,” in Matt Pharr, ed., *GPU Gems 2*, Addison-Wesley, pp. 361–380, 2005. Cited on p. 371, 577, 589
- [930] Nguyen, Tuan, “Apple Sued for Deceptive MacBook and MacBook Pro Advertising,” *DailyTech*, May 18, 2007. Cited on p. 832
- [931] Hubert Nguyen, ed., *GPU Gems 3*, Addison-Wesley, 2007. Cited on p. 885
- [932] Nicodemus, F.E., J.C. Richmond, J.J. Hsia, I.W. Ginsberg, and T. Limperis, “Geometric Considerations and Nomenclature for Reflectance,” National Bureau of Standards (US), October 1977. Cited on p. 223, 225, 226, 404
- [933] Nielsen, Kasper Høy, *Real-Time Hardware-Based Photorealistic Rendering*, Master’s Thesis, Informatics and Mathematical Modeling, The Technical University of Denmark, 2000. Cited on p. 391
- [934] Nielsen, Frank, “Interactive Image Segmentation Based on GPU Cellular Automata,” in Engel, Wolfgang, ed., *ShaderX<sup>5</sup>*, Charles River Media, pp. 543–552, 2006. Cited on p. 443
- [935] Nienhuys, Han-Wen, Jim Arvo, and Eric Haines, “Results of Sphere in Box Ratio Contest,” in Eric Haines, ed., *Ray Tracing News*, vol. 10, no. 1, January 1997. Cited on p. 735
- [936] Nishita, Tomoyuki, Thomas W. Sederberg, and Masanori Kakimoto, “Ray Tracing Trimmed Rational Surface Patches,” *Computer Graphics (SIGGRAPH ’90 Proceedings)*, pp. 337–345, August 1990. Cited on p. 751
- [937] Nishita, Tomoyuki, Takao Sirai, Katsumi Tadamura, and Eihachiro Nakamae, “Display of The Earth Taking into Account Atmospheric Scattering,” *Computer Graphics (SIGGRAPH 93 Proceedings)*, pp. 175–182, August 1993. Cited on p. 499
- [938] Nijasare, Mangesh, Sumanta N. Pattanaik, and Vineet Goel, “Real-Time Global Illumination on GPUs,” *Journal of graphics tools*, vol. 10, no. 2, pp. 55–71, 2005. Cited on p. 425
- [939] Nguyen, Hubert, “Casting Shadows on Volumes,” *Game Developer*, vol. 6, no. 3, pp. 44–53, March 1999. Cited on p. 339
- [940] Northrup, J.D., and Lee Markosian, “Artistic Silhouettes: A Hybrid Approach,” *Proceedings of the First International Symposium on Non-photorealistic Animation and Rendering (NPAR)*, pp. 31–37, June 2000. Cited on p. 522
- [941] Novosad, Justin, “Advanced High-Quality Filtering,” in Matt Pharr, ed., *GPU Gems 2*, Addison-Wesley, pp. 417–435, 2005. Cited on p. 122, 471, 473
- [942] Nuebel, Markus, “Introduction to Different Fog Effects,” in Wolfgang Engel, ed., *ShaderX<sup>2</sup>: Introductions and Tutorials with DirectX 9*, Wordware, pp. 151–179, 2003. Cited on p. 500
- [943] Nuebel, Markus, “Hardware-Accelerated Charcoal Rendering,” in Engel, Wolfgang, ed., *ShaderX<sup>3</sup>*, Charles River Media, pp. 195–204, 2004. Cited on p. 525

- [944] NVIDIA developer website. <http://developer.nvidia.com> Cited on p. 50
- [945] *NVIDIA SDK 10*. <http://developer.nvidia.com> Cited on p. 42, 173, 369, 453, 505
- [946] NVIDIA Corporation, “NVIDIA GPU Programming Guide,” NVIDIA developer website, 2005. [http://developer.nvidia.com/object/gpu\\_programming\\_guide.html](http://developer.nvidia.com/object/gpu_programming_guide.html) Cited on p. 38, 282, 699, 700, 701, 702, 712, 722
- [947] NVIDIA Corporation, “GPU Programming Exposed: The Naked Truth Behind NVIDIA’s Demos,” Exhibitor Tech Talk, SIGGRAPH 2005. [http://developer.nvidia.com/object/siggraph\\_2005\\_presentations.html](http://developer.nvidia.com/object/siggraph_2005_presentations.html) Cited on p. 317, 391, 486
- [948] NVIDIA Corporation, “GeForce 8800 GPU Architecture Overview,” *Technical brief, TB-02787-001\_v01*, 2006. Cited on p. 847, 876
- [949] NVIDIA Corporation, “Solid Wireframe,” White Paper, WP-03014-001\_v01, February 2007. <http://developer.download.nvidia.com/SDK/10/direct3d/samples.html> Cited on p. 528
- [950] Oat, Chris, “Adding Spherical Harmonic Lighting to the Sushi Engine,” *Game Developers Conference*, March 2004. <http://developer.download.nvidia.com/SDK/10/direct3d/samples.html> Cited on p. 436
- [951] Oat, Chris, “A Steerable Streak Filter,” in Engel, Wolfgang, ed., *ShaderX<sup>3</sup>*, Charles River Media, pp. 341–348, 2004. Cited on p. 472, 482, 483
- [952] Oat, Chris, “Irradiance Volumes for Games,” *Game Developers Conference*, March 2005. [http://www.ati.com/developer/gdc/GDC2005\\_PracticalPRT.pdf](http://www.ati.com/developer/gdc/GDC2005_PracticalPRT.pdf) Cited on p. 424
- [953] Oat, Chris, “Irradiance Volumes for Real-time Rendering,” in Engel, Wolfgang, ed., *ShaderX<sup>5</sup>*, Charles River Media, pp. 333–344, 2006. Cited on p. 424
- [954] Oat, Christopher, and Pedro V. Sander, “Ambient Aperture Lighting,” *SIGGRAPH 2006 Advanced Real-Time Rendering in 3D Graphics and Games course notes*, 2006. Cited on p. 429
- [955] Oat, Christopher, and Pedro V. Sander, “Ambient Aperture Lighting,” *ACM Symposium on Interactive 3D Graphics and Games (I3D 2007)*, pp. 61–64, 2007. Cited on p. 429
- [956] Oat, Christopher, and Thorsten Scheuermann, “Computing Per-Pixel Object Thickness in a Single Render Pass,” in Wolfgang Engel, ed., *ShaderX<sup>6</sup>*, Charles River Media, pp. 57–62, 2008. Cited on p. 501
- [957] Ofek, E., and A. Rappoport, “Interactive Reflections on Curved Objects,” *Computer Graphics (SIGGRAPH 98 Proceedings)*, pp. 333–342, July 1998. Cited on p. 387, 391
- [958] Olano, Marc, John Hart, Wolfgang Heidrich, and Michael McCool, *Real-Time Shading*, A K Peters Ltd., 2002. Cited on p. 283
- [959] Olano, Marc, Bob Kuehne, and Maryann Simmons, “Automatic Shader Level of Detail,” *ACM SIGGRAPH/Eurographics Workshop on Graphics Hardware*, pp. 7–14, 2003. Cited on p. 681
- [960] Olano, Marc, “Modified Noise for Evaluation on Graphics Hardware,” *ACM SIGGRAPH/Eurographics Workshop on Graphics Hardware*, pp. 105–110, July 2005. Cited on p. 178
- [961] Olick, Jon, “Segment Buffering,” in Matt Pharr, ed., *GPU Gems 2*, Addison-Wesley, pp. 69–73, 2005. Cited on p. 711
- [962] Oliveira, Gustavo, “Refractive Texture Mapping, Part Two,” *Gamasutra*, November 2000. Cited on p. 396

- [963] Oliveira, Manuel M., Gary Bishop, and David McAllister, “Relief Texture Mapping,” *Computer Graphics (SIGGRAPH 2000 Proceedings)*, pp. 359–368, July 2000. Cited on p. 194, 464
- [964] Oliveira, Manuel M., and Fabio Policarpo, “An Efficient Representation for Surface Details,” *UFRGS Technical Report RP-351*, January 26, 2005. Cited on p. 197
- [965] Oliveira, Manuel M., and Maicon Brauwers, “Real-Time Refraction Through Deformable Objects,” *ACM Symposium on Interactive 3D Graphics and Games (I3D 2007)*, pp. 89–96, 2007. Cited on p. 397
- [966] Omohundro, Stephen M., “Five Balltree Construction Algorithms,” Technical Report no. 89-063, International Computer Science Institute, 1989. Cited on p. 803, 804
- [967] O’Neil, Sean, “Accurate Atmospheric Scattering,” in Matt Pharr, ed., *GPU Gems 2*, Addison-Wesley, pp. 253–268, 2005. Cited on p. 499
- [968] *OpenEXR File Format*, Cited on p. 481
- [969] OpenGL Architecture Review Board, M. Woo, J. Neider, T. Davis, and D. Shreiner, *OpenGL Programming Guide*, Sixth Edition, Addison-Wesley, 2007. Cited on p. 27, 51, 153, 154, 155, 537, 551, 573
- [970] OpenGL Architecture Review Board, *OpenGL Reference Manual*, Fourth Edition, Addison-Wesley, 2004. Cited on p. 93
- [971] *OpenGL Volumizer Programmer’s Guide*, Silicon Graphics Inc., 1998. Cited on p. 502
- [972] *OpenSG* scene graph system. Cited on p. 552, 573
- [973] Oren, Michael, and Shree K. Nayar, “Generalization of Lambert’s Reflectance Model,” *Computer Graphics (SIGGRAPH 94 Proceedings)*, pp. 239–246, July 1994. Cited on p. 252, 262
- [974] O’Rourke, John, “Integrating Shaders into Applications,” in Randima Fernando, ed., *GPU Gems*, Addison-Wesley, pp. 601–615, 2004. Cited on p. 45, 50, 51
- [975] O’Rourke, Joseph, *Computational Geometry in C*, Second Edition, Cambridge University Press, Cambridge, 1998. Cited on p. 536, 537, 751, 910
- [976] Osman, Brian, Mike Bukowski, and Chris McEvoy, “Practical Implementation of Dual Paraboloid Shadow Maps,” *ACM SIGGRAPH Symposium on Video Games (Sandbox 2006)*, pp. 103–106, 2006. Cited on p. 361
- [977] O’Sullivan, Carol, and John Dingliana, “Real vs. Approximate Collisions: When Can We Tell the Difference?”, *Visual Proceedings (SIGGRAPH 2001)*, p. 249, August 2001. Cited on p. 816, 824
- [978] O’Sullivan, Carol, and John Dingliana, “Collisions and Perception,” *ACM Transactions on Graphics*, vol. 20, no. 3, pp. 151–168, 2001. Cited on p. 816, 824
- [979] O’Sullivan, Carol, John Dingliana, Fabio Ganovelli, and Garet Bradshaw, “T6: Collision Handling for Virtual Environments,” *Eurographics 2001 Tutorial proceedings*, 2001. Cited on p. 827
- [980] Owens, John D., William J. Dally, Ujval J. Kapasi, Scott Rixner, Peter Mattson, Ben Mowery, “Polygon Rendering on a Stream Architecture,” *ACM SIGGRAPH/Eurographics Workshop on Graphics Hardware*, pp. 23–32, June 2000. Cited on p. 875
- [981] Owens, John, “Streaming Architectures and Technology Trends,” in Matt Pharr, ed., *GPU Gems 2*, Addison-Wesley, pp. 457–470, 2005. Cited on p. 278, 847, 877

- [982] Paeth, Alan W., ed., *Graphics Gems V*, Academic Press, 1995. Cited on p. 97, 792
- [983] Pagán, Tito, “Efficient UV Mapping of Complex Models,” *Game Developer*, vol. 8, no. 8, pp. 28–34, August 2001. Cited on p. 151, 153
- [984] Pallister, Kim, and Dean Macri, “Building Scalable 3D Games for the PC,” *Gamasutra*, November 1999. Cited on p. 561
- [985] Pallister, Kim, “Generating Procedural Clouds Using 3D Hardware,” in Mark DeLoura, ed., *Game Programming Gems 2*, Charles River Media, pp. 463–473, 2001. Cited on p. 452
- [986] Pangerl, David, “ZT-Buffer Algorithm,” in Wolfgang Engel, ed., *ShaderX<sup>5</sup>*, Charles River Media, pp. 151–157, 2006. Cited on p. 138
- [987] Pangerl, David, “Quantized Ring Clipping,” in Wolfgang Engel, ed., *ShaderX<sup>6</sup>*, Charles River Media, pp. 133–140, 2008. Cited on p. 573
- [988] Paris, Sylvain, Pierre Kornprobst, Jack Tumblin, and Frédéric Durand, “A Gentle Introduction to Bilateral Filtering and Its Applications,” *Course 13 notes at SIGGRAPH 2007*, 2007. Cited on p. 472
- [989] Parker, Steven, William Martin, Peter-Pike J. Sloan, Peter Shirley, Brian Smits, Charles Hansen, “Interactive Ray Tracing,” *Proceedings 1999 Symposium on Interactive 3D Graphics*, pp. 119–134, April 1999. Cited on p. 324
- [990] Pattanaik, S., J. Tumblin, H. Yee, and D. Greenberg, “Time-Dependent Visual Adaptation for Fast, Realistic Image Display,” *Computer Graphics (SIGGRAPH 2000 Proceedings)*, pp. 47–54, July 2000. Cited on p. 475
- [991] Patterson, J.W., S.G. Hoggar, and J.R. Logie, “Inverse Displacement Mapping,” *Computer Graphics Forum*, vol. 10 no. 2, pp. 129–139, March 1991. Cited on p. 193
- [992] Paul, Richard P.C., *Robot Manipulators: Mathematics, Programming, and Control*, MIT Press, Cambridge, Mass., 1981. Cited on p. 69
- [993] Peercy, Mark S., Marc Olano, John Airey, and P. Jeffrey Ungar, “Interactive Multi-Pass Programmable Shading,” *Computer Graphics (SIGGRAPH 2000 Proceedings)*, pp. 425–432, July 2000. Cited on p. 33, 35
- [994] Peercy, Mark S., Mark Segal, and Derek Gerstmann, “A Performance-Oriented Data Parallel Virtual Machine for GPUs,” *SIGGRAPH 2006 Technical Sketch*, 2006. Cited on p. 36, 841, 883
- [995] Pellacini, Fabio, and Kiril Vidimče, “Cinematic Lighting,” in Randima Fernando, ed., *GPU Gems*, Addison-Wesley, pp. 167–183, 2004. Cited on p. 223
- [996] Pellacini, Fabio, “User-Configurable Automatic Shader Simplification,” *ACM Transactions on Graphics (SIGGRAPH 2005)*, vol. 24, no. 3, pp. 445–452, August, 2005. Cited on p. 681
- [997] Pellacini, Fabio, Kiril Vidimče, Aaron Lefohn, Alex Mohr, Mark Leone, and John Warren, “Lpics: a Hybrid Hardware-Accelerated Relighting Engine for Computer Cinematography,” *ACM Transactions on Graphics (SIGGRAPH 2005)*, vol. 24, no. 3, pp. 464–470, August, 2005. Cited on p. 442
- [998] Pellacini, Fabio, Miloš Hašan, and Kavita Bala, “Interactive Cinematic Relighting with Global Illumination,” in Hubert Nguyen, ed., *GPU Gems 3*, Addison-Wesley, pp. 183–202, 2007. Cited on p. 442
- [999] Pelzer, Kurt, “Combined Depth and ID-Based Shadow Buffers,” in Kirmse, Andrew, ed., *Game Programming Gems 4*, Charles River Media, pp. 411–425, 2004. Cited on p. 351

- [1000] Pelzer, Kurt, “Rendering Countless Blades of Waving Grass,” in Randima Fernando, ed., *GPU Gems*, Addison-Wesley, pp. 107–121, 2004. Cited on p. 182
- [1001] Pelzer, Kurt, “Indicator Materials,” in Engel, Wolfgang, ed., *ShaderX<sup>4</sup>*, Charles River Media, pp. 513–521, 2005. Cited on p. 698
- [1002] Perthuis, Cedric, “Introduction to the graphics pipeline of the PS3,” *Eurographics 2006*, Graphics Meets Games Talks, 2006. Cited on p. 864, 868
- [1003] Perlin, Ken, “An Image Synthesizer,” *Computer Graphics (SIGGRAPH '85 Proceedings)*, pp. 287–296, July 1985. Cited on p. 178
- [1004] Perlin, Ken, and Eric M. Hoffert, “Hypertexture,” *Computer Graphics (SIGGRAPH '89 Proceedings)*, pp. 253–262, July 1989. Cited on p. 178
- [1005] Perlin, Ken, “Improving Noise,” *ACM Transactions on Graphics (SIGGRAPH 2002)*, vol. 21, no. 3, pp. 681–682, 2002. Cited on p. 178
- [1006] Perlin, Ken, “Implementing Improved Perlin Noise,” in Randima Fernando, ed., *GPU Gems*, Addison-Wesley, pp. 73–85, 2004. Cited on p. 178
- [1007] Persson, Emil, “Selective Supersampling,” in Engel, Wolfgang, ed., *ShaderX<sup>5</sup>*, Charles River Media, pp. 177–183, 2006. Cited on p. 133
- [1008] Persson, Emil, “Post-Tonemapping Resolve for High-Quality HDR Anti-aliasing in D3D10,” in Wolfgang Engel, ed., *ShaderX<sup>6</sup>*, Charles River Media, pp. 161–164, 2008. Cited on p. 480
- [1009] Pfister, Hans-Peter, Matthias Zwicker, Jeroen van Barr, and Markus Gross, “Surfels: Surface Elements as Rendering Primitives,” *Computer Graphics (SIGGRAPH 2000 Proceedings)*, pp. 335–342, July 2000. Cited on p. 694
- [1010] Pharr, Matt, and Greg Humphreys, *Physically Based Rendering: From Theory to Implementation*, Morgan Kaufmann, 2004. Cited on p. 210, 437, 476, 480
- [1011] Pharr, Matt, “Fast Filter Width Estimates with Texture Maps,” in Randima Fernando, ed., *GPU Gems*, Addison-Wesley, pp. 417–424, 2004. Cited on p. 165
- [1012] Pharr, Matt, and Simon Green, “Ambient Occlusion,” in Randima Fernando, ed., *GPU Gems*, Addison-Wesley, pp. 279–292, 2004. Cited on p. 377, 426
- [1013] Pharr, Matt, ed., *GPU Gems 2*, Addison-Wesley, 2005. Cited on p. 885
- [1014] Phong, Bui Tuong, “Illumination for Computer Generated Pictures,” *Communications of the ACM*, vol. 18, no. 6, pp. 311–317, June 1975. Cited on p. 112, 115, 201, 249, 252, 266
- [1015] Piegl, L., and W. Tiller, *The NURBS Book*, Springer-Verlag, Berlin/Heidelberg, Second Edition, 1997. Cited on p. 643
- [1016] Pineda, Juan, “A Parallel Algorithm for Polygon Rasterization,” *Computer Graphics (SIGGRAPH '88 Proceedings)*, pp. 17–20, August 1988. Cited on p. 840
- [1017] Piponi, Dan, and George Borshukov, “Seamless Texture Mapping of Subdivision Surfaces by Model Peeling and Texture Blending,” *Computer Graphics (SIGGRAPH 2000 Proceedings)*, pp. 471–478, July 2000. Cited on p. 629
- [1018] Placeres, Frank Puig, “Overcoming Deferred Shading Drawbacks,” in Wolfgang Engel, ed., *ShaderX<sup>5</sup>*, Charles River Media, pp. 115–130, 2006. Cited on p. 281, 283
- [1019] Pletinckx, Daniel, “Quaternion calculus as a basic tools in computer graphics,” *The Visual Computer*, vol. 5, pp. 2–13, 1989. Cited on p. 97
- [1020] Policarpo, Fabio, “Relief Mapping in a Pixel Shader using Binary Search,” Technical report, September 2004. Cited on p. 193

- [1021] Policarpo, Fabio, Manuel M. Oliveira, and João L.D. Comba, “Real-Time Relief Mapping on Arbitrary Polygonal Surfaces,” *ACM Symposium on Interactive 3D Graphics and Games (I3D 2005)*, pp. 155–162, April 2005. Cited on p. 193, 194, 195
- [1022] Policarpo, Fabio, and Manuel M. Oliveira, “Relief Mapping of Non-Height-Field Surface Details,” *ACM Symposium on Interactive 3D Graphics and Games (I3D 2006)*, pp. 55–62, March 2006. Cited on p. 464, 465
- [1023] Policarpo, Fabio, and Manuel M. Oliveira, “Relaxed Cone Stepping for Relief Mapping,” in Hubert Nguyen, ed., *GPU Gems 3*, Addison-Wesley, pp. 409–428, 2007. Cited on p. 196
- [1024] Popescu, Voicu, John Eyles, Anselmo Lastra, Joshua Steinhurst, Nick England, and Lars Nyland, “The WarpEngine: An Architecture for the Post-Polygonal Age,” *Computer Graphics (SIGGRAPH 2000 Proceedings)*, pp. 433–442, July 2000. Cited on p. 875
- [1025] Porcino, Nick, “Lost Planet Parallel Rendering,” *Meshula.net* website, October 2007. <http://meshula.net/wordpress/?p=124> Cited on p. 488, 495, 496, 504
- [1026] Porter, Thomas, and Tom Duff, “Compositing digital images,” *Computer Graphics (SIGGRAPH '84 Proceedings)*, pp. 253–259, July 1984. Cited on p. 135, 139
- [1027] Poulin, P., and A. Fournier, “A Model for Anisotropic Reflection,” *Computer Graphics (SIGGRAPH '90 Proceedings)*, pp. 273–282, August 1990. Cited on p. 252, 266, 268
- [1028] Poynton, Charles, *Digital Video and HDTV: Algorithms and Interfaces*, Morgan Kaufmann, 2003. Related resource: *Gamma FAQ*. Cited on p. 141, 143, 146, 216
- [1029] Pranckevičius, Aras, “Soft Projected Shadows,” in Wolfgang Engel, ed., *Shader X<sup>4</sup>*, Charles River Media, pp. 279–288, 2005. Cited on p. 338
- [1030] Praun, Emil, Adam Finkelstein, and Hugues Hoppe, “Lapped Textures,” *Computer Graphics (SIGGRAPH 2000 Proceedings)*, pp. 465–470, July 2000. Cited on p. 524
- [1031] Praun, Emil, Hugues Hoppe, Matthew Webb, and Adam Finkelstein, “Real-time Hatching,” *Computer Graphics (SIGGRAPH 2001 Proceedings)*, pp. 581–586, August 2001. Cited on p. 524
- [1032] Preetham, Arcot J., Peter Shirley, and Brian Smitsc, “A Practical Analytic Model for Daylight,” *Computer Graphics (SIGGRAPH 99 Proceedings)*, pp. 91–100, August 1999. Cited on p. 499
- [1033] Preparata, F.P., and M.I. Shamos, *Computational Geometry: An Introduction*, Springer-Verlag, 1985. Cited on p. 537, 751
- [1034] Press, William H., Saul A. Teukolsky, William T. Vetterling, and Brian P. Flannery, “Numerical Recipes in C,” Cambridge University Press, Cambridge, 1992. Cited on p. 731, 734, 786, 903
- [1035] Proakis, John G., and Dimitris G. Manolakis, *Digital Signal Processing: Principles, Algorithms, and Applications*, Third Edition, Macmillan Publishing Co., 1995. Cited on p. 117, 119, 122, 124
- [1036] Pulli, Kari, and Mark Segal, “Fast Rendering of Subdivision Surfaces,” *7th Eurographics Workshop on Rendering*, pp. 61–70, June 1996. Cited on p. 643
- [1037] Pulli, Kari, Tomi Aarnio, Ville Miettinen, Kimmo Roimela, Jani Vaarala, *Mobile 3D Graphics: with OpenGL ES and M3G*, Morgan Kaufmann, 2007. Cited on p. 877

- [1038] Purcell, Timothy J., Ian Buck, William R. Mark, and Pat Hanrahan, “Ray Tracing on Programmable Graphics Hardware,” *ACM Transactions on Graphics (SIGGRAPH 2002)*, vol. 21, no. 3, pp. 703–712, July 2002. Cited on p. 416
- [1039] Purcell, Timothy J., Craig Donner, Mike Cammarano, Henrik Wann Jensen, and Pat Hanrahan, “Photon Mapping on Programmable Graphics Hardware,” *SIGGRAPH/Eurographics Workshop on Graphics Hardware*, pp. 41–50, 2003. Cited on p. 417
- [1040] Purnomo, Budirijanto, Jonathan Bilodeau, Jonathan D. Cohen, and Subodh Kumar, “Hardware-Compatible Vertex Compression Using Quantization and Simplification,” *Graphics Hardware*, pp. 53–61, 2005. Cited on p. 713
- [1041] Qin, Zheng, Michael D. McCool, and Craig S. Kaplan, “Real-Time Texture-Mapped Vector Glyphs,” *ACM Symposium on Interactive 3D Graphics and Games (I3D 2006)*, pp. 63–69, 2006. Cited on p. 159
- [1042] Quinlan, S., “Efficient distance computation between non-convex objects,” *IEEE Conference on Robotics and Automation*, pp. 3324–3329, 1994. Cited on p. 826
- [1043] Rafferty, Matthew, Daniel Aliaga, Voicu Popescu, and Anselmo Lastra, “Images for Accelerating Architectural Walkthroughs,” *IEEE Computer Graphics and Applications*, vol. 18, no. 6, pp. 38–45, Nov./Dec. 1998. Cited on p. 461
- [1044] Ragan-Kelley, Jonathan, Charlie Kilpatrick, Brian W. Smith, Doug Epps, “The Lightspeed Automatic Interactive Lighting Preview System,” *ACM Transactions on Graphics (SIGGRAPH 2007)*, vol. 26, no. 3, 25:1–25:11, July, 2007. Cited on p. 441, 442
- [1045] Ramamoorthi, Ravi, and Pat Hanrahan, “An Efficient Representation for Irradiance Environment Maps,” *Computer Graphics (SIGGRAPH 2001 Proceedings)*, pp. 497–500, August 2001. Cited on p. 314, 320, 321, 322, 323, 424
- [1046] Raskar, Ramesh, and Michael Cohen, “Image Precision Silhouette Edges,” *Proceedings 1999 Symposium on Interactive 3D Graphics*, pp. 135–140, April 1999. Cited on p. 513, 514, 515
- [1047] Raskar, Ramesh, “Hardware Support for Non-photorealistic Rendering,” *ACM SIGGRAPH/Eurographics Workshop on Graphics Hardware*, pp. 41–46, 2001. Cited on p. 515, 517
- [1048] Raskar, Ramesh, and Jack Tumblin, *Computational Photography: Mastering New Techniques for Lenses, Lighting, and Sensors*, A K Peters Ltd., 2007. Cited on p. 444, 533
- [1049] Rasmusson, J., J. Hasselgren, and T. Akenine-Möller, “Exact and Error-Bounded Approximate Color Buffer Compression and Decompression,” *Graphics Hardware*, pp. 41–48, 2007. Cited on p. 856
- [1050] Ratcliff, John W., “Sphere Trees for Fast Visibility Culling, Ray Tracing, and Range Searching,” in Mark DeLoura, ed., *Game Programming Gems 2*, Charles River Media, pp. 384–387, 2001. Cited on p. 650
- [1051] Reddy, Martin, *Perceptually Modulated Level of Detail for Virtual Environments*, Ph.D. Thesis, University of Edinburgh, 1997. Cited on p. 691
- [1052] Reeves, William T., “Particle Systems—A Technique for Modeling a Class of Fuzzy Objects,” *ACM Transactions on Graphics*, vol. 2, no. 2, pp. 91–108, April 1983. Cited on p. 455
- [1053] Reeves, William T., David H. Salesin, and Robert L. Cook, “Rendering Antialiased Shadows with Depth Maps,” *Computer Graphics (SIGGRAPH '87 Proceedings)*, pp. 283–291, July 1987. Cited on p. 362

- [1054] Rege, Ashu, "Optimization for DirectX 9 Graphics," *Game Developers Conference*, March 2004. [http://developer.nvidia.com/object/optimizations\\_for\\_dx9.html](http://developer.nvidia.com/object/optimizations_for_dx9.html) Cited on p. 551
- [1055] Rege, Ashu, "Shader Model 3.0," NVIDIA Developer Technology Group, 2004. [ftp://download.nvidia.com/developer/presentations/2004/GPU\\_Jackpot/Shader\\_Model\\_3.pdf](ftp://download.nvidia.com/developer/presentations/2004/GPU_Jackpot/Shader_Model_3.pdf) Cited on p. 38
- [1056] Reif, Ulrich, "A Unified Approach to Subdivision Algorithms Near Extraordinary Vertices," *Computer Aided Geometric Design*, vol. 12, no. 2, pp. 153–174, 1995. Cited on p. 643
- [1057] Reimer, Jeremy, "Valve goes multicore," *ars technica* website, Nov. 5, 2006. <http://arstechnica.com/articles/paedia/cpu/valve-multicore.ars> Cited on p. 722
- [1058] Reinhard, Erik, Mike Stark, Peter Shirley, and James Ferwerda, "Photographic Tone Reproduction for Digital Images," *ACM Transactions on Graphics (SIGGRAPH 2002)*, vol. 21, no. 3, pp. 267–276, July 2002. Cited on p. 478
- [1059] Reinhard, Erik, Greg Ward, Sumanta Pattanaik, and Paul Debevec, *High Dynamic Range Imaging: Acquisition, Display, and Image-Based Lighting*, Morgan Kaufmann, 2006. Cited on p. 325, 480, 481
- [1060] Reinhard, Erik, Erum Arif Khan, Ahmet Oguz Akyüz, and Garrett Johnson, *Color Imaging: Fundamentals and Applications*, A K Peters Ltd., 2008. Cited on p. 217, 283
- [1061] Reis, Aurelio, "Per-Pixel Lit, Light Scattering Smoke," in Engel, Wolfgang, ed., *Shader X<sup>5</sup>*, Charles River Media, pp. 287–294, 2006. Cited on p. 450
- [1062] Ren, Zhong Ren, Rui Wang, John Snyder, Kun Zhou, Xinguo Liu, Bo Sun, Peter-Pike Sloan, Hujun Bao, Qunsheng Peng, and Baining Guo, "Real-Time Soft Shadows in Dynamic Scenes using Spherical Harmonic Exponentiation," *ACM Transactions on Graphics*, vol. 25, no. 3, pp. 977–986, July 2006. Cited on p. 381, 385
- [1063] Reuter, Patrick, Johannes Behr, and Marc Alexa, "An Improved Adjacency Data Structure for Fast Triangle Stripping," *journal of graphics tools*, vol. 10, no. 2, pp. 41–50, 2005. Cited on p. 543, 553, 554, 573
- [1064] Rhodes, Graham, "Fast, Robust Intersection of 3D Line Segments," in Mark DeLoura, ed., *Game Programming Gems 2*, Charles River Media, pp. 191–204, 2001. Cited on p. 782
- [1065] Riguer, Guennadi, "Performance Optimization Techniques for ATI Graphics Hardware with DirectX 9.0," ATI whitepaper, 2002. [http://ati.amd.com/developer/dx9/ATI-DX9\\_Optimization.pdf](http://ati.amd.com/developer/dx9/ATI-DX9_Optimization.pdf) Cited on p. 282, 558, 699, 856, 857
- [1066] Riguer, Guennadi, "DirectX 10: porting, performance, and "gotchas"," *Game Developers Conference*, March 2007. [http://developer.amd.com/assets/Riguer-DX10\\_tips\\_and\\_tricks\\_for\\_print.pdf](http://developer.amd.com/assets/Riguer-DX10_tips_and_tricks_for_print.pdf) Cited on p. 708
- [1067] Risser, Eric, "True Impostors," in Hubert Nguyen, ed., *GPU Gems 3*, Addison-Wesley, pp. 481–490, 2007. Cited on p. 465
- [1068] Risser, Eric, Musawir Shah, and Sumanta Pattanaik, "Faster Relief Mapping Using the Secant Method," *journal of graphics tools*, vol. 12, no. 3, pp. 17–24, 2007. Cited on p. 195
- [1069] Risser, Eric, "Truer Impostors," *Game Developers Conference*, February 2008. <http://www.ericroisser.com/> Cited on p. 466
- [1070] Ritter, Jack, "An Efficient Bounding Sphere," in Andrew S. Glassner, ed., *Graphics Gems*, Academic Press, pp. 301–303, 1990. <http://www.graphicsgems.org> Cited on p. 732

- [1071] Robertson, Barbara, "Shades of Davy Jones," CGSociety Technology Focus, 22 December 2006. Cited on p. 381
- [1072] Rockwood, Alyn, and Peter Chambers, "Interactive Curves and Surfaces: A Multimedia Tutorial on CAGD," Morgan Kaufmann, 1996. Cited on p. 576
- [1073] Rohleder, Paweł, and Maciej Jamrozik, "Sunlight with Volumetric Light Rays," *ShaderX<sup>6</sup>*, Charles River Media, pp. 325–330, 2008. Cited on p. 499
- [1074] Röttger, Stefan, Wolfgang Heidrich, Philipp Slusallek, Hans-Peter Seidel, "Real-Time Generation of Continuous Levels of Detail for Height Fields," *Proc. 6th Int. Conf. in Central Europe on Computer Graphics and Visualization*, pp. 315–322, 1998. Cited on p. 549, 573
- [1075] Röttger, Stefan, Alexander Irion, and Thomas Ertl, "Shadow Volumes Revisited," *10th International Conference in Central Europe on Computer Graphics, Visualization and Computer Vision 2002 (WSCG)*, pp. 373–379. Cited on p. 342
- [1076] Rogers, David F., *Mathematical Elements for Computer Graphics*, Second Edition, McGraw-Hill, 1989. Cited on p. 643
- [1077] Rogers, David F., *Procedural Elements for Computer Graphics*, Second Edition, McGraw-Hill, 1998. Cited on p. 11, 22, 535
- [1078] Rogers, David F., *An Introduction to NURBS: With Historical Perspective*, Morgan Kaufmann, 2000. Cited on p. 643
- [1079] Rohlf, J., and J. Helman, "IRIS Performer: A High Performance Multiprocessing Toolkit for Real-Time 3D Graphics," *Computer Graphics (SIGGRAPH 94 Proceedings)*, pp. 381–394, July 1994. Cited on p. 691, 718, 720
- [1080] Roimela, Kimmo, Tomi Aarnio ,and Joonas Itäranta, "High Dynamic Range Texture Compression," *ACM Transactions on Graphics*, vol. 25, no. 3, pp. 707–712, 2006. Cited on p. 178
- [1081] Rokne, Jon, "The Area of a Simple Polygon," in James Arvo, ed., *Graphics Gems II*, Academic Press, pp. 5–6, 1991. Cited on p. 910
- [1082] Rosado, Gilberto, "Motion Blur as a Post-Processing Effect," in Hubert Nguyen, ed., *GPU Gems 3*, Addison-Wesley, pp. 575–581, 2007. Cited on p. 495
- [1083] Rossignac, J., and M. van Emmerik, M., "Hidden contours on a frame-buffer," *7th Eurographics Workshop on Computer Graphics Hardware*, pp. 188–204, 1992. Cited on p. 513
- [1084] Rost, Randi J., *OpenGL Shading Language (2nd Edition)*, Addison-Wesley, 2006. Cited on p. 31, 35, 50, 470
- [1085] Rost, Randi J., "Antialiasing Procedural Shaders," in *OpenGL Shading Language (2nd Edition)*, Addison-Wesley, 2006. Cited on p. 180
- [1086] Roth, Marcus, and Dirk Reiners, "Sorted Pipeline Image Composition," *Eurographics Symposium on Parallel Graphics and Visualization (EGPGV 2006)*, pp. 119–126, 2006. Cited on p. 844, 846
- [1087] Rule, Keith, *3D Graphics File Formats: A Programmer's Reference*, Addison-Wesley, 1996. Cited on p. 534, 573
- [1088] Rundberg, Peter, *An Optimized Collision Detection Algorithm*, M.S. Thesis, Department of Computer Engineering, Chalmers University of Technology, Gothenburg, 1999. Cited on p. 770
- [1089] Rusinkiewicz, Szymon, "A Survey of BRDF Representation for Computer Graphics," written for CS348C, Stanford University, 1997. Cited on p. 202, 226, 265

- [1090] Rusinkiewicz, Szymon, "A New Change of Variables for Efficient BRDF Representation," *9th Eurographics Workshop on Rendering*, pp. 11–22, June–July 1998. Cited on p. 267, 268
- [1091] Rusinkiewicz, Szymon, and Marc Levoy, "QSplat: A Multiresolution Point Rendering System for Large Meshes," *Computer Graphics (SIGGRAPH 2000 Proceedings)*, pp. 343–352, July 2000. Cited on p. 694
- [1092] Rusinkiewicz, Szymon, Michael Burns, and Doug DeCarlo, "Exaggerated Shading for Depicting Shape and Detail," *ACM Transactions on Graphics*, vol. 25, no. 3, July 2006. Cited on p. 509
- [1093] Ryu, David, "500 Million and Counting: Hair Rendering on Ratatouille," Pixar Technical Memo 07-09, May 2007. Cited on p. 879
- [1094] "S3TC DirectX 6.0 Standard Texture Compression," S3 Inc., 1998. Cited on p. 174
- [1095] Sagan, Hans, *Space-Filling Curves*, Springer-Verlag, 1994. Cited on p. 556
- [1096] Sagar, Mark, John Monos, John Schmidt, Dan Ziegler, Sing-choong Foo, Remington Scott, Jeff Stern, Chris Waegner, Peter Nofz, Tim Hawkins, and Paul Debevec, "Reflectance Field Rendering of Human Faces in *Spider-Man 2*," *SIGGRAPH 2004 Technical Sketch*, 2004. Cited on p. 265
- [1097] Saito, Takafumi, and Tokiichiro Takahashi, "Comprehensible Rendering of 3-D Shapes," *Computer Graphics (SIGGRAPH '90 Proceedings)*, pp. 197–206, August 1990. Cited on p. 279, 518
- [1098] Samet, Hanan, *Applications of Spatial Data Structures: Computer Graphics, Image Processing and GIS*, Addison-Wesley, 1989. Cited on p. 654, 827
- [1099] Samet, Hanan, *The Design and Analysis of Spatial Data Structures*, Addison-Wesley, 1989. Cited on p. 651, 654, 666, 827
- [1100] Samet, Hanan, *Foundations of Multidimensional and Metric Data Structures*, Morgan Kaufmann, 2006. Cited on p. 827
- [1101] Samosky, Joseph, *SectionView: A system for interactively specifying and visualizing sections through three-dimensional medical image data*, M.S. Thesis, Department of Electrical Engineering and Computer Science, Massachusetts Institute of Technology, 1993. Cited on p. 754
- [1102] Sancer, M. I., "Shadow Corrected Electromagnetic Scattering from Randomly Rough Surfaces," *IEEE Transactions on Antennas and Propagation*, vol. 17, no. 5, pp. 577–585, September 1969. Cited on p. 262
- [1103] Sander, Pedro V., Xianfeng Gu, Steven J. Gortler, Hugues Hoppe, and John Snyder, "Silhouette Clipping," *Computer Graphics (SIGGRAPH 2000 Proceedings)*, pp. 327–334, July 2000. Cited on p. 561, 664
- [1104] Sander, Pedro V., John Snyder, Steven J. Gortler, and Hugues Hoppe, "Texture Mapping Progressive Meshes," *Computer Graphics (SIGGRAPH 2001 Proceedings)*, pp. 409–416, August 2001. Cited on p. 561, 567
- [1105] Sander, Pedro V., "A Fixed Function Shader in HLSL," ATI Research, October 2003. <http://www2.ati.com/misc/samples/dx9/FixedFuncShader.pdf> Cited on p. 50
- [1106] Sander, Pedro V., David Gosselin, and Jason L. Mitchell, "Real-Time Skin Rendering on Graphics Hardware," *SIGGRAPH 2004 Technical Sketch*, 2004. Cited on p. 405

- [1107] Sander, Pedro V., and Jason L. Mitchell, “Progressive Buffers: View-dependent Geometry and Texture LOD Rendering,” *SIGGRAPH 2006 Advanced Real-Time Rendering in 3D Graphics and Games* course notes, 2006. Cited on p. 687
- [1108] Sander, Pedro V., Natalya Tatarchuk, and Jason L. Mitchell, “Explicit Early-Z Culling for Efficient Fluid Flow Simulation,” in Engel, Wolfgang, ed., *ShaderX<sup>5</sup>*, Charles River Media, pp. 553–564, 2006. Cited on p. 472, 857
- [1109] Sander, Pedro V., Diego Nehab, and Joshua Barczak, “Fast Triangle Reordering for Vertex Locality and Reduced Overdraw,” *ACM Transactions on Graphics*, vol. 26, no. 3, article 89, 2007. Cited on p. 555
- [1110] Salvi, Marco, “Rendering Filtered Shadows with Exponential Shadow Maps,” in Engel, Wolfgang, ed., *ShaderX<sup>6</sup>*, Charles River Media, pp. 257–274, 2008. Cited on p. 370
- [1111] Saransaari, Hannu, “Incremental Instant Radiosity,” in Wolfgang Engel, ed., *ShaderX<sup>6</sup>*, Charles River Media, pp. 381–392, 2008. Cited on p. 417
- [1112] Schaufler, Gernot, “Dynamically Generated Impostors,” *GI Workshop on Modeling—Virtual Worlds—Distributed Graphics*, D.W. Fellner, ed., Infix Verlag, pp. 129–135, November 1995. Cited on p. 458, 459, 460
- [1113] Schaufler, G., and W. Stürzlinger, “A Three Dimensional Image Cache for Virtual Reality,” *Computer Graphics Forum*, vol. 15, no. 3, pp. 227–236, 1996. Cited on p. 459, 461
- [1114] Schaufler, Gernot, “Exploiting Frame to Frame Coherence in a Virtual Reality System,” *VRAIS ’96*, Santa Clara, California, pp. 95–102, April 1996. Cited on p. 461
- [1115] Schaufler, Gernot, “Nailboards: A Rendering Primitive for Image Caching in Dynamic Scenes,” *Eurographics Rendering Workshop 1997*, pp. 151–162, 1997. Cited on p. 463, 464
- [1116] Schaufler, Gernot, “Per-Object Image Warping with Layered Impostors,” *9th Eurographics Workshop on Rendering*, pp. 145–156, June–July 1998. Cited on p. 461, 464
- [1117] Schaufler, Gernot, Julie Dorsey, Xavier Decoret, and François Sillion, “Conservative Volumetric Visibility with Occluder Fusion,” *Computer Graphics (SIGGRAPH 2000 Proceedings)*, pp. 229–238, July 2000. Cited on p. 680
- [1118] Scheib, Vincent, “Introduction to Demos & The Demo Scene,” *Gamasutra*, February 2001. Cited on p. 415
- [1119] Scherzer, Daniel, “Robust Shadow Maps for Large Environments.” *Central European Seminar on Computer Graphics 2005*, pp. 15–22, 2005. Cited on p. 353, 357
- [1120] Scherzer, Daniel, Stefan Jeschke, and Michael Wimmer, “Pixel-Correct Shadow Maps with Temporal Reprojection and Shadow Test Confidence,” *Eurographics Symposium on Rendering (2007)*, 45–50, June 2007. Cited on p. 358
- [1121] Scheuermann, Thorsten, and Natalya Tatarchuk, “Improved Depth-of-Field Rendering,” in Engel, Wolfgang, ed., *ShaderX<sup>3</sup>*, Charles River Media, pp. 363–377, 2004. Related article on website. <http://www.ati.com/developer/techpapers.html> Cited on p. 488, 489
- [1122] Scheuermann, T., and J. Hensley, “Efficient Histogram Generation Using Scattering on GPUs,” *ACM SIGGRAPH Symposium on Interactive 3D Graphics and Games*, pp. 33–37, 2007. Cited on p. 477

- [1123] Schilling, Andreas, G. Knittel, and Wolfgang Straßer, “Texram: A Smart Memory for Texturing,” *IEEE Computer Graphics and Applications*, vol. 16, no. 3, pp. 32–41, May 1996. Cited on p. 169
- [1124] Schilling, Andreas, “Towards Real-Time Photorealistic Rendering: Challenges and Solutions,” *ACM SIGGRAPH/Eurographics Workshop on Graphics Hardware* Los Angeles, CA, pp. 7–16, August 1997. Cited on p. 251, 275
- [1125] Schilling, Andreas, “Antialiasing of Environment Maps,” *Computer Graphics Forum*, vol. 20, no. 1, pp. 5–11, March 2001. Cited on p. 275
- [1126] Schlag, John, “Using Geometric Constructions to Interpolate Orientations with Quaternions,” in James Arvo, ed., *Graphics Gems II*, Academic Press, pp. 377–380, 1991. Cited on p. 97
- [1127] Schlag, John, “Fast Embossing Effects on Raster Image Data,” in Paul S. Heckbert, ed., *Graphics Gems IV*, Academic Press, pp. 433–437, 1994. Cited on p. 187
- [1128] Schlick, Christophe, “An Inexpensive BDRF Model for Physically based Rendering,” *Computer Graphics Forum*, vol. 13, no. 3, Sept. 1994, pp. 149–162. Cited on p. 233, 240, 262
- [1129] Schlick, Christophe, “A Survey of Shading and Reflectance Models,” *Computer Graphics Forum*, vol. 13, no. 2, June 1994, pp. 121–131. Cited on p. 252, 264
- [1130] Schmalstieg, Dieter, and Robert F. Tobler, “Fast Projected Area Computation for Three-Dimensional Bounding Boxes,” *journal of graphics tools*, vol. 4, no. 2, pp. 37–43, 1999. Also collected in [71]. Cited on p. 689
- [1131] Schneider, Philip, and David Eberly, *Geometric Tools for Computer Graphics*, Morgan Kaufmann, 2003. Cited on p. 536, 537, 573, 733, 751, 791, 792, 827
- [1132] Schneider, Jens, and Rüdiger Westermann, “GPU-Friendly High-Quality Terrain Rendering,” *Journal of WSCG*, vol. 14, no. 1-3, pp. 49–56, 2006. Cited on p. 549, 573
- [1133] Schorn, Peter and Frederick Fisher, “Testing the Convexity of Polygon,” in Paul S. Heckbert, ed., *Graphics Gems IV*, Academic Press, pp. 7–15, 1994. Cited on p. 537, 549, 573
- [1134] Schroders, M.F.A., and R.V. Gulik, “Quadtree Relief Mapping,” *ACM SIGGRAPH/Eurographics Workshop on Graphics Hardware*, pp. 61–66, 2006. Cited on p. 197
- [1135] Schröder, Peter, and Wim Sweldens, “Spherical Wavelets: Efficiently Representing Functions on the Sphere,” *Computer Graphics (SIGGRAPH 95 Proceedings)*, pp. 161–172, August 1995. Cited on p. 266
- [1136] Schröder, Peter, “What Can We Measure?” *SIGGRAPH 2006 Discrete Differential Geometry course notes*, 2006. Cited on p. 736
- [1137] Schroeder, Tim, “Collision Detection Using Ray Casting,” *Game Developer*, vol. 8, no. 8, pp. 50–56, August 2001. Cited on p. 763, 784, 787, 788, 789, 798
- [1138] Schüler, Christian, “Eliminating Surface Acne with Gradient Shadow Mapping,” in Wolfgang Engel, ed., *ShaderX<sup>4</sup>*, Charles River Media, pp. 289–297, 2005. Cited on p. 351
- [1139] Schüler, Christian, “Normal Mapping without Precomputed Tangents,” in Engel, Wolfgang, ed., *ShaderX<sup>5</sup>*, Charles River Media, pp. 131–140, 2006. Cited on p. 186

- [1140] Schüller, Christian, “Multisampling Extension for Gradient Shadow Maps,” in Wolfgang Engel, ed., *ShaderX<sup>5</sup>*, Charles River Media, pp. 207–218, 2006. Cited on p. 351, 366
- [1141] Schumacher, Dale A., “General Filtered Image Rescaling,” in David Kirk, ed., *Graphics Gems III*, Academic Press, pp. 8–16, 1992. Cited on p. 164
- [1142] Schwarz, Michael, and Marc Stamminger, “Bitmask Soft Shadows,” *Computer Graphics Forum*, vol. 26, no. 3, pp. 515–524, 2007. Cited on p. 372
- [1143] Scott, N., D. Olsen, and E. Gannett, “An Overview of the VISUALIZE fx Graphics Accelerator Hardware,” *Hewlett-Packard Journal*, pp. 28–34, May 1998. Cited on p. 674
- [1144] Sears, Chris, “The Elements of Cache Programming Style,” *Proceedings of the 4th Annual Linux Showcase and Conference*, October 2000. Cited on p. 705
- [1145] Sekulic, Dean, “Efficient Occlusion Culling,” in Randima Fernando, ed., *GPU Gems*, Addison-Wesley, pp. 487–503, 2004. Cited on p. 483, 666, 675
- [1146] Segal, M., C. Korobkin, R. van Widenfelt, J. Foran, and P. Haeberli, “Fast Shadows and Lighting Effects Using Texture Mapping,” *Computer Graphics (SIGGRAPH '92 Proceedings)*, pp. 249–252, July 1992. Cited on p. 153, 222, 339, 350
- [1147] Segovia, Benjamin, Jean-Claude Iehl, Richard Mitanchey, and Bernard Péroche, “Bidirectional Instant Radiosity,” *Eurographics Symposium on Rendering (2006)*, pp.389–397 , June 2006. Cited on p. 417
- [1148] Selan, Jeremy, “Using Lookup Tables to Accelerate Color Transformations,” in Matt Pharr, ed., *GPU Gems 2*, Addison-Wesley, pp. 381–408, 2005. Cited on p. 474, 475
- [1149] Sen, Pradeep, Mike Cammarano, and Pat Hanrahan, “Shadow Silhouette Maps,” *ACM Transactions on Graphics (SIGGRAPH 2003)*, vol. 22, no. 3, pp. 521–526, 2003. Cited on p. 357
- [1150] Seetzen, Helge, Wolfgang Heidrich, Wolfgang Stuerzlinger, Greg Ward, Lorne Whitehead, Matthew Trentacoste, Abhijeet Ghosh, and Andrejs Vorozcovs, “High Dynamic Range Display Systems,” *ACM Transactions on Graphics (SIGGRAPH 2004)*, vol. 23, no. 3, pp. 760–768, August, 2004. Cited on p. 832
- [1151] Shade, J., D. Lischinski, D. Salesin, T. DeRose, and J. Snyder, “Hierarchical Image Caching for Accelerated Walkthroughs of Complex Environments,” *Computer Graphics (SIGGRAPH 96 Proceedings)*, pp. 75–82, August 1996. Cited on p. 461
- [1152] Shade, J., Steven Gortler, Li-Wei He, and Richard Szeliski, “Layered Depth Images,” *Computer Graphics (SIGGRAPH 98 Proceedings)*, pp. 231–242, July 1998. Cited on p. 464
- [1153] Shah, Musawir A., Jaakko Konttinen, and Sumanta Pattanaik, “Caustics Mapping: An Image-space Technique for Real-time Caustics,” *IEEE Transactions on Visualization and Computer Graphics*, vol. 13, no. 2, pp. 272–280, Mar.-Apr. 2007. Cited on p. 399
- [1154] Shankel, Jason, “Rendering Distant Scenery with Skyboxes,” in Mark DeLoura, ed., *Game Programming Gems 2*, Charles River Media, pp. 416–420, 2001. Cited on p. 444
- [1155] Shankel, Jason, “Fast Heightfield Normal Calculation,” in Dante Treglia, ed., *Game Programming Gems 3*, Charles River Media, pp. 344–348, 2002. Cited on p. 547
- [1156] Shanmugam, Perumaal, and Okan Arikan, “Hardware Accelerated Ambient Occlusion Techniques on GPUs,” *ACM Symposium on Interactive 3D Graphics and Games (I3D 2007)*, pp. 73–80, 2007. Cited on p. 385

- [1157] Sharma, Gaurav, "Comparative Evaluation of Color Characterization and Gamut of LCDs versus CRTs," *Proc. SPIE: Color Imaging: Device Independent Color, Color Hard Copy, and Applications VII*, January 2002, vol. 4663, pp. 177–186. Cited on p. 141
- [1158] Sharp, Brian, "Implementing Curved Surface Geometry," *Game Developer*, vol. 6, no. 6, pp. 42–53, June 1999. Cited on p. 639
- [1159] Sharp, Brian, "Subdivision Surface Theory," *Game Developer*, vol. 7, no. 1, pp. 34–42, January 2000. Cited on p. 620, 643
- [1160] Sharp, Brian, "Implementing Subdivision Surface Theory," *Game Developer*, vol. 7, no. 2, pp. 40–45, February 2000. Cited on p. 618, 620, 629, 643
- [1161] Shastry, Anirudh S., "High Dynamic Range Rendering," GameDev.net website, 2004. <http://www.gamedev.net/reference/articles/article2108.asp> Cited on p. 484
- [1162] Shen, Hao, Pheng Ann Heng, and Zesheng Tang, "A Fast Triangle-Triangle Overlap Test Using Signed Distances," *journals of graphics tools*, vol. 8, no. 1, pp. 17–24, 2003. Cited on p. 757
- [1163] Shene, Ching-Kuang, "Computing the Intersection of a Line and a Cylinder," in Paul S. Heckbert, ed., *Graphics Gems IV*, Academic Press, pp. 353–355, 1994. Cited on p. 741
- [1164] Shene, Ching-Kuang, "Computing the Intersection of a Line and a Cone," in Alan Paeth, ed., *Graphics Gems V*, Academic Press, pp. 227–231, 1995. Cited on p. 741
- [1165] Shene, Ching-Kuang, "CS3621 Introduction to Computing with Geometry Notes," Michigan Technological University, website, 2007. <http://www.cs.mtu.edu/~shene/COURSES/cs3621/NOTES/notes.html> Cited on p. 583
- [1166] Shilov, Anton, Yaroslav Lyssenko, and Alexey Stepin, "Highly Defined: ATI Radeon HD 2000 Architecture Review," Xbit Laboratories website, August 2007. [http://www.xbitlabs.com/articles/video/display/r600-architecture\\_8.html](http://www.xbitlabs.com/articles/video/display/r600-architecture_8.html) Cited on p. 133
- [1167] Shimizu, Clement, Amit Shesh, and Baoquan Chen, "Hardware Accelerated Motion Blur Generation Clement Shimizu," University of Minnesota Computer Science Department Technical Report 2003-01. Cited on p. 493
- [1168] Shinya, M., and M-C Forgue, "Interference Detection through Rasterization," *The Journal of Visualization and Computer Animation*, vol. 2, no. 3, pp. 132–134, 1991. Cited on p. 824
- [1169] Shirley, Peter, *Physically Based Lighting Calculations for Computer Graphics*, Ph.D. Thesis, University of Illinois at Urbana Champaign, December 1990. Cited on p. 131, 146, 240
- [1170] Shirley, Peter, Helen Hu, Brian Smits, Eric Lafortune, "A Practitioners' Assessment of Light Reflection Models," *Pacific Graphics '97*, pp. 40–49, October 1997. Cited on p. 240, 252, 264
- [1171] Shirley, Peter, and R. Keith Morley, *Realistic Ray Tracing, Second Edition*, A.K. Peters Ltd., 2003. Cited on p. 415, 437
- [1172] Shirley, Peter, Michael Ashikhmin, Michael Gleicher, Stephen Marschner, Erik Reinhard, Kelvin Sung, William Thompson, and Peter Willemse, *Fundamentals of Computer Graphics, Second Edition*, A.K. Peters Ltd., 2005. Cited on p. 97, 146
- [1173] Shirman, Leon A., and Salim S. Abi-Ezzi, "The Cone of Normals Technique for Fast Processing of Curved Patches," *Computer Graphics Forum*, vol. 12, no. 3, pp. 261–272, 1993. Cited on p. 664

- [1174] Shishkovtsov, Oles, “Deferred Shading in S.T.A.L.K.E.R.,” in Matt Pharr, ed., *GPU Gems 2*, Addison-Wesley, pp. 143–166, 2005. Cited on p. 281, 361, 480
- [1175] Shiue, Le-Jeng, Ian Jones, and Jörg Peters, “A Realtime GPU Subdivision Kernel,” *ACM Transactions on Graphics*, vol. 24, no. 3, pp. 1010–1015, 2005. Cited on p. 643
- [1176] Shoemake, Ken, “Animating Rotation with Quaternion Curves,” *Computer Graphics (SIGGRAPH '85 Proceedings)*, pp. 245–254, July 1985. Cited on p. 67, 72, 76, 79
- [1177] Shoemake, Ken, “Quaternions and  $4 \times 4$  Matrices,” in James Arvo, ed., *Graphics Gems II*, Academic Press, pp. 351–354, 1991. Cited on p. 76, 77
- [1178] Shoemake, Ken, “Polar Matrix Decomposition,” in Paul S. Heckbert, ed., *Graphics Gems IV*, Academic Press, pp. 207–221, 1994. Cited on p. 70
- [1179] Shoemake, Ken, “Euler Angle Conversion,” in Paul S. Heckbert, ed., *Graphics Gems IV*, Academic Press, pp. 222–229, 1994. Cited on p. 66, 69
- [1180] Sigg, Christian, and Markus Hadwiger, “Fast Third-Order Texture Filtering,” in Matt Pharr, ed., *GPU Gems 2*, Addison-Wesley, pp. 313–329, 2005. Cited on p. 170
- [1181] Sillion, François, and Claude Puech, *Radiosity and Global Illumination*, Morgan Kaufmann, 1994. Cited on p. 408
- [1182] Sillion, François, G. Drettakis, and B. Bodelet, “Efficient Impostor Manipulation for Real-Time Visualization of Urban Scenery,” *Computer Graphics Forum*, vol. 16, no. 3, pp. 207–218, 1997. Cited on p. 467
- [1183] Skiena, Steven, *The Algorithm Design Manual*, Springer Verlag, 1997. Cited on p. 563
- [1184] Sloan, Peter-Pike, Michael F. Cohen, and Steven J. Gortler, “Time Critical Lumigraph Rendering,” *Proceedings 1997 Symposium on Interactive 3D Graphics*, pp. 17–23, April 1997. Cited on p. 444
- [1185] Sloan, Peter-Pike J., and Michael F. Cohen, “Interactive Horizon Mapping,” *11th Eurographics Workshop on Rendering*, pp. 281–286, June 2000. Cited on p. 428
- [1186] Sloan, Peter-Pike, Jan Kautz, and John Snyder, “Precomputed Radiance Transfer for Real-Time Rendering in Dynamic, Low-Frequency Lighting Environments,” *ACM Transactions on Graphics (SIGGRAPH 2002)*, vol. 21, no. 3, pp. 527–536, July 2002. Cited on p. 431, 436
- [1187] Sloan, Peter-Pike, Jesse Hall, John Hart, and John Snyder, “Clustered Principal Components for Precomputed Radiance Transfer,” *ACM Transactions on Graphics (SIGGRAPH 2003)*, vol. 22, no. 3, pp. 382–391, 2003. Cited on p. 436
- [1188] Sloan, Peter-Pike, Ben Luna, and John Snyder, “Local, Deformable Precomputed Radiance Transfer,” *ACM Transactions on Graphics (SIGGRAPH 2005)*, vol. 24, no. 3, pp. 1216–1224, August, 2005. Cited on p. 436
- [1189] Sloan, Peter-Pike, “Normal Mapping for Precomputed Radiance Transfer,” *ACM Symposium on Interactive 3D Graphics and Games (I3D 2006)*, pp. 23–26, March 2006. Cited on p. 421, 436
- [1190] Sloan, Peter-Pike, Naga K. Govindaraju, Derek Nowrouzezahrai, and John Snyder, “Image-Based Proxy Accumulation for Real-Time Soft Global Illumination,” *Pacific Graphics 2007*, pp. 97–105, October 2007. Cited on p. 385, 417
- [1191] Sloan, Peter-Pike. Personal communication, 2008. Cited on p. 257

- [1192] Sloan, Peter-Pike, “Stupid Spherical Harmonics (SH) Tricks,” *Game Developers Conference*, February 2008. <http://www.ppsloan.org/publications/>. Cited on p. 320, 321, 322, 323
- [1193] Smith, Bruce G., “Geometrical Shadowing of a Random Rough Surface,” *IEEE Transactions on Antennas and Propagation*, vol. 15, no. 5, pp. 668–671, September 1967. Cited on p. 262
- [1194] Smith, Alvy Ray, *Digital Filtering Tutorial for Computer Graphics*, Technical Memo 27, revised March 1983. Cited on p. 124, 146
- [1195] Smith, Alvy Ray, *Digital Filtering Tutorial, Part II*, Technical Memo 44, revised May 1983. Cited on p. 146
- [1196] Smith, Alvy Ray, “A Pixel is Not a Little Square, a Pixel is Not a Little Square, a Pixel is Not a Little Square! (And a Voxel is Not a Little Cube),” Technical Memo 6, Microsoft Research, July 1995. Cited on p. 125, 146
- [1197] Smith, Alvy Ray, and James F. Blinn, “Blue Screen Matting,” *Computer Graphics (SIGGRAPH 96 Proceedings)*, pp. 259–268, August 1996. Cited on p. 139
- [1198] Smith, Alvy Ray, “The Stuff of Dreams,” *Computer Graphics World*, pp. 27–29, July 1998. Cited on p. 880
- [1199] Smith, Andrew, Yoshifumi Kitamura, Haruo Takemura, and Fumio Kishino, “A Simple and Efficient Method for Accurate Collision Detection Among Deformable Polyhedral Objects in Arbitrary Motion,” *IEEE Virtual Reality Annual International Symposium*, pp. 136–145, 1995. Cited on p. 822
- [1200] Smits, Brian, “Efficiency Issues for Ray Tracing,” *journal of graphics tools*, vol. 3, no. 2, pp. 1–14, 1998. Also collected in [71]. Cited on p. 705, 744
- [1201] Snook, Greg, “Simplified Terrain Using Interlocking Tiles,” in Mark DeLoura, ed., *Game Programming Gems 2*, Charles River Media, pp. 377–383, 2001. Cited on p. 571
- [1202] Snyder, John, Ronen Barzel, and Steve Gabriel, “Motion Blur on Graphics Workstations,” in David Kirk, ed., *Graphics Gems III*, Academic Press, pp. 374–382, 1992. Cited on p. 831
- [1203] Snyder, John, “Area Light Sources for Real-Time Graphics,” Microsoft Research Technical Report, MSR-TR-96-11 Microsoft Research, March 1996. Cited on p. 294
- [1204] Snyder, John, and Jed Lengyel, “Visibility Sorting and Compositing without Splitting for Image Layer Decompositions,” *Computer Graphics (SIGGRAPH 98 Proceedings)*, pp. 219–230, July 1998. Cited on p. 446, 488
- [1205] Soler, Cyril, and François Sillion, “Fast Calculation of Soft Shadow Textures Using Convolution,” *Computer Graphics (SIGGRAPH 98 Proceedings)*, pp. 321–332, July 1998. Cited on p. 338, 370
- [1206] Sousa, Tiago, “Adaptive Glare,” in Engel, Wolfgang, ed., *ShaderX<sup>3</sup>*, Charles River Media, pp. 349–355, 2004. Cited on p. 477, 478, 484
- [1207] Sowizral, Henry, Kevin Rushforth, and Michael Deering, *The Java 3D API Specification*, Addison Wesley, 1997. Cited on p. 707
- [1208] Spencer, Greg, Peter Shirley, Kurt Zimmerman, and Donald Greenberg, “Physically-Based Glare Effects for Digital Images,” *Computer Graphics (SIGGRAPH 95 Proceedings)*, pp. 325–334, August 1995. Cited on p. 482
- [1209] Spörl, Marco, “A Practical Analytic Model for Daylight with Shaders,” in Engel, Wolfgang, ed., *ShaderX<sup>3</sup>*, Charles River Media, pp. 597–610, 2004. Cited on p. 499

- [1210] St. Amour, Jean-François, Eric Paquette, Pierre Poulin, and Philippe Beaudoin “Real-Time Soft Shadows Using the PDSM Technique,” in Wolfgang Engel, ed., *ShaderX<sup>4</sup>*, Charles River Media, pp. 299–311, 2005. Cited on p. 371
- [1211] Stam, Jos, “Multiple Scattering as a Diffusion Process,” *6th Eurographics Workshop on Rendering*, pp. 41–50, June 1995. Cited on p. 404
- [1212] Stam, Jos, “Exact Evaluation of Catmull-Clark Subdivision Surfaces at Arbitrary Parameter Values,” *Computer Graphics (SIGGRAPH 98 Proceedings)*, pp. 395–404, July 1998. Cited on p. 643
- [1213] Stam, Jos, “Diffraction Shaders,” *Computer Graphics (SIGGRAPH 99 Proceedings)*, pp. 101–110, August 1999. Cited on p. 241, 249, 252, 262
- [1214] Stamate, Vlad, “Reduction of Lighting Calculations Using Spherical Harmonics,” in Engel, Wolfgang, ed., *ShaderX<sup>3</sup>*, Charles River Media, pp. 251–262, 2004. Cited on p. 323
- [1215] Stamate, Vlad, “Real Time Photon Mapping Approximation on the GPU,” in Wolfgang Engel, ed., *ShaderX<sup>6</sup>*, Charles River Media, pp. 393–400, 2008. Cited on p. 417
- [1216] Stamminger, Marc, and George Drettakis, “Perspective Shadow Mapping,” *ACM Transactions on Graphics (SIGGRAPH 2002)*, vol. 21, no. 3, pp. 557–562, July 2002. Related article in [669]. Cited on p. 353, 355
- [1217] Stark, Michael M., James Arvo, and Brian Smits, “Barycentric Parameterizations for Isotropic BRDFs,” *IEEE Transactions on Visualization and Computer Graphics*, vol. 11, no. 2, pp. 126–138, Mar. 2005. Cited on p. 268
- [1218] Steed, Paul, *Animating Real-Time Game Characters*, Charles River Media, 2002. Cited on p. 84
- [1219] Stewart, A.J., and M.S. Langer, “Towards Accurate Recovery of Shape from Shading Under Diffuse Lighting,” *IEEE Trans. on Pattern Analysis and Machine Intelligence*, vol. 19, no. 9, Sept. 1997, pp. 1020–1025. Cited on p. 379
- [1220] Stich, Martin, Carsten Wächter, and Alexander Keller, “Efficient and Robust Shadow Volumes Using Hierarchical Occlusion Culling and Geometry Shaders,” in Hubert Nguyen, ed., *GPU Gems 3*, Addison-Wesley, pp. 239–256, 2007. Cited on p. 346, 347
- [1221] Stokes, Jon, “Clearing up the confusion over Intel’s Larrabee, part II,” Ars Technica website, June 4, 2007. <http://arstechnica.com/news.ars/post/20070604-clearing-up-the-confusion-over-intels-larrabee-part-ii.html> Cited on p. 841, 883, 884
- [1222] Stokes, Jon, “Intel talks Penryn, Nehalem at IDF,” Ars Technica website, September 18, 2007. <http://arstechnica.com/news.ars/post/20070918-intel-talks-penryn-nehalem-at-idf.html> Cited on p. 883
- [1223] Stokes, Michael, Matthew Anderson, Srinivasan Chandrasekar, and Ricardo Motta, “A Standard Default Color Space for the Internet—sRGB,” Version 1.10, Nov. 1996. Cited on p. 143
- [1224] Stone, Maureen, *A Field Guide to Digital Color*, A K Peters Ltd., August 2003. Cited on p. 215, 217
- [1225] Stone, Maureen, “Representing Colors as Three Numbers,” *IEEE Computer Graphics and Applications*, vol. 25, no. 4, pp. 78–85, July/August 2005. Cited on p. 210, 216
- [1226] Strothotte, Thomas, and Stefan Schlechtweg *Non-Photorealistic Computer Graphics: Modeling, Rendering, and Animation*, Morgan Kaufmann, 2002. Cited on p. 508, 522

- [1227] Ström, Jacob, and Tomas Akenine-Möller, “iPACKMAN: High-Quality, Low-Complexity Texture Compression for Mobile Phones,” *Graphics Hardware*, pp. 63–70, 2005. Cited on p. 176, 873
- [1228] Suffern, Kevin, *Ray Tracing from the Ground Up*, A K Peters Ltd., 2007. Cited on p. 415, 437
- [1229] Sun, Bo, Ravi Ramamoorthi, Srinivasa Narasimhan, and Shree Nayar, “A Practical Analytic Single Scattering Model for Real Time Rendering,” *ACM Transactions on Graphics (SIGGRAPH 2005)*, vol. 24, no. 3, pp. 1040–1049, 2005. Cited on p. 499
- [1230] Sunday, Dan, “Area of Triangles and Polygons (2D and 3D),” GeometryAlgorithms.com, 2001. Also collected in [71] as “Fast Polygon Area and Newell Normal Computation.” Cited on p. 911
- [1231] Sutherland, Ivan E., Robert F. Sproull, and Robert F. Schumacker, “A Characterization of Ten Hidden-Surface Algorithms,” *Computing Surveys*, vol. 6, no. 1, March 1974. Cited on p. 887
- [1232] Svarovsky, Jan, “View-Independent Progressive Meshing,” in Mark DeLoura, ed., *Game Programming Gems*, Charles River Media, pp. 454–464, 2000. Cited on p. 563, 567, 574
- [1233] Szécsi, László, “Alias-Free Hard Shadows with Geometry Maps,” in Wolfgang Engel, ed., *ShaderX<sup>5</sup>*, Charles River Media, pp. 219–237, 2006. Cited on p. 357
- [1234] Szirmay-Kalos, László, Barnabás Aszódi, and István Lazányi, “Ray Tracing Effects without Tracing Rays,” in Engel, Wolfgang, ed., *ShaderX<sup>4</sup>*, Charles River Media, pp. 397–407, 2005. Cited on p. 307, 399
- [1235] Szirmay-Kalos, László, and Umenhoffer, Tamás, “Displacement Mapping on the GPU—State of the Art,” *Computer Graphics Forum*, vol. 27, no. 1, 2008. Cited on p. 198
- [1236] Tabellion, Eric, and Arnauld Lamorlette, “An Approximate Global Illumination System for Computer Generated Films,” *ACM Transactions on Graphics (SIGGRAPH 2004)*, vol. 23, no. 3, pp. 469–476, August, 2004. Cited on p. 26, 422
- [1237] Tadamura, Katsumi, Xueying Qin, Guofang Jiao, and Eihachiro Nakamae, “Rendering Optimal Solar Shadows Using Plural Sunlight Depth Buffers,” *Computer Graphics International 1999*, pp. 166, 1999. Cited on p. 359
- [1238] Tamura, Naoki, Henry Jonah, Bing-Yu Chen, and Tomoyuki Nishita, “A Practical and Fast Rendering Algorithm for Dynamic Scenes Using Adaptive Shadow Fields,” *Pacific Graphics 2006*, pp. 702–712, October 2006. Cited on p. 430
- [1239] Tan, Ping, Stephen Lin, Long Quan, Baining Guo, and Heung-Yeung Shum, “Multiresolution Reflectance Filtering,” *Rendering Techniques 2005: 16th Eurographics Workshop on Rendering*, pp. 111–116, June–July 2005. Cited on p. 275
- [1240] Tan, Ping, Stephen Lin, Long Quan, Baining Guo, and Harry Shum, “Filtering and Rendering of Resolution-Dependent Reflectance Models,” *IEEE Transactions on Visualization and Computer Graphics*, vol. 14, no. 2, pp. 412–425, Mar.–Apr. 2008. Cited on p. 275
- [1241] Tanner, Christopher C., Christopher J. Migdal, and Michael T. Jones, “The Clipmap: A Virtual Mipmap,” *Computer Graphics (SIGGRAPH 98 Proceedings)*, pp. 151–158, July 1998. Cited on p. 173
- [1242] Tarini, Marco, Kai Hormann, Paolo Cignoni, and Claudio Montani, “PolyCube-Maps,” *ACM Transactions on Graphics (SIGGRAPH 2004)*, vol. 23, no. 3, pp. 853–860, August, 2004. Cited on p. 151

- [1243] Tatarchuk, Natalya, Chris Brennan, Alex Vlachos, and John Isidoro, “Motion Blur Using Geometry and Shading Distortion,” in Engel, Wolfgang, ed., *ShaderX<sup>2</sup>: Shader Programming Tips and Tricks with DirectX 9*, Wordware, pp. 299–308, 2004. Cited on p. 494
- [1244] Tatarchuk, Natalya, “Dynamic Parallax Occlusion Mapping with Approximate Soft Shadows,” *SIGGRAPH 2006 Advanced Real-Time Rendering in 3D Graphics and Games course notes*, 2006. Cited on p. 193, 194, 195, 197, 199
- [1245] Tatarchuk, Natalya, Chris Oat, Pedro V. Sander, Jason L. Mitchell, Carsten Wenzel, and Alex Evans, *SIGGRAPH 2006 Advanced Real-Time Rendering in 3D Graphics and Games course notes*, 2006. Cited on p. 997
- [1246] Tatarchuk, Natalya, “Artist-Directable Real-Time Rain Rendering in City Environments,” *SIGGRAPH 2006 Advanced Real-Time Rendering in 3D Graphics and Games course notes*, 2006. Cited on p. 2, 472, 501, 505
- [1247] Tatarchuk, Natalya, “Rendering Multiple Layers of Rain with a Postprocessing Composite Effect,” in Engel, Wolfgang, ed., *ShaderX<sup>5</sup>*, Charles River Media, pp. 303–313, 2006. Cited on p. 2
- [1248] Tatarchuk, Natalya, “Practical Parallax Occlusion Mapping with Approximate Soft Shadows for Detailed Surface Rendering,” *SIGGRAPH 2006 Advanced Real-Time Rendering in 3D Graphics and Games course notes*, 2006. Cited on p. 193, 194, 195, 199
- [1249] Tatarchuk, Natalya, “ATI: ToyShop,” *Best of Eurographics Animation Festival*, Eurographics, September 2006. <http://www.ati.com/developer/techpapers.html> Cited on p. 2
- [1250] Tatarchuk, Natalya, and Jeremy Shopf, “Real-Time Medical Visualization with FireGL,” *SIGGRAPH 2007*, AMD Technical Talk, August 2007. Cited on p. 503, 607
- [1251] Tatarchuk, Natalya, Christopher Oat, Jason L. Mitchell, Chris Green, Johan Andersson, Martin Mittring, Shanon Drone, and Nico Galoppo, *SIGGRAPH 2007 Advanced Real-Time Rendering in 3D Graphics and Games course notes*, 2007. Cited on p. 971
- [1252] Tatarchuk, Natalya, “Real-Time Tessellation on GPU,” *SIGGRAPH 2007 Advanced Real-Time Rendering in 3D Graphics and Games course notes*, 2007. Cited on p. 632, 633, 635
- [1253] Taubin, Gabriel, André Guéziec, William Horn, and Francis Lazarus, “Progressive Forest Split Compression,” *Computer Graphics (SIGGRAPH 98 Proceedings)*, pp. 123–132, July 1998. Cited on p. 562
- [1254] Taylor, Philip, “Per-Pixel Lighting,” In *Driving DirectX* web column, November 2001. <http://msdn2.microsoft.com/en-us/library/ms810494.aspx> Cited on p. 325
- [1255] Tchou, Chris, Jessi Stumpfel, Per Einarsson, Marcos Fajardo, and Paul Debevec, “Unlighting the Parthenon,” *SIGGRAPH 2004 Technical Sketch*, 2004. Cited on p. 265
- [1256] Team Beyond3D, “Intel Presentation Reveals the Future of the CPU-GPU War,” Beyond3D.com website, 11th Apr 2007. <http://www.beyond3d.com/content/articles/31/> Cited on p. 883, 884
- [1257] Teixeira, Diogo, “Baking Normal Maps on the GPU,” in Hubert Nguyen, ed., *GPU Gems 3*, Addison-Wesley, pp. 491–512, 2007. Cited on p. 681
- [1258] Teller, Seth J., and Carlo H. Séquin, “Visibility Preprocessing For Interactive Walkthroughs,” *Computer Graphics (SIGGRAPH '91 Proceedings)*, pp. 61–69, July 1991. Cited on p. 667

- [1259] Teller, Seth J., *Visibility Computations in Densely Occluded Polyhedral Environments*, Ph.D. Thesis, Department of Computer Science, University of Berkeley, 1992. Cited on p. 667
- [1260] Teller, Seth, and Pat Hanrahan, “Global Visibility Algorithms for Illumination Computations,” *Computer Graphics (SIGGRAPH 94 Proceedings)*, pp. 443–450, July 1994. Cited on p. 667
- [1261] Teschner, M., B. Heidelberger, M. Mueller, D. Pomeranets, and M. Gross, “Optimized Spatial Hashing for Collision Detection of Deformable Objects,” *Vision, Modeling, Visualization*, pp. 47–54, November 2003. Cited on p. 814
- [1262] Teschner, M., S. Kimmerle, B. Heidelberger, G. Zachmann, L. Raghupathi, A. Fuhrmann, M. Cani, F. Faure, N. Magnenat-Thalmann, W. Strasser, and P. Volino, “Collision Detection for Deformable Objects,” *Computer Graphics Forum*, vol. 24, no. 1, pp. 61–81 , 2005. Cited on p. 827
- [1263] Tessman, Thant, “Casting Shadows on Flat Surfaces,” *Iris Universe*, pp. 16–19, Winter 1989. Cited on p. 333
- [1264] Tevs, A., I. Ihrke, and H.-P. Seidel, “Maximum Mipmaps for Fast, Accurate, and Scalable Dynamic Height Field Rendering,” *ACM Symposium on Interactive 3D Graphics and Games (I3D 2008)*, pp. 183–190, February 2008. Cited on p. 197
- [1265] Thomas, Spencer W., “Decomposing a Matrix into Simple Transformations,” in James Arvo, ed., *Graphics Gems II*, Academic Press, pp. 320–323, 1991. Cited on p. 68, 70
- [1266] Thürmer, Grit, and Charles A. Wüthrich, “Computing Vertex Normals from Polygonal Facets,” *journal of graphics tools*, vol. 3, no. 1, pp. 43–46, 1998. Also collected in [71]. Cited on p. 546
- [1267] Toksvig, Michael, “Mipmapping Normal Maps,” *journal of graphics tools*, vol. 10, no. 3, pp. 65–71, 2005. Cited on p. 274
- [1268] Torborg, J., and J.T. Kajiya, “Talisman: Commodity Realtime 3D Graphics for the PC,” *Computer Graphics (SIGGRAPH 96 Proceedings)*, pp. 353–363, August 1996. Cited on p. 446
- [1269] Rafael P. Torchelsen, Rafael P., João L. D. Comba, and Rui Bastos, “Practical Geometry Clipmaps for Rendering Terrains in Computer Games,” in Wolfgang Engel, ed., *ShaderX<sup>6</sup>*, Charles River Media, pp. 103–114, 2008. Cited on p. 573
- [1270] Torrance, K., and E. Sparrow, “Theory for Off-Specular Reflection From Roughened Surfaces,” *J. Optical Society of America*, vol. 57, September 1967. Cited on p. 229, 246, 247, 248, 258, 261
- [1271] Trapp, Matthias, and Jürgen Döllner, “Automated Combination of Real-Time Shader Programs,” *Eurographics 2007*, short presentation, pp. 53–56, September 2007. Cited on p. 50, 277
- [1272] Treglia, Dante, ed., *Game Programming Gems 3*, Charles River Media, 2002. Cited on p. 952
- [1273] Tsai, Yu-Ting, and Zen-Chung Shih, “All-Frequency Precomputed Radiance Transfer using Spherical Radial Basis Functions and Clustered Tensor Approximation,” *ACM Transactions on Graphics*, vol. 25, no. 3, pp. 967–976, July 2006. Cited on p. 436
- [1274] Tumblin, Jack, J.K. Hodgins, and B. Guenter, “Two Methods for Display of High Contrast Images,” *ACM Transactions on Graphics*, vol. 18, no. 1, pp. 56–94, January 1999. Cited on p. 475

- [1275] Turk, Greg, *Interactive Collision Detection for Molecular Graphics*, Technical Report TR90-014, University of North Carolina at Chapel Hill, 1990. Cited on p. 814
- [1276] Turkowski, Ken, "Filters for Common Resampling Tasks," in Andrew S. Glassner, ed., *Graphics Gems*, Academic Press, pp. 147–165, 1990. Cited on p. 122
- [1277] Turkowski, Ken, "Properties of Surface-Normal Transformations," in Andrew S. Glassner, ed., *Graphics Gems*, Academic Press, pp. 539–547, 1990. Cited on p. 64
- [1278] Turner, Bryan, "Real-Time Dynamic Level of Detail Terrain Rendering with ROAM," *Gamasutra*, April 2000. Cited on p. 569
- [1279] Ulrich, Thatcher, "Loose Octrees," in Mark DeLoura, ed., *Game Programming Gems*, Charles River Media, pp. 444–453, 2000. Cited on p. 656
- [1280] Umenhoffer, Tamás, Lázló Szirmay-Kalos, Gábor Szijártó, "Spherical Billboards and Their Application to Rendering Explosions," *Graphics Interface 2006*, pp. 57–63, 2006. Cited on p. 453
- [1281] Umenhoffer, Tamás, László Szirmay-Kalos and Gábor Szijártó, "Spherical Billboards for Rendering Volumetric Data," in Engel, Wolfgang, ed., *ShaderX<sup>5</sup>*, Charles River Media, pp. 275–285, 2006. Cited on p. 453
- [1282] Umenhoffer, Tamás, Gustavo Patow, and Lázló Szirmay-Kalos, "Robust Multiple Specular Reflections and Refractions," in Hubert Nguyen, ed., *GPU Gems 3*, Addison-Wesley, pp. 387–407, 2007. Cited on p. 392
- [1283] Upstill, S., *The RenderMan Companion: A Programmer's Guide to Realistic Computer Graphics*, Addison-Wesley, 1990. Cited on p. 33, 199, 283
- [1284] Uralsky, Yury, "Efficient Soft-Edged Shadows Using Pixel Shader Branching," in Matt Pharr, ed., *GPU Gems 2*, Addison-Wesley, pp. 269–282, 2005. Cited on p. 363
- [1285] Valient, Michal, "Accelerated Real-Time Rendering," M.Sc. Thesis, Comenius University, Bratislava, Slovakia, 2003. Cited on p. 263
- [1286] Valient, Michal, "Advanced Lighting and Shading with Direct3D 9," in Engel, Wolfgang, ed., *ShaderX<sup>2</sup> : Introductions&Tutorials with DirectX9*, Wordware, pp. 83–150, 2004. Cited on p. 263
- [1287] Valient, Michal, and Willem H. de Boer, "Fractional-Disk Soft Shadows," in Engel, Wolfgang, ed., *ShaderX<sup>3</sup>*, Charles River Media, pp. 411–424, 2004. Cited on p. 364, 366
- [1288] Valient, Michal, "Deferred Rendering in Killzone," *Develop Conference*, Brighton, July 2007. Cited on p. 280, 281, 283
- [1289] Valient, Michal, "Stable Rendering of Cascaded Shadow Maps," in Wolfgang Engel, ed., *ShaderX<sup>6</sup>*, Charles River Media, pp. 231–238, 2008. Cited on p. 359
- [1290] van den Bergen, G., "Efficient Collision Detection of Complex Deformable Models Using AABB Trees," *journal of graphics tools*, vol. 2, no. 4, pp. 1–13, 1997. Also collected in [71]. Cited on p. 807, 808, 809, 820, 821
- [1291] van den Bergen, G., "A Fast and Robust GJK Implementation for Collision Detection of Convex Objects," *journal of graphics tools*, vol. 4, no. 2, pp. 7–25, 1999. Cited on p. 809, 818, 820
- [1292] van den Bergen, Gino, *Collision Detection in Interactive 3D Computer Animation*, Ph.D. Thesis, Eindhoven University of Technology, 1999. Cited on p. 808, 809, 820

- [1293] van den Bergen, Gino, "Proximity Queries and Penetration Depth Computation on 3D Game Objects," *Game Developers Conference*, pp. 821–837, March 2001. <http://www.win.tue.nl/~gino/solid/gdc2001depth.pdf> Cited on p. 820
- [1294] van den Bergen, Gino, *Collision Detection in Interactive 3D Environments*, Morgan Kaufmann, 2003. Cited on p. 809, 826
- [1295] van der Burg, John, "Building an Advanced Particle System," *Gamasutra*, June 2000. Cited on p. 455
- [1296] van Emde Boas, P., R. Kaas, and E. Zijlstra, "Design and Implementation of an Efficient Priority Queue," *Mathematical Systems Theory*, vol. 10, no. 1, pp. 99–127, 1977. Cited on p. 657
- [1297] van Overveld, C.V.A.M., and B. Wyvill, "Phong Normal Interpolation Revisited," *ACM Transaction on Graphics*, vol. 16, no. 4, pp. 397–419, October 1997. Cited on p. 602
- [1298] van Overveld, C.V.A.M., and B. Wyvill, "An Algorithm for Polygon Subdivision Based on Vertex Normals," *Computer Graphics International '97*, pp. 3–12, June 1997. Cited on p. 599
- [1299] Velho, Luiz, "Simple and Efficient Polygonization of Implicit Surfaces," *journal of graphics tools*, vol. 1, no. 2, pp. 5–24, 1996. Cited on p. 607
- [1300] Velho, Luiz, and Luiz Henrique de Figueiredo, "Optimal Adaptive Polygonal Approximation of Parametric Surfaces," Technical Report CS-96-23, University of Waterloo, 1996. Cited on p. 637
- [1301] Verbeck, Channing, and Donald P. Greenberg, "A Comprehensive Light Source Description for Computer Graphics," *IEEE Computer Graphics & Applications*, vol. 4, no. 7, pp. 66–75, 1984. Cited on p. 221
- [1302] *Virtual Terrain Project* website. <http://www.vterrain.org> Cited on p. 505, 569, 573, 574
- [1303] Vlachos, Alex, and Jason L. Mitchell, "Refraction Mapping in Liquid Containers," in Mark DeLoura, ed., *Game Programming Gems*, Charles River Media, pp. 594–600, 2000. Cited on p. 398
- [1304] Vlachos, Alex, Jörg Peters, Chas Boyd, and Jason L. Mitchell, "Curved PN Triangles," *ACM Symposium on Interactive 3D Graphics 2001*, pp. 159–166, 2001. Cited on p. 599, 601, 603
- [1305] Vlachos, Alex, and John Isidoro, "Smooth  $C^2$  Quaternion-based Flythrough Paths," in Mark DeLoura, ed., *Game Programming Gems 2*, Charles River Media, pp. 220–227, 2001. Cited on p. 97
- [1306] Vlachos, Alex, "Approximating Fish Tank Refractions," in Mark DeLoura, ed., *Game Programming Gems 2*, Charles River Media, pp. 402–405, 2001. Cited on p. 397
- [1307] Volino, Pascal, and Nadia Magnenat Thalmann, "Collision and Self-Collision Detection: Efficient and Robust Solutions for Highly Deformable Surfaces," *Eurographics Workshop on Animation and Simulation '95*, pp. 55–65, September 1995. Cited on p. 826
- [1308] Volino, Pascal, and Nadia Magnenat Thalmann, "Implementing Fast Cloth Simulation with Collision Response," *Computer Graphics International 2000*, pp. 257–268, June 2000. Cited on p. 826
- [1309] Voorhies, Douglas, "Space-Filling Curves and a Measure of Coherence," in James Arvo, ed., *Graphics Gems II*, Academic Press, pp. 26–30, 1991. Cited on p. 556

- [1310] International Standard ISO/IEC 14772-1:1997 (VRML). Cited on p. 69
- [1311] Walbourn, Chuck, ed., “Introduction to Direct3D 10,” *Course 5 notes at SIGGRAPH 2007*, 2007. Cited on p. 711
- [1312] Wald, Ingo, Philipp Slusallek, and Carsten Benthin, “Interactive Distributed Ray-Tracing of Highly Complex Models,” *12th Eurographics Workshop on Rendering*, pp. 274–285, June 2001. Cited on p. 415
- [1313] Wald, Ingo, Carsten Benthin, Markus Wagner, and Philipp Slusallek, “Interactive Rendering with Coherent Ray-Tracing,” *Computer Graphics Forum*, vol. 20, no. 3, pp. 153–164, 2001. Cited on p. 415
- [1314] Wald, Ingo, William R. Mark, Johannes Günther, Solomon Boulos, Thiago Ize, Warren Hunt, Steven G. Parker, and Peter Shirley, “State of the Art in Ray Tracing Animated Scenes,” *State of the Art Reports, EUROGRAPHICS 2007*, pp. 89–116, September 2007. Cited on p. 416, 736
- [1315] Walker, R., and J. Snoeyink, “Using CSG Representations of Polygons for Practical Point-in-Polygon Tests,” *Visual Proceedings (SIGGRAPH 97)*, p. 152, August 1997. Cited on p. 751
- [1316] Walter, Bruce, “Notes on the Ward BRDF,” Technical Report PCG-05-06, Program of Computer Graphics, Cornell University, Ithaca, New York, 2005. Cited on p. 258
- [1317] Wan, Liang, Tien-Tsin Wong, and Chi-Sing Leung, “Isocube: Exploiting the Cubemap Hardware,” *IEEE Transactions on Visualization and Computer Graphics*, vol. 13, no. 4, pp. 720–731, July 2007. Cited on p. 306
- [1318] Wan, Liang, Tien-Tsin Wong, Chi-Sing Leung, and Chi-Wing Fu, “Isocube: A Cubemap with Uniformly Distributed and Equally Important Texels,” in Wolfgang Engel, ed., *ShaderX<sup>6</sup>*, Charles River Media, pp. 83–92, 2008. Cited on p. 306
- [1319] Wang, Niniane, “Realistic and Fast Cloud Rendering,” *journal of graphics tools*, vol. 9, no. 3, pp. 21–40, 2004. Cited on p. 452
- [1320] Wang, Niniane, “Let There Be Clouds!” *Game Developer Magazine*, vol. 11, no. 1, pp. 34–39, January 2004. Cited on p. 452
- [1321] Wang, Yulan, and Steven Molnar, “Second-depth Shadow Mapping,” TR94-019, Department of Computer Science, The University of North Carolina at Chapel Hill, 1994. Cited on p. 352
- [1322] Wang, X., X. Tong, S. Lin, S. Hu, B. Guo, and H.-Y. Shum, “Generalized Displacement Maps,” *Eurographics Symposium on Rendering (2004)*, pp. 227–233, June 2004. Cited on p. 195
- [1323] Wang, L., X. Wang, P. Sloan, L. Wei, Xin Tong, and B. Guo, “Rendering from Compressed High Dynamic Range Textures on Programmable Graphics Hardware,” *ACM Symposium on Interactive 3D Graphics and Games*, pp. 17–23, 2007. Cited on p. 178
- [1324] Wanger, Leonard, “The effect of shadow quality on the perception of spatial relationships in computer generated imagery,” *Computer Graphics (1992 Symposium on Interactive 3D Graphics)*, vol. 25, no. 2, pp. 39–42, 1992. Cited on p. 333
- [1325] Ward, Greg, “Real Pixels,” in James Arvo, ed., *Graphics Gems II*, Academic Press, pp. 80–83, 1991. Cited on p. 481
- [1326] Ward, Gregory, “Measuring and Modeling Anisotropic Reflection,” *Computer Graphics (SIGGRAPH '92 Proceedings)*, pp. 265–272, July 1992. Cited on p. 249, 252, 258, 260, 264, 265, 266

- [1327] Ward, Kelly, Florence Bertails, Tae-Yong Kim, Stephen R. Marschner, Marie-Paule Cani, and Ming Lin, “A Survey on Hair Modeling: Styling, Simulation, and Rendering,” *IEEE Transactions on Visualization and Computer Graphics (TVCG)*, vol. 13, no. 2, pp. 213–234, March/April 2007. Cited on p. 371
- [1328] Warren, Joe, and Henrik Weimer, *Subdivision Methods for Geometric Design: A Constructive Approach*, Morgan Kaufmann, 2001. Cited on p. 576, 609, 610, 612, 615, 616, 643
- [1329] Watson, Benjamin, and David Luebke, “The Ultimate Display: Where Will All the Pixels Come From?” *Computer*, pp. 54–61, August 2005. Cited on p. 1, 645, 719, 835
- [1330] Watt, Alan, and Mark Watt, *Advanced Animation and Rendering Techniques—Theory and Practice*, Addison-Wesley, 1992. Cited on p. 67, 97, 117, 199, 643
- [1331] Watt, Alan, *3D Computer Graphics*, Second Edition, Addison-Wesley, 1993. Cited on p. 199, 455
- [1332] Watt, Alan, and Fabio Policarpo, *The Computer Image*, Addison-Wesley, 1998. Cited on p. 117, 119, 199
- [1333] Watt, Alan, and Fabio Policarpo, *3D Games: Real-Time Rendering and Software Technology*, Addison-Wesley, 2001. Cited on p. 199
- [1334] Watt, Alan, and Fabio Policarpo, *Advanced Game Development with Programmable Graphics Hardware*, A K Peters Ltd., 2005. Cited on p. 197, 199
- [1335] Webb, Matthew , Emil Praun, Adam Finkelstein, and Hugues Hoppe, “Fine tone control in hardware hatching,” *2nd International Symposium on Non-Photorealistic Animation and Rendering (NPAR)*, pp. 53–58, June 2002. Cited on p. 525
- [1336] Weghorst, H., G. Hooper, and D. Greenberg, “Improved Computational Methods for Ray Tracing,” *ACM Transactions on Graphics*, vol. 3, no. 1, pp. 52–69, 1984. Cited on p. 806
- [1337] Wei, Li-Yi, “Tile-Based Texture Mapping,” in Matt Pharr, ed., *GPU Gems 2*, Addison-Wesley, pp. 189–199, 2005. Cited on p. 156
- [1338] Welsh, Terry, “Parallax Mapping with Offset Limiting: A Per-Pixel Approximation of Uneven Surfaces,” Infiscape Corp., 2004. Also collected in [309]. Cited on p. 191, 192
- [1339] Welzl, Emo, “Smallest Enclosing Disks (Balls and Ellipsoids),” in H. Maurer, ed., *New Results and New Trends in Computer Science, LNCS 555*, 1991. Cited on p. 733
- [1340] Wenzel, Carsten, “Far Cry and DirectX,” *Game Developers Conference*, March 2005. [http://ati.amd.com/developer/gdc/D3DTutorial08\\_FarCryAndDX9.pdf](http://ati.amd.com/developer/gdc/D3DTutorial08_FarCryAndDX9.pdf) Cited on p. 485, 710
- [1341] Wenzel, Carsten, “Real-Time Atmospheric Effects in Games,” *SIGGRAPH 2006 Advanced Real-Time Rendering in 3D Graphics and Games course notes*, 2006. Cited on p. 282, 453, 499, 500
- [1342] Wenzel, Carsten, “Real-time Atmospheric Effects in Games Revisited,” *Game Developers Conference*, March 2007. Related article in [1245]. [http://ati.amd.com/developer/gdc/2007/D3DTutorial\\_Crytek.pdf](http://ati.amd.com/developer/gdc/2007/D3DTutorial_Crytek.pdf) Cited on p. 447, 452, 499, 500, 881
- [1343] Wernecke, Josie, *The Inventor Mentor*, Addison-Wesley, 1994. Cited on p. 695
- [1344] Westin, Stephen H., James R. Arvo, and Kenneth E. Torrance, “Predicting Reflectance Functions from Complex Surfaces,” *Computer Graphics (SIGGRAPH '92 Proceedings)*, pp. 255–264, July 1992. Cited on p. 266

- [1345] Westin, Stephen H., Hongsong Li, and Kenneth E. Torrance, “A Field Guide to BRDF Models,” Research Note PCG-04-01, Cornell University Program of Computer Graphics, January 2004. Cited on p. 241, 245, 252, 264
- [1346] Westin, Stephen H., Hongsong Li, and Kenneth E. Torrance, “A Comparison of Four BRDF Models,” Research Note PCG-04-02, Cornell University Program of Computer Graphics, April 2004. Cited on p. 241, 245, 252, 264
- [1347] Westover, Lee, “Footprint Evaluation for Volume Rendering,” *Computer Graphics (SIGGRAPH '90 Proceedings)*, pp. 367–376, August 1990. Cited on p. 502
- [1348] Wexler, Daniel, Larry Gritz, Eric Enderton, and Jonathan Rice, “GPU-Accelerated High-Quality Hidden Surface Removal,” *ACM SIGGRAPH/Eurographics Workshop on Graphics Hardware*, pp. 7–14, 2005. Cited on p. 141
- [1349] Weyrich, Tim, Wojciech Matusik, Hanspeter Pfister, Bernd Bickel, Craig Donner, Chien Tu, Janet McAndless, Jinho Lee, Addy Ngan, Henrik Wann Jensen, and Markus Gross, “Analysis of Human Faces Using a Measurement-Based Skin Reflectance Model,” *ACM Transactions on Graphics*, vol. 25, no. 3, pp. 1013–1024, July 2006. Cited on p. 265
- [1350] Whatley, David “Towards Photorealism in Virtual Botany,” in Matt Pharr, ed., *GPU Gems 2*, Addison-Wesley, pp. 7–45, 2005. Cited on p. 183, 685
- [1351] Wiley, Abe, and Thorsten Scheuermann, “The Art and Technology of Whiteout,” *SIGGRAPH 2007*, AMD Technical Talk, August 2007. Cited on p. 316
- [1352] Williams, Amy, Steve Barrus, R. Keith Morley, and Peter Shirley, “An Efficient and Robust Ray-Box Intersection Algorithm,” *journal of graphics tools*, vol. 10, no. 1, pp. 49–54, 2005. Cited on p. 744
- [1353] Williams, Lance, “Casting Curved Shadows on Curved Surfaces,” *Computer Graphics (SIGGRAPH '78 Proceedings)*, pp. 270–274, August 1978. Cited on p. 348
- [1354] Williams, Lance, “Pyramidal Parametrics,” *Computer Graphics*, vol. 7, no. 3, pp. 1–11, July 1983. Cited on p. 163, 165, 301
- [1355] Wilson, A. E., Larsen, D. Manocha, and M.C. Lin, “Partitioning and Handling Massive Models for Interactive Collision Detection,” *Computer Graphics Forum*, vol. 18, no. 3, pp. 319–329, 1999. Cited on p. 826
- [1356] Wilson, Andy, and Dinesh Manocha, “Simplifying Complex Environments using Incremental Textured Depth Meshes,” *ACM Transactions on Graphics (SIGGRAPH 2003)*, vol. 22, no. 3, pp. 678–688, 2003. Cited on p. 467
- [1357] Wimmer, Michael, and Dieter Schmalstieg, “Load balancing for smooth LODs,” Technical Report TR-186-2-98-31, Institute of Computer Graphics and Algorithms, Vienna University of Technology, December 1998. Cited on p. 693
- [1358] Wimmer, Michael, Peter Wonka, and François Sillion, “Point-Based Impostors for Real-Time Visualization,” *12th Eurographics Workshop on Rendering*, pp. 163–176, June 2001. Cited on p. 457, 466
- [1359] Wimmer, Michael, Daniel Scherzer, and Werner Purgathofer, “Light Space Perspective Shadow Maps,” *Eurographics Symposium on Rendering (2004)*, pp. 143–151, June 2004. Cited on p. 356
- [1360] Wimmer, Michael, and Jiří Bittner, “Hardware Occlusion Queries Made Useful,” in Matt Pharr, ed., *GPU Gems 2*, Addison-Wesley, pp. 91–108, 2005. Cited on p. 674, 676

- [1361] Wimmer, Michael, and Daniel Scherzer, “Robust Shadow Mapping with Light-Space Perspective Shadow Maps,” in Wolfgang Engel, ed., *ShaderX<sup>4</sup>*, Charles River Media, pp. 313–330, 2005. Cited on p. 356
- [1362] Winner, Stephanie, Mike Kelley, Brent Pease, Bill Rivard, and Alex Yen, “Hardware Accelerated Rendering of Antialiasing Using a Modified A-Buffer Algorithm,” *Computer Graphics (SIGGRAPH 97 Proceedings)*, pp. 307–316, August 1997. Cited on p. 126, 130
- [1363] Witkin, Andrew, David Baraff, and Michael Kass, “Physically Based Modeling,” *Course 25 notes at SIGGRAPH 2001*, 2001. Cited on p. 812, 813, 823, 824
- [1364] Wloka, Matthias, “Implementing Motion Blur & Depth of Field using DirectX 8,” *Meltdown 2001*, July 2001. Cited on p. 488, 493
- [1365] Wloka, Matthias, “Batch, Batch, Batch: What Does It Really Mean?” *Game Developers Conference*, March 2003. <http://developer.nvidia.com/docs/IO/8230/BatchBatchBatch.pdf> Cited on p. 708
- [1366] Wood, Daniel N., Daniel I. Azuma, Ken Aldinger, Brian Curless, Tom Duchamp, David H. Salesin, and Werner Stuetzle, “Surface Light Fields for 3D Photography,” *Computer Graphics (SIGGRAPH 2000 Proceedings)*, pp. 287–296, July 2000. Cited on p. 444
- [1367] Wolberg, George, *Digital Image Warping*, IEEE Computer Society Press, 1990. Cited on p. 117, 119, 122, 146, 180, 199
- [1368] Wong, Tien-Tsin, Chi-Sing Leung, and Kwok-Hung Choy, “Lighting Precomputation Using the Relighting Map,” in Engel, Wolfgang, ed., *ShaderX<sup>3</sup>*, Charles River Media, pp. 379–392, 2004. Cited on p. 437
- [1369] Wonka, Peter, and Dieter Schmalstieg, “Occluder Shadows for Fast Walkthroughs of Urban Environments,” *Computer Graphics Forum*, vol. 18, no. 3, pp. 51–60, 1999. Cited on p. 679
- [1370] Wonka, Peter, Michael Wimmer, and Dieter Schmalstieg, “Visibility Preprocessing with Occluder Fusion for Urban Walkthroughs,” *11th Eurographics Workshop on Rendering*, pp. 71–82, June 2000. Cited on p. 679
- [1371] Wonka, Peter, Michael Wimmer, and François X. Sillion, “Instant Visibility,” *Computer Graphics Forum*, vol. 20, no. 3, pp. 411–421, 2001. Cited on p. 679, 680
- [1372] Wonka, Peter, *Occlusion Culling for Real-Time Rendering of Urban Environments*, Ph.D. Thesis, The Institute of Computer Graphics and Algorithms, Vienna University of Technology, June, 2001. Cited on p. 679
- [1373] Woo, Andrew, “Fast Ray-Box Intersection,” in Andrew S. Glassner, ed., *Graphics Gems*, Academic Press, pp. 395–396, 1990. Cited on p. 744
- [1374] Woo, Andrew, “The Shadow Depth Map Revisited,” in David Kirk, ed., *Graphics Gems III*, Academic Press, pp. 338–342, 1992. Cited on p. 352
- [1375] Woo, Andrew, Andrew Pearce, and Marc Ouellette, “It’s Really Not a Rendering Bug, You See...,” *IEEE Computer Graphics and Applications*, vol. 16, no. 5, pp. 21–25, September 1996. Cited on p. 539
- [1376] Woodland, Ryan, “Filling the Gaps—Advanced Animation Using Stitching and Skinning,” in Mark DeLoura, ed., *Game Programming Gems*, Charles River Media, pp. 476–483, 2000. Cited on p. 81, 83
- [1377] Woodland, Ryan, “Advanced Texturing Using Texture Coordinate Generation,” in Mark DeLoura, ed., *Game Programming Gems*, Charles River Media, pp. 549–554, 2000. Cited on p. 180, 222

- [1378] Woop, Sven, Jörg Schmittler, and Philipp Slusallek, “RPU: A Programmable Ray Processing Unit for Realtime Ray Tracing,” *ACM Transactions on Graphics*, vol. 24, no. 3, pp. 434–444, August, 2005. Cited on p. 876
- [1379] Worley, Steven, “Advanced Antialiasing,” in *Texturing and Modeling: A Procedural Approach*, third edition, Morgan Kaufmann, 2002. Cited on p. 180
- [1380] Wright, Richard, “Understanding and Using OpenGL Texture Objects,” *Gamasutra*, July 23, 1999. Cited on p. 172, 174, 712
- [1381] Wrotek, Paweł, Alexander Rice, Morgan McGuire, “Real-Time Collision Deformations using Graphics Hardware,” *Journal of graphics tools*, vol. 10, no. 4, pp. 1–22, 2005. Cited on p. 826
- [1382] Wu, David. Personal communication, 2002. Cited on p. 512, 516, 517, 520, 521, 522
- [1383] Wyatt, Rob, “Hardware Accelerated Spherical Environment Mapping using Texture Matrices,” *Gamasutra*, August 2000. Cited on p. 304
- [1384] Wyatt, Rob, “Curves on the RSX,” Insomniac Games presentation, 2007. Cited on p. 583
- [1385] Wyman, Chris, and Charles Hansen, “Penumbra Maps: Approximate Soft Shadows in Real-Time,” *Eurographics Symposium on Rendering (2003)*, pp. 202–207, June 2003. Cited on p. 371
- [1386] Wyman, Chris, “Interactive Image-Space Refraction of Nearby Geometry,” *GRAPHITE 2005*, pp. 205–211, November 2005. Cited on p. 398
- [1387] Wyman, Chris, “Interactive Refractions and Caustics Using Image-Space Techniques,” in Engel, Wolfgang, ed., *ShaderX<sup>5</sup>*, Charles River Media, pp. 359–371, 2006. Cited on p. 399
- [1388] Wyman, Chris, “Hierarchical Caustic Maps,” *ACM Symposium on Interactive 3D Graphics and Games (I3D 2008)*, pp. 163–172, February 2008. Cited on p. 398, 399
- [1389] Wynn, Chris, “Real-Time BRDF-based Lighting using Cube-Maps,” NVIDIA White Paper, 2001. <http://developer.nvidia.com> Cited on p. 267
- [1390] Wyszecki, Günther, and W. S. Stiles, *Color Science: Concepts and Methods, Quantitative Data and Formulae*, second edition, John Wiley & Sons, Inc., 1982. Cited on p. 283
- [1391] Wyvill, Brian, “Symmetric Double Step Line Algorithm,” in Andrew S. Glassner, ed., *Graphics Gems*, Academic Press, pp. 101–104, 1990. Cited on p. 11
- [1392] Xia, Julie C., Jihad El-Sana, and Amitabh Varshney, “Adaptive Real-Time Level-of-detail-based Rendering for Polygonal Objects,” *IEEE Transactions on Visualization and Computer Graphics*, vol. 3, no. 2, June 1997. Cited on p. 637
- [1393] Xiang, X., M. Held, and J.S.B. Mitchell, “Fast and Effective Stripification of Polygonal Surface Models,” *Proceedings 1999 Symposium on Interactive 3D Graphics*, pp. 71–78, April 1999. Cited on p. 554, 556
- [1394] Kun Xu, Kun, Yun-Tao Jia, Hongbo Fu, Shimin Hu, and Chiew-Lan Tai, “Spherical Piecewise Constant Basis Functions for All-Frequency Precomputed Radiance Transfer,” *IEEE Transactions on Visualization and Computer Graphics*, vol. 14, no. 2, pp. 454–467, Mar.–Apr. 2008. Cited on p. 436
- [1395] Yoon, Sung-Eui, Peter Lindstrom, Valerio Pascucci, and Dinesh Manocha “Cache-oblivious Mesh Layouts,” *ACM Transactions on Graphics*, vol. 24, no. 3, pp. 886–893, July 2005. Cited on p. 557, 658

- [1396] Yoon, Sung-Eui, and Dinesh Manocha “Cache-Efficient Layouts of Bounding Volume Hierarchies,” *Computer Graphics Forum*, vol. 25, no. 3, pp. 853–857, 2006. Cited on p. 658
- [1397] Yoon, Sung-Eui, Sean Curtis, and Dinesh Manocha, “Ray Tracing Dynamic Scenes using Selective Restructuring,” *Eurographics Symposium on Rendering (2007)*, pp. 73–84, June 2007. Cited on p. 822
- [1398] Yuksel, Cem, and John Keyser, “Deep Opacity Maps,” *Computer Graphics Forum*, vol. 27, no. 2, 2008. Cited on p. 371
- [1399] Zachmann, Gabriel, “Rapid Collision Detection by Dynamically Aligned DOP-Trees,” *Proceedings of IEEE Virtual Reality Annual International Symposium—VRAIS ’98*, Atlanta, Georgia, pp. 90–97, March 1998. Cited on p. 807
- [1400] Zarge, Jonathan, and Richard Huddy, “Squeezing Performance out of your Game with ATI Developer Performance Tools and Optimization Techniques,” *Game Developers Conference*, March 2006. [http://ati.amd.com/developer/gdc/2006/GDC06-ATI\\_Session-Zarge-PerfTools.pdf](http://ati.amd.com/developer/gdc/2006/GDC06-ATI_Session-Zarge-PerfTools.pdf) Cited on p. 270, 699, 700, 701, 702, 712, 713, 722, 847
- [1401] Zarge, Jonathan, Seth Sowerby, and Guennadi Riguer “AMD DirectX 10 Performance Tools and Techniques,” in Wolfgang Engel, ed., *ShaderX<sup>6</sup>*, Charles River Media, pp. 557–582, 2008. Cited on p. 698, 722
- [1402] Zhang, H., D. Manocha, T. Hudson, and K.E. Hoff III, “Visibility Culling using Hierarchical Occlusion Maps,” *Computer Graphics (SIGGRAPH 97 Proceedings)*, pp. 77–88, August 1997. Cited on p. 679
- [1403] Zhang, Hansong, *Effective Occlusion Culling for the Interactive Display of Arbitrary Models*, Ph.D. Thesis, Department of Computer Science, University of North Carolina at Chapel Hill, July 1998. Cited on p. 673, 679, 720
- [1404] Zhang, Fan, Hanqiu Sun, Leilei Xu, and Kit-Lun Lee, “Parallel-Split Shadow Maps for Large-Scale Virtual Environments,” *ACM International Conference on Virtual Reality Continuum and Its Applications 2006*, pp. 311–318, June 2006. Cited on p. 359
- [1405] Zhang, Fan, Hanqiu Sun, and Oskari Nyman, “Parallel-Split Shadow Maps on Programmable GPUs,” in Hubert Nguyen, ed., *GPU Gems 3*, Addison-Wesley, pp. 203–237, 2007. Cited on p. 359, 360
- [1406] Zhang, X., S. Redon, M. Lee, and Y.J. Kim, “Continuous Collision Detection for Articulated Models using Taylor Models and Temporal Culling,” *ACM Transactions on Graphics (SIGGRAPH 2005)*, vol. 26, no. 3, article 15, 2007. Cited on p. 827
- [1407] Zhou, Kun, Yaohua Hu, Stephen Lin, Baining Guo, and Heung-Yeung Shum, “Precomputed Shadow Fields for Dynamic Scenes,” *ACM Transactions on Graphics (SIGGRAPH 2005)*, vol. 24, no. 3, pp. 1196–1201, 2005. Cited on p. 430
- [1408] Zhou, Kun, Qiming Hou, Minmin Gong, John Snyder, Baining Guo, and Heung-Yeung Shum, “Fogshop: Real-Time Design and Rendering of Inhomogeneous, Single-Scattering Media,” *Pacific Graphics 2007*, pp. 116–125, October 2007. Cited on p. 500
- [1409] Zhukov, Sergei, Andrei Iones, Grigorij Kronin, “An Ambient Light Illumination Model,” *9th Eurographics Workshop on Rendering*, pp. 45–56, June–July 1998. Cited on p. 378, 381, 383
- [1410] Zioma, Renaldas, “Better Geometry Batching Using Light Buffers,” in Engel, Wolfgang, ed., *ShaderX<sup>4</sup>*, Charles River Media, pp. 5–16, 2005. Cited on p. 281, 282

- [1411] Zorin, Denis, Peter Schröder, and Wim Sweldens, “Interpolating Subdivision for Meshes with Arbitrary Topology,” *Computer Graphics (SIGGRAPH 96 Proceedings)*, pp. 189–192, August 1996. Cited on p. 616, 618
- [1412] Zorin, Denis, *C<sup>k</sup> Continuity of Subdivision Surfaces*, Caltech CS-TR-96-23, 1996. Cited on p. 643
- [1413] Zorin, Denis, *Stationary Subdivision and Multiresolution Surface Representations*, Ph.D. thesis, Caltech CS-TR-97-32, 1997. Cited on p. 614, 616, 618, 620
- [1414] Zorin, Denis, “A Method for Analysis of C1-Continuity of Subdivision Surfaces,” *SIAM Journal of Numerical Analysis*, vol. 37, no. 5, pp. 1677–1708, 2000. Cited on p. 643
- [1415] Zorin, Denis, Peter Schröder, Tony DeRose, Leif Kobbelt, Adi Levin, and Wim Sweldens, “Subdivision for Modeling and Animation.” *Course notes at SIGGRAPH 2000*, 2000. Cited on p. 610, 612, 615, 616, 618, 623, 624, 643
- [1416] Zwillinger, Dan, “CRC Standard Mathematical Tables and Formulas,” 31st Edition, CRC Press, 2002. Cited on p. 911, 919

# Index

- 1-ring, 614, 615
- 2-ring, 618
- 2.5 dimensions, 486
- 3DNow, 706
- A*-buffer, *see* buffer
- AABB, 650, 729, 731, 760, 762, 807
  - creation, 732
  - orthographic projection, 90
  - plane/box intersection, 755–756
  - ray/box intersection, 741–746
- AABB/AABB intersection, *see* intersection testing
- AABB/plane intersection, *see* intersection testing
- AABB/ray intersection, *see* intersection testing
- AABB/sphere intersection, *see* intersection testing
- absorption, 104
- acceleration algorithms, 15, 533, 645–695, 806, *see also* optimization
- accessibility shading, 378
- accumulation buffer, *see* buffer
- adaptive refinement, 133, 441
- adjacency graph, 543
- adjoint, *see* matrix
- AFR, 836
- albedo texture, 280
- aliasing, 117, 118
  - crawlies, 117
  - jaggies, 117, 119
  - perspective, 353
  - projective, 353
  - self-shadow, 350
  - shadow map, 350
  - temporal, 119, 161
  - texture, 161, 166
- alpha, 136, 137–141, 146, 181–183
  - blending, 135–136, 183
  - channel, 24, 139, 140, 182, 832
- LOD, *see* level of detail
- mapping, *see* texturing
- premultiplied, 139–140
- unmultiplied, 140
- alpha test, 24
- alpha to coverage, 135, 183, 491
- alternate frame rendering, 836
- AltiVec, 706
- ambient
  - aperture lighting, 429
  - color, 296
  - cube, 325, 424
  - light, 102, 295–296
- occlusion
  - dynamic, 373–385
  - field, 427
  - precomputed, 425–427
- reflectance, 296
- term, *see* lighting model
- angle difference relations, *see* trigonometry
- angle sum relations, *see* trigonometry
- animation, 77, 81, 180, 659
  - cel, 508
  - impostor, 461
  - particle system, 455
  - sprite, 445
  - subdivision, 643
  - texture, *see* texturing
  - vertex blending, *see* transform
- anisotropic
  - filtering, *see* texturing, minification
  - reflection, *see* BRDF
  - scaling, *see* transform, scaling, nonuniform
- anti-shadow, *see* shadow
- antialiasing, 116–134, 146
  - coverage sampling, 128–129
  - custom filter, 133
  - edge, 138
  - edge detect, 134

- full-scene, 126
- HRAA, 132
- jittering, 131
- line, 124
- multisampling, 128–132, 137
- N-rooks*, 131
- Quincunx, 132
- RGSS, 128
- screen based, 124–134, 183
- supersampling, 126, 126
  - rotated grid, 128, 873
  - texture, *see* texturing, minification
- application stage, *see* pipeline
- approximating
  - subdivision curve, *see* curves, subdivision
  - subdivision surface, *see* surfaces, subdivision
- $\arccos$ , *see* trigonometry
- $\arcsin$ , *see* trigonometry
- $\arctan$ , *see* trigonometry
- area calculation, 910–911
  - parallelogram, 910
  - triangle, 910
- artistic rendering, *see* non-photorealistic rendering
- Ashikhmin model, *see* BRDF
- aspect graph, *see* spatial data structure
- Assassin's Creed*, 495, 887
- $\text{atan2}$ , 7, 68
- atmospheric scattering, 499
- autostereoscopic, 837
- average cache miss ratio, 555
- axis-aligned bounding box, *see* AABB
- axis-aligned BSP tree, *see* spatial data structure, BSP tree
- B-spline, *see* curves, *and* surfaces
- Bézier
  - curves, *see* curves
  - patch, *see* surfaces
  - triangle, *see* surfaces
- back buffer, *see* buffer
- back plane, 90n
- backface culling, *see* culling
- backprojection, 372
- backwards mapping, 488
- baking, 537, 681
- balancing the pipeline, *see* pipeline
- banding artifacts, 128, 217, 832
- bandlimited signal, *see* sampling
- bandwidth, 847, 850–853
  - bus, 853
  - memory, 842, 850–852
- barycentric coordinates, 539, 747–748
- basis, 185, 301, 892–894
  - functions, 317
    - orthogonal, 317
    - orthonormal, 318
  - orientation, 901
  - orthogonal, 894
  - orthonormal, 894–895, 904
  - projection, 318, 431
  - standard, 7, 70, 319, 895, 904
  - tangent space, 628
- batch, 709
- BC, *see* texturing, compression
- Beer's Law, *see* Beer-Lambert Law
- Beer-Lambert Law, 393, 498
- bell curve, 468
- benchmarking, 834
- bent normal, 375–378
- Bernoulli number, 914
- Bernstein
  - form
    - Bézier curve, 581
    - Bézier patch, 594
    - Bézier triangle, 598
  - polynomial, 581, 594
  - Bézier triangle, 598
- bevel plane, 800
- BGR, 832n
- bias, 335
- bias factor, *see* shadow, shadow map
- bias parameter, *see* curves
- bidirectional reflectance distribution function, *see* BRDF
- bidirectional texture function, 461
- bilateral filter, 472
- bilinear interpolation, *see* interpolation
- billboard, 446–462, 500, *see also* impostor
  - axial, 454–455, 456
  - cloud, 462
  - particle, 455, 456
  - screen-aligned, 448
  - spherical, 454
  - world oriented, 448–454
- binary space partitioning tree, *see* spatial data structure, BSP tree
- binary tree, *see* tree
- binocular parallax, 836
- binormal vector, 185
- bintree, 569–570
- biquadratic surface, *see* surfaces
- bitangent vector, 185, 258, 269
- bitmask, 689
- blend shapes, *see* transform, morph targets

- blending, 24  
additive, 139, 486  
function, 581, 582, 588, 589  
    implicit surface, 607  
operations, *see* texturing  
surfaces, *see* surfaces, implicit
- Blinn and Newell's environment mapping,  
    *see* environment mapping
- Blinn lighting equation, *see* lighting  
    equation and BRDF
- blitting, 835
- blocking, *see* stage blocking
- bloom, 482
- BLT swapping, *see* blitting
- blue-screen matting, 140
- blur, 468–472  
    radial, 495, 499
- bokeh, 487
- Boost*, 705
- border, *see* texturing
- bottleneck, 12, 697, 699–702, 846
- bottom-up, *see* collision detection
- bounded Bézier curve, *see* curves
- bounding volume, 647, 762, 763  
    creation, 732–734  
    hierarchy, *see* spatial data structure  
    temporal, 650
- bowtie, *see* polygon
- box/plane intersection, *see* intersection  
    testing
- box/ray intersection, *see* intersection  
    testing
- box/sphere intersection, *see* intersection  
    testing
- BOXTREE, 803
- BRDF, 223–275  
    acquisition, 265  
    anisotropic, 229  
    Ashikhmin-Shirley, 241, 258, 261,  
        266  
    Banks, *see* BRDF, Kajiya-Kay  
    basis projection, 266–267  
    Blinn, 311  
    Blinn-Phong, 229, 257, 266  
    Cook-Torrance, 229, 261, 266  
    Cook-Torrance model, 267  
    databases, 265  
    diffraction, 262  
    environment map, 308–313  
    factorization, 267–268  
    fitting to measured data, 265–266  
    Hapke model, 229  
    HTSG, 266  
    HTSG model, 262  
    implementing, 269–275  
    isotropic, 224  
    Kajiya-Kay, 258  
    Lafortune, 266  
    Lambertian, 110, 227, 229  
    Lommel-Seeliger model, 229  
    lunar, 229  
    normalization, 253  
    Oren-Nayar, 262  
    Phong, 229, 252, 311  
    Poulin-Fournier, 266  
    re-parameterization, 267  
    reflectance lobe, 228, 229, 309–312  
    specular lobe, 228, 229, 309–312  
    theoretical models, 251–264  
    visibility term, 260  
    Ward, 258, 260, 266
- breadth-first traversal, 817
- BrightSide, 832
- BSDF, 226
- BSP tree, *see* spatial data structure
- BSSRDF, 225, 404
- BTDF, 226
- buffer  
    A-buffer, 129–131, 135  
    accumulation, 24  
        antialiasing, 126–128, 131–133  
        depth of field, 486  
        glossy effects, 389  
        motion blur, 492  
        soft shadow, 337  
    back, 25, 834  
    color, 23, 829–831, 831–832  
    compression, 854–856  
    deep, 279  
    double, 25, 834–835, 835  
    dual depth, 137  
    dynamic, 712  
    frame, 24, 829  
    front, 25, 834  
    G-buffer, 279, 441, 518  
    identification, 522, 726  
    memory, 837–838  
    pending, 835  
    photon, 399  
    single, 702, 833–834  
    static, 712  
    stencil, 24, 44, 838  
        glossy effects, 389  
        projection shadow, 335  
        reflection, 387–389  
        shadow volume, 340–348  
    stereo, 836–837  
    triple, 835–836

- Z-buffer*, 23–24, 44, 833, 838, 854, 888
  - compression, 854–856
  - hierarchical, *see* culling
  - shadow map, 348
- bump mapping, 147, 183–199
  - dot product, 187n
  - heightfield, 186–187
  - normal map, 176, 187–190, 270, 271, 419, 567
  - offset vector, 186
- bus, 850
  - bus bandwidth, *see* bandwidth
- BV, *see* bounding volume
- BV/BV intersection, *see* intersection testing
- BVH, *see* spatial data structure, bounding volume hierarchy
- $C^0$ -continuity, *see* continuity
- $C^1$ -continuity, *see* continuity
- cache, 703
  - memory, 172, 704
  - post T&L, 865
  - post-transform, 550, 866
  - pre T&L, 865
  - primitive assembly, 866
  - texture, 172–174, 847–849, 853, 867
    - thrashing, 712
  - vertex, 550, 865–866
- cache-oblivious mesh, *see* triangle mesh
- CAD, 441
- CAGD, 643
- camera gamma, *see* encoding gamma
- camera space, 17
- canonical view volume, 18, 90
- capability bits, 37
- capping, 343
- Cars*, 880
- cartoon rendering, *see* shading, toon
- cathode-ray tube, *see* CRT
- Catmull-Clark subdivision, *see* surfaces, subdivision
- Catmull-Rom spline, *see* curves
- caustics, 399–401
- ceil, 632
- Cel Damage*, 508, 512, 516
- cel rendering, *see* shading, toon
- cell, *see* culling, portal
- Cell Broadband Engine<sup>TM</sup>, 868–870
  - PPE, 868
  - SPE, 869
- cell-based visibility, 672, 679, 680
- central differencing, *see* differencing scheme
- centroid, 733
- CFAA, *see* antialiasing, custom filter
- Cg, 31, 51
- CgFX, 45
- Chaikin subdivision, *see* curves, subdivision
- change of base, *see* matrix
- character animation, *see* transform, vertex blending
- charcoal, 508
- chroma-keying, 140
- chromatic aberration, 396
- chromaticity, 214
  - diagram, 214
- Chromium*, 844
- CIE, 210, 212
- CIE chromaticity diagram, 214–215
- CIE XYZ, 213–217
- CIELAB, 216
- CIELUV, 216
- ciliary corona, 482
- circle of confusion, 487
- clamp, *see* texturing
- ClearType, 134
- clipmap, *see* texturing geometry, 573
- clipping, 19
  - clipping plane, 19
    - user-defined, 19, 389
  - clock gating, 874
- CLOD, *see* level of detail, continuous
- closed model, 545
- clouds, 371, 452
- CMYK, 217
- $C^n$ -continuity, *see* continuity
- code optimization, *see* optimization
- code profiler, 703
- CodeAnalyst*, 700, 705
- cofactor, *see* matrix, subdeterminant
- coherence
  - frame-to-frame, 458, 666, 693
    - collision detection, 812, 813
    - spatial, 556, 666
    - temporal, *see* coherence, frame-to-frame
- COLLADA FX, 45
- collision detection, 15, 793–827
  - bottom-up, 803, 821
  - bounding volume, 807
    - hierarchy, 802, 803
  - broad phase, 811–815, 824–826
  - cost function, 806–807

- COLLIDE, 824  
deformable, 820–822  
distance queries, 818–820  
dynamic, 797–802, 826  
GJK, 818  
GPU-based, 824–826  
grids, 814–815  
hierarchical, 802–807  
    grids, 815  
hierarchy building, 802–804  
incremental tree-insertion, 803–804  
multiple objects, 811–815  
OBBTree, 807–811  
parallel close proximity, 807  
pseudocode, 805  
RAPID, 811  
rigid-body motion, 794, 810  
SOLID, 809, 826  
sweep-and-prune, 812–814  
time-critical, 795, 816–817  
top-down, 803, 804, 821  
    OBBTree, 809–810, 826  
with rays, 795–796  
collision determination, 793  
collision handling, 793  
collision response, 784, 793, 817, 822–824  
    elastic, 823  
    restitution, 823  
color, 8, 146, 210–217  
    bleeding, 408  
    buffer, *see* buffer  
    correction, 474–475  
    matching, 210–213  
    mode, 831  
        high color, 831–832  
        true color, 831–832  
    perception, 217  
colorimetry, 210–217  
combine functions, *see* texturing,  
    blending operations  
common-shader core, 30, 36  
communication, 846  
compositing, 139, 146  
compression, *see* texturing, *see also* buffer,  
    Z-buffer, 854  
computational photography, 444, 533  
Computer Aided Geometric Design, 643  
concatenation, *see* transform  
consolidation, *see* polygonal techniques  
constant buffer, 32  
constant register, 32  
constructive solid geometry, 606  
continuity, *see also* curves and surfaces  
     $C^0$ , 587, 600, 604  
     $C^1$ , 587, 604, 606  
     $C^n$ , 587  
     $G^1$ , 587, 605, 606  
     $G^n$ , 587  
continuity parameter, *see* curves  
continuous signal, *see* sampling  
contour, *see* polygon  
contour lines, 154  
contouring artifacts, *see* banding artifacts  
control mesh, 612  
control points, 579  
convex hull, 733, 765, 766, 798, 810,  
    909–910  
    Bézier curve, 581  
    Bézier patch, 595  
    Bézier triangle, 599  
    Loop, 616  
convex region, *see* polygon  
convolution, 122  
    spherical, 321  
Cook-Torrance model, *see* BRDF  
cookie, 222, 340  
*Coolbits*, 701  
coordinate system  
    left-handed, 89, 92  
    right-handed, 89, 542, 893  
corner cutting, 608  
corona, *see* ciliary corona  
cos, *see* trigonometry  
counterclockwise vertex order, 59, 542,  
    543, 662  
coverage mask  
    A-buffer, 129  
CPU, 864  
CPU-limited, 700  
cracking, 539–541, 632  
    Bézier triangle, 603  
    fractional tessellation, 631  
    N-patch, 603  
    polygon edge, 539–541  
    quadtree, 639  
    terrain, 570  
    tessellation, 635  
Cramer's rule, *see* matrix, inverse  
crawlies, *see* aliasing, 117  
crease, 625  
critical angle, 237  
cross product, 73n, 896–897  
    notation, 7  
CrossFire X, 835  
crossings test, *see* intersection testing  
CRT, 141, 830–831  
phosphors, 216

- Crysis*, 190, 197, 378, 382, 384, 395, 437, 453, 502, 881
- CSAA, *see* antialiasing, coverage sampling
- CSG, 606
- CSM, *see* shadow, map, cascaded
- CTM, 36, 841, 883
- cube map, 154, 171
- cube texture, 171
- cube/polygon intersection, *see* intersection testing
- CubeMapGen, 172, 310, 312
- cubic convolution, *see* texturing, magnification
- cubic curve, *see* curves
- cubic environment mapping, *see* environment mapping
- CUDA, 36, 478, 841, 883
- culling, 660–680
  - approximate visibility, 679
  - backface, 662–664, 714
    - orientation consistency, 59
    - PLAYSTATION® 3, 866
  - clustered backface, 664
  - detail, 670
  - early-Z, 643, 857–858, 873
  - frontface, 663
  - hardware occlusion query, 674–677
  - hierarchical Z-buffering, 677–679
  - hierarchical view frustum, 664–667, 718, 771
  - image-space, 672, 674, 677, 679
  - incremental occlusion maps, 680
  - object-space, 672
  - occlusion, 652, 670–680, 720
    - hardware, 856–857
    - PLAYSTATION® 3, 866
    - representation, 672
  - portal, 461, 667–670, 720
  - programmable, 858–859
  - ray-space, 672
  - shaft occlusion, 680
  - view frustum, 664–667, 718, 771- Z, 643, 677, 854, 856–857, 858, 862, 866, 872, 876
- Zmax, 856–857
- Zmin, 857

curve segment, 589

curved surfaces, *see* surfaces

curves
 
  - B-spline, 609, 610
  - Bézier, 578–583
    - Bernstein, 581–583
    - de Casteljau, 579
  - derivative, 583
  - rational, 583–584

bias parameter, 590

bounded Bézier, 584–585

Catmull-Rom spline, 590

continuity, 585–587

continuity parameter, 591

cubic, 579, 582, 589

degree, 579

GPU rendering, 584–585

Hermite, 587–589, 589

Kochanek-Bartels, 589–592

parametric, 576–592

piecewise, 585

quadratic, 579, 581, 582

quartic, 579

S-shaped, 587, 637

spline, 589, 643

subdivision, 608–611
 
  - approximating, 609
  - Chaikin, 608
  - interpolating, 609
  - limit, 608
  - tension parameter, 589, 609

cylinder, 798–799

D3D runtime, 700

DAC, *see* digital-to-analog converter

DAG, *see* directed acyclic graph

dart, 625

data reduction, *see* simplification, 561

dataflow, 841

*Day of Defeat: Source*, 475

DDRAM, 852

de Casteljau
 
  - Bézier curves, 579
  - Bézier patches, 594
  - Bézier triangles, 598

decaling, 181

decimation, *see* simplification, 561

deferred shading, *see* shading

demo scene, 415

dependent texture read, *see* texture depth
 
  - buffer, *see* buffer, Z-buffer
  - clamp, 344
  - complexity, 282, 670, 671, 715, 716, 851
  - cueing, 496
  - of field, 126, 484, 486–489
  - peeling, 136, 137, 282, 352, 372, 392, 395, 398, 501, 825
  - sprite, *see* impostor

- determinant, *see* matrix  
    notation, 7
- dielectric, 235
- difference object, 818
- differential pulse code modulation, 855
- diffuse color, 228, 240
- diffuse term, 105
- diffusion, 404  
    texture space, 404
- digital visual interface, 830
- digital-to-analog converter, 830
- dihedral angle, 510, 517, 546
- dimension reduction, *see* intersection testing
- direct memory access, *see* DMA
- Direct3D, 21n
- directed acyclic graph, 659
- direction  
    principal, 526
- directional light, *see* light, source, directional
- directional occlusion  
    precomputed, 428–430
- discrete geometry LOD, *see* level of detail
- discrete oriented polytope, *see* k-DOP
- discretized signal, *see* sampling
- displaced subdivision, *see* surfaces, subdivision
- displacement mapping, 148, 196, 198–199, 626, 627, 633
- display gamma, 142
- display hardware, 829–831
- display list, 660
- DisplayPort, 830
- distance attenuation, *see* lighting equation
- distance fields, 160, 382, 826
- distance queries, *see* collision detection
- dithering, 832
- division, 706
- DMA, 869
- domain, 577  
    rectangular, 593  
    triangular, 598
- Doom, 653, 695
- dot product, 73n, 891, 894  
    notation, 7
- dots per inch, 645
- double angle relations, *see* trigonometry
- double buffer, *see* buffer
- downsampling, 123, 471, 483
- DRAM, 703
- draw call, 31
- driver, *see* graphics, driver
- dual-color blending, 45, 141
- dueling frusta, 357
- DVI, 830
- DXTC, *see* texturing, compression
- dynamic  
    intersection testing, *see* intersection testing  
    separating axis test, *see* intersection testing, separating axis test
- dynamic buffer, *see* buffer, dynamic
- dynamically adjusted BSP tree, *see* spatial data structure, BSP tree
- ear clipping, 536
- early z pass, 282, 716, 858
- early-Z culling, *see* culling
- edge, 510–512, *see also* line border, 510  
    boundary, 510, 511, 518, 522, 543, 566
- bridge, 537
- collapse, *see* simplification
- crease, 510, 511, 517, 518, 546, 566, 603
- detection  
    Sobel, 518
- feature, 510
- hard, 510
- highlighting, *see* line
- join, 537
- keyholed, 537
- material, 511, 511  
    preservation, 546
- ridge, 511, 517
- stitching, *see* polygon
- valley, 511, 517
- eigenvalue, *see* matrix
- eigenvector, *see* matrix
- elastic collision response, *see* collision response
- electron beam, 830
- EM, *see* environment mapping
- EMBM, *see* bump mapping, environment map
- emissive term, *see* lighting model
- encoding gamma, 142
- energy efficiency, 870
- enveloping, *see* transform, vertex blending
- environment map bump mapping, *see* bump mapping
- environment mapping, 297–313  
    Blinn and Newell's method, 300–301, 304
- BRDF, *see* BRDF

- cubic, 304–307, 316
- filtering, 308–313
- irradiance, 314–325, 423
- limitations of, 298, 313
- parabolic mapping, 307–308, 361
- silhouette rendering, 512
- sphere mapping, 301–304
- with normal mapping, 299
- Ericsson Texture Compression, *see* texturing, compression
- ETC, *see* texturing, compression, Ericsson
- Euclidean space, 889–892
- Euler angles, 55, 66, 69, 78
- Euler transform, *see* transform
- Euler–Mascheroni constant, 716
- Euler–Poincaré formula, 554, 562
- EVS, *see* exact visible set
- EWA, 170
- exact visible set, 661
- exitance, 105, 204, 411
- explicit surface, *see* surfaces
- extraordinary vertex, 614
- eye space, 17, 26
- faceter, 533
- factorization, *see* BRDF
- fairness, 616
- falloff function, 219, 293
- false shadow, *see* shadow
- fan, *see* triangle fan
- Far Cry*, 277, 421, 485, 710
- far plane, 90, 96, 771
- Feline, 170
- FIFO, 719, 720, 846
- fill bounded, *see* fill limited
- fill rate, 702
- film frame rate, 490
- filter
  - rotation-invariant, 468
  - separable, 471, 484
  - steerable, 483
- filtering, 117, 117–124, 132, 468
  - box filter, 120, 144
  - Gaussian filter, 123, 132, 468, 484
  - kernel, 471
  - lowpass filter, 121, 124
  - nearest neighbor, 120
  - sinc filter, 122–123, 468
  - support, 471
  - television, 831
  - tent filter, 120
  - triangle filter, 120
- fin, 504, 522
- final gather, 417
- first principal direction, 526
- five times rule, 206
- fixed-function pipeline, *see* pipeline, fixed-function
- fixed-view effects, 440–443
- flat shading, *see* shading
- FLIPQUAD, 133
- floor, 632
- flow control, 33
  - dynamic, 33
  - static, 33
- fluorescence, *see* light, emission
- flush, *see* pipeline
- fog, 496–502
  - color, 496
  - exponential, 497
  - factor, 496
  - glossy reflection, 389
  - linear, 497
  - pixel level, 498
  - radial, 499
  - vertex level, 498
  - volumetric, 501
- force feedback, 15
- form factor, 409
- forward differencing, *see* differencing scheme
- forward mapping, 487
- fps, 702
- fragment, 22, 137
  - A-buffer, 129
  - generation, 843
  - merge, 843
  - shader, *see* pixel, shader
- frame
  - buffer, *see* buffer
  - map, 270
  - rate, 1, 719
    - constant, 461, 691–692
- frame-to-frame coherence, *see* coherence
- frames per second, 13
- Fresnel effect, 232
- Fresnel equations, 230
- Fresnel reflectance, 230
  - Schlick approximation, 233, 247, 297
- front buffer, *see* buffer
- Frostbite*, 882
- frosted glass, 389
- frustum, 19, 771
  - intersection, *see* intersection testing
  - plane extraction, 773–774
- frustum/object intersection, *see* intersection testing
- FSAA, *see* antialiasing, full-scene

- Fusion*, 883  
*FX Composer*, 36, 40, 45, 46, 49, 50, 886
- $G^1$ -continuity, *see* continuity  
gamma correction, 141–145, 146, 164  
gamut, 215–216, 236  
    sRGB, 236  
gather operation, 488  
Gaussian elimination, *see* matrix, inverse  
genus, 554  
geodesic curve, 78  
geometric sum, 649  
geometrical attenuation factor, *see* geometry, factor  
geometry  
    factor, 248  
    patch, 640  
    shader, 29, 40–42, 113, 306, 467, 487, 490, 504, 522, 558, 576, 700, 711, 727  
    particles, 456  
    shadows, 347  
    stage, *see* pipeline  
    unit, 842  
    PLAYSTATION® 3, 865  
geomorph LOD, *see* level of detail  
gimbal lock, *see* transform, Euler  
GJK, *see* collision detection  
glare effects, 482  
global illumination, 328, 389, 416, 444  
    full, 407  
glow, 481  
`glPolygonOffset`, 335, 514  
GLSL, 31, 35, 51, 871  
GLslang, 35  
 $G^n$ -continuity, *see* continuity  
gobo, 222, 340, 502  
golden thread, 441  
goniometer, 265  
Gooch shading, 45, 519  
Gouraud shading, *see* shading  
GPGPU, 36, 841, 861, 883  
GPU, 14, 840, 864, *see also* hardware  
gradient  
    pixel, 43, 165  
graftals, 526  
graphics  
    driver, 700, 712, 834, 841  
    processing unit, *see* GPU  
    rendering pipeline, *see* pipeline  
graphics processing unit, *see* GPU  
grayscale  
    conversion to, 215–216  
greedy algorithm, 553
- green-screen matting, 140  
grids, *see* collision detection
- hair, 371, 504–505  
hairy ball theorem, 67  
half vector, 111, 247  
half-angle relations, *see* trigonometry  
half-edge, 543  
*Half-Life 2*, 276, 420, 421, 424, 425, 429, 436  
*Half-Life 2: Lost Coast*, 479  
half-plane  
    test, 907, 909  
half-space, 6  
halo, 482  
haloing, *see* line  
handedness, 893  
    left-handed basis, 893, 901  
    right-handed basis, 893, 901  
hard real time, 691  
hardware  
    GeForce 256, 29, 840  
    GeForce 7800, 864  
    GeForce 8800, 876  
    GeForce256, 840  
    GeForce3, 34, 344, 841, 853  
    InfiniteReality, 117, 131  
    Mali, 844  
    Mali architecture, 870–875  
    MBX/SGX, 871  
    Pixel-Planes, 8n, 871, 875  
    PixelFlow, 846, 875  
    PLAYSTATION® 3, 845, 850, 863–870  
    Pomegranate, 846  
    PowerVR, 871  
    Radeon, 169, 855  
    Radeon HD 2000, 133, 630  
    Talisman, 170, 446  
    VISUALIZE fx, 675  
    Voodoo 1, 1  
    Voodoo 2, 840  
    Wii, 26, 35  
    Xbox, 849  
    Xbox 360, 849, 859–863  
harmonic series, 716  
HDMI, 830  
HDR, 480–481  
HDRI, 481  
HDTV, 143  
    phosphors, 216  
He's lighting model, *see* lighting model  
head, 66, 68  
headlight, 324

- heads-up display, 455  
height correlation, 249  
heightfield, 463–466, 569, *see also* bump mapping  
terrain, 568, 569  
*Hellgate: London*, 299, 332, 358, 359, 504  
Helmholtz reciprocity, 226, 240  
hemisphere lighting, 324, 425  
Hermite curves, *see* curves  
Hermite interpolation, *see* interpolation  
Hertz, 13  
hidden line rendering, *see* line  
hierarchical  
  Z-buffering, *see* culling  
  image caching, *see* impostor  
  occlusion map, *see* culling, HOM algorithm  
  spatial data structure, *see* spatial data structure  
  view frustum culling, *see* culling, *see also* culling  
hierarchical grids, *see* collision detection  
hierarchy building, *see* collision detection  
high color mode, *see* color  
high dynamic range imaging, *see* HDRI  
high level shading language, *see* HLSL  
high-definition multimedia interface, 830  
highlighting  
  selection, 527  
Hilbert curve, 556  
histogram, 477  
hither, 90n  
HLS, 217  
HLSL, 31, 35, 51  
HLSL FX, 45  
homogeneous notation, 5, 54, 58, 153, 905–906  
homogenization, 59, 89, 905  
horizon mapping, 428  
horizontal refresh rate, *see* refresh rate  
horizontal retrace, *see* retrace  
hourglass, *see* polygon  
HSB, 217  
HUD, 455  
hue, 214  
hyperbolic interpolation, *see* interpolation  
HyperZ, 857  
hysteresis, *see* level of detail  
HZB culling, *see* culling, hierarchical  
  Z-buffering  
IBR, *see* image-based rendering  
IHV, 37  
 Illuminant E, 214  
image  
  geometry, 467  
  processing, 467–473  
  pyramid, 677, 678  
  size, *see* texturing  
image-based rendering, 208, 439  
imaging sensor, 107–110  
IMMPACT, 826  
implicit surface, *see* surfaces  
importance sampling, 414, 426  
impostor, 450, 457–462, 693  
  depth sprite, 463–464  
  hierarchical image caching, 461  
  layered depth image, 464  
  multimesh, 466  
  point-based, 467  
  sprite, 457  
incandescence, *see* light, emission  
incremental occlusion maps, *see* culling  
incremental tree-insertion, *see* collision detection  
index buffer, *see* vertex buffer, 558–561  
index of refraction, 231  
indexed vertex buffer, *see* vertex, buffer  
inflection, 587  
inline code, 707  
inner product, 317  
input assembler, 38  
instance, 16, 659  
instancing, 39, 711  
insulator, 235  
intensity, 205  
interactivity, 1  
interface, *see* hardware  
interlacing, 831  
interleaved sampling, 131  
intermediate language, 31  
interpolating  
  subdivision curve, *see* curves, subdivision  
  subdivision surface, *see* surfaces, subdivision  
interpolation, 643  
  barycentric, 747  
  bicubic, 158  
  bilinear, 158–159, 161, 592–593  
  centroid, 128  
  Hermite, 587–592  
  hyperbolic, 838  
  linear, 578  
  perspective-correct, 838–840  
  quadrilinear, 170  
  rational linear, 839

- repeated, 598
  - bilinear, 594
  - linear, 578–581
- rotation invariant, 539
- trilinear, 166
- intersection testing, 725–792
  - $k$ -DOP/ $k$ -DOP, 765–767
  - $k$ -DOP/ray, 744
  - AABB/AABB, 765
  - box/plane, 755–757
  - box/ray, 741–746
    - ray slope, 746
    - slabs method, 742–744
  - BV/BV, 762–771
  - convex polyhedron/ray, 744
  - crossings test, 752–755
  - dimension reduction, 737
  - dynamic, 783–791, 797–802
  - dynamic separating axis test, *see* intersection testing, separating axis test
  - dynamic sphere/plane, 784–785
  - dynamic sphere/polygon, 787–791
  - dynamic sphere/sphere, 785–786
  - frustum, 771–778
  - frustum/box, 777–778
  - frustum/ray, 744
  - frustum/sphere, 774–777
  - hardware-accelerated, 726–727
  - interval overlap method, 757–760
  - line/line, 780–782
  - OBB/OBB, 767–771
    - SAT lite, 808
  - octant test, 776, 778
  - picking, 725–726
  - plane/ray, 751
  - polygon/ray, 750–755
  - rejection test, 731
  - rules of thumb, 737–738
  - separating axis, 731
  - separating axis test, 731, 744, 757, 760, 761, 766, 767, 777
    - dynamic, 791
    - lite, 808
  - shaft/box, 778–780
  - sphere/box, 763–765
  - sphere/ray, 738–741
  - sphere/sphere, 763
  - static, 783
  - three planes, 782–783
  - triangle/box, 760–762
  - triangle/ray, 746–750
  - triangle/triangle, 757–760
- interval arithmetic, 858
- interval overlap method, *see* intersection testing
- intrinsic functions, 33
- inverse displacement mapping, *see* texturing, relief
- irradiance, 102, 203, 314, 409
  - map, *see* environment mapping
  - volume, 423
- irregular vertex, 614
- isocube, 306
- isosurface, 502, 606, 607
- isotropic scaling, *see* transform, scaling, uniform
- jaggies, *see* aliasing, 117
- Java ME, 877
- jittering, 60, *see* antialiasing, 389
- joint, 578, 585, 587, 590
- Jordan curve theorem, 752
- joule, 203
- $k$ -ary tree, *see* tree
- $k$ -d tree, *see* spatial data structure
- $k$ -DOP, 675, 730, 731, 744, 762, 765, 783, 807
  - collision detection, 807
  - creation, 732
- key, 479
- Killzone 2, 280, 493
- Kochanek-Bartels curves, *see* curves
- LAB, 216
- Lafortune model, *see* BRDF
- Lambert's law, 110
- Lambertian shading, *see* BRDF, Lambertian
- Nehalem, 883
- latency, 1, 704, 717, 719–721, 835, 842, 847, 853–854, 861
  - occlusion query, 674
- latitude, 300, 728
- law of cosines, *see* trigonometry
- law of sines, *see* trigonometry
- law of tangents, *see* trigonometry
- layered depth image, *see* impostor
- layered distance map, 392
- lazy creation, 804
- LCD, 134, 830–831
- LDI, *see* impostor, layered depth image
- least-crossed criterion, 653
- left-handed, *see* coordinate system
  - basis, *see* handedness
- lens flare, 482
- lenticular display, 837

- level of detail, 576, 680–693, 718, 720  
 alpha, 684–686  
 benefit function, 687, 692  
 bias, 166, *see also* texturing  
 blend, 684  
 continuous, 562, 569, 571, 573, 630, 686  
 cost function, 691  
 discrete geometry, 683  
 fractional tessellation, 631  
 generation, 681  
 geomorph, 686–691  
 hysteresis, 690–691  
 N-patch, 603  
 popping, 567, 683, 684, 685  
 projected area-based, 688–690  
 range-based, 688  
 selection, 681, 687–691  
 simplification, 567  
 subdivision surface, 611  
 switching, 681, 683–687  
 time-critical, 680, 691–693
- LIC, *see* line, integral convolution  
 LIDAR, 533  
 light  
   absorption, 393  
   adaptation, 475, 478  
   attenuation mask, 340  
   back, 324  
   baking on, 714  
   bidirectional, 324  
   bleeding, 369  
   field, 208  
   fill, 324  
   key, 324  
   leak, 352–353, 369, 370  
   mapping, *see* texturing  
   meter, 103, 204, 210  
   probe, 301  
   rim, 324  
   source, 100–104, 713  
     area, 289–295, 331, 337  
     directional, 100  
     point, 206  
     spot, 220  
     spotlight, 418  
     volume, 331  
   three-point, 324  
   vector, 100  
 light-field rendering, 444  
 lighting equation, 146, *see also* BRDF  
   Phong, 201  
 Lightspeed Memory Architecture, 857
- limit  
   curve, 608, 610  
   surface, 615  
   tangent, 618
- Lindstrom, 569
- line, 19, 527–530, 906–908, *see also* edge drawing, 11  
 edge highlighting, 527  
 haloing, 528, 530  
 hidden-line rendering, 528–529  
 integral convolution, 492  
 polygon edge rendering, 527–528  
 three-dimensional, 908  
   explicit, 908  
   implicit, 908  
 two-dimensional, 906–908  
   explicit, 906  
   implicit, 906
- line/line intersection, *see* intersection testing
- linear algebra, 889–911  
 linear independence, 892–893  
 linear interpolation, *see* interpolation  
 linear speedup, 721  
 LiSPSM, *see* shadow, map, light space perspective  
*LittleBigPlanet*, 425, 886  
 LMA, 857  
 load balance, 846  
 load balancing, 861  
 local frame, 258  
 local lighting model, *see* lighting model  
 LOD, *see* levels of detail  
 log, 8  
 longitude, 300, 728  
 look-up table, 474, 689  
 loop, *see* silhouette, *see* polygon  
 Loop subdivision, *see* surfaces, subdivision  
 loop unrolling, 707  
 loose octree, *see* spatial data structure  
 lossy compression, *see* texturing, compression  
*Lost Planet*, 495, 504  
 LSPSM, *see* shadow, map, light space perspective  
 LU decomposition, *see* matrix, inverse  
 Lumigraph, 444  
 luminaire, 217  
 luminance, 212, 215  
 luminescence, *see* light, emission  
 LUT, *see* look-up table  
 LUV, 216

- M3G, 877  
Möbius strips, 543  
Macbeth ColorChecker, *see* Munsell ColorChecker  
Mach banding, 832, 832  
MacLaurin series, *see* trigonometry  
macroscale, 107, 184, 271  
magnification, *see* texturing  
mailbox, 651  
main axes, 7  
manifold, 352, 545  
map  
  caustic, 400  
marching cubes, 607  
marching tetrahedra, 607  
mask, 614  
masking  
  perceptual, 217  
  shader, 31  
material, 104–107  
matrix, 897–905, *see also* transform  
  addition, 898  
  adjoint, 901–902  
  change of base, 904–905  
  column-major, 61n, 890  
  definition, 897  
  determinant, 59, 900–901  
  eigenvalue, 903–904  
  eigenvector, 734, 903–904  
  homogeneous form, 905  
  identity, 897, 903, 904  
  multiplication, 899  
  orthogonal, 65, 68, 76, 904  
    rotation, 57, 66  
  row-major, 61n, 92  
  scalar multiplication, 898  
  subdeterminant, 901  
  trace, 57, 76, 898  
  transpose, 59, 898  
    notation, 7  
matte, 139  
MB subdivision, *see* surfaces, subdivision,  
  modified butterfly  
MBX/SGX, *see* hardware  
mean width, 736  
memory  
  allocation, 705  
  architecture, 849–850  
  bandwidth, *see* bandwidth  
  bank, 853  
  dynamic random access, 703  
  optimization, *see* optimization  
  tiled, 868  
UMA, 849  
  unified, *see* unified memory  
  architecture  
memory hierarchy, 703  
mental mill, 36  
merging  
  pixel, 23–25  
merging stage, 23–24, 44–45  
mesh, *see* polygon  
mesh parameterization, 153  
mesoscale, 107, 183–184, 271  
message-passing architecture, *see*  
  multiprocessing  
metaball, 42, 533, 606  
metal, 235  
metamers, 212  
microfacets, 246–249  
microgeometry, 241–246  
  masking, 244  
  shadowing, 243  
micropatch, 372  
micropolygon, 26  
microscale, 107, 184, 241, 271  
minification, *see* texturing  
Minkowski sum, 787, 789, 791, 798, 819  
mipmap chain, 163  
mipmapping, *see* texturing, minification  
mirror transform, *see* transform, reflection  
model space, 16, 842  
modeler, 532–533, 535, 547  
  solid, 532–533  
  surface, 533  
modified butterfly subdivision, *see*  
  surfaces, subdivision  
modulate, *see* texturing, blending  
  operations  
Mollweide's formula, *see* trigonometry  
monitor, 141, 830–831  
  gamut, 216  
Moore's Law, 880  
morph targets, *see* transform  
morphing, *see* transform  
Morton sequence, 849  
mosaicing, *see* texturing, tiling  
motion blur, 126, 490–496  
motion parallax, 837  
MRT, 44  
MSAA, *see* antialiasing, multisampling  
multi-view rendering, 836–837  
multicore, 717  
multipass lighting, 278  
multipass rendering, 857  
multiple angle relations, *see* trigonometry

multiprocessing, 716–722, 846  
  dynamic assignment, 721  
  message-passing, 716  
  parallel, 720–722  
  pipeline, 717–720  
  shared memory multiprocessor, 716  
  static assignment, 721  
  symmetric, 717

multisampling, *see* antialiasing

multitexturing, *see* texturing

multum in parvo, 163

Munsell ColorChecker, 145

N-patch, *see* surfaces

nailboard, *see* impostor, depth sprite

NDF, *see* normal, distribution function

near plane, 90, 96, 688, 771

nearest neighbor, *see* texturing and filtering

negatively oriented, *see* handedness, left-handed basis

*Nehalem*, 883

Newell's formula, 535

Newton's formula, *see* trigonometry

node, 648–649  
  internal, 648  
  leaf, 648  
  root, 648

noise function, *see* texturing

non-photorealistic rendering, 507–526  
  stylistic rendering, 507

noncommutativity, 61, 72, 899

norm of vector, *see* vector

normal  
  cone, 664  
  distribution function, 246, 273  
  map, 258  
  incidence, 232  
  map, *see* bump mapping  
  transform, *see* transform

normal-patches, *see* surfaces, N-patch

normalize vector, *see* vector

normalized device coordinates, 19, 90

north bridge, 859, 860

NPR, *see* non-photorealistic rendering

*N*-rooks sampling, 131

NTSC, 217  
  phosphors, 216

NURBS, *see* surfaces

Nusselt analog, 410

`NV_depth_clamp`, 344

`NvTriStrip`, 552, 573

Nyquist limit, *see* sampling

OBB, 729–730, 731, 762, 807  
  collision detection, 807–809  
  plane/box intersection, 757  
  ray/box intersection, 742–744

OBB/OBB intersection, *see* intersection testing

OBB/plane intersection, *see* intersection testing

OBB/ray intersection, *see* intersection testing

OBBTTree, *see* collision detection

obscuration, 378, 379, 381, 383, 426

occluder, 673  
  shrinking, 679  
  virtual, 680

occluding power, 673

occlusion  
  culling, *see* culling  
  horizons, *see* culling  
  reflection, 430

octant test, *see* intersection testing

octree, *see* spatial data structure

octree texture, 171

*Okami*, 508, 509, 881

omni light, 218

opacity  
  spectral, 141

OpenEXR format, 481

OpenGL ARB, 37

OpenGL ES, 176, 870, 873, 877

OpenRT, 646

OpenSG, 552, 573

optimal placement, *see* simplification

optimization  
  application stage, 703–707  
  code, 703–707  
  geometry stage, 713–714  
  lighting, 713–714  
  memory, 704–707  
  pipeline, 697–723  
  pixel shader, 711, 716, 857  
  rasterizer stage, 714  
  vertex shader, 711

ordinary vertex, 614

Oren and Nayar model, *see* BRDF

orientation, 56, 65, *see* polygon

oriented bounding box, *see* OBB

orthogonal  
  decomposition, 895  
  vectors, 891

outline, *see* polygon, with multiple outlines

over operator, 136–140, 393, 684

overblurring, 166

- overclock, 701  
overdraw, 851  
oversampling, *see* supersampling
- packed pixel format, 832  
padding, 705  
page flipping, 834  
painter's algorithm, 654  
painterly rendering, 508  
parabola, 579  
parabolic mapping, *see* environment mapping  
paraboloid mapping, *see* environment mapping  
parallax, 443, 460, 460  
    barrier display, 837  
    mapping, 191–193  
    occlusion mapping, *see* texturing, relief
- parallel  
    close proximity, *see* collision detection  
    graphics, 723, 842  
    processing, *see* multiprocessing  
    projection, *see* projection, orthographic
- parallelism, 720  
    spatial, 717  
    temporal, 717
- parameter space values, *see* texturing
- parametric  
    curves, *see* curves  
    surfaces, *see* surfaces
- particle, 39n  
    soft, 452–454  
    system, 455–456
- patch, 593
- path planning, 818
- PCF, *see* percentage-closer filtering
- PCI Express, 712, 849, 850, 883
- PCIe, 850
- PCU, *see* culling, programmable, 876
- PDI, 422
- Peano curve, 556
- pen and ink, 508
- pending buffer, *see* buffer
- penetration depth, 818
- penumbra, *see* shadow
- penumbra map, *see* shadow, map,  
    penumbra method
- penumbra wedge, 348
- per-polygon operations, *see* per-vertex operations
- per-vertex operations, 15
- percentage-closer filtering, 361–366
- performance measurement, 702
- perf dot product, 6, 780, 781
- perspective projection, *see* projection
- perspective-correct interpolation, *see* interpolation
- Peter Panning, 352
- Phong lighting equation, *see* lighting equation and BRDF
- Phong lobe, 257
- Phong shading, *see* shading
- phosphor, 214–216
- phosphorescence, *see* light, emission
- photogrammetry, 532, 533
- photometric curve, 209, 212, 216
- photometry, 209–210
- photon mapping, 399, 416
- photons, 202
- photorealistic rendering, 440, 507
- pick window, *see* intersection testing
- picking, 725–726, 728, 740
- piecewise  
    Bézier curves, *see* curves  
    smooth subdivision, *see* surfaces, subdivision
- ping-pong buffers, 472, 483
- pipeline, 11–27, 697–723  
    application stage, 12, 14–15, 697  
    conceptual stages, 12  
    fixed-function, 26, 201, 220, 467,  
        496, 701  
        lighting, 219  
    flush, 711, 854  
    functional stages, 13  
    geometry stage, 12, 15–20, 697  
    rasterizer stage, 12, 21–25, 697  
    software, 718  
    speedup, 12  
    stage, 12–14, 841–842
- Pirates of the Caribbean*, 381
- pitch, 66, 68
- pixel, 21n, 125n  
    overdraw, 716  
    processor, *see* pixel, shader  
    shader, 29, 42–44, 137  
        depth sprite, 464  
    PLAYSTATION® 3, 866–868
- Pixel-Planes, *see* hardware
- pixelation, 158
- PixelFlow, *see* hardware
- pixels per second, 702
- Planck's constant, 202
- plane, 6, 908–909  
    axis-aligned, 7

- coordinate, 7
- explicit, 908
- implicit, 908
- sweep, 535
- plane/AABB intersection, *see* intersection testing
- plane/box intersection, *see* intersection testing
- plane/OBB intersection, *see* intersection testing
- plane/ray intersection, *see* intersection testing
- PLAYSTATION® 3, 35
- PLAYSTATION® 3, *see* hardware
- PN triangle, *see* surfaces, N-patch
- point, 893, 905, 906
- point clouds, 533
- point rendering, 534, 693–695
- point-based visibility, 672
- pointer indirection, 704
- Poisson disk, 132, 365, 366, 488
- polycube maps, 151
- polygon
  - area, 910–911
  - bowtie, 535
  - contour, 537
  - convex region, 536
  - degree, 552
  - edge cracking, *see* cracking
  - edge stitching, 541
  - edges for joining outlines, 537
  - hourglass, 535
  - loop, 537
  - mesh, 542
  - orientation, 542–544
  - sorting, 136–137, 654, 715–716
  - soup, 541, 794, 802, 809
  - star-shaped, 537
  - T-vertex, 541
    - with multiple outlines, 537
- polygon-aligned BSP tree, *see* spatial data structure, BSP tree
- polygon/cube intersection, *see* intersection testing
- polygon/ray intersection, *see* intersection testing
- polygonal techniques, 531–574
  - consolidation, 531, 541–547
  - merging, 541–542
  - simplification, *see* simplification
  - smoothing, 545–547
  - tessellation, 531, 534–541, 681
  - triangulation, 531, 534–537, 538
- polygonalization, 533
- polypostor, 461
- polytope, 765n
- POM, 193
- Pomegranate, *see* hardware
- popping, *see* level of detail
- port, 850
- portal culling, *see* culling
- positively oriented, *see* handedness, right-handed basis
- post processing, 467
- post T&L vertex cache, *see* cache
- potentially visible set, 373, 661
- Poulin-Fournier model, *see* BRDF
- PowerStrip*, 701
- PowerVR, *see* hardware
- pre T&L vertex cache, *see* cache
- pre-order traversal, 665
- precision, 713
  - color, 167, 831
  - depth, 350
  - floating point, 707
  - half, 481, 713
  - subpixel, 541
- precomputed lighting, 417–425
- precomputed radiance transfer, 407, 430–437
- prefetch, 842
  - texture, 173, 847–849, 853
- prelighting, 417, 537
- preshaded, 537
- printer gamut, 216
- probability
  - geometric, 735–737
- procedural modeling, 199, 526, 532
- procedural texturing, *see* texturing
- processor
  - stream, 841
- product relations, *see* trigonometry
- programmable culling, *see* culling, programmable
- progressive refinement, 411, 441n
- progressive scan, 831
- projected area, 409
- projection, 18–19, 89–97
  - 3D polygon to 2D, 751
  - 3D triangle to 2D, 746
  - bounding volume, 688–691
  - cylindrical, 152
  - orthogonal vector, 895
  - orthographic, 18–19, 55, 89–92
  - parallel, *see* projection, orthographic
  - perspective, 18, 19, 55, 92–97, 833
  - planar, 152
  - spherical, 152

- projective texturing, *see* texturing  
projector function, *see* texturing  
proxy object, 648  
PRT, *see* precomputed radiance transfer  
PSM, *see* shadow, map, perspective  
purple fringing, 396  
PVS, *see* potentially visible set  
Pythagorean relation, *see* trigonometry
- quadratic curve, *see* curves  
quadratic equation, 739, 786  
quadtree, *see* spatial data structure, 654  
*Quake*, 695  
*Quake II*, 418  
*Quake III*, 33, 424  
quartic curve, *see* curves  
quaternion, 67, 72–80  
    addition, 73  
    conjugate, 73, 74  
    definition, 72  
    dual, 85  
    identity, 73  
    imaginary units, 72  
    inverse, 73  
    laws of multiplication, 74  
    logarithm, 74  
    matrix conversion, 76–77  
    multiplication, 73  
    norm, 73, 74  
    power, 74  
    slerp, 77–79  
    spherical linear interpolation, 77–78  
    spline interpolation, 78–79  
    transforms, 75–80  
    unit, 74, 75
- R11G11B10 float format, 481  
R9G9B9E5 format, 481  
radian, 205  
radiance, 108, 206–208, 212, 311, 316, 409, 411, 442  
radiance distribution, 208  
radiance transfer, 430  
radian  
    energy, 203  
    exitance, *see* exitance  
    flux, 203  
    intensity, *see* intensity  
    power, 203  
radiometry, 101  
radiosity, *see* exitance, 408–412, 537  
    equation, 410  
    normal mapping, 420  
    simplification, 566
- range-based fog, *see* fog  
RAPID, *see* collision detection  
raster operations, 24  
rasterization equation, 852  
rasterizer  
    perspective-correct, 838  
    stage, *see* pipeline  
    unit, 842  
PLAYSTATION® 3, 866  
*Ratatouille*, 406, 879, 880, 884  
rational  
    Bézier curve, *see* curves, Bézier  
    Bézier patch, *see* surfaces, Bézier  
    linear interpolation, *see* interpolation  
ray, 727–728  
    tracing, 26, 301, 412, 412–416, 437, 736, 804, 806, 814, 841, 875, 876, 883, 884  
    Monte Carlo, 413  
    reflection, 391  
ray/object intersection, *see* intersection testing  
reciprocity, 226  
reconstruction, 118, 120–123  
refinement phase, *see* surfaces, subdivision  
reflectance  
    anisotropic, 243  
    body, 229  
    directional-hemispherical, 226  
    equation, 288, 327  
    isotropic, 243  
    lobe, *see* BRDF  
    surface, 229  
    volume, *see* reflectance, body  
reflection, 105, 228, 229, 386–392  
    curved, 391–392  
    environment mapping, 298, 301, 307  
    equation, *see* reflectance, equation  
    external, 232  
    glossy, 389  
    internal, 232, 236  
        total, 237, 395, 398  
    law of, 386  
    map, 309–312  
    mapping, 298  
    occlusion, 430  
    planar, 386–391, 669  
    transform, 59, 387  
reflectometer, 265  
refraction, 105, 135, 396–401  
    glossy, 389  
    image-space, 398  
refractive index, *see* index of refraction

- refresh rate
  - horizontal, 830
  - vertical, 830
- register combiners, 34
- regular
  - setting, 617
  - vertex, 614
- rejection test, *see* intersection testing
- relief texture mapping, *see* texturing
- render target, 38
- rendering
  - equation, 327–328, 414
  - spectrum, 440
  - speed, 13, 14
  - state, 711
- RenderMan*, 33, 35, 199, 275, 283, 875, 880, 884
- RenderMonkey*, 50, 886
- repeat, *see* texturing
- repeated linear interpolation, *see* interpolation
- replace, *see* texturing, blending operations
- resampling, 123–124
- restitution, *see* collision response
- retrace
  - horizontal, 830
  - vertical, 25, 830, 834
- retro-reflection, 245
- reverse mapping, 488
- REYES, 875, 884
- RGB, 156
  - color cube, 213
  - color mode, *see* color, mode, true color
  - to grayscale, 215
- RGBA, 136, 139, 832
  - texture, 156
- RGBE format, 481
- RGSS, 128
- right triangle laws, *see* trigonometry
- right-handed, *see* coordinate system
  - basis, *see* handedness
- rigid-body
  - transform, *see* transform
- riplmap, *see* texturing, minification
- ROAM, 569
- roll, 66, 68
- ROP, 24
- roping, 144
- rotation, *see* transform
- RSX®, *see* hardware,
- PLAYSTATION® 3
- S3 texture compression, *see* texturing, compression
- S3TC, *see* texturing, compression
- sampling, 117–125, 128, *see also* antialiasing
  - bandlimited signal, 119–120
  - centroid, 128
  - continuous signal, 118
  - discretized signal, 118
  - Nyquist limit, 119, 163, 166
  - pattern, 128, 146
  - stochastic, 131
  - stratified, 131
  - theorem, 119
- Sarrus’s scheme
  - cross product, 897
  - determinant, 900
- SAT, *see* intersection testing, separating axis test
- saturation, 214
- SBRDF, *see* SVBRDF
- scalable link interface, 835
- scalar product, *see* dot product
- scaling, *see* transform
- scan conversion, 21, 22
- scanline, 830
  - interleave, 835
- scanner gamut, 216
- scatter operation, 487
- scattering, 104
  - multiple, 403
  - single, 403
- scattering albedo, 239–241
- scene graph, *see* spatial data structure
- screen
  - coordinates, 20
  - mapping, 20
  - space, 842
  - space coverage, 637, 688
- SDRAM, 852
- Sea of Images, 444
- second-order equation, 739
- sectioning, 19
- self-shadowing, *see* aliasing
- semi-regular setting, 617
- sensor, *see* imaging sensor
- separating axis test, *see* intersection testing
- separating hyperplane theorem, 731
- SGI algorithm, *see* triangle strip
- Sh, 35, 51
- shade tree, 33

- shader
    - unified, *see* unified shader architecture
  - Shader Model, 35
  - shading, 17, 110–116
    - deferred, 279–283, 373, 442, 846, 875
    - equation, 17, 149
    - flat, 113, 115
    - Gouraud, 115
    - hard, 508
    - language, 31
    - mode, 113
    - Phong, 115
    - pixel, 22, *see also* pixel shader problems, 537–539
    - texture palette, 523–525
    - toon, 508–510
    - vertex, 17–18, *see* vertex shader
  - shadow, 331–373
    - anti-shadow, 336
    - buffer, 349
    - depth map, 349
    - field, 430
    - hard, 331
    - map, 339, 348, 348–372
      - adaptive, 358
      - bias, 350–353
      - cascaded, 358–361
      - convolution, 370
      - deep, 370, 407
      - hierarchical, 372
      - light space perspective, 356
      - minmax, 372
      - omnidirectional, 361
      - opacity, 371
      - parallel split, 359
      - penumbra, 371
      - perspective, 355
      - second depth, 352
      - silhouette, 357
      - trapezoidal, 356
      - variance, 367–370
    - on curved surfaces, 339–340
    - optimization, 372–373
    - penumbra, 331, 337
    - planar, 333–339
      - soft, 336–339
    - projection, 333–336
    - soft, 331–333, 336–340, 348, 361–372, 412
    - texture, 339
    - umbra, 331, 339
    - volume, 340–348
  - shaft, 778
  - shaft occlusion culling, *see* culling
  - shape blending, *see* transform, morph targets
  - shared memory multiprocessor, *see* multiprocessing
  - shear, *see* transform
  - shell, 504
  - shell mapping, 198, 516
  - shortest arc, 78
  - shower door effect, 523
  - Shrek*, 879
  - Shrek 2*, 422
  - silhouette, 338, 510–522, 626, 638
    - backface rendered, 513–517
    - bias rendered, 513
  - detection
    - hardware, 347
  - edge detection, 520–522
  - environment mapped, 512
  - fattening, 514–515
  - halo, 516
  - hybrid, 522
  - image, 517–520
  - loop, 520, 522
  - procedural geometry, 513–517
  - shadow volume, 347
  - shell, 515–517
- SIMD, 31, 37
  - simplex, 819
  - simplification, 532, 561–573, 681, 713
    - cost function, 563–566
    - edge collapse, 562–564
    - level of detail, 567
    - optimal placement, 563
    - reversibility, 562
  - sin, *see* trigonometry
  - single buffer, *see* buffer
  - skeleton-subspace deformation, *see* transform, vertex blending
  - skinning, *see* transform, vertex blending
  - skybox, 443–444, 452
  - slab, 730, 742n, 766
  - slabs method, *see* intersection testing
  - slerp, *see* quaternion
  - SLI, 835
  - small batch problem, 551, 560, 708
  - smoothies, 371
  - smoothing, *see* polygonal techniques
  - smoothing phase, *see* surfaces, subdivision
  - SMOOTHVISION, 131
  - SMP, 717
  - Snell's Law, 231, 237
  - Sobel edge detection, 518
  - software pipelining, *see* multiprocessing

- SOLID, *see* collision detection, SOLID  
 solid, 544
  - angle, 205, 690
  - volume of, 544*Sorbetto*, 442  
 sort, 652
  - bubble sort, 813
  - insertion sort, 813
  - space, 842*Sort-Everywhere*, 846  
 sort-first, 843, 843
  - PLAYSTATION® 3, 866*sort-last*, 843  
*sort-last fragment*, 845
  - PLAYSTATION® 3, 866*sort-last image*, 846
  - PixelFlow, 846*sort-middle*, 843, 844, 871, 875
  - Mali, 844
  - south bridge, 860, 864
  - space subdivision, 647
  - space-filling curve, 556, 849
  - span, 892
  - spatial data structure, 647–660
    - aspect graph, 661
    - bounding volume hierarchy, 647, 647–650, 725, 762
    - BSP tree, 647, 650–654, 666, 796
      - axis-aligned, 650–652
      - collision detection, 796
      - dynamically adjusted, 797–802
      - polygon-aligned, 652–654
    - cache-aware, 657–658
    - cache-oblivious, 657–658
    - collision testing, 805–806
    - hierarchical, 647
    - hierarchy building, 802–804
    - irregular, 647
    - k-d tree*, 651, 876
    - loose octree, 656
    - octree, 647, 654–656, 666, 677, 822
    - quadtree, 654
      - restricted, 571, 639
    - regular, 647
    - scene graph, 658–660, 660, 670, 688
      - LOD, 688
    - triangle binary tree, 569–570
  - spatial relationship, 328
  - spatialization, 660*SPE*, *see* Cell Broadband Engine™, SPE  
 spectrum, 210, 211, 212, 214–215
  - visible, 202*specular*
  - highlight, *see* highlight
- light map, *see* texturing  
 lobe, *see* BRDF  
 term, 105  
*SpecVar maps*, 275  
*SpeedTree*, 455  
 sphere, 533, 807
  - formula, 728, 729, 738*sphere mapping*, *see* environment mapping  
*sphere/box intersection*, *see* intersection testing  
*sphere/frustum intersection*, *see* intersection testing  
*sphere/plane intersection*, *see* intersection testing, dynamic  
*sphere/ray intersection*, *see* intersection testing  
*sphere/sphere intersection*, *see* intersection testing, dynamic, *see* intersection testing  
*spherical*
  - coordinates, 300, 728
  - harmonics, 266, 317–323, 381, 424, 430, 894
  - gradients, 323, 424
  - linear interpolation, *see* quaternion*splat*, 399, 461, 502, 694–695  
*spline*
  - curves, *see* curves
  - surfaces, *see* surfaces*sprite*, 39n, 445–446, *see also* impostor
  - layered, 445
  - point, 456*SPU*, *see* Cell Broadband Engine™, SPU  
*SRGB*, 143–145, 235, 236  
*SSE*, 706, 763–765  
*stage*
  - blocking, 720
  - starving, 720*star-shaped polygon*, *see* polygon  
*starving*, *see* stage starving  
*state*
  - changes, 711, 718
  - sorting, 718*static buffer*, *see* buffer, static  
*static intersection testing*, *see* intersection testing  
*stationary subdivision*, *see* surfaces, subdivision  
*stencil*, 614
  - buffer, *see* buffer*steradian*, 205  
*stereo*
  - buffer, *see* buffer

- rendering, 836–837  
vision, 836
- stereolithography, 533, 545
- stereophotogrammetry, 532
- stereopsis, 836
- stitching, *see* polygon, edge stitching
- stochastic sampling, 131
- stream output, 42, 456, 560
- stride, 558
- strip, *see* triangle strip
- stroke, 525–526
- stylistic rendering, *see* non-photorealistic rendering
- subdeterminant, *see* matrix
- subdivision
- curves, *see* curves
  - surfaces, *see* surfaces
- subpixel addressing, 541
- subsurface scattering, 225
  - global, 401–407
  - local, 238–241
- subtexture, *see* texturing
- sum object, 818
- summed-area table, *see* texturing, minification
- superscalar, 15
- supershader, 277
- supporting plane, 751n
- surface
- acne, 350, 356, 366
  - area
    - heuristic, 736
  - light fields, 444
- surfaces
- B-spline, 624
  - Bézier patch, 592–597
    - Bernstein, 594
    - de Casteljau, 594
    - degree, 594
    - derivatives, 595
    - rational, 597
  - Bézier triangle, 597–599, 600
    - Bernstein, 598
    - de Casteljau, 598
    - degree, 597
    - derivatives, 598
  - biquadratic, 594
  - continuity, 604–606
  - explicit, 728–729
    - sphere, 728, 729
    - triangle, 729, 747
  - implicit, 606–608, 728
    - blending, 606
- derivatives, 606
- sphere, 738
- N-patch, 592, 599–603
  - shadows, 348
- NURBS, 643
- parametric, 151, 592–603
- spline, 539, 616
- subdivision, 611–629
  - $\sqrt{3}$ , 621–622
  - approximating, 613
  - Catmull-Clark, 623–624
  - color interpolation, 629
  - displaced, 626–628
  - interpolating, 617
  - limit position, 615
  - limit surface, 615
  - limit tangents, 615
  - Loop, 613–616, 617, 620–622, 624, 626–628, 643
  - mask, 614
  - modified butterfly, 613, 616, 616–620, 621, 622, 628
  - normal interpolation, 628–629
  - piecewise smooth, 624–626
  - polygon-based, 612
  - refinement phase, 612
  - smoothing phase, 612
  - stationary, 612
  - stencil, 614
  - texture interpolation, 629
  - triangle-based, 612
  - uniform, 612
  - tensor product, 592- tessellation, *see* tessellation
- surfel, 694
- surround effect, 142
- SVBRDF, 226
- swap
  - buffer, 25, 834, 835
  - strip, *see* triangle strip
- sweep-and-prune, *see* collision detection
- swizzling, 31, *see* texturing
- synchronization
  - monitor, 702, 830, 835, 837
- T221 display, 645
- TAM, *see* tonal art map
- tan, *see* trigonometry
- tangent
  - patch, 640
  - space, *see* basis
  - vector, 185, 589
- taxonomy
- parallel architectures, 843

- Taylor series, *see* trigonometry  
*Team Fortress 2*, 160, 161  
 tearing, 834  
 technical illustration, 507, 508, 527, 530  
 television  
     color space, 217  
 temporal  
     aliasing, *see* aliasing, temporal  
     coherence, 522, *see* coherence,  
         frame-to-frame  
     delay, 1  
 temporary register, 32  
 tension parameter, *see* curves  
 tensor product surfaces, *see* surfaces  
 tessellation, 629–641, *see also* polygonal  
     techniques, tessellation  
     adaptive, 633–639  
     evaluation shader, 633–634  
     fractional, 631–633, 687  
     surface, 592  
     uniform, 629  
 texel, 149  
 Texram, 169  
 text, 159, 585  
 texture  
     coordinates, 47  
     cube map, 171  
     dependent read, 34, 35, 196, 299  
     displacement, 198  
     lapped, 524  
     lookup, 508  
     matrix, 154n, 304, 308  
     palette, *see* shading  
     periodicity, 155  
     space, 149  
     volume, 170–171  
     volumetric, 504  
 textured depth mesh, 467  
 texturing, 22, 147–199  
     alpha mapping, 156, 181–183, 447,  
         482  
     animation, 180, 183, 418  
     antialiasing, *see* antialiasing  
     bandwidth, *see* bandwidth  
     border, 155  
     bump mapping, *see* bump mapping  
     cache, *see* cache  
     cellular, 179  
     clamp, 155  
     clipmap, 173  
     compression, 174–178, 853  
         Ericsson, 873  
         lossy, 175  
         normal, 176–177  
     corresponder function, 149, 154–156  
     decaling, 181  
     detail, 159  
     diffuse color map, 181  
     distortion, 538–539  
     environment mapping, *see*  
         environment mapping  
     filtering, *see* texturing, sampling and  
         filtering  
     gloss map, 181  
     image, 156–178  
     image size, 157  
     level of detail bias, 166  
     light mapping, 339, 411, 417–419  
         dot3, 421  
     magnification, 157, 157–161  
         bilinear interpolation, 158  
         cubic convolution, 158  
         nearest neighbor, 158  
     minification, 157, 161–170  
         anisotropic filtering, 168–169  
         bilinear interpolation, 161  
         Elliptical Weighted Average, 170  
         level of detail, 165  
         mipmapping, 163–166  
         nearest neighbor, 161  
         quadrilinear interpolation, 170  
         riplmap, 166, 168  
         summed-area table, 167–168  
         trilinear interpolation, 166  
     mirror, 155  
     noise, 178, 444  
     one-dimensional, 154  
     pipeline, 148–156  
     prefetch, *see* prefetch  
     procedural, 178–180  
     projective, 222, 539  
     projector function, 149–154  
     relief, 193–198, 199, 280, 398, 450,  
         464–465, 504, 681, 682  
     repeat, 154  
     specular color map, 181  
     subtexture, 163  
     swizzling, 848–849  
     tiling, 712  
     value transform function, 149  
     vector, 159  
     wrap, 154  
     three plane intersection, *see* intersection  
         testing  
     throughput, 14, 697, 719  
     tile, 871  
         screen, 844, 854  
     texture, *see* texturing

- tile table, 854  
tiled memory, *see* memory  
tiled rasterization, *see* rasterizer  
tiling, *see* texturing  
time-critical rendering, 691  
timestamping, 651  
timing, 14, 737  
TIN, 568  
tolerance verification, 818  
tonal art maps, 524  
tone mapping, 475–481  
tone reproduction, 475  
toon rendering, *see* shading  
top-down, *see* collision detection  
Torrance-Sparrow model, *see* BRDF  
*Toy Story*, 880  
trace of matrix, *see* matrix  
transfer function, 141, 430  
    display, 142  
    encoding, 142  
    end-to-end, 142  
transform, 53, 905, *see also* matrix  
    affine, 54, 64, 906  
    angle preserving, 62  
    bounded, *see* transform, limited  
    concatenation of, 61–62  
    constraining a, 69  
    decomposition, 69–70  
    Euler, 65–69  
        extracting parameters, 68–69  
        gimbal lock, 67  
    inverse, 56–60, 62, 63, 65, 66, 71,  
        902–903, 905  
    adjoint method, 65  
    Cramer’s rule, 65, 748, 902–903  
    Gaussian elimination, 65, 903  
    LU decomposition, 65  
length preserving, 62  
linear, 53  
mirror, *see* transform, reflection  
model, 16–17  
morph targets, 85–89  
morphing, 85–89  
normal, 63–64  
orthographic, *see* projection  
perspective, *see* projection  
quaternion, 76  
reflection, 59, 663  
rigid-body, 56, 62–63, 70, 80  
    collision detection, 810  
rotation, 56–58  
    about an arbitrary axis, 70–71  
    from one vector to another, 79–80  
rotation around a point, 57  
scaling, 58–59  
    anisotropic, *see* transform,  
        scaling, nonuniform  
    isotropic, *see* transform, scaling,  
        uniform  
    nonuniform, 58  
        uniform, 58  
shear, 60–61  
translation, 56  
vertex blending, 80–85, 87, 97, 850  
    enveloping, 81  
    skeleton-subspace deformation, 81  
    skinning, 81  
view, 16–17  
volume preserving, 61  
translation, *see* transform  
transmission, 105  
transparency, 135–141, 389, 718  
    screen-door, 135, 685  
    sorting, 136, 652  
transparency adaptive antialiasing, 183  
tree  
    balanced, 648, 804, 810  
    binary, 649, 803  
    full, 649  
    k-ary tree, 648, 803  
trees  
    rendering, 181–182, 454–456,  
        461–462  
triangle  
    area, 910  
    degree, 552  
    fan, 537, 548–549  
    formula, 729, 747  
    mesh, 542, 554–557  
        cache-oblivious, 556–557  
        universal, 556–557  
setup, 22, 840  
strip, 549–551  
    creating, 552–554  
    generalized, 550  
    sequential, 550  
    swap, 550  
traversal, 22, 862  
triangle/triangle intersection, *see*  
    intersection testing  
triangulated irregular network, 568  
triangulation, *see* polygonal techniques  
trigonometry, 913–919  
    angle difference relations, 918  
    angle sum relations, 918  
arccos, 914–915  
arcsin, 914–915  
arctan, 914–915

cos, 913  
 derivatives of functions, 915  
 double angle relations, 917  
 formulae, 915–919  
 function sums & differences, 919  
 functions, 913–915  
 half-angle relations, 919  
 inverses of functions, 914  
 law of cosines, 916  
 law of sines, 916  
 law of tangents, 916  
 MacLaurin series, 914  
 Mollweide's formula, 917  
 multiple angle relations, 917  
 Newton's formula, 917  
 product relations, 918  
 Pythagorean relation, 916  
 right triangle laws, 915  
 sin, 913  
 tan, 913  
 Taylor series, 913  
 trigonometric identity, 917  
 twilight, 325  
 trilinear interpolation, *see* interpolation  
 triple buffer, *see* buffer  
 tristimulus values, 213  
 true color mode, *see* color  
 TSM, *see* shadow, map, trapezoidal  
 T-vertex, *see* polygon  
 two-and-a-half-dimensions, *see*  $2\frac{1}{2}$ D  
  
 uberlight, 223  
 ubershader, 277, 278, 281  
 UMA, *see* unified memory architecture  
 umbra, *see* shadow  
 under operator, 137  
 underclock, 701  
 unified memory architecture, 849, 849,  
     859  
 unified shader architecture, 31n, 700, 846,  
     860, 860  
 uniform tessellation, *see* tessellation  
 unsharp mask, 385  
 upsampling, 123  
  
 valence, 614  
*Valgrind*, 705  
 van Emde Boas layout, 657  
 vector, 889–890  
     addition, 890, 893  
     geometrical, 893, 905, 906  
     irradiance, 290, 421  
     length, 893  
  
 norm, 891–893  
     notation, 7  
 normalize, 894  
 product, *see* cross product  
 scalar multiplication, 890, 893  
 zero, 890–891  
 velocity buffer, 492–496  
 vertex  
     array, *see* vertex, buffer, *see* vertex,  
         buffer  
     buffer, 550, 557–561, 707  
     cache, *see* cache  
     correspondence, 85  
     processor, *see* vertex, shader  
     shader, 29, 38–40  
         animation, 40  
         data compression, 713  
         effects, 39  
         particle systems, 456  
         PLAYSTATION® 3, 864–866  
         shadows, 347  
         skinning, 83–85  
         vertex blending, 83–85  
     stream, 558  
     texture, 40, 165, 198, 198n  
 vertical  
     refresh rate, *see* refresh rate  
     retrace, *see* retrace  
     sync, *see* synchronization, monitor  
 vertices per second, 702  
 video  
     color space, 217  
     controller, 830  
     memory, 830, 849  
 view  
     frustum culling, *see* culling  
     ray, 110  
     transform, *see* transform  
     vector, 109  
 view-independent progressive meshing,  
     562  
 VIPM, 562  
 visibility test, 672  
 Vista, 30  
 visual appearance, 99  
 visual phenomena, 99–100  
 volume  
     calculation  
         parallelepiped-box, 911  
     rendering, 502–505  
     solid, *see* solid  
 volumetric shadows, *see* shadow  
 voxel, 502, 760

- VSM, *see* shadow, map, variance  
*VTune*, 700, 705
- Wang tiles, 155
- Ward model, *see* BRDF
- watercolor, 508
- watertight model, 545
- watt, 203
- wavelets, 179, 266, 894
- W*-buffer, *see* buffer
- welding vertices, 542
- wheel of reincarnation, 883
- white point, 214
- Wii, *see* hardware
- winding number, 753
- window coordinates, 20
- wireframe, 528, 529
- Woo's method, *see* intersection testing
- world space, 16, 17, 833
- wrap, *see* texturing, repeat
- wrap lighting, 294, 403
- Xbox, *see* hardware
- Xbox 360, 35, *see* hardware
- yaw, 66n
- YIQ, 217
- yon, 90n
- YUV, 217, 474
- Z*-buffer, *see* buffer
- Z*-compression, 854–856
- z*-fighting, 833n
- Z*-max culling, *see* culling
- Z*-min culling, *see* culling
- zonal harmonics, 321
- z*-partitioning, 359
- Z*-pyramid, 677

# Real-Time Rendering

Third Edition

Tomas Akenine-Möller  
Eric Haines  
Naty Hoffman

Thoroughly revised, this third edition focuses on modern techniques used to generate synthetic three-dimensional images in a fraction of a second. With the advent of programmable shaders, a wide variety of new algorithms have arisen and evolved over the past few years. This edition discusses current, practical rendering methods used in games and other applications. It also presents a solid theoretical framework and relevant mathematics for the field of interactive computer graphics, all in an approachable style.

New chapters provide broad coverage of the field, such as:

- The Graphics Processing Unit
- Image-Based Effects
- Curves and Curved Surfaces
- Area and Environmental Lighting
- Acceleration Algorithms

With topics including:

- Ambient Occlusion
- Displacement Mapping
- Deferred Shading
- High Dynamic Range Imaging and Lighting
- Global Subsurface Scattering
- PlayStation 3 and Xbox 360 Console Case Studies

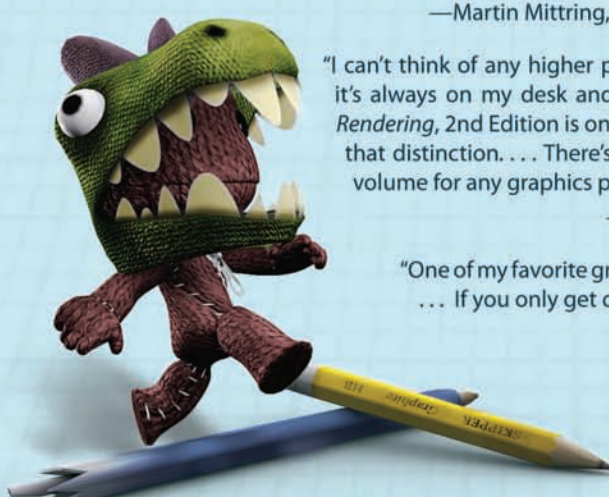
## Praise for *Real-Time Rendering*

"*Real-Time Rendering* has been a required reference for professional graphics practitioners for nearly a decade. This latest edition is as relevant as ever, covering topics from essential mathematical foundations to advanced techniques used by today's cutting edge games."

—Gabe Newell, President, Valve

"*Real-Time Rendering* provides a solid introduction to the essential techniques every graphics programmer should know. It also serves as a great reference for finding relevant publications and is a joy to read."

—Martin Mittring, Lead graphics programmer, Crytek



"I can't think of any higher praise for a book than the fact that it's always on my desk and within easy reach, and *Real-Time Rendering*, 2nd Edition is one of the few books that qualifies for that distinction. . . . There's no doubt that this is a must-have volume for any graphics programmer."

—Herb Marselas, Ensemble Studios

"One of my favorite graphics books is *Real-Time Rendering*. . . . If you only get one graphics book, get this one."

—Ron Fosner, author of *Real-Time Shader Programming*



A K Peters, Ltd.

Sackboys and Sackgirls  
from  


Cover Design by Daniel Wittenberg

ISBN 978-1-56881-424-7



9 781568 814247